
GEOTECHNICAL EARTHQUAKE ENGINEERING



STEVEN L. KRAMER

Geotechnical Earthquake Engineering

PRENTICE-HALL INTERNATIONAL SERIES
IN CIVIL ENGINEERING AND ENGINEERING MECHANICS
William J. Hall, Editor

Au and Christiano, *Fundamentals of Structural Analysis*
Au and Christiano, *Structural Analysis*
Barson and Rolfe, *Fracture and Fatigue Control in Structures, 2/e*
Bathe, *Finite Element Procedures in Engineering Analysis*
Berg, *Elements of Structural Dynamics*
Biggs, *Introduction to Structural Engineering*
Chajes, *Structural Analysis, 2/e*
Chopra, *Dynamics of Structures: Theory and Applications to Earthquake Engineering*
Collins and Mitchell, *Prestressed Concrete Structures*
Cooper and Chen, *Designing Steel Structures*
Cording et al., *The Art and Science of Geotechnical Engineering*
Gallagher, *Finite Element Analysis*
Hendrickson and Au, *Project Management for Construction*
Higdon et al., *Engineering Mechanics, 2nd Vector Edition*
Hultz and Kovacs, *Introduction in Geotechnical Engineering*
Humar, *Dynamics of Structures*
Johnston, Lin, and Galambos, *Basic Steel Design, 3/e*
Kelkar and Sewell, *Fundamentals of the Analysis and Design of Shell Structures*
Kramer, *Geotechnical Earthquake Engineering*
MacGregor, *Reinforced Concrete: Mechanics and Design, 2/e*
Mehta and Monteiro, *Concrete: Structure, Properties and Materials, 2/e*
Melosh, *Structural Engineering Analysis by Finite Elements*
Meredith et al., *Design and Planning of Engineering Systems, 2/e*
Mindess and Young, *Concrete*
Nawy, *Prestressed Concrete*
Nawy, *Reinforced Concrete: A Fundamental Approach, 2/e*
Pfeffer, *Solid Waste Management*
Popov, *Engineering Mechanics of Solids*
Popov, *Introduction to the Mechanics of Solids*
Popov, *Mechanics of Materials, 2/e*
Schneider and Dickey, *Reinforced Masonry Design, 2/e*
Wang and Salmon, *Introductory Structural Analysis*
Weaver and Johnson, *Structural Dynamics by Finite Elements*
Wolf, *Dynamic Soil-Structure Interaction*
Wray, *Measuring Engineering Properties of Soils*
Yang, *Finite Element Structural Analysis*

Geotechnical Earthquake Engineering

Steven L. Kramer
University of Washington

Prentice-Hall International Series
in Civil Engineering and Engineering Mechanics



Prentice Hall
Upper Saddle River, New Jersey 07458

Library of Congress Cataloging-in-Publication Data

Kramer, Steven Lawrence.
Geotechnical earthquake engineering / Steven L. Kramer.
p. cm. -- (Prentice-Hall civil engineering and engineering
mechanics series)
Includes bibliographical references and index.
ISBN 0-13-374943-6
1. Earthquake engineering. 2. Engineering geology. I. Title.
II. Series.
TA654.6.K72 1996
624.1'762--dc20
CIP

95-33020

Acquisitions editor: **BILL STENQUIST**
Production editor: **IRWIN ZUCKER**
Cover director: **JAYNE CONTE**
Buyer: **JULIA MEEHAN**
Editorial assistant: **MEG WEIST**



©1996 by Prentice-Hall, Inc.
Simon & Schuster / A Viacom Company
Upper Saddle River, NJ 07458

All rights reserved. No part of this book may be
reproduced, in any form or by any means,
without permission in writing from the publisher.

The author and publisher of this book have used their best efforts in preparing this book. These efforts include the development, research, and testing of the theories and programs to determine their effectiveness. The author and publisher make no warranty of any kind, expressed or implied, with regard to these programs or the documentation contained in this book. The author and publisher shall not be liable in any event for incidental or consequential damages in connection with, or arising out of, the furnishing, performance, or use of these programs.

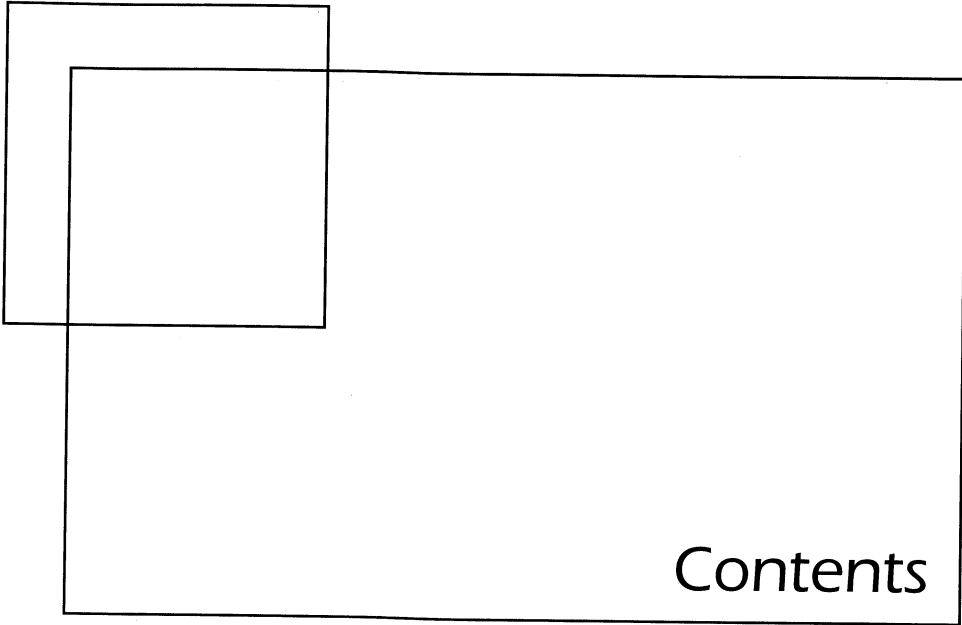
Printed in the United States of America

10 9 8 7 6 5 4 3

ISBN 0-13-374943-6

Prentice-Hall International (UK) Limited, London
Prentice-Hall of Australia Pty. Limited, Sydney
Prentice-Hall Canada Inc., Toronto
Prentice-Hall Hispanoamericana, S.A., Mexico
Prentice-Hall of India Private Limited, New Delhi
Prentice-Hall of Japan, Inc., Tokyo
Simon & Schuster Asia Pte. Ltd., Singapore
Editora Prentice-Hall do Brasil, Ltda., Rio de Janeiro

To my parents



	Preface	xv
1	Introduction to Geotechnical Earthquake Engineering	1
1.1	Introduction	1
1.2	Background	1
1.3	Seismic Hazards	2
	1.3.1 Ground Shaking,	2
	1.3.2 Structural Hazards,	3
	1.3.3 Liquefaction,	5
	1.3.4 Landslides,	9
	1.3.5 Retaining Structure Failures,	11
	1.3.6 Lifeline Hazards,	11
	1.3.7 Tsunami and Seiche Hazards,	13
1.4	Mitigation of Seismic Hazards	14
1.5	Significant Historical Earthquakes	14

2	Seismology and Earthquakes	18
2.1	Introduction	18
2.2	Internal Structure of the Earth	18
	2.2.1 <i>Seismic Waves</i> ,	19
	2.2.2 <i>Internal Structure</i> ,	20
2.3	Continental Drift and Plate Tectonics	23
	2.3.1 <i>Plate Tectonics</i> ,	24
	2.3.2 <i>Plate Boundaries</i> ,	29
2.4	Faults	33
	2.4.1 <i>Fault Geometry</i> ,	33
	2.4.2 <i>Fault Movement</i> ,	34
2.5	Elastic Rebound Theory	36
	2.5.1 <i>Relationship to Earthquake Recurrence</i> ,	39
	2.5.2 <i>Relationship to Tectonic Environment</i> ,	41
	2.5.3 <i>Seismic Moment</i> ,	42
2.6	Other Sources of Seismic Activity	42
2.7	Geometric Notation	43
2.8	Location of Earthquakes	44
2.9	Size of Earthquakes	45
	2.9.1 <i>Earthquake Intensity</i> ,	45
	2.9.2 <i>Earthquake Magnitude</i> ,	46
	2.9.3 <i>Earthquake Energy</i> ,	50
2.10	Summary	51
3	Strong Ground Motion	54
3.1	Introduction	54
3.2	Strong-Motion Measurement	56
	3.2.1 <i>Seismographs</i> ,	56
	3.2.2 <i>Data Acquisition and Digitization</i> ,	59
	3.2.3 <i>Strong-Motion Processing</i> ,	61
	3.2.4 <i>Strong-Motion Instrument Arrays</i> ,	62
	3.2.5 <i>Strong-Motion Records</i> ,	64
3.3	Ground Motion Parameters	65
	3.3.1 <i>Amplitude Parameters</i> ,	66
	3.3.2 <i>Frequency Content Parameters</i> ,	70
	3.3.3 <i>Duration</i> ,	79
	3.3.4 <i>Other Measures of Ground Motion</i> ,	82
	3.3.5 <i>Discussion</i> ,	84

3.4	Estimation of Ground Motion Parameters	84
3.4.1	<i>Magnitude and Distance Effects</i> ,	85
3.4.2	<i>Development of Predictive Relationships</i> ,	86
3.4.3	<i>Estimation of Amplitude Parameters</i> ,	88
3.4.4	<i>Estimation of Frequency Content Parameters</i> ,	91
3.4.5	<i>Estimation of Duration</i> ,	95
3.4.6	<i>Estimation of Other Parameters</i> ,	95
3.5	Spatial Variability of Ground Motions	100
3.6	Summary	102
4	Seismic Hazard Analysis	106
4.1	Introduction	106
4.2	Identification and Evaluation of Earthquake Sources	107
4.2.1	<i>Geologic Evidence</i> ,	107
4.2.2	<i>Tectonic Evidence</i> ,	113
4.2.3	<i>Historical Seismicity</i> ,	113
4.2.4	<i>Instrumental Seismicity</i> ,	114
4.3	Deterministic Seismic Hazard Analysis	114
4.4	Probabilistic Seismic Hazard Analysis	117
4.4.1	<i>Earthquake Source Characterization</i> ,	118
4.4.2	<i>Predictive Relationships</i> ,	126
4.4.3	<i>Temporal Uncertainty</i> ,	127
4.4.4	<i>Probability Computations</i> ,	129
4.5	Summary	138
5	Wave Propagation	143
5.1	Introduction	143
5.2	Waves in Unbounded Media	144
5.2.1	<i>One-Dimensional Wave Propagation</i> ,	144
5.2.2	<i>Three-Dimensional Wave Propagation</i> ,	149
5.3	Waves in a Semi-infinite Body	156
5.3.1	<i>Rayleigh Waves</i> ,	156
5.3.2	<i>Love Waves</i> ,	162
5.3.3	<i>Higher-Mode Surface Waves</i> ,	164
5.3.4	<i>Dispersion of Surface Waves</i> ,	164
5.3.5	<i>Phase and Group Velocities</i> ,	165
5.4	Waves in a Layered Body	165
5.4.1	<i>One-Dimensional Case: Material Boundary in an Infinite Rod</i> ,	165
5.4.2	<i>Three-Dimensional Case: Inclined Waves</i> ,	170
5.5	Attenuation of Stress Waves	174
5.5.1	<i>Material Damping</i> ,	175
5.5.2	<i>Radiation Damping</i> ,	179
5.6	Summary	180

6	Dynamic Soil Properties	184
6.1	Introduction	184
6.2	Representation of Stress Conditions by the Mohr Circle	185
	6.2.1 <i>Principal Stresses</i> ,	187
	6.2.2 <i>Stress Paths</i> ,	188
6.3	Measurement of Dynamic Soil Properties	191
	6.3.1 <i>Field Tests</i> ,	191
	6.3.2 <i>Laboratory Tests</i> ,	215
	6.3.3 <i>Interpretation of Observed Ground Response</i> ,	228
6.4	Stress–Strain Behavior of Cyclically Loaded Soils	228
	6.4.1 <i>Some Basic Aspects of Particulate Matter Behavior</i> ,	228
	6.4.2 <i>Equivalent Linear Model</i> ,	230
	6.4.3 <i>Cyclic Nonlinear Models</i> ,	240
	6.4.4 <i>Discussion</i> ,	244
6.5	Strength of Cyclically Loaded Soils	244
	6.5.1 <i>Definitions of Failure</i> ,	244
	6.5.2 <i>Cyclic Strength</i> ,	245
	6.5.3 <i>Monotonic Strength</i> ,	246
6.6	Summary	248
7	Ground Response Analysis	254
7.1	Introduction	254
7.2	One-Dimensional Ground Response Analysis	255
	7.2.1 <i>Linear Approach</i> ,	256
	7.2.2 <i>Nonlinear Approach</i> ,	275
	7.2.3 <i>Comparison of One-Dimensional Ground Response Analyses</i> ,	279
7.3	Two-Dimensional Ground Response Analysis	280
	7.3.1 <i>Dynamic Finite-Element Analysis</i> ,	281
	7.3.2 <i>Equivalent Linear Approach</i> ,	284
	7.3.3 <i>Nonlinear Approach</i> ,	286
	7.3.4 <i>Other Approaches to Two-Dimensional Ground Response Problems</i> ,	286
	7.3.5 <i>Comparison of Two-Dimensional Ground Response Analyses</i> ,	291
7.4	Three-Dimensional Ground Response Analysis	291
	7.4.1 <i>Equivalent Linear Finite-Element Approach</i> ,	292
	7.4.2 <i>Nonlinear Finite-Element Approach</i> ,	292
	7.4.3 <i>Shear Beam Approach</i> ,	293
	7.4.4 <i>Comparison of Three-Dimensional Ground Response Analyses</i> ,	294
7.5	Soil–Structure Interaction	294
	7.5.1 <i>Illustration of Soil–Structure Interaction Effects</i> ,	295
	7.5.2 <i>Methods of Analysis</i> ,	300
7.6	Summary	303

8	Local Site Effects and Design Ground Motions	308
8.1	Introduction	308
8.2	Effects of Local Site Conditions on Ground Motion	309
	8.2.1 Evidence from Theoretical Ground Response Analyses,	309
	8.2.2 Evidence from Measured Amplification Functions,	310
	8.2.3 Evidence from Measured Surface Motions,	312
	8.2.4 Compilations of Data on Local Site Effects,	317
	8.2.5 Effects of Surface Topography and Basin Geometry,	319
8.3	Design Parameters	323
	8.3.1 Design Earthquakes,	324
	8.3.2 Design Spectra,	325
8.4	Development of Design Parameters	327
	8.4.1 Site-Specific Development,	327
	8.4.2 Code-Based Development,	328
8.5	Development of Ground Motion Time Histories	340
	8.5.1 Modification of Actual Ground Motion Records,	340
	8.5.2 Time-Domain Generation,	341
	8.5.3 Frequency-Domain Generation,	343
	8.5.4 Green's Function Techniques,	343
	8.5.5 Limitations of Artificial Ground Motions,	345
8.6	Summary	345
9	Liquefaction	348
9.1	Introduction	348
9.2	Liquefaction-Related Phenomena	349
	9.2.1 Flow Liquefaction,	349
	9.2.2 Cyclic Mobility,	349
9.3	Evaluation of Liquefaction Hazards	350
9.4	Liquefaction Susceptibility	351
	9.4.1 Historical Criteria,	352
	9.4.2 Geologic Criteria,	353
	9.4.3 Compositional Criteria,	354
	9.4.4 State Criteria,	355
9.5	Initiation of Liquefaction	361
	9.5.1 Flow Liquefaction Surface,	361
	9.5.2 Influence of Excess Pore Pressure,	366
	9.5.3 Evaluation of Initiation of Liquefaction,	368
9.6	Effects of Liquefaction	397
	9.6.1 Alteration of Ground Motion,	398
	9.6.2 Development of Sand Boils,	400
	9.6.3 Settlement,	402
	9.6.4 Instability,	408
9.7	Summary	417

10	<i>Seismic Slope Stability</i>	423
10.1	Introduction	423
10.2	Types of Earthquake-Induced Landslides	424
10.3	Earthquake-Induced Landslide Activity	426
10.4	Evaluation of Slope Stability	429
10.5	Static Slope Stability Analysis	430
	10.5.1 <i>Limit Equilibrium Analysis</i> ,	430
	10.5.2 <i>Stress-Deformation Analyses</i> ,	433
10.6	Seismic Slope Stability Analysis	433
	10.6.1 <i>Analysis of Inertial Instability</i> ,	433
	10.6.2 <i>Analysis of Weakening Instability</i> ,	450
10.7	Summary	462
11	<i>Seismic Design of Retaining Walls</i>	466
11.1	Introduction	466
11.2	Types of Retaining Walls	466
11.3	Types of Retaining Wall Failures	467
11.4	Static Pressures on Retaining Walls	469
	11.4.1 <i>Rankine Theory</i> ,	469
	11.4.2 <i>Coulomb Theory</i> ,	472
	11.4.3 <i>Logarithmic Spiral Method</i> ,	474
	11.4.4 <i>Stress-Deformation Analysis</i> ,	476
11.5	Dynamic Response of Retaining Walls	477
11.6	Seismic Pressures on Retaining Walls	477
	11.6.1 <i>Yielding Walls</i> ,	478
	11.6.2 <i>Nonyielding Walls</i> ,	484
	11.6.3 <i>Effects of Water on Wall Pressures</i> ,	486
	11.6.4 <i>Finite-Element Analysis</i> ,	489
11.7	Seismic Displacements of Retaining Walls	489
	11.7.1 <i>Richards–Elms Method</i> ,	489
	11.7.2 <i>Whitman–Liao Method</i> ,	492
	11.7.3 <i>Finite-Element Analysis</i> ,	493
11.8	Seismic Design Considerations	494
	11.8.1 <i>Gravity Walls</i> ,	494
	11.8.2 <i>Cantilever Walls</i> ,	495
	11.8.3 <i>Braced Walls</i> ,	495
	11.8.4 <i>Reinforced Soil Walls</i> ,	500
11.9	Summary	503

12 Soil Improvement for Remediation of Seismic Hazards 506

- 12.1 Introduction 506
- 12.2 Densification Techniques 507
 - 12.2.1 *Vibro Techniques*, 508
 - 12.2.2 *Dynamic Compaction*, 510
 - 12.2.3 *Blasting*, 512
 - 12.2.4 *Compaction Grouting*, 513
 - 12.2.5 *Areal Extent of Densification*, 514
- 12.3 Reinforcement Techniques 515
 - 12.3.1 *Stone Columns*, 515
 - 12.3.2 *Compaction Piles*, 516
 - 12.3.3 *Drilled Inclusions*, 516
- 12.4 Grouting and Mixing Techniques 517
 - 12.4.1 *Grouting*, 518
 - 12.4.2 *Mixing*, 519
- 12.5 Drainage Techniques 521
- 12.6 Verification of Soil Improvement 522
 - 12.6.1 *Laboratory Testing Techniques*, 522
 - 12.6.2 *In Situ Testing Techniques*, 523
 - 12.6.3 *Geophysical Testing Techniques*, 523
- 12.7 Other Considerations 524
- 12.8 Summary 524

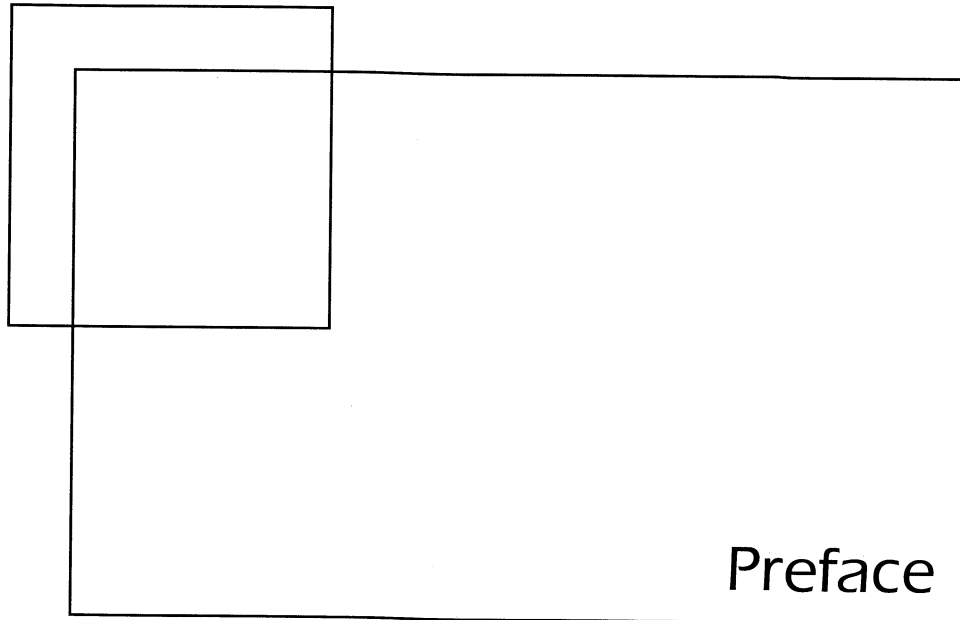
A Vibratory Motion 527

- A.1 Introduction 527
- A.2 Types of Vibratory Motion 527
 - A.2.1 *Simple Harmonic Motion*, 528
 - A.2.2 *Trigonometric Notation for Simple Harmonic Motion*, 529
 - A.2.3 *Other Measures of Motion*, 533
- A.3 Fourier Series 536
 - A.3.1 *Trigonometric Form*, 536
 - A.3.2 *Exponential Form*, 539
 - A.3.3 *Discrete Fourier Transform*, 541
 - A.3.4 *Fast Fourier Transform*, 541
 - A.3.5 *Power Spectrum*, 542

B Dynamics of Discrete Systems 543

- B.1 Introduction 543
- B.2 Vibrating Systems 544
- B.3 Single-Degree-of-Freedom Systems 544

B.4	Equation of Motion for SDOF System	545
	<i>B.4.1 Equation of Motion: External Loading,</i>	<i>545</i>
	<i>B.4.2 Equation of Motion: Vibration of Supports (Base Shaking),</i>	<i>547</i>
B.5	Response of Linear SDOF Systems	547
	<i>B.5.1 Undamped Free Vibrations,</i>	<i>548</i>
	<i>B.5.2 Damped Free Vibrations,</i>	<i>551</i>
	<i>B.5.3 Response of SDOF Systems to Harmonic Loading,</i>	<i>553</i>
	<i>B.5.4 Response of SDOF Systems to Periodic Loading,</i>	<i>561</i>
	<i>B.5.5 Response of SDOF Systems to General Loading,</i>	<i>564</i>
B.6	Damping	567
	<i>B.6.1 Viscous Damping,</i>	<i>567</i>
	<i>B.6.2 Other Measures of Energy Dissipation,</i>	<i>569</i>
	<i>B.6.3 Complex Stiffness,</i>	<i>570</i>
B.7	Response Spectra	571
B.8	Response of Nonlinear SDOF Systems to General Loading	572
	<i>B.8.1 Incremental Equation of Motion,</i>	<i>572</i>
	<i>B.8.2 Numerical Integration,</i>	<i>574</i>
B.9	Multiple-Degree-of-Freedom Systems	575
	<i>B.9.1 Equations of Motion,</i>	<i>575</i>
	<i>B.9.2 Undamped Free Vibrations,</i>	<i>577</i>
	<i>B.9.3 Mode Superposition Method,</i>	<i>579</i>
	<i>B.9.4 Response Spectrum Analysis,</i>	<i>581</i>
	<i>B.9.5 Discussion,</i>	<i>582</i>
C	Probability Concepts	583
C.1	Introduction	583
C.2	Sample Spaces and Events	583
C.3	Axioms of Probability	584
C.4	Probabilities of Events	585
C.5	Random Variables	588
C.6	Expected Values and Standard Deviations	589
C.7	Common Probability Distributions	590
	<i>C.7.1 Uniform Distribution,</i>	<i>590</i>
	<i>C.7.2 Normal Distribution,</i>	<i>591</i>
	<i>C.7.3 Lognormal Distribution,</i>	<i>594</i>
	References	596
	Index	643



Compared to most disciplines of civil engineering, geotechnical earthquake engineering is quite young. While the damaging effects of earthquakes have been known for centuries, the strong contribution of soils to the magnitude and pattern of earthquake damage was not widely appreciated until relatively recently. Following damaging earthquakes in 1964 in Niigata, Japan and Alaska, and spurred by the growth of the nuclear power industry in the 1960s and 1970s, the field of geotechnical earthquake engineering has grown rapidly. Although much remains to be learned, the field has matured to the point where generally accepted theories and analytical procedures now exist for many important problems.

The purpose of this book is to introduce the reader to the concepts, theories, and procedures of geotechnical earthquake engineering. It is intended for use as a text in graduate courses on geotechnical earthquake engineering and as a reference book for practicing engineers. Recognizing that geotechnical earthquake engineering is a broad, multidisciplinary field, the book draws from seismology, geology, structural engineering, risk analysis, and other technical disciplines.

The book is written at a level suitable for students with knowledge equivalent to that of a senior (fourth-year) civil engineering student. The student should have had basic courses in soil mechanics, structural engineering, and hydraulics; introductory courses in geology and probability/statistics would also be helpful. Many graduate students will have

had courses in structural dynamics or soil dynamics by the time they begin study of geotechnical earthquake engineering. For those readers without prior exposure, introductions to the nomenclature and mathematics of dynamic systems, structural dynamics, and probability are presented in three appendices.

ORGANIZATION

The subject matter falls into two main categories. The appendices and the first six chapters present fundamental principles of seismology, ground motion, dynamics, and soil behavior. Applications of these principles to the practical problems most commonly encountered in geotechnical earthquake engineering practice are presented in the last six chapters.

Chapter 1 introduces the reader to the types of damage that can occur during earthquakes and to the problems they present to geotechnical earthquake engineers. Basic concepts of earthquake seismology and the terminology used to describe earthquakes and their effects are described in Chapter 2. Chapter 3 describes ground motion measurement, the parameters used to characterize strong ground motion, and methods for prediction of those parameters. Deterministic and probabilistic seismic hazard analyses are presented in Chapter 4. Chapter 5 introduces the reader to wave propagation, beginning with simple one-dimensional body waves in homogeneous materials and extending to surface waves and multidimensional, layered systems. The properties of soil that control their wave propagation behavior are described in Chapter 6. Field and laboratory techniques for measurement of these properties are also described.

Chapter 7 presents methods for analysis of ground response during earthquakes, beginning with one-dimensional ground response analysis and moving through two- and three-dimensional dynamic response analyses. Both frequency- and time-domain approaches are described. Chapter 7 concludes with an introduction to the basic concepts and effects of soil-structure interaction. The effects of local soil conditions on ground motions and earthquake damage are described in Chapter 8. Chapter 8 also introduces the concept of design ground motions, and how they are obtained from site-specific analyses and from building codes. Chapter 9 deals with liquefaction—it begins with a conceptual framework for understanding various liquefaction-related phenomena and then presents practical procedures for evaluation of liquefaction hazards. Seismic stability of slopes is covered in Chapter 10, and seismic design of retaining structures in Chapter 11. Chapters 10 and 11 address their respective topics initially from pseudo-static and then from permanent displacement standpoints. Chapter 12 introduces commonly used soil improvement techniques for mitigation of seismic hazards.

PEDAGOGY

This book is the first to deal explicitly with the topic of geotechnical earthquake engineering. During its preparation, a great deal of time and effort was devoted to decisions regarding content and organization. The final form naturally reflects my own preference, but the text has been reviewed by many engineers from both academia and professional practice. Preparation of the text also involved a great deal of interpretation of information from a

wide variety of sources. While the text reflects my own interpretation of this information, it is heavily referenced to allow readers to explore background or more detailed information on various geotechnical earthquake engineering topics.

A couple features are noteworthy. Two ground motions from the Loma Prieta earthquake, one from a rock outcrop and one from the surface of a nearby deep soil deposit, are used to illustrate a number of concepts throughout the book. Differences in the amplitudes, frequency contents, and durations of the motions are emphasized in Chapter 3. The reasons for these differences later become apparent in Chapters 7 and 8. The book also emphasizes the use of transfer functions, particularly in the solution of ground response problems. The transfer function approach helps students form a more complete understanding of ground response—in the frequency domain as well as the time domain. With the advent of computer programs such as MATLAB, MathCad, and Mathematica, the Fourier analyses required in the transfer function approach are quite simple; students use MATLAB extensively in my soil dynamics and geotechnical earthquake engineering courses.

The book contains worked examples and homework problems. The example problems are intended to illustrate the basic concepts of the problems they address; to allow the results to be checked, a number involve calculations carried out to more significant figures than the accuracy of the procedures (and typical input data) would justify. Many of the important problems of geotechnical earthquake engineering, however, do not lend themselves to the type of short, well-defined homework problem that is readily placed in a book. My preference is to assign longer, project-oriented assignments based on actual case histories, and I recommend that the homework problems in this book be supplemented by such assignments.

UNITS

As in many other fields, the use of units in geotechnical earthquake engineering is neither uniform nor consistent. The current state of knowledge in geotechnical earthquake engineering has resulted from advances in a variety of technical fields and a variety of countries, many of which customarily use different units. Fortunately, most conform to relatively standard metric or British systems. Rather than attempt to force the use of one system or the other, this book uses dual units. In recognition of their origins, the most common units for each quantity is listed first with the alternative following in parentheses. The approach is intended to allow all readers to proceed through the material without stopping to convert (mentally or otherwise) from one set of units to another. To encourage familiarity with both sets of units, some example and homework problems are specified in metric units and some in British units.

ACKNOWLEDGMENTS

A number of people have helped directly and indirectly in the preparation of this book. The professional and academic portions of my career have benefited greatly from a number of people that I have worked closely with, particularly (in chronological order) Bill Houston, Tom Tejima, H.B. Seed, Joe Mahoney, and Bob Holtz. Their assistance, advice, and encouragement has taken many forms, and I am grateful to each.

As this book evolved from a collection of lecture notes and handouts, it was continually improved by comments and suggestions from many students in my soil dynamics and geotechnical earthquake engineering courses. Their assistance is greatly appreciated. I am also grateful to many colleagues who provided constructive critical reviews of different parts of the book, including Dr. Donald G. Anderson, Dr. Juan Baez, Mr. David Baska, Dr. Gopal Biswas, Prof. Ross W. Boulanger, Dr. C.B. Crouse, Prof. Emeritus William J. Hall, Ms. Karen Henry, Prof. Carlton L. Ho, Prof. William D. Kovacs, Prof. Roberto T. Leon, Prof. Gregory R. MacRae, Dr. Lelio H. Mejia, Dr. Robert Pyke, Prof. Peter K. Robertson, Prof. Raj Siddharthan, Prof. Stewart Smith, Prof. Timothy D. Stark, and Prof. George M. Turkiyyah. Each made suggestions that improved the quality of the book. Prof. Geoffrey R. Martin and Prof. T. Leslie Youd reviewed substantial portions of the book; their efforts are particularly appreciated.

Finally, I am most grateful to my wife, Diane, and to my daughters, Katie and Megan. Preparation of this book involved several years of long working hours; I could not have done it without their cheerful understanding and encouragement.



1

Introduction to Geotechnical Earthquake Engineering

1.1 INTRODUCTION

Earthquake engineering deals with the effects of earthquakes on people and their environment and with methods of reducing those effects. It is a very young discipline, many of its most important developments having occurred in the past 30 to 40 years. Earthquake engineering is a very broad field, drawing on aspects of geology, seismology, geotechnical engineering, structural engineering, risk analysis, and other technical fields. Its practice also requires consideration of social, economic, and political factors. Most earthquake engineers have entered the field from structural engineering or geotechnical engineering backgrounds, a fact that is reflected in the practice of earthquake engineering. This book covers geotechnical aspects of earthquake engineering. Although its primary audience is geotechnical engineering students and practitioners, it contains a great deal of information that should be of interest to the structural engineer and the engineering seismologist.

1.2 BACKGROUND

The study of earthquakes dates back many centuries. Written records of earthquakes in China date as far back as 3000 years. Japanese records and records from the eastern Mediterranean region go back nearly 1600 years. In the United States the historical record of

earthquakes is much shorter, about 350 years. On the seismically active west coast of the United States, earthquake records go back only about 200 years. Compared with the millions of years over which earthquakes have been occurring, humankind's experience with earthquakes is very brief.

Today, hundreds of millions of people throughout the world live with a significant risk to their lives and property from earthquakes. Billions of dollars of public infrastructure are continuously at risk of earthquake damage. The health of many local, regional, and even national economies are also at risk from earthquakes. These risks are not unique to the United States, Japan, or any other country. Earthquakes are a global phenomenon and a global problem.

Earthquakes have occurred for millions of years and will continue in the future as they have in the past. Some will occur in remote, undeveloped areas where damage will be negligible. Others will occur near densely populated urban areas and subject their inhabitants and the infrastructure they depend on to strong shaking. It is impossible to prevent earthquakes from occurring, but it is possible to mitigate the effects of strong earthquake shaking: to reduce loss of life, injuries, and damage.

1.3 SEISMIC HAZARDS

A number of naturally occurring events, such as earthquakes, hurricanes, tornados, and floods, are capable of causing deaths, injuries, and property damage. These *natural hazards* cause tremendous damage around the world each year. Hazards associated with earthquakes are commonly referred to as *seismic hazards*. The practice of earthquake engineering involves the identification and mitigation of seismic hazards. The most important seismic hazards are described in the following sections.

1.3.1 Ground Shaking

When an earthquake occurs, seismic waves radiate away from the source and travel rapidly through the earth's crust. When these waves reach the ground surface, they produce shaking that may last from seconds to minutes. The strength and duration of shaking at a particular site depends on the size and location of the earthquake and on the characteristics of the site. At sites near the source of a large earthquake, ground shaking can cause tremendous damage. In fact, ground shaking can be considered to be the most important of all seismic hazards because all the other hazards are caused by ground shaking. Where ground shaking levels are low, these other seismic hazards may be low or nonexistent. Strong ground shaking, however, can produce extensive damage from a variety of seismic hazards.

Although seismic waves travel through rock over the overwhelming majority of their trip from the source of an earthquake to the ground surface, the final portion of that trip is often through soil, and the characteristics of the soil can greatly influence the nature of shaking at the ground surface. Soil deposits tend to act as "filters" to seismic waves by attenuating motion at certain frequencies and amplifying it at others. Since soil conditions often vary dramatically over short distances, levels of ground shaking can vary significantly within a small area. One of the most important aspects of geotechnical earthquake engineering practice involves evaluation of the effects of local soil conditions on strong ground motion. In this book, Chapter 3 presents methods for quantifying the most important

characteristics of strong ground motions, and Chapters 4 through 7 provide the background and techniques for site-specific ground motion prediction.

1.3.2 Structural Hazards

Without doubt the most dramatic and memorable images of earthquake damage are those of structural collapse. From the predictable collapse of the unreinforced masonry and adobe structures in which many residents of underdeveloped areas of the world live (Figure 1.1) to the surprising destruction of more modern construction (Figures 1.2 to 1.4), structural damage is the leading cause of death and economic loss in many earthquakes. However, structures need not collapse to cause death and damage. Falling objects such as brick facings and parapets on the outside of a structure or heavy pictures and shelves within a structure have caused casualties in many earthquakes. Interior facilities such as piping, lighting, and storage systems can also be damaged during earthquakes.

Over the years, considerable advances have been made in earthquake-resistant design of structures, and seismic design requirements in building codes have steadily improved. As earthquake-resistant design has moved from an emphasis on structural strength to emphases on both strength and ductility, the need for accurate predictions of ground motions has increased. In current design practice, the geotechnical earthquake engineer is often responsible for providing the structural engineer with appropriate design ground motions. In this book, Chapter 8 describes the effects of local soil conditions on ground motions and provides guidance for the development of site-specific design ground motions.



Figure 1.1 Damage to buildings in Huaras, Peru following the 1970 Peru earthquake. The adobe structures in the foreground were destroyed, but the reinforced concrete structure in the background suffered little damage (photo by G. Plafker, courtesy of USGS).

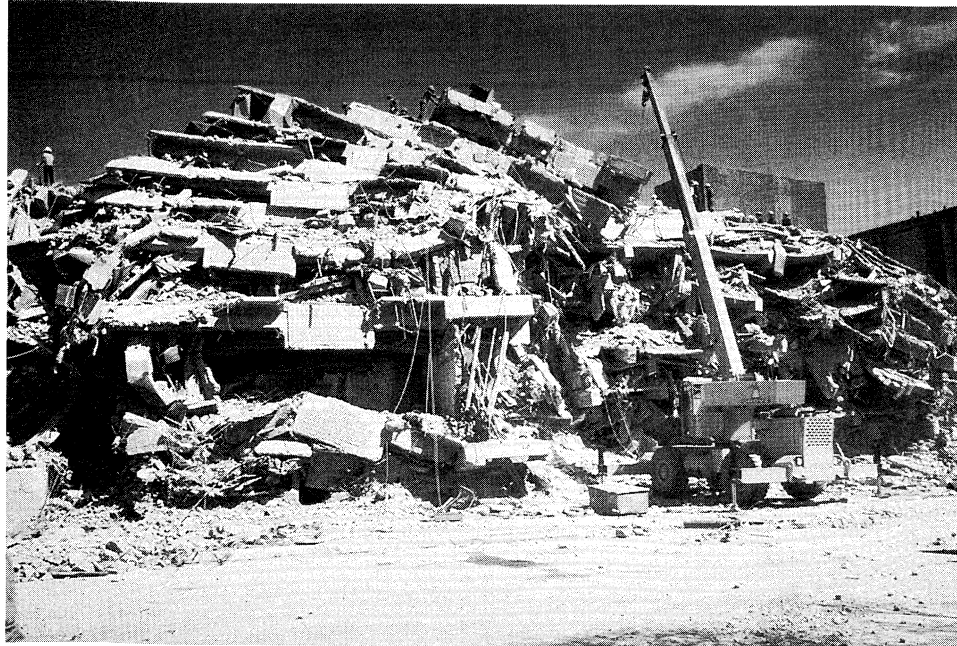


Figure 1.2 Collapsed portion of the reinforced concrete Hospital Juarez in Mexico City following the 1985 Mexico earthquake (photo by E.V. Leyendecker, courtesy of EERI).

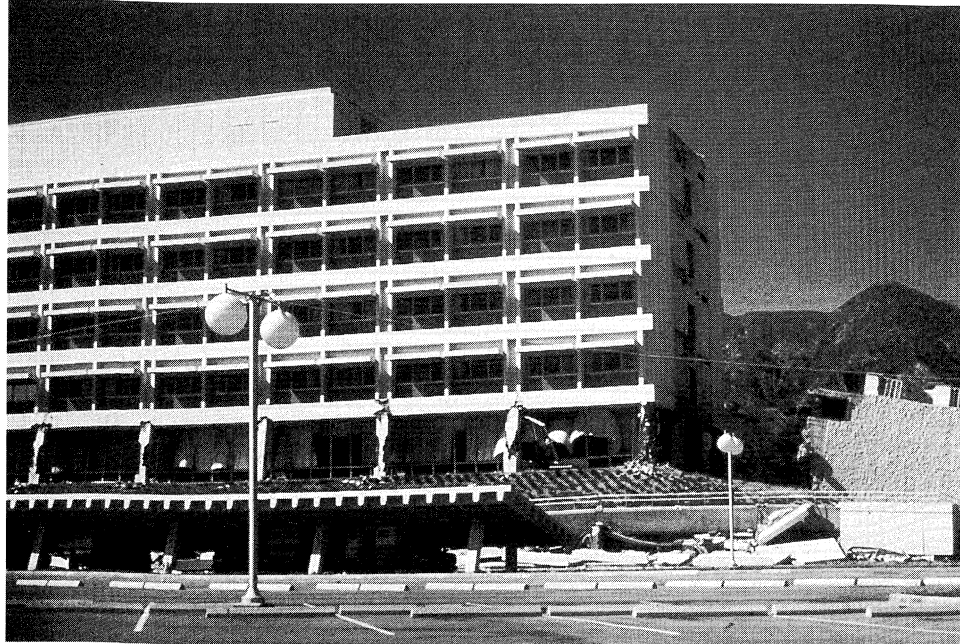


Figure 1.3 Effects of column failures at Olive View Hospital in the 1971 San Fernando earthquake. Collapse of the canopy in the foreground pinned the ambulances beneath them, rendering them useless (courtesy of EERI).

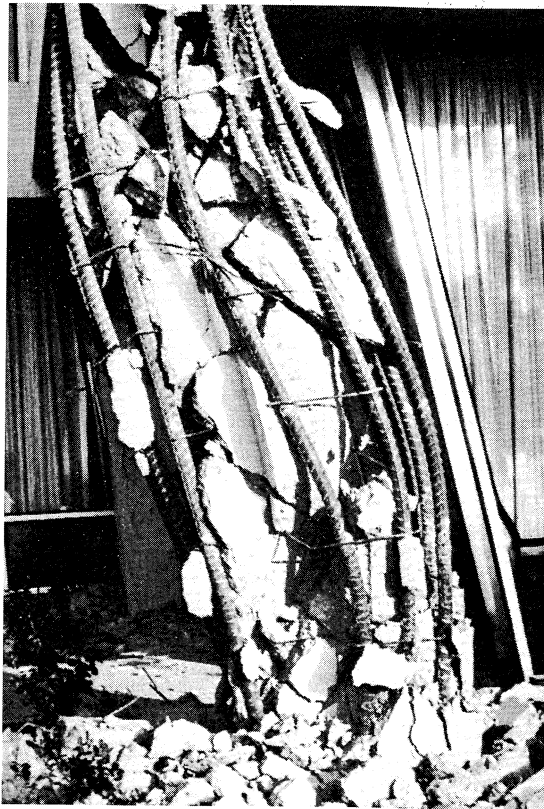


Figure 1.4 Reinforced concrete column at Olive View Hospital following the 1971 San Fernando earthquake. Insufficient transverse reinforcement was unable to provide adequate confinement (courtesy of USGS).

1.3.3 Liquefaction

Some of the most spectacular examples of earthquake damage have occurred when soil deposits have lost their strength and appeared to flow as fluids. In this phenomenon, termed *liquefaction*, the strength of the soil is reduced, often drastically, to the point where it is unable to support structures or remain stable. Because it only occurs in saturated soils, liquefaction is most commonly observed near rivers, bays, and other bodies of water.

The term *liquefaction* actually encompasses several related phenomena. Flow failures, for example, can occur when the strength of the soil drops below the level needed to maintain stability under static conditions. Flow failures are therefore driven by static gravitational forces and can produce very large movements. Flow failures have caused the collapse of earth dams (Figure 1.5) and other slopes, and the failure of foundations (Figure 1.6). The 1971 San Fernando earthquake caused a flow failure in the upstream slope of the Lower San Fernando Dam (Figure 1.7) that nearly breached the dam. Thousands could have been killed in the residential area immediately below the dam. Lateral spreading is a related phenomenon characterized by incremental displacements during earthquake shaking. Depending on the number and strength of the stress pulses that exceed the strength of the soil, lateral spreading can produce displacements that range from negligible to quite large. Lateral spreading is quite common near bridges, and the displacements it produces can damage the abutments, foundations, and superstructures of bridges (Figures 1.8 and 1.9). Finally, the



Figure 1.5 Liquefaction failure of Sheffield Dam following the 1925 Santa Barbara earthquake (K. Steinbrugge collection; courtesy of EERC, Univ. of California).



Figure 1.6 Liquefaction-induced bearing capacity failures of the Kawagishi-cho apartment buildings following the 1964 Niigata earthquake (courtesy of USGS).



Figure 1.7 Lower San Fernando Dam following liquefaction failure of its upstream slope in the 1971 San Fernando earthquake (K. Steinbrugge collection; courtesy of EERC, Univ. of California).

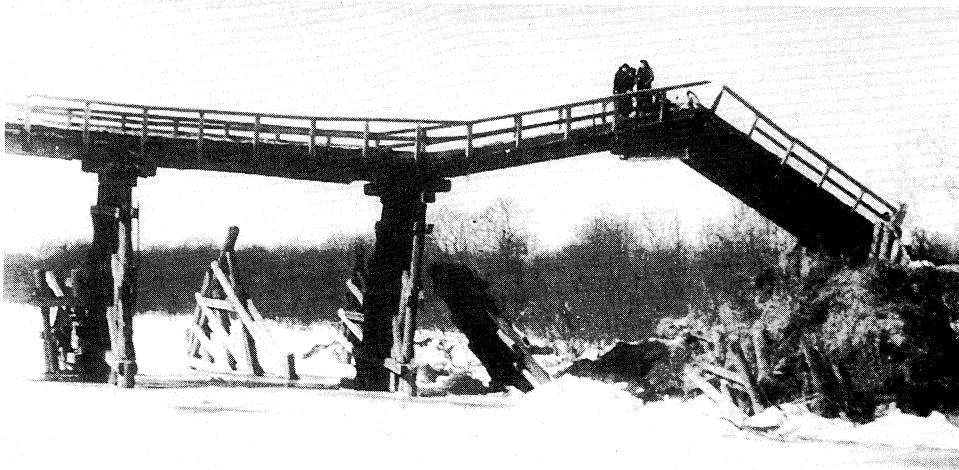


Figure 1.8 Effect of lateral spreading on a small bridge in Japan following the 1952 Tokachi-Oki earthquake. Lateral spreading of the soil at the abutment buckled the bridge deck (K. Steinbrugge collection; courtesy of EERC, Univ. of California).



Figure 1.9 The Showa Bridge following the 1964 Niigata earthquake. Lateral spreading caused bridge pier foundations to move and rotate sufficiently for simply supported bridge spans to fall (courtesy of USGS).

phenomenon of level-ground liquefaction does not involve large lateral displacements but is easily identified by the presence of sand boils (Figure 1.10) produced by groundwater rushing to the surface. Although not particularly damaging by themselves, sand boils indicate the presence of high groundwater pressures whose eventual dissipation can produce subsidence and damaging differential settlements.

Liquefaction is a complicated phenomenon, but research has progressed to the point where an integrated framework of understanding can be developed. Chapter 9 of this book presents the basic concepts with which the susceptibility, triggering conditions, and effects of all liquefaction phenomena can be understood, together with practical procedures for evaluation of liquefaction hazards.

1.3.4 Landslides

Strong earthquakes often cause landslides. Although the majority of such landslides are small, earthquakes have also caused very large slides. In a number of unfortunate cases, earthquake-induced landslides have buried entire towns and villages (Figure 1.11). More commonly, earthquake-induced landslides cause damage by destroying buildings, or disrupting bridges and other constructed facilities (Figures 1.12 and 1.13). Many earthquake-induced landslides result from liquefaction phenomena, but many others simply represent the failures of slopes that were marginally stable under static conditions. Various types of seismic slope failures, their frequency of occurrence, and procedures for their analysis are described in Chapter 10.



Figure 1.10 Sand boil in rice field following the 1964 Niigata earthquake (K. Steinbrugge collection; courtesy of EERC, Univ. of California).

1.3.5 Retaining Structure Failures

Anchored bulkheads, quay walls, and other retaining structures are frequently damaged in earthquakes. Damage is usually concentrated in waterfront areas such as ports and harbors (Figure 1.14). Because such facilities are often essential for the movement of goods upon which local economies often rely, the business losses associated with their failure can go far beyond the costs of repair or reconstruction. The seismic design of retaining structures is covered in Chapter 11.

1.3.6 Lifeline Hazards

A network of facilities that provide the services required for commerce and public health can be found in virtually any developed area. These networks, which include electrical power and telecommunications, transportation, water and sewage, oil and gas distribution, and waste storage systems, have collectively come to be known as *lifelines*. Lifeline systems may include power plants, transmission towers, and buried electrical cables; roads, bridges, harbors, and airports; water treatment facilities, reservoirs and elevated water tanks, and buried water distribution systems; liquid storage tanks and buried oil and gas pipelines; and municipal solid waste and hazardous waste landfills. Lifeline systems and the facilities that comprise them provide services that many take for granted but which are essential in modern industrial areas. Lifeline failures not only have severe economic consequences but can also adversely affect the environment and quality of life following an earthquake.



(a)



(b)

Figure 1.11 Village of Yungay, Peru, (a) before and (b) after being buried by a giant landslide in the 1970 Peruvian earthquake. The same palm trees are visible at the left side of both photographs. The landslide involved 50 million cubic meters of material that eventually covered an area of some 8000 square kilometers. About 25,000 people were killed by this landslide, over 18,000 in the villages of Yungay and Ranrahirca (K. Steinbrugge collection; courtesy of EERC, Univ. of California).



Figure 1.12 A wing of Government Hill School in Anchorage, Alaska, straddled the head scarp of the Government Hill landslide in the 1964 Good Friday earthquake (K. Steinbrugge collection; courtesy of EERC, Univ. of California).

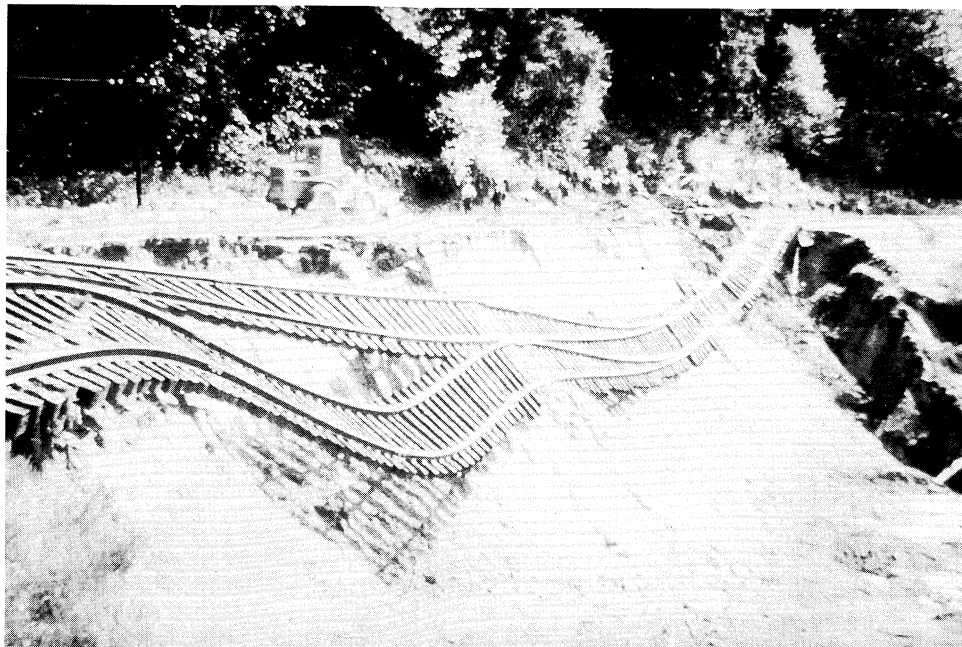


Figure 1.13 Earthquake-induced landslide along railroad tracks near Olympia, Washington (photo by G.W. Thorsen).



Figure 1.14 Failure of a quay wall on Rokko Island in Kobe, Japan in the 1995 Hyogo-Ken Nanbu earthquake (photo by S. L. Kramer).

Lifeline failure can cause disruption and economic losses that greatly exceed the cost of repairing facilities directly damaged by earthquake shaking. The 1989 Loma Prieta and 1994 Northridge earthquakes caused economic losses estimated at \$8 billion and \$30 billion in the state of California alone. These losses had severe local and regional repercussions but had only minor effects on most U.S. citizens. The 1972 Managua earthquake, on the other hand, caused losses of \$2 billion, 40% of Nicaragua's gross national product that year. The high costs of reconstruction produced a national debt that triggered inflation, increased unemployment, and eventually contributed to the destabilization of the Nicaraguan government. More recently, the Hyogo-Ken Nanbu earthquake devastated the city of Kobe, Japan; total damages have been estimated in excess of \$100 billion.

Lifeline failures can also hamper emergency response and rescue efforts immediately following damaging earthquakes. Most of the damage in the 1906 San Francisco earthquake, for example, was caused by a fire that could not be fought properly because of broken water mains. Eighty-three years later, television allowed the world to watch another fire in San Francisco following the Loma Prieta earthquake. These fires were caused by broken natural gas pipes, and again, firefighting was hampered by broken water mains. The Loma Prieta earthquake also caused the collapse and near collapse of several elevated highways and the collapse of a portion of the San Francisco–Oakland Bay Bridge. Loss of these transportation lifelines caused gridlock throughout the area. Some of the elevated highways were still out of service five years after the earthquake.

1.3.7 Tsunami and Seiche Hazards

Rapid vertical seafloor movements caused by fault rupture during earthquakes can produce long-period sea waves called *tsunamis*. In the open sea, tsunamis travel great distances at high speeds but are difficult to detect—they usually have heights of less than 1 m and wavelengths (the distance between crests) of several hundred kilometers. As a tsunami approaches shore, however, the decreasing water depth causes its speed to decrease and the height of the wave to increase. In some coastal areas, the shape of the seafloor may amplify the wave, producing a nearly vertical wall of water that rushes far inland and causes devastating damage (Figure 1.15). The Great Hōei Tokaidō–Nōhaidō tsunami killed 30,000 people in Japan in 1707. The 1960 Chilean earthquake produced a tsunami that not only killed 300 people in Chile, but also killed 61 people in Hawaii and, 22 hours later, 199 people in distant Japan (Iida et al., 1967).

Earthquake-induced waves in enclosed bodies of water are called *seiches*. Typically caused by long-period seismic waves that match the natural period of oscillation of the water in a lake or reservoir, seiches may be observed at great distances from the source of an earthquake. The 1964 Good Friday earthquake in Alaska, for example, produced damaging waves up to 5 ft high in lakes in Louisiana and Arkansas (Spaeth and Berkman, 1967). Another type of seiche can be formed when faulting causes permanent vertical displacements within a lake or reservoir. In 1959, vertical fault movement within Hebgen Lake produced a seiching motion that alternately overtopped Hebgen Dam and exposed the lake bottom adjacent to the dam in 1959 (Steinbrugge and Cloud, 1962).



Figure 1.15 Tsunami damage in Kodiak, Alaska, following the 1964 Good Friday earthquake (courtesy of USGS).

1.4 MITIGATION OF SEISMIC HAZARDS

Ultimately, the goal of the earthquake engineer is to mitigate seismic hazards. For new construction, hazard mitigation is embedded in the process of earthquake-resistant design. Details of earthquake-resistant design of structures are beyond the scope of this book, but some aspects of earthquake loading of structures are described in Chapter 8. Earthquake-resistant design of slopes, dams, embankments, and retaining structures is based on topics presented in Chapters 9 to 11. Mitigation of existing seismic hazards is also very important. The important topic of remediation of soil deposits for seismic hazard mitigation is covered in Chapter 12.

1.5 SIGNIFICANT HISTORICAL EARTHQUAKES

Earthquakes occur almost continuously around the world. Fortunately, most are so small that they cannot be felt. Only a very small percentage of earthquakes are large enough to cause noticeable damage, and a small percentage of those are large enough to be considered major earthquakes. Throughout recorded history, some of these major earthquakes can be regarded as being particularly significant, either because of their size and the damage they produced or because of what scientists and engineers were able to learn from them. A partial list of significant earthquakes, admittedly biased toward U.S. earthquakes and earthquakes with significant geotechnical earthquake engineering implications, is given in Table 1-1.

TABLE 1-1 Significant Historical Earthquakes

Date	Location	Magnitude	Deaths	Comments
780 B.C.	China			One of the first reliable written accounts of a strong earthquake; produced widespread damage west of Xian in Shaanxi Province
A.D. 79	Italy			Sixteen years of frequent earthquakes culminating with the eruption of Mt. Vesuvius, which buried the city of Pompeii
893	India		180,000	Widespread damage; many killed in collapse of earthen homes
1556	China	8.0 (est.)	530,000	Occurred in densely populated region near Xian; produced thousands of landslides, which killed inhabitants of soft rock caves in hillsides; death estimate of questionable accuracy
1755	Portugal	8.6	60,000	Lisbon earthquake; first scientific description of earthquake effects
1783	Italy		50,000	Calabria earthquake; first scientific commission for earthquake investigation formed

TABLE 1-1 Significant Historical Earthquakes (continued)

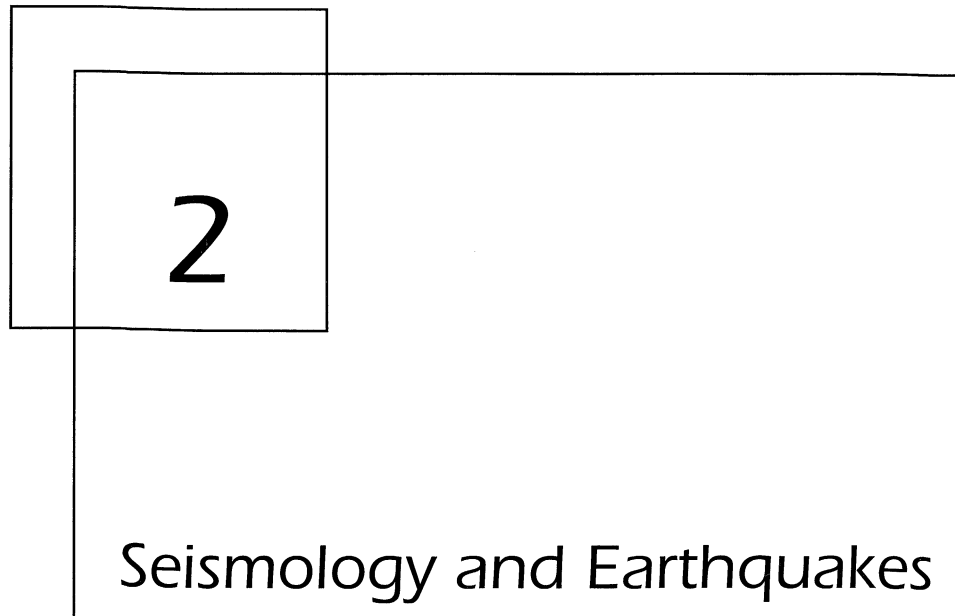
1811–1812	Missouri	7.5, 7.3, 7.8	Several	Three large earthquakes in less than two months in New Madrid area; felt all across central and eastern United States
1819	India		1,500	Cutch earthquake; first well-documented observations of faulting
1857	California	8.3	1	Fort Tejon earthquake; one of the largest earthquakes known to have been produced by the San Andreas Fault; fault ruptured for 250 miles (400 km) with up to 30 ft (9 m) offset
1872	California	8.5	27	Owens Valley earthquake; one of the strongest ever to have occurred in the United States
1886	South Carolina	7.0	110	Strongest earthquake to strike east coast of United States; produced significant liquefaction
1906	California	7.9	700	First great earthquake to strike densely populated area in United States; produced up to 21 ft (7 m) offset in 270-mile (430-km) rupture of San Andreas Fault; most damage caused by fire; extent of ground shaking damage correlated to geologic conditions in postearthquake investigation
1908	Italy	7.5	83,000	Messina and surrounding area devastated; Italian government appointed engineering commission that recommended structures be designed for equivalent static lateral loads
1923	Japan	7.9	99,000	Kanto earthquake; caused major damage in Tokyo-Yokohama area, much due to fire in Tokyo and tsunami in coastal regions; strongly influenced subsequent design in Japan
1925	California	6.3	13	Santa Barbara earthquake; caused liquefaction failure of Sheffield Dam; led to first explicit provisions for earthquake resistance in U.S. building codes

TABLE 1-1 Significant Historical Earthquakes (continued)

1933	California	6.3	120	Considerable building damage; schools particularly hard-hit, with many children killed and injured; led to greater seismic design requirements in building codes, particularly for public school buildings
1940	California	7.1	9	Large ground displacements along Imperial Fault near El Centro; first important accelerogram for engineering purposes was recorded
1959	Montana	7.1	28	Hebgen Lake earthquake; faulting within reservoir produced large seiche that overtopped earth dam
1960	Chile	9.5	2,230	Probably the largest earthquake ever recorded
1964	Alaska	9.2	131	The Good Friday earthquake; caused severe damage due to liquefaction and many earthquake-induced landslides
1964	Japan	7.5	26	Widespread liquefaction caused extensive damage to buildings, bridges, and port facilities in Niigata; along with Good Friday earthquake in Alaska, spurred intense interest in the phenomenon of liquefaction
1967	Venezuela	6.5	266	Caused collapse of relatively new structures in Caracas; illustrated effects of local soil conditions on ground motion and damage
1971	California	6.6	65	San Fernando earthquake; produced several examples of liquefaction, including near collapse of Lower San Fernando Dam; caused collapse of several buildings and highway bridges; many structural lessons learned, particularly regarding need for spiral reinforcement of concrete columns; many strong motion records obtained
1975	China	7.3	1,300	Evacuation following successful prediction saved thousands of lives in Haicheng, Liaoning Province
1976	China	7.8	700,000	Thought to be the most deadly earthquake in history; destroyed city of Tangshan, Hebei Province; not predicted; death estimate of questionable accuracy

TABLE 1-1 Significant Historical Earthquakes (continued)

1985	Mexico	8.1	9,500	Epicenter off Pacific Coast, but most damage occurred over 220 miles (360 km) away in Mexico City; illustrated effect of local soil conditions on ground motion amplification and damage; subsequent studies led to better understanding of dynamic properties of fine-grained soils
1989	California	7.1	63	Loma Prieta earthquake; extensive ground motion amplification and liquefaction damage in San Francisco Bay area
1994	California	6.8	61	Northridge earthquake; occurred on previously unknown fault beneath heavily populated area; buildings, bridges, lifelines extensively damaged; produced extraordinarily strong shaking at several locations
1995	Japan	6.9	5,300	Hyogo-Ken Nanbu earthquake; caused tremendous damage to Kobe, Japan; widespread liquefaction in reclaimed lands constructed for port of Kobe; landslides and damage to retaining walls and underground subway stations also observed



2

Seismology and Earthquakes

2.1 INTRODUCTION

The study of geotechnical earthquake engineering requires an understanding of the various processes by which earthquakes occur and their effects on ground motion. The field of *seismology* (from the Greek *seismos* for earthquake and *logos* for science) developed from a need to understand the internal structure and behavior of the earth, particularly as they relate to earthquake phenomena. Although earthquakes are complex phenomena, advances in seismology have produced a good understanding of the mechanisms and rates of occurrence of earthquakes in most seismically active areas of the world. This chapter provides a brief introduction to the structure of the earth, the reasons why earthquakes occur, and the terminology used to describe them. More complete descriptions of these topics may be found in a number of seismology texts, such as Gutenberg and Richter (1954), Richter (1958), Bullen (1975), Bath (1979), Bullen and Bolt (1985), Gubbins (1990), and Lay and Wallace (1995). A very readable description of seismology and earthquakes is given by Bolt (1993).

2.2 INTERNAL STRUCTURE OF THE EARTH

The earth is roughly spherical, with an equatorial diameter of 12,740 km (7918 miles) and a polar diameter of 12,700 km (7893 miles), the higher equatorial diameter being caused by

higher equatorial velocities due to the earth's rotation. The earth weighs some 5.4×10^{21} tons (4.9×10^{24} kg), which indicates an average specific gravity of about 5.5. Since the specific gravity of surficial rocks is known to be on the order of 2.7 to 3, higher specific gravities are implied at greater depths.

One of the first important achievements in seismology was the determination of the internal structure of the earth. Large earthquakes produce enough energy to cause measurable shaking at points all around the world. As the different types of seismic waves travel through the earth, they are refracted and reflected at boundaries between different layers, reaching different points on the earth's surface by different paths. Studies of these refractions and reflections early in this century revealed the layered structure of the earth and provided insight into the characteristics of each layer.

2.2.1 Seismic Waves

When an earthquake occurs, different types of seismic waves are produced: *body waves* and *surface waves*. Although seismic waves are discussed in detail in Chapter 5, the brief description that follows is necessary to explain some of the concepts of Chapters 2 to 4.

Body waves, which can travel through the interior of the earth, are of two types: *p-waves* and *s-waves* (Figure 2.1). P-waves, also known as primary, compressional, or longitudinal waves, involve successive compression and rarefaction of the materials through which they pass. They are analogous to sound waves; the motion of an individual particle that a p-wave travels through is parallel to the direction of travel. Like sound waves, *p-waves can travel through solids and fluids*. S-waves, also known as secondary, shear, or transverse waves, cause shearing deformations as they travel through a material. The motion of an individual particle is perpendicular to the direction of s-wave travel. The direction of particle movement can be used to divide s-waves into two components, SV (vertical

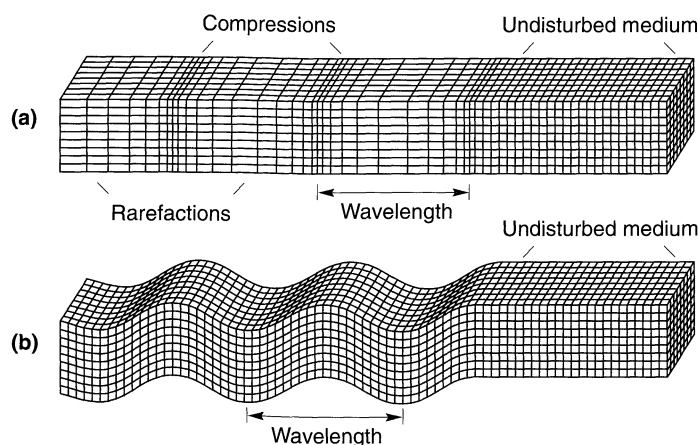


Figure 2.1 Deformations produced by body waves: (a) p-wave; (b) SV-wave. From *Earthquakes* by Bolt. Copyright © 1993 by W.H. Freeman and Company. Used with permission.

plane movement) and SH (horizontal plane movement). The speed at which body waves travel varies with the stiffness of the materials they travel through. Since geologic materials are stiffest in compression, p-waves travel faster than other seismic waves and are therefore the first to arrive at a particular site. Fluids, which have no shearing stiffness, cannot sustain s-waves.

Surface waves result from the interaction between body waves and the surface and surficial layers of the earth. They travel along the earth's surface with amplitudes that decrease roughly exponentially with depth (Figure 2.2). Because of the nature of the interactions required to produce them, surface waves are more prominent at distances farther from the source of the earthquake. At distances greater than about twice the thickness of the earth's crust, surface waves, rather than body waves, will produce peak ground motions. The most important surface waves, for engineering purposes, are *Rayleigh waves* and *Love waves*. Rayleigh waves, produced by interaction of p- and SV-waves with the earth's surface, involve both vertical and horizontal particle motion. They are similar, in some respects, to the waves produced by a rock thrown into a pond. Love waves result from the interaction of SH-waves with a soft surficial layer and have no vertical component of particle motion.

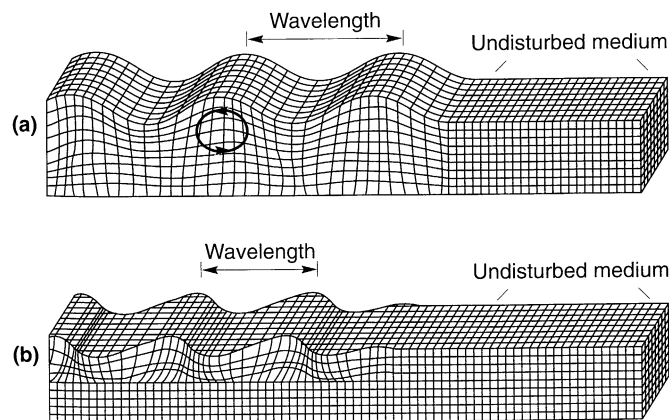


Figure 2.2 Deformations produced by surface waves: (a) Rayleigh wave; and (b) Love wave. From *Earthquakes* by Bolt. Copyright ©1993 by W.H. Freeman and Company. Used with permission.

2.2.2 Internal Structure

The *crust*, on which human beings live, is the outermost layer of the earth. The thickness of the crust ranges from about 25 to 40 km (15 to 25 miles) beneath the continents (although it may be as thick as 60 to 70 km (37 to 44 miles) under some young mountain ranges) to as thin as 5 km (3 miles) or so beneath the oceans—only a very small fraction of the earth's diameter (Figure 2.3). The internal structure of the crust is complex but can be represented by a basaltic layer that is overlain by a granitic layer at continental locations. Since it is

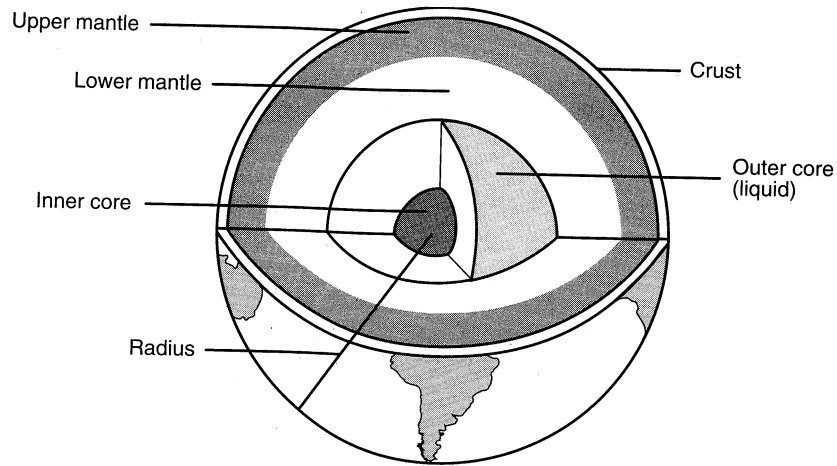


Figure 2.3 Internal structure of the earth.

exposed to the oceans or the atmosphere, the crust is cooler than the materials below it (Figure 2.4). In addition to being thinner, the oceanic crust is generally more uniform and more dense than the continental crust.

A distinct change in wave propagation velocity marks the boundary between the crust and the underlying *mantle*. This boundary is known as the *Mohorovičić discontinuity*, or the *Moho*, named after the seismologist who discovered it in 1909. Although the specific nature of the Moho itself is not well understood, its role as a reflector and refractor of seismic waves is well established. The mantle is about 2850 km (1770 miles) thick and can be

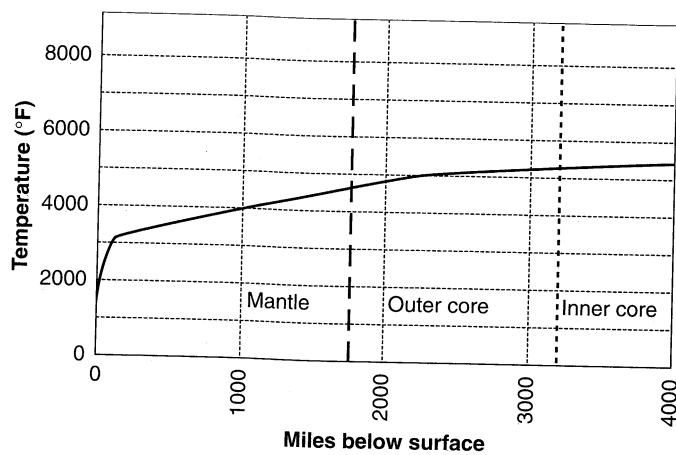


Figure 2.4 Estimated variation of temperature below the surface of the earth. (After Verhoogan, 1960.)

divided into the *upper mantle* (shallower than about 650 km (404 miles)) and the *lower mantle*. No earthquakes have been recorded in the lower mantle, which exhibits a uniform velocity structure and appears to be chemically homogeneous, except near its lower boundary. The mantle is cooler near the crust than at greater depths but still has an average temperature of about 4000°F. As a result, the mantle materials are in a viscous, semimolten state. They behave as a solid when subjected to rapidly applied stresses, such as those associated with seismic waves, but can slowly flow like a fluid in response to long-term stresses. The mantle material has a specific gravity of about 4 to 5.

The *outer core*, or *liquid core*, is some 2260 km (1400 miles) thick. As a liquid, it cannot transmit s-waves. As shown in Figure 2.5, the s-wave velocity drops to zero at the core–mantle boundary, or *Gutenberg discontinuity*; note also the precipitous drop in p-wave velocity. The outer core consists primarily of molten iron (which helps explain its high specific gravity of 9 to 12). The *inner core*, or *solid core*, is a very dense (specific gravity up to about 15), solid nickel–iron material compressed under tremendous pressures. The temperature of the inner core is estimated to be relatively uniform at over 5000°F.

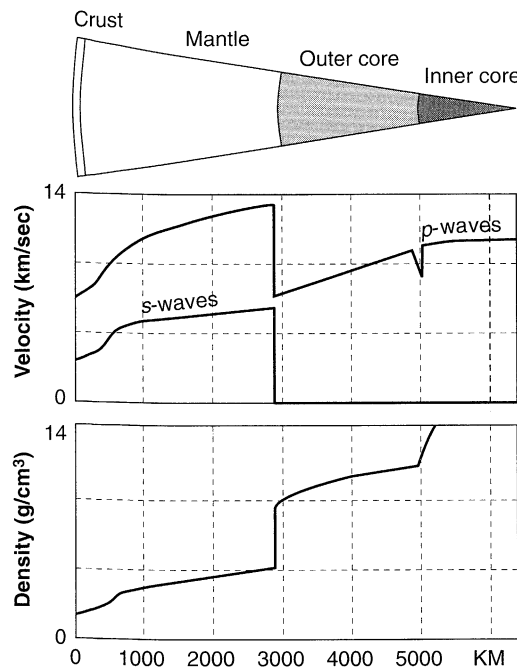


Figure 2.5 Variation of p- and s-wave velocity and density within the earth. (After Eiby, 1980.)

Figure 2.6 shows the influence of the earth's structure on the distribution of seismic waves during earthquakes. Since wave propagation velocities generally increase with depth, wave paths are usually refracted back toward the earth's surface. An exception is at the core–mantle boundary, where the outer core velocity is lower than the mantle velocity.

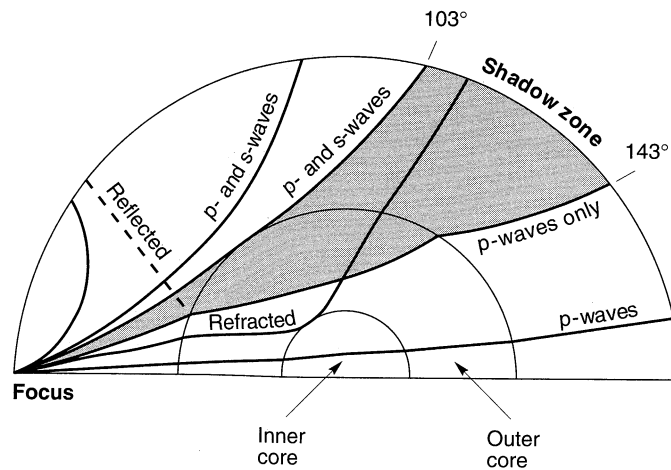


Figure 2.6 Seismic wave paths illustrating reflection and refraction of seismic waves from the source (focus) of the earthquake by the different layers of the earth. Note that p- and s-waves can reach the earth's surface between 0 and 103°, but the liquid nature of the outer core allows only p-waves to reach the surface between 143 and 180°. In the shadow zone between angles of 103 and 143°, only paths reflected from the inner core can reach the earth's surface. (From Sumner, 1969.)

2.3 CONTINENTAL DRIFT AND PLATE TECTONICS

Although observations of similarity between the coastlines and geology of eastern South America and the western Africa and the southern part of India and northern part of Australia had intrigued scientists since the seventeenth century (Glen 1975; Kearey and Vine, 1990), the theory that has come to be known as *continental drift* was not proposed until the early twentieth century (Taylor, 1910; Wegener, 1915). Wegener, for example, believed that the earth had only one large continent called Pangaea 200 million years ago. He believed that Pangaea broke into pieces that slowly drifted (Figure 2.7) into the present configuration of the continents. A more detailed view of the current similarity of the African and South American coasts is shown in Figure 2.8.

The theory of continental drift did not receive much attention until about 1960, when the current worldwide network of seismographs was able to define earthquake locations accurately, and to confirm that long-term deformations were concentrated in narrow zones between relatively intact blocks of crust. Also, exploration of the ocean floor did not begin in earnest until after World War II, when new techniques such as deep-water echo sounding, seismic refraction, and piston coring became available. The geology of the ocean floor is young, representing only about 5% of the earth's history (Gubbins, 1990), and relatively simple. Its detailed study provided strong supporting evidence of the historical movement of the continents as assumed in the theory of continental drift. Within 10 years, the theory of continental drift had become widely accepted and acknowledged as the greatest advance in the earth sciences in a century.

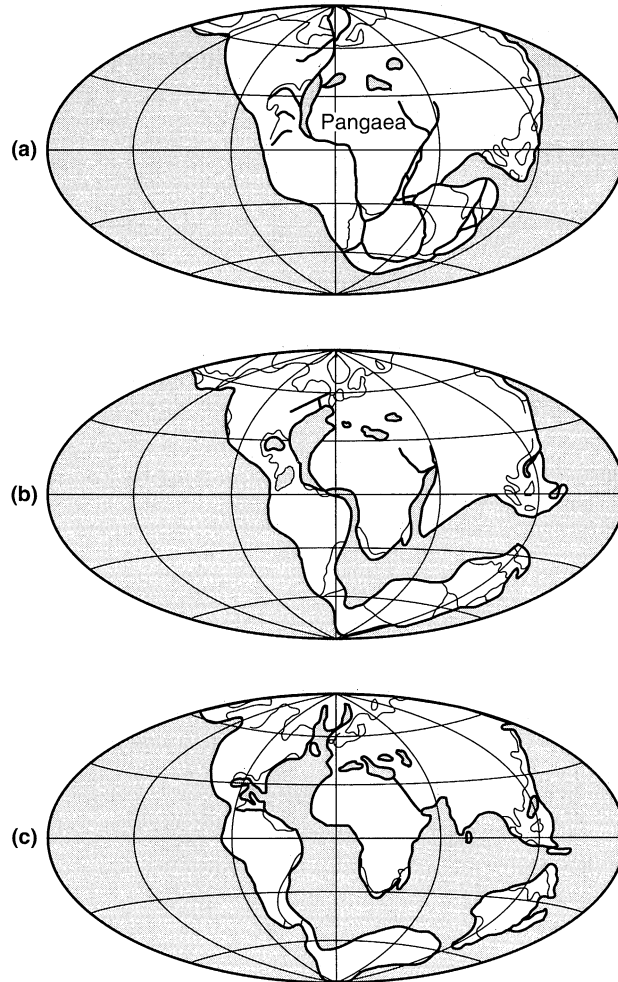


Figure 2.7 Wegener's theory of continental drift: (a) 270 million years ago; (b) 150 million years ago; (c) 1 million years ago. (After Verney, 1979.)

2.3.1 Plate Tectonics

The original theory of continental drift suggested images of massive continents pushing through the seas and across the ocean floor. It was well known, however, that the ocean floor was too strong to permit such motion, and the theory was originally discredited by most earth scientists. From this background, however, the modern theory of *plate tectonics* began to evolve. The basic hypothesis of plate tectonics is that the earth's surface consists of a number of large, intact blocks called *plates*, and that these plates move with respect to

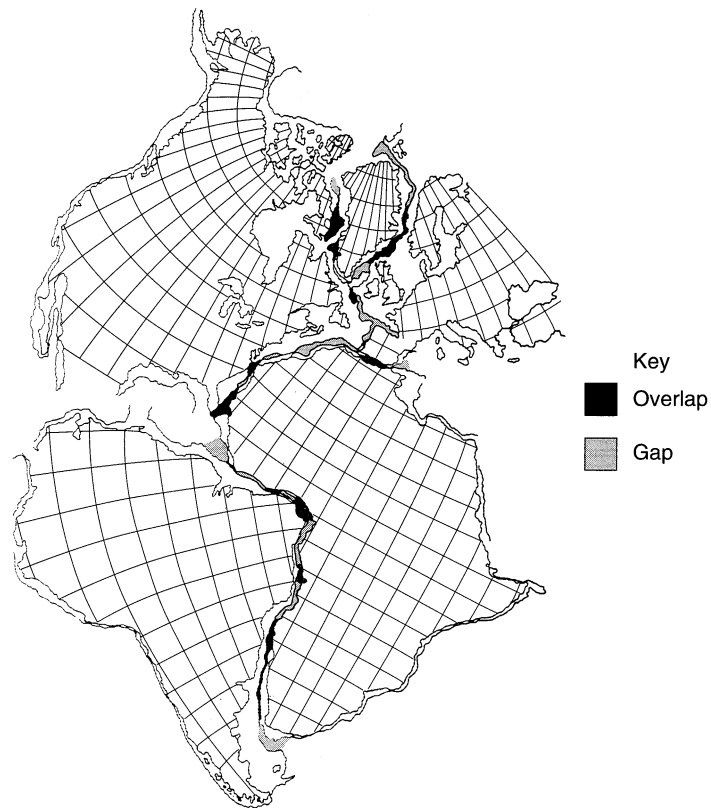
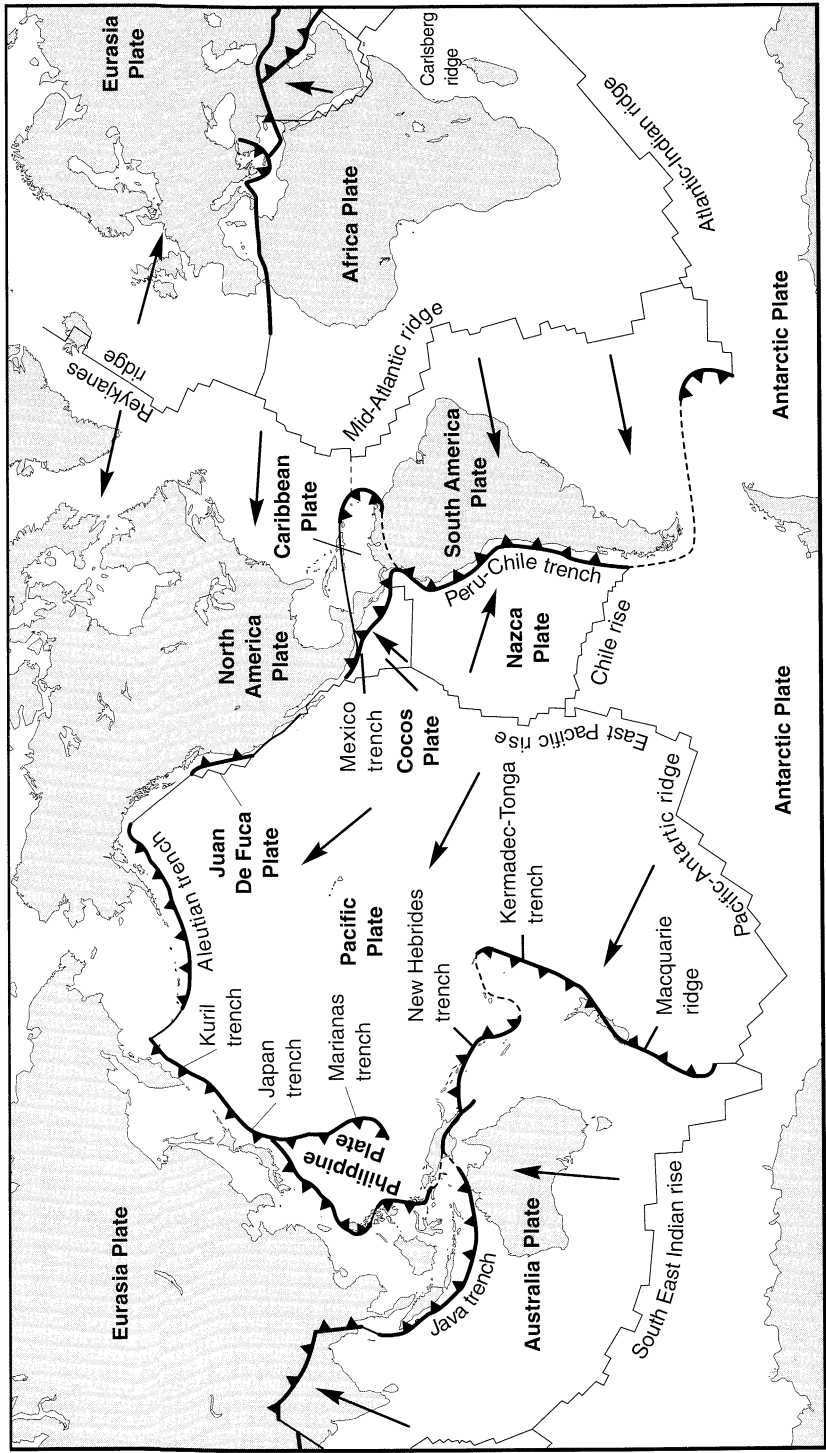


Figure 2.8 Statistical spherical fit of several continents using the continental slopes rather than the coastlines. (After Bullard et al., 1965, with permission of the Royal Society.)

each other. The earth's crust is divided into six continental-sized plates (African, American, Antarctic, Australia-Indian, Eurasian, and Pacific) and about 14 of subcontinental size (e.g., Caribbean, Cocos, Nazca, Philippine, etc.). The major plates are shown in Figure 2.9. Smaller *platelets*, or *microplates*, have broken off from the larger plates in the vicinity of many of the major plate boundaries but are not shown here. The relative deformation between plates occurs only in narrow zones near their boundaries. This deformation of the plates can occur slowly and continuously (*aseismic deformation*) or can occur spasmodically in the form of earthquakes (*seismic deformation*). Since the deformation occurs predominantly at the boundaries between the plates, it would be expected that the locations of earthquakes would be concentrated near plate boundaries. The map of earthquake epicenters shown in Figure 2.10 confirms this expectation, thereby providing strong support for the theory of plate tectonics.

The theory of plate tectonics is a kinematic theory (i.e., it explains the geometry of plate movement without addressing the cause of that movement). Something must drive the movement, however, and the tremendous mass of the moving plates requires that the



Key
 —▲— Subduction zone
 —▲— Strike-slip (transform) faults
 - - - - - Uncertain plate boundary
 — Ridge axis

Figure 2.9 The major tectonic plates, mid-oceanic ridges, trenches, and transform faults of the earth. Arrows indicate directions of plate movement. (After Fowler, 1990.)

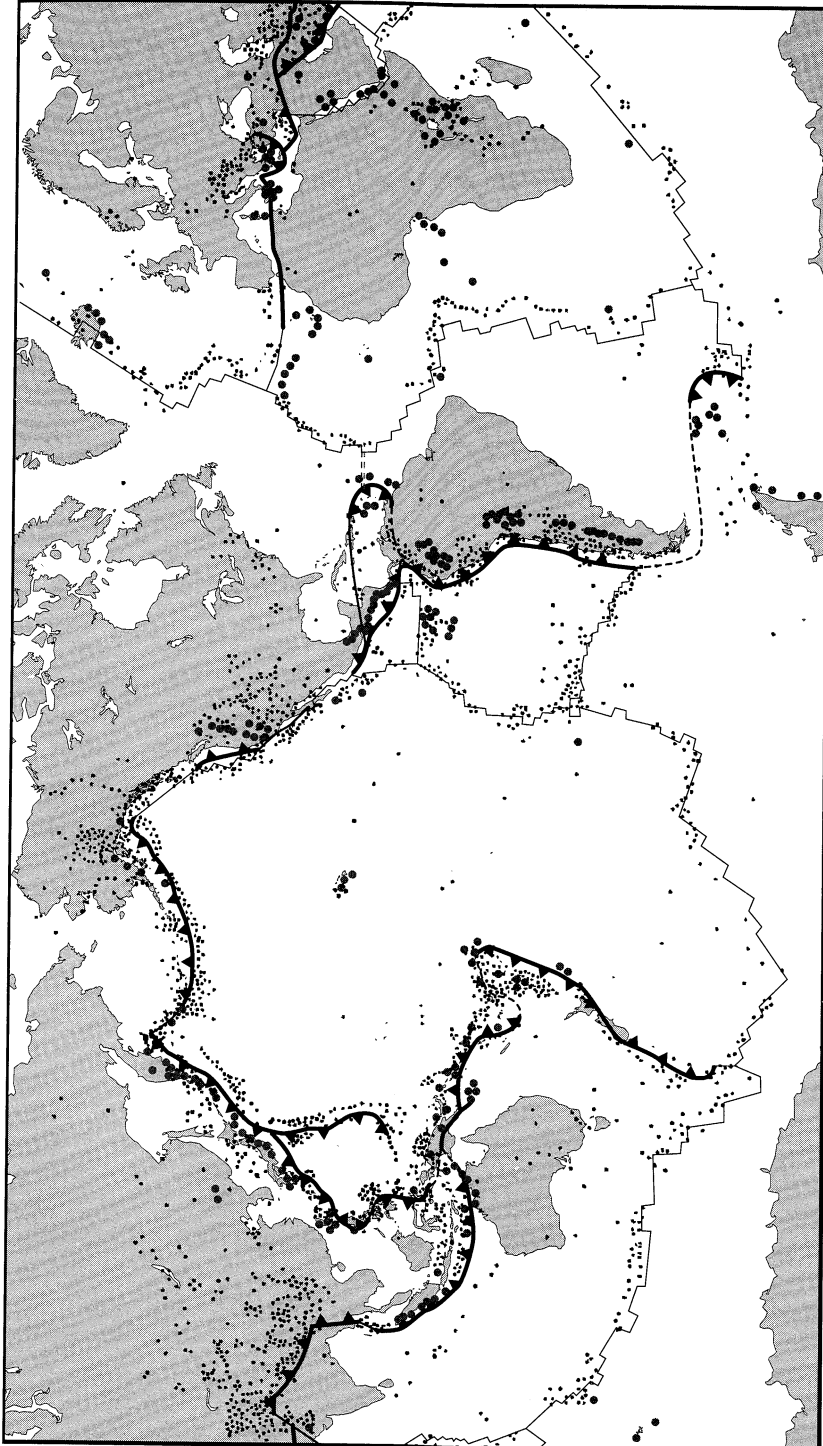


Figure 2.10 Worldwide seismic activity. The dots represent the epicenters of significant earthquakes. It is apparent that the locations of the great majority of earthquakes correspond to the boundaries between plates. (After Bolt, 1988.)

driving forces be very large. The most widely accepted explanation of the source of plate movement relies on the requirement of thermomechanical equilibrium of the earth's materials. The upper portion of the mantle is in contact with the relatively cool crust while the lower portion is in contact with the hot outer core. Obviously, a temperature gradient must exist within the mantle (see Figure 2.4). The variation of mantle density with temperature produces the unstable situation of denser (cooler) material resting on top of less dense (warmer) material. Eventually, the cooler, denser material begins to sink under the action of gravity and the warmer, less dense material begins to rise. The sinking material gradually warms and becomes less dense; eventually, it will move laterally and begin to rise again as subsequently cooled material begins to sink. This process is the familiar one of *convection*.

Convection currents in the semimolten rock of the mantle, illustrated schematically in Figure 2.11, impose shear stresses on the bottom of the plates, thus "dragging" them in various directions across the surface of the earth. Other phenomena, such as *ridge push* or *slab pull*, may also contribute to the movement of plates (Hager, 1978).

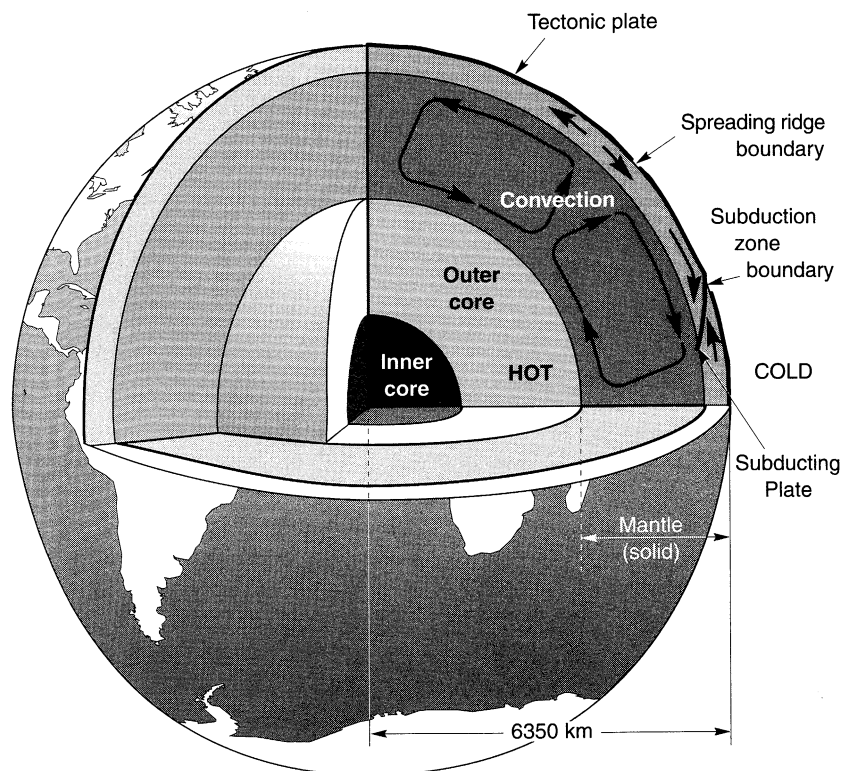


Figure 2.11 Convection currents in mantle. Near the bottom of the crust, horizontal component of convection currents impose shear stresses on bottom of crust, causing movement of plates on earth's surface. The movement causes the plates to move apart in some places and to converge in others. (After Noson et al., 1988.)

2.3.2 Plate Boundaries

Three distinct types of plate boundaries have been identified, and understanding the movement associated with each will aid in the understanding of plate tectonics. The characteristics of the plate boundaries also influence the nature of the earthquakes that occur along them.

2.3.2.1 Spreading Ridge Boundaries

✓ In certain areas the plates move apart from each other (Figure 2.12) at boundaries known as *spreading ridges* or *spreading rifts*. Molten rock from the underlying mantle rises to the surface where it cools and becomes part of the spreading plates. In this way, the plates “grow” at the spreading ridge. Spreading rates range from approximately 2 to 18 cm/yr (1 to 7 in/yr); the highest rates are found in the Pacific Ocean ridges and the lowest along the Mid-Atlantic Ridge. It is estimated (Garfunkel, 1975) that new oceanic crust is currently formed at a rate of about 3.1 km²/yr (1.2 miles²/yr) worldwide. The crust, mainly young, fresh basalt, is thin in the vicinity of the spreading ridges. It may be formed by relatively slow upward movement of magma, or it may be ejected quickly during seismic activity. Underwater photographs have shown formations of pillow lava and have even recorded lava eruptions in progress. Volcanic activity, much of which occurs beneath the ocean surface, is common in the vicinity of spreading-ridge boundaries. Spreading ridges can protrude above the ocean; the island of Iceland, where volcanic activity is nearly continuous (there are 150 active volcanos), is such an example.

The mantle material cools after it reaches the surface in the gap between the spreading plates. As it cools, it becomes magnetized (*remnant magnetism*) with a polarity that depends on the direction of the earth’s magnetic field at that time. The magnetic field of the earth is not constant on a geological time scale; it has fluctuated and reversed at irregular historical intervals, thus imposing magnetic anomalies (reversals of polarity) in the rock that forms at the

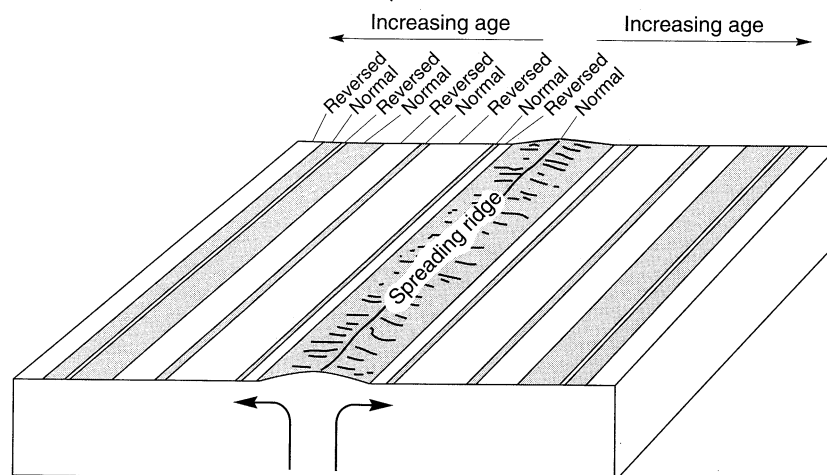


Figure 2.12 Spreading ridge boundary. Magma rises to surface and cools in gap formed by spreading plates. Magnetic anomalies are shown as stripes of normal and reversed magnetic polarity. (After Foster, 1971.)

spreading ridge boundaries. Measurement of the magnetic field in a direction perpendicular to a spreading ridge plate boundary reveals a fluctuating pattern of magnetic intensity, as illustrated for the eastern Pacific Ocean region in Figure 2.13. These magnetic anomalies have allowed large portions of the major plates to be dated. Comparison of the ages of various materials allows identification of the geometry and movement of various plates and has proven invaluable in the verification and acceptance of the theory of plate tectonics.

2.3.2.2 Subduction Zone Boundaries

Since the size of the earth remains constant, the creation of new plate material at spreading ridges must be balanced by the consumption of plate material at other locations. This occurs at *subduction zone* boundaries where the relative movement of two plates is toward each other. At the point of contact, one plate plunges, or *subducts*, beneath the other,

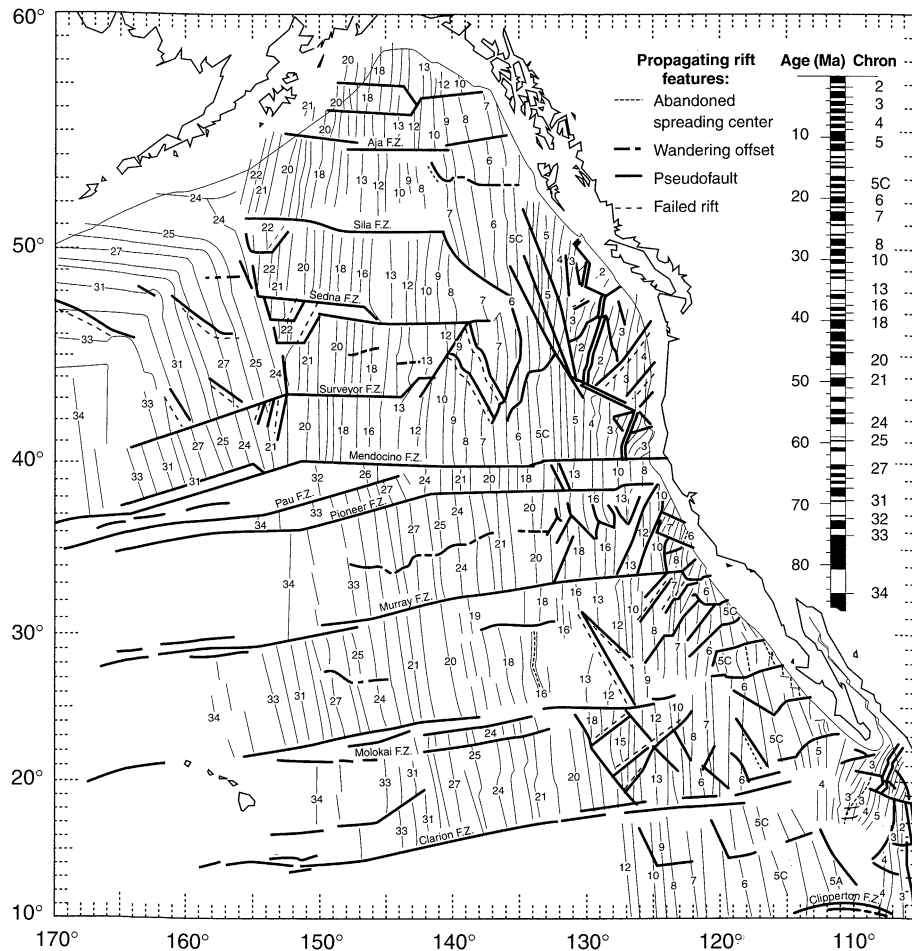


Figure 2.13 Magnetic anomalies in the eastern Pacific Ocean. The dark lines represent bands of common magnetic polarity. (After Atwater and Sveringhaus, 1989.)

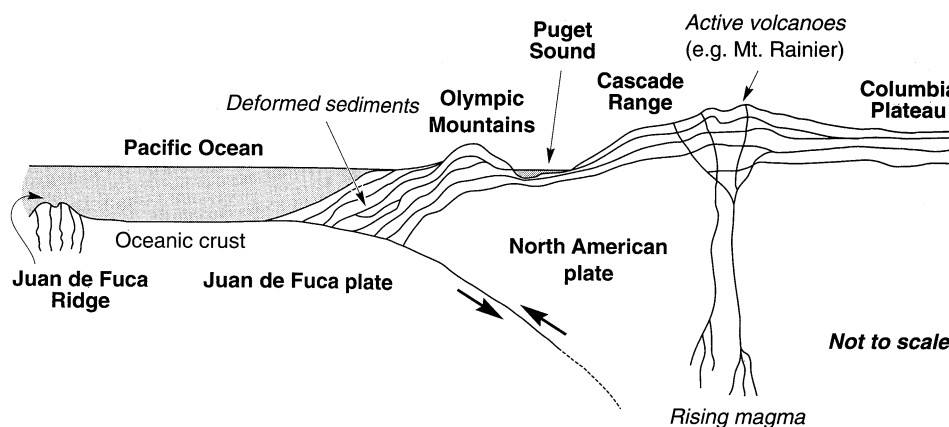


Figure 2.14 Cascadia subduction zone off the coasts of Washington and Oregon. The Juan de Fuca plate originates at the Juan de Fuca spreading ridge and subducts beneath the North American plate. Magma rising from the deeper part of the subduction zone has formed a series of volcanoes that run roughly parallel to the subduction zone. One of these, Mt. St. Helens, erupted explosively in 1980. (After Noson et al., 1988.)

as shown in Figure 2.14. Subduction zone plate boundaries exist off the western coasts of Mexico and Chile, south of the Aleutian Island chain of Alaska, and off the eastern coast of Japan. The Cascadia subduction zone off the coast of Washington and British Columbia is shown in Figure 2.14.

Subduction zone boundaries are often found near the edges of continents. Because the oceanic crust is generally cold and dense, it sinks under its own weight beneath the lighter continental crust. When the rate of plate convergence is high, a trench is formed at the boundary between plates. In fact, subduction zone boundaries are sometimes called trench boundaries. Earthquakes are generated in the sloping *Benioff zone* at the interface between the subducting and overriding plates. When the rate of convergence is slow, sediments accumulate in an *accretionary wedge* on top of the crustal rock, thus obscuring the trench.

The subducting plate warms and becomes less brittle as it sinks. Eventually, it becomes so ductile as to be incapable of producing earthquakes; the greatest recorded earthquake depth of approximately 700 km (435 miles) supports this hypothesis. Portions of the subducting plate melt, producing magma that can rise to the surface to form a line of volcanoes roughly parallel to the subduction zone on the overriding plate.

When plates carrying continents move toward each other, *continental collisions* can lead to the formation of mountain ranges. The Himalayas consist of two crustal layers that have formed as the Australia–Indian plate has collided with the Eurasian plate. Continental collision of the plates carrying Africa and Europe are currently reducing the size of the Mediterranean Sea and will eventually lead to the formation of a collision-type mountain range (McKenzie, 1970).

2.3.2.3 Transform Fault Boundaries

Transform faults occur where plates move past each other without creating new crust or consuming old crust. They are usually found offsetting spreading ridges as illustrated in Figure 2.15. These transform faults are identified by offsets in magnetic anomalies and, where preserved, scarps on the surface of the crust. Magnetic anomaly offsets defining *fracture zones* may be observed over thousands of kilometers; however, it is only the segment of the fracture zone between the spreading ridges that is referred to as the transform fault. As illustrated in Figure 2.15, the motion on the portions of the fracture zone that extend beyond the transform fault is in the same direction on either side of the fracture zone; hence there is generally no relative motion. These inactive portions of the fracture zone can be viewed as fossil faults that are not producing earthquakes.

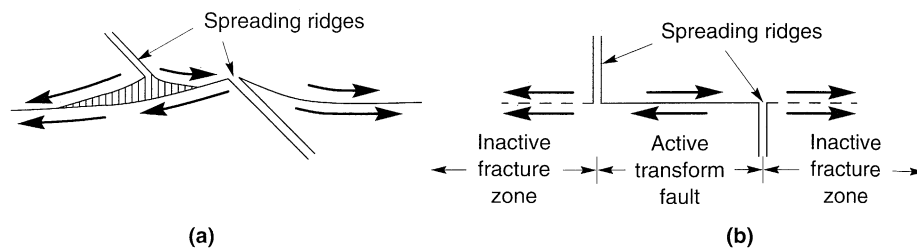


Figure 2.15 (a) Oblique and (b) plan views of transform fault and adjacent inactive fracture zones.

The San Andreas fault, for example, has been characterized as a transform fault (Wilson, 1965) connecting the East Pacific ridge off the coast of Mexico with the Juan de Fuca ridge off the coast of Washington state. In reality, the geometry of transform faults is usually quite complex with many bends and kinks, and they are often divided into a number of *fault segments*. Their depth is typically limited but can extend horizontally over very long distances. Other important transform faults include the Motagua fault (which separates the North American and Caribbean plates), the Alpine fault of New Zealand, and the Dead Sea fault system that connects the Red Sea to the Bitlis Mountains of Turkey (Kearey and Vine, 1990).

Plate tectonics provides a very useful framework for understanding and explaining movements on the earth's surface and the locations of earthquakes and volcanoes. Plate tectonics accounts for the formation of new and consumption of old crustal materials in terms of the three types of plate movement illustrated in Figure 2.16. It does not, however, explain all observed tectonic seismicity. For example, it is known that *intraplate earthquakes* (earthquakes that occur within a plate, away from its edges) have occurred on most continents. Well-known North American examples are the series of midplate earthquakes that occurred in the vicinity of New Madrid, Missouri, in 1811–1812, and the 1886 Charleston (South Carolina) earthquake. The 1976 Tangshan (China) and 1993 Marathwada (India) earthquakes are more recent examples of damaging intraplate earthquakes.

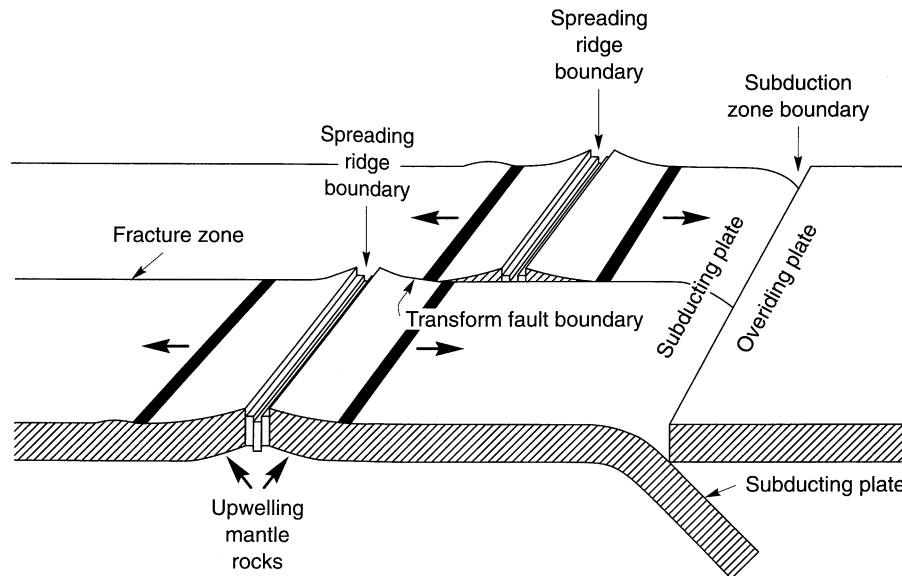


Figure 2.16 Interrelationships among spreading ridge, subduction zone, and transform fault plate boundaries.

2.4 FAULTS

While the theory of plate tectonics generally assigns the relative movement of plates to one of the three preceding types of plate boundaries, examination on a smaller scale reveals that the movement at a particular location can be quite complicated. In some regions, plate boundaries are distinct and easy to identify, while in others they may be spread out with the edges of the plates broken to form smaller *platelets* or *microplates* trapped between the larger plates. Locally, the movement between two portions of the crust will occur on new or preexisting offsets in the geologic structure of the crust known as *faults*.

Faults may range in length from several meters to hundreds of kilometers and extend from the ground surface to depths of several tens of kilometers. Their presence may be obvious, as reflected in surficial topography, or they may be very difficult to detect. The presence of a fault does not necessarily mean that earthquakes can be expected; movement can occur aseismically, or the fault may be inactive. The lack of observable surficial faulting, on the other hand, does not imply that earthquakes cannot occur; in fact, fault rupture does not reach the earth's surface in most earthquakes. The activity of faults is discussed in more detail in Chapter 4.

2.4.1 Fault Geometry

Standard geologic notation is used to describe the orientation of a fault in space. While the surface of a large fault may be irregular, it can usually be approximated, at least over short distances, as a plane. The orientation of the fault plane is described by its *strike* and *dip*. The

strike of a fault is the horizontal line produced by the intersection of the fault plane and a horizontal plane as shown in Figure 2.17. The azimuth of the strike (e.g., N60°E) is used to describe the orientation of the fault with respect to due north. The downward slope of the fault plane is described by the *dip angle*, which is the angle between the fault plane and the horizontal plane measured perpendicular to the strike. A vertical fault would have a dip angle of 90°.

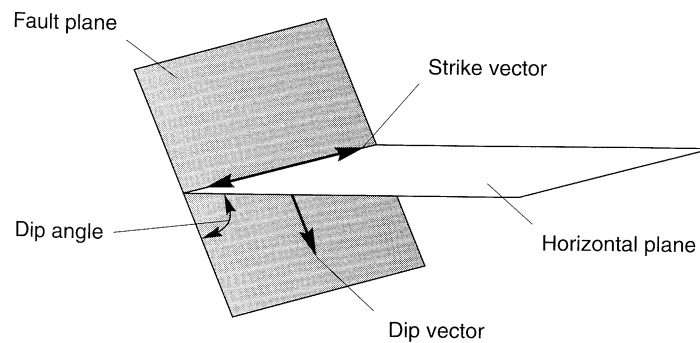


Figure 2.17 Geometric notation for description of fault plane orientation.

2.4.2 Fault Movement

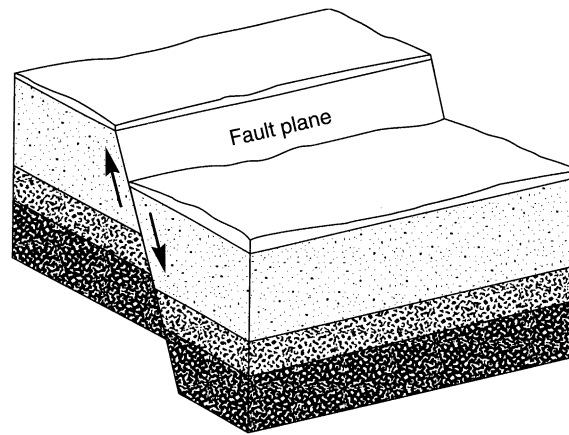
The type of movement occurring on a fault is usually reduced to components in the directions of the strike and dip. While some movement in both directions is inevitable, movement in one direction or the other will usually predominate.

2.4.2.1 Dip Slip Movement

Fault movement that occurs primarily in the direction of the dip (or perpendicular to the strike) is referred to as *dip slip* movement. There are different types of dip slip movements, classified according to the direction of movement and the dip angle of the fault. *Normal faults*, illustrated in Figure 2.18, occur when the horizontal component of dip slip movement is extensional and when the material above the inclined fault (sometimes referred to as the *hanging wall*) moves downward relative to the material below the fault (the *foot wall*). Normal faulting is generally associated with tensile stresses in the crust and results in a horizontal lengthening of the crust. When the horizontal component of dip slip movement is compressional and the material above the fault moves upward relative to the material below the fault, *reverse faulting* is said to have occurred. Movement on reverse faults, illustrated in Figure 2.19, results in a horizontal shortening of the crust. A special type of reverse fault is a *thrust fault*, which occurs when the fault plane has a small dip angle. Very large movements can be produced by thrust faulting; the European Alps are an excellent example of thrust structure.

2.4.2.2 Strike-Slip Movement

Fault movement occurring parallel to the strike is called *strike-slip* movement. *Strike-slip faults* are usually nearly vertical and can produce large movements. Strike-slip faults are further categorized by the relative direction of movement of the materials on either side of the fault. An observer standing near a *right lateral strike-slip fault* would observe the ground on



(a)



(b)

Figure 2.18 (a) Normal faulting (after Noson et al., 1988); (b) scarp of the normal fault that produced the 1954 Dixie-Fairview earthquake in Nevada (K. Steinbrugge collection; courtesy of EERC, Univ. of California).

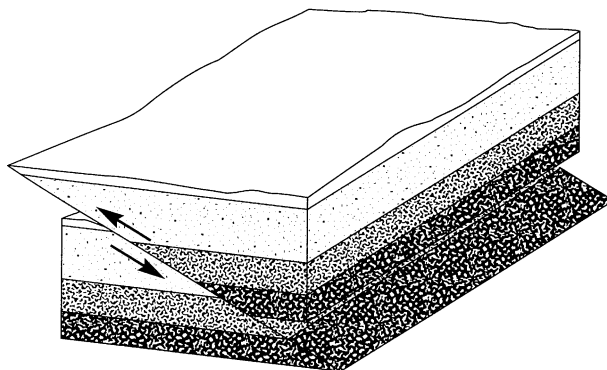


Figure 2.19 Reverse faulting. Because the dip angle is so small, this reverse fault would probably be classified as a thrust fault. (After Noson et al., 1988.)

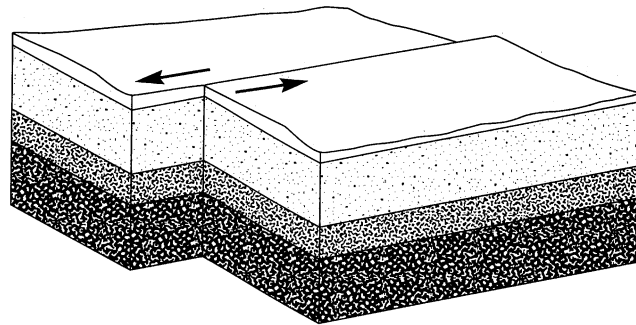
the other side of the fault moving to the right. Similarly, an observer adjacent to a *left lateral strike-slip fault* would observe the material on the other side moving to the left. The strike-slip fault shown in Figure 2.20a would be characterized as a left lateral strike-slip fault. The San Andreas fault in California is an excellent example of right lateral strike-slip faulting; in the 1906 San Francisco earthquake, several roads and fences north of San Francisco were offset by nearly 6 m (20 ft) (Figure 2.20b).

Oblique fault movement (i.e., movement with both dip-slip and strike-slip components) often occurs. The 1971 San Fernando earthquake ruptured the ground surface over a length of 15 km (9 miles). The maximum vertical displacement (produced by reverse fault movement) was 1.46 m (4.8 ft), and the maximum horizontal displacement (from left lateral strike-slip movement) was 2.13 m (7.0 ft) (Berlin, 1980).

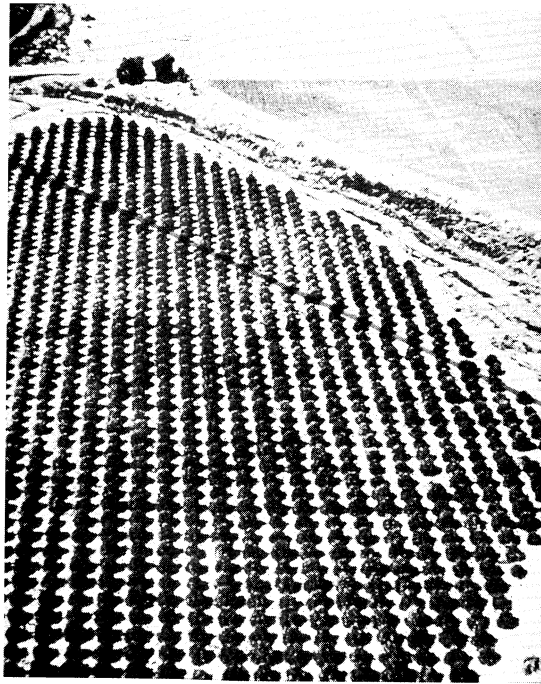
2.5 ELASTIC REBOUND THEORY

The plates of the earth are in constant motion, and plate tectonics indicates that the majority of their relative movement occurs near their boundaries. The long-term effects of this movement can be observed in the geologic record, which reflects deformations that have occurred over very long periods of time. With the advent of modern electronic distance measurement equipment, however, movements can also be observed over much shorter time scales. Figure 2.21 shows a set of survey lines established across the San Andreas and Calaveras faults by the California Department of Water Resources and Division of Mines and Geology. The shortening of chords 17 and 19, and the lengthening of 20 and 23, indicate that fault movement is occurring. Chord 21, which lies entirely east of the Calaveras fault, shows very little change in length.

As relative movement of the plates occurs, *elastic strain energy* is stored in the materials near the boundary as shear stresses increase on the fault planes that separate the plates. When the shear stress reaches the shear strength of the rock along the fault, the rock fails and the accumulated strain energy is released. The effects of the failure depend on the nature of the rock along the fault. If it is weak and ductile, what little strain energy that could be stored



(a)



(b)

Figure 2.20 (a) Left lateral strike-slip faulting (from Noson et al., 1988); (b) trees offset by strike-slip faulting through citrus grove in 1940 Imperial Valley earthquake (courtesy of U.S. Geological Survey).

will be released relatively slowly and the movement will occur aseismically. If, on the other hand, the rock is strong and brittle, the failure will be rapid. Rupture of the rock will release the stored energy explosively, partly in the form of heat and partly in the form of the stress waves that are felt as earthquakes. The theory of *elastic rebound* (Reid, 1911) describes this

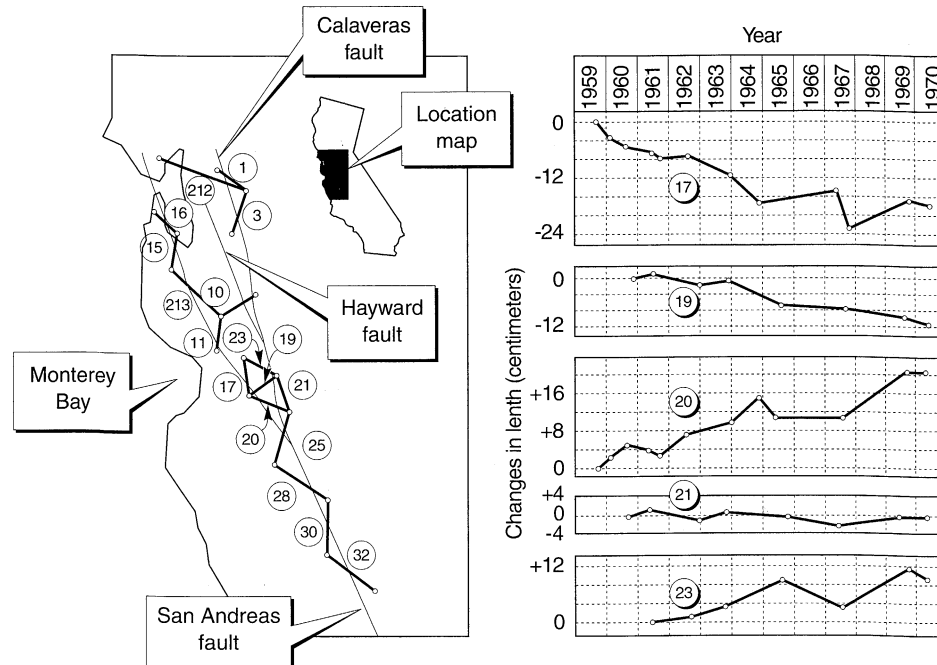


Figure 2.21 (a) Survey lines across San Andreas and Calaveras faults in California; (b) change in chord length (extension positive). (From *Earthquakes* by Bolt. Copyright © 1993 by W.H. Freeman and Company. Used with permission.)

process of the successive buildup and release of strain energy in the rock adjacent to faults. It is often illustrated as shown in Figure 2.22.

The nature of the buildup and release of stress is of interest. Faults are not uniform, either geometrically or in terms of material properties—both strong and weak zones can exist over the surface of a fault. The stronger zones, referred to as *asperities* by some (Kanamori and Stewart, 1978) and *barriers* by others (Aki, 1979), are particularly important. The *asperity model* of fault rupture assumes that the shear stresses prior to an earthquake are not uniform across the fault because of stress release in the weaker zones by creep or *foreshocks*. Release of the remaining stresses held by the asperities produces the main earthquake that leaves the rupture surface in a state of uniform stress. In the *barrier model*, the pre-earthquake stresses on the fault are assumed to be uniform. When the main earthquake occurs, stresses are released from all parts of the fault except for the stronger barriers; *aftershocks* then occur as the rock adjusts to the new uniform stress field. Since both foreshocks and aftershocks are commonly observed, it appears that some strong zones behave as asperities and others as barriers (Aki, 1984). The engineering significance of asperities and barriers lies in their influence on ground-shaking characteristics close to the fault. A site located close to one of these strong zones may experience stronger shaking than a site equally close

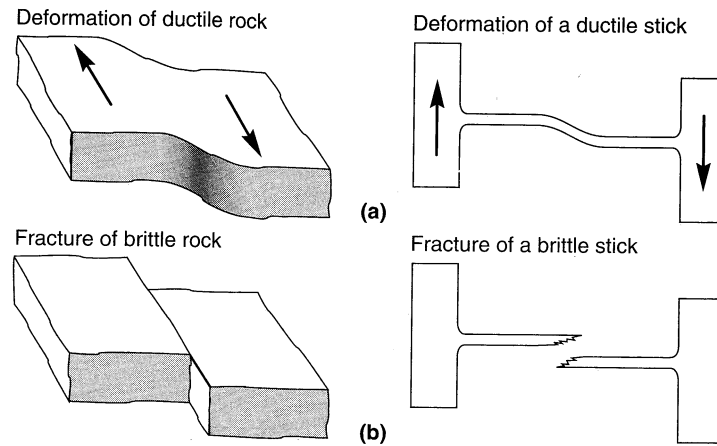


Figure 2.22 Elastic rebound theory of earthquakes. In (a) the slow deformation of rock in the vicinity of a plate boundary results in a buildup of strain energy in the rock in the same way that strain energy builds up in a ductile stick deformed as shown on the right. If the strength of the rock is exceeded, it will rupture, releasing strain energy in the form of vibrations, much as the energy in the stick would be released when the stick breaks. After the earthquake, the rock is displaced from its original position. The total relative displacement of the plates is the sum of the slip displacement at the fault and possible displacements due to warping distortion of the edges of the plates near the fault. (After Foster, R.J., *General Geology*, 5/e, © 1988. Adapted by permission of Prentice Hall, Upper Saddle River, New Jersey.)

to the fault but farther from a strong zone. At larger distances from the fault the effects of fault nonuniformity decrease. Unfortunately, methods for locating these strong zones prior to rupture have not yet been developed.

Rupture generally progresses across a fault as a series of dislocations (some *multiple-event* earthquakes can be thought of as a series of small earthquakes that occur in close spatial and temporal proximity). Small earthquakes can be modeled as point processes since their rupture surfaces usually span only a few kilometers. Large earthquakes, however, can rupture over distances of tens, or even hundreds, of kilometers, and the nature of ground shaking can be influenced by the characteristics of the rupture process. For example, waves emanate from the fault with different strengths in different directions; such *directivity* effects can produce azimuthal differences in ground motion characteristics (Benioff, 1955; Ben-Menachem, 1961). Constructive interference of waves produced by successive dislocations can produce strong pulses of large displacement called *fling* (Figure 2.23) at nearby sites toward which the rupture is progressing (Benioff, 1955; Singh, 1985).

2.5.1 Relationship to Earthquake Recurrence

The theory of elastic rebound implies that the occurrence of earthquakes will relieve stresses along the portion of a fault on which rupture occurs, and that subsequent rupture

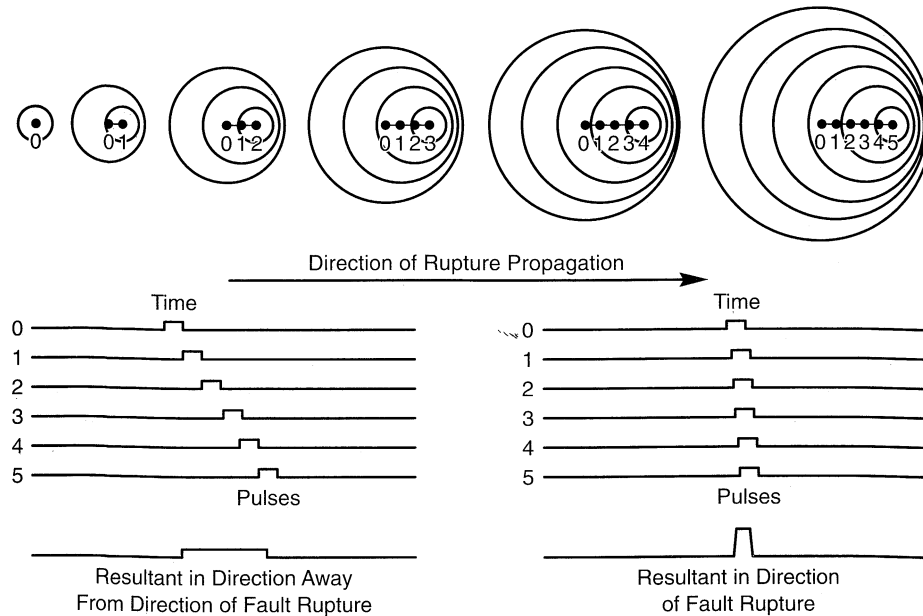


Figure 2.23 Schematic illustration of directivity effect on ground motions at sites toward and away from direction of fault rupture. Overlapping of pulses can lead to strong fling pulse at sites toward which the fault ruptures. (After Singh, 1985; used by permission of EERI).

will not occur on that segment until the stresses have had time to build up again. The chances of an earthquake occurring on a particular fault segment should therefore be related in some way to the time that has elapsed since the last earthquake and, perhaps, to the amount of energy that was released. In a probabilistic sense, then, individual earthquakes on a particular fault segment should not be considered as random, independent events. This characteristic is important in seismic hazard analysis.

Because earthquakes relieve the strain energy that builds up on faults, they should be more likely to occur in areas where little or no seismic activity has been observed for some time. By plotting fault movement and historical earthquake activity along a fault, it is possible to identify *gaps* in seismic activity at certain locations along faults. According to elastic rebound theory, either the movement is occurring aseismically or strain energy is building in the vicinity of these seismic gaps. In areas where the latter is known to be the case, seismic gaps should represent the most likely locations for future earthquakes. A number of seismic gaps have been identified around the world and large earthquakes have subsequently been observed on several of them. The 1989 Loma Prieta earthquake occurred on a segment of the San Andreas fault that had previously been identified as a gap, as shown in Figure 2.24. The use of seismic gaps offers promise for improvement in earthquake prediction capabilities and seismic risk evaluation.

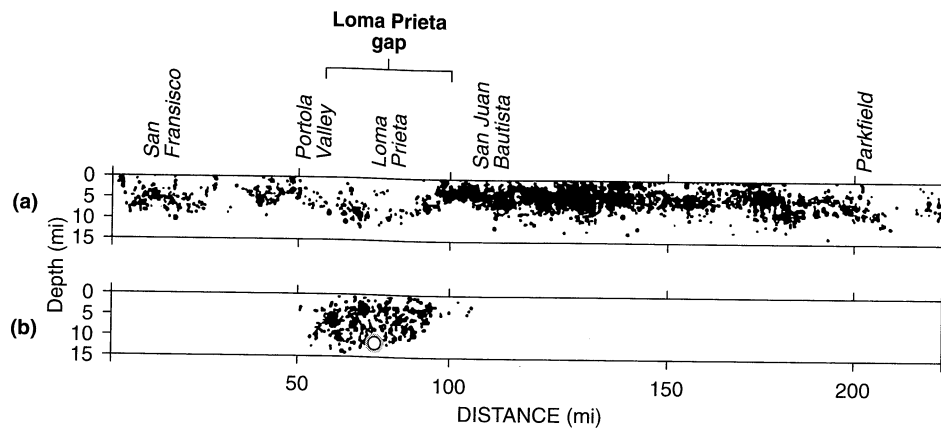


Figure 2.24 Cross section of the San Andreas fault from north of San Francisco to south of Parkfield: (a) seismicity in the 20 years prior to the 1989 Loma Prieta earthquake is shown with the Loma Prieta gap highlighted; (b) main shock (open circle) and aftershocks of the Loma Prieta earthquake. Note the remaining gaps between San Francisco and Portola Valley and south of Parkfield. (After Housner et al., 1990.)

2.5.2 Relationship to Tectonic Environment

Elastic rebound also implies that tectonic environments capable of storing different amounts of energy will produce earthquakes of different size. Consider, for example, the tectonic environment in the vicinity of a spreading ridge plate boundary. First, the crust is thin; hence the volume of rock in which strain energy can build up is small. Second, the horizontal component of the relative plate movement is extensional; hence the normal stress on the fault plane, and with it the rupture strength, is low. Third, the rock is relatively warm and ductile, so it will not release strain energy suddenly. Taken together, these factors limit the total strain energy that can build up and be suddenly released at a spreading ridge boundary. These factors explain the observed absence of very large earthquakes at spreading ridge boundaries.

By the time the oceanic crust has moved from a spreading ridge to a subduction zone, it has cooled and become much thicker and stronger. Relative movement of the plates is toward each other, so high compressive normal stresses increase the rupture strength on the fault plane. Because subduction zone plate boundaries are inclined, the potential rupture area is large. All of these factors support the potential buildup of very large amounts of strain energy that, when suddenly released, can produce great earthquakes. In fact, the largest recorded earthquakes have been produced by subduction zones.

At transform faults, the rock is generally cool and brittle, but large compressive stresses do not usually develop because the faults are often nearly vertical and movement is typically of a strike-slip nature. Because the depth of transform faulting is limited, the total

amount of strain energy that can be stored is controlled by the length of rupture. Very large earthquakes involving rupture lengths of hundreds of kilometers have been observed on transform faults, but truly “great” earthquakes may not be possible.

2.5.3 Seismic Moment

The concept of elastic rebound theory can be used to develop a useful measure of the size of an earthquake. The *seismic moment* of an earthquake is given by

$$M_0 = \mu A \bar{D} \quad (2.1)$$

where μ is the rupture strength of the material along the fault, A the rupture area, and \bar{D} the average amount of slip. The seismic moment is named for its units of force times length; however, it is more a measure of the work done by the earthquake. As such, the seismic moment correlates well with the energy released during an earthquake. The seismic moment can be estimated from geologic records for historical earthquakes, or obtained from the long-period components of a seismogram (Bullen and Bolt, 1985).

2.6 OTHER SOURCES OF SEISMIC ACTIVITY

The sudden release of strain energy by rupture of the rock at plate boundaries is the primary cause of seismic activity around the world. There are, however, other sources of seismic activity that produce smaller earthquakes that may be important in localized regions.

Earthquakes have been associated with volcanic activity. Shallow volcanic earthquakes may result from sudden shifting or movement of magma. In 1975, a magnitude 7.2 earthquake on the big island of Hawaii produced significant damage and was followed shortly by an eruption of the Kilauea volcano. The 1980 eruption of Mt. St. Helens in southern Washington was actually triggered by a small ($M_s = 5.1$), shallow, volcanic earthquake that triggered a massive landslide on the north slope of the volcano. The unloading of the north slope allowed the main eruption to occur approximately 30 sec later. Volcanic eruptions themselves can release tremendous amounts of energy essentially at the earth's surface and may produce significant ground motion.

Seismic waves may be produced by underground detonation of chemical explosives or nuclear devices (Bolt, 1975). Many significant developments in seismology during the Cold War years stemmed from the need to monitor nuclear weapons testing activities of other countries. Collapse of mine or cavern roofs, or *mine bursts*, can cause small local earthquakes, as can large landslides. A 1974 landslide involving $1.6 \times 10^9 \text{ m}^3$ ($2.1 \times 10^9 \text{ yd}^3$) of material along the Montaro River in Peru produced seismic waves equivalent to those of a magnitude 4.5 earthquake (Bolt, 1989).

Reservoir-induced earthquakes have been the subject of considerable study and some controversy. Local seismicity increased significantly after the filling of Lake Mead behind Hoover Dam on the Nevada–Arizona border in 1935. When the Koyna Dam (India) reservoir was filled, local shallow earthquakes became common in an area previously thought to have been virtually aseismic. In 1967, five years after filling of the Koyna reservoir had

begun, a magnitude 6.5 earthquake killed 177 persons and injured more than 2000 more. Local seismicity has been observed to increase seasonally with seasonal increases in reservoir level. In 1975, seven years after the filling of Oroville Dam in an area of low historical seismicity in northern California, a swarm of earthquakes culminated in a magnitude 5.7 main shock. After construction of the High Dam, a magnitude 5.6 earthquake occurred in Aswan, Egypt where very little significant seismic activity had been observed in the 3000-year history of the area. In these cases, seismic activity appears to have been triggered by the presence of the reservoir. While the effect of the weight of the impounded water is likely to be negligible at the depths of the induced seismic activity, an increase in porewater pressure that migrates as a "pulse" away from the reservoir after filling may have been sufficient to reduce the strength of the rock to the point where rupture could occur.

2.7 GEOMETRIC NOTATION

To describe the location of an earthquake, it is necessary to use accepted descriptive terminology. Earthquakes result from rupture of the rock along a fault, and even though the rupture may involve thousands of square kilometers of fault plane surface, it must begin somewhere. The point at which rupture begins and the first seismic waves originate is called the *focus*, or *hypocenter*, of the earthquake (Figure 2.25). From the focus, the rupture spreads across the fault at velocities of 2 to 3 km/sec (1.2 to 1.9 miles/sec) (Bolt, 1989). Although fault rupture can extend to the ground surface, the focus is located at some *focal depth* (or *hypocentral depth*) below the ground surface. The point on the ground surface directly above the focus is called the *epicenter*. The distance on the ground surface between an observer or site and the epicenter is known as the *epicentral distance*, and the distance between the observer and the focus is called the *focal distance* or *hypocentral distance*.

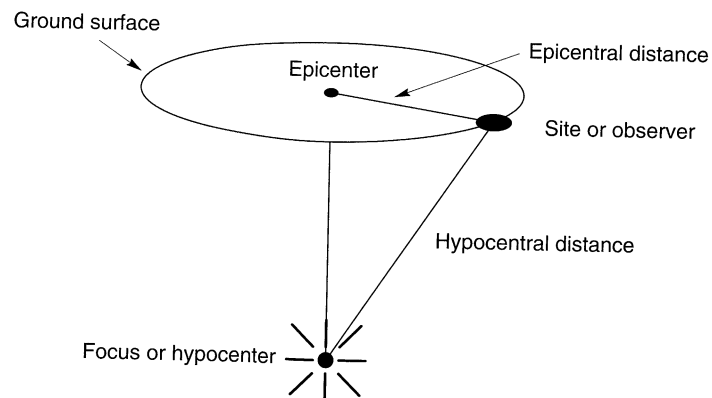


Figure 2.25 Notation for description of earthquake location.

2.8 LOCATION OF EARTHQUAKES

The location of an earthquake is often initially specified in terms of the location of its epicenter. Preliminary epicentral location is a simple and straightforward matter, but refinement of the final location can be considerably more complex. Preliminary location is based on the relative arrival times of p- and s-waves at a set of at least three seismographs.

Since p-waves travel faster than s-waves, they will arrive first at a given seismograph. The difference in arrival times will depend on the difference between the p- and s-wave velocities, and on the distance between the seismograph and the focus of the earthquake, according to

$$d = \frac{\Delta t_{p-s}}{1/v_s - 1/v_p} \quad (2.2)$$

where Δt_{p-s} is the difference in time between the first p- and s-wave arrivals, and v_p and v_s are the p- and s-wave velocities, respectively. In bedrock, p-wave velocities are generally 3 to 8 km/sec (1.9 to 5 miles/sec) and s-wave velocities range from 2 to 5 km/sec (1.2 to 3.1 miles/sec). At any single seismograph it is possible to determine the epicentral distance but not the direction of the epicenter. This limited knowledge is expressed graphically by plotting a circle of radius equal to the epicentral distance. When the epicentral distance from a second seismograph is plotted as a circle about its location, the possible location of the epicenter is narrowed to the two points of intersection of the circles. Obviously, a third seismograph is necessary to identify the most likely location of the epicenter as illustrated in Figure 2.26. More refined estimates of the epicentral, or hypocentral, location are made using multiple seismographs, a three-dimensional seismic velocity model of the earth, and numerical optimization techniques. The accuracy of these techniques depends on the number, quality, and geographic distribution of the seismographs and on the accuracy of the seismic velocity model (Dewey, 1979).

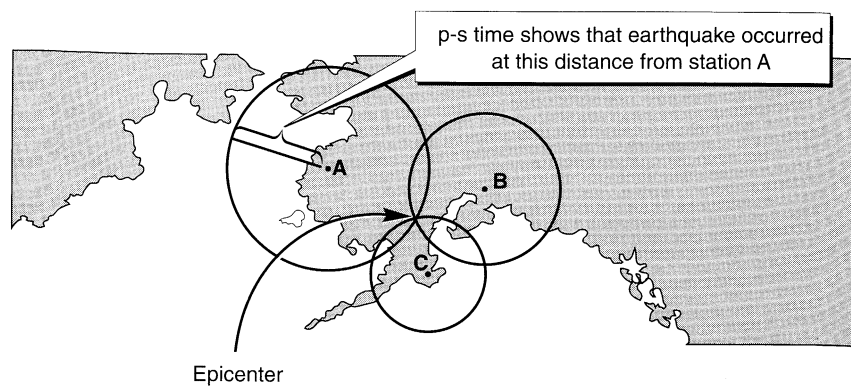


Figure 2.26 Preliminary location of epicenter from differential wave-arrival-time measurements at seismographs A, B, and C. Most likely epicentral location is at the intersection of the three circles. (After Foster, R.J., *General Geology*, 5e, © 1988. Adapted by permission of Prentice Hall, Upper Saddle River, New Jersey.)

2.9 SIZE OF EARTHQUAKES

The “size” of an earthquake is obviously a very important parameter, and it has been described in different ways. Prior to the development of modern instrumentation, methods for characterizing the size of earthquakes were based on crude and qualitative descriptions of the effects of the earthquakes. More recently, modern seismographs have allowed the development of a number of quantitative measures of earthquake size. Since several of these measures are commonly used in both seismology and earthquake engineering, the distinguishing features of each should be understood.

2.9.1 Earthquake Intensity

The oldest measure of earthquake size is the earthquake *intensity*. The intensity is a qualitative description of the effects of the earthquake at a particular location, as evidenced by observed damage and human reactions at that location. Because qualitative descriptions of the effects of earthquakes are available throughout recorded history, the concept of intensity can be applied to historical accounts to estimate the locations and sizes of earthquakes that occurred prior to the development of modern seismic instruments (*preinstrumental* earthquakes). This application has been very useful in characterizing the rates of recurrence of earthquakes of different sizes in various locations, a critical step in evaluation of the likelihood of seismic hazards. Intensities can also be used to estimate strong ground motion levels (Section 3.3.1.1), for comparison of earthquake effects in different geographic regions, and for earthquake loss estimation.

The Rossi–Forel (RF) scale of intensity, describing intensities with values ranging from I to X, was developed in the 1880s and used for many years. It has largely been replaced in English-speaking countries by the modified Mercalli intensity (MMI) scale originally developed by the Italian seismologist Mercalli and modified in 1931 to better represent conditions in California (Richter, 1958). The MMI scale is illustrated in Table 2-1. The qualitative nature of the MMI scale is apparent from the descriptions of each intensity level.

The Japanese Meteorological Agency (JMA) has its own intensity scale, and the Medvedev–Spoonheuer–Karnik (MSK) scale is used in central and eastern Europe. A comparison of the RF, MMI, JMA, and MSK scales is shown in Figure 2.27.

Earthquake intensities are usually obtained from interviews of observers after the event. The interviews are often done by mail, but in some seismically active areas, permanent observers are organized and trained to produce rational and unemotional accounts of ground shaking. Since human observers and structures are scattered more widely than any seismological observatory could reasonably hope to scatter instruments, intensity observations provide information that helps characterize the distribution of ground shaking in a region. A plot of reported intensities at different locations on a map allows contours of equal intensity, or *isoseisms*, to be plotted. Such a map is called an *isoseismal map* (Figure 2.28). The intensity is generally greatest in the vicinity of the epicenter of the earthquake, and the term *epicentral intensity* is often used as a crude description of earthquake size. Isoseismal maps show how the intensity decreases, or attenuates, with increasing epicentral distance.



Table 2-1 Modified Mercalli Intensity Scale of 1931

I	Not felt except by a very few under especially favorable circumstances
II	Felt by only a few persons at rest, especially on upper floors of buildings; delicately suspended objects may swing
III	Felt quite noticeably indoors, especially on upper floors of buildings, but many people do not recognize it as an earthquake; standing motor cars may rock slightly; vibration like passing of truck; duration estimated
IV	During the day felt indoors by many, outdoors by few; at night some awakened; dishes, windows, doors disturbed; walls make cracking sound; sensation like heavy truck striking building; standing motor cars rocked noticeably
V	Felt by nearly everyone, many awakened; some dishes, windows, etc., broken; a few instances of cracked plaster; unstable objects overturned; disturbances of trees, piles, and other tall objects sometimes noticed; pendulum clocks may stop
VI	Felt by all, many frightened and run outdoors; some heavy furniture moved; a few instances of fallen plaster or damaged chimneys; damage slight
VII	Everybody runs outdoors; damage negligible in buildings of good design and construction, slight to moderate in well-built ordinary structures, considerable in poorly built or badly designed structures; some chimneys broken; noticed by persons driving motor cars
VIII	Damage slight in specially designed structures, considerable in ordinary substantial buildings, with partial collapse, great in poorly built structures; panel walls thrown out of frame structures; fall of chimneys, factory stacks, columns, monuments, walls; heavy furniture overturned; sand and mud ejected in small amounts; changes in well water; persons driving motor cars disturbed
IX	Damage considerable in specially designed structures; well-designed frame structures thrown out of plumb; great in substantial buildings, with partial collapse; buildings shifted off foundations; ground cracked conspicuously; underground pipes broken
X	Some well-built wooden structures destroyed; most masonry and frame structures destroyed with foundations; ground badly cracked; rails bent; landslides considerable from river banks and steep slopes; shifted sand and mud; water splashed over banks
XI	Few, if any (masonry) structures remain standing; bridges destroyed; broad fissures in ground; underground pipelines completely out of service; earth slumps and land slips in soft ground; rails bent greatly
XII	Damage total; practically all works of construction are damaged greatly or destroyed; waves seen on ground surface; lines of sight and level are distorted; objects thrown into the air

2.9.2 Earthquake Magnitude

The possibility of obtaining a more objective, quantitative measure of the size of an earthquake came about with the development of modern instrumentation for measuring ground motion during earthquakes. In the past 60 years, the development of seismic instruments, and our understanding of the quantities they measure, have increased dramatically. Seismic instruments allow an objective, quantitative measurement of earthquake size called *earthquake magnitude* to be made. Most measurements of earthquake magnitude are instrumental (i.e., based on some measured characteristic of ground shaking).

MMI	I	II	III	IV	V	VI	VII	VIII	IX	X	XI	XII
RF	I	II	III	IV	V	VI	VII	VIII	IX	X		
JMA	I		II	III	IV	V	VI	VII				
MSK	I	II	III	IV	V	VI	VII	VIII	IX	X	XI	XII

Figure 2.27 Comparison of intensity values from modified Mercalli (MMI), Rossi-Forel (RF), Japanese Meteorological Agency (JMA), and Medvedev-Spoonheuer-Karnik (MSK) scales. (After Richter (1958) and Murphy and O'Brien (1977).)

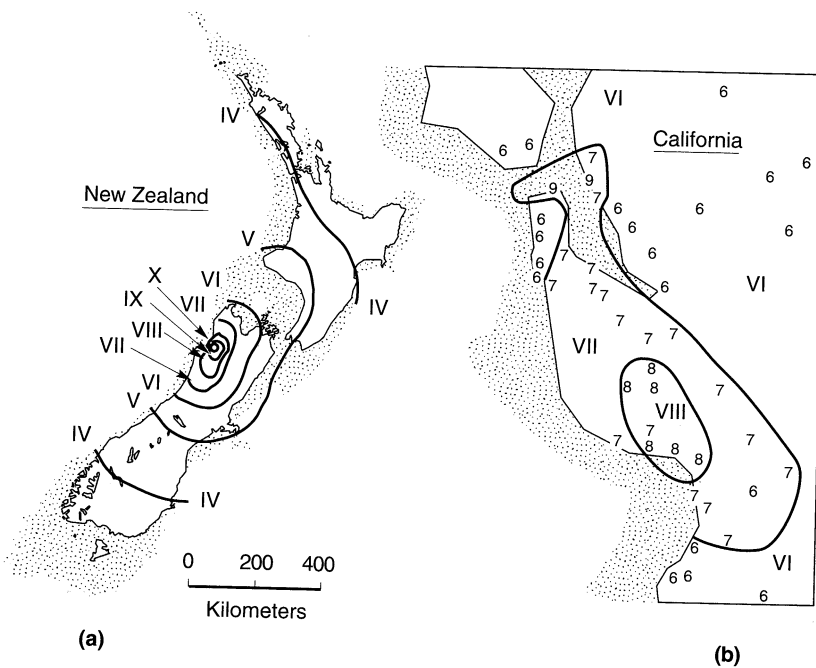


Figure 2.28 Isoseismal maps from (a) the 1968 Inangahua earthquake in New Zealand (After Eiby, 1980) and (b) the 1989 Loma Prieta earthquake in northern California (Modified Mercalli intensities). (After Housner, 1990.)

2.9.2.1 Richter Local Magnitude

In 1935, Charles Richter used a Wood–Anderson seismometer to define a *magnitude* scale for shallow, local (epicentral distances less than about 600 km (375 miles)) earthquakes in southern California (Richter, 1935). Richter defined what is now known as the *local magnitude* as the logarithm (base 10) of the maximum trace amplitude (in micrometers) recorded on a Wood–Anderson seismometer located 100 km (62 miles) from the epicenter of the earthquake. The Richter local magnitude (M_L) is the best known magnitude scale, but it is not always the most appropriate scale for description of earthquake size.

2.9.2.2 Surface Wave Magnitude

The Richter local magnitude does not distinguish between different types of waves. Other magnitude scales that base the magnitude on the amplitude of a particular wave have been developed. At large epicentral distances, body waves have usually been attenuated and scattered sufficiently that the resulting motion is dominated by surface waves. The *surface wave magnitude* (Gutenberg and Richter, 1936) is a worldwide magnitude scale based on the amplitude of Rayleigh waves with a period of about 20 sec. The surface wave magnitude is obtained from

$$M_s = \log A + 1.66 \log \Delta + 2.0 \quad (2.3)$$

where A is the maximum ground displacement in micrometers and Δ is the epicentral distance of the seismometer measured in degrees (360° corresponding to the circumference of the earth). Note that the surface wave magnitude is based on the maximum ground displacement amplitude (rather than the maximum trace amplitude of a particular seismograph); therefore, it can be determined from any type of seismograph. The surface wave magnitude is most commonly used to describe the size of shallow (less than about 70 km (44 miles) focal depth), distant (farther than about 1000 km (622 miles)) moderate to large earthquakes.

2.9.2.3 Body Wave Magnitude

For deep-focus earthquakes, surface waves are often too small to permit reliable evaluation of the surface wave magnitude. The *body wave magnitude* (Gutenberg, 1945) is a worldwide magnitude scale based on the amplitude of the first few cycles of p-waves which are not strongly influenced by the focal depth (Bolt, 1989). The body wave magnitude can be expressed as

$$m_b = \log A - \log T + 0.01 \Delta + 5.9 \quad (2.4)$$

where A is the p-wave amplitude in micrometers and T is the period of the p-wave (usually about one sec). Body wave magnitude can also be estimated from the amplitude of one-second-period, higher-mode Rayleigh waves (Nuttli, 1973); the resulting magnitude, m_{bLg} , is commonly used to describe intraplate earthquakes.

2.9.2.4 Other Instrumental Magnitude Scales

Magnitude scales using different parts of the instrumental record have also been proposed. The *coda* of an earthquake motion are the backscattered waves (Aki, 1969) that follow passage of the primary (unreflected) body and surface waves. Aki (1969), showing that certain characteristics of the coda are independent of the travel path, developed a *coda magnitude*, M_c , that could be obtained from those characteristics. The duration magnitude,

M_D , which is based on the total duration of the earthquake, can be used to describe small earthquakes that are often of more interest to seismologists than engineers (Real and Teng, 1973). The Japanese Meteorological Agency uses long-period waves to determine a local magnitude scale, M_{JMA} , for Japanese earthquakes.

2.9.2.5 Moment Magnitude

It is important to realize that the previously described magnitude scales are empirical quantities based on various instrumental measurements of ground-shaking characteristics. As the total amount of energy released during an earthquake increases, however, the ground-shaking characteristics do not necessarily increase at the same rate. For strong earthquakes, the measured ground-shaking characteristics become less sensitive to the size of the earthquake than for smaller earthquakes. This phenomenon is referred to as *saturation*; the body wave and Richter local magnitudes saturate at magnitudes of 6 to 7 and the surface wave magnitude saturates at about $M_s = 8$. To describe the size of very large earthquakes, a magnitude scale that does not depend on ground-shaking levels, and consequently does not saturate, would be desirable. The only magnitude scale that is not subject to saturation is the *moment magnitude* (Kanamori, 1977; Hanks and Kanamori, 1979) since it is based on the seismic moment, which is a direct measure of the factors that produce rupture along the fault. The moment magnitude is given by

$$M_w = \frac{\log M_0}{1.5} - 10.7 \quad (2.5)$$

where M_0 is the seismic moment (Section 2.5.3) in dyne-cm.

The relationship between the various magnitude scales can be seen in Figure 2.29. Saturation of the instrumental scales is indicated by their flattening at higher magnitude

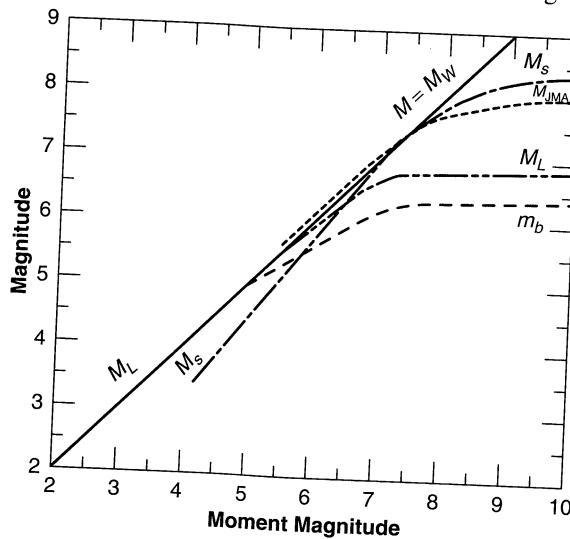


Figure 2.29 Saturation of various magnitude scales: M_w (moment magnitude), M_L (Richter local magnitude), M_s (surface wave magnitude), m_b (short-period body wave magnitude), m_B (long-period body wave magnitude), and M_{JMA} (Japanese Meteorological Agency magnitude). (After Idriss, 1985.)

values. As an example of the effects of magnitude saturation, both the 1906 San Francisco and 1960 Chile earthquakes produced ground shaking that led to surface wave magnitudes of 8.3, even though the sizes of their rupture surfaces, illustrated by the shaded areas in Figure 2.30, were vastly different. The great disparity in energy release was, however, reflected in the moment magnitudes of the earthquakes: 7.9 for San Francisco and 9.5 for Chile.

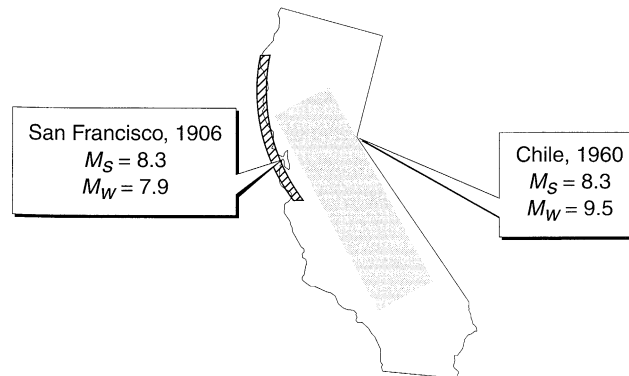


Figure 2.30 Comparison of relative areas of fault rupture (shaded) and magnitudes for 1906 San Francisco and 1960 Chile earthquakes. Although the shaking of both earthquakes produced surface wave magnitudes of 8.3, the amounts of energy released were very different, as reflected in their moment magnitudes. (After Boore, 1977. The motion of the ground during earthquakes, *Scientific American*, Vol. 237, No. 6, used with permission.)

Bolt (1989) suggests that M_L or m_b be used for shallow earthquakes of magnitude 3 to 7, M_s for magnitudes 5 to 7.5, and M_w for magnitudes greater than 7.5.

2.9.3 Earthquake Energy

The total seismic energy released during an earthquake is often estimated from the relationship (Gutenberg and Richter, 1956)

$$\log E = 11.8 + 1.5M_s \quad (2.6)$$

where E is expressed in ergs. This relationship was later shown (Kanamori, 1983) to be applicable to moment magnitude as well. It implies that a unit change in magnitude corresponds to a $10^{1.5}$ or 32-fold increase in seismic energy. A magnitude 5 earthquake therefore would release only about 0.001 times the energy of a magnitude 7 earthquake, thereby illustrating the ineffectiveness of small earthquakes in relieving the buildup of strain energy that causes very large earthquakes. Combining equations (2.5) and (2.6) (using M_w) shows that the amount of energy released during an earthquake is proportional to the seismic moment.

The amount of energy released by earthquakes is often difficult to comprehend; although a single erg is small (1 erg = 7.5×10^{-8} ft-lb), the energy released in an atomic bomb of the size used at Hiroshima (20,000-ton TNT equivalent) would correspond to a magnitude 6.0 earthquake. On that basis, the 1960 Chile earthquake ($M_w = 9.5$) released as much energy as 178,000 such atomic bombs (Figure 2.31).

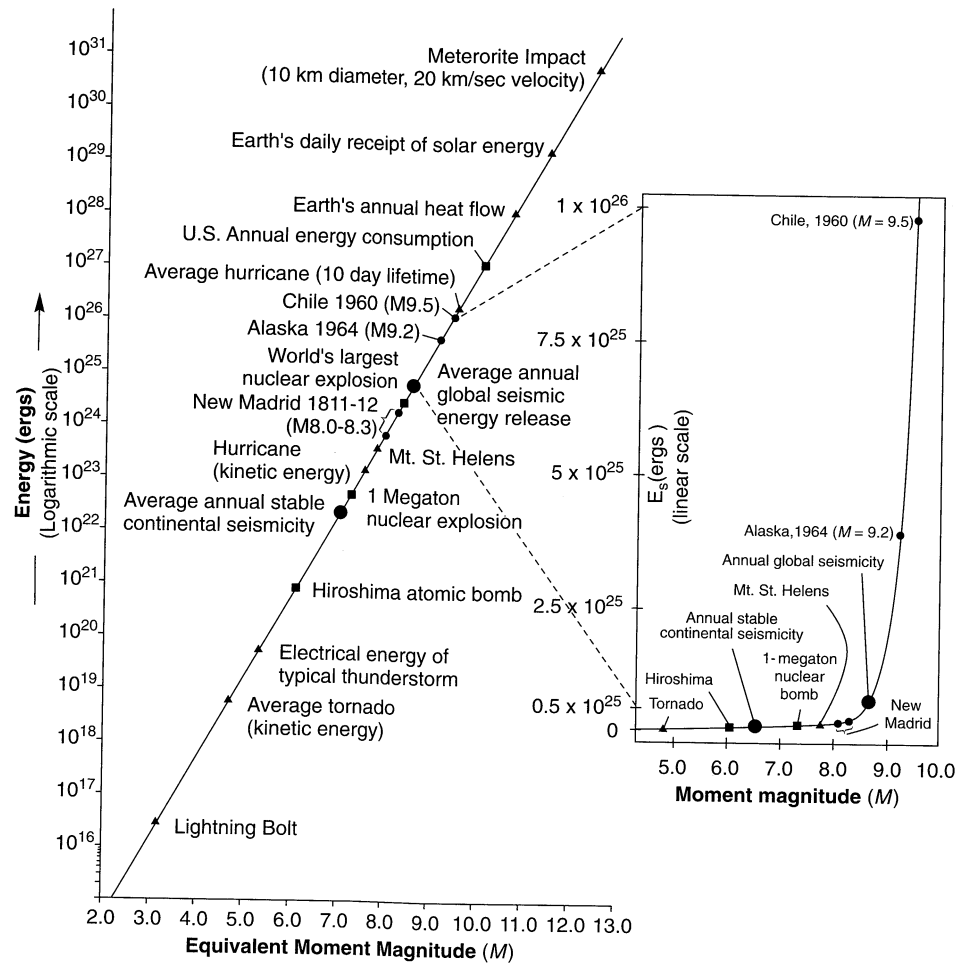


Figure 2.31 Relative energy of various natural and human-made phenomena. (After Johnston, 1990. Reprinted by permission of USGS.)

2.10 SUMMARY

1. The earth has a layered structure—the surficial crust is underlain in turn by the mantle, the outer core, and the inner core. The temperature of each layer increases with depth. The temperature gradient in the mantle causes the semimolten rock to move slowly by convection.
2. The crust is broken into a number of large plates and smaller platelets. Shear stresses on the bottoms of the plates, caused by lateral movement of the convecting mantle, and gravitational forces cause the plates to move with respect to each other.
3. Relative movement of the plates causes stresses to build up on their boundaries. As movement occurs, strain energy accumulates in the vicinity of the boundaries. This

energy is eventually dissipated: either smoothly and continuously or in a stick-slip manner that produces earthquakes. The size of an earthquake depends on the amount of energy released.

4. There are three different types of plate boundaries and their characteristics influence the amount of strain energy that can build up near them. As a result, the different types of boundaries have different earthquake capabilities: subduction zone boundaries can produce the largest earthquakes, followed by transform fault boundaries and then spreading ridge boundaries.
5. The surfaces on which relative movements occur are called faults. At a particular location, a fault is assumed to be planar with an orientation described by its strike and dip. Fault movement is divided into dip-slip components (normal and reverse faulting) and strike-slip components (left lateral and right lateral faulting).
6. The energy-releasing function of earthquakes suggests that a period of time for strain energy accumulation should be expected between large earthquakes at the same location. It also suggests that earthquakes should be most likely to occur along portions of a fault for which little seismic activity has been observed—unless the plate movement has occurred aseismically.
7. Earthquake intensity is a qualitative measure of the effects of an earthquake at a particular location. It is related to the size of the earthquake but is also influenced by other factors. Isoleismal maps can be used to describe the spatial variation of intensity for a given earthquake. Because no instrumental measurements are required, historical accounts can be used to estimate intensity values for preinstrumental earthquakes.
8. Earthquake magnitude is a quantitative measure of the size of an earthquake. Most magnitude scales are based on measured ground motion characteristics. The local magnitude is based on the trace amplitude of a particular seismometer, the surface wave magnitude on the amplitude of Rayleigh waves, and the body wave magnitude on the amplitude of p-waves. Because these amplitudes tend to reach limiting values, these magnitude scales may not accurately reflect the size of very large earthquakes. The moment magnitude, which is not obtained from ground motion characteristics, is able to describe the size of any earthquake.
9. Earthquake magnitude scales are logarithmic, hence a unit change in magnitude corresponds to a 10-fold change in the magnitude parameter (ground motion characteristic or seismic moment). The energy released by an earthquake is related to magnitude in such a way that a unit change in magnitude corresponds to a 32-fold change in energy.

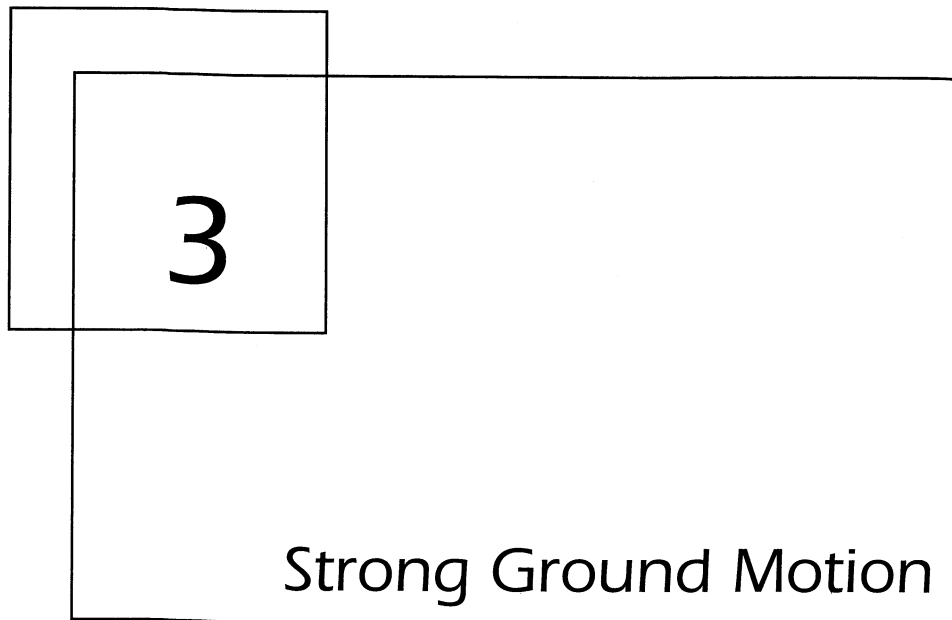
HOMWORK PROBLEMS

- 2.1 Convection caused by thermal gradients in the upper mantle is thought to be a primary cause of continental drift. Estimate the average thermal gradient in the upper mantle.
- 2.2 The coefficient of thermal expansion of the upper mantle is about $2.5 \times 10^{-5}/^{\circ}\text{K}$. Estimate the ratio of the density at the top of the upper mantle to that at the bottom on the upper mantle.

- 2.3 Using the data from Figure 2.21, determine whether the San Andreas and Calaveras faults are undergoing right lateral or left lateral strike slip faulting.
- 2.4 Using the data from Figure 2.21, estimate the average rate of relative movement along the San Andreas and Calaveras faults during the period from 1959 to 1970.
- 2.5 Assuming p- and s-waves traveled through the crust at 6 km/sec and 3 km/sec, respectively, estimate the epicentral location (latitude and longitude) of the hypothetical earthquake whose characteristics are given below:

Seismograph			
Latitude	Longitude	p-wave arrival time	s-wave arrival time
37°22'30"	121°52'30"	06:11:18.93	06:11:26.90
37°45'00"	122°20'00"	06:11:14.84	06:11:18.71
37°52'33"	121°43'38"	06:11:17.26	06:11:23.53

- 2.6 Using a map of California, determine which fault the hypothetical earthquake of Problem 2.5 would most likely have occurred on?
- 2.7 An earthquake causes an average of 2.5 m strike-slip displacement over an 80 km long, 23 km deep portion of a transform fault. Assuming that the rock along the fault had an average rupture strength of 175 kPa, estimate the seismic moment and moment magnitude of the earthquake.



3.1 INTRODUCTION

The earth is far from quiet—it vibrates almost continuously at periods ranging from milliseconds to days and amplitudes ranging from nanometers to meters. The great majority of these vibrations are so weak that they cannot be felt or even detected without specialized measurement equipment. Such *microseismic activity* is of greater importance to seismologists than engineers. Earthquake engineers are interested primarily in *strong ground motion* (i.e., motion of sufficient strength to affect people and their environment). Evaluation of the effects of earthquakes at a particular site requires objective, quantitative ways of describing strong ground motion.

The ground motions produced by earthquakes can be quite complicated. At a given point, they can be completely described by three components of translation and three components of rotation. In practice, the rotational components are usually neglected; three orthogonal components of translational motion are most commonly measured. Typical ground motion records, such as the acceleration-time histories shown in Figure 3.1, contain a tremendous amount of information. To express all of this information precisely (i.e., to reproduce each of the three time histories exactly), every twist and turn in each plot must be described. The motions shown in Figure 3.1, for example, were determined from 2000 acceleration values measured at time increments of 0.02 sec. This large amount of information makes precise description of a ground motion rather cumbersome.

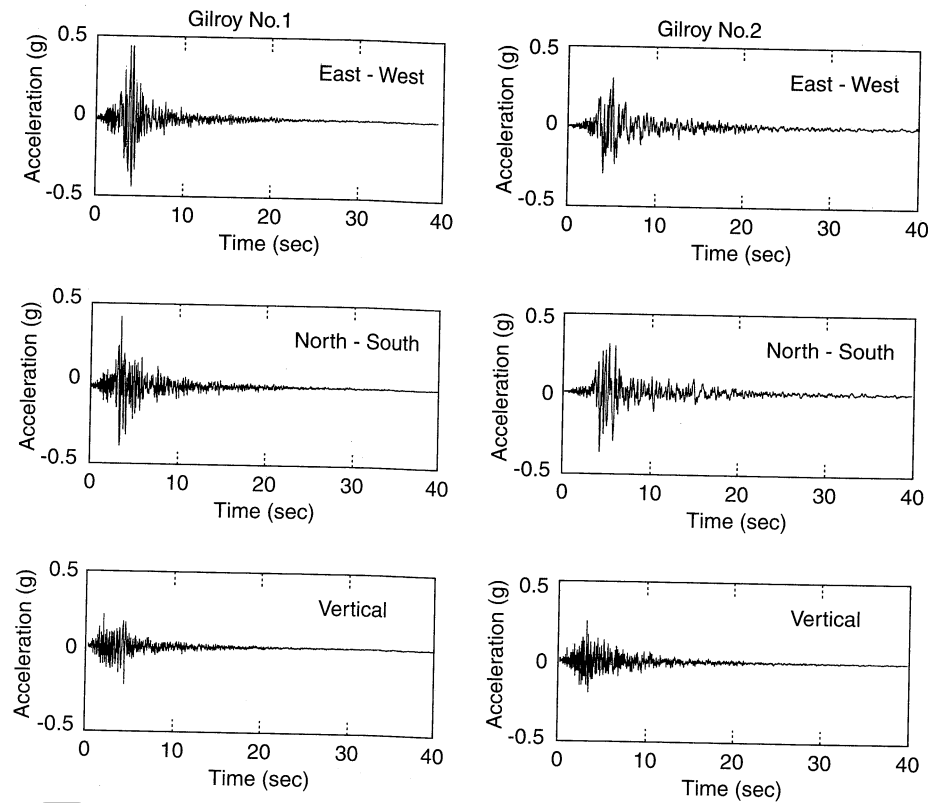


Figure 3.1 Acceleration time histories recorded at two sites in Gilroy, California during the 1989 Loma Prieta earthquake. The Gilroy No. 1 instrument was located on an outcrop of Franciscan sandstone, while the Gilroy No. 2 instrument was underlain by 165 m (540 ft) of stiff, alluvial soils. The Gilroy No. 1 (rock) and Gilroy No. 2 (soil) sites were located at epicentral distances of 21.8 km (13.5 miles) and 22.8 km (14.2 miles), respectively.

Fortunately, it is not necessary to reproduce each time history exactly to describe the ground motion adequately for engineering purposes. It is necessary, however, to be able to describe the characteristics of the ground motion that are of engineering significance and to identify a number of *ground motion parameters* that reflect those characteristics. For engineering purposes, three characteristics of earthquake motion are of primary significance: (1) the amplitude, (2) frequency content, and (3) duration of the motion. A number of different ground motion parameters have been proposed, each of which provides information about one or more of these characteristics. In practice, it is usually necessary to use more than one of these parameters to characterize a particular ground motion adequately.

This chapter describes the instruments and techniques used to measure strong ground motion, and the procedures by which measured motions are corrected. It then presents a variety of parameters that can be used to characterize the amplitude, frequency content, and duration of strong ground motions. Relationships that can be used to predict these parameters are also presented. The chapter concludes with a brief description of the spatial variability of

ground motions. Before proceeding further, the reader should review the topics discussed in Appendices A and B—familiarity with the concepts presented in those appendices is assumed in this chapter and the remainder of the book.

3.2 STRONG-MOTION MEASUREMENT

The identification and evaluation of ground motion parameters requires access to measurements of strong ground motions in actual earthquakes. Accurate, quantitative measurement of strong ground motion is critical for both seismological and earthquake engineering applications. As stated by the National Research Council Committee on Earthquake Engineering Research (Housner, 1982): “The recording of strong ground motion provides the basic data for earthquake engineering. Without a knowledge of the ground shaking generated by earthquakes, it is not possible to assess hazards rationally or to develop appropriate methods of seismic design.”

3.2.1 Seismographs

Although written descriptions of earthquakes date back as far as 780 B.C., the first accurate measurements of destructive ground motions were made during the 1933 Long Beach, California earthquake (Hudson, 1984). Measurement of ground motion has advanced considerably since then, most rapidly in the past 20 years or so.

Various instruments are available for ground motion measurement. *Seismographs* are used to measure relatively weak ground motion; the records they produce are called *seismograms*. Strong ground motions are usually measured by *accelerographs* and expressed in the form of *accelerograms*. The simplest type of seismograph can be illustrated by a mass–spring–damper single-degree-of-freedom (SDOF) system, as shown in Figure 3.2. A rotating drum is connected to the seismograph housing with a stylus attached to a mass. The mass is connected to the housing by a spring and dashpot arranged in parallel, and the housing is connected to the ground. Since the spring and dashpot are not rigid, the motion of the mass will not be identical to the motion of the ground during an earthquake. The relative movement of the mass and the ground will be indicated by the trace made by the stylus on

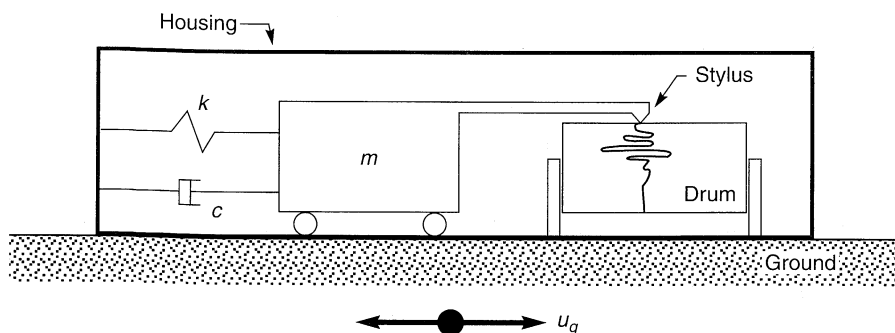


Figure 3.2 Simple mass–spring–dashpot type of seismograph. The housing is firmly connected to the ground. When the ground shakes, the stylus marks a trace on the rotating drum that shows the relative displacement between the mass and the ground. Most modern instruments are more complicated than the one shown here.

the rotating drum. A typical seismograph station may have three seismographs oriented to record motion in the vertical and two perpendicular horizontal directions.

Seismographs can be designed to measure various ground motion characteristics. To understand how this can be done it is necessary to consider the dynamic response of a simple seismograph such as the one shown in Figure 3.2. This seismograph is a SDOF oscillator whose response to shaking is given by the equation of motion (Appendix B)

$$m\ddot{u} + c\dot{u} + ku = -m\ddot{u}_g \quad (3.1)$$

where u is the seismograph trace displacement (the relative displacement between the seismograph and the ground) and u_g is the ground displacement.

If the ground displacement is simple harmonic at a circular frequency ω_g , the displacement response ratio (the ratio of trace displacement amplitude to ground displacement amplitude) will be

$$\frac{|u|}{|u_g|} = \frac{\beta^2}{\sqrt{(1 - \beta^2)^2 + (2\xi\beta)^2}} \quad (3.2)$$

where $\beta (= \omega_g/\omega_0)$ is the *tuning ratio*, $\omega_0 (= \sqrt{k/m})$ is the *undamped natural circular frequency*, and $\xi (= c/2\sqrt{km})$ is the *damping ratio*. Figure 3.3a shows how the displacement response ratio varies with frequency and damping. For ground motion frequencies well above the natural frequency of the seismograph (i.e., large values of β), the trace amplitude is equal to the ground motion amplitude. The lowest frequency for which this equality holds (within a given range of accuracy) depends on the damping ratio. Because the frequency response is flat and phase angles are preserved at damping ratios of 60%, SDOF displacement seismographs are usually designed with damping ratios in that range (Richart et al., 1970).

Similarly, the acceleration response ratio (the ratio of trace displacement amplitude to ground acceleration amplitude) is given by

$$\frac{|u|}{|\ddot{u}_g|} = \frac{1}{\omega_0^2 \sqrt{(1 - \beta^2)^2 + (2\xi\beta)^2}} \quad (3.3)$$

The variation of acceleration response ratio with frequency and damping is shown in Figure 3.3b. The trace amplitude is proportional to the ground acceleration amplitude for frequencies well below the natural frequency of the seismograph (i.e., low values of β). A seismograph with 60% damping will accurately measure accelerations at frequencies up to about 55% of its natural frequency. Most seismographs of this type have natural frequencies of about 25 Hz with damping ratios near 60%, with desirable flat response (constant acceleration response ratio) at frequencies up to about 13 Hz.

The preceding paragraphs show how the same physical system can act as both a displacement seismograph and an accelerograph. It measures displacements at frequencies well above and accelerations at frequencies well below its natural frequency. The Wood-Anderson seismograph, used by Richter to develop the first earthquake magnitude scale, used a small mass suspended eccentrically on a thin tungsten torsion wire. A mirror attached to the wire allowed optical recording with a ground motion magnification of about 3000. Damping was provided electromagnetically at 80% of critical; the damped natural period was about 0.8 sec.

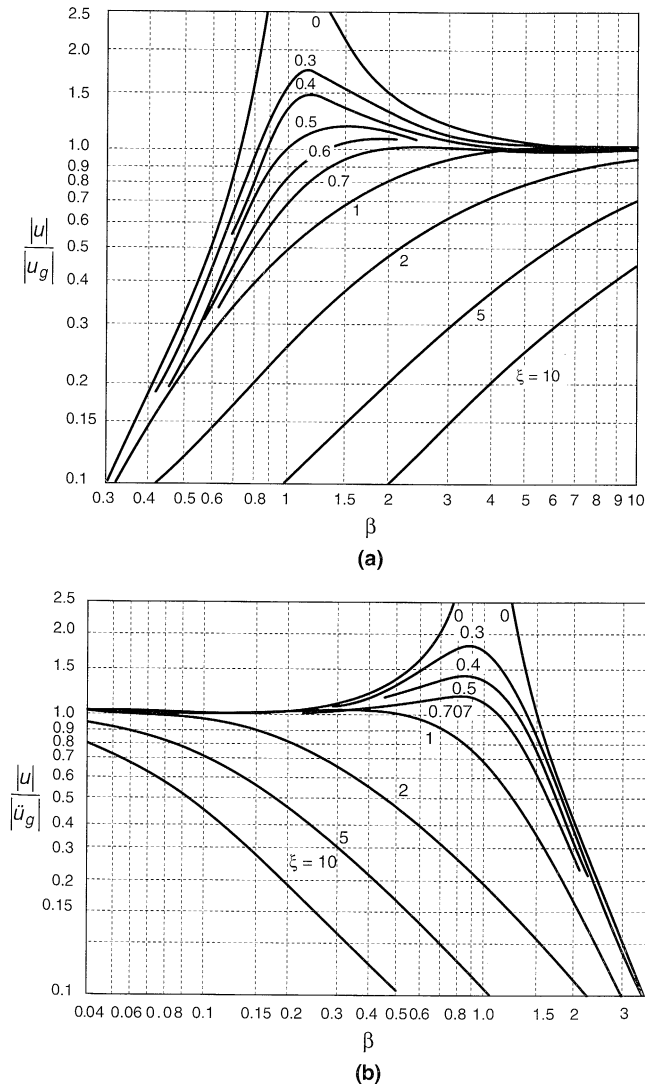


Figure 3.3 (a) Displacement response ratio and (b) acceleration response ratio ($\omega_0 = 1$ rad/sec) for SDOF system subjected to simple harmonic base motion.

In most modern seismographs, an electronic transducer often referred to as a *seismometer* senses the motion and produces an analog (continuous) electrical signal that is recorded for subsequent processing. Most accelerographs currently in use are *accelerometers*, electronic transducers that produce an output voltage proportional to acceleration. A number of different types of accelerometers are available. *Servo* (or *force balance*) accelerometers use a suspended mass to which a displacement transducer is attached. When the housing is accelerated, the signal produced by the relative displacement between the

housing and mass is used to generate a restoring force that pushes the mass back toward its equilibrium position. The restoring force is proportional to the acceleration and can be measured electronically. Servo accelerometers can provide very good accuracy over the range of frequencies of greatest interest in earthquake engineering. *Piezoelectric accelerometers* use a mass attached to a piezoelectric material (usually quartz, tourmaline, or a ferroelectric ceramic) to sense accelerations. The piezoelectric material acts as the spring in the diagram of Figure 3.2; damping is generally negligible. When accelerated, the inertial force of the mass strains the piezoelectric material, which develops an electrical charge on its surfaces. The resulting voltage is (if the dielectric constant does not vary with charge) proportional to acceleration. Because piezoelectric materials are quite stiff, their natural frequencies are very high, so they are particularly useful for high-frequency measurements. Their response at low frequencies, however, can be strongly influenced by signal conditioning system characteristics. Triaxial accelerometers, in which three orthogonal components of acceleration are measured with a common time base, are commonly used. From the three components, the acceleration in any direction can be computed. Some seismographs use velocity transducers, or *geophones*, in addition or as an alternative to accelerometers.

Seismographs, accelerographs, and ancillary equipment are protected by an instrument shelter (Figure 3.4). An important component of a seismograph or accelerograph is an accurate clock, particularly when more than one component of motion is measured or when the ground motion at one location is being compared with that at another. Most modern instruments maintain time accuracy by synchronizing on a daily basis with radio time signals transmitted by a standard time service or by recording such signals along with the ground-motion data. Universal Coordinated Time (the scientific equivalent of Greenwich Mean Time) is used as a common worldwide time basis.

A *seismoscope* (Hudson, 1958) is a relatively inexpensive ground motion instrument. Seismoscopes are conical pendulums (Figure 3.5a) in which a metal stylus attached to a suspended mass inscribes a record of ground motion on a smoked glass plate, producing a two-dimensional record of the type shown in Figure 3.5b. Scott (1972) found that small oscillations of the trace were related to the instrument rather than the earthquake and that they could be used to provide a time scale to the seismoscope trace. The time scale allows accelerograms to be computed from the seismoscope trace.

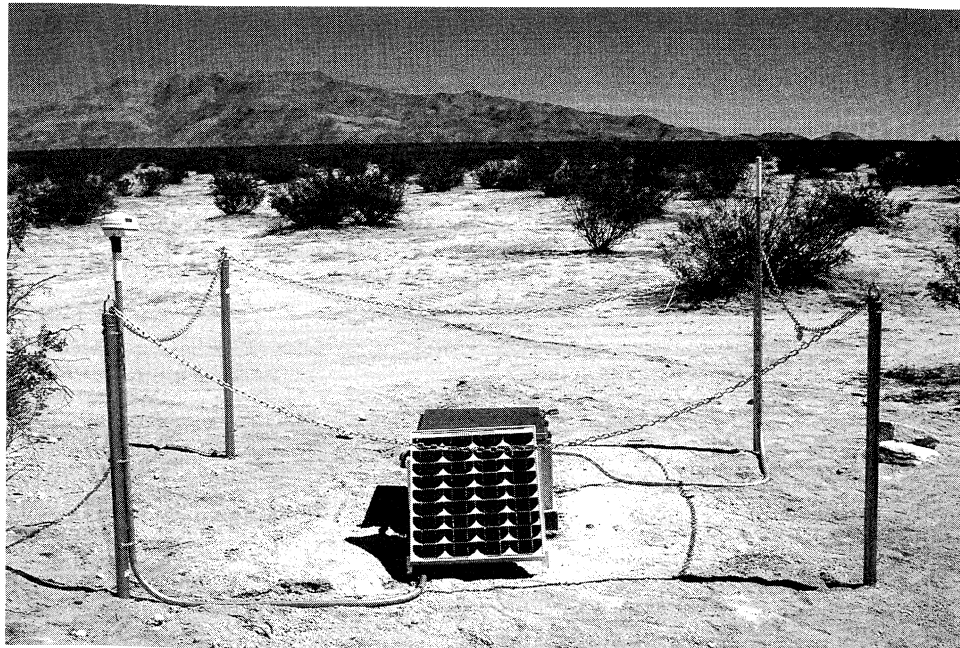
3.2.2 Data Acquisition and Digitization

Early ground motion instruments transformed the motion of the ground to the motion of a physical mechanism. The mechanism, perhaps in the form of a pen or stylus or reflective mirror, caused the motion to be recorded in analog form on paper or photographic film attached to a rotating drum. Later-generation instruments recorded motions electronically in analog form on magnetic tape. Rather than record continuously, instruments of these types lay dormant until triggered by the exceedance of a small threshold acceleration at the beginning of the earthquake motion. As a result, any vibrations that may have preceded triggering were not recorded, thereby introducing a *baseline error* into the acceleration record.

To use the recorded ground motions for engineering computations, the analog ground motion records must be digitized. Originally, digitization was performed manually with paper, pencil, and an engineering scale. Semiautomatic digitizers, with which a user moved a lens with crosshairs across an accelerogram mounted on a digitizing table, were commonly used in the late



(a)



(b)

Figure 3.4 (a) Modern digital strong motion instrument (solar-powered, 16-bit resolution, 250 samples/sec, GPS timing, and cellular modem) mounted in cast-in-place reinforced concrete vault, and (b) completed installation with insulated cover and solar panel (courtesy of Terra Technology Corp, Redmond, Washington).

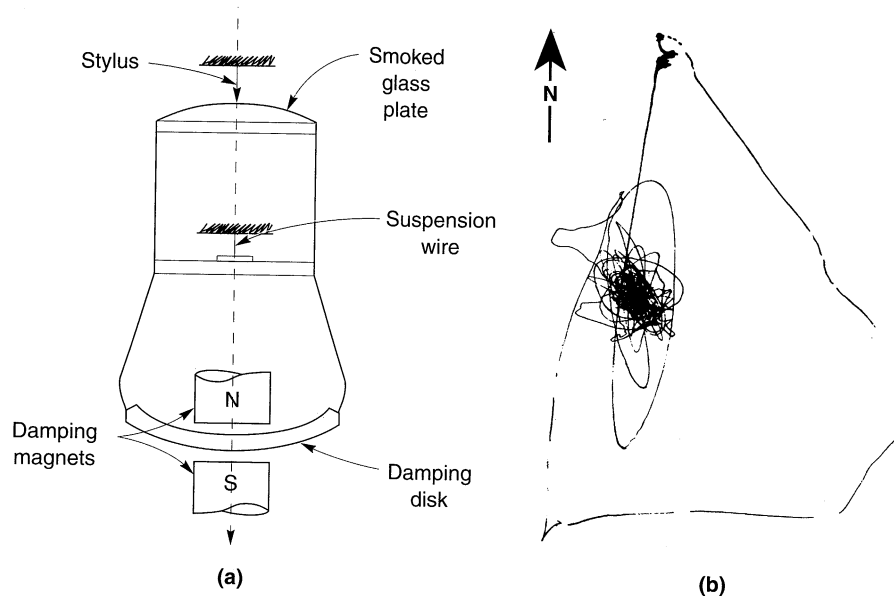


Figure 3.5 (a) Typical Wilmot-type seismoscope in which a fixed stylus scribes a record of relative motion on a smoked glass plate mounted on the suspended seismoscope; (b) typical seismoscope record. (After Newmark and Rosenblueth, 1971.)

1970s. By pressing a foot-operated switch, the coordinates of the crosshairs were recorded. These forms of digitizing involved exacting and tiring work; operator accuracy and fatigue were important considerations (Hudson, 1979). Fully automatic computer-based digitization, typically at sampling rates of 200 or more samples per second, is now commonplace.

In recent years, *digital seismographs* have become much more commonly used. Although they use analog transducers, digital instruments convert the analog signal to digital form in the field. They record ground motions continuously at rates of 200 to 1000 samples/sec with 12- to 16-bit resolution, saving the recorded data only if a triggering acceleration is exceeded. Their on-board memories can typically save 4 to 6 Mb worth of data, from before an earthquake begins until after it ends, thereby preserving the initial portion of the record that is lost with triggered analog systems. Because digital systems are more complex, more expensive, and more difficult to maintain in the field, they have not yet replaced analog systems.

3.2.3 Strong-Motion Processing

The raw data obtained from a strong-motion instrument may include errors from several possible sources, each of which must be carefully evaluated and corrected to produce an accurate record of the actual ground motion. Raw data often include background noise from different sources. Microseisms from ocean waves can be detected by sensitive instruments. Other noise may be caused by traffic, construction activity, wind (transmitted to the ground by vibration of trees, buildings, etc.), and even atmospheric pressure changes. Obviously, this range of sources can produce nonseismic noise at both low and high frequencies. To isolate the motion actually produced by the earthquake, background noise must be removed or at least suppressed.

All accelerographs have their own dynamic response characteristics, or *instrument response*, that can influence the motions they measure. Consequently, instrument response must be corrected for in strong-motion processing. Instrument response corrections are usually performed by modeling the instrument itself as a SDOF system and using the SDOF model to decouple the response of the instrument from the actual ground motion. For most modern accelerographs with flat frequency response up to about 12 to 13 Hz, the instrument correction is only important for frequencies above the usual range of engineering interest. However, some accelerographs are located in buildings (usually on the ground floor or in the basement) or near the abutments of dams or bridges. The motions they record can be affected at frequencies of interest by the response of the structure in or near which they are located. Even the motions recorded by strong motion instruments located in the *free field* (away from the influence of large structures) may be influenced by the response of their instrument shelter (Bycroft, 1978; Crouse et al., 1984), although these effects are usually important only at relatively high frequencies (Crouse and Hushmand, 1989) for typical instrument shelters.

Another correction is required to reduce the effects of errors in ground motion measurement, such as those associated with the triggering of analog seismographs. If a seismograph does not start until some triggering level of motion is reached, the entire accelerogram is in error by the level of motion at the time of triggering. Integration of an uncorrected acceleration time history, for example, will produce a linear error in velocity and a quadratic error in displacement. An acceleration error as small as 0.001g at the beginning of a 30-sec-long accelerogram would erroneously predict a permanent displacement of 441 cm at the end of the motion. Correction of such errors, termed *baseline correction*, was originally accomplished by subtracting a best-fit parabola from the accelerogram before integrating to velocity and displacement but is now performed using high-pass filters and modern data processing techniques (Joyner and Boore, 1988). The motions shown in Figure 3.1, for example, were bandpass filtered to remove frequencies below 0.08 Hz and frequencies above 23 Hz. Computer software for processing strong-ground-motion records (Converse, 1992) is available from the U.S. Geological Survey (USGS).

3.2.4 Strong-Motion Instrument Arrays

Large earthquakes produce ground motions with different characteristics at different points on the ground surface. The spatial variation of ground motion, whether on worldwide, regional, or local scales, is important in both seismology and earthquake engineering. Arrays and networks of strong motion instruments have proven useful in determining the spatial variation of strong ground motion.

3.2.4.1 Worldwide and Regional Arrays

Understanding of earthquake and tectonic processes improved dramatically with the establishment of the *Worldwide Standard Seismograph Network (WWSSN)* in 1961. The WWSSN was originally developed, in large part, to monitor compliance with nuclear weapons testing bans. Before that time, worldwide seismicity data were obtained from a wide variety of very different types of instruments operated by many different organizations. Differences in instruments and operating procedures made comparison of results difficult. WWSSN stations use standardized instruments; each station has at least two three-component analog seismographs to monitor both short- and long-period motions. The capabilities of the WWSSN instruments, however, are limited by modern standards (Aki and Richards,

1980), and they are being replaced by digital instruments such as those of the *Global Digital Seismometer Network* (GDSN) and the *Global Seismographic Network* (GSN). The Incorporated Research Institutions for Seismology (IRIS), a consortium of U.S. and foreign research institutions, oversees operation of the GSN and a set of portable instruments that can be deployed to monitor aftershocks following large earthquakes.

Regional arrays of seismographs are now operating in most seismically active countries. In the United States, for example, the USGS operates regional arrays in different parts of the country. In the California Strong Motion Instrumentation Program (CSMIP), the California Division of Mines and Geology operates an extensive array of free-field seismographs (Figure 3.6) as well as seismographs in buildings and bridges.

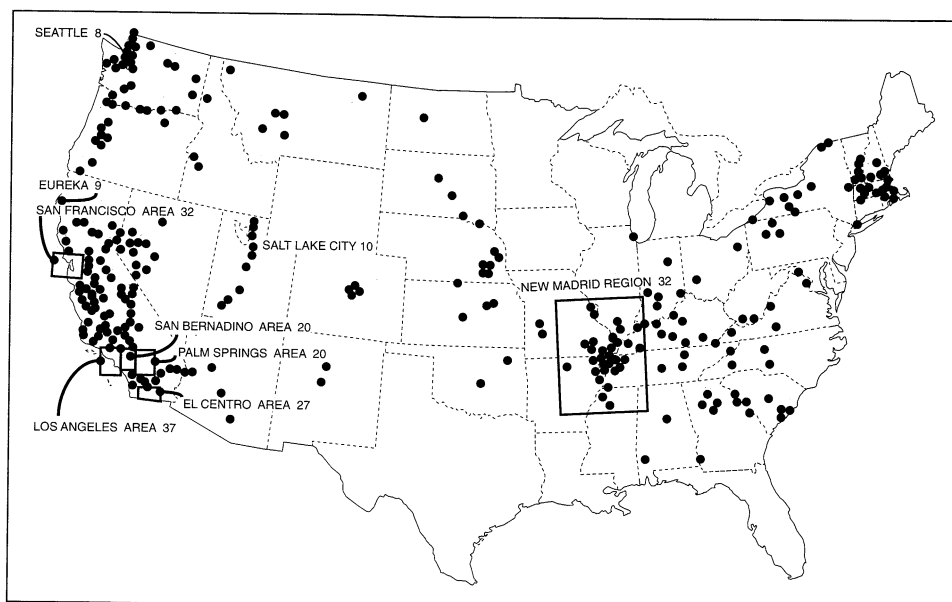


Figure 3.6 Locations of strong motion instruments operated by the U.S. Geological Survey in cooperation with other agencies as of April, 1990. Boxes in northern and southern California indicate areas with high instrument density. (After Joyner and Boore, *Geotechnical News*, March, 1991, p. 24. Used by permission of BiTech Publishers, Ltd..)

3.2.4.2 Local and Dense Arrays

While widely spaced regional and worldwide arrays are useful for studying earthquake mechanisms and the spatial distribution of many important earthquake parameters, geotechnical earthquake engineering often requires spatial distribution information on a smaller areal scale and below the ground surface. In recent years a number of local and dense arrays, some with downhole instrumentation, have been installed at various locations around the world.

Japan has been very active in the installation of local strong-motion instrument arrays. The three-dimensional dense accelerometer array at Chiba (Katayama and Sato, 1982), for example, includes 44 three-component accelerometers, 15 of which are at the ground surface and the remainder at depths of up to 40 m (130 ft.). In Taiwan, the SMART-1 dense accelerometer array near Lotung (Figure 3.7) consists of a central accelerometer surrounded

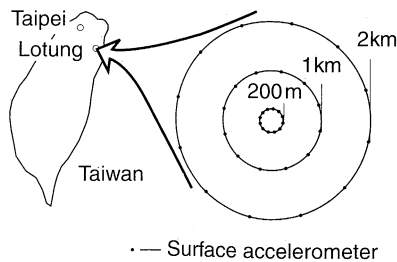


Figure 3.7 Original configuration of SMART-1 array in Lotung, Taiwan.

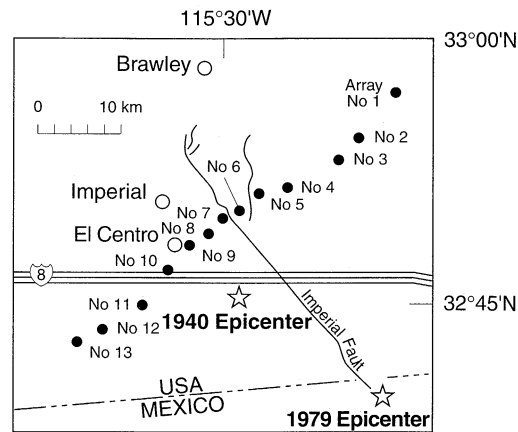


Figure 3.8 The El Centro Array in southern California. The El Centro Differential Array is located near Station 9.

by three rings of 12 accelerometers each at radii of 200 m (650 ft), 1 km (0.6 mi), and 2 km (1.2 mi). A few years after the SMART-1 array was installed, $\frac{1}{4}$ - and $\frac{1}{12}$ -scale models of nuclear containment structures were constructed in its midst (Tang, 1987). The structures were instrumented to record their response during earthquakes, and additional surface and downhole (to depths of 47 m (154 ft)) ground motion instruments were installed adjacent to the $\frac{1}{4}$ -scale model and in the free-field.

In the United States, one of the most important local arrays has been the El Centro Array, a 45-km-long (28 mi) array of 13 stations that crosses the Imperial and Brawley faults in southern California (Figure 3.8). It also contains the El Centro Differential Array, a dense array consisting of six three-component accelerometers along a 305-m (1000 ft) line. Shortly after installation, the arrays recorded the 1979 Imperial Valley earthquake ($M_s = 6.9$), which occurred only 5.6 km away and produced very useful information on near-field ground motions. Near Anza, California, an array of ten three-component stations along a 30-km (19 mi) stretch of the San Jacinto fault was installed to study various earthquake characteristics (Berger et al., 1984). Data are telemetered by digital VHF radio to a nearby mountain peak station and then on to another station in La Jolla, California.

These are but a few of the many strong-motion arrays that have been installed in seismically active countries around the world. The rapid proliferation of local, regional, and worldwide seismograph arrays in recent years has come hand in hand with technological advances in data acquisition, storage, and communication. The ability to acquire and store large quantities of digital seismic data at high speeds, and to retrieve the data from remote locations by telemetry, has and will continue to make such data more plentiful.

3.2.5 Strong-Motion Records

Strong-motion records can now be easily obtained from a number of sources. The U.S. Geological Survey, for example, published a compact disk (Seekins et al., 1992) that contained uncorrected strong motion records from North American earthquakes between 1933 and 1986; more than 4000 records were included. A number of strong-motion databases can be accessed over the Internet, with individual records downloaded by anonymous ftp (file transfer protocol)

procedures. The Gilroy records shown in Figure 3.1 were obtained from the database maintained by the Lamont–Doherty Earth Observatory at Columbia University in conjunction with the National Center for Earthquake Engineering Research at SUNY Buffalo. An example of the information provided with such records is shown in Figure 3.9. A useful World Wide Web site with links to many sources of ground motion and earthquake information is maintained at the University of Washington (<http://www.geophys.washington.edu/seismosurfing.html>). A variety of geotechnical earthquake engineering information can be found at a web site maintained at the University of Southern California (<http://rccg01.usc.edu/eqdata/home.html>).

```

NCEER ASCII STRONG-MOTION DATA FORMAT
EVENT PARAMETERS:
DATE: year=1989 month=10 day=18
TIME: hour|minute (24hr)=0004 second= 2.200 time code=UTC
LOCATION: latitude= 37.03700 longitude= -121.80300 depth (km)= 18.0
NAME: SANTA CRUZ MTNS (LOMA PRIETA) EARTHQUAKE
SITE PARAMETERS:
LOCATION: latitude= 36.97300 longitude= -121.57200 elevation (m)= 0.0
SITE ID: 47379 - GILROY #1 - GAVILAN COLLEGE, WATER TANK
CODE: 47379
RECORD/TRACE PARAMETERS:
START DATE: year=1989 month=10 day=18
START TIME: hour|minute (24hr)=0004 second=23.900 time code=UTC
EPICENTRAL DISTANCE: distance (km)= 21.8 azimuth (deg)=N289.1
SPECS: sampling rate (sec)=0.020
        number of points= 2000
        units=CM/SEC/SEC
        type of data=ACCELERATION
        data format=10F8.2 INTERPOLATED
COMPONENT OF MOTION: azimuth=N0 (HORIZONTAL)
COMMENT: POLARITY OF MOTION RELATIVE TO GROUND
DATA:
-15.68 -3.95 5.46 -3.90 -6.74 9.49 -1.38 -9.81 -0.19 3.15
-3.67 -5.76 7.40 -4.94 -20.14 3.44 11.68 -15.90 2.78 5.54
-8.23 -17.18 -3.88 -4.98 -8.69 15.80 3.82 -20.33 -15.56 -5.71
-0.33 5.18 -9.95 -10.07 -10.64 -3.87 29.66 -2.16 -13.34 -3.92
-22.97 0.31 0.25 14.43 12.96 -23.51 -16.04 15.48 -12.18 -5.45
19.23 -37.29 -15.52 41.53 -23.24 -14.09 37.65 -26.03 -43.07 12.52
26.86 -6.89 -17.72 -20.30 39.13 15.81 -25.54 15.76 -46.07 -25.70
74.64 -31.37 -89.33 24.91 -4.54 8.83 67.54 1.26 -32.89 -42.30
. . . . .
. . . . .
. . . . .

```

Figure 3.9 Event, size, and record information preceding the digitized acceleration data for the Gilroy No. 1 (rock) strong-motion record.

3.3 GROUND MOTION PARAMETERS

Ground motion parameters are essential for describing the important characteristics of strong ground motion in compact, quantitative form. Many parameters have been proposed

to characterize the amplitude, frequency content, and duration of strong ground motions; some describe only one of these characteristics, while others may reflect two or three. Because of the complexity of earthquake ground motions, identification of a single parameter that accurately describes all important ground motion characteristics is regarded as impossible (Jennings, 1985; Joyner and Boore, 1988).

3.3.1 Amplitude Parameters

The most common way of describing a ground motion is with a time history. The motion parameter may be acceleration, velocity, or displacement, or all three may be displayed as shown in Figure 3.10. Typically, only one of these quantities is measured directly with the others computed from it by integration and/or differentiation. Note the different predominant frequencies in the acceleration, velocity, and displacement time histories. The acceleration time history shows a significant proportion of relatively high frequencies. Integration produces a smoothing or filtering effect [in the frequency domain, $\tilde{v}(\omega) = \tilde{a}(\omega)/\omega$ and

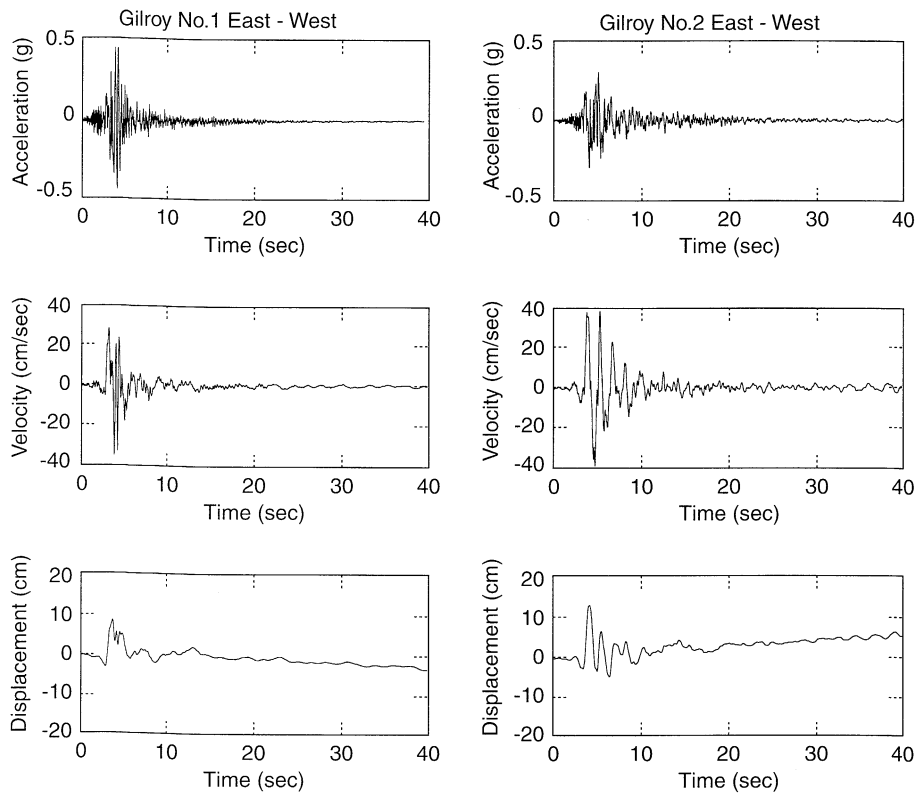


Figure 3.10 Acceleration, velocity, and displacement time histories for the E-W components of the Gilroy No. 1 (rock) and Gilroy No. 2 (soil) strong motion records. The velocities and displacements were obtained by integrating the acceleration records shown in Figure 3.1 using the trapezoidal rule. Note that the Gilroy No. 1 (rock) site experienced higher accelerations, but the Gilroy No. 2 (soil) site experienced higher velocities and displacements.

$\tilde{u}(\omega) = \tilde{v}(\omega)/\omega$, where \tilde{u} , \tilde{v} , and \tilde{a} are the transformed displacement, velocity, and acceleration, respectively]. Therefore, the velocity time history shows substantially less high-frequency motion than the acceleration time history. The displacement time history, obtained by another round of integration, is dominated by relatively low frequency motion.

3.3.1.1 Peak Acceleration

The most commonly used measure of the amplitude of a particular ground motion is the peak horizontal acceleration (PHA). The PHA for a given component of motion is simply the largest (absolute) value of horizontal acceleration obtained from the accelerogram of that component. By taking the vector sum of two orthogonal components, the maximum resultant PHA (the direction of which will usually not coincide with either of the measured components) can be obtained.

Horizontal accelerations have commonly been used to describe ground motions because of their natural relationship to inertial forces; indeed, the largest dynamic forces induced in certain types of structures (i.e., very stiff structures) are closely related to the PHA. The PHA can also be correlated to earthquake intensity (e.g., Trifunac and Brady, 1975a; Murphy and O'Brien, 1977; Krinitzky and Chang, 1987). Although this correlation is far from precise, it can be very useful for estimation of PHA when only intensity information is available, as in the cases of earthquakes that occurred before strong motion instruments were available (preinstrumental earthquakes). A number of intensity–acceleration relationships have been proposed, several of which are shown in Figure 3.11. The use of intensity–attenuation relationships also allows estimation of the spatial variability of peak acceleration from the isoseismal maps of historical earthquakes.

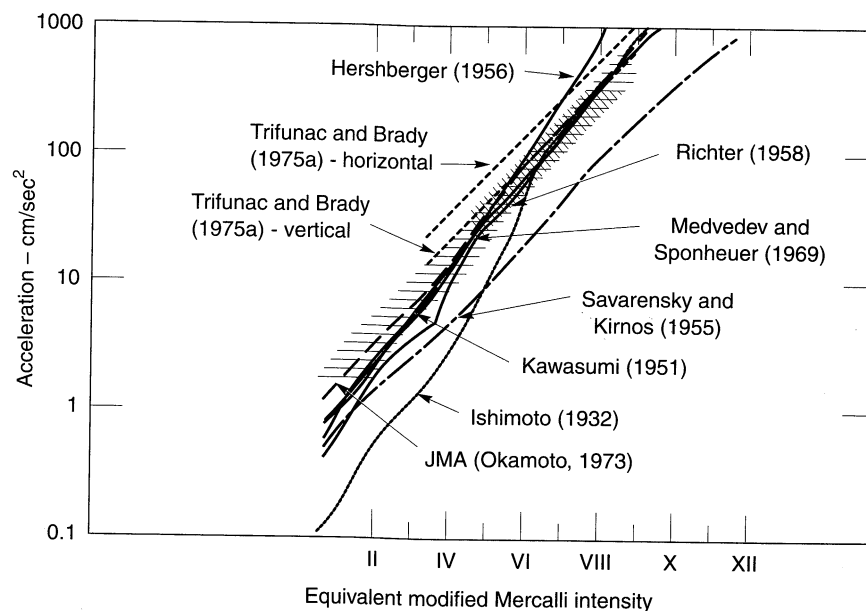


Figure 3.11 Proposed relationships between PHA and MMI. (After Trifunac and Brady, 1975a. Used by permission of the Seismological Society of America.)

Vertical accelerations have received less attention in earthquake engineering than horizontal accelerations, primarily because the margins of safety against gravity-induced static vertical forces in constructed works usually provide adequate resistance to dynamic forces induced by vertical accelerations during earthquakes. For engineering purposes, the peak vertical acceleration (PVA) is often assumed to be two-thirds of the PHA (Newmark and Hall, 1982). The ratio of PVA to PHA, however, has more recently been observed to be quite variable but generally to be greater than two-thirds near the source of moderate to large earthquakes and less than two-thirds at large distances (Campbell, 1985; Abrahamson and Litehiser, 1989). Peak vertical accelerations can be quite large; a PVA of 1.74g was measured between the Imperial and Brawley faults in the 1979 Imperial Valley earthquake.

Ground motions with high peak accelerations are usually, but not always, more destructive than motions with lower peak accelerations. Very high peak accelerations that last for only a very short period of time may cause little damage to many types of structures. A number of earthquakes have produced peak accelerations in excess of 0.5g but caused no significant damage to structures because the peak accelerations occurred at very high frequencies and the duration of the earthquake was not long. Although peak acceleration is a very useful parameter, it provides no information on the frequency content or duration of the motion; consequently, it must be supplemented by additional information to characterize a ground motion accurately.

3.3.1.2 Peak Velocity

The peak horizontal velocity (PHV) is another useful parameter for characterization of ground motion amplitude. Since the velocity is less sensitive to the higher-frequency components of the ground motion, as illustrated in Figure 3.10, the PHV is more likely than the PHA to characterize ground motion amplitude accurately at intermediate frequencies. For structures or facilities that are sensitive to loading in this intermediate-frequency range (e.g., tall or flexible buildings, bridges, etc.), the PHV may provide a much more accurate indication of the potential for damage than the PHA. PHV has also been correlated to earthquake intensity (e.g., Trifunac and Brady, 1975a; Krinitzsky and Chang, 1987).

3.3.1.3 Peak Displacement

Peak displacements are generally associated with the lower-frequency components of an earthquake motion. They are, however, often difficult to determine accurately (Campbell, 1985; Joyner and Boore, 1988), due to signal processing errors in the filtering and integration of accelerograms and due to long-period noise. As a result, peak displacement is less commonly used as a measure of ground motion than is peak acceleration or peak velocity.

Example 3.1

Determine the peak accelerations, velocities, and displacements for the E-W components of the Gilroy No. 1 (rock) and Gilroy No. 2 (soil) ground motions.

Solution The peak amplitude values can be estimated graphically from Figure 3.9. The actual peak values, based on the data from which Figure 3.9 was plotted, are:

Parameter	Gilroy No. 1 (Rock)	Gilroy No. 2 (Soil)
Peak acceleration	0.442g	0.332g
Peak velocity (cm/sec)	33.7	39.2
Peak displacement (cm)	8.5	13.3

3.3.1.4 Other Amplitude Parameters

Although the parameters discussed previously are easily determined, they describe only the peak amplitudes of single cycles within the ground motion time history. In some cases, damage may be closely related to the peak amplitude, but in others it may require several repeated cycles of high amplitude to develop. Newmark and Hall (1982) described the concept of an *effective acceleration* as “that acceleration which is most closely related to structural response and to damage potential of an earthquake. It differs from and is less than the peak free-field ground acceleration. It is a function of the size of the loaded area, the frequency content of the excitation, which in turn depends on the closeness to the source of the earthquake, and to the weight, embedment, damping characteristic, and stiffness of the structure and its foundation.”

Some time histories are characterized by single-cycle peak amplitudes that are much greater than the amplitudes of other cycles. An example of such a case is the Stone Canyon record shown in Figure 3.12a. These single cycles often occur at high frequencies and consequently have little effect on structures with lower natural frequencies. In other time histories, such as the Koyna record of Figure 3.12b, a number of peaks of similar amplitude are observed.

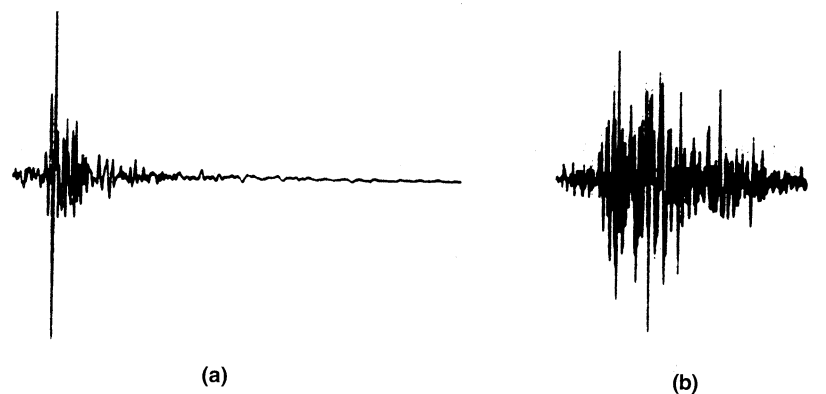


Figure 3.12 Accelerograms from (a) the N29W Melendy Ranch record of the 1972 Stone Canyon ($M = 4.6$) earthquake and (b) the longitudinal record from the 1967 Koyna ($M = 6.5$) earthquake. The time and acceleration scales are identical for both records. Peak accelerations are very close, illustrating the limitations of using peak amplitude as a sole measure of strong ground motion. (After Hudson, 1979; used by permission of EERI.)

Sustained Maximum Acceleration and Velocity. Nuttli (1979) used lower peaks of the accelerogram to characterize strong motion by defining the *sustained maximum acceleration* for three (or five) cycles as the third (or fifth) highest (absolute) value of acceleration in the time history. The *sustained maximum velocity* was defined similarly. Although the PHA values for the 1972 Stone Canyon earthquake and 1967 Koyna earthquake records (Figure 3.12) were nearly the same, a quick visual inspection indicates that their sustained maximum accelerations (three- or five-cycle) were very different. For a structure that required several repeated cycles of strong motion to develop damage, the

Koyna motion would be much more damaging than the Stone Canyon motion, even though they had nearly the same PHA. For these motions, the sustained maximum acceleration would be a better indicator of damage potential than the PHA.

Example 3.2

Determine the three- and five-cycle sustained maximum accelerations and velocities for the E-W components of the Gilroy No. 1 (rock) and Gilroy No. 2 (soil) ground motions.

Solution The sustained maximum acceleration and velocity values can be obtained graphically from Figure 3.10. The actual values, based on the data from which Figure 3.10 was plotted, are:

Parameter	Gilroy No. 1 (Rock)	Gilroy No. 2 (Soil)
Sustained maximum acceleration		
Three-cycle	0.434g	0.312g
Five-cycle	0.418g	0.289g
Sustained maximum velocity (cm/sec)		
Three-cycle	31.6	38.4
Five-cycle	29.9	38.2

Effective Design Acceleration. The notion of an effective design acceleration, with different definitions, has been proposed by at least two researchers. Since pulses of high acceleration at high frequencies induce little response in most structures, Benjamin and Associates (1988) proposed that an *effective design acceleration* be taken as the peak acceleration that remains after filtering out accelerations above 8 to 9 Hz. Kennedy (1980) proposed that the effective design acceleration be 25% greater than the third highest (absolute) peak acceleration obtained from a filtered time history.

3.3.2 Frequency Content Parameters

Only the simplest of analyses (see Section B.5.3 of Appendix B) are required to show that the dynamic response of compliant objects, be they buildings, bridges, slopes, or soil deposits, is very sensitive to the frequency at which they are loaded. Earthquakes produce complicated loading with components of motion that span a broad range of frequencies. The *frequency content* describes how the amplitude of a ground motion is distributed among different frequencies. Since the frequency content of an earthquake motion will strongly influence the effects of that motion, characterization of the motion cannot be complete without consideration of its frequency content.

3.3.2.1 Ground Motion Spectra

Any periodic function (i.e., any function that repeats itself exactly at a constant interval) can be expressed using Fourier analysis as the sum of a series of simple harmonic terms of different frequency, amplitude, and phase. Using the Fourier series (see Section A.3 of Appendix A), a periodic function, $x(t)$, can be written as

$$x(t) = c_0 + \sum_{n=1}^{\infty} c_n \sin(\omega_n t + \phi_n) \quad (3.4)$$

In this form, c_n and ϕ_n are the amplitude and phase angle, respectively, of the n th harmonic of the Fourier series [see equations (A.10) and (A.11) for their definitions]. The Fourier series provides a complete description of the ground motion since the motion can be completely recovered by the inverse Fourier transform.

Fourier Spectra. A plot of Fourier amplitude versus frequency [c_n versus ω_n from equation (3.4)] is known as a *Fourier amplitude spectrum*; a plot of Fourier phase angle (ϕ_n versus ω_n) gives the *Fourier phase spectrum*. The Fourier amplitude spectrum of a strong ground motion shows how the amplitude of the motion is distributed with respect to frequency (or period). It expresses the frequency content of a motion very clearly.

The Fourier amplitude spectrum may be narrow or broad. A narrow spectrum implies that the motion has a dominant frequency (or period), which can produce a smooth, almost sinusoidal time history. A broad spectrum corresponds to a motion that contains a variety of frequencies that produce a more jagged, irregular time history. The Fourier amplitude spectra for the E-W components of the Gilroy No. 1 (rock) and Gilroy No. 2 (soil) motions shown in Figure 3.13. The jagged shapes of the spectra are typical of those observed for

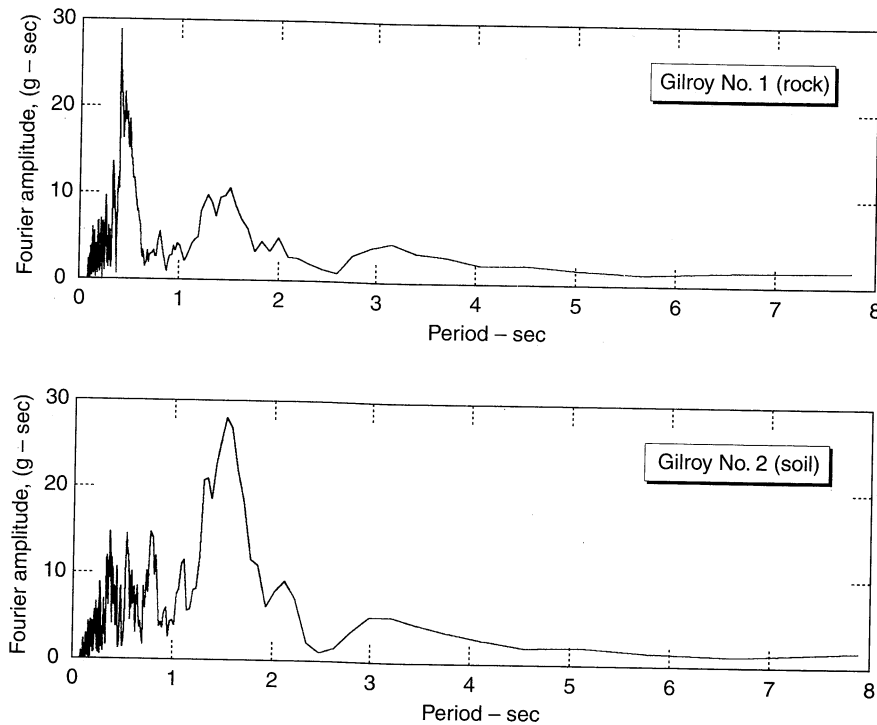


Figure 3.13 Fourier amplitude spectra for the E-W components of the Gilroy No. 1 (rock) and Gilroy No. 2 (soil) strong motion records. Fourier spectra were obtained by discrete Fourier transform (Section A.3.3 of Appendix A) and consequently have units of velocity. Fourier amplitude spectra can also be plotted as functions of frequency (see Figure E3.3).

individual ground motions. The shapes of the spectra are quite different: the Gilroy No. 1 (rock) spectrum is strongest at low periods (or high frequencies) while the reverse is observed for the Gilroy No. 2 (soil) record. A difference in frequency content can be detected by closely examining the motions in the time domain (Figure 3.1), but the difference is explicitly illustrated by the Fourier amplitude spectra.

When the Fourier amplitude spectra of actual earthquake motions are smoothed and plotted on logarithmic scales, their characteristic shapes can be seen more easily. As illustrated in Figure 3.14, Fourier acceleration amplitudes tend to be largest over an intermediate range of frequencies bounded by the *corner frequency* f_c on the low side and the *cutoff frequency* f_{\max} on the high side. The corner frequency can be shown theoretically (Brune, 1970, 1971) to be inversely proportional to the cube root of the seismic moment. This result indicates that large earthquakes produce greater low-frequency motions than do smaller earthquakes. The cutoff frequency is not well understood; it has been characterized both as a near-site effect (Hanks, 1982) and as a source effect (Papageorgiou and Aki, 1983) and is usually assumed to be constant for a given geographic region.

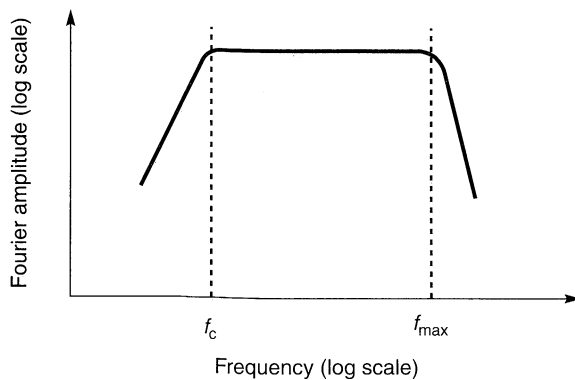


Figure 3.14 Idealized shape of smoothed Fourier amplitude spectrum illustrating the corner frequency, f_c , and cutoff frequency, f_{\max} .

Since phase angles control the times at which the peaks of harmonic motions occur (Appendix A), the Fourier phase spectrum influences the variation of ground motion with time. In contrast to Fourier amplitude spectra, Fourier phase spectra from actual earthquake records do not display characteristic shapes.

Power Spectra. The frequency content of a ground motion can also be described by a *power spectrum* or *power spectral density function*. The power spectral density function can also be used to estimate the statistical properties of a ground motion and to compute stochastic response using random vibration techniques (Clough and Penzien, 1975; Vanmarcke, 1976; Yang, 1986).

The total intensity of a ground motion of duration T_d is given in the time domain by the area under the time history of squared acceleration:

$$I_0 = \int_0^{T_d} [a(t)]^2 dt \quad (3.5)$$

Using Parseval's theorem, the total intensity can also be expressed in the frequency domain, as

$$I_0 = \frac{1}{\pi} \int_0^{\omega_N} c_n^2 d\omega \quad (3.6)$$

where $\omega_N = \pi / \Delta t$ is the *Nyquist frequency* (the highest frequency in the Fourier series). The average intensity, λ_0 , can be obtained by dividing equations (3.5) and (3.6) by the duration,

$$\lambda_0 = \frac{1}{T_d} \int_0^{T_d} [a(t)]^2 dt = \frac{1}{\pi T_d} \int_0^{\omega_N} c_n^2 d\omega \quad (3.7)$$

Notice that the average intensity is equal to the mean-squared acceleration. The *power spectral density*, $G(\omega)$, is defined such that

$$\lambda_0 = \int_0^{\omega_N} G(\omega) d\omega \quad (3.8)$$

from which we can easily see, by comparing equations (3.7) and (3.8), that

$$G(\omega) = \frac{1}{\pi T_d} c_n^2 \quad (3.9)$$

The close relationship between the power spectral density function and the Fourier amplitude spectrum is apparent from equation (3.9). The power spectral density is often normalized by dividing its values by the area beneath it

$$G^n(\omega) = \frac{1}{\lambda_0} G(\omega) \quad (3.10)$$

where λ_0 , as before, is the mean-squared acceleration.

The power spectral density function is useful in characterizing the earthquake as a random process. The power spectral density function by itself can describe a *stationary random process* (i.e., one whose statistical parameters do not vary with time). Actual strong motion accelerograms, however, frequently show that the intensity builds up to a maximum value in the early part of the motion, then remains approximately constant for a period of time, and finally decreases near the end of the motion. Such *nonstationary random process* behavior is often modeled by multiplying a stationary time history by a deterministic intensity function (e.g., Hou, 1968; Shinozuka, 1973; Saragoni and Hart, 1983). Changes in frequency content during the motion have been described using an *evolutionary power spectrum* approach (Priestley, 1965, 1967; Liu, 1970).

Response Spectra. A third type of spectrum is used extensively in earthquake engineering practice. The *response spectrum* describes the maximum response of a single-degree-of-freedom (SDOF) system to a particular input motion as a function of the natural frequency (or natural period) and damping ratio of the SDOF system (Section B.7 of Appendix B). Computed response spectra for the Gilroy No. 1 (rock) and Gilroy No. 2 (soil) records are illustrated in Figure 3.15.

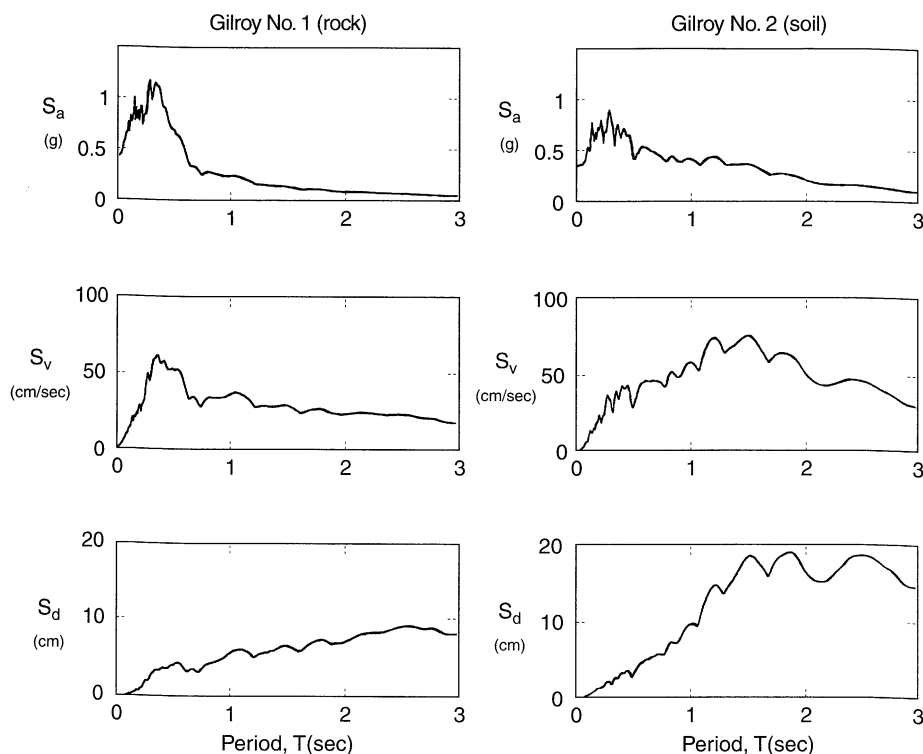


Figure 3.15 Response spectra (5% damping) for Gilroy No. 1 (rock) and Gilroy No. 2 (soil) strong motion records. The frequency contents of the two motions are reflected in the response spectra. The Gilroy 1 (rock) motion, for example, produced higher spectral accelerations at low periods than did the Gilroy 2 (soil) motion, and lower spectral accelerations at higher periods. The higher long-period content of the Gilroy 2 (soil) motion produced spectral velocities and displacements much higher than those of the Gilroy 1 (rock) motion.

Response spectra may be plotted individually to arithmetic scales, or may be combined, by virtue of the relationships of equation (3.11), in tripartite plots (Section A.2.2). The tripartite plot displays spectral velocity on the vertical axis, natural frequency (or period) on the horizontal axis, and acceleration and displacement on inclined axes. The acceleration and displacement axes are reversed when the spectral values are plotted against natural period rather than natural frequency. The shapes of typical response spectra indicate that peak spectral acceleration, velocity, and displacement values are associated with different frequencies (or periods). At low frequencies the average spectral displacement is nearly constant; at high frequencies the average spectral acceleration is fairly constant. In between lies a range of nearly constant spectral velocity. Because of this behavior, response spectra are often divided into *acceleration-controlled* (high-frequency), *velocity-controlled* (intermediate-frequency), and *displacement-controlled* (low-frequency) portions.

Elastic response spectra assume linear structural force–displacement behavior. For many real structures, however, inelastic behavior may be induced by earthquake ground

motions. An inelastic response spectrum (i.e., one that corresponds to a nonlinear force–displacement relationship, can be used to account for the effects of inelastic behavior. Figure 3.16 shows inelastic response spectra for acceleration and yield displacement for various values of the *ductility factor* $\mu = u_{\max}/u_y$, where u_{\max} is the maximum allowable displacement and u_y is the yield displacement. A separate inelastic spectrum must be plotted to show total (elastic plus plastic) displacement. Spectral accelerations decrease with increasing ductility, but total displacements increase.

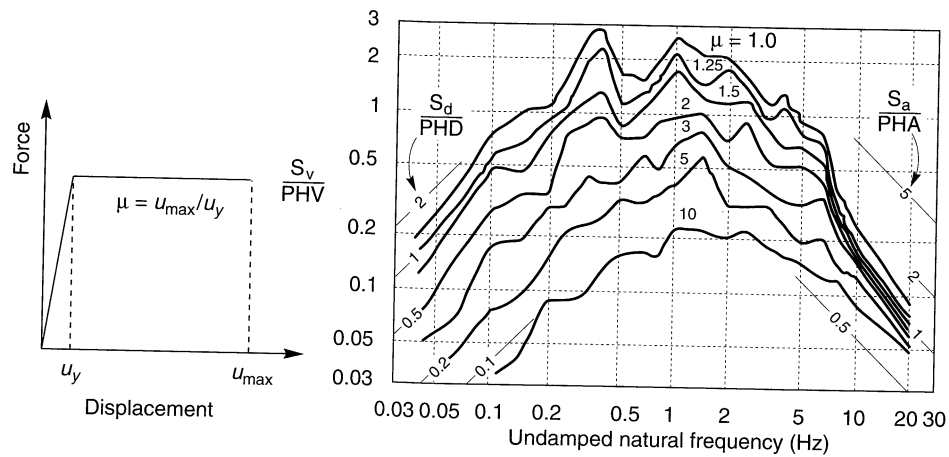


Figure 3.16 Inelastic response spectra for the El Centro N-S component of the 1940 Imperial Valley earthquake. Only the elastic component of the displacement is plotted. Spectral accelerations are correct, but spectral velocities are not. (After Newmark and Hall, 1982; used by permission of EERI.)

Response spectra reflect strong ground motion characteristics indirectly, since they are “filtered” by the response of a SDOF structure. The amplitude, frequency content, and to a lesser extent, duration of the input motion all influence spectral values. The different frequency contents of the Gilroy No. 1 (rock) and Gilroy No. 2 (soil) ground motions are clearly illustrated by the different shapes of their respective response spectra (Figure 3.15).

It is important to remember that response spectra represent only the maximum responses of a number of different structures. However, the response of structures is of great importance in earthquake engineering, and the response spectrum has proven to be an important and useful tool for characterization of strong ground motion.

3.3.2.2 Spectral Parameters

Section 3.3.2.1 described three types of spectra that can be used to characterize strong ground motion. The Fourier amplitude spectrum and the closely related power spectral density, combined with the phase spectrum, can describe a ground motion completely. The response spectrum does not describe the actual ground motion, but it does provide valuable additional information on its potential effects on structures. Each of these spectra is a complicated function and, as with time histories, a great many data are required to describe them completely. A number of *spectral parameters* have been proposed to extract important pieces of information from each spectrum.

Predominant Period. A single parameter that provides a useful, although somewhat crude representation of the frequency content of a ground motion is the *predominant period*, T_p . The predominant period is defined as the period of vibration corresponding to the maximum value of the Fourier amplitude spectrum. To avoid undue influence of individual spikes of the Fourier amplitude spectrum, the predominant period is often obtained from a smoothed spectrum. While the predominant period provides some information regarding the frequency content, it is easy to see (Figure 3.17) that motions with radically different frequency contents can have the same predominant period.

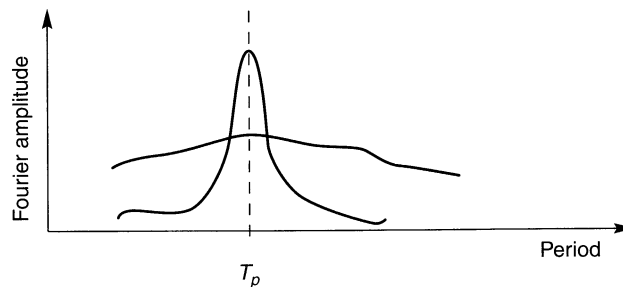


Figure 3.17 Two hypothetical Fourier amplitude spectra with the same predominant period but very different frequency contents. The upper curve describes a wideband motion and the lower a narrowband motion.

Example 3.3

Determine the predominant periods for the E-W components of the Gilroy No. 1 (rock) and Gilroy No. 2 (soil) ground motions.

Solution The Fourier amplitude spectra of most ground motions are quite jagged in the vicinity of their peaks, so some smoothing is required to identify the predominant period. The smoothing and predominant period identification is most easily accomplished by plotting the Fourier amplitude spectrum as a function of frequency. By numerically smoothing their Fourier amplitude spectra (Figure E3.3), the predominant periods are

$$\text{Gilroy No. 1 (rock): } T_p = 0.39 \text{ sec}$$

$$\text{Gilroy No. 2 (soil): } T_p = 0.53 \text{ sec}$$

Note that the predominant period of the Gilroy No. 2 (soil) motion is greater than that of the Gilroy No. 1 (rock) motion, thereby illustrating the relative strength of the longer period (lower-frequency) components of the Gilroy No. 1 (soil) motion.

Bandwidth. The predominant period can be used to locate the peak of the Fourier amplitude spectrum; however, it provides no information on the dispersion of spectral amplitudes about the predominant period. The *bandwidth* of the Fourier amplitude spectrum is the range of frequency over which some level of Fourier amplitude is exceeded. Bandwidth is usually measured at the level where the power of the spectrum is half its maximum value; this corresponds to a level of $1/\sqrt{2}$ times the maximum Fourier amplitude. The irregular shape of individual Fourier amplitude spectra often renders bandwidth difficult to evaluate. It is determined more easily for smoothed spectra.

Central Frequency. The power spectral density function can be used to estimate statistical properties of the ground motion. Defining the n th spectral moment of a ground motion by

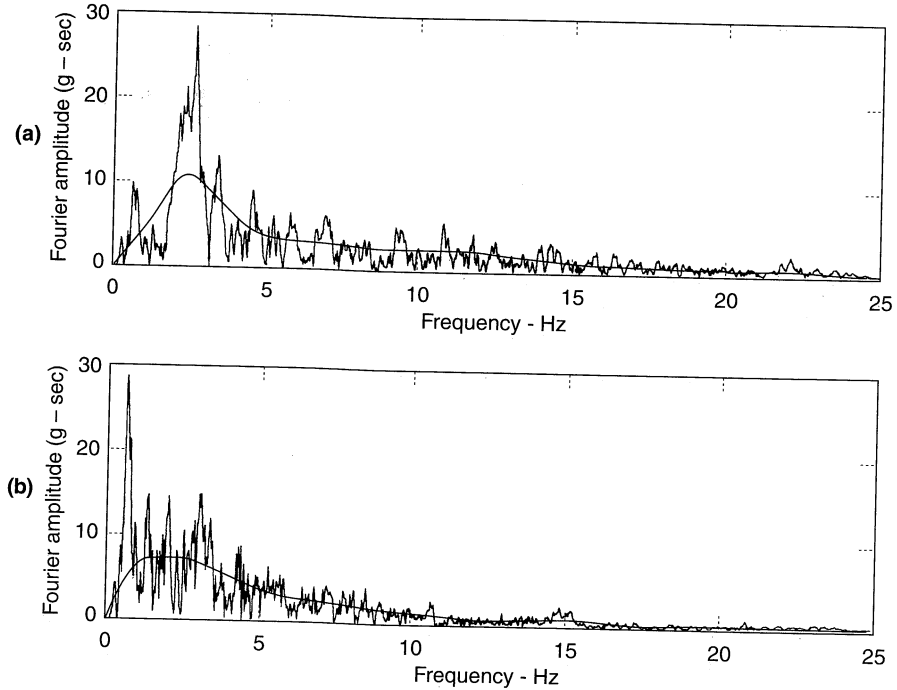


Figure E3.3 Raw and smoothed FAS for Gilroy No.1 (rock) and Gilroy No.2 (soil) motions.

$$\lambda_n = \int_0^{\omega_N} \omega^n G(\omega) d\omega \quad (3.11)$$

the *central frequency* Ω (Vanmarcke, 1976) is given by

$$\Omega = \sqrt{\frac{\lambda_2}{\lambda_0}} \quad (3.12)$$

The central frequency is a measure of the frequency where the power spectral density is concentrated. It can also be used, along with the average intensity and duration, to calculate the theoretical median peak acceleration

$$\dot{u}_{\max} = \sqrt{2\lambda_0 \ln\left(2.8 \frac{\Omega T_d}{2\pi}\right)} \quad (3.13)$$

Shape Factor. The *shape factor* (Vanmarcke, 1976) indicates the dispersion of the power spectral density function about the central frequency:

$$\delta = \sqrt{1 - \frac{\lambda_1^2}{\lambda_0 \lambda_2}} \quad (3.14)$$

The shape factor always lies between 0 and 1, with higher values corresponding to larger bandwidths.

Kanai-Tajimi Parameters. Although individual power spectral density functions may have highly irregular shapes, averaging a number of normalized power spectral density functions for similar strong ground motions reveals a smooth characteristic shape. Kanai (1957) and Tajimi (1960) used a limited number of strong motion records to propose the following three-parameter model for power spectral density:

$$G(\omega) = G_0 \frac{1 + [2\xi_g(\omega/\omega_g)]^2}{[1 - (\omega/\omega_g)^2]^2 + [2\xi_g(\omega/\omega_g)]^2} \quad (3.15)$$

where the parameters G_0 , ξ_g , and ω_g determine the shape of the function (Figure 3.18).

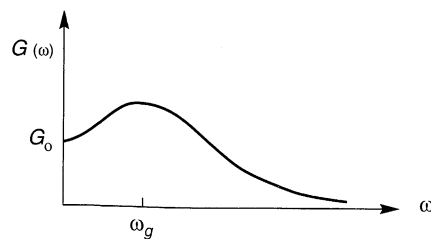


Figure 3.18 Shape of the Kanai-Tajimi power spectral density function.

The displacement response of a SDOF system with natural frequency ω_g and damping ratio ξ_g to white noise base motion would be described by a Kanai-Tajimi power spectral density function. As such, high-frequency components of the input motion will be attenuated, and frequency components in the vicinity of ω_g will be amplified. Typical values of Kanai-Tajimi parameters for various site conditions are shown in Table 3-1.

Clough and Penzien (1975) proposed a correction to the Kanai-Tajimi power spectral density function to prevent excessive velocities and displacements at very low frequencies. The corrected Kanai-Tajimi power spectral density function requires two additional parameters to describe the power spectral density.

3.3.2.3 v_{\max}/a_{\max}

Because peak velocities and peak accelerations are usually associated with motions of different frequency, the ratio v_{\max}/a_{\max} should be related to the frequency content of the motion (Newmark, 1973; Seed et al., 1976; McGuire, 1978). For a simple harmonic motion

Table 3-1 Ground Intensity, Ground Frequency, and Ground Damping for Various Site Conditions

Ground Motion	Site Conditions	Number of Records	Ground Intensity, G_0	Ground Frequency, ω_g	Ground Damping, ξ_g
Horizontal	Alluvium	161	0.102	18.4	0.34
	Alluvium on rock	60	0.078	22.9	0.30
	Rock	26	0.070	27.0	0.34
Vertical	Alluvium	78	0.080	26.2	0.46
	Alluvium on rock	29	0.072	29.1	0.46
	Rock	13	0.053	38.8	0.46

Source: Elghadamsi et al. (1988).

of period T , for example, $v_{\max}/a_{\max} = T/2\pi$. For earthquake motions that include many frequencies, the quantity $2\pi(v_{\max}/a_{\max})$ can be interpreted as the period of vibration of an equivalent harmonic wave, thus providing an indication of which periods of the ground motion are most significant. Seed and Idriss (1982) suggested the following representative average values for different site conditions less than 50 km from the source:

Site Condition	v_{\max}/a_{\max}
Rock	55 cm/sec/g = 0.056 sec
Stiff soils (<200 ft)	110 cm/sec/g = 0.112 sec
Deep stiff soils (>200 ft)	135 cm/sec/g = 0.138 sec

The corresponding periods of equivalent harmonic waves for the rock, stiff soil, and deep stiff soil site conditions are 0.35 sec, 0.70 sec, and 0.87 sec, respectively, which indicates a shift toward longer-period (lower-frequency) motion on softer soil deposits.

Example 3.4

Determine the ratio v_{\max}/a_{\max} for the N-S components of the Gilroy No. 1 (rock) and Gilroy No. 2 (soil) ground motions. Compare the quantities $2\pi(v_{\max}/a_{\max})$ with the predominant periods of the motions.

Solution Based on the v_{\max} and a_{\max} values from Example 3.1,

$$\text{Gilroy No.1 (rock): } \frac{v_{\max}}{a_{\max}} = \frac{33.7 \text{ cm/sec}}{0.442 (981 \text{ cm/sec}^2)} = 0.078 \text{ sec}$$

$$\text{Gilroy No.2 (soil): } \frac{v_{\max}}{a_{\max}} = \frac{39.2 \text{ cm/sec}}{0.322 (981 \text{ cm/sec}^2)} = 0.124 \text{ sec}$$

The quantity $2\pi(v_{\max}/a_{\max})$ is equal to the predominant period of a simple harmonic motion. To see how well it corresponds to the predominant period of the Gilroy No. 1 (rock) and Gilroy No. 2 (soil) ground motions,

$$\text{Gilroy No.1 (rock): } 2\pi \frac{v_{\max}}{a_{\max}} = 0.49 \text{ sec} \quad T_p = 0.39 \text{ sec}$$

$$\text{Gilroy No.2 (soil): } 2\pi \frac{v_{\max}}{a_{\max}} = 0.78 \text{ sec} \quad T_p = 0.53 \text{ sec}$$

Though the ratio v_{\max}/a_{\max} certainly indicates that the Gilroy No. 1 (rock) motion has a higher frequency content than the Gilroy No. 2 (soil) motion, it overestimates the predominant period of both the Gilroy No. 1 (rock) motion and Gilroy No.2 (soil) motions. Due to the approximate nature of the predominant period and the stochastic nature of both v_{\max} and a_{\max} , close agreement between v_{\max}/a_{\max} and predominant period should not be expected.

3.3.3 Duration

The duration of strong ground motion can have a strong influence on earthquake damage. Many physical processes, such as the degradation of stiffness and strength of certain types of structures and the buildup of porewater pressures in loose, saturated sands, are sensitive to the number of load or stress reversals that occur during an earthquake. A motion of short duration may not produce enough load reversals for damaging response to build up in a structure, even if the amplitude of the motion is high. On the other hand, a motion with moderate amplitude but long duration can produce enough load reversals to cause substantial damage.

The duration of a strong ground motion is related to the time required for release of accumulated strain energy by rupture along the fault. As the length, or area, of fault rupture increases, the time required for rupture increases. As a result, the duration of strong motion increases with increasing earthquake magnitude. While this relationship has been supported by empirical evidence for many years, advances in source mechanism modeling (Hanks and McGuire, 1981) have provided theoretical support, indicating that the duration should be proportional to the cube root of the seismic moment. When *bilateral rupture* [i.e., rupture that propagates in opposite directions from the focus (as in the case of the 1989 Loma Prieta earthquake)] occurs, the strong motion duration may be considerably lower.

An earthquake accelerogram generally contains all accelerations from the time the earthquake begins until the time the motion has returned to the level of background noise. For engineering purposes, only the strong-motion portion of the accelerogram is of interest. Different approaches have been taken to the problem of evaluating the duration of strong motion in an accelerogram. The *bracketed duration* (Bolt, 1969) is defined as the time between the first and last exceedances of a threshold acceleration (usually 0.05g). Another definition of duration (Trifunac and Brady, 1975b) is based on the time interval between the points at which 5% and 95% of the total energy has been recorded. Boore (1983) has taken the duration to be equal to the *corner period* (i.e., the inverse of the corner frequency). The rate of change of cumulative root-mean-square (rms) acceleration has also been used as the basis for evaluation of strong-motion duration (McCann and Shah, 1979). Power spectral density concepts can also be used to define a strong-motion duration (Vanmarcke and Lai, 1977). Other definitions of strong-motion duration have been proposed (Perez, 1974; Trifunac and Westermo, 1977). Because it implicitly reflects the strength of shaking, the bracketed duration is most commonly used for earthquake engineering purposes.

The duration of strong motion has been investigated by interpretation of accelerograms from earthquakes of different magnitudes. Using a 0.05g threshold acceleration, Chang and Krinitzky (1977) estimated the bracketed durations for soil and rock sites at short (less than 10 km) epicentral distances shown in Table 3-2.

Duration has also been expressed in terms of equivalent cycles of ground motion. One such approach was developed in conjunction with an early procedure for evaluation of liquefaction potential (Seed et al., 1975). To represent an irregular time history of shear stress

Table 3-2 Typical Earthquake Durations at Epicentral Distances Less Than 10 km

Magnitude	Duration (sec)	
	Rock Sites	Soil Sites
5.0	4	8
5.5	6	12
6.0	8	16
6.5	11	23
7.0	16	32
7.5	22	45
8.0	31	62
8.5	43	86

Source: Chang and Krinitzky (1977).

by a uniform series of harmonic stress cycles, the concept of an equivalent number of significant stress cycles was developed. The equivalent number of uniform stress cycles, shown in Table 3-3, was selected to cause pore pressure buildup equivalent to that of an actual shear stress-time history at a harmonic stress amplitude of 65% of the maximum actual shear stress.

Table 3-3 Equivalent Number of Uniform Stress Cycles

Earthquake Magnitude	Number of Significant Stress Cycles
$5\frac{1}{4}$	2-3
6	5
$6\frac{3}{4}$	10
$7\frac{1}{2}$	15
$8\frac{1}{2}$	26

Example 3.5

Determine the bracketed durations of the E-W components of the Gilroy No. 1 (rock) and Gilroy No. 2 (soil) ground motions.

Solution Based on a threshold acceleration of 0.05g, the bracketed durations can be obtained graphically from the accelerograms shown in Figure E3.5.

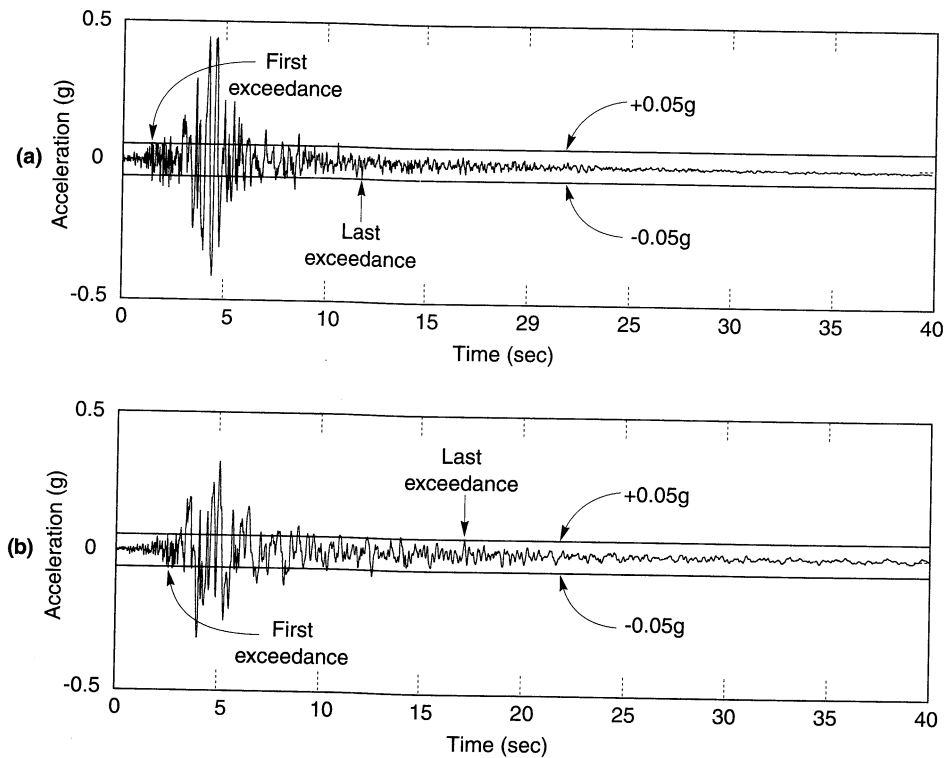


Figure E3.5

Gilroy No.1 (rock):	$T_d = 9.8$ sec
Gilroy No.2 (soil):	$T_d = 14.7$ sec

3.3.4 Other Ground Motion Parameters

The preceding parameters related primarily to the amplitude, frequency content, or duration of a ground motion. Since all of these characteristics are important, ground motion parameters that reflect more than one are very useful. The following paragraphs present a number of parameters that reflect two or three important ground motion characteristics.

A single parameter that includes the effects of the amplitude and frequency content of a strong motion record is the *rms acceleration*, defined as

$$a_{\text{rms}} = \sqrt{\frac{1}{T_d} \int_0^{T_d} [a(t)]^2 dt} = \sqrt{\lambda_0} \quad (3.16)$$

where T_d is the duration of the strong motion and λ_0 is the average intensity (or mean-squared acceleration). Because the integral in equation (3.16) is not strongly influenced by large, high-frequency accelerations (which occur only over a very short period of time) and because it is influenced by the duration of the motion, the rms acceleration can be very useful for engineering purposes. Its value, however, can be sensitive to the method used to define strong motion duration.

A parameter closely related to the rms acceleration is the *Arias intensity* (Arias, 1970), defined as

$$I_a = \frac{\pi}{2g} \int_0^{\infty} [a(t)]^2 dt \quad (3.17)$$

The Arias intensity has units of velocity and is usually expressed in meters per second. Since it is obtained by integration over the entire duration rather than over the duration of strong motion, its value is independent of the method used to define the duration of strong motion.

Example 3.6

Determine the rms accelerations and Arias intensities of the E-W components of the Gilroy No. 1 (rock) and Gilroy No. 2 (soil) ground motions.

Solution By integrating the accelerograms of the Gilroy No. 1 (rock) and Gilroy No. 2 (soil) ground motions numerically, the rms accelerations and Arias intensities are

Gilroy No.1 (rock):	$a_{\text{rms}} = 0.112g$	$I_a = 1.667$ m/sec
Gilroy No.2 (soil):	$a_{\text{rms}} = 0.072g$	$I_a = 1.228$ m/sec

The *characteristic intensity*, defined as

$$I_c = a_{\text{rms}}^{1.5} T_d^{0.5} \quad (3.18)$$

is related linearly to an index of structural damage due to maximum deformations and absorbed hysteretic energy (Ang, 1990).

The *cumulative absolute velocity* is simply the area under the absolute accelerogram:

$$\text{CAV} = \int_0^{T_d} |a(t)| dt \quad (3.19)$$

The cumulative absolute velocity has been found to correlate well with structural damage potential. For example, a CAV of 0.30g-sec (obtained after filtering out frequencies above 10 Hz) corresponds to the lower limit for MMI VII shaking (Benjamin and Associates, 1988).

Since many structures have fundamental periods between 0.1 and 2.5 sec, the response spectrum ordinates in this period range should provide an indication of the potential response of these structures. The *response spectrum intensity* (Housner, 1959) was therefore defined as

$$\text{SI}(\xi) = \int_{0.1}^{2.5} \text{PSV}(\xi, T) dT \quad (3.20)$$

(i.e., the area under the pseudovelocity response spectrum between periods of 0.1 sec and 2.5 sec. The response spectrum intensity, as indicated in equation (3.20), can be computed for any structural damping ratio. It captures important aspects of the amplitude and frequency content (in the range of primary importance for structures) in a single parameter.

Von Thun et al. (1988) referred to the response spectrum intensity for 5% damping as the *velocity spectrum intensity*. The velocity spectrum intensity was suggested as being useful for evaluation of the response of earth and rockfill dams, which typically have fundamental periods between 0.6 and 2.0 sec (Makdisi and Seed, 1978). To characterize strong ground motion for analysis of concrete dams, which generally have fundamental periods of less than 0.5 sec, Von Thun et al. (1988) introduced the *acceleration spectrum intensity*, defined as

$$\text{ASI} = \int_{0.1}^{0.5} S_a(\xi=0.05, T) dT \quad (3.21)$$

(i.e., the area under the acceleration response spectrum between periods of 0.1 sec and 0.5 sec).

The Applied Technology Council (1978) defined two factors by which standard response spectra could be normalized. The *effective peak acceleration* (EPA) was defined as the average spectral acceleration over the period range 0.1 to 0.5 sec divided by 2.5 (the standard amplification factor for a 5% damping spectrum). The *effective peak velocity* (EPV) was defined as the average spectral velocity at a period of 1 sec divided by 2.5. Determination of EPA and EPV is shown schematically in Figure 3.19. The process of averaging the spectral accelerations and velocities over a range of periods minimizes the influence of local spikes in the response spectrum on the EPA and EPV. The EPA and EPV have been used in the specification of smoothed design response spectra in building codes (Chapter 8).

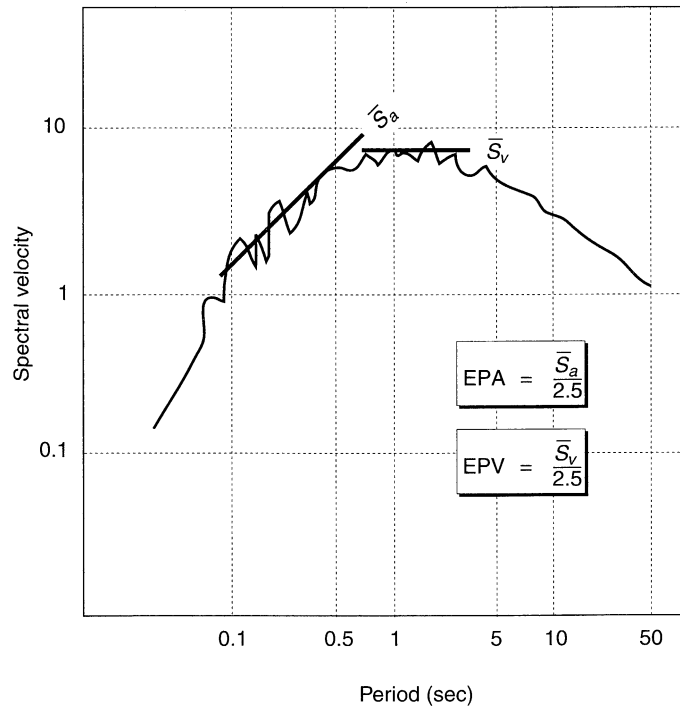


Figure 3.19 Determination of effective peak acceleration and effective peak velocity from response spectra. (After Applied Technology Council, 1978.)

3.3.5 Discussion

A wide variety of strong motion parameters have been presented. Some describe only the amplitude of the motion, others only the frequency content or duration. Some of these parameters are influenced by two or three of these important ground motion characteristics. Table 3-4 indicates which ground motion characteristics strongly influence the various ground motion parameters.

Seismic hazard analyses (Chapter 4) and the development of design ground motions (Chapter 8) rely heavily on the characterization of strong ground motion by ground motion parameters. Characterization by a single parameter is only rarely appropriate; the use of several parameters is usually required to describe adequately the important characteristics of a particular ground motion. Since different engineering problems are influenced by different ground motion characteristics, the significance of different parameters depends on the types of problems for which they are used.

3.4 ESTIMATION OF GROUND MOTION PARAMETERS

Proper design of earthquake-resistant structures and facilities requires estimation of the level of ground shaking to which they will be subjected. Since the level of shaking is most

Table 3-4 Ground Motion Characteristics That Are Strongly Reflected in Various Ground Motion Parameters

Ground Motion Parameter	Ground Motion Characteristic		
	Amplitude	Frequency Content	Duration
Peak acceleration, PHA and PHV	×		
Peak velocity, PHV	×		
Sustained maximum acceleration, SMA	×		
Effective design acceleration, EDA	×		
Predominant period, T_p		×	
Bandwidth		×	
Central frequency, Ω		×	
Shape factor, δ		×	
Power spectrum intensity, G_0	×	×	×
Ground frequency, ω_g		×	
Ground damping, ξ_g		×	
$v_{\max} a_{\max}$		×	
Duration, T_d			×
rms acceleration, a_{rms}	×	×	
Characteristic intensity, I_c	×	×	×
Arias intensity, I_a	×	×	×
Cumulative absolute velocity, CAV	×	×	×
Response spectrum intensity, SI(ξ)	×	×	
Velocity spectrum intensity, VSI	×	×	
Acceleration spectrum intensity, ASI	×	×	
Effective peak acceleration, EPA	×	×	
Effective peak velocity, EPV	×	×	

conveniently described in terms of ground motion parameters, methods for estimating ground motion parameters are required. *Predictive relationships*, which express a particular ground motion parameter in terms of the quantities that affect it most strongly, are used to estimate ground motion parameters. Predictive relationships play an important role in seismic hazard analyses (Chapter 4) used for seismic design.

3.4.1 Magnitude and Distance Effects

Much of the energy released by rupture along a fault takes the form of stress waves. Since the amount of energy released in an earthquake is strongly related to its magnitude, the characteristics of the stress waves will also be strongly related to magnitude. Figure 3.20 illustrates the influence of earthquake magnitude on actual ground motion characteristics in the time domain. Each earthquake came from essentially the same source, and each accelerometer was measured at about the same distance from the source. The variations in amplitude, frequency content, and duration with magnitude are apparent.

As stress waves travel away from the source of an earthquake, they spread out and are partially absorbed by the materials they travel through. As a result, the *specific energy* (energy per unit volume) decreases with increasing distance from the source. Since the characteristics of stress waves are strongly related to specific energy, they will also be strongly related to distance. The distance between the source of an earthquake and a

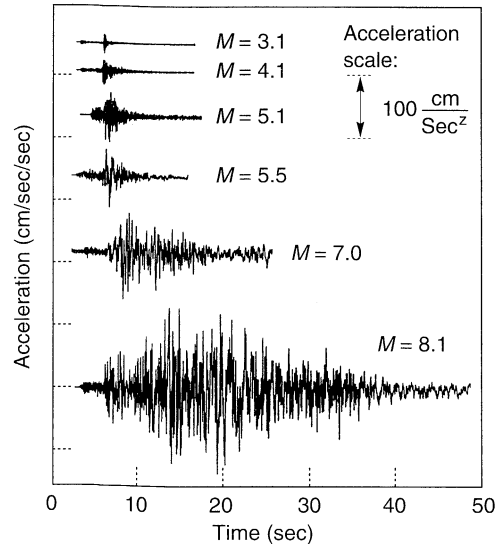


Figure 3.20 Accelerograms from six earthquakes off the Pacific coast of Mexico. Each accelerogram was measured at nearly the same epicentral distance. The record from the $M = 8.1$ (1985 Michoacan) earthquake continues for another 25 sec. (After Anderson, 1991, *Geotechnical News*, Vol. 9, No. 1, p. 35. Used by permission of BiTech Publishers, Ltd.)

particular site can be interpreted in different ways. Figure 3.21 illustrates some of the most commonly used measures of distance. R_1 and R_2 are the hypocentral and epicentral distances, which are the easiest distances to determine after an earthquake. If the length of fault rupture is a significant fraction of the distance between the fault and the site, however, energy may be released closer to the site, and R_1 and R_2 may not accurately represent the "effective distance." R_3 is the distance to the zone of highest energy release. Since rupture of this zone is likely to produce the peak ground motion amplitudes, it represents the best distance measure for peak amplitude predictive relationships. Unfortunately, its location is difficult to determine after an earthquake and nearly impossible to predict before an earthquake. R_4 is the closest distance to the zone of rupture (not including sediments overlying basement rock) and R_5 is the closest distance to the surface projection of the fault rupture. R_4 and R_5 have both been used extensively in predictive relationships.

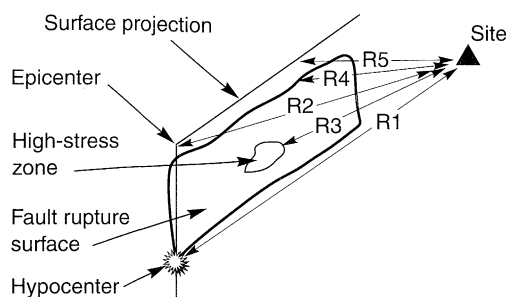


Figure 3.21 Various measures of distance used in strong-motion predictive relationships. (After Shakal and Bernreuter, 1981.)

3.4.2 Development of Predictive Relationships

Predictive relationships usually express ground motion parameters as functions of magnitude, distance, and in some cases, other variables, for example,

$$Y = f(M, R, P_i) \quad (3.22)$$

where Y is the ground motion parameter of interest, M the magnitude of the earthquake, R a measure of the distance from the source to the site being considered, and the P_i are other parameters (which may be used to characterize the earthquake source, wave propagation path, and/or local site conditions). Predictive relationships are developed by regression analyses of recorded strong motion databases. As such, they change with time as additional strong motion data become available. Most predictive relationships are updated in the literature every 3 to 5 years or shortly after the occurrence of large earthquakes in well-instrumented regions.

The functional form of the predictive relationship is usually selected to reflect the mechanics of the ground motion process as closely as possible. This minimizes the number of empirical coefficients and allows greater confidence in application of the predictive relationship to conditions (magnitudes and distances) that are poorly represented in the database. Common forms for predictive relationships are based on the following observations:

1. Peak values of strong motion parameters are approximately lognormally distributed (i.e., the logarithms of the parameters are approximately normally distributed). As a result, the regression is usually performed on the logarithm of Y rather than on Y itself.
2. Earthquake magnitude is typically defined as the logarithm of some peak motion parameter (Section 2.9.2). Consequently, $\ln Y$ should be approximately proportional to M .
3. The ^{amplitude} spreading of stress waves as they travel away from the source of an earthquake causes body wave [p- and s-wave (Section 5.2.2.5)] amplitudes to decrease according to $1/R$ and surface wave [primarily Rayleigh wave (Section 5.3.1)] amplitudes to decrease according to $1/\sqrt{R}$.
4. The area over which fault rupture occurs increases with increasing earthquake magnitude (Section 4.2.1.2). As a result, some of the waves that produce strong motion at a site arrive from a distance, R , and some arrive from greater distances. The effective distance, therefore, is greater than R by an amount that increases with increasing magnitude.
5. Some of the energy carried by stress waves is absorbed by the materials they travel through [material damping (Section 5.5.1)]. This material damping causes ground motion amplitudes to decrease exponentially with R .
6. Ground motion parameters may be influenced by source characteristics (e.g. strike-slip, normal, or reverse faulting) or site characteristics (e.g. hard rock, soft rock, alluvium, etc.).

Combining these observations, a typical predictive relationship may have the form

$$\ln Y = \underbrace{C_1}_{\textcircled{1}} + \underbrace{C_2 M + C_3 M^{C_4}}_{\textcircled{2}} + \underbrace{C_5 \ln[R + C_6 \exp(C_7 M)]}_{\textcircled{4}} + \underbrace{C_8 R}_{\textcircled{5}} + \underbrace{f(\text{source}) + f(\text{site})}_{\textcircled{6}} \quad \sigma_{\ln Y} = C_9 \quad (3.23)$$

where the circled numbers indicate the observations associated with each term. Some predictive relationships utilize all these terms (and some have even more) and others do not.

The $\sigma_{\ln Y}$ term describes uncertainty in the value of the ground motion parameter given by the predictive relationship. Statistically, it represents an estimate of the standard deviation of $\ln Y$ at the magnitude and distance of interest. Historically, most $\sigma_{\ln Y}$ values have been constants, but several recent predictive relationships indicate $\sigma_{\ln Y}$ values that vary with magnitude. At a given magnitude, therefore, the probability that the ground motion parameter will exceed a value Y^* would be $1 - F_Z(z^*)$ where $F_Z(z^*)$ is the value of the standard cumulative distribution function (see Section C7.2 of Appendix C) at $z^* = (\ln Y^* - \bar{\ln Y})/\sigma_{\ln Y}$.

When using any predictive relationship, it is very important to know how parameters such as M and R are defined and to use them in a consistent manner. It is also important to recognize that different predictive relationships are usually obtained from different data sets. To make reasonable predictions of ground motion parameters, a predictive relationship based on data that are consistent with the conditions relevant to the prediction is required.

3.4.3 Estimation of Amplitude Parameters

Predictive relationships for parameters that decrease with increasing distance (such as peak acceleration and peak velocity) are often referred to as *attenuation relationships*. A few of a large number of useful attenuation relationships for different geographic and tectonic environments are described in the following sections.

3.4.3.1 Peak Acceleration

Since peak acceleration is the most commonly used ground motion parameter, many peak acceleration attenuation relationships have been developed. All are best suited to conditions similar to those in the databases from which they were developed. As additional strong motion data have become available, attenuation relationships have become more refined. Consider, for example, two attenuation relationships developed some 13 years apart.

In 1981, Campbell (1981) used worldwide data to develop an attenuation relationship for the mean PHA for sites within 50 km of the fault rupture in magnitude 5.0 to 7.7 earthquakes:

$$\begin{aligned} \ln \text{PHA}(g) &= -4.141 + 0.868M - 1.09 \ln[R + 0.0606 \exp(0.7M)] \\ \sigma_{\ln \text{PHA}} &= 0.37 \end{aligned} \quad (3.24)$$

where M is the local magnitude or surface wave magnitude for magnitudes less than or greater than 6, respectively, and R is the closest distance to the fault rupture in kilometers. In this relatively simple attenuation relationship, which represented the state of the art in 1981, the peak acceleration was taken as a function of M and R only and $\sigma_{\ln \text{PHA}}$ was constant. In 1994, Campbell and Bozorgnia (1994) used worldwide accelerograms from earthquakes of moment magnitude ranging from 4.7 to 8.1 to develop the attenuation relationship

$$\begin{aligned} \ln \text{PHA}(\text{gals}) &= -3.512 + 0.904M_w - 1.328 \ln \sqrt{R^2 + [0.149 \exp(0.647M_w)]^2} \\ &+ (1.125 - 0.112 \ln R - 0.0957M_w)F + (0.440 - 0.171 \ln R)S_{\text{SR}} \\ &+ (0.405 - 0.222 \ln R)S_{\text{HR}} \end{aligned} \quad (3.25)$$

$$\sigma_{\ln \text{PHA}} = \begin{cases} 0.889 - 0.0691M & M \leq 7.4 \\ 0.38 & M > 7.4 \end{cases}$$

where R is the closest distance (≤ 60 km) to seismic rupture in kilometers (with minimum values of 7.3, 5.8, 3.5, and 3.0 km for magnitudes of 5.0, 5.5, 6.0, and 6.5, respectively); the source term, F , takes on values of 0 for strike-slip and normal faulting, and 1 for reverse, reverse-oblique, and thrust faulting; $S_{SR} = 1$ for soft-rock sites (sedimentary deposits of Tertiary age), $S_{HR} = 1$ for hard-rock sites (primarily older sedimentary deposits, metamorphic rock, and crystalline rock), and $S_{SR} = S_{HR} = 0$ for alluvium sites. The 1994 relationship, which is based on more data, is clearly more specific (and more complicated) than the 1981 relationship. The incorporation of additional terms reflecting source and site characteristics are typical of the refinement of predictive relationships that has taken place in recent years.

Boore et al. (1993) used data from western North America earthquakes of magnitude 5.0 to 7.7 at distances within 100 km (62 mi) of the surface projection of the fault to develop the predictive relationship

$$\log \text{PHA}(g) = b_1 + b_2(M_w - 6) + b_3(M_w - 6)^2 + b_4R + b_5 \log R + b_6G_B + b_7G_C \quad (3.26)$$

where $R = \sqrt{d^2 + h^2}$, d is the closest distance to the surface projection of the fault in kilometers, and

$$G_B = \begin{cases} 0 & \text{for site class A} \\ 1 & \text{for site class B} \\ 0 & \text{for site class C} \end{cases} \quad G_C = \begin{cases} 0 & \text{for site class A} \\ 0 & \text{for site class B} \\ 1 & \text{for site class C} \end{cases}$$

Note that the Boore et al. (1993) attenuation relationship is expressed in terms of the common (base 10) logarithm rather than the natural logarithm. The site classes are defined on the basis of the average shear wave velocity in the upper 30 m (100 ft) (Table 3-5). Coefficients for the Boore et al. (1993) attenuation relationship were developed for two measures of peak acceleration: the randomly oriented component and the larger horizontal component (the former considers two orthogonal horizontal records at a particular site as separate events and the latter considers only the larger of the two). The coefficients are given in Table 3-6.

Table 3-5 Definitions of Site Classes for Boore et al. (1993) Attenuation Relationship

Site Class	\bar{v}_s in Upper 30 m (100 ft)
A	> 750 m/sec (2500 ft/sec)
B	360–750 m/sec (1200–2500 ft/sec)
C	180–360 m/sec (600–1200 ft/sec)

Table 3-6 Coefficients for Boore et al. (1993) Attenuation Relationship

	Component								
	b_1	b_2	b_3	b_4	b_5	b_6	b_7	h	$\sigma_{\log \text{PHA}}$
Random	-0.105	0.229	0.0	0.0	-0.778	0.162	0.251	5.57	0.230
Larger	-0.038	0.216	0.0	0.0	-0.777	0.158	0.254	5.48	0.205

Since the continental crust in eastern North America is stronger and more intact than the crust in western North America, peak accelerations tend to be higher. For the mid-continental portion of eastern North America, Toro et al. (1994) developed an attenuation relationship for peak horizontal rock acceleration:

$$\ln \text{PHA}(g) = 2.20 + 0.81 (M_w - 6) - 1.27 \ln R_m + 0.11 \max\left(\ln \frac{R_m}{100}, 0\right) - 0.0021 R_m \quad \sigma_{\ln \text{PHA}} = \sqrt{\sigma_M^2 + \sigma_R^2} \quad (3.27)$$

where $R_m = \sqrt{R^2 + 9.3^2}$, R is the closest horizontal distance to the earthquake rupture (in km), $\sigma_M = 0.36 + 0.07(M_w - 6)$, and

$$\sigma_R = \begin{cases} 0.54 & \text{for } R < 5 \text{ km} \\ 0.54 - 0.0227(R - 5) & \text{for } 5 \text{ km} \leq R \leq 20 \text{ km} \\ 0.20 & \text{for } R > 20 \text{ km} \end{cases}$$

Subduction zone earthquakes generally occur at greater hypocentral depths than earthquakes that occur on transform faults. Consequently, the seismic waves that emanate from subduction zone earthquakes follow different paths from those of transform faults. Youngs et al. (1988) used strong-motion measurements obtained on rock from 60 earthquakes and numerical simulations of $M_w \geq 8$ earthquakes to develop a subduction zone attenuation relationship:

$$\ln \text{PHA}(g) = 19.16 + 1.045 M_w - 4.738 \ln [R + 205.5 \exp(0.0968 M_w)] + 0.54 Z_t \quad \sigma_{\ln \text{PHA}} = 1.55 - 0.125 M_w \quad (3.28)$$

where R is the closest distance to the zone of rupture in kilometers and Z_t is 0 for interface events and 1 for intraslab events.

The four preceding attenuation relationships are shown graphically for earthquake magnitudes 5.5, 6.5, and 7.5 in Figure 3.22. The shapes of the attenuation relationships are similar, despite the fact that they represent different geographic regions and different source mechanisms and use different measures of distance.

Peak Velocity. Regression analysis of PHV data has provided a number of useful relationships describing the attenuation of that parameter. Joyner and Boore (1988), for example, used strong-motion records from earthquakes of moment magnitude between 5.0 and 7.7 to develop the attenuation relationship

$$\log \text{PHV}(\text{cm/sec}) = j_1 + j_2 (M - 6) + j_3 (M - 6)^2 + j_4 \log R + j_5 R + j_6 \quad (3.29)$$

where PHV can be selected as the randomly oriented or larger horizontal component, $R = \sqrt{r_0^2 + j_7^2}$, and r_0 is the shortest distance (in kilometers) from the site to the vertical projection of the earthquake fault rupture on the surface of the earth. The coefficients for the Joyner and Boore (1988) attenuation relationship are given in Table 3-7.

Table 3-7 Coefficients for Joyner and Boore (1988) Peak Horizontal Velocity Attenuation Relationship

Component	j_1	j_2	j_3	j_4	j_5	j_6	j_7	$\sigma_{\log \text{PHV}}$
Random	2.09	0.49	0.0	-1.0	-0.0026	0.17	4.0	0.33
Larger	2.17	0.49	0.0	-1.0	-0.0026	0.17	4.0	0.33

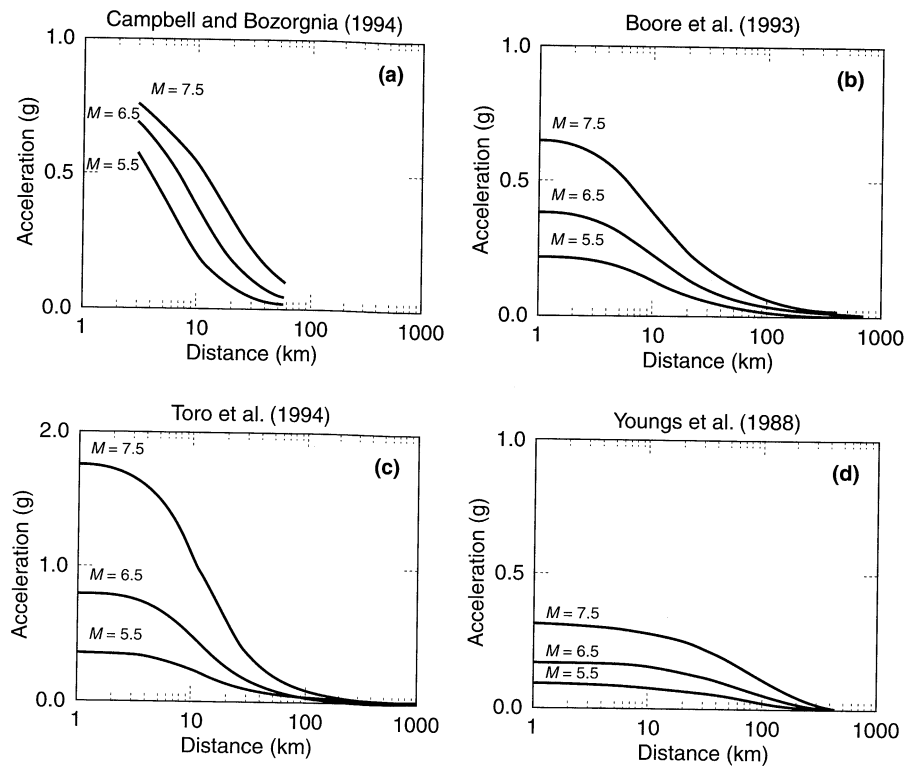


Figure 3.22 Variation of peak horizontal acceleration with distance for $M = 5.5$, $M = 6.5$, and $M = 7.5$ earthquakes according to various attenuation relationships: (a) Campbell and Bozorgnia (1994), soft rock sites and strike-slip faulting; (b) Boore et al. (1993), site class B; (c) Toro et al. (1994); and (d) Youngs et al. (1988), intraslab event.

3.4.4 Estimation of Frequency Content Parameters

Large earthquakes produce larger and longer-period ground motions than do smaller earthquakes; consequently, the frequency content of a ground motion is related to the earthquake magnitude. As seismic waves travel away from a fault, their higher-frequency components are scattered and absorbed more rapidly than are their lower-frequency components. As a result, the frequency content also changes with distance.

3.4.4.1 Predominant Period

One aspect of the change in frequency content with distance involves the shifting of the peak of the Fourier amplitude spectrum to lower frequencies (or higher periods). As a result, the predominant period increases with increasing distance, as illustrated in Figure 3.23.

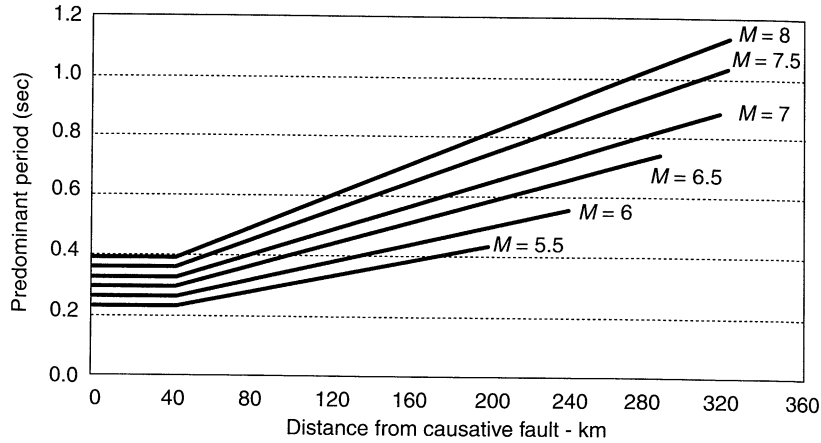


Figure 3.23 Variation of predominant period at rock outcrops with magnitude and distance. (After Seed et al., 1969.)

Example 3.7

Determine the predominant period that would have been expected for the recorded motion at the Gilroy No. 1 (rock) site.

Solution The Gilroy No. 1 (rock) motion was recorded at a site located at an epicentral distance of 21.8 km from the Loma Prieta ($M = 7.1$) earthquake. From Figure 3.23, the expected predominant period would be 0.33 sec. As determined in Example 3.3, the actual predominant period of the Gilroy No. 1 (rock) motion was 0.39 sec.

3.4.4.2 Fourier Amplitude Spectra

Ordinates of the Fourier amplitude spectrum can be estimated empirically by regression on the Fourier spectral ordinates of actual strong-motion data (e.g., Trifunac, 1976; McGuire et al., 1984; Trifunac and Lee, 1987; Castro et al., 1990). Alternatively, a physically based model of source, travel path, and site behavior may be calibrated to predict Fourier amplitude spectra.

Based on Brune's (1970, 1971) solution for instantaneous slip of a circular rupture surface, the Fourier amplitudes for a far-field event at distance R can be expressed (McGuire and Hanks, 1980; Boore, 1983) as

$$|A(f)| = \left[CM_0 \frac{f^2}{1 - (f/f_c)^2} \frac{1}{\sqrt{1 + (f/f_{\max})^8}} \right] \frac{e^{-\pi f R/Q(f) v_s}}{R} \quad (3.30)$$

where f_c is the corner frequency (see Figure 3.14), f_{\max} the cutoff frequency (Figure 3.14), $Q(f)$ is the frequency-dependent *quality factor* (inversely proportional to the damping ratio of the rock; see Section 5.5.1), and C is a constant given by

$$C = \frac{R_{\theta\phi} FV}{4\pi\rho v_s^3} \quad (3.31)$$

where $R_{\theta\phi}$ (≈ 0.55) accounts for the radiation pattern, F ($= 2$) accounts for the free-surface effect, V ($= \sqrt{2}/2$) accounts for partitioning the energy into two horizontal components, ρ is the density of the rock along the rupture surface, and v_s is the shear wave velocity of the rock.

If f_{\max} is assumed constant for a given geographic region (15 Hz and 40 Hz are typical values for western and eastern North America, respectively), the spectra for different earthquakes are functions of the seismic moment, M_o , and f_c , which can be related (Brune, 1970, 1971) by

$$f_c = 4.9 \times 10^6 v_s \left(\frac{\Delta\sigma}{M_o} \right)^{1/3} \quad (3.32)$$

where v_s is in km/sec, M_o is in dyne-cm, and $\Delta\sigma$ is referred to as the *stress parameter* or *stress drop* in bars. Stress parameters of 50 bars and 100 bars are commonly used for sources in western and eastern North America, respectively. Figure 3.24a shows how the Fourier amplitude spectra predicted by equation (3.30) vary with magnitude. Note the strong influence of magnitude on both the amplitude and frequency content of the motion. As the magnitude increases, the bandwidth increases and the corner frequency decreases, implying that more low-frequency (long-period) motion will occur. Figure 3.24b shows time histories of acceleration generated from the spectra of equation (3.30) for magnitude 4 and magnitude 7 events. The stress parameter and seismic moment are commonly used to specify the *source spectrum*, given by the expression in brackets in equation (3.30). The final expression is the *travel path operator*, which describes attenuation of the Fourier amplitudes as the energy travels away from the site. An expression that describes the effects of soil response (a *site operator*) can be added to equation (3.31), if necessary, to account for near-surface effects. The response of soil deposits during earthquakes is discussed in detail in Chapter 7.

Since it is based on the mechanics of source rupture and wave propagation, equation (3.30) offers significant advantages over purely empirical methods for magnitudes and distances for which few or no data are available.

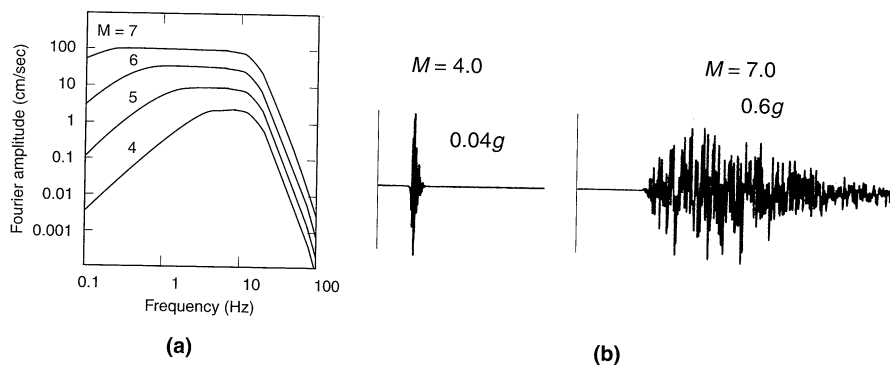


Figure 3.24 (a) Variation of Fourier amplitude spectra at $R = 10$ km for different moment magnitudes ($\Delta\sigma = 100$ bars); (b) accelerograms generated from the $M = 4$ and $M = 7$ spectra. (After Boore, 1983. Used by permission of the Seismological Society of America.)

3.4.4.3 Ratio v_{\max}/a_{\max}

As a measure of the frequency content of a ground motion, the ratio v_{\max}/a_{\max} is also related to earthquake magnitude and distance. This dependence has been studied by several investigators, with a summary of their results provided by McGuire (1978), who proposed the magnitude and distance dependencies shown in Table 3-8. The table indicates that, as expected, the v_{\max}/a_{\max} ratio increases with increasing earthquake magnitude and increasing source-to-site distance.

Table 3-8 Magnitude and Distance Dependence of v_{\max}/a_{\max} ^a

Site Conditions	Magnitude Dependence	Distance Dependence
Rock sites	$e^{0.40M}$	$R^{0.12}$
Soil sites	$e^{0.15M}$	$R^{0.23}$

Source: After McGuire (1978).

^aThe ratio v_{\max}/a_{\max} is proportional to these dependence relationships.

Example 3.8

Estimate the values of v_{\max}/a_{\max} that would be observed at rock and soil sites 40 km from the source of a $M = 6$ earthquake located near the 1989 Loma Prieta earthquake.

Solution Using the values from the Gilroy No. 1 (rock) and Gilroy No. 2 (soil) sites, and recalling that those sites were located 21.8 km and 22.8 km, respectively, from the $M = 7.1$ Loma Prieta earthquake,

$$\begin{aligned} \text{Rock site:} \quad \frac{v_{\max}}{a_{\max}} &\approx 0.078 \text{ sec} \frac{e^{(0.40)(6)}}{e^{(0.40)(7.1)}} \frac{40^{0.12}}{21.8^{0.12}} = 0.054 \text{ sec} \\ \text{Soil site:} \quad \frac{v_{\max}}{a_{\max}} &\approx 0.124 \text{ sec} \frac{e^{(0.15)(6)}}{e^{(0.15)(7.1)}} \frac{40^{0.23}}{22.8^{0.23}} = 0.120 \text{ sec} \end{aligned}$$

3.4.4.4 Response Spectrum Ordinates

The importance of response spectra in earthquake engineering has led to the development of methods for predicting them directly. For many years, the shapes of all response spectra were, for a given class of soil conditions, assumed to be identical. Design spectra were developed by scaling standard spectral shapes by some ground motion parameter, usually the PHA. As more recorded motions became available, the magnitude dependence of spectral shapes was recognized increasingly. For example, Figure 3.25 shows the response spectra computed from the accelerograms shown in Figure 3.21. The difference in spectral shapes at different magnitudes, particularly in the long-period range, are apparent. This shape dependence was later accounted for, at least approximately, by using PHA, PHV, and peak displacement to scale design spectra in different frequency ranges (Newmark and Hall, 1978, 1982), as discussed in Section 8.3.2. More recently, regression analyses have been used to develop predictive relationships for spectral ordinates at various oscillator periods (e.g., Joyner and Boore, 1982, 1988; Crouse, 1991; Boore et al., 1993).

For example, Boore et al. (1993) determined values of coefficients that when used with equation (3.26), predict pseudospectral velocities for oscillators of different natural periods. These attenuation relationships, the coefficients of which are presented in

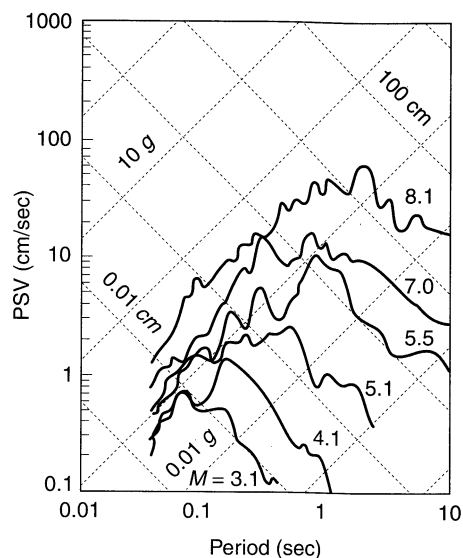


Figure 3.25 Response spectra computed from the accelerograms of Figure 3.20. Epicentral distances from each accelerogram were nearly equal. Note that the shapes, as well as the values, of the spectra vary with earthquake magnitude. (After Anderson, 1991. *Geotechnical News*, Vol. 9, No.1, p.35. Used by permission of BiTech Publishers, Ltd.)

Tables 3-9 and 3-10, are applicable to the same conditions as the attenuation relationship of equation (3.26). These coefficients produce smooth response spectra, as illustrated in Figure 3.26. Although the smooth response spectra are limited to periods of 2.0 sec, their general shapes are similar to those of actual spectra.

3.4.5 Estimation of Duration

The duration of strong ground motion increases with increasing earthquake magnitude. However, the manner in which strong motion duration varies with distance depends on how it is defined. Since acceleration amplitudes decrease with distance, durations based on absolute acceleration levels, such as the bracketed duration, would be expected to decrease with distance; at some distance all accelerations will drop below the threshold acceleration and the bracketed duration will be zero. Page et al. (1972) and Chang and Krinitzky (1977) confirmed this, as shown in Figure 3.27. Durations based on relative acceleration levels (e.g., Trifunac and Brady, 1975b; Dobry et al., 1978) increase with increasing distance and may have long durations even when the acceleration amplitudes are very low. For engineering purposes, the bracketed duration appears to provide the most reasonable indication of the influence of duration on potential damage.

3.4.6 Estimation of Other Parameters

Parameters that reflect more than one important characteristic of strong ground motion are likely to see increasing use. For most, however, only limited data for the development of predictive relationships are currently available.

Table 3-9 Smoothed Coefficients of Predictive Relationships for the Larger Horizontal Component of 5% Damped PSV

T	b_1	b_2	b_3	b_4	b_5	b_6	b_7	h	$\sigma_{\log Y}$
0.10	1.700	0.321	-0.104	0.0	-0.921	0.039	0.128	6.18	0.194
0.11	1.777	0.320	-0.110	0.0	-0.929	0.065	0.150	6.57	0.194
0.12	1.837	0.320	-0.113	0.0	-0.934	0.087	0.169	6.82	0.193
0.13	1.886	0.321	-0.116	0.0	-0.938	0.106	0.187	6.99	0.193
0.14	1.925	0.322	-0.117	0.0	-0.939	0.123	0.203	7.09	0.193
0.15	1.956	0.323	-0.117	0.0	-0.939	0.137	0.217	7.13	0.194
0.16	1.982	0.325	-0.117	0.0	-0.939	0.149	0.230	7.13	0.194
0.17	2.002	0.326	-0.117	0.0	-0.938	0.159	0.242	7.10	0.195
0.18	2.019	0.328	-0.115	0.0	-0.936	0.169	0.254	7.05	0.195
0.19	2.032	0.330	-0.114	0.0	-0.934	0.177	0.264	6.98	0.196
0.20	2.042	0.332	-0.112	0.0	-0.931	0.185	0.274	6.90	0.196
0.22	2.056	0.336	-0.109	0.0	-0.926	0.198	0.291	6.70	0.198
0.24	2.064	0.341	-0.105	0.0	-0.920	0.208	0.306	6.48	0.199
0.26	2.067	0.345	-0.101	0.0	-0.914	0.217	0.320	6.25	0.201
0.28	2.066	0.349	-0.096	0.0	-0.908	0.224	0.333	6.02	0.202
0.30	2.063	0.354	-0.092	0.0	-0.902	0.231	0.344	5.79	0.204
0.32	2.058	0.358	-0.088	0.0	-0.897	0.236	0.354	5.57	0.205
0.34	2.052	0.362	-0.083	0.0	-0.891	0.241	0.363	5.35	0.206
0.36	2.045	0.366	-0.079	0.0	-0.886	0.245	0.372	5.14	0.208
0.38	2.038	0.369	-0.076	0.0	-0.881	0.249	0.380	4.94	0.209
0.40	2.029	0.373	-0.072	0.0	-0.876	0.252	0.388	4.75	0.211
0.42	2.021	0.377	-0.068	0.0	-0.871	0.255	0.395	4.58	0.213
0.44	2.013	0.380	-0.065	0.0	-0.867	0.258	0.401	4.41	0.213
0.46	2.004	0.383	-0.061	0.0	-0.863	0.261	0.407	4.26	0.215
0.48	1.996	0.386	-0.058	0.0	-0.859	0.263	0.413	4.11	0.216
0.50	1.988	0.390	-0.055	0.0	-0.856	0.265	0.418	3.97	0.217
0.55	1.968	0.397	-0.048	0.0	-0.848	0.270	0.430	3.67	0.221
0.60	1.949	0.404	-0.042	0.0	-0.842	0.275	0.441	3.43	0.223
0.65	1.932	0.410	-0.037	0.0	-0.837	0.279	0.451	3.23	0.226
0.70	1.917	0.416	-0.033	0.0	-0.833	0.283	0.459	3.08	0.229
0.75	1.903	0.422	-0.029	0.0	-0.830	0.287	0.467	2.97	0.232
0.80	1.891	0.427	-0.025	0.0	-0.827	0.290	0.474	2.89	0.234
0.85	1.881	0.432	-0.022	0.0	-0.826	0.294	0.481	2.85	0.237
0.90	1.872	0.436	-0.020	0.0	-0.825	0.297	0.486	2.83	0.240
0.95	1.864	0.440	-0.018	0.0	-0.825	0.301	0.492	2.84	0.242
1.00	1.858	0.444	-0.016	0.0	-0.825	0.305	0.497	2.87	0.245
1.10	1.849	0.452	-0.014	0.0	-0.828	0.312	0.506	3.00	0.249
1.20	1.844	0.458	-0.013	0.0	-0.832	0.319	0.514	3.19	0.254
1.30	1.842	0.464	-0.012	0.0	-0.837	0.326	0.521	3.44	0.258
1.40	1.844	0.469	-0.013	0.0	-0.843	0.334	0.527	3.74	0.262
1.50	1.849	0.474	-0.014	0.0	-0.851	0.341	0.533	4.08	0.267
1.60	1.857	0.478	-0.016	0.0	-0.859	0.349	0.538	4.46	0.270
1.70	1.866	0.482	-0.019	0.0	-0.868	0.357	0.543	4.86	0.274
1.80	1.878	0.485	-0.022	0.0	-0.878	0.365	0.547	5.29	0.279
1.90	1.891	0.488	-0.025	0.0	-0.888	0.373	0.551	5.74	0.283
2.00	1.905	0.491	-0.028	0.0	-0.898	0.381	0.554	6.21	0.287

Source: After Boore et al., (1993).

Table 3-10 Smoothed Coefficients of Predictive Relationships for the Random Horizontal Component of 5% Damped PSV

T	b_1	b_2	b_3	b_4	b_5	b_6	b_7	h	$\sigma_{\log Y}$
0.10	1.653	0.327	-0.098	0.0	-0.934	0.046	0.136	6.27	0.208
0.11	1.725	0.318	-0.100	0.0	-0.937	0.071	0.156	6.65	0.208
0.12	1.782	0.313	-0.101	0.0	-0.939	0.093	0.174	6.91	0.208
0.13	1.828	0.309	-0.101	0.0	-0.939	0.111	0.191	7.08	0.209
0.14	1.864	0.307	-0.100	0.0	-0.938	0.127	0.206	7.18	0.209
0.15	1.892	0.305	-0.099	0.0	-0.937	0.140	0.221	7.23	0.211
0.16	1.915	0.305	-0.098	0.0	-0.935	0.153	0.234	7.24	0.211
0.17	1.933	0.305	-0.096	0.0	-0.933	0.163	0.246	7.21	0.212
0.18	1.948	0.306	-0.094	0.0	-0.930	0.173	0.258	7.16	0.213
0.19	1.959	0.308	-0.092	0.0	-0.927	0.182	0.269	7.10	0.215
0.20	1.967	0.309	-0.090	0.0	-0.924	0.190	0.279	7.02	0.215
0.22	1.978	0.313	-0.086	0.0	-0.918	0.203	0.297	6.83	0.218
0.24	1.982	0.318	-0.082	0.0	-0.912	0.214	0.314	6.62	0.220
0.26	1.982	0.323	-0.078	0.0	-0.906	0.224	0.329	6.39	0.222
0.28	1.979	0.329	-0.073	0.0	-0.899	0.232	0.343	6.17	0.225
0.30	1.974	0.334	-0.070	0.0	-0.893	0.239	0.356	5.94	0.226
0.32	1.967	0.340	-0.066	0.0	-0.888	0.245	0.367	5.72	0.228
0.34	1.959	0.345	-0.062	0.0	-0.882	0.251	0.378	5.50	0.230
0.36	1.950	0.350	-0.059	0.0	-0.877	0.256	0.387	5.30	0.232
0.38	1.940	0.356	-0.055	0.0	-0.872	0.260	0.396	5.10	0.235
0.40	1.930	0.361	-0.052	0.0	-0.867	0.264	0.405	4.91	0.236
0.42	1.920	0.365	-0.049	0.0	-0.862	0.267	0.413	4.74	0.238
0.44	1.910	0.370	-0.047	0.0	-0.858	0.271	0.420	4.57	0.239
0.46	1.900	0.375	-0.044	0.0	-0.854	0.273	0.427	4.41	0.241
0.48	1.890	0.379	-0.042	0.0	-0.850	0.276	0.433	4.26	0.243
0.50	1.881	0.384	-0.039	0.0	-0.846	0.279	0.439	4.13	0.244
0.55	1.857	0.394	-0.034	0.0	-0.837	0.284	0.452	3.82	0.248
0.60	1.835	0.403	-0.030	0.0	-0.830	0.289	0.464	3.57	0.251
0.65	1.815	0.411	-0.026	0.0	-0.823	0.293	0.474	3.36	0.254
0.70	1.797	0.418	-0.023	0.0	-0.818	0.297	0.483	3.20	0.257
0.75	1.781	0.425	-0.020	0.0	-0.813	0.300	0.490	3.07	0.259
0.80	1.766	0.431	-0.018	0.0	-0.809	0.303	0.497	2.98	0.261
0.85	1.753	0.437	-0.016	0.0	-0.805	0.306	0.503	2.92	0.264
0.90	1.742	0.442	-0.015	0.0	-0.802	0.309	0.508	2.89	0.266
0.95	1.732	0.446	-0.014	0.0	-0.800	0.312	0.513	2.88	0.268
1.00	1.724	0.450	-0.014	0.0	-0.798	0.314	0.517	2.90	0.270
1.10	1.710	0.457	-0.013	0.0	-0.795	0.319	0.523	2.99	0.274
1.20	1.701	0.462	-0.014	0.0	-0.794	0.324	0.528	3.14	0.277
1.30	1.696	0.466	-0.015	0.0	-0.793	0.328	0.532	3.36	0.280
1.40	1.695	0.469	-0.017	0.0	-0.794	0.333	0.535	3.62	0.283
1.50	1.696	0.471	-0.019	0.0	-0.796	0.338	0.537	3.92	0.285
1.60	1.700	0.472	-0.022	0.0	-0.798	0.342	0.538	4.26	0.286
1.70	1.706	0.473	-0.025	0.0	-0.801	0.347	0.539	4.62	0.289
1.80	1.715	0.472	-0.029	0.0	-0.804	0.351	0.539	5.01	0.290
1.90	1.725	0.472	-0.032	0.0	-0.808	0.356	0.538	5.42	0.292
2.00	1.737	0.471	-0.037	0.0	-0.812	0.360	0.537	5.85	0.293

Source: After Boore et al., (1993).

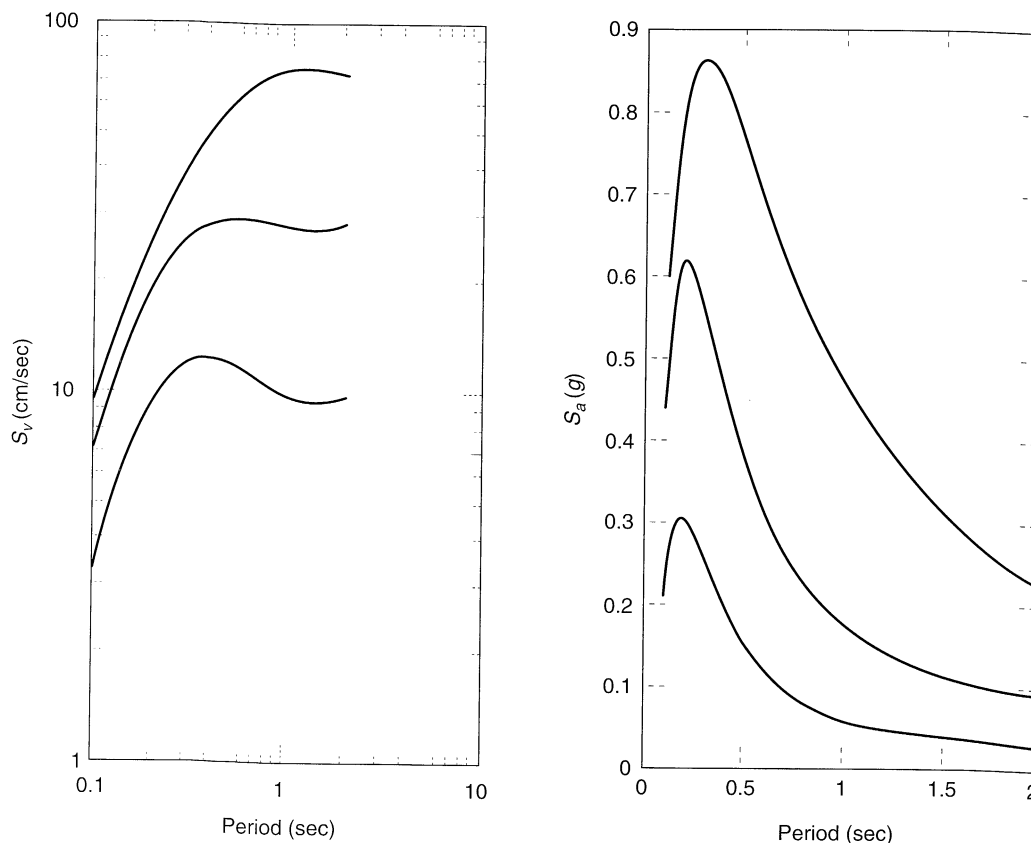


Figure 3.26 Response spectra for the random component of ground motion at a site class B site at $R = 10$ km according to the predictive relationship of Boore et al. (1993): (a) pseudospectral velocity computed directly from equation (3.27) and Table 3-10, and (b) pseudospectral acceleration computed from the pseudospectral velocities.

3.4.6.1 RMS Acceleration

Hanks and McGuire (1981) used a database of California earthquakes of local magnitude 4.0 to 7.0 to develop an attenuation relationship for rms acceleration for hypocentral distances between 10 and 100 km (6.2 and 62 mi):

$$a_{\text{rms}} = 0.119 \frac{\sqrt{f_{\text{max}}/f_c}}{R} \quad (3.33)$$

where f_c is the corner frequency, f_{max} is the cutoff frequency, and R is in kilometers.

Kavazanjian et al. (1985) used the definition of duration proposed by Vanmarcke and Lai (1980) with a database of 83 strong motion records from 18 different earthquakes to obtain

$$a_{\text{rms}} = 0.472 + 0.268M_w + 0.129 \log\left(\frac{0.966}{R^2} + \frac{0.255}{R}\right) - 0.1167R \quad (3.34)$$

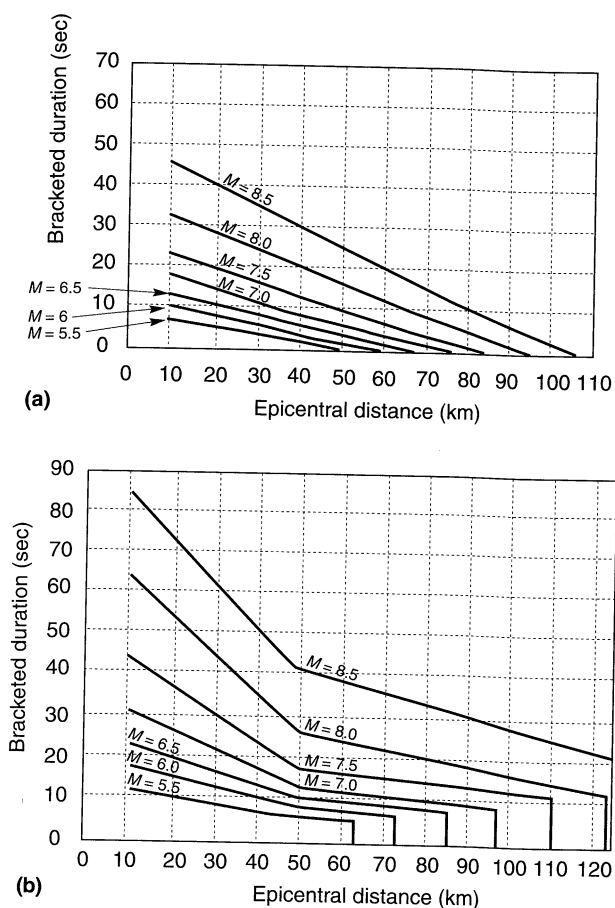


Figure 3.27 Variation of bracketed duration (0.05g threshold) with magnitude and epicentral distance: (a) rock sites; (b) soil sites. (After Chang and Krinitzsky, 1977.)

where R is the distance to the closest point of rupture on the fault. The database was restricted to $M_w > 5$, $R < 110$ km (68 mi), rupture depths less than 30 km (19 mi), and soil thicknesses greater than 10 m (33 ft).

3.4.6.2 Arias Intensity

Campbell and Duke (1974) used data from California earthquakes to predict the variation of Arias intensity within 15 to 110 km (9 to 68 mi) of magnitude 4.5 to 8.5 events.

$$I_a \text{ (m/sec)} = 313 \frac{e^{M_s(0.33M_s - 1.47)}}{R^{3.79}} S \quad (3.35)$$

$$\text{where } S = \begin{cases} 0.57R^{0.46} & \text{for basement rock} \\ 1.02R^{0.51} & \text{for sedimentary rock} \\ 0.37R^{0.81} & \text{for alluvium } \leq 60\text{ft thick} \\ 0.65R^{0.74} & \text{for alluvium } > 60\text{ft thick} \end{cases}$$

and R is the distance from the center of energy release in kilometers.

Wilson (1993) analyzed strong motion records from California to develop an attenuation relationship which, using the Arias intensity definition of equation (3.17), can be expressed as

$$\log I_a \text{ (m/sec)} = M_w - 2 \log R - kR - 3.990 + 0.365 (1 - P) \quad (3.36)$$

where $R = \sqrt{D^2 + h^2}$, D is the minimum horizontal distance to the vertical projection of the fault plane, h is a correction factor (with a default value of 7.5 km (4.7 mi)), k is a coefficient of anelastic absorption (with a default value of zero), and P is the exceedance probability.

Acceleration and Velocity Spectrum Intensities. Von Thun et al. (1988) used 30 strong motion records, primarily from rock outcrops in the western United States and Italy, to develop the attenuation relationships for acceleration spectrum intensity and velocity spectrum intensity shown graphically in Figure 3.28. Large earthquakes in these areas are generally accompanied by surface faulting. The use of these attenuation relationships is recommended only for areas with similar tectonic conditions.

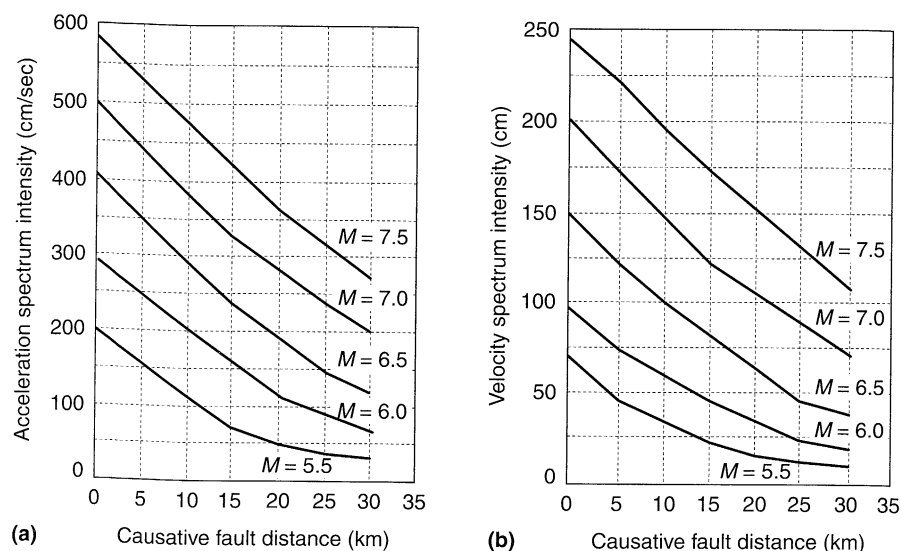


Figure 3.28 Attenuation of (a) acceleration spectrum intensity and (b) velocity spectrum intensity. (After Von Thun et al., 1988. Earthquake ground motions for design and analysis of dams, *Earthquake Engineering and Soil Dynamics II*. Reprinted by permission of ASCE.)

3.5 SPATIAL VARIABILITY OF GROUND MOTIONS

The preceding sections considered the spatial variation of ground motions on a regional scale. Ground motions also vary spatially on local scales, and this local variation can be important for certain types of structures. The longest dimension of most structures is usually small enough that the ground motion at one end is virtually the same as that at the other end. For structures such as bridges and pipelines that extend over considerable distances, different ground motions may occur beneath different parts of the structure. In such cases the

local spatial variation (or *incoherence*) of the ground motion may exert an important influence on the response of the structure.

Spatial incoherence can be caused by a number of factors. One is the traveling-wave or *wave-passage* effect, in which nonvertical waves reach different points on the ground surface at different times, producing a time shift between the motions at those points (Figure 3.29a). A cause of incoherence in the nearfield is the *extended source effect*, in which differences in the relative geometry of the source and sites produce different time shifts, and consequently different motions, at the sites (Figure 3.29b). Finally, *ray-path effects* caused by scattering (reflection, refraction, etc.) of waves by inhomogeneities along the travel path (Figure 3.30c) can cause incoherence.

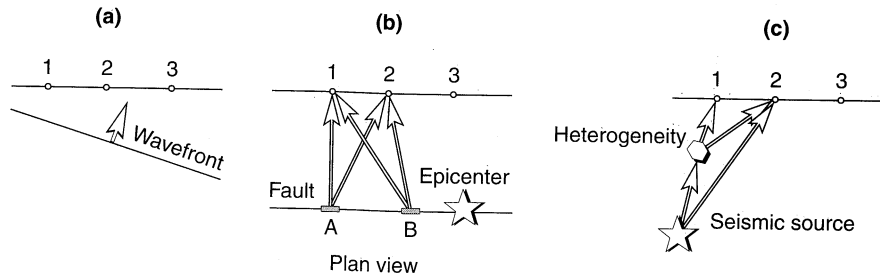


Figure 3.29 Sources of incoherent ground motions: (a) wave-passage effect causes inclined wavefront to reach locations 1, 2, and 3 at different times; (b) extended source effect causes waves due to rupture at A and B to reach points 1 and 2 at different times; (c) scattering of waves by heterogeneity causes different waves to arrive at different locations at different times. (After Abrahamson, 1991.)

The similarity between ground motions at different locations can be described in the time domain or the frequency domain. Consider two points j and k at which accelerograms $a_j(t)$ and $a_k(t)$ are recorded. The similarity of the motions can be described in the time domain by the *cross covariance*

$$C_{jk}(\tau) = \sum_{i=1}^N a_j(t_i) a_k(t_i + \tau) \quad (3.37)$$

where τ is a time increment and N is the number of time samples. The *autocovariance*, C_{jj} (or C_{kk}), is obtained by analyzing the covariance of an accelerogram against itself. The maximum value of the autocovariance will, obviously, correspond to a value of $\tau = 0$. The similarity of the motions in the frequency domain can be described by the *coherency*

$$\gamma_{jk}(\omega) = \frac{S_{jk}(\omega)}{\sqrt{S_{jj}(\omega) S_{kk}(\omega)}} \quad (3.38)$$

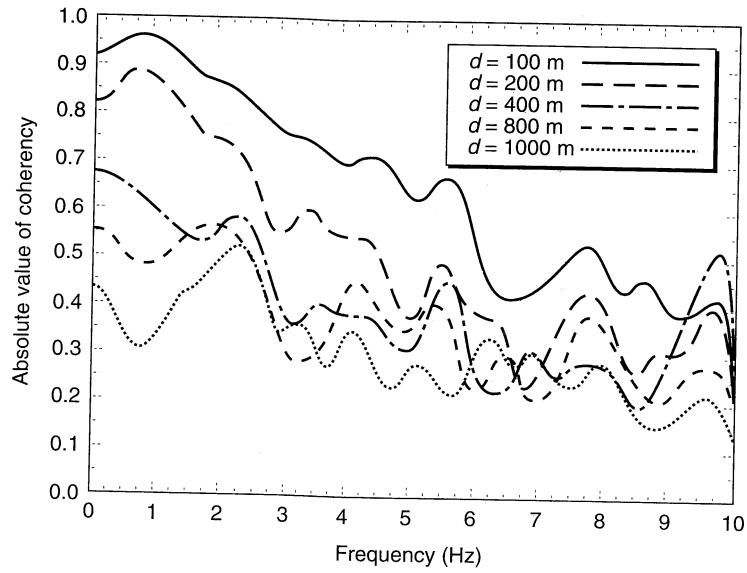
where the smoothed cross-spectrum, $S_{jk}(\omega)$, is the Fourier transform of the cross-covariance and the autospectra, $S_{jj}(\omega)$ and $S_{kk}(\omega)$, are the Fourier transforms of the autocovariances, $C_{jj}(\tau)$ and $C_{kk}(\tau)$. The coherency describes the degree of positive or negative correlation between the amplitudes and phase angles of two time histories at each of their component frequencies. A value of 1 indicates full coherence (or perfect correlation), while a value of

zero indicates full incoherence (or no correlation). The modulus of the coherency (the square root of the sum of the squares of the real and imaginary parts) is called the *lagged coherency*. Because the wave passage effect from a point source simply introduces a phase shift at each frequency, it does not influence the lagged coherency.

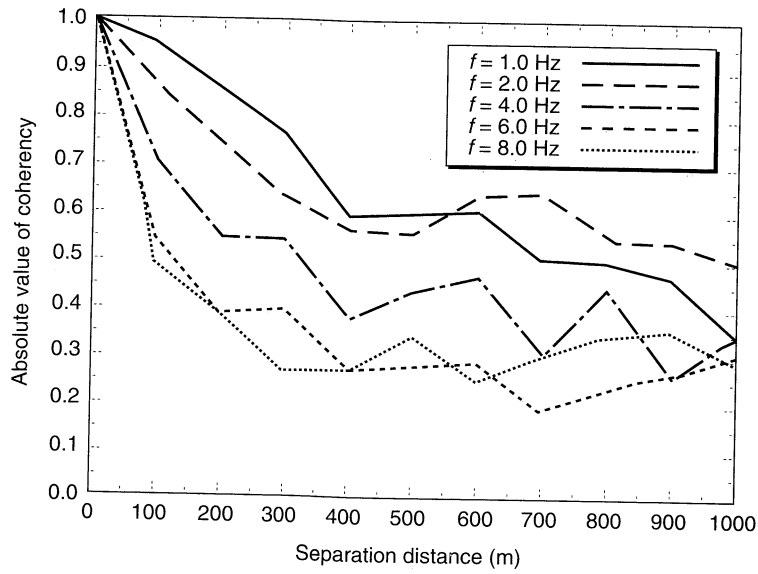
Ground motions recorded by dense arrays show that coherency decreases with increasing distance between measuring points and with increasing frequency, as shown in Figure 3.30. Measured coherency functions from dense arrays in California and Japan are similar to those from the SMART-1 array, suggesting that they may be applicable to other areas as well, although research in this area is continuing (Abrahamson, 1991). Smooth analytical coherency functions (coherency as a function of separation distance and frequency) that match the most significant trends in measured coherency functions have been proposed (Haricharan and Vanmarcke, 1986; Luco and Wong, 1986; Hao et al., 1989; Abrahamson et al., 1991).

3.6 SUMMARY

1. Complete description of a strong ground motion involves three components of translation and three components of rotation. In practice, only the translational components are usually measured, and they are usually measured in orthogonal directions.
2. A number of different instruments can be used for strong-motion measurement. Each has its own dynamic response characteristics that determine the conditions for which it is best suited. Older strong-motion instruments are likely to acquire data in analog form, while newer instruments often acquire data digitally.
3. Raw strong-motion data may include errors from several sources that require correction to produce accurate strong motion records. Strong motion processing is often required to minimize background noise, correct for the dynamic response of the transducer, and to correct for measurement errors.
4. Strong ground motions can be quite complicated, and their complete description involves a large amount of data. For engineering purposes, the essential characteristics of a strong ground motion can be described in much more compact form using ground motion parameters.
5. From an earthquake engineering standpoint, the most important characteristics of a strong ground motion are the amplitude, frequency content, and duration. All of these characteristics can significantly influence earthquake damage. Consequently, knowledge of the amplitude, frequency content, or duration alone may not be sufficient to describe accurately the damage potential of a ground motion.
6. A variety of parameters are available for description of strong ground motions. Some of these parameters describe ground motion amplitude, some describe frequency content, and others describe duration. Other parameters reflect two or more of these important characteristics. More than one parameter is generally required to characterize a strong ground motion.
7. Commonly used amplitude parameters include peak acceleration, peak velocity, and peak displacement. The peak acceleration provides a good indication of the high-frequency component of a ground motion. The peak velocity and peak displacement describe the amplitudes of the intermediate- and low-frequency components, respectively.



(a)



(b)

Figure 3.30 Measured decay of coherency with increasing frequency and separation distance for $M = 6.9$ event at hypocentral depth of 30.6 km and epicentral distance of 116.6 km from SMART-1 dense array at Lotung, Taiwan. (After Haricharan and Vanmarcke, 1986. Stochastic variation of earthquake ground motion in space and time, *Journal of Engineering Mechanics*, Vol. 112, No. 2. Reprinted by permission of ASCE.)

8. The frequency content of a strong ground motion is generally described through the use of different types of spectra. Fourier spectra and power spectra directly illustrate the frequency content of the motion itself. Response spectra reflect the influence of the ground motion on structures of different natural periods. A variety of spectral parameters are available to describe the frequency content of a strong ground motion.
9. Strong-motion durations can be described in absolute or relative terms. The bracketed duration, defined as the time between the first and last exceedances of a threshold acceleration, is based on an absolute measure of acceleration (the threshold acceleration). Measures of duration based on relative ground motion levels can define very long durations for weak ground motions. For engineering purposes, the bracketed duration is most commonly used.
10. Some parameters reflect the amplitude, frequency content, and duration of a strong ground motion. Although these parameters, such as rms acceleration, Arias intensity, and response spectrum intensity, may be more difficult to calculate than parameters more commonly used, they often reflect the potential of the motion to produce damage more accurately.
11. The characteristics of a ground motion at a particular site depend on earthquake magnitude and on the distance between the source of the earthquake and the site. Consequently, ground motion parameters also vary with earthquake magnitude and source-to-site distance.
12. Measured ground motion data have been used to develop relationships that predict values of ground motion parameters as functions of earthquake magnitude and source-to-site distance. Predictive relationships are generally empirical; each is obtained by regression on a specific set of data. Consequently, each predictive relationship is appropriate for conditions that are consistent with the conditions of the database.
13. Predictive relationships are not precise; they typically express the mean value of a ground motion parameter and include a measure of the distribution of values about the mean. The standard deviation of the parameter (or the natural logarithm of the parameter) is usually estimated in the development of the predictive relationship.
14. Predictive relationships for variables that decrease with increasing source-to-site distance are frequently referred to as attenuation relationships. Many attenuation relationships have been reported in the literature, and the most commonly used relationships are updated every few years.
15. Ground motions vary on local as well as regional scales. Local variations may cause differential movements of the supports of long structures such as bridges and pipelines. Design and analysis of such structures may require consideration of local variations.
16. The local variability of ground motions is usually expressed in terms of coherency. The coherency of two ground motions can be computed—it is a measure of the correlation of the amplitudes and phase angles of the motions at different frequencies. The coherency of two closely spaced ground motions is higher than that of two distant ground motions. Also, the coherency of the low-frequency (long-wavelength) components of a pair of motions is higher than that of the high-frequency (short-wavelength) components.

HOMEWORK PROBLEMS

Strong motion records can be obtained from a variety of sources over the Internet, often by anonymous ftp. Download the strong motion record indicated by your instructor and use it to solve Problems 3.1 - 3.6. The use of a mathematical analysis program such as MATLAB is highly recommended; it will greatly simplify the required computations.

- 3.1 Plot the time history of acceleration and determine:
 - (a) The peak acceleration.
 - (b) The sustained maximum acceleration (3rd cycle and 5th cycle).
 - (c) The bracketed duration.
- 3.2 Integrate the time history of acceleration to produce time histories of velocity and displacement. Plot the time histories of velocity and displacement and determine the peak velocity and peak displacement.
- 3.3 Compute and plot the Fourier amplitude spectrum of the strong motion record.
- 3.4 Determine the predominant period of the strong motion record.
- 3.5 Compute the rms acceleration for the strong motion record.
- 3.6 Compute the Arias intensity for the strong motion record.
- 3.7 Determine and plot the variations of peak horizontal acceleration with distance for a $M_w = 6.5$ earthquake using the attenuation relationship of Campbell (1981).
- 3.8 Determine and plot the variations of peak horizontal acceleration with distance for a $M_w = 6.5$ earthquake at soft rock, hard rock, and alluvium sites using the attenuation relationship of Campbell and Bozorgnia (1994). Which of these conditions agrees best with the attenuation relationship of Campbell (1981)?
- 3.9 Using the attenuation relationship of Toro et al. (1994), determine the probability that a $M_w = 7$ earthquake in mid-continental eastern North America would produce a peak acceleration greater than 0.30 g at a point located 50 km from the closest point of rupture.
- 3.10 Determine the peak horizontal velocity that would have a 10% probability of being exceeded by a $M_w = 7.5$ earthquake occurring at a distance of 40 km. Use the Joyner and Boore (1988) attenuation relationship.
- 3.11 Using the Boore et al. (1994) attenuation relationship, determine and plot the mean and mean \pm one standard deviation response spectra for a $M_w = 6.75$ earthquake that occurs at a distance of 70 km.
- 3.12 Determine the values of Arias intensity that have 10%, 25%, 50%, 75%, and 90% probabilities of being exceeded by a $M_w = 7.25$ earthquake at a distance of 45 km. Use the attenuation relationship of Wilson (1993) with zero anelastic absorption.



4

Seismic Hazard Analysis

4.1 INTRODUCTION

In many areas of the world, the threat to human activities from earthquakes is sufficient to require their careful consideration in the design of structures and facilities. The goal of *earthquake-resistant design* is to produce a structure or facility that can withstand a certain level of shaking without excessive damage. That level of shaking is described by a *design ground motion*, which can be characterized by *design ground motion parameters*. The specification of design ground motion parameters is one of the most difficult and most important problems in geotechnical earthquake engineering.

Much of the difficulty in design ground motion specification results from its unavoidable reliance on subjective decisions that must be made with incomplete or uncertain information. These decisions largely revolve around the definition of the boundary between acceptable and excessive damage, and uncertainty in the size, time, and location of future earthquakes. If very little damage is acceptable, a relatively strong level of shaking must be designed for, and the measures required to resist that shaking can be quite expensive. If greater levels of damage are tolerable, lower design levels of shaking may be considered and the resulting design will be less expensive. Obviously, there are trade-offs between the short-term cost of providing an earthquake-resistant design and the potential long-term cost (which, for many structures, may never be realized) of earthquake-induced damage.

Seismic hazard analyses involve the quantitative estimation of ground-shaking hazards at a particular site. Seismic hazards may be analyzed deterministically, as when a particular earthquake scenario is assumed, or probabilistically, in which uncertainties in earthquake size, location, and time of occurrence are explicitly considered. Although seismic hazard analysis is a critical part of the development of design ground motions, it is not the only part. This chapter presents different methods for analysis of seismic hazards; the broader problem of design ground motions is addressed in Chapter 8.

4.2 IDENTIFICATION AND EVALUATION OF EARTHQUAKE SOURCES

To evaluate seismic hazards for a particular site or region, all possible sources of seismic activity must be identified and their potential for generating future strong ground motion evaluated. Identification of seismic sources requires some detective work; nature's clues, some of which are obvious and others quite obscure, must be observed and interpreted.

The availability of modern seismographs and seismographic networks has made observation and interpretation of current earthquakes rather convenient. The occurrence of a large earthquake is now recorded by hundreds of seismographs around the world. Within hours, seismologists are able to determine its magnitude, locate its rupture surface, and even evaluate source parameters. In the 1990s, it is virtually impossible for a significant earthquake anywhere in the world to go undetected.

The current ability to identify and locate all earthquake sources is a relatively recent development, particularly when compared with the time scales on which large earthquakes usually occur. The fact that no strong motions have been instrumentally recorded in a particular area does not guarantee that they have not occurred in the past or that they will not occur in the future. In the absence of an instrumental seismic record, other clues of earthquake activity must be uncovered. These may take the form of geologic and tectonic evidence, or historical (preinstrumental) seismicity.

4.2.1 Geologic Evidence

The theory of plate tectonics assures us that the occurrence of earthquakes is written in the geologic record, primarily in the form of offsets, or relative displacements, of various strata. Study of the geologic record of past earthquake activity is called *paleoseismology* (Wallace, 1981). In some parts of the world, this geologic record is easily accessible and relatively easily interpreted by the trained seismic geologist. In other locations, however, the geologic record may be very complex or it may be hidden by thick layers of recent sediments that have not been displaced by seismic activity. The identification of seismic sources from geologic evidence is a vital, though often difficult part of a seismic hazard analysis.

The search for geologic evidence of earthquake sources centers on the identification of faults. A variety of tools and techniques are available to the geologist, including the review of published literature; interpretation of air photos and remote sensing (e.g., infrared photograph) imagery; field reconnaissance including logging of trenches (Figure 4.1); test pits and borings; and geophysical techniques. Criteria for identification of faults are described in numerous textbooks on structural geology, field geology and geomorphology (Adair, 1979). The following list of features that suggest faulting is that of Reiter (1990):

- Unit descriptions**
- Lithologic units**
- ① Bonneville Lake deposits
- ② Post-provo alluvial fan deposit

Sag fill derived from the north and associated colluvium

- ④A Colluvium
- ④B Transitional deposit
- ④C Pond deposit

Locally derived SAG fill and associated colluvium

- ④A Colluvium-basal facies
- ④B Colluvium
- ④C Pond deposit
- ④D Channel (?) deposit
- ④E Mudflow deposit
- ⑤ Pond deposit

Young scarp colluvium

- ⑥A Colluvium-basal facies
- ⑥B Colluvium/slopewash deposit

Pre-settlement deposit

- ⑦ Pond deposit soil

Historical deposit

- ⑧ Alluvium and pond deposits

Soil units

- ⑤1 Soil developed on post-Provo alluvial-fan deposits
- ⑤2 Paleontisol soil developed on 4B
- ⑤3 Paleontisol soil developed on 3B
- ⑤3 Topsoil

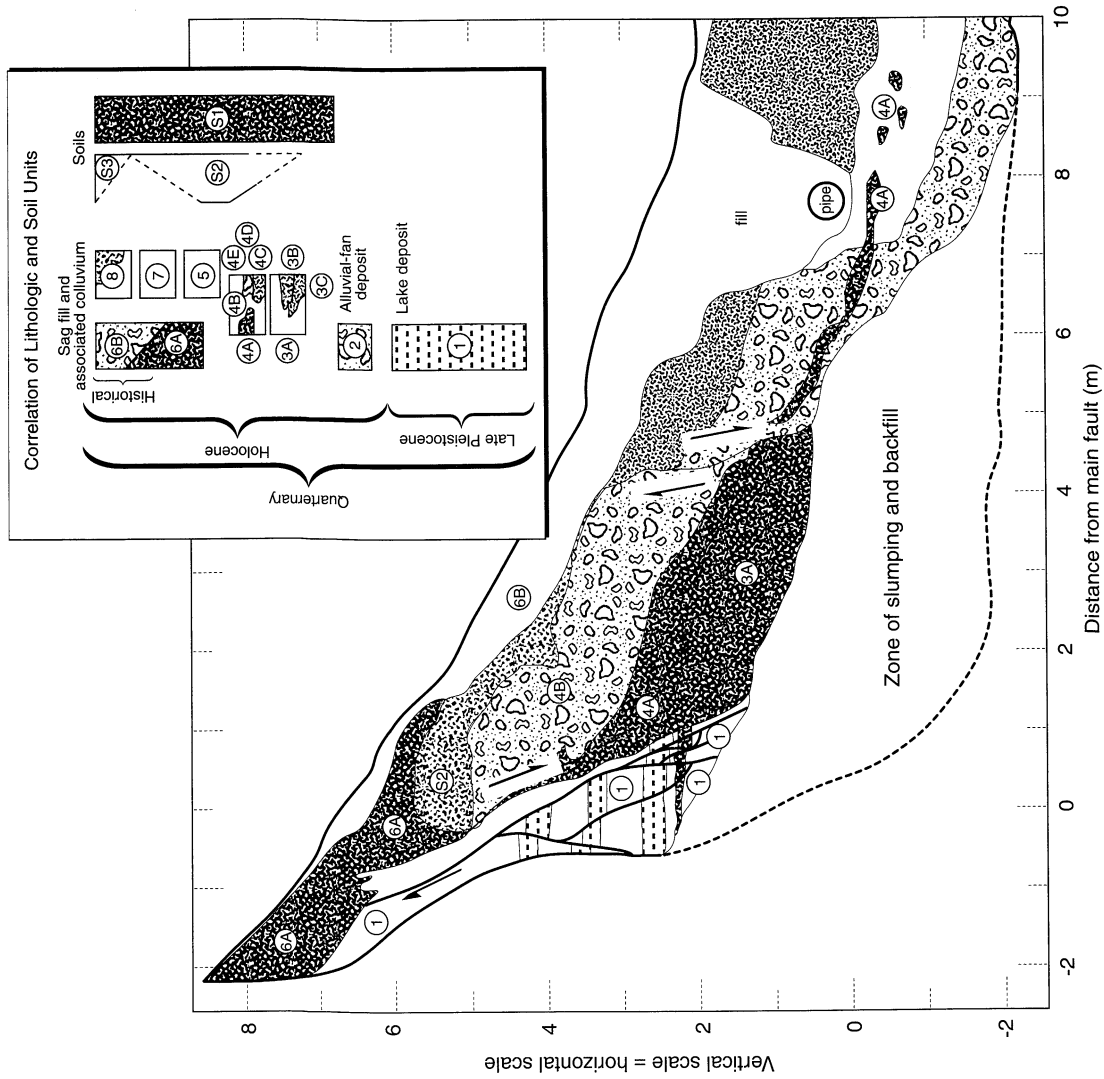


Figure 4.1 Trench log across the Wasatch fault near Kaysville, Utah. Colluvial units 3A, 4A/4B/S2, and 6A are three separate deposits. Each resulted from erosion of the scarp produced by a surface-faulting earthquake. (After Swan et al., 1980; Schwartz, 1988.)

1. Directly observable fracture surfaces and indicators of fracturing. These include disruption of the ground surface and evidence of the movement and grinding of the two sides of the fault (*slickensides*, *fault gouge*, and *fault breccia*).
2. Geologically mappable indicators. These include the juxtaposition of dissimilar materials, missing or repeated strata and the truncation of strata or structures.
3. Topographic and *geomorphic* (surface landform) indicators [Figure 4.2]. These include topographic scarps or triangular facets on ridges, offset streams or drainage, tilting or changes in elevation of terraces or shorelines, *sag ponds* (water ponded by depressions near strike-slip faults) and anomalous stream gradients.
4. Secondary geologic features. These include abrupt changes in groundwater levels, gradients, and chemical composition, alignment of springs or volcanic vents and the presence of hot springs.
5. Lineaments on remote sensing imagery. These may be caused by topography, vegetation, or tonal contrasts.
6. Geophysical indicators of subsurface faulting. These include steep linear gravity or magnetic gradients, differences in seismic wave velocities, and offset of seismic reflection horizons.
7. Geodetic indicators. These include fault movement appearing in geodetic surveys as tilting and changes in the distance between fixed points.

4.2.1.1 Fault Activity

The mere presence of a fault, however, does not indicate the likelihood of future earthquakes. The notion of *fault activity* is important and has been a topic of considerable discussion and controversy over the years. Although there is general agreement concerning the use of the terms *active fault* to describe a fault that poses a current earthquake threat and *inactive fault* to describe one on which past earthquake activity is unlikely to be repeated, there is no consensus as to how fault activity should be evaluated.

Formal definitions of fault activity are important because they often trigger legal requirements for special investigations or special design provisions. However, there are wide variations in the criteria for fault activity in the commonly used definitions. Slemmons and McKinney (1977), for example, found 31 different definitions of the term *active fault*. Most were based on the elapsed period of time since the most recent fault movement. The California Division of Mines and Geology defines an active fault as one that has produced surface displacement within Holocene time (approximately the past 10,000 years). For dams, the U.S. Army Corps of Engineers has used a time period of 35,000 years, and the U.S. Bureau of Reclamation has used 100,000 years (Idriss, 1985). The U.S. Nuclear Regulatory Commission (*Code of Federal Regulations*, 1978), on the other hand, has used the term *capable fault* (rather than active fault) for those that exhibit

1. movement at or near the ground surface at least once within the past 35,000 years or movement of a recurring nature within the past 500,000 years;
2. macroseismicity instrumentally determined with records of sufficient precision to demonstrate a direct relationship with the fault; or

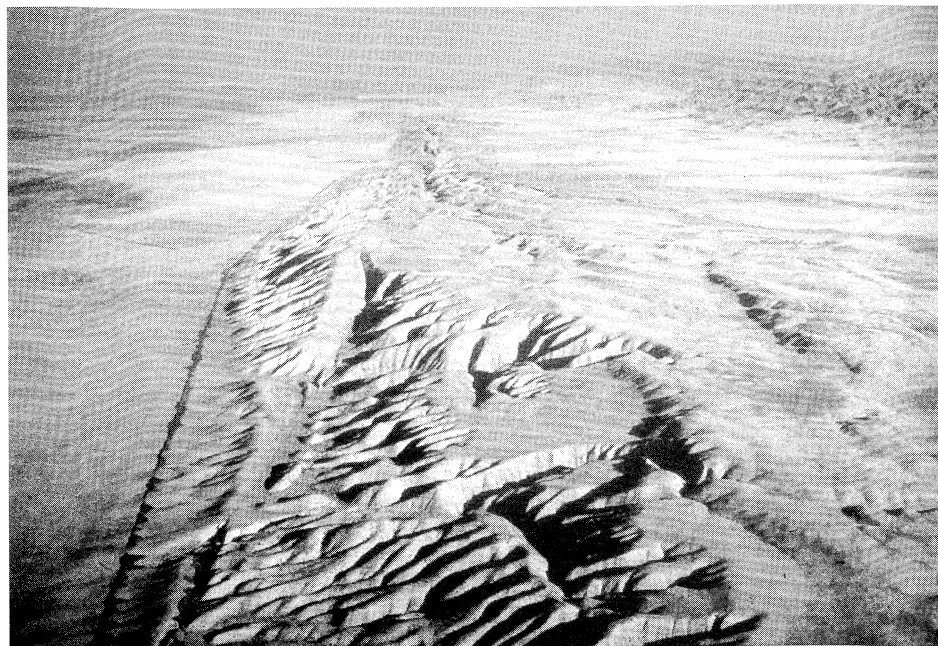
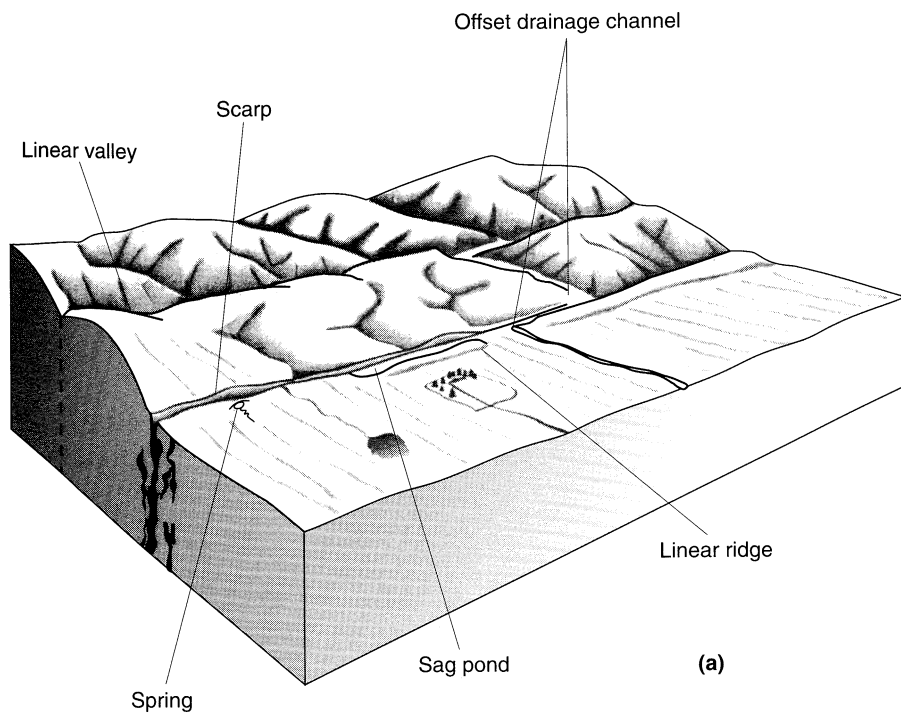


Figure 4.2 Typical terrain in the vicinity of a fault (a) showing topographic and geomorphic indicators of faulting (After Wesson et al., 1975.) and (b) an aerial view of such terrain along the San Andreas fault in the Carrizo Plain (photo by Robert Wallace; used by permission of U.S. Geological Survey.)

3. a structural relationship to a capable fault according to characteristics (1) or (2) above, such that movement on one could reasonably be expected to be accompanied by movement on the other.

Actually, the specification of fault activity by specific time intervals is not very realistic (Cluff et al., 1972; Cluff and Cluff, 1984); faults do not suddenly become inactive on the 10,000th or 35,000th anniversary of their last movement. Rather, fault activity is relative and can change as faults move from active to inactive states over geologic time. Cluff and Cluff (1984) suggested six classes (and five subclasses) of fault activity based on characteristics such as slip rate, slip per event, rupture length, earthquake size, and recurrence interval. Approaches of this type offer a more satisfying framework for characterization of fault activity but can be difficult to implement in the political and economic environment in which many seismic hazard analyses are conducted.

4.2.1.2 Magnitude Indicators

Geologic evidence can also be used to estimate the magnitude of past earthquakes by correlating observed deformation characteristics with the known magnitudes of recorded earthquakes. Studies of worldwide earthquakes have shown that faults do not rupture over their entire lengths or areas during individual events. Instead, individual fault segments with physically controlled boundaries (Schwartz and Coppersmith, 1986; Schwartz, 1988) rupture repeatedly. Rupture length, rupture area, and fault displacement can be evaluated by postearthquake, field geological investigations. Correlation of magnitude with such quantities involves regression on limited data sets and, consequently, produces an estimate of the expected value of the magnitude. The uncertainty in these estimates, which can be considerable, must be recognized when applying them.

Fault rupture length has often been used to estimate earthquake magnitude. A number of studies (e.g., Tocher, 1958; Bonilla and Buchanan, 1970; Mark and Bonilla, 1977; Slemmons, 1977, 1982; Acharaya, 1979; Chen, 1984; Bonilla et al., 1984; Wells and Coppersmith, 1994) have illustrated the general nature of the relationship between fault rupture length and magnitude. Estimation of magnitude based on fault rupture length does not account for variations in the width of the rupture surface; rupture length methods are best suited to cases in which the rupture surface is fairly narrow, typically less than about 20 km (12.4 mi) (Bonilla et al., 1984). Obviously, they are not useful for cases in which rupture does not extend to the ground surface. Fault rupture area, by virtue of its relationship to seismic moment, would appear to be more fundamentally related to magnitude than fault rupture length alone. Indeed, for faults of width greater than about 20 km (12.4 mi), magnitudes are more closely correlated to fault rupture area than are any other parameter (Wyss, 1979; Wells and Coppersmith, 1994). Although the average fault displacement is used to evaluate the seismic moment, the unavailability of fault displacement measurements over an entire rupture surface renders its determination impossible. Instead, maximum surface displacements (Slemmons, 1982; Wells and Coppersmith, 1994) have been correlated to magnitude. Empirical relationships based on statistical analyses of worldwide historical earthquake data are presented in Table 4-1 and Figure 4.3.

The relationships in Table 4-1 can be used to predict mean values of the dependent variables (M_w , $\log L$, $\log A$, and $\log D$); the standard deviations of the dependent variables can be used (see Appendix C) to compute values other than the mean.

Table 4-1 Empirical Relationships between Moment Magnitude, M_w , Surface Rupture Length, L (km), Rupture Area, A (km²), and Maximum Surface Displacement, D (m)

Fault Movement	Number of Events	Relationship	σ_{M_w}	Relationship	$\sigma_{\log L, A, D}$
Strike slip	43	$M_w = 5.16 + 1.12 \log L$	0.28	$\log L = 0.74M_w - 3.55$	0.23
Reverse	19	$M_w = 5.00 + 1.22 \log L$	0.28	$\log L = 0.63M_w - 2.86$	0.20
Normal	15	$M_w = 4.86 + 1.32 \log L$	0.34	$\log L = 0.50M_w - 2.01$	0.21
All	77	$M_w = 5.08 + 1.16 \log L$	0.28	$\log L = 0.69M_w - 3.22$	0.22
Strike Slip	83	$M_w = 3.98 + 1.02 \log A$	0.23	$\log A = 0.90M_w - 3.42$	0.22
Reverse	43	$M_w = 4.33 + 0.90 \log A$	0.25	$\log A = 0.98M_w - 3.99$	0.26
Normal	22	$M_w = 3.93 + 1.02 \log A$	0.25	$\log A = 0.82M_w - 2.87$	0.22
All	148	$M_w = 4.07 + 0.98 \log A$	0.24	$\log A = 0.91M_w - 3.49$	0.24
Strike slip	43	$M_w = 6.81 + 0.78 \log D$	0.29	$\log D = 1.03M_w - 7.03$	0.34
Reverse ^a	21	$M_w = 6.52 + 0.44 \log D$	0.52	$\log D = 0.29M_w - 1.84$	0.42
Normal	16	$M_w = 6.61 + 0.71 \log D$	0.34	$\log D = 0.89M_w - 5.90$	0.38
All	80	$M_w = 6.69 + 0.74 \log D$	0.40	$\log D = 0.82M_w - 5.46$	0.42

Source: Wells and Coppersmith (1994).

^aRegression relationships are not statistically significant at a 95% probability level (note inconsistency of regression coefficients and standard deviations).

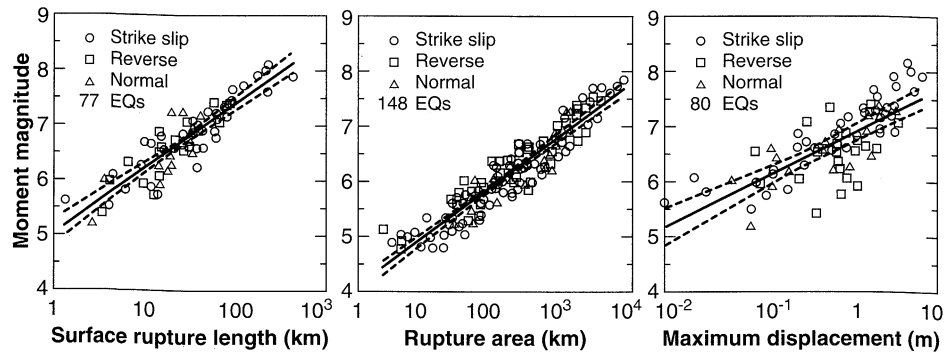


Figure 4.3 Scatter inherent in databases from which correlations of Table 4-1 were developed. (After Wells and Coppersmith, 1994. Used by permission of the Seismological Society of America.)

Example 4.1

Compute the probability that a moment magnitude 7.0 earthquake on the San Andreas fault would cause a surface rupture longer than 100 km.

Solution The San Andreas fault is known to produce strike-slip movement (Section 2.4.2.2). From Table 4-1, the mean surface rupture length for a $M_w = 7.0$ earthquake would be computed as

$$\log L = 0.74M_w - 3.55 = 0.74(7.0) - 3.55 = 1.63$$

Then the mean, or expected, value of L is given by

$$L = 10^{1.63} = 42.7 \text{ km}$$

The standard normal variate (Section C.7.2 of Appendix C) for a 100-km-long surface rupture would be

$$z = \frac{\log 100 - \log 42.7}{0.28} = 1.32$$

From Table C-1, the probability that the surface rupture length would exceed 100 km is 0.0934 or 9.34%.

4.2.2 Tectonic Evidence

Plate tectonics and elastic rebound theory tell us that earthquakes occur to relieve the strain energy that accumulates as plates move relative to each other. The rate of movement, therefore, should be related to the rate of strain energy accumulation and also to the rate of strain energy release (Smith, 1976; Woodward-Clyde Consultants, 1979; Idriss, 1985). For major subduction zones, Ruff and Kanamori (1980) related maximum magnitude to both the rate of convergence and the age of the subducted slab according to

$$M_w = -0.0089T + 0.134V + 7.96 \quad (4.1)$$

where T is the age in millions of years and V is the rate of convergence in cm/yr. Heaton and Kanamori (1984) used this relationship to suggest that the Cascadia subduction zone off the coasts of Oregon, Washington, and British Columbia could be capable of generating great earthquakes of magnitude well above 8 (Figure 4.4). Subsequently, geologic evidence of historical great earthquakes was discovered (e.g., Atwater, 1987; Atwater et al., 1987) along the coasts of Washington and Oregon.

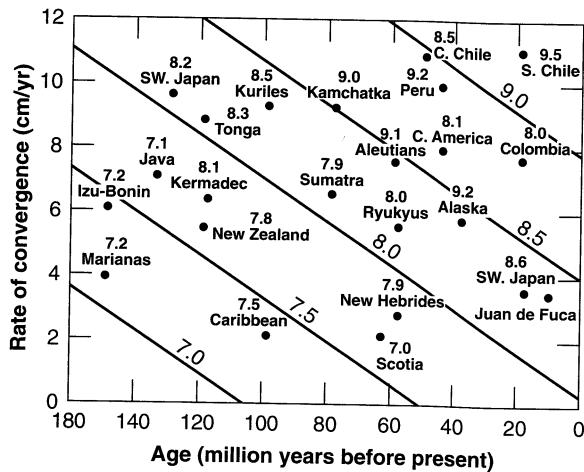


Figure 4.4 Relationship between earthquake magnitude, age, and rate of convergence in subduction zone environments. Diagonal lines correspond to equation (4.1). Data points represent actual earthquakes. (After Heaton and Kanamori, 1984. Used by permission of the Seismological Society of America.)

4.2.3 Historical Seismicity

Earthquake sources may also be identified from records of historical (preinstrumental) seismicity. The written historical record extends back only a few hundred years or less in the United States; in Japan and the Middle East it may extend about 2000 years and up to 3000 years or so in China (Ambraseys, 1971, 1978; Allen, 1975; Bolt, 1988).

Historical accounts of ground-shaking effects can be used to confirm the occurrence of past earthquakes and to estimate their geographic distributions of intensity. When sufficient data are available, the maximum intensity can be determined and used to estimate the location of the earthquake epicenter and the magnitude of the event. Although the accuracy of locations determined in this way depends strongly on population density and the rate of

earthquake recurrence, a geographic pattern of historic epicenters provides strong evidence for the existence of earthquake source zones. Since historical records are dated, they can also be used to evaluate the rate of recurrence of earthquakes, or *seismicity*, in particular areas.

4.2.4 Instrumental Seismicity

Over the past 80 or 90 years, about 10 earthquakes of $M_s > 7$ have occurred somewhere in the world each year (Kanamori, 1988). Instrumental records from large earthquakes have been available since about 1900, although many from before 1960 are incomplete or of uneven quality. Nevertheless, instrumental recordings represent the best available information for the identification and evaluation of earthquake sources. Their most significant limitation is the short period of time, compared with the average period of time between large earthquakes, for which they have been available. Again, the alignment of instrumentally located epicenters or hypocenters indicates the existence of earthquake sources. Analysis of aftershocks can also aid in the delineation of earthquake source zones.

4.3 DETERMINISTIC SEISMIC HAZARD ANALYSIS

In the early years of geotechnical earthquake engineering, the use of *deterministic seismic hazard analysis* (DSHA) was prevalent. A DSHA involves the development of a particular seismic scenario upon which a ground motion hazard evaluation is based. The scenario consists of the postulated occurrence of an earthquake of a specified size occurring at a specified location. A typical DSHA can be described as a four-step process (Reiter, 1990) consisting of:

1. Identification and characterization of all earthquake sources capable of producing significant ground motion at the site. Source characterization includes definition of each source's geometry (the *source zone*) and earthquake potential.
2. Selection of a source-to-site distance parameter for each source zone. In most DSHAs, the shortest distance between the source zone and the site of interest is selected. The distance may be expressed as an epicentral distance or hypocentral distance, depending on the measure of distance of the predictive relationship(s) used in the following step.
3. Selection of the *controlling earthquake* (i.e., the earthquake that is expected to produce the strongest level of shaking), generally expressed in terms of some ground motion parameter, at the site. The selection is made by comparing the levels of shaking produced by earthquakes (identified in step 1) assumed to occur at the distances identified in step 2. The controlling earthquake is described in terms of its size (usually expressed as magnitude) and distance from the site.
4. The hazard at the site is formally defined, usually in terms of the ground motions produced at the site by the controlling earthquake. Its characteristics are usually described by one or more ground motion parameters obtained from predictive relationships of the types presented in Chapter 3. Peak acceleration, peak velocity, and response spectrum ordinates are commonly used to characterize the seismic hazard.

The DSHA procedure is shown schematically in Figure 4.5. Expressed in these four compact steps, DSHA appears to be a very simple procedure, and in many respects it is.

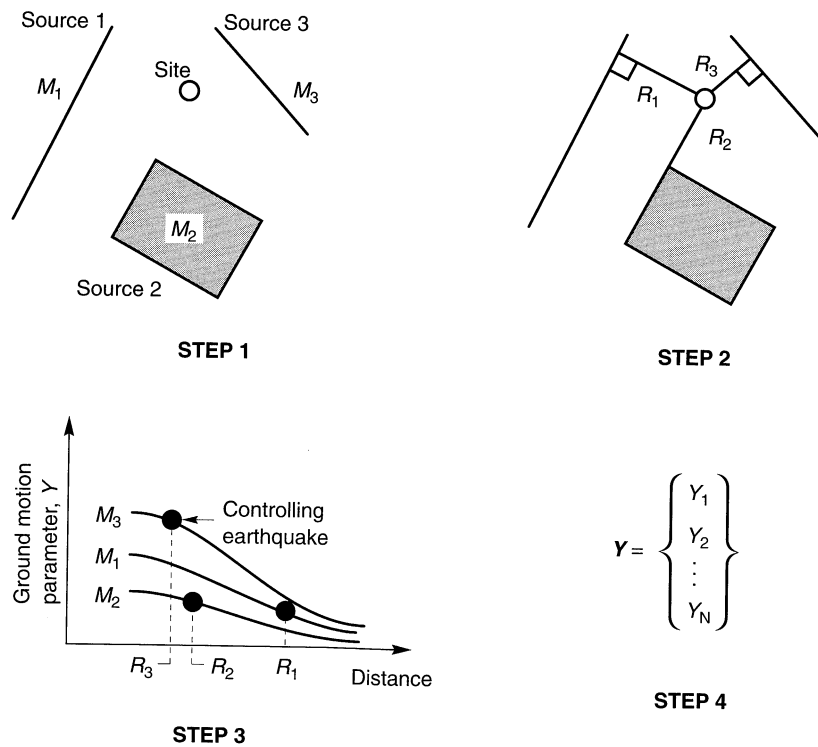


Figure 4.5 Four steps of a deterministic seismic hazard analysis.

Handwritten note: This is the controlling earthquake

When applied to structures for which failure could have catastrophic consequences, such as nuclear power plants and large dams, DSHA provides a straightforward framework for evaluation of worst-case ground motions. However, it provides no information on the likelihood of occurrence of the controlling earthquake, the likelihood of it occurring where it is assumed to occur, the level of shaking that might be expected during a finite period of time (such as the useful lifetime of a particular structure or facility), or the effects of uncertainties in the various steps required to compute the resulting ground motion characteristics.

Perhaps most important, DSHA involves subjective decisions, particularly regarding earthquake potential (step 1), that can require the combined expertise and opinions of seismologists, seismic geologists, engineers, risk analysts, economists, social scientists, and government officials. The broad range of backgrounds and often divergent goals of such professionals can cause difficulty in reaching a consensus on earthquake potential. Over the years there have been many terms used to describe earthquake potential; among them the *maximum credible earthquake* (MCE), *design basis earthquake* (DBE), *safe shutdown earthquake* (SSE), *maximum probable earthquake* (MPE), *operating basis earthquake* (OBE), and *seismic safety evaluation earthquake*. The MCE, for example, is usually defined as the maximum earthquake that appears capable of occurring under the known tectonic framework. The DBE and SSE are usually defined in essentially the same way. The MPE has been defined as the maximum historical earthquake and also as the maximum earthquake

likely to occur in a 100-year interval. Many DSHAs have used the two-pronged approach of evaluating hazards for both the MCE and MPE (or SSE and OBE). Disagreements over the definition and use of these terms have forced the delay, and even cancellation, of a number of large construction projects. The Committee on Seismic Risk of the Earthquake Engineering Research Institute (EERI) has stated that terms such as MCE and MPE “are misleading . . . and their use is discouraged” (Committee on Seismic Risk, 1984).

Example 4.2

The site shown in Figure E4.2 is located in the vicinity of three independent seismic sources represented by source zones 1, 2, and 3. Using a deterministic seismic hazard analysis, compute the peak acceleration.

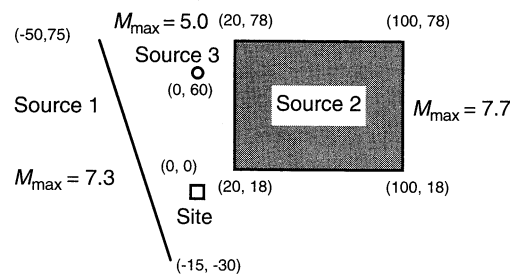


Figure E4.2

Solution Taking the site as the center of a local x - y coordinate system, the coordinates of the source zone boundaries (in kilometers) are given in parentheses. Source zone 1 is a 111-km-long linear source zone that can produce a maximum magnitude of 7.3 at any point along its length. Source zone 2 is an areal source zone of 4800 km² capable of generating a magnitude 7.7 earthquake anywhere within its boundaries. Source zone 3 is a point source that can produce a maximum magnitude of 5.0. Following the four-step procedure described earlier:

1. The problem statement provides the location and maximum magnitude of each source zone. In real DSHAs, this is often an extremely complex and difficult task.
2. The source-to-site distance can be represented by the minimum between the site and any part of each source zone. On that basis, the distances are:

Source Zone	Distance, R (km)
1	23.7
2	25.0
3	60.0

3. If the level of shaking is assumed to be adequately characterized by the peak horizontal acceleration, an appropriate attenuation relationship can be used to select the controlling earthquake. Using the relationship of Cornell et al. (1979), developed with data from $M = 3.0$ to 7.7 earthquakes at distances of 20 to 200 km in the western United States,

$$\ln \text{PHA (gals)} = 6.74 + 0.859M - 1.80 \ln (R + 25)$$

the PHA values generated by each of the source zones would be:

Source Zone	M	R (km)	PHA
1	7.3	23.7	0.42g
2	7.7	25.0	0.57g
3	5.0	60.0	0.02g

On this basis, the source zone 2 event would be selected as the controlling earthquake. (Note: Though currently out of date, the Cornell et al. relationship is used here because of its simplicity which will make a subsequent example on probabilistic seismic hazard analysis much easier to understand.)

4. The hazard would be taken as that which would result from a magnitude 7.7 earthquake occurring at a distance of 25 km. This motion would produce a peak acceleration of 0.57g; other ground motion parameters could be obtained from the predictive relationships described in Chapter 3.

4.4 PROBABILISTIC SEISMIC HAZARD ANALYSIS

In the past 20 to 30 years the use of probabilistic concepts has allowed uncertainties in the size, location, and rate of recurrence of earthquakes and in the variation of ground motion characteristics with earthquake size and location to be explicitly considered in the evaluation of seismic hazards. *Probabilistic seismic hazard analysis* (PSHA) provides a framework in which these uncertainties can be identified, quantified, and combined in a rational manner to provide a more complete picture of the seismic hazard.

Understanding the concepts and mechanics of PSHA requires familiarity with some of the terminology and basic concepts of probability theory. Such background information can be found in Appendix C. The PSHA methodology described in this section is similar in many respects to the well-established methods developed by Cornell (1968), and Algermissen et al. (1982).

The PSHA can also be described as a procedure of four steps (Reiter, 1990), each of which bear some degree of similarity to the steps of the DSHA procedure, as illustrated in Figure 4.6.

1. The first step, identification and characterization of earthquake sources, is identical to the first step of the DSHA, except that the probability distribution of potential rupture locations within the source must also be characterized. In most cases, uniform probability distributions are assigned to each source zone, implying that earthquakes are equally likely to occur at any point within the source zone. These distributions are then combined with the source geometry to obtain the corresponding probability distribution of source-to-site distance. The DSHA, on the other hand, implicitly assumes that the probability of occurrence is 1 at the points in each source zone closest to the site, and zero elsewhere.
2. Next, the seismicity or temporal distribution of earthquake recurrence must be characterized. A *recurrence relationship*, which specifies the average rate at which an earthquake of some size will be exceeded, is used to characterize the seismicity of each source zone. The recurrence relationship may accommodate the maximum size earthquake, but it does not limit consideration to that earthquake, as DSHAs often do.

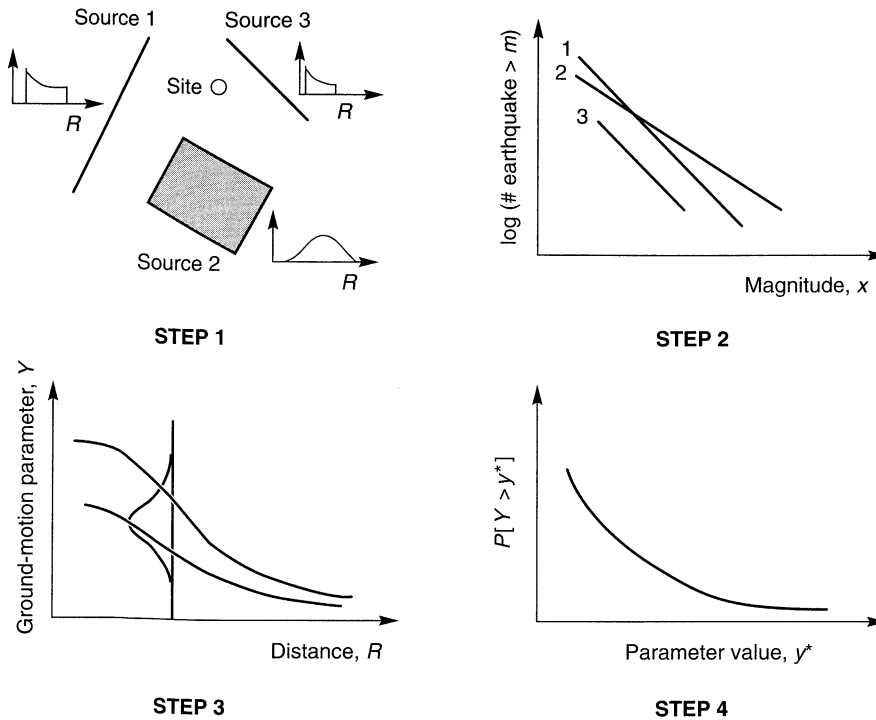


Figure 4.6 Four steps of a probabilistic seismic hazard analysis.

3. The ground motion produced at the site by earthquakes of any possible size occurring at any possible point in each source zone must be determined with the use of predictive relationships. The uncertainty inherent in the predictive relationship is also considered in a PSHA.
4. Finally, the uncertainties in earthquake location, earthquake size, and ground motion parameter prediction are combined to obtain the probability that the ground motion parameter will be exceeded during a particular time period.

The proper performance of a PSHA requires careful attention to the problems of source characterization and ground motion parameter prediction and to the mechanics of the probability computations.

4.4.1 Earthquake Source Characterization

Characterization of an earthquake source requires consideration of the spatial characteristics of the source and of the distribution of earthquakes within that source, of the distribution of earthquake size for each source, and of the distribution of earthquakes with time. Each of these characteristics involves some degree of uncertainty.

4.4.1.1 Spatial Uncertainty

The geometries of earthquake sources depend on the tectonic processes involved in their formulation. Earthquakes associated with volcanic activity, for example, generally

originate in zones near the volcanoes that are small enough to allow them to be characterized as *point sources*. Well-defined fault planes, on which earthquakes can occur at many different locations, can be considered as two-dimensional *areal sources*. Areas where earthquake mechanisms are poorly defined, or where faulting is so extensive as to preclude distinction between individual faults, can be treated as three-dimensional *volumetric sources*.

For the purposes of a seismic hazard analysis, the *source zones* may be similar to or somewhat different than the actual source, depending on the relative geometry of the source and site of interest and on the quality of information about the sources. For example, the relatively short fault in Figure 4.7a can be modeled as a point source since the distance between any point along its length and the site is nearly constant. Similarly, the depth of the fault plane shown in Figure 4.7b is sufficiently small that variations in hypocentral depth have little influence on hypocentral distance. In such a case the hazard analysis can be simplified with negligible loss of accuracy by approximating the planar source as a linear source zone. In Figure 4.7c, the available data are insufficient to determine accurately the actual geometry of the source, so it is represented as a volumetric source.

Earthquakes are usually assumed to be uniformly distributed within a particular source zone (i.e., earthquakes are considered equally likely to occur at any location). The assumption of uniformity is by no means required; nonuniform distributions may be used when sufficient information is by no means required; nonuniform distributions may be used when sufficient information to justify them exists. A uniform distribution within the source zone does not, however, often translate into a uniform distribution of source-to-site distance. Since predictive relationships express ground motion parameters in terms of some measure of source-to-site distance, the spatial uncertainty must be described with respect to the appropriate distance parameter. The uncertainty in source-to-site distance can be described by a probability density function.

For the point source of Figure 4.8a, the distance, R , is known to be r_s ; consequently, the probability that $R = r_s$ is assumed to be 1 and the probability that $R \neq r_s$, zero. Other cases are not as simple. For the linear source of Figure 4.8b, the probability that an earthquake occurs on the small segment of the fault between $L = l$ and $L = l + dl$ is the same as the probability that it occurs between $R = r$ and $R = r + dr$; that is,

$$f_L(l) dl = f_R(r) dr \quad (4.2)$$

where $f_L(l)$ and $f_R(r)$ are the probability density functions for the variables L and R , respectively. Consequently,

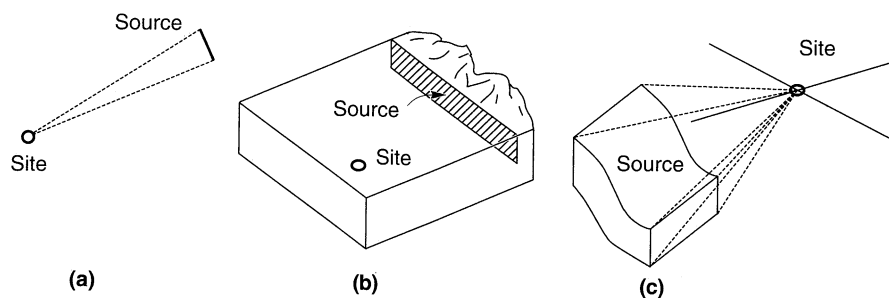


Figure 4.7 Examples of different source zone geometries: (a) short fault that can be modeled as a point source; (b) shallow fault that can be modeled as a linear source; (c) three-dimensional source zone.

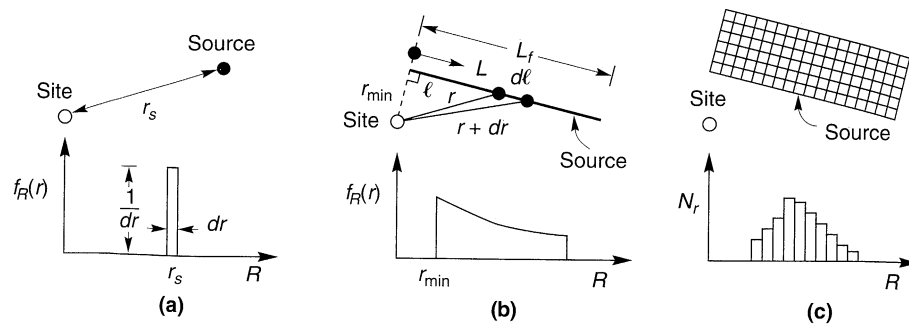


Figure 4.8 Examples of variations of source-to-site distance for different source zone geometries. The shape of the probability distribution can be visualized by considering the relative portions of the source zone that would fall between each of a series of circles (or spheres for three-dimensional problems) with equal differences in radius.

$$f_R(r) = f_L(l) \frac{dl}{dr} \quad (4.3)$$

If earthquakes are assumed to be uniformly distributed over the length of the fault, $f_L(l) = l/L_f$. Since $l^2 = r^2 - r_{\min}^2$ the probability density function of R is given by

$$f_R(r) = \frac{r}{L_f \sqrt{r^2 - r_{\min}^2}} \quad (4.4)$$

For source zones with more complex geometries, it is easier to evaluate $f_R(r)$ by numerical rather than analytical methods. For example, dividing the irregular source zone of Figure 4.8c into a large number of discrete elements of equal area, a histogram that approximates $f_R(r)$ can be constructed by tabulating the values of R that correspond to the center of each element.

The preceding discussion assumes that all the energy is released at the hypocenter of the earthquake. However, energy is released over the entire fault rupture surface, parts of which may be much closer to the site than the hypocenter. Der-Kiureghian and Ang (1977) noted that the rupture surface of a large earthquake with a distant hypocenter could release energy much closer to the site, and developed methods to account for rupture surface dimensions in PSHA.

4.4.1.2 Size Uncertainty

Once an earthquake source is identified and its corresponding source zone characterized, the seismic hazard analyst's attention is turned toward evaluation of the sizes of earthquakes that the source zone can be expected to produce. All source zones have a maximum earthquake magnitude that cannot be exceeded; it can be large for some and small for others. In general, the source zone will produce earthquakes of different sizes up to the maximum earthquake, with smaller earthquakes occurring more frequently than larger ones. The strain energy may be released aseismically, or in the form of earthquakes. Assuming that all strain energy is released by earthquakes of magnitude 5.5 to 9.0 and that the average fault displacement is one-half the maximum surface displacement, Slemmons (1982) showed how the rate of movement was related to earthquake magnitude and recurrence interval (Figure 4.9). The distribution of earthquake sizes in a given period of time is described by

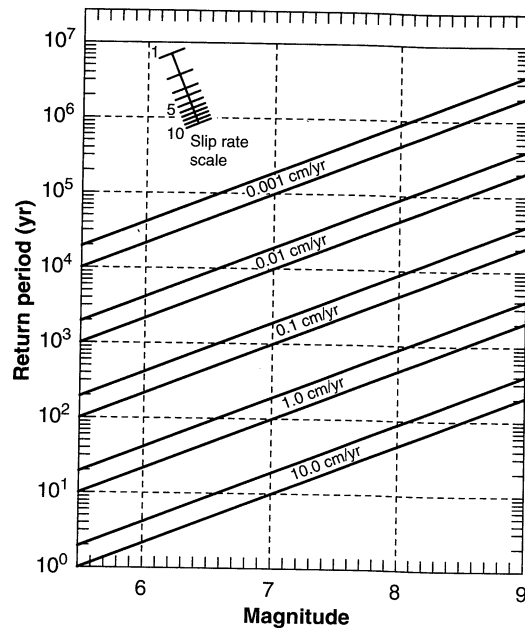


Figure 4.9 Effect of fault slip rate and earthquake magnitude on return period. (After Slemmons, 1982.)

a *recurrence law*. A basic assumption of PSHA is that the recurrence law obtained from past seismicity is appropriate for the prediction of future seismicity.

Gutenberg–Richter Recurrence Law. Gutenberg and Richter (1944) gathered data for southern California earthquakes over a period of many years and organized the data according to the number of earthquakes that exceeded different magnitudes during that time period. They divided the number of exceedances of each magnitude by the length of the time period to define a *mean annual rate of exceedance*, λ_m of an earthquake of magnitude m . As would be expected, the mean annual rate of exceedance of small earthquakes is greater than that of large earthquakes. The reciprocal of the annual rate of exceedance for a particular magnitude is commonly referred to as the *return period* of earthquakes exceeding that magnitude. When the logarithm of the annual rate of exceedance of southern California earthquakes was plotted against earthquake magnitude, a linear relationship was observed. The resulting *Gutenberg–Richter law* for earthquake recurrence was expressed as

$$\log \lambda_m = a - bm \tag{4.5}$$

where λ_m is the mean annual rate of exceedance of magnitude m , 10^a is the mean yearly number of earthquakes of magnitude greater than or equal to zero, and b (the *b value*) describes the relative likelihood of large and small earthquakes. The Gutenberg–Richter law is illustrated schematically in Figure 4.10a. As the b value increases, the number of larger magnitude earthquakes decreases compared to those of smaller magnitudes. The Gutenberg–Richter law is not restricted to the use of magnitude as a descriptor of earthquake size; epicentral intensity has also been used. Worldwide recurrence data are shown in Figure 4.10b.

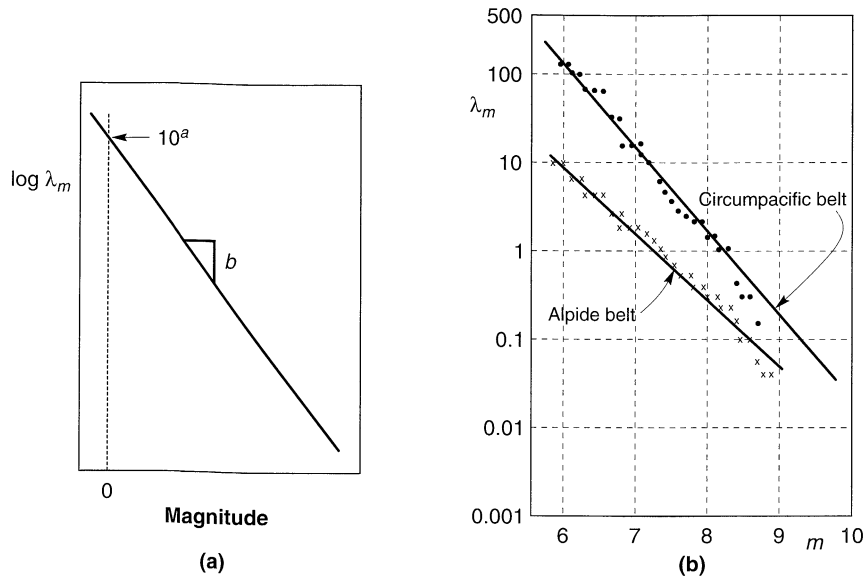


Figure 4.10 (a) Gutenberg–Richter recurrence law, showing meaning of a and b parameters; and (b) application of Gutenberg–Richter law to worldwide seismicity data. (After Esteva, 1970.)

Example 4.3

Using Figure 4.10b, compute the return period of $M = 8$ earthquakes on the Circumpacific and Alpidic belts.

Solution At a magnitude of 8, Figure 4.10b indicates that the Circumpacific and Alpidic belts have mean annual rates of exceedance of 1.76 per year and 0.31 per year, respectively. Therefore, the corresponding return periods are

$$\text{Circumpacific: } T_R = \frac{1}{\lambda_m} = \frac{1}{1.76/\text{yr}} = 0.6 \text{ year}$$

$$\text{Alpidic: } T_R = \frac{1}{\lambda_m} = \frac{1}{0.31/\text{yr}} = 3.2 \text{ years}$$

The a and b parameters are generally obtained by regression on a database of seismicity from the source zone of interest. Unless the source zone is extremely active, the database is likely to be relatively sparse. Since the use of both instrumental and historical events is usually required, the database may contain both magnitude (possibly based on different scales) and intensity data, necessitating the conversion of one measure of size to the other. In some areas, the record of seismicity may be distorted by the presence of *dependent events* such as aftershocks and foreshocks (Merz and Cornell, 1973). Although such dependent events can cause significant damage, a PSHA is intended to evaluate the hazard from discrete, independent releases of seismic energy. Therefore, dependent events must be removed from the seismicity database and their effects accounted for in separate analyses. Completeness of the database must also be considered. The historical record is usually more complete for large earthquakes than for small earthquakes; small earthquakes can go undetected for a

variety of physical and demographic reasons. Fitting a straight line such as that implied by the Gutenberg–Richter law through recurrence data in which the mean rate of exceedance of small earthquakes is underestimated will tend to flatten the line. As a result, the actual mean rate of small earthquakes will be underpredicted and the mean rate of large earthquakes will be overpredicted. Different methods have been proposed (Stepp, 1972; Weichert, 1980; EPRI, 1986) to correct incomplete records.

Bounded Gutenberg–Richter Recurrence Laws. The standard Gutenberg–Richter recurrence law of equation (4.5) may also be expressed as

$$\lambda_m = 10^{a-bm} = \exp(\alpha - \beta m) \quad (4.6)$$

where $\alpha = 2.303a$ and $\beta = 2.303b$. Equation (4.6) shows that the Gutenberg–Richter law implies that earthquake magnitudes are exponentially distributed. The standard Gutenberg–Richter law covers an infinite range of magnitudes, from $-\infty$ to $+\infty$. For engineering purposes, the effects of very small earthquakes are of little interest and it is common to disregard those that are not capable of causing significant damage. If earthquakes smaller than a lower threshold magnitude m_0 are eliminated, the mean annual rate of exceedance can be written (McGuire and Arabasz, 1990) as

$$\lambda_m = \nu \exp[-\beta(m - m_0)] \quad m > m_0 \quad (4.7)$$

where $\nu = \exp(\alpha - \beta m_0)$. In most PSHAs, the lower threshold magnitude is set at values from about 4.0 to 5.0 since magnitudes smaller than that seldom cause significant damage. The resulting probability distribution of magnitude for the Gutenberg–Richter law with lower bound can be expressed in terms of the *cumulative distribution function* (CDF):

$$F_M(m) = P[M < m | M > m_0] = \frac{\lambda_{m_0} - \lambda_m}{\lambda_{m_0}} = 1 - e^{-\beta(m - m_0)} \quad (4.8)$$

or the probability density function (PDF):

$$f_M(m) = \frac{d}{dm} F_M(m) = \beta e^{-\beta(m - m_0)} \quad (4.9)$$

At the other end of the magnitude scale, the standard Gutenberg–Richter law predicts nonzero mean rates of exceedance for magnitudes up to infinity. This implies, for example, that the Circumpacific belt (Figure 4.10b), would produce a magnitude 10 earthquake at a mean annual exceedance rate of about 0.02 per year (a return period of only 50 years), even though earthquakes of that size have never been observed. Some maximum magnitude, m_{\max} , is associated with all source zones. If it is known or can be estimated, the mean annual rate of exceedance can be expressed (McGuire and Arabasz, 1990) as

$$\lambda_m = \nu \frac{\exp[-\beta(m - m_0)] - \exp[-\beta(m_{\max} - m_0)]}{1 - \exp[-\beta(m_{\max} - m_0)]} \quad m_0 \leq m \leq m_{\max} \quad (4.10)$$

The bounded recurrence law of equation (4.10) is shown in Figure 4.11a for conditions of constant rate of seismicity (i.e., constant mean annual rate of exceedance of m_0). An alternative interpretation, based on a constant rate of seismic moment (hence energy) release, produces the recurrence curves of Figure 4.11b. In the constant moment rate model, increasing the maximum magnitude requires a substantial decrease in the mean annual rate of exceedance of

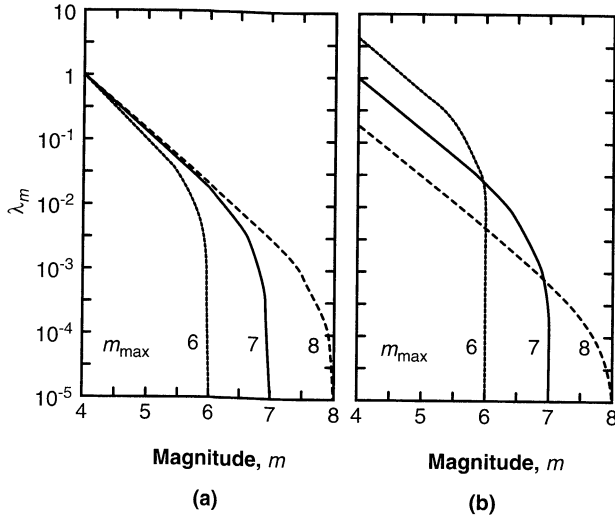


Figure 4.11 Bounded Gutenberg–Richter recurrence laws for $m_0 = 4$ and $m_{\max} = 6, 7,$ and 8 constrained by (a) constant seismicity rate and (b) constant moment rate. (After Youngs and Coppersmith, 1985.)

lower magnitude events to account for the extra energy released in large earthquakes. Since the seismic moment is proportional to the amount of slip (displacement) that occurs in an earthquake, the moment rate is proportional to the slip rate. Hence the constant-moment-rate model is equivalent to a constant-slip-rate model and can be used when the slip rate is known to be constant. The extent to which actual slip rates vary with time, however, appears to be different for different faults and can even fluctuate with time along the same fault.

The CDF and PDF for the Gutenberg–Richter law with upper and lower bounds can be expressed as

$$F_M(m) = P[M < m | m_0 \leq m \leq m_{\max}] = \frac{1 - \exp[-\beta(m - m_0)]}{1 - \exp[-\beta(m_{\max} - m_0)]} \quad (4.11)$$

$$f_M(m) = \frac{\beta \exp[-\beta(m - m_0)]}{1 - \exp[-\beta(m_{\max} - m_0)]} \quad (4.12)$$

Characteristic Earthquake Recurrence Laws. The Gutenberg–Richter law was developed from a set of regional data that included many different seismic sources. Since PSHAs are usually conducted for specific sites rather than large regions, the earthquake-generating characteristics of individual faults is important. In recent years the ability of the Gutenberg–Richter law to represent the behavior of a single source has been called into question (Schwartz and Coppersmith, 1984; Schwartz, 1988).

Paleoseismic studies indicate that individual points on faults and fault segments tend to move by approximately the same distance in each earthquake. This has been interpreted to suggest that individual faults repeatedly generate earthquakes of similar (within about one-half magnitude unit) size, known as *characteristic earthquakes*, at or near their maximum magnitude. Alternatively, the apparently repetitive nature of fault movement at individual points may be controlled by localized geologic constraints and, consequently, not reflect earthquake magnitude very accurately. Resolution of these alternative interpretations awaits further paleoseismic research.

By dating these characteristic earthquakes, their historical rate of recurrence can be estimated. Geologic evidence indicates the characteristic earthquakes occur more frequently than would be implied by extrapolation of the Gutenberg–Richter law from high exceedance rates (low magnitude) to low exceedance rates (high magnitude). The result is a more complex recurrence law that is governed by seismicity data at low magnitudes and geologic data at high magnitudes, as shown in Figure 4.12.

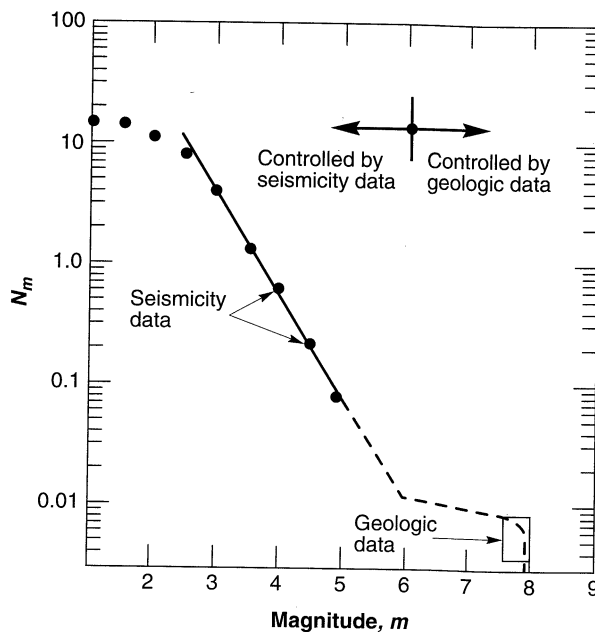


Figure 4.12 Inconsistency of mean annual rate of exceedance as determined from seismicity data and geologic data. (After Youngs and Coppersmith, 1985.)

Youngs and Coppersmith (1985) developed a generalized magnitude-frequency density function that combined an exponential magnitude distribution at lower magnitudes with a uniform distribution in the vicinity of the characteristic earthquake. Recurrence relationships derived from the Youngs and Coppersmith model and the bounded Gutenberg–Richter model, assuming the same m_{\max} , b value, and slip rate, are shown in Figure 4.13. The characteristic earthquake model predicts higher rates of exceedance at magnitudes near the characteristic earthquake magnitude and lower rates at lower magnitudes. Other models that account for characteristic earthquakes have been developed by Wesnorsky et al. (1984) and Wu et al. (1995).

Other Recurrence Laws. A number of other recurrence laws have been proposed. Merz and Cornell (1973a) used a quadratic expression to describe the mean annual rate at which earthquakes of magnitude greater than m_0 and less than m_{\max} are exceeded. Shah et al. (1975) used a bilinear recurrence law in an evaluation of seismic risk for Nicaragua. In another approach, the Gutenberg–Richter law was modified on the basis of seismic moment and fault slip (Lomnitz-Adler and Lomnitz, 1979).

Discussion. Available evidence is insufficient to determine whether the Gutenberg–Richter, characteristic earthquake, or some other recurrence law is correct. Evaluation of which model is most appropriate for a given source is hampered by the brevity of historical

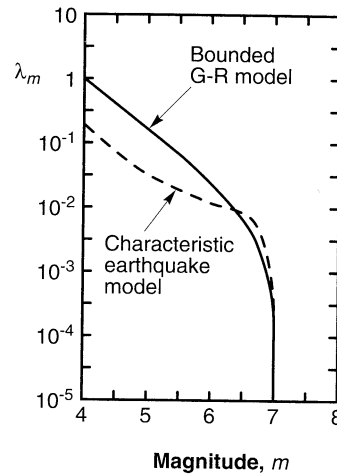


Figure 4.13 Comparison of recurrence laws from bounded Gutenberg–Richter and characteristic earthquake models. (After Youngs and Coppersmith, 1985.)

and/or instrumental records. Based on five decades of seismicity records for the major seismic sources of southern California, Wesnousky (1994) concluded that while the available data were not sufficient to disprove the Gutenberg–Richter recurrence law, the characteristic earthquake model better represented the observed distribution of earthquake magnitudes. Additional research in this area is in progress and will undoubtedly be an active topic of discussion in the forthcoming seismology literature.

4.4.2 Predictive Relationships

Predictive relationships are nearly always obtained empirically by least-squares regression on a particular set of strong motion parameter data. Despite attempts to remove questionable data and the use of quality-based weighting schemes, some amount of scatter in the data is inevitable. The scatter results from randomness in the mechanics of rupture and from variability and heterogeneity of the source, travel path, and site conditions. Scatter in the data can be quantified by confidence limits (Campbell, 1985) or by the standard deviation of the predicted parameter. Reflecting the form of most predictive relationships, the standard deviation of the (natural) logarithm of the predicted parameter is usually computed. This considerable uncertainty must be accounted for in computation of seismic hazards. The probability that a particular ground motion parameter Y exceeds a certain value, y^* , for an earthquake of a given magnitude, m , occurring at a given distance, r , is illustrated graphically in Figure 4.14. In probabilistic terms, it is given by

$$P[Y > y^* | m, r] = 1 - F_Y(y^*) \quad (4.13)$$

where $F_Y(y)$ is the value of the CDF of Y at m and r . The value of $F_Y(y)$ depends on the probability distribution used to represent Y . In general, ground motion parameters are usually assumed to be lognormally distributed (the logarithm of the parameter is normally distributed); however, the unbounded characteristics of that distribution can attribute a nonzero probability to unrealistic values of the ground motion parameter. For example, a hypothetical PHA attenuation relationship that predicts a mean PHA of $0.5g$ with $\sigma_{\ln y} = 0.5$ would imply a 0.06% probability that the PHA would exceed $2.5g$. The use of distributions that impose an upper limit on Y have been studied by Kulkarni et al. (1979), Bender (1984), and Zemell (1984).

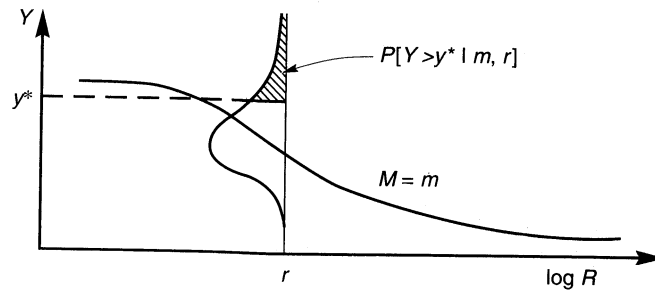


Figure 4.14 Schematic illustration of conditional probability of exceeding a particular value of a ground motion parameter for a given magnitude and distance.

Example 4.4

Using the predictive relationship of Campbell and Bozorgnia (1994) given as equation (3.25), compute the probability that a $M_w = 7$ earthquake on a strike-slip fault would cause a peak horizontal acceleration greater than $0.4g$ at a soft-rock site 15 km from the closest point on the rupture surface.

Solution. For equation (3.26), the parameters $F = 0$ and $S_{HR} = 0$ and $S_{SR} = 1$, so the mean value of the natural logarithm of peak horizontal acceleration is given by

$$\begin{aligned} \overline{\ln \text{PHA}} \text{ (gal)} &= 3.512 + 0.904 M_w - 1.328 \sqrt{R^2 + [0.149 \exp(0.647 M_w)]^2} \\ &\quad + 0.904 - 0.171 \ln R \\ &= 3.512 + (0.904)(7) - 1.328 \sqrt{15^2 + [0.149 \exp(0.647 \times 7)]^2} \\ &\quad + 0.904 - 0.171 \ln(15) \\ &= 6.31 \end{aligned}$$

from which $\text{PHA} = e^{6.31} = 552$ gal. Then, from Section C.7.2 of Appendix C, the standard normal variate is

$$z = \frac{\ln \text{PHA} - \overline{\ln \text{PHA}}}{\sigma_{\ln \text{PHA}}} = \frac{\ln[(0.40g)(981 \text{ gal/g})] - \ln(552 \text{ gal})}{0.405} = -0.843$$

From Table C-1,

$$F_z(-0.843) = P[z < 0.843] = P[a_{\max} < 0.4g] = 0.200$$

so the desired probability

$$P[\text{PHA} > 0.40g | M = 7.0, R = 15 \text{ km}] = 1 - 0.200 = 0.800$$

4.4.3 Temporal Uncertainty

To calculate the probabilities of various hazards occurring in a given time period, the distribution of earthquake occurrence with respect to time must be considered. Earthquakes have long been assumed to occur randomly with time, and in fact, examination of available seismicity records has revealed little evidence (when aftershocks are removed) of temporal patterns in earthquake recurrence. The assumption of random occurrence allows the use of simple probability models, but is inconsistent with the implications of elastic rebound theory (Section 2.5.1).

4.4.3.1 Poisson Model

The temporal occurrence of earthquakes is most commonly described by a Poisson model. The Poisson model provides a simple framework for evaluating probabilities of events that follow a *Poisson process*, one that yields values of a random variable describing the number of occurrences of a particular event during a given time interval or in a specified spatial region. Since PSHAs deal with temporal uncertainty, the spatial applications of the Poisson model will not be considered further. Poisson processes possess the following properties:

1. The number of occurrences in one time interval are independent of the number that occur in any other time interval.
2. The probability of occurrence during a very short time interval is proportional to the length of the time interval.
3. The probability of more than one occurrence during a very short time interval is negligible.

These properties indicate that the events of a Poisson process occur randomly, with no “memory” of the time, size, or location of any preceding event.

For a Poisson process, the probability of a random variable N , representing the number of occurrences of a particular event during a given time interval is given by

$$P[N = n] = \frac{\mu^n e^{-\mu}}{n!} \quad (4.14)$$

where μ is the average number of occurrences of the event in that time interval. The time between events in a Poisson process can be shown to be exponentially distributed. To characterize the temporal distribution of earthquake recurrence for PSHA purposes, the Poisson probability is usually expressed as

$$P[N = n] = \frac{(\lambda t)^n e^{-\lambda t}}{n!} \quad (4.15)$$

where λ is the average rate of occurrence of the event and t is the time period of interest. Note that the probability of occurrence of at least one event in a period of time t is given by

$$\begin{aligned} P[N \geq 1] &= P[N = 1] + P[N = 2] + P[N = 3] + \dots \\ &+ P[N = \infty] = 1 - P[N = 0] = 1 - e^{-\lambda t} \end{aligned} \quad (4.16)$$

When the event of interest is the exceedance of a particular earthquake magnitude, the Poisson model can be combined with a suitable recurrence law to predict the probability of at least one exceedance in a period of t years by the expression

$$P[N \geq 1] = 1 - e^{-\lambda_m t} \quad (4.17)$$

4.4.3.2 Other Models

Elastic rebound theory suggests that the occurrence of earthquakes on a particular fault or fault segment should *not* be independent of past seismicity. If earthquakes occur to release strain energy that builds up over extended periods of time, the occurrence of a large earthquake should substantially reduce the chances of another independent, large earthquake

(from the same source) occurring shortly thereafter. If earthquakes are triggered when the stress on a fault reaches some limiting value, the chances of occurrence should depend on the times, sizes, and locations of preceding events.

A number of models that account for prior seismicity have been proposed (Anagnos and Kiremidjian, 1988). *Nonhomogeneous Poisson models* (e.g., Vere-Jones and Ozaki, 1982) allow the annual rate of exceedance to vary with time. *Renewal models* (Esteva, 1970; Hagiwara, 1974; Savy et al., 1980; Kiremidjian and Anagnos, 1984; Cornell and Winterstein, 1986) use arrival-time distributions other than exponential (implied by the homogeneous Poisson model) to allow the hazard rate to increase with time since the last event; gamma and Weibull distributions are most common. *Time-predictable models* specify a distribution of the time to the next earthquake that depends on the magnitude of the most recent earthquake; *slip-predictable models* consider the distribution of earthquake magnitude to depend on the time since the most recent earthquake. *Markov models* incorporate a type of memory that describes the chances that a process moves from some past "state" to a particular future state. The time for which the process stays in a particular state before moving to another state is exponentially distributed; *semi-Markov models* are not restricted to the exponential distribution. Both Markov models (Vere-Jones, 1966; Vagliente, 1973; Veneziano and Cornell, 1974; Nishioka and Shah, 1980) and semi-Markov models (Patwardhan et al., 1980; Cluff et al., 1980; Coppersmith, 1981; Guagenti-Grandori and Molina, 1984) have been used in seismic hazard analysis. The semi-Markov models of Patwardhan et al. (1980) and Cluff et al. (1980), for example, relate the probability of future earthquakes of various sizes to the size of the most recent event and the elapsed time since its occurrence. *Trigger models* (Vere-Jones and Davies, 1966; Shlien and Tokosz, 1970; Merz and Cornell, 1973b; Lai, 1977) can account for clusters of events (aftershocks) that occur after triggering events.

4.4.3.3 Model Applicability

Investigations of the applicability of Poisson and non-Poissonian models (Cornell and Winterstein, 1986) have shown that the Poisson model is useful for practical seismic risk analysis except when the seismic hazard is dominated by a single source for which the time interval since the previous significant event is greater than the average interevent time and when the source displays strong "characteristic-time" behavior. For this and other reasons related to simplicity, ease of use, and lack of sufficient data to support more sophisticated models, the Poisson model is the most widely used in contemporary PSHA.

Each of the more sophisticated models uses a "pattern" of earthquake occurrence to reconcile their computed probabilities with the mechanics of the elastic rebound process of earthquake generations. As a result, each requires additional parameters whose values must be evaluated from historical and instrumental seismicity records that are, in most cases, too sparse to permit accurate evaluation. As time passes and additional data becomes available, the use of these models will undoubtedly increase.

4.4.4 Probability Computations

The results of a PSHA can be expressed in many different ways. All involve some level of probabilistic computations to combine the uncertainties in earthquake size, location, frequency, and effects to estimate seismic hazards. A common approach involves the development of *seismic hazard curves*, which indicate the annual probability of exceedance of

different values of a selected ground motion parameter. The seismic hazard curves can then be used to compute the probability of exceeding the selected ground motion parameter in a specified period of time.

4.4.4.1 Seismic Hazard Curves

Seismic hazard curves can be obtained for individual source zones and combined to express the aggregate hazard at a particular site. The basic concept of the computations required for development of seismic hazard curves is fairly simple. The probability of exceeding a particular value, y^* , of a ground motion parameter, Y , is calculated for one possible earthquake at one possible source location and then multiplied by the probability that that particular magnitude earthquake would occur at that particular location. The process is then repeated for all possible magnitudes and locations with the probabilities of each summed. The required calculations are described in the following paragraphs.

For a given earthquake occurrence, the probability that a ground motion parameter Y will exceed a particular value y^* can be computed using the total probability theorem, that is,

$$P[Y > y^*] = P[Y > y^* | \mathbf{X}] P[\mathbf{X}] = \int P[Y > y^* | \mathbf{X}] f_{\mathbf{X}}(\mathbf{X}) d\mathbf{X} \quad (4.18)$$

where \mathbf{X} is a vector of random variables that influence Y . In most cases the quantities in \mathbf{X} are limited to the magnitude, M , and distance, R . Assuming that M and R are independent, the probability of exceedance can be written as

$$P[Y > y^*] = \iint P[Y > y^* | m, r] f_M(m) f_R(r) dm dr \quad (4.19)$$

where $P[Y > y^* | m, r]$ is obtained from the predictive relationship and $f_M(m)$ and $f_R(r)$ are the probability density functions for magnitude and distance, respectively.

If the site of interest is in a region of N_S potential earthquake sources, each of which has an average rate of threshold magnitude exceedance, $v_i [= \exp(\alpha_i - \beta_i m_0)]$, the total average exceedance rate for the region will be given by

$$\lambda_{y^*} = \sum_{i=1}^{N_S} v_i \iint P[Y > y^* | m, r] f_{M_i}(m) f_{R_i}(r) dm dr \quad (4.20)$$

The individual components of equation (4.20) are, for virtually all realistic PSHAs, sufficiently complicated that the integrals cannot be evaluated analytically. Numerical integration, which can be performed by a variety of different techniques, is therefore required. One approach, used here for simplicity rather than efficiency, is to divide the possible ranges of magnitude and distance into N_M and N_R segments, respectively. The average exceedance rate can then be estimated by

$$\lambda_{y^*} = \sum_{i=1}^{N_S} \sum_{j=1}^{N_M} \sum_{k=1}^{N_R} v_i P[Y > y^* | m_j, r_k] f_{M_i}(m_j) f_{R_i}(r_k) \Delta m \Delta r \quad (4.21)$$

where $m_j = m_0 + (j - 0.5)(m_{\max} - m_0)/N_M$, $r_k = r_{\min} + (k - 0.5)(r_{\max} - r_{\min})/N_R$, $\Delta m = (m_{\max} - m_0)/N_M$, and $\Delta r = (r_{\max} - r_{\min})/N_R$. This is equivalent to assuming that each source is capable of generating only N_M different earthquakes of magnitude, m_j , at only N_R different source-to-site distances, r_k . Equation (4.21) is then equivalent to

$$\lambda_{y^*} \approx \sum_{i=1}^{N_S} \sum_{j=1}^{N_M} \sum_{k=1}^{N_R} v_i P[Y > y^* | m_j, r_k] P[M = m_j] P[R = r_k] \quad (4.22)$$

The accuracy of the crude numerical integration procedure described above increases with increasing N_M and N_R . More refined methods of numerical integration will provide greater accuracy at the same values of N_M and N_R .

Example 4.5

The basic procedures of a typical PSHA can be illustrated for the site shown in Figure 4-6 if the recurrence relationships for each of the source zones is known. Assuming that the seismicity of the respective source zones are described by

Source zone 1: $\log \lambda_m = 4.4 - 1.0M$

Source zone 2: $\log \lambda_m = 3.5 - 0.8M$

Source zone 3: $\log \lambda_m = 2.7 - 1.2M$

the PSHA can be performed in the four previously described steps:

1. The problem statement provides the location, geometry, and maximum magnitude of each source zone. The distribution of source-to-site distance must also be characterized. To limit the number of computations involved in this simple example, we will characterize the distribution of source-to-site distance by a relatively coarse histogram. Consider first source zone 1. It is a simple matter to show that the shortest possible source-to-site distance will be 23.72 km and that the longest will be 90.12 km. We can divide this total range into 10 distance intervals of length $(90.12 \text{ km} - 23.72 \text{ km})/10 = 6.64 \text{ km}$. If we divide the source zone into a large number of segments of equal length, we can characterize the distribution of source-to-site distance by determining how many of the segments fall within each distance interval. For 1000 segments, the normalized histogram of source-to-site distance is shown in Figure E4.5a. The ordinates of the normalized histogram represent the relative frequency that would be equal to the probability if an infinite number of segments were used, but which is an approximation to the probability in this case. The probability that the source-to-site distance is between 23.72 and 30.36 km (or about equal to the midpoint of that range, 27.04 km) is approximately 0.336. For source zone 2, the source-to-site range 25 to 125 km can be divided into 10 intervals of 10-km length; dividing the areal source zone into 2500 elements of equal area, the normalized histogram of Figure E4.5b is obtained. Since there is only one possible source-to-site distance, obtaining the normalized histogram of Figure E4.5c for source zone 3 is trivial matter.

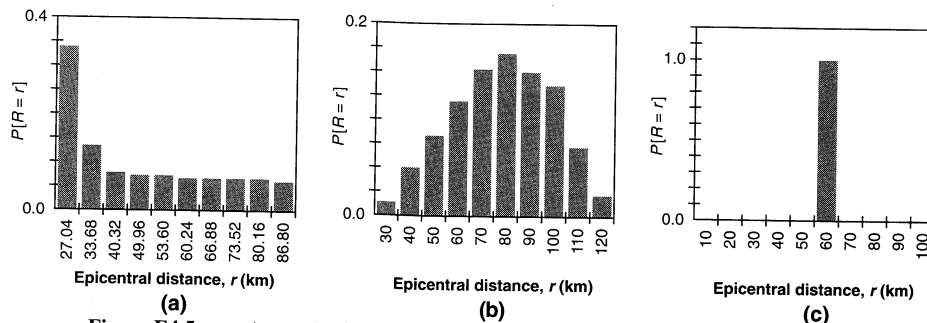


Figure E4.5a-c Approximations to source-to-site probability distributions for source zones (a)1, (b)2, and (c)3.

- The temporal distribution of earthquake recurrence can be characterized using the recurrence relationships provided in the problem statement. Assuming that earthquakes of magnitude less than 4.0 do not contribute to the seismic hazard, the mean rates of exceedance of magnitude 4.0 events from each of the source zones are

$$\text{Source zone 1: } \nu_1 = 10^{4.4 - 1.0(4.0)} = 2.512$$

$$\text{Source zone 2: } \nu_2 = 10^{3.5 - 0.8(4.0)} = 1.995$$

$$\text{Source zone 3: } \nu_3 = 10^{2.7 - 1.2(4.0)} = 0.008$$

giving $\nu_{\text{total}} = 4.515$. For each source zone, the probability that the magnitude will be within an interval between a lower bound m_l and an upper bound m_u is given by

$$P[m_l < m < m_u] = \int_{M=m_l}^{M=m_u} f_M(m) dm \approx f_M\left(\frac{m_l + m_u}{2}\right)(m_u - m_l)$$

where $f_M(m)$ is given in equation (4.12). If $N_M = 10$, the lowest magnitude interval for source zone 1 will be from $M = 4.0$ to $M = 4.33$. The probability that the magnitude would fall within that interval would be

$$P[4.0 < M < 4.33] \approx \frac{2.303e^{-2.303(4.165 - 4.0)}}{1 - e^{-2.303(7.3 - 4.0)}}(4.33 - 4.0) = 0.522$$

The probabilities of various magnitudes for each source zone are as shown in Figure E4.5d–f.

- To compare the results of this PSHA with those from the DSHA example, we will use the same predictive relationship: that is, the Cornell et al. (1979) relationship

$$\ln \text{PHA (gals)} = 6.74 + 0.859M - 1.80 \ln(R + 25)$$

Uncertainty in this relationship is expressed by the standard deviation $\sigma_{\ln y} = 0.57$.

- Finally, we compute the total seismic hazard as the sum of the contributions from each possible combination of source-to-site distance and earthquake magnitude on each of the three source zones. First, we consider source zone 1. For the lowest magnitude interval ($j = 1$),

$$P[M = m_1] = P[M = 4.165] = 0.522$$

as computed in step 2. For the lowest distance interval ($k = 1$),

$$P[R = r_1] = P[R = 27.04 \text{ km}] = 0.336$$

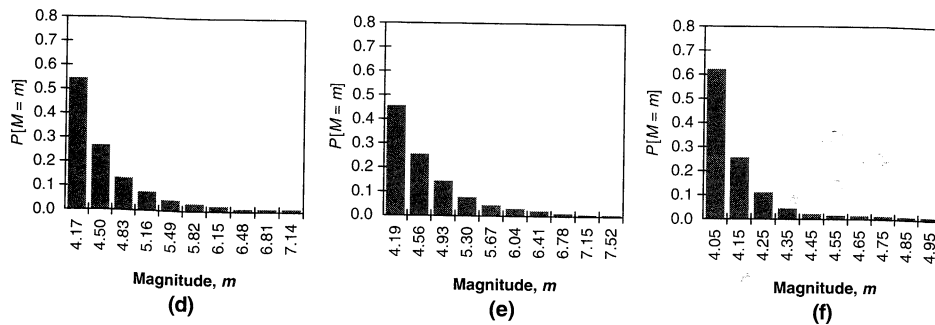


Figure E4.5d–f Approximations to magnitude probability distributions for source zones (d)1, (e)2, and (f)3.

as computed in step 1. This combination of magnitude and distance indicates an expected value of $\ln \text{PHA}$ of

$$\overline{\ln \text{PHA}} = 3.204$$

Now we can calculate the probabilities that various target peak acceleration levels will be exceeded. For $a^* = 0.01g$ (9.81 gals), the corresponding standard normal variable is

$$z^* = \frac{\ln a^* - \overline{\ln \text{PHA}}}{\sigma_{\ln y}} = \frac{\ln(9.81) - 3.204}{0.57} = -1.63$$

Then the probability that the peak acceleration is greater than 0.01g, using Table 4-2, is

$$\begin{aligned} P[\text{PHA} > 0.01g | M = 4.165, R = 27.04 \text{ km}] &= P[z^* > -1.63] \\ &= 1 - P[z^* < -1.63] \\ &= 1 - F_z(-1.63) \\ &= 0.9484 \end{aligned}$$

Annual rate of exceedance of a peak acceleration of 0.01g by an earthquake of magnitude 4.165 at a distance of 27.04 km on source zone 1 (given that an earthquake of $M > m_0$ occurs on source zone 1) will be

$$\begin{aligned} \lambda_{0.01g} &= \nu_1 P[\text{PHA} > 0.01g | M = 4.165, R = 27.04 \text{ km}] \\ &\quad \times P[M = 4.165] P[R = 27.04] \\ &= 2.512 (0.9484) (0.522) (0.336) \\ &= 0.4181 \end{aligned}$$

If the preceding calculations are repeated for the 99 other possible combinations of magnitude and distance for source zone 1, the contributions of each will be

Magnitude	Distance (km)									
	27.04	33.68	40.32	46.96	53.60	60.24	66.88	73.52	80.16	86.80
4.165	0.4181	0.1501	0.0805	0.0676	0.0559	0.0456	0.0369	0.0293	0.0231	0.0179
4.495	0.2027	0.0753	0.0424	0.0376	0.0331	0.0289	0.0250	0.0213	0.0181	0.0149
4.825	0.0957	0.0363	0.0209	0.1092	0.0177	0.0162	0.0148	0.0134	0.0120	0.0106
5.155	0.0452	0.0172	0.0100	0.0093	0.0088	0.0084	0.0079	0.0074	0.0070	0.0065
5.485	0.0212	0.0081	0.0047	0.0045	0.0042	0.0041	0.0040	0.0038	0.0037	0.0035
5.815	0.0099	0.0037	0.0022	0.0021	0.0020	0.0019	0.0019	0.0018	0.0018	0.0018
6.145	0.0045	0.0018	0.0010	0.0010	0.0010	0.0010	0.0009	0.0009	0.0009	0.0009
6.475	0.0023	0.0009	0.0005	0.0005	0.0005	0.0005	0.0005	0.0004	0.0004	0.0004
6.805	0.0011	0.0004	0.0003	0.0002	0.0002	0.0002	0.0002	0.0002	0.0002	0.0002
7.135	0.0005	0.0002	0.0001	0.0001	0.0001	0.0001	0.0001	0.0001	0.0001	0.0001

Summing all of these contributions indicates that the mean annual rate at which an acceleration of 0.01g will be exceeded by an earthquake on source zone 1 will be 1.923. Repeating all of these calculations for the other source zones yields equivalent exceedance rates of 1.016 for source zone 2 and 0.005 for source zone 3. Consequently, the probability that a target acceleration of 0.01g will be exceeded by an earthquake of $M > m_0$ on any of the three source zones will be $1.923 + 1.016 + 0.005 = 2.944$. This implies a return period of 0.34 year for this low acceleration. By repeating this process for different target accelerations, the seismic hazard curves of Figure E4.5g can be developed.

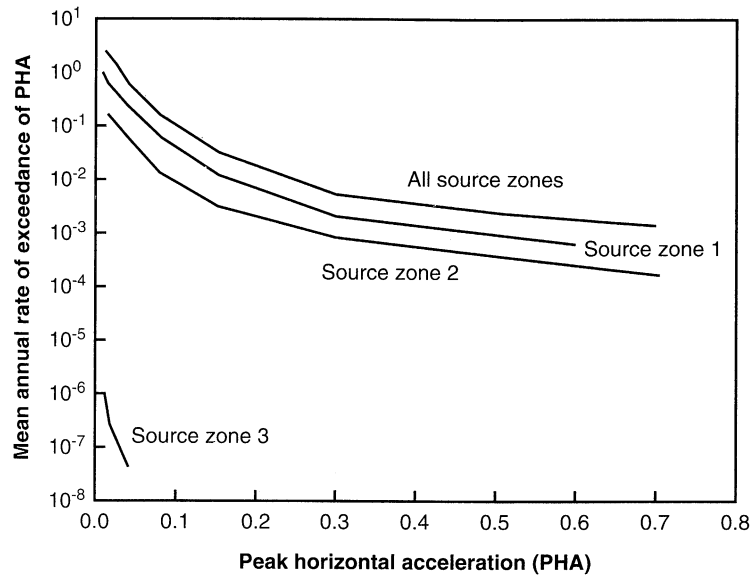


Figure E4.5g Seismic hazard curves for source zones 1, 2, and 3 and total seismic hazard curve for all sources.

4.4.4.2 Finite Time Periods

The seismic hazard curve can easily be combined with the Poisson model to estimate probabilities of exceedance in finite time intervals. From equation (4.17), the probability of exceedance of y^* in a time period T is

$$P[Y_T > y^*] = 1 - e^{-\lambda_{y^*} T} \quad (4.23)$$

Example 4.6

Returning to Example 4.5, the probability that an acceleration of 0.10g would be exceeded in a 30-year period would be

$$P[\text{PHA} > 0.10g \text{ in } 30 \text{ years}] = 1 - e^{-\lambda_{y^*} T} = 1 - e^{-(0.0822)(30)} = 0.915 = 91.5\%$$

It is often necessary to compute the value of a ground motion parameter corresponding to a particular probability of exceedance in a given time period. For example, the acceleration level that has a 10% probability of exceedance in a 50-year period would be that with an annual rate of exceedance, obtained by rearranging equation (4.23), of

$$\lambda_{y^*} = \frac{\ln(1 - P[Y_T > y^*])}{T} = \frac{\ln(1 - 0.1)}{50} = 0.00211$$

From the total seismic hazard curve of Figure 4.18, that acceleration level would be approximately 0.63g.

These types of analyses have been performed for a variety of seismically active areas within the United States. As the exposure time, T , increases, the probability of exceeding a particular ground motion parameter value also increases. Similarly, the value of a ground motion parameter with a particular probability of exceedance increases with increasing exposure time. Figure 4.15 illustrates the peak acceleration with a 10% probability of

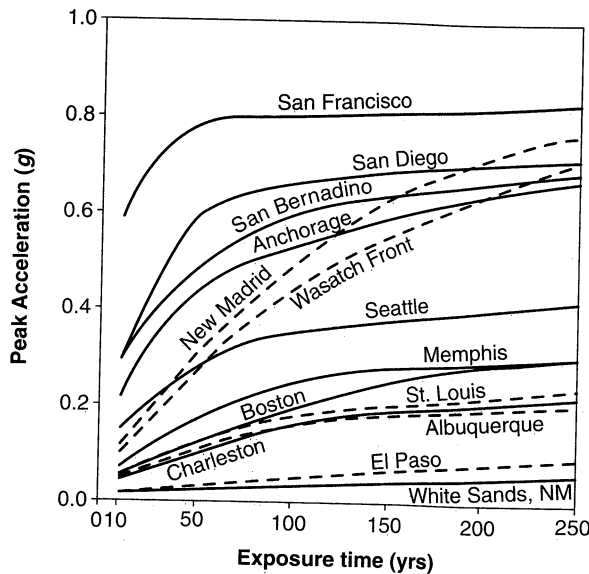


Figure 4.15 Peak horizontal bedrock accelerations with 10% probability of exceedance over various exposure times for 14 areas in North America. (After NEHRP, 1993.)

exceedance for a number of metropolitan areas within the United States. Seismic hazard maps, such as that shown in Figure 4.16, have been developed to express the relative seismicity of different regions in building codes (Chapter 8).

4.4.4.3 Deaggregation

The PSHA procedures described in the preceding sections allow computation of the mean annual rate of exceedance at a particular site based on the aggregate risk from potential earthquakes of many different magnitudes occurring at many different source-site distances. The rate of exceedance computed in a PSHA, therefore, is not associated with any particular earthquake magnitude or source-site distance.

In some cases, however, it may be useful to estimate the most likely earthquake magnitude and/or the most likely source-site distance. These quantities may be used, for example, to select existing ground motion records (recorded in earthquakes of similar magnitude at similar source-site distance) for response analyses. This process of *deaggregation* requires that the mean annual rate of exceedance be expressed as a function of magnitude and/or distance. Computationally, this simply involves the removal of terms from the summations of Equation 4.22. For example, the mean annual rate of exceedance can be expressed as a function of magnitude by

$$\lambda_{y^*}(m_j) \approx P[M = m_j] \sum_{i=1}^{N_s} \sum_{k=1}^{N_R} v_i P[Y > y^* | m_j, r_k] P[R = r_k] \quad (4.24)$$

Similarly, the mean annual rate of exceedance can be expressed as a function of source-site distance by

$$\lambda_{y^*}(r_k) \approx P[R = r_k] \sum_{i=1}^{N_s} \sum_{j=1}^{N_M} v_i P[Y > y^* | m_j, r_k] P[M = m_j] \quad (4.25)$$



Figure 4.16 Contours of mean horizontal acceleration on rock (expressed as a percentage of gravity) with 10% probability of exceedance in 50 years. (After Algermissen et al., 1990.)

Finally, it is possible to compute the mean annual rate of exceedance as functions of both earthquake magnitude and source-site distance, i.e.

$$\lambda_{y^*}(m_j, r_k) \approx P[M = m_j] P[R = r_k] \sum_{i=1}^{N_S} v_i P[Y > y^* | m_j, r_k] \quad (4.26)$$

4.4.4.4 Logic Tree Methods

The probability computations described previously allow systematic consideration of uncertainty in the values of the parameters of a particular seismic hazard model. In some cases, however, the best choices for elements of the seismic hazard model itself may not be clear. The use of *logic trees* (Power et al., 1981; Kulkarni et al., 1984; Coppersmith and Youngs, 1986) provides a convenient framework for the explicit treatment of model uncertainty.

The logic tree approach allows the use of alternative models, each of which is assigned a weighting factor that is interpreted as the relative likelihood of that model being correct. It consists of a series of nodes, representing points at which models are specified and branches that represent the different models specified at each node. The sum of the probabilities of all branches connected to a given node must be 1. The simple logic tree shown in Figure 4.17 allows uncertainty in selection of models for attenuation, magnitude distribution, and maximum magnitude to be considered. In this logic tree, attenuation according to the models of Campbell and Bozorgnia (1994) and Boore et al. (1993) are considered equally likely to be correct, hence each is assigned a relative likelihood of 0.5. Proceeding to the next level of nodes, the Gutenberg–Richter magnitude distribution is considered to be 50% more likely to be correct than the characteristic earthquake distribution. At the final level of nodes, different relative likelihoods are assigned to the maximum magnitude. This logic tree terminates with a total of $2 \times 2 \times 3 = 12$ (no. of attenuation

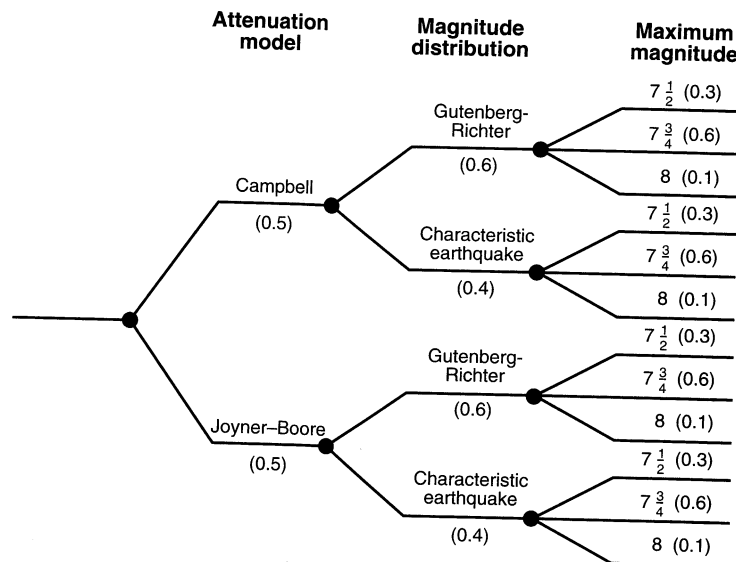


Figure 4.17 Simple logic tree for incorporation of model uncertainty.

models \times no. of magnitude distributions \times no. of maximum magnitudes) branches. The relative likelihood of the combination of models and/or parameters implied by each terminal branch is given by the product of the relative likelihood of the terminal branch and all prior branches leading to it. Hence the relative likelihood of the combination of the Campbell attenuation model, Gutenberg–Richter magnitude distribution, and maximum magnitude of 7.5 is $0.5 \times 0.6 \times 0.3 = 0.09$. The sum of the relative likelihoods of the terminal branches, or of those at any prior level, is equal to 1.

To use the logic tree, a seismic hazard analysis is carried out for the combination of models and/or parameters associated with each terminal branch. The result of each analysis is weighted by the relative likelihood of its combination of branches, with the final result taken as the sum of the weighted individual results.

It is easy to see that the required computational effort increases quickly with increasing numbers of nodes and branches. Parameters best characterized by continuous distributions (e.g., the maximum magnitude in the example of Figure 4.17) are difficult to treat in the logic tree without resorting to large numbers of branches. Nevertheless, the logic tree is a very useful tool for the analysis of seismic hazards.

4.5 SUMMARY

1. Earthquake-resistant design seeks to produce structures that can withstand a certain level of shaking without excessive damage. That level of shaking is described by a design ground motion which is usually determined with the aid of a seismic hazard analysis.
2. Seismic hazard analyses involve the quantitative estimation of ground motion characteristics at a particular site. They may be conducted deterministically or probabilistically.
3. Seismic hazard analyses require the identification and characterization of all potential sources of seismic activity that could produce significant ground motions at the site of interest. Earthquake sources may be identified on the basis of geologic, tectonic, historical, and instrumental evidence.
4. Deterministic seismic hazard analyses involve the assumption of some scenario—the occurrence of an earthquake of a particular size at a particular location—for which ground motion characteristics are determined. In practice, DSHAs often assume that earthquakes of the largest possible magnitude occur at the shortest possible distance to the site within each source zone. The earthquake that produces the most severe site motion is then used to compute site-specific ground motion parameters.
5. When applied to structures for which failure could have catastrophic consequences, such as nuclear power plants and large dams, DSHA provides a straightforward framework for evaluation of “worst-case” ground motions. However, it provides no information on the likelihood of occurrence of the controlling earthquake, the likelihood of it occurring where it is assumed to occur, the level of shaking that might be expected during a finite period of time (such as the useful lifetime of a particular structure or facility), or the effects of uncertainties in the various steps required to compute the resulting ground motion characteristics.

6. Probabilistic seismic hazard analyses allow uncertainties in the size, location, rate of recurrence, and effects of earthquakes to be explicitly considered in the evaluation of seismic hazards. A PSHA requires that uncertainties in earthquake location, size, recurrence, and ground shaking effects be quantified.
7. For each source zone, uncertainty in earthquake location is characterized by a probability density function of source-to-site distance. Evaluation of the probability density function requires estimation of the geometry of the source zone and of the distribution of earthquakes within it.
8. Uncertainty in the sizes of earthquakes produced by each source zone can be described by various recurrence laws. The Gutenberg–Richter recurrence law, which assumes an exponential distribution of magnitude, is commonly used with modifications to account for minimum and maximum magnitudes. A more recent interpretation of fault activity has produced the characteristic earthquake recurrence law. Which of these two recurrence laws is more correct has not yet been determined; it is not uncommon to incorporate both into a PSHA by means of a logic tree.
9. The level of shaking produced by an earthquake of a given size occurring at a given source-to-site distance is determined from predictive relationships. The uncertainty in these ground motions is a function of the scatter in the databases from which the predictive relationships were developed.
10. The probabilities of earthquakes of various sizes occurring in finite periods of time are usually computed assuming that earthquakes occur as Poisson processes. Although the Poisson model assumes an independence of events that is not consistent with elastic rebound theory, it remains the most commonly used model in contemporary PSHA.
11. Standard methods of probability analysis can be used to combine the quantified uncertainties in earthquake size, location, recurrence, and effects to compute ground motion levels with various probabilities of exceedance in different periods of time. Because of the complex and empirical nature of the probability density functions, exceedance probabilities are usually computed by numerical, rather than analytical, methods.
12. The accuracy of a PSHA depends on the accuracy with which uncertainty in earthquake size, location, recurrence, and effects can be characterized. Although models and procedures for characterization of uncertainty of these parameters are available, they may be based on data collected over periods of time that, geologically, are very short. Engineering judgment must be applied to the interpretation of PSHA results.
13. Model uncertainties can be incorporated into a PSHA by means of a logic tree. A logic tree allows the use of alternative models, each of which is assigned a weighting factor related to the likelihood of that model being correct. The weighting factors are usually assigned subjectively, often using expert opinion.

HOMWORK PROBLEMS

- 4.1 Estimate the surface rupture lengths, rupture areas, and maximum surface displacements for earthquakes of $M_w = 6$ and $M_w = 8$.

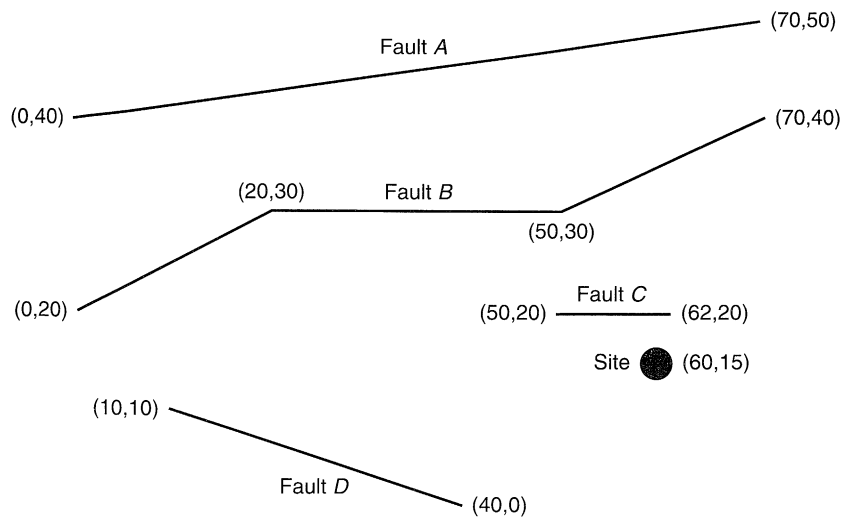


Figure P4.2

4.2 The site shown in Figure P4.2 is located near four active faults in California. Fault A is a normal fault. Faults B and C are strike-slip faults, and Fault D is a reverse fault. The coordinates of the site and faults shown above are in km. Assuming that only linear segments can rupture in an individual event, perform a deterministic seismic hazard analysis to:

- Determine the anticipated peak acceleration at the site. Use the attenuation relationship(s) from Chapter 3 you believe are most appropriate and briefly justify your selection.
- Determine and plot the anticipated response spectrum at the site.
- Assuming that the site consists of a bedrock outcrop, determine the anticipated duration of strong motion at the site.
- Estimate the anticipated Arias Intensity at the site.

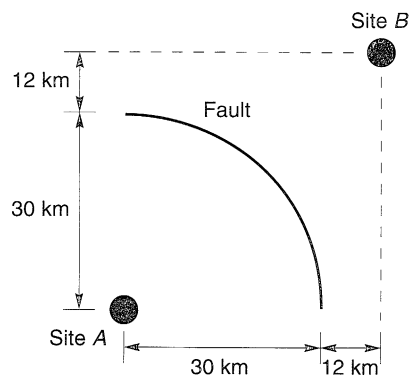


Figure P4.3

- 4.3 The hypothetical vertical fault segment shown in Figure P4.3 is represented as a quarter-circle. On the same graph, plot histograms of expected epicentral distance for motions at Site A and Site B assuming:
- Earthquakes are equally likely to occur at any point on the fault segment.
 - Earthquakes are twice as likely to occur at the midpoint of the fault segment as at either end and the likelihood is linearly distributed between the midpoint and the ends.
- 4.4 In a hypothetical seismically active region, earthquakes have been recorded over an 80-year period. Part of the record is instrumental, but part is not. Combining all available data, it appears that the earthquakes have been distributed as follows:

MOMENT MAGNITUDE	NUMBER OF EARTHQUAKES
3–4	~1800
4–5	~150
5–6	11
> 6	1

- Estimate the Gutenberg–Richter parameters for the region.
 - Neglecting earthquakes of magnitude less than 3, compute the probability that an earthquake in the region will have a moment magnitude between 5.5 and 6.5.
 - Repeat Part(b) assuming that paleoseismic evidence indicates that the region is not capable of producing earthquakes of moment magnitude greater than 6.5.
- 4.5 The seismicity of a particular region is described by the Gutenberg–Richter recurrence law:

$$\log \lambda_m = 4.0 - 0.7M$$

- What is the probability that at least one earthquake of magnitude greater than 7.0 will occur in a 10-year period? In a 50-year period? In a 250-year period?
 - What is the probability that exactly one earthquake of magnitude greater than 7.0 will occur in a 10-year period? In a 50-year period? In a 250-year period?
 - Determine the earthquake magnitude that would have a 10% probability of being exceeded at least once in a 50-year period.
- 4.6 A hypothetical site is located at the end of a hypothetical 300 km long linear feature known as Holtz's Fault. Historical data indicates that the seismicity of Holtz's Fault can be described by the relationship

$$\log \lambda_m = 3.0 - 0.75M$$

Peak accelerations in the region of Holtz's Fault can be described by the simple attenuation relationship of Campbell (1981), even for distances greater than 50 km.

Given the above information:

- Develop a seismic hazard curve for peak acceleration at the site.
- Determine the probability that an acceleration of 0.25 g will be exceeded at least once in a 100-year period.
- Determine the peak acceleration that would have a 10% probability of being exceeded at least once in a 50-year period.

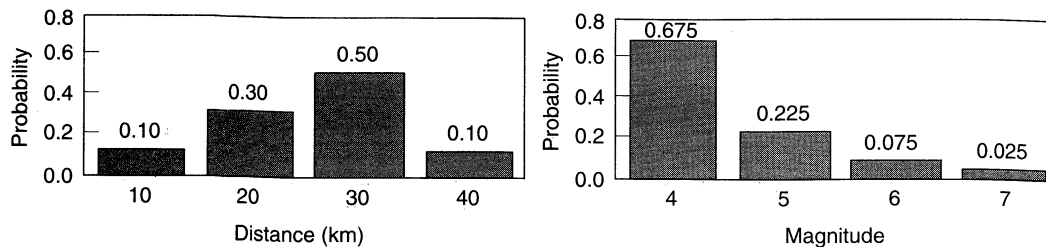


Figure P4.7

- 4.7** A new seismic source is identified in the vicinity of the site described in Problem 6. The geometry of the source is such that the source-site distance is distributed as indicated by the simple histogram above. The source is expected to produce an earthquake of magnitude 4 or more every 5 years, on average, and the magnitudes are expected to be distributed as indicated in the simple histogram above. Assuming that earthquakes of magnitude 4, 5, 6, or 7 can occur at distances of 10, 20, 30, or 40 km, and using the attenuation relationship given in Problem 6,
- Develop and plot a seismic hazard curve for peak acceleration at the site that considers both Holtz's Fault and the new seismic source. Plot the individual seismic hazard curves on the same graph.
 - Considering both sources, determine the probability that an acceleration of 0.25 g will be exceeded at least once in a 100-year period.
 - Considering both sources, determine the peak acceleration that would have a 10% probability of being exceeded at least once in a 50-year period.

5

Wave Propagation

5.1 INTRODUCTION

It is the continuous nature of geologic materials that causes soil dynamics and geotechnical earthquake engineering to diverge from their structural counterparts. While most structures can readily be idealized as assemblages of discrete masses with discrete sources of stiffness, geologic materials cannot. They must be treated as continua, and their response to dynamic disturbances must be described in the context of wave propagation.

Some basic concepts of wave propagation have been alluded to in previous chapters; a more fundamental treatment of the basic concepts is presented in this chapter. The presentation follows a repeated pattern of simple-to-complex applications. The relatively simple problem of waves in unbounded media is followed by the more complicated problem of waves in bounded and layered media. Within each, the concepts are presented first for the simple case of one-dimensional wave propagation, and then for the more general three-dimensional case. The careful reader will note that the basic techniques and principles used to solve the more complicated cases are generally the same as those used for the simple cases; the additional complexity simply results from the need to consider more dimensions.



5.2 WAVES IN UNBOUNDED MEDIA

The propagation of stress waves is most easily understood by first considering an unbounded, or “infinite,” medium [i.e., one that extends infinitely in the direction(s) of wave propagation]. A simple, one-dimensional idealization of an unbounded medium is that of an infinitely long rod or bar. Using the basic requirements of equilibrium of forces and compatibility of displacements, and using strain–displacement and stress–strain relationships, a one-dimensional wave equation can be derived and solved. The process can be repeated, using the same requirements and relationships, for the more general case of wave propagation in a medium that extends infinitely in three orthogonal directions.

5.2.1 One-Dimensional Wave Propagation

Three different types of vibration can occur in a thin rod: longitudinal vibration during which the axis of the rod extends and contracts without lateral displacement; torsional vibration in which the rod rotates about its axis without lateral displacement of the axis; and flexural vibration during which the axis itself moves laterally. The flexural vibration problem has little application in soil dynamics and will not be considered further. For the first two cases, however, the operative wave equations are easily derived and solved.

5.2.1.1 Longitudinal Waves in an Infinitely Long Rod

Consider the free vibration of an infinitely long, linear elastic, constrained rod with cross-sectional area A , Young’s modulus E , Poisson’s ratio ν , and density ρ , as shown in Figure 5.1. If the rod is constrained against radial straining, then particle displacements caused by a longitudinal wave must be parallel to the axis of the rod. Assume that cross-sectional planes will remain planar and that stresses will be distributed uniformly over each cross section. As a stress wave travels along the rod and passes through the small element shown in Figure 5.2, the axial stress at the left end of the element ($x = x_0$) is σ_{x_0} . At the right end ($x = x_0 + dx$), the axial stress is $\sigma_{x_0} + (\partial\sigma_x/\partial x) dx$. Then dynamic equilibrium of the element requires that

$$\left(\sigma_{x_0} + \frac{\partial\sigma_x}{\partial x} dx\right)A - \sigma_{x_0}A = \rho A dx \frac{\partial^2 u}{\partial t^2} \quad (5.1)$$

where u is the displacement in the x -direction. This simply states that the unbalanced external forces acting on the ends of the element [the left side of Equation (5.1)] must equal the inertial force induced by acceleration of the mass of the element (the right side). Simplifying yields the one-dimensional *equation of motion*

$$\frac{\partial\sigma_x}{\partial x} = \rho \frac{\partial^2 u}{\partial t^2} \quad (5.2)$$

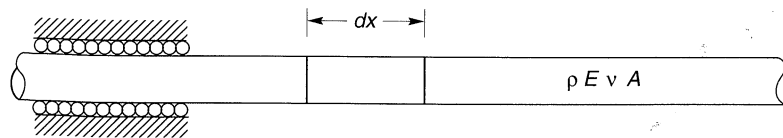


Figure 5.1 Constrained, infinite rod for one-dimensional wave propagation. Constraint against radial straining schematically represented by rollers.

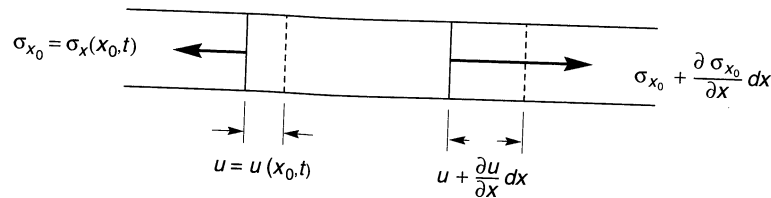


Figure 5.2 Stresses and displacements at ends of element of length dx and cross-sectional area, A .

In this form, the equation of motion is valid for any stress-strain behavior but cannot be solved directly because it mixes stresses [on the left side of equation (5.2)] with displacements (on the right side). To simplify the equation of motion, the left side can be expressed in terms of displacement by using the *stress-strain relationship*, $\sigma_x = M\epsilon_x$, where the *constrained modulus* $M = \{(1 - \nu)/[(1 + \nu)(1 - 2\nu)]\}E$, and the *strain-displacement relationship*, $\epsilon_x = \partial u/\partial x$. These substitutions allow the one-dimensional equation of motion to be written in the familiar form of the one-dimensional *longitudinal wave equation* for a constrained rod:

$$\frac{\partial^2 u}{\partial t^2} = \frac{M}{\rho} \frac{\partial^2 u}{\partial x^2} \quad (5.3)$$

The one-dimensional wave equation can be written in the alternative form

$$\frac{\partial^2 u}{\partial t^2} = v_p^2 \frac{\partial^2 u}{\partial x^2} \quad (5.4)$$

where v_p is the *wave propagation velocity*; for this case, the wave travels at $v_p = \sqrt{M/\rho}$. Note that the wave propagation velocity depends only on the properties of the rod material (its stiffness and density) and is independent of the amplitude of the stress wave. The wave propagation velocity increases with increasing stiffness and with decreasing density. The wave propagation velocity is an extremely important material property that is relied upon heavily in soil dynamics and geotechnical earthquake engineering.

The wave propagation velocity is the velocity at which a stress wave would travel along the rod. It is not the same as the *particle velocity*, which is the velocity at which a single point within the rod would move as the wave passes through it. Knowing that $\partial u = \epsilon_x \partial x$ (from the strain-displacement relationship), $\epsilon_x = \sigma_x/M$ (from the stress-strain relationship), and $\partial x = v_p \partial t$ (from the definition of wave propagation velocity), the particle velocity \dot{u} can be shown to be

$$\dot{u} = \frac{\partial u}{\partial t} = \frac{\epsilon_x \partial x}{\partial t} = \frac{\sigma_x v_p \partial t}{M \partial t} = \frac{\sigma_x}{M} v_p = \frac{\sigma_x}{\rho v_p^2} v_p = \frac{\sigma_x}{\rho v_p} \quad (5.5)$$

Equation (5.5) shows that the particle velocity is proportional to the axial stress in the rod. The coefficient of proportionality, ρv_p , is called the *specific impedance* of the material. The specific impedance is another important property that influences the behavior of waves at boundaries (Section 5.4).

Example 5.1

Compute v_p for steel, vulcanized rubber, and water.

Solution The constrained moduli and specific gravities of steel, rubber, and water can be found in a number of reference books; typical values are summarized below:

MATERIAL	SPECIFIC GRAVITY, SG	M (PSI)
Steel	7.85	40.4×10^6
Vulcanized Rubber	1.2	167×10^6
Water	1.0	0.34×10^6

With this information, the v_p -values can be calculated from:

$$v_p = \sqrt{\frac{M}{\rho}} = \sqrt{\frac{M}{(\text{SG})\rho_w}} = \sqrt{\frac{Mg}{(\text{SG})\gamma_w}}$$

For steel,

$$v_p = \sqrt{\frac{(40.4 \times 10^6 \text{ psi})(144 \text{ in}^2/\text{ft}^2)(32.2 \text{ ft}/\text{sec}^2)}{(7.85)(62.4 \text{ pcf})}} = 19556 \text{ ft}/\text{sec}$$

For vulcanized rubber,

$$v_p = \sqrt{\frac{(167 \times 10^6 \text{ psi})(144 \text{ in}^2/\text{ft}^2)(32.2 \text{ ft}/\text{sec}^2)}{(1.20)(62.4 \text{ pcf})}} = 101691 \text{ ft}/\text{sec}$$

For water,

$$v_p = \sqrt{\frac{(0.34 \times 10^6 \text{ psi})(144 \text{ in}^2/\text{ft}^2)(32.2 \text{ ft}/\text{sec}^2)}{(1.00)(62.4 \text{ pcf})}} = 5026 \text{ ft}/\text{sec}$$

5.2.1.2 Torsional Waves in an Infinitely Long Rod

Torsional waves involve rotation of the rod about its own axis. In the case of the longitudinal wave, the direction of particle motion was parallel to the direction of wave propagation. For torsional waves, particle motion is constrained to planes perpendicular to the direction of wave propagation. Development of a wave equation for torsional vibrations, however, follows exactly the same steps as for longitudinal vibration. Consider the short segment of a cylindrical rod shown in Figure 5.3 as a torsional wave of torque amplitude T travels along the rod. Dynamic torsional equilibrium requires that the unbalanced external torque [left side of equation (5.6)] is equal to the inertial torque (right side):

$$\left(T_{x_0} + \frac{\partial T}{\partial x} dx \right) - T_{x_0} = \rho J dx \frac{\partial^2 \theta}{\partial t^2} \quad (5.6)$$

where J is the polar moment of inertia of the rod about its axis. This equilibrium equation can be simplified to produce the equation of motion

$$\frac{\partial T}{\partial x} = \rho J \frac{\partial^2 \theta}{\partial t^2} \quad (5.7)$$

Now, incorporating the torque–rotation relationship

$$T = GJ \frac{\partial \theta}{\partial x} \quad (5.8)$$

where G is the *shear modulus* of the rod, the torsional wave equation can be written as

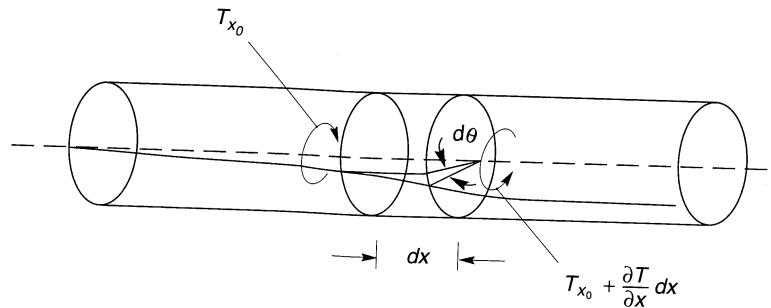


Figure 5.3 Torque and rotation at ends of element of length dx and cross-sectional area, A .

$$\frac{\partial^2 \theta}{\partial t^2} = \frac{G}{\rho} \frac{\partial^2 \theta}{\partial x^2} = v_s^2 \frac{\partial^2 \theta}{\partial x^2} \quad (5.9)$$

where $v_s = \sqrt{G/\rho}$ is the velocity of propagation of the torsional wave. Note that the form of the wave equation for torsional waves [equation (5.9)] is identical to that for longitudinal waves [equation (5.3)], but the wave propagation velocities are different. The wave propagation velocity depends both on the stiffness of the rod in the mode of deformation induced by the wave and on the material density but is independent of the amplitude of the stress wave.

Example 5.2

Compute v_s for steel, vulcanized rubber, and water.

Solution The shear moduli of steel, rubber, and water can be found in a number of reference books; typical values are summarized below:

MATERIAL	G (PSI)
Steel	11.5×10^6
Vulcanized Rubber	0.167×10^6
Water	0

With this information, the v_s -values can be calculated from

$$v_s = \sqrt{\frac{G}{\rho}} = \sqrt{\frac{G g}{(SG)\gamma_w}}$$

For steel,

$$v_s = \sqrt{\frac{(11.5 \times 10^6 \text{ psi}) (144 \text{ in}^2/\text{ft}^2) (32.2 \text{ ft}/\text{sec}^2)}{(7.85) (62.4 \text{ pcf})}} = 10434 \text{ ft}/\text{sec}$$

For vulcanized rubber,

$$v_s = \sqrt{\frac{(0.167 \times 10^6 \text{ psi}) (144 \text{ in}^2/\text{ft}^2) (32.2 \text{ ft}/\text{sec}^2)}{(1.20) (62.4 \text{ pcf})}} = 3216 \text{ ft}/\text{sec}$$

For water,

$$v_s = 0$$

The last result is obvious—as an inviscid fluid, water can produce no resistance to shear stresses and consequently cannot transmit torsional waves.

5.2.1.3 Solution of the One-Dimensional Equation of Motion

The one-dimensional wave equation is a partial differential equation of the form

$$\frac{\partial^2 u}{\partial t^2} = v^2 \frac{\partial^2 u}{\partial x^2} \quad (5.10)$$

where v represents the wave propagation velocity corresponding to the type of stress wave of interest. The solution of such an equation can be written in the form

$$u(x, t) = f(vt - x) + g(vt + x) \quad (5.11)$$

where f and g can be any arbitrary functions of $(vt - x)$ and $(vt + x)$ that satisfy equation (5.10). Note that the argument of f remains constant when x increases with time (at velocity v), and the argument of g remains constant when x decreases with time. Therefore, the solution of equation (5.11) describes a displacement wave $[f(vt - x)]$ traveling at velocity v in the positive x -direction and another $[g(vt + x)]$ traveling at the same speed in the negative x -direction. It also implies that the shapes of the waves do not change with position or time.

If the rod is subjected to some steady-state harmonic stress $\sigma(t) = \sigma_0 \cos \bar{\omega}t$ where σ_0 is the stress wave amplitude and $\bar{\omega}$ is the circular frequency of the applied loading, the solution can be expressed using the *wave number*, $k = \bar{\omega}/v$, in the form

$$u(x, t) = A \cos(\bar{\omega}t - kx) + B \cos(\bar{\omega}t + kx) \quad (5.12)$$

Here the first and second terms describe harmonic waves propagating in the positive and negative x -directions, respectively. The wave number is related to the *wavelength*, λ , of the motion by

$$\lambda = v\bar{T} = \frac{v}{f} = \frac{2\pi}{\bar{\omega}}v = \frac{2\pi}{k} \quad (5.13)$$

where \bar{T} is the period of the applied loading (note that wave number is to wavelength as circular frequency is to period) and $f = 1/\bar{T}$. Note that at a given frequency, the wavelength increases with increasing wave propagation velocity. Equation (5.12) indicates that the displacement varies harmonically with respect to both time and position as illustrated in Figure 5.4. Equation 5.13 and Figure 5.4 show that the wave number is to the wavelength as the circular frequency is to the period of vibration. For a wave propagating in the positive x -direction only ($B = 0$), differentiating $u(x, t)$ twice with respect to x and twice with respect to t and substituting into the wave equation [equation (5.10)] gives

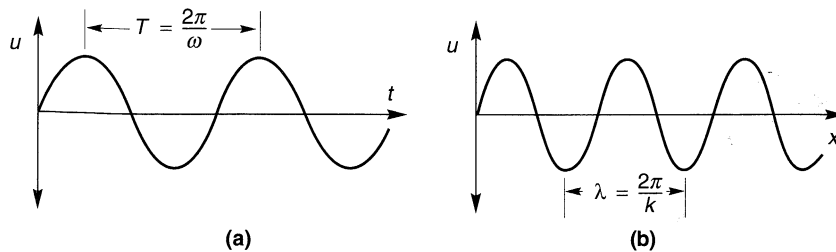


Figure 5.4 Particle displacement (a) as function of time, and (b) as function of position along the rod.

$$-\bar{\omega}^2 A \cos(\bar{\omega}t - kx) = -v^2 k^2 A \cos(\bar{\omega}t - kx) \quad (5.14)$$

which reduces to the identity $\bar{\omega} = kv$, thereby verifying equation (5.12) as a solution to the wave equation.

Using complex notation (Appendix A), the equivalent form of the solution can be written as

$$u(x, t) = C e^{i(\bar{\omega}t - kx)} + D e^{i(\bar{\omega}t + kx)} \quad (5.15)$$

This form of the solution can be verified in the same way as the trigonometric form.

Example 5.3

Calculate the wavelengths of harmonic longitudinal and torsional waves traveling along constrained steel and vulcanized rubber rods. Assume that the waves are harmonic at a frequency of 10 Hz.

Solution Using equation 5.13 and the wave propagation velocities computed in Examples 5.1 and 5.2,

Longitudinal waves

$$\text{Steel:} \quad \lambda = \frac{v_p}{f} = \frac{19556 \text{ ft/sec}}{10 \text{ sec}^{-1}} = 1956 \text{ ft}$$

$$\text{Vulcanized rubber:} \quad \lambda = \frac{v_p}{f} = \frac{101691 \text{ ft/sec}}{10 \text{ sec}^{-1}} = 10169 \text{ ft}$$

Torsional waves

$$\text{Steel:} \quad \lambda = \frac{v_s}{f} = \frac{10434 \text{ ft/sec}}{10 \text{ sec}^{-1}} = 1043 \text{ ft}$$

$$\text{Vulcanized rubber:} \quad \lambda = \frac{v_s}{f} = \frac{3216 \text{ ft/sec}}{10 \text{ sec}^{-1}} = 322 \text{ ft}$$

5.2.2 Three-Dimensional Wave Propagation

The preceding discussion of wave propagation in rods illustrates some of the basic principles of wave propagation, but an infinite rod is hardly an adequate model for describing the propagation of seismic waves through the earth. Since the earth is three-dimensional and sources of seismic energy are three-dimensional, seismic waves must be described in terms of three-dimensional wave propagation.

Derivations of three-dimensional equations of motion follow the same steps as those used for one-dimensional propagation; the equations of motion are formulated from equilibrium considerations, stress-strain relationships, and strain-displacement relationships. In the three-dimensional case, however, the various relationships are more complex and the derivation more cumbersome. Brief reviews of three-dimensional stress and strain notation and three-dimensional stress-strain behavior will precede derivation of the equations of motion.

5.2.2.1 Review of Stress Notation

The stress at a point on some plane passing through a solid does not usually act normal to that plane but has both normal and shear components. Considering a small element with one corner at the center of an x - y - z Cartesian coordinate system (Figure 5.5), a total of nine components of stress will act on its faces. These stresses are denoted by σ_{xx} , σ_{xy} , σ_{xz} , and

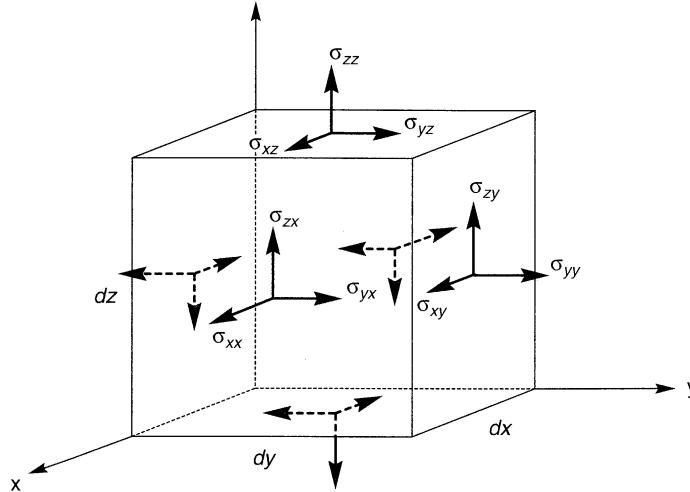


Figure 5.5 Stress notation for element of dimensions dx by dy by dz .

so on, where the first and second letters in the subscript describe the direction of the stress itself and the axis perpendicular to the plane in which it acts. Thus σ_{xx} , σ_{yy} , and σ_{zz} , are *normal stresses*, while the other six components represent *shear stresses*. Moment equilibrium of the element requires that

$$\sigma_{xy} = \sigma_{yx} \quad \sigma_{xz} = \sigma_{zx} \quad \sigma_{yz} = \sigma_{zy} \quad (5.16)$$

which means that only six independent components of stress are required to define the state of stress of the element completely. In some references, the notation σ_x , σ_y , σ_z , τ_{xy} , τ_{yz} , and τ_{xz} is used to describe σ_{xx} , σ_{yy} , σ_{zz} , σ_{xy} , σ_{yz} , and σ_{xz} , respectively.

5.2.2.2 Review of Strain Notation

Components of strain are easily visualized by considering the two-dimensional strain in the x - y plane shown in Figure 5.6. The point P , at coordinates (x_0, y_0) , is at one corner of the infinitesimal element $PQRS$ which has a square shape before deformation. After deformation, the infinitesimal element has been displaced, distorted, and rotated into the shape $P'Q'R'S'$. From Figure 5.6, $\tan \alpha_1 = dv/dx$ and $\tan \alpha_2 = du/dy$, where u and v represent displacements in the x - and y -directions, respectively. The shear strain in the x - y plane is given by $\epsilon_{xy} = \alpha_1 + \alpha_2$. For small deformations, the angles may be taken equal to their tangents so that the relationship between the shear strain and the displacements is $\epsilon_{xy} = dv/dx + du/dy$. The rotation of the element about the z -axis is given by $\Omega_z = (\alpha_1 - \alpha_2)/2$. Analogous definitions can be developed for the x - z and y - z planes. For the three-dimensional case, the strain-displacement relationships are defined by



$$\begin{aligned} \epsilon_{xx} &= \frac{du}{dx} & \epsilon_{yy} &= \frac{dv}{dy} & \epsilon_{zz} &= \frac{dw}{dz} \\ \epsilon_{xy} &= \frac{dv}{dx} + \frac{du}{dy} & \epsilon_{yz} &= \frac{dw}{dy} + \frac{dv}{dz} & \epsilon_{zx} &= \frac{du}{dz} + \frac{dw}{dx} \end{aligned} \quad (5.17)$$

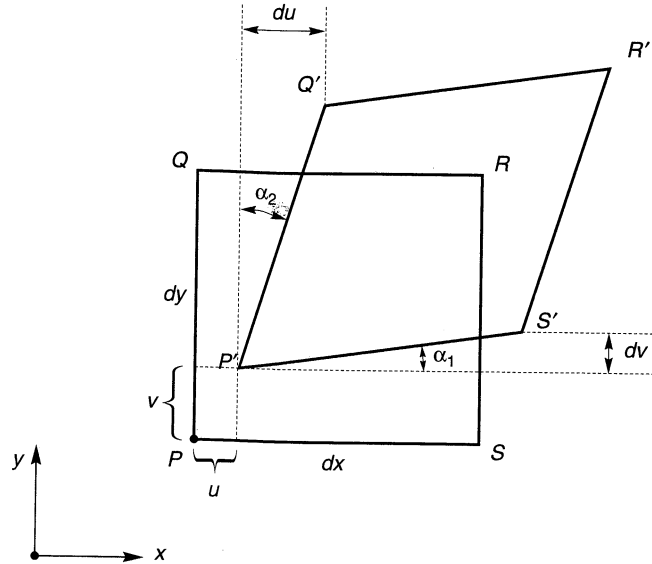


Figure 5.6 Square element subjected to plane strain deformation.

Rigid-body rotation about the x -, y -, and z -axes are given by the *rotation-displacement relationships*

$$\Omega_x = \frac{1}{2} \left(\frac{dw}{dy} - \frac{dv}{dz} \right) \quad \Omega_y = \frac{1}{2} \left(\frac{du}{dz} - \frac{dw}{dx} \right) \quad \Omega_z = \frac{1}{2} \left(\frac{dv}{dx} - \frac{du}{dy} \right) \quad (5.18)$$

The first three quantities, ϵ_{xx} , ϵ_{yy} , and ϵ_{zz} , represent the extensional and compressional strain parallel to the x -, y -, and z -axes, and are called *normal strains*. The second three quantities, ϵ_{xy} , ϵ_{yz} , and ϵ_{zx} , represent the components of shear strain in the planes corresponding to their suffixes. These six quantities are the components of strain that correspond to the deformation at P . In some references, the notation ϵ_x , ϵ_y , ϵ_z , γ_{xy} , γ_{yz} , and γ_{xz} is used to describe ϵ_{xx} , ϵ_{yy} , ϵ_{zz} , ϵ_{xy} , ϵ_{yz} , and ϵ_{zx} , respectively.

5.2.2.3 Review of Stress-Strain Relationships

Stresses and strains are proportional in a linear elastic body. The stress-strain relationship can be described by *Hooke's law*, which can be written in generalized form as

$$\begin{aligned} \sigma_{xx} &= c_{11}\epsilon_{xx} + c_{12}\epsilon_{yy} + c_{13}\epsilon_{zz} + c_{14}\epsilon_{xy} + c_{15}\epsilon_{yz} + c_{16}\epsilon_{zx} \\ \sigma_{yy} &= c_{21}\epsilon_{xx} + c_{22}\epsilon_{yy} + c_{23}\epsilon_{zz} + c_{24}\epsilon_{xy} + c_{25}\epsilon_{yz} + c_{26}\epsilon_{zx} \\ \sigma_{zz} &= c_{31}\epsilon_{xx} + c_{32}\epsilon_{yy} + c_{33}\epsilon_{zz} + c_{34}\epsilon_{xy} + c_{35}\epsilon_{yz} + c_{36}\epsilon_{zx} \\ \sigma_{xy} &= c_{41}\epsilon_{xx} + c_{42}\epsilon_{yy} + c_{43}\epsilon_{zz} + c_{44}\epsilon_{xy} + c_{45}\epsilon_{yz} + c_{46}\epsilon_{zx} \\ \sigma_{yz} &= c_{51}\epsilon_{xx} + c_{52}\epsilon_{yy} + c_{53}\epsilon_{zz} + c_{54}\epsilon_{xy} + c_{55}\epsilon_{yz} + c_{56}\epsilon_{zx} \\ \sigma_{zx} &= c_{61}\epsilon_{xx} + c_{62}\epsilon_{yy} + c_{63}\epsilon_{zz} + c_{64}\epsilon_{xy} + c_{65}\epsilon_{yz} + c_{66}\epsilon_{zx} \end{aligned} \quad (5.19)$$

where the 36 coefficients represent the elastic constants of the material. The requirement that the elastic strain energy must be a unique function of the strain (which requires that $c_{ij} = c_{ji}$ for all i and j) reduces the number of independent coefficients to 21. If the material is isotropic, the coefficients must be independent of direction, so that

$$\begin{aligned} c_{12} &= c_{21} = c_{13} = c_{31} = c_{23} = c_{32} = \lambda \\ c_{44} &= c_{55} = c_{66} = \mu \\ c_{11} &= c_{22} = c_{33} = \lambda + 2\mu \end{aligned} \quad (5.20)$$

and all other constants are zero. Therefore, Hooke's law for an isotropic, linear, elastic material allows all components of stress and strain to be expressed in terms of the two *Lamé constants*, λ and μ :

$$\begin{aligned} \sigma_{xx} &= \lambda \bar{\epsilon} + 2\mu \epsilon_{xx} & \sigma_{xy} &= \mu \epsilon_{xy} \\ \sigma_{yy} &= \lambda \bar{\epsilon} + 2\mu \epsilon_{yy} & \sigma_{yz} &= \mu \epsilon_{yz} \\ \sigma_{zz} &= \lambda \bar{\epsilon} + 2\mu \epsilon_{zz} & \sigma_{zx} &= \mu \epsilon_{zx} \end{aligned} \quad (5.21)$$

where the *volumetric strain* $\bar{\epsilon} = \epsilon_{xx} + \epsilon_{yy} + \epsilon_{zz}$. Note that the symbol λ is used universally for both Lamé's constant and for wavelength; the context in which it is used should make its meaning obvious.

For convenience, several other parameters are often used to describe the stress-strain behavior of isotropic, linear, elastic materials, each of which can be expressed in terms of Lamé's constants. Some of the more common of these are

$$\text{Young's modulus:} \quad E = \frac{\mu(3\lambda + 2\mu)}{\lambda + \mu} \quad (5.22a)$$

$$\text{Bulk modulus:} \quad K = \lambda + \frac{2\mu}{3} \quad (5.22b)$$

$$\text{Shear modulus:} \quad G = \mu \quad (5.22c)$$

$$\text{Poisson's ratio:} \quad \nu = \frac{\lambda}{2(\lambda + \mu)} \quad (5.22d)$$

Hooke's law for an isotropic, linear, elastic material can be expressed using any combination of two of these parameters and/or Lamé's constants.

5.2.2.4 Equations of Motion for a Three-Dimensional Elastic Solid

The three-dimensional equations of motion for an elastic solid are obtained from equilibrium requirements in much the same way as for the one-dimensional rod, except that equilibrium must be ensured in three perpendicular directions. Consider the variation in stress across an infinitesimal cube aligned with its sides parallel to the x - y - z axes shown in Figure 5.7. Assuming that the average stress on each face of the cube is represented by the stress shown at the center of the face, the resultant forces acting in the x -, y -, and z -directions can be evaluated. In the x -direction, the unbalanced external forces must be balanced by an inertial force in that direction, so that

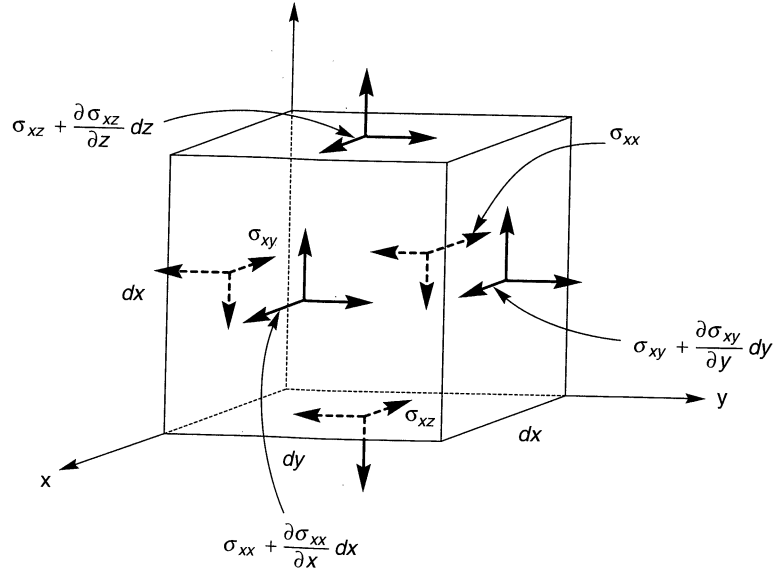


Figure 5.7 Stresses in x-direction on infinitesimal cube.

$$\begin{aligned}
 \rho \, dx \, dy \, dz \frac{\partial^2 u}{\partial t^2} &= \left(\sigma_{xx} + \frac{\partial \sigma_{xx}}{\partial x} dx \right) dy \, dz - \sigma_{xx} \, dy \, dz \\
 &+ \left(\sigma_{xy} + \frac{\partial \sigma_{xy}}{\partial y} dy \right) dx \, dz - \sigma_{xy} \, dx \, dz \\
 &+ \left(\sigma_{xz} + \frac{\partial \sigma_{xz}}{\partial z} dz \right) dx \, dy - \sigma_{xz} \, dx \, dy
 \end{aligned} \tag{5.23}$$

which simplifies to

$$\rho \frac{\partial^2 u}{\partial t^2} = \frac{\partial \sigma_{xx}}{\partial x} + \frac{\partial \sigma_{xy}}{\partial y} + \frac{\partial \sigma_{xz}}{\partial z} \tag{5.24}$$

Repeating this operation in the y- and z-directions gives

$$\rho \frac{\partial^2 v}{\partial t^2} = \frac{\partial \sigma_{yx}}{\partial x} + \frac{\partial \sigma_{yy}}{\partial y} + \frac{\partial \sigma_{yz}}{\partial z} \tag{5.24b}$$

$$\rho \frac{\partial^2 w}{\partial t^2} = \frac{\partial \sigma_{zx}}{\partial x} + \frac{\partial \sigma_{zy}}{\partial y} + \frac{\partial \sigma_{zz}}{\partial z} \tag{5.24c}$$

Equations (5.24) represent the *three-dimensional equations of motion* of an elastic solid. Note that these equations of motion were derived solely on the basis of equilibrium considerations and thus apply to solids of any stress–strain behavior. To express these equations of motion in terms of displacements, it is again necessary to use a stress–strain relationship and a strain–displacement relationship. Using Hooke’s law as developed in Section 5.2.2.3, the first of the equations of motion [equation (5.24a)] can be written in terms of strains as.

$$\rho \frac{\partial^2 u}{\partial t^2} = \frac{\partial}{\partial x}(\lambda \bar{\epsilon} + 2\mu \epsilon_{xx}) + \frac{\partial}{\partial y}(\mu \epsilon_{xy}) + \frac{\partial}{\partial z}(\mu \epsilon_{xz}) \quad (5.25)$$

Substituting the strain–displacement relationships

$$\epsilon_{xx} = \frac{\partial u}{\partial x} \quad \epsilon_{xy} = \frac{\partial v}{\partial x} + \frac{\partial u}{\partial y} \quad \epsilon_{xz} = \frac{\partial w}{\partial x} + \frac{\partial u}{\partial z}$$

into equation (5.25) produces the desired equation of motion in terms of displacements:

$$\rho \frac{\partial^2 u}{\partial t^2} = (\lambda + \mu) \frac{\partial \bar{\epsilon}}{\partial x} + \mu \nabla^2 u \quad (5.26a)$$

where the *Laplacian operator* ∇^2 represents

$$\nabla^2 = \frac{\partial^2}{\partial x^2} + \frac{\partial^2}{\partial y^2} + \frac{\partial^2}{\partial z^2}$$

Repeating this process in the y and z directions gives

$$\rho \frac{\partial^2 v}{\partial t^2} = (\lambda + \mu) \frac{\partial \bar{\epsilon}}{\partial y} + \mu \nabla^2 v \quad (5.26b)$$

$$\rho \frac{\partial^2 w}{\partial t^2} = (\lambda + \mu) \frac{\partial \bar{\epsilon}}{\partial z} + \mu \nabla^2 w \quad (5.26c)$$

5.2.2.5 Solutions of the Three-Dimensional Equations of Motion

Together, equations (5.26) represent the three-dimensional equations of motion for an isotropic, linear, elastic solid. It turns out that these equations can be manipulated to produce two wave equations. Consequently, only two types of waves can travel through such an unbounded solid. The characteristics of each type of wave will be revealed by their respective wave equations.

The solution for the first type of wave can be obtained by differentiating each of equations (5.26) with respect to x , y , and z and adding the results together to give

$$\begin{aligned} \rho \left(\frac{\partial^2 \epsilon_{xx}}{\partial t^2} + \frac{\partial^2 \epsilon_{yy}}{\partial t^2} + \frac{\partial^2 \epsilon_{zz}}{\partial t^2} \right) &= (\lambda + \mu) \left(\frac{\partial^2 \bar{\epsilon}}{\partial x^2} + \frac{\partial^2 \bar{\epsilon}}{\partial y^2} + \frac{\partial^2 \bar{\epsilon}}{\partial z^2} \right) \\ &+ \mu \left(\frac{\partial^2 \epsilon_{xx}}{\partial x^2} + \frac{\partial^2 \epsilon_{yy}}{\partial y^2} + \frac{\partial^2 \epsilon_{zz}}{\partial z^2} \right) \end{aligned}$$

or

$$\rho \frac{\partial^2 \bar{\epsilon}}{\partial t^2} = (\lambda + \mu) \nabla^2 \bar{\epsilon} + \mu \nabla^2 \bar{\epsilon} \quad (5.27)$$

Rearranging yields the wave equation

$$\frac{\partial^2 \bar{\epsilon}}{\partial t^2} = \frac{\lambda + 2\mu}{\rho} \nabla^2 \bar{\epsilon} \quad (5.28)$$

Recalling that $\bar{\epsilon}$ is the volumetric strain (which describes deformations that involve no shearing or rotation), this wave equation describes an *irrotational*, or *dilatational*, wave. It indicates that a dilatational wave will propagate through the body at a velocity

$$v_p = \sqrt{\frac{\lambda + 2\mu}{\rho}} \quad (5.29)$$

This type of wave is commonly known as a *p-wave* (or *primary wave*) and v_p is referred to as the *p-wave velocity* of the material. The general nature of p-wave motion was illustrated in Figure 2.1a. Note that particle displacements are parallel to the direction of wave propagation, just as they were in the constrained rod of Section 5.2.1.1. The longitudinal wave in the constrained rod is actually a p-wave. Using equations (5.22c) and (5.22d), v_p can be written in terms of the shear modulus and Poisson's ratio as

$$v_p = \sqrt{\frac{G(2 - 2\nu)}{\rho(1 - 2\nu)}} \quad (5.30)$$

As ν approaches 0.5 (at which point the body becomes incompressible, i.e., infinitely stiff with respect to dilatational deformations), v_p approaches infinity.

To obtain the solution for the second type of wave, $\bar{\epsilon}$ is eliminated by differentiating equation (5.26b) with respect to z and equation (5.26c) with respect to y , and subtracting one from the other:

$$\rho \frac{\partial}{\partial t^2} \left(\frac{\partial w}{\partial y} - \frac{\partial v}{\partial z} \right) = \mu \nabla^2 \left(\frac{\partial w}{\partial y} - \frac{\partial v}{\partial z} \right) \quad (5.31)$$

Recalling the definition of rotation [equation (5.19)], equation (5.31) can be written in the form of the wave equation

$$\frac{\partial^2 \Omega_x}{\partial t^2} = \frac{\mu}{\rho} \nabla^2 \Omega_x \quad (5.32)$$

which describes an *equivoluminal*, or *distortional* wave, of rotation about the x -axis. Similar expressions can be obtained by the same process for rotation about the y - and z -axes. Equation (5.32) shows that a distortional wave will propagate through the solid at a velocity

$$v_s = \sqrt{\frac{\mu}{\rho}} = \sqrt{\frac{G}{\rho}} \quad (5.33)$$

This type of wave is commonly known as a *s-wave* (or *shear wave*) and v_s is referred to as the *shear wave velocity* of the material. Note that the particle motion is constrained to a plane perpendicular to the direction of wave propagation, just as it was in the case of the torsional wave of Section 5.2.1.2. Consequently, the torsional wave represented a form of an *s-wave*. The close relationship between s-wave velocity and shear modulus is used to advantage in many of the field and laboratory tests discussed in Chapter 6. The general nature of s-wave motion was illustrated in Figure 2.1b.

S-waves are often divided into two types, or resolved into two perpendicular components. SH-waves are s-waves in which particle motion occurs only in a horizontal plane. SV-waves are s-waves whose particle motion lies in a vertical plane. A given s-wave with arbitrary particle motion can be represented as the vector sum of its SH and SV components.

In summary, only two types of waves, known as *body waves*, can exist in an unbounded (infinite) elastic solid. P-waves involve no rotation of the material they pass through and travel at velocity, v_p . S-waves involve no volume change and travel at velocity, v_s . The velocities of p- and s-waves depend on the stiffnesses of the solid with respect to the types of deformation induced by each wave. Comparing the velocities [equations (5.30) and (5.33)]

$$\frac{v_p}{v_s} = \sqrt{\frac{2-2\nu}{1-2\nu}} \quad (5.34)$$

the p-wave velocity can be seen to exceed the s-wave velocity by an amount that depends on the compressibility (as reflected in Poisson's ratio) of the body. For a typical Poisson's ratio of 0.3 for geologic materials, the ratio $v_p/v_s = 1.87$.

5.3 WAVES IN A SEMI-INFINITE BODY

The earth is obviously not an infinite body—it is a very large sphere with an outer surface on which stresses cannot exist. For near-surface earthquake engineering problems, the earth is often idealized as a semi-infinite body with a planar free surface (the effects of the earth's curvature are neglected). The boundary conditions associated with the free surface allow additional solutions to the equations of motion to be obtained. These solutions describe waves whose motion is concentrated in a shallow zone near the free surface (i.e., *surface waves*). Since earthquake engineering is concerned with the effects of earthquakes on humans and their environment, which are located on or very near the earth's surface, and since they attenuate with distance more slowly than body waves, surface waves are very important.

Two types of surface waves are of primary importance in earthquake engineering. One, the *Rayleigh wave*, can be shown to exist in a homogeneous, elastic half-space. The other surface wave, the *Love wave*, requires a surficial layer of lower s-wave velocity than the underlying half-space. Other types of surface waves exist but are much less significant from an earthquake engineering standpoint.

5.3.1 Rayleigh Waves

Waves that exist near the surface of a homogeneous elastic half-space were first investigated by Rayleigh (1885) and are known to this date as *Rayleigh waves*. To describe Rayleigh waves, consider a *plane wave* (Figure 5.8) that travels in the x -direction with zero particle displacement in the y -direction ($v = 0$). The z -direction is taken as positive downward, so all particle motion occurs in the x - z plane. Two *potential functions*, Φ and Ψ , can be defined to describe the displacements in the x - and z -directions:

$$u = \frac{\partial \Phi}{\partial x} + \frac{\partial \Psi}{\partial z} \quad (5.35a)$$

$$w = \frac{\partial \Phi}{\partial z} - \frac{\partial \Psi}{\partial x} \quad (5.35b)$$

The volumetric strain, or *dilatation*, $\bar{\epsilon}$, of the wave is given by $\bar{\epsilon} = \epsilon_{xx} + \epsilon_{zz}$, or

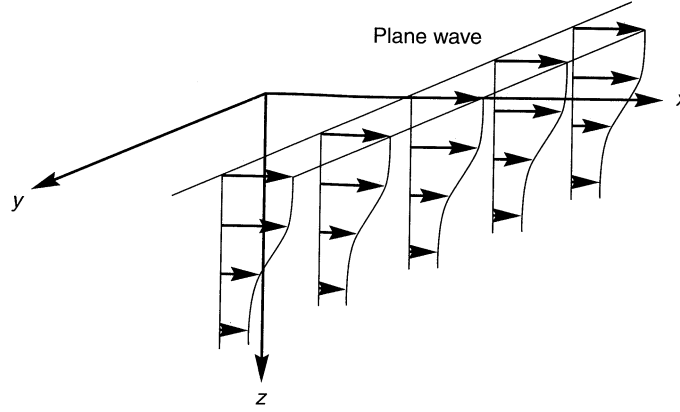


Figure 5.8 Motion induced by a typical plane wave that propagates in the x -direction. Wave motion does not vary in the y -direction.

$$\bar{\epsilon} = \frac{\partial u}{\partial x} + \frac{\partial w}{\partial z} = \frac{\partial}{\partial x} \left(\frac{\partial \Phi}{\partial x} + \frac{\partial \Psi}{\partial z} \right) + \frac{\partial}{\partial z} \left(\frac{\partial \Phi}{\partial z} - \frac{\partial \Psi}{\partial x} \right) = \frac{\partial^2 \Phi}{\partial x^2} + \frac{\partial^2 \Phi}{\partial z^2} = \nabla^2 \Phi \quad (5.36)$$

The rotation in the x - z plane is given [equation (5.19)] by

$$2\Omega_y = \frac{\partial u}{\partial z} - \frac{\partial w}{\partial x} = \frac{\partial}{\partial z} \left(\frac{\partial \Phi}{\partial x} + \frac{\partial \Psi}{\partial z} \right) - \frac{\partial}{\partial x} \left(\frac{\partial \Phi}{\partial z} - \frac{\partial \Psi}{\partial x} \right) = \frac{\partial^2 \Psi}{\partial z^2} + \frac{\partial^2 \Psi}{\partial x^2} = \nabla^2 \Psi \quad (5.37)$$

Use of the potential functions allows separation of the effects of dilatation and rotation [i.e., equations (5.36) and (5.37) indicate that Φ and Ψ are associated with dilatation and rotation, respectively]. Therefore, Rayleigh waves can be thought of as combinations of p- and s-waves (SV waves for this case, since the x - z plane is vertical) that satisfy certain boundary conditions. Substitution of the expressions for u and w into the equations of motion as written in equations (5.26a) and (5.26c) gives

$$\rho \frac{\partial}{\partial x} \left(\frac{\partial^2 \Phi}{\partial t^2} \right) + \rho \frac{\partial}{\partial z} \left(\frac{\partial^2 \Psi}{\partial t^2} \right) = (\lambda + 2\mu) \frac{\partial}{\partial x} (\nabla^2 \Phi) + \mu \frac{\partial}{\partial z} (\nabla^2 \Psi) \quad (5.38a)$$

$$\rho \frac{\partial}{\partial z} \left(\frac{\partial^2 \Phi}{\partial t^2} \right) - \rho \frac{\partial}{\partial x} \left(\frac{\partial^2 \Psi}{\partial t^2} \right) = (\lambda + 2\mu) \frac{\partial}{\partial z} (\nabla^2 \Phi) - \mu \frac{\partial}{\partial x} (\nabla^2 \Psi) \quad (5.38b)$$

Solving equations (5.38) simultaneously for $\partial^2 \Phi / \partial t^2$ and $\partial^2 \Psi / \partial t^2$ shows

$$\frac{\partial^2 \Phi}{\partial t^2} = \frac{\lambda + 2\mu}{\rho} \nabla^2 \Phi = v_p^2 \nabla^2 \Phi \quad (5.39a)$$

$$\frac{\partial^2 \Psi}{\partial t^2} = \frac{\mu}{\rho} \nabla^2 \Psi = v_s^2 \nabla^2 \Psi \quad (5.39b)$$

If the wave is harmonic with frequency ω and wave number k_R , so that it propagates with Rayleigh wave velocity $v_R = \omega/k_R$, the potential functions can be expressed as

$$\Phi = F(z) e^{i(\omega t - k_R x)} \quad (5.40a)$$

$$\Psi = G(z)e^{i(\omega t - k_R x)} \quad (5.40b)$$

where F and G are functions that describe the manner in which the amplitude of the dilational and rotational components of the Rayleigh wave vary with depth. Substituting these expressions for Φ and Ψ into equations (5.39) gives

$$-\frac{\omega^2}{v_p^2}F(z) = -k_R^2 F(z) + \frac{d^2 F(z)}{dz^2} \quad (5.41a)$$

$$-\frac{\omega^2}{v_s^2}G(z) = -k_R^2 G(z) + \frac{d^2 G(z)}{dz^2} \quad (5.41b)$$

which can be rearranged to give the second-order differential equations

$$\frac{d^2 F}{dz^2} - \left(k_R^2 - \frac{\omega^2}{v_p^2} \right) F = 0 \quad (5.42a)$$

$$\frac{d^2 G}{dz^2} - \left(k_R^2 - \frac{\omega^2}{v_s^2} \right) G = 0 \quad (5.42b)$$

The general solution to these equations can be written in the form

$$F(z) = A_1 e^{-qz} + B_1 e^{qz} \quad (5.43a)$$

$$G(z) = A_2 e^{-sz} + B_2 e^{sz} \quad (5.43b)$$

where

$$q^2 = k_R^2 - \frac{\omega^2}{v_p^2}$$

$$s^2 = k_R^2 - \frac{\omega^2}{v_s^2}$$

The second term of equations (5.43) corresponds to a disturbance whose displacement amplitude approaches infinity with increasing depth. Since this type of behavior is not realistic, B_1 and B_2 must be zero, and the potential functions can finally be written as

$$\Phi = A_1 e^{-qz + i(\omega t - k_R x)} \quad (5.44a)$$

$$\Psi = A_2 e^{-sz + i(\omega t - k_R x)} \quad (5.44b)$$

Since neither shear nor normal stresses can exist at the free surface of the half-space, $\sigma_{xz} = 0$ and $\sigma_{zz} = 0$ when $z = 0$. Therefore,

$$\sigma_{zz} = \lambda \bar{\epsilon} + 2\mu \epsilon_{zz} = \lambda \bar{\epsilon} + 2\mu \frac{dw}{dz} = 0 \quad (5.45a)$$

$$\sigma_{xz} = \mu \epsilon_{xz} = \mu \left(\frac{dw}{dx} + \frac{du}{dz} \right) = 0 \quad (5.45b)$$

Using the potential function definitions of u and w [equations (5.35)] and the solution for the potential functions [equation (5.44)], the free surface boundary conditions can be rewritten as

$$\sigma_{zz}(z=0) = A_1 [(\lambda + 2\mu)q^2 - \lambda k_R^2] - 2iA_2\mu k_R s = 0 \quad (5.46a)$$

$$\sigma_{xz}(z=0) = 2iA_1 k_R q + A_2(s^2 + k_R^2) = 0 \quad (5.46b)$$

which can be rearranged to yield

$$\frac{A_1(\lambda + 2\mu)q^2 - \lambda k_R^2}{A_2 2i\mu k_R s} - 1 = 0 \quad (5.47a)$$

$$\frac{A_1}{A_2} \frac{2iqk_R}{s^2 + k_R^2} + 1 = 0 \quad (5.47b)$$

With these results, the velocities and displacement patterns of Rayleigh waves can be determined.

5.3.1.1 Rayleigh Wave Velocity

The velocity at which Rayleigh waves travel is of interest in geotechnical earthquake engineering. As discussed in Chapter 6, Rayleigh waves are often mechanically generated and their velocities measured in the field to investigate the stiffness of surficial soils. Adding equations (5.47) and cross-multiplying gives

$$4q\mu s k_R^2 = (s^2 + k_R^2)[(\lambda + 2\mu)q^2 - \lambda k_R^2] \quad (5.48)$$

which, upon introducing the definitions of q and s and factoring out a $G^2 k_R^8$ term, yields

$$16 \left(1 - \frac{\omega^2}{v_p^2 k_R^2}\right) \left(1 - \frac{\omega^2}{v_s^2 k_R^2}\right) = \left(2 - \frac{\lambda + 2\mu}{\mu} \frac{\omega^2}{v_p^2 k_R^2}\right)^2 \left(2 - \frac{\omega^2}{v_s^2 k_R^2}\right)^2 \quad (5.49)$$

Defining K_{Rs} as the ratio of the Rayleigh wave velocity to the s-wave velocity

$$K_{Rs} = \frac{v_R}{v_s} = \frac{\omega}{v_s k_R}$$

then

$$\frac{v_R}{v_p} = \frac{\omega}{v_p k_R} = \frac{\omega}{v_s k_R \sqrt{(\lambda + 2\mu)/\mu}} = \alpha K_{Rs}$$

where $\alpha = \sqrt{\mu/(\lambda + 2\mu)} = \sqrt{(1 - 2\nu)/(2 - 2\nu)}$. Then equation (5.49) can be rewritten as

$$16 (1 - \alpha^2 K_{Rs}^2)(1 - K_{Rs}^2) = \left(2 - \frac{1}{\alpha^2} \alpha^2 K_{Rs}^2\right)^2 (2 - K_{Rs}^2)^2 \quad (5.50)$$

which can be expanded and rearranged into the equation

$$K_{Rs}^6 - 8K_{Rs}^4 + (24 - 16\alpha^2)K_{Rs}^2 + 16(\alpha^2 - 1) = 0 \quad (5.51)$$

This equation is cubic in K_{Rs}^2 , and real solutions for K_{Rs} can be found for various values of Poisson's ratio. These allow evaluation of the ratios of the Rayleigh wave velocity to both s- and p-wave velocities as functions of ν . The solution shown in Figure 5.9 shows that Rayleigh waves travel slightly slower than s-waves for all values of Poisson's ratio except 0.5.

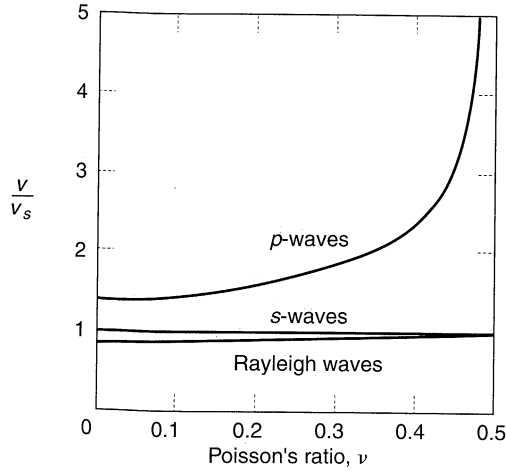


Figure 5.9 Variation of Rayleigh wave and body wave propagation velocities with Poisson's ratio.

5.3.1.2 Rayleigh Wave Displacement Amplitude

Section 5.3.1.1 showed how the velocity of a Rayleigh wave compares with that of p- and s-waves. Some of the intermediate results of that section can be used to illustrate the nature of particle motion during the passage of Rayleigh waves. Substituting the solutions for the potential functions Φ and Ψ [equations (5.44)] into the expressions for u and w [equation 5.35] and carrying out the necessary partial differentiations yields

$$u = -A_1 i k_R e^{-qz + i(\omega t - k_R x)} - A_2 s e^{-sz + i(\omega t - k_R x)} \quad (5.52a)$$

$$w = (-A_1 i k_R e^{-qz + i(\omega t - k_R x)}) + A_2 i k_R e^{-sz + i(\omega t - k_R x)} \quad (5.52b)$$

From equation (5.47b),

$$A_2 = -\frac{2qik_R}{s^2 + k_R^2} A_1$$

which, substituting into equations (5.52), gives

$$u = A_1 \left(-ik_R e^{-qz} + \frac{2iqsk_R}{s^2 + k_R^2} e^{-sz} \right) e^{i(\omega t - k_R x)} \quad (5.53a)$$

$$w = A_1 \left(\frac{2qk_R^2}{s^2 + k_R^2} e^{-sz} - q e^{-qz} \right) e^{i(\omega t - k_R x)} \quad (5.53b)$$

where the terms in parentheses describe the variation of the amplitudes of u and w with depth. These horizontal and vertical displacement amplitudes are illustrated for several values of

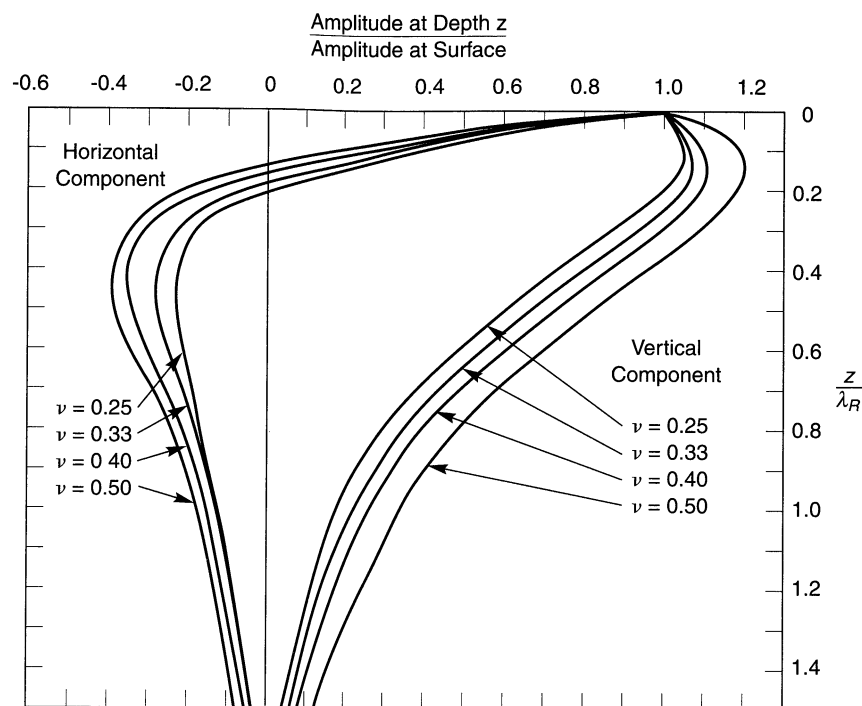


Figure 5.10 Horizontal and vertical motion of Rayleigh waves. A negative amplitude ratio indicates that the displacement is in the opposite direction of the surface displacement. (After Richart et al., 1970.)

Poisson's ratio in Figure 5.10. Examination of equations (5.53) indicates that the horizontal and vertical displacements are out of phase by 90° . Hence the horizontal displacement will be zero when the vertical displacement reaches its maximum (or minimum), and vice versa. The motion of a particle near the surface of the half-space is in the form of a retrograde ellipse (as opposed to the prograde ellipse particle motion observed at the surface of water waves). The general nature of Rayleigh wave motion was illustrated in Figure 2.2a.

The Rayleigh waves produced by earthquakes were once thought to appear only at very large epicentral distances (several hundred km). It is now recognized, however, that they can be significant at much shorter distances (a few tens of kilometers). The ratio of minimum epicentral distance, R , to focal depth, h , at which Rayleigh waves first appear in a homogeneous medium is given by

$$\frac{R}{h} = \frac{1}{\sqrt{(v_p/v_R)^2 - 1}} \quad (5.54)$$

where v_p and v_R are the wave propagation velocities of p-waves and Rayleigh waves, respectively (Ewing et al., 1957).

5.3.2 Love Waves

In a homogeneous elastic half-space, only p-waves, s-waves, and Rayleigh waves can exist. If the half-space is overlain by a layer of material with lower body wave velocity, however, Love waves can develop (Love, 1927). Love waves essentially consist of SH-waves that are trapped by multiple reflections within the surficial layer. Consider the case of a homogeneous surficial layer of thickness H overlying a homogeneous half-space as shown in Figure 5.11. A Love wave traveling in the $+x$ -direction would involve particle displacements only in the y -direction (SH-wave motion), and could be described by the equation

$$v(x, z, t) = V(z) e^{i(k_L x - \omega t)} \quad (5.55)$$

where v is the particle displacement in the y -direction, $V(z)$ describes the variation of v with depth, and k_L is the wave number of the Love wave. The Love wave must satisfy the wave equations for s-waves in both the surficial layer and the half-space

$$\frac{\partial^2 v}{\partial t^2} = \begin{cases} \frac{G_1}{\rho_1} \left(\frac{\partial^2 v}{\partial x^2} + \frac{\partial^2 v}{\partial z^2} \right) & \text{for } 0 \leq z \leq H \\ \frac{G_2}{\rho_2} \left(\frac{\partial^2 v}{\partial x^2} + \frac{\partial^2 v}{\partial z^2} \right) & \text{for } z \geq H \end{cases} \quad (5.56a)$$

$$\quad (5.56b)$$

The amplitude can be shown (Aki and Richards, 1980) to vary with depth according to

$$V(z) = \begin{cases} A_1 e^{-v_1 z} + B_1 e^{v_1 z} & \text{for } 0 \leq z \leq H \\ A_2 e^{-v_2 z} + B_2 e^{v_2 z} & \text{for } z \geq H \end{cases} \quad (5.57a)$$

$$\quad (5.57b)$$

where the A and B coefficients describe the amplitudes of downgoing and upgoing waves, respectively, and

$$v_1 = \sqrt{\frac{k_L^2 - \omega^2}{G_1/\rho_1}} \quad v_2 = \sqrt{\frac{k_L^2 - \omega^2}{G_2/\rho_2}} \quad (5.58)$$

Since the half-space extends to infinite depth, B_2 must be zero (no energy can be supplied or reflected at infinite depth to produce an upgoing wave). The requirement that all stresses vanish at the ground surface is satisfied if

$$\frac{\partial v}{\partial z} = \frac{\partial V(z)}{\partial z} e^{i(k_L x - \omega t)} = -A_1 v_1 e^{-v_1 z} + v_1 B_1 e^{v_1 z} = (A_1 - B_1) v_1 (e^{-v_1 z} + e^{v_1 z}) = 0$$

in other words, if $A_1 = B_1$. The amplitudes can now be rewritten in terms of the two remaining unknown amplitudes as

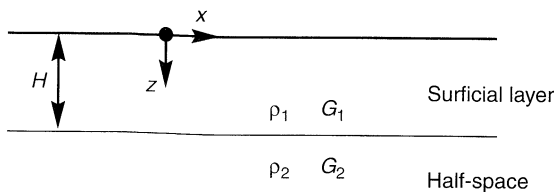


Figure 5.11 Schematic illustration of softer surficial layer ($G_1/\rho_1 < G_2/\rho_2$) overlying elastic half-space, the simplest conditions for which Love waves can exist.

$$V(z) = \begin{cases} A_1(e^{-v_1 z} + e^{v_1 z}) & \text{for } 0 \leq z \leq H \\ A_2 e^{-v_2 z} & \text{for } z \geq H \end{cases} \quad (5.59a)$$

$$A_2 e^{-v_2 z} \quad \text{for } z \geq H \quad (5.59b)$$

At the $z = H$ interface, continuity of stresses requires that

$$2iG_1 v_1 A_1 \sin(iv_1 H) = G_2 v_2 A_2 e^{-v_2 H} \quad (5.60)$$

and compatibility of displacements requires that

$$2A_1 \cos(iv_1 H) = A_2 e^{-v_2 H} \quad (5.61)$$

Using equations (5.60) and (5.61), A_2 can be expressed in terms of A_1 by

$$A_2 = \frac{2 \cos(iv_1 H)}{e^{-v_2 H}} A_1 \quad (5.62)$$

Substituting equations (5.59) and (5.60) into (5.55) gives

$$v(x, z, t) = \begin{cases} 2A_1 \cos \left[\omega \left(\frac{1}{v_{s1}^2} - \frac{1}{v_L^2} \right)^{1/2} z \right] e^{i(k_L x - \omega t)} & \text{for } 0 \leq z \leq H \\ 2A_1 \cos \left[\omega \left(\frac{1}{v_{s1}^2} - \frac{1}{v_L^2} \right)^{1/2} H \right] \exp \left[-\omega \left(\frac{1}{v_L^2} - \frac{1}{v_{s2}^2} \right)^{1/2} (z - H) \right] e^{i(k_L x - \omega t)} & \text{for } z \geq H \end{cases} \quad (5.63a)$$

$$v(x, z, t) = \begin{cases} 2A_1 \cos \left[\omega \left(\frac{1}{v_{s1}^2} - \frac{1}{v_L^2} \right)^{1/2} z \right] e^{i(k_L x - \omega t)} & \text{for } 0 \leq z \leq H \\ 2A_1 \cos \left[\omega \left(\frac{1}{v_{s1}^2} - \frac{1}{v_L^2} \right)^{1/2} H \right] \exp \left[-\omega \left(\frac{1}{v_L^2} - \frac{1}{v_{s2}^2} \right)^{1/2} (z - H) \right] e^{i(k_L x - \omega t)} & \text{for } z \geq H \end{cases} \quad (5.63b)$$

where v_{s1} and v_{s2} are the shear wave velocities of materials 1 and 2, respectively, and v_L is the velocity of the Love wave. Equation (5.63) shows, as illustrated in Figure 5.12, that the Love wave displacement amplitude varies sinusoidally with depth in the surficial layer and decays exponentially with depth in the underlying half-space. Because of this, Love waves are often described as SH-waves that are trapped in the surficial layer. The general nature of Love wave displacement was shown in Figure 2.2a.

The Love wave velocity is given by the solution of

$$\tan \omega H \left(\frac{1}{v_{s1}^2} - \frac{1}{v_L^2} \right)^{1/2} = \frac{G_2 \sqrt{1/v_L^2 - 1/v_{s2}^2}}{G_1 \sqrt{1/v_{s1}^2 - 1/v_L^2}} \quad (5.64)$$

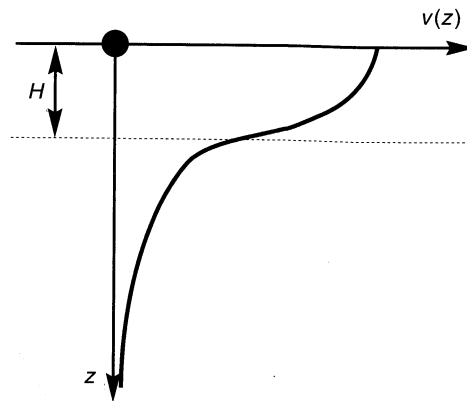


Figure 5.12 Variation of particle displacement amplitude with depth for Love waves.

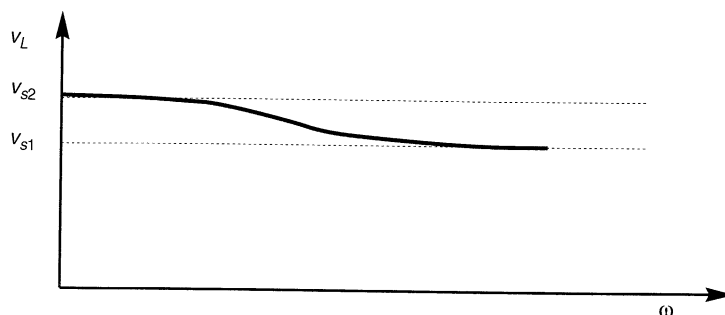


Figure 5.13 Variation of Love wave velocity with frequency.

which indicates, as illustrated in Figure 5.13 that Love wave velocities range from the s-wave velocity of the half-space (at very low frequencies) to the s-wave velocity of the surficial layer (at very high frequencies). This frequency dependence indicates that Love waves are dispersive (Section 5.3.4).

5.3.3 Higher-Mode Surface Waves

Any surface wave must (1) satisfy the equation of motion, (2) produce zero stress at the ground surface, and (3) produce zero displacement at infinite depth. Nontrivial solutions do not exist for arbitrary combinations of frequency and wave number; rather, a set of discrete and unique wave numbers exist for a given frequency. Each wave number describes a different displacement pattern, or *mode*, of the surface wave. The preceding derivations have been limited to the *fundamental modes* of Rayleigh and Love waves, which are the most important for earthquake engineering applications. Detailed treatment of higher-mode surface waves can be found in most advanced seismology texts.

5.3.4 Dispersion of Surface Waves

For a homogeneous half-space, the Rayleigh wave velocity was shown to be related to the body wave velocities by Poisson's ratio. Since the body wave velocities are constant with depth, the Rayleigh wave velocity in a homogeneous half-space is independent of frequency. The velocity of the Love wave, on the other hand, varies with frequency between an upper and a lower limit.

Dispersion is a phenomenon in which waves of different frequency (and different wavelength) propagate at different velocities. Hence Love waves are clearly *dispersive*, and Rayleigh waves in a homogeneous half-space are *nondispersive*. Near the earth's surface, however, soil and rock stiffnesses usually increase with depth. Since the depth to which a Rayleigh wave causes significant displacement increases with increasing wavelength (Figure 5.10), Rayleigh waves of long wavelength (low frequency) can propagate faster than Rayleigh waves of short wavelength (high frequency). Therefore, in the real world of heterogeneous materials, Rayleigh waves are also dispersive. The dispersion of Rayleigh waves can be used to evaluate subsurface stiffness profiles by field testing techniques described in Chapter 6.

Since the velocities of both Rayleigh waves and Love waves decrease with increasing frequency, the low-frequency components of surface waves produced by earthquakes can

be expected to arrive at a particular site before their high-frequency counterparts. This tendency to spread the seismic energy over time is an important effect of dispersion.

5.3.5 Phase and Group Velocities

The solutions for Rayleigh wave velocity, v_R , and Love wave velocity, v_L , were based on the assumption of harmonic loading which produces an infinite wave train. These velocities describe the rate at which points of constant phase (e.g., peaks, troughs, or zero points) travel through the medium and are called *phase velocities*. A transient disturbance may produce a packet of waves with similar frequencies. This packet of waves travels at the *group velocity*, c_g , given by

$$c_g = c + k \frac{dc}{dk} \quad (5.65)$$

where c is the phase velocity (equal to v_R or v_L , depending on which type of wave is being considered) and k is the wave number (equal to ω/v_R or ω/v_L). In a nondispersive material, $dc/dk = 0$, so the group velocity is equal to the phase velocity. Since both v_R and v_L generally decrease with increasing frequency in geologic materials, dc/dk is less than zero and the group velocity is lower than the phase velocity. Consequently, a wave packet would appear to consist of a series of individual peaks that appear at the back end of the packet, move through the packet to the front, and then disappear. The opposite behavior can be observed by (for $c < c_g$) dropping a rock into a calm pond of water and watching the resulting ripples carefully.

5.4 WAVES IN A LAYERED BODY

The model of a homogeneous elastic half-space is useful for explaining the existence of body waves and Rayleigh waves, and the addition of a softer surficial layer allows Love waves to be described. In the earth, however, conditions are much more complicated with many different materials of variable thickness occurring in many areas. To analyze wave propagation under such conditions, and to understand the justification for idealizations of actual conditions when all features cannot be explicitly analyzed, the general problem of wave behavior at interfaces must be investigated.

5.4.1 One-Dimensional Case: Material Boundary in an Infinite Rod

Consider a harmonic stress wave traveling along a constrained rod in the $+x$ direction and approaching an interface between two different materials, as shown in Figure 5.14. Since the wave is traveling toward the interface, it will be referred to as the *incident wave*. Since it is traveling in material 1, its wavelength will be $\lambda_1 = 2\pi/k_1$, and it can therefore be described by

$$\sigma_I(x, t) = \sigma_I e^{i(\omega t - k_1 x)} \quad (5.66a)$$

When the incident wave reaches the interface, part of its energy will be transmitted through the interface to continue traveling in the positive x -direction through material 2. This *transmitted wave* will have a wavelength $\lambda_2 = 2\pi/k_2$. The remainder will be reflected at the interface and will travel back through material 1 in the negative x -direction as a *reflected wave*. The transmitted and reflected waves can be described by

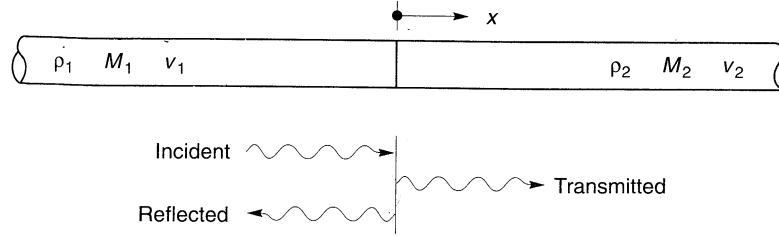


Figure 5.14 One-dimensional wave propagation at material interface. Incident and reflected waves travel in opposite directions in material 1. The transmitted wave travels through material 2 in the same direction as the incident wave.

$$\sigma_T(x, t) = \sigma_t e^{i(\omega t - k_2 x)} \quad (5.66b)$$

$$\sigma_R(x, t) = \sigma_r e^{i(\omega t + k_1 x)} \quad (5.66c)$$

Assuming that the displacements associated with each of these waves are of the same harmonic form as the stresses that cause them; that is,

$$u_I(x, t) = A_i e^{i(\omega t - k_1 x)} \quad (5.67a)$$

$$u_R(x, t) = A_r e^{i(\omega t + k_1 x)} \quad (5.67b)$$

$$u_T(x, t) = A_t e^{i(\omega t - k_2 x)} \quad (5.67c)$$

Stress–strain and strain–displacement relationships can be used to relate the stress amplitudes to the displacement amplitudes:

$$\sigma_I(x, t) = M_1 \frac{\partial u_I(x, t)}{\partial x} = -ik_1 M_1 A_i e^{i(\omega t - k_1 x)} \quad (5.68a)$$

$$\sigma_R(x, t) = M_1 \frac{\partial u_R(x, t)}{\partial x} = +ik_1 M_1 A_r e^{i(\omega t + k_1 x)} \quad (5.68b)$$

$$\sigma_T(x, t) = M_2 \frac{\partial u_T(x, t)}{\partial x} = -ik_2 M_2 A_t e^{i(\omega t - k_2 x)} \quad (5.68c)$$

From these, the stress amplitudes are related to the displacement amplitudes by

$$\sigma_i = -ik_1 M_1 A_i \quad (5.69a)$$

$$\sigma_r = +ik_1 M_1 A_r \quad (5.69b)$$

$$\sigma_t = -ik_2 M_2 A_t \quad (5.69c)$$

At the interface, both compatibility of displacements and continuity of stresses must be satisfied. The former requires that

$$u_I(0, t) + u_R(0, t) = u_T(0, t) \quad (5.70)$$

and the latter that

$$\sigma_I(0, t) + \sigma_R(0, t) = \sigma_T(0, t) \quad (5.71)$$

Substituting equations (5.67) and (5.66) into equations (5.70) and (5.71), respectively, indicates that

$$A_i + A_r = A_t \quad (5.72)$$

$$\sigma_i + \sigma_r = \sigma_t \quad (5.73)$$

at the interface. Substituting equations (5.69) into equation (5.73) and using the relationship $kM = \omega\rho v$, gives

$$-\rho_1 v_1 A_i + \rho_1 v_1 A_r = -\rho_2 v_2 A_t = -\rho_2 v_2 (A_i + A_r) \quad (5.74)$$

Equation (5.74) can be rearranged to relate the displacement amplitude of the reflected wave to that of the incident wave:

$$A_r = \frac{\rho_1 v_1 - \rho_2 v_2}{\rho_1 v_1 + \rho_2 v_2} A_i = \frac{1 - \rho_2 v_2 / \rho_1 v_1}{1 + \rho_2 v_2 / \rho_1 v_1} A_i \quad (5.75)$$

and knowing A_i and A_r , equation (5.72) can be used to determine A_t as

$$A_t = \frac{2\rho_1 v_1}{\rho_1 v_1 + \rho_2 v_2} A_i = \frac{2}{1 + \rho_2 v_2 / \rho_1 v_1} A_i \quad (5.76)$$

✓ Remember that the product of the density and the wave propagation velocity is the specific impedance of the material. Equations (5.75) and (5.76) indicate that the partitioning of energy at the interface depends only on the ratio of the specific impedances of the materials on either side of the interface. Defining the *impedance ratio* as $\alpha_z = \rho_2 v_2 / \rho_1 v_1$, the displacement amplitudes of the reflected and transmitted waves are

$$A_r = \frac{1 - \alpha_z}{1 + \alpha_z} A_i \quad (5.77)$$

$$A_t = \frac{2}{1 + \alpha_z} A_i \quad (5.78)$$

After evaluating the effect of the interface on the displacement amplitudes of the reflected and transmitted waves, its effect on stress amplitudes can be investigated. From equations (5.69)

$$A_i = -\frac{\sigma_i}{ik_1 M_1} \quad (5.79a)$$

$$A_r = \frac{\sigma_r}{ik_1 M_1} \quad (5.79b)$$

$$A_t = -\frac{\sigma_t}{ik_2 M_2} \quad (5.79c)$$

Substituting equations (5.79) into equations (5.77) and (5.78) and rearranging gives

$$\sigma_r = \frac{\alpha_z - 1}{1 + \alpha_z} \sigma_i \quad (5.80)$$

$$\sigma_t = \frac{2\alpha_z}{1 + \alpha_z} \sigma_i \quad (5.81)$$

The importance of the impedance ratio in determining the nature of reflection and transmission at interfaces can clearly be seen. Equations (5.77), (5.78), (5.80), and (5.81) indicate that fundamentally different types of behavior occur when the impedance ratio is less than or greater than 1. When the impedance ratio is less than 1, an incident wave can be thought of as approaching a “softer” material. For this case, the reflected wave will have a smaller stress amplitude than the incident wave and its sign will be reversed (an incident compression pulse will be reflected as a tensile pulse, and vice versa). If the impedance ratio is greater than 1, the incident wave is approaching a “stiffer” material in which the stress amplitude of the transmitted wave will be greater than that of the incident wave and the stress amplitude of the reflected wave will be less than, but of the same sign, as that of the incident wave. The displacement amplitudes are also affected by the impedance ratio. The relative stress and displacement amplitudes of reflected and transmitted waves at boundaries with several different impedance ratios are illustrated in Table 5-1.

The cases of $\alpha_z = 0$ and $\alpha_z = \infty$ are of particular interest. An impedance ratio of zero implies that the incident wave is approaching a “free end” across which no stress can be transmitted ($\sigma_t = 0$). To satisfy this zero stress boundary condition, the displacement of the boundary (the transmitted displacement) must be twice the displacement amplitude of the incident wave ($A_t = 2A_i$). The reflected wave has the same amplitude as the incident wave but is of the opposite polarity ($\sigma_r = -\sigma_i$). In other words, a free end will reflect a compression wave as a tension wave of identical amplitude and shape and a tension wave as an identical compression wave. An infinite impedance ratio implies that the incident wave is approaching a “fixed end” at which no displacement can occur ($u_t = 0$). In that case the stress at the boundary is twice that of the incident wave ($\sigma_t = 2\sigma_i$) and the reflected wave has the same amplitude and polarity as the incident wave ($A_r = -A_i$).

The case of $\alpha_z = 1$, in which the impedances on each side of the boundary are equal, is also of interest. Equations (5.77), (5.78), (5.80), and (5.81) indicate that no reflected wave

Table 5-1 Influence of Impedance Ratio on Displacement and Stress Amplitudes of Reflected and Transmitted Waves

Impedance Ratio, α_z	Displacement Amplitudes			Stress Amplitudes		
	Incident	Reflected	Transmitted	Incident	Reflected	Transmitted
0	A_i	A_i	$2A_i$	σ_i	$-\sigma_i$	0
$\frac{1}{4}$	A_i	$3A_i/5$	$8A_i/5$	σ_i	$-3\sigma_i/5$	$2\sigma_i/5$
$\frac{1}{2}$	A_i	$A_i/3$	$4A_i/3$	σ_i	$-\sigma_i/3$	$2\sigma_i/3$
1	A_i	0	A_i	σ_i	0	σ_i
2	A_i	$-A_i/3$	$2A_i/3$	σ_i	$\sigma_i/3$	$4\sigma_i/3$
4	A_i	$-3A_i/5$	$2A_i/5$	σ_i	$3\sigma_i/5$	$8\sigma_i/5$
∞	A_i	$-A_i$	0	σ_i	σ_i	$2\sigma_i$



is produced and that the transmitted wave has, as expected, the same amplitude and polarity as the incident wave. In other words, all of the elastic energy of the wave crosses the boundary unchanged and travels away, never to return. Another way of looking at a boundary with an impedance ratio of unity is as a boundary between two identical, semi-infinite rods. A harmonic wave traveling in the positive x -direction (Figure 5.15a) would impose an axial force [see equation (5.5)] on the boundary:

$$F = \sigma_x A = \rho v_m A \dot{u}$$

This axial force is identical to that which would exist if the semi-infinite rod on the right side of the boundary were replaced by a dashpot (Figure 5.15b) of coefficient $c = \rho v_m A$. In other words, the dashpot would absorb all the elastic energy of the incident wave, so the response of the rod on the left would be identical for both cases illustrated in Figure 5.15. This result has important implications for ground response and soil–structure interaction analyses (Chapter 7), where the replacement of a semi-infinite domain by discrete elements such as dashpots can provide tremendous computational efficiencies.

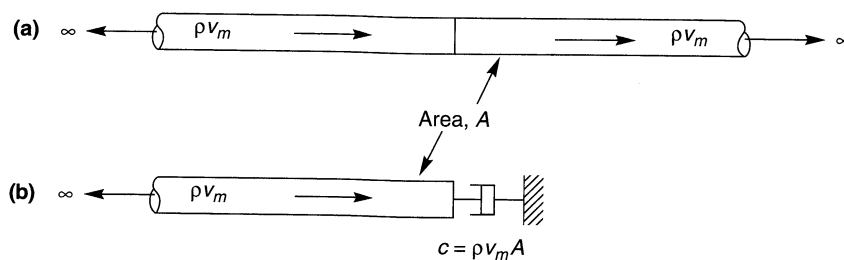


Figure 5.15 (a) Harmonic wave traveling along two connected semi-infinite rods; (b) semi-infinite rod attached to dashpot. With proper selection of dashpot coefficient, response in semi-infinite rod on left will be identical for both cases.

Example 5.4

A vertically propagating shear wave travels upward through a layered soil deposit. Compute the amplitudes of the reflected and transmitted waves that develop when the shear wave reaches the boundary shown in Figure E5.4.

Solution Although the transmission-reflection behavior in the preceding section was derived for constrained longitudinal waves, extension to the case of shear waves is straightforward. The (shear wave) impedance ratio for an upward-traveling wave is

$$\alpha_z = \frac{(1.76 \text{ Mg/m}^3)(400 \text{ m/sec})}{(2.24 \text{ Mg/m}^3)(750 \text{ m/sec})} = 0.419$$

The stress amplitude of the reflected wave is given by equation (5.79)

$$\sigma_r = \frac{\alpha_z - 1}{1 + \alpha_z} \sigma_i = \frac{0.419 - 1}{1 + 0.419} (100 \text{ kPa}) = -40.9 \text{ kPa}$$

From equation (5.80), the stress amplitude of the transmitted wave is

$$\sigma_t = \frac{2\alpha_z}{1 + \alpha_z} \sigma_i = \frac{2(0.419)}{1 + 0.419} (100 \text{ kPa}) = 59.1 \text{ kPa}$$

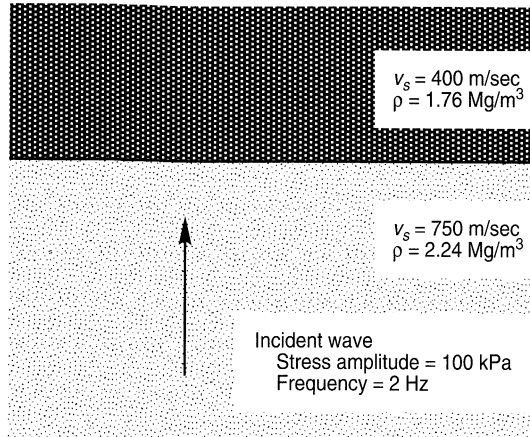


Figure E5.4

The displacement amplitude of the incident wave can be computed from the shear wave equivalent of equation 5.78a

$$A_i = -\frac{\alpha_i}{ik_1 G_1} = \frac{i\alpha_i}{\rho_1 \omega v_{s1}}$$

$$= \frac{i(100 \text{ kN/m}^2)(1 \text{ Mg}/9.807 \text{ kN})(9.807 \text{ m/sec}^2)}{(2.24 \text{ Mg/m}^3) 2\pi(2 \text{ Hz})(750 \text{ m/sec})} = 0.00477 \text{ m} = 4.77 \text{ mm}$$

The i term simply describes the 90° phase angle between stresses and displacements. Then, using equations (5.76) and (5.77), the displacement amplitudes of the reflected and transmitted waves are

$$A_r = \frac{1 - \alpha_z}{1 + \alpha_z} A_i = \frac{1 - 0.419}{1 + 0.419} (4.77 \text{ mm}) = 1.95 \text{ mm}$$

$$A_t = \frac{2}{1 + \alpha_z} A_i = \frac{2}{1 + 0.419} (4.77 \text{ mm}) = 6.72 \text{ mm}$$

In this example, the incident wave travels from a material of higher impedance to a material of lower impedance. As a result, the displacement amplitude of the transmitted wave is greater than that of the incident wave, but the stress amplitude is smaller.

5.4.2 Three-Dimensional Case: Inclined Waves

In general, waves will not approach interfaces at 90° angles as they did in Section 5.4.1. The orientation of an *inclined body wave* can strongly influence the manner in which energy is reflected and transmitted across an interface. Fermat's principle defines the propagation time of a seismic pulse between two arbitrary points A and B as the minimum travel time along any continuous path that connects A and B . The path that produces the minimum travel time is called a *ray path*, and its direction is often represented by a vector called a *ray*. A *wavefront* is defined as a surface of equal travel time, consequently, a ray path must (in an isotropic material) be perpendicular to the wavefront as illustrated in Figure 5.16. Snell considered the change of direction of ray paths at interfaces between materials with different wave propagation velocities. Using Fermat's principle, Snell showed that

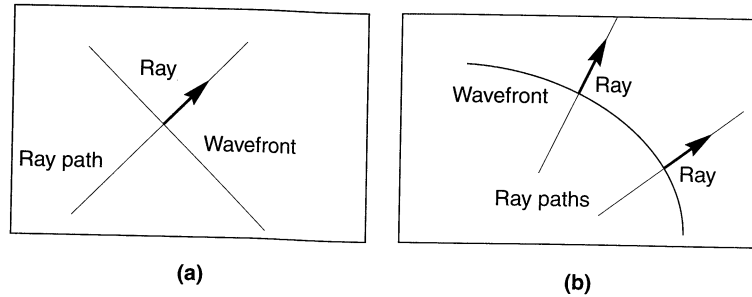


Figure 5.16 Ray path, ray, and wavefront for (a) plane wave and (b) curved wavefront.

$$\frac{\sin i}{v} = \text{constant} \quad (5.82)$$

where i is the angle between the ray path and the normal to the interface and v is the velocity of the wave (p- or s-wave) of interest. This relationship holds for both reflected and transmitted waves. It indicates that the transmitted wave will be *refracted* (except when $i = 0$) when the wave propagation velocities are different on each side of the interface.

Consider the case of two half-spaces of different elastic materials in contact with each other. As for the previous case, the requirements of equilibrium and compatibility and the theory of elasticity can be used to determine the nature of and distribution of energy among the reflected and transmitted waves for the cases of an incident p-wave, an incident SV-wave, and an incident SH-wave.

The types of waves produced by incident p-, SV-, and SH-waves are shown in Figure 5.17. Since incident p- and SV-waves involve particle motion perpendicular to the plane of the interface; they will each produce both reflected and refracted p- and SV-waves. An incident SH-wave does not involve particle motion perpendicular to the interface; consequently, only SH-waves are reflected and refracted. The directions and relative amplitudes of the waves produced at the interface depend on both the direction and amplitude of the

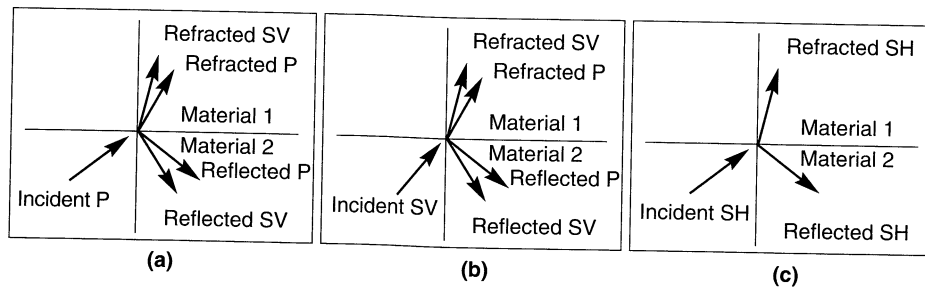


Figure 5.17 Reflected and refracted rays resulting from incident (a) p-wave, (b) SV-wave, and (c) SH-wave.

incident wave. Using Snell's law and the requirements of equilibrium and compatibility, these directions and amplitudes can be determined. Using the notation of Richter (1958):

Wave Type	Velocity	Amplitude	Angle with Normal
Incident p	U	A	a
Incident s	V	B	b
Reflected p	U	C	c
Reflected s	V	D	d
Refracted p	Y	E	e
Refracted s	Z	F	f

the directions of all waves are easily related to the direction of the incident wave using Snell's law:

$$\frac{\sin a}{U} = \frac{\sin b}{V} = \frac{\sin c}{U} = \frac{\sin d}{V} = \frac{\sin e}{Y} = \frac{\sin f}{Z} \quad (5.83)$$

Since incident and reflected waves travel through the same material, $a = c$ and $b = d$, which shows that the *angle of incidence* is equal to the *angle of reflection* for both p- and s-waves.

The *angle of refraction* is uniquely related to the angle of incidence by the ratio of the wave velocities of the materials on each side of the interface. Snell's law indicates that waves traveling from higher-velocity materials into lower-velocity materials will be refracted closer to the normal to the interfaces. In other words, waves propagating upward through horizontal layers of successively lower velocity (as is common near the earth's surface) will be refracted closer and closer to a vertical path (Figure 5.18). This phenomenon is relied upon heavily by many of the methods of ground response analysis presented in Chapter 7.

The *critical angle of incidence*, i_c , is defined as that which produces a refracted wave that travels parallel to the interface (e or $f = 90^\circ$). Therefore,

$$i_c = \sin^{-1} \frac{U}{Y} = \sin^{-1} \frac{V}{Z} \quad (5.84)$$

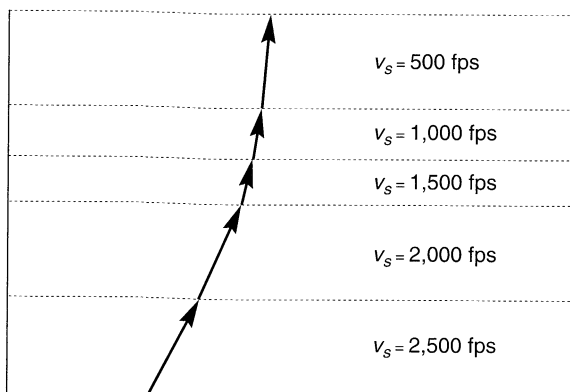


Figure 5.18 Refraction of an SH-wave ray path through series of successively softer (lower v_s) layers. Note that orientation of ray path becomes closer to vertical as ground surface is approached. Reflected rays are not shown.

The concept of critical refraction is used in the interpretation of seismic refraction tests (Section 6.3.1.1).

Assuming that the incident wave is simple harmonic, satisfaction of the requirements of equilibrium and compatibility at the interface give rise to the following systems of simultaneous equations (Richter, 1958), which allows the amplitudes of the reflected and refracted waves (C , D , E , and F) to be expressed in terms of the amplitude of the incident p-wave (A).

$$\begin{aligned}
 (A - C) \sin a + D \cos b - E \sin e + F \cos f &= 0 \\
 (A + C) \cos a + D \sin b - E \cos e - F \sin f &= 0 \\
 - (A + C) \sin 2a + D \frac{U}{V} \cos 2b + EK \left(\frac{Z}{V} \right)^2 \frac{U}{Y} \sin 2e - FK \left(\frac{Z}{V} \right)^2 \frac{U}{Z} \cos 2f &= 0 \\
 - (A - C) \cos 2b + D \frac{V}{U} \sin 2b + EK \frac{Y}{U} \cos 2f - FK \frac{Z}{U} \sin (2f) &= 0
 \end{aligned} \quad (5.85)$$

where $K = \rho_1/\rho_2$ (the subscripts 1 and 2 refer to materials 1 and 2, respectively). Note that the amplitudes are functions of the angle of incidence, the velocity ratio, and the density ratio. Figure 5.19 shows the variation of amplitude with angle of p-wave incidence for the following conditions: $U = 8.000$, $Y = 2.003$, $K = 0.606$, and $v = 0.25$. The sensitivity of the reflected and refracted wave amplitudes to the angle of incidence is apparent. SV-waves are neither reflected nor refracted at angles of incidence of 0 and 90° , but can carry the majority of the wave energy away from the interface at intermediate angles.

For an incident SV-wave, both SV- and p-waves are reflected and refracted. The equilibrium/compatibility equations relating the relative amplitudes are

$$\begin{aligned}
 (B + D) \sin b + C \cos a - E \cos e - F \sin f &= 0 \\
 (B - D) \cos b + C \sin a + E \sin e - F \cos f &= 0 \\
 (B + D) \cos 2b - C \frac{V}{U} \sin 2a + EK \frac{Z^2}{VY} \sin 2e - FK \frac{Z}{V} \cos 2f &= 0 \\
 - (B - D) \sin 2b + C \frac{U}{V} \cos 2b + EK \frac{Y}{V} \cos 2f + FK \frac{Z}{V} \sin 2f &= 0
 \end{aligned} \quad (5.86)$$

which produce the amplitude behavior shown in Figure 5.20. For angles of incidence greater than $\sin^{-1}(V/U)$, about 36° in Figure 5.20(a), no p-wave can be reflected, so the incident wave energy must be carried away by the remaining waves. A more detailed discussion of this phenomenon can be found in McCamy et al. (1962).

An incident SH-wave involves no particle motion perpendicular to the interface; consequently, it cannot produce p-waves ($C = E = 0$) or SV-waves. The equilibrium/compatibility equations are considerably simplified and easily solved as

$$\begin{aligned}
 D &= \frac{1 - K \frac{Z \cos f}{V \cos b}}{1 + K \frac{Z \cos f}{V \cos b}} B \\
 F &= B \left(1 + \frac{1 - K \frac{Z \cos f}{V \cos b}}{1 + K \frac{Z \cos f}{V \cos b}} \right)
 \end{aligned} \quad (5.87)$$

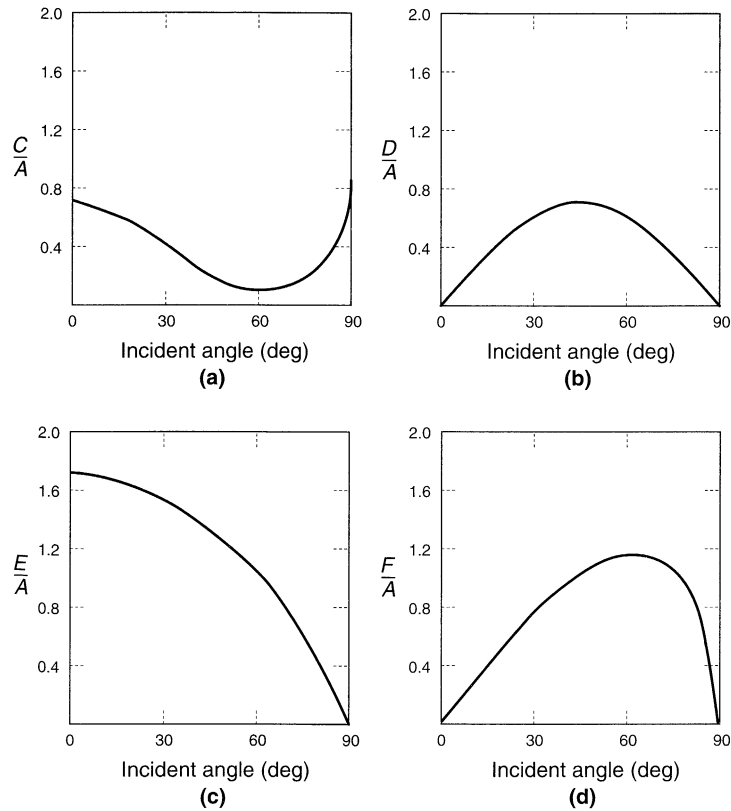


Figure 5.19 Ratio of amplitudes of (a) reflected p-wave, (b) reflected SV-wave, (c) refracted p-wave, and (d) refracted SV-wave to amplitude of incident p-wave versus angle of incidence.

The preceding results show that the interaction of stress waves with boundaries can be quite complicated. As seismic waves travel away from the source of an earthquake, they invariably encounter heterogeneities and discontinuities in the earth's crust. The creation of new waves and the reflection and refraction of ray paths by these heterogeneities cause seismic waves to reach a site by many different paths. Since the paths have different lengths, the motion at the site is spread out in time by this *scattering* effect.

5.5 ATTENUATION OF STRESS WAVES

The preceding sections have considered only the propagation of waves in linear elastic materials. In a homogeneous linear elastic material, stress waves travel indefinitely without change in amplitude. This type of behavior cannot occur, however, in real materials. The amplitudes of stress waves in real materials, such as those that comprise the earth, attenuate with distance. This attenuation can be attributed to two sources, one of which involves the

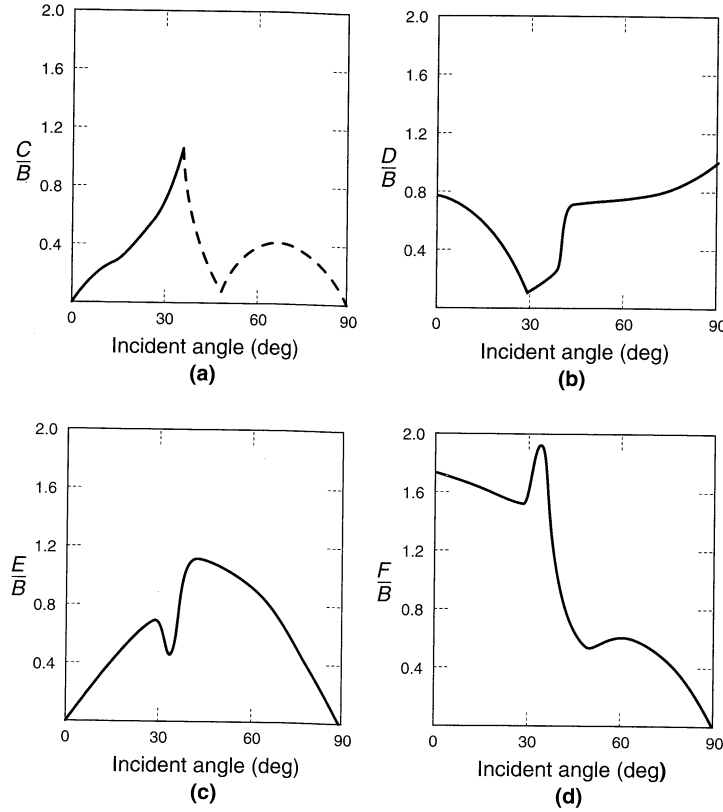


Figure 5.20 Ratio of amplitudes of (a) reflected p-wave, (b) reflected SV-wave, (c) refracted p-wave, and (d) refracted SV-wave to amplitude of incident SV-wave versus angle of incidence.

materials through which the waves travel and the other the geometry of the wave propagation problem.

5.5.1 Material Damping

In real materials, part of the elastic energy of a traveling wave is always converted to heat. The conversion is accompanied by a decrease in the amplitude of the wave. Viscous damping, by virtue of its mathematical convenience, is often used to represent this dissipation of elastic energy. For the purposes of viscoelastic wave propagation, soils are usually modelled as Kelvin–Voigt solids (i.e., materials whose resistance to shearing deformation is the sum of an elastic part and a viscous part). A thin element of a Kelvin–Voigt solid can be illustrated as in Figure 5.21.

The stress–strain relationship for a Kelvin–Voigt solid in shear can be expressed as

$$\tau = G\gamma + \eta \frac{\partial \gamma}{\partial t} \tag{5.88}$$

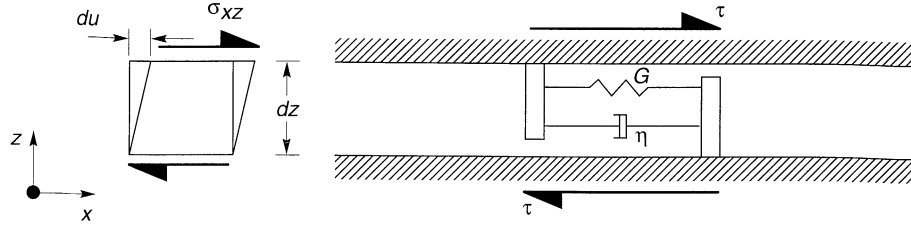


Figure 5.21 Thin element of a Kelvin–Voigt solid subjected to horizontal shearing. Total resistance to shearing deformation is given by the sum of an elastic (spring) component and a viscous (dashpot) component.

where $\tau (= \sigma_{xz})$ is the shear stress, $\gamma (= \partial u / \partial z)$ is the shear strain, and η is the viscosity of the material. Thus the shear stress is the sum of an elastic part (proportional to strain) and a viscous part (proportional to strain rate). For a harmonic shear strain of the form

$$\gamma = \gamma_0 \sin \omega t \tag{5.89}$$

the shear stress will be

$$\tau = G\gamma_0 \sin \omega t + \omega \eta \gamma_0 \cos \omega t \tag{5.90}$$

Together, equations (5.89) and (5.90) show that the stress–strain loop of a Kelvin–Voigt solid is elliptical. The elastic energy dissipated in a single cycle is given by the area of the ellipse, or

$$\Delta W = \int_{t_0}^{t_0 + 2\pi/\omega} \tau \frac{\partial \gamma}{\partial t} dt = \pi \eta \omega \gamma_0^2$$

which indicates that the dissipated energy is proportional to the frequency of loading. Real soils, however, dissipate elastic energy hysteretically, by the slippage of grains with respect to each other. As a result, their energy dissipation characteristics are insensitive to frequency. For discrete Kelvin–Voigt systems (Appendix B), the damping ratio, ξ , was shown to be related to the force–displacement (or, equivalently, the stress–strain) loop as shown in Figure 5.22. Since the peak energy stored in the cycle is

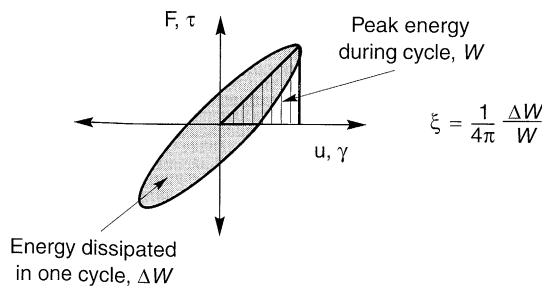


Figure 5.22 Relationship between hysteresis loop and damping ratio.

$$W = \frac{1}{2}G\gamma_0^2$$

then

$$\xi = \frac{1}{4\pi} \frac{\pi\eta\omega\gamma_0^2}{\frac{1}{2}G\gamma_0^2} = \frac{\eta\omega}{2G} \quad (5.91)$$

To eliminate frequency dependence while maintaining the convenience of the viscoelastic formulation, equation (5.91) is often rearranged to produce an equivalent viscosity that is inversely proportional to frequency. The use of this equivalent viscosity ensures that the damping ratio is independent of frequency:

$$\eta = \frac{2G\xi}{\omega} \quad (5.92)$$

A Kelvin–Voigt solid for vertically propagating SH-waves may be represented by a stack of infinitesimal elements of the type shown schematically in Figure 5.21. The one-dimensional equation of motion for vertically propagating SH-waves can be written as

$$\rho \frac{\partial^2 u}{\partial t^2} = \frac{\partial \sigma_{xz}}{\partial z} \quad (5.93)$$

Substituting equation (5.88) into (5.93) with $\tau = \sigma_{xz}$ and $\gamma = \partial u / \partial z$, and differentiating the right side allows the wave equation to be expressed as

$$\rho \frac{\partial^2 u}{\partial t^2} = G \frac{\partial^2 u}{\partial z^2} + \eta \frac{\partial^3 u}{\partial z^2 \partial t} \quad (5.94)$$

For harmonic waves, the displacements can be written as

$$u(z, t) = U(z) e^{i\omega t} \quad (5.95)$$

which, when substituted into the wave equation (5.94) yields the ordinary differential equation

$$(G + i\omega\eta) \frac{d^2 U}{dz^2} = -\rho\omega^2 U \quad (5.96)$$

or

$$G^* \frac{d^2 U}{dz^2} = -\rho\omega^2 U \quad (5.97)$$

where $G^* = G + i\omega\eta$ is the *complex shear modulus*. The complex shear modulus is analogous to the complex stiffness described in Section B.6.3 of Appendix B. Using equation (5.92) to eliminate frequency dependence, the complex shear modulus can also be expressed as $G^* = G(1 + 2i\xi)$. This equation of motion has the solution

$$u(z, t) = A e^{i(\omega t - k^* z)} + B e^{i(\omega t + k^* z)} \quad (5.98)$$

where A and B depend on the boundary conditions and $k^* = \omega\sqrt{\rho/G^*}$ is the *complex wave number*. It can be shown (after Kolsky, 1963) that k^* is given by

$$k^* = k_1 + ik_2 \quad (5.99)$$

where

$$\begin{aligned} k_1^2 &= \frac{\rho\omega^2}{2G(1+4\xi^2)}(\sqrt{1+4\xi^2}+1) \\ k_2^2 &= \frac{\rho\omega^2}{2G(1+4\xi^2)}(\sqrt{1+4\xi^2}-1) \end{aligned} \quad (5.100)$$

and only the positive root of k_1 and the negative root of k_2 have physical significance. Note that for the inviscid case ($\eta = \xi = 0$), $k_2 = 0$ and $k_1 = k$. For a wave propagating in the positive z -direction, the solution can be written as

$$u(z, t) = Ae^{k_2 z} e^{i(\omega t - k_1 z)} \quad (5.101)$$

which shows (since k_2 is negative) that material damping produces exponential attenuation of wave amplitude with distance.

Although the Kelvin–Voigt model is by far the most commonly used model for soils, it represents only one of an infinite number of rheological models. By rearranging and adding more springs and dashpots, many different types of behavior can be modeled, although the complexity of the wave equation solution increases dramatically as the number of springs and dashpots increases.

Example 5.5

A harmonic plane wave with a period of 0.3 sec travels through a viscoelastic material ($G = 1.6 \times 10^6$ psf, $\eta = 9000$ lb-sec/ft², $\gamma = 140$ pcf). Determine the distance over which the displacement amplitude of the plane wave would be halved.

Solution From equation (5.101), the displacement amplitude at $z = z_1$ is

$$u(z_1) = A \exp(k_2 z_1)$$

If $z = z_2$ represents the location at which the displacement amplitude is halved, then

$$u(z_2) = A \exp(k_2 z_2) = \frac{1}{2} A \exp(k_2 z_1)$$

which leads to

$$\exp[k_2(z_2 - z_1)] = \frac{1}{2}$$

or

$$z_2 - z_1 = \frac{\ln(1/2)}{k_2}$$

For this case

$$\xi = \frac{\eta\omega}{2G} = \frac{2\pi\eta}{2GT} = \frac{2\pi(9000 \text{ lb-sec/ft}^2)}{2(1.6 \times 10^6 \text{ lb/ft}^2)(0.3 \text{ sec})} = 0.059$$

Then, from equation (5.100)

$$k_2 = \sqrt{\frac{\frac{140 \text{ lb/ft}^2}{32.2 \text{ ft/sec}^2} (2\pi/0.3 \text{ sec})^2}{2(1.6 \times 10^6 \text{ lb/ft}^2)(1 + 4(0.059)^2)}} (\sqrt{1 + 4(0.059)^2} - 1) = -0.002$$

so

$$z_2 - z_1 = \frac{\ln(0.5)}{-0.002} = 347 \text{ ft}$$

5.5.2 Radiation Damping

Since material damping absorbs some of the elastic energy of a stress wave, the *specific energy* (elastic energy per unit volume) decreases as the wave travels through a material. The reduction of specific energy causes the amplitude of the stress wave to decrease with distance. The specific energy can also decrease by another common mechanism, which can be illustrated by the propagation of stress waves along an undamped conical rod.

Consider the unconstrained conical rod of small apex angle shown in Figure 5.23 and assume that it is subjected to stress waves of wavelength considerably larger than the diameter of the rod in the area of interest. If the apex angle is sufficiently small, the normal stress will be uniform across each of two spherical surfaces that bound an element of width dr , and will act in a direction virtually parallel to the axis of the rod. Letting u represent the displacement parallel to the axis of the rod, the equation of motion in that direction can be written, using exactly the same approach used in Section 5.2.1.1, as

$$\rho r^2 \alpha dr \frac{\partial^2 u}{\partial t^2} = \left(\sigma + \frac{\partial \sigma}{\partial r} dr \right) (r + dr)^2 \alpha - \sigma r^2 \alpha \quad (5.102)$$

which simplifies to

$$\rho r \frac{\partial^2 u}{\partial t^2} = r \frac{\partial \sigma}{\partial r} + 2\sigma \quad (5.103)$$

Substituting the stress-strain and strain-displacement relationships (assuming now that the ends of the element are planar) gives

$$\rho r \frac{\partial^2 u}{\partial t^2} = Er \frac{\partial^2 u}{\partial r^2} + 2E \frac{\partial u}{\partial r} \quad (5.104)$$

or

$$\frac{\partial^2(ur)}{\partial t^2} = \frac{E}{\rho} \frac{\partial^2(ur)}{\partial r^2} \quad (5.105)$$

which is the now-familiar wave equation. Its solution will be of the form

$$u(r, t) = \frac{1}{r} [f(vt - r) + g(vt + r)] \quad (5.106)$$

where $v = \sqrt{E/\rho}$. Equation (5.106) indicates that the amplitude of the wave will decrease with distance (even though the total elastic energy remains the same). The reduction is of

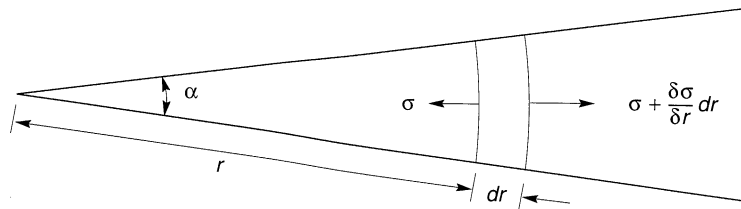


Figure 5.23 Conical rod of apex angle α .

purely geometric origin, resulting from the decrease in specific energy that occurs as the area of the rod increases.

Even though elastic energy is conserved (no conversion to other forms of energy takes place), this reduction in amplitude due to spreading of the energy over a greater volume of material is often referred to as *radiation damping* (also as *geometric damping* and *geometric attenuation*). It should be distinguished from material damping in which elastic energy is actually dissipated by viscous, hysteretic, or other mechanisms.

When earthquake energy is released from a fault below the ground surface, body waves travel away from the source in all directions. If the rupture zone can be represented as a point source, the wavefronts will be spherical and the preceding analysis can easily be extended to show that geometric attenuation causes the amplitude to decrease at a rate of $1/r$. It can also be shown (Bullen, 1953) that geometric attenuation of surface waves causes their amplitudes to decrease at a rate of essentially $1/(\sqrt{r})$; in other words, surface waves attenuate (geometrically) much more slowly than body waves. This explains the greater proportion of surface wave motion (relative to body wave motion) that is commonly observed at large epicentral distances. This explains the advantages of the surface wave magnitude, relative to body wave magnitude, for characterization of distant earthquakes.

For problems in which energy is released from a finite source, ranging from the large-scale case of rupture along an earthquake fault to the smaller-scale case of a vibrating foundation, radiation damping can be extremely important. In such cases the effects of radiation damping often dominate those of material damping.

5.6 SUMMARY

1. Only body waves can travel through an unbounded, homogeneous solid. There are two types of body waves: p- and s-waves. P-waves are irrotational, or dilatational, waves—they induce volumetric but not shearing deformations in the materials they travel through. The direction of particle movement caused by p-waves is parallel to the direction in which the wave is traveling. S-waves, also known as shear waves, involve shearing but not volumetric deformations. The passage of an s-wave causes particle movement perpendicular to the direction of wave travel.
2. Body waves travel at velocities that depend on the stiffness and density of the material they travel through. Because geologic materials are stiffer in volumetric compression than in shear, p-waves travel faster through them than do s-waves.
3. The interaction of inclined body waves with the stress-free surface of the earth produces surface waves. The motions produced by surface waves are concentrated in a shallow zone near the surface.
4. Rayleigh waves are the most important type of surface wave for earthquake engineering applications. In a homogeneous elastic half-space, Rayleigh waves would travel slightly more slowly than s-waves and would produce both vertical and horizontal particle motions that follow a retrograde elliptical pattern.
5. The depth to which Rayleigh waves induce significant motion is inversely proportional to the frequency of the wave. Low-frequency Rayleigh waves can produce particle motion at large depths, but the motions produced by high-frequency Rayleigh waves are confined to shallow depths.

6. When body wave velocities increase with depth, as they generally do in the earth's crust, Rayleigh wave velocities are frequency dependent. Low-frequency Rayleigh waves, which induce motion in deeper, stiffer materials, travel faster than high-frequency Rayleigh waves. Waves with frequency-dependent velocities are said to be dispersive.
7. Love waves are surface waves that can develop in the presence of a soft surficial layer. Love waves are dispersive—their velocities vary with frequency between the shear wave velocity of the surficial layer (at high frequencies) and the shear wave velocity of the underlying material (at low frequencies).
8. When a body wave strikes a rigid boundary oriented perpendicular to its direction of travel, the wave is perfectly reflected as an identical wave traveling back in the opposite direction. The zero-displacement boundary condition requires that the stress at the boundary be twice that of the wave away from the boundary. When a body wave strikes a stress-free boundary oriented perpendicular to its direction of travel, the wave is reflected as an identical wave of opposite polarity travelling back in the same direction. The zero-stress boundary condition requires that the particle motion at the boundary be twice as large as the particle motion away from the boundary.
9. When a body wave strikes a normal boundary between two different materials, part of the wave energy is reflected and part is transmitted across the boundary. The behavior of the wave at the boundary is governed by the ratio of the specific impedances of the materials on either side of the boundary. This impedance ratio determines the amplitudes and polarities of the reflected and transmitted waves.
10. When body waves strike boundaries between different materials at angles other than 90° , part of the wave energy is reflected and part is refracted as it crosses the boundary. If the direction of particle motion is parallel to the boundary, the reflected and refracted waves will be of the same form as the incident wave. If not, new types of waves can be created; for example, an inclined p-wave that strikes a horizontal boundary will produce reflected p- and SV-waves, and also refracted p- and SV-waves.
11. When an inclined wave travels upward through horizontal layers that become successively softer, the portion of the wave that crosses each layer boundary will be refracted closer and closer to a vertical direction.
12. The amplitude of a stress wave decreases as the wave travels through the earth's crust. There are two primary mechanisms that cause this attenuation of wave amplitude. The first, material damping, is due to absorption of energy by the materials the wave is traveling through. The second, radiation damping, results from the spreading of wave energy over a greater volume of material as it travels away from its source.

HOMEWORK PROBLEMS

- 5.1 Determine the wave propagation velocity of a longitudinal wave in a constrained rod of: (a) steel, (b) cast iron, (c) concrete with $f'_c = 4,000$ psi.
- 5.2 Determine the wave propagation velocity of a torsional wave in a constrained rod of: (a) steel, (b) cast iron, (c) concrete with $f'_c = 4,000$ psi.
- 5.3 Derive an expression for the wave propagation velocity of a longitudinal wave in an unconstrained elastic rod with Young's modulus, E , Poisson's ratio, ν , and density, ρ . Neglect the

effects of radial displacements in your derivation. How does this velocity compare with that of a longitudinal wave in a constrained rod?

- 5.4 A constrained steel rod is subjected to a harmonic axial stress at a frequency of 1 Hz.
- Determine the wavelength of the axial displacements along the rod.
 - Determine the phase angle between displacements measured at points on the rod located 1 ft, 10 ft, 100 ft, 1000 ft, and 10000 ft apart.
 - Repeat Part (a) for loading frequencies of 10 Hz, 100 Hz, 1 kHz, and 1 MHz.
- 5.5 A constrained steel rod is subjected to a harmonic torsional stress at a frequency of 1 Hz.
- Determine the wavelength of the angular rotations along the rod.
 - Determine the phase angle between rotations measured at points on the rod located 1 ft, 10 ft, 100 ft, 1000 ft, and 10000 ft apart.
 - Repeat Part (a) for loading frequencies of 10 Hz, 100 Hz, 1 kHz, and 1 MHz.
- 5.6 Determine the depth at which the vertical displacement amplitude of a Rayleigh wave is equal to one-half of the vertical displacement amplitude at the ground surface. For Rayleigh waves traveling through crystalline bedrock with a constant shear modulus of 57 ksi and specific gravity of 2.7, plot the variation of this depth with frequency for $f = 0.1$ Hz to $f = 20$ Hz.

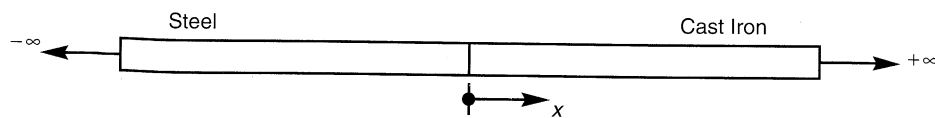


Figure P5.7

- 5.7 The infinite rod shown above is half steel and half cast iron. If a stress pulse of amplitude 100 psi (compression positive) and frequency 1000 Hz travels through the steel in the $+x$ -direction, determine the displacement amplitude of the transmitted wave that travels through the cast iron.

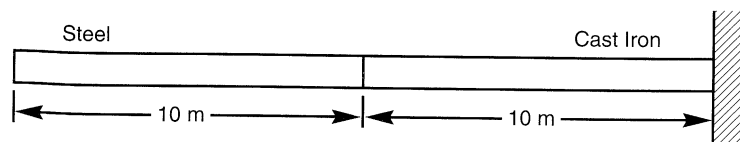


Figure P5.8

- 5.8 The finite rod shown above is subjected to an impact load that produces a rectangular axial stress pulse of amplitude 100 psi and duration 0.1 msec at its left end. The left end of the rod is free and the right end is fixed. Assuming that the impact began at $t = 0$, determine and plot the axial stress at the mid-point of the cast iron section from $t = 0$ to $t = 15$ msec.

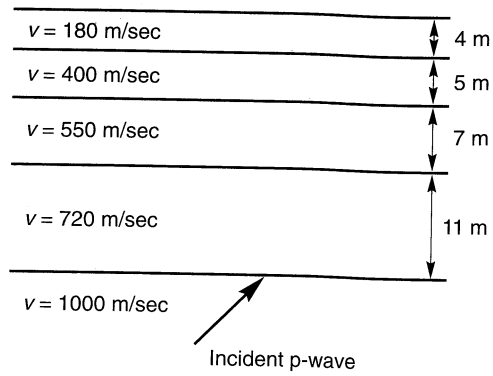


Figure P5.9

- 5.9 Consider the layered soil deposit shown above. Determine and plot the paths of the refracted and reflected rays if an incident raypath strikes the lowest boundary at a 45° angle. Show only the first reflection and refraction at each layer boundary.
- 5.10 Seismologists usually describe the effects of material damping by the quality factor. Quality factor values on the order of 300 and 500 are typically used for waves travelling through the earth's crust in western North America (WNA) and eastern North America (ENA), respectively. Why are higher quality factors used for ENA? What damping ratios do these quality factors correspond to?

6

Dynamic Soil Properties

6.1 INTRODUCTION

The nature and distribution of earthquake damage is strongly influenced by the response of soils to cyclic loading. This response is controlled in large part by the mechanical properties of the soil. Geotechnical earthquake engineering encompasses a wide range of problems involving many types of loading and many potential mechanisms of failure, and different soil properties influence the behavior of the soil for different problems. For many important problems, particularly those dominated by wave propagation effects, only low levels of strain are induced in the soil. For other important problems, such as those involving the stability of masses of soil, large strains are induced in the soil. The behavior of soils subjected to dynamic loading is governed by what have come to be popularly known as *dynamic soil properties*. While recognizing that the properties themselves are not dynamic (indeed, they apply to a host of nondynamic problems), that term will be used in this book because of its conciseness and familiarity.

Detailed treatment of every aspect of the behavior of cyclically loaded soils is beyond the scope of a book such as this. This chapter addresses the most important aspects of their behavior in the context of the various geotechnical earthquake engineering problems addressed in the following chapters. It presents a variety of methods by which low- and high-strain soil behavior can be measured in the field and in the laboratory. The behavior of cyclically loaded soils, and different approaches to its characterization, are also described.

6.2 REPRESENTATION OF STRESS CONDITIONS BY THE MOHR CIRCLE

The cyclic properties of soils depend on the state of stress in the soil prior to loading and on the stresses imposed by the loading. To discuss soil properties and their relationship to the various types of cyclic loading encountered in geotechnical earthquake engineering problems, the concepts and terminology used to describe stresses must be specified. Although such concepts are ordinarily presented early in a first course on soil mechanics, their importance in the understanding and solution of geotechnical earthquake engineering problems (particularly the liquefaction problems discussed in Chapter 9) is sufficient to warrant their repetition here.

The stress conditions at any point in a mass of soil can be described by the normal and shear stresses acting on a particular plane passing through that point. Because most normal stresses in soils are compressive (soils cannot, in general, resist tensile stresses), it is customary in geotechnical engineering to describe compressive stresses as positive. Consequently, positive shear stresses are those that tend to cause counterclockwise rotation of the body they act upon, and clockwise angles are positive. Figure 6.1 illustrates the sign conventions for normal and shear stresses; σ_x and σ_y are the normal stresses acting on planes normal to the x - and y -axes, respectively, τ_{xy} (and τ_{yx}) is the shear stress in the y -direction (x -direction) on the plane normal to the x -axis (y -axis), and σ_α and τ_α are the normal and shear stresses on the plane inclined at angle α . In structural mechanics, the opposite conventions are generally used.

The notation used to describe the foregoing stresses is different than that used to develop the equations of motion for three-dimensional wave propagation in Chapter 5. For that problem of solid mechanics, the standard notation of solid mechanics was used. For this chapter and the remainder of the book, the notation above, which is most commonly used in geotechnical engineering, is used. The equivalence of the two notations was discussed in Section 5.2.2.1.

It is often necessary to consider the stresses on several different planes that pass through a particular point. Equilibrium requirements can be used (e.g., Holtz and Kovacs, 1981) to express the normal and shear stresses on a plane inclined at an angle, α , to the x -axis as

$$\sigma_\alpha = \frac{\sigma_x + \sigma_y}{2} + \frac{\sigma_y - \sigma_x}{2} \cos 2\alpha - \tau_{xy} \sin 2\alpha \tag{6.1a}$$

$$\tau_\alpha = \frac{\sigma_x - \sigma_y}{2} \sin 2\alpha - \tau_{xy} \cos 2\alpha \tag{6.1b}$$

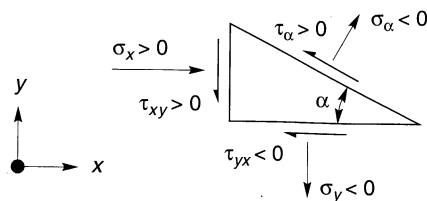


Figure 6.1 Sign conventions for normal and shear stresses.

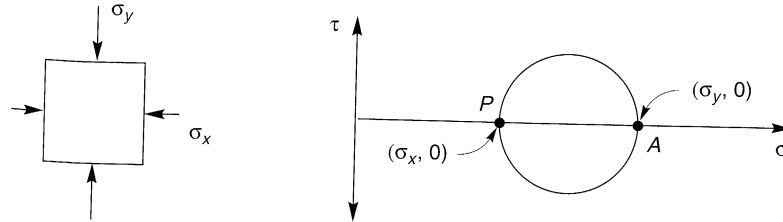


Figure 6.2 Mohr circle of stress for element subjected to major principal stress, σ_y , and minor principal stress, σ_x . Location of pole denoted by P .

Equations (6.1) describe a circle whose center is at $[\sigma = (\sigma_x + \sigma_y)/2, \tau = 0]$ and whose radius is $\sqrt{[(\sigma_y - \sigma_x)/2]^2 + \tau_{xy}^2}$. This circle, shown in Figure 6.2, is the well-known *Mohr circle of stress*. The Mohr circle simply illustrates the stress conditions acting on an element graphically and, as such, is very useful for understanding states of stress and stresses induced by external loading. It will be used often in the remainder of this book.

Equations (6.1) allow the stresses on planes of different inclination to be determined analytically, but they can also be determined graphically using the *pole* of the Mohr circle. The pole has a useful property: any line drawn through the pole will intersect the Mohr circle at a point that describes the shear and normal stresses on a plane parallel to that line. Consider the element shown in Figure 6.2 subjected to a vertical normal stress, σ_y , and a horizontal normal stress, σ_x . The shear stresses on the boundaries are zero. The stress conditions on the horizontal plane are known: $\sigma = \sigma_y$ and $\tau = 0$. Since the property of the pole states that a horizontal line drawn through it must intersect the Mohr circle at a point describing those stress conditions, a horizontal line drawn through the point describing those stress conditions will intersect the Mohr circle at the pole. For the case of Figure 6.2, the point of known stress conditions is point A and the plane for which the stress conditions are known is horizontal. Consequently, a horizontal line drawn through point A must intersect the Mohr circle at the pole, labeled as point P .

Example 6.1

Compute the normal and shear stresses on a plane passing through the element shown in Figure E6.1a and inclined at 45° clockwise from horizontal.

Solution The stresses on the horizontal plane are $\sigma = 4$ and $\tau = +1$. Drawing a horizontal line through this point reveals the location of the pole at point P . Note that the known stresses on the

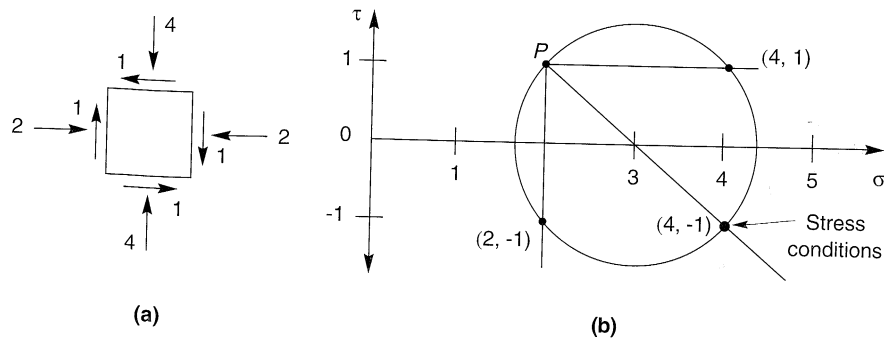


Figure E6.1

vertical plane, $\sigma = 2$ and $\tau = -1$, could just as easily have been used with a vertical line to determine the location of the pole. Once the pole has been identified, the stress conditions on any plane can be determined. Drawing a line through the pole parallel to the plane of interest (Figure E6.1b) shows that the stresses on that plane are $\sigma = 4$ and $\tau = -1$.

6.2.1 Principal Stresses

Two points on the Mohr circle are of particular interest. The points where the circle intersects the normal stress axis describe the normal stresses on planes where no shear stresses exist. Those planes are called *principal stress planes* and the normal stresses that act on them are called *principal stresses*. The *principal stress axes* are aligned in the directions of the principal stresses; therefore, they are perpendicular to the principal stress planes. The largest principal stress is the *major principal stress*, σ_1 , and the smallest is the *minor principal stress*, σ_3 . There is also an *intermediate principal stress*, σ_2 , that can take on any value between σ_1 and σ_3 ; a complete Mohr diagram would include σ_2 , as shown in Figure 6.3. Since the mechanical behavior of soils is much more sensitive to the relationship between σ_1 and σ_3 than to the value of σ_2 , and since σ_2 and σ_3 are often nearly equal, the value of σ_2 is usually not shown.

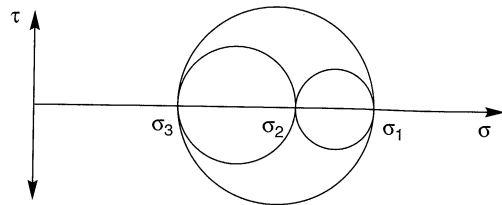


Figure 6.3 Mohr circles of stress including intermediate principal stress, σ_2 .

The pole can be used to determine the orientation of the principal stress planes. The fact that the angle between two lines passing through any point on a semicircle and the “corners” of the semicircle is 90° confirms that the major and minor principal stresses act perpendicular to each other (the intermediate principal stress acts mutually perpendicular to the major and minor principal stresses). Figure 6.4a shows the orientation of the principal stress axes on the element shown previously in Figure E6.1b. If the shear stress, τ_{xy} , is increased from 1 to 2

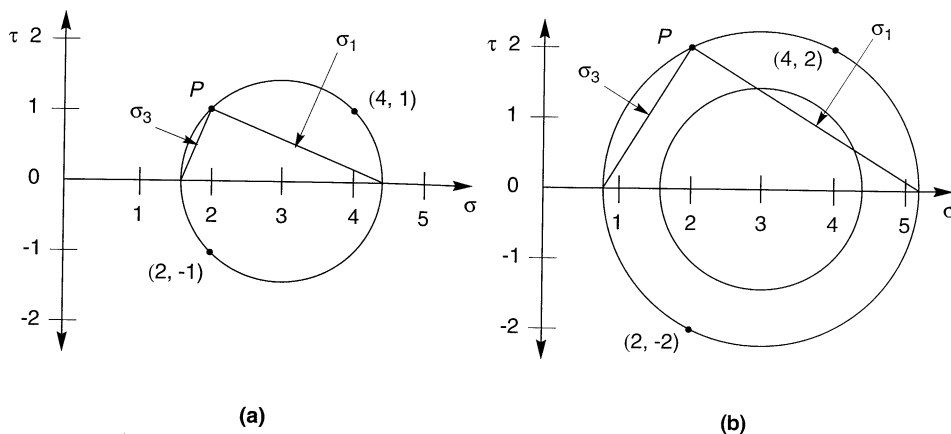


Figure 6.4 Orientation of principal stress axes for (a) $\tau_{xy} = 1$ and (b) $\tau_{xy} = 2$. Note the rotation of principal stress axes that accompanies the change in τ_{xy} .

with σ_x and σ_y held constant, the Mohr circle grows to the size shown in Figure 6.4b. Note that the increase in shear stress is accompanied by rotation of the principal stress axes.

6.2.2 Stress Paths

The variation in stress conditions acting on an element of soil can be tracked by plotting the Mohr circle at various stages in the loading sequence, but such a plot can quickly become difficult to decipher for many loading sequences. It is much simpler to observe the stress conditions by plotting the variation of the position of a single point on the Mohr circle. The *stress point* usually selected is the very top of the Mohr circle, as shown in Figure 6.5. The path taken by the stress point during loading is called the *stress path*. Since many properties of soil are dependent on the stress path induced by the applied loading, the stress path is a very useful tool in geotechnical engineering. [In a considerable body of geotechnical engineering literature, particularly that relating to the constitutive modelling of soils, the stress point is defined according to $p = (\sigma_1 + \sigma_2 + \sigma_3)/3$ and $q = \sigma_1 - \sigma_3$. Although each form has its own merits, they essentially present the same information; the form of Figure 6.5 is more commonly used in geotechnical earthquake engineering and will be used hereafter.]

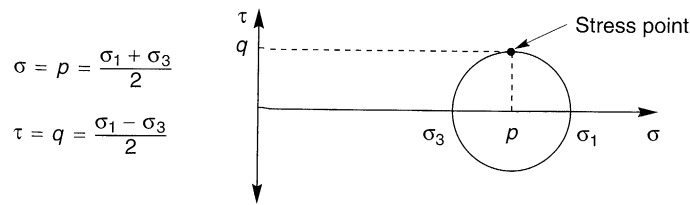


Figure 6.5 Location and definition of stress point on which stress path is based.

Stress paths can be expressed in terms of total or effective stresses. Since the effective stress is equal to the difference between the total stress and the pore pressure, the effective stress path is described by

$$p' = \frac{\sigma'_1 + \sigma'_3}{2} = \frac{(\sigma_1 - u) + (\sigma_3 - u)}{2} = \frac{\sigma_1 + \sigma_3}{2} - \frac{2u}{2} = p - u \quad (6.2a)$$

$$q' = \frac{\sigma'_1 - \sigma'_3}{2} = \frac{(\sigma_1 - u) - (\sigma_3 - u)}{2} = \frac{\sigma_1 - \sigma_3}{2} = q \quad (6.2b)$$

Total and effective stress paths are often plotted together; the horizontal distance between the two is equal to the pore pressure.

Many soil deposits are formed by sedimentation of soil particles through water. As more and more soil is deposited, consolidation causes the volume to decrease and the effective stresses to increase. If the process is one-dimensional (i.e., if the soil particles move only in the vertical direction), the minor principal stress will be proportional to the major principal stress and the effective stress path of an element of soil below the ground surface will move from A to B in Figure 6.6. The slope of the stress path in this range is given by

$$m_0 = \frac{dq}{dp'} = \frac{d\left(\frac{\sigma'_1 - \sigma'_3}{2}\right)}{d\left(\frac{\sigma'_1 + \sigma'_3}{2}\right)} = \frac{\sigma'_1 - \sigma'_3}{\sigma'_1 + \sigma'_3} = \frac{\sigma'_1(1 - K_0)}{\sigma'_1(1 + K_0)} = \frac{1 - K_0}{1 + K_0} \quad (6.3)$$

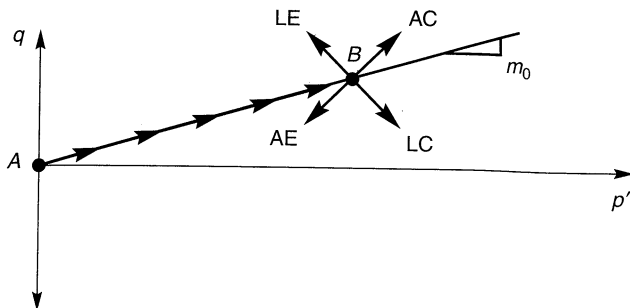


Figure 6.6 Effective stress paths for K_0 consolidation (A to B) and subsequent drained loading along axial compression (AC), axial extension (AE), lateral compression (LC), and lateral extension (LE) stress paths.

where $K_0 = \sigma_3'/\sigma_1'$ is the *coefficient of lateral earth pressure at rest*. If the ground surface is level, the principal stress axes will be vertical and horizontal.

After the soil has consolidated, slow (drained) external loading can cause the stress path to move in a variety of directions. If the vertical stress increases while the horizontal stress remains constant (a condition often approximated by foundation loading), the stress path will move in the direction labeled AC in Figure 6.6. If the horizontal stress decreases with constant vertical stress (as in the development of *active earth pressure* conditions), the stress path moves in the direction LE . If the vertical stress is decreased with constant horizontal stress (as beneath an excavation), the stress path moves in the AE direction, and if the horizontal stress increases with constant vertical stress (*passive earth pressure* conditions), the stress path moves in the direction labeled LC . For each of these idealized conditions, no shear stresses are induced on vertical or horizontal planes; consequently, the principal stress axes remain vertical and horizontal (although they will instantaneously exchange positions if the p' -axis is crossed).

Most realistic loading conditions involve simultaneous changes in horizontal and vertical stresses and/or the development of shear stresses on horizontal and vertical planes. Consider an element of soil beneath a level ground surface (Figure 6.7a) subjected to vertically propagating s-waves. At stage A, the element is under at-rest conditions with the Mohr circle as indicated in Figure 6.7b and the stress path at point A in Figure 6.7c. Since the major principal stress is vertical, the pole of the Mohr circle is at the point $(\sigma'_h, 0)$ in Figure 6.7b. A vertically propagating shear wave will produce shear stresses on horizontal and vertical planes and distort the element as shown in stage B of Figure 6.7a. Since the shear stresses increase while the vertical and horizontal stresses remain constant, the radius of the Mohr circle increases but the center does not move (Figure 6.7b). The stress path (Figure 6.7c) moves vertically, as does the position of the pole (Figure 6.7b), which indicates that the principal stress axes are rotated from their initial vertical and horizontal positions. Since the horizontal shear stresses are cyclic in nature, their direction will reverse after going back through the $\tau_{hv} = \tau_{vh} = 0$ position in stage C. Note that the stress conditions at stage C are identical to those of stage A, and that the principal stress axes have rotated back to the vertical and horizontal positions. At stage D, the shear stresses act in the opposite direction and the principal stress axes rotate in the opposite direction as in stage B. Thus the loading induced by vertically propagating shear waves can be described by the stress path of Figure 6.7c and a principal stress axis rotation. Note that the stress path never indicates isotropic stress conditions (it never reaches the p' -axis) and that the principal stress axes rotate continuously.

The nature of principal stress axis rotation is significant. Research (e.g., Wong and Arthur, 1986; Symes et al., 1988; Sayao and Vaid, 1989) has shown that principal stress

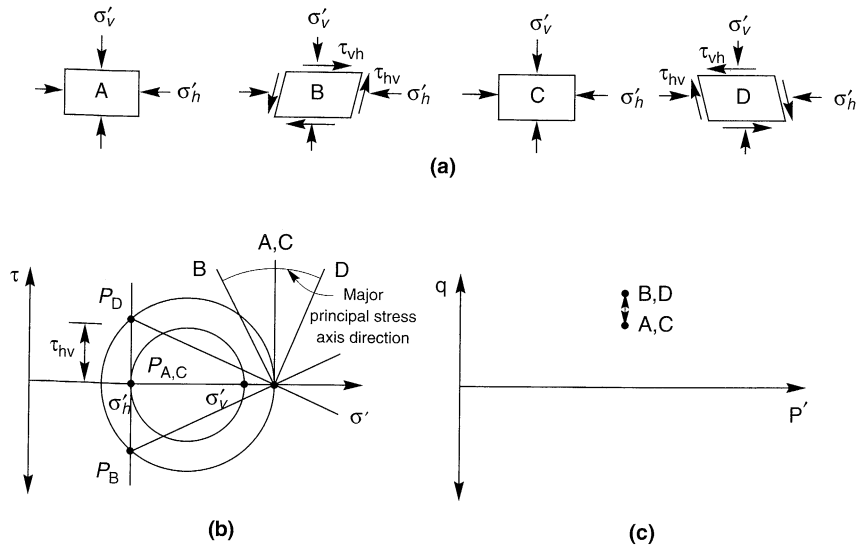


Figure 6.7 (a) Stress and strain conditions imposed on element of soil below level ground surface by vertically propagating shear waves at four different times; (b) Mohr circles, locations of poles, and orientations of major principal stress axis; (c) stress path.

rotation can cause shear and volumetric strain by itself (i.e., even if the stress point does not move). Hence some of the strain induced by vertically propagating shear waves results from principal stress rotation; this effect is not present in many field and laboratory tests.

Example 6.2

A reconstituted triaxial specimen of dry sand is consolidated isotropically to an effective confining pressure of 200 kPa, and then loaded in drained triaxial compression to a deviator stress ($\sigma_1 - \sigma_3$) of 200 kPa. At that point the specimen is subjected to a harmonic deviator stress that oscillates between 100 and 300 kPa. Plot the total and estimated effective stress paths.

Solution Because the sand is dry, no pore pressures exist, so the total and effective stresses are equal. During preparation, the stresses acting on the specimen are very small, so the stress path is at point A in Figure E6.2. Isotropic consolidation takes the stress path to point B, and drained triaxial compression takes it to point C. Harmonic loading then causes the stress path to oscillate between points D and E.

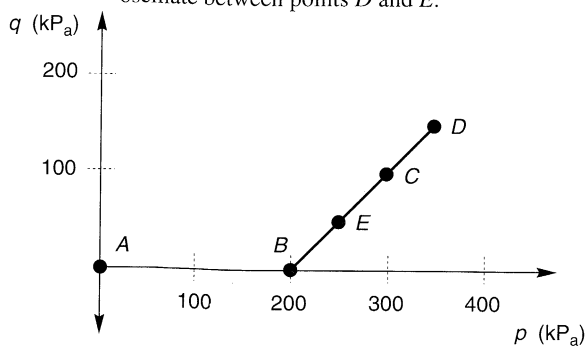


Figure E6.2

6.3 MEASUREMENT OF DYNAMIC SOIL PROPERTIES

The measurement of dynamic soil properties is a critical task in the solution of geotechnical earthquake engineering problems. A wide variety of field and laboratory techniques are available, each with different advantages and limitations with respect to different problems. Many are oriented toward measurement of low-strain properties and many others toward properties mobilized at larger strains. The selection of testing techniques for measurement of dynamic soil properties requires careful consideration and understanding of the specific problem at hand. Efforts should always be made to use tests or test procedures that replicate the initial stress conditions and the anticipated cyclic loading conditions as closely as possible.

Soil properties that influence wave propagation and other low-strain phenomena include stiffness, damping, Poisson's ratio, and density. Of these, stiffness and damping are the most important; the others have less influence and tend to fall within relatively narrow ranges. The stiffness and damping characteristics of cyclically loaded soils are critical to the evaluation of many geotechnical earthquake engineering problems—not only at low strains but because soils are nonlinear materials, also at intermediate and high strains. At high levels of strain, the influence of the rate and number of cycles of loading on shear strength may also be important. Volume change characteristics are also important at high strain levels.

The measurement of these important soil properties in field and laboratory tests is presented in the following sections. Many of the tests have been developed specifically to measure dynamic soil properties; others are modified versions of tests commonly used to measure soil behavior under monotonic loading conditions. The applicability of the various tests to dynamic soil properties is emphasized here—descriptions of their applications to static properties may be found in standard geotechnical engineering texts (e.g., Lambe and Whitman, 1969; Holtz and Kovacs, 1981).

Any investigation of dynamic soil properties should be performed with due recognition of the inevitable uncertainty in measured properties. Sources of uncertainty include the inherent variability of soils (a result of the geologic environment in which they were deposited), inherent anisotropy (a function of the soil structure or "fabric"), induced anisotropy (caused by anisotropic stress conditions), drilling and sampling disturbance, limitations of field and/or laboratory testing equipment, testing errors, and interpretation errors. Some of these sources of uncertainty can be minimized by careful attention to test details, but others cannot.

6.3.1 Field Tests

Field tests allow the properties of the soil to be measured in situ (i.e., in their existing state where the complex effects of existing stress, chemical, thermal, and structural conditions are reflected in the measured properties). The measurement of dynamic soil properties by field tests has a number of advantages. Field tests do not require sampling, which can alter the stress, chemical, thermal, and structural conditions in soil specimens. Many field tests measure the response of relatively large volumes of soil, thereby minimizing the potential for basing property evaluation upon small, unrepresentative specimens. Many field tests induce soil deformations that are similar to those of the problem of interest, particularly for wave propagation and foundation design problems. On the other hand, field tests do not allow the effects of conditions other than the in situ conditions to be investigated easily, nor do they

allow porewater drainage to be controlled. In many field tests, the specific soil property of interest is not measured but must be determined indirectly, by theoretical analysis or empirical correlation.

Some field tests can be performed from the ground surface, while others require the drilling of boreholes or the advancement of a probe into the soil. Surface tests are often less expensive and can be performed relatively quickly. They are particularly useful for materials in which drilling and sampling or penetration is difficult. Borehole tests, on the other hand, have the advantage of the information gained directly from the boring: visual and laboratory-determined soil characteristics, water table location, and so on. Also, the interpretation of borehole tests is usually more direct than that of surface tests.

6.3.1.1 Low-Strain Tests

Low-strain tests generally operate at strain levels that are not large enough to induce significant nonlinear stress-strain behavior in the soil, typically at shear strains below about 0.001%. As such, most are based on the theory of wave propagation in linear materials. Many involve the measurement of body wave velocities which can easily be related to low-strain soil moduli. Others involve the development of standing waves, whose measured frequencies and/or wavelengths can be used to compute low-strain moduli.

Seismic geophysical tests represent an important class of field tests for determination of dynamic soil properties. Seismic tests involve the creation of transient and/or steady-state stress waves and the interpretation of their behavior from measurements made at one or more different locations. In many seismic tests, a source produces a "pulse" of waves whose times of arrival are measured at distant receivers. The source, which may range from a sledgehammer blow to the ground surface to a buried explosive charge, will generally produce p-waves, s-waves, and surface waves. The relative amplitudes of each depend on how the impulse is generated. Explosive sources and vertical impact sources (Figure 6.8a and b) are rich in p-wave content. SH-waves are produced most efficiently by striking the end of a beam pressed tightly against the ground surface (Figure 6.8c).

Since p-waves travel fastest, their arrivals at distant receivers are most easily detected and their arrival times most easily measured. S-wave resolution can be improved markedly by reversing the polarity of the impulse, as is easily accomplished for SH-waves by striking the other end of the beam of Figure 6.8c. Since the polarity of the train of p-waves is not reversed, subtracting the reversed record from the original record will diminish the p-wave amplitudes while enhancing the s-wave amplitudes. Wave arrivals can also be enhanced by adding, or "stacking," records from multiple impulses; the random noise portions of the records tend to cancel each other while the actual waves are reinforced.

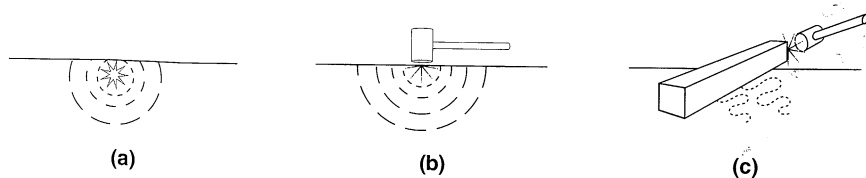


Figure 6.8 Different methods for creation of impulsive disturbances for seismic geophysical tests: (a) shallow explosives; (b) vertical impact; (c) horizontal impact.

Careful consideration of groundwater conditions is essential for proper interpretation of seismic geophysical test measurements. P-waves travel through groundwater at about 5000 ft/sec, depending on temperature and salinity. Soft, saturated soils may propagate p-waves at these high velocities even though the velocity is not indicative of the stiffness of the soil skeleton. Failure to consider groundwater effects can result in significant overestimation of soil stiffness. The groundwater problem can largely be avoided by using s-waves which are propagated by the soil skeleton and not the groundwater.

Seismic Reflection Test. The seismic reflection test allows the wave propagation velocity and thickness of surficial layers to be determined from the ground surface or in offshore environments. The test and its interpretation are conceptually very simple. The reflection test is most useful for investigation of large-scale and/or very deep stratigraphy. It is rarely used for delineation of shallow soil layers.

For the simple profile shown in Figure 6.9a, the test is performed by producing an impulse (usually rich in p-waves) at the source, *S*, and measuring the arrival time at the receiver, *R*. The impulse produces stress waves that radiate away from the source in all directions with a hemispherical wavefront. Some of the wave energy follows a direct path from *S* to *R* and arrives at *R* at

$$t_d = \frac{\text{distance of travel}}{\text{wave velocity}} = \frac{x}{v_{p1}} \quad (6.4)$$

By measuring *x* and *t_d*, the p-wave velocity of the upper layer, *v_{p1}*, can easily be determined. Another portion of the impulse energy travels downward and strikes the horizontal layer boundary at an angle of incidence

$$i = \tan^{-1} \frac{x}{2H} \quad (6.5)$$

The part of that wave that is reflected back toward the ground surface arrives at the receiver at

$$t_r = \frac{\text{distance of travel}}{\text{wave velocity}} = \frac{2\sqrt{H^2 + (x/2)^2}}{v_{p1}} = \frac{\sqrt{4H^2 + x^2}}{v_{p1}} \quad (6.6)$$

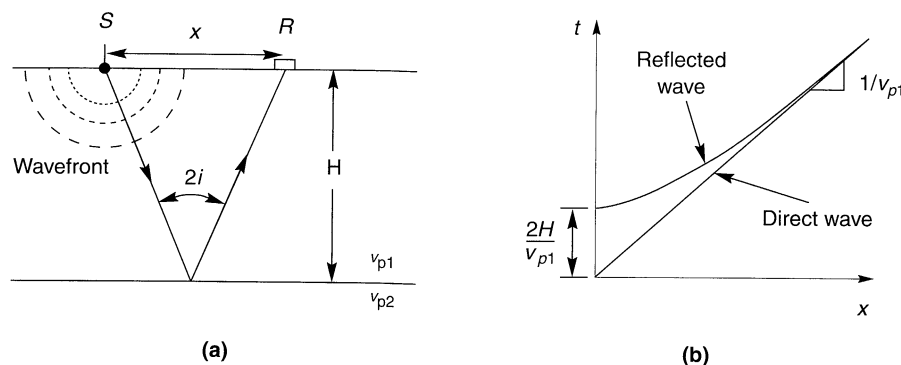


Figure 6.9 (a) Ray path for incident and reflected p-wave from horizontal layer boundary; (b) variation of travel time for direct and reflected waves. Difficulty in resolution increases with increasing source-receiver separation.

By measuring t_r and knowing x and v_{p1} from the direct wave calculation, the thickness of the upper layer can be calculated as

$$H = \frac{1}{2} \sqrt{t_r^2 v_{p1}^2 - x^2} \quad (6.7)$$

Figure 6.9b shows how the arrival times for the direct and reflected waves are related; the difference in arrival times decreases with increasing distance. When, as is usually the case, actual conditions differ from the simple assumptions of horizontal layering above, multiple measurements must be made. In the case of the inclined layer boundary shown in Figure 6.10, for example, travel-time measurements at receivers A and B can be used to determine the angle of inclination as

$$\sin \alpha = \frac{v_{p1}^2 (t_{RA} + t_{RB})(t_{RB} - t_{RA})}{4z_\alpha (x_B - x_A)} - \frac{x_A + x_B}{4z_\alpha} \quad (6.8)$$

where $v_{p1} = x_A/t_{dA} = x_B/t_{dB}$ and t_{dA} and t_{dB} are the direct wave arrival times at receivers A and B , respectively. If receiver A is placed at the source ($x_A = 0$), then

$$z_\alpha = \frac{t_{RA} v_{p1}}{2} \quad (6.9)$$

$$\sin \alpha = \frac{v_{p1}^2 (t_{RA} + t_{RB})(t_{RB} - t_{RA}) - x_B^2}{2t_{RA} v_{p1} x_B} \quad (6.10)$$

The characteristics of deeper layers may be evaluated using reflections from deeper interfaces (Griffiths and King, 1965; Ewing et al., 1957; Kley, 1983). The method is limited, however, by the difficulty associated with determining the arrival time of the reflected waves, particularly for cases in which reflected waves arrive while the receivers are still responding to direct waves. Interpretation of results for profiles with low-velocity layers may also be difficult.

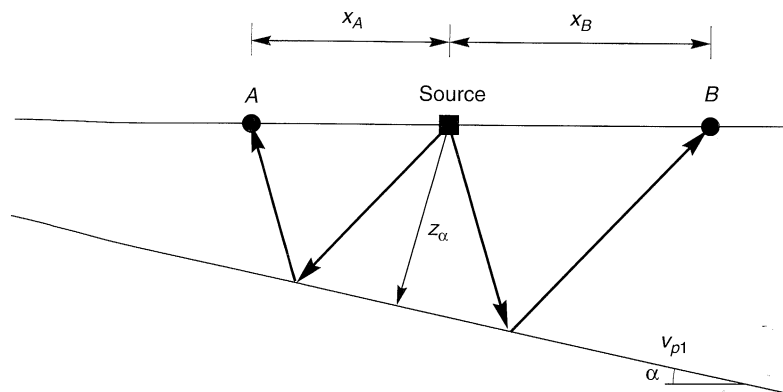


Figure 6.10 Source and receiver layout for reflection test with inclined layer boundary.

Example 6.3

A loose deposit of overconsolidated clay is underlain by bedrock. Previous subsurface investigations in the area suggest that the bedrock surface is nearly horizontal. A seismic reflection

survey shows the arrival of distinct p-waves at a geophone 38 msec and 200 msec after an impulsive load is applied at a point 20 m from the geophone. Determine the thickness and the p-wave velocity of the clay deposit.

Solution Assuming that the first p-wave arrival is caused by the direct p-wave, the p-wave velocity is given by

$$v_{p1} = \frac{x}{t_d} = \frac{20 \text{ m}}{0.038 \text{ sec}} = 526 \text{ m/sec}$$

If the second p-wave is due to the reflected wave, the thickness of the deposit is given by

$$H = \frac{1}{2} \sqrt{t_R^2 v_{p1}^2 - x^2} = \frac{1}{2} \sqrt{(0.200 \text{ sec})^2 (526 \text{ m/sec})^2 - (20 \text{ m})^2} = 51.6 \text{ m}$$

Seismic Refraction Test. The seismic refraction test eliminates the most important limitation of the seismic reflection test by using the arrival times of the first waves, regardless of path, to reach a given receiver. The test involves measurement of the travel times of p- and/or s-waves from an impulse source to a linear array of points along the ground surface at different distances from the source. Although the seismic refraction test is more commonly used than the seismic reflection test, its greatest earthquake engineering application is also for delineation of major stratigraphic units.

A typical test setup is shown in Figure 6.11. An impulsive energy source, which can be mechanical or explosive, is located at or near the ground surface. A series of receivers, usually geophones, are placed in a linear array. One receiver is located at the source. The output of all of the receivers is recorded when the impulse load is triggered. From these recordings the arrival times of the first waves to reach each receiver can be determined and

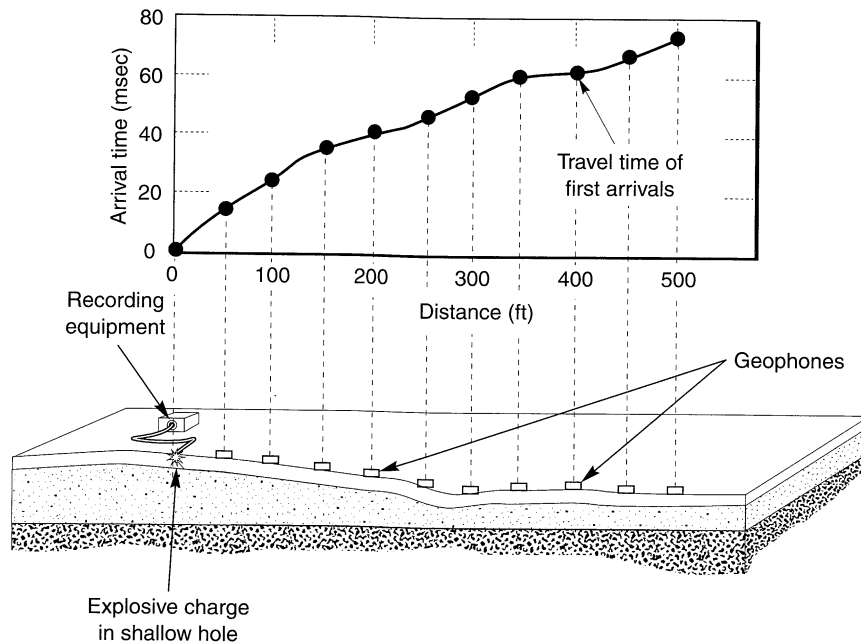


Figure 6.11 Seismic refraction test setup. (After Redpath, 1973.)

plotted as a function of source–receiver distance, as shown in Figure 6.11. If the receivers were all excited by a single stress wave traveling along the ground surface at constant velocity, v (the test can be performed and interpreted with p- or s-waves, so v could be v_p or v_s), the arrival time–distance plot would be a straight line of slope $1/v$ that passed through the origin. Figure 6.11 shows that this is clearly not the case—a different, more complicated mechanism is at work.

Horizontal Layering. Assume that the seismic refraction test is being conducted on the surface of a two-layered elastic half-space as shown in Figure 6.13. The impulse produces stress waves that travel away from the source in all directions with a hemispherical wavefront. Some of the energy travels directly from the source to the receivers in the form of a *direct wave*, arriving at the n th receiver at a travel time

$$t_{dn} = \frac{x_n}{v_1} \quad (6.11)$$

where v_1 is the wave propagation velocity of material 1. Other rays travel downward toward the boundary between materials 1 and 2. At that boundary, these rays are reflected and refracted, with the directions of the refracted rays determined by Snell's law (Section 5.4.2). At the critical angle of incidence, i_c , the refracted ray will travel parallel to the boundary. According to Huygens' principle (which says that any point on a wavefront acts as the source of a new disturbance) and Snell's law, this critically refracted wave will produce a *head wave* in material 1 that will travel at v_1 in a direction inclined at $(90^\circ - i_c)$ to the boundary. The resulting wavefront can have a portion controlled by the direct wave and a portion controlled by the head wave, as illustrated in Figure 6.12. Note that the direct wave produces the first wave arrival at short source–receiver distances, but the head wave arrives before the direct wave at distances greater than the *critical distance*, x_c .

At distances greater than x_c , a ray that travels downward at velocity v_1 through material 1, is critically refracted to travel in material 2 at velocity v_2 and is then critically refracted back up through material 1 at velocity, v_1 will reach a receiver faster than a ray that travels along the shorter direct path at velocity v_1 . The travel time required for the head wave to reach the n th receiver (Figure 6.13) can be written as

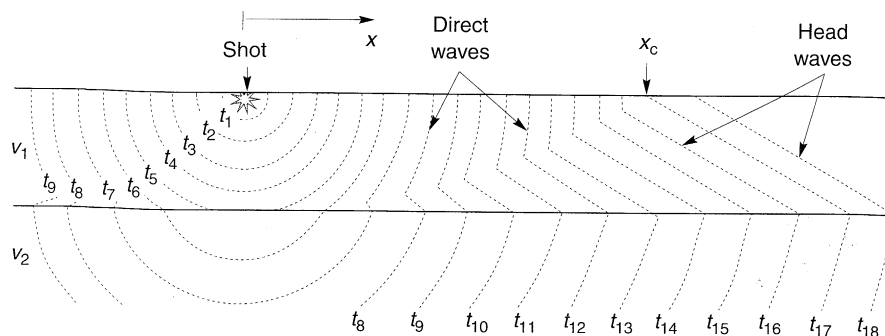


Figure 6.12 Wavefronts for first-arriving waves in a seismic refraction survey. Note that first arrivals near the source are from direct waves but, at distances greater than the critical distance, x_c , the first arrivals are from head waves. (After Corps of Engineers, 1979.)

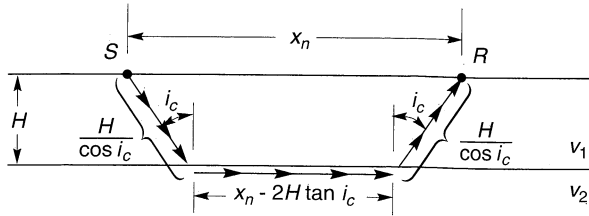


Figure 6.13 Travel path for first arrival when $x_n > x_c$.

$$t_{hn} = \frac{H}{v_1 \cos i_c} + \frac{x_n - 2H \tan i_c}{v_2} + \frac{H}{v_1 \cos i_c} \quad (6.12)$$

Substituting the result of Snell's law for critical incidence, $\sin i_c = v_1/v_2$, and the trigonometric identity $\cos^2 i_c = 1 - \sin^2 i_c$, and rearranging yields

$$t_{hn} = \frac{x_n}{v_2} + 2H \sqrt{\frac{1}{v_1^2} - \frac{1}{v_2^2}} \quad (6.13)$$

If a receiver was placed exactly at the critical distance, x_c , the direct wave and the head wave would reach it at exactly the same time (i.e., $t_{dn} = t_{hn}$). Consequently, from equations (6.11) and (6.13),

$$\frac{x_c}{v_1} = \frac{x_c}{v_2} + 2H \sqrt{\frac{1}{v_1^2} - \frac{1}{v_2^2}} \quad (6.14)$$

from which

$$H = \frac{x_c}{2} \sqrt{\frac{v_2 - v_1}{v_2 + v_1}} \quad (6.15)$$

Therefore, the travel time–distance diagram allows three important characteristics of the subsurface conditions, namely v_1 , v_2 , and H , to be obtained.

For the case of multiple horizontal layers, the travel time–distance diagram will exhibit more than one break in slope, as illustrated in Figure 6.14. The distances corresponding to these slope breaks can be used, along with the slopes themselves, to determine the thicknesses of deeper layers. The thickness of the k th layer, for example, would be given by (Corps of Engineers, 1979)

$$H_k = \frac{x_{ck}}{2} \sqrt{\frac{v_{k+1} - v_k}{v_{k+1} + v_k}} + \sum_{j=1}^{k-1} \frac{H_j}{v_j} \frac{v_{k+1} \sqrt{v_k^2 - v_j^2} - v_k \sqrt{v_{k+1}^2 - v_j^2}}{\sqrt{v_{k+1}^2 - v_k^2}} \quad (k \geq 2) \quad (6.16)$$

In the preceding paragraphs, it has been explicitly assumed that the velocity of each layer is smaller than the layer immediately below it. For many geologic conditions this is a good assumption, but when it is not, the results of a seismic refraction test can be misleading. A low-velocity layer underlying a higher-velocity layer (i.e., a *velocity reversal*) will not appear as an individual segment on the travel time–distance diagram. Instead, it will cause the computed depths of the layer boundaries to be greater than the actual depths (Redpath, 1973). Also, *blind zones*, where a subsurface layer exists but is not indicated by the travel time–distance diagram, can be caused by insufficient layer thickness or insufficient velocity

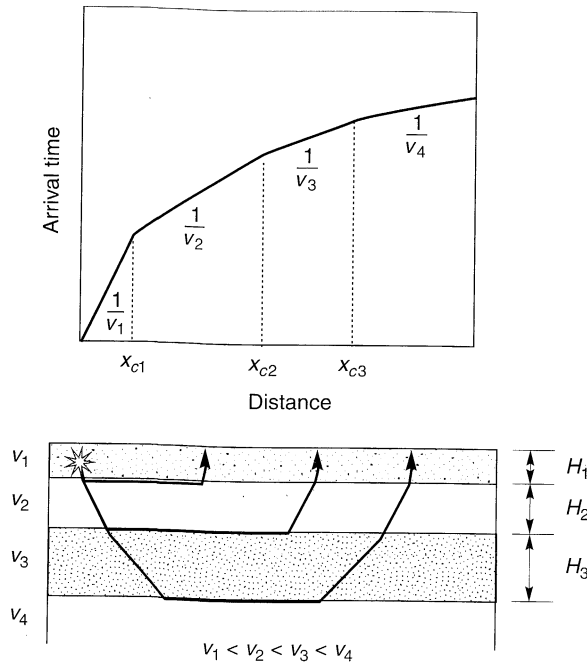


Figure 6.14 Travel time–distance diagram for multiple horizontal layers. (After Redpath, 1973.)

contrast (Soske, 1959). In such cases the head wave from a deeper layer can overtake the head wave of an intermediate layer before it reaches the ground surface. The undetected existence of a blind zone will cause the computed depth of the deeper layer to be less than the actual depth (Redpath, 1973). In cases where the velocity increases continuously with depth (e.g., sands, gravels, normally consolidated clays), ray paths will be curved rather than straight, as previously assumed. For the case where velocity is proportional to depth (Figure 6.15), the ray paths will become circular arcs. The resulting time–distance curves can be transformed into curves of velocity versus depth (Redpath, 1973; Corps of Engineers, 1979).

Inclined or Irregular Layering. When the boundaries between layers are not parallel, the travel time–distance diagram will not yield the true velocities of all layers directly since the apparent velocity (the distance between adjacent receivers divided by the difference in their arrival times) is influenced by the slope of the layer boundaries and the critical angles of incidence. Referring to Figure 6.16, the apparent velocity from a seismic refraction test in the down-dip direction, v_{2D} , is lower than the apparent velocity, v_{2U} , from an identical test in the up-dip direction. From Snell's law,

$$\sin(i_c + \alpha) = \frac{v_1}{v_{2D}} \quad (6.17a)$$

$$\sin(i_c - \alpha) = \frac{v_1}{v_{2U}} \quad (6.17b)$$

which can be rearranged to produce the *apparent dip angle* (the dip angle in the vertical plane of the array of receivers)

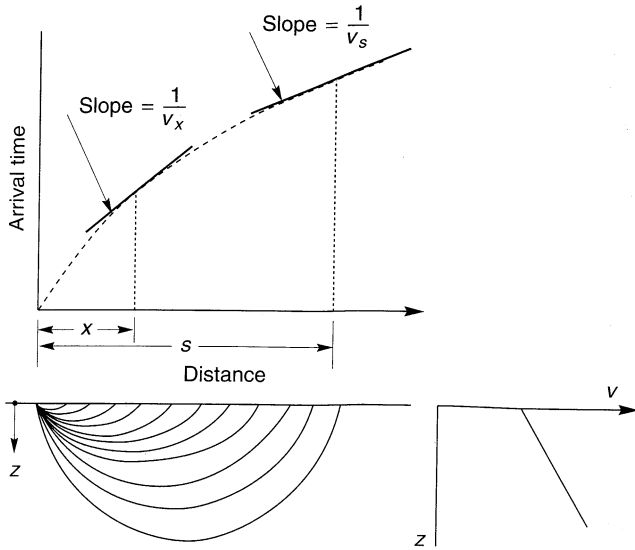


Figure 6.15 Ray paths and travel time-distance diagram for a single layer with linearly increasing velocity. (After Redpath, 1973.)

$$\alpha = \frac{1}{2} \left(\sin^{-1} \frac{v_1}{v_{2D}} - \sin^{-1} \frac{v_1}{v_{2U}} \right) \quad (6.18)$$

The apparent dip angle is equal to the true dip angle only when the dip vector lies within the plane of the receiver array. In other cases, another survey utilizing a nonparallel array of receivers is required to determine the true dip (Richart et al., 1970). The thickness of the upper layer, measured perpendicular to the layer boundary at each shot point, can be computed as

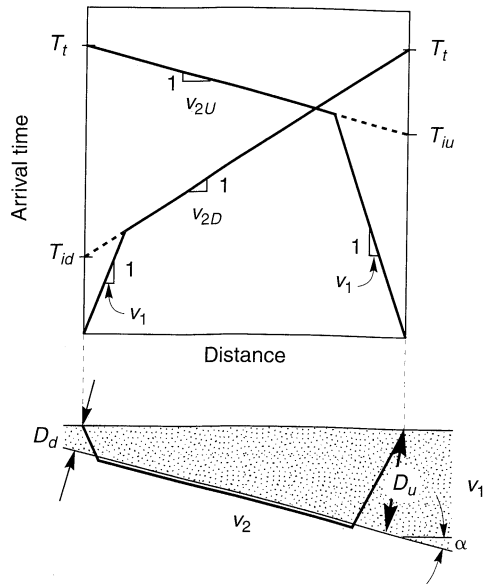


Figure 6.16 Reverse profiling used to identify irregular or sloping interfaces. Concept of apparent velocity in underlying layer is also illustrated. (After Redpath, 1973.)

$$D_d = \frac{v_1 T_{id}}{2 \cos \alpha} \tag{6.19a}$$

$$D_u = \frac{v_1 T_{iu}}{2 \cos \alpha} \tag{6.19b}$$

The true value of v_2 is given by

$$v_2 = \frac{2v_{2D}v_{2U}}{v_{2D} + v_{2U}} \cos \alpha \tag{6.20}$$

The preceding discussion illustrates the importance of reverse profiling for cases of inclined layering. Since the nature of the layering is not often known in advance, as well as to provide additional data, reverse profiling is routinely performed.

Example 6.4

A seismic refraction survey with reverse profiling between two shot points located 120 m apart shows the p-wave arrival times listed below. Determine the thickness of the surficial layer of soil.

Geophone	Distance from Shot Point A	p-Wave Arrival Time (msec)	Distance from Shot Point B	p-Wave Arrival Time (msec)
A	0	0	120	88
B	5	11	100	78
C	10	26	80	67
D	20	49	60	58
E	40	65	40	47
F	60	71	20	37
G	80	76	10	26
H	100	83	5	12
I	120	88	0	0

Solution The arrival time–distance diagrams for the forward and reverse profiles are plotted in Figure E6.4.

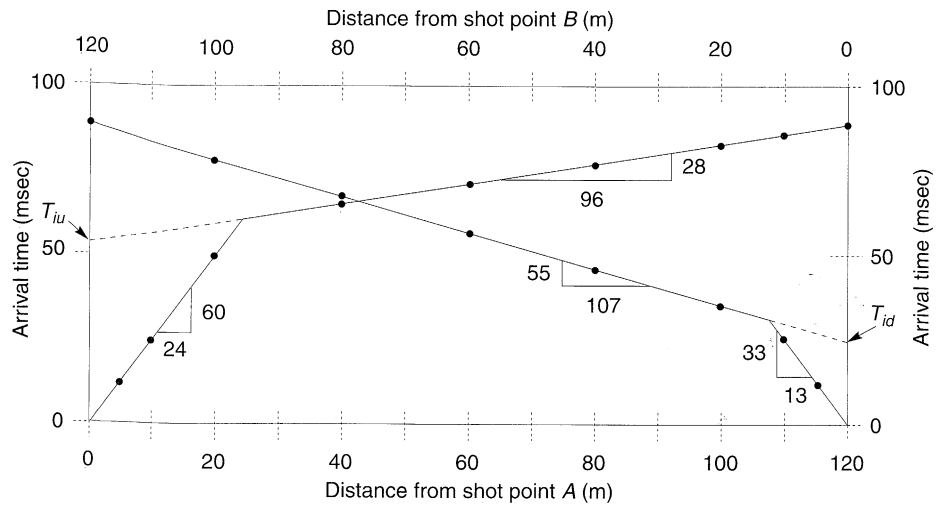


Figure E6.4

From the initial slopes of the travel-time diagrams, the average p-wave velocity of the surficial layer is given by

$$v_1 = \frac{1}{2} \left(\frac{24 \text{ m}}{0.060 \text{ sec}} + \frac{13 \text{ m}}{0.033 \text{ sec}} \right) = 397 \text{ m/sec}$$

The apparent velocities in the down-dip and up-dip directions are

$$v_{2D} = \frac{107 \text{ m}}{0.055 \text{ sec}} = 1945 \text{ m/sec}$$

$$v_{2U} = \frac{96 \text{ m}}{0.028 \text{ sec}} = 3429 \text{ m/sec}$$

The apparent dip angle can then be computed as

$$\alpha = \frac{1}{2} \left(\sin^{-1} \frac{v_1}{v_{2D}} - \sin^{-1} \frac{v_1}{v_{2U}} \right) = \frac{1}{2} \left(\sin^{-1} \frac{397}{1945} - \sin^{-1} \frac{397}{3429} \right) = 2.56^\circ$$

Then the depths of the layer boundary, measured perpendicular to the boundary, at shot points A and B are

$$D_A = \frac{v_1 T_{id}}{2 \cos \alpha} = \frac{(397 \text{ m/sec})(0.029 \text{ sec})}{2 \cos 2.56^\circ} = 5.8 \text{ m}$$

$$D_B = \frac{v_1 T_{iu}}{2 \cos \alpha} = \frac{(397 \text{ m/sec})(0.053 \text{ sec})}{2 \cos 2.56^\circ} = 10.5 \text{ m}$$

A more general procedure can be developed to interpret the results of tests on soil profiles with layers of variable thickness. Consider the site of Figure 6.17, where waves from the two sources SP₁ and SP₂ reach a receiver at point D at arrival times T_{D1} and T_{D2}, respectively. The total time [i.e., the total travel time from the location of SP₁ to that of SP₂ (and vice versa)], is given by

$$T_t = \frac{AB}{v_1} + \frac{BCEF}{v_2} + \frac{FG}{v_1} = \frac{z_1}{v_1 \cos i_c} + \frac{s - z_1 \tan i_c - z_2 \tan i_c}{v_2} + \frac{z_2}{v_1 \cos i_c} \quad (6.21)$$

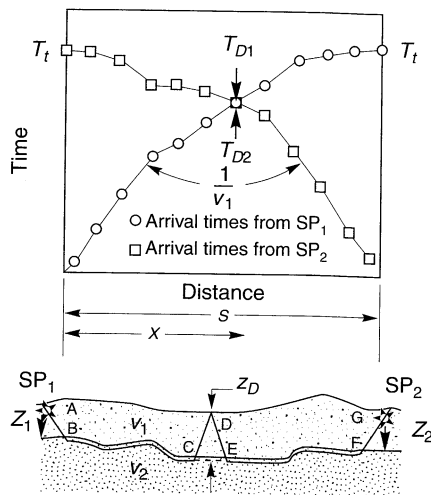


Figure 6.17 Forward and reverse profiles for layer of irregular thickness. (After Corps of Engineers, 1979.)

where z_1 and z_2 are the vertical thicknesses of the surficial layer at SP_1 and SP_2 , respectively. The arrival times at point D are given by

$$T_{D1} = \frac{AB}{v_1} + \frac{BC}{v_2} + \frac{CD}{v_1} = \frac{z_1}{v_1 \cos i_c} + \frac{x_D - z_1 \tan i_c - z_D \tan i_c}{v_2} + \frac{z_D}{v_1 \cos i_c} \quad (6.22)$$

$$T_{D2} = \frac{FG}{v_1} + \frac{EF}{v_2} + \frac{DE}{v_1} = \frac{z_2}{v_1 \cos i_c} + \frac{(s - x_D) - z_2 \tan i_c - z_D \tan i_c}{v_2} + \frac{z_D}{v_1 \cos i_c} \quad (6.23)$$

The velocity of the lower layer, v_2 , is inversely proportional to the difference between the arrival times from the forward and reverse profiles (i.e., a plot of arrival time difference versus distance has a slope of $2/v_2$). Combining equations (6.21) through (6.23) and substituting $v_2 = v_1/\sin i_c$ yields

$$T_{D1} + T_{D2} - T_t = \frac{2z_D}{v_1} \frac{1 - \sin^2 i_c}{\cos i_c} \quad (6.24)$$

Therefore

$$z_D = \frac{1}{2} \frac{(T_{D1} + T_{D2} - T_t)v_1}{\cos i_c} \quad (6.25)$$

By moving the receiver (point D) to different locations (or using multiple geophones), the variation of surficial layer thickness between SP_1 and SP_2 can be determined. Implicit in the preceding derivation is the assumption that the first arrivals at D are from head waves from the same layer rather than from direct waves. Long arrays may be required to ensure the validity of this assumption over distances of interest.

Suspension Logging Test. Suspension logging, although commonly used in petroleum exploration, has only recently been applied to geotechnical earthquake engineering problems. A probe 5 to 6 m (15 to 20 ft) long is lowered into an uncased borehole filled with water or drilling fluid. A horizontal reversible-polarity solenoid located near the base of the probe produces a sharp, impulsive pressure wave in the drilling fluid. Upon reaching the borehole wall, the pressure wave produces both p- and s-waves in the surrounding soil. These waves travel through the soil and eventually transmit energy back through the drilling fluid to two biaxial geophones located about 1 m (3 ft) apart near the top of the probe. To enhance identification of p- and s-wave arrivals, the procedure is repeated with an impulse of opposite polarity. Differences in arrival times are used to compute the average p- and s-wave velocities of the soil between the geophones. The suspension test allows measurement of wave propagation velocities in a single, uncased borehole, but the frequencies of the waves (500 to 2,000 Hz for s-waves and 1000 to 3000 Hz for p-waves) are much higher than those of interest in geotechnical earthquake engineering.

Because the solenoid travels with the geophones down the borehole, the amplitude of the signals is relatively constant at all depths. As a result, the suspension logging test is effective at great depths—up to 2 km (Nigbor and Imai, 1994). By overlapping measurement points, resolutions of less than 1 m (3.1 ft) can be obtained. This capability is particularly useful at sites that may have thin layers of soft or weak soil. The presence of tube waves may limit the effectiveness of the suspension logging test in cased boreholes.

Steady-State Vibration (Rayleigh Wave) Test. The problem of detecting wave arrivals and measuring arrival times is eliminated in tests that interpret properties from the characteristics of steady-state vibrations. The displacements along the ground surface adjacent to a vertically vibrating circular footing are caused primarily by Rayleigh waves (Miller and Pursey, 1955). Since Rayleigh waves produce both vertical and horizontal displacements, the ground surface will, for a constant loading frequency, be distorted as shown in exaggerated form in Figure 6.18. By placing a receiver at the center of the footing and moving another receiver to points at different distances from the receiver, the locations of points vibrating in-phase can be determined. The horizontal distances between such points are equal to the wavelength of the Rayleigh wave. By measuring the Rayleigh wavelength, the Rayleigh wave phase velocity, v_R , can be calculated as

$$v_R = \omega\lambda_R/2\pi = f\lambda_R \quad (6.26)$$

From the phase velocity, Poisson's ratio, and Figure 5.10, the shear wave velocity can be estimated. For many soils, $v_s \approx 1.09v_R$.

For soils whose stiffness varies with depth, dispersion will cause the Rayleigh wave phase velocity to vary with frequency. The shape of the Rayleigh wave displacement profile (Figure 5.10) suggests that the measured phase velocity corresponds to the soil properties at a depth of about $\lambda_R/3$ (Gazetas, 1991) to $\lambda_R/2$ (Heukelom and Foster, 1960; Richart et al., 1970). By varying the loading frequency in the field, the variation of shear wave velocity with depth can be estimated. The steady-state vibration test is useful for determining the near-surface shear wave velocity but cannot easily provide detailed resolution of highly variable velocity profiles. For geotechnical earthquake engineering applications, the steady-state vibration test has largely been supplanted by the spectral analysis of surface waves test.

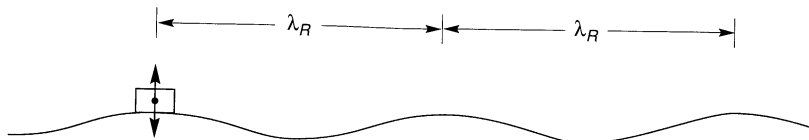


Figure 6.18 Rayleigh wave-induced deformation of ground surface adjacent to vertically vibrating footing. (After Richart et al., 1970.)

Spectral Analysis of Surface Waves Test. The shape of a *dispersion curve* [i.e., a plot of Rayleigh wave velocity versus frequency (or wavelength)], at a particular site is related to the variation of body wave velocities with depth. The preceding steady-state test can be used to generate a dispersion curve by repeating the test at different loading frequencies. This process, however, tends to be quite time consuming in the field. With the use of digital data acquisition and signal-processing equipment, a dispersion curve can be obtained from an impulsive or random noise load. The measurement and interpretation of dispersion curves obtained in this way, known as *spectral analysis of surface waves* (SASW) (Heisey et al., 1982; Nazarian and Stokoe, 1983; Stokoe et al., 1994), is one of the most significant recent advances in shallow seismic exploration.

The SASW test is performed by placing two vertical receivers on the ground surface in line with an impulsive or random noise source, as illustrated in Figure 6.19. The output of both

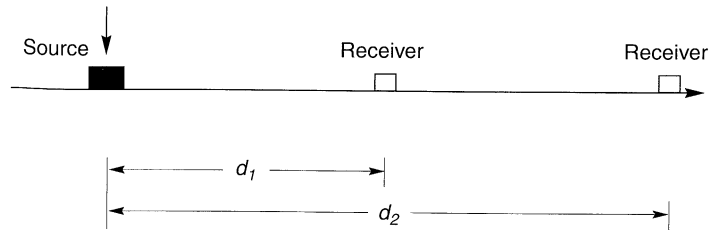


Figure 6.19 Typical configuration of source and receivers in a SASW test. Receiver spacing is changed in such a way that $d_1 + d_2$ remains constant.

receivers is recorded and transformed to the frequency domain using the fast Fourier transform. After transformation, the phase difference, $\phi(f)$, can be computed for each frequency. The corresponding travel time between receivers can be calculated for each frequency from

$$\Delta t(f) = \frac{\phi(f)}{2\pi f} \quad (6.27)$$

Since the distance between receivers, $\Delta d = d_2 - d_1$, is known, the Rayleigh wave phase velocity and wavelength can be calculated as functions of frequency:

$$v_R(f) = \frac{\Delta d}{\Delta t(f)} \quad (6.28)$$

$$\lambda_R(f) = \frac{v_R(f)}{f} \quad (6.29)$$

With modern electronic instrumentation, these calculations can be performed in the field virtually in real time. The results can be used to plot the experimental dispersion curve (Figure 6.20). While the test should, in theory, yield good results for a single receiver spacing, practical considerations dictate that several different receiver spacings be used. At each spacing, the midpoint between the two receivers is kept at the same distance from the source.

Identification of the thickness and shear wave velocity of subsurface layers involves the iterative matching of a theoretical dispersion curve to the experimental dispersion curve. The Haskell–Thomson solution (Thomson, 1950; Haskell, 1953) for a series of uniform elastic layers of infinite horizontal extent is used to predict the theoretical dispersion curve. Initial estimates of the thickness and shear wave velocity of each layer are then adjusted until the values that produce the best fit to the experimental dispersion curve are identified. This identification procedure is usually referred to as *inversion* (Nazarian, 1984). For profiles in which the shear wave velocity varies irregularly with depth, the dispersion curve may be influenced by higher-mode Rayleigh waves (Gucunski and Woods, 1991; Tokimatsu et al., 1992).

SASW tests have a number of important advantages over other field tests. They can be performed quickly, they require no borehole, they can detect low-velocity layers, and they can be used to considerable depth (>100 m). Comparison of shear wave velocity profiles obtained from SASW testing and cross-hole testing (see the next section) have shown good agreement (Hiltunen and Woods, 1988). SASW testing is particularly useful at sites where drilling and sampling are difficult; it has been used successfully in such materials as

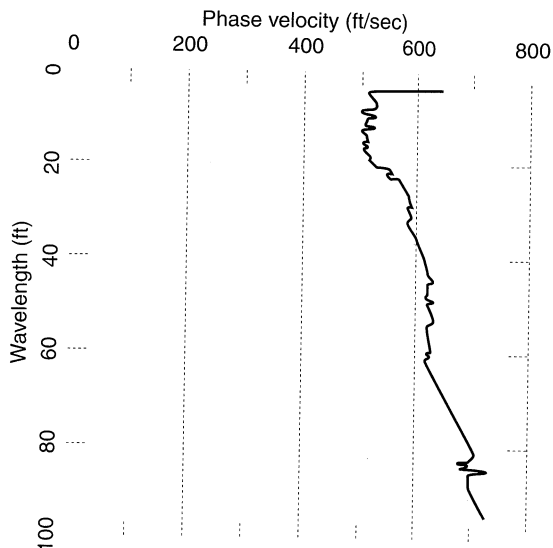


Figure 6.20 Experimental dispersion curve from SASW test. (After Gucunski and Woods, 1991; used by permission of the University of Missouri-Rolla.)

gravels and debris flow deposits (Stokoe et al., 1988) and landfills (Kavazanjian et al., 1994). The procedure does, however require specialized equipment and experienced operators. Its applicability is also limited to sites at which the assumptions of the Haskell-Thomson solution (e.g., horizontal layering) are at least approximately satisfied.

Seismic Cross-Hole Test. Seismic cross-hole tests use two or more boreholes to measure wave propagation velocities along horizontal paths. The simplest cross-hole test configuration (Figure 6.21a) consists of two boreholes, one of which contains an impulse energy source and the other a receiver. By fixing both the source and the receiver at the same depth in each borehole, the wave propagation velocity of the material between the boreholes at that depth is measured. By testing at various depths, a velocity profile can be obtained. When possible, use of more than two boreholes is desirable (Figure 6.21b) to minimize possible inaccuracies resulting from trigger time measurement, casing and backfill (material placed between the casing and the borehole wall) effects, and site anisotropy. Wave propagation velocities can then be calculated from differences in arrival times at adjacent pairs of boreholes. Arrival times can be determined by eye using points of common phase (first arrival, first peak, first trough, etc.) or by the type of cross-correlation techniques commonly used in petroleum exploration (Roesler, 1977).

Since the impulse sources must be located in the borehole, variation of the p-wave/s-wave content is more difficult than for methods in which it is at the surface. When explosive sources are used, the wave content is shifted toward higher p-wave content when larger charges are used, particularly when detonated above the ground surface (Woods, 1978). A number of mechanical impulse sources have been used, including the driving of a standard penetration test (Section 6.3.1.2) sampler, vertical impact loading of rods connected to borehole packers or jacks, torsional impact loading of a torque foot at the bottom of the borehole (Stokoe and Hoar, 1978), and other techniques (Applegate, 1974; Stokoe and Abdel-razzak, 1975; Auld, 1977). The best results are generally obtained when the polarity of the impulse

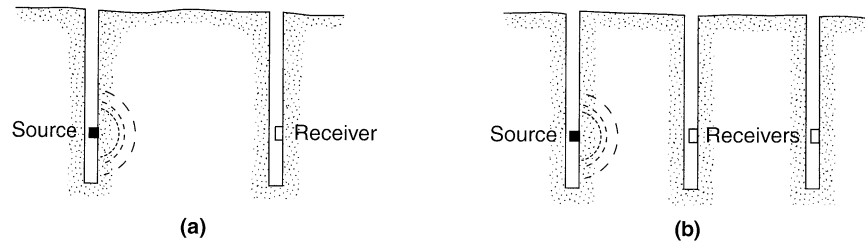


Figure 6.21 Seismic cross-hole test: (a) direct measurement using two-hole configuration; (b) interval measurement using three-hole configuration.

source is reversible, hence the frequent preference for mechanical sources over explosive sources.

The cross-hole test often allows individual soil layers to be tested since layer boundaries are frequently nearly horizontal. It can also detect hidden layers that can be missed by seismic refraction surveys. Cross-hole tests can yield reliable velocity data to depths of 30 to 60 m (100 to 200 ft) using mechanical impulse sources, and to greater depths with explosive sources. On the other hand, the sensitivity of the measured velocities to source–receiver distance often requires borehole deviation surveys, particularly for boreholes more than 15 to 20 m (50 to 65 ft) deep. The measured velocities may not be equal to the actual velocities when higher-velocity layers exist nearby. In such cases, more advanced methods of interpretation that can account for refraction (e.g., Butler et al., 1978) are required. Hryciw (1989) presented methods for correction of ray-path curvature in materials of continuously varying velocity.

Amplitude attenuation measurements from cross-hole tests involving three or more boreholes has been used to compute the material damping ratio of soils (Hoar and Stokoe, 1984; Mok et al., 1988; EPRI, 1993). The procedure requires accurately calibrated and oriented receivers that are well coupled to the borehole wall. By assuming a radiation pattern, the effects of geometric attenuation (radiation damping) can be separated from the measured attenuation to leave the attenuation due to material damping. The required assumptions render such approaches best suited to sites of simple geometry and homogeneous soil conditions.

Example 6.5

Determine the SV-wave velocity from the cross-hole test trigger and geophone records shown in Figure E6.5. The trigger and geophone are located 5 m apart. The solid line represents the response from a downward impact on a mechanical source and the dotted line represents the response from an upward impact.

Solution There is an obvious wave arrival at the geophone at about 2 msec after impact at the source. However, close examination of the geophone record shows that the polarity of this early arrival was not influenced by the polarity of the impact; consequently, the early arrival can be identified as a p-wave. At a later point, the arrival of waves whose polarity is reversed by the reversal of impact polarity is observed. These represent SV-waves—the arrival time of 23 msec after impact (determined graphically) indicates an SV-wave velocity of

$$v_s = \frac{x}{\Delta t} = \frac{5 \text{ m}}{0.023 \text{ sec}} = 217 \text{ m/sec}$$

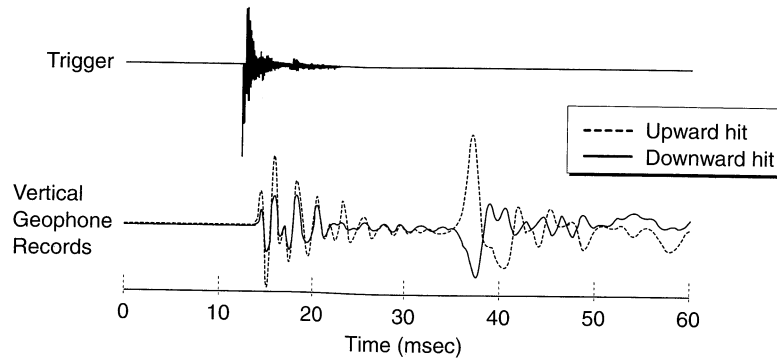


Figure E6.5

Seismic Down-Hole (Up-Hole) Test. Seismic down-hole (or up-hole) tests can be performed in a single borehole. In the down-hole test, an impulse source is located on the ground surface adjacent to the borehole. A single receiver that can be moved to different depths, or a string of multiple receivers at predetermined depths, is fixed against the walls of the borehole, and a single triggering receiver is located at the energy source (Figure 6.22). All receivers are connected to a high-speed recording system so that their output can be measured as a function of time. In the up-hole test, a movable energy source is located in the borehole with a single receiver on the ground surface adjacent to the borehole.

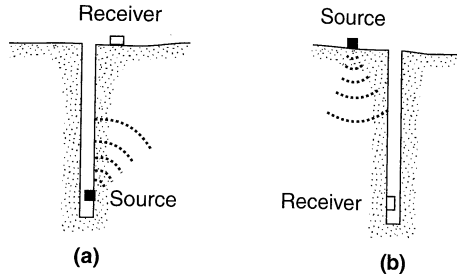


Figure 6.22 (a) Seismic up-hole test, and (b) seismic down-hole test.

The objective of the down-hole (or up-hole) test is to measure the travel times of p- and/or s-waves from the energy source to the receiver(s). By properly locating the receiver positions, a plot of travel time versus depth can be generated (Figure 6.23). The slope of the travel-time curve at any depth represents the wave propagation velocity at that depth.

S-waves can be generated much more easily in the down-hole test than the up-hole test; consequently, the down-hole test is more commonly used. With an SH-wave source, the down-hole test measures the velocity of waves similar to those that carry most seismic energy to the ground surface. Because the waves must travel through all materials between the impulse source and the receivers, the down-hole test allows detection of layers that can be hidden in seismic refraction surveys. Potential difficulties with down-hole (and up-hole) tests and their interpretation can result from disturbance of the soil during drilling of the borehole, casing and borehole fluid effects, insufficient or excessively large impulse sources, background

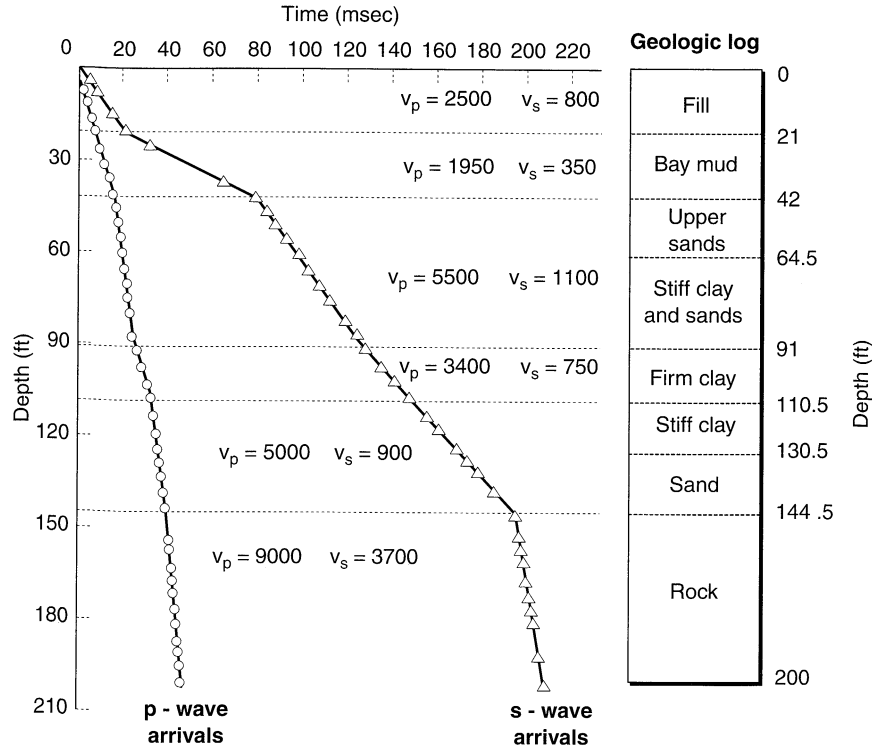


Figure 6.23 Travel-time curve from down-hole test in San Francisco Bay area. (After Schwarz and Musser, 1972.)

noise effects, and groundwater table effects. The effects of material and radiation damping on waveforms can make identification of s-wave arrivals difficult at depths greater than 30 to 60 m (100 to 200 ft). Efforts toward measurement of damping ratios in the down-hole test have also been made (Redpath et al., 1982; Redpath and Lee, 1986; EPRI, 1993).

Seismic Cone Test. The seismic cone test (Robertson et al., 1985) is very similar to the down-hole test, except that no borehole is required. A seismic cone penetrometer consists of a conventional cone penetrometer (Section 6.3.1.2) outfitted with a geophone or accelerometer mounted just above the friction sleeve. At different stages in the cone penetration sounding, penetration is stopped long enough to generate impulses at the ground surface, often by striking each end of a beam pressed against the ground by the outriggers of the cone rig, with an instrumented hammer. Travel time–depth curves can be generated and interpreted in the same way as for down-hole tests. Although down-hole (and up-hole) tests have usually been performed to complement other tests or to provide redundancy, the efficiency of the seismic cone test may lead to its more common use. Cross-hole seismic tests using two seismic cones have also been performed (e.g., Baldi et al., 1988).

6.3.1.2 High-Strain Tests

The field of in situ testing of soils has expanded tremendously in the past 25 years as a number of new devices and procedures have been developed and implemented. While

these tests are most commonly used to measure high-strain characteristics such as soil strength, their results have also been correlated to low-strain soil properties. For geotechnical earthquake engineering problems, the standard penetration test, cone penetration test, dilatometer test, and pressuremeter test are of particular interest.

Standard Penetration Test. The *standard penetration test* (SPT) is by far the oldest and most commonly used in situ test in geotechnical engineering. It is also commonly used in a number of geotechnical earthquake engineering applications. In the SPT, a standard split-barrel sampler (Figure 6.24) is driven into the soil at the bottom of a borehole by repeated blows (30 to 40 blows per minute) of a 140-lb (63.6 kg) hammer released from a height of 30 in (76 cm). The standard SPT sampler should have a constant inside diameter; the use of samplers designed to accommodate internal sample liners can underestimate penetration resistance by 10 to 20% when the liners are not in place. The sampler is usually driven 18 in. (46 cm); the number of blows required to achieve the last 12 in. (30 cm) of penetration is taken as the *standard penetration resistance*, N . The N value is a function of the soil type, confining pressure, and soil density, but is also influenced by the test equipment and procedures. In fact, studies have shown that different equipment and procedures are quite common both within the United States and other countries, and that they strongly influence the energy delivered to the soil by each blow of the hammer (Kovacs et al., 1977; Schmertmann et al., 1978; Kovacs and Salomone, 1982). Seed et al. (1985) recommended that the test be performed in 4- to 5-in.-diameter (10 to 13 cm) rotary boreholes with upward deflection of bentonite drilling mud using a tricone or baffled drag bit. The recommended sampler should have a constant inside diameter and be connected to A or AW [for depths less than 15 m (50 ft)] or N or NW (for greater depths) drill rods. Driving at a rate of 30 to 40 blows per minute with 60% of the theoretical free-fall energy delivered to the sampler was also recommended. It has become common to normalize the N value to an overburden pressure of 1 ton/ft² (100 kPa) and to correct it to an energy ratio of 60% (the average ratio of the actual energy delivered by safety hammers to the theoretical free-fall energy) according to

$$(N_1)_{60} = N_m C_N \frac{E_m}{0.60 E_{ff}} \quad (6.30)$$

where N_m is the measured penetration resistance, C_N an overburden correction factor (Figure 6.25), E_m the actual hammer energy, and E_{ff} the theoretical free-fall hammer energy. The corrected standard penetration resistance, $(N_1)_{60}$, has been correlated to many important properties of coarse-grained soils. Correlations for the properties of fine-grained soils are much less reliable.

Example 6.6

A site in Japan had the measured SPT resistances indicated in table E6.6. Ishihara (1993) indicated that the SPT procedures used in Japan deliver about 72% of the theoretical free-fall energy to the sampler. Assuming that the sands have an average void ratio of 0.44 and that the water table is at a depth of 1.5 m, compute the corresponding $(N_1)_{60}$ values.

Solution Given the void ratio of 0.44, and assuming that $G_s = 2.7$, the average dry and submerged densities of the sand are 1.874 Mg/m³ and 1.180 Mg/m³, respectively. These densities can be used to compute the vertical effective stress values that correspond to each depth at which the SPT resistance was measured (column 3 below). For example, the vertical effective stress at a depth of 6.2 m is given by

Table E6-6

Depth (m)	N_m	Depth (m)	N_m
1.2	7	11.2	23
2.2	4	12.2	13
3.2	3	13.2	11
4.2	3	14.2	11
5.2	5	15.2	24
6.2	9	16.2	27
7.2	12	17.2	5
8.2	12	18.2	6
9.2	14	19.2	4
10.2	9	20.2	38

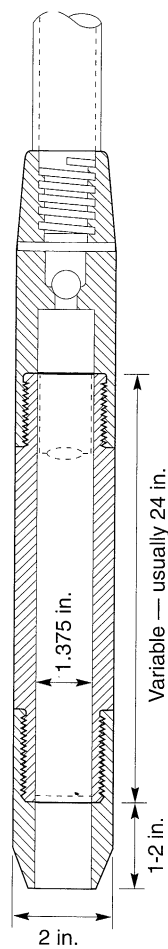


Figure 6.24 SPT sampler.

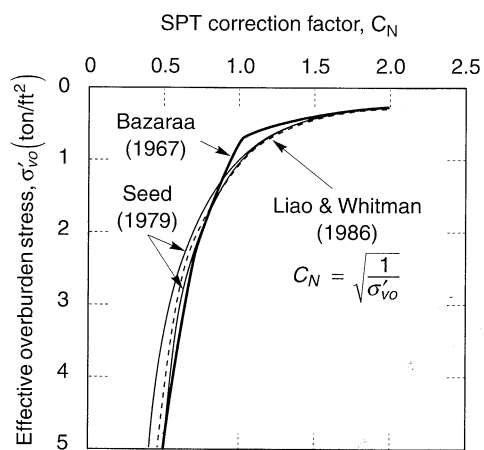


Figure 6.25 SPT overburden correction factor. (After Liao and Whitman, 1986.)

$$\sigma'_{v0} = \left[(1.5 \text{ m}) \left(1.874 \frac{\text{Mg}}{\text{m}^3} \right) + (4.7 \text{ m}) \left(1.180 \frac{\text{Mg}}{\text{m}^3} \right) \right] \left(9.81 \frac{\text{m}}{\text{sec}^2} \right) = 82.0 \text{ kPa}$$

By converting the vertical effective stresses from units of kPa to units of tons/ft², the value of the correction factor at each depth can be computed by the relationship of Liao and Whitman (1986) (column 4 below). For example, the correction factor at a depth of 6.2 m is given by

$$C_N = \sqrt{\frac{1}{(82.0 \text{ kPa})[(0.01044 \text{ tons/ft}^2)/\text{kPa}]}]} = 1.08$$

Then the corrected SPT resistances can be computed using equation (6.30) (column 6 below). For a depth of 6.2 m,

$$(N_1)_{60} = N_m C_N \frac{E_m}{0.60 E_{ff}} = (9)(1.08) \frac{0.72 E_{ff}}{0.60 E_{ff}} = 11.7$$

The appropriate values for all depths are tabulated below.

(1) Depth (m)	(2) N_m	(3) σ'_{v0} (kPa)	(4) C_N	(5) E_m/E_{ff}	(6) $(N_1)_{60}$
1.2	7	22.1	2.08	0.72	17.3
2.2	4	35.7	1.64	0.72	7.9
3.2	3	47.3	1.42	0.72	5.1
4.2	3	58.8	1.28	0.72	4.6
5.2	5	70.4	1.16	0.72	7.0
6.2	9	82.0	1.08	0.72	11.7
7.2	12	93.6	1.01	0.72	14.6
8.2	12	105.3	0.95	0.72	13.7
9.2	14	116.8	0.91	0.72	15.2
10.2	9	128.4	0.86	0.72	9.3
11.2	23	140.0	0.83	0.72	22.8
12.2	13	151.5	0.79	0.72	12.4
13.2	11	163.1	0.77	0.72	10.1
14.2	11	174.7	0.74	0.72	9.8
15.2	24	186.3	0.72	0.72	20.7
16.2	27	197.9	0.70	0.72	22.5
17.2	5	209.4	0.68	0.72	4.1
18.2	6	221.1	0.66	0.72	4.7
19.2	4	232.7	0.64	0.72	3.1
20.2	38	244.3	0.63	0.72	28.5

For gravelly soils, the *Becker hammer penetration test* (BPT) can be used in the same way as the SPT is for sands. In a recommended BPT procedure (Harder and Seed, 1986), a closed 6.6-in.-OD drill bit at the end of a 6.6-in. (16.8 cm) OD steel casing is driven into the soil by an ICE 180 diesel pile-driving hammer (8100 ft-lb/blow (110 N-m/blow) rated energy). The BPT resistance is taken as the number of blows per foot of penetration, corrected for variations in the diesel hammer bounce chamber pressure (which reflect the effects of soil resistance and combustion conditions on hammer energy). By comparing the results from the BPT and SPT at the same sandy sites, Harder and Seed (1986) found that the BPT and SPT resistances were related as shown in Table 6-1.

Rather than relying on bounce chamber pressures, Sy and Campanella (1994) used a pile driving analyzer to measure the maximum transferred energy, ENTHRU. With energy

Table 6.1 Equivalence of Corrected BPT and SPT Resistances

Corrected BPT Blowcount, N_{BC}	Corrected SPT Blowcount, N_{60}
0	0
20	~20
40	~34
60	~46
80	~58
100	~70

measurements, the BPT resistance can be corrected to a reference ENTHRU level of 30% of the rated energy of an ICE 180 diesel hammer

$$N_{b30} = N_b \frac{\text{ENTHRU}}{30}$$

where ENTHRU is expressed as a percentage. Considering the effects of skin resistance along the sides of the BPT casing, the graphical correlation with SPT resistance shown in Figure 6.26 was developed.

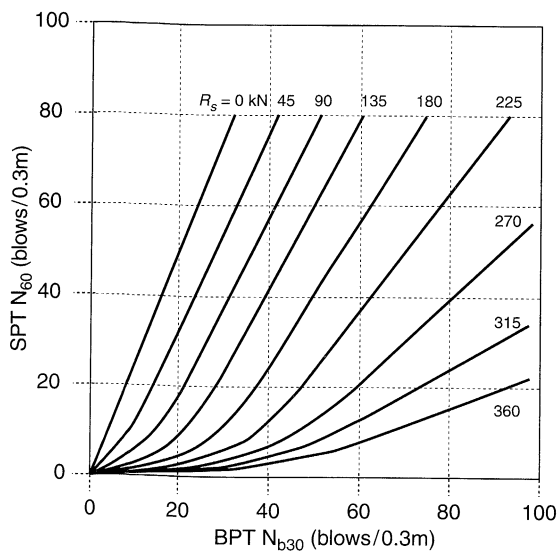


Figure 6.26 BPT-SPT correlations for different BPT shaft resistances. (After Sy and Campanella, 1984; used with permission.)

Cone Penetration Test. In recent years, use of the cone penetration test (CPT) in geotechnical engineering practice has increased sharply. The CPT involves the steady penetration of a standard cone penetrometer (Figure 6.27a) into the ground. The standard cone penetrometer has a conical tip of 10 cm^2 (1.55 in^2) area and 60° apex angle immediately below a cylindrical friction sleeve of 150 cm^2 (23.3 in^2) surface area. The penetrometer is pushed into the ground at a constant rate of 2 cm/sec (0.8 in/sec). The tip and friction sleeve are each connected to load cells that measure the tip resistance, q_c , and sleeve resistance, f_s , during penetration (Figure 6.27b). The friction ratio, $\text{FR} = f_s/q_c$, is also

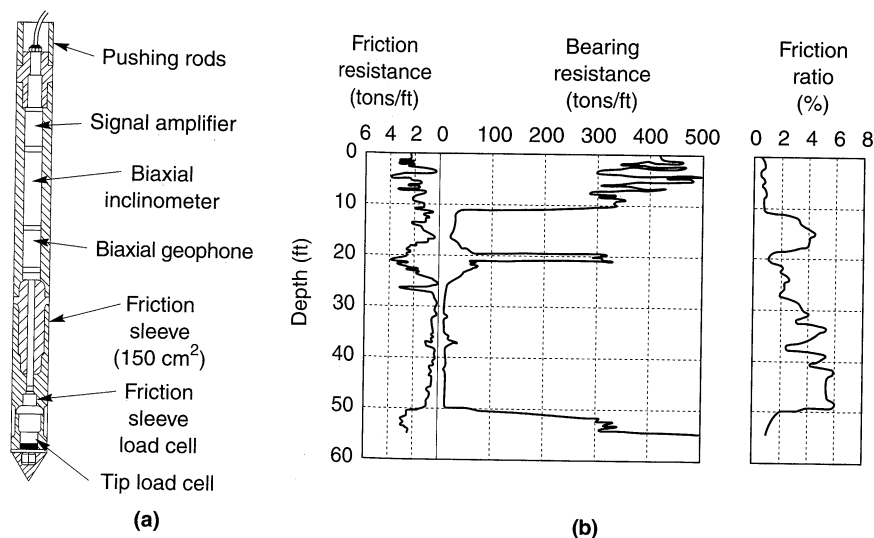


Figure 6.27 (a) Typical cone penetrometer with seismic cone capabilities (after Baldi et al., 1988); (b) results of cone penetration sounding (after Ward, 1986).

a useful parameter—it is high in cohesive soils and low in cohesionless soils. The absolute and relative magnitudes of the penetration resistances can be correlated to many of the same properties as the SPT, and also to soil type.

The CPT can be performed rapidly (usually about four times faster than drilling and sampling) and relatively inexpensively. It provides a continuous profile of penetration resistance that can detect the presence of thin layers or seams that are easily missed in SPT testing. The capabilities of cone penetrometers can be enhanced by adding additional transducers to measure additional variables such as porewater pressure (in the *piezocone*) or wave propagation velocity [in the *seismic CPT* (Section 6.3.1.1)]. However, the CPT cannot be used at sites with very stiff and/or very dense soils without damaging the probe or rods. The presence of gravel-size particles can also limit the use of the CPT.

Dilatometer Test. The *dilatometer test* (DMT) uses a flat dilatometer (Figure 6.28), a stainless steel blade with a thin flat circular expandable steel membrane on one side (Marchetti, 1980). The dilatometer is jacked into the ground with the membrane surface flush with the surrounding blade surface. At intervals of 10 to 20 cm (4 to 8 in.), penetration is stopped and the membrane inflated by pressurized gas. The pressure at which the membrane moves by 0.05 mm (0.002 in.) (the lift-off pressure, p_0) and the pressure at which its center moves 1.1 mm (0.043 in.) (p_1) are recorded, corrected, and used with the hydrostatic pressure, u_0 , and the effective overburden pressure, σ'_{v0} , to compute various indices to which soil properties can be correlated. The most commonly used of these indices are the material index, I_D , the horizontal stress index, K_D , and the dilatometer modulus, E_D , given by

$$I_D = \frac{p_1 - p_0}{p_1 - u_0} \quad (6.31)$$

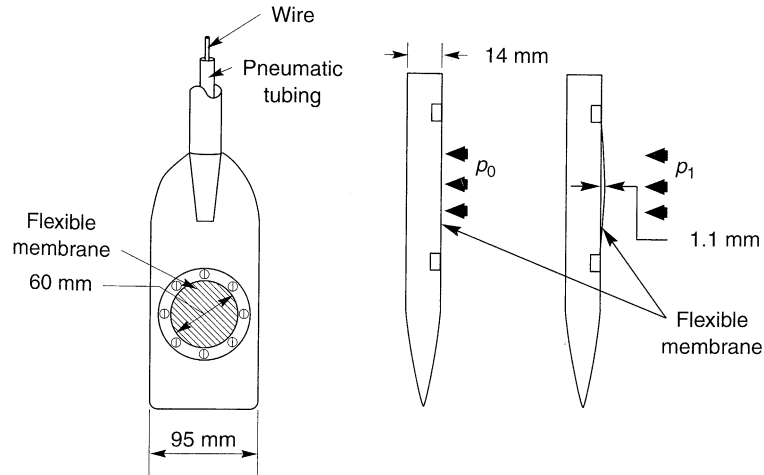


Figure 6.28 Front and side views of the Marchetti flat dilatometer. (After Baldi et al., 1986.)

$$K_D = \frac{p_0 - u_0}{\sigma'_{v0}} \tag{6.32}$$

$$E_D = \alpha(p_1 - p_0) \tag{6.33}$$

where α is equal to 34.7 for a 60-mm (2.4 in.) membrane diameter and a membrane deflection of 1.1 mm (0.043 in.). Dilatometer parameters have been correlated to low-strain soil stiffness (Section 6.4.2.1) and liquefaction resistance (Section 9.5.3.1).

Pressuremeter Test. The *pressuremeter test* (PMT) is the only in situ test capable of measuring stress–strain, as well as strength, behavior (Mair and Wood, 1987). The pressuremeter (Figure 6.29a) is a cylindrical device that uses a flexible membrane to

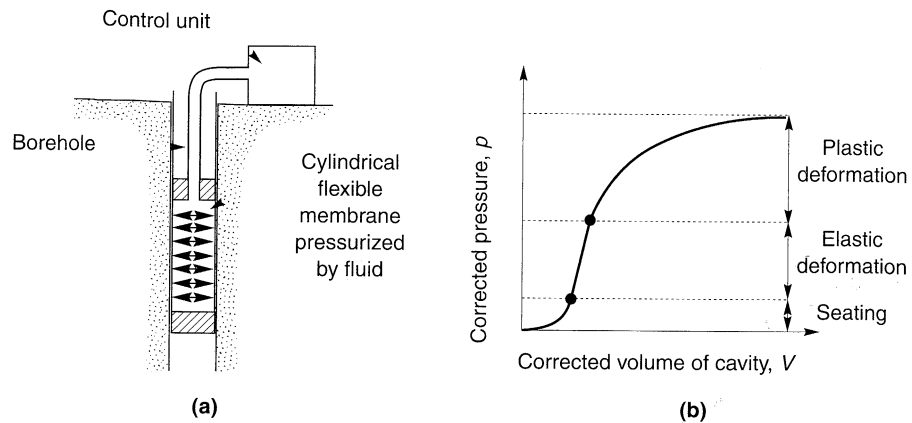


Figure 6.29 Pressuremeter test: (a) test setup; (b) typical pressuremeter curve. (After Mair and Wood, 1987.)

apply a uniform pressure to the walls of a borehole. Deformation of the soil can be measured by the volume of fluid injected into the flexible membrane or by feeler arms for pressuremeters that use compressed gas. After correcting the measured pressures and volume changes for system compliance, elevation differences, and membrane effects, a pressure–volume curve (Figure 6.29b) can be developed. Using cavity expansion theory, the pressure–volume curve can be used to compute the stress–strain behavior. Self-boring pressuremeters, which minimize soil disturbance, and push-in pressuremeters, which can penetrate soft soils very quickly, have also been developed.

Other Field Tests. A number of variations of the preceding tests have been used to measure dynamic soil properties, and new tests are also being developed. The concept of *geotomography* follows from advances in the medical imaging field (Johnson et al., 1978; Lytle, 1978). Using multiple sources and receivers, a large matrix of source–receiver travel times can be measured and compared with predictions of a ray-tracing model that can account for refraction and reflection at possible material boundaries between the sources and receivers. The number, position, and inclination of material boundaries are adjusted until the computed travel-time matrix matches the observed matrix. Although geotomography is still in its infancy, it offers the potential for rapid, detailed resolution of two- and three-dimensional subsurface structures. An apparatus that measures electrical conductivity of soil–porewater systems (Arulmoli et al., 1985) has been used to estimate in situ density and low-strain stiffness and to evaluate liquefaction potential. An *in situ borehole torsional test system* (Henke and Henke, 1991) advances two thin, concentric tubes into the soil at the bottom of a borehole. Records of rotation versus cyclic torque applied to the inner tube have shown behavior similar to that of stress–strain curves in controlled laboratory tests.

6.3.2 Laboratory Tests

Laboratory tests are usually performed on relatively small specimens that are assumed to be representative of a larger body of soil. The specimens are tested as *elements* (i.e., they are subjected to uniform initial stresses and uniform changes in stress or strain conditions). In other laboratory tests, specimens are tested as *models* and the results must be interpreted in terms of the nonuniform boundary conditions acting on the model.

The ability of laboratory tests to provide accurate measurements of soil properties depends on their ability to replicate the initial conditions and loading conditions of the problem of interest. No laboratory test can represent all possible stress and strain paths with general rotation of principal stress axes; consequently, different tests will be most suitable for different problems.

6.3.2.1 Sampling

Element tests are performed on soil specimens. For problems involving the response of soils to be placed as fills, specimens can be constructed from bulk or disturbed samples by simulating the compaction process as closely as possible in the laboratory. When the properties of an existing soil are needed, however, the problem becomes more difficult. Tests on existing soils can be performed on undisturbed or reconstituted specimens. However, in many instances the results will be different between these tests because of differences in soil fabric between natural and reconstituted soil specimens, even when densities and applied stresses are similar.

Dynamic soil properties are influenced by many factors, including density and stress conditions, and other factors, such as soil fabric or structure, age, stress and strain history, and cementation. While the void ratio and stress conditions can be recreated in a reconstituted specimen, the effects of the other factors cannot. Since the effects of these other factors are manifested primarily at low strain levels, they are easily destroyed by sample disturbance. For the results of laboratory tests to reflect the actual behavior of the in situ soil as closely as possible, high-quality undisturbed samples must be obtained.

For cohesive soils, procedures for the preparation of test specimens by carefully trimming thin-walled tube or block samples are fairly well established. Undisturbed sampling of cohesionless soils such as clean sands and gravels is more difficult. Even thin-walled sampling tubes can cause significant disturbance of clean sands, causing densification of loose sands and dilation of dense sands (Marcuson et al., 1977). The use of block sampling (Horn, 1978) has proven effective, but the process is laborious and may not be practical below certain depths. The use of freezing and coring was first described by Hvorslev (1949). This approach has been shown to be effective when the confining pressure is maintained and when free drainage is maintained continuously at the freezing front (Singh et al., 1979). Konno et al. (1993), for example, described the successful retrieval of undisturbed samples by coring through a 140-cm-diameter column of sandy gravel frozen by liquid nitrogen circulating through a central 73-mm steel tube for a period of about 160 hrs.

6.3.2.2 Low-Strain Element Tests

Only a limited number of laboratory tests are able to determine the properties of soils at low strain levels. These include the resonant column test, the ultrasonic pulse test, and the piezoelectric bender element test.

Resonant Column Test. The resonant column test is the most commonly used laboratory test for measuring the low-strain properties of soils. It subjects solid or hollow cylindrical specimens to harmonic torsional or axial loading by an electromagnetic loading system (Figure 6.30a). The loading systems usually apply harmonic loads for which the frequency and amplitude can be controlled, but random noise loading (Al-Sanad and Aggour, 1984) and impulse loading (Tawfiq et al., 1988) have also been used.

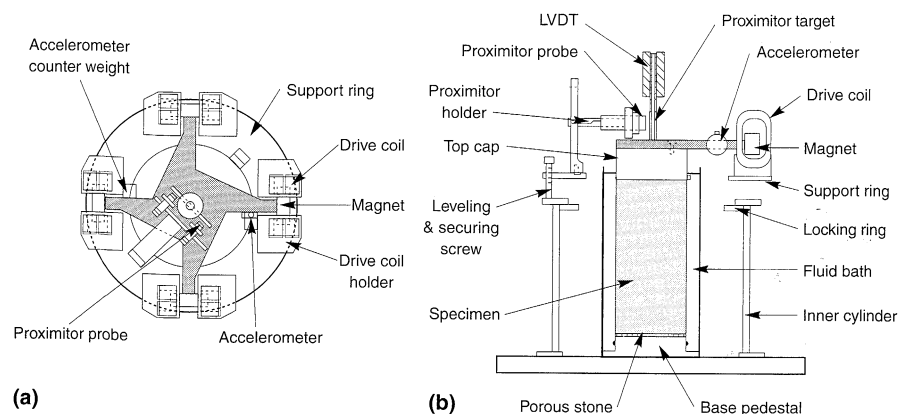


Figure 6.30 Typical resonant column test apparatus: (a) top view of loading system, and (b) profile view of loading system and soil specimen. (After EPRI, 1993.)

After the resonant column specimen has been prepared and consolidated, cyclic loading is begun. The loading frequency is initially set at a low value and is then gradually increased until the response (strain amplitude) reaches a maximum. The lowest frequency at which the response is locally maximized is the fundamental frequency of the specimen. The fundamental frequency is a function of the low-strain stiffness of the soil, the geometry of the specimen, and certain characteristics of the resonant column apparatus.

The shear modulus can be related to the fundamental frequency by the following procedure. Consider a resonant column specimen of height, h , fixed against rotation of its base, with polar moment of inertia, J , subjected to harmonic torsional loading (Figure 6.30b). From equation (5.8), the elastic resistance of the specimen produces a torque at its top,

$$T = GJ \frac{\partial \theta}{\partial z} = G \frac{I}{\rho} \frac{\partial \theta}{\partial z} \quad (6.34)$$

where I is the mass polar moment of inertia of the specimen. This torque must be equal to the inertial torque of the loading system. If the elements of the torsional loading system connected to the top of the specimen have a mass polar moment of inertia, I_0 , the inertial torque is

$$T = -I_0 h \frac{\partial^2 \theta}{\partial t^2} \quad (6.35)$$

Assuming that the rotations of the specimen are also harmonic, they can be described by

$$\theta(z, t) = \Theta(z)(C_1 \cos \omega t + C_2 \sin \omega t) \quad (6.36)$$

where $\Theta(z) = C_3 \cos kz + C_4 \sin kz$. The zero rotation boundary condition at the base ($z = 0$) requires $C_3 = 0$, and the equality of equations (6.34) and (6.35) requires, at the fundamental frequency, $\omega_n = k_n v_s$, so that

$$\begin{aligned} & G \frac{I}{\rho} C_4 k_n \cos k_n h (C_1 \cos \omega_n t + C_2 \sin \omega_n t) \\ &= -I_0 h (-\omega_n^2 C_4 \sin k_n h) (C_1 \cos \omega_n t + C_2 \sin \omega_n t) \end{aligned}$$

which can be expressed as

$$\frac{I}{I_0} = \frac{\omega_n h}{v_s} \tan \frac{\omega_n h}{v_s} \quad (6.37)$$

For a given specimen, I , I_0 , and h are generally known at the time that cyclic loading begins. The fundamental frequency is then obtained experimentally, and equation (6.37) is used to calculate v_s . The shear modulus is then obtained from $G = \rho v_s^2$. Damping can be determined from the frequency response curve using the half-power bandwidth method (Section B.6.1 of Appendix B) or from the logarithmic decrement by placing the specimen in free vibration.

For longitudinal loading, the analogous equation is

$$\frac{W}{W_0} = \frac{\omega_n h}{v_l} \tan \frac{\omega_n h}{v_l} \quad (6.38)$$

where W is the weight of the specimen, W_0 the weight of the loading system, and $v_l = \sqrt{E/\rho}$ the longitudinal wave propagation velocity.

If the loading system was massless ($I_0 = 0$), equation (6.37) would degrade to

$$v_s = \frac{2\omega_n h}{\pi} = 4f_n h \quad (6.39)$$

where f_n is the fundamental frequency in hertz. In this case the rotations would follow a quarter-sine-wave pattern over the height of the specimen at the fundamental frequency. Adding the mass of the loading system results in a more linear variation of rotation and, consequently, more uniform strain conditions over the height of the specimen.

The shear strain in a solid cylindrical resonant column specimen loaded in torsion varies from zero at the centerline of the specimen to a maximum value at its outer edge. In situations in which the shear modulus varies with shear strain amplitude, the effects of nonuniform strain can be significant (Drnevich, 1967, 1972). The use of hollow specimens minimizes the variation of shear strain amplitude across the specimen.

Large-diameter resonant column devices have been used for gravelly soils (Woods, 1991) and rock (Prange, 1981). Konno et al. (1993) performed what could be described as in situ resonant column tests of gravelly soils at a potential nuclear power plant site in Japan. In these tests the material in two 10-m-ID (32.8 ft) circular trenches was excavated and replaced with water-filled bags to depths of 5 m (16 ft) and 9 m (30 ft). Concrete cap blocks 3 (10 ft) and 5 m (16 ft) thick were cast on top of each of the resulting soil columns. Vibratory shakers were placed on top of the blocks near the edges; cyclic torsional loading was applied to the soil column by operating the jacks 180° out of phase. By performing frequency sweeps, the response of the soil columns could be measured at shear strain amplitudes up to 0.01%.

Example 6.7

A 6-in.-high specimen of soft silty clay with a unit weight of 105 lb/ft³ is tested in a resonant column device with $I/I_0 = 0.4$. From the frequency response curve shown in Figure E6.7, determine the shear modulus of the specimen.

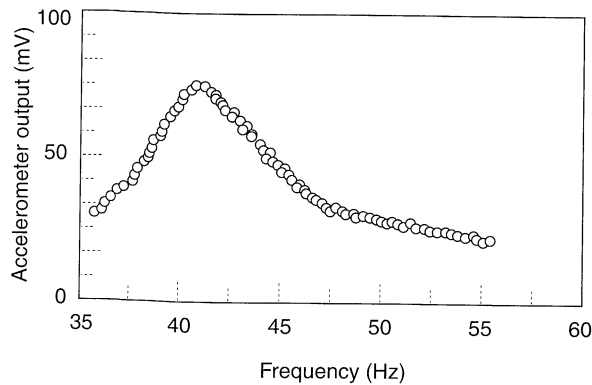


Figure E6.7

Solution The maximum amplitude of the accelerometer output occurs at the fundamental frequency of the specimen, determined graphically to be

$$f_n = 41 \text{ Hz}$$

Then equation (6.37) can be written as

$$\frac{I}{I_0} = \frac{\omega_n h}{v_s} \tan \frac{\omega_n h}{v_s} = 0.4$$

which is satisfied when $\omega_n h/v_s = 0.593$. Then

$$v_s = \frac{\omega_n h}{0.593} = \frac{2\pi f_n h}{0.593} = \frac{2\pi(41)(0.5)}{0.593} = 212 \text{ ft/sec}$$

$$G = \rho v_s^2 = \frac{105 \text{ lb/ft}^3}{32.2 \text{ ft/sec}^2} (212 \text{ ft/sec})^2 = 146,557 \text{ lb/ft}^2$$

The resonant column test allows stiffness and damping characteristics to be measured under controlled conditions. The effects of effective confining pressure, strain amplitude, and time can readily be investigated. However, measurement of porewater pressure is difficult, and the material properties are usually measured at frequencies above those of most earthquake motions.

Ultrasonic Pulse Test. Wave propagation velocities can be measured in the laboratory by means of the ultrasonic pulse test (Lawrence, 1963; Nacci and Taylor, 1967). Ultrasonic transmitters and receivers are attached to platens that can be placed at each end of a specimen with the distance separating them carefully measured. The transmitters and receivers are made of piezoelectric materials which exhibit changes in dimensions when subjected to a voltage across their faces, and which produce a voltage across their faces when distorted. A high-frequency electrical pulse applied to the transmitter causes it to deform rapidly and produce a stress wave that travels through the specimen toward the receiver. When the stress wave reaches the receiver, it generates a voltage pulse that is measured. The distance between the transmitter and receiver is divided by the time difference between the voltage pulses to obtain the wave propagation velocity. The ultrasonic pulse test is particularly useful for very soft materials, such as seafloor sediments, since it can be performed while the soil is still in the sampling tube (Woods, 1978).

Piezoelectric Bender Element Test. Another type of test that allows measurement of shear wave velocity on laboratory specimens makes use of piezoelectric bender elements (Shirley and Anderson, 1975; De Alba et al., 1984; Dyvik and Madhus, 1985). Bender elements are constructed by bonding two piezoelectric materials together in such a way that a voltage applied to their faces causes one to expand while the other contracts, causing the entire element to bend as shown in Figure 6.31. Similarly, a lateral disturbance of the bender element will produce a voltage, so the bender elements can be used as both s-wave transmitters and receivers.

In most setups, the bender elements protrude into opposite ends of a soil specimen. A voltage pulse is applied to the transmitter element, which causes it to produce an s-wave.

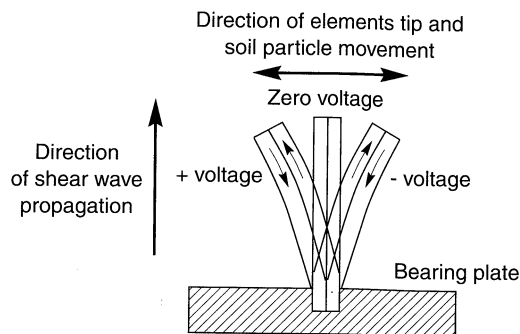


Figure 6.31 Piezoelectric bender element. Positive voltage causes element to bend one way, negative voltage causes it to bend the other.

When the s-wave reaches the other end of the specimen, distortion of the receiver element produces another voltage pulse. The time difference between the two voltage pulses is measured with an oscilloscope and divided into the distance between the tips of the bender elements to give the s-wave velocity of the specimen.

Piezoelectric bender elements have been incorporated into conventional and cubical triaxial devices, direct simple shear devices, oedometers, and model tests. Since the specimen is not disturbed during the bender element test, it can be subsequently tested for other soil characteristics.

6.3.2.3 High-Strain-Element Tests

At high shear strain amplitudes, soils generally exhibit volume change tendencies. Under drained loading conditions, these tendencies are allowed to manifest themselves in the form of volumetric strain, but under undrained conditions they result in changes in pore pressure (and effective stress). Since soil behavior is governed by effective stresses, all methods of testing soils at high strain levels must be capable of controlling porewater drainage from the specimen and measuring volume changes and/or pore pressures accurately. The problem of *system compliance* (volume changes due to the testing apparatus rather than the soil), which can lead to errors in volume change/pore pressure measurement, is important in the interpretation of high-strain test results. *Membrane penetration* in coarse-grained soil is an important contributor to system compliance.

Cyclic Triaxial Test. Just as the triaxial compression test is the most commonly used laboratory test for measurement of soil properties under static loading conditions, the cyclic triaxial test has been the most commonly used test for measurement of dynamic soil properties at high strain levels. In the triaxial test, a cylindrical specimen is placed between top and bottom loading platens and surrounded by a thin rubber membrane (Figure 6.32). The specimen is subjected to a radial stress, usually applied pneumatically, and an axial stress. By virtue of these boundary conditions, the principal stresses in the specimen are always vertical and horizontal.

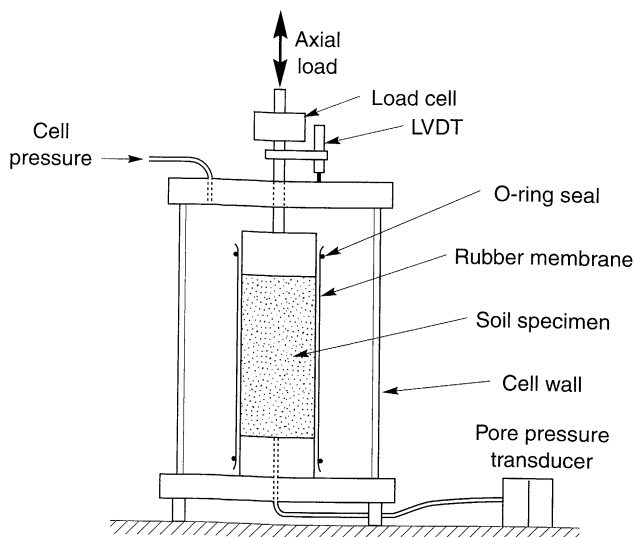


Figure 6.32 Typical triaxial apparatus.

The difference between the axial stress and the radial stress is called the *deviator stress*. In the cyclic triaxial test, the deviator stress is applied cyclically, either under stress-controlled conditions (typically by pneumatic or hydraulic loaders), or under strain-controlled conditions (by servohydraulic or mechanical loaders). Cyclic triaxial tests are most commonly performed with the radial stress held constant and the axial stress cycled at a frequency of about 1 Hz.

As with the static triaxial test, the cyclic triaxial test can be performed under isotropically consolidated or anisotropically consolidated conditions, thereby producing the stress paths shown in Figure 6.33. Figure 6.33a shows the cyclic deviator stress and total stress path for an isotropically consolidated specimen. Isotropically consolidated tests are commonly used to represent level-ground sites where no initial shear stresses exist on horizontal planes. The test begins with zero shear stress (point A) and the deviator stress is initially increased. Since the axial stress is then greater than the radial stress, the major and minor principal stress axes are vertical and horizontal, respectively. After the deviator stress reaches its maximum value (point B), it decreases and approaches a value of zero (point C). Just before it reaches point C, the major principal stress axis is still vertical, but it rotates instantaneously to horizontal as point C is passed and the deviator stress becomes negative. At point C, no shear stress exists on the specimen. This process of stress reversal repeats itself throughout the test, with instantaneous 90° rotations of the principal stress axes occurring every time the deviator stress passes through zero.

To model conditions in and beneath slopes where initial static shear stresses exist, anisotropically consolidated triaxial tests are performed. Figure 6.33b refers to an anisotropically consolidated specimen for which the cyclic deviator stress amplitude is greater than the deviator stress during consolidation. Stress reversals also exist in this situation, even though the cyclic deviator stress is no longer symmetric about the *p*-axis. If the cyclic deviator stress

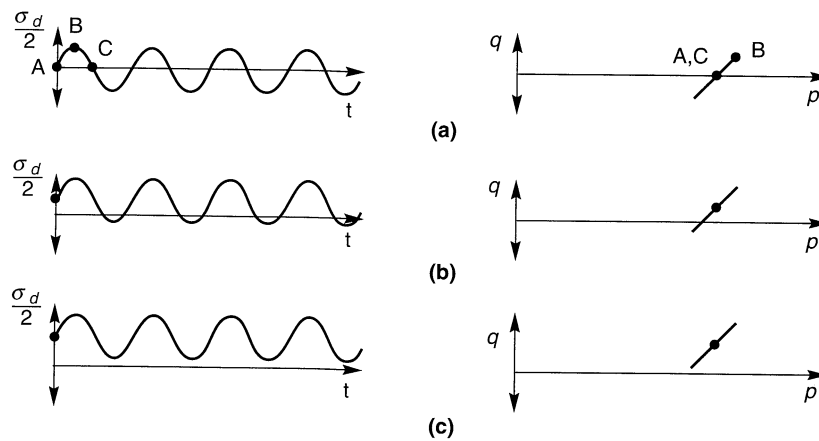


Figure 6.33 Time histories of deviator stress and stress paths for (a) isotropically consolidated conditions, (b) anisotropically consolidated conditions with cyclic deviator stress amplitude greater than deviator stress during consolidation (producing stress reversals), and (c) anisotropically consolidated conditions with cyclic deviator stress amplitude less than deviator stress during consolidation (no stress reversals).

amplitude is smaller than the deviator stress during consolidation (Figure 6.33c), no stress reversals will occur. For this case, the principal stress axes will not rotate and the specimen will never reach the zero shear stress condition. The stress paths in Figure 6.33 are obviously different with respect to initial stress conditions, stress path, and principal stress axis rotation than those imposed on the element of soil subjected to vertically propagating *s*-waves shown in Figure 6.7. These differences illustrate the fundamental difficulty in the direct application of properties obtained from the cyclic triaxial test to actual wave propagation problems.

In some cases, the cell pressure is also applied cyclically. By decreasing (or increasing) the cell pressure by the same amount that the deviator stress is increased (or decreased) by, the Mohr circle can be made to expand and contract about a constant center point. The resulting stress path will then oscillate vertically, much like that shown for the case of vertically propagating *s*-waves (Figure 6.7). Although the stress path of such a triaxial test can be made to match that induced by a vertically propagating *s*-wave, the principal stresses in the triaxial test remain constrained to the vertical and horizontal direction rather than rotating continuously as caused by the *s*-wave.

The stresses and strains measured in the cyclic triaxial test can be used to compute the shear modulus and damping ratio (Section 6.4.2). The cyclic triaxial test allows stresses to be applied uniformly, although stress concentrations can exist at the cap and base, and allows drainage conditions to be accurately controlled (when the effects of membrane penetration are mitigated). It requires only minor modification of standard triaxial testing equipment. On the other hand, the cyclic triaxial test cannot model stress conditions that exist in most actual seismic wave propagation problems. Bedding errors and system compliance effects generally limit measurements to shear strains greater than about 0.01%, although local strain measurement (e.g., Burland and Symes, 1982; Ladd and Dutko, 1985; Goto et al., 1991) can produce accurate measurements at strain levels as small as 0.0001%.

Membrane penetration effects can be important in cyclic triaxial tests of coarse sands and gravels. After consolidation, the thin triaxial membrane will penetrate the perimeter voids of coarse sand and gravel specimens. As excess pore pressures develop during cyclic loading, the net pressure on the membrane decreases and its penetration decreases. When this happens, the effective volume of the voids increases and the excess pore pressure drops below the level it would have had if true constant-volume conditions had been maintained. Because they allow the effective stresses to be higher than they would be under constant-volume conditions, membrane penetration effects can lead to inaccurate stiffness and damping measurements and unconservative estimation of liquefaction resistance (Chapter 9). Procedures have been developed for measurement (Vaid and Negussey, 1984; Kramer and Sivaneswaran, 1989a), minimization (Lade and Hernandez, 1977; Raju and Venkataramana, 1980), compensation (Seed and Anwar, 1986; Tokimatsu and Nakamura, 1986), and posttest correction (Martin et al., 1978; Kramer and Sivaneswaran, 1989b) of membrane penetration effects.

Example 6.8

A cyclic triaxial test on a saturated clay specimen produces the stress–strain loop shown in Figure E6.8. Determine the secant shear modulus and damping ratio.

Solution Graphically, the slope of a straight line between the ends of the stress–strain curve shows that

$$E_{\text{sec}} = \frac{236 \text{ kPa}}{0.014} = 16,857 \text{ kPa}$$

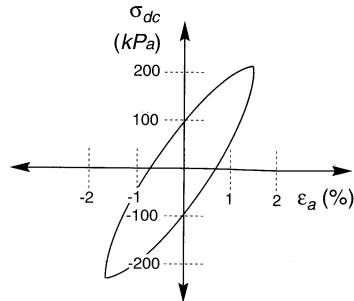


Figure E6.8

Then, assuming that the saturated clay is loaded under undrained conditions, $\nu = 0.5$, so

$$G_{\text{sec}} = \frac{E}{2(1 + \nu)} = \frac{16,857 \text{ kPa}}{2(1 + 0.5)} = 5619 \text{ kPa}$$

The area of the hysteresis loop is 4.52 kPa and the area of the triangle denoting the maximum strain energy is 1.65 kPa. Then

$$\xi = \frac{1}{4\pi} \frac{\text{area of hysteresis loop}}{\text{area of triangle}} = \frac{4.52 \text{ kPa}}{1.65 \text{ kPa}} = 0.218$$

Cyclic Direct Simple Shear Test. The cyclic direct simple shear test is capable of reproducing earthquake stress conditions much more accurately than is the cyclic triaxial test. It is most commonly used for liquefaction testing. In the cyclic direct simple shear test, a short, cylindrical specimen is restrained against lateral expansion by rigid boundary platens (Cambridge-type device), a wire-reinforced membrane (NGI-type device), or a series of stacked rings (SGI-type device). By applying cyclic horizontal shear stresses to the top or bottom of the specimen, the test specimen is deformed (Figure 6.34) in much the same way as an element of soil subjected to vertically propagating s-waves (Figure 6.7).

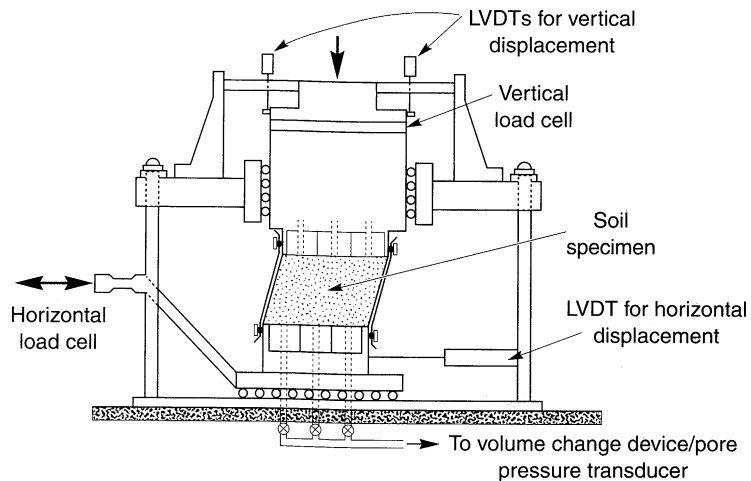


Figure 6.34 NGI cyclic simple shear apparatus. Soil specimen is contained within wire-reinforced rubber membrane. (After Airey and Wood, 1987.)

The simple shear apparatus, however, applies shear stresses only on the top and bottom surfaces of the specimen. Since no complementary shear stresses are imposed on the vertical sides, the moment caused by the horizontal shear stresses must be balanced by non-uniformly distributed shear and normal stresses. The effects of nonuniformity of stresses can be reduced by increasing the diameter/height ratio of the specimen; such effects are small at diameter/height ratios greater than about 8:1 (Kovacs and Leo, 1981). Conventional simple shear apparatuses are limited by their inability to impose initial stresses other than those corresponding to K_0 conditions. In recent years, simple shear devices that allow independent control of vertical and horizontal stresses have been developed. To better simulate actual earthquake conditions, Pyke (1973) used a large shaking table to produce a two-directional large-scale simple shear apparatus with a diameter/height ratio of about 9 in one direction and 20 in the other. Small-scale, bidirectional, cyclic simple shear apparatuses have also been developed (Boulanger et al., 1993).

Cyclic Torsional Shear Test. Many of the difficulties associated with the cyclic triaxial and cyclic direct simple shear tests can be avoided by loading cylindrical soil specimens in torsion. Cyclic torsional shear tests allow isotropic or anisotropic initial stress conditions and can impose cyclic shear stresses on horizontal planes with continuous rotation of principal stress axes. They are most commonly used to measure stiffness and damping characteristics over a wide range of strain levels.

Ishihara and Li (1972) developed a torsional triaxial test that used solid specimens. Dobry et al. (1985) used strain-controlled cyclic torsional loading along with stress-controlled axial loading of solid specimens to develop a CyT-CAU test that has proven effective for measurement of liquefaction behavior. Torsional testing of solid specimens, however, produces shear strains that range from zero along the axis of the specimen to a maximum value at the outer edge. To increase the radial uniformity of shear strains, others (e.g., Drnevich, 1967, 1972) developed hollow cylinder cyclic torsional shear apparatuses (Figure 6.35). While hollow cylinder tests offer perhaps the best uniformity and control

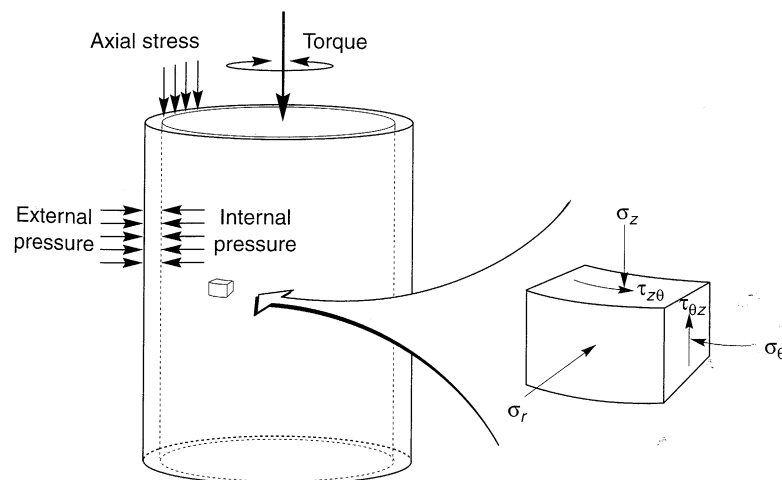


Figure 6.35 Hollow cylinder apparatus. The specimen is enclosed within internal and external membranes on which internal and external pressures can be applied independently. Application of cyclic torque induces cyclic shear stresses on horizontal planes.

over stresses and drainage, specimen preparation can be difficult and the equipment is not widely available.

6.3.2.4 Model Tests

In contrast to element tests, model tests usually attempt to reproduce the boundary conditions of a particular problem by subjecting a small-scale physical model of a full-scale *prototype structure* to cyclic loading. Model tests may be used to evaluate the performance of a particular prototype or to study the effects of different parameters on a general problem. While model testing is very useful for identification of important phenomena and verification of predictive theories, it has not yet developed to the point of being used directly for design of significant structures or facilities.

The behavior of soils is sensitive to stress level; soils that exhibit contractive behavior under high normal stresses may exhibit dilative behavior at lower stress levels. One of the most significant challenges in model testing, therefore, is the problem of testing models whose stress dependency matches that of the full-scale prototype. Because this is very difficult under the gravitational field of the earth, one common approach involves testing under increased gravitational fields. Model tests can therefore be divided into those performed under the gravitational field of the earth (1g model tests) and those performed under higher gravitational accelerations. The 1g tests are most commonly performed with the use of shaking tables; tests under increased gravitational fields are usually performed in a geotechnical centrifuge.

Both shaking table and centrifuge model tests share certain drawbacks, among the most important of which are similitude and boundary effects. Because different aspects of the response of a 1/N-scale model are governed by different scale factors, similitude cannot be assured for all parameters simultaneously. Boundary effects are usually associated with the metallic bins or boxes in which shaking table and centrifuge models are usually constructed. The sidewalls can restrain soil movement and reflect energy that would radiate away in the prototype problem. The industrial filler material Duxseal has been used as an absorbent wall lining with some success (Steedman, 1991).

Shaking Table Tests. In the early years of geotechnical earthquake engineering, virtually all physical model testing was performed on shaking tables. Shaking table research has provided valuable insight into liquefaction, postearthquake settlement, foundation response, and lateral earth pressure problems. Most shaking tables utilize a single horizontal translation degree of freedom, but shaking tables with multiple degrees of freedom have also been developed. Shaking tables are usually driven by servohydraulic actuators (Figure 6.36); their dynamic loading capacities are controlled by the capacity of the hydraulic pumps that serve the actuators. Large pumps and large actuators are required to produce large displacements of heavy models at moderate or high frequencies.

Shaking tables of many sizes have been used for geotechnical earthquake engineering research. Some are quite large, allowing models with dimensions of several meters to be tested. Thus shaking tables can often utilize actual, prototype soils rather than resorting to the smaller particle sizes often required for smaller scale model tests. For these large models, soils can be placed, compacted relatively easily, and instrumented relatively easily. Shaking table models can be easily viewed from different perspectives during testing.

On the other hand, high gravitational stresses cannot be produced in a shaking table test. Though the contractive behavior associated with high normal stresses at significant

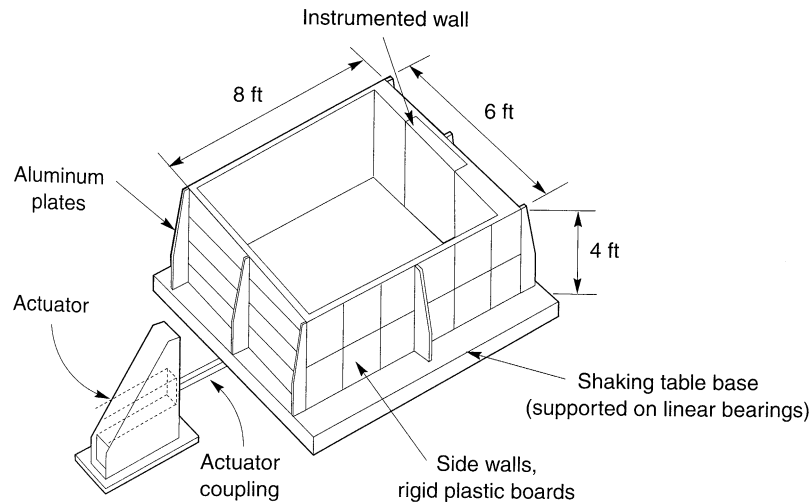


Figure 6.36 Shaking table with soil bin used for dynamic earth pressure research. (After Sherif et al., 1982.)

depths can be simulated by placing soil very loosely during model preparation, the process of preparing such models is quite difficult. Because of the low normal stress levels, the contribution of factors that produce a cohesive component of strength will be greater in the model than in the prototype. Correction procedures (e.g., Hettler and Gudehus, 1985; Iai, 1989) have been developed to aid in the interpretation of shaking table test results.

Centrifuge Tests. In a centrifuge test, a $1/N$ -scale model located at a distance, r , from the axis of a centrifuge (Figure 6.37) is rotated at a rotational speed, $\Omega = \sqrt{N/r}$, which is sufficient to raise the acceleration field at the location of the model to N times the acceleration of gravity. In principle, the stress conditions at any point in the model should then be identical to those at the corresponding point in the full-scale prototype. The overall behavior (e.g., displacements, failure mechanisms, etc.) should also be identical.

Centrifuge tests are restricted to much smaller models than even moderate-sized shaking tables. Since the gravitational field increases with radial distance, the gravitational

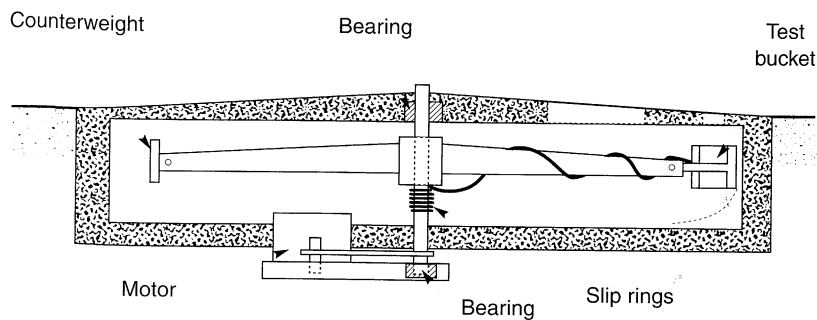


Figure 6.37 Cross section through a geotechnical centrifuge. (After O'Reilly, 1991.)

acceleration at the top of the model is lower than that at the bottom of the model. Since the gravitational field acts in the radial direction, the horizontal plane is curved (O'Reilly, 1991) by an amount that decreases with increasing centrifuge radius.

Similitude considerations are very important in the planning and interpretation of centrifuge tests. Scaling factors for a number of parameters are shown in Table 6-2. The scaling factors show how dynamic events are speeded up in the centrifuge. For example, the stresses and strains in a 30-m (100-ft)-high prototype earth dam could be modeled with a 30-cm (1-ft)-high centrifuge model accelerated to 100g (of course, the particle size of the model soil will correspond to a prototype particle size that is 100 times larger, too). A harmonic 1-Hz base motion lasting 10 sec at the prototype scale would be modeled by a 100-Hz motion lasting 0.1 sec in the model. The dissipation of any generated pore pressures, however, would occur 10,000 times as fast in the model as in the field. For this reason, viscous fluids such as glycerin or silicon oil are often used as pore fluids in centrifuge models. Improved estimates of prototype behavior can be obtained using the modeling of models technique (Schofield, 1980), which involves comparing the response of models of different size at the same prototype scale.

Obviously, high-speed transducers and data acquisition systems are required to obtain useful results in dynamic centrifuge tests. Because the scaling laws apply to all parts of the model, miniaturized transducers and cables are required to minimize their influence on the response of the model.

Table 6-2 Scaling Factors for Centrifuge Modeling^a.

Type of Event	Quantity	$\frac{\text{Model Dimension}}{\text{Prototype Dimension}}$
All events	Stress	1
	Strain	1
	Length	1/N
	Mass	1/N ³
	Density	1
	Force	1/N ²
Dynamic events	Gravity	N
	Time	1/N
	Frequency	N
	Acceleration	N
Diffusion events	Strain rate	N
	Time	1/N ²
	Strain rate	N ²

Source: After Kutter and James (1989).

^aValues are based on the assumption that the same soils and fluid are used in the model and the prototype and that the soil properties are not rate dependent.

Other Model Tests. In recent years the hydraulic gradient similitude test, originally developed by Zelikson (1969), has been used to measure dynamic soil properties (e.g., Yan and Byrne, 1990, 1991). The hydraulic gradient similitude test achieves high body forces by subjecting a model to a controlled, downward-acting hydraulic gradient. Since the body forces are aligned with flow lines, the presence of flow obstructions or nonuniform soil

conditions can cause “gravity” to act in different directions at different locations. Such effects complicate interpretation of the test results and restrict the use of the test to a relatively narrow range of problems.

6.3.3 Interpretation of Observed Ground Response

Interpretation of the response of instrumented, full-scale structures subjected to dynamic loading or earthquakes can provide invaluable information on dynamic soil properties and other geotechnical earthquake engineering parameters. This approach requires well-instrumented sites, either with vertical arrays or closely spaced instruments at soil and rock sites. At such sites the actual motions at the base and surface of a soil deposit can be used with a suitable ground response model (Chapter 7) to identify the dynamic soil properties (specifically, shear modulus and damping) that produce the best agreement between predicted and actual motions (e.g., Abdel-Ghaffar and Scott, 1979; Tokimatsu and Midorikawa, 1981; Chang et al., 1991; Glaser, 1995). Obviously, this approach requires an earthquake to produce ground motions, and the strain levels to which the dynamic soil properties can be measured are controlled by the strains produced by the earthquake. Examples of observed ground response from which dynamic soil properties can be identified are presented in Sections 8.2.2 and 8.2.3. As instrumentation and remote data acquisition systems continue to improve, more full-scale response data are likely to become available.

6.4 STRESS–STRAIN BEHAVIOR OF CYCLICALLY LOADED SOILS

The mechanical behavior of soils can be quite complex under static, let alone seismic loading conditions. Geotechnical engineers are constantly challenged by the need to characterize the most important aspects of cyclic soil behavior as accurately as possible with simple, rational models. The point at which the conflicting requirements of simplicity and accuracy are balanced depends on many factors, and many combinations have been proposed.

For the purposes of this book, three broad classes of soil models will be discussed: *equivalent linear models*, *cyclic nonlinear models*, and *advanced constitutive models*. Of these, equivalent linear models are the simplest and most commonly used but have limited ability to represent many aspects of soil behavior under cyclic loading conditions. At the other end of the spectrum, advanced constitutive models can represent many details of dynamic soil behavior, but their complexity and difficulty of calibration currently renders them impractical for many common geotechnical earthquake engineering problems. Nevertheless, each class of soil model reveals important information about the cyclic behavior of soils.

6.4.1 Some Basic Aspects of Particulate Matter Behavior

Before considering specific stress–strain models, it is useful to examine some basic aspects of the mechanical behavior of particulate media. Several important aspects of low-strain soil behavior can be illustrated by considering the soil as an assemblage of discrete elastic particles. Hertz (1881) studied the behavior of identical spheres of radius, R , compressed against each other by a normal force, N (Timoshenko and Goodier, 1951), and showed that

$$N = \frac{2\sqrt{2}GR^{3/2}}{3(1-\nu)}\delta_N^{3/2} \quad (6.40)$$

where G and ν are the elastic constants of the spheres and δ_N is the change in distance between the centers of the spheres. For a cubically packed array of spheres loaded along one of the packing axes (Figure 6.38), the average normal stress is obtained by dividing the normal force by its tributary area, that is,

$$\sigma = \frac{N}{(2R)^2} = \frac{N}{4R^2} \tag{6.41}$$

Then the tangent modulus for uniaxial loading is given by

$$E_{\text{tan}} = \frac{d\sigma}{d\varepsilon} = \frac{dN/4R^2}{d\delta_N/2R} = \frac{1}{2R} \frac{dN}{d\delta_N} = \frac{3}{2} \left[\frac{2G}{3(1-\nu)} \right]^{2/3} \sigma^{1/3} \tag{6.42}$$

which suggests that the stiffness should, theoretically, vary with the cube root of the axial stress. When a tangential force, T , is applied, elastic distortion causes the centers of the spheres to be displaced perpendicular to their original axis (Mindlin and Deresiewicz, 1953; Dobry et al., 1982) by an amount

$$\delta_T = \left[1 - \left(1 - \frac{T}{fN} \right)^{2/3} \right] \left\{ \frac{3fN}{4E} (2-\nu)(1+\nu) \left[\frac{3(1-\nu^2)NR}{4E} \right]^{-1/3} \right\} \quad T \leq fN \tag{6.43}$$

where f is the coefficient of friction between the spheres (note that δ_T is a nonlinear function of T). When T becomes equal to fN , gross sliding of the particle contacts occurs (though slippage of part of the contact can occur before this point). This gross sliding is required for permanent particle reorientation; consequently, volume changes (drained conditions) cannot occur and excess pore pressures (undrained conditions) cannot be generated when gross sliding does not occur. The shear strain corresponding to the initiation of gross sliding

$$\gamma_{iv} = \frac{\delta_T(T = fN)}{2R} = 2.08 \frac{(2-\nu)(1+\nu)f}{(1-\nu^2)^{1/2} E^{2/3}} \sigma^{2/3} \tag{6.44}$$

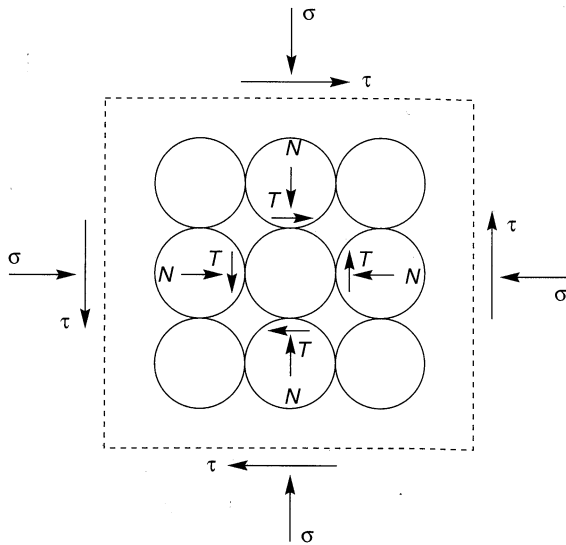


Figure 6.38 Cubically packed assemblage of spheres subjected to normal stress, σ , and shear stress, τ , that produce interparticle contact forces N and T . (After Dobry et al., 1982.)

is called the *volumetric threshold shear strain*. When the properties of quartz ($E = 11 \times 10^6$ psi (7.6×10^7 kPa), $\nu = 0.31$, $f = 0.50$) are substituted into equation (6.44), the threshold shear strain is given by

$$\gamma_{tv}(\%) = 0.000175 \sigma^{2/3} \quad (6.45)$$

where σ is in psf. For confining pressures of practical interest (500 to 4000 psf (25 to 200 kPa)), equation (6.44) would predict a threshold shear strain between 0.01 and 0.04%. Real soils, of course, do not consist of regular arrays of spherical particles, but the existence of a threshold shear strain very close to that predicted by equation (6.44) has been observed experimentally for sands under both drained (Drnevich and Richart, 1970; Youd, 1972; Pyke, 1973) and undrained (Park and Silver, 1975; Dobry and Ladd, 1980; Dobry et al., 1982) loading conditions. The simple idealized analysis of a regular array of spheres helps illustrate the reason for its existence. Experimental evidence suggests that the volumetric threshold shear strain increases with plasticity index (PI); the volumetric threshold shear strain of a clay with PI = 50 is approximately one order of magnitude greater than that of a sand, with PI = 0 (Vucetic, 1994). Experimental evidence also indicates (Vucetic, 1994) that soils exhibit linear elastic behavior below a linear cyclic threshold shear strain, γ_{tl} , that is approximately 30 times smaller than γ_{tv} .

Such analyses of the interaction of individual soil particles can provide insight into the mechanical behavior of soils. In recent years, tremendous advances have been made in *micromechanical modeling* of soils. Micromechanical models account for the kinematics and contact interactions of individual soil particles, thereby eliminating the need for a global constitutive model. A number of computational models have been developed with various restrictions on dimensionality, particle shape and size distribution, particle kinematics, and contact behavior (e.g., Cundall and Strack, 1979; Ting et al., 1989; Ng and Dobry, 1994). Although the computational effort involved in tracking the motion of each individual particle is currently too large to allow their use for practical problems with complicated boundary conditions, they have provided useful insight into several aspects of soil behavior.

6.4.2 Equivalent Linear Model

A typical soil subjected to symmetric cyclic loading as would be expected beneath a level ground surface far from adjacent structures, might exhibit a hysteresis loop of the type shown in Figure 6.39. This hysteresis loop can be described in two ways: first, by the actual path of the loop itself, and second, by parameters that describe its general shape. In general terms, two important characteristics of the shape of a hysteresis loop are its inclination and its breadth. The inclination of the loop depends on the stiffness of the soil, which can be described at any point during the loading process by the *tangent shear modulus*, G_{tan} . Obviously, G_{tan} varies throughout a cycle of loading, but its average value over the entire loop can be approximated by the secant shear modulus

$$G_{sec} = \frac{\tau_c}{\gamma_c} \quad (6.46)$$

where τ_c and γ_c are the shear stress and shear strain amplitudes, respectively. Thus G_{sec} describes the general inclination of the hysteresis loop. The breadth of the hysteresis loop is

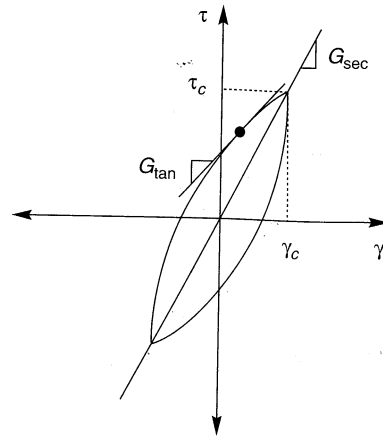


Figure 6.39 Secant shear modulus, G_{sec} , and tangent shear modulus, G_{tan} .

related to the area, which as a measure of energy dissipation, can conveniently be described (Section B.6.1) by the damping ratio

$$\xi = \frac{W_D}{4\pi W_S} = \frac{1}{2\pi} \frac{A_{\text{loop}}}{G_{\text{sec}} \gamma_c^2} \quad (6.47)$$

where W_D is the dissipated energy, W_S the maximum strain energy, and A_{loop} the area of the hysteresis loop. The parameters G_{sec} and ξ are often referred to as *equivalent linear* material parameters. For certain types of ground response analyses, they are used directly to describe the soil behavior; other types of analyses require the actual path of the hysteresis loop as described by a cyclic nonlinear or advanced constitutive model. Both types of ground response analysis are described in Chapter 7.

Because some of the most commonly used methods of ground response analysis are based on the use of equivalent linear properties, considerable attention has been given to the characterization of G_{sec} and ξ for different soils. It is important to recognize, however, that the equivalent linear model is only an approximation of the actual nonlinear behavior of the soil. The assumption of linearity embedded in its use has important implications when it is used for ground response analysis, as discussed in Chapter 7. It also means that it cannot be used directly for problems involving permanent deformation or failure; equivalent linear models imply that the strain will always return to zero after cyclic loading, and since a linear material has no limiting strength, failure cannot occur. Nevertheless, the assumption of linearity allows a very efficient class of computational models to be used for ground response analyses, and it is commonly employed for that reason.

6.4.2.1 Shear Modulus

Laboratory tests have shown that soil stiffness is influenced by cyclic strain amplitude, void ratio, mean principal effective stress, plasticity index, overconsolidation ratio, and number of loading cycles. The secant shear modulus of an element of soil varies with cyclic shear strain amplitude. At low strain amplitudes, the secant shear modulus is high, but it decreases as the strain amplitude increases. The locus of points corresponding to the tips of hysteresis loops of various cyclic strain amplitudes is called a *backbone* (or *skeleton*)

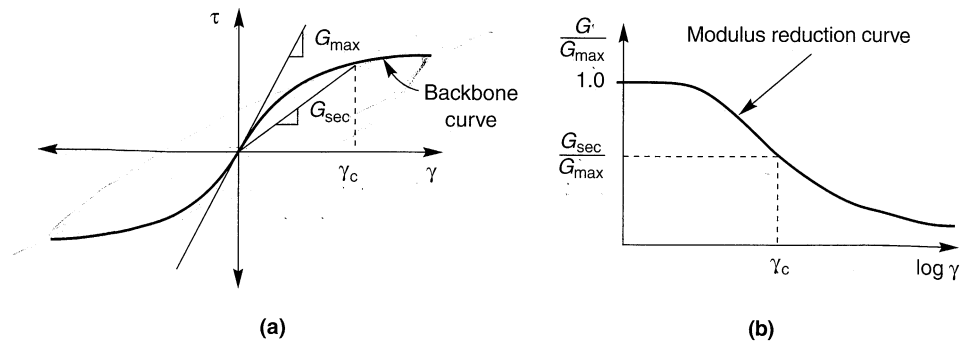


Figure 6.40 Backbone curve showing typical variation of G_{sec} with shear strain.

curve (Figure 6.40a); its slope at the origin (zero cyclic strain amplitude) represents the largest value of the shear modulus, G_{max} . At greater cyclic strain amplitudes, the modulus ratio $G_{\text{sec}}/G_{\text{max}}$ (the “sec” subscript will hereafter be dropped for convenience and consistency with the notation commonly used in the geotechnical earthquake engineering literature) drops to values of less than 1. Characterization of the stiffness of an element of soil therefore requires consideration of both G_{max} and the manner in which the modulus ratio G/G_{max} varies with cyclic strain amplitude and other parameters. The variation of the modulus ratio with shear strain is described graphically by a modulus reduction curve (Figure 6.40b). The modulus reduction curve presents the same information as the backbone curve; either one can be determined from the other.

Maximum Shear Modulus, G_{max} . Since most seismic geophysical tests induce shear strains lower than about $3 \times 10^{-4}\%$, the measured shear wave velocities can be used to compute G_{max} as

$$G_{\text{max}} = \rho v_s^2 \quad (6.48)$$

The use of measured shear wave velocities is generally the most reliable means of evaluating the in situ value of G_{max} for a particular soil deposit, and the seismic geophysical tests described in Section 6.3.1.1 are commonly used for that purpose. Care must be taken in the interpretation of shear wave velocity, particularly at sites with anisotropic stress conditions, which can cause measured shear wave velocities to vary with the direction of wave propagation and particle movement (Roesler, 1979; Stokoe et al., 1985; Yan and Byrne, 1991).

When shear wave velocity measurements are not available, G_{max} can be estimated in several different ways. Laboratory test data suggest that the maximum shear modulus can be expressed as

$$G_{\text{max}} = 625 F(e) (\text{OCR})^k p_a^{1-n} (\sigma'_m)^n \quad (6.49)$$

where $F(e)$ is a function of the void ratio, OCR the overconsolidation ratio, k an overconsolidation ratio exponent (Table 6-3), σ'_m the mean principal effective stress [$\sigma'_m = (\sigma'_1 + \sigma'_2 + \sigma'_3)/3$], n a stress exponent, and p_a is atmospheric pressure in the same units as σ'_m and G_{max} . Hardin (1978) proposed that $F(e) = 1/(0.3 + 0.7e^2)$, while Jamiolkowski et al. (1991) suggested that $F(e) = 1/e^{1.3}$. The stress exponent is often taken as $n = 0.5$ but can be computed

Table 6-3 Overconsolidation Ratio Exponent, K

Plasticity Index	k
0	0.00
20	0.18
40	0.30
60	0.41
80	0.48
≥ 100	0.50

Source: After Hardin and Drnevich (1972b).

for individual soils from the results of laboratory tests at different effective confining pressures. It should be apparent that G_{max} , p_a , and σ'_m must be expressed in the same units. Equation (6.49) can also be used to adjust measured G_{max} values to represent conditions that are different (e.g., increased effective stresses) from those at which the measurements were made.

Other empirical relationships have been proposed for specific soil types. The maximum shear modulus of sand, for example, is often estimated as

$$G_{max} = 1000 K_{2,max} (\sigma'_m)^{0.5} \tag{6.50}$$

where $K_{2,max}$ is determined from the void ratio or relative density (Table 6-4) and σ'_m is in lb/ft^2 (Seed and Idriss, 1970). Field tests have consistently shown that shear wave velocities of gravels are significantly higher than those of sands, indicating that G_{max} of gravel is higher than that of sand. $K_{2,max}$ values for gravels are typically in the range 80 to 180 (Seed et al., 1984). For fine-grained soils, preliminary estimates of the maximum shear modulus can be obtained from plasticity index, overconsolidation ratio, and undrained strength (Table 6-5). Because undrained strengths are highly variable and because shear moduli an undrained strengths vary differently with effective confining pressure, these results must be used carefully.

Table 6-4 Estimation of $K_{2,max}$

e	$K_{2,max}$	D_r (%)	$K_{2,max}$
0.4	70	30	34
0.5	60	40	40
0.6	51	45	43
0.7	44	60	52
0.8	39	75	59
0.9	34	90	70

Source: Adapted from Seed and Idriss (1970).

The maximum shear modulus can also be estimated from in situ test parameters. A number of empirical relationships between G_{max} and various in situ test parameters have been developed; some of the more widely published are presented in Table 6-6. The inherent difficulty of correlating a small strain parameter such as G_{max} with penetration parameters that relate to much larger strains is evident from the scatter in the data on which they are based and from the variability of the results obtained by different investigators. As such, the usefulness of such correlations is currently limited to preliminary estimates of G_{max} .

Table 6-5 Values of G_{\max}/s_u ^a

Plasticity Index	Overconsolidation Ratio, OCR		
	1	2	5
15–20	1100	900	600
20–25	700	600	500
35–45	450	380	300

Source: After Weiler (1988).

^aUndrained strength measured in CU triaxial compression.

However, the application of in situ testing to geotechnical earthquake engineering problems is only in its early stages, and significant advances can be expected as additional data become available.

Evaluation of shear modulus can be complicated by rate and time effects (Anderson and Woods, 1975, 1976; Anderson and Stokoe, 1978; Isenhowe and Stokoe, 1981). Rate effects can cause G_{\max} to increase with increasing strain rate. The influence of strain rate on G_{\max} increases with increasing soil plasticity; for San Francisco Bay mud (PI \approx 40), G_{\max} increases about 4% per tenfold increase in strain rate. Rate effects can be significant when comparing G_{\max} values obtained from field shear wave velocity measurements (usually made with the use of impulsive disturbances which produce relatively high frequencies) with values obtained from laboratory tests. The shear wave velocity, and hence G_{\max} , increases approximately linearly with the logarithm of time past the end of primary consolidation to an extent that cannot be attributed solely to the effects of secondary compression. The change of stiffness with time can be described by

$$\Delta G_{\max} = N_G (G_{\max})_{1000} \quad (6.51)$$

where ΔG_{\max} is the increase in G_{\max} over one log cycle of time and $(G_{\max})_{1000}$ is the value of G_{\max} at a time of 1000 min past the end of primary consolidation. N_G increases with increasing plasticity index, PI, and decreases with increasing OCR (Kokushu et al., 1982). For normally consolidated clays, N_G can be estimated from the relationship

$$N_G \approx 0.027 \sqrt{\text{PI}}$$

Anderson and Woods (1975) showed that some of the discrepancy between G_{\max} values from field and laboratory tests could be explained by time effects, and that N_G could be used to correct the G_{\max} values from laboratory tests to better represent actual in situ conditions.

A brief summary of the effects of environmental and loading conditions on the maximum shear modulus of normally and moderately overconsolidated soils is presented in Table 6-7.

Modulus Reduction, G/G_{\max} . In the early years of geotechnical earthquake engineering, the modulus reduction behaviors of coarse- and fine-grained soils were treated separately (e.g., Seed and Idriss, 1970). Recent research, however, has revealed a gradual transition between the modulus reduction behavior of nonplastic coarse-grained soil and plastic fine-grained soil.

Zen et al. (1978) and Kokushu et al. (1982) first noted the influence of soil plasticity on the shape of the modulus reduction curve; the shear modulus of highly plastic soils was

Table 6-6 Empirical Relationships between G_{max} and In Situ Test Parameters

In Situ Test	Relationship	Soil Type	References	Comments
SPT	$G_{max} = 20,000(N_1)_{60}^{0.333}(\sigma'_m)^{0.5}$	Sand	Ohta and Goto (1976), Seed et al. (1986)	G_{max} and σ'_m in lb/ft ²
	$G_{max} = 325N_{60}^{0.68}$	Sand	Imai and Tonouchi (1982)	G_{max} in kips/ft ²
	$G_{max} = 1634(q_c)^{0.250}(\sigma'_v)^{0.375}$	Quartz sand	Rix and Stokoe (1991)	G_{max} , q_c , and σ'_v in kPa; Based on field tests in Italy and on calibration chamber tests
DMT	(Figure 6.41)	Silica sand	Baldi et al. (1986)	G_{max} , q_c , and σ'_v in kPa; Based on field tests in Italy
	$G_{max} = 406(q_c)^{0.695}e^{-1.130}$	Clay	Mayne and Rix (1993)	G_{max} , q_c , and σ'_v in kPa; Based on field tests at worldwide sites
	$G_{max} / E_d = 2.72 \pm 0.59$	Sand	Baldi et al. (1986)	Based on calibration chamber tests
	$G_{max} / E_d = 2.2 \pm 0.7$	Sand	Bellotti et al. (1986)	Based on field tests
	$G_{max} = \frac{530}{(\sigma'_v / p_a)^{0.25}} \frac{\gamma_D / \gamma_w - 1}{2.7 - \gamma_D / \gamma_w} K_0^{0.25} (p_a \sigma'_v)^{0.5}$	Sand, silt, clay	Hryciw (1990)	G_{max} , p_a , σ'_v in same units; γ_D is dilatometer-based unit weight of soil; based on field tests
PMT	$3.6 \leq \frac{G_{max}}{G_{ur,c}} \leq 4.8$	Sand	Bellotti et al. (1986)	$G_{ur,c}$ is corrected unloading-reloading modulus from cyclic PMT
	$G_{max} = \frac{1.68}{\alpha_p} G_{ur}$	Sand	Byrne et al. (1991)	G_{ur} is secant modulus of unloading-reloading portion of PMG; α_p is factor that depends on unloading-reloading stress conditions; based on theory and field test data

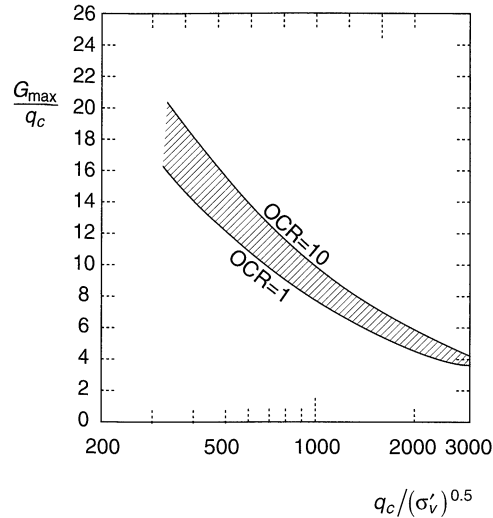


Figure 6.41 Estimation of G_{\max} from CPT tip resistance for uncemented silica sands. (After Baldi et al., 1989.)

Table 6-7 Effect of Environmental and Loading Conditions on Maximum Shear Modulus of Normally Consolidated and Moderately Overconsolidated Soils

Increasing Factor	G_{\max}
Effective confining pressure, σ'_m	Increases with σ'_m
Void ratio, e	Decreases with e
Geologic age, t_g	Increases with t_g
Cementation, c	Increases with c
Overconsolidation ratio, OCR	Increases with OCR
Plasticity index, PI	Increases with PI if OCR > 1; stays about constant if OCR = 1
Strain rate, $\dot{\gamma}$	No effect for non-plastic soils; increases with $\dot{\gamma}$ for plastic soils (up to ~10% increase per log cycle increase in $\dot{\gamma}$)
Number of loading cycles, N	Decreases after N cycles of large γ_c , but recovers later with time in clays; increases with N for sand

Source: Modified from Dobry and Vucetic (1987).

observed to degrade more slowly with shear strain than did low-plasticity soils. After reviewing experimental results from a broad range of materials, Dobry and Vucetic (1987) and Sun et al. (1988) concluded that the shape of the modulus reduction curve is influenced more by the plasticity index than by the void ratio and presented curves of the type shown in Figure 6.42. These curves show that the linear cyclic threshold shear strain, γ_{th} , is greater for highly plastic soils than for soils of low plasticity. This characteristic is extremely important; it can strongly influence the manner in which a soil deposit will amplify or attenuate earthquake motions. The $PI = 0$ modulus reduction curve from Figure 6.42 is very similar to the

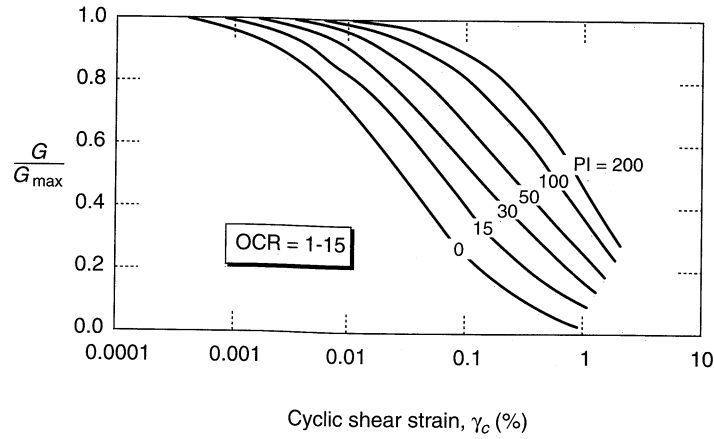


Figure 6.42 Modulus reduction curves for fine-grained soils of different plasticity. (After Vucetic and Dobry (1991). Effect of soil plasticity on cyclic response. *Journal of Geotechnical Engineering*, Vol. 117, No. 1. Reprinted by permission of ASCE.)

average modulus reduction curve that was commonly used for sands (Seed and Idriss, 1970) when coarse- and fine-grained soils were treated separately. This similarity suggests that the modulus reduction curves of Figure 6.42 may be applicable to both fine- and coarse-grained soils (this conclusion should be confirmed for individual coarse-grained soils, particularly those that could exhibit aging or cementation effects). The difficulty of testing very large specimens has precluded the widespread testing of gravelly soils in the laboratory, but available test data indicate that the average modulus reduction curve for gravel is similar to, though slightly flatter than, that of sand (Seed et al., 1986; Yasuda and Matsumoto, 1993).

Modulus reduction behavior is also influenced by effective confining pressure, particularly for soils of low plasticity (Iwasaki et al., 1978; Kokoshu, 1980). The linear cyclic threshold shear strain, γ_{tb} , is greater at high effective confining pressures than at low effective confining pressures. The effects of effective confining pressure and plasticity index on modulus reduction behavior were combined by Ishibashi and Zhang (1993) in the form

$$\frac{G}{G_{\max}} = K(\gamma, \text{PI}) (\sigma'_m)^{m(\gamma, \text{PI}) - m_o} \quad (6.52)$$

where

$$K(\gamma, \text{PI}) = 0.5 \left\{ 1 + \tanh \left[\ln \left(\frac{0.000102 + n(\text{PI})}{\gamma} \right)^{0.492} \right] \right\}$$

$$m(\gamma, \text{PI}) - m_o = 0.272 \left\{ 1 - \tanh \left[\ln \left(\frac{0.000556}{\gamma} \right)^{0.47} \right] \right\} \exp(-0.0145 \text{PI}^{1.3})$$

$$n(\text{PI}) = \begin{cases} 0.0 & \text{for PI} = 0 \\ 3.37 \times 10^{-6} \text{PI}^{1.404} & \text{for } 0 < \text{PI} \leq 15 \\ 7.0 \times 10^{-7} \text{PI}^{1.976} & \text{for } 15 < \text{PI} \leq 70 \\ 2.7 \times 10^{-5} \text{PI}^{1.115} & \text{for PI} > 70 \end{cases}$$

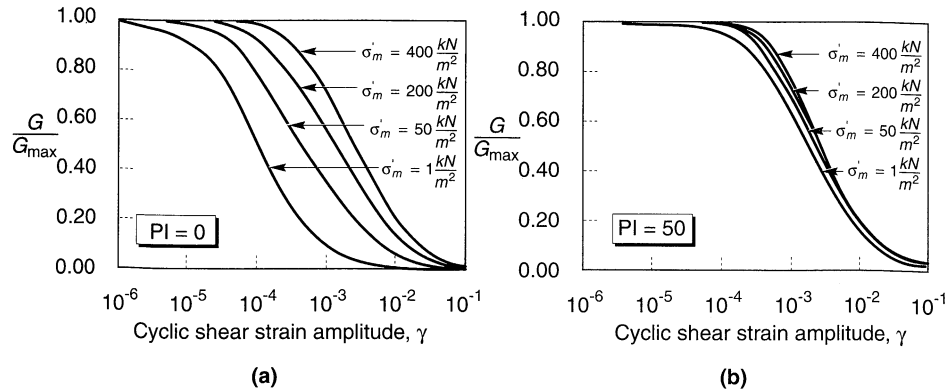


Figure 6.43 Influence of mean effective confining pressure on modulus reduction curves for (a) nonplastic ($PI = 0$) soil, and (b) plastic ($PI = 50$) soil. (After Ishibashi (1992). Discussion, *Journal of Geotechnical Engineering*, Vol. 118, No. 5. Reprinted by permission of ASCE.)

The effect of confining pressure on modulus reduction behavior of low- and high-plasticity soils is illustrated in Figure 6.43.

Under stress-controlled harmonic loading conditions, pore pressure generation and structural changes can cause the shear strain amplitude of a soil specimen to increase with increasing number of cycles. If clay or saturated sand specimens are loaded harmonically under strain-controlled undrained conditions, the shear stress amplitude would be observed to decrease with increasing number of cycles. Both conditions illustrate the tendency for repeated cyclic loads to degrade the stiffness of the specimen. For cohesive soils, the value of the shear modulus after N cycles, G_N , can be related to its value in the first cycle, G_1 , by

$$G_N = \delta G_1 \quad (6.53)$$

where the *degradation index*, δ , is given by $\delta = N^{-t}$ and t is the *degradation parameter* (Idriss et al., 1978). The degradation parameter has been shown to decrease with increasing PI and increasing overconsolidation ratio, and to increase with increasing cyclic strain amplitude (Idriss et al., 1980; Vucetic and Dobry, 1989; Tan and Vucetic, 1989). The effects of stiffness degradation on modulus reduction behavior is shown in Figure 6.44.

The influence of various environmental and loading conditions on the modulus ratio of normally consolidated and moderately overconsolidated clays is described in Table 6-8.

6.4.2.2 Damping Ratio

Theoretically, no hysteretic dissipation of energy takes place at strains below the linear cyclic threshold shear strain. Experimental evidence, however, shows that some energy is dissipated even at very low strain levels (the mechanism is not well understood), so the damping ratio is never zero. Above the threshold strain, the breadth of the hysteresis loops exhibited by a cyclically loaded soil increase with increasing cyclic strain amplitude, which indicates that the damping ratio increases with increasing strain amplitude.

Just as modulus reduction behavior is influenced by plasticity characteristics, so is damping behavior (Kokushu et al., 1982; Dobry and Vucetic, 1987; Sun et al., 1988). Damping ratios of highly plastic soils are lower than those of low plasticity soils at the same

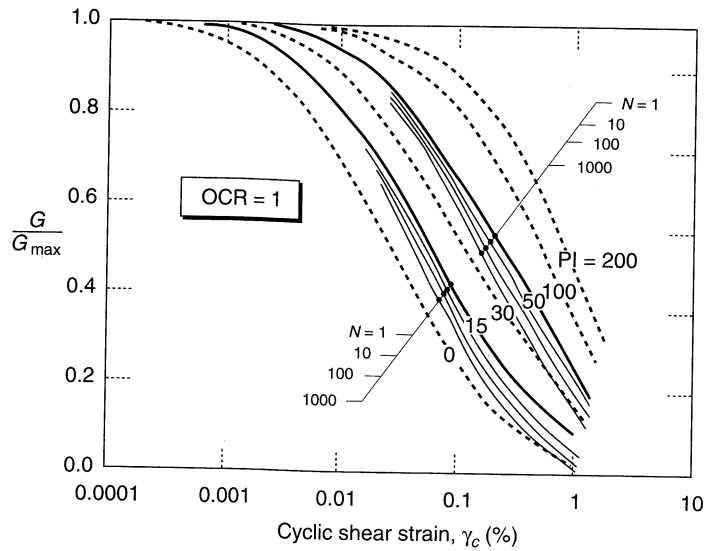


Figure 6.44 Effect of cyclic degradation on shear modulus. (After Vucetic and Dobry (1991). Effect of soil plasticity on cyclic response, *Journal of Geotechnical Engineering*, Vol 117, No. 1. Reprinted by permission of ASCE.)

Table 6-8. Effect of Environmental and Loading Conditions on Modulus Ratio (at a Given Strain Level) of Normally Consolidated and Moderately Overconsolidated Soils

Increasing Factor	G/G_{max}
Confining pressure, σ'_m	Increases with σ'_m ; effect decreases with increasing PI
Void ratio, e	Increases with e
Geologic age, t_g	May increase with t_g
Cementation, c	May increase with c
Overconsolidation ratio, OCR	Not affected
Plasticity index, PI	Increases with PI
Cyclic strain, γ_c	Decreases with γ_c
Strain rate, $\dot{\gamma}$	G increases with $\dot{\gamma}$ but G/G_{max} probably not affected if G and G_{max} are measured at same $\dot{\gamma}$
Number of loading cycles, N	Decreases after N cycles of large γ_c (G_{max} measured before N cycles) for clays; for sands, can increase (under drained conditions) or decrease (under undrained conditions)

Source: Modified from Dobry and Vucetic (1987).

cyclic strain amplitude (Figure 6.45). The PI = 0 damping curve from Figure 6.45 is nearly identical to the average damping curve that was used for coarse-grained soils when they

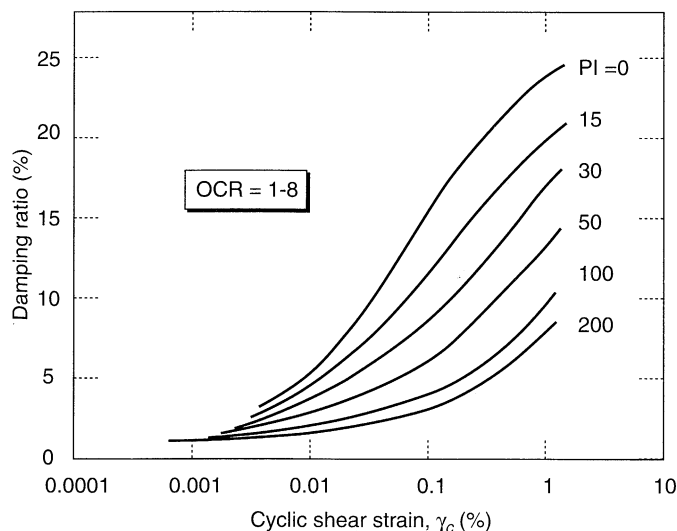


Figure 6.45 Variation of damping ratio of fine-grained soil with cyclic shear strain amplitude and plasticity index. (After Vucetic and Dobry (1991). Effect of soil plasticity on cyclic response, *Journal of Geotechnical Engineering*, Vol. 117, No. 1. Reprinted by permission of ASCE.)

were treated separately from fine-grained soils. This similarity suggests that the damping curves of Figure 6.45 can be applied to both fine- and coarse-grained soils. The damping behavior of gravel is very similar to that of sand (Seed et al., 1984).

Damping behavior is also influenced by effective confining pressure, particularly for soils of low plasticity. Ishibashi and Zhang (1993) developed an empirical expression for the damping ratio of plastic and nonplastic soils. Using equation (6.52) to compute the modulus reduction factor, G/G_{\max} , the damping ratio is given by

$$\xi = 0.333 \frac{1 + \exp(-0.0145PI^{1.3})}{2} \left[0.586 \left(\frac{G}{G_{\max}} \right)^2 - 1.547 \frac{G}{G_{\max}} + 1 \right] \quad (6.54)$$

The influence of various environmental and loading conditions on the damping ratio of normally consolidated and moderately overconsolidated soils is described in Table 6-9.

6.4.3 Cyclic Nonlinear Models

The nonlinear stress–strain behavior of soils can be represented more accurately by cyclic nonlinear models that follow the actual stress–strain path during cyclic loading. Such models are able to represent the shear strength of the soil, and with an appropriate pore pressure generation model, changes in effective stress during undrained cyclic loading. A variety of cyclic nonlinear models have been developed; all are characterized by (1) a backbone curve and (2) a series of “rules” that govern unloading–reloading behavior, stiffness degradation, and other effects. The simplest of these models have relatively simple backbone curves and only a few basic rules. More complex models may incorporate many additional rules that allow the model to better represent the effects of irregular loading, densification, pore pressure generation, or

Table 6-9. Effect of Environmental and Loading Conditions on Damping Ratio of Normally Consolidated and Moderately Overconsolidated Soils

Increasing Factor	Damping ratio, ξ
Confining pressure, σ'_m	Decreases with σ'_m ; effect decreases with increasing PI
Void ratio, e	Decreases with e
Geologic age, t_g	Decreases with t_g
Cementation, c	May decrease with c
Overconsolidation ratio, OCR	Not affected
Plasticity index, PI	Decreases with PI
Cyclic strain, γ_c	Increases with γ_c
Strain rate, $\dot{\gamma}$	Stays constant or may increase with $\dot{\gamma}$
Number of loading cycles, N	Not significant for moderate γ_c and N

Source: Modified from Dobry and Vucetic (1987).

other effects. The applicability of cyclic nonlinear models, however, is generally restricted to a fairly narrow, albeit important range of initial conditions and stress paths.

The performance of cyclic nonlinear models can be illustrated by a very simple example in which the shape of the backbone curve is described by $\tau = F_{bb}(\gamma)$. The shape of any backbone curve is tied to two parameters, the initial (low-strain) stiffness and the (high-strain) shear strength of the soil. For the simple example, the backbone function, $F_{bb}(\gamma)$, can be described by a hyperbola

$$F_{bb}(\gamma) = \frac{G_{\max}\gamma}{1 + (G_{\max}/\tau_{\max})|\gamma|} \tag{6.55}$$

The shape of the hyperbolic backbone curve is illustrated in Figure 6.46. Other expressions [e.g., the Ramberg–Osgood model (Ramberg and Osgood, 1943)] can also be used to describe the backbone curve. Alternatively, backbone curves can be constructed from modulus reduction curves.

The quantities G_{\max} and τ_{\max} may be measured directly, computed, or obtained by empirical correlation. For the example model, the response of the soil to cyclic loading is governed by the following four rules:

1. For initial loading, the stress–strain curve follows the backbone curve.

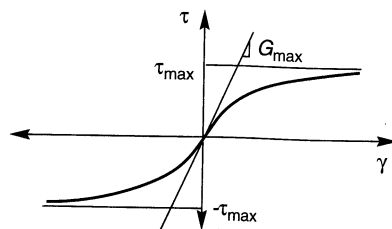


Figure 6.46 Hyperbolic backbone curve asymptotic to $\tau = G_{\max}\gamma$ and to $\tau = \tau_{\max}$ (and $\tau = -\tau_{\max}$).

2. If a stress reversal occurs at a point defined by (γ_r, τ_r) , the stress–strain curve follows a path given by

$$\frac{\tau - \tau_r}{2} = F_{bb} \left(\frac{\gamma - \gamma_r}{2} \right)$$

In other words, the unloading and reloading curves have the same shape as the backbone curve (with the origin shifted to the loading reversal point) but is enlarged by a factor of 2. These first two rules, which describe *Masing behavior* (Masing, 1926), are not sufficient to describe soil response under general cyclic loading. As a result, additional rules are needed.

3. If the unloading or reloading curve exceeds the maximum past strain and intersects the backbone curve, it follows the backbone curve until the next stress reversal.
4. If an unloading or reloading curve crosses an unloading or reloading curve from the previous cycle, the stress–strain curve follows that of the previous cycle.

Models that follow these four rules are often called *extended Masing models*. An example of the extended Masing model is shown in Figure 6.47. Cyclic loading begins at point A, and the stress–strain curve during initial loading (from A to B) follows the backbone curve as required by rule 1. At point B, the loading is reversed and the unloading portion of the stress–strain curve moves away from B along the path required by rule 2. Note that the initial unloading modulus is equal to G_{\max} . The unloading path intersects the backbone curve at point C and, according to rule 3, continues along the backbone curve until the next loading reversal at point D. The reloading curve then moves away from D as required by rule 2, and the process is repeated for the remainder of the applied loading. Although this model is very simple and is expressed only in terms of effective stresses, it inherently incorporates the hysteretic nature of damping and the strain–dependence of the shear modulus and damping ratio. Other unloading–reloading models are available (e.g., Iwan, 1967; Finn et al., 1977; Vucetic, 1990); the Cundall–Pyke model (Pyke, 1979) is particularly straightforward and easily implemented into ground response analyses. To avoid spurious response at very low strain levels, some cyclic nonlinear models require the addition of a small

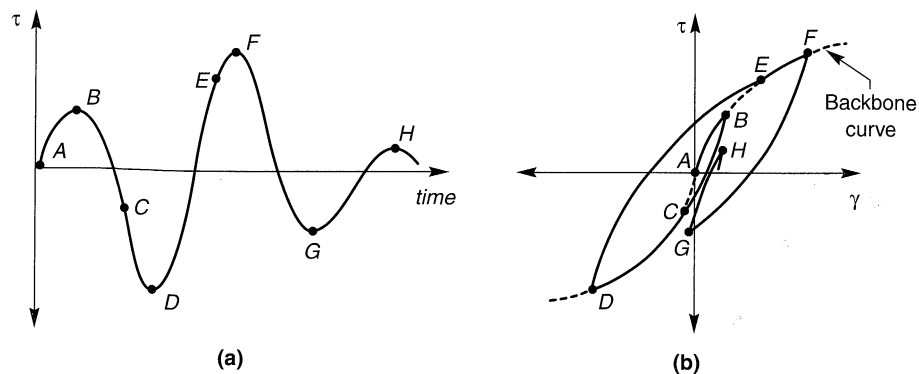


Figure 6.47 Extended Masing rules: (a) variation of shear stress with time; (b) resulting stress–strain behavior (backbone curve indicated by dashed line).

amount of low strain damping. Note that the cyclic nonlinear model does not require the shear strain to be zero when the shear stress is zero. The ability to represent the development of permanent strains is one of the most important advantages of cyclic nonlinear models over equivalent linear models.

This simple example model does not, however, allow for the determination of shear-induced volumetric strains that can lead to hardening under drained conditions or to pore pressure development with attendant stiffness degradation under undrained conditions. Such factors are accounted for in the majority of the cyclic nonlinear models commonly used in geotechnical earthquake engineering practice (e.g., Finn et al., 1977; Pyke, 1979, 1985).

The ability to compute changes in pore pressure, hence also changes in effective stress, represents another significant advantage of cyclic nonlinear models over equivalent linear models. As pore pressures increase, effective stresses decrease, and consequently the values of G_{\max} and τ_{\max} decrease. Since the shape and position of the backbone curve depends on G_{\max} and τ_{\max} , the backbone curve “degrades” with increasing pore pressure. As with actual soils, the stiffness in a stress–strain model depends not only on the cyclic strain amplitude, as implied by the equivalent linear model, but also on the stress history of the soil. When incorporated into computational models for ground response analysis, cyclic nonlinear models allow prediction of the generation, redistribution, and eventual dissipation of pore pressures during and after earthquake shaking. These capabilities are very useful for evaluation of liquefaction hazards (Chapter 9).

6.4.4 Advanced Constitutive Models

The most accurate and general methods for representation of soil behavior are based on advanced constitutive models that use basic principles of mechanics to describe observed soil behavior for (a) general initial stress conditions, (b) a wide variety of stress paths, (c) rotating principal stress axes, (d) cyclic or monotonic loading, (e) high or low strain rates, and (f) drained or undrained conditions.

Such models generally require a *yield surface* that describes the limiting stress conditions for which elastic behavior is observed, a *hardening law* that describes changes in the size and shape of the yield surface as plastic deformation occurs, and a *flow rule* that relates increments of plastic strain to increments of stress. The Cam–Clay (Roscoe and Schofield, 1963) and modified Cam–Clay (Roscoe and Burland, 1968) models were among the first of this type. Improvements in the prediction of shear strains have resulted from the use of multiple nested yield loci within the yield surface (Mroz, 1967; Prevost, 1977) and the development of bounding surface models (Dafalias and Popov, 1979) which incorporate a smooth transition from elastic to plastic behavior. Detailed treatment of such advanced constitutive models is beyond the scope of this book. The interested reader can refer to a number of sources, including Desai and Siriwardane (1984), Dafalias and Herrmann (1982), Wroth and Houlsley (1985), Lade (1988), and Wood (1991).

Although advanced constitutive models allow considerable flexibility and generality in modeling the response of soils to cyclic loading, their description usually requires many more parameters than equivalent linear models or cyclic nonlinear models. Evaluation of these parameters can be difficult, and the parameters obtained from one type of test can be different from those obtained from another. Although the use of advanced constitutive models will undoubtedly increase, these practical problems have, to date, limited their use in geotechnical earthquake engineering practice.

6.4.5 Discussion

A hierarchy of models are available for characterization of the stress–strain behavior of cyclically loaded soils. The models range considerably in complexity and accuracy; a model that is appropriate for one type of problem may not be appropriate for another. No single stress–strain model is appropriate for all problems. Selection of a stress–strain model requires careful consideration of the problem to which it is to be applied, recognition of the assumptions and limitations of the available models, and a good understanding of how the model is used in all required analyses.

6.5 STRENGTH OF CYCLICALLY LOADED SOILS

The effect of cyclic loading on the limiting strength of soils is of considerable importance in geotechnical earthquake engineering. Problems of slope stability, foundation performance, and retaining wall behavior, among others, are strongly influenced by the strength that the soil can mobilize at large strains.

Soil strength behavior is most conveniently discussed in terms of coarse-grained cohesionless soils and fine-grained cohesive soils under drained and undrained conditions. Earthquake loading is generally applied so rapidly that all but the most permeable of soils are loaded under undrained conditions. The strength of cohesionless soils is inextricably tied to the phenomenon of liquefaction, a problem so important in geotechnical earthquake engineering that it is treated in a separate chapter (Chapter 9). The following discussion is directed toward the effect of cyclic loading on the undrained shear strength of cohesive soils.

6.5.1 Definitions of Failure

The shear strength of an element of soil is typically defined as the shear stress mobilized at the point of “failure,” but failure can be defined in many different ways. In the field, failure is usually associated with deformations that exceed some serviceability limit. Since deformation results from the integration of strains over some volume of soil, the point of failure of an element of soil is often defined in terms of a limiting strain.

Consider an element of soil in drained equilibrium under anisotropic stress conditions in a cyclic direct simple shear test (point A in Figure 6.48). The application of a cyclic shear stress, τ_{cyc} , produces (under stress-controlled conditions) a cyclic shear strain, γ_{cyc} , but also an increase in the average strain, γ_{ave} . The average shear strain increases with increasing numbers of loading cycles. Clearly, the strength of the soil during cyclic loading could be defined in terms of limiting values of γ_{cyc} or γ_{ave} or of some combination of the two. The available strength of the soil under monotonic loading (after the cyclic loading has ended) may also be of interest.

The following sections discuss two measures of the strength of a cyclically loaded soil. The “cyclic” strength is based on a limiting value of cyclic and/or average strain *during cyclic loading* (although the soil may not actually be in a state of failure as defined by effective stress conditions). The “monotonic” strength is the ultimate static strength that can be mobilized *after cyclic loading has ended*.

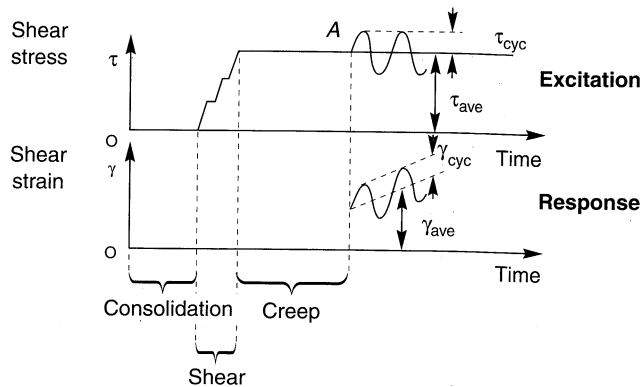


Figure 6.48 Definitions of average and cyclic shear stress and shear strain. (After Goulois et al., 1985. Used by permission of ASTM.)

6.5.2 Cyclic Strength

The levels of both cyclic and permanent deformations are of interest in a number of geotechnical earthquake engineering problems. They are also important in the design of foundations for marine structures subjected to wave loading, and much of the current state of knowledge of cyclic strength has come from research in that area. The cyclic strength of an element of soil depends on the relationship between the average shear stress, τ_{ave} , and the cyclic shear stress, τ_{cyc} . When the average shear stress is low, unidirectional strains will accumulate slowly, so the average shear strain will also be low. The amplitude of the cyclic strain, however, may become large if the cyclic shear stress is large. If, on the other hand, the average shear stress is high (relative to the static shear strength, s_u), substantial unidirectional strains can develop even when the cyclic shear stress is small.

For the case of $\tau_{ave} = 0$, no unidirectional strain will develop, so failure must be defined in terms of the cyclic shear strain, γ_{cyc} . When failure is defined in terms of a specific level of cyclic shear strain (often 3 percent), the *cyclic strength ratio*, defined as τ_{cyc}/s_u , decreases with increasing numbers of cycles, as shown in Figure 6.49. At cyclic stress ratios below some limiting value, however, the failure strain will never be reached (i.e., stable response will be achieved). This limiting cyclic stress ratio, referred to as the *critical level of repeated loading* (CLRL) by Sangrey et al. (1969), increases with increasing soil plasticity. Hermann and Houston (1980) found CLRL values ranging from 0.05 for a nonplastic silt to 0.55 for San Francisco Bay mud.

For cases in which τ_{ave} is greater than zero, both γ_{cyc} and γ_{ave} will depend on τ_{cyc} and τ_{ave} (Seed and Chan, 1966). Investigations of the cyclic response of marine clays (e.g., Meimon and Hicher, 1980; Goulois et al., 1985; Andersen et al., 1988) have shown that γ_{cyc} depends predominantly on τ_{cyc} and the number of cycles, and γ_{ave} depends predominantly on τ_{ave} and the number of cycles (Figure 6.50).

In the development of a procedure for estimating earthquake-induced permanent deformations in dams and embankments, Makdisi and Seed (1978) defined the dynamic yield strength of soils that exhibit small changes in pore pressure under undrained loading as 80% of the undrained strength of the soil. Substantial permanent deformations can develop when the total (static plus cyclic) shear stress exceeds the dynamic yield strength.

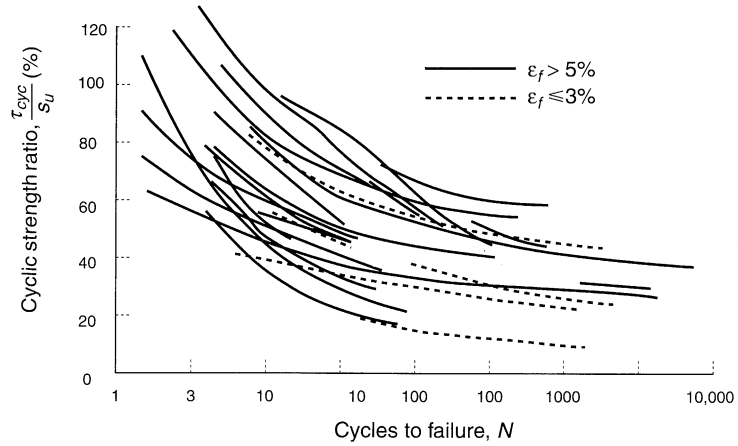


Figure 6.49 Variation of cyclic strength ratio with number of cycles for different soils. (After Lee and Focht, 1976.)

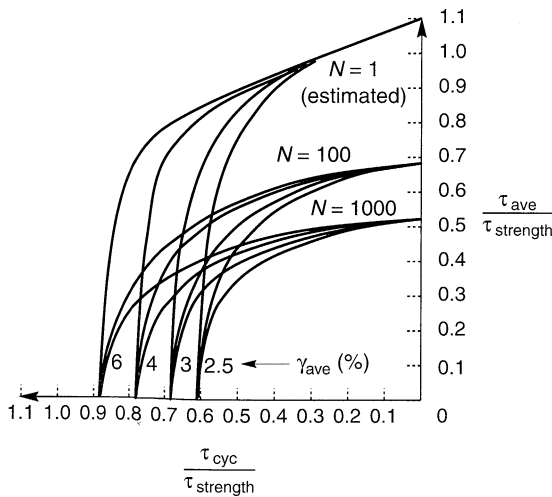


Figure 6.50 Variation of average shear strain with average shear stress, cyclic shear stress, and number of cycles in cyclic direct simple shear tests on plastic Drammen clay. τ_{strength} is a reference strength measured under slow loading conditions with $\tau_{\text{ave}} = 0$. Cyclic loading applied at a period of 10 sec. (After Goulois et al., 1985. Used by permission of ASTM.)

6.5.3 Monotonic Strength

Evaluation of the static stability of slopes and retaining walls and the capacity of foundations after earthquake shaking has ended is another important problem in geotechnical earthquake engineering. Such problems require evaluation of the available shear strength of the soil after the earthquake has ended. This postearthquake strength must reflect any effects of cyclic loading imposed by the earthquake.

As pointed out by Castro and Christian (1976), the ultimate (residual, high-strain) undrained shear strength of a saturated soil is controlled by its void ratio and structure. Barring any change in soil structure, a saturated soil at a particular void ratio will mobilize a

specific undrained strength, with little influence of the history of stresses and strains by which that strength is arrived at. For such soil conditions, the undrained strength after cyclic loading will be equal to the undrained strength before undrained loading (at the same strain rate). Since cyclic loading induces positive excess pore pressures, the effective stress in an element of soil sheared monotonically after being subjected to cyclic loading will be lower than that in an identical element that is sheared monotonically without prior cyclic loading. Consequently, the element that had been cycled would be expected to exhibit more dilative behavior but to have a lower stiffness in the early stages of monotonic undrained loading than the element that had not been cycled.

Changes in monotonic strength can be caused by disturbance of the soil structure during cyclic loading. The extent to which the structure of the soil is disturbed is influenced by the relationship between the cyclic strain amplitude and the strain at which failure occurs under monotonic loading conditions (Thiers and Seed, 1969). Substantial structural disturbance can modify the stress-strain behavior and reduce the monotonic shear strength. The six triaxial specimens shown in Figure 6.51 had similar void ratios (except specimen 6, which had a somewhat higher void ratio than the rest) at the end of consolidation. Specimen 1 was sheared monotonically immediately after consolidation, but specimens 2 to 6 were first subjected to varying levels of cyclic loading. Since the void ratios were nearly the same, the specimens would therefore be expected to have similar monotonic strengths. As shown by the stress-strain curves and stress paths, they behaved largely as would be expected. After being subjected to different levels of cyclic strain, their ultimate (large strain) strengths were similar (except specimen 6, which was lower than the others). Differences in the ultimate strength can be explained by small differences in the void ratios and also by differences in the extent of structural disturbance induced by the cyclic loading.

Thiers and Seed (1969) found that the ultimate strength of three clays decreased by less than 10% when the cyclic strain amplitude was less than one-half of the failure strain from monotonic tests. At higher cyclic strain amplitudes, the reduction in strength was more

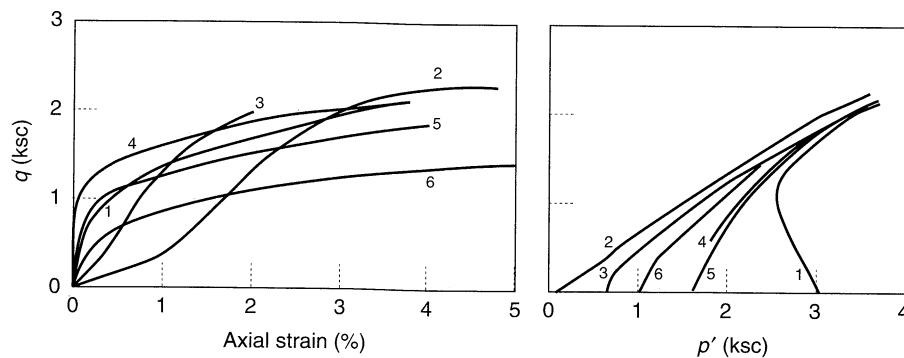


Figure 6.51 Effect of cyclic loading on subsequent monotonic undrained loading behavior of triaxial specimens of a slightly plastic silt: (a) stress-strain behavior; (b) effective stress path behavior. Specimen 1 was tested in conventional CU test with no prior cyclic loading. Specimens 2 to 6 were subjected to different levels of cyclic loading prior to monotonic loading. Note the dilative nature of the stress paths of specimens 2 to 6 compared to specimen 1. (After Castro and Christian, 1976.)

dramatic, as illustrated in Figure 6.52. Similar results have been obtained by others (e.g., Koutsoftas, 1978; Byrne et al., 1984).

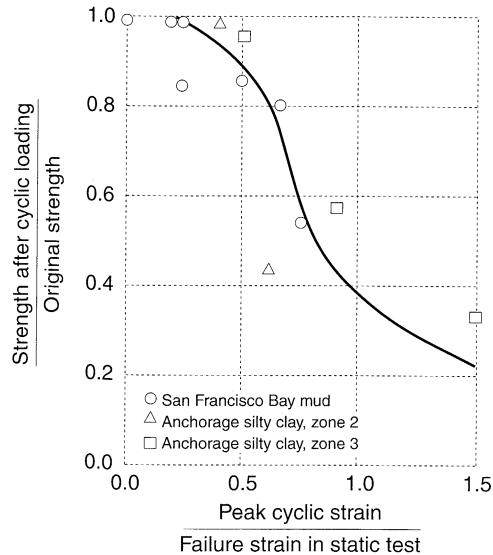


Figure 6.52 Effect of peak cyclic strain on monotonic strength after cyclic loading. (After Thiers and Seed, 1969. Used by permission of ASTM.)

6.6 SUMMARY

1. Earthquake damage is strongly influenced by the dynamic response of soil deposits. The cyclic nonlinear and strength characteristics of soils govern their dynamic response during earthquakes.
2. The measurement of dynamic soil properties is an important aspect of geotechnical earthquake engineering. A variety of field and laboratory techniques are available; some are oriented toward measurement of low-strain behavior and others toward measurement of soil behavior at high strain levels.
3. Field tests allow measurement of soil properties in situ; the complex effects of existing stress, chemical, thermal, and structural conditions are therefore reflected in the measured soil properties. Many field tests measure the response of large volumes of soil and induce soil deformation similar to those induced by earthquakes. Because in situ conditions cannot be easily controlled or varied, field tests do not allow measurement of the behavior of the soil under other stress states or soil conditions.
4. A number of field tests measure low-strain soil properties, particularly wave propagation velocities. These tests include seismic reflection, seismic refraction, steady-state vibration, spectral analysis of surface waves, seismic crosshole, seismic downhole (and uphole), and seismic cone tests. Other field tests, such as the standard penetration, cone penetration, dilatometer, and pressuremeter tests, measure the properties of the soil at higher strain levels.

5. Laboratory tests allow the control and measurement of stresses, strains, and porewater pressures. As a result, they can often simulate anticipated initial and dynamic stress conditions better than field tests. The results of laboratory tests, however, may be influenced by sample disturbance. Sample disturbance has a particularly strong effect on low-strain properties.
6. Several laboratory tests measure low-strain soil properties. Among these are the resonant column test, the ultrasonic pulse test, and the piezoelectric bender element test. The cyclic triaxial test, cyclic direct shear test, and cyclic torsional shear test can be used to measure dynamic soil properties at higher strain levels.
7. Dynamic soil properties may also be inferred from the results of model tests. Shaking table tests can accommodate relatively large models, but their inability to produce high gravitational stresses can make extrapolation to prototype conditions difficult. Centrifuge tests can satisfy similitude requirements much better than shaking table tests but must be performed on relatively small models.
8. Soils exhibit nonlinear, inelastic, stress–strain behavior under cyclic loading conditions. At low strain levels, the stiffness of a soil is greatest and the damping is smallest. At higher strain levels, the effects of nonlinearity and inelasticity increase, producing lower stiffness and greater damping. Complete characterization of such behavior is very complicated. For the great majority of geotechnical earthquake engineering analyses, however, approximate characterization is sufficient. Three broad classes of stress–strain models are used for geotechnical earthquake engineering analyses: equivalent linear models, cyclic nonlinear models, and advanced constitutive models.
9. Equivalent linear models treat soils as a linear viscoelastic materials. Nonlinear behavior is accounted for by the use of strain-dependent stiffness and damping parameters. The stiffness of the soil is usually characterized by the maximum shear modulus, which is mobilized at low strains, and a modulus reduction curve, which shows how the shear modulus decreases at larger strains. Damping behavior is characterized by the damping ratio, which increases with increasing strain amplitude. The shapes of the modulus reduction and damping curves are influenced by soil plasticity and, for soils of very low plasticity, by effective confining pressure.
10. Cyclic nonlinear models represent the nonlinear, inelastic behavior of soils using a nonlinear backbone curve and a series of rules that govern unloading–reloading behavior. Backbone curves are usually described by simple functions that reflect the transition from the initial stiffness (at low strain levels) to the ultimate strength (at high strain levels). The unloading–reloading rules control the behavior of the model during stress reversals and ensure that it behaves in a manner similar to that exhibited by actual soils subjected to irregular cyclic loading. In contrast to equivalent linear models, cyclic nonlinear models allow permanent strains to develop. Cyclic nonlinear models can also be coupled with pore pressure generation models to predict changes in effective stress during cyclic loading. Modeling such behavior requires that the original backbone curve be degraded (softened) as pore pressures increase.

11. Advanced constitutive models use basic principles of mechanics to describe soil behavior for general initial stress conditions, a wide variety of stress paths with rotating principal stresses, cyclic or monotonic loading, high or low strain rates, and drained or undrained conditions. As such, they are much more general than equivalent linear or cyclic nonlinear models. The penalty for this increased generality comes in the form of increased complexity, an increased number of model parameters (some of which can be difficult to determine), and increased computational effort when incorporated into ground response or soil–structure interaction analyses.
12. The shear strength of soil can be influenced by cyclic loading. The level of permanent strain that develops in a cyclically loaded element of soil depends on the relationship between the average (static) shear stress and the cyclic shear stress. If the average shear stress is zero, only cyclic strains will develop and failure is defined in terms of a limiting cyclic strain level. If the average shear stress is greater than zero, cyclic stresses can produce unidirectional as well as cyclic shear strains. The rate at which unidirectional strain develops is influenced by the relative magnitudes of the average and cyclic shear stresses. The ultimate strength of a soil loaded monotonically after an episode of cyclic loading is also important. Because the undrained strength of a saturated soil is controlled by its density and structure, the postearthquake undrained strength will (barring structural changes) be essentially the same as the static undrained strength, even if excess pore pressures have developed during cyclic loading.

HOMEWORK PROBLEMS

- 6.1 At a level site, bedrock is overlain by a layer of overconsolidated clay of variable thickness. A seismic refraction survey is conducted with 13 receivers placed on a straight line between two shot points located 1,000 ft apart. From the p-wave arrival times listed below, determine and plot the subsurface profile in the central 800 ft portion of the survey. Determine the p-wave velocities of the overconsolidated clay and the underlying bedrock.

Receiver	Distance from SP 1	Arrival time from SP 1 (msec)	Distance from SP 2	Arrival time from SP 2 (msec)
A	0	0	1000	124
B	50	15	950	119
C	100	30	900	114
D	200	48	800	105
E	300	58	700	96
F	400	67	600	85
G	500	78	500	75
H	600	91	400	73
I	700	108	300	68
J	800	113	200	47
K	900	115	100	30
L	950	119	50	15
M	1000	124	0	0

- 6.2 The figure below shows the vertical response of geophones located at the same depths in vertical boreholes spaced 5 m apart. The waves recorded at the geophones resulted from downward (solid lines) and upward (dashed lines) impacts on a mechanical source at the same depth in a third borehole that was colinear with the other two boreholes. Determine the average SV-wave velocity of the soil between the geophones.

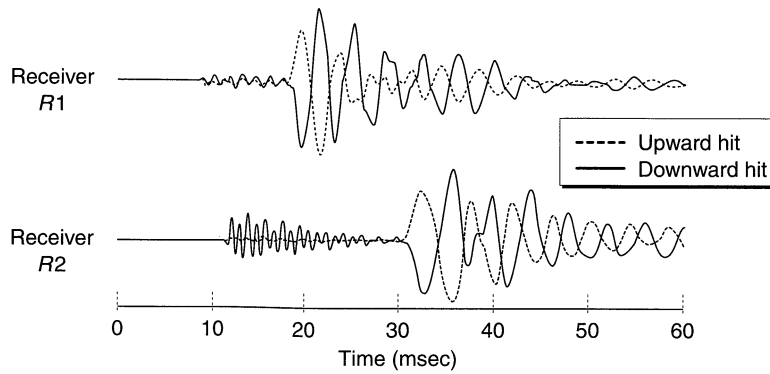


Figure P6.2

- 6.3 Estimate the damping ratio of the resonant column specimen from which the frequency response curve of Figure E6.7 was obtained.
- 6.4 Portions of the time histories of deviator stress and axial strain from a stress-controlled cyclic triaxial test are shown below. Compute the secant shear modulus and damping ratio of the test specimen. Assuming that the soil is saturated and its response is consistent with the Masing criteria, estimate the maximum shear modulus of the soil.

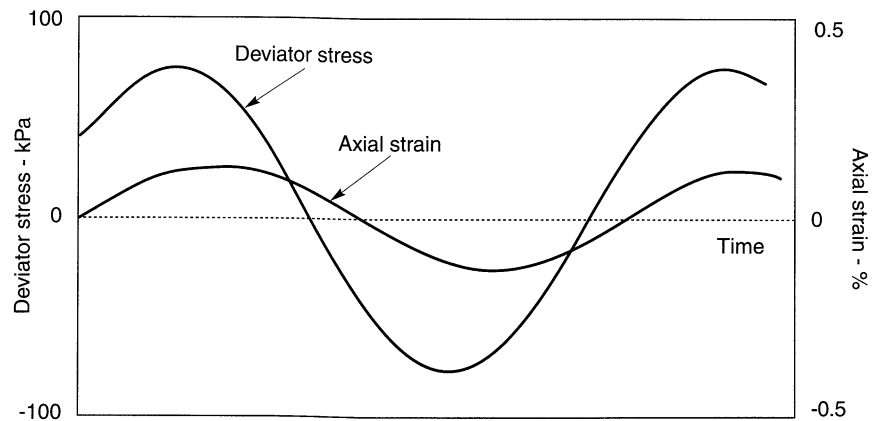


Figure P6.4

- 6.5 A site is underlain by about 14 m of hydraulic fill sand with the following properties.

Grain size characteristics: $D_{10} < 0.074$ mm

$D_{30} = 0.14$ mm

$D_{50} = 0.17$ mm

$D_{60} = 0.20$ mm

Saturated unit weight = 18.8 kN/m^3

Average uncorrected SPT resistance = 6 blows/ft

Average cone tip resistance = 3 MPa

The groundwater table is located at a depth of 2m.

- (a) Estimate the shear wave velocity of the hydraulic fill at a depth of 5 m by as many procedures as the available data will support.
- (b) Shear wave velocity measurements at this site have indicated hydraulic fill shear wave velocities ranging from about 120 m/sec - 200 m/sec at 5 m depth with an average value of about 170 m/sec. Comment on the level of agreement between the estimated shear wave velocities from Part (a) and the measured shear wave velocities.
- 6.6 At the site described in Problem 6.5, the hydraulic fill is underlain by a 15 m thick deposit of medium stiff, normally consolidated silty clay with the following properties:

Water content = 40%

Liquid limit = 46

Plastic limit = 23

Saturated unit weight = 15.9 kN/m^3

Cone tip resistance = 8 to 14 kg/cm^2

Undrained shear strength = 27 to 61 kPa

- (a) Estimate the shear wave velocity of the silty clay at a depth of 20 m by as many procedures as the available data will support.
- (b) Shear wave velocity measurements at this site have indicated silty clay shear wave velocities ranging from about 120 m/sec - 180 m/sec at 20 m depth with an average value of about 155 m/sec. Comment on the level of agreement between the estimated shear wave velocities from Part (a) and the measured shear wave velocities.
- 6.7 Determine and plot the backbone curve that would correspond to the Vucetic-Dobry modulus reduction curve for a clay with $PI = 15$.
- 6.8 Compute and plot the modulus reduction curve for a silty clay ($PI = 30$) at a mean effective confining pressure of 40 kPa using the relationship of Ishibashi and Zhang (1993). How does this curve compare with that shown in Figure 6.42?

- 6.9** Compute and plot the damping ratio curves that correspond to the modulus reduction curves shown in Figure 6.43. Comment on the influence of effective confining pressure on damping characteristics of low and high plasticity soils.
- 6.10** An element of soil with a maximum shear modulus of 700,000 psf and an undrained strength of 1000 psf is subjected to the time history of shear stress shown below. Assuming that the backbone curve is hyperbolic, and that the soil follows the extended Masing criteria, plot the resulting stress-strain behavior. Mark all points at which the unloading-reloading rules governing the stress-strain behavior change (i.e. mark as 1-2 at the point where control over the stress-strain response shifts from Rule 1 to Rule 2).

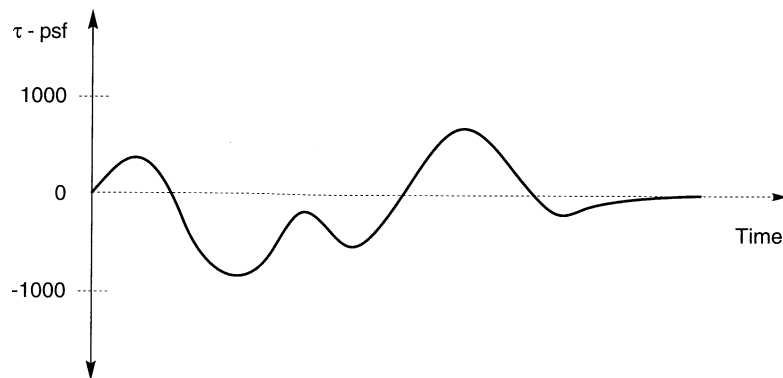


Figure P6.10

7

Ground Response Analysis

7.1 INTRODUCTION

One of the most important and most commonly encountered problems in geotechnical earthquake engineering is the evaluation of ground response. *Ground response analyses* are used to predict ground surface motions for development of design response spectra, to evaluate dynamic stresses and strains for evaluation of liquefaction hazards, and to determine the earthquake-induced forces that can lead to instability of earth and earth-retaining structures.

Under ideal conditions, a complete ground response analysis would model the rupture mechanism at the source of an earthquake, the propagation of stress waves through the earth to the top of bedrock beneath a particular site, and would then determine how the ground surface motion is influenced by the soils that lie above the bedrock. In reality, the mechanism of fault rupture is so complicated and the nature of energy transmission between the source and the site so uncertain that this approach is not practical for common engineering applications. In practice, empirical methods based on the characteristics of recorded earthquakes are used to develop predictive relationships of the types discussed in Chapter 3. These predictive relationships are often used in conjunction with a seismic hazard analysis to predict bedrock motion characteristics at the site. The problem of ground response analysis then becomes one of determining the response of the soil deposit to the motion of the bedrock immediately beneath it. Despite the fact that seismic waves may travel through tens

of kilometers of rock and often less than 100 m of soil, the soil plays a very important role in determining the characteristics of the ground surface motion.

The influence of local soil conditions on the nature of earthquake damage has been recognized for many years. Since the 1920s, seismologists and, more recently, geotechnical earthquake engineers have worked toward the development of quantitative methods for predicting the influence of local soil conditions on strong ground motion. Over the years, a number of techniques have been developed for ground response analysis. The techniques are often grouped according to the dimensionality of the problems they can address, although many of the two- and three-dimensional techniques are relatively straightforward extensions of corresponding one-dimensional techniques. This chapter describes the most commonly used methods for one-, two-, and three-dimensional ground response, and introduces the problem of soil–structure interaction.

7.2 ONE-DIMENSIONAL GROUND RESPONSE ANALYSIS

When a fault ruptures below the earth's surface, body waves travel away from the source in all directions. As they reach boundaries between different geologic materials, they are reflected and refracted. Since the wave propagation velocities of shallower materials are generally lower than the materials beneath them, inclined rays that strike horizontal layer boundaries are usually reflected to a more vertical direction. By the time the rays reach the ground surface, multiple refractions have often bent them to a nearly vertical direction (Figure 7.1). One-dimensional ground response analyses are based on the assumption that all boundaries are horizontal and that the response of a soil deposit is predominantly caused by SH-waves propagating vertically from the underlying bedrock. For one-dimensional ground response analysis, the soil and bedrock surface are assumed to extend infinitely in the horizontal direction. Procedures based on this assumption have been shown to predict ground response that is in reasonable agreement with measured response in many cases.

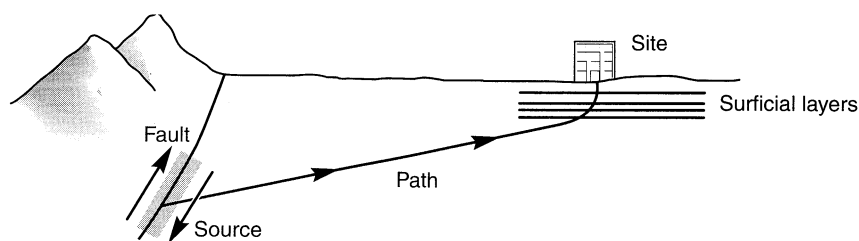


Figure 7.1 Refraction process that produces nearly vertical wave propagation near the ground surface.

Before describing any of the ground response models, it is necessary to define several terms that are commonly used to describe ground motions. With reference to Figure 7.2a, the motion at the surface of a soil deposit is the *free surface motion*. The motion at the base of the soil deposit (also the top of bedrock) is called a *bedrock motion*. The motion at a location where bedrock is exposed at the ground surface is called a *rock outcropping motion*. If the soil deposit was not present (Figure 7.2b), the motion at the top of bedrock would be the *bedrock outcropping motion*.

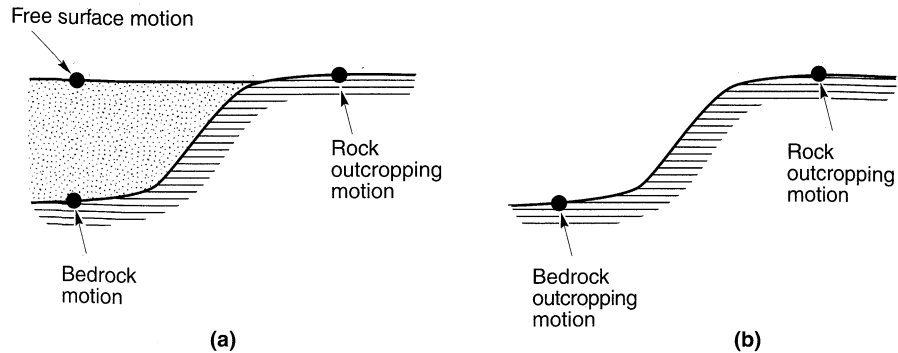


Figure 7.2 Ground response nomenclature: (a) soil overlying bedrock; (b) no soil overlying bedrock. Vertical scale is exaggerated.

7.2.1 Linear Approach

The manner in which transfer functions can be used to compute the response of single-degree-of-freedom systems is illustrated in Appendix B (Section B.5.4.2). An important class of techniques for ground response analysis is also based on the use of transfer functions. For the ground response problem, transfer functions can be used to express various response parameters, such as displacement, velocity, acceleration, shear stress, and shear strain, to an input motion parameter such as bedrock acceleration. Because it relies on the principle of superposition, this approach is limited to the analysis of linear systems. Non-linear behavior can be approximated, however, using an iterative procedure with equivalent linear soil properties.

The mathematical aspects of the transfer function approach were described in Section B.5.4.2 of Appendix B. Although the calculation involve manipulation of complex numbers, the approach itself is quite simple. A known time history of bedrock (input) motion is represented as a Fourier series, usually using the FFT (Section A.3.4). Each term in the Fourier series of the bedrock (input) motion is then multiplied by the transfer function to produce the Fourier series of the ground surface (output) motion. The ground surface (output) motion can then be expressed in the time domain using the inverse FFT. Thus the transfer function determines how each frequency in the bedrock (input) motion is amplified, or deamplified, by the soil deposit.

7.2.1.1 Evaluation of Transfer Functions

The key to the linear approach is the evaluation of transfer functions. In the following sections, transfer functions are derived for a series of successively more complicated geotechnical conditions. Although the simplest of these may only rarely be applicable to actual problems, they illustrate some of the important effects of soil deposits on ground motion characteristics without undue mathematical complexity. The more complex are capable of describing the most important aspects of ground response and are very commonly used in geotechnical earthquake engineering practice.

Uniform Undamped Soil on Rigid Rock. First, consider a uniform layer of isotropic, linear elastic soil overlying rigid bedrock as shown in Figure 7.3. Harmonic horizontal motion of the bedrock will produce vertically propagating shear waves in the overlying soil. The resulting horizontal displacement can be expressed, using the results of Section 5.2.1.3, as

$$u(z, t) = Ae^{i(\omega t + kz)} + Be^{i(\omega t - kz)} \quad (7.1)$$

where ω is the circular frequency of ground shaking, k the wave number ($= \omega/v_s$) and A and B the amplitudes of waves traveling in the $-z$ (upward) and $+z$ (downward) directions, respectively. At the free surface ($z = 0$), the shear stress, and consequently the shear strain, must vanish; that is,

$$\tau(0, t) = G\gamma(0, t) = G \frac{\partial u(0, t)}{\partial z} = 0 \quad (7.2)$$

Substituting (7.1) into (7.2) and differentiating yields

$$Gik(Ae^{ik(0)} - Be^{-ik(0)})e^{i\omega t} = Gik(A - B)e^{i\omega t} = 0 \quad (7.3)$$

which is satisfied (nontrivially) when $A = B$. The displacement can then be expressed as

$$u(z, t) = 2A \frac{e^{ikz} + e^{-ikz}}{2} e^{i\omega t} = 2A \cos kz e^{i\omega t} \quad (7.4)$$

which describes a standing wave of amplitude $2A \cos kz$. The standing wave is produced by the constructive interference of the upward and downward traveling waves and has a fixed shape with respect to depth. Equation (7.4) can be used to define a transfer function that describes the ratio of displacement amplitudes at any two points in the soil layer. Choosing these two points to be the top and bottom of the soil layer gives the transfer function

$$F_1(\omega) = \frac{u_{\max}(0, t)}{u_{\max}(H, t)} = \frac{2Ae^{i\omega t}}{2A \cos kHe^{i\omega t}} = \frac{1}{\cos kH} = \frac{1}{\cos(\omega H/v_s)} \quad (7.5)$$

The modulus of the transfer function is the amplification function

$$|F_1(\omega)| = \sqrt{\{\text{Re}[F_1(\omega)]\}^2 + \{\text{Im}[F_1(\omega)]\}^2} = \frac{1}{|\cos(\omega H/v_s)|} \quad (7.6)$$

which indicates that the surface displacement is always at least as large as the bedrock displacement (since the denominator can never be greater than 1) and, at certain frequencies, is

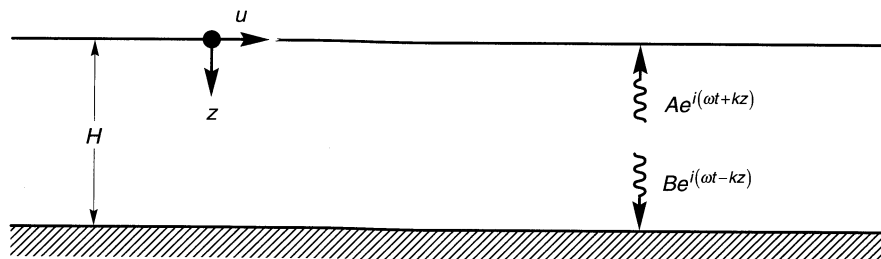


Figure 7.3 Linear elastic soil deposit of thickness H underlain by rigid bedrock.

much larger. Thus $|F_1(\omega)|$ is the ratio of the free surface motion amplitude to the bedrock motion amplitude (or, since the bedrock is rigid in this case, the bedrock outcropping motion). As $\omega H/v_s$ approaches $\pi/2 + n\pi$, the denominator of equation (7.6) approaches zero, which implies that infinite amplification, or resonance, will occur (Figure 7.4). Even this very simple model illustrates that the response of a soil deposit is highly dependent upon the frequency of the base motion, and that the frequencies at which strong amplification occurs depend on the geometry (thickness) and material properties (s-wave velocity) of the soil layer.

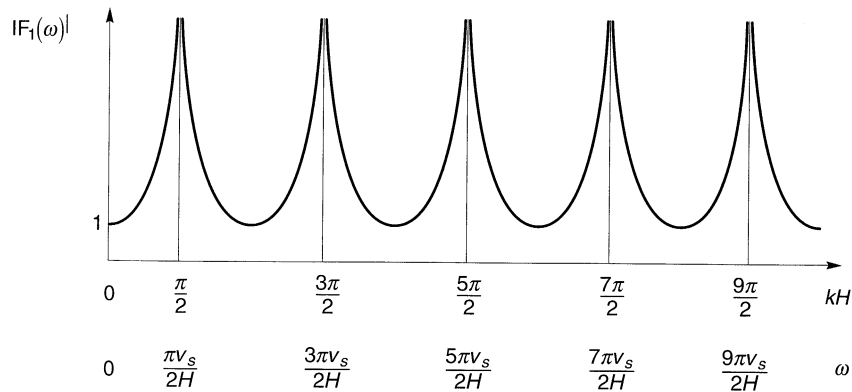


Figure 7.4 Influence of frequency on steady-state response of undamped linear elastic layer.

Example 7.1

Compute the time history of acceleration at the surface of the linear elastic soil deposit shown in Figure E7.1a in response to the E-W component of the Gilroy No. 1 (rock) motion (Figure 3.1).

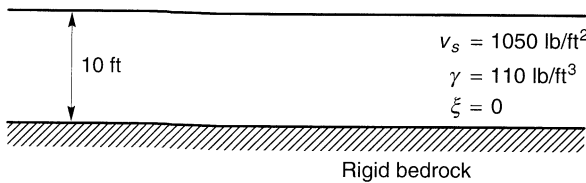


Figure E7.1a

Solution Computation of the ground surface motion from the bedrock motion can be accomplished in the following series of steps:

1. Obtain the time history of acceleration of the input motion. In this case the input motion is the E-W component of the Gilroy No. 1 (rock) motion shown in Figure E7.1b. The Gilroy No. 1 record consists of 2000 acceleration values at 0.02-sec intervals.
2. Compute the Fourier series of the bedrock (input) motion. The Fourier series is complex valued; its one-sided Fourier amplitude spectrum (Section A.3 of Appendix A) is shown in Figure E7.1c. The Fourier amplitude spectrum is defined for frequencies up to $1/2\Delta t = 25$ Hz, but most of the energy in the bedrock motion is at frequencies less than 5 to 10 Hz.
3. Compute the transfer function that relates the ground surface (output) motion to the bedrock (input) motion. From equation (7.5), the transfer function (Figure E7.1d) for the case of undamped soil is real valued. The transfer function has values of 1 below frequencies

of about 10 Hz. However, at frequencies that approach the fundamental frequency of the soil deposit ($f_0 = v_s/4H = 26.25$ Hz), the transfer function begins to take on large values.

4. Compute the Fourier series of the ground surface (output) motion as the product of the transfer function and the Fourier series of the bedrock (input) motion. At frequencies less than 5 to 10 Hz, the Fourier spectrum of the ground surface motion is virtually the same as that of the bedrock motion. Although the transfer function indicates that frequencies above 20 Hz or so will be amplified strongly, the input motion is weak in that frequency range. The one-sided amplitude spectrum is shown in Figure E7.1e. Examination of this Fourier amplitude spectrum indicates that the ground surface motion has somewhat more high frequency motion, but is generally similar to that of the bedrock motion.
5. Obtain the time history of the ground surface motion by inverting its Fourier series. As illustrated in Figure E7.1f, the time history of ground surface motion has a somewhat greater content of high-frequency components, but is generally similar to the time history of bedrock motion.

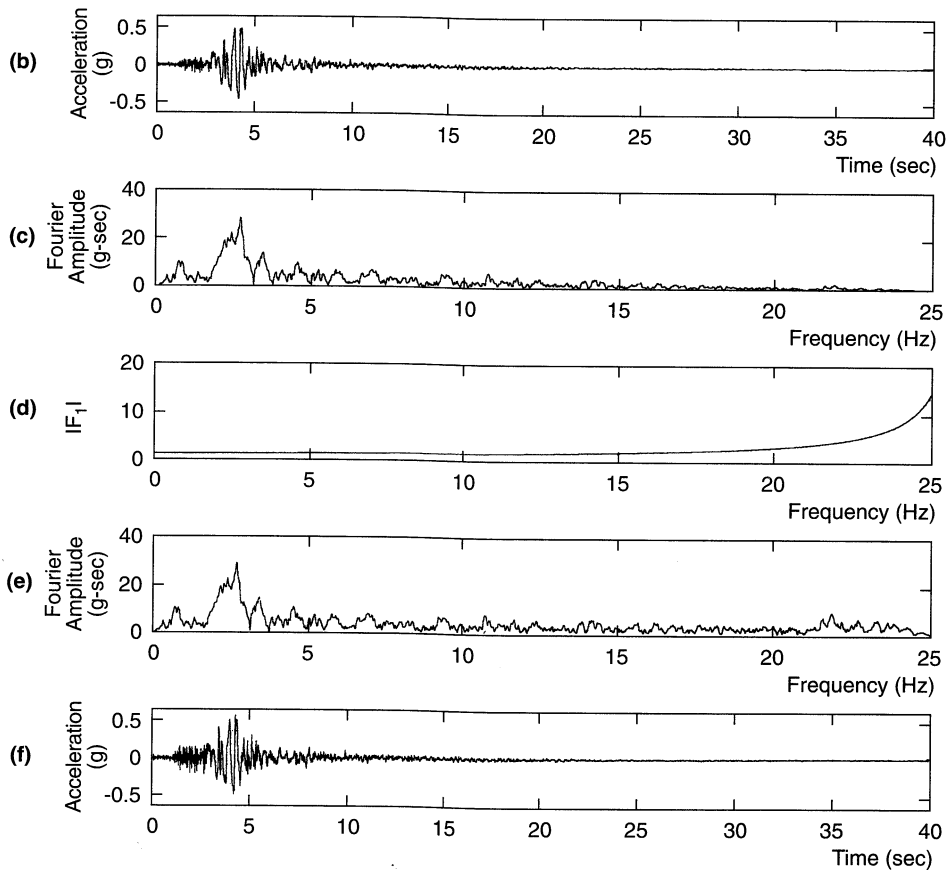


Figure E7.1b-f

Because the soil layer had a high natural frequency (intentionally selected to avoid the extremely large transfer function values that exist near the natural frequency of an undamped layer), its effect on the ground surface motion was relatively small.

Uniform, Damped Soil on Rigid Rock. Obviously, the type of unbounded amplification predicted by the previous analysis cannot physically occur. The previous analysis assumed no dissipation of energy, or damping, in the soil. Since damping is present in all materials, more realistic results can be obtained by repeating the analysis with damping. Assuming the soil to have the shearing characteristics of a Kelvin–Voigt solid, the wave equation can be written [equation (5.94)] as

$$\rho \frac{\partial^2 u}{\partial t^2} = G \frac{\partial^2 u}{\partial z^2} + \eta \frac{\partial^3 u}{\partial z^2 \partial t} \quad (7.7)$$

As shown in equation (5.94), the solution to this wave equation is of the form

$$u(z, t) = A e^{i(\omega t + k^* z)} + B e^{i(\omega t - k^* z)}$$

where k^* is a complex wave number with real part k_1 and imaginary part k_2 . Repeating the previous algebraic manipulations with the complex wave number, the transfer function for the case of damped soil over rigid rock can be expressed as

$$F_2(\omega) = \frac{1}{\cos k^* H} = \frac{1}{\cos(\omega H/v_s^*)} \quad (7.8)$$

Since the frequency-independent complex shear modulus (Section 5.5.1) is given by $G^* = G(1 + i2\xi)$, the complex shear wave velocity can be expressed as

$$v_s^* = \sqrt{\frac{G^*}{\rho}} = \sqrt{\frac{G(1 + i2\xi)}{\rho}} \approx \sqrt{\frac{G}{\rho}}(1 + i\xi) = v_s(1 + i\xi) \quad (7.9)$$

for small ξ . Then the complex wave number can be written, again for small ξ , as

$$k^* = \frac{\omega}{v_s^*} = \frac{\omega}{v_s(1 + i\xi)} \approx \frac{\omega}{v_s}(1 - i\xi) = k(1 - i\xi) \quad (7.10)$$

and finally, the transfer function, as

$$F_2(\omega) = \frac{1}{\cos k(1 - i\xi)H} = \frac{1}{\cos[\omega H/v_s(1 + i\xi)]} \quad (7.11)$$

Using the identity $|\cos(x + iy)| = \sqrt{\cos^2 x + \sinh^2 y}$, the amplification function can be expressed as

$$|F_2(\omega)| = \frac{1}{\sqrt{\cos^2 kH + \sinh^2 \xi kH}} \quad (7.12)$$

Since $\sinh^2 y \approx y^2$ for small y , the amplification function can be simplified to

$$|F_2(\omega)| \approx \frac{1}{\sqrt{\cos^2 kH + (\xi kH)^2}} = \frac{1}{\sqrt{\cos^2(\omega H/v_s) + [\xi(\omega H/v_s)]^2}} \quad (7.13)$$

For small damping ratios, equation (7.13) indicates that amplification by a damped soil layer also varies with frequency. The amplification will reach a local maximum whenever $kH \approx \pi/2 + n\pi$ but will never reach a value of infinity since (for $\xi > 0$) the denominator will

always be greater than zero. The frequencies that correspond to the local maxima are the *natural frequencies* of the soil deposit. The variation of amplification factor with frequency is shown for different levels of damping in Figure 7.5. This amplification factor is also equal to the ratio of the free surface motion amplitude to the bedrock (or bedrock outcropping) motion amplitude. Comparing Figures 7.4 and 7.5 shows that damping affects the response at high frequencies more than at lower frequencies.

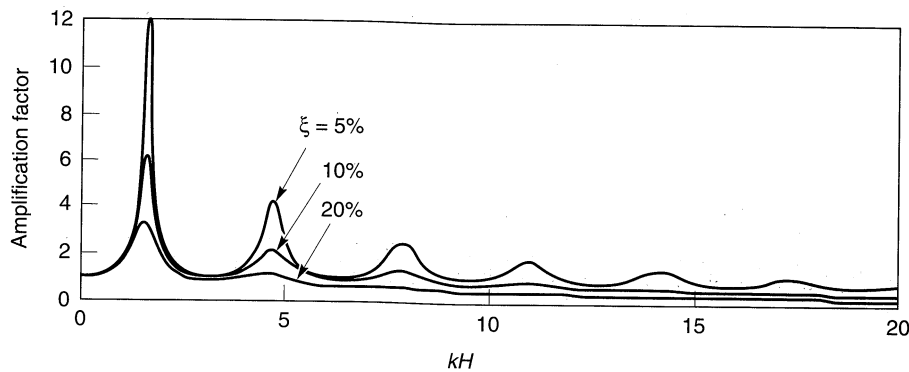


Figure 7.5 Influence of frequency on steady-state response of damped, linear elastic layer.

The n th natural frequency of the soil deposit is given by

$$\omega_n \approx \frac{v_s}{H} \left(\frac{\pi}{2} + n\pi \right) \quad n = 0, 1, 2, \dots, \infty \quad (7.14)$$

Since the peak amplification factor decreases with increasing natural frequency, the greatest amplification factor will occur approximately at the lowest natural frequency, also known as the *fundamental frequency*.

$$\omega_0 = \frac{\pi v_s}{2H} \quad (7.15)$$

The period of vibration corresponding to the fundamental frequency is called the *characteristic site period*,

$$T_s = \frac{2\pi}{\omega_0} = \frac{4H}{v_s} \quad (7.16)$$

The characteristic site period, which depends only on the thickness and shear wave velocity of the soil, provides a very useful indication of the period of vibration at which the most significant amplification can be expected.

At each natural frequency, a standing wave develops in the soil. Normalized deformed shapes, or mode shapes, for the first three natural frequencies are shown in Figure 7.6. Note that the soil displacements are in phase at all depths in the fundamental mode, but not in the higher modes. At frequencies above the fundamental frequency, part of the soil deposit may be moving in one direction while another part is moving in the opposite direction. This phenomenon must be considered in the evaluation of inertial forces in soil masses required for seismic stability analyses (Chapter 10).

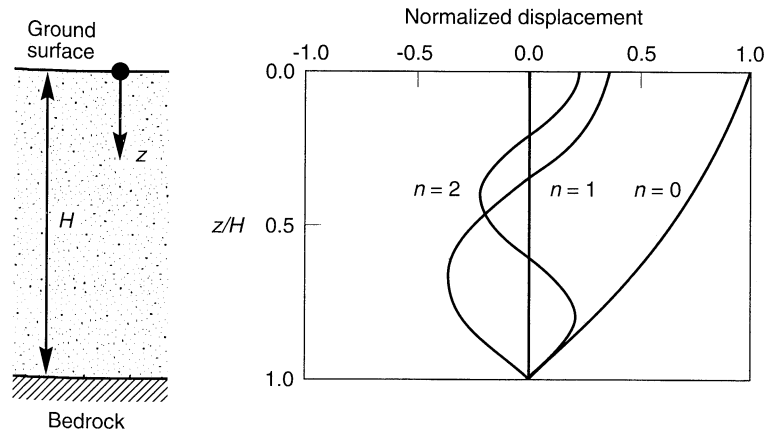


Figure 7.6 Displacement patterns for standing waves at fundamental ($n = 0$), second ($n = 1$) and third ($n = 2$) natural frequencies for a soil layer with $\xi = 5\%$. Displacements are normalized by maximum displacement at the fundamental frequency.

Example 7.2

The site at which the Gilroy No. 2 (soil) earthquake motion shown in Figure 3.1 was recorded is underlain by some 540 ft of soil underlain by shale and serpentinite bedrock. The shear wave velocity of the soil varies from about 1000 ft/sec at depths less than about 130 ft to about 2000 ft/sec at greater depths. Assuming an average shear wave velocity of 1500 ft/sec², an average unit weight of 125 lb/ft³, a damping ratio of 5%, and rigid bedrock (Figure E7.2a), compute the ground surface motion that would occur if the bedrock was subjected to the E-W component of the Gilroy No. 1 (rock) motion.

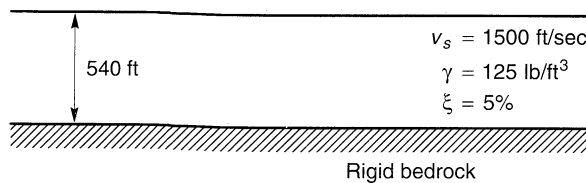


Figure E7.2a

Solution Computation of the ground surface motion from the bedrock motion can be accomplished in the same five steps as described in Example 7.1:

1. Obtain the time history of acceleration of the input motion. This step is identical to step 1 in Example 7.1; the motion is shown in Figure E7.2b.
2. Compute the Fourier series of the bedrock (input) motion. This step is also identical to step 2 in Example 7.1; the result is shown in Figure E7.2c.
3. Compute the transfer function that relates the ground surface (output) motion to the bedrock (input) motion. From equation (7.11), the transfer function for the case of damped soil is complex valued. The modulus of the transfer function is shown in Figure E7.2d. The shape of the transfer function indicates that significant amplification will occur at several natural frequencies, and that higher frequencies (greater than about 10 Hz) will be suppressed.

4. Compute the Fourier series of the ground surface (output) motion as the product of the transfer function and the Fourier series of the bedrock (input) motion. The Fourier spectrum of the ground surface motion (Figure E7.2e) shows amplification at the natural frequencies of the soil deposit and little high-frequency motion.
5. Obtain the time history of the ground surface motion by inverting the Fourier series. The time history of ground surface motion (Figure E7.2f) indicates that peak accelerations at the ground surface and bedrock levels are similar, but the frequency contents are different. Because the ground surface motion is weighted toward lower frequencies, the peak velocity and displacement at the ground surface are likely to be considerably greater than at bedrock.

The rigid bedrock analysis predicts a peak ground surface acceleration of 0.452 g, which is considerably greater than the peak acceleration of 0.322g actually recorded at the Gilroy No. 2 (soil) station.

Uniform, Damped Soil on Elastic Rock. The preceding two sections developed expressions for amplification factors for soils overlying rigid bedrock. If the bedrock is rigid, its motion will be unaffected by motions in, or even the presence of, the overlying

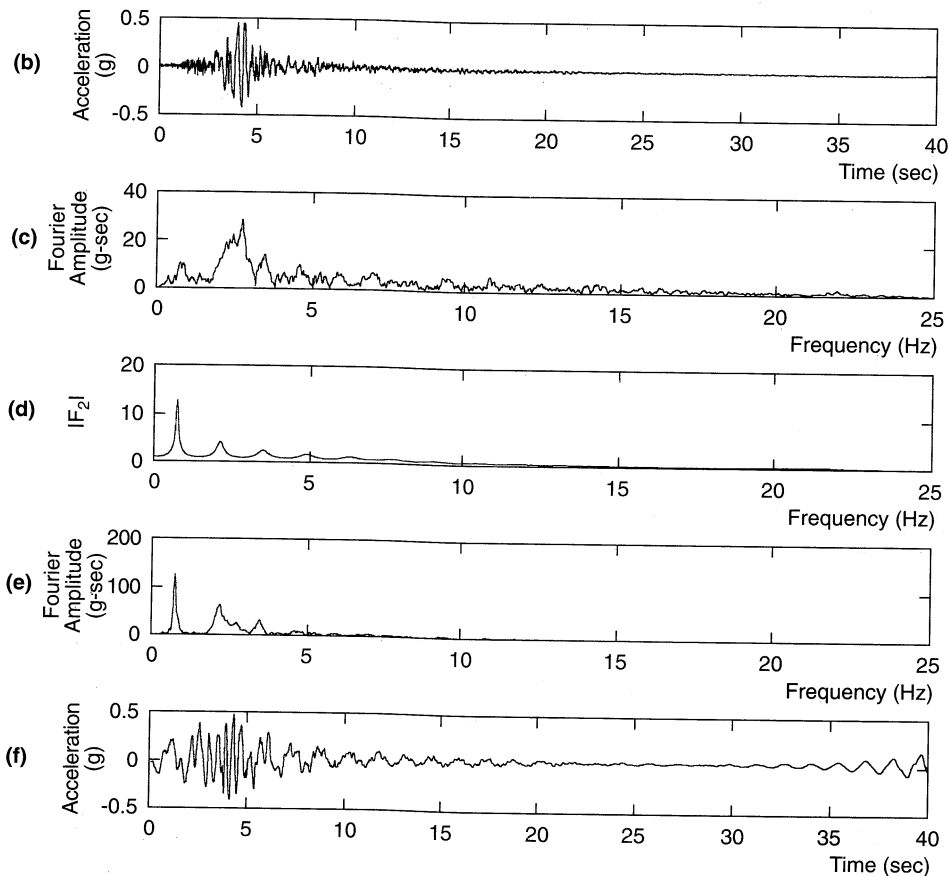


Figure E7.2b-f

✓ soil. It acts as a fixed end (Section 5.4.1) boundary. Any downward-traveling waves in the soil will be completely reflected back toward the ground surface by the rigid layer, thereby trapping all of the elastic wave energy within the soil layer.

If the rock is elastic, however, downward-traveling stress waves that reach the soil–rock boundary will be reflected only partially; part of their energy will be transmitted through the boundary to continue traveling downward through the rock. If the rock extends to great depth (large enough that waves reflected from any deeper material boundaries do not return to the soil–rock boundary soon enough, or with sufficient amplitude, to influence the response of the soil deposit), the elastic energy of these waves will effectively be removed from the soil layer. This is a form of radiation damping, and it causes the free surface motion amplitudes to be smaller than those for the case of rigid bedrock.

Consider the case of a soil layer overlying a halfspace of elastic rock (Figure 7.7). If the subscripts s and r refer to soil and rock, respectively, the displacements due to vertically propagating s-waves in each material can be written as

$$u_s(z_s, t) = A_s e^{i(\omega t + k_s^* z_s)} + B_s e^{i(\omega t - k_s^* z_s)} \quad (7.17a)$$

$$u_r(z_r, t) = A_r e^{i(\omega t + k_r^* z_r)} + B_r e^{i(\omega t - k_r^* z_r)} \quad (7.17b)$$

The free surface effect, as before, requires that $A_s = B_s$, and compatibility of displacements and continuity of stresses at the soil–rock boundary require that

$$u_s(z_s = H) = u_r(z_r = 0) \quad (7.18)$$

$$\tau_s(z_s = H) = \tau_r(z_r = 0) \quad (7.19)$$

Substituting equations (7.17) into equation (7.18) yields

$$A_s(e^{ik_s^* H} + e^{-ik_s^* H}) = A_r + B_r \quad (7.20)$$

From equation (7.19) and the definition of shear stress ($\tau = G \partial u / \partial z$)

$$A_s i G_s k_s^* (e^{ik_s^* H} - e^{-ik_s^* H}) = i G_r k_r^* (A_r - B_r) \quad (7.21)$$

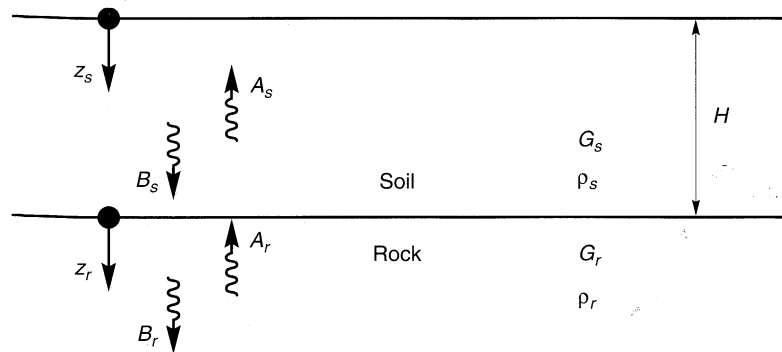


Figure 7.7 Nomenclature for the case of a soil layer overlying a half-space of elastic rock.

or

$$\frac{G_s k_s^*}{G_r k_r^*} A_s (e^{ik_s^* H} - e^{-ik_s^* H}) = A_r - B_r \quad (7.22)$$

The ratio

$$\frac{G_s k_s^*}{G_r k_r^*} = \frac{\rho_s v_{ss}^*}{\rho_r v_{sr}^*} = \alpha_z^* \quad (7.23)$$

where v_{ss}^* and v_{sr}^* are the complex shear wave velocities of the soil and rock, respectively, and α_z^* is the complex impedance ratio (see Section 5.4.1). Solving equations (7.20) and (7.22) simultaneously gives

$$A_r = \frac{1}{2} A_s [(1 + \alpha_z^*) e^{ik_s^* H} + (1 - \alpha_z^*) e^{-ik_s^* H}] \quad (7.24a)$$

$$B_r = \frac{1}{2} A_s [(1 - \alpha_z^*) e^{ik_s^* H} + (1 + \alpha_z^*) e^{-ik_s^* H}] \quad (7.24b)$$

Suppose that a vertically propagating shear wave of amplitude, A , traveled upward through the rock. If the soil was not present, the free surface effect at the rock outcrop would produce a bedrock outcropping motion of amplitude $2A$. With the soil present, the free surface motion amplitude would be

$$2A_s = \frac{4A}{(1 + \alpha_z^*) e^{ik_s^* H} + (1 - \alpha_z^*) e^{-ik_s^* H}}$$

Defining the transfer function, F_3 , as the ratio of the soil surface amplitude to the rock outcrop amplitude,

$$F_3(\omega) = \frac{2}{(1 + \alpha_z^*) e^{ik_s^* H} + (1 - \alpha_z^*) e^{-ik_s^* H}} \quad (7.25)$$

which, using Euler's law, can be rewritten as

$$F_3(\omega) = \frac{1}{\cos k_s^* H + i \alpha_z^* \sin k_s^* H} = \frac{1}{\cos(\omega H / v_{ss}^*) + i \alpha_z^* \sin(\omega H / v_{ss}^*)} \quad (7.26)$$

The modulus of $F_3(\omega)$ cannot be expressed in a very compact form when soil damping exists. To illustrate the important effect of bedrock elasticity, however, the amplification factor for undamped soil can be expressed as

$$|F_3(\omega, \xi = 0)| = \frac{1}{\sqrt{\cos^2 k_s H + \alpha_z^2 \sin^2 k_s H}} \quad (7.27)$$

Note that resonance cannot occur (the denominator is always greater than zero, even when the soil is undamped). The effect of the bedrock stiffness, as reflected by the impedance ratio, on amplification behavior is illustrated in Figure 7.8. Note the similarity between the effects of soil damping and bedrock elasticity by comparing the shapes of the amplification factor curves in Figure 7.8 and those in Figure 7.5. The elasticity of the rock affects amplification

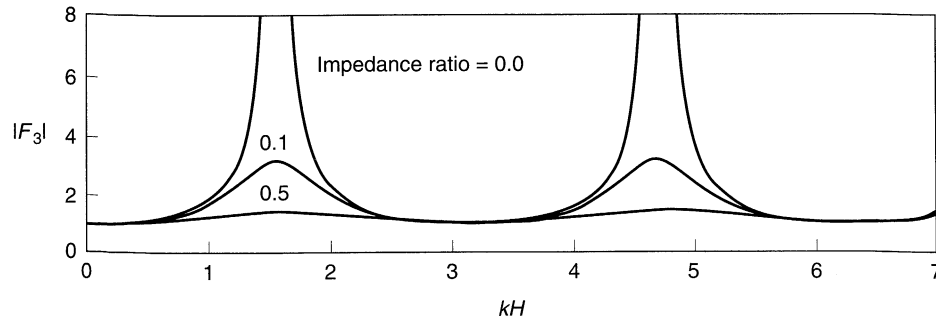


Figure 7.8 Effect of impedance ratio on amplification factor for case of undamped soil.

similarly to the damping ratio of the soil—both prevent the denominator from reaching zero. This radiation damping effect has significant practical importance, particularly in the eastern United States, where bedrock is substantially harder than that typically found in the western states. The stiffer bedrock means that greater amplification may occur in the east and that design criteria established on the basis of empirical evidence from western earthquakes may be somewhat unconservative in the east.

Example 7.3

Repeat Example 7.2 assuming that the bedrock is not rigid. Assume a shear wave velocity of 5000 ft/sec, a unit weight of 160 lb/ft³, and 2% damping for bedrock at the Gilroy No. 2 site (Figure E7.3a).

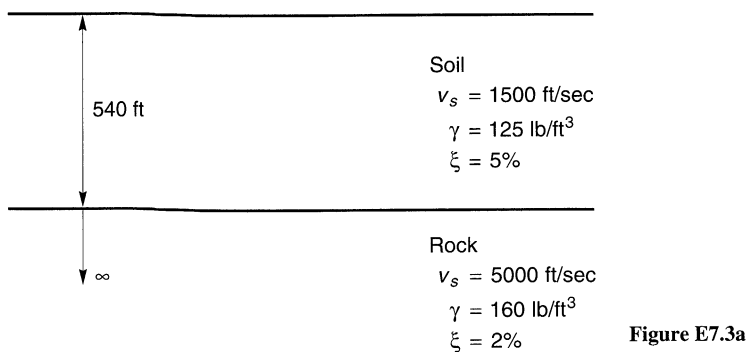


Figure E7.3a

Solution Computation of the ground surface motion from the bedrock motion can be accomplished in the same five steps described in Example 7.2. The only difference is that the transfer function in this example will include the effects of bedrock compliance.

1. Obtain the time history of acceleration of the input motion. This step is identical to step 1 in Examples 7.1 and 7.2; the motion is shown in Figure E7.3b.
2. Compute the Fourier series of the bedrock (input) motion. Again, this step is identical to step 2 in Examples 7.1 and 7.2; the result is shown in Figure E7.3c.
3. Compute the transfer function that relates the ground surface (output) motion to the bedrock (input) motion. From Equation 7.25, the transfer function for the case of damped

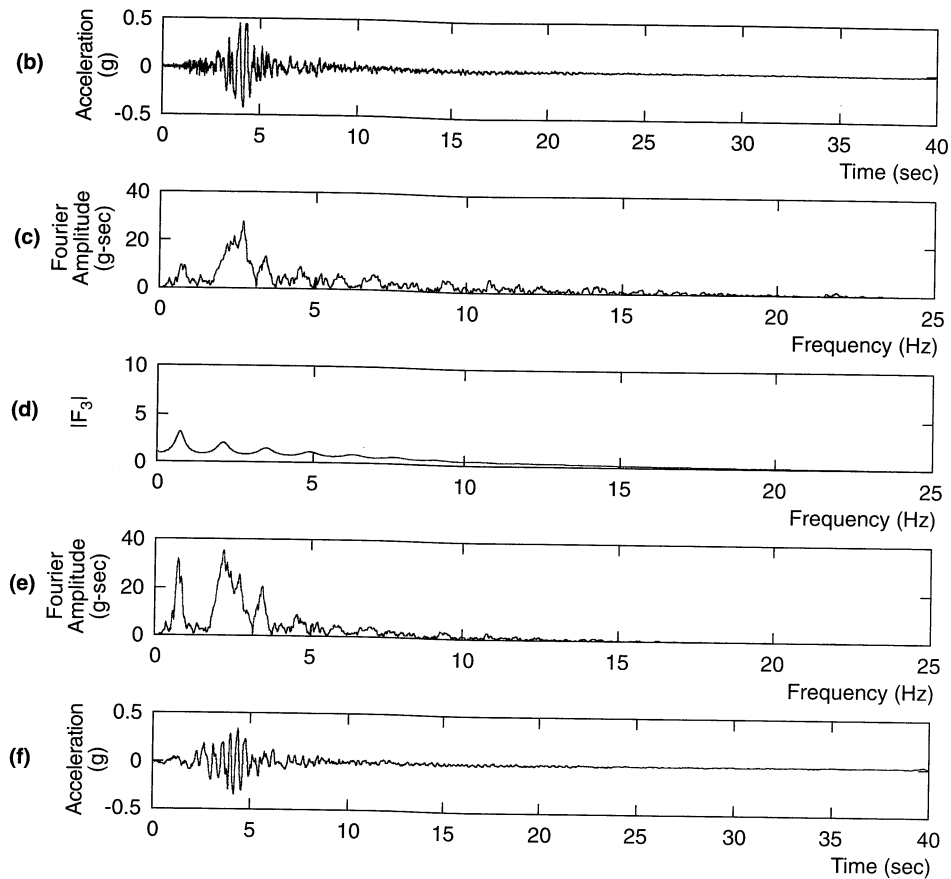


Figure E7.3b-f

soil is complex valued. The modulus of the transfer function, shown in Figure E7.3d, indicates that less amplification will occur than in the case of rigid bedrock.

4. Compute the Fourier series of the ground surface (output) motion as the product of the transfer function and the Fourier series of the bedrock (input) motion. The Fourier series of the ground surface motion (Figure E7.3e) shows less amplification than in the case of rigid bedrock.
5. Obtain the time history of the ground surface motion by inverting the Fourier series. The time history of ground surface motion (Figure E7.3f) indicates that the peak accelerations at the ground surface is lower than the peak acceleration at the bedrock level; the frequency contents are also different.

The compliant bedrock analysis predicts a peak ground surface acceleration of $0.339g$, which agrees well with the peak acceleration of $0.322g$ recorded at the Gilroy No. 2 (soil) station. The good agreement between peak accelerations, however, does not mean that this simple analysis has predicted all aspects of the Gilroy No. 2 (soil) motion. Comparison of the Fourier amplitude spectrum of the predicted motion (Figure E7.3e) with that of the recorded motion (Figure 3.13b) shows significant differences in frequency content.

Layered, Damped Soil on Elastic Rock. While the uniform elastic layer models are useful for illustration of the influence of soil conditions on several ground motion characteristics, they are seldom suitable for analysis of practical ground response problems. Real ground response problems usually involve soil deposits with layers of different stiffness and damping characteristics with boundaries at which elastic wave energy will be reflected and/or transmitted. Such conditions require the development of transfer functions for layered soil deposits.

Consider a soil deposit consisting of N horizontal layers where the N th layer is bedrock (Figure 7.9). Assuming that each layer of soil behaves as a Kelvin–Voigt solid, the wave equation is of the form given in equation (5.94). The solution to the wave equation can be expressed in the form

$$u(z, t) = Ae^{i(\omega t + k^*z)} + Be^{i(\omega t - k^*z)} \quad (7.28)$$

where A and B represent the amplitudes of waves traveling in the $-z$ (upward) and $+z$ (downward) directions, respectively. The shear stress is then given by the product of the complex shear modulus, G^* , and the shear strain, so

$$\tau(z, t) = G^* \frac{\partial u}{\partial z} = (G + i\omega\eta) \frac{\partial u}{\partial z} = G(1 + 2i\xi) \frac{\partial u}{\partial z} \quad (7.29)$$

Introducing a local coordinate system, Z , for each layer, the displacement at the top and bottom of layer m will be

$$u_m(Z_m = 0, t) = (A_m + B_m)e^{i\omega t} \quad (7.30a)$$

$$u_m(Z_m = h_m, t) = (A_me^{ik_m^*h_m} + B_me^{-ik_m^*h_m})e^{i\omega t} \quad (7.30b)$$

Displacements at layer boundaries must be compatible (i.e., the displacement at the top of a particular layer must be equal to the displacement at the bottom of the overlying layer).

✓ Applying the compatibility requirement to the boundary between layer m and layer $m + 1$, that is,

$$u_m(Z_m = h_m, t) = u_{m+1}(Z_{m+1} = 0, t)$$

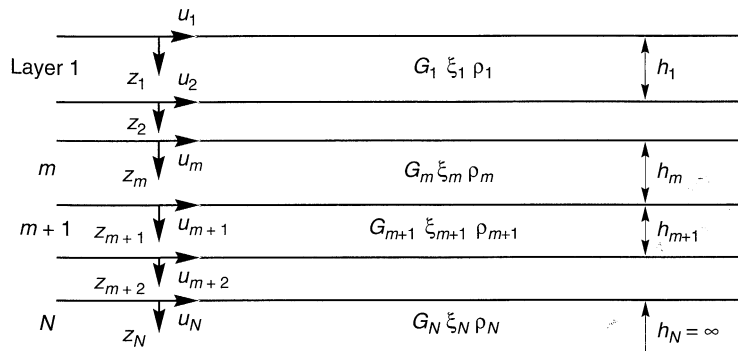


Figure 7.9 Nomenclature for layered soil deposit on elastic bedrock.

yields

$$A_{m+1} + B_{m+1} = A_m e^{ik_m^* h_m} + B_m e^{-ik_m^* h_m} \quad (7.31)$$

The shear stresses at the top and bottom of layer m are

$$\tau_m(Z_m = 0, t) = ik_m^* G_m^* (A_m - B_m) e^{i\omega t} \quad (7.32a)$$

$$\tau_m(Z_m = h_m, t) = ik_m^* G_m^* (A_m e^{ik_m^* h_m} - B_m e^{-ik_m^* h_m}) e^{i\omega t} \quad (7.32b)$$

✓ Since stresses must be continuous at layer boundaries,

$$\tau_m(Z_m = h_m, t) = \tau_{m+1}(Z_{m+1} = 0, t)$$

so

$$A_{m+1} - B_{m+1} = \frac{k_m^* G_m^*}{k_{m+1}^* G_{m+1}^*} (A_m e^{ik_m^* h_m} - B_m e^{-ik_m^* h_m}) \quad (7.33)$$

Adding (7.31) and (7.33) and subtracting (7.33) from (7.31) gives the recursion formulas

$$A_{m+1} = \frac{1}{2} A_m (1 + \alpha_m^*) e^{ik_m^* h_m} + \frac{1}{2} B_m (1 - \alpha_m^*) e^{-ik_m^* h_m} \quad (7.34a)$$

$$B_{m+1} = \frac{1}{2} A_m (1 - \alpha_m^*) e^{ik_m^* h_m} + \frac{1}{2} B_m (1 + \alpha_m^*) e^{-ik_m^* h_m} \quad (7.34b)$$

where α_m^* is the complex impedance ratio at the boundary between layers m and $m+1$:

$$\alpha_m^* = \frac{k_m^* G_m^*}{k_{m+1}^* G_{m+1}^*} = \frac{\rho_m (v_s^*)_m}{\rho_{m+1} (v_s^*)_{m+1}} \quad (7.35)$$

✓ At the ground surface, the shear stress must be equal to zero, which requires [from equation (7.32a)] that $A_1 = B_1$. If the recursion formulas of equation (7.34) are applied repeatedly for all layers from 1 to m , functions relating the amplitudes in layer m to those in layer 1 can be expressed by

$$A_m = a_m(\omega) A_1 \quad (7.36a)$$

$$B_m = b_m(\omega) B_1 \quad (7.36b)$$

The transfer function relating the displacement amplitude at layer i to that at layer j is given by

$$F_{ij}(\omega) = \frac{|u_i|}{|u_j|} = \frac{a_i(\omega) + b_i(\omega)}{a_j(\omega) + b_j(\omega)} \quad (7.37)$$

Because $|\ddot{u}| = \omega|\dot{u}| = \omega^2|u|$ for harmonic motion, equation (7.37) also describes the amplification of accelerations and velocities from layer i to layer j . Equation (7.37) indicates that the motion in any layer can be determined from the motion in any other layer. Hence if the motion at any one point in the soil profile is known, the motion at any other point can be contributed. This result allows a very useful operation called *deconvolution* (Section 7.2.1.4) to be performed.

Example 7.4

As part of a comprehensive investigation of ground motion estimation techniques, the Electric Power Research Institute performed a detailed subsurface investigation at the site of the Gilroy

No. 2 (soil) recording station (EPRI, 1993). A rough approximation to the measured shear wave velocity profile is listed below.

Depth Range (ft)	Average Shear Wave Velocity (ft/sec)
0–20	500
20–45	700
45–70	1500
70–130	1000
130–540	2000
> 540	5000

Assuming, as in Examples 7.2 and 7.3, an average soil unit weight of 125 lb/ft^3 and 5% soil damping, compute the expected ground surface response when the bedrock is subjected to the Gilroy No. 1 (rock) motion.

Solution As in the previous examples of this chapter, this problem requires evaluation of the transfer function that relates the ground surface motion to the bedrock motion. Because of multiple reflections within the layered system, the transfer function [equation (7.36)] for this example is considerably more complicated than for the single-layered cases of the previous examples. While the transfer function can be evaluated by hand, it has also been coded in the computer program SHAKE (Schnabel et al., 1972). SHAKE was used, with constant soil stiffness and damping ratio, to obtain the transfer function shown in Figure E7.4c. As in the previous examples, the Fourier series of the ground surface motion (Figure E7.4d) was computed as the product of the transfer function and the Fourier series of the bedrock motion. Inversion of this Fourier series produces the time history of ground surface acceleration (Figure E7.4e).

Examination of Figure E7.4c shows that the transfer function for the layered system is indeed more complicated than the transfer functions for the single-layered cases of Examples 7.1, 7.2, and 7.3. The spikes in the transfer function at frequencies of about 3.5 and 5.5 Hz help produce a peak acceleration of $0.499g$ that is considerably larger than the peak acceleration of $0.322g$ that was actually recorded at the Gilroy No. 2 (soil) station. Differences in the frequency contents of the predicted and recorded motions can be seen by comparing Figures E7.4d and 3.13b.

7.2.1.2 Equivalent Linear Approximation of Nonlinear Response

Since the nonlinearity of soil behavior is well known, the linear approach must be modified to provide reasonable estimates of ground response for practical problems of interest. As discussed in Chapter 6, the actual nonlinear hysteretic stress–strain behavior of cyclically loaded soils can be approximated by equivalent linear soil properties. The equivalent linear shear modulus, G , is generally taken as a secant shear modulus and the equivalent linear damping ratio, ξ , as the damping ratio that produces the same energy loss in a single cycle as the actual hysteresis loop. The strain-dependent nature of these equivalent linear properties was described in Section 6.4.2.

Since the linear approach requires that G and ξ be constant for each soil layer, the problem becomes one of determining the values that are consistent with the level of strain induced in each layer. To address this problem, an objective definition of strain level is needed. The laboratory tests from which modulus reduction and damping ratio curves (e.g., those shown in Figures 6.47 and 6.50) have been developed used simple harmonic loading

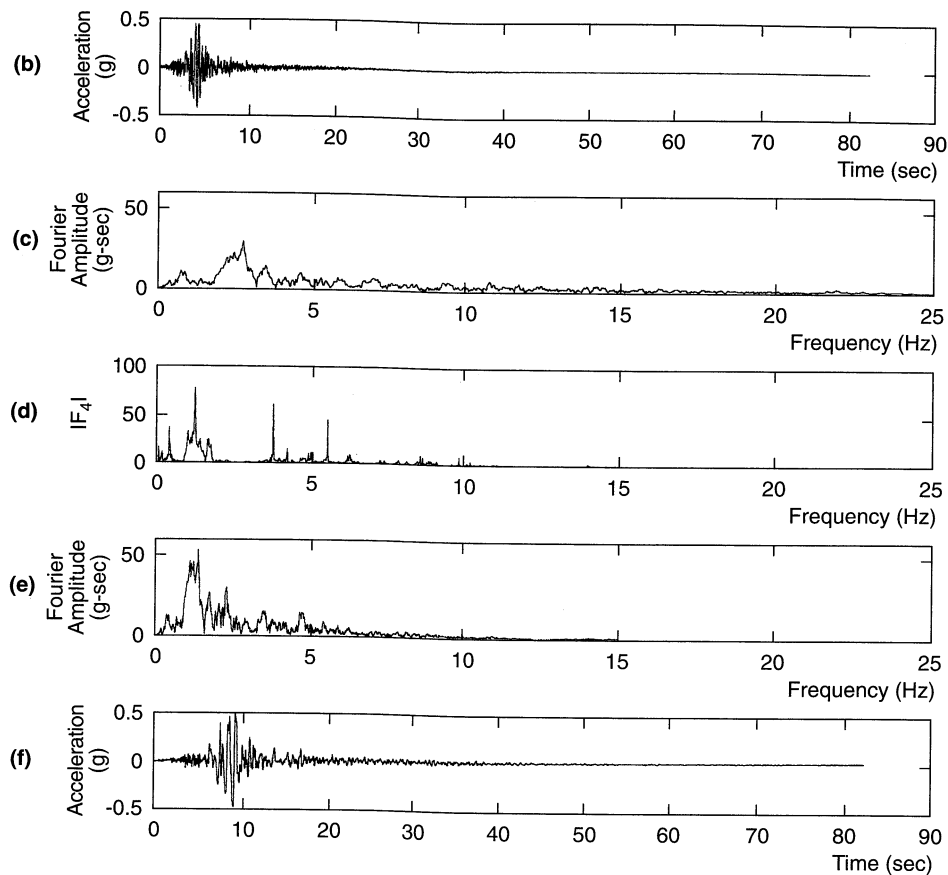


Figure E7.4

and characterized the strain level by the peak shear strain amplitude. The time history of shear strain for a typical earthquake motion, however, is highly irregular with a peak amplitude that may only be approached by a few spikes in the record. Figure 7.10 shows both harmonic (as in a typical laboratory test) and transient (as in a typical earthquake) shear strain time histories that have the same peak cyclic shear strain. Clearly, the harmonic record represents a more severe loading condition than the transient record, although their peak values are identical. As a result, it is common to characterize the strain level of the transient record in terms of an effective shear strain which has been empirically found to vary between about 50 and 70% of the maximum shear strain. The computed response is not particularly sensitive to this percentage, however, and the effective shear strain is often taken as 65% of the peak strain.

Since the computed strain level depends on the values of the equivalent linear properties, an iterative procedure is required to ensure that the properties used in the analysis are compatible with the computed strain levels in all layers. Referring to Figure 7.11, the iterative procedure operates as follows:

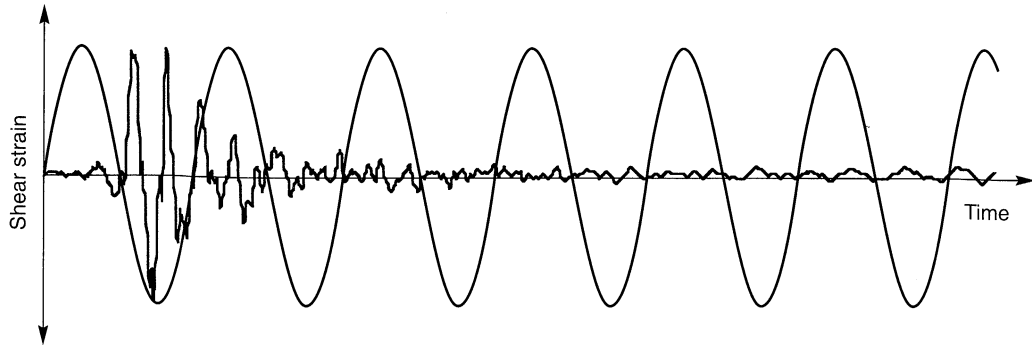


Figure 7.10 Two shear strain time histories with identical peak shear strains. For the transient motion of an actual earthquake, the effective shear strain is usually taken as 65% of the peak strain.

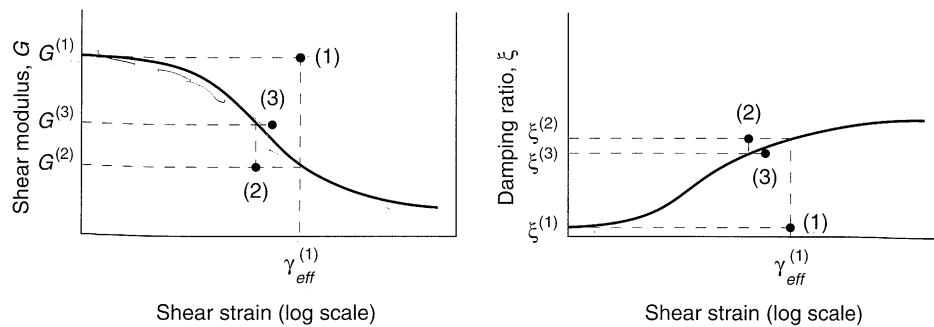


Figure 7.11 Iteration toward strain-compatible shear modulus and damping ratio in equivalent linear analysis. Using initial estimates, $G^{(1)}$ and $\xi^{(1)}$, the equivalent linear analysis predicts an effective shear strain, $\gamma_{eff}^{(1)}$. Because this strain is greater than those corresponding to $G^{(1)}$ and $\xi^{(1)}$, an iteration is required. The next iteration uses parameters, $G^{(2)}$ and $\xi^{(2)}$, that are compatible with $\gamma_{eff}^{(1)}$. The equivalent linear analysis is repeated and the parameters checked until strain-compatible value of G and ξ are obtained.

1. Initial estimates of G and ξ are made for each layer. The initially estimated values usually correspond to the same strain level; the low-strain values are often used for the initial estimate.
2. The estimated G and ξ values are used to compute the ground response, including time histories of shear strain for each layer.
3. The effective shear strain in each layer is determined from the maximum shear strain in the computed shear strain time history. For layer j

$$\gamma_{effj}^{(i)} = R_{\gamma} \gamma_{maxj}^{(i)}$$

where the superscript refers to the iteration number and R_{γ} is the ratio of the effective shear strain to maximum shear strain. R_{γ} depends on earthquake magnitude (Idriss and Sun, 1992) and can be estimated from

$$R_\gamma = \frac{M-1}{10}$$

4. From this effective shear strain, new equivalent linear values, $G^{(i+1)}$ and $\xi^{(i+1)}$ are chosen for the next iteration.
5. Steps 2 to 4 are repeated until differences between the computed shear modulus and damping ratio values in two successive iterations fall below some predetermined value in all layers. Although convergence is not absolutely guaranteed, differences of less than 5 to 10% are usually achieved in three to five iterations (Schnabel et al., 1972).

Even though the process of iteration toward strain-compatible soil properties allows nonlinear soil behavior to be approximated, it is important to remember that the complex response method is still a linear method of analysis. The strain-compatible soil properties are constant throughout the duration of the earthquake, regardless of whether the strains at a particular time are small or large. The method is incapable of representing the changes in soil stiffness that actually occur during the earthquake. The equivalent linear approach to one-dimensional ground response analysis of layered sites has been coded into a widely used computer program called SHAKE (Schnabel et al., 1972).

Example 7.5

An extensive laboratory testing program conducted by EPRI (1993) produced detailed information on the modulus reduction and damping characteristics of the soils beneath the Gilroy No. 2 (soil) recording station. Although the soil conditions varied with depth, a rough approximation to the average modulus reduction and damping characteristics is given below.

	Strain (%)										
	10^{-4}	$10^{-3.5}$	10^{-3}	$10^{-2.5}$	10^{-2}	$10^{-1.5}$	10^{-1}	$10^{-0.5}$	10^0	$10^{0.5}$	10^1
G/G_{\max}	1.00	1.00	1.00	0.99	0.90	0.71	0.47	0.24	0.10	0.05	0.04
ξ (%)	3.00	3.00	3.00	3.53	4.83	7.68	12.3	18.5	24.4	27.0	30.0

Repeat the analysis of Example 7.4 with the data listed above using the iterative equivalent linear approach.

Solution As in the case of Example 7.4, the transfer function was evaluated using the computer program SHAKE (Schnabel et al., 1972). In this example the first iteration used the same stiffness and damping values used in Example 7.4. Subsequent iterations used stiffness and damping values that were consistent with the modulus reduction and damping behavior listed above. After a total of eight iterations, the shear moduli and damping ratios had converged to within 1% of strain-compatible values. Because the strain-compatible shear moduli were smaller than the low-strain shear moduli on which the analysis of Example 7.4 was based (the iterations converged to strains at which G/G_{\max} values were less than 1.0), the transfer function (Figure E7.5c) was shifted toward lower frequencies. As in the previous examples, the Fourier series of the ground surface motion (Figure E7.5d) was computed as the product of the transfer function and the Fourier series of the bedrock motion. Inversion of this Fourier series produced the time history of ground surface acceleration shown in Figure E7.5e.

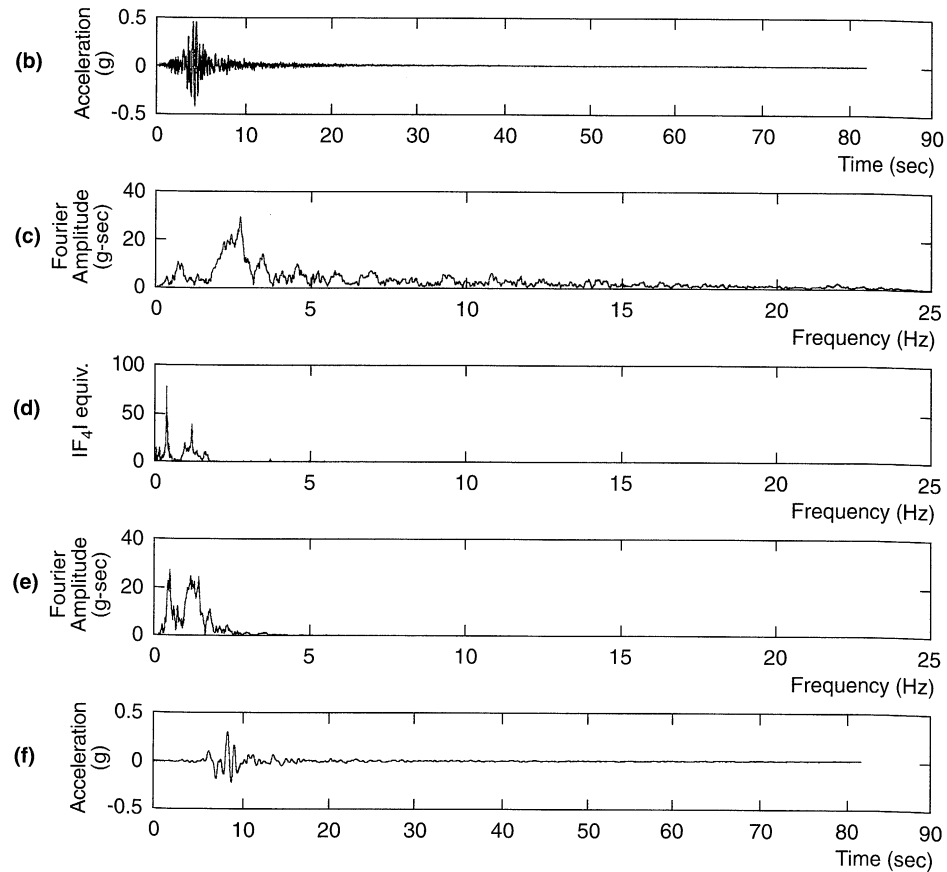


Figure E7.5

The softer soil behavior indicated by the iterative equivalent linear analysis is clearly reflected in the transfer function (Figure E7.5c), the Fourier series of the ground surface motion (Figure E7.5d), and the time history of ground surface acceleration (Figure E7.5e). The predicted peak ground surface acceleration of 0.304g compares well with the peak acceleration of 0.322g recorded at the Gilroy No. 2 (soil) station, but comparison of the overall motions in the time domain (Figure E7.5e versus Figure 3.1) and frequency domain (Figure E7.5d versus Figure 3.13b) shows significant differences.

The analysis described in this example was intended to illustrate the effects of the equivalent linear approach to approximation of nonlinear soil behavior on computed ground motions. Like Examples 7.2 to 7.4, it characterized the actual soil conditions at the Gilroy No. 2 (soil) site in a simplified manner. More detailed characterization (EPRI, 1993) produced significantly better agreement between predicted and recorded motions.

7.2.1.3 Deconvolution

Because the equivalent linear approach utilizes a linear analysis, the response at any point can be related to the response at any other point. Although the transfer functions developed in Section 7.1.1.1 related to the computation of free surface motion from bedrock

motion, transfer functions relating motions at other depths can also be derived without difficulty. An important problem of practical interest involves the computation of bedrock motion from a known free surface motion. This process, known as *deconvolution*, is particularly useful in the interpretation of actual ground motions recorded on the surfaces of soil deposits.

Although deconvolution of a linear elastic system should theoretically produce a unique solution, practical difficulties often arise. Some of these may be of a numerical nature, particularly when iteration toward strain-compatible soil properties are required (Roesset, 1977) and strain levels are large. Others are associated with limitations in the accuracy of the assumption that all motion results from vertically propagating shear waves. Silva (1988) found that about 75% of the power (87% of the amplitude) in a free surface motion could be attributed to vertically propagating shear waves at frequencies up to 15 Hz; the remainder was attributed to scattered waves and surface waves. Silva suggested a deconvolution procedure based on the use of a prefiltered (15 Hz low-pass to eliminate the tendency to develop unrealistically large accelerations at depth) free surface motion and iteration toward strain-compatible properties using 87% of the input motion amplitudes before deconvolving using the filtered free surface motion at full (100%) amplitude. Deconvolution should be performed with great care and the reasonableness of any deconvolved motion evaluated carefully.

7.2.2 Nonlinear Approach

Although the equivalent linear approach is computationally convenient and provides reasonable results for many practical problems, it remains an approximation to the actual nonlinear process of seismic ground response. An alternative approach is to analyze the actual nonlinear response of a soil deposit using direct numerical integration in the time domain. By integrating the equation of motion in small time steps, any linear or nonlinear stress-strain model (Section 6.4.3) or advanced constitutive model (Section 6.4.4) can be used. At the beginning of each time step, the stress-strain relationship is referred to to obtain the appropriate soil properties to be used in that time step. By this method, a nonlinear inelastic stress-strain relationship can be followed in a set of small incrementally linear steps.

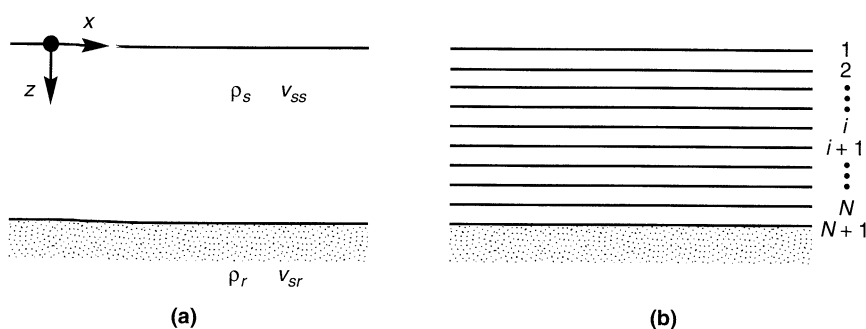
Most currently available nonlinear one-dimensional ground response analysis computer programs characterize the stress-strain behavior of the soil by cyclic stress-strain models (Section 6.4.3) such as the hyperbolic model, modified hyperbolic model, Ramberg-Osgood model, Hardin-Drnevich-Cundall-Pyke (HDCP) model, Martin-Davidenkova model, and Iwan-type model. Others have been based on advanced constitutive models (Section 6.4.4), such as the nested yield surface model. Some of the most commonly used computer programs for nonlinear one-dimensional ground response analysis are listed in Table 7-1. A number of techniques can be used to integrate the equations of motion. Of these, the explicit finite-difference technique is most easily explained.

Consider the soil deposit of infinite lateral extent shown in Figure 7.12a. If the soil layer is subjected to horizontal motion at the bedrock level, the response will be governed by the equation of motion

$$\frac{\partial \tau}{\partial z} = \rho \frac{\partial^2 u}{\partial t^2} = \rho \frac{\partial \dot{u}}{\partial t} \quad (7.38)$$

Table 7-1 Computer Programs for Nonlinear One-Dimensional Ground Response Analysis

Program	Soil Model	Reference
CHARSOIL	Ramberg-Osgood	Streeter et al. (1973)
DESRA-2	Hyperbolic	Lee and Finn (1978)
DYNA1D	Nested yield surface	Prevost (1989)
MASH	Martin-Davidenkov	Martin and Seed (1978)
NONLI3	Iwan-type	Joyner (1977)
TESS1	HDCP	Pyke (1985)

**Figure 7.12** (a) Nomenclature for uniform soil deposit of infinite lateral extent overlying bedrock; (b) discretization of soil deposit into N sublayers.

To introduce the explicit finite-difference method, consider the function $f(x)$ shown in Figure 7.13. The first derivative of $f(x)$ at $x = \tilde{x}$ is given by

$$\frac{df(\tilde{x})}{dx} = \lim_{\Delta x \rightarrow 0} \frac{f(\tilde{x} + \Delta x) - f(\tilde{x})}{\Delta x} \quad (7.39)$$

A reasonable approximation to the first derivative can be made by removing the restriction of the limit and using a small but finite value of Δx . In this way the expression of equation (7.39) is referred to as a *forward-difference* approximation to $df(\tilde{x})/dx$. Figure 7.13 illustrates that the forward difference actually provides a better approximation to the derivative at $x = \tilde{x} + \Delta x/2$ than at $x = \tilde{x}$.

Dividing the soil layer into N sublayers of thickness, Δz (Figure 7.12b), and proceeding through time in small time increments of length, Δt , the notation $u_{i,t} = u(z = i \Delta z, t)$ can be used to write finite-difference approximations to the derivatives

$$\frac{\partial \tau}{\partial z} \approx \frac{\tau_{i+1,t} - \tau_{i,t}}{\Delta z} \quad (7.40a)$$

$$\frac{\partial \dot{u}}{\partial t} \approx \frac{\dot{u}_{i,t+\Delta t} - \dot{u}_{i,t}}{\Delta t} \quad (7.40b)$$

Substituting equations (7.40) into the equation of motion allows that differential equation to be approximated by the explicit finite-difference equation

$$\frac{\tau_{i+1,t} - \tau_{i,t}}{\Delta z} = \rho \frac{\dot{u}_{i,t+\Delta t} - \dot{u}_{i,t}}{\Delta t} \quad (7.41)$$

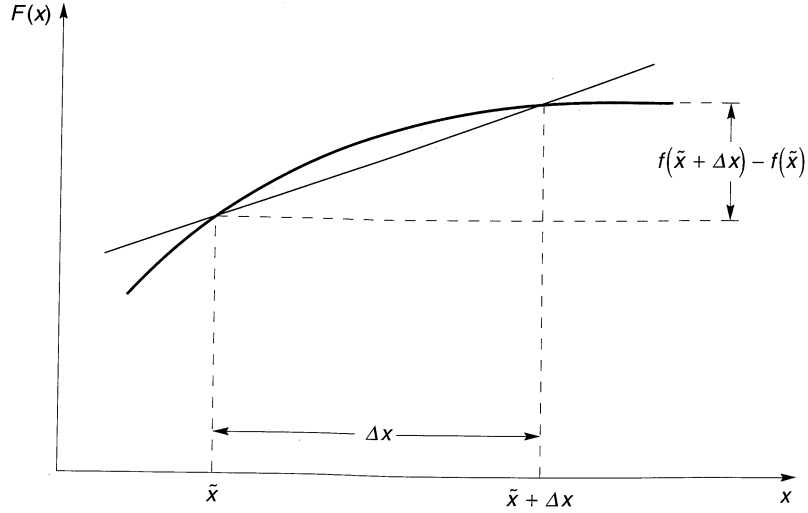


Figure 7.13 Forward-difference approximation of $f'(x)$ is given by slope of line passing through function at $x = \tilde{x}$ and $x = \tilde{x} + \Delta x$. Approximation becomes exact as $\Delta x \rightarrow 0$.

Solving for $\dot{u}_{i,t+\Delta t}$ gives

$$\dot{u}_{i,t+\Delta t} = \dot{u}_{i,t} + \frac{\Delta t}{\rho \Delta z} (\tau_{i+1,t} - \tau_{i,t}) \quad (7.42)$$

Equation (7.42) simply shows how the conditions at time, t , can be used to determine the conditions at time, $t + \Delta t$. Using equation (7.42) for all i , the velocity profile can be determined at time $t + \Delta t$. Using the computed velocities at the end of each time step as the initial velocities for the next time step, the repeated application of equation (7.42) allows the equation of motion to be integrated in a series of small time steps.

As with any integration problem, however, the boundary conditions must be satisfied. Since the ground surface is a free surface, $\tau_1 = 0$, so

$$\dot{u}_{1,t+\Delta t} = \dot{u}_{1,t} + \frac{\Delta t}{\rho \Delta z} \tau_{2,t} \quad (7.43)$$

The boundary condition at the bottom of the soil deposit depends on the nature of the underlying bedrock. If the bedrock is rigid, its particle velocity, $\dot{u}_b(t) = \dot{u}_{N+1,t}$, can be specified directly as the input motion. If the bedrock is elastic, continuity of stresses requires that the shear stress at the bottom of the soil layer, $\tau_{N+1,t}$, be equal to the shear stress at the top of the rock layer, $\tau_{r,t}$. Thus

$$\dot{u}_{N+1,t+\Delta t} = \dot{u}_{N+1,t} + \frac{\Delta t}{\rho \Delta z} (\tau_{r,t} - \tau_{N,t}) \quad (7.44)$$

If an incident wave traveling upward through the rock has a particle velocity $\dot{u}_r(t)$ at the soil-rock boundary, the shear stress at the boundary is approximated (Joyner and Chen, 1975) by

$$\tau_{r,t} \approx \rho_r v_{sr} (2\dot{u}_r(t + \Delta t) - \dot{u}_{N+1,t+\Delta t}) \quad (7.45)$$

Substituting equation (7.45) into equation (7.44) and solving for $\dot{u}_{N+1,t+\Delta t}$ gives

$$\dot{u}_{N+1,t+\Delta t} = \frac{\dot{u}_{N+1,t} + \frac{\Delta t}{\rho \Delta z} [2\rho_r v_{sr} \dot{u}_r(t+\Delta t) - \tau_{N,t}]}{1 + (\Delta t / \rho \Delta z) \rho_r v_{sr}} \quad (7.46)$$

Once the boundary conditions have been established, the integration calculations proceed from the bottom ($i = N + 1$) to the top ($i = 1$) of the soil deposit in each time step, and step by step in time. Computation of the velocity at the end of each time step, however, requires knowledge of the shear stress in that time step.

If the soil deposit is initially at rest, then $\dot{u}_{i,t=0} = 0$ and $\tau_{i,t=0}$ for all i . When the input motion, in the form of $\dot{u}_b(t)$ (rigid bedrock) or $\dot{u}_r(t)$ (elastic bedrock), imparts some velocity to the base of the soil deposit, \dot{u}_{N+1} will take on a nonzero value. In subsequent time steps, $\dot{u}_N, \dot{u}_{N-1}, \dot{u}_{N-2}, \dots$ will all take on nonzero values as the soil deposit moves in response to the input motion. The incremental displacement in each time step is given by

$$\Delta u_{i,t} = \dot{u}_{i,t} \Delta t \quad (7.47)$$

Summing the incremental displacements allows the total displacement, $u_{i,t}$, to be determined at the beginning of each time step. The shear strain in each sublayer is given by

$$\gamma_{i,t} = \frac{\partial u_{i,t}}{\partial z} \approx \frac{u_{i+1,t} - u_{i,t}}{\Delta z} \quad (7.48)$$

If the soil is assumed to be linear elastic, the shear stress depends only on the current shear strain, (i.e., $\tau_{i,t} = G_i \gamma_{i,t}$). If the soil is nonlinear and inelastic, however, the shear stress will depend on the current shear strain and the stress–strain history. In such cases the computed shear strain, $\gamma_{i,t}$, and the cyclic stress–strain relationship (or advanced constitutive model) are used to determine the corresponding shear stress, $\tau_{i,t}$. The integration process can then be summarized as follows:

1. At the beginning of each time step, the particle velocity, $\dot{u}_{i,t}$, and total displacement, $u_{i,t}$, are known at each layer boundary.
2. The particle displacement profile is used to determine the shear strain, $\gamma_{i,t}$, within each layer.
3. The stress–strain relationship is used to determine the shear stress, $\tau_{i,t}$, in each layer. The stress–strain curve may be linear or nonlinear. If nonlinear inelastic soil behavior is assumed, stress reversals are checked and accounted for (e.g., by application of the Masing criteria) in each layer.
4. The input motion is used to determine the motion of the base of the soil layer at time $t + \Delta t$.
5. The motion of each layer boundary at time $t + \Delta t$ is calculated, working from bottom to top. The process is then repeated from step 1 to compute the response in the next time step.

Because the particle velocities are computed at times that differ by one-half time step from those at which the shear stresses are best approximated, the explicit method can become numerically unstable if the time step is too large (i.e., if $\Delta t > \Delta z / v_{ss}$) (Davis, 1986).

Using different difference expressions, an *implicit finite-difference* formulation can eliminate the stability problem, thereby allowing the use of longer time steps. Implicit formulations, however, involve the solution of a set of $N + 1$ simultaneous equations (which can be computationally time consuming for large N) at each time step. Whether it is more efficient to perform the rapid calculations of the explicit method at a large number of time steps, or the more time-consuming calculations of the implicit method at fewer time steps, is often difficult to predict. Most existing computer programs for nonlinear ground response analysis use the explicit formulation.

7.2.3 Comparison of One-Dimensional Ground Response Analyses

Although equivalent linear and nonlinear methods are both used to solve one-dimensional ground response analysis problems, their formulations and underlying assumptions are quite different. Consequently, it is reasonable to expect to find some differences in their results.

The results of equivalent linear and nonlinear ground response analyses have been compared on a number of occasions (e.g., Joyner and Chen, 1975; Martin and Seed, 1978; Dikmen and Ghaboussi, 1984) with the following general conclusions:

1. The inherent linearity of equivalent linear analyses can lead to *spurious resonances* (i.e., high levels of amplification that result from coincidence of a strong component of the input motion with one of the natural frequencies of the equivalent linear soil deposit). Since the stiffness of an actual nonlinear soil changes over the duration of a large earthquake, such high amplification levels will not develop in the field.
2. The use of an effective shear strain in an equivalent linear analysis can lead to an over-softened and overdamped system when the peak shear strain is much larger than the remainder of the shear strains, or to an under-softened, underdamped system when the shear strain amplitude is nearly uniform.
3. Equivalent linear analyses can be much more efficient than nonlinear analyses, particularly when the input motion can be characterized with acceptable accuracy by a small number of terms in a Fourier series. For example, most earthquakes contain relatively little elastic wave energy at frequencies above 15 to 20 Hz. Consequently, the response can usually be computed with reasonable accuracy by considering only the frequencies below 15 to 20 Hz (or lower, in some cases). As the power, speed, and accessibility of computers have increased in recent years, the practical significance of differences in the efficiency of one-dimensional ground response analyses has decreased substantially.
4. Nonlinear methods can be formulated in terms of effective stresses to allow modeling of the generation, redistribution, and eventual dissipation of excess pore pressure during and after earthquake shaking. Equivalent linear methods do not have this capability.
5. Nonlinear methods require a reliable stress-strain or constitutive model. The parameters that describe such models are not as well established as those of the equivalent linear model. A substantial field and laboratory testing program may be required to evaluate nonlinear model parameters.

6. Differences between the results of equivalent linear and nonlinear analyses depend on the degree of nonlinearity in the actual soil response. For problems where strain levels remain low (stiff soil profiles and/or relatively weak input motions), both analyses can produce reasonable estimates of ground response. For problems involving high strain levels, particularly problems in which the induced shear stresses approach the available shear strength of the soil, nonlinear analyses are likely to provide reasonable results.

In summary, both equivalent linear and nonlinear techniques can and have been used successfully for one-dimensional ground response analysis. The use and interpretation of each requires knowledge of their underlying assumptions, understanding of their operation, and recognition of their limitations. Neither can be considered mathematically rigorous or precise, yet their accuracy is not inconsistent with the variability in soil conditions, uncertainty in soil properties, and scatter in the experimental data upon which many of their input parameters are based.

7.3 TWO-DIMENSIONAL DYNAMIC RESPONSE ANALYSIS

The methods of one-dimensional ground response analysis described in previous sections are useful for level or gently sloping sites with parallel material boundaries. Such conditions are not uncommon and one-dimensional analyses are widely used in geotechnical earthquake engineering practice. For many other problems of interest, however, the assumptions of one-dimensional wave propagation are not acceptable. Sloping or irregular ground surfaces, the presence of heavy structures or stiff, embedded structures, or walls and tunnels all require two-dimensional or possibly even three-dimensional analysis. Problems in which one dimension is considerably greater than others can often be treated as two-dimensional plane strain problems. A number of common cases are shown in Figure 7.14.

The following sections discuss a number of methods that can be applied to two-dimensional dynamic response problems. Techniques for the solution of such problems have been developed using both frequency-domain (complex response) methods and time-domain (direct integration) methods. These techniques have been applied to many practical problems such as those shown in Figure 7.14. Two- and three-dimensional dynamic response and soil-structure interaction problems are most commonly solved using dynamic finite-element analyses. Although a detailed treatment of the finite-element method is

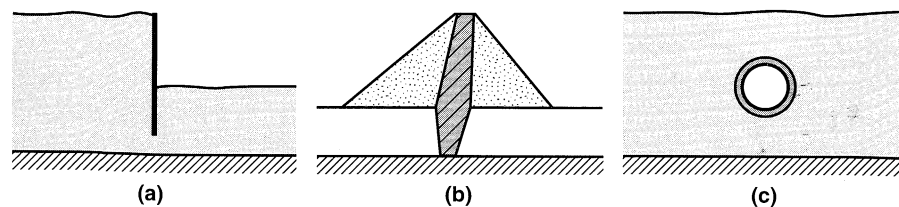


Figure 7.14 Examples of common problems typically analyzed by two-dimensional plane strain dynamic response analyses: (a) cantilever retaining wall; (b) earth dam; (c) tunnel.

beyond the scope of this book, a brief introduction precedes the description of two- and three-dimensional dynamic response analyses.

7.3.1 Dynamic Finite-Element Analysis

The finite-element method treats a continuum as an assemblage of discrete *elements* whose boundaries are defined by *nodal points*, and assumes that the response of the continuum can be described by the response of the nodal points. The following section presents a very brief summary of the finite-element method that is intended only to provide a basic description of its principles to the unfamiliar reader. Complete descriptions of the finite-element method may be found in a number of books devoted to that topic (e.g., Desai and Abel, 1972; Bathe, 1982; Zienkiewicz and Taylor, 1989).

7.3.1.1 Elemental Equations of Motion

In the finite-element method, the problem of interest is first discretized by dividing it into elements as shown in Figure 7.15. The displacement of the soil at any point within an element, $\{\mathbf{v}\}^T = \{u \ v\}$, is expressed in terms of the nodal point displacements, $\{\mathbf{q}\}^T = \{u_1 \ u_2 \ u_3 \ u_4 \ v_1 \ v_2 \ v_3 \ v_4\}$, by

$$\{\mathbf{v}\} = [\mathbf{N}] \{\mathbf{q}\} \tag{7.49}$$

where $[\mathbf{N}]$ is a matrix of *shape functions*. The *strain–displacement matrix*, $[\mathbf{B}]$, allows the strains to be determined from the nodal point displacements

$$\{\boldsymbol{\epsilon}\} = [\mathbf{B}] \{\mathbf{q}\} \tag{7.50}$$

and the stress–strain matrix, $[\mathbf{D}]$, relates stresses to strains:

$$\{\boldsymbol{\sigma}\} = [\mathbf{D}] \{\boldsymbol{\epsilon}\} \tag{7.51}$$

Defining a local coordinate system, (s, t) , that maps the quadrilateral elements into squares as shown in Figure 7.16, and using the strain–displacement and stress–strain relationships, an *element stiffness matrix* can be written (assuming unit thickness in the z -direction) as

$$[\mathbf{k}_e] = \int_{-1}^1 \int_{-1}^1 [\mathbf{B}]^T [\mathbf{D}] [\mathbf{B}] |J| ds dt \tag{7.52}$$

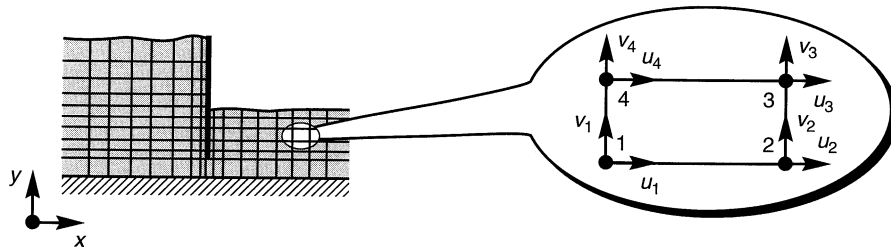


Figure 7.15 Finite-element discretization of retaining structure illustrating the degrees of freedom of a typical four-noded element.

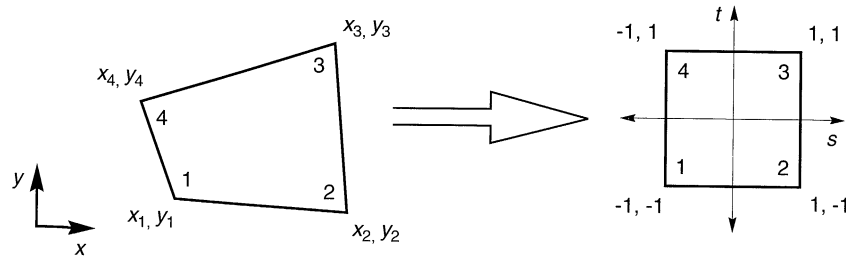


Figure 7.16 Mapping of quadrilateral element from irregular shape in x - y coordinate system to square shape in s - t coordinate system.

where the Jacobian

$$|J| = \sum_{i=1}^4 \sum_{j=1}^4 x_i \left(\frac{\partial N_i}{\partial s} \frac{\partial N_j}{\partial t} - \frac{\partial N_i}{\partial t} \frac{\partial N_j}{\partial s} \right) y_j$$

A consistent element mass matrix can be written, assuming constant density within the element, as

$$[\mathbf{m}_e] = \rho \int_{-1}^1 \int_{-1}^1 [\mathbf{N}]^T [\mathbf{N}] |J| ds dt \quad (7.53)$$

As an alternative, a *lumped-element mass matrix* can be developed by assuming that the mass of the element is concentrated at the nodal points. Experience has shown that use of the consistent element matrix tends to overestimate the natural frequencies of a system and that the lumped mass matrix tends to underestimate them by about the same amount. Lysmer et al. (1974) suggested the use of a *mixed element mass matrix*, which is simply the average of the consistent and lumped mass matrices.

Damping matrices can be troublesome because of the implications of various formulations on the frequency dependence of damping. For nonlinear ground response analyses, however, damping results primarily from the hysteretic behavior of the soil and is therefore accounted for by variations in the stiffness matrix under cyclic loading conditions. Some small amount of viscous damping may be included in a two-dimensional ground response analysis to account for damping at very small strains and to minimize numerical problems that can arise in the complete absence of damping. A consistent damping matrix can be obtained from

$$[\mathbf{c}_e] = \rho \int_{-1}^1 \int_{-1}^1 [\mathbf{B}]^T [\boldsymbol{\eta}] [\mathbf{B}] |J| ds dt \quad (7.54)$$

where $[\boldsymbol{\eta}]$ is a matrix of damping terms. The equations of motion for the element can then be written as

$$[\mathbf{m}_e] \{\ddot{\mathbf{q}}\} + [\mathbf{c}_e] \{\dot{\mathbf{q}}\} + [\mathbf{k}_e] \{\mathbf{q}\} = \{\mathbf{Q}(\mathbf{t})\} \quad (7.55)$$

where the element force vector is given by

$$\{\mathbf{Q}(t)\} = \int_{-1}^1 \int_{-1}^1 [\mathbf{N}]^T \{\mathbf{W}\} |J| ds dt + \int_s [\mathbf{N}]^T \{\mathbf{T}\} dS$$

and $\{\mathbf{W}\}$ is the vector of prescribed body forces and $\{\mathbf{T}\}$ is a vector of external tractions that may be applied to some surface, S .

7.3.1.2 Global Equations of Motion

Once the equations of motion for each element are obtained, they are combined in a way that satisfies compatibility of displacements to obtain the *global equations of motion*

$$[\mathbf{M}] \{\ddot{\mathbf{u}}\} + [\mathbf{C}] \{\dot{\mathbf{u}}\} + [\mathbf{K}] \{\mathbf{u}\} = \{\mathbf{R}(t)\} \quad (7.56a)$$

where $[\mathbf{M}]$ is the *global mass matrix*, $[\mathbf{C}]$ the *global damping matrix*, $[\mathbf{K}]$ the *global stiffness matrix*, $\{\mathbf{u}\}$ the *global nodal point displacement vector*, and $\{\mathbf{R}(t)\}$ the *global nodal point force vector*. For the case of loading induced by base motion, the global equation of motion is

$$[\mathbf{M}] \{\ddot{\mathbf{u}}\} + [\mathbf{C}] \{\dot{\mathbf{u}}\} + [\mathbf{K}] \{\mathbf{u}\} = -[\mathbf{M}] [\mathbf{1}] \ddot{u}_b(t) \quad (7.56b)$$

7.3.1.3 Discretization Considerations

The response of both equivalent linear and nonlinear finite-element models can be influenced by discretization. In particular, the use of coarse finite-element meshes can result in the filtering of high-frequency components whose short wavelengths cannot be modeled by widely spaced nodal points. The maximum dimension of any element should be limited to one-eighth (Kuhlemeyer and Lysmer, 1973) to one-fifth (Lysmer et al., 1975) of the shortest wavelength considered in the analysis.

7.3.1.4 Boundary Conditions

For computational efficiency it is desirable to minimize the number of elements in a finite-element analysis. Since the maximum dimensions of the elements are generally controlled by the wave propagation velocity and frequency range of interest, minimizing the number of elements usually becomes a matter of minimizing the size of the discretized region. As the size of the discretized region decreases, the influence of boundary conditions becomes more significant.

For many dynamic response and soil-structure interaction problems, rigid or near-rigid boundaries such as bedrock are located at considerable distances, particularly in the horizontal direction, from the region of interest. As a result, wave energy that travels away from the region of interest may effectively be permanently removed from that region. In a dynamic finite-element analysis, it is important to simulate this type of radiation damping behavior. The most commonly used boundaries for finite-element analyses can be divided into three groups (Christian et al., 1977; Wolf, 1985).

Elementary Boundaries. Conditions of zero displacement or zero stress are specified at *elementary boundaries* (Figure 7.17a). Elementary boundaries can be used to model the ground surface accurately as a free (zero stress) boundary. For lateral or lower

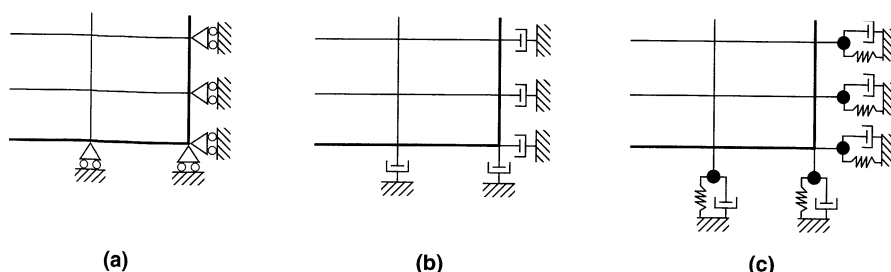


Figure 7.17 Three types of finite-element mesh boundaries: (a) elementary boundary in which zero displacements are specified; (b) local boundary consisting of viscous dashpots; (c) lumped-parameter consistent boundary (actual lumped parameter would consist of more masses, springs, and dashpots than shown).

boundaries, however, the perfect reflection characteristics of elementary boundaries can trap energy in the mesh that in reality would radiate past the boundaries and away from the region of interest. The resulting “box effect” can produce serious errors in a ground response or soil–structure interaction analysis. If elementary boundaries are placed far enough from the region of interest, reflected waves may be damped sufficiently to negate their influence.

Local Boundaries. Section 5.4.1 showed how a viscous dashpot could be used to simulate a semi-infinite region for the case of normally incident body waves. The use of viscous dashpots (Figure 7.17b) represents a common type of *local boundary*. It can be shown (e.g., Wolf, 1985) that the value of the dashpot coefficient necessary for perfect energy absorption depends on the angle of incidence of the impinging wave. Since waves are likely to strike the boundary at different angles of incidence, a local boundary with specific dashpot coefficients will always reflect some of the incident wave energy. Additional difficulties arise when dispersive surface waves reach a local boundary; since their phase velocity depends on frequency, a frequency-dependent dashpot would be required to absorb all their energy. The effects of reflections from local boundaries can be reduced by increasing the distance between the boundary and the region of interest.

Consistent Boundaries. Boundaries that can absorb all types of body waves and surface waves at all angles of incidence and all frequencies are called *consistent boundaries*. Consistent boundaries can be represented by frequency-dependent boundary stiffness matrices obtained from boundary integral equations or the boundary element method. Wolf (1991), for example, developed a lumped-parameter model consisting of an assemblage of discrete springs, masses, and dashpots which can approximate the behavior of a consistent boundary. A greatly simplified example of such an assemblage is shown in Figure 7.17c.

7.3.2 Equivalent Linear Approach

The two-dimensional equivalent linear approach is very similar to the one-dimensional approach. A soil–structure system is represented by a two-dimensional finite-element model. The input motion is represented by a Fourier series and the equations of motion are solved for each frequency of the series (or at selected frequencies with interpretation in between) with the results summed to obtain the total response.

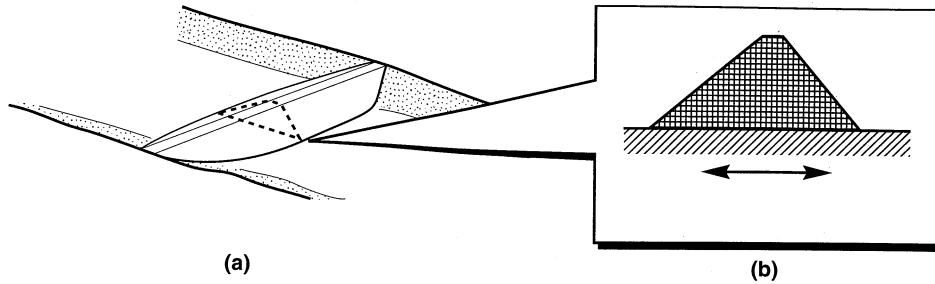


Figure 7.18 Practical situation where two-dimensional ground response analyses are used: (a) plane strain conditions can be assumed at center of long dam, allowing (b) center section of dam to be modeled in two dimensions.

Consider the problem of the earth dam shown in Figure 7.18a. Assuming that the axis of the dam is long relative to its height, the response of the center portion of the dam can be assumed to be two-dimensional. Dynamic equilibrium of the model shown in Figure 7.18b requires that the following equations of motion be satisfied:

$$[\mathbf{M}] \{\ddot{\mathbf{u}}\} + [\mathbf{K}^*] \{\mathbf{u}\} = -[\mathbf{M}] [\mathbf{1}] \ddot{u}_b(t) \quad (7.57)$$

where $[\mathbf{M}]$ is the mass matrix, $[\mathbf{K}^*]$ the *complex stiffness matrix*, $[\mathbf{K}^*] = [\mathbf{K}] + i\omega[\mathbf{C}]$, $\{\mathbf{u}\}$ the vector of unknown nodal point displacements (relative to the base), and $\ddot{u}_b(t)$ is the time history of base acceleration. The mass and stiffness matrices are assembled from the corresponding element stiffness matrices using standard finite-element procedures and damping is introduced into the analysis through the use of complex shear moduli when forming the complex element stiffness matrices.

If the base motion is assumed to be harmonic, the relative displacement vector can be expressed as

$$\{\mathbf{u}\} = \{\mathbf{H}(\omega)\} \tilde{u}_b(\omega) e^{i\omega t} \quad (7.58)$$

where $\{\mathbf{H}(\omega)\}$ is a vector of transfer functions and $\tilde{u}_b(\omega)$ is the Fourier transform of $\ddot{u}_b(t)$. Substituting equation (7.58) into the equation of motion gives

$$-\omega^2 [\mathbf{M}] \{\mathbf{H}(\omega)\} \tilde{u}_b(\omega) e^{i\omega t} + [\mathbf{K}^*] \{\mathbf{H}(\omega)\} \tilde{u}_b(\omega) e^{i\omega t} = -[\mathbf{M}] [\mathbf{1}] \tilde{u}_b(\omega) e^{i\omega t}$$

Rearranging allows the transfer function vector to be expressed as

$$\{\mathbf{H}(\omega)\} = \frac{[\mathbf{M}]}{\omega^2 [\mathbf{M}] - [\mathbf{K}^*]} \quad (7.59)$$

Once the transfer function vector has been obtained, computation of the response follows the same procedures used for one-dimensional complex response analysis (Section 7.1.1.2). In this approach the primary computational effort is associated with evaluation of the transfer functions. For large problems, the mass and stiffness matrices are large, and evaluation of the transfer functions can be quite time consuming. For computational efficiency, the transfer functions are often explicitly evaluated at only a limited number of frequencies, with values at intermediate frequencies obtained by interpolation (Lysmer et al.,

1975; Tajirian, 1981). Iteration toward strain-compatible material properties (Section 7.1.1.3) can be incorporated on an element-by-element basis. Analyses of this type are performed by the widely used computer program FLUSH (Lysmer et al., 1975). The use of *generalized hyperelements* in the computer program GROUND2D greatly reduces the number of degrees of freedom required for two-dimensional dynamic response analyses (Deng et al., 1995).

7.3.3 Nonlinear Approach

Two-dimensional nonlinear analyses can be used to estimate permanent displacements of slopes (Chapter 10), retaining structures (Chapter 11), and other constructed facilities. Two-dimensional nonlinear dynamic response analyses are performed by writing the global equations of motion [equation (7.57)] from a finite-element idealization in incremental form and then integrating them in the time domain. Such analyses can be divided into two main groups according to the manner in which the soil behavior is represented. One group uses cyclic nonlinear stress-strain models (Section 6.4.3) and the other uses advanced constitutive models (Section 6.4.4).

Finn et al. (1986) extended the hyperbolic model with extended Masing criteria and a residual pore pressure model from one to two dimensions in the computer program TARA-3. The program has been used to back-analyze full-scale case histories and the results of various centrifuge model tests. Even with its relatively simple cyclic stress-strain model, the program has been able to capture the most important aspects of ground response with good accuracy. According to Finn (1988), the simplicity of the stress-strain model can produce substantial computational efficiency relative to models based on more complicated soil models.

Methods based on advanced constitutive models have been developed. The program DYNFLOW (Prevost, 1981) uses a multiple yield surface model to predict deformations and pore pressures. It has been applied to problems of earth dams with good results. A consortium of Japanese construction firms have developed the program DIANA (Kawai, 1985) that can perform static and dynamic analyses with different advanced constitutive models. A number of other programs incorporating advanced constitutive models have been developed in recent years.

7.3.4 Other Approaches to Two-Dimensional Dynamic Response Problems

In an attempt to capture the most significant aspects of various two-dimensional dynamic response problems without the computational cost and complexity of dynamic finite-element analyses, a number of investigators have developed alternative approaches to specific problems. These approaches typically involve simplifying assumptions that allow two-dimensional problems to be solved by one-dimensional analyses.

7.3.4.1 Shear Beam Approach

One of the earliest approaches to the dynamic analysis of two-dimensional geotechnical systems was the *shear beam analysis* applied to earth dams by Mononobe et al. (1936). The approach has since been verified and extended to cover a variety of conditions; a comprehensive review was prepared by Gazetas (1987). The shear beam approach is based on the assumption that a dam deforms in simple shear, thereby producing only horizontal displacements.

Hatanaka (1952) and others have verified the accuracy of this assumption, at least for rigid foundation conditions. The shear beam approach also assumes that either shear stresses or shear strains are uniform across horizontal planes. These assumptions have also been verified (Chopra, 1966; Dakoulas, 1985); stresses and strain are nearly constant across the dam except in small zones near the upstream and downstream faces where they decrease to zero (Gazetas, 1987).

Consider the homogeneous, infinitely long dam shown in Figure 7.19. Assuming horizontal displacements to be constant at a given depth, the horizontal displacement relative to the base, $\ddot{u}(z, t)$, is independent of x . The resultant shearing force on the upper surface of a slice of thickness, dz , is

$$S_z(t) = \int_{-x_u}^{x_d} \tau(x, z, t) dx$$

The corresponding resultant shearing force on the bottom of the slice is

$$S_{z+dz}(t) = \int_{-x_u}^{x_d} \left[\tau(x, z, t) + \frac{\partial \tau(x, z, t)}{\partial z} dz \right] dx$$

The resultant inertial force acting on the slice depends on the total acceleration, that is,

$$I_z(t) = \rho \left[\ddot{u}(z, t) + \ddot{u}_b(t) \right] \frac{2Bz}{H} dz$$

For equilibrium in the x -direction,

$$S_{z+dz}(t) - S_z(t) = I_z(t) \quad (7.60)$$

or

$$-\frac{\partial}{\partial z} \left[\int_{-x_u}^{x_d} \tau(x, z, t) dx \right] dz = \rho \left[\ddot{u}(z, t) + \ddot{u}_b(t) \right] \frac{2Bz}{H} dz$$

Substituting $\tau(x, z, t) = G(x, z)\gamma(z, t)$ and $\gamma(z, t) = \partial u(z, t)/\partial z$, the shear beam equation can be written as

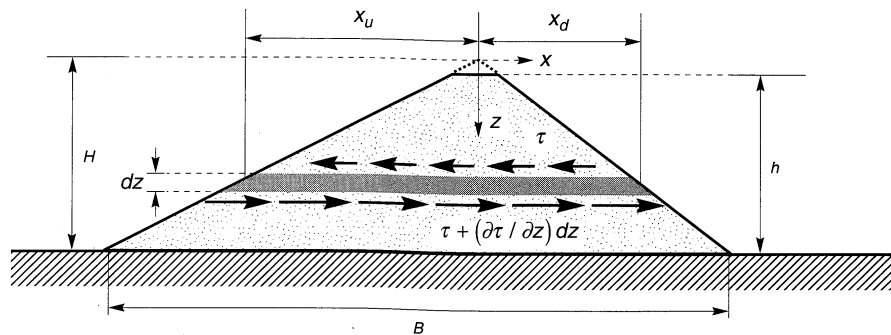


Figure 7.19 Earth dam, showing stresses acting on an element of thickness, dz .

$$\rho(\ddot{u} + \ddot{u}_b) = \frac{1}{z} \frac{\partial}{\partial z} \left[\bar{G}(z) z \frac{\partial u}{\partial z} \right] \quad (7.61)$$

where the average shear modulus, \bar{G} , is given by

$$\bar{G}(z) = \frac{1}{x_u + x_d} \int_{-x_n}^{x_d} G(x, z) dx$$

Equation (7.62) is simply a one-dimensional wave equation (i.e., the shear beam approach allows the two-dimensional dam section to be represented as a one-dimensional system).

Gazetas (1982) developed solutions to the shear beam wave equation for the case where the shear modulus increases as a power function of depth according to $G(z) = G_b(z/H)^m$, where G_b is the average shear modulus at the base of the dam. For such conditions, the n th natural circular frequency (assuming $h/H = 1$) is given by

$$\omega_n = \frac{\bar{v}_{ss}}{H} \frac{\beta_n}{8} (4 + m)(2 - m) \quad (7.62)$$

where \bar{v}_{ss} is the average shear wave velocity of the soil in the dam and β_n is the n th root of a period relation (Dakoulas and Gazetas, 1985) tabulated in Table 7-2 for the first five modes of vibration.

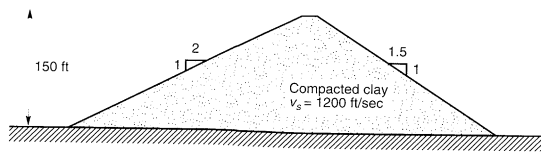


Figure E7.6

Table 7-2 Values of β_n for First Five Modes of Vibration of an Earth Dam

m	n				
	1	2	3	4	5
0	2.404	5.520	8.654	11.792	14.931
$\frac{1}{2}$	2.903	6.033	9.171	12.310	15.451
$\frac{4}{7}$	2.999	6.133	9.273	12.413	15.544
$\frac{2}{3}$	3.142	6.283	9.525	12.566	15.708
1	3.382	7.106	10.174	13.324	16.471

Equation (7.62) produces a fundamental period of

$$T_1 = \frac{16\pi}{(4 + m)(2 - m)\beta_1} \frac{H}{\bar{v}_{ss}} \quad (7.63)$$

Example 7.6

The earth dam shown in Figure E 7.6 is constructed of compacted clay with a shear wave velocity of 1200 ft/sec. Compute the first three natural frequencies of the dam.

Solution Because the crest of the dam is so narrow, $H \approx h$. Then, from equation (7.62), the first three natural frequencies can be calculated as

$$\begin{aligned} \omega_1 &= \frac{\bar{v}_{ss}}{H} \frac{\beta_1}{8} (4 + m)(2 - m) = \frac{1200}{150} \frac{2.404}{8} (4)(2) = 19.2 \text{ rad/sec} & f_1 &= 3.1 \text{ Hz} \\ \omega_2 &= \frac{\bar{v}_{ss}}{H} \frac{\beta_2}{8} (4 + m)(2 - m) = \frac{1200}{150} \frac{5.520}{8} (4)(2) = 44.2 \text{ rad/sec} & f_2 &= 7.0 \text{ Hz} \\ \omega_3 &= \frac{\bar{v}_{ss}}{H} \frac{\beta_3}{8} (4 + m)(2 - m) = \frac{1200}{150} \frac{8.654}{8} (4)(2) = 69.2 \text{ rad/sec} & f_3 &= 11.0 \text{ Hz} \end{aligned}$$

The mode shape at the n th natural frequency is given by

$$U_n(z) = \left(\frac{z}{H}\right)^{-m/2} J_q \left[\beta_n \left(\frac{z}{H}\right)^{1-m/2} \right] \tag{7.64}$$

where J_q is a Bessel function of the first kind of order, $q = m/(2 - m)$, which can be evaluated from

$$J_q(x) = \sum_{k=0}^{\infty} \frac{(-1)^k}{k! \Gamma(q+k+1)} \left(\frac{x}{2}\right)^{q+2k} \tag{7.65}$$

where $\Gamma(\cdot)$ is the gamma function (Table 7-3).

Table 7-3 Recursion Relationship and Values of Gamma Function

$$\Gamma(x) = \int_0^{\infty} e^{-x} x^{x-1} dx; \quad \Gamma(x+1) = x\Gamma(x)$$

x	$\Gamma(x)$	x	$\Gamma(x)$	x	$\Gamma(x)$	x	$\Gamma(x)$
1.00	1.00000	1.25	0.90640	1.50	0.88623	1.75	0.91906
1.01	0.99433	1.26	0.90440	1.51	0.88659	1.76	0.92137
1.02	0.98884	1.27	0.90250	1.52	0.88704	1.77	0.92376
1.03	0.98335	1.28	0.90072	1.53	0.88757	1.78	0.92623
1.04	0.97884	1.29	0.89904	1.54	0.88818	1.79	0.92877
1.05	0.97350	1.30	0.89747	1.55	0.88887	1.80	0.93138
1.06	0.96874	1.31	0.89600	1.56	0.88964	1.81	0.93408
1.07	0.96415	1.32	0.89464	1.57	0.89049	1.82	0.93685
1.08	0.95973	1.33	0.89338	1.58	0.89142	1.83	0.93969
1.09	0.95546	1.34	0.89222	1.59	0.89243	1.84	0.94261
1.10	0.95135	1.35	0.89115	1.60	0.89352	1.85	0.94561
1.11	0.94739	1.36	0.89018	1.61	0.89468	1.86	0.94869
1.12	0.94359	1.37	0.88931	1.62	0.89592	1.87	0.95184
1.13	0.93993	1.38	0.88854	1.63	0.89724	1.88	0.95507
1.14	0.93642	1.39	0.88785	1.64	0.89864	1.89	0.95838
1.15	0.93304	1.40	0.88726	1.65	0.90012	1.90	0.96177
1.16	0.92980	1.41	0.88676	1.66	0.90167	1.91	0.96523
1.17	0.92670	1.42	0.88636	1.67	0.90330	1.92	0.96878
1.18	0.92373	1.43	0.88604	1.68	0.90500	1.93	0.97240
1.19	0.92088	1.44	0.88580	1.69	0.90678	1.94	0.97610
1.20	0.91817	1.45	0.88565	1.70	0.90864	1.95	0.97988
1.21	0.91558	1.46	0.88560	1.71	0.91057	1.96	0.98374
1.22	0.91311	1.47	0.88563	1.72	0.91258	1.97	0.98768
1.23	0.91075	1.48	0.88575	1.73	0.91466	1.98	0.99171
1.24	0.90852	1.49	0.88595	1.74	0.91683	1.99	0.99581
						2.00	1.00000

The first and second mode shapes are shown in Figure 7.20 for various values of the stiffness parameter, m . As m increases, the shear beam analysis produces a “whiplash effect” characterized by large shear strain and high acceleration near the crest of the dam in the second and higher modes. Under strong shaking, nonlinear behavior of the materials in an actual earth dam may prevent the development of the high accelerations predicted by the shear beam analysis.

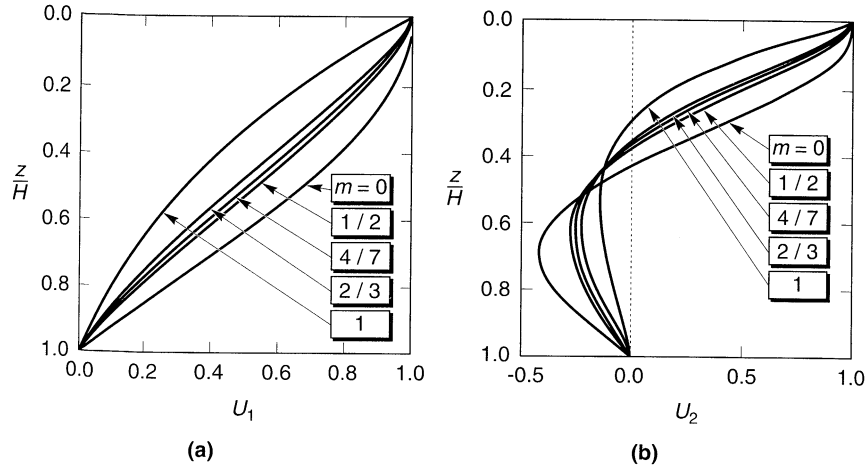


Figure 7.20 Mode shapes for (a) first mode and (b) second mode of earth dam response. Note rapid change of U with depth near crest of dam for second mode at $m = 1$ (whiplash effect). (After Dakoulas and Gazetas, 1985.)

The midcrest and base accelerations are related by the transfer function

$$H(\omega) = \frac{\ddot{u}(z=0) + \ddot{u}_b}{\ddot{u}_b} = \frac{(a_0/2)^q}{\Gamma(q+1)J_q(a_0)} \frac{1}{i\alpha_z J_{q+1}(a_0)} \quad (7.66)$$

where $a_0 = \omega H / \bar{v}_{ss}$, and $\alpha_z = \rho_s v_{ss} / \rho_r v_{sr}$ is the impedance ratio at the soil–rock interface.

In the preceding derivation, the soil was assumed to be linear and undamped. The effects of soil damping can easily be included by repeating the derivation with the soil characterized by a complex stiffness. The results, as expressed in equations (7.62) through (7.66), would be identical except for the replacement of v_{ss} by the complex shear wave velocity, $v_{ss}^* = v_{ss}(1 + i\xi)$.

The shear beam approach is an excellent example of a procedure that through the judicious use of appropriate assumptions, greatly simplifies an important class of ground response problems. It allows rapid estimation of many important response parameters, and can be used to check the reasonableness of the results of more sophisticated analyses. The shear beam transfer function can be used in an equivalent linear analysis, or nonlinear inelastic stress–strain behavior can be assumed in an incremental nonlinear analysis.

7.3.4.2 Other Approaches

The *layered inelastic shear beam* (Stara-Gazetas, 1986) combines the shear beam approach with a one-dimensional nonlinear ground response analysis. In this approach, a series of static nonlinear finite-element analyses are performed with incrementally increasing horizontal pseudoinertial forces to determine the nonlinear backbone curve for an entire horizontal layer, or “superelement.” The backbone curves for each layer are then used with the extended Masing criteria (Section 6.4.3) in a nonlinear shear beam analysis of the dam. Other approaches include the simplified nonlinear method of Dakoulas (1985) and the nonlinear hysteretic method of Elgamel et al. (1985).

7.3.5 Comparison of Two-Dimensional Dynamic Response Analyses

Differences in the underlying assumptions and formulations of two-dimensional dynamic response analyses lead to differences in their results. The proper use of these analyses requires understanding of these differences. The two-dimensional equivalent linear method can suffer from the spurious resonances and difficulties associated with effective strain determination described for the one-dimensional equivalent linear method in Section 7.2.3. In addition, the different modes of vibration associated with the extra degrees of freedom (vertical translation and rotation) in the two-dimensional case complicate the computation of the maximum shear strain, require the use of another material parameter (such as Poisson's ratio) in addition to the shear modulus, and produce much more complicated stress paths. Again, the equivalent linear approach is restricted to total stress analyses.

Two-dimensional nonlinear methods have the enormously beneficial capability of computing pore pressures (hence effective stresses) and permanent deformations. The accuracy with which they can be computed, however, depends on the accuracy of the constitutive models on which they are based. While great progress in the constitutive modeling of soils has been made in the past 20 years, additional refinement is required before precise a priori predictions of permanent displacement are possible.

The shear beam models are fundamentally different from the equivalent linear and nonlinear finite-element models in that they restrict particle movement to the horizontal plane. Finite-element analyses are capable of modeling an actual dam's tendency to respond vertically as well as horizontally, but the shear beam model forces all of the elastic wave energy to produce horizontal deformations. As a result, shear beam models generally overestimate the fundamental frequency of most dams by about 5%, and higher natural frequencies by increasingly greater amounts. Shear beam displacements compare well (within about 10%) with those computed by finite-element analyses, but shear beam crest accelerations for flexible dams can be up to 50% greater than those from finite-element analyses. This discrepancy is related to the whiplash effect produced by the higher shear beam modes. For stiff dams where these higher modes are associated with frequencies greater than those associated with earthquake motions, the computed accelerations match much more closely.

7.4 THREE-DIMENSIONAL DYNAMIC RESPONSE ANALYSIS

In some instances the two-dimensional idealizations of the preceding sections may not be appropriate and three-dimensional dynamic response analyses are necessary. Such conditions can arise, as illustrated in Figure 7.21, when soil conditions vary three-dimensionally, when problem boundaries vary three-dimensionally, and when the response of three-dimensional structures is of interest.

Three-dimensional dynamic response problems are treated in much the same way as two-dimensional problems. Dynamic finite-element analyses are available, using both equivalent linear and nonlinear approaches. A number of three-dimensional analyses have been developed with an emphasis on soil-structure interaction problems (Section 7.5.2). For the important problem of earth dams, shear beam analyses have been developed for the approximate response of dams in narrow canyons.

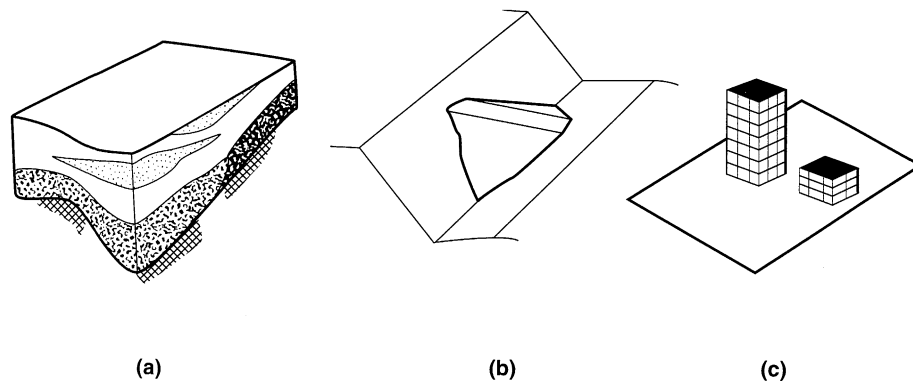


Figure 7.21 Three situations requiring three-dimensional dynamic response or soil-structural interaction analysis: (a) site where soil conditions vary significantly in three dimensions; (b) earth dam in narrow canyon; (c) site where response of soil is influenced by response of structures (and vice versa) and where response of one structure may influence response of another.

7.4.1 Equivalent Linear Finite-Element Approach

Computationally, three-dimensional equivalent linear dynamic response analyses are virtually identical to the two-dimensional analyses described in Section 7.2.2. Three-dimensional finite elements (usually in the shapes of “bricks” or tetrahedra) have more nodal points with more degrees of freedom than corresponding two-dimensional elements, but the basic process of element mass, damping, and stiffness formulation, and assembly into global equations of motion, is identical.

To analyze the seismic response of earth dams in narrow canyons, Kagawa (1977) implemented three-dimensional finite elements into a predecessor of the two-dimensional equivalent linear program FLUSH (Lysmer et al., 1975). Mejia and Seed (1981) eliminated several restrictions that resulted from Kagawa’s original assumptions while developing the three-dimensional equivalent linear program TLUSH (Kagawa et al., 1981).

Three-dimensional equivalent linear analyses have also been developed for soil-structure interaction (Section 7.4) problems. Computer programs such as SASSI (Lysmer et al., 1981), CLASSI (Luco and Wong, 1982), and HASSI (Katayama et al., 1991) use both soil and structural elements to model soil-structure systems.

7.4.2 Nonlinear Finite-Element Approach

Three-dimensional nonlinear ground response analyses are also relatively straightforward extensions of their two-dimensional counterparts. The computer program DYNFLOW (Prevost, 1981), based on a multiple yield surface plasticity model, has three-dimensional as well as two-dimensional capabilities. When applied to the back-analysis of earth dams (e.g., Prevost et al., 1985), it realistically represented dam response while accounting for all three components of ground shaking and all modes of vibration. Three-dimensional nonlinear soil-structure interaction analyses can also be performed with programs such as TRANL (Baylor et al., 1974) and FLEX (Vaughan, 1983). Many of the large multipurpose finite-element codes (e.g., ANSYS, ADINA, etc.) are also capable of performing three-dimensional nonlinear

analyses, although they are not specifically oriented toward soil–structure problems or earthquake loading.

7.4.3 Shear Beam Approach

Many earth dams are constructed in relatively narrow canyons where abutment boundary conditions influence the response of the dam. Hatanaka (1952) and Ambraseys (1960) developed shear beam-type solutions for earth dams in rectangular canyons of different width/height ratios. Dakoulas and Gazetas (1986) developed a closed-form solution for a homogeneous ($v_{ss} = \text{constant}$) earth dam in a semicylindrical valley of width, L , and depth, H , showing

$$\begin{aligned} \omega_n &= \frac{n\pi v_{ss}}{H} \\ T_1 &= \frac{2H}{v_{ss}} \\ U_n(y = 0, z) &= \frac{\sin(n\pi z/H)}{n\pi z/H} \end{aligned} \tag{7.67}$$

and

$$H(\omega) = \frac{\ddot{u}(y = 0, z = 0) + \ddot{u}_b}{\ddot{u}_b} \tag{7.68}$$

where all variables are as defined for equations (7.62) to (7.66) and the origin of axes is at the center of the crest of the dam. Note that the natural frequencies of a three-dimensional dam are always greater than the corresponding natural frequencies of its two-dimensional maximum section, thereby illustrating the “stiffening” effects of the abutments. This stiffening effect is also observed for dams in canyons of different shapes, although the effect decreases as the crest length/dam height ratio increases (Figure 7.22a).

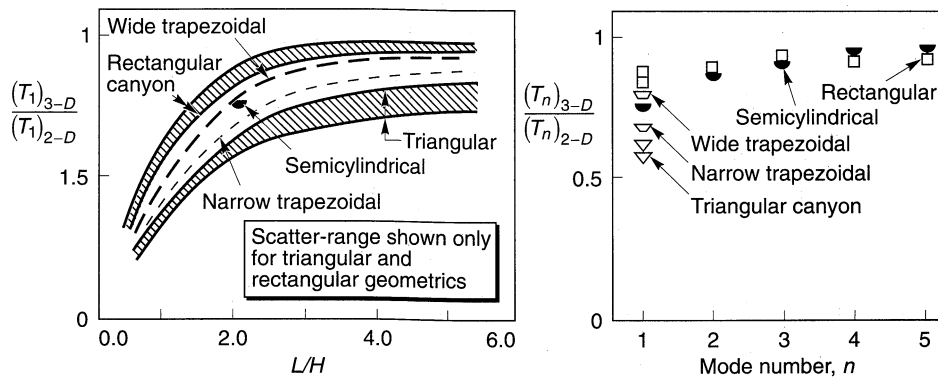


Figure 7.22 Effect of three-dimensional boundary effects on (a) fundamental frequencies for different crest length/dam height ratios, and (b) natural periods for first five modes of earth dams ($L/H = 2$) in canyons of different shape. (After Gazetas, 1987. Used with kind permission from Elsevier Science, Ltd, The Boulevard, Langford Lane, Kidlington OX5 1GB UK.)

7.4.4 Comparison of Three-Dimensional Dynamic Response Analyses

The relative capabilities and limitations of the various approaches to three-dimensional dynamic response analysis are very similar to those of their two-dimensional counterparts. Of special interest for three-dimensional problems, however, are the relative computational efficiencies of the various approaches.

The shear beam approach is simple and consequently very efficient for earth dam problems, but it makes quite restrictive assumptions about the mode of dam response. The nonlinear finite-element approach offers the greatest potential, in terms of its ability to compute permanent displacements and variations in effective stress, but it requires solution of the incremental equations of motion at every time step. For large three-dimensional problems, this can involve very large systems of simultaneous equations and many time steps. The equivalent linear approach, through the use of the cutoff frequency and interpolation of the transfer functions, requires large matrix computations at only a relatively small number of frequencies. The equivalent linear approach can therefore be more computationally efficient than the nonlinear approach.

7.5 SOIL-STRUCTURE INTERACTION

All of the ground response analyses described thus far have considered cases in which no structures are present. Ground motions that are not influenced by the presence of structures are referred to as *free-field motions*. When a structure founded on solid rock is subjected to an earthquake, the extremely high stiffness of the rock constrains the rock motion to be very close to the free-field motion. Structures founded on rock are considered to be *fixed-base structures*. Computation of their response is relatively simple using the methods described in Appendix B.

On the other hand, the same structure would respond differently if supported on a soft soil deposit. First, the inability of the foundation to conform to the deformations of the free-field motion would cause the motion of the base of the structure to deviate from the free-field motion. Second, the dynamic response of the structure itself would induce deformation of the supporting soil. This process, in which the response of the soil influences the motion of the structure and the response of the structure influences the motion of the soil, is referred to as *soil-structure interaction*.

Soil-structure interaction has little effect on the dynamic response of many structures and foundation systems. In other cases, however, its effects can be significant. Whether the neglect of its effects is conservative or unconservative depends on the details of the problem at hand and must be evaluated on a case-by-case basis. The analysis of soil-structure interaction can be quite complicated; a detailed treatment is beyond the scope of this book. For more details, the work of Wolf (1985) and the Committee on Nuclear Structures and Materials (1979) are helpful. The purpose of the following sections is simply to provide a basic description of soil-structure interaction phenomena, to provide insight into the conditions under which it can be significant, and to introduce some of the methods that are commonly used to evaluate its effects.

7.5.1 Illustration of Soil-Structure Interaction Effects

A simple analysis is sufficient to illustrate the most important effects of soil-structure interaction. Following the approach of Wolf (1985), consider the case of the simple SDOF system mounted on a rigid, massless, L-shaped foundation (Figure 7.23a) supported on an elastic soil deposit. The structure is characterized by its mass, m , stiffness, k , and damping coefficient, c . If the material supporting the foundation is rigid, the natural frequency of the resulting fixed-base system would depend only on the mass and stiffness of the structure, that is,

$$\omega_0 = \sqrt{\frac{k}{m}} \tag{7.69}$$

and the hysteretic damping ratio would be

$$\xi = \frac{c\omega_0}{2k} \tag{7.70}$$

If the supporting material is compliant, however, the foundation can translate and rotate. The stiffness and damping characteristics of the compliant soil-foundation system can be represented by the translational and rotational springs and dashpots shown in Figure 7.23b. The foundation dashpots represent two sources of damping: material damping caused by inelastic behavior of the soil supporting the foundation, and radiation damping that occurs as dynamic forces in the structure cause the foundation to deform the soil, producing stress waves that travel away from the foundation. The amount of material damping will depend on the level of strain induced in the soil; if the strains are high, material damping can be substantial, but if they are low, the material damping may be negligible. In contrast, radiation damping is a purely geometric effect that exists at low as well as high strain amplitudes. For typical foundations, radiation damping is often much greater than material damping.

The total displacements of the mass and the base of the structure can be split into their individual components (Figure 7.23c):

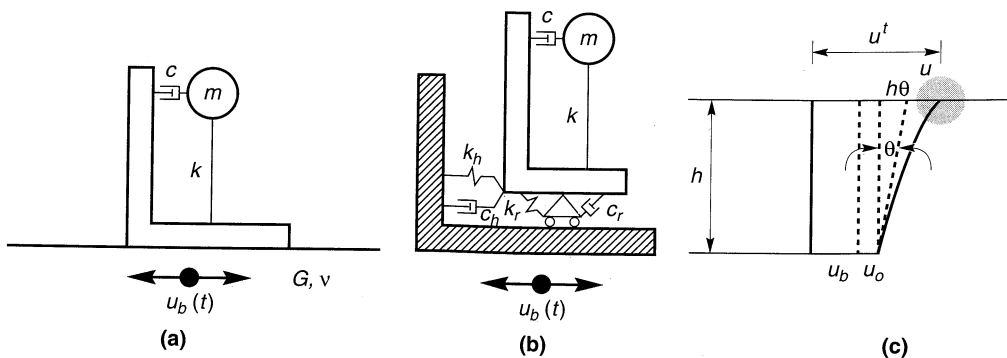


Figure 7.23 Compliant base model with one dynamic degree of freedom: (a) SDOF system on an elastic soil deposit; (b) idealized discrete system in which compliance of base is represented by translational and rotational springs and dashpots; (c) components of motion of base and mass.

$$u^t = u_b + u_0 + h\theta + u \quad (7.71a)$$

$$u_0^t = u_b + u_0 \quad (7.71b)$$

where the symbols are defined as shown in Figure 7.23c. Neglecting material damping in the soil ($\xi_g = 0$), the horizontal force imposed on the soil by the foundation would be

$$P_x = k_x u_0 + c_x \dot{u}_0 \quad (7.72)$$

where the subscript x refers to the horizontal direction for $\xi_g = 0$ conditions. For harmonic excitation at frequency ω , material damping can be introduced by the use of a complex stiffness, so that

$$P_h = k_x(1 + i2\xi_x + i2\xi_g)u_0 \quad (7.73)$$

Since $P_h = k_h u_0 + c_h \dot{u}_0$, the horizontal stiffness and damping coefficients are

$$k_h = k_x \quad (7.74a)$$

$$c_h = c_x + \frac{2}{\omega} \xi_g k_x \quad (7.74b)$$

The first term on the right side of equation (7.74b) corresponds to radiation damping, and the second to material damping. If the structure was rigid ($k = \infty$) and the foundation unable to rotate ($k_r = \infty$), the natural frequency for translational vibration would be

$$\omega_h = \sqrt{\frac{k_h}{m}} \quad (7.75)$$

Repeating the same process for the rocking mode of vibration produces

$$k_r = k_\theta \quad (7.76a)$$

$$c_r = c_\theta + \frac{2}{\omega} \xi_g k_\theta \quad (7.76b)$$

where the subscript θ denotes the absence of material damping. If the structure was rigid ($k = \infty$) and the foundation unable to translate ($k_h = \infty$), the natural frequency for rocking would be

$$\omega_r = \sqrt{\frac{k_r}{mh^2}} \quad (7.77)$$

Insight into the soil–structure interaction problem can now be gained by developing an equivalent SDOF system (i.e., a SDOF system that responds in essentially the same way as the system of Figure 7.23). Using the subscript e to describe the properties of this equivalent system, the equation of motion (for harmonic motion) can be written as

$$(-m\omega^2 + i\omega c_e + k_e)u = m\omega^2 U_b$$

where U_b is the equivalent seismic input motion. Note that the mass is the same for the equivalent and actual models. For the equivalent system

$$k_e = m\omega_e^2$$

$$\xi_e = \frac{c_e\omega}{2k_e}$$

The natural frequency of the equivalent model, ω_e , is the frequency at which the response of the equivalent system goes to infinity for $\xi_e = 0$. This occurs when

$$\frac{1}{\omega_e^2} = \frac{1}{\omega_0^2} + \frac{1}{\omega_h^2} + \frac{1}{\omega_r^2}$$

or at

$$\omega_e = \frac{\omega_0}{\sqrt{1 + k/k_h + kh^2/k_r}} \quad (7.78)$$

Equation (7.78) indicates that the natural frequency of the equivalent system is always lower than that of the fixed-base structure. In other words, an important effect of soil-structure interaction is to reduce the natural frequency of the soil-structure system to a value lower than that of the structure under fixed-base conditions.

By neglecting second-order damping ratio terms, the equivalent hysteretic damping ratio can be expressed as

$$\xi_e = \frac{\omega_e^2}{\omega_0^2}\xi + \left(1 - \frac{\omega_e^2}{\omega_0^2}\right)\xi_g + \frac{\omega_e^2}{\omega_h^2}\xi_x + \frac{\omega_e^2}{\omega_r^2}\xi_\theta \quad (7.79)$$

Equation (7.79) indicates that the damping ratio of the equivalent system will, for typical soils and foundations, be larger than the damping ratio of the structure itself. Consequently, another important effect of soil-structure interaction is to increase the effective damping ratio to a value greater than that of the structure itself.

For the fixed-base case, no translation or rotation of the base is possible, but the base translation of the equivalent system can be shown to be

$$u_0 = \frac{\omega_0^2}{\omega_h^2}(1 + 2\xi_i - 2\xi_x i - 2\xi_g i)u \quad (7.80)$$

and the base rotation

$$\theta = \frac{1}{h} \frac{\omega_0^2}{\omega_r^2}(1 + 2\xi_i - 2\xi_\theta i - 2\xi_g i)u \quad (7.81)$$

Then the motion of the mass relative to the free-field motion is given by the sum of the base displacement, u_0 , the displacement of the top of the rod due to rotation of the base, $h\theta$, and the displacement due to distortion of the structure, u ,

$$u + u_0 + h\theta = \omega_0^2 \left[\frac{1}{\omega_e^2} + 2(\xi - \xi_g) i \left(\frac{1}{\omega_e^2} - \frac{1}{\omega_0^2} \right) - \frac{2\xi_x i}{\omega_h^2} - \frac{2\xi_\theta i}{\omega_r^2} \right] u \quad (7.82)$$

The effects of soil–structure interaction are easily illustrated in terms of the following dimensionless parameters:

Stiffness ratio: $\bar{s} = \frac{\omega_0 h}{v_s}$ where v_s is the soil shear wave velocity

Slenderness ratio: $\bar{h} = \frac{h}{a}$ where a is characteristic length of the foundation (radius for circular shape)

Mass ratio: $\bar{m} = \frac{m}{\rho a^3}$ where ρ is the mass density of the soil

Large values of the stiffness ratio correspond to situations where a relatively stiff structure rests on a relatively soft soil. The fixed-base condition is realized at zero stiffness ratio.

Actual foundation stiffness and damping coefficients are frequency dependent. To illustrate the effects of soil–structure interaction, however, the following simplified, frequency-independent expressions can be used to estimate the stiffness and damping coefficients of a rigid circular footing of radius a

$$k_x = \frac{8Ga}{2-\nu} \quad c_x = \frac{4.6}{2-\nu} \rho v_s a^2$$

$$k_\theta = \frac{8Ga^3}{3(1-\nu)} \quad c_\theta = \frac{0.4}{1-\nu} \rho v_s a^4$$

The graphs in Figures 7.24 and 7.25 show the influence of soil–structure interaction on the natural frequency, damping ratio, and displacement characteristics of the equivalent SDOF system. Comparing the response characteristics of the equivalent system with the fixed-base system illustrates the effects of soil–structure interaction.

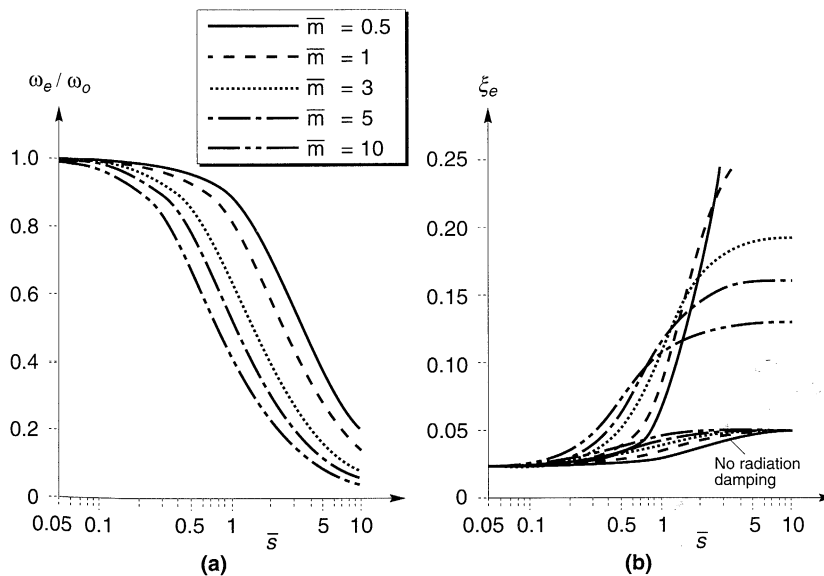


Figure 7.24 Effect of stiffness ratio and mass ratio on (a) natural frequency, and (b) damping ratio of soil–structure systems ($\bar{h} = 1, \nu = 0.33, \xi = 0.025, \xi_g = 0.05$). (After Wolf, 1985.)

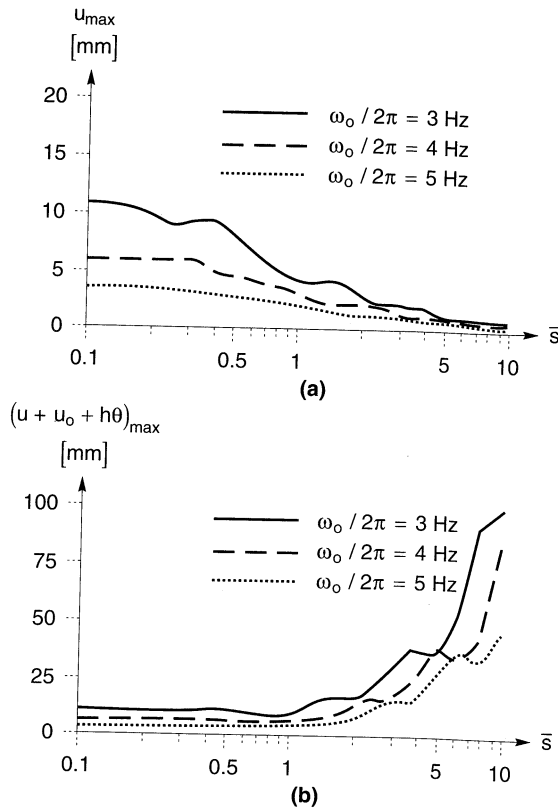


Figure 7.25 Response of equivalent soil-structure system to artificial time history ($\bar{h} = 1, \bar{m} = 3, \nu = 0.33, \xi = 0.025, \xi_g = 0.05$): (a) maximum structural distortion; (b) maximum displacement of mass relative to free field. (After Wolf, 1985.)

Figure 7.24a shows how the natural frequency of the equivalent SDOF system drops below that of the fixed-base system as the stiffness ratio increases. The effects of soil-structure interaction on the natural frequency is small at low stiffness ratios, i.e., when the stiffness of the soil (as reflected in the shear wave velocity) is large relative to the stiffness of the structure. For the fixed-base condition ($\bar{s} = 0$), the natural frequency of the equivalent system is equal to the fixed-base natural frequency. Figure 7.24b illustrates the influence of soil-structure interaction on the damping ratio of the equivalent SDOF system. For the fixed-base condition, the damping ratio of the equivalent system is equal to the structural damping ratio, but as the stiffness ratio increases, the effects of radiation and soil damping become more apparent. At high stiffness ratios, structural damping represents only a small part of the total damping of the system.

The effects of soil-structure interaction on displacements is illustrated in Figure 7.25. The indicated maximum responses are for an artificial input motion that produced an NRC response spectrum scaled to $a_{\max} = 1.0g$. In this case, the effects of soil-structure interaction were to reduce the maximum structural distortion, u_{\max} , by an amount that increased with increasing stiffness ratio and to increase the overall displacement (relative to the free field) by an amount that increased with increasing stiffness ratio. Thus soil-structure interaction tends to reduce the demands on the structure, but because the foundation can translate and rotate, increase the overall displacement. These effects can be important for tall, slender

structures or for closely spaced structures that may be subject to *pounding* when relative displacements become large.

7.5.2 Methods of Analysis

While the preceding analysis illustrated several important effects of soil–structure interaction, it is not suitable for the detailed analysis of practical soil–structure interaction problems. Methods for the analysis of soil–structure interaction can be divided into two main categories: *direct methods* and *multistep methods*.

7.5.2.1 Direct Method

In the direct method, the entire soil–foundation–structure system is modeled and analyzed in a single step. As illustrated in Figure 7.26, free-field input motions are specified along the base and sides of the model and the resulting response of the interacting system is computed (for a finite-element model) from the equations of motion

$$[\mathbf{M}]\{\ddot{\mathbf{u}}\} + [\mathbf{K}^*]\{\mathbf{u}\} = -[\mathbf{M}]\{\ddot{\mathbf{u}}_{\text{ff}}(t)\} \quad (7.83)$$

where $\{\ddot{\mathbf{u}}_{\text{ff}}(t)\}$ are the specified free-field accelerations at the boundary nodal points. The use of the direct method requires a computer program that can treat the behavior of both the soil and the structure with equal rigor.

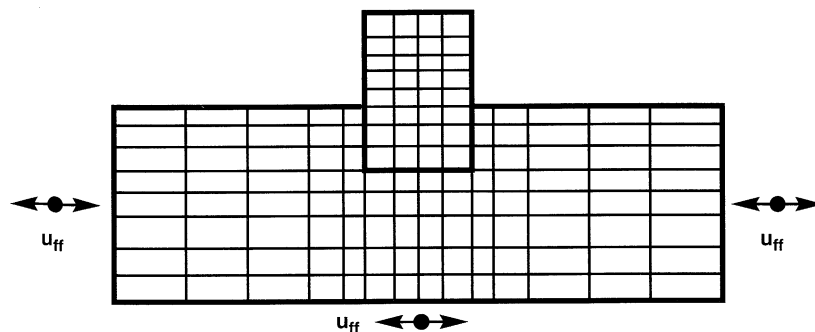


Figure 7.26 Direct method of soil–structure interaction analysis. Entire problem is modeled and response to free-field motion applied at boundaries is determined in a single step.

7.5.2.2 Multistep Method

Multistep methods use the principle of superposition to isolate the two primary causes of soil–structure interaction: the inability of the foundation to match the free-field deformation and the effect of the dynamic response of the structure–foundation system on the movement of the supporting soil. Because they rely on superposition, they are limited to the analysis of linear (or equivalent linear) systems.

Kinematic Interaction. In the free field, an earthquake will cause soil displacements in both the horizontal and vertical directions. If a foundation on the surface of, or embedded in, a soil deposit is so stiff that it cannot follow the free-field deformation pattern, its motion will be influenced by *kinematic interaction*, even if it has no mass. For

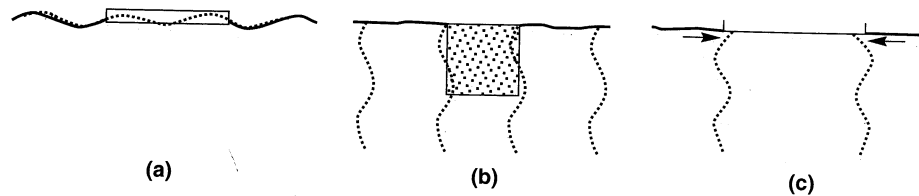


Figure 7.27 Kinematic interaction with free-field motions indicated by dashed lines: (a) flexural stiffness of surface foundation prevents it from following vertical component of free-field displacement; (b) rigidity of block foundation prevents it from following horizontal component of free-field displacement; (c) axial stiffness of surface foundation prevents immediately underlying soil from deforming incoherently.

example, the flexural stiffness of the massless mat foundation in Figure 7.27a prevents it from following the horizontally varying vertical component of the free-field motion. The rigidity of the massless embedded foundation in Figure 7.27b keeps it from following the vertically varying horizontal free-field motion. The axial stiffness of the slab in Figure 7.27c prevents development of the incoherent free-field motion. In each of these cases, the motion of the foundation is influenced by kinematic interaction. Kinematic interaction, however, is not present in all problems. If the surface foundation of Figure 7.27a was subjected to vertically propagating s-waves (horizontal particle motion only), it would not restrict the movement of the soil; consequently, no kinematic interaction would exist. Kinematic interaction will occur whenever the stiffness of the foundation system impedes development of the free-field motions.

Kinematic interaction can also induce different modes of vibration in a structure. Consider the embedded foundation of Figure 7.28a. When subjected to vertically propagating s-waves with a wavelength equal to the depth of embedment, a net overturning moment can be applied to the foundation, thereby causing the foundation to rock as well as translate, even though the free-field motion is purely translational. At a different frequency (Figure 7.28b), the wavelength may be such that rotation is inhibited. Horizontally propagating waves can, in a similar manner, induce torsional vibration of the foundation.

The deformations due to kinematic interaction alone can be computed by assuming that the foundation has stiffness but no mass. The equations of motion for this case are

$$[M_{\text{soil}}]\{\ddot{u}_{\text{KI}}\} + [K^*]\{u_{\text{KI}}\} = -[M_{\text{soil}}]\ddot{u}_b(t) \quad (7.84)$$

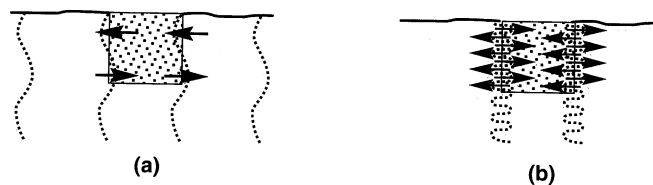


Figure 7.28 Excitation of rocking vibrations in an embedded foundation by vertically propagating s-waves: (a) at certain frequencies, the wavelength is such that unbalanced overturning moments cause rocking; (b) at other frequencies (and wavelengths), rocking may be suppressed.

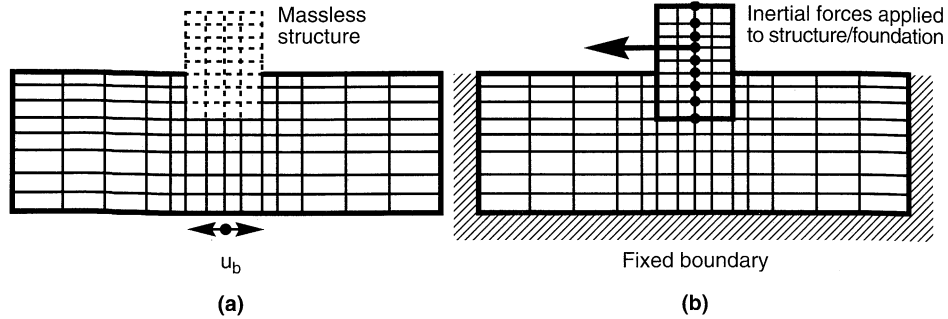


Figure 7.29 (a) Kinematic interaction analysis and (b) inertial interaction analysis. Mass of structure in inertial interaction analysis shown as being lumped at the center of the structure.

where $[M_{\text{soil}}]$ is the mass matrix assuming that the structure and foundation are massless. Equation (7.84) describes the problem illustrated in Figure 7.29a. Equation (7.84) is solved for $\{u_{\text{KI}}\}$, which is referred to as the *foundation input motion*.

Inertial Interaction. The structure and foundation do have mass, however, and this mass causes them to respond dynamically. If the supporting soil is compliant, the forces transmitted to it by the foundation will produce foundation movement that would not occur in a fixed-base structure. The effects of soil compliance on the resulting response are due to *inertial interaction*.

The deformations due to inertial interaction can be computed from the equations of motion

$$[M]\{\ddot{u}_{\text{II}}\} + [K^*]\{u_{\text{II}}\} = -[M_{\text{structure}}]\{\ddot{u}_{\text{KI}}(t) + \ddot{u}_{\text{b}}(t)\} \quad (7.85)$$

where $[M_{\text{structure}}]$ is the mass matrix assuming that the soil is massless. Note that the right side of equation (7.85) represents the inertial loading on the structure–foundation system. This inertial loading depends on the base motion and the foundation input motion, which reflects the effects of kinematic interaction. In the inertial interaction analysis, the inertial loading is applied only to the structure; the base of the soil deposit is stationary. Equation (7.85) corresponds to the problem illustrated in Figure 7.29b.

Combination of Kinematic and Inertial Interaction. The kinematic interaction analysis produces the motion of the massless foundation–structure system (relative to the base) due to kinematic interaction. This motion is combined with the base motion to produce the total kinematic motion of the foundation–structure system. When the inertial loading that results from this kinematic motion is applied to the foundation–structure system resting on massless soil, equation (7.85) allows computation of the relative (to the total kinematic) motion. Adding equations (7.84) and (7.85) gives

$$\begin{aligned} [M_{\text{soil}}]\{\ddot{u}_{\text{KI}}\} + [M]\{\ddot{u}_{\text{II}}\} + [K^*](\{u_{\text{KI}}\} + \{u_{\text{II}}\}) \\ = -([M_{\text{soil}}] + [M_{\text{structure}}])\ddot{u}_{\text{b}} - [M_{\text{structure}}]\{\ddot{u}_{\text{KI}}\} \end{aligned} \quad (7.86)$$

Since $\{u_{\text{KI}}\} + \{u_{\text{II}}\} = \{u\}$ and $[M_{\text{soil}}] + [M_{\text{structure}}] = [M]$, equation (7.86) is equivalent to the original equations of motion

$$[M]\{\ddot{u}\} + [K^*]\{u\} = -[M]\{\ddot{u}_{\text{b}}(t)\}$$

which proves that the solution to the entire soil–structure interaction problem is equal to the sum of the solutions of the kinematic and inertial interaction analyses. Therefore, the multi-step procedure can be summarized as follows:

1. A kinematic interaction analysis, in which the foundation–structure system is assumed to have stiffness but no mass, is performed. This analysis produces the foundation input motion.
2. The foundation input motion is used to apply inertial loads to the structure in an inertial interaction analysis, in which the soil, foundation, and structure are all assumed to have stiffness and mass.

If the foundation itself is rigid, the soil can be replaced by a set of equivalent springs and dashpots in the inertial interaction analysis. The inertial interaction analysis can then be performed by applying inertial forces to the masses of the structure (Figure 7.30a) or by applying the input motion to the supports (Figure 7.30b); the two methods are mathematically equivalent. Considerable research, involving analytical, numerical, and experimental modeling, has produced a variety of techniques for the evaluation of spring and dashpot constants for foundation systems. Gazetas (1991) provided a very useful, practical series of charts and tables for estimation of spring and dashpot coefficients for a variety of foundation types and soil conditions. For more complicated soil and foundation conditions, computer programs such as DYNA4 (Novak et al., 1993) allow computation of complete foundation stiffness and damping matrices.

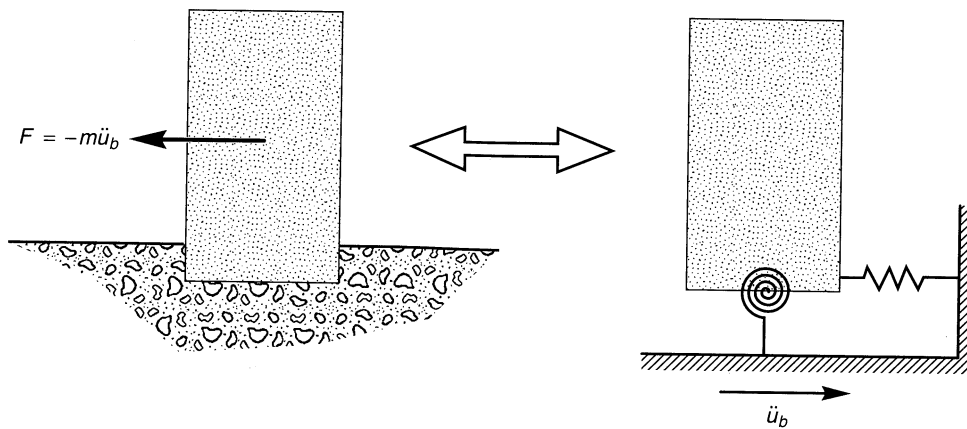


Figure 7.30 Equivalent formulations of inertial interaction analysis for structures with rigid foundation: (a) inertia forces applied to each element; (b) foundation motion applied through frequency-dependent springs and dashpots (not shown).

7.6 SUMMARY

1. Analysis of the response of soil deposits and earthen structures to earthquake motions is one of the most important aspects of geotechnical earthquake engineering practice. Ground response problems are often grouped into categories for which one-, two-, and three-dimensional ground response analyses are appropriate.

2. Ground response analyses are generally performed by one of two methods: equivalent linear analysis or nonlinear analysis. Equivalent linear analyses are linear analyses in which the soil stiffness and damping characteristics are adjusted until they are compatible with the level of strain induced in the soil. Nonlinear analyses actually consider the nonlinear inelastic stress–strain behavior of soils by integrating the equations of motion in small time steps. Equivalent linear analyses are generally more computationally efficient than nonlinear analyses.
3. One-dimensional ground response analyses are based on the assumption that the ground surface and all material boundaries below the ground surface are horizontal and extend infinitely in all lateral directions. Although these assumptions can never be strictly satisfied, they are satisfied sufficiently for engineering purposes at many sites.
4. The equivalent linear approach makes use of transfer functions to relate parameters of interest (such as ground surface acceleration or velocity) to known parameters (such as bedrock acceleration). The nature of a transfer function is influenced by the thickness, stiffness, and damping characteristics of each soil layer. The transfer function is also influenced by bedrock properties.
5. During an earthquake, stress waves that reach the ground surface are perfectly reflected (i.e., with no loss of energy) to travel downward toward bedrock. When a downward traveling wave reaches bedrock, part of the wave will be reflected, and unless the rock is perfectly rigid, part will be transmitted to continue traveling downward through the rock. If the elastic bedrock is relatively homogeneous, the transmitted wave effectively removes energy from the soil deposit and causes its response to be lower than it would have been for the case of rigid bedrock. This phenomenon represents a form of radiation damping.
6. Because the equivalent linear approach is fundamentally linear, the response at any two points in a soil deposit are uniquely related to each other. As a result, an object motion can be specified at any point in the soil deposit and the corresponding motion computed at any other point. This feature allows use of a motion recorded on the surface of a soil deposit to compute the bedrock motion that would have caused it. This useful operation, known as deconvolution, does not provide a unique solution when performed with nonlinear analyses.
7. Nonlinear analyses integrate the equations of motion in small time steps. At the beginning of each time step, the stress–strain relationship is referred to to obtain the appropriate soil properties to be used in that time step. By this method, a nonlinear inelastic stress–strain relationship can be followed in a set of small incrementally linear steps.
8. Both equivalent linear and nonlinear approaches have been used successfully for ground response analysis. Their use and interpretation, however, requires knowledge of their underlying assumptions, understanding of their operation, and recognition of their limitations. Neither can be considered mathematically rigorous or precise, yet their accuracy is not inconsistent with the variability in soil conditions, uncertainty in soil properties, and scatter in the experimental data upon which many of their input parameters are based.
9. Two- and three-dimensional ground response analyses are usually performed using dynamic finite-element analyses. These analyses can be performed using equivalent

linear or nonlinear approaches. Both equivalent linear and nonlinear dynamic finite element analyses are analogous to their one-dimensional counterparts, and many of the same advantages and limitations apply to each.

10. Analysis of the response of certain two- and three-dimensional earth structures, such as earth dams and embankments, can be greatly simplified by the shear beam approach. The shear beam approach allows two- and three-dimensional problems to be idealized as equivalent one-dimensional problems.
11. Ground motions that are not influenced by the presence of structures are called free-field motions. When structures are present, they interact with the soil through a process referred to as soil–structure interaction. Soil–structure interaction has little effect on the response of some systems and a large effect on the response of others. Its effects are most significant for stiff and/or heavy structures supported on relatively soft soils. For soft and/or light structures founded on stiff soils, soil–structure interaction effects are generally small.
12. In general, soil–structure interaction will cause the natural frequency of a soil–structure system to be lower than the natural frequency of the structure itself. Also, radiation damping will generally cause the total damping of a soil–structure system to be greater than that of the structure itself. Because of these effects, soil–structure interaction tends to reduce the demands on the structure, but because the foundation can translate and rotate, can increase the overall displacement.
13. Soil–structure interaction is caused by two phenomena: the inability of the foundation to match the free-field deformation (kinematic interaction) and the effect of the dynamic response of the structure–foundation system on the movement of the supporting soil (inertial interaction). Kinematic interaction can induce modes of deformation (e.g., rocking and torsion) that are not present in a free-field motion. Inertial interaction occurs when the forces transmitted to the soil by the dynamic response of the structure produce foundation movements that would not occur in a fixed-base structure. The effects of inertial interaction are usually more pronounced than the effects of kinematic interaction.
14. For linear or equivalent linear analyses, the effects of kinematic interaction and inertial interaction can be separated. The effects of kinematic interaction are first determined and then used as input to an inertial interaction analysis. Combining the results of both analyses allows the overall response to be determined.

HOMework PROBLEMS

- 7.1 For the case of a uniform layer of undamped soil overlying rigid bedrock, develop a transfer function that relates shear stress, $\tau(z = H/2, t)$, to the bedrock acceleration, $\ddot{u}_b(t)$. Plot the modulus of the transfer function from $kH = 0$ to $kH = 2\pi$.
- 7.2 An acceleration reduction factor can be defined as the ratio of the peak acceleration at depth, z , to the peak ground surface acceleration, i.e.

$$r_d = \frac{\ddot{u}_{\max}(z)}{\ddot{u}_{\max}(z = 0)}$$

For the case of a uniform layer of undamped soil overlying rigid bedrock, develop an expression for the reduction factor as a function of the thickness and shear wave velocity of the soil layer, and the frequency of the input motion.

- 7.3 Plot the reduction factor determined in Problem 7.2 with depth for a 15 m thick soil deposit with a shear wave velocity of 300 m/sec at input motion frequencies of 0.5 Hz, 1.0 Hz, 2.0 Hz, 3.0 Hz, and 5.0 Hz.
- 7.4 Derive a transfer function that relates the displacement of the ground surface to the displacement of bedrock for the site illustrated below.
- Define the complex wave numbers, k_1^* and k_2^* .
 - Define the complex impedance ratio, α^* .
 - Express the transfer function in terms of h_1 , h_2 , k_1^* , k_2^* , and α^* .

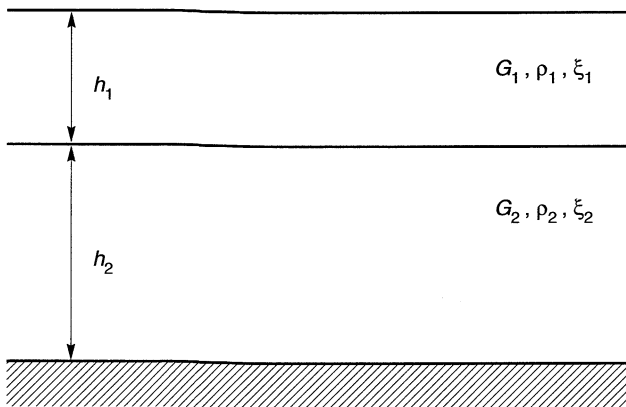


Figure P7.4

- 7.5 The shear modulus of the soil within the earth dam shown below increases linearly with depth. The shear wave velocity of the soil just above the base of the dam is 800m/sec. Compute the first two natural frequencies of the dam.

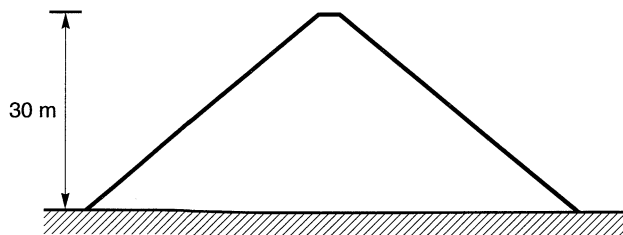


Figure P7.5

- 7.6 If the dam section shown in Problem 7.5 represented the maximum section of a dam in a semi-cylindrical channel, estimate the first two natural frequencies of the dam.

- 7.7 The SDOF system shown below is supported by a 10 ft diameter circular footing. The mass of the footing is small compared to the mass of the structure. Compute the damped natural period of the soil-structure system:
- (a) assuming fixed base conditions,
 - (b) assuming that the footing can translate horizontally (but not rotate), and
 - (c) assuming that the footing can both translate and rotate.

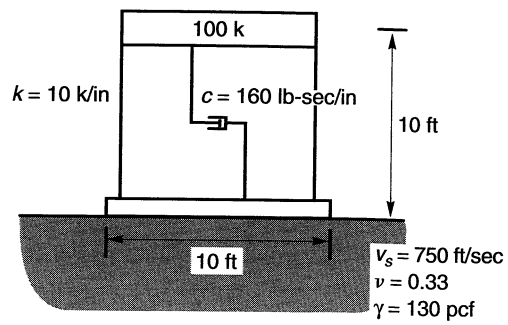


Figure P7.7

8

Local Site Effects and Design Ground Motions

8.1 INTRODUCTION

The influence of local geologic and soil conditions on the intensity of ground shaking and earthquake damage has been known for many years. MacMurdo (1824) noted that “buildings situated on rock were not by any means so much affected . . . as those whose foundations did not reach to the bottom of the soil” in the 1819 earthquake in Cutch, India. In his report on the 1857 Neapolitan earthquake, Mallet (1862) noted the effect of local geologic conditions on damage. Wood (1908) and Reid (1910) showed that the intensity of ground shaking in the 1906 San Francisco earthquake was related to local soil and geologic conditions. Gutenberg (1927) developed site-dependent amplification factors from recordings of microseisms at sites with different subsurface conditions. Since these early observations, the effects of local site conditions on ground motions have been illustrated in earthquakes around the world. More recently, the availability of strong-motion instruments has allowed local site effects to be measured quantitatively in recent years.

Local site effects play an important role in *earthquake-resistant design* and must be accounted for on a case-by-case basis. This is usually accomplished by the development of one or more *design ground motions* (i.e., motions that reflect the levels of strong motion amplitude, frequency content, and duration that a structure or facility at a particular site should be designed for). The development of site-specific design ground motions involves

concepts presented in all of the preceding chapters of this book; it is one of the most important aspects of geotechnical earthquake engineering.

Despite considerable evidence, the existence of local site effects was a matter of some debate in past years. Indeed, provisions specifically accounting for local site effects did not appear in building codes until the 1970s. This chapter presents theoretical, instrumental, and historical evidence for the existence of local site effects. It discusses procedures that are commonly used for the development of site-specific design ground motions and reviews the manner in which local site effects are treated in the specification of design ground motions by contemporary building codes and standards.

8.2 EFFECTS OF LOCAL SITE CONDITIONS ON GROUND MOTION

Local site conditions can profoundly influence all of the important characteristics—amplitude, frequency content, and duration—of strong ground motion. The extent of their influence depends on the geometry and material properties of the subsurface materials, on site topography, and on the characteristics of the input motion. The nature of local site effects can be illustrated in several ways: by simple, theoretical ground response analyses, by measurements of actual surface and subsurface motions at the same site, and by measurements of ground surface motions from sites with different subsurface conditions.

8.2.1 Evidence from Theoretical Ground Response Analyses

There are important theoretical reasons why ground surface motions should be influenced by local site conditions. At most sites the density and s-wave velocity of materials near the surface are smaller than at greater depths. If the effects of scattering and material damping are neglected, the conservation of elastic wave energy requires that the flow of energy (energy flux, $\rho v_s \dot{u}^2$) from depth to the ground surface be constant. Therefore, since ρ and v_s decrease as waves approach the ground surface, the particle velocity, \dot{u} , must increase.

The characteristics of local soil deposits can also influence the extent to which ground motion amplification will occur when the specific impedance is constant. The basis for such amplification can be illustrated analytically using simple, theoretical ground response analyses. Consider, for example, the two soil deposits shown in Figure 8.1; their geometries are identical, but one is considerably stiffer than the other. If each soil is assumed to be linearly

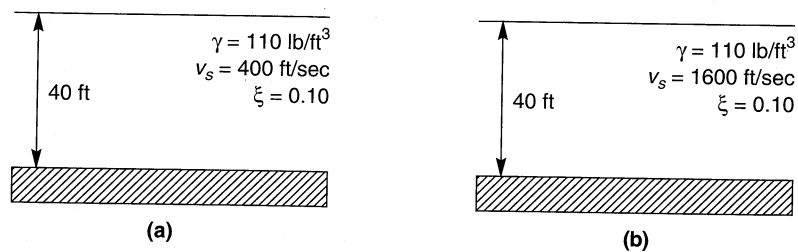


Figure 8.1 Two hypothetical soil deposits overlying rigid bedrock: (a) site A; (b) site B. Soils are identical, except the s-wave velocity of the soil at site B is four times greater than that at site A.

elastic and bedrock to be rigid, the amplification functions of each site [from equation (7.13)] are as illustrated in Figure 8.2. Clearly, the softer site (site A) will amplify low-frequency (long-period) bedrock motions more than the stiff site (site B); the reverse would be observed for high-frequency (short-period) motions. Since earthquakes produce bedrock motion over a range of frequencies, some components of an actual bedrock motion will be amplified more than others, as illustrated in Examples 7.1 to 7.5. For the more realistic condition of elastic bedrock, the nature of the local site amplification will be influenced by the specific impedance of the bedrock. Consequently, any description of local site conditions should include the density and stiffness of the bedrock. For example, the harder crystalline bedrock found in much of the eastern United States would be expected to produce amplification factors about 50% higher than those associated with the softer rock conditions typically found in California (Jacob, 1991) for equivalent soil conditions.

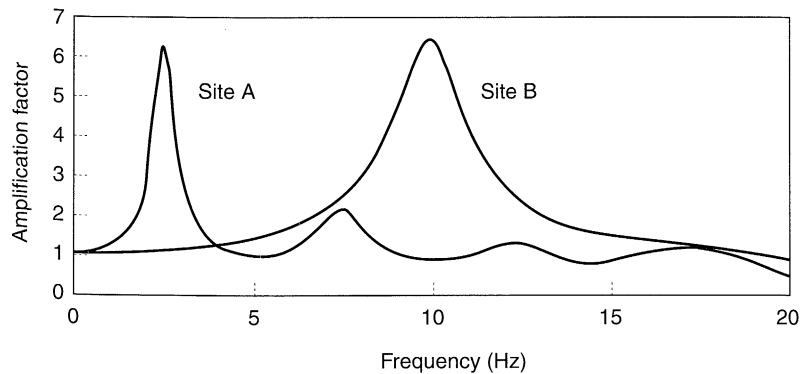


Figure 8.2 Amplification functions for sites A and B. Note that the softer soil at site A will amplify low-frequency input motions much more strongly than will the stiffer soils of site B. At higher frequencies, the opposite behavior would be expected.

8.2.2 Evidence from Measured Amplification Functions

The idealized assumptions of simple one-dimensional ground response analyses (uniform materials, horizontal layering, vertically propagating s-waves, etc.) produce smooth amplification functions such as those shown in Figure 8.2. Since these conditions rarely exist in the field, actual amplification functions are not so smooth.

Interpretation of strong motion data from sites where both surface and subsurface instruments had been installed allows actual amplification functions to be computed (e.g., Joyner et al., 1976; Johnson and Silva, 1981; Chang et al., 1986). The strong amplification at the natural frequencies of the soil deposit shown in Figure 8.3 clearly illustrates the importance of local soil conditions on ground response. The site consists of various soils of relatively uniform shear wave velocity overlying bedrock; consequently, the frequency dependence of the actual amplification function is qualitatively similar to that predicted by simple ground response analyses. For sites with more complicated subsurface conditions, or

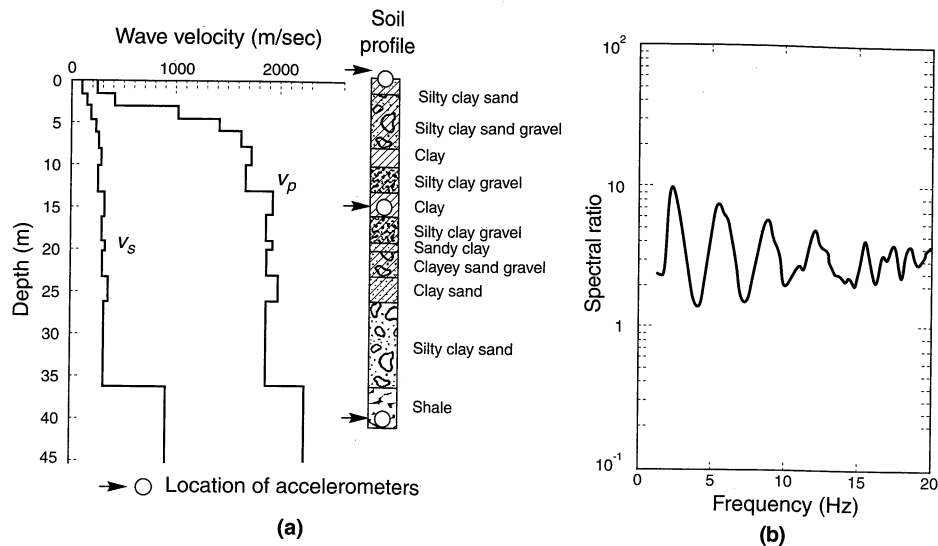


Figure 8.3 (a) Subsurface profile at Richmond field station (after Johnson and Silva, 1981). (b) Surface–bedrock amplification functions from response measured during the Briones Hills ($M_L = 4.3$) earthquake (after Silva, 1988). Fourier spectra were smoothed over a 1-Hz window prior to spectral ratio computation.

for stronger earthquakes in which soil nonlinearity may become significant, the ability of simple ground response analyses to predict the irregular peaks and valleys of actual amplification functions decreases. The effects of soil nonlinearity also cause amplification functions from strong motions to differ from those of weak motions (e.g., Aki, 1993).

Example 8.1

Compute the spectral ratio of the Gilroy No. 1 (rock) and Gilroy No. 2 (soil) motions.

Solution The actual transfer function relating the Gilroy No. 1 (rock) and Gilroy No. 2 (soil) motions can be computed from the Fourier series of the individual motions. The process can be performed in three steps:

1. Compute the Fourier series for the Gilroy No. 1 (rock) motion. The Fourier amplitude spectrum of this motion was originally shown in Figure 3.13a, and is repeated in Figure E8.1a. Also shown is a smoothed version of the spectrum (the smoothed version was smoothed numerically, but not as extensively as required for evaluation of the predominant period in Example 3.3).
2. Compute the Fourier series for the Gilroy No. 2 (soil) motion. Raw and smoothed Fourier amplitude spectra for this motion are shown in Figure E8.1b.
3. Compute the transfer function as the ratio of the Fourier amplitudes of the Gilroy No. 2 (soil) motion to the Fourier amplitudes of the Gilroy No. 1 (rock) motion. The result, shown in Figure E8.1c, shows that low-frequency components of the Gilroy No. 1 (rock) motion were amplified by the soils underlying the Gilroy No. 2 (soil) station; high-frequency components were attenuated.

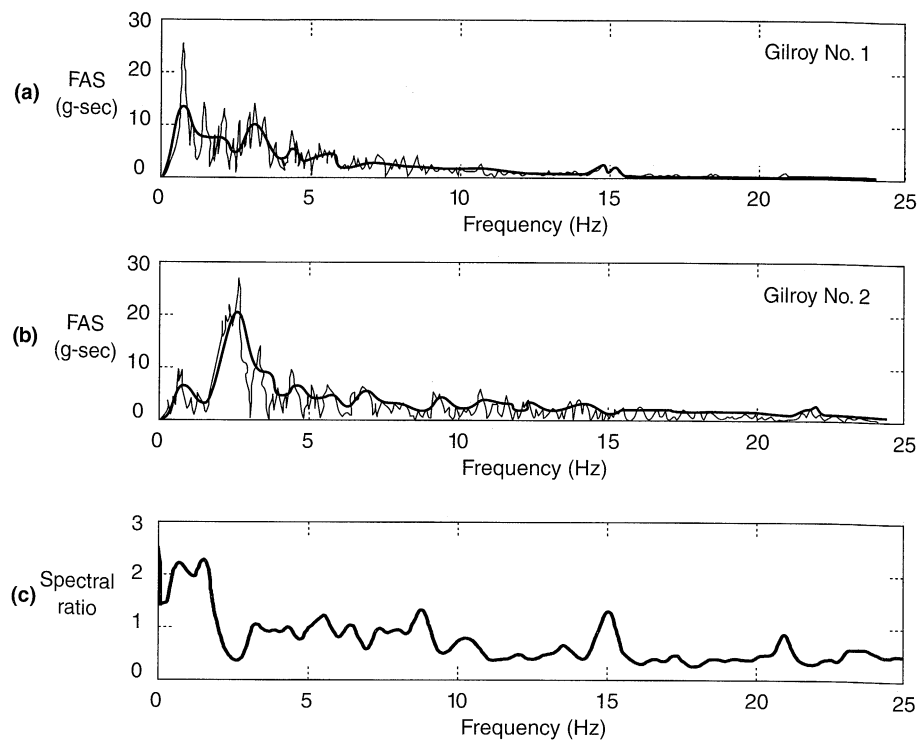


Figure E8.1

8.2.3 Evidence from Measured Surface Motions

Further evidence of the importance of local site conditions can be gained by comparing ground surface motions measured at different sites. For example, recordings of ground motion at several locations in San Francisco were made during a nearby $M \approx 5.3$ earthquake in 1957. Variations in ground motion, expressed in terms of peak horizontal acceleration and response spectra, are shown along with variation in soil conditions along a 4-mile section through the city in Figure 8.4. Ground surface motions at the rock outcrops (Market and Guerrero, Mason and Pine, Harrison and Main) were quite similar, but the amplitude and frequency content of the motions at sites underlain by thick soil deposits were markedly different.

Similar effects have been observed in many other earthquakes. From the standpoint of local site effects, two of the most significant recent earthquakes were the 1985 Michoacan (Mexico) earthquake (Stone et al., 1987) and the 1989 Loma Prieta (California) earthquake (Seed et al., 1990). These well-documented earthquakes produced strong motion records at sites underlain by a variety of different subsurface conditions in Mexico City and the San Francisco Bay area. A brief examination of these case histories illustrates the importance of local site effects.

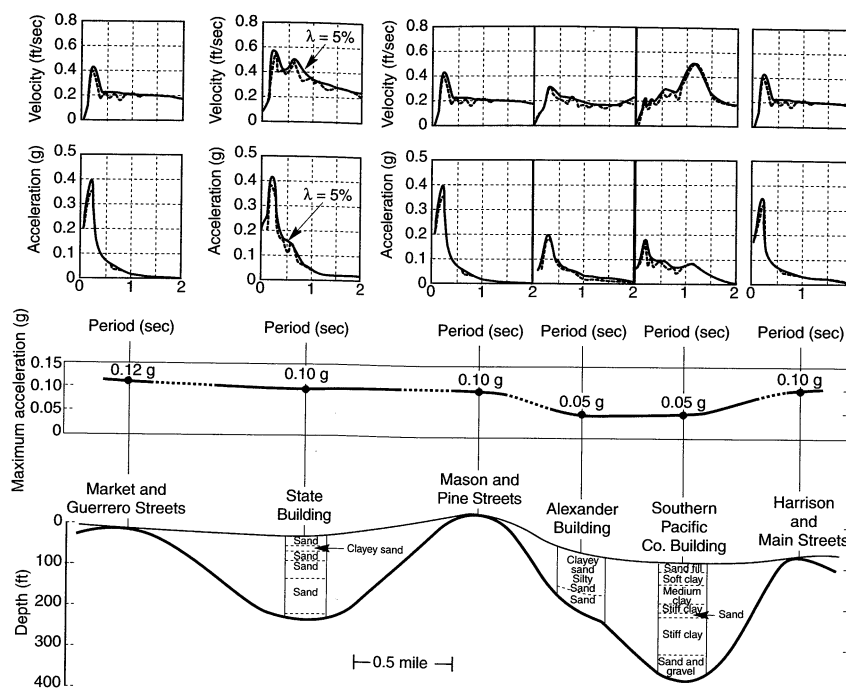


Figure 8.4 Variation of spectral velocity, spectral acceleration, and peak horizontal acceleration along a 4-mile section through San Francisco in the 1957 San Francisco earthquake. (After Idriss and Seed, 1968. Used by permission of the Seismological Society of America.)

8.2.3.1 Mexico City, 1985

The September 19, 1985 Michoacan ($M_s = 8.1$) earthquake caused only moderate damage in the vicinity of its epicenter (near the Pacific coast of Mexico) but caused extensive damage some 350 km away in Mexico City. Studies of ground motions recorded at different sites in Mexico City illustrated the significant relationship between local soil conditions and damaging ground motions and led to important advances in understanding the cyclic response of plastic clays (e.g., Dobry and Vucetic, 1987).

For seismic zonation purposes, Mexico City is often divided into three zones with different subsurface conditions (Figure 8.5a). Shallow, compact deposits of mostly granular soil, basalt, or volcanic tuff are found in the *Foothill Zone*, located west of downtown. In the *Lake Zone*, thick deposits of very soft soils formed from the pluviation of airborne silt, clay, and ash from nearby volcanoes through the waters of ancient Lake Texcoco extend to considerable depths, as shown by the contours of Figure 8.5b. These soft soils generally consist of two soft clay (Mexico City Clay) layers separated by a 0- to 6-m-thick (0 to 20 ft) compact sandy layer called the *capa dura*. Groundwater is generally found at a depth of about 2 m over most of the Lake Zone. Between the Foothill and Lake Zones lies the *Transition Zone*, where the soft soil deposits are thin and interspersed erratically with alluvial deposits.

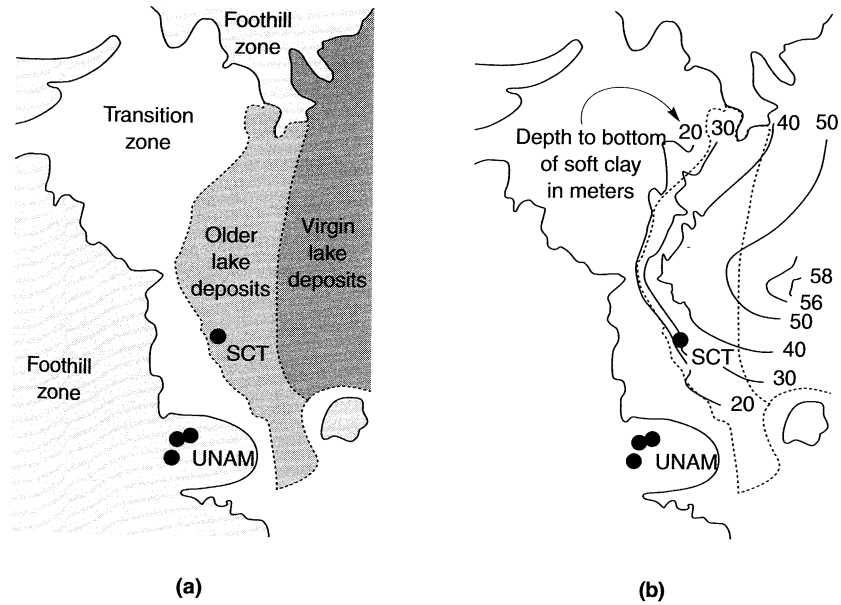


Figure 8.5 Strong-motion instruments and geotechnical conditions in Mexico City: (a) locations of strong motion instruments relative to Foothill, Transition, and Lake Zones; (b) contours of soft soil thickness. (After Stone et al., 1987.)

Prior to 1985, a number of strong-motion instruments had been deployed in Mexico City. Shown in Figure 8.5 are the locations of those at the Universidad Nacional Autonoma de Mexico (UNAM) and the Secretary of Communications and Transportation (SCT) site. The UNAM site was located in the Foothill Zone on 3 to 5 m (10 to 16 ft) of basaltic rock underlain by softer strata of unknown thickness. The SCT site was located on the soft soils of the Lake Zone.

Although the Michoacan earthquake was quite large, its great distance from Mexico City produced accelerations at the UNAM (rock) site of only 0.03g to 0.04g (Figure 8.6). In

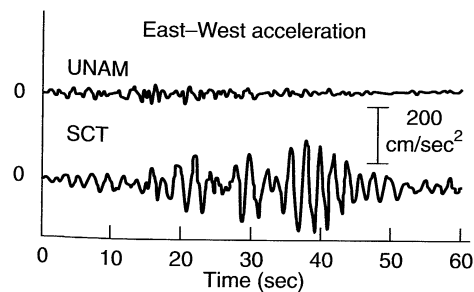


Figure 8.6 Time histories of acceleration recorded by strong motion instruments at UNAM and SCT sites. (After Stone et al., 1987.)

the Transition Zone, peak accelerations at the VIV site were slightly greater than those at UNAM but still quite low. In the Lake Zone, however, peak accelerations at the CDA and SCT sites were up to five times greater than those at UNAM. The frequency contents of the SCT and CDA motions were also much different than that of the UNAM motion; the predominant period was about 2 sec at SCT and slightly longer at CDA. Strong levels of shaking persisted over a very long duration at the SCT and CDA sites. The response spectra shown in Figure 8.7 illustrate the pronounced effects of the Lake Zone soils: at periods of approximately 2 sec, spectral accelerations at the SCT site were about 10 times greater than those at the UNAM site. The SCT site was underlain by 35 to 40 m (115 to 131 ft) of soft clay with an average s -wave velocity of about 75 m/sec (250 ft/sec). As a result, its characteristic site period [equation (7.16)] was $T_s = 4H/v_s \approx 4(37.5)/75 = 2$ sec, a value consistent with the peak in the SCT response spectrum of Figure 8.7.

Structural damage in Mexico City was highly selective; large parts of the city experienced no damage while other areas suffered pronounced damage. Damage was negligible in the Foothill Zone and minimal in the Transition Zone. The greatest damage occurred in those portions of the Lake Zone underlain by 38 to 50 m (125 to 164 ft) of soft soil (Stone et al., 1987), where the characteristic site periods were estimated at 1.9 to 2.8 sec. Even within this area, damage to buildings of less than five stories and modern buildings greater than 30 stories was slight. Most buildings in the five- to 20-story range, however, either collapsed or were badly damaged. Using the crude rule of thumb that the fundamental period of an N -story building is approximately $N/10$ sec, most of the damaged buildings had fundamental periods equal to or somewhat less than the characteristic site period. Accounting for the period-lengthening effect of soil-structure interaction (Section 7.4) and the tendency for the fundamental period of a structure to increase during a strong earthquake (due to the reduction in stiffness caused by cumulative architectural and structural damage), it seems likely that the damaged structures were subjected to many cycles of large dynamic forces at periods near their fundamental periods. This "double-resonance" condition (amplification of bedrock motion by the soil deposit and amplification of the soil motion by the structure) combined with structural design and construction deficiencies to cause locally devastating damage.

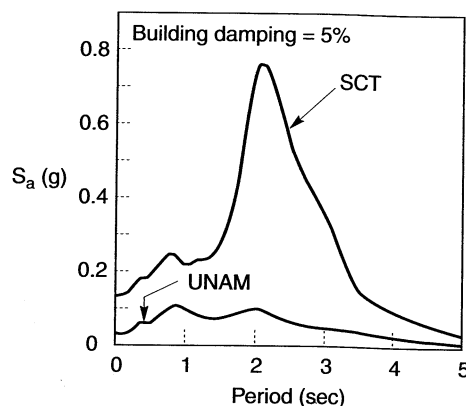


Figure 8.7 Response spectra computed from recorded motions at UNAM and SCT sites. (After Romo and Seed, 1986.)

8.2.3.2 San Francisco Bay Area, 1989

On October 19, 1989, a $M_s = 7.1$ earthquake occurred near Mt. Loma Prieta located about 100 km south of San Francisco and Oakland, California. The Loma Prieta earthquake produced MMI VIII shaking in the epicentral region, but intensities were actually higher, MMI IX, in portions of San Francisco and Oakland. The fact that the earthquake caused extensive damage in certain areas, and relatively little damage in others, suggested that local site effects were important.

The San Francisco Bay basin is largely filled with alluvial deposits of clays and silty to sandy clays with some layers of sandy and gravelly soils. The deeper deposits were overconsolidated by historical glacial sea-level drawdown, but the upper unit was deposited after the last drawdown episode. This material, known as San Francisco Bay Mud, is a normally consolidated silty clay. It is highly compressible and its strength grades from soft near the ground surface to medium stiff at depth. For purposes of seismic zonation, the Bay area can be divided into the three zones shown in Figure 8.8. The San Francisco Bay Mud is generally found at the margins of the bay, where its thickness varies from zero up to several tens of feet.

Both the epicentral region and the San Francisco Bay area were well instrumented with seismographs and accelerometers. Peak horizontal accelerations were recorded at the locations shown in Figure 8.8. These accelerations were high near the epicenter but attenuated with distance from the source. The attenuation, however, occurs much more rapidly for sites in the Rock/Shallow Residual Soil zone than in the Alluvium or Bay Mud zones (Figure 8.8).

The response of two instruments, those located at Yerba Buena Island and Treasure Island in the middle of San Francisco Bay, are particularly instructive. Yerba Buena Island

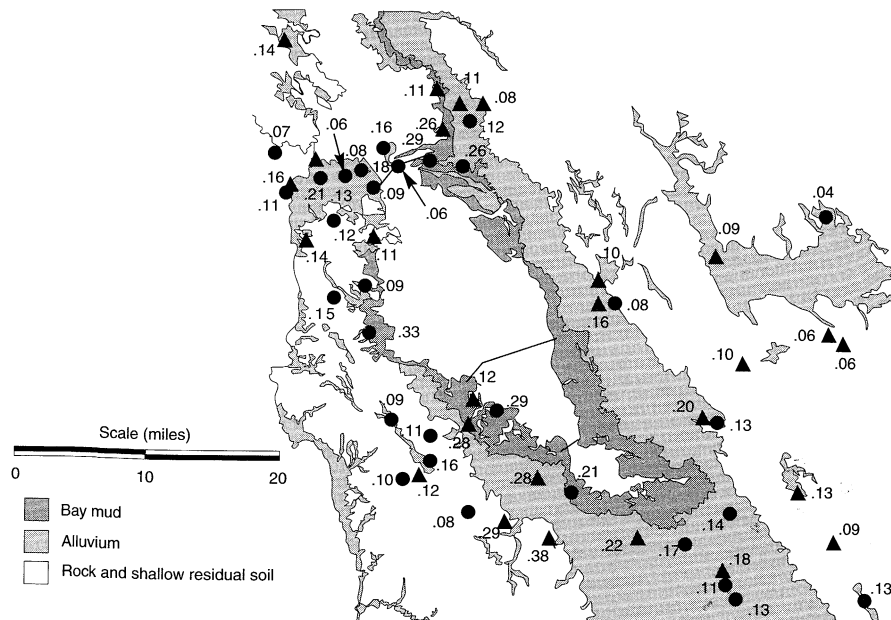


Figure 8.8 Measured peak horizontal accelerations (in g's) in the San Francisco Bay area during the 1989 Loma Prieta earthquake. Note the variation of peak acceleration for different site conditions. (After Seed et al., 1990.)

is a rock outcrop and Treasure Island is a 400-acre man-made hydraulic fill placed partially on the Yerba Buena shoals, a sandbar located immediately northwest of Yerba Buena Island. Treasure Island is underlain by a variable thickness of San Francisco Bay Mud; the Treasure Island seismograph was underlain by 45 ft (13.7 m) of loose sandy soil (hydraulic fill and natural soils) over 55 ft (16.8 m) of San Francisco Bay Mud. The Yerba Buena Island seismograph was located directly on rock. Though the Yerba Buena Island and Treasure Island instruments were virtually the same distance from the source, they recorded dramatically different ground surface motions (Figure 8.9a). Peak accelerations at Yerba Buena Island were 0.06g in the E-W direction and 0.03g in the N-S direction; the corresponding values at Treasure Island were 0.16g and 0.11g. Response spectra for the two sites are shown in Figure 8.9b. Clearly, the presence of the soft soils at the Treasure Island site caused significant amplification of the underlying bedrock motion.

Amplification of ground motion by soft soil deposits in other areas contributed significantly to damage in other parts of the San Francisco Bay area. The northern portion of the I-880 Cypress Viaduct that collapsed in the earthquake was underlain by San Francisco Bay Mud; the southern part that remained standing was not.

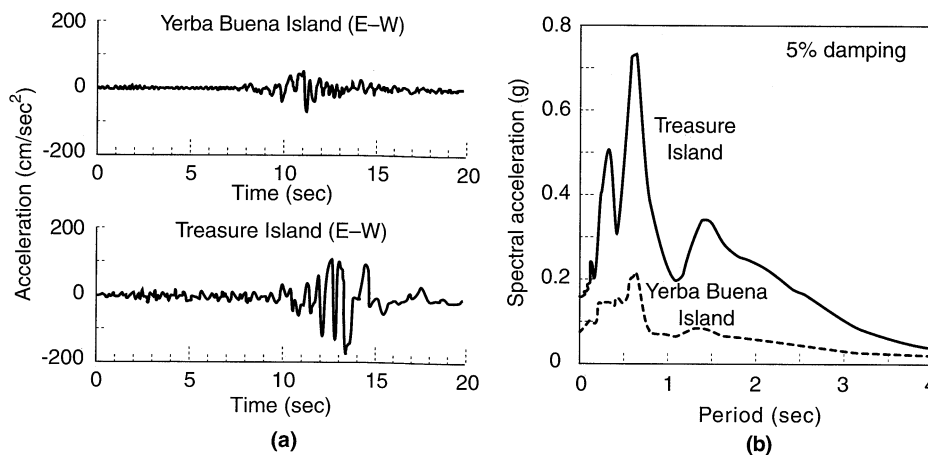


Figure 8.9 Ground surface motions at Yerba Buena Island and Treasure Island in the 1989 Loma Prieta earthquake: (a) time histories; (b) response spectra. (After Seed et al., 1990.)

8.2.4 Compilations of Data on Local Site Effects

The preceding section illustrates the important influence of local site conditions on the characteristics of ground surface motions. Case histories of ground response in Mexico City, the San Francisco Bay area, and many other locations have clearly shown that local site conditions strongly influence peak acceleration amplitudes and the amplitudes and shapes of response spectra.

Comparisons of peak acceleration attenuation relationships for sites underlain by different types of soil profiles show distinct trends in amplification behavior (Seed et al., 1976). Although attenuation data are scattered, overall trends suggest that peak accelerations at the surfaces of soil deposits are slightly greater than on rock when peak accelerations are small and somewhat smaller at higher acceleration levels (Figure 8.10). Based on data from Mexico

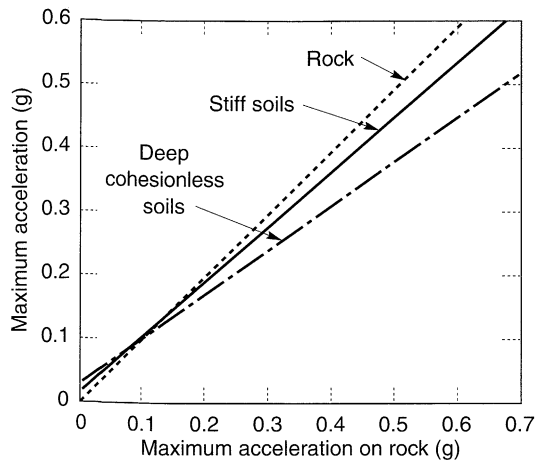


Figure 8.10 Approximate relationships between peak accelerations on rock and other local site conditions. (After Seed et al., 1976.)

City and the San Francisco Bay area, and on additional ground response analyses, Idriss (1990) related peak accelerations on soft soil sites to those on rock sites (Figure 8.11). At low to moderate acceleration levels (less than about $0.4g$), peak accelerations at soft sites are likely to be greater than on rock sites. In some cases, such as Mexico City in 1985 and the San Francisco Bay area in 1989, relatively small rock accelerations may cause high accelerations at the surfaces of soft soil deposits. At higher acceleration levels, however, the low stiffness and nonlinearity of soft soils often prevent them from developing peak accelerations as large as those observed on rock.

Local site conditions also influence the frequency content of surface motions and hence the response spectra they produce. Seed et al. (1976) computed response spectra from ground motions recorded at sites underlain by four categories of site conditions: rock sites, stiff soil sites (less than 200 ft (61 m) deep), deep cohesionless soil sites (greater than 250 ft (76 m) deep), and sites underlain by soft to medium-stiff clay deposits. Normalizing the computed spectra (by dividing spectral accelerations by the peak ground acceleration) illustrates

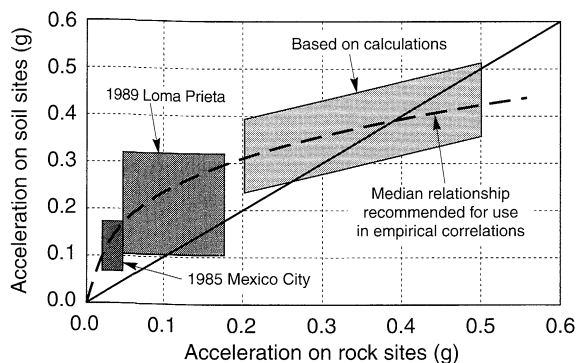


Figure 8.11 Approximate relationship between peak accelerations on rock and soft soil sites. (After Idriss, 1990, *H. Bolton Seed Memorial Symposium Proceedings*, Vol. 2, p. 285. Used by permission of BiTech Publishers, Ltd.)

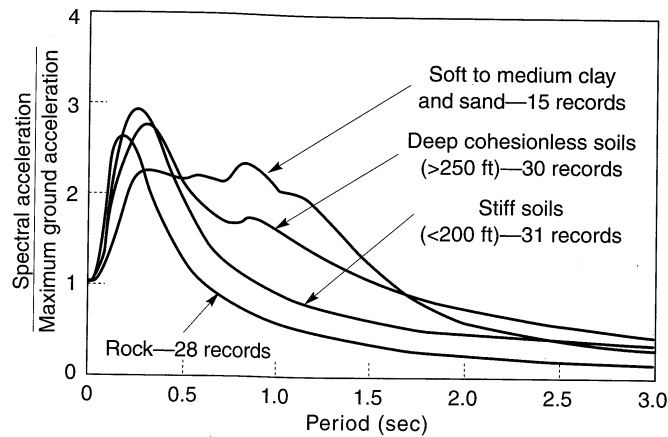


Figure 8.12 Average normalized response spectra (5% damping) for different local site conditions. (After Seed et al., 1976.)

the effects of local soil conditions on the shapes of the spectra (Figure 8.12). The effects are apparent: at periods above about 0.5 sec, spectral amplifications are much higher for soil sites than for rock sites. At longer periods, the spectral amplification increases with decreasing subsurface profile stiffness. Figure 8.12 clearly shows that deep and soft soil deposits produce greater proportions of long-period (low-frequency) motion. This effect can be very significant, particularly when long-period structures such as bridges and tall buildings are founded on such deposits. These results also show that the use of a single response spectrum shape for all site conditions is not appropriate, a finding that has strongly influenced the development of building codes and standards (Section 8.4.2).

8.2.5 Effects of Surface Topography and Basin Geometry

The effects of topographic irregularities and alluvial basin geometry on ground motions can be significant. Perhaps the best known example of apparent topographic effects was produced by an accelerograph on the abutment of Pacoima Dam in southern California. The Pacoima Dam accelerograph recorded peak horizontal accelerations of about 1.25g in each of two perpendicular directions in the 1971 San Fernando ($M_L = 6.4$) earthquake, values that were considerably larger than expected for an earthquake of this magnitude. The accelerograph, however, was located at the crest of a narrow, rocky ridge adjacent to the dam (Trifunac and Hudson, 1971). Subsequent investigations have attributed a good part of the unusually high peak accelerations to dynamic response of the ridge itself—a topographic effect. In the cases where alluvial valleys have been filled with soft soils, one-dimensional ground response analyses are often able to capture most essential aspects of response. They may not, however, be able to describe the complex wave fields and long durations produced by multiple reflections in some of these basins. The effects of surface topography and basin geometry are illustrated in the following sections.

8.2.5.1 Topography

The topographic effects caused by simple irregularities can be estimated from exact solutions to idealized problems (Aki, 1988). For a triangular infinite wedge subjected to vertically propagating SH-waves (with particle motion parallel to its axis), apex displacements are amplified by a factor $2\pi/\phi$, where ϕ is the vertex angle of the wedge (Figure 8.13a). This approach can be used to approximate topographic effects for certain cases of ridge-valley terrain (Figure 8.13b). Different geometries and different wave fields have also been considered (e.g., Geli et al., 1988; Sanchez-Sesma, 1990; Faccioli, 1991).

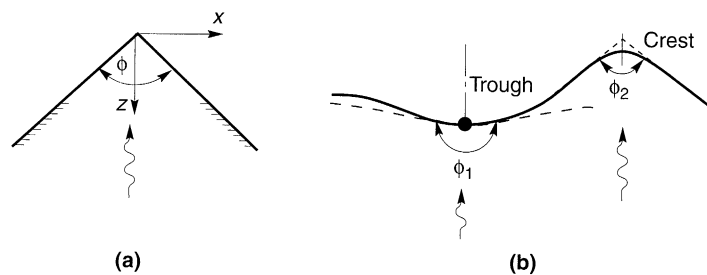


Figure 8.13 Characterization of simple topographic irregularities: (a) notation for a triangular wedge; (b) approximation of actual ground surface (solid line) at trough and crest by wedges. (After Faccioli, 1991.)

Increased amplification near the crest of a ridge was measured in five earthquakes in Matsuzaki, Japan (Jibson, 1987). Figure 8.14 shows how the normalized peak acceleration varied at different points along the ridge. The average peak crest acceleration was about 2.5 times the average base acceleration. Similar patterns of amplification on ridges are suggested

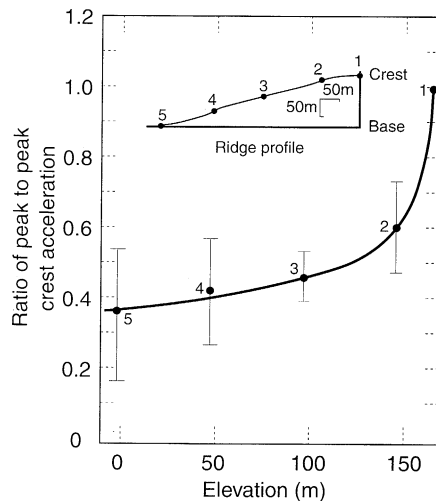


Figure 8.14 Normalized peak accelerations (means and error bars) recorded on mountain ridge at Matsuzaki, Japan. (After Jibson, 1987.)

by damage patterns in earthquakes in Italy and Chile (Finn, 1991). Analysis of topographic irregularities is a complicated problem; the interaction of waves can produce complex patterns of amplification and deamplification, depending on the geometry of the irregularity and on the types, frequencies, and angles of incidence of the incoming waves (Sanchez-Sesma and Campillo, 1993).

8.2.5.2 Basins

Since many large cities are located on or near alluvial valleys, the effects of basin geometry on ground motion is of great interest in geotechnical earthquake engineering. The curvature of a basin in which softer alluvial soils have been deposited can trap body waves and cause some incident body waves to propagate through the alluvium as surface waves (Vidale and Helmberger, 1988). These waves can produce stronger shaking and longer durations than would be predicted by one-dimensional analyses that consider only vertically propagating s-waves.

King and Tucker (1984) measured ground motions along transverse and longitudinal profiles across the Chusal Valley near the Afghanistan border of the former Soviet Union. Interpretation of the response in a series of small ($M_L \leq 4.0$) earthquakes suggested that one-dimensional ground response analyses could predict the average response of sediments near the center of the valley but not at the edges. Significant differences between the amplification functions at the center and edges of the valley were observed, explaining why the motions at those locations were considerably different. Similar effects have been observed for other valleys (e.g., Caracas in 1967, San Fernando in 1971, and Leninakan, Armenia in 1988) in different earthquakes.

Bard and Gariel (1986) used an analytical approach to study the two-dimensional response of shallow and deep alluvial valleys. By comparing computed amplification functions for the two-dimensional case with those based on the assumption of one-dimensional wave propagation, the accuracy of the one-dimensional assumption could be demonstrated. As shown in Figure 8.15a, the one- and two-dimensional amplification functions at the center of a shallow, flat valley (Station 8) were quite similar, which indicates that one-dimensional analyses would be appropriate in that area. Closer to the edge of the valley (Station 4), however, the amplification functions were considerably different. For the deep valley shown in Figure 8.15b, agreement between the one- and two-dimensional amplification functions was much better at the center of the valley than near the edges, but was not as good as for the shallow valley. For alluvial valleys of irregular shape, such combined concave/convex regions, theoretical studies (e.g., Rial et al., 1992) indicate that very complex, even chaotic, motions can result.

The potential for significant differential motion across such alluvial valleys has important implications for the design of long-span structures, such as bridges and pipelines, that often cross valleys. Differential movements can induce large loads and cause heavy damage to these types of structures.

8.2.5.3 Evaluation of Effects

Evaluation of the effects of topographic and subsurface irregularities requires two- and in some cases, three-dimensional analyses. Such analyses are often complicated and time consuming and may require more detailed site characterization than may be feasible.

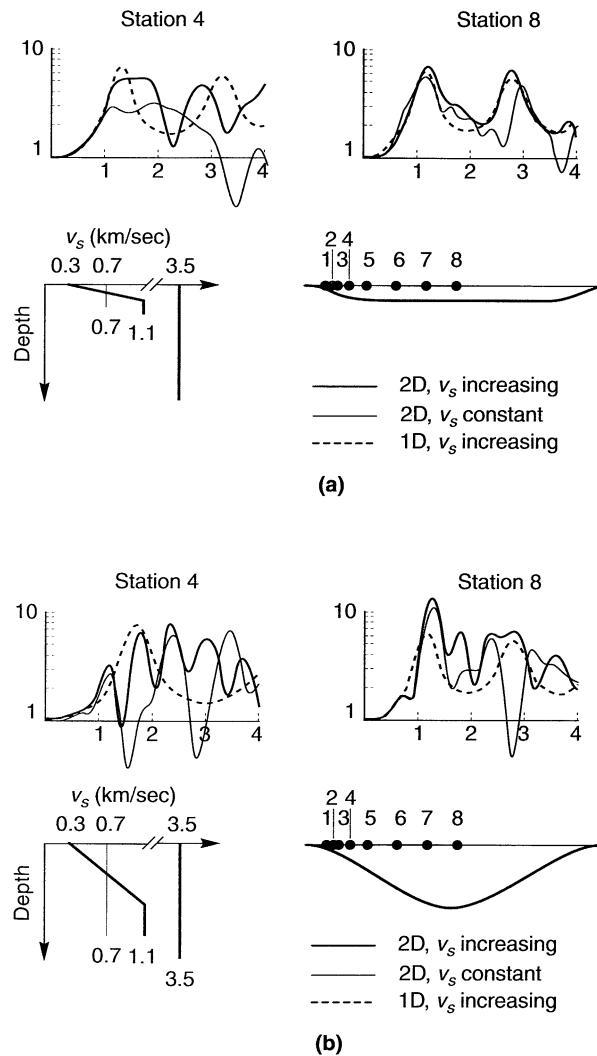


Figure 8.15 Comparison of amplification factors for one- and two-dimensional analyses of (a) shallow, flat basin, and (b) deep basin. (After Bard and Gariel, 1986. Used by permission of the Seismological Society of America.)

Although they may be difficult to predict, there is little doubt that such effects exist. Silva (1988) summarized the effects of topographic and subsurface irregularities, with comments on their quantitative predictability, as shown in Table 8-1.

Although provisions for considering topographic effects have been incorporated into a French building code (French Association for Earthquake Engineering, 1990), participants in a recent site effects workshop (Whitman, 1992) considered the introduction of such provisions into U.S. codes to be premature.

Table 8-1 Effects of Topographic and Subsurface Irregularities

Structure	Conditions	Type	Size	Quantitative Predictability
Surface topography	Sensitive to shape ratio, largest for ratio between 0.2 and 0.6; most pronounced when $\lambda \approx$ mountain width	Amplification at top of structure, amplification and deamplification at base, rapid changes in amplitude phase along slopes	Ranges up to a factor of 30 but generally from about 2 to 10	Poor: generally underpredict size; may be due to ridge-ridge interaction and three-dimensional effects
Sediment-filled valleys	Local changes in shallow sediment thickness	Increased duration	Duration of significant motions can be doubled	Fair
	Generation of long-period surface waves from body waves at shallow incidence angles	Increased amplification and duration due to trapped surface waves	Duration and amplification of significant motions may be increased over one-dimensional projections	Good at periods exceeding 1 sec
Shallow and wide (depth/width < 0.25) sediment-filled valleys	Effects most pronounced near edges; largely vertically propagating shear waves away from edges	Broadband amplification near edges due to generation of surface waves	One-dimensional models may underpredict at higher frequencies by about 2 near edges	Good: away from edges one dimension works well, near edges extend one dimension to higher frequencies
Deep and narrow (depth/width > 0.25) sediment-filled valleys	Effects throughout valley width	Broadband amplification across valley due to whole valley modes	One-dimensional models may underpredict for a wide bandwidth by about 2 to 4; resonant frequencies shifted from one dimension	Fair: given detailed description of vertical and lateral changes in material properties

Source: After Silva (1988).

8.3 DESIGN PARAMETERS

Earthquake-resistant design of new structures and evaluation of the safety of existing structures requires analysis of their response to earthquake shaking. Evaluation of geotechnical hazards, such as liquefaction and slope failure, also requires analysis with respect to some level of shaking. The level of shaking for which satisfactory performance is expected is often referred to as a *design level* of shaking and is described by a *design ground motion*. Design ground motions can, depending on how they are to be used, be specified in many different ways. Many analyses of soil and structural response require an entire time history of motion; others require only one or more of the ground motion parameters described in Chapter 3. The parameters most commonly used to specify design ground motions are peak horizontal acceleration, peak horizontal velocity, predominant period, response spectrum ordinates, and duration.

8.3.1 Design Earthquakes

Historically, design parameters were most commonly determined from a specified *design earthquake*, and some regulatory agencies still require that earthquake-resistant design be performed with respect to the motion produced by a design earthquake. The specification of a design earthquake implies a level of determinism in the seismic hazard analysis; that is, after the design earthquake is characterized (which can be done deterministically or probabilistically), its effects at the site of interest are computed deterministically. Historically, design earthquakes have been associated with *two-level design*, in which a structure or facility is required both to remain operational at one level of motion, and to avoid catastrophic failure at another, more severe level.

Many different terms have been used to describe the levels of severity associated with design earthquakes; some of them have been defined differently by different organizations. The Maximum Credible Earthquake (MCE) is usually defined as the largest earthquake that can reasonably be expected (although the meaning of the word *reasonably* may be open to interpretation) from a particular source. The Safe Shutdown Earthquake (SSE), used in the design of nuclear power plants, is specifically defined (Christian, 1988) as the earthquake that produces the maximum peak horizontal acceleration for the following cases: (1) moving the epicenter of the largest anticipated event in the surrounding seismotectonic province (region of uniform seismicity) to the site, (2) moving the epicenters of the largest events in the adjacent seismotectonic provinces to the nearest points on their boundaries and attenuating their motions to the site, and (3) moving the foci of the largest events on any capable faults to the closest points on the faults to the site and then attenuating their motions to the site. In many geographic regions, the MCE and SSE have similar characteristics. Other terms that have been used to describe similar worst-case levels of shaking include Maximum Capable Earthquake, Maximum Design Earthquake, Contingency Level Earthquake, Safety Level Earthquake, Credible Design Earthquake, and Contingency Design Earthquake. The two-level design approach generally requires that structures of facilities be designed to avoid catastrophic failure at the levels of shaking produced by these upper-level design earthquakes.

A lower but more likely level of shaking would be produced by an Operating Basis Earthquake (OBE); it is an earthquake that should be expected during the life of a structure (Krinitsky et al., 1993). The OBE has been taken as an earthquake with half the peak acceleration of the SSE (Christian, 1988), as an earthquake that produces motion with a 50% probability of exceedance in 50 years (USCOLD, 1985), and as an earthquake with a return period of about 110 years (Christian et al., 1978). Other terms that have been used to describe design earthquakes of similar size are Operating Level Earthquake, Maximum Probable Earthquake, Probable Design Earthquake, and Strength Level Earthquake. Two-level design requires that structures and facilities be designed to remain operational after being subjected to the levels of shaking associated with these lower-level design earthquakes.

Design earthquakes are often specified without regard to their likelihood of occurrence, even though a MCE may have a return period of 200 years in one location and 10,000 years in another. Their use in the development of design ground motions has decreased as probabilistic seismic hazard analysis techniques have developed. Still, some believe (e.g., Krinitsky et al., 1993) that the assumptions of the probabilistic approach are insufficiently supported by observational data to allow its reliable use for critical structures and facilities. This lack of data is particularly significant for large earthquakes.

8.3.2 Design Spectra

Response spectra are often used to represent seismic loading for the dynamic analysis of structures. As a result, design ground motions are often expressed in terms of *design spectra*. Design spectra and the response spectra of actual earthquakes are not the same. Response spectra from earthquakes are highly irregular (e.g., Figure 3.16); their shapes reflect the details of their specific frequency contents and phasing. Design spectra, on the other hand, are generally quite smooth; they are usually determined by smoothing, averaging, or enveloping the response spectra of multiple motions. The use of smooth design response spectra implicitly recognizes the uncertainty with which soil and structural properties are known by avoiding sharp fluctuations in spectral accelerations with small changes in structural period.

Newmark and Hall (1973), for example, recommended that design response spectra be developed from a series of straight lines on a tripartite plot (Section A.2.2 of Appendix A) corresponding to the acceleration-, velocity-, and displacement-controlled portions (Section 3.3.2.1) of the spectrum. A Newmark–Hall design spectrum is obtained by multiplying the peak ground acceleration, velocity, and displacement values by the factors shown in Table 8-2. At periods below about 0.17 sec (frequencies above about 6 Hz), the spectral accelerations are tapered down to the peak ground acceleration. A peak ground velocity of 48 in./sec (122 cm/sec) and peak ground displacement of 36 in. (91 cm) are assumed to be consistent with a peak ground acceleration of 1.0g; each of these parameters can be scaled by the ratio of the design peak ground acceleration to 1.0g to produce a design spectrum.

Table 8-2 Amplification factors for Newmark–Hall Design Spectra

Structural Damping Ratio	Amplification Factors for:		
	Displacement	Velocity	Acceleration
0	2.5	4.0	6.4
2	1.8	2.8	4.3
5	1.4	1.9	2.6
10	1.1	1.3	1.5
20	1.0	1.1	1.2

Source: After Newmark and Hall (1973).

Example 8.2

Develop a Newmark–Hall design spectrum for 5% damping and a peak ground acceleration of 0.25g.

Solution For 5% damping, the acceleration, velocity, and displacement amplification factors are 2.6, 1.9, and 1.4, respectively. Consequently, the peak spectral values are:

$$\text{Spectral acceleration: } S_a = 2.6(0.25g) = 0.65g$$

$$\text{Spectral velocity: } S_v = 1.9 \frac{0.25g}{1.00g} (48 \text{ in./sec}) = 22.8 \text{ in./sec}$$

$$\text{Spectral displacement: } S_d = 1.4 \frac{0.25g}{1.00g} (36 \text{ in.}) = 12.6 \text{ in.}$$

A tripartite plot of the resulting design spectrum is shown in Figure E8.2.

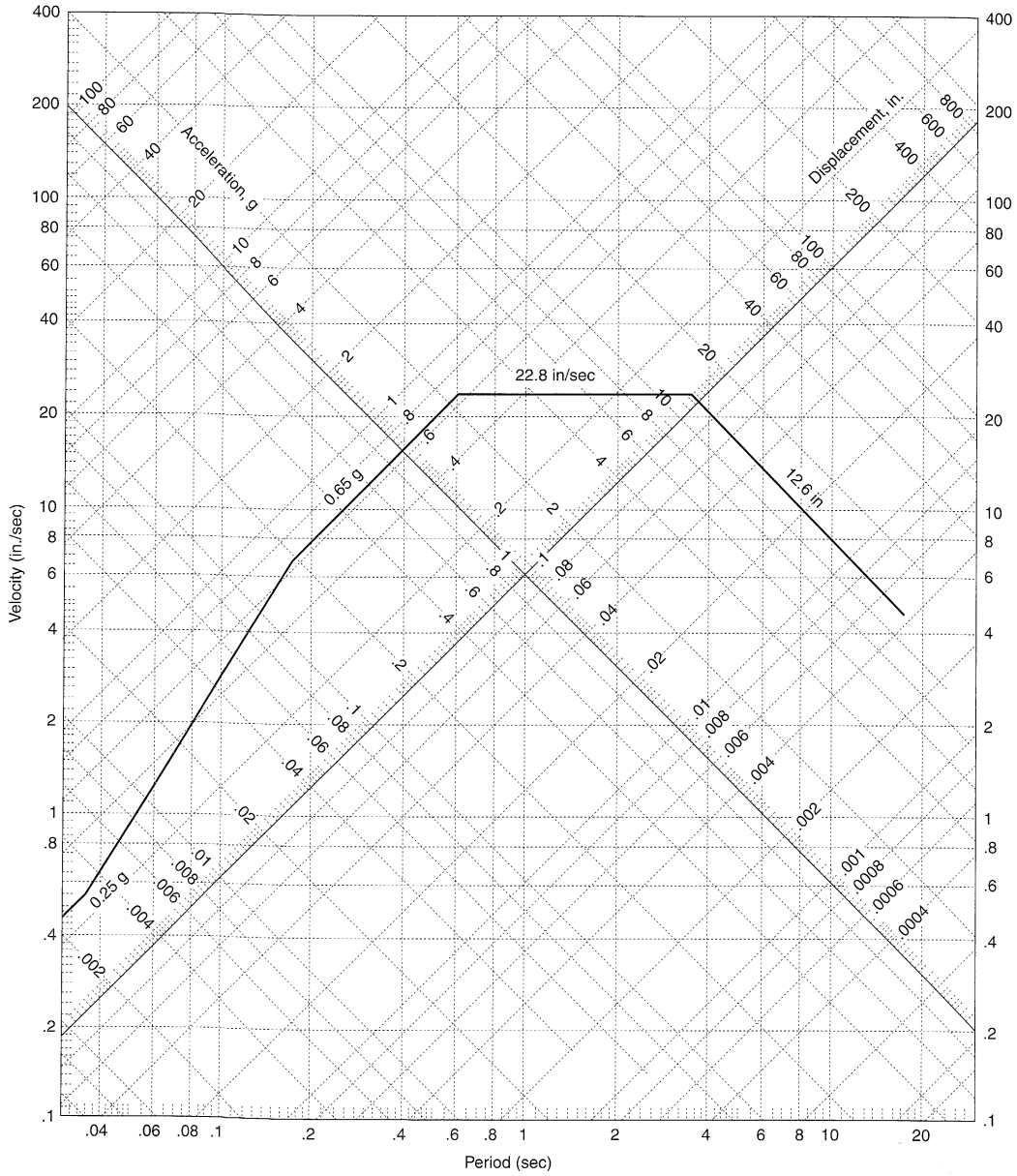


Figure E8.2

For sites that could be subjected to shaking from more than one seismic source, development of a design spectrum can be complicated. A site in California, for example, may be subjected to strong short-period (high-frequency) motion from small earthquakes on nearby faults and strong long-period (low-frequency) motion from large earthquakes on more distant faults. The development of predictive relationships for the ordinates of response spectra

(Section 3.4.4.4) have allowed *uniform risk spectra* (e.g., Trifunac et al., 1987), in which spectral ordinates are obtained by individual PSHAs, to be generated with proper consideration of all seismic sources. With this approach, the design spectrum has an equal probability of exceedance at all periods of vibration. Because of the averaging procedures inherent in the attenuation relationships on which they are based, uniform risk spectra have smooth shapes that are unlike the response spectra from individual ground motions.

8.4 DEVELOPMENT OF DESIGN PARAMETERS

The characteristics of the design ground motion at a particular site are influenced by the location of the site relative to potential seismic sources, the seismicity of those sources, the nature of rupture at the source, travel path effects between the source and the site, local site effects, and the importance of the structure or facility for which the ground motion is to be used. The manner in which the motion is to be used should also be considered.

Design ground motions are usually developed in one of two ways: from site-specific analyses or from the provisions of building codes and standards.

8.4.1 Site-Specific Development

Site-specific design ground motions reflect the detailed effects of the particular subsurface conditions at the sites of interest. The usual process for developing site-specific ground motions involves a seismic hazard analysis and a ground response analysis. The seismic hazard analysis can be performed deterministically or probabilistically using the techniques described in Chapter 4. The use of probabilistic seismic hazard analyses requires that the design motion be associated with some level of risk, or return period. Selection of such a quantity can be quite complex; various social, economic, and political considerations are often involved. For many structures and facilities in the United States, design ground motions have been based on parameters with a 10% probability of exceedance in 50 years (or a 475-year return period). The requirements of most contemporary building codes, for example, are based on that level of risk though some experts believe that higher return periods would be more appropriate (Matthiesen et al., 1982; Whitman, 1989). Different regulatory agencies may require different return periods for different types of structures and facilities.

The seismic hazard analysis will produce a set of ground motion parameters that may, or may not, correspond to the subsurface conditions at the site of interest. Both deterministic and probabilistic seismic hazard analyses utilize predictive relationships (Section 3.4) that usually correspond to a fairly narrow range of subsurface conditions; if the site of interest is located on a similar profile, these parameters may be taken directly as the *design ground motion parameters*. If it is not, however, the parameters from the seismic hazard analysis must be modified to account for the effects of local site conditions.

This parameter modification process may be performed empirically, using prior observations such as those shown in Figures 8.12 and 8.13, or analytically. In the analytical approach, both deconvolution (Section 7.1.1.4) and conventional ground response analyses may be required, as illustrated in Figure 8.16. The seismic hazard analysis will produce parameters that describe a ground motion at the surface (point A) of a site with subsurface

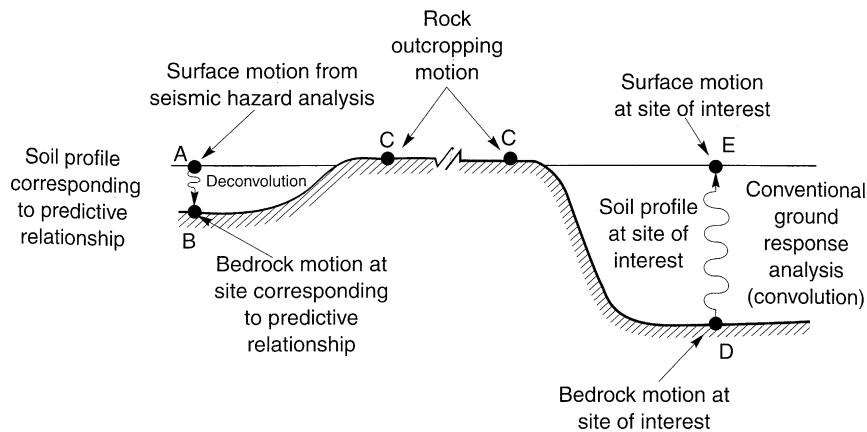


Figure 8.16 Procedure for modifying ground motion parameters from a seismic hazard analysis to account for the effects of local site conditions.

conditions that corresponds to those of the sites in the database from which the predictive relationship was developed. To determine the corresponding parameters at the surface of the site of interest, a time history of ground surface motion that is consistent with the predicted parameters is generated; procedures for generating such time histories are described in Section 8.5. This motion is then deconvolved through a soil profile corresponding to the predictive relationship to determine the time history of bedrock motion (at point *B*) that would produce the time history of motion at point *A*. The corresponding rock at cropping motion produces the bedrock motion applied at the base (point *D*) of the soil profile at the site of interest. A conventional ground response analysis is then performed to predict the motion at the surface of the soil profile of interest (point *E*). This motion, which is consistent with the results of the seismic hazard analysis and also with the local site conditions, can be taken as the design ground motion. It can be used to compute site-specific design parameters such as peak acceleration and velocity, response spectral ordinates, and duration.

8.4.2 Code-Based Development

Alternatively, design ground motions can be developed on the basis of building code provisions. Consideration of earthquake and other effects in the design of new structures is mandated by modern building codes which may be adopted as law by various city, county, and state governments. The purpose of codes such as the *Uniform Building Code* (UBC) is "to provide minimum standards to safeguard life or limb, health, property, and public welfare by regulating and controlling the design, construction, quality of materials, use and occupancy, location and maintenance of buildings" (ICBO, 1991). Codes for highway bridges, nuclear power plants, and other types of structures have been produced by various regulatory agencies.

The provisions of building codes are developed by consensus of a broad group of experienced practitioners and researchers. Although contemporary codes do consider site effects, they usually do so by lumping groups of similar soil profiles together so that their provisions apply to broad ranges of soil conditions within which the local conditions of a particular site are expected to fall. Because of this, design ground motions developed from

code provisions are usually more conservative (i.e., correspond to stronger levels of shaking) than those developed from site-specific analyses. This relationship between site-specific and code-based design ground motions provides an economic incentive that implicitly encourages the development of site-specific design ground motions.

8.4.2.1 Background

The first building code, motivated primarily by insurance losses due to fire, was published in 1905. In 1927, the first edition of the *UBC* was published by what is now the International Conference of Building Officials. The *UBC* has become widely adopted, particularly in the western United States, where seismic hazards are high. As a result, the *UBC* has been near the forefront of activity on issues relating to earthquake-resistant design. In the United States, the Building Officials and Code Administrators International (BOCA) Code, Standard Building Code (SBC), and National Building Code (NBC) are frequently used in the midwest, south, and northeast, respectively.

Historically, building code provisions relating to earthquake safety have developed incrementally, with each increment occurring shortly after the occurrence of a damaging earthquake in the United States. Although building codes go back as far as about 2100 B.C. (Berg, 1983), explicit provisions for earthquake resistance did not appear in U.S. building codes until after the 1925 Santa Barbara earthquake ($M_L = 6.3$). Those provisions, however, were listed only in an appendix and were not mandatory. After the 1933 Long Beach, California earthquake ($M_L = 6.3$), in which the potentially tragic consequences of the collapse of many school buildings were averted by the earthquake's occurrence after school hours, the state of California passed a bill known as the Field Act, which required that all new school construction be designed for higher levels of earthquake resistance and that school construction be closely supervised in the field. Shortly thereafter, California also passed the Riley Act, which established mandatory design requirements for nearly all occupied buildings in the state.

In 1959, the Structural Engineers Association of California (SEAOC) published a document titled *Recommended Lateral Force Requirements and Tentative Commentary*, more commonly known as the *SEAOC Blue Book*, whose provisions were incorporated into the 1961 *UBC*. Since then the Blue Book has been modified about every three years with its revised provisions adopted first by the ICBO in the *UBC* and then by the other major regional codes. These codes developed in an incremental, evolutionary manner as new research and experience was gained. The provisions of the *UBC*, for example, have historically been based on those of the *SEAOC Blue Book* (e.g., SEAOC, 1990). In 1975 the Applied Technology Council began, with support from the National Science Foundation and the National Bureau of Standards (now the National Institute for Standards and Technology), to take a fresh look at all aspects of earthquake-resistant design, with the aim of developing code provisions that could be adopted nationwide. In 1978, ATC published a report titled *Tentative Provisions for the Development of Seismic Regulations for Buildings* (ATC, 1978), popularly known as *ATC 3-06*. This document included many innovations, including several relating to the treatment of local site effects and development of design ground motions. Years later, many of the provisions of *ATC 3-06* were incorporated into the NEHRP (National Earthquake Hazards Reduction Program) *Recommended Provisions for the Development of Seismic Regulations for New Buildings* produced by the Building Seismic Safety Council (BSSC, 1991a, b).

The *UBC* and *NEHRP Provisions* are the most influential contemporary documents that describe minimum standards for earthquake-resistant design of buildings in the United States. Although codes and provisions change with time, both the *UBC* and *NEHRP Provisions* address the issue of local site conditions and present commonly used approaches to the development of design ground motions. The following sections describe the manner in which local site effects and design ground motions are specified in the most recent (1994) versions of the *UBC* and *NEHRP Provisions*. These descriptions are intended only to illustrate the philosophies and basic approaches of the documents; they are not complete.

8.4.2.2 Uniform Building Code

Building codes are not intended to eliminate earthquake damage completely. Indeed, the commentary to the 1990 *SEAOC Blue Book*, upon which the 1991 *UBC* is based, says that “structures designed in conformance [with the *Blue Book* recommendations] should, in general, be able to: (1) resist a minor level of earthquake ground motion without damage; (2) resist a moderate level of earthquake ground motions without structural damage, but possibly experience some nonstructural damage; (3) resist a major level of earthquake ground motion having an intensity equal to the strongest either experienced or forecast for the building site, without collapse, but possibly with some structural as well as nonstructural damage” (SEAOC, 1990). These expectations illustrate the basic philosophy of earthquake-resistant structural design, as the commentary goes on to state that it “would in most cases be economically prohibitive to design buildings to remain elastic for all levels of earthquake ground motions. A fundamental tenet of seismic design is that inelastic yielding is allowed to accommodate seismic loadings as long as such yielding does not impair the vertical load capacity of the structure. In other words, damage is allowed in the maximum expected earthquake loading case only if it does not pose a significant probability of the structure’s collapse.”

The *UBC* allows two basic approaches to the earthquake-resistant design of buildings: a static approach in which the effects of ground motions are represented by static lateral forces, and a dynamic approach in which ground motion is characterized by a design response spectrum. The simpler static approach is allowed only for certain conditions of geometric regularity, occupancy, and height.

Static Approach. The static approach is based on determination of a *design base shear* force, which is then distributed in a specified pattern over the height of the structure for structural analysis of lateral load resistance. The total design base shear in a given direction (the structure must be able to resist it in any direction) is given by

$$V = \frac{ZIC}{R_w} W \quad (8.1)$$

where Z is a *seismic zone factor* (Figure 8.17), I is an *importance factor* (Table 8-3), R_w is a numerical coefficient that reflects the ductility of the structure (Table 8-4), W is the *seismic dead load* (which includes permanent equipment and portions of live loads, partition loads, and snow loads), and

$$C = \frac{1.25S}{T^{2/3}} \quad (8.2)$$

In equation (8.2), S is a soil coefficient (Table 8-5) and T is the fundamental period of the structure in seconds. The value of C need not exceed 2.75, and the minimum value of C/R_w ,



Figure 8.17 Map and table for evaluation of UBC seismic zone factor, Z (Reproduced from the 1994 edition of the *Uniform Building Code*™, copyright © 1994, with permission of the publisher, the International Conference of Building Officials.)

Table 8-3 UBC Importance Factor, *I*.

Occupancy Category	<i>I</i>
Essential Facilities ^a	1.25
Hazardous Facilities ^b	1.25
Special Occupancy Structures ^c	1.00
Standard Occupancy Structures ^d	1.00
Miscellaneous Structures ^e	1.00

^a Includes hospitals and other medical facilities having surgery and emergency treatment areas; fire and police stations; tanks or other structures containing, housing or supporting water or other fire-suppression materials or equipment required for the protection of essential or hazardous facilities, or special occupancy structures; structures and shelters in emergency-preparedness centers; standby power-generating equipment for essential facilities; structures and equipment in government communication centers and other facilities required for emergency response; garages and shelters for emergency vehicles and emergency aircraft; aviation control towers; standby power generating equipment for essential facilities.

^b Includes occupancies and structures therein housing or supporting toxic or explosive chemicals or substances. Nonbuilding structures housing, supporting, or containing quantities of toxic or explosive substances which, if contained in a building, would cause that building to be classified as a hazardous facility.

^c Occupancies with a capacity > 300 persons; buildings for schools through secondary or day-care centers - capacity > 250 students; occupancies used for colleges or adult education schools - capacity > 500 students; medical facilities with 50 or more resident incapacitated patients, but not included above; jails and detention facilities, all structures with occupancy > 5,000 persons; structures and equipment in power-generating stations and other public utility facilities not included above, and required for continued operation.

^d All structures having occupancies or functions not listed above, and occupancy towers.

^e Group U occupancies except for towers.

under most conditions, is set at 0.075. The fundamental period of the structure can be determined by different methods; in the simplest it is approximated by

$$T = C_t(h_n)^{3/4} \quad (8.3)$$

where C_t has values of 0.035 for steel moment-resisting frames, 0.030 for reinforced concrete moment-resisting frames and eccentrically braced steel frames, and 0.020 for all other structures, and h_n is the height (in feet) of the uppermost level of the main portion of the structure above the base.

Dynamic Approach. The dynamic approach of the *UBC* allows the response of the structure to be determined by response spectrum analysis or by time-history analysis. Hence design ground motions can be specified in terms of design response spectra or design ground motion time histories. In both cases, the *UBC* requires that the design ground motion correspond to a 10% probability of exceedance in a 50-year period (475-year return period).

Design response spectra can be determined in one of two ways: from site-specific ground response analyses of the type described in Section 8.4.1, or from smooth, normalized spectral shapes (Figure 8.18). The normalized spectral shapes follow from the results of Seed et al. (1976) and Newmark and Hall (1982) (see Figure 8.12), and account for the frequency-dependent amplification of ground motion by different local site conditions. These normalized spectra are presented for three subsurface profiles; as would be expected, greater long-period spectral accelerations are associated with softer and deeper soil profiles.

Table 8-4 Values of UBC reduction factor, R_w

Basic Structural System	Lateral Load Resisting System	R_w	
Bearing Wall System	Light-framed walls with shear panels		
	a. Wood structural panel walls for structures three stories or less	8	
	b. All other light-framed walls	6	
	Shear walls		
	a. Concrete	6	
	b. Masonry	6	
	Light steel-framed bearing walls with tension-only bracing	4	
	Braced frames where bracing carries gravity loads		
	a. Steel	6	
	b. Concrete	4	
	c. Heavy timber	4	
	Building Frame System	Steel eccentrically braced frame	10
		Light-framed walls with shear panels	
a. Wood structural panel walls for structures three stories or less		9	
b. All other light-framed walls		7	
Shear walls			
a. Concrete		8	
b. Masonry		8	
Ordinary braced frames			
a. Steel		8	
b. Concrete		8	
c. Heavy timber		8	
Special concentrically braced frames			
a. Steel		9	
Moment-Resisting Frame System	Special moment-resisting frames (SMRF)		
	a. Steel	12	
	b. Concrete	12	
	Concrete intermediate moment-resisting frames (IMRF)	8	
	Ordinary moment-resisting frames (OMRF)		
	a. Steel	6	
	b. Concrete	5	
Masonry moment-resisting wall frame	9		
Dual Systems	Shear walls		
	a. Concrete with SMRF	12	
	b. Concrete with steel OMRF	6	
	c. Concrete with concrete IMRF	9	
	d. Masonry with SMRF	8	
	e. Masonry with OMRF	6	
	f. Masonry with concrete IMRF	7	
	Steel eccentrically braced frame		
	a. With steel SMRF	12	
	b. With steel OMRF	6	
	Ordinary braced frames		
	a. Steel with steel SMRF	10	
	b. Steel with steel OMRF	6	
	c. Concrete with concrete SMRF	9	
	d. Concrete with concrete IMRF	6	
	Special concentrically braced frames		
	a. Steel with steel SMRF	11	
b. Steel with steel OMRF	6		

Table 8-5 UBC Soil Coefficient, S .

Type	Description	S
S1	A soil profile with either: (a) A rock-like material characterized by a shear wave velocity greater than 2,500 feet per second or by other suitable means of classification, or (b) Medium-dense to dense or medium-stiff to stiff soil condition where the soil depth is less than 200 feet.	1.0
S2	A soil profile with predominantly medium dense to dense or medium-stiff to stiff soil conditions, where the soil depth exceeds 200 feet or more.	1.2
S3	A soil profile containing more than 20 feet of soft to medium stiff clay but not more than 40 feet of soft clay.	1.5
S4	A soil profile containing more than 40 feet of soft clay characterized by a shear wave velocity less than 500 feet per second.	2.0

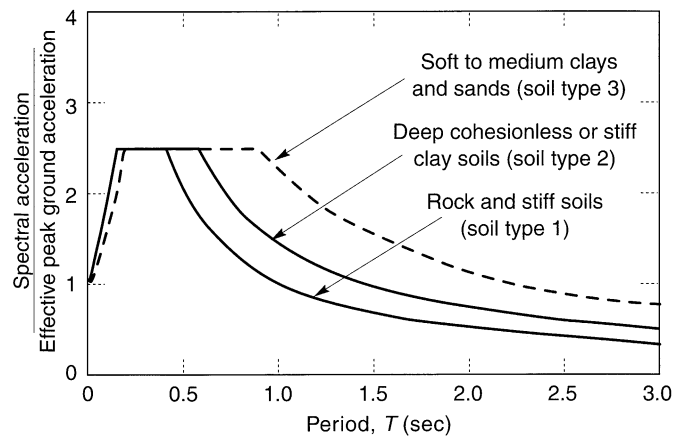


Figure 8.18 Site-dependent normalized response spectra. (Reproduced from the 1994 edition of the *Uniform Building Code*™, copyright © 1994, with permission of the publisher, the International Conference of Building Officials.)

The design response spectrum is obtained by multiplying the ordinates of the normalized spectrum by the effective peak ground acceleration, which can be taken as the value of the seismic zone factor, Z , expressed as a fraction of gravity. Note that the shape of the design spectrum is constant—the spectral ordinates are linearly scaled by the peak acceleration alone. Since important ground motion characteristics such as frequency content and duration are influenced by earthquake magnitude and distance, the probabilities of exceedance of a constant-shape design spectrum may be different at low periods than at high periods. The use of such a design spectrum may produce structural designs with different probabilities of failure. Uniform risk spectra (Section 8.3.2) minimize this possibility.

The *UBC* requires that design ground motion time histories be developed on a site-specific basis. The use of several time histories is recommended. Response spectra computed from the time histories must, either individually or in combination, approximate the site-specific design response spectrum. Site-specific analyses are required for flexible structures (fundamental periods greater than 0.7 seconds) located on soil profile S4.

Other Code Provisions. The UBC also sets forth requirements dealing with site grading, foundations, and retaining structures. In seismic zones 3 and 4, building officials may require that “the potential for soil liquefaction and soil strength loss during earthquakes shall be evaluated during the geotechnical investigation. The geotechnical report shall assess potential consequences of any liquefaction and soil strength loss, including estimation of differential settlement, lateral movement or reduction in foundation soil-bearing capacity, and discuss mitigating measures.” The topic of soil liquefaction is discussed in detail in Chapter 9.

8.4.2.3 NEHRP Provisions

The *NEHRP Provisions* is not a building code; rather, it is a source document intended to aid in the development of building codes in areas of seismic exposure. Their purpose is to “present criteria for the design and construction of buildings and nonbuilding structures subject to earthquake ground motions. Their purposes are to minimize the hazard to life for all buildings and nonbuilding structures, to increase the expected performance of higher occupancy structures as compared to ordinary structures, and to improve the capability of essential facilities to function during and after an earthquake . . . (they provide) the minimum criteria considered to be prudent and economically justified for the protection of life safety in buildings subject to earthquakes at any location in the United States. . . The ‘design’ earthquake ground motion levels specified . . . may result in both structural and non-structural damage. For most structures designed and constructed according to these provisions, it is expected that structural damage from a major earthquake may be repairable but it may not be economical. . . For motions larger than the design levels, the intent of these provisions is that there be a low likelihood of building collapse.” (BSSC, 1991b).

Ground Motion Parameters. The *NEHRP Provisions* use the effective peak acceleration, EPA, and effective peak velocity, EPV (Section 3.3.4), to describe ground motions. These parameters can be thought of as normalizing factors for the development of smooth response spectra; the EPA is proportional to the average spectral acceleration at low periods (0.1 to 0.5 sec) and the EPV is proportional to the spectral velocity at longer periods (about 1 sec). The EPA is usually somewhat lower than the peak acceleration of a specific ground motion and can be substantially lower for ground motions with very high frequencies. The EPV is usually greater than the peak velocity, particularly at large distances from strong earthquakes. To compute various design coefficients, the EPA and EPV are replaced by the dimensionless acceleration coefficients, A_a and A_v . The *effective peak acceleration coefficient*, A_a , is numerically equal to the EPA when expressed as a decimal fraction of gravity (i.e., $A_a = 0.2$ when $EPA = 0.2g$). The *effective peak velocity-related acceleration coefficient*, A_v , is numerically equal to $EPV/30$ when the EPV is expressed in in./sec (i.e., $A_v = 0.2$ when $EPV = 6$ in./sec). Note that A_v is an acceleration coefficient, even though it is obtained from the spectral velocity; it provides a useful measure of the longer-period (lower-frequency) components of a ground motion. At any particular location, the design of a building may be governed by A_a or A_v . The NEHRP provisions contain maps, based on probabilistic seismic hazard analyses with a 10% probability of exceedance in a 50-year period, that divide the United States into seven seismic loading zones (Figure 8.19). The coefficients A_a and A_v can be determined from these maps and Table 8-6.

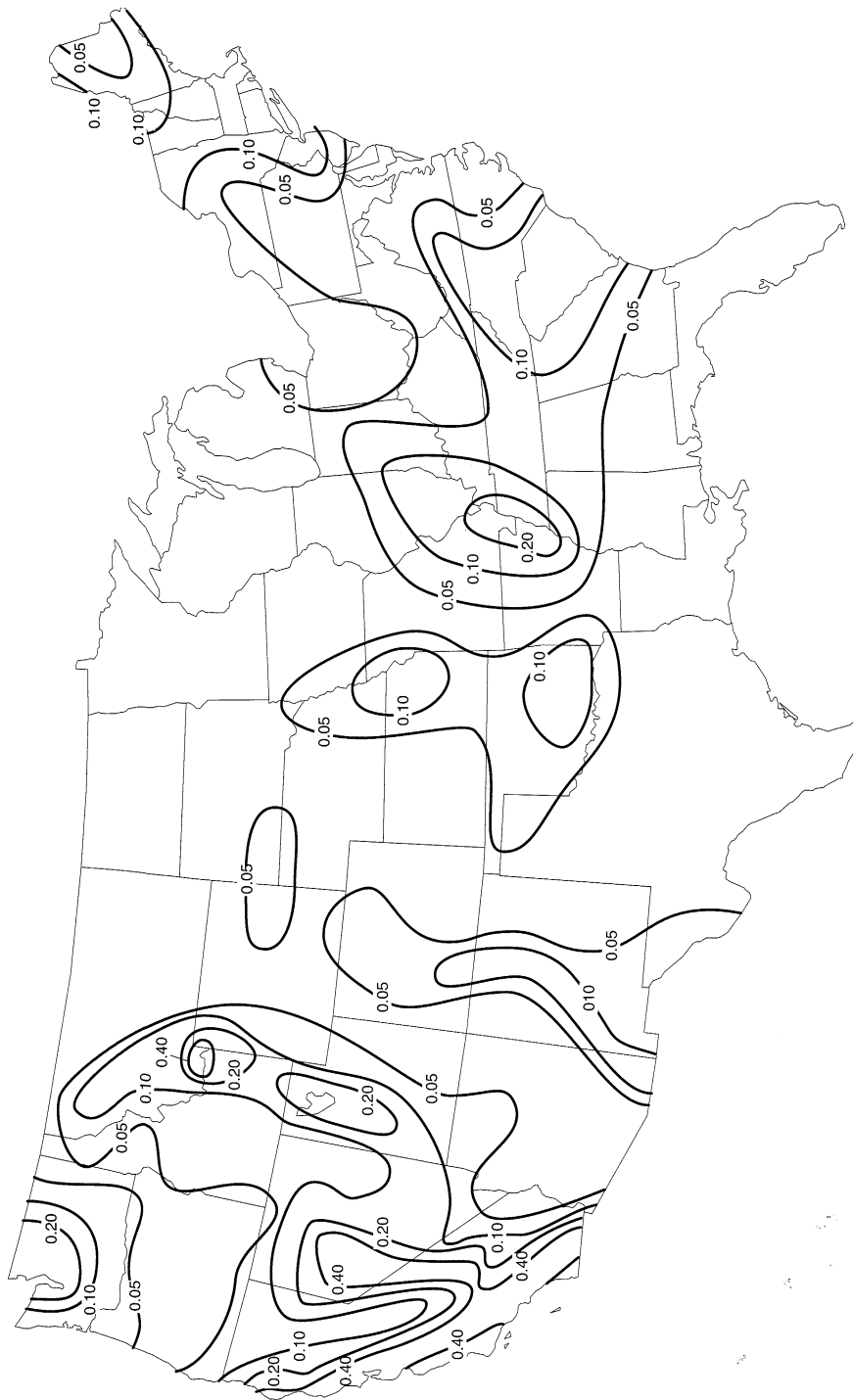


Figure 8.19 Maps of NEHRP seismic loading zones: (a) map 1 for A_{ps} ; and (b) map 2 for A_{ps} . (After BSSC, 1994.)

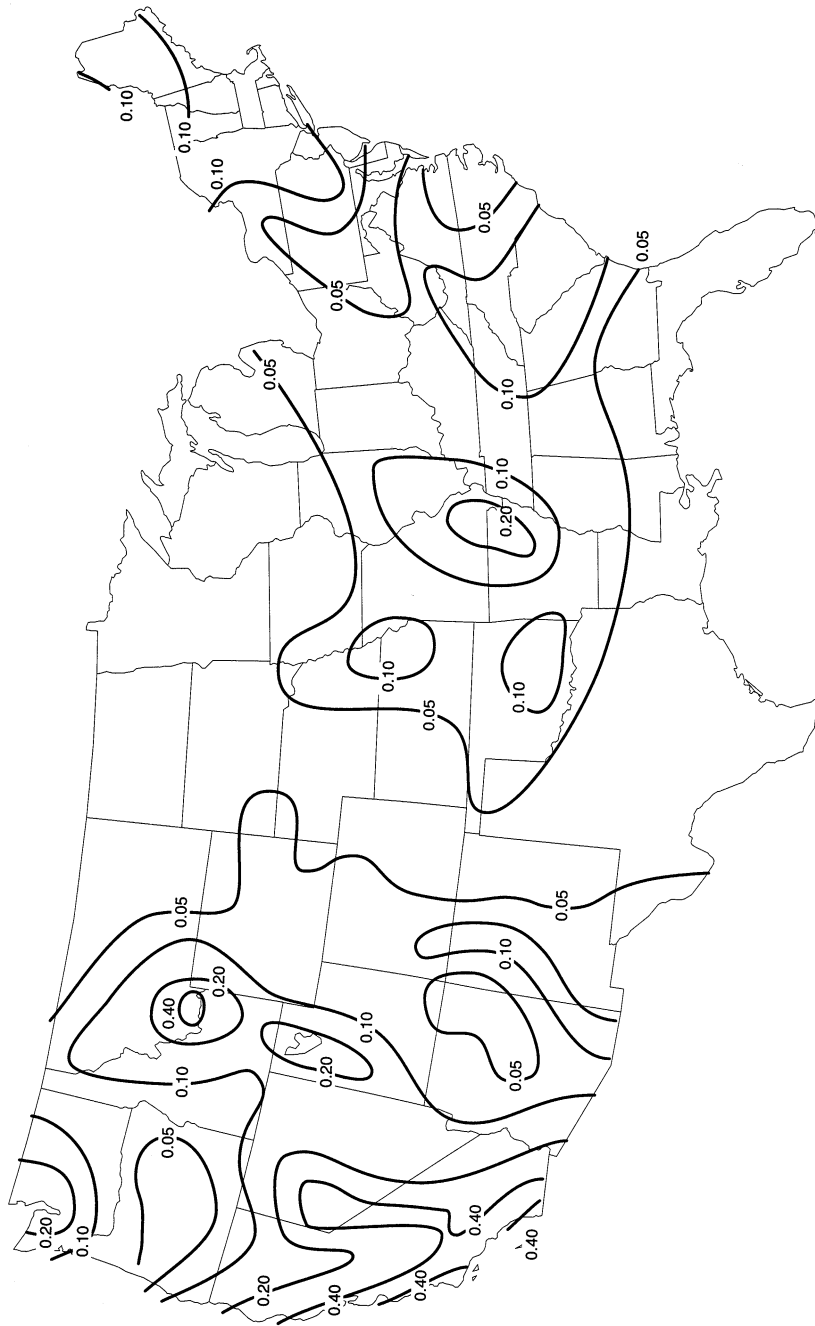


Figure 8.19 (continued)

Table 8-6 NEHRP Coefficients A_a and A_v

Map Area from Map 1 (for A_a) or Map 2 (for A_v)	Value of A_a and A_v
7	0.40
6	0.30
5	0.20
4	0.15
3	0.10
2	0.05
1	< 0.05 ^a

^a For equations or expressions incorporating the terms A_a or A_v , a value of 0.05 shall be used.

Equivalent Lateral Force Procedure. Like the *UBC*, the *NEHRP Provisions* account for local soil conditions in the determination of design loading. The *NEHRP Provisions*, however, address the effects of local soil conditions in greater detail than the *UBC*. The remainder of this section focuses on the differences between this aspect of the *UBC* and *NEHRP Provisions*, as illustrated by their static (or equivalent lateral force) approaches to seismic design.

The equivalent lateral force procedure of the *NEHRP Provisions* requires that the seismic base shear that is proportional to the weight of the structure.

$$V = C_s W \quad (8.4)$$

where W includes the total dead load and applicable portions of other loads (e.g., permanent equipment, partitions, live loads) and the seismic response coefficient, C_s , is the smaller of

$$C_s = \frac{1.2C_v}{RT^{2/3}} \quad (8.5a)$$

or

$$C_s = \frac{2.5C_a}{R} \quad (8.5b)$$

In Equations 8.5, R is a response modification factor (analogous but not identical to the R_w factor in the *UBC*) and T is the fundamental period of the structure. The long-period seismic coefficient, C_v , and the short-period seismic coefficient, C_a , reflect both local soil conditions and site seismicity. These coefficients are defined as

$$C_a = F_a A_a \quad (8.6a)$$

$$C_v = F_v A_v \quad (8.6b)$$

where F_a and F_v depend on soil type and A_a and A_v depend on site seismicity. The effective peak acceleration, A_a , and effective peak velocity-related acceleration, A_v , are obtained from Table 8-6 and Figure 8.20. The site coefficients, F_a and F_v , are shown in Table 8-7.

Table 8-7 Values of F_a and F_v for different site conditions and shaking intensities.

Soil Profile Type	Values of F_a				
	Shaking Intensity				
	$A_a \leq 0.1$	$A_a = 0.2$	$A_a = 0.3$	$A_a = 0.4$	$A_a \geq 0.5$
A	0.8	0.8	0.8	0.8	0.8
B	1.0	1.0	1.0	1.0	1.0
C	1.2	1.2	1.1	1.0	1.0
D	1.6	1.4	1.2	1.1	1.0
E	2.5	1.7	1.2	0.9	SS ¹
F	SS	SS	SS	SS	SS

Soil Profile Type	Values of F_v				
	Shaking Intensity				
	$A_v \leq 0.1$	$A_v = 0.2$	$A_v = 0.3$	$A_v = 0.4$	$A_v \geq 0.5$
A	0.8	0.8	0.8	0.8	0.8
B	1.0	1.0	1.0	1.0	1.0
C	1.7	1.6	1.5	1.4	1.3
D	2.4	2.0	1.8	1.6	1.5
E	3.5	3.2	2.8	2.4	SS ¹
F	SS	SS	SS	SS	SS

¹ Site-specific geotechnical investigation and dynamic site response analyses shall be performed.

Soil Profile Type	Description
A	Hard rock with measured shear wave velocity, $\bar{v}_s > 5000$ ft/sec (1500 m/sec)
B	Rock with 2500 ft/sec $< \bar{v}_s \leq 5000$ ft/sec (760 m/sec $< \bar{v}_s \leq 1500$ m/sec)
C	Very dense soil and soft rock with 1200 ft/sec $< \bar{v}_s \leq 2500$ ft/sec (360 m/sec $< \bar{v}_s \leq 760$ m/sec) or with either $\bar{N} > 50$ or $\bar{s}_u \geq 2000$ psf (100 kPa)
D	Stiff soil with 600 ft/sec $< \bar{v}_s \leq 1200$ ft/sec (180 m/sec $< \bar{v}_s \leq 360$ m/sec) or with either $15 \leq \bar{N} \leq 50$ or 1000 psf $\leq \bar{s}_u \leq 2000$ psf (50 kPa $\leq \bar{s}_u \leq 100$ kPa)
E	A soil profile with $\bar{v}_s < 600$ ft/sec (180 m/sec) or any profile with more than 10 ft (3 m) of soft clay defined as soil with $PI > 20$, $w \geq 40\%$, and $s_u < 500$ psf (25 kPa)
F	Soil requiring site-specific evaluations: <ol style="list-style-type: none"> 1. Soils vulnerable to potential failure or collapse under seismic loading such as liquefiable soils, quick and highly sensitive clays, collapsible weakly cemented soils. 2. Peats and/or highly organic clays ($H > 10$ ft (3 m) of peat and/or highly organic clay where H = thickness of soil) 3. Very high plasticity clays ($H > 25$ ft (8 m) with $PI > 75$) 4. Very thick soft/medium stiff clays ($H > 120$ ft (36 m))

Exception: When the soil properties are not shown in sufficient detail to determine the Soil Profile Type, Type D shall be used. Soil Profile Types E or F need not be assumed unless the regulatory agency determines that Types E or F may be present at the site or in the event that Types E or F are established by the geotechnical data.

8.5 DEVELOPMENT OF GROUND MOTION TIME HISTORIES

On many occasions, ground motion parameters alone do not adequately describe the effects of ground shaking. For analysis of nonlinear problems such as the response of inelastic structures or the permanent deformation of an unstable slope, time histories of motion are required. Time histories can also be required in the development of site-specific design ground motions, as illustrated in Figure 8.19. In these cases, time histories that match *target ground motion parameters* such as peak accelerations, velocities, or spectral ordinates are required.

In some cases, the local and regional geologic and tectonic conditions of the site of interest may be so similar to those of sites where actual strong motions have previously been measured that those strong motion records can be used directly. Usually, this is not the case, and artificial ground motions must be developed. Artificial ground motions can be developed in a number of different ways. The main challenges in their development are to ensure that they are consistent with the target parameters and that they are realistic (i.e., that their characteristics are consistent with those of actual earthquakes). This is not as easy as it might appear; many motions that appear reasonable in the time domain may not when examined in the frequency domain, and vice versa. Many reasonable-looking time histories of acceleration produce, after integration, unreasonable time histories of velocity and/or displacement. The quality of an artificial ground motion is very difficult to discern by eye.

The most commonly used methods for generation of artificial ground motions fall into four main categories: (a) modification of actual ground motion records, (b) generation of artificial motions in the time domain, (c) generation of artificial motions in the frequency domain, and (d) generation of artificial motions using Green's function techniques.

8.5.1 Modification of Actual Ground Motion Records

Perhaps the simplest approach to the generation of artificial ground motions is the modification of actual recorded ground motions. Maximum motion levels, such as peak acceleration and peak velocity, have been used to rescale actual strong motion records to higher or lower levels of shaking (Figure 8.20). Krinitszky and Chang (1979) recommended that the scaling factor (the ratio of the target amplitude to the amplitude of the record being scaled) should be kept as close to 1 as possible, and always between 0.25 and 4.0, and that analyses be conducted with several scaled records. Vanmarcke (1979), noting that simple amplitude scaling fails to account for differences in important characteristics such as frequency content and duration, suggested that limits on the scaling factor should be related to the type of problem to which the resulting motion is to be applied. For analysis of linear elastic structures, the limits of Krinitszky and Chang (1979) were considered suitable, but for liquefaction a scaling factor range of 0.5 to 2.0 was recommended.

This type of rescaling procedure requires careful selection of the actual motion that is to be used. A desirable ground motion record will not only have a peak acceleration or velocity close to the target value, but will have magnitude, distance, and local site characteristics that are similar to those of the target motion. Such a record is most likely to have a similar frequency content and duration to the target motion. Computer programs (e.g., Dussom et al., 1991; Ferritto, 1992) that contain, or at least interact with, strong motion databases are available to aid in the selection of actual ground motions for rescaling.

Rescaling of the time scale has been used to modify the frequency content of an actual ground motion record. This is usually accomplished by multiplying the time step of a digitized

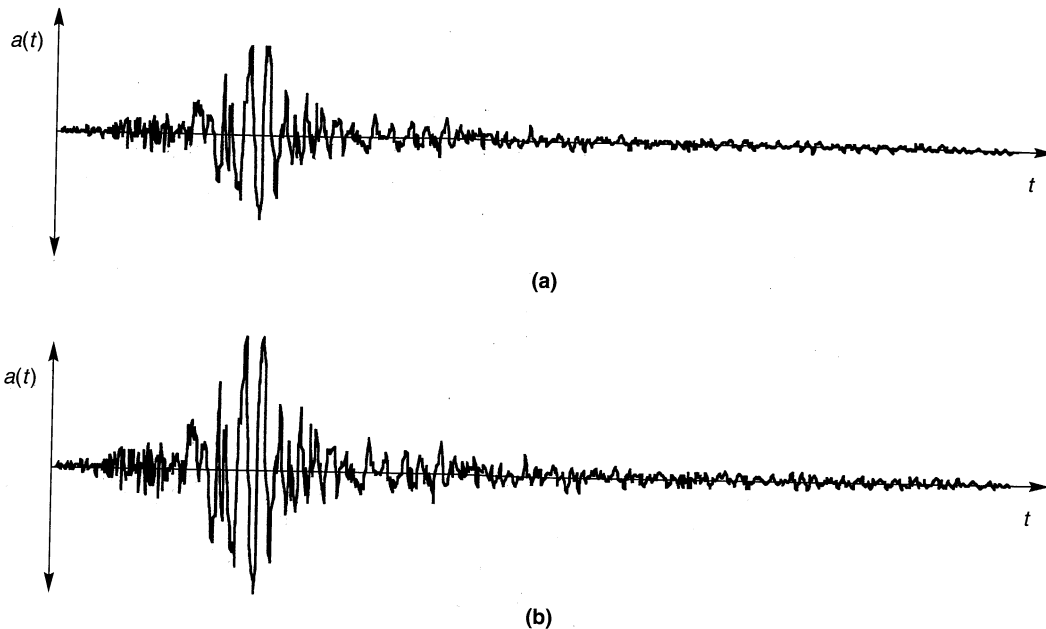


Figure 8.20 (a) Original accelerogram from actual earthquake; (b) rescaled version of original accelerogram in which accelerations were scaled upward by a factor of 1.5 to match target peak acceleration.

actual record by the ratio of the predominant period (Section 3.3.2.2) of the target motion to the predominant period of the actual motion (Figure 8.21). Since this approach changes the frequency content over the entire spectrum as well as the duration of the rescaled record, it should be used carefully to avoid unintended consequences.

To generate artificial ground motions of long duration without significantly changing the frequency content, some (e.g., Seed and Idriss, 1969) have spliced parts of actual ground motion records together. Procedures of this type must also be used with caution. Careful examination of the reasonableness of spliced motions in both the time and frequency domains is advised.

8.5.2 Time-Domain Generation

The resemblance of ground motion time histories to transient stochastic processes was noted years ago (Housner, 1947). Since then, a number of procedures that treat ground motions as stochastic processes have been developed. Many of these operate entirely in the time domain.

A stationary stochastic process is one whose statistics remain constant with time. A stationary accelerogram, for example, would have a constant mean acceleration, constant standard deviation of acceleration, and a constant frequency content—the accelerations would continue indefinitely. The fact that the acceleration amplitude of actual ground motions varies with time (ground motions have a beginning and an end, after all) renders their amplitudes nonstationary. Studies have also shown that the frequency content of a typical ground motion is also nonstationary—it changes over the duration of shaking.

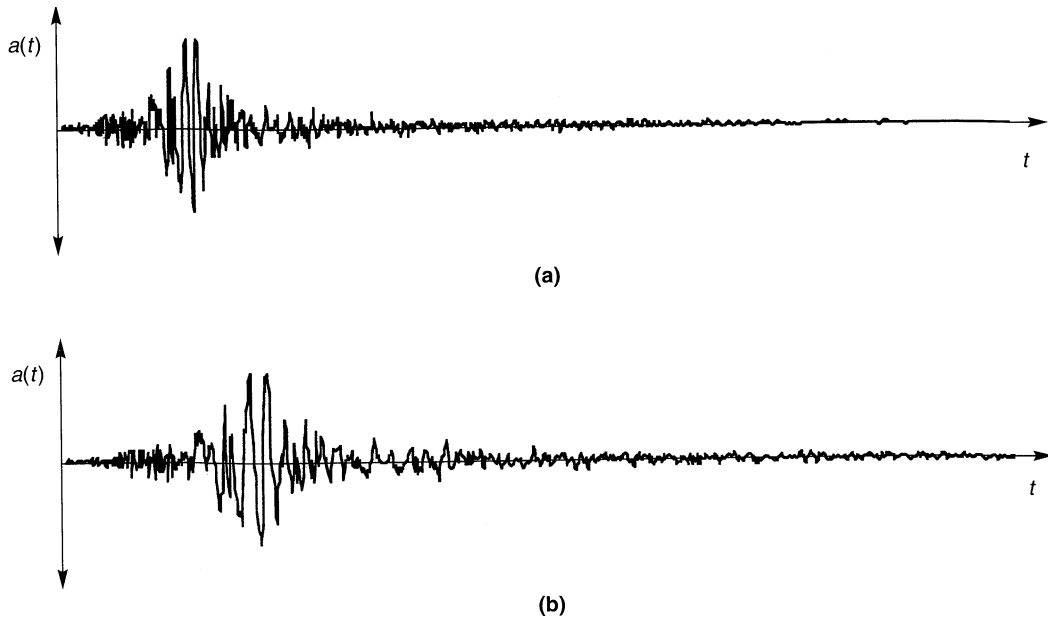


Figure 8.21 (a) Original accelerogram from actual earthquake; (b) rescaled version of original accelerogram in which time scale was scaled upward by a factor of 1.3 to match target predominant period. Note that the duration has also been increased by a factor of 1.3.

Generation of an artificial ground motion time history in the time domain typically involves multiplying a stationary, filtered white noise (or filtered Poisson process) signal by an envelope function that describes the buildup and subsequent decay (nonstationarity) of ground motion amplitude (Shinozuka and Deodatis, 1988), as illustrated in Figure 8.22. More recently, models that consider the nonstationarity of both amplitude and frequency content (e.g., Sharma and Shah, 1986; Shinozuka and Deodatis, 1988) have been developed. The use of autoregressive moving average (ARMA) models (e.g., Chang et al., 1982; Kozin, 1988) has also increased in recent years.

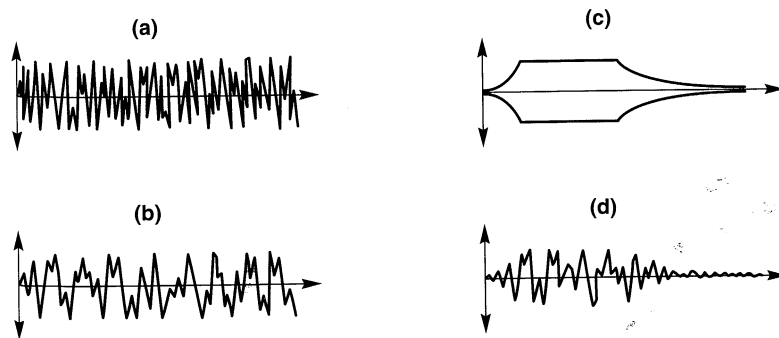


Figure 8.22 Example of time-domain generation of synthetic time history: (a) time history of white noise is filtered in the time domain to produce (b) time history of filtered white noise. Filtered white noise is multiplied by envelope function in (c) to produce the artificial ground motion shown in (d).

8.5.3 Frequency-Domain Generation

Ground motions can be generated quite conveniently in the frequency domain by combining a Fourier amplitude spectrum with a Fourier phase spectrum. The amplitude spectrum may be computed from an actual ground motion spectrum or may be represented by some theoretical means, such as a Brune spectrum or a power spectral density function (Section 3.3.2.1). The phase spectrum may be obtained from an actual ground motion or may be computed from a time history given by the product of white noise and an envelope function (Figure 8.23). Some investigators (e.g., Ohsaki, 1979; Abrahamson and Singh, 1986) have used phase difference distributions as an indicator of phase structure to develop nonrandom, artificial phase spectra.

Frequency-domain methods are particularly useful for generating motions that are consistent with target response spectra. Computer programs such as EQGEN (Chang et al., 1986b) and RASCAL (Silva, 1987) assume initial Fourier amplitude and phase spectra, and then iteratively adjust the ordinates of the Fourier amplitude spectrum until a motion consistent with the target response spectrum is produced. The origin of the target response spectrum must be kept in mind when generating spectrum-compatible motions. Constant risk spectra (Chapter 4), for example, represent the aggregate effect of potential earthquakes of many different magnitudes occurring at many different distances. Because a constant risk spectrum does not correspond to any particular seismic event, a motion generated from a constant risk target spectrum should not be expected to correspond to a particular seismic event (Naiem and Lew, 1995).

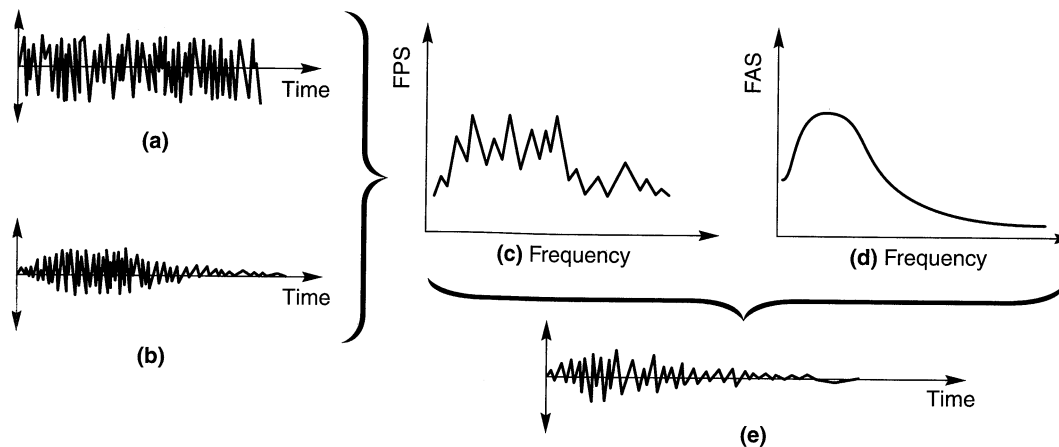


Figure 8.23 Example of frequency-domain generation of synthetic time history: (a) time history of white noise is shaped by envelope function to produce (b) time history of enveloped white noise. Fourier transform of enveloped white noise is performed to obtain (c) phase spectrum. Phase spectrum is combined with (d) amplitude spectrum to produce (e) synthetic time history.

8.5.4 Green's Function Techniques

The Green's function approach to ground motion modeling is based on the idea that the total motion at a particular site is equal to the sum of the motions produced by a series of individual ruptures of many small patches on the causative fault. Obtaining the site motion

requires defining the geometry of the earthquake source, dividing the source into a finite number of patches, defining the sequence in which the patches rupture, defining the slip functions (functions describing the variation of slip displacement with time for each patch) across the source, and defining Green's functions (functions that describe the motion at the site due to an instantaneous unit slip at the source; see Figure 8.24) across the source. Combining the Green's function with the slip function gives the motion at the site due to slip of each individual patch. Summing the effects of the slips of each patch while accounting for the order in which they rupture produces the overall ground motion at the site. Obviously, the summation procedure assumes that all materials remain linear.

Calculation of Green's functions requires knowledge of the velocity structure of the crustal materials between the source and site. However, estimation of the velocity structure, particularly with respect to heterogeneities responsible for the scattering that produces late-arriving coda waves, is a very difficult problem. Considerable computational effort is also required to calculate Green's function; finite-element, finite-difference, and ray theory techniques are usually used for this purpose. Hartzell (1978) bypassed these computations by using the weak motions of small earthquakes as *empirical Green's functions* to simulate the strong motion of large earthquakes. Empirical Green's functions have the benefit of automatically retaining the effects of the crustal velocity structure.

The Green's function approach is particularly useful for generating *near-field* motions, that is, motions at sites close enough to the fault that the fault dimensions become significant (for *far-field* sites, the fault can be treated as a point source without undue loss of accuracy). The nature of the rupture pattern, including the general direction in which rupture progresses, and the site azimuth (relative to the fault) can strongly influence ground motion in the near field. The Green's function approach allows phenomena such as directivity and fling (Section 2.5) to be reflected in artificial motions.

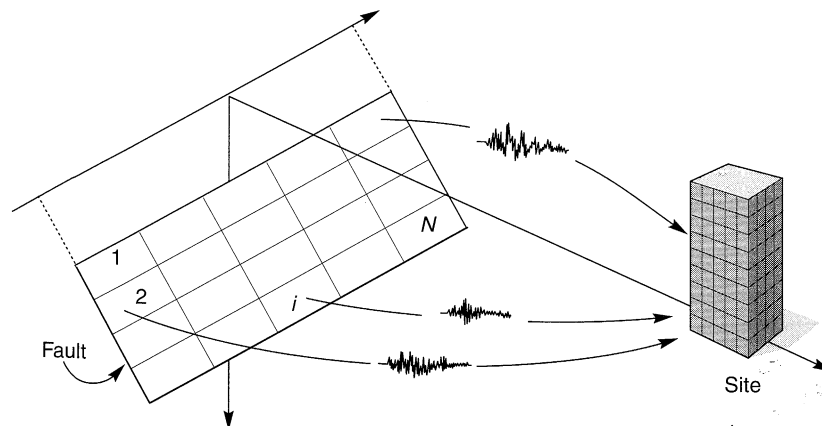


Figure 8.24 Schematic of Green's functions for a fault divided into N patches. Differences in the Green's functions for the different patches are due to differences in focal depth, epicentral distance, and geologic structure along the source-site path. Once Green's functions have been determined, site motions can easily be simulated for a variety of fault rupture patterns and slip functions.

8.5.5 Limitations of Artificial Ground Motions

As discussed in Chapter 3, actual ground motions are complicated—they are influenced by, and consequently reflect, characteristics of the seismic source, the rupture process, the source–site travel path, and local site conditions. Although it is convenient to characterize them with a small number of parameters, it is important to remember that such characterizations can never be complete.

Artificial motions that match a small number of target parameters are not unique; many different motions can produce the same target parameters. If such a set of motions are used to analyze problems for which damage correlates well to the target parameters, the predicted damage is likely to be consistent. For example, a set of different motions with the same peak acceleration will produce similar base shears in a stiff, linear elastic structure founded on rock. The same set of motions, however, might produce a broad range of base shears in a flexible and/or inelastic structure or in a structure founded on soft soil. They could also produce significantly different estimates of permanent slope movement or liquefaction potential. When using artificial motions, the eventual use(s) of the motions must always be reconciled with the criteria from which they were developed.

8.6 SUMMARY

1. Historical references to the correlation between earthquake damage and local site conditions extend back nearly 200 years. Provisions that specifically accounted for local site conditions did not appear in building codes, however, until the early 1970s.
2. Evidence for the existence of local site effects is compelling. In addition to theoretical evidence, amplification functions computed from measurements of surface and bed-rock motions at the same location, and comparisons of surface motion characteristics from nearby sites with different subsurface conditions, all confirm the important effects of local site conditions on earthquake ground motions.
3. Geometric effects can also influence ground motions. Though topographic irregularities scatter seismic waves to produce complicated patterns of amplification and deamplification, motions at the crests of ridges are generally amplified. Alluvial basins filled with soft sediments can, depending on their shapes, trap body waves and produce surface waves within the alluvium. Ground motion in an alluvial basin may be considerably different than those that would be predicted by one-dimensional ground response analyses, particularly near the edges of the basin.
4. Earthquake-resistant design of new structures and evaluation of the seismic vulnerability of existing structures involves prediction of their response to design ground motions. Design ground motions are obtained from design parameters developed from a prescribed design earthquake or from a seismic hazard analysis.
5. Design parameters may be developed on a site-specific basis or they may be obtained from building codes. For a typical site, parameters based on site-specific analyses are likely to be more accurate than code-based parameters. They are also likely to result in more economical designs.

6. Building codes have historically developed on an incremental basis as new knowledge is obtained. The seismic provisions of building codes have followed the same trend with the most significant changes occurring after major earthquakes.
7. Building codes are not intended to eliminate earthquake damage completely. Instead, they aim to produce designs that will resist small ground motions without damage, moderate motions without structural damage, and severe motions without collapse.
8. Ground motion time histories with specified target parameters can be developed by several different procedures. When design parameters are used as targets, these procedures will produce design ground motions. Procedures based on scaling of recorded ground motions and generation of artificial ground motions are widely used.

HOMWORK PROBLEMS

- 8.1 Compute and compare the response spectrum intensities at the State Building, Alexander Building, and Southern Pacific Company Building in the 1957 San Francisco earthquake (see Figure 8.4).
- 8.2 An earthquake produces a peak acceleration of $0.25g$ on a rock outcrop in the far-field. Estimate the peak ground surface accelerations that would be expected at stiff soil, deep cohesionless soil, and soft soil sites at the same distance from the source of the earthquake.
- 8.3 How would the frequency content of the bedrock motion influence the relationships shown in Figures 8.10 and 8.11. Comment on the ranges of applicability of these relationships.
- 8.4 Consider the Gilroy No. 1 (rock) and Gilroy No. 2 (soil) ground motions described in Chapter 3. Soil conditions at the Gilroy No. 2 (soil) site were described in Example 7.4. How well do the motions at these sites agree with the approximate relationships between peak accelerations on rock and soil outcrops shown in Figure 8.12?
- 8.5 How well do the shapes of the response spectra of the Gilroy No. 1 (rock) and Gilroy No. 2 (soil) motions (Figure 3.15) agree with the average normalized spectra shown in Figure 8.12?
- 8.6 Vertically propagating shear waves with a displacement amplitude of 1 cm at a great depth approach the ground surface illustrated below. Assuming that the topographic effects can be approximated by the triangular infinite wedge solution, estimate the displacement amplitudes at points A, B, C, and D.

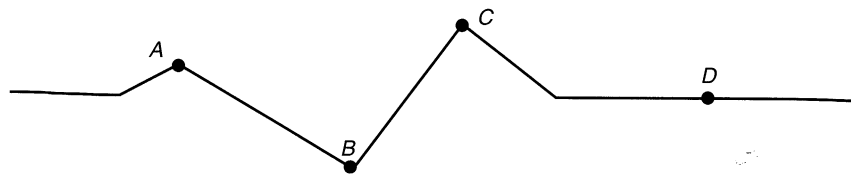
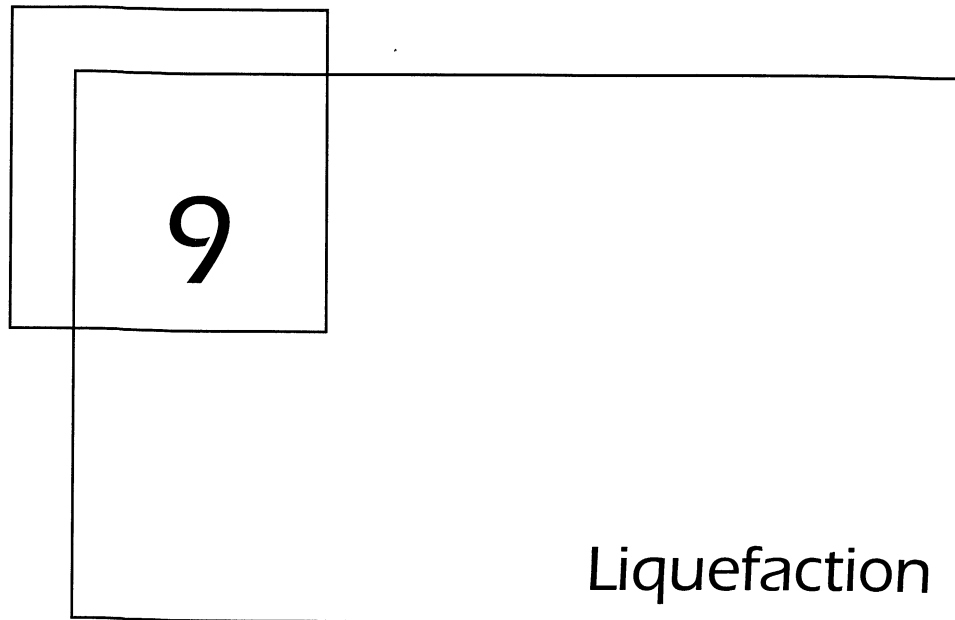


Figure P8.6

- 8.7 Determine and plot (on arithmetic scales) Newmark-Hall design spectra (5% damping) for a peak acceleration of $0.442g$. Label the acceleration-controlled, velocity-controlled, and displacement-controlled portions of the spectrum. How well does this design spectrum correspond to the response spectrum of the Gilroy No. 1 (rock) ground motion?

- 8.8** Using the provisions of the Uniform Building Code, evaluate design base shear coefficients (the ratio of the design base shear to the weight of the structure) for 8-story hospital buildings in Denver, Seattle, and San Francisco. Assume that the hospitals are constructed as ordinary moment-resisting steel frames. Bedrock outcrops at the ground surface at the Denver site. The Seattle site is located on 700 feet of dense, glacially overconsolidated soils. The San Francisco hospital site is underlain by 45 feet of soft San Francisco Bay Mud.
- 8.9** Use the provisions of the Uniform Building Code to develop design response spectra for the Denver and Seattle hospital sites from Problem 8.8. Briefly describe the steps that would be required to develop a design response spectrum for the San Francisco site.



9.1 INTRODUCTION

Liquefaction is one of the most important, interesting, complex, and controversial topics in geotechnical earthquake engineering. Its devastating effects sprang to the attention of geotechnical engineers in a three-month period in 1964 when the Good Friday earthquake ($M_W = 9.2$) in Alaska was followed by the Niigata earthquake ($M_S = 7.5$) in Japan. Both earthquakes produced spectacular examples of liquefaction-induced damage, including slope failures, bridge and building foundation failures, and flotation of buried structures. In the 30 years since these earthquakes, liquefaction has been studied extensively by hundreds of researchers around the world. Much has been learned, but the road has not been smooth. Different terminologies, procedures, and methods of analysis have been proposed, and a prevailing approach has been slow to emerge.

In recent years, many of these differences have been reconciled by the realization that their causes were due, in large part, to semantics. The term *liquefaction* has been used to describe a number of different, though related phenomena. Rather than try to trace the convoluted development of the current state of knowledge regarding liquefaction, this chapter will present a basic framework for the conceptual understanding of liquefaction-related soil behavior and use it to describe the various methods by which liquefaction hazards can be evaluated. To do this, the chapter introduces some new terminology to distinguish between

phenomena that have frequently been lumped together under the heading of *liquefaction*. The new terminology allows these phenomena to be illustrated in a way that simplifies understanding of their mechanics and the manner in which they contribute to earthquake damage.

9.2 LIQUEFACTION-RELATED PHENOMENA

The term *liquefaction*, originally coined by Mogami and Kubo (1953), has historically been used in conjunction with a variety of phenomena that involve soil deformations caused by monotonic, transient, or repeated disturbance of saturated cohesionless soils under undrained conditions. The generation of excess pore pressure under undrained loading conditions is a hallmark of all liquefaction phenomena. The tendency for dry cohesionless soils to densify under both static and cyclic loading is well known. When cohesionless soils are saturated, however, rapid loading occurs under undrained conditions, so the tendency for densification causes excess pore pressures to increase and effective stresses to decrease. Liquefaction phenomena that result from this process can be divided into two main groups: *flow liquefaction* and *cyclic mobility*.

Both flow liquefaction and cyclic mobility are very important, and any evaluation of liquefaction hazards should carefully consider both. In the field, flow liquefaction occurs much less frequently than cyclic mobility but its effects are usually far more severe. Cyclic mobility, on the other hand, can occur under a much broader range of soil and site conditions than flow liquefaction; its effects can range from insignificant to highly damaging. In this book, the generic term *liquefaction* will be taken to include both flow liquefaction and cyclic mobility. Flow liquefaction and cyclic mobility will be identified individually when necessary.

9.2.1 Flow Liquefaction

Flow liquefaction produces the most dramatic effects of all the liquefaction-related phenomena—tremendous instabilities known as *flow failures*. Flow liquefaction can occur when the shear stress required for static equilibrium of a soil mass (the *static shear stress*) is greater than the shear strength of the soil in its liquefied state. Once triggered *the large deformations produced by flow liquefaction are actually driven by static shear stresses*. The cyclic stresses may simply bring the soil to an unstable state at which its strength drops sufficiently to allow the static stresses to produce the flow failure. Flow liquefaction failures are characterized by the sudden nature of their origin, the speed with which they develop, and the large distance over which the liquefied materials often move. The flow slide failures of Sheffield Dam (Figure 1.5) and Lower San Fernando Dam (Figure 1.7) are examples of flow liquefaction. The fluid nature of liquefied soil is illustrated in Figure 9.1.

9.2.2 Cyclic Mobility

Cyclic mobility is another phenomenon that can also produce unacceptably large permanent deformations during earthquake shaking. In contrast to flow liquefaction, cyclic mobility occurs when the static shear stress is less than the shear strength of the liquefied soil. *The deformations produced by cyclic mobility failures develop incrementally during earthquake*



Figure 9.1 A small flow slide along the shore of Lake Merced in San Francisco in 1957 (photo by M. Bonilla; courtesy of USGS).

shaking. In contrast to flow liquefaction, the deformations produced by cyclic mobility are driven by both cyclic and static shear stresses. These deformations, termed *lateral spreading*, can occur on very gently sloping ground or on virtually flat ground adjacent to bodies of water (Figure 9.2). When structures are present, lateral spreading can cause significant damage (Figure 1.8 and 1.9).

A special case of cyclic mobility is level-ground liquefaction. Because static horizontal shear stresses that could drive lateral deformations do not exist, level-ground liquefaction can produce large, chaotic movement known as ground oscillation during earthquake shaking, but produces little permanent lateral soil movement. Level-ground liquefaction failures are caused by the upward flow of water that occurs when seismically induced excess pore pressures dissipate. Depending on the length of time required to reach hydraulic equilibrium, level-ground liquefaction failure may occur well after ground shaking has ceased. Excessive vertical settlement and consequent flooding of low-lying land and the development of sand boils (Figure 9.3) are characteristic of level-ground liquefaction failure.

9.3 EVALUATION OF LIQUEFACTION HAZARDS

Both flow liquefaction and cyclic mobility can produce damage at a particular site, and a complete evaluation of liquefaction hazards requires that the potential for each be addressed. When faced with such a problem, the geotechnical earthquake engineer can systematically evaluate potential liquefaction hazards by addressing the following questions:

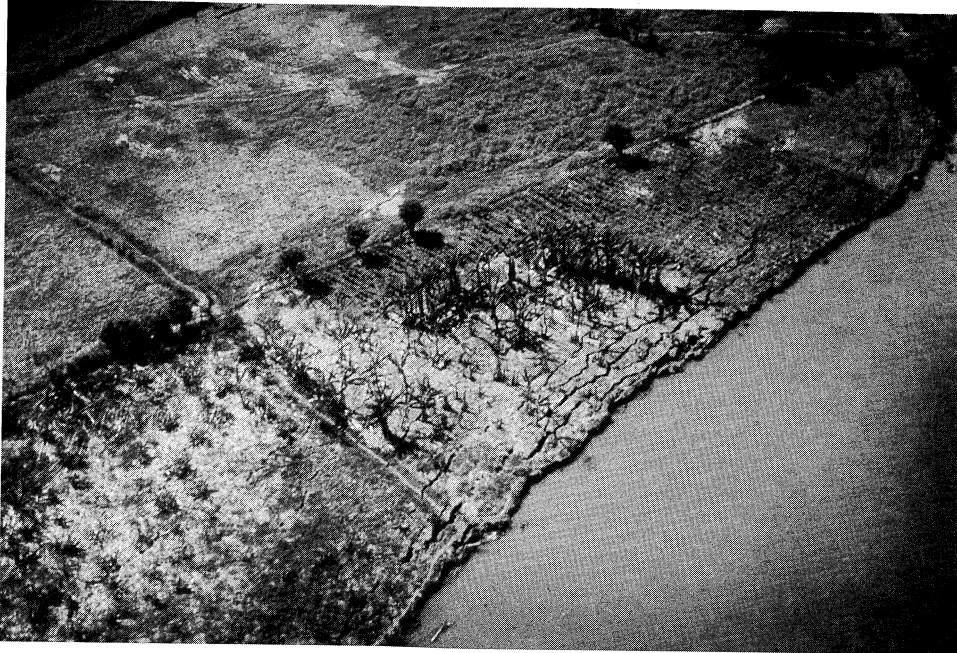


Figure 9.2 Lateral spreading of very flat ground toward the Motagua River following the 1976 Guatemala earthquake. Note orientation of ground surface cracks parallel to river bank (photo by G. Plafker; courtesy of USGS).

1. Is the soil susceptible to liquefaction?
2. If the soil is susceptible, will liquefaction be triggered?
3. If liquefaction is triggered, will damage occur?

If the answer to the first question is no, the liquefaction hazard evaluation can be terminated with the conclusion that liquefaction hazards do not exist. If the answer is yes, the next question must be addressed. In some cases it may be more efficient to reverse the order of the second and third questions, particularly when damage appears unlikely. If the answers to all three are yes, a problem exists; if the anticipated level of damage is unacceptable, the site must be abandoned or improved (Chapter 12) or on-site structures strengthened. These questions pertain to the three most critical aspects of liquefaction hazard evaluation: *susceptibility, initiation, and effects*. All three must be considered in a comprehensive evaluation of liquefaction hazards.

9.4 LIQUEFACTION SUSCEPTIBILITY

Not all soils are susceptible to liquefaction; consequently, the first step in a liquefaction hazard evaluation is usually the evaluation of liquefaction susceptibility. If the soil at a particular site is not susceptible, liquefaction hazards do not exist and the liquefaction hazard evaluation can be ended. If the soil is susceptible, however, the matters of liquefaction initiation and



Figure 9.3 Sand boils near Niigata, Japan following the 1964 Niigata earthquake. Sand boils are often aligned along cracks in the ground (photo by K. Steinbrugge; courtesy of Earthquake Engineering Research Center, University of California).

effects must be addressed. There are several criteria by which liquefaction susceptibility can be judged, and some are different for flow liquefaction and cyclic mobility. These include historical, geologic, compositional, and state criteria.

9.4.1 Historical Criteria

A great deal of information on liquefaction behavior has come from postearthquake field investigations, which have shown that liquefaction often recurs at the same location when soil and groundwater conditions have remained unchanged (Youd, 1984a). Thus liquefaction case histories can be used to identify specific sites, or more general site conditions, that may be susceptible to liquefaction in future earthquakes. Youd (1991) described a number of instances where historical evidence of liquefaction has been used to map liquefaction susceptibility.

Postearthquake field investigations have also shown that liquefaction effects have historically been confined to a zone within a particular distance of the seismic source. Ambraseys (1988) compiled worldwide data from shallow earthquakes to estimate a limiting epicentral distance beyond which liquefaction has not been observed in earthquakes of different magnitudes (Figure 9.4). The distance to which liquefaction can be expected

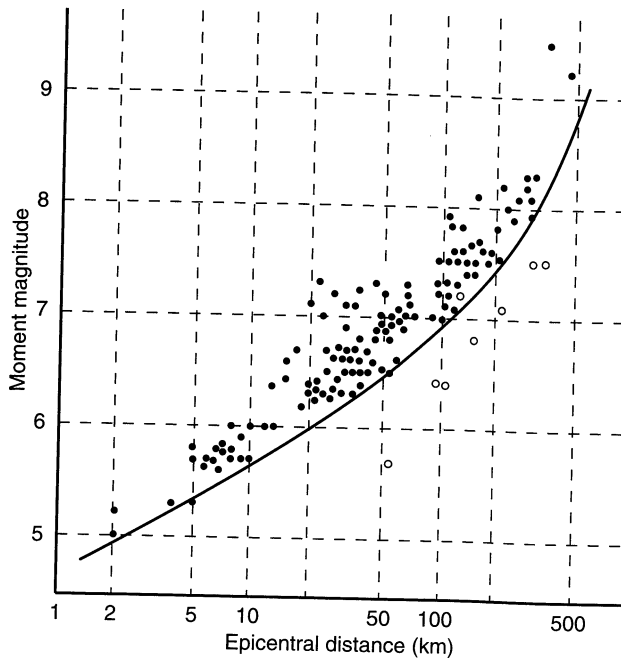


Figure 9.4 Relationship between limiting epicentral distance of sites at which liquefaction has been observed and moment magnitude for shallow earthquakes. Deep earthquakes (focal depths > 50 km) have produced liquefaction at greater distances. After Ambraseys (1988).

increases dramatically with increasing magnitude. While relationships of the type shown in Figure 9.4 offer no guarantee that liquefaction cannot occur at greater distances, they are helpful for estimation of regional liquefaction hazard scenarios.

9.4.2 Geologic Criteria

Soil deposits that are susceptible to liquefaction are formed within a relatively narrow range of geological environments (Youd, 1991). The depositional environment, hydrological environment, and age of a soil deposit all contribute to its liquefaction susceptibility (Youd and Hoose, 1977).

Geologic processes that sort soils into uniform grain size distributions and deposit them in loose states produce soil deposits with high liquefaction susceptibility. Consequently, fluvial deposits, and colluvial and aeolian deposits when saturated, are likely to be susceptible to liquefaction. Liquefaction has also been observed in alluvial-fan, alluvial-plain, beach, terrace, playa, and estuarine deposits, but not as consistently as in those listed previously. The susceptibility of older soil deposits to liquefaction is generally lower than that of newer deposits. Soils of Holocene age are more susceptible than soils of Pleistocene age, although susceptibility decreases with age within the Holocene. Liquefaction of pre-Pleistocene deposits is rare.

Liquefaction occurs only in saturated soils, so the depth to groundwater (either free or perched) influences liquefaction susceptibility. Liquefaction susceptibility decreases with increasing groundwater depth; the effects of liquefaction are most commonly observed at

sites where groundwater is within a few meters of the ground surface. At sites where groundwater levels fluctuate significantly, liquefaction hazards may also fluctuate.

Human-made soil deposits also deserve attention. Loose fills, such as those placed without compaction, are very likely to be susceptible to liquefaction. The stability of hydraulic fill dams and mine tailings piles, in which soil particles are loosely deposited by settling through water, remains an important contemporary seismic hazard. Well-compacted fills, on the other hand, are unlikely to satisfy state criteria (Section 9.4.4) for liquefaction susceptibility.

9.4.3 Compositional Criteria

Since liquefaction requires the development of excess pore pressure, liquefaction susceptibility is influenced by the compositional characteristics that influence volume change behavior. Compositional characteristics associated with high volume change potential tend to be associated with high liquefaction susceptibility. These characteristics include particle size, shape, and gradation.

For many years, liquefaction-related phenomena were thought to be limited to sands. Finer-grained soils were considered incapable of generating the high pore pressures commonly associated with liquefaction, and coarser-grained soils were considered too permeable to sustain any generated pore pressure long enough for liquefaction to develop. More recently, the bounds on gradation criteria for liquefaction susceptibility have broadened.

Liquefaction of nonplastic silts has been observed (Ishihara, 1984, 1985) in the laboratory and the field, indicating that plasticity characteristics rather than grain size alone influence the liquefaction susceptibility of fine-grained soils. Coarse silts with bulky particle shape, which are nonplastic and cohesionless, are fully susceptible to liquefaction (Ishihara, 1993); finer silts with flaky or platelike particles generally exhibit sufficient cohesion to inhibit liquefaction. Clays remain nonsusceptible to liquefaction, although sensitive clays can exhibit strain-softening behavior similar to that of liquefied soil. Fine-grained soils that satisfy each of the following four Chinese criteria (Wang, 1979) may be considered susceptible to significant strength loss:

Fraction finer than 0.005 mm \leq 15%

Liquid limit, LL \leq 35%

Natural water content \geq 0.9 LL

Liquidity index \leq 0.75

To account for differences in Chinese and U.S. practice, the U.S. Army Corps of Engineers modified the measured index properties (by decreasing the fines content by 5%, increasing the liquid limit by 1%, and increasing the natural water content by 2%) before applying the Chinese criteria to a clayey silt in the foundation of Sardis Dam (Finn et al., 1994).

At the other end of the grain size spectrum, liquefaction of gravels has been observed in the field (Coulter and Migliaccio, 1966; Chang, 1978; Wong, 1984; Youd et al., 1985; Yegian et al., 1994) and in the laboratory (Wong et al., 1975; Evans and Seed, 1987). The effects of membrane penetration (Section 6.3.2.3) are now thought to be responsible for the high liquefaction resistance observed in early laboratory investigations of gravelly soils. When pore pressure dissipation is impeded by the presence of impermeable layers so that truly undrained conditions exist, gravelly soils can also be susceptible to liquefaction.

Liquefaction susceptibility is influenced by gradation. Well-graded soils are generally less susceptible to liquefaction than poorly graded soils; the filling of voids between larger particles by smaller particles in a well-graded soil results in lower volume change potential under drained conditions and, consequently, lower excess pore pressures under undrained conditions. Field evidence indicates that most liquefaction failures have involved uniformly graded soils.

Particle shape can also influence liquefaction susceptibility. Soils with rounded particle shapes are known to densify more easily than soils with angular grains. Consequently, they are usually more susceptible to liquefaction than angular-grained soils. Particle rounding frequently occurs in the fluvial and alluvial environments where loosely deposited saturated soils are frequently found, and liquefaction susceptibility is often high in those areas.

9.4.4 State Criteria

Even if a soil meets all of the preceding criteria for liquefaction susceptibility, it still may or may not be susceptible to liquefaction. Liquefaction susceptibility also depends on the initial *state* of the soil (i.e., its stress and density characteristics at the time of the earthquake). Since the tendency to generate excess pore pressure of a particular soil is strongly influenced by both density and initial stress conditions, liquefaction susceptibility depends strongly on the initial state of the soil. These liquefaction susceptibility criteria, unlike those discussed previously, are different for flow liquefaction and cyclic mobility.

To introduce contemporary methods for evaluating state criteria (and to provide a background for evaluating the effects of liquefaction), a brief historical review of some basic concepts of cohesionless soil behavior is required.

9.4.4.1 Critical Void Ratio

In his pioneering work on the shear strength of soils, Casagrande (1936) performed drained, strain-controlled triaxial tests on initially loose and initially dense sand specimens. The results (Figure 9.5), which form the cornerstone of modern understanding of soil

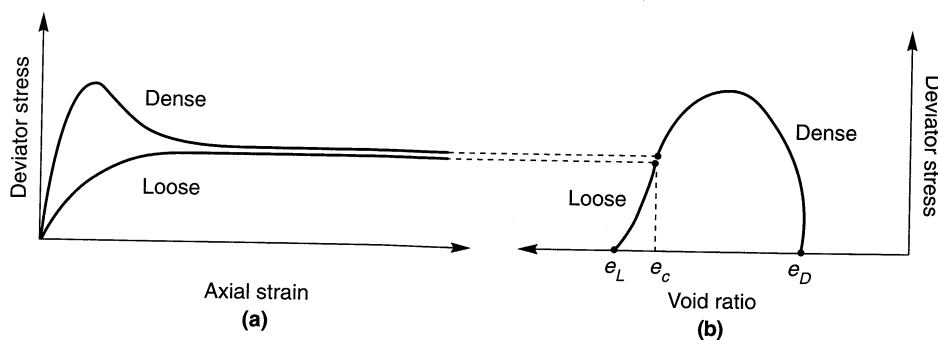


Figure 9.5 (a) Stress–strain and (b) stress–void ratio curves for loose and dense sands at the same effective confining pressure. Loose sand exhibits contractive behavior (decreasing void ratio) and dense sand exhibits dilative behavior (increasing void ratio) during shearing. By the time large strains have developed, both specimens have reached the critical void ratio and mobilize the same large-strain shearing resistance.

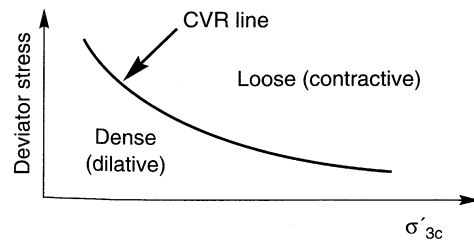


Figure 9.6 Use of the CVR line as a boundary between loose contractive states and dense dilative states.

strength behavior, showed that all specimens tested at the same effective confining pressure approached the same density when sheared to large strains. Initially loose specimens contracted, or densified, during shearing and initially dense specimens first contracted, but then very quickly began to dilate. At large strains, all specimens approached the same density and continued to shear with constant shearing resistance. The void ratio corresponding to this constant density was termed the *critical void ratio, e_c* . By performing tests at different effective confining pressures, Casagrande found that the critical void ratio was uniquely related to the effective confining pressure, and called the locus the *critical void ratio (CVR) line* (Figure 9.6). By defining the state of the soil in terms of void ratio and effective confining pressure, the CVR line could be used to mark the boundary between loose (contractive) and dense (dilative) states.

The equipment needed to measure pore pressure was not available at the time, but Casagrande hypothesized that strain-controlled undrained testing would produce positive excess pore pressure (due to the tendency for contraction) in loose specimens, and negative excess pore pressure (due to the tendency for dilation) in dense specimens (Figure 9.7), until the CVR line was reached. This hypothesis was subsequently verified experimentally. The CVR line therefore described the state toward which any soil specimen would migrate at large strains, whether by volume changes under drained conditions, changes in effective confining pressure under undrained conditions, or some combination under partially drained conditions.

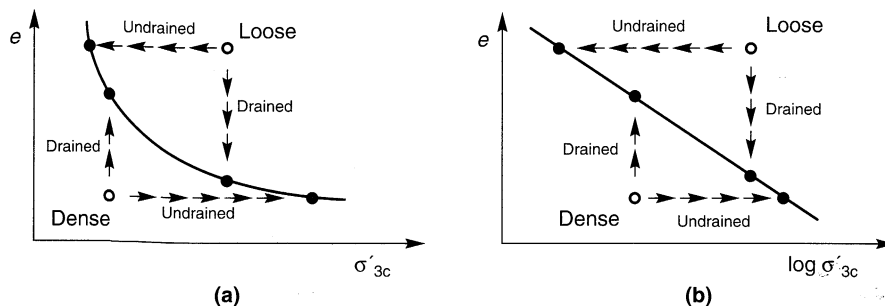


Figure 9.7 Behavior of initially loose and dense specimens under drained and undrained conditions for (a) arithmetic and (b) logarithmic effective confining pressure scales.

Since the CVR line marked the boundary between contractive and dilative behavior, it was considered to mark the boundary between states in which a particular soil was or was not susceptible to flow liquefaction (Figure 9.8). Saturated soils with initial void ratios high

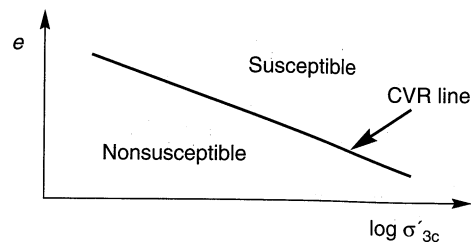


Figure 9.8 Use of CVR line as a boundary between initial states that are and are not susceptible to flow liquefaction.

enough to plot above the CVR line were considered susceptible to flow liquefaction, and soils with initial states plotting below the CVR line were considered nonsusceptible. However, when Fort Peck Dam in Montana suffered a static flow liquefaction failure of its upstream slope during construction in 1938 (Middlebrooks, 1942), a postfailure investigation showed that the initial state of soils that had obviously liquefied actually plotted somewhat below the CVR line (i.e., in the nonsusceptible region). Casagrande attributed this discrepancy to the inability of strain-controlled drained tests to replicate all of the phenomena that influence soil behavior under the stress-controlled undrained conditions of an actual flow liquefaction failure. Over the years, Casagrande developed the hypothesis that a flowing liquefied sand has a “flow structure” in which grains continuously rotate to orient themselves in a structure of minimum frictional resistance (Casagrande, 1976). Casagrande was unable to achieve a flow structure in the laboratory until the late 1960s, when one of his students performed an important series of stress-controlled undrained triaxial tests (Castro, 1969).

9.4.4.2 Steady State of Deformation

Castro (1969) performed static and cyclic triaxial tests on isotropically consolidated specimens and several static tests on anisotropically consolidated specimens. Three different types of stress-strain behavior, illustrated for anisotropically consolidated specimens in Figure 9.9 were observed. Very loose specimens (such as specimen A in Figure 9.9) exhibited a peak undrained strength at a small shear strain and then “collapsed” to flow rapidly to large strains at low effective confining pressure and low large-strain strength. This type of behavior now recognized as flow liquefaction was described at that time as “liquefaction.” Dense specimens (specimen B) initially contracted but then dilated until a relatively high constant effective confining pressure and large-strain strength was reached. At intermediate densities (specimen C) the exceedance of a peak strength at low strain was followed by a limited period of strain-softening behavior, which ended with the onset of dilation at intermediate strains. [This reversal from contractive to dilative behavior occurs at the *phase transformation point* (Ishihara et al., 1975).] Further loading produced continued dilation to higher effective confining pressures and, consequently, higher large-strain strengths. This type of behavior was termed *limited liquefaction*.

The testing program showed a unique relationship between void ratio and effective confining pressure at large strains. Graphically, this relationship plotted below and roughly parallel to the CVR line obtained from drained strain-controlled tests; the difference being attributed to development of the flow structure under stress-controlled conditions. The state in which the soil flowed continuously under constant shear stress and constant effective confining pressure at constant volume and constant velocity was later defined (Castro and

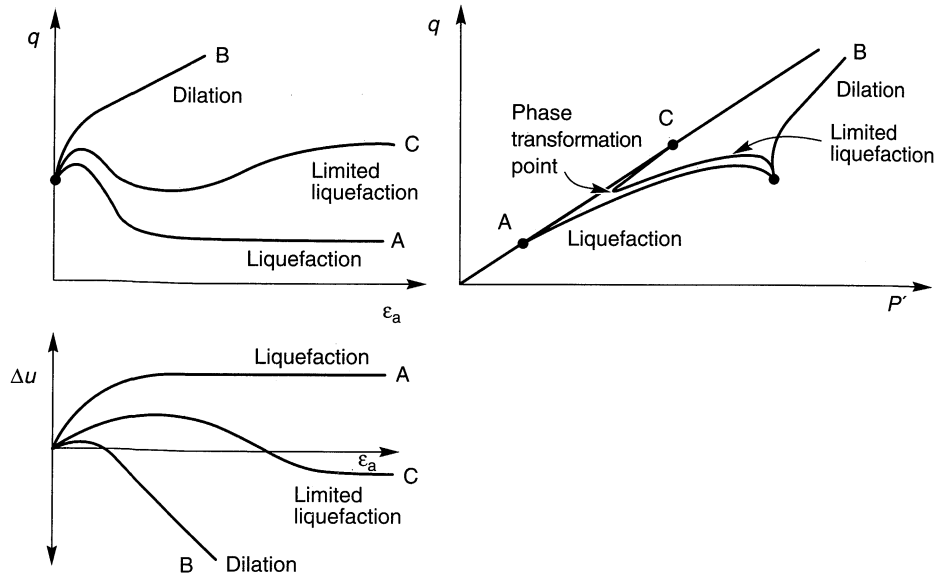


Figure 9.9 Liquefaction, limited liquefaction, and dilation in monotonic loading tests.

Poulos, 1977; Poulos, 1981) as the *steady state of deformation*. Since the steady state of deformation is reached only at large strains (after the effects of initial conditions such as soil fabric, stress and strain history, and loading conditions have been obscured), the effective confining pressure in an element of soil in the steady state of deformation was considered to depend only on the density of the soil. Relatively recently it has been shown that the steady-state conditions are different for compressive and extensional stress paths (e.g., Vaid et al., 1990; Reimer and Seed, 1992; Vaid and Thomas, 1995), particularly when the soil is deposited with inherently anisotropic structure. Specifically, pluviated sands exhibit contractive behavior over a wider range of densities when loaded in extension than in compression; a particular element of sand at an intermediate density may exhibit dilative behavior in compression but contractive behavior when loaded in extension. As a result, the depositional conditions, stress conditions, and loading conditions that exist in the field should be matched as closely as possible in laboratory investigations of steady-state behavior.

The locus of points describing the relationship between void ratio and effective confining pressure in the steady state of deformation is called the *steady-state line* (SSL). In its most general form, the SSL can be viewed as a three-dimensional curve in $e-\sigma'-\tau$ (Figure 9.10) or $e-p'-q$ space. The SSL shown in Figure 9.7a therefore represents the projection of the three-dimensional SSL onto a plane of constant τ . The SSL can also be projected onto planes of constant effective confining pressure ($\sigma' = \text{constant}$) and constant density ($e = \text{constant}$). The SSL can also be expressed in terms of the steady-state strength, S_{su} ; since the shearing resistance of the soil in the steady state of deformation is proportional to the effective confining pressure, the strength-based SSL is parallel to the effective confining pressure-based SSL when both are plotted on logarithmic scales (Figure 9.11).

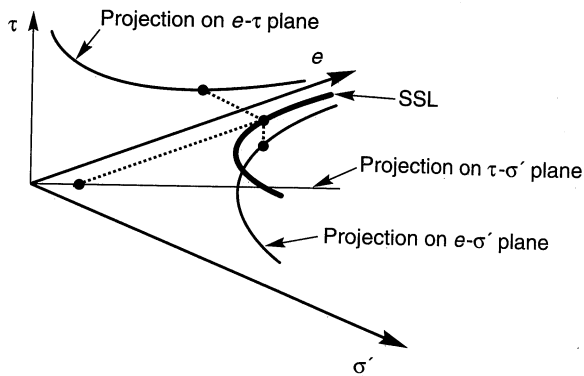


Figure 9.10 Three-dimensional steady-state line showing projections on e - τ plane, e - σ' plane, and τ - σ' plane. A similar plot can be developed using the stress path parameters q and p' instead of τ and σ' .

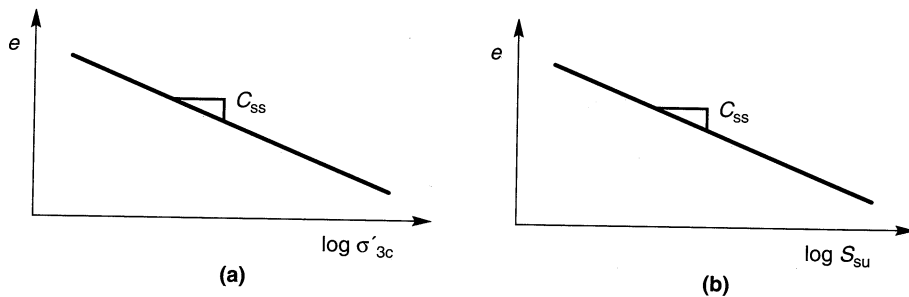


Figure 9.11 Proportionality of S_{su} to σ'_{3c} produces strength-based and effective confining pressure-based steady-state lines with identical slopes.

The SSL is useful for identifying the conditions under which a particular soil may or may not be susceptible to flow liquefaction (Figure 9.12). Soils whose state plots below the SSL are not susceptible to flow liquefaction. A soil whose state lies above the SSL will be susceptible to flow liquefaction *only if the static shear stress exceeds its steady state (or residual) strength*. Since the SSL can be used to evaluate the shearing resistance of liquefied soils, it is also useful for evaluating the potential effects of liquefaction (Section 9.6). Although determination of the position of the SSL can be difficult in practice (Section 9.6.4.1), the SSL is very useful for understanding the basic concepts of liquefaction.

Cyclic mobility, on the other hand, can occur in soils whose state plot above or below the SSL. In other words, *cyclic mobility can occur in both loose and dense soils*.

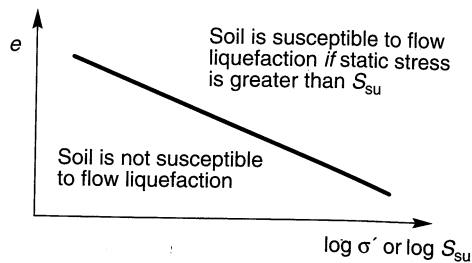


Figure 9.12 State criteria for flow liquefaction susceptibility. Soils with combinations of initial density and stress conditions that plot above the SSL are susceptible to flow liquefaction when the static shear strength is greater than the steady-state strength. Initial conditions that plot below the SSL are not susceptible to flow liquefaction.

The location of the SSL is sensitive to the compositional characteristics of the soil—its vertical position is strongly influenced by gradation and its slope by particle angularity. Soils with rounded particles usually have flat SSLs—a characteristic that often leads to difficulty in the estimation of in situ steady-state strength.

9.4.4.3 State Parameter

The nature of the steady-state line illustrates the limited applicability of absolute measures of density, such as void ratio and relative density, for characterization of a potentially liquefiable soil. As illustrated in Figure 9.12, an element of soil at a particular void ratio (hence a particular density and relative density) can be susceptible to flow liquefaction under a high effective confining pressure but nonsusceptible at a low effective confining pressure.

Using concepts of critical-state soil mechanics, the behavior of a cohesionless soil should be more closely related to the proximity of its initial state to the steady-state line than to absolute measures of density (Roscoe and Pooroshasb, 1963). In other words, soils in states located at the same distance from the steady-state line should exhibit similar behavior. Using this logic, a *state parameter* (Been and Jeffries, 1985) can be defined as

$$\psi = e - e_{ss} \quad (9.1)$$

where e_{ss} is the void ratio of the steady-state line at the effective confining pressure of interest (Figure 9.13). When the state parameter is positive, the soil exhibits contractive behavior and may be susceptible to flow liquefaction. When it is negative, dilative behavior will occur and the soil is not susceptible to flow liquefaction. The state parameter has been related to friction angle, dilation angle, CPT resistance (Been et al., 1986, 1987; Sladen, 1985), PMT results (Yu, 1994), and DMT results (Konrad, 1988). Ishihara (1993) showed that the ability of the state parameter to characterize soil behavior of very loose sands under low effective confining pressures may be limited and proposed an analogous parameter (the *state index*) based on the relative distance between the initial state and the *quasi-steady-state line* (a line analogous to and located slightly below the SSL which corresponds to the stress and density conditions at the phase transformation points observed in cases of limited liquefaction).

The concept of the state parameter is very useful and the possibility of determining its value from in situ tests is appealing. The accuracy with which the state parameter can be determined, however, is influenced by the accuracy with which the position of the SSL can be determined (Section 9.6.3.1).

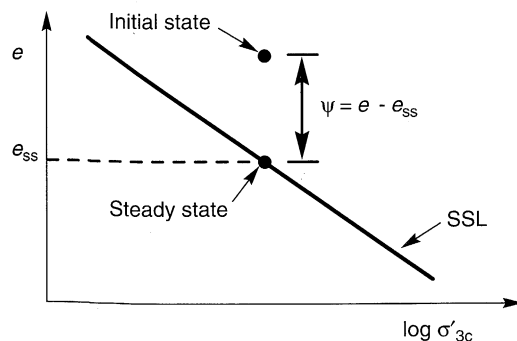


Figure 9.13 State parameter.

9.5 INITIATION OF LIQUEFACTION

The fact that a soil deposit is susceptible to liquefaction does not mean that liquefaction will necessarily occur in a given earthquake. Its occurrence requires a disturbance that is strong enough to initiate, or trigger, it. Evaluation of the nature of that disturbance is one of the most critical parts of a liquefaction hazard evaluation. Any discussion of the initiation of liquefaction must specify which liquefaction-related phenomena are being considered. Many previous studies of liquefaction initiation have implicitly lumped flow liquefaction and cyclic mobility together, but since they are distinctly different phenomena, it is more appropriate to consider each separately.

Although cyclic mobility is an earthquake related phenomenon, flow liquefaction can be initiated in a variety of ways. Flow slides triggered by monotonic loading (*static liquefaction*) have been observed in natural soil deposits (Koppejan et al., 1948; Andersen and Bjerrum, 1968; Bjerrum, 1971; Kramer, 1988), man-made fills (Middlebrooks, 1942; Cornforth et al., 1975; Mitchell, 1984), and mine tailings piles (Kleiner, 1976; Jennings, 1979; Eckersley, 1985). Flow liquefaction has also been triggered by nonseismic sources of vibration, such as pile driving (Jakobsen, 1952; Broms and Bennermark, 1967), train traffic (Fellenius, 1953), geophysical exploration (Hryciw et al., 1990), and blasting (Conlon, 1966; Carter and Seed, 1988). Perhaps somewhat ironically, the study of static liquefaction over the past 10 to 15 years has contributed greatly to improved understanding of seismically induced liquefaction by identifying the effective stress conditions at which liquefaction phenomena are initiated.

Understanding the initiation of liquefaction requires identification of the state of the soil when liquefaction is triggered. In the following sections, these conditions will be presented in a framework that allows the mechanics of both flow liquefaction and cyclic mobility to be clearly understood. Subsequently, practical and commonly used procedures for determining the nature of the disturbance required to move from initial state to the state at which liquefaction is triggered will be presented.

9.5.1 Flow Liquefaction Surface

The conditions at which flow liquefaction is initiated are most easily illustrated with the aid of the stress path (Section 6.2.2). Hanzawa et al. (1979) first showed that the effective stress conditions at which strain-softening behavior occurred in loose, saturated sands could be described very simply in stress path space. As discussed in the following sections, the effective stress conditions at the initiation of flow liquefaction can be described in stress path space by a three-dimensional surface that will be referred to hereafter as the *flow liquefaction surface* (FLS). While some practical difficulties in the measurement of the FLS for general stress paths remain, it provides (in conjunction with steady-state concepts) a very useful framework for conceptual understanding of the relationships between the various liquefaction phenomena. This conceptual understanding is vital for proper evaluation of the behavior of liquefiable soils both during and after earthquake shaking.

9.5.1.1 Monotonic Loading

The conditions at the initiation of flow liquefaction can be seen most easily when the soil is subjected to monotonically increasing stresses. Consider, for example, the response of an isotropically consolidated specimen of very loose, saturated sand in undrained,

stress-controlled triaxial compression (Figure 9.14). Immediately prior to undrained shearing (point A), the specimen is in drained equilibrium under an initial effective confining pressure, σ'_{3c} , with zero shear stress (Figure 9.14a,b) and zero excess pore pressure (Figure 9.14c). Since its initial state is well above the SSL (Figure 9.14d), the sand will exhibit contractive behavior. When undrained shearing begins, the contractive specimen generates positive excess pore pressure as it mobilizes shearing resistance up to a peak value (point B) that occurs at a relatively small strain. The excess pore pressure at point B is also relatively small; the pore pressure ratio, $r_u = u_{\text{excess}}/\sigma'_{3c}$, is well below 1.00. At point B, however, the specimen becomes unstable, and because it is loaded under stress-controlled conditions, collapses (the axial strain may increase from less than 1% to more than 20% in a fraction of a second). As the specimen strains from point B to point C, the excess pore pressure increases dramatically. At and beyond point C, the specimen is in the steady state of deformation and the effective confining pressure is only a small fraction of the initial effective confining pressure. This specimen has exhibited flow liquefaction behavior; the static shear stresses required for equilibrium (at point B) were greater than the available shear strength (at point C) of the liquefied soil. Flow liquefaction was initiated at the instant it became irreversibly unstable (i.e., at point B).

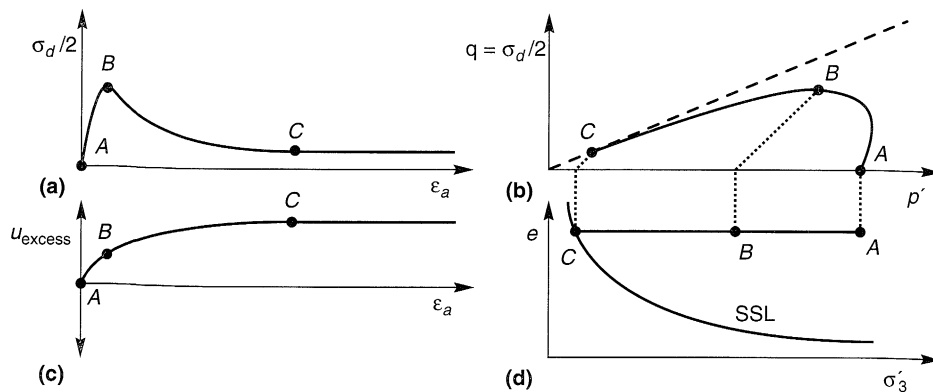


Figure 9.14 Response of isotropically consolidated specimen of loose, saturated sand: (a) stress-strain curve; (b) effective stress path; (c) excess pore pressure; (d) effective confining pressure.

Now consider the response of a series of triaxial specimens initially consolidated to the same void ratio at different effective confining pressures. Since all of the specimens have the same void ratio, they will all reach the same effective stress conditions at the steady state, but they will get there by different stress paths. Figure 9.15 illustrates the response of each specimen under monotonic loading. The initial states of specimens A and B are below the SSL, so they exhibit dilative behavior upon shearing. Specimens C, D, and E all exhibit contractive behavior; each reaches a peak undrained strength after which they strain rapidly toward the steady state. For specimens C, D, and E, flow liquefaction is initiated at the peak of each stress path (at the points marked with an X). Hanzawa et al. (1979), Vaid and Chern (1983), and a number of more recent investigations have shown that the locus of points

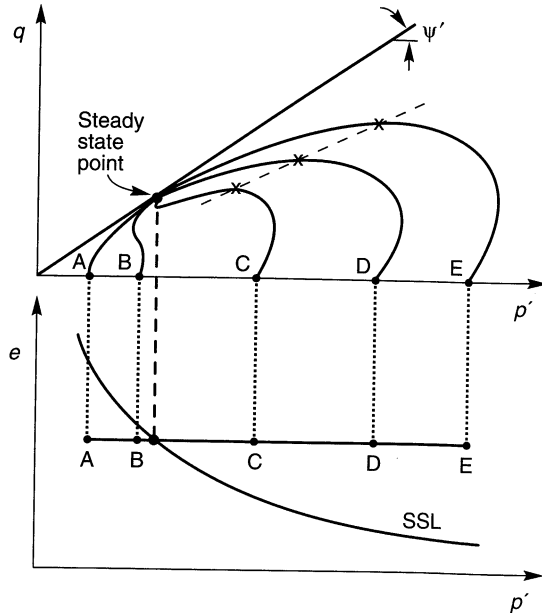


Figure 9.15 Response of five specimens isotropically consolidated to the same initial void ratio at different initial effective confining pressures. Flow liquefaction in specimens C, D, and E is initiated at the points marked with an \times . The dotted line passing through these points is a line of constant principal effective stress ratio, K_L .

describing the effective stress conditions at the initiation of flow liquefaction is a straight line (the dotted line in Figure 9.15) that projects through the origin of the stress path. Graphically, these points may be used to define the *flow liquefaction surface* (FLS) in stress path space; since flow liquefaction cannot occur if the stress path is below the steady-state point, the FLS is truncated at that level (Figure 9.16). This form of the FLS was first proposed (with a different name) by Vaid and Chern (1985). It should be noted that Sladen et al. (1985) proposed an analogous surface (called the *collapse surface*) that was assumed to project linearly through the steady-state point; since the preponderance of current experimental evidence appears to support projection through the origin, the term *FLS* is used in this book. For very loose samples, the steady-state point may be so close to the origin that the practical difference between the FLS and the collapse surface is negligible.

The FLS marks the boundary between stable and unstable states in undrained shear. If the stress conditions in an element of soil reach the FLS under undrained conditions, whether by monotonic or cyclic loading, flow liquefaction will be triggered and the shearing

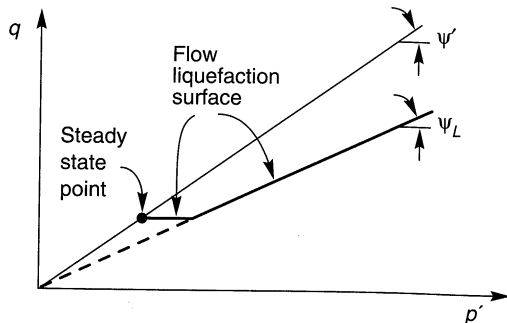


Figure 9.16 Orientation of the flow liquefaction surface in stress path space.

resistance will be reduced to the steady-state strength. Therefore, *the FLS describes the conditions at which flow liquefaction is initiated.*

For isotropic initial conditions, the slope of the FLS is often about two-thirds the slope of the drained failure envelope for clean sands. Specimens tested under anisotropic initial conditions, however, indicate that the FLS is steeper for soils with high initial (drained) shear stress compared to soils with lower initial shear stress at the same void ratio (Figure 9.17). The FLS may be very close to the initial stress point when initial shear stresses are large, in which case flow liquefaction may be initiated by only a very small undrained disturbance (Kramer and Seed, 1988). Case histories that have been attributed to *spontaneous liquefaction* probably involved initial shear stresses that were high enough that the small undrained disturbance required to initiate flow liquefaction was not observed.

The *limited liquefaction* behavior exhibited by specimens *C* and *D* (Figure 9.16) is significant for cases in which the static shear stress increases (as in the case of monotonic loading described in this section). In such cases the shearing resistance may drop to values at the point of phase transformation (or the quasi-steady state) that are lower than the steady-state strength. This temporary drop in shearing resistance may produce shear strains of 5% to 20% (Ishihara, 1993) and result in unacceptably large permanent deformations. Because the effects of initial conditions are not erased completely at these strain levels, they influence the quasi-steady-state strength. Procedures for estimation of quasi-steady-state strength are given by Ishihara (1993). Because the static component of shear stress generally remains constant or decreases during earthquakes, the quasi-steady state is less likely to be reached as a result of earthquake shaking.

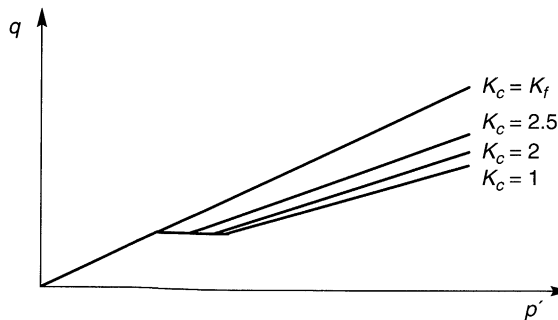


Figure 9.17 Variation of flow liquefaction surface inclination with initial principal effective stress ratio for constant void ratio.

9.5.1.2 Cyclic Loading

Vaid and Chern (1983) first showed that the FLS applied to both cyclic and monotonic loading, and a considerable amount of independent experimental evidence supports that observation. Other experimental evidence (e.g., Alarcon-Guzman et al., 1988) suggests that the effective stress path can move somewhat beyond the FLS before liquefaction is initiated by cyclic loading. Whether liquefaction is initiated precisely at the FLS under cyclic as well as monotonic loading is not currently known with certainty. Because the FLS is used as part of a conceptual model of liquefaction behavior in this book, and because it is slightly more conservative to do so, the FLS will be assumed to apply to both cyclic and monotonic loading.

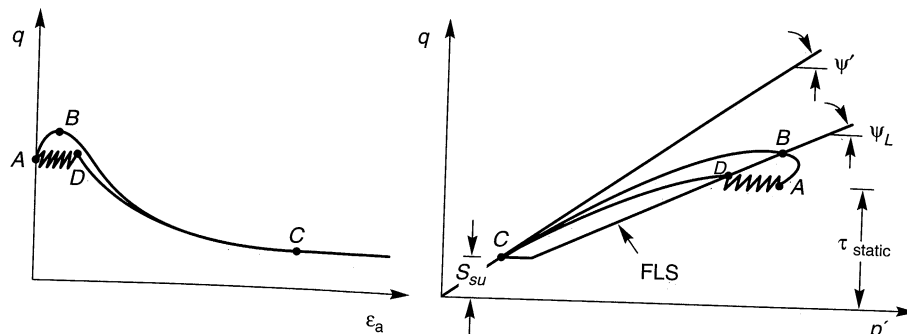


Figure 9.18 Initiation of flow liquefaction by cyclic and monotonic loading. Although the stress conditions at the initiation of liquefaction are different for the two types of loading (points *B* and *D*), both lie on the FLS.

Consider the responses of two identical, anisotropically consolidated, triaxial specimens of loose, saturated sand (Figure 9.18). Initially, the specimens are in drained equilibrium (point *A*) under a static shear stress, τ_{static} , that is greater than the steady-state strength, S_{su} . The first specimen is loaded monotonically (under undrained conditions): the shearing resistance builds up to a peak value when the stress path reaches the FLS (point *B*). At that point the specimen becomes unstable and strains rapidly toward the steady state (point *C*). The second specimen is loaded cyclically (also under undrained conditions): the effective stress path moves to the left as positive excess pore pressures develop and permanent strains accumulate. When the effective stress path reaches the FLS (at point *D*), the specimen becomes unstable and strains toward the steady state of deformation (point *C*). Although the effective stress conditions at the initiation of liquefaction (points *B* and *D*) were different, they fell in both cases on the FLS. The FLS, therefore, marks the onset of the instability that produces flow liquefaction. Lade (1992) provided a detailed description of this instability from a continuum mechanics standpoint.

9.5.1.3 Development of Flow Liquefaction

Flow liquefaction occurs in two stages. The first stage, which takes place at small strain levels, involves the generation of sufficient excess pore pressure to move the stress path from its initial position to the FLS. This excess pore pressure may be generated by undrained monotonic or cyclic loading. When the effective stress path reaches the FLS, the soil becomes inherently unstable and the second stage begins. The second stage involves strain-softening (and additional excess pore pressure generation) that is driven by the shear stresses required for static equilibrium. These shear stresses are the *driving stresses*—they must be distinguished from the *locked-in stresses* that develop during deposition and consolidation of the soil (Castro, 1991). Locked-in shear stresses, such as those that exist beneath level ground when $K_0 \neq 1$, cannot drive a flow liquefaction failure. Large strains develop in the second stage as the effective stress path moves from the FLS to the steady state. If the first stage takes the soil to the FLS under undrained, stress-controlled conditions, the second stage is inevitable.

9.5.2 Influence of Excess Pore Pressure

The generation of excess pore pressure is the key to the initiation of liquefaction. Without changes in pore pressure, hence changes in effective stress, neither flow liquefaction nor cyclic mobility can occur. The different phenomena can, however, require different levels of pore pressure to occur.

9.5.2.1 Flow Liquefaction

Flow liquefaction can be initiated by cyclic loading only when the shear stress required for static equilibrium is greater than the steady-state strength. In the field, these shear stresses are caused by gravity and remain essentially constant until large deformations develop. Therefore, initial states that plot in the shaded region of Figure 9.19 are susceptible to flow liquefaction. The occurrence of flow liquefaction, however, requires an undrained disturbance strong enough to move the effective stress path from its initial point to the FLS.

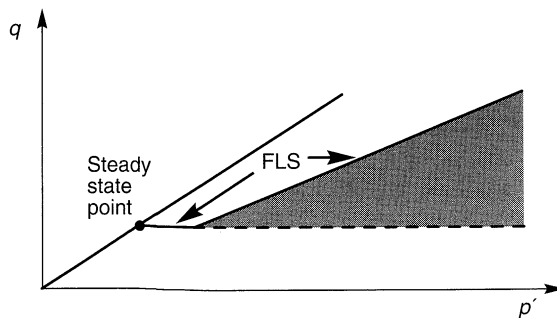


Figure 9.19 Zone of susceptibility to flow liquefaction. If initial conditions fall within the shaded zone, flow liquefaction will occur if an undrained disturbance brings the effective stress path from the point describing the initial conditions to the FLS.

If the initial stress conditions plot near the FLS, as they would in an element of soil subjected to large shear stresses under drained conditions, flow liquefaction can be triggered by small excess pore pressures (Kramer and Seed, 1988). The liquefaction resistance will be greater if the initial stress conditions are farther from the flow liquefaction surface. The FLS can be used to estimate the pore pressure ratio at the initiation of flow liquefaction; it decreases substantially with increasing initial stress ratio (Figure 9.20) for soils at a particular void ratio. At high initial stress ratios, flow liquefaction can be triggered by very small static or dynamic disturbances.

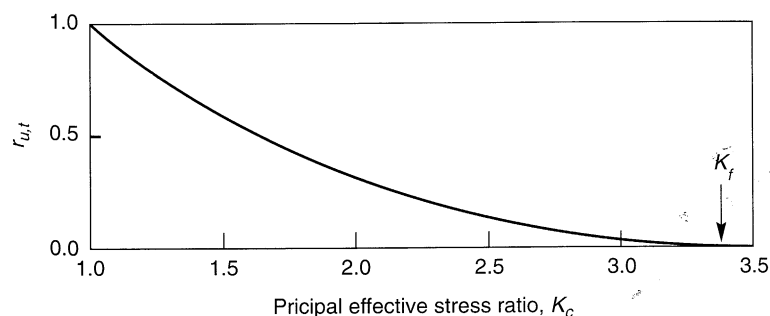


Figure 9.20 Variation of pore pressure ratio ($r_{u,t} = u_t / \sigma'_{vc}$) required to trigger flow liquefaction in triaxial specimens of Sacramento River Fine Sand with initial principal effective stress ratio.

9.5.2.2 Cyclic Mobility

Although flow liquefaction cannot occur, cyclic mobility can develop when the static shear stress is smaller than the steady-state shear strength. Therefore, initial states that plot in the shaded region of Figure 9.21 are susceptible to cyclic mobility. Note that cyclic mobility can occur in both loose and dense soils (the shaded region of Figure 9.21 extends from very low to very high effective confining pressures and corresponds to states that would plot both above and below the SSL). The development of cyclic mobility can be illustrated by the response of soils in cyclic triaxial tests. Three combinations of initial conditions and cyclic loading conditions generally produce cyclic mobility.

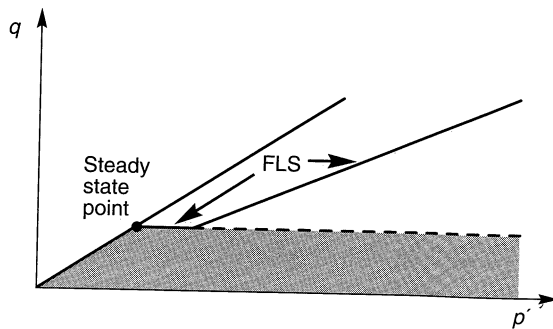


Figure 9.21 Zone of susceptibility to cyclic mobility. If initial conditions plot within shaded zone, cyclic mobility can occur.

The first, illustrated in Figure 9.22a, occurs when $\tau_{static} - \tau_{cyc} > 0$ (i.e., no shear stress reversal) and $\tau_{static} + \tau_{cyc} < S_{su}$ (no exceedance of steady-state strength). In this case the effective stress path moves to the left until it reaches the drained failure envelope. Since it cannot cross the drained failure envelope, additional loading cycles simply cause it to move up and down along the envelope. As a result, the effective stress conditions stabilize. Flow-type deformations cannot develop because any unidirectional straining would induce dilation. The effective confining pressure has decreased significantly, and the resulting low stiffness can allow significant permanent strains to develop within each loading cycle.

The second condition (Figure 9.22b) occurs when $\tau_{static} - \tau_{cyc} > 0$ (no stress reversal) and $\tau_{static} + \tau_{cyc} > S_{su}$ (steady-state strength is exceeded momentarily). Again, cyclic loading will cause the effective stress path to move to the left. When it touches the FLS, momentary periods of instability will occur. Significant permanent strain may develop during these

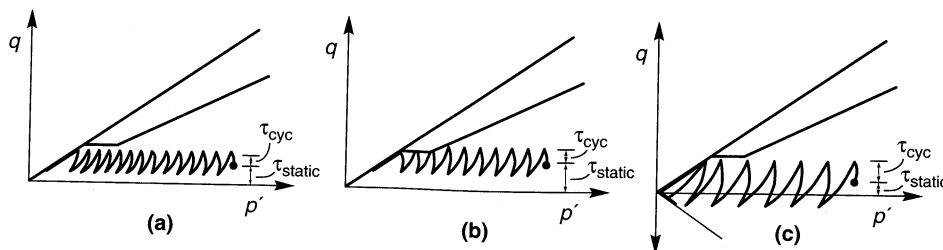


Figure 9.22 Three cases of cyclic mobility: (a) no stress reversal and no exceedance of the steady-state strength; (b) no stress reversal with momentary periods of steady-state strength exceedance; (c) stress reversal with no exceedance of steady-state strength.

periods, particularly if τ_{static} is greater than the quasi-static shear strength, but the straining will generally cease at the end of cyclic loading when the shear stress returns to τ_{static} .

The final condition is that in which $\tau_{\text{static}} - \tau_{\text{cyc}} < 0$ (stress reversal occurs) and $\tau_{\text{static}} + \tau_{\text{cyc}} < S_{su}$ (steady-state strength is not exceeded). In this case (Figure 9.22c) the direction of the shear stress changes so that each cycle includes both compressional and extensional loading. Experimental evidence (e.g., Dobry et al., 1982; Mohamad and Dobry, 1986) has shown that the rate of pore pressure generation increases with increasing degree of stress reversal. Hence the effective stress path moves relatively quickly to the left (because excess pore pressure builds up quickly) and eventually oscillates along the compression and extension portions of the drained failure envelope. Each time the effective stress path passes through the origin (it does so twice during each loading cycle), the specimen is in an instantaneous state of zero effective stress ($r_u = 100\%$). Although this state of zero effective stress is referred to as *initial liquefaction* (Seed and Lee, 1966), it should not be taken to imply that the soil has no shear strength. If monotonic loading is applied at the state of initial liquefaction, the specimen will dilate until the steady-state strength is mobilized (Figure 9.23). Significant permanent strains may accumulate during cyclic loading, but flow failure cannot occur. Note that initial liquefaction can only occur when stress reversals occur.

In contrast to flow liquefaction, there is no clearcut point at which cyclic mobility is initiated. Permanent strains, and the permanent deformations they produce, accumulate incrementally. Their magnitude depends on the static shear stress and the duration of the ground motion. For ground motions of short duration at nearly level sites, permanent deformations may be small. For moderately sloping sites or gently sloping sites subjected to ground motions of long duration, cyclic mobility can produce damaging levels of soil deformation.

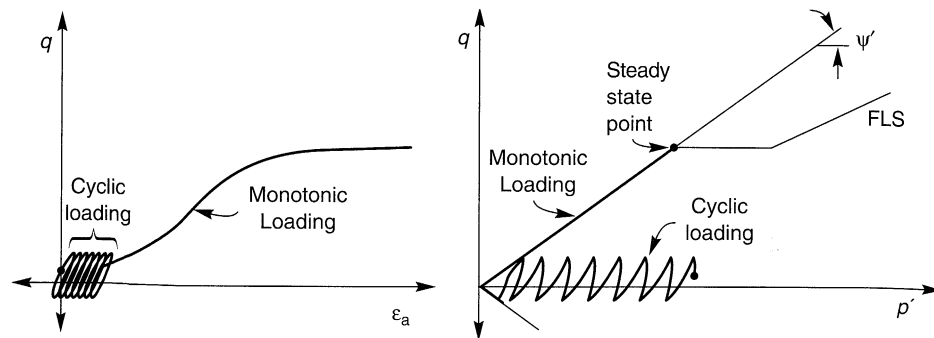


Figure 9.23 Dilative behavior of specimen loaded monotonically after occurrence of cyclic mobility. Cyclic loading with stress reversal causes the effective confining pressure to decrease rapidly, eventually reaching momentary values of zero. Subsequent monotonic loading, however, causes dilation as the steady-state strength is mobilized.

9.5.3 Evaluation of Initiation of Liquefaction

The combination of steady-state and flow liquefaction surface concepts described in Section 9.5.2 provides a framework in which the basic mechanisms of liquefaction can be understood. This framework integrates liquefaction susceptibility with liquefaction initiation and

liquefaction effects. It also illustrates the important influence of excess pore pressure generation on the extent of liquefaction-related hazards.

A number of approaches to evaluation of the potential for initiation of liquefaction have developed over the years. In the following sections, the most common of these—the *cyclic stress approach* and a useful alternative, the *cyclic strain approach*—are presented. Each has advantages and limitations, and each is preferred by different groups of engineers. For particularly important projects, it is not unusual to use more than one approach in a liquefaction hazard evaluation.

9.5.3.1 Cyclic Stress Approach

In the 1960s and 1970s, many advances in the state of knowledge of liquefaction phenomena resulted from the pioneering work of H. B. Seed and his colleagues at the University of California at Berkeley. This research was directed largely toward evaluation of the loading conditions required to trigger liquefaction. This loading was described in terms of cyclic shear stresses, and liquefaction potential was evaluated on the basis of the amplitude and number of cycles of earthquake-induced shear stress. The general approach has come to be known as the *cyclic stress approach*.

Seed and Lee (1966) defined *initial liquefaction* as the point at which the increase in pore pressure is equal to the initial effective confining pressure [i.e., when $u_{\text{excess}} = \sigma'_{3c}$ (or when $r_u = 100\%$)]. Because most of the early laboratory testing investigations were based on cyclic triaxial tests on isotropically consolidated specimens (consequently, with complete stress reversal), initial liquefaction could be produced in both loose and dense specimens. According to the definitions of Section 9.2, this behavior would now be classified (since the static shear stress was zero) as cyclic mobility. The use of the term *initial liquefaction* led many to the erroneous belief that flow liquefaction could be initiated in any loose or dense cohesionless soil.

The cyclic stress approach is conceptually quite simple: the earthquake-induced loading, expressed in terms of cyclic shear stresses, is compared with the liquefaction resistance of the soil, also expressed in terms of cyclic shear stresses. At locations where the loading exceeds the resistance, liquefaction is expected to occur. Application of the cyclic stress approach, however, requires careful attention to the manner in which the loading conditions and liquefaction resistance are characterized.

Characterization of Earthquake Loading. The level of excess pore pressure required to initiate liquefaction is related to the amplitude and duration of earthquake-induced cyclic loading. The cyclic stress approach is based on the assumption that excess pore pressure generation is fundamentally related to the cyclic shear stresses, hence seismic loading is expressed in terms of cyclic shear stresses. The loading can be predicted in two ways: by a detailed ground response analysis or by the use of a simplified approach.

Ground response analyses (Chapter 7) can be used to predict time histories of shear stress at various depths within a soil deposit. Such analyses produce time histories with the transient, irregular characteristics of actual earthquake motions. However, the laboratory data from which liquefaction resistance can be estimated are usually obtained from tests in which the cyclic shear stresses have uniform amplitudes. Therefore, comparison of earthquake-induced loading with laboratory-determined resistance requires conversion of an irregular time history of shear stress to an equivalent series of uniform stress cycles. Seed et

al. (1975a) applied a weighting procedure to a set of shear stress time histories from recorded strong ground motions to determine the number of uniform stress cycles, N_{eq} (at an amplitude of 65% of the peak cyclic shear stress, i.e., $\tau_{cyc} = 0.65\tau_{max}$) that would produce an increase in pore pressure equivalent to that of the irregular time history (Figure 9.24). Similar relationships have been developed for other stress levels (e.g., Haldar and Tang, 1981) but the 65% level is most commonly used. In all cases, the equivalent number of uniform stress cycles increases with increasing earthquake magnitude (just as strong-motion duration increases with increasing earthquake magnitude).

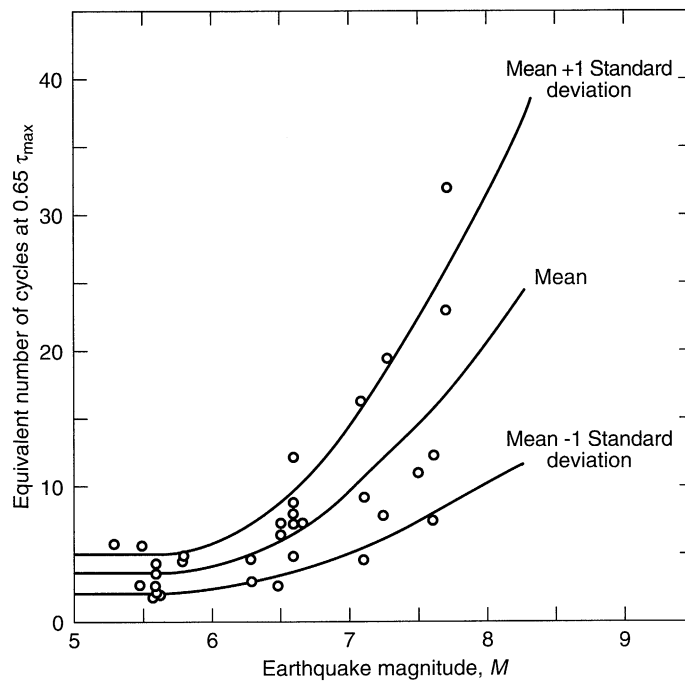


Figure 9.24 Number of equivalent uniform stress cycles, N_{eq} , for earthquakes of different magnitude. (After Seed, et al., 1975a.)

Example 9.1

Figure E9.1 shows a typical irregular time history of shear stress that was produced by a $M_w = 7.0$ earthquake. Estimate the amplitude and number of loading cycles of an equivalent series of uniform stress cycles.

Solution Figure E9.1 shows that the maximum shear stress is 780 lb/ft^2 (37.4 kPa). Consequently, the amplitude of the equivalent series of uniform stress cycles is

$$\tau_{cyc} = 0.65\tau_{max} = (0.65)(780 \text{ lb/ft}^2) = 507 \text{ lb/ft}^2 \text{ (24.3 kPa)}$$

Referring to Figure 9.28, the corresponding equivalent number of cycles is approximately 10 (although values ranging from 5 to 14 would fall within one standard deviation of that value).

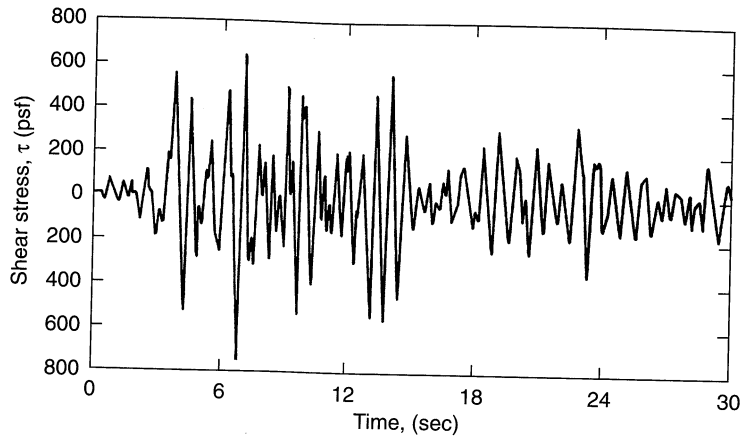


Figure E9.1 Typical irregular time history of shear stress. For liquefaction purposes, 10 cycles of harmonic shear stress at 510 lb/ft² would be considered equivalent to this time history.

The uniform cyclic shear stress amplitude for level (or gently sloping) sites can also be estimated from a simplified procedure (Seed and Idriss, 1971) as

$$\tau_{cyc} = 0.65 \frac{a_{max}}{g} \sigma_v r_d \tag{9.2}$$

where a_{max} is the peak ground surface acceleration, g the acceleration of gravity, σ_v the total vertical stress, and r_d the value of a stress reduction factor (Figure 9.25) at the depth of interest. This uniform cyclic shear stress is assumed to be applied for the equivalent number of cycles shown in Figure 9.24.

Regardless of whether a detailed ground response analysis or the simplified procedure is used, the earthquake-induced loading is characterized by a level of uniform cyclic shear stress that is applied for an equivalent number of cycles.

Example 9.2

The site shown in Figure E9.2a is subjected to earthquake shaking that produces a peak ground acceleration of 0.22g. Estimate and plot the variation of maximum shear stress with depth. Compute and plot the variation of equivalent uniform cyclic shear stress with depth.

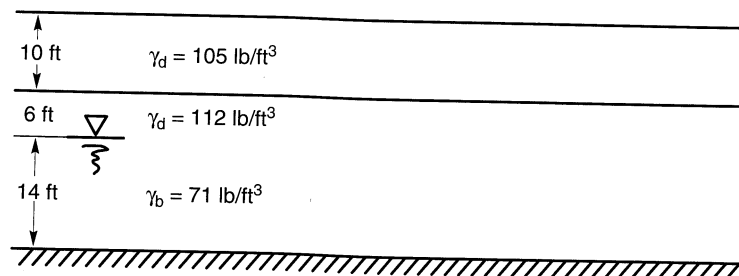


Figure E9.2a

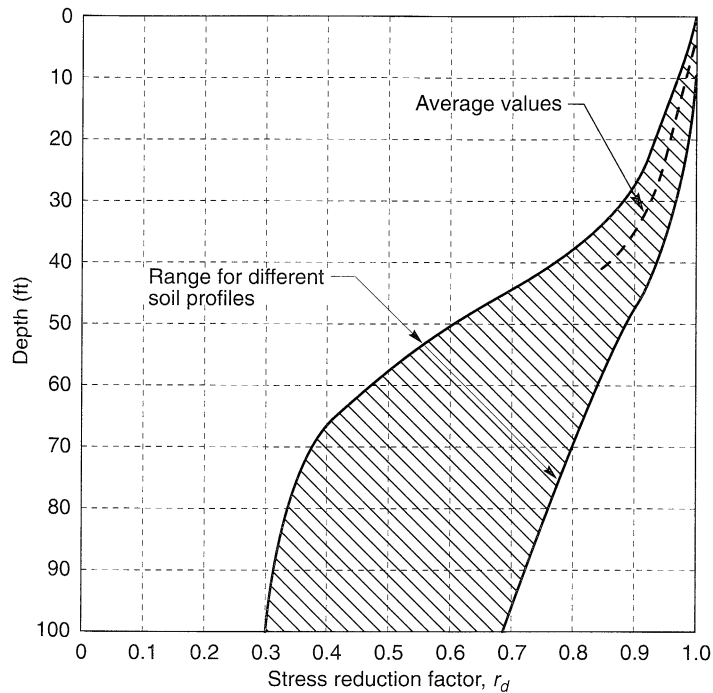


Figure 9.25 Reduction factor to estimate the variation of cyclic shear stress with depth below level or gently sloping ground surfaces. (After Seed and Idriss, 1971.)

Solution Using the simplified procedure of Seed and Idriss (1971), the maximum shear stress can be estimated from

$$\tau_{\max} = \frac{a_{\max}}{g} \sigma_v r_d$$

Estimation of the variation of τ_{\max} with depth requires evaluation of the variation of total vertical stress, σ_v , and stress reduction factor, r_d , with depth. At depths of 5 ft and 25 ft, for example, the total vertical stresses are

$$\sigma_v(z = 5 \text{ ft}) = (5 \text{ ft})(105 \text{ lb/ft}^3) = 525 \text{ lb/ft}^2$$

$$\begin{aligned} \sigma_v(z = 25 \text{ ft}) &= (10 \text{ ft})(105 \text{ lb/ft}^3) + (6 \text{ ft})(112 \text{ lb/ft}^3) + (9 \text{ ft})(71 \text{ lb/ft}^3 + 62.4 \text{ lb/ft}^3) \\ &= 2923 \text{ lb/ft}^2 \end{aligned}$$

At the same depths, Figure 9.29 indicates that the stress reduction factor has values of

$$r_d(z = 5 \text{ ft}) = 0.992$$

$$r_d(z = 25 \text{ ft}) = 0.947$$

The maximum shear stresses at depths of 5 ft and 25 ft can then be estimated as

$$\tau_{\max}(z = 5 \text{ ft}) = (0.22)(525 \text{ lb/ft}^2)(0.992) = 115 \text{ lb/ft}^2$$

$$\tau_{\max}(z = 25 \text{ ft}) = (0.22)(2923 \text{ lb/ft}^2)(0.947) = 609 \text{ lb/ft}^2$$

The equivalent uniform cyclic shear stresses are simply taken as 65% of the maximum shear stresses, i.e.

$$\tau_{\text{cyc}} = (z = 5 \text{ ft}) = 0.65\tau_{\text{max}}(z = 5 \text{ ft}) = (0.65)(115 \text{ lb/ft}^2) = 75 \text{ lb/ft}^2$$

$$\tau_{\text{cyc}} = (z = 5 \text{ ft}) = 0.65\tau_{\text{max}}(z = 5 \text{ ft}) = (0.65)(609 \text{ lb/ft}^2) = 396 \text{ lb/ft}^2$$

By repeating this process for other depths, the variations of τ_{max} and τ_{cyc} can be determined and plotted as in Figure E9.2b.

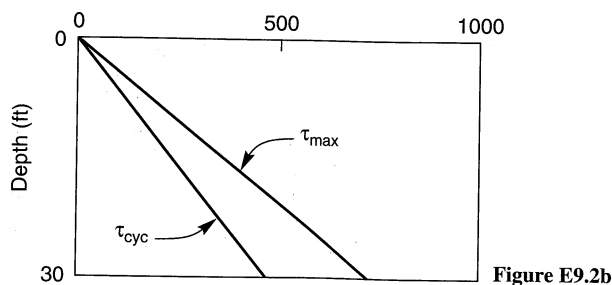


Figure E9.2b

Characterization of Liquefaction Resistance. The liquefaction resistance of an element of soil depends on how close the initial state of the soil is to the state corresponding to “failure” and on the nature of the loading required to move it from the initial state to the failure state. As the preceding sections have shown, however, the failure state is different for flow liquefaction and cyclic mobility. The failure state for flow liquefaction is easily defined using the FLS, and its initiation is easily recognized in the field. The definition of failure for cyclic mobility is imprecise—a certain level of deformation caused by cyclic mobility may be excessive at some sites and acceptable at others. In contrast to flow liquefaction, there is no distinct point at which cyclic mobility “failure” can be defined. Cyclic mobility failure is generally considered to occur when pore pressures become large enough to produce ground oscillation, lateral spreading, or other evidence of damage at the ground surface. This definition of failure is imprecise; in practice the presence of sand boils is frequently taken as evidence of cyclic mobility. The development of sand boils, however, depends not only on the characteristics of the liquefiable sand but also on the characteristics (e.g., thickness, permeability, and intactness) of any overlying soils (Section 9.6.2).

In the field, where stresses and pore pressures are seldom measured, it is often difficult to distinguish between different liquefaction phenomena after an earthquake has occurred. When the cyclic stress approach was developed, little distinction was made between the different liquefaction phenomena—cases of flow liquefaction and cyclic mobility were lumped together under the general heading of “liquefaction.” Characterization of liquefaction resistance developed along two lines: methods based on the results of laboratory tests, and methods based on in situ tests and observations of liquefaction behavior in past earthquakes.

Characterization Based on Laboratory Tests. The early development of the cyclic stress approach emphasized laboratory testing for characterization of liquefaction resistance. To create an initial condition of zero driving stress (to simulate the stress conditions on

horizontal planes beneath level ground), most laboratory tests were performed on isotropically consolidated triaxial specimens or on K_0 -consolidated simple shear specimens. In these tests, "liquefaction failure" was usually defined as the point at which initial liquefaction was reached or at which some limiting cyclic strain amplitude (commonly 5% for dense specimens) was reached.

Laboratory tests show that the number of loading cycles required to produce liquefaction failure, N_L , decreases with increasing shear stress amplitude and with decreasing density (Figure 9.26). While liquefaction failure can occur in only a few cycles in a loose specimen subjected to large cyclic shear stresses, thousands of cycles of low-amplitude shear stresses may be required to cause liquefaction failure of a dense specimen. The relationship between density, cyclic stress amplitude, and number of cycles to liquefaction failure can be expressed graphically by laboratory *cyclic strength curves*, such as those shown in Figure 9.27. Cyclic strength curves are frequently normalized by the initial effective overburden pressure to produce a *cyclic stress ratio* (CSR). The CSR must be defined differently for different types of tests. For the cyclic simple shear test, the CSR is taken as the ratio of the cyclic shear stress to the initial vertical effective stress [i.e., $(CSR)_{ss} = \tau_{cyc}/\sigma'_{v0}$]. For the cyclic triaxial test, it is taken as the ratio of the maximum cyclic shear stress to the initial effective confining pressure [i.e., $(CSR)_{tx} = \sigma_{dc}/2\sigma'_{3c}$]. As discussed in Chapter 6, the cyclic simple shear and cyclic triaxial tests impose quite different loading, and their cyclic stress ratios are not equivalent. For liquefaction testing, the two are usually related by

$$(CSR)_{ss} = c_r(CSR)_{tx} \quad (9.3)$$

where the correction factor, c_r , is estimated from Table 9-1.

In contrast to laboratory cyclic simple shear and cyclic triaxial tests, earthquakes produce shear stresses in different directions. Multidirectional shaking has been shown (Pyke, et al., 1975) to cause pore pressures to increase more rapidly than does unidirectional shaking. Seed, et al. (1975b) suggested that the CSR required to produce initial liquefaction in

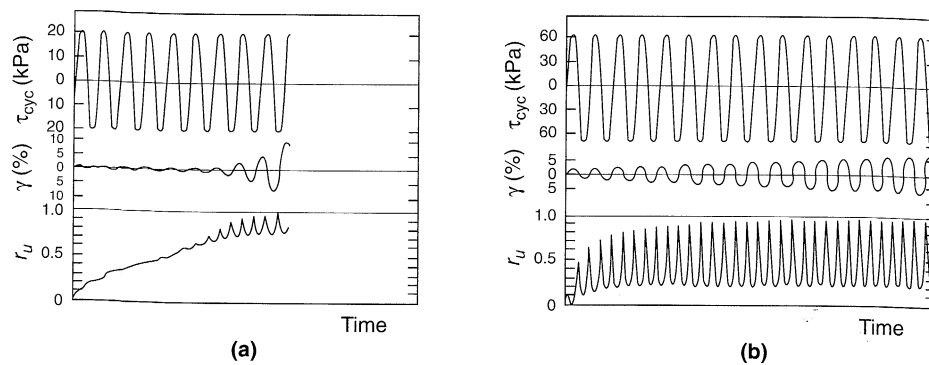


Figure 9.26 Results of torsional shear tests on isotropically consolidated ($\sigma'_0 = 98$ kPa) specimens of (a) loose sand (47% relative density) and (b) dense sand (75% relative density). Loose specimen reached initial liquefaction ($r_u = 1.00$) on 10th loading cycle. Despite much higher loading, dense specimen has not quite reached initial liquefaction after 17 cycles. (After Ishihara, 1985; used by permission of Kluwer Academic Publishers.)

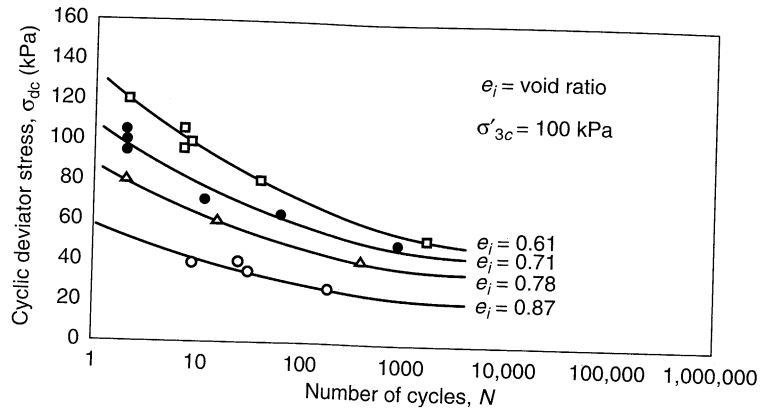


Figure 9.27 Cyclic stresses required to produce initial liquefaction and 20% axial strain in isotropically consolidated Sacramento River Sand triaxial specimens. (After Seed and Lee, 1965.)

Table 9-1 Values of CSR Correction Factor, c_r

Reference	Equation	c_r for:	
		$K_0 = 0.4$	$K_0 = 1.0$
Finn et al. (1971)	$c_r = (1 + K_0)/2$	0.7	1.0
Seed and Peacock (1971)	Varies	0.55–0.72	1.0
Castro (1975)	$c_r = 2(1 + 2K_0)/3\sqrt{3}$	0.69	1.15

the field was about 10% less than that required in unidirectional cyclic simple shear tests. Therefore, the liquefaction resistance of an element of soil in the field is given by the cyclic stress ratio

$$(CSR)_{\text{field}} = \frac{\tau_{\text{cyc}}}{\sigma'_{v0}} = 0.9(CSR)_{ss} = 0.9c_r(CSR)_{tx} \quad (9.4)$$

Example 9.3

A 2-m-thick layer of Sacramento River Sand ($e = 0.87$; $\phi' = 33^\circ$) is overlain by 4 m of compacted fill ($\rho_r = 2.1 \text{ Mg/m}^3$). The water table is at the bottom of the fill. Using the cyclic triaxial test results shown in Figure 9.27, estimate the maximum cyclic shear stress required to initiate liquefaction in the sand in a magnitude 7.5 earthquake.

Solution The sand is under an average effective vertical stress of

$$\sigma'_{v0} = [(4 \text{ m})(2.1 \text{ Mg/m}^3) + (1.0 \text{ m})(0.91 \text{ Mg/m}^3)] \left(9.81 \frac{\text{m}}{\text{sec}^2} \right) = 91.3 \text{ kPa}$$

which is close to the effective confining pressures of the cyclic triaxial test data shown in Figure 9.27.

Using Figure 9.24, a magnitude 7.5 earthquake would be expected to produce about 14 uniform stress cycles (at 65% of the maximum shear stress). From Figure 9.27, the cyclic deviator

stress that would cause initial liquefaction in 14 cycles would be about 39 kPa. Then the triaxial cyclic stress ratio is

$$(\text{CSR})_{tx} = \frac{\sigma_{dc}}{2\sigma_{3c}} = \frac{39 \text{ kPa}}{(2)(100 \text{ kPa})} = 0.195$$

The corresponding field cyclic stress ratio can be determined using equation (9.4). Letting $K_0 = 1 - \sin \phi' = 0.46$, we have

$$(\text{CSR})_{\text{field}} = 0.9c_r(\text{CSR})_{tx} = 0.9 \frac{1+0.46}{2}(0.195) = 0.128$$

Then

$$\tau_{\text{cyc}} = (\text{CSR})_{\text{field}}\sigma'_{v0} = (0.128)(91.3 \text{ kPa}) = 11.7 \text{ kPa}$$

$$\tau_{\text{max}} = \frac{\tau_{\text{cyc}}}{0.65} = \frac{11.7 \text{ kPa}}{0.65} = 18.0 \text{ kPa}$$

Therefore, a peak shear stress of 18 kPa would be required to initiate liquefaction in the Sacramento River Sand in a magnitude 7.5 earthquake.

Laboratory tests can also reveal the manner in which excess pore pressure is generated. For stress-controlled cyclic tests with uniform loading, Lee and Albaisa (1974) and DeAlba et al. (1975) found that the pore pressure ratio, r_u , is related to the number of loading cycles by

$$r_u = \frac{1}{2} + \frac{1}{\pi} \sin^{-1} \left[2 \left(\frac{N}{N_L} \right)^{1/\alpha} - 1 \right] \quad (9.5)$$

where N_L is the number of cycles required to produce initial liquefaction ($r_u = 1.00$) and α is a function of the soil properties and test conditions. As illustrated in Figure 9.28, excess pore pressures increase quickly in the first and last loading cycles. Equation (9.5) can be used to estimate the excess pore pressure generated when initial liquefaction does not occur (i.e., when $N_{\text{eq}} < N_L$). In an approach that could address irregular loading, Martin et al.

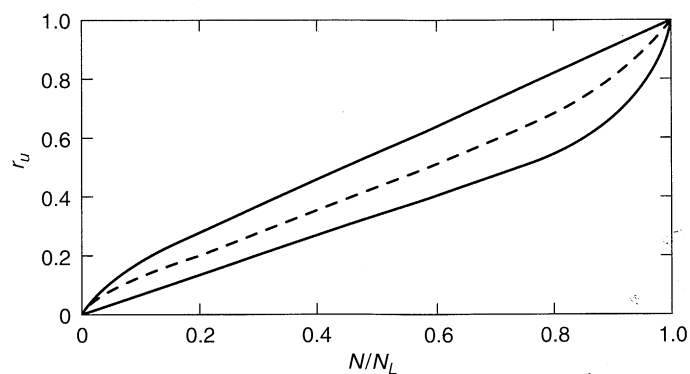


Figure 9.28 Rate of pore pressure generation in cyclic simple shear tests. The dashed line was generated from equation (9.5) with $\alpha = 0.7$. (After De Alba et al., 1975.)

(1975) developed a fundamental model that combined data on the rate of settlement of cyclically loaded dry sand with data on the rebound and stress–deformation characteristics of the soil to predict pore pressure generation. The model has been incorporated into non-linear ground response analyses to provide an effective stress-based approach to liquefaction analysis (Section 9.5.3.3).

For a number of years, liquefaction resistance was commonly characterized by cyclic stresses determined from laboratory tests. However, subsequent work showed that cyclic stress-based measures of liquefaction resistance are influenced by factors other than the initial density and stress conditions. For example, liquefaction resistance is influenced by differences in the structure of the soil (or *soil fabric*) produced by different methods of specimen preparation (Ladd, 1974; Mulilis et al., 1975; Toki et al., 1986; Tatsuoka et al., 1986). The history of prior seismic straining also influences liquefaction resistance [i.e., the liquefaction resistance of a specimen that has been subjected to prior seismic straining is greater than that of a specimen of the same density that has not (Finn et al., 1970; Seed et al., 1975b)]. Also, liquefaction resistance increases with increasing overconsolidation ratio and lateral earth pressure coefficient (Seed and Peacock, 1971). Finally, the length of time under sustained pressure has been shown (Ohsaki, 1969; Seed, 1979; Yoshimi et al., 1989) to increase the liquefaction resistance. These additional parameters are all functions of the depositional and historical environment of a soil deposit, and they tend to influence soil behavior primarily at the low strain levels associated with the initiation of liquefaction. These low-strain effects are easily destroyed by sampling disturbance, and are very difficult to replicate in reconstituted specimens. Because of these factors, characterization of liquefaction resistance by laboratory testing is extremely difficult and has been supplanted by methods based on in situ test results for many projects. Truly undisturbed sampling (e.g., by careful ground freezing and coring) is required for laboratory tests to be able to characterize liquefaction resistance reliably.

Cyclic triaxial tests of liquefaction resistance can also be complicated by specimen nonuniformity. As high pore pressures develop in a cyclic triaxial test specimen, the soil grains tend to settle causing densification of the lower part and loosening of the upper part of the specimen. The nonuniform density leads to nonuniform strain, and eventually to thinning or *necking* of the upper portion of the specimen. This nonuniformity can cause considerable uncertainty in the application of cyclic triaxial test results to field conditions.

Characterization Based on In Situ Tests. An alternative approach, first described by Whitman (1971), is to use liquefaction case histories to characterize liquefaction resistance in terms of measured in situ test parameters. Previous case histories can be characterized by the combination of a loading parameter, \mathcal{L} , and a liquefaction resistance parameter, \mathcal{R} , which can be plotted with a symbol that indicates whether liquefaction was or was not observed (Figure 9.29). A boundary can then be drawn between the \mathcal{L} – \mathcal{R} combinations that have and have not produced liquefaction in past earthquakes. The boundary is usually drawn conservatively such that all cases in which liquefaction has been observed lie above it. In this approach, the cyclic stress ratio is usually used as the loading parameter, and in situ test parameters that reflect the density and pore pressure generation characteristics of the soil are used as liquefaction resistance parameters.

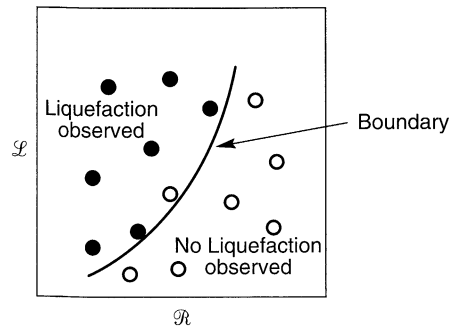


Figure 9.29 Typical plot showing combinations of loading parameter, \mathcal{L} , and liquefaction resistance parameter, \mathcal{R} , for cases where liquefaction has been observed (solid circles) and not observed (open circles). Boundary indicates minimum value of liquefaction resistance parameter required to prevent liquefaction.

1. Standard Penetration Resistance. In the United States and most other countries, the standard penetration test (SPT) has been the most commonly used in situ test for characterization of liquefaction resistance; factors that tend to increase liquefaction resistance (e.g. density, prior seismic straining, overconsolidation ratio, lateral earth pressures, and time under sustained pressure) also tend to increase SPT resistance. Seed et al. (1983) compared the corrected SPT resistance (Section 6.3.1.2) and cyclic stress ratio for clean sand (Figure 9.30) and silty sand (Figure 9.31) sites at which liquefaction was or was not observed in earthquakes of $M = 7.5$ to determine the minimum cyclic stress ratio at which liquefaction could be expected in a clean sand of a given SPT resistance.

The presence of fines can affect SPT resistance and therefore must be accounted for in the evaluation of liquefaction resistance (Seed et al., 1985; Ishihara and Kosecki, 1989; Koester, 1994). Examination of Figures 9.30 and 9.31 shows that the liquefaction resistance of sands is not influenced by fines unless the fines comprise more than 5% of the soil. At higher fines contents, the fines tend to inhibit liquefaction [i.e., the CSR required to initiate liquefaction (for a given $(N_1)_{60}$ value)]. The plasticity of the fines can also influence liquefaction resistance; the adhesion of plastic fines tends to resist the relative movement of individual soil particles and thereby reduce the generation of excess pore pressure during earthquakes. Laboratory tests (Ishihara and Koseki, 1989) indicate little influence at plasticity indices below 10, and a gradual increase in liquefaction resistance at plasticity indices greater than 10. Ishihara (1993) suggested that the effects of plasticity could be accounted for by multiplying the CSR by the factor

$$F = \begin{cases} 1.0 & \text{PI} \leq 10 \\ 1.0 + 0.022(\text{PI} - 10) & \text{PI} > 10 \end{cases} \quad (9.6)$$

Since most sandy soils in alluvial deposits and man-made fills have plasticity indices less than about 15, the effect of fines plasticity is usually small.

Because strong-motion duration (hence equivalent number of uniform stress cycles) increases with earthquake magnitude, the minimum cyclic stress ratio required to initiate liquefaction decreases with increasing magnitude. The minimum cyclic stress ratio for other magnitudes may be obtained by multiplying the cyclic stress ratio for $M = 7.5$ earthquakes by the factors shown in Table 9-2.

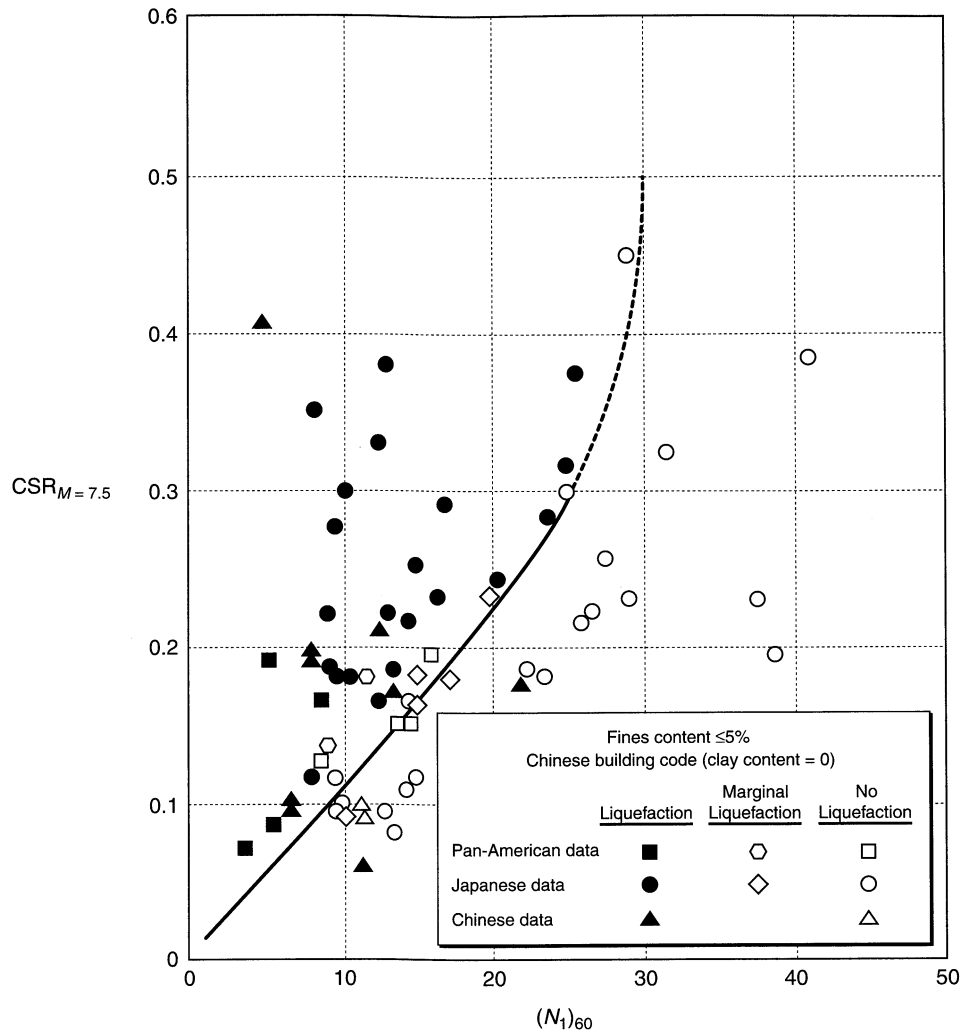


Figure 9.30 Relationship between cyclic stress ratios causing liquefaction and $(N_1)_{60}$ values for clean sands in $M = 7.5$ earthquakes. (After Seed et al. (1975). Influence of SPT procedures in soil liquefaction resistance evaluations, *Journal of Geotechnical Engineering*, Vol. 111, No. 12. Reprinted by permission of ASCE.)

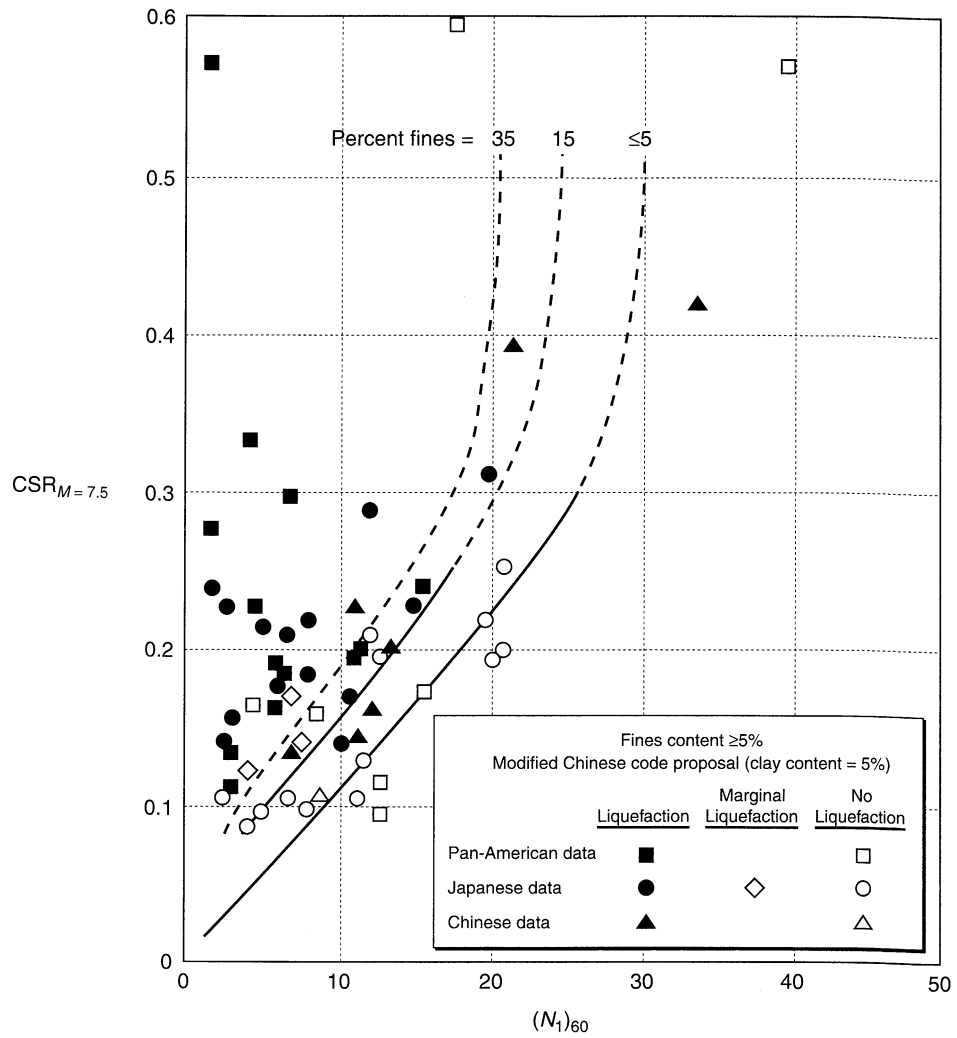


Figure 9.31 Relationship between cyclic stress ratios causing liquefaction and $(N_1)_{60}$ values for silty sands in $M = 7.5$ earthquakes. (After Seed et al. (1975). Influence of SPT procedures in soil liquefaction resistance evaluations, *Journal of Geotechnical Engineering*, Vol. 111, No. 12. Reprinted by permission of ASCE.)

Table 9-2 Magnitude Correction Factors for Cyclic Stress Approach

Magnitude, M	$CSR_M/CSR_{M=7.5}$
$5\frac{1}{4}$	1.50
6	1.32
$6\frac{3}{4}$	1.13
$7\frac{1}{2}$	1.00
$8\frac{1}{2}$	0.89

The data from which Figures 9.30 and 9.31 were developed correspond primarily to level-ground sites with relatively shallow deposits of potentially liquefiable soil. At sites with sloping ground conditions or at sites that support heavy structures, the presence of initial static shear stresses will influence liquefaction resistance. For conditions in which the static shear stress is greater than the steady-state strength, the initial conditions are closer to the FLS and the liquefaction resistance is reduced. Laboratory tests show that the cyclic shear stress required to trigger liquefaction increases at high effective confining pressures (greater than those of the field performance database). Seed (1983) proposed that the effects of initial shear stress and high effective confining pressures be accounted for by modifying the cyclic stress ratio as follows:

$$(CSR_{field})_{\alpha, \sigma} = (CSR_{field})_{\alpha=0, \sigma < 1 \text{ ton/ft}^2} K_{\alpha} K_{\sigma} \tag{9.7}$$

where $\alpha = \tau_{h, static} / \sigma'_{v0}$, and K_{α} and K_{σ} are correction factors for initial shear stress (Figure 9.32) and effective overburden pressure (Figure 9.33), respectively. The values of K_{α} and K_{σ} vary for different soils and should be evaluated on a site-specific basis whenever possible.

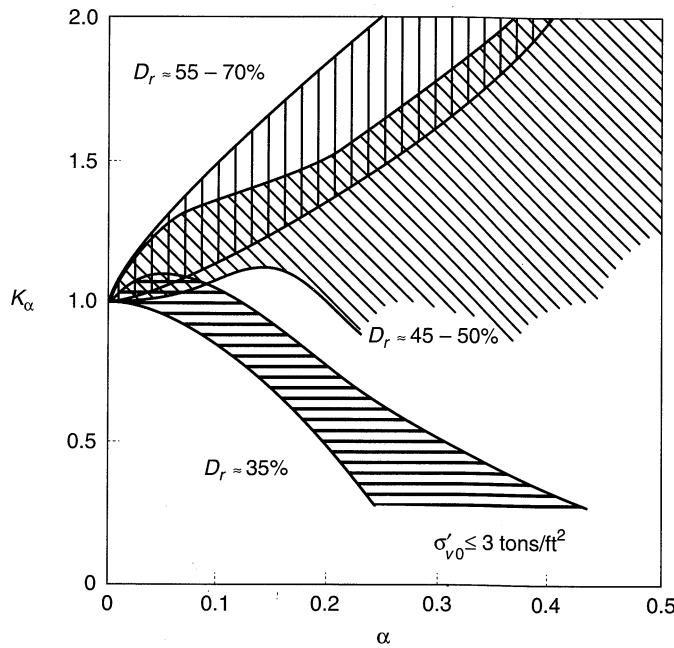


Figure 9.32 Variation of correction factor, K_{α} , with initial shear/normal stress ratio. (After Seed and Harder, 1990. *H. Bolton Seed Memorial Symposium Proceedings*, Vol. 2, p. 364. Used by permission of BiTech Publishers, Ltd.)

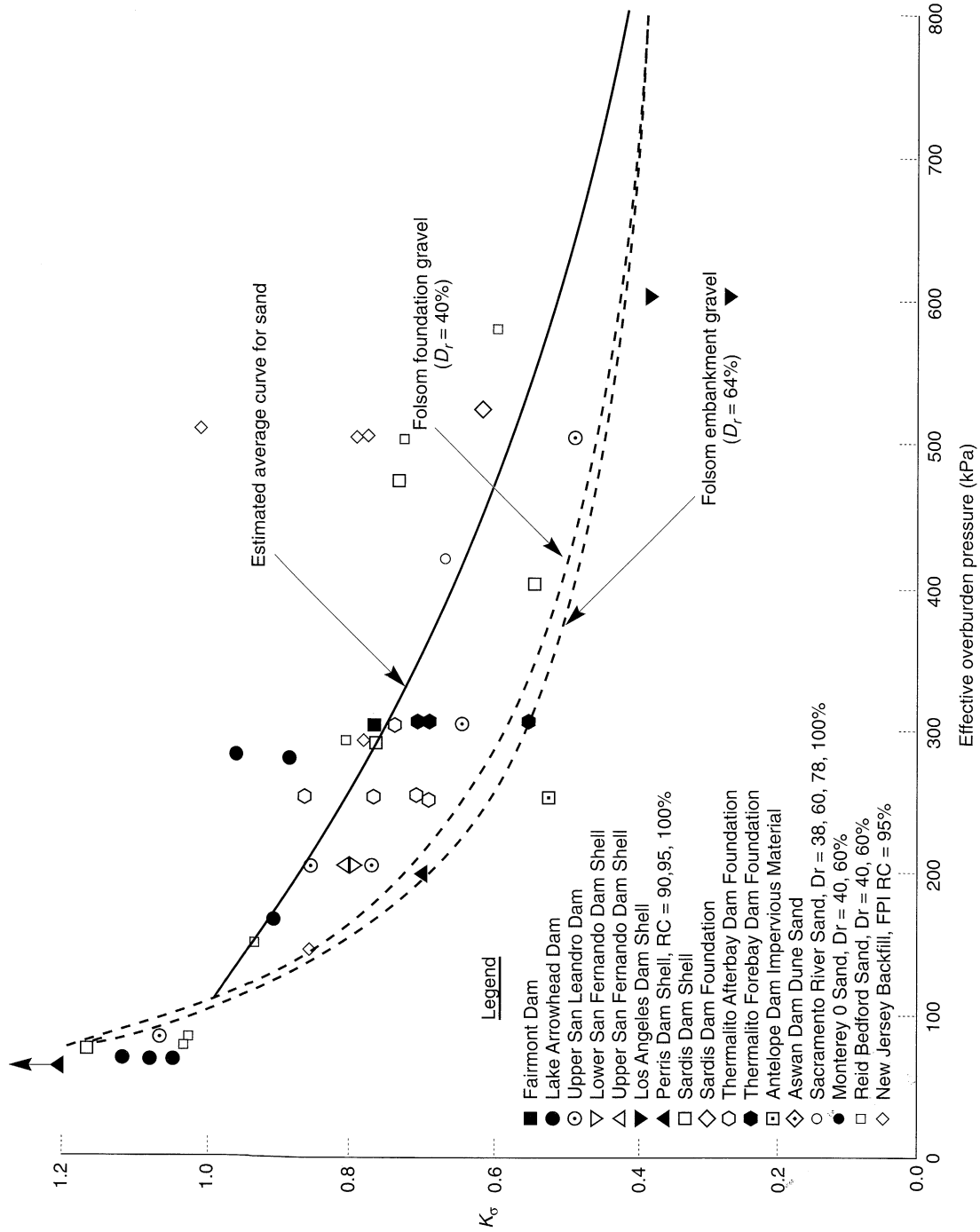


Figure 9.33 Variation of correction factor, K_g , with effective overburden pressure. (After Marcuson et al., 1990. Used by permission of EERI.)

2. Cone Penetration Resistance. The tip resistance from the cone penetration test (CPT) can also be used as a measure of liquefaction resistance; indeed, it has a pronounced advantage over the SPT in its ability to detect thin seams of loose soil. The database of sites at which CPT resistance has been measured and where the occurrence or nonoccurrence of liquefaction has been documented, although growing rapidly, remains fairly small. By supplementing these data with correlations between CPT and SPT resistances, the minimum cyclic stress ratio at which liquefaction can be expected in a clean sand of a given CPT resistance can be determined (e.g., Robertson and Campanella, 1985; Seed and DeAlba, 1986). Since the CPT-SPT correlation depends on grain size, CPT-based liquefaction curves have been developed for different mean grain sizes (Figure 9.34a). Mitchell and Tseng (1990) developed curves based on laboratory tests and theoretically derived values of CPT resistance (Figure 9.34b). CPT-SPT correlation that make use of the friction ratio as well as the tip resistance (Douglas et al., 1981; Martin, 1992) eliminate the need for measurement of mean grain size (and the drilling and sampling required to do so). In CPT-based liquefaction evaluations, the tip resistance is normalized to a standard effective overburden pressure of 1 ton/ft² (96 kPa) by

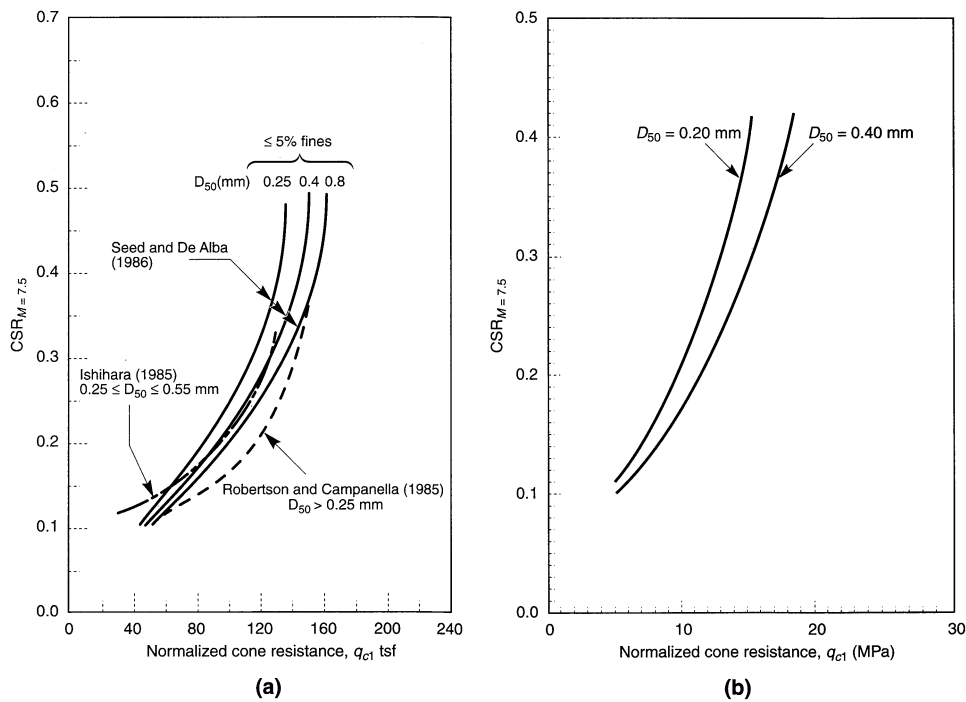


Figure 9.34 CPT-based liquefaction curves: (a) based on correlations with SPT data; (b) based on theoretical/experimental results. (After Mitchell and Tseng, 1990, H. Bolton Seed Memorial Symposium Proceedings, Vol. 2, p. 347. Used by permission of BiTech Publishers, Ltd.)

$$q_{c1} = q_c \left(\frac{p_a}{\sigma'_{v0}} \right)^{0.5} \quad (9.8a)$$

or

$$q_{c1} = \frac{1.8}{0.8 + \sigma'_{v0}} q_c \quad (9.8b)$$

where σ'_{v0} is in tons/ft² (Kayen et al., 1992). Adjustment for magnitudes other than 7.5 can be made using the CSR correction factors presented in Table 9-2. Kayen et al. (1992) found that liquefaction observations in the 1989 Loma Prieta earthquake agreed well with the curves of Robertson and Campanella (1985) and Mitchell and Tseng (1990).

For silty sands (> 5% fines), the effects of fines can be estimated by adding the following tip resistance increments to the measured tip resistance to obtain an equivalent clean sand tip resistance (Ishihara, 1993)

Fines Content (%)	Tip Resistance Increment (tons/ft ²)
≤ 5	0
~ 10	12
~ 15	22
~ 35	40

3. *Shear Wave Velocity.* Improved methods of in situ shear wave velocity measurements and studies related to development of the cyclic strain approach (Section 9.5.3.2) have contributed to the recognition of shear wave velocity as a useful measure of liquefaction resistance. Measured shear wave velocities can be normalized to a standard effective overburden pressure of 1 ton/ft² (96 kPa) by

$$v_{s1} = v_s (\sigma'_{v0})^{-1/n} \quad (9.9)$$

where σ'_{v0} is in tons/ft² and n has been taken as 3 (Tokimatsu et al., 1991) or 4 (Finn, 1991; Kayen et al., 1992). Stokoe et al. (1988) used the cyclic strain approach and equivalent linear ground response analyses to explore the relationship between peak ground surface acceleration (for stiff soil site conditions) and shear wave velocity. The results were used to develop bounds for the conditions under which liquefaction could be expected; the results agreed well with observed behavior in two earthquakes in the Imperial Valley of California (Figure 9.35). Tokimatsu et al. (1991) used the results of laboratory tests to develop curves showing the CSR required to produce a cyclic strain amplitude of 2.5% in various numbers of cycles as a function of corrected shear wave velocity (Figure 9.36).

The observation that the shear wave velocity of sand is insensitive to factors (e.g., soil fabric, overconsolidation ratio, prior cyclic straining) that are known to influence liquefaction resistance suggests that shear wave velocity measurements alone may not be sufficient to evaluate the liquefaction potential of all soil deposits (Jamiolkowsky and LoPresti, 1992; Verdugo, 1992).

4. *Dilatometer Index.* Correlations for liquefaction potential with the horizontal stress index of the dilatometer test (DMT) have also been proposed (Marchetti, 1982; Robertson

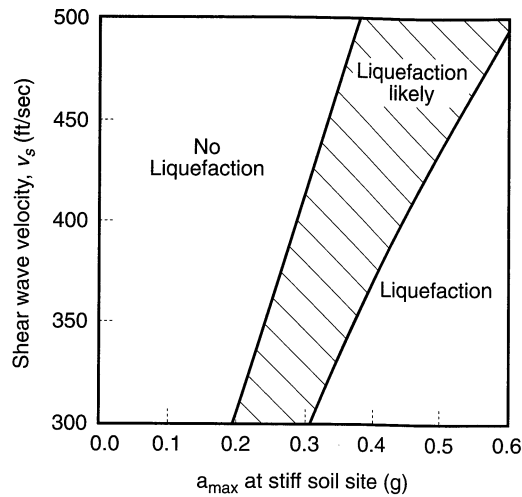


Figure 9.35 Chart for evaluation of liquefaction potential from shear wave velocity and peak ground acceleration (10 cycles). (After Stokoe et al., 1988.)

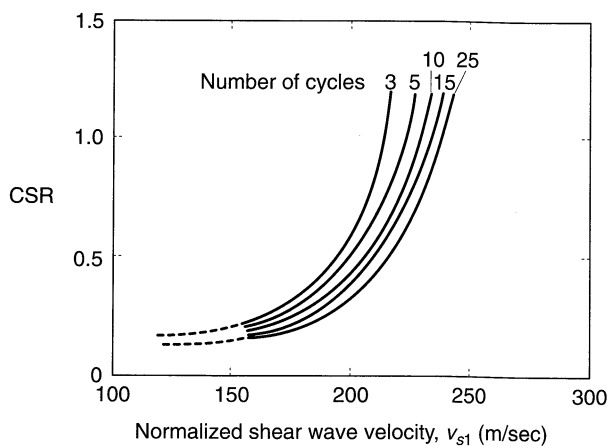


Figure 9.36 Correlations between cyclic stress ratio required to produce cyclic strain amplitude of 2.5% in clean sand and shear wave velocity. (After Tokimatsu et al., 1991.)

and Camponella, 1986; Reyna and Chameau, 1991). Figure 9.37 illustrates the performance of three such correlations when applied to data from several sites in the Imperial Valley of California. New correlations for the DMT should be expected as additional experience with this relatively new in situ test is obtained.

5. Use of In Situ Test Results. SPT resistance is by far the most commonly used in situ test parameter for characterization of liquefaction resistance. The SPT allows a sample to be retrieved (for identification, measurement of fines content, etc.) and has the largest case history database of any in situ test. However, the CPT is becoming much more commonly used for characterization of liquefaction resistance. The CPT provides a continuous record of penetration resistance (an important benefit when thin layers of seams of potentially liquefiable soil may exist) and is much faster and less expensive than the SPT. Because CPT-based liquefaction resistance is influenced by grain size characteristics (Figure 9.34), complementary borings with sampling may be required.

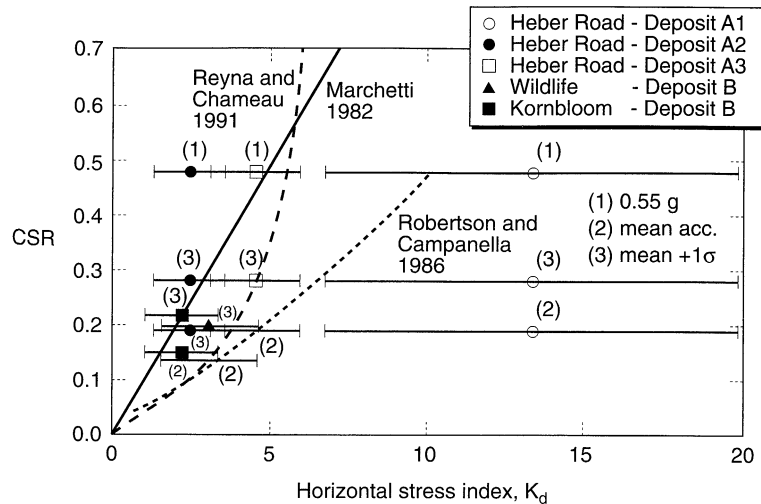


Figure 9.37 Suggested relationships between cyclic stress ratio required to produce liquefaction and horizontal stress index from dilatometer test. (After Reyna and Chameau, 1991.)

Regardless of which is used, the in situ test parameters allow estimation of CSR_L —the CSR required to initiate liquefaction. Using the definition of cyclic stress ratio, the cyclic shear stress required to initiate liquefaction is given by

$$\tau_{cyc,L} = CSR_L \sigma'_{v0} \quad (9.10)$$

Evaluation of Initiation of Liquefaction. Once the cyclic loading imposed by an earthquake and the liquefaction resistance of the soils have been characterized, liquefaction potential can be evaluated. The cyclic stress approach characterizes earthquake loading by the amplitude of an equivalent uniform cyclic stress and liquefaction resistance by the amplitude of the uniform cyclic stress required to produce liquefaction in the same number of cycles. The evaluation of liquefaction potential is thus reduced to a comparison of loading and resistance throughout the soil deposit of interest.

The evaluation is easily performed graphically. First, the variation of equivalent cyclic shear stress (earthquake loading, τ_{cyc}), with depth is plotted as in Figure 9.38 (the number of equivalent cycles, N_{eq} , corresponding to the earthquake magnitude must be determined if liquefaction resistance is to be characterized using laboratory test results). The variation of the cyclic shear stress required to cause liquefaction (liquefaction resistance, $\tau_{cyc,L}$) with depth is then plotted on the same graph (the values of $\tau_{cyc,L}$ must correspond to the same earthquake magnitude, or same number of equivalent cycles, as τ_{cyc}). Liquefaction can be expected at depths where the loading exceeds the resistance or when the factor of safety against liquefaction, expressed as

$$FS_L = \frac{\text{cyclic shear stress required to cause liquefaction}}{\text{equivalent cyclic shear stress induced by earthquake}} = \frac{\tau_{cyc,L}}{\tau_{cyc}} = \frac{CSR_L}{CSR} \quad (9.11)$$

is less than 1.

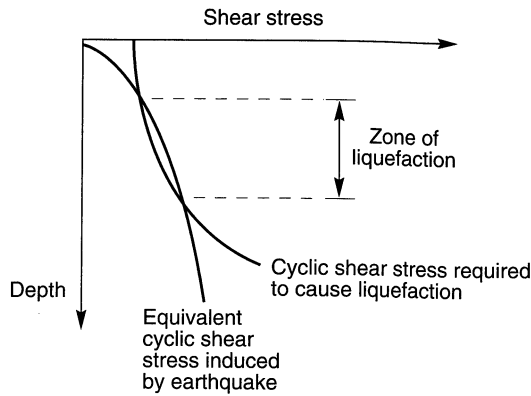


Figure 9.38 Process by which zone of liquefaction is identified.

It should be noted that significant excess pore pressure can develop even if the computed factor of safety is greater than 1. At level-ground sites, for example, the magnitude of this excess pore pressure can be estimated from Figure 9.39. The reduction in effective stress associated with such excess pore pressures can reduce the stiffness of the soil, and significant settlement can occur as the excess pore pressures dissipate (Section 9.6.3.2).

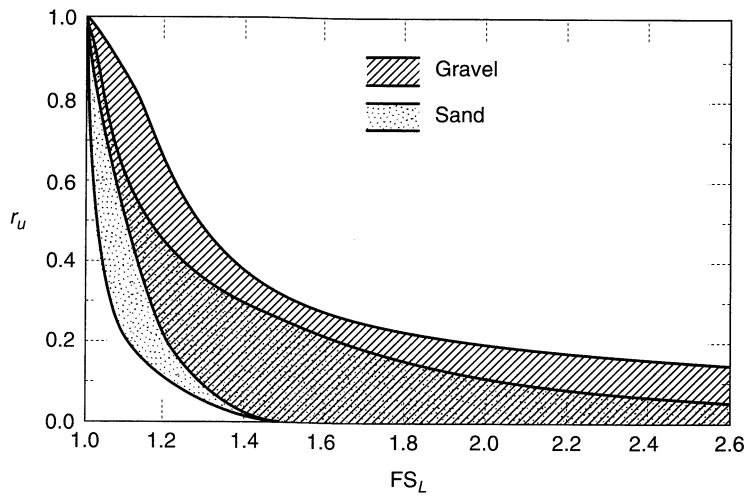


Figure 9.39 Relationship between residual excess pore pressure and factor of safety against liquefaction for level-ground sites. (After Marcuson and Hynes, 1990.)

Example 9.4

A site in Japan underlain by clean, potentially liquefiable sand was described in Example 6.6. SPT tests were performed at the site using standard Japanese SPT techniques; the process by which the measured SPT resistances are corrected to obtain $(N_1)_{60}$ values was described in Example 6.6. Using the information available, determine the extent to which liquefaction would have been expected in the 1964 Niigata earthquake ($M = 7.5$) if the peak horizontal acceleration at the ground surface was $0.16g$.

Solution Evaluation of liquefaction potential by the cyclic stress approach involves comparison of the level of cyclic stress induced by the earthquake with the level of cyclic stress required to initiate liquefaction. The level of cyclic stress induced by the earthquake can be estimated from the information available using the simplified procedure of Seed and Idriss (1971). The variation of total vertical stress with depth is easily computed (column 2 below). For example, the total vertical stress at a depth of 6.2 m is given by

$$\sigma_{v0} = (1.5 \text{ m}) \left(1.874 \frac{\text{Mg}}{\text{m}^3} \right) + (4.7 \text{ m}) \left(2.180 \frac{\text{Mg}}{\text{m}^3} \right) \left(9.81 \frac{\text{m}}{\text{sec}^2} \right) = 128.1 \text{ kPa}$$

The value of the stress reduction factor can be obtained graphically from Figure 9.25 (column 3 below). At a depth of 6.2 m, $r_d = 0.960$. Knowing the peak ground surface acceleration, the cyclic shear stress is computed (column 4 below) by equation (9.2). At a depth of 6.2 m,

$$\tau_{\text{cyc}} = 0.65 \frac{0.16g}{g} (128.1 \text{ kPa}) (0.960) = 12.8 \text{ kPa}$$

The level of cyclic shear stress required to initiate liquefaction depends on the liquefaction resistance of the soil. For this example, liquefaction resistance can be characterized by the $(N_1)_{60}$ values (column 5 below—from column 6 in Example 6.6). Using the chart for less than 5% fines in Figure 9.31, the cyclic stress ratios required to initiate liquefaction can be found graphically (column 6 below). At a depth of 6.2 m, the value $(N_1)_{60} = 11.7$ corresponds to $\text{CSR}_{M=7.5} = 0.130$. Because the magnitude of the Niigata earthquake was 7.5, the magnitude correction factor (Table 9-2) has a value of 1.0. Then

$$\text{CSR}_L = (\text{CSR}_{M=7.5})(1.0) = 0.130$$

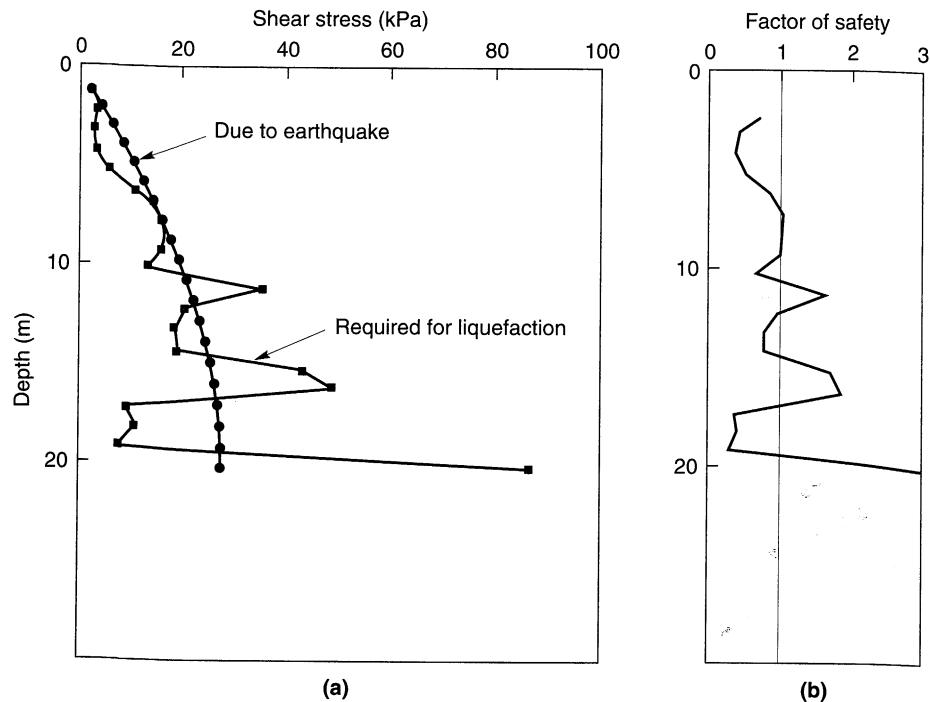


Figure E9.4

Knowing CSR_L and the variation of vertical effective stress with depth (column 7 below—from column 3 of Example 6.6), the cyclic stress required to initiate liquefaction can be computed (column 8 below and Figure E9.4a). At a depth of 6.2 m,

$$\tau_{cyc,L} = CSR_L \sigma'_{v0} = (0.130)(82.0 \text{ kPa}) = 10.7 \text{ kPa}$$

Finally, the cyclic stress induced by the earthquake can be compared to the cyclic stress required to initiate liquefaction. Using the concept of a factor of safety against liquefaction [equation (9.11)], the variation of factor of safety with depth can be determined (column 9 below and Figure E9.4b). At a depth of 6.2 m,

$$FS_L = \frac{\tau_{cyc,L}}{\tau_{cyc}} = \frac{10.7 \text{ kPa}}{12.8 \text{ kPa}} = 0.84$$

As illustrated in Figure E9.4b, the factor of safety against liquefaction is greater than one where the cyclic stress induced by the earthquake is lower than the cyclic stress required to initiate liquefaction ($\tau_{cyc} < \tau_{cyc,L}$). At this site, extensive liquefaction would have been expected in the upper 8 to 10 m and at some greater depths as well.

The conditions of this example are representative of those in the Kawagishi-Cho area of Niigata, Japan (Figure 1.6) though the actual peak accelerations may have been on the order of 0.2 to 0.3g. The extensive liquefaction predicted in this example is consistent with what was actually observed in that area in the 1964 Niigata earthquake.

(1) D (m)	(2) σ_{v0}	(3) r_d	(4) τ_{cyc}	(5) $(N_1)_{60}$	(6) CSR_L	(7) σ'_{v0}	(8) $\tau_{cyc,L}$	(9) FS_L
1.2	22.1	0.994	2.28	17.3	—	22.1	—	—
2.2	42.6	0.989	4.38	7.9	0.087	36.4	3.17	0.72
3.2	64.0	0.982	6.53	5.1	0.056	47.3	2.65	0.41
4.2	85.3	0.976	8.66	4.6	0.051	58.8	3.00	0.35
5.2	106.7	0.968	10.8	7.0	0.077	70.4	5.42	0.50
6.2	128.1	0.960	12.8	11.7	0.130	82.0	10.7	0.84
7.2	149.5	0.951	14.8	14.6	0.161	93.6	15.1	1.02
8.2	170.9	0.940	16.7	13.7	0.151	105.3	15.9	0.95
9.2	192.3	0.926	18.5	15.2	0.167	116.8	19.5	1.05
10.2	213.8	0.910	20.2	9.3	0.102	128.4	13.1	0.65
11.2	235.1	0.886	21.7	22.8	0.250	140.0	35.0	1.61
12.2	256.5	0.864	23.1	12.4	0.136	151.5	20.6	0.89
13.2	277.9	0.835	24.1	10.1	0.111	163.1	18.1	0.75
14.2	299.3	0.813	25.3	9.8	0.108	174.7	18.9	0.75
15.2	320.7	0.767	25.6	20.7	0.228	186.3	42.5	1.66
16.2	342.1	0.739	26.3	22.5	0.245	197.9	48.5	1.84
17.2	363.5	0.704	26.6	4.1	0.045	209.4	9.42	0.35
18.2	384.8	0.671	26.9	4.7	0.052	221.1	11.5	0.43
19.2	406.2	0.642	27.1	3.1	0.034	232.7	7.91	0.29
20.2	427.7	0.625	27.8	28.5	0.350	244.3	85.5	3.08

Because of their physical significance, the initiation of liquefaction has been presented in terms of cyclic stresses in this section. After developing an understanding of the relationship between the cyclic shear stresses induced by an earthquake and the cyclic shear stresses required to initiate liquefaction, many engineers will find it more convenient to characterize earthquake loading and liquefaction resistance in terms of the cyclic stress

ratios, CSR and CSR_L , both of which vary over a much smaller range than the cyclic shear stresses themselves.

9.5.3.2 Cyclic Strain Approach

The large number of factors that influence the cyclic stresses required to produce liquefaction can make laboratory evaluation of liquefaction resistance in the cyclic stress approach difficult. As Seed (1976) pointed out, "the liquefaction characteristics of in situ sand deposits are determined by a number of complex factors, of which relative density is only one, and careful evaluations of all of these factors is required in selecting soil characteristics for use in design."

In an effort to develop a more robust approach to the liquefaction problem, Dobry and Ladd (1980) and Dobry et al. (1982) described an approach that used cyclic strains rather than cyclic stresses to characterize earthquake-induced loading and liquefaction resistance. The approach is based on experimental evidence that shows densification of dry sands to be controlled by cyclic strains rather than cyclic stresses (e.g., Silver and Seed, 1971; Youd, 1972) and the existence of the threshold volumetric shear strain (Section 6.4.1) below which densification does not occur. Since the tendency for a sand to densify when dry is directly related to its tendency to develop excess pore pressure when saturated, it follows that pore pressure generation should be more fundamentally related to cyclic strains than cyclic stresses.

Characterization of Loading Conditions. In the cyclic strain approach, earthquake-induced loading is expressed in terms of cyclic strains. The time history of cyclic strain in an actual earthquake is transient and irregular. To compare the loading with laboratory-measured liquefaction resistance, it must be represented by an equivalent series of uniform strain cycles. The conversion procedure is analogous to that used in the cyclic stress approach.

The time history of cyclic shear strain may be computed in a ground response analysis. This is perhaps the weakest link in the cyclic strain approach since cyclic strains are considerably more difficult to predict accurately than cyclic stresses (Seed, 1980). Dobry et al. (1982) proposed a simplified method for estimating the amplitude of the uniform cyclic strain from the amplitude of the uniform cyclic stress of equation (9.2):

$$\gamma_{cyc} = 0.65 \frac{a_{max}}{g} \frac{\sigma_v r_d}{G(\gamma_{cyc})} \quad (9.12)$$

where $G(\gamma_{cyc})$ is the shear modulus of the soil at $\gamma = \gamma_{cyc}$. Since γ_{cyc} influences both sides of equation (9.12), the value of $G(\gamma_{cyc})$ must be obtained iteratively from a measured G_{max} profile and appropriate modulus reduction curves (Section 6.4.2.1). The equivalent number of strain cycles, N_{cq} , depends on the earthquake magnitude, and can be estimated from Figure 9.24.

Once γ_{cyc} is determined, it can be compared with the threshold shear strain, γ_t . If $\gamma_{cyc} < \gamma_t$, no pore pressure will be generated and, consequently, liquefaction cannot be initiated. The liquefaction hazard evaluation would end at that point. If $\gamma_{cyc} > \gamma_t$, liquefaction is possible and the liquefaction resistance of the soil must be evaluated.

Characterization of Liquefaction Resistance. The cyclic strain approach simplifies the interpretation of liquefaction resistance from laboratory tests. Experimental evidence indicates that factors that increase the cyclic stresses required to initiate

liquefaction (e.g., density, soil fabric, strain history, overconsolidation ratio, length of time under sustained pressure) also increase the shear modulus of the soil. Because these factors influence both τ_{cyc} and G similarly, their influence on the ratio $\gamma_{cyc} = \tau_{cyc} / G$ is much smaller. Consequently, they have little influence on pore pressure generation when interpreted in terms of cyclic strains. Dobry and Ladd (1980) provided striking evidence of this result; Figure 9.40 shows the pore pressure ratio produced by 10 strain-controlled cycles of loading on two different sands prepared by three different methods at three different initial effective confining pressures. The insensitivity of the generated pore pressure to factors other than cyclic strain amplitude illustrated in Figure 9.40 is a hallmark of the cyclic strain approach.

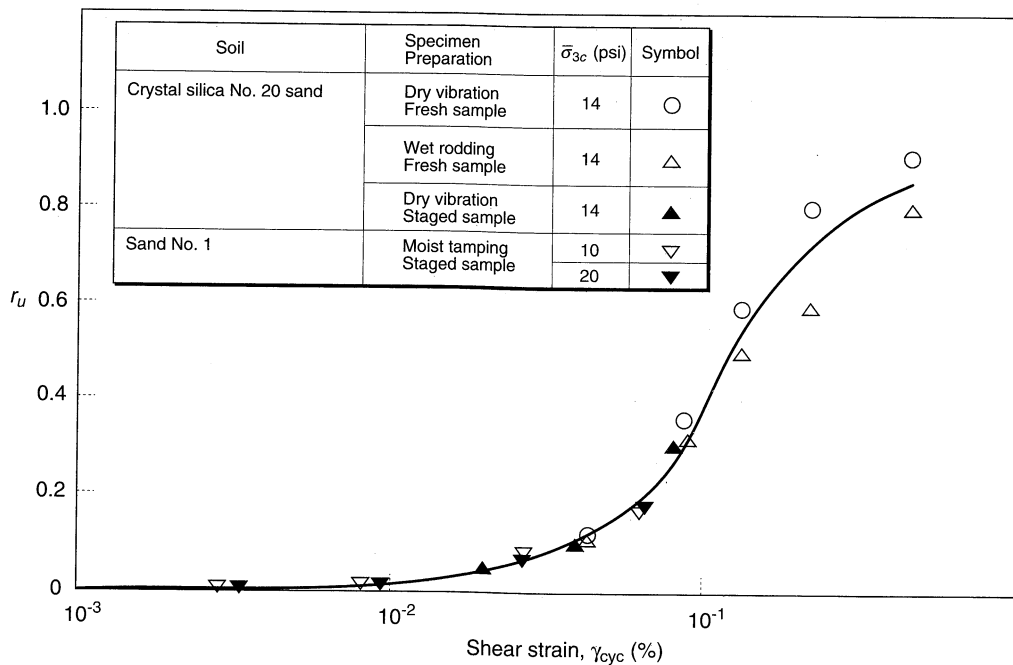


Figure 9.40 Measured pore pressure ratio after 10 cycles of loading in strain-controlled cyclic triaxial tests. After Dobry and Ladd, (1980). Discussion, *Journal of the Geotechnical Engineering Division*, Vol. 106, No. GT6. Reprinted by permission of ASCE.

Dobry et al. (1984) developed an innovative axial/torsional triaxial test called the CyT-CAU test for measurement of liquefaction resistance. In this test a solid cylindrical triaxial specimen is anisotropically consolidated under a *stress-controlled* static deviator stress. Cyclic strains are then imposed under undrained conditions by *strain-controlled* cyclic torsion while the stress-controlled deviator stress remains constant. The cyclic shear strains induce excess pore pressure in the specimen. If the effective stress conditions reach the FLS and the steady-state strength is less than the static shear stress, flow liquefaction will occur. This test closely models the behavior of soils that experience flow liquefaction

in the field: excess pore pressures are generated by cyclic shear strains, but flow failure is driven by static shear stresses.

Vasquez-Herrera and Dobry (1988) used the CyT-CAU test to investigate the generation of excess pore pressure and initiation of flow liquefaction. Confirming the existence of a FLS for several sands, Vasquez-Herrera and Dobry also observed that the excess pore pressure required to trigger liquefaction decreased with increasing initial principal effective stress ratio (see Figure 9.20), and a corresponding decrease in the number of strain cycles required to trigger liquefaction (Figure 9.41). The cyclic strain amplitude required to trigger liquefaction in N_{eq} cycles can be expressed in the form

$$\gamma_{cyc} = 0.01 + \left[\frac{r_{u,t}}{\alpha N_{eq} (2 - r_{u,t})} \right]^{1/\beta} \quad (9.13)$$

where α and β are experimentally determined functions of K_c used to characterize liquefaction resistance in the cyclic strain approach. The rate at which excess pore pressures develop is also influenced by K_c ; normalized pore pressures increase more quickly in the first cycles for specimens at lower K_c values (Figure 9.42).

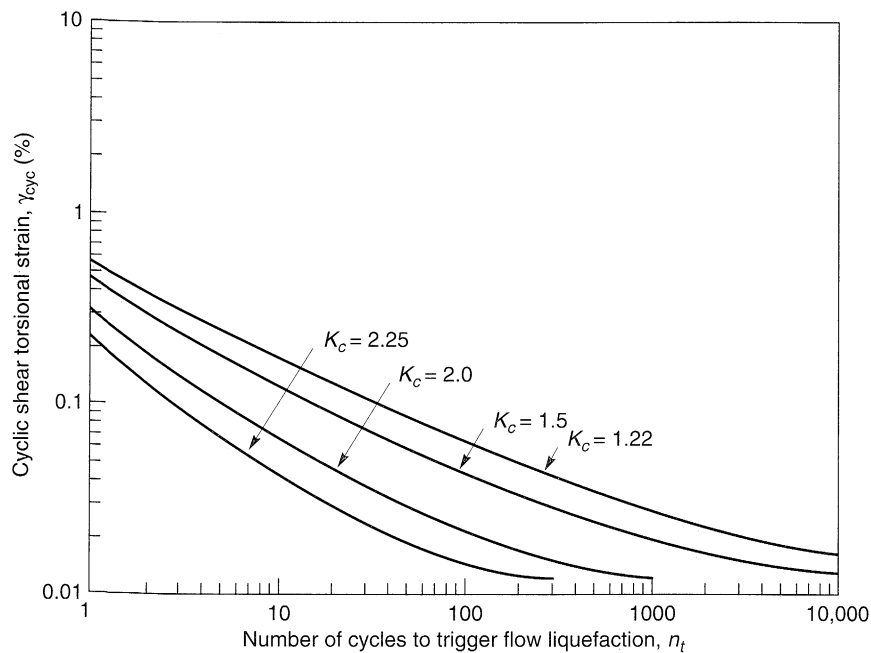


Figure 9.41 Liquefaction resistance curves for a sand obtained from an actual liquefaction failure. For this sand, $\alpha = 4.78$ to $1.91K_c$ and $\beta = 2.96$ to $0.78K_c$. Note the significant reduction in liquefaction resistance with increasing level of initial shear stress. (After Vasquez-Herrera and Dobry, 1988.)

Evaluation of Liquefaction Potential. Liquefaction potential may be evaluated in the cyclic strain approach in a manner similar to that used in the cyclic stress approach. The cyclic loading imposed by the earthquake, characterized by the amplitude of

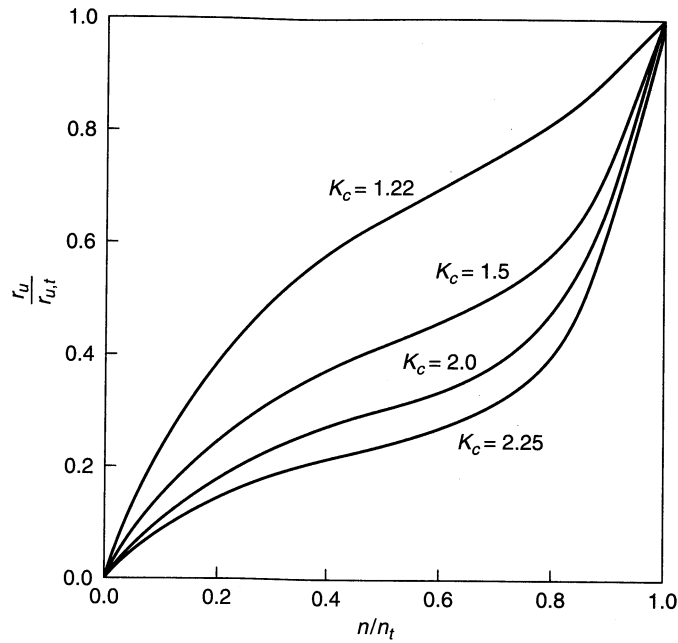


Figure 9.42 Normalized rate of pore pressure generation for sands subjected to different levels of initial shear stress. (After Vasquez-Herrera and Dobry, 1988.)

a series of N_{eq} uniform strain cycles, is compared with the liquefaction resistance, which is expressed in terms of the cyclic strain amplitude required to initiate liquefaction in the same number of cycles. Liquefaction can be expected at depths where the cyclic loading exceeds the liquefaction resistance (Figure 9.43). Since loading and resistance are characterized in terms of strains rather than stresses, the cyclic strain approach does not yield a factor of safety against liquefaction.

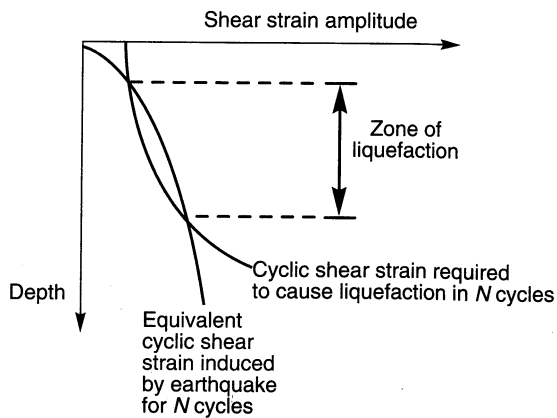


Figure 9.43 Process by which the zone of liquefaction is identified in the cyclic strain approach.

The primary advantage of the cyclic strain approach derives from the strong relationship between pore pressure generation and cyclic strain amplitude. For a given soil, excess pore pressure can be predicted more accurately from cyclic strains than from cyclic stresses. However, cyclic strains are considerably more difficult to predict accurately than cyclic stresses. The cyclic strain approach is not used as commonly as the cyclic stress approach in geotechnical earthquake engineering practice.

9.5.3.3 Other Approaches to the Initiation of Liquefaction

Although the cyclic stress and cyclic strain approaches are the most commonly used in geotechnical earthquake engineering practice, other approaches have also been developed. Two that offer considerable promise are the *dissipated energy approach* and the *effective stress-based response analysis approach*. As these approaches are refined, and as additional data with which to calibrate them become available, their use is likely to increase.

Energy Dissipation Approach. The use of dissipated energy as a measure of liquefaction resistance offers a number of advantages; it is related to both cyclic stresses and cyclic strains, and it can be related to inherently stochastic earthquake ground motions in a way that methods based on peak ground motion parameters alone cannot, it is a scalar quantity, and it can be related to fundamental earthquake parameters.

The densification of dry soil involves rearrangement of grains and hence the expenditure of energy. As a cyclically loaded dry soil densifies and approaches its minimum void ratio, the amount of energy required to rearrange individual soil grains increases. For a saturated soil, however, the tendency for densification causes the pore pressure to increase and the interparticle contact forces to decrease. As these contact forces decrease, the amount of energy needed to rearrange soil grains decreases. By combining these observations, Nemat-Nasser and Shokoh (1979) developed a simple, unified theory that related densification under drained conditions and pore pressure generation under undrained conditions to dissipated energy. Others have since attempted to characterize the relationship between excess pore pressure and dissipated energy experimentally (e.g., Simcock et al., 1983; Law et al., 1990; Figueroa and Dahisaria, 1991). Although some of the data are quite scattered, the excess pore pressure can be predicted by a relationship of the form

$$\frac{\Delta u}{\sigma'_{v0}} = \alpha W_N^\beta \quad (9.14)$$

where W_N is a dimensionless energy term (Law et al., 1990) and α and β are coefficients determined from laboratory tests.

Davis and Berrill (1982) demonstrated the potential for using energy to relate liquefaction behavior to fundamental earthquake parameters such as magnitude and distance. By combining an estimate of the energy content of seismic waves at a distance R from an earthquake of magnitude M with a simple energy dissipation function calibrated by experimental results and field observations of liquefaction behavior, an expression for excess pore pressure was developed.

$$\Delta u = \frac{450}{R^2 N_1^2 \sqrt{\sigma'_{v0}}} 10^{1.5M} \quad (9.15)$$

where R is in meters, N_1 is the SPT resistance corrected to an effective overburden pressure of 1 ton/ft² (96 kPa), and Δu and σ'_{v0} are in kPa. Law et al. (1990) used energy principles to develop the following criterion for liquefaction failure in sands:

$$\frac{10^{1.5M}}{2.28 \times 10^{-10} N_1^{1.5} R^{4.3}} \geq 1.0 \quad (9.16)$$

where R is the hypocentral distance in kilometers.

Effective Stress-Based Response Analysis Approach. Stress–strain modeling of soil behavior has been a subject of intense research activity for many years, and the task of replicating the complex behavior of potentially liquefiable soils with simple constitutive models has proven challenging. As discussed in Section 6.4, the nonlinear stress–strain behavior of soils can be described by cyclic nonlinear stress–strain models and by advanced constitutive models.

Cyclic nonlinear stress–strain models (Section 6.4.3) use an empirical backbone curve and a series of unloading–reloading rules that govern cyclic behavior. Pore pressure prediction is accomplished by pore pressure models (e.g., Martin et al., 1975; Ishihara and Towhata, 1980; Finn and Bhatia, 1981) that can predict the generation of pore pressure under irregular cyclic loading conditions. The computed pore pressure is used to degrade, or soften, the backbone curve as the effective stress (and soil stiffness) decreases.

In the Martin et al. (1975) model, for example, the pore pressure generated in an increment of undrained loading is related to the volumetric strain that would have occurred in the same loading increment under drained conditions by

$$\Delta u = \bar{E}_r \Delta \varepsilon_{vd} \quad (9.17)$$

where \bar{E}_r is the rebound modulus and $\Delta \varepsilon_{vd}$ is the incremental volumetric strain under drained conditions. The rebound modulus can be expressed as

$$\bar{E}_r = \frac{(\sigma'_v)^{1-m}}{m K_2 (\sigma'_{v0})^{n-m}} \quad (9.18)$$

where σ'_v and σ'_{v0} are the current and initial vertical effective stresses and m , n , and K_2 are experimentally determined from a rebound test in a consolidometer. The incremental volumetric strain is computed as

$$\Delta \varepsilon_{vd} = C_1 (\gamma - C_2 \varepsilon_{vd}) + \frac{C_3 \varepsilon_{vd}^2}{\gamma + C_4 \varepsilon_{vd}} \quad (9.19)$$

where γ and ε_{vd} are the cyclic shear and volumetric strains, respectively, and C_1 – C_4 are constants determined from the results of drained cyclic simple shear tests. Martin et al. (1981) developed a procedure for estimation of these constants without laboratory test results. When incorporated into nonlinear ground response analyses, cyclic nonlinear and pore pressure models allow computation of the generation, redistribution, and dissipation of pore pressures. Hence the effective stress conditions throughout a soil deposit can be monitored throughout and even after an earthquake to evaluate liquefaction hazards.

Advanced constitutive models (Section 6.4.4) provide a more rigorous approach to prediction of soil behavior under a wide variety of loading conditions. Such models describe the increments of volumetric and deviatoric strain produced by increments of volumetric and deviatoric stress. By setting the incremental volumetric strain to zero to represent undrained conditions, changes in effective stresses can be computed. Such models can be incorporated into nonlinear ground response and dynamic response analyses. The one-dimensional nonlinear ground response program DYNA1D (Prevost, 1989), for example, uses a nested yield surface constitutive model to account for nonlinear, anisotropic, hysteretic soil behavior to predict the generation, redistribution, and dissipation of excess pore pressure during and after earthquake shaking.

Probabilistic Approach. There are many potential sources of uncertainty in both the loading and resistance aspects of liquefaction problems, and probabilistic approaches have been developed to deal with them. Uncertainties in cyclic loading can be evaluated using the standard probabilistic seismic hazard analyses described in Section 4.4. Uncertainties in liquefaction resistance can be treated in one of two general ways.

One group of methods is based on probabilistic characterization of the parameters shown by laboratory tests to influence pore pressure generation. Haldar and Tang (1979) characterized uncertainty in the parameters of the simplified cyclic stress approach described in Section 9.5.3.1. Fardis and Veneziano (1982) used a similar approach with total stress and effective stress models. Chameau and Clough (1983) described pore pressure generation probabilistically using experimental data and an effective stress model. Each of these methods can compute the probability of liquefaction due to a particular set of loading conditions. Their accuracy depends on the accuracy of the underlying liquefaction/pore pressure model and on how accurately the uncertainty of the model parameters can be determined.

An alternative group of methods are based on in situ test-based characterization of liquefaction resistance (e.g., Christian and Swiger, 1975; Yegian and Whitman, 1978; Veneziano and Liao, 1984; Liao et al., 1988). These methods use various statistical classification and regression analyses to assign probabilities of liquefaction to different combinations of loading and resistance parameters. Liao et al. (1988), for example, analyzed 278 case studies to produce the following expression for the probability of liquefaction:

$$P_L = \frac{1}{1 + \exp [-(\beta_0 + \beta_1 \ln(\text{CSR}) + \beta_2(N_1)_{60})]} \quad (9.20)$$

where the parameters β_0 - β_2 are shown in Table 9-3. Liquefaction probability curves for the clean and silty sand cases are shown graphically in Figure 9.44.

Example 9.5

Use the approach of Liao et al. (1988) to estimate the probabilities of liquefaction at the site described in Example 9.4.

Solution The σ'_{v0} and τ_{cyc} data from Example 9.4 can be used to compute the cyclic stress ratio (column 4 below). Using this cyclic stress ratio and the $(N_1)_{60}$ values evaluated originally in Example 6.6, probabilities of liquefaction at each depth in the soil profile using equation (9.20) (with the clean sand regression coefficients).

Although the results of this analysis are expressed in terms of a probability of liquefaction rather than a factor of safety against liquefaction (as in Example 9.4), both indicate that

D (m)	τ_{cyc} (kPa)	σ'_{vo} (kPa)	CSR	$(N_1)_{60}$	P_L
1.2	2.28	22.1	0.103	17.3	—
2.2	4.38	36.4	0.120	7.9	0.403
3.2	6.53	47.3	0.138	5.1	0.835
4.2	8.66	58.8	0.147	4.6	0.903
5.2	10.8	70.4	0.153	7.0	0.823
6.2	12.8	82.0	0.156	11.7	0.469
7.2	14.8	93.6	0.158	14.6	0.218
8.2	16.7	105.3	0.159	13.7	0.293
9.2	18.5	116.8	0.158	15.2	0.180
10.2	20.2	128.4	0.157	9.3	0.687
11.2	21.7	140.0	0.155	22.8	0.009
12.2	23.1	151.5	0.152	12.4	0.342
13.2	24.1	163.1	0.148	10.1	0.522
14.2	25.3	174.7	0.145	9.8	0.519
15.2	25.6	186.3	0.137	20.7	0.010
16.2	26.3	197.9	0.133	22.5	0.003
17.2	26.6	209.4	0.127	4.1	0.815
18.2	26.9	221.1	0.122	4.7	0.729
19.2	27.1	232.7	0.116	3.1	0.785
20.2	27.8	244.3	0.114	28.5	0.0001

Table 9-3 Regression Parameters for Calculating Probability of Liquefaction

Data ^a	Number of Cases	β_0	β_1	β_2
All cases	278	10.167	4.1933	-0.24375
Clean sand cases only	182	16.447	6.4603	-0.39760
Silty sand cases only	96	6.4831	2.6854	-0.18190

Source: After Liao et al. (1988).

^a A fines content of 12% is used as the boundary between clean and silty sands.

extensive liquefaction would have been expected at this particular site in the 1964 Niigata earthquake. Widespread liquefaction was indeed observed at sites with soil conditions similar to these in that earthquake.

9.6 EFFECTS OF LIQUEFACTION

Liquefaction phenomena can affect buildings, bridges, buried pipelines, and other constructed facilities in many different ways. Liquefaction can also influence the nature of ground surface motions. Flow liquefaction can produce massive flow slides and contribute to the sinking or tilting of heavy structures, the floating of light buried structures, and to the failure of retaining structures. Cyclic mobility can cause slumping of slopes, settlement of

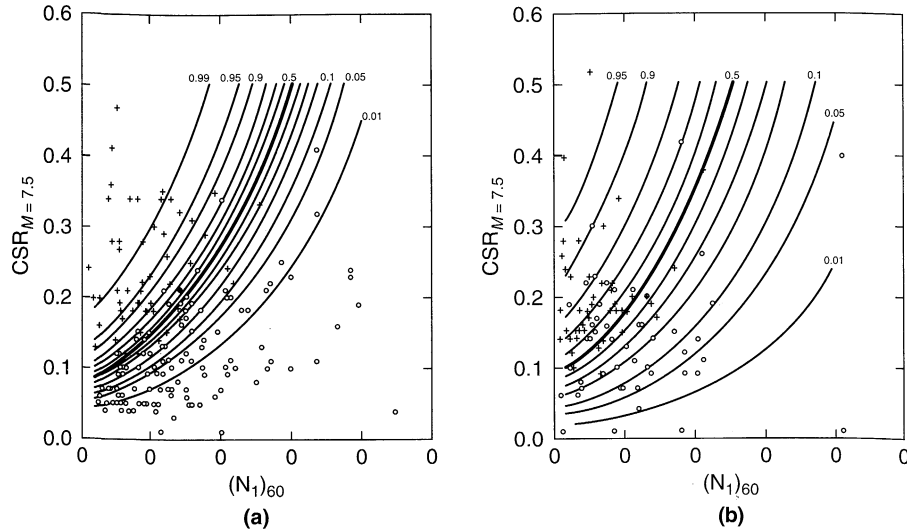


Figure 9.44 Contours of equal probability of liquefaction for (a) clean sand (less than 12% fines), and (b) silty sands (greater than 12% fines). (After Liao et al., 1988. Regression models for evaluating liquefaction probability, *Journal of Geotechnical Engineering*, Vol. 114, No. 4. Reprinted by permission of ASCE.)

buildings, lateral spreading, and retaining wall failure. Substantial ground oscillation, ground surface settlement, sand boils, and postearthquake stability failures can develop at level-ground sites.

The effects of liquefaction can be better appreciated by studying well-documented case histories. In addition to the regularly published journals that deal with geotechnical earthquake engineering, an excellent compilation of case histories can be found in Hamada and O'Rourke (1992).

9.6.1 Alteration of Ground Motion

The influence of the shear modulus and damping characteristics of soils on ground response is well established. Several examples of the effects of these characteristics presented in Chapter 8 showed that soft soil deposits respond differently than stiff soil deposits to the same motion.

The development of positive excess pore pressures causes soil stiffness to decrease during an earthquake. A deposit of liquefiable soil that is relatively stiff at the beginning of the earthquake may be much softer by the end of the motion. As a result, the amplitude and frequency content of the surface motion may change considerably throughout the earthquake. In the most extreme case, the development of very high pore pressures can cause the stiffness (and strength) of even a thin layer to be so low that the high-frequency components of a bedrock motion cannot be transmitted to the ground surface. An example of this effect is shown in Figure 9.45. It is not difficult to identify the point at which liquefaction-induced reduction of the stiffness of the underlying soil took place—the acceleration amplitude and frequency content both changed dramatically about 7 sec after the motion began. The fact

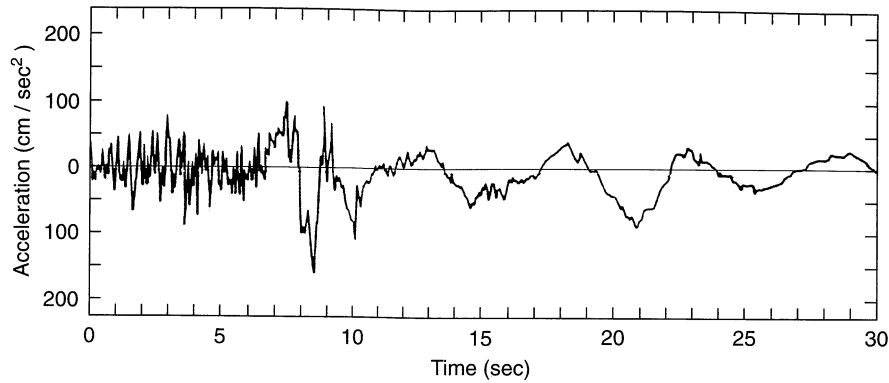


Figure 9.45 Accelerogram from site near apartment building resting on liquefiable soil (shown in Figure 1.6) in 1964 Niigata earthquake. (After Aki, 1988.)

that surface acceleration amplitudes decrease when pore pressures become large does not mean that damage potential is necessarily reduced because low acceleration amplitudes at low frequencies can still produce large displacements. These displacements may be of particular concern for buried structures, utilities, and structures supported on pile foundations that extend through liquefied soils (Figure 9.46).

The occurrence of liquefaction at depth beneath a flat ground surface can decouple the liquefied soils from the surficial soils and produce large, transient ground oscillations. The surficial soils are often broken into blocks (Figure 9.47) separated by fissures that can open and close during the earthquake. Ground waves with amplitudes of up to several feet have been observed during ground oscillation, but permanent displacements are usually small.

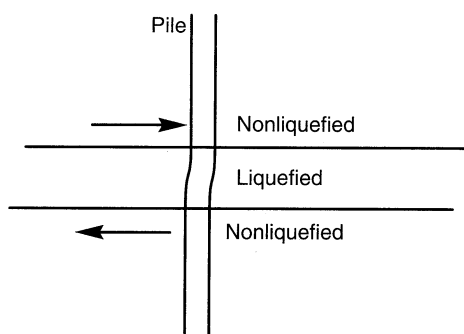


Figure 9.46 Potential effects of subsurface liquefaction on pile foundations. The large strains that may develop in a liquefied layer can induce high bending moments in piles that extend through it.

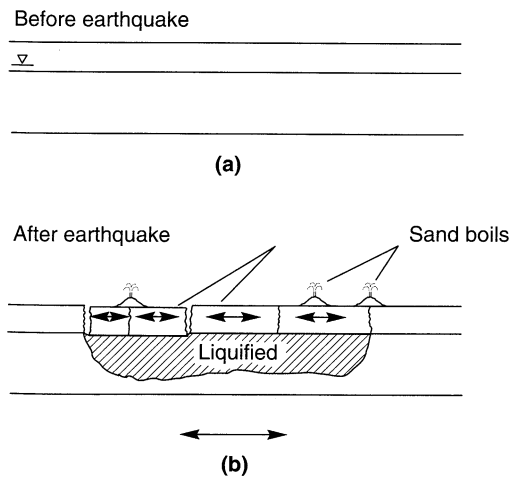


Figure 9.47 Ground oscillation (a) before and (b) after earthquake. (After Youd, 1984b.)

Youd (1993) attributed to ground oscillation most of the chaotic ground movements that fractured and buckled pavements in the Marina District of San Francisco during the 1989 Loma Prieta earthquake. Prediction of the amplitude of ground oscillation at a particular site is very difficult; even detailed nonlinear ground response analyses can provide only crude estimates.

9.6.2 Development of Sand Boils

Liquefaction is often accompanied by the development of sand boils. During and following earthquake shaking, seismically induced excess pore pressures are dissipated predominantly by the upward flow of porewater. This flow produces upward-acting forces on soil particles [these forces can loosen the upper portion of the deposit and leave it in a state susceptible to liquefaction in a future earthquake (Youd, 1984a)]. If the hydraulic gradient driving the flow reaches a critical value, the vertical effective stress will drop to zero and the soil will be in a *quick* condition. In such cases, the water velocities may be sufficient to carry soil particles to the surface. In the field, soil conditions are rarely uniform so the escaping porewater tends to flow at high velocity through localized cracks or channels. Sand particles can be carried through these channels and ejected at the ground surface to form sand boils. The development of sand boils is a complicated and somewhat random process; it depends on the magnitude of the excess pore pressure; the thickness, density, and depth of the zone of excess pore pressure; and the thickness, permeability, and intactness of any soil layers that overlay the zone of high excess pore pressure. There are pitfalls to reliance upon the presence of sand boils for evidence of liquefaction-related phenomena; liquefaction at great depths or in thin layers may not produce sand boils, but lower excess pore pressures in thick layers at shallow depths may. Also, the low permeability of silty sand may prevent porewater from flowing quickly enough to produce sand boils, even if high excess pore pressures develop. Ishihara (1985) examined the soil conditions associated with various liquefaction-related damage reports from the 1983 Nihonkai-chubu earthquake ($M = 7.7$) and 1976 Tangshan ($M = 7.7$) earthquakes (Gao et al. 1983) and produced estimates of the thickness of the overlying layer required to prevent level-ground liquefaction-related damage (Figure 9.48). These estimates have been validated against a much larger database for sites not susceptible to ground oscillation or lateral spreading, but are insufficient for predicting damage at other sites (Youd and Garris, 1995).

Sand boils are of little engineering significance by themselves, but they are useful indicators of high excess pore pressure generation. Shaking table (Liu and Qiao, 1984) and centrifuge (Fiegel and Kutter, 1992) tests have shown that porewater draining from the voids of the loose layers can accumulate beneath the less pervious layers and form *water interlayers* (Figure 9.49). Sand boils can develop when the water interlayers break through to the ground surface. Some redistribution of soil grains is also likely to accompany the formation of water interlayers; specifically the sand immediately beneath the water interlayer may be loosened by the upward flow of water toward the interlayer. If such conditions develop beneath an inclined ground surface, the presence of the water interlayer and the reduced steady state strength of the loosened sand immediately beneath it can contribute to large flow deformations (Section 9.6.4).

Ground surface settlement results from the volumetric strain that develops as seismically induced pore pressures dissipate. The phenomenon is illustrated for an element of soil

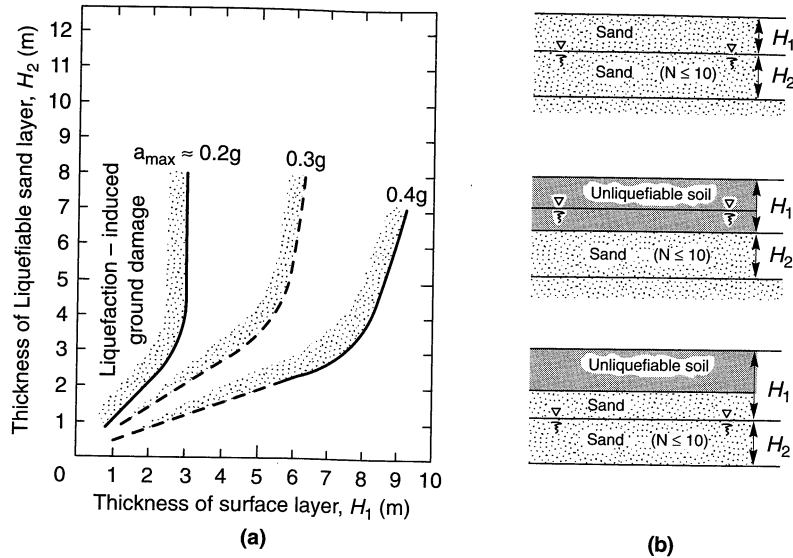


Figure 9.48 (a) Relationship between thickness of liquefiable layer and thickness of overlying layer at sites for which surface manifestation of level-ground liquefaction has been observed, and (b) guides to evaluation of respective layer thicknesses. (After Ishihara, 1985; used by permission of Kluwer Academic Publishers.)

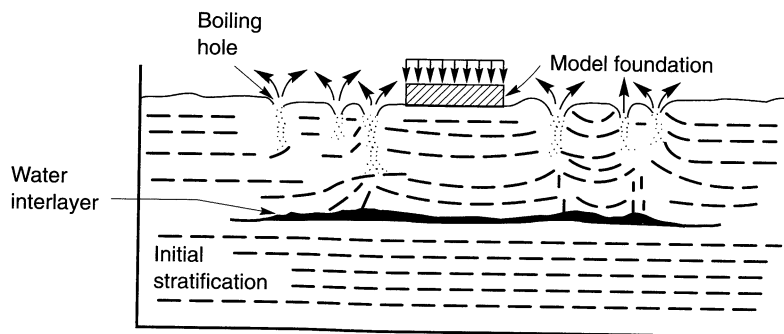


Figure 9.49 Formation of water interlayers in shaking table tests of Liu and Qiao (1984).

in Figure 9.50. Initially, the element is in drained equilibrium (zero excess pore pressure) at point A. Earthquake shaking causes excess pore pressure to build up under undrained conditions, thereby reducing the effective stress to that shown at point B. The excess pore pressure produces a hydraulic gradient that drives the porewater out of the voids. The flow of water reduces the hydraulic gradient until the excess pore pressure has completely dissipated (point C). As the water flows from the voids, the volume of the element decreases. As Figure 9.50 clearly illustrates, the magnitude of the volume change increases with the magnitude of the seismically induced excess pore pressure. Even small excess pore pressures,

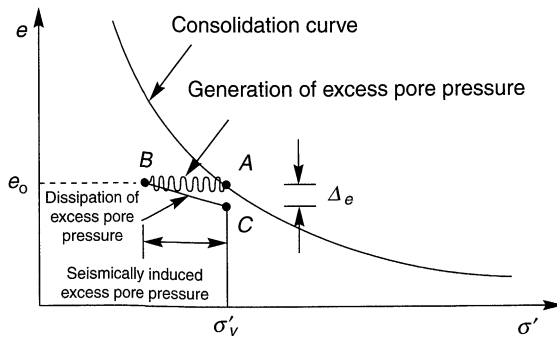


Figure 9.50 Process of earthquake-induced settlement from dissipation of seismically induced excess pore pressure.

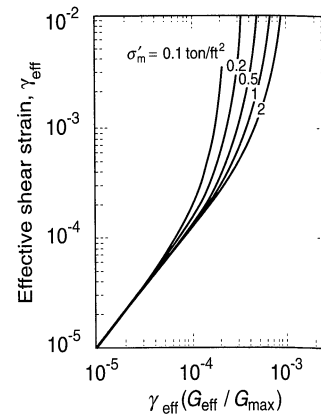


Figure 9.51 Plot for determination of effective cyclic shear strain in sand deposits. (After Tokimatsu and Seed, 1987. Evaluation of settlements in sand due to earthquake shaking, *Journal of Geotechnical Engineering*, Vol. 113, No. 8. Reprinted by permission of ASCE.)

which may not be sufficient to produce flow liquefaction or cyclic mobility, can produce some postearthquake settlement.

9.6.3 Settlement

The tendency of sands to densify when subjected to earthquake shaking is well documented. Subsurface densification is manifested at the ground surface in the form of settlement. Earthquake-induced settlement frequently causes distress to structures supported on shallow foundations, damage to utilities that serve pile-supported structures, and damage to life-lines that are commonly buried at shallow depths.

Dry sands densify very quickly; settlement of a dry sand deposit is usually complete by the end of an earthquake. The settlement of a saturated sand deposit requires more time—settlement can occur only as earthquake-induced pore pressures dissipate. The time required for this settlement to occur depends on the permeability and compressibility of the soil, and on the length of the drainage path—it can range from a few minutes up to about a day.

Estimation of earthquake-induced settlements of sands is difficult. Errors of 25 to 50% are common in static settlement predictions; even less accuracy should be expected for the more complicated case of seismic loading. Nevertheless, the following procedures have been shown to produce results that agree reasonably well with many cases of observed field behavior.

9.6.3.1 Settlement of Dry Sands

The densification of dry sands subjected to earthquake loading depends on the density of the sand, the amplitude of the cyclic shear strain induced in the sand, and the number of cycles of shear strain applied during the earthquake (Silver and Seed, 1971). Settlements

can be estimated using detailed ground response analyses with corrections for the effects of multidirectional shaking (Seed and Silver, 1972; Pyke et al., 1975), or by simplified procedures (Tokimatsu and Seed, 1987). In the simplified procedure, the effective cyclic shear strain, γ_{cyc} , is estimated by a procedure similar to that proposed for the cyclic strain approach to the initiation of liquefaction (Section 9.5.3.2):

$$\gamma_{cyc} = 0.65 \frac{a_{max}}{g} \frac{\sigma_v r_d}{G(\gamma_{cyc})} \tag{9.21}$$

Since the shear modulus varies with γ_{cyc} , several iterations may be required to calculate a value of γ_{cyc} that is consistent with the shear modulus. Figure 9.51 may be used to estimate γ_{cyc} when G_{max} is known. The effective cyclic shear strain can then be used, along with the relative density or SPT resistance of the sand, to estimate the volumetric strain due to compaction, ϵ_c , from Figure 9.52. The data from Figure 9.52 are based on 15 cycles of strain, which corresponds to a $M = 7.5$ earthquake. For earthquakes of other magnitudes, the volumetric strain due to compaction can be determined from the volumetric strain ratio presented in Table 9-4.

Following the experimental results of Pyke et al. (1975), the effect of multidirectional shaking is accounted for by doubling $\epsilon_{c,M}$. Pyke et al. (1975) also suggested that the vertical component of ground motion could cause an additional 50% increase in settlement (above that caused by the horizontal components); the effect of vertical motion is not explicitly accounted for in the simplified procedure of Tokimatsu and Seed (1987). Since the stiffness, density, and shear strain amplitudes typically vary with depth, a given soil deposit is usually divided into sublayers, with the settlement of each sublayer computed and summed to obtain the total ground surface settlement.

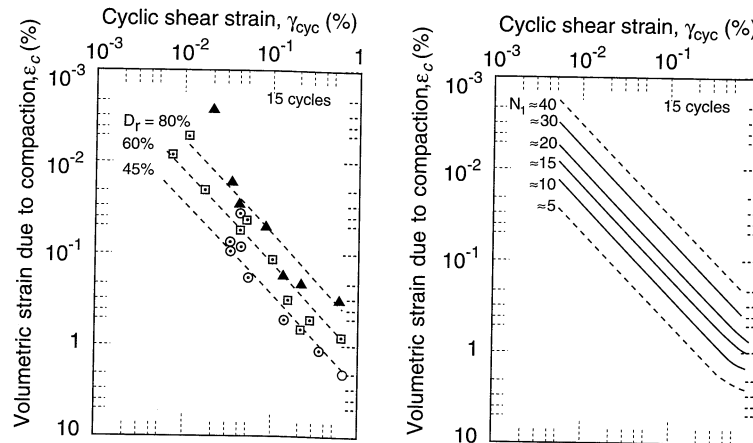


Figure 9.52 Relationship between volumetric shear strain, $\epsilon_{c,M=7.5}$ and cyclic shear strain, γ_{cyc} , in terms of (a) relative density and (b) standard penetration resistance. (After Tokimatsu and Seed, 1987. Evaluation of settlements in sand due to earthquake shaking, *Journal of Geotechnical Engineering*, Vol. 113, No. 8. Reprinted by permission of ASCE.)

Table 9-4 Influence of Earthquake Magnitude on Volumetric Strain for Dry Sands

Earthquake Magnitude	$\frac{\epsilon_{c,M}}{\epsilon_{c,M=7.5}}$
$5\frac{1}{4}$	0.4
6	0.6
$6\frac{3}{4}$	0.85
$7\frac{1}{2}$	1.0
$8\frac{1}{2}$	1.25

Source: After Tokimatsu and Seed, 1987

Example 9.6

The settlement of a 50-ft-thick deposit of loose sand ($D_r = 45\%$) with an average corrected SPT resistance of 9 was estimated for an earthquake of magnitude 6.6 by Seed and Silver (1972) and Tokimatsu and Seed (1987).

Solution The deposit can be divided into a series of layers; six layers are used in this example as illustrated in tabular form below. Based on the given $(N_1)_{60}$ values, G_{\max} can be estimated using the relationship of Ohto and Goto (1976) given in Table 6-6 (column 5 below). This allows estimation of γ_{cyc} (column 6 below) using Figure 9.51. The resulting volumetric strain (for a magnitude 7.5 earthquake) can then be obtained from Figure 9.52 (column 7 below). Using Table 9-5, the volumetric strain in a $M = 6.6$ earthquake should be about 80% of that in a magnitude 7.5 earthquake (column 8 below). Accounting for multidirectional shaking, the volumetric strains are then doubled (column 9 below). Finally, the settlement of each layer can be estimated as the product of the volumetric strain and the thickness of the layer (column 10 below).

(1) Layer Number	(2) Thickness (ft)	(3) D_r (%)	(4) $(N_1)_{60}$	(5) G_{\max} (ksf)	(6) γ_{cyc}	(7) $\epsilon_{c,M=7.5}$ (%)	(8) $\epsilon_{c,M=6.6}$ (%)	(9) $2\epsilon_{c,M=6.6}$ (%)	(10) Settlement (in.)
1	5	45	9	520	0.0005	0.14	0.11	0.22	0.13
2	5	45	9	900	0.0008	0.23	0.18	0.36	0.22
3	10	45	9	1270	0.0012	0.35	0.28	0.56	0.67
4	10	45	9	1630	0.0014	0.40	0.32	0.64	0.77
5	10	45	9	1930	0.0015	0.45	0.36	0.72	0.86
6	10	45	9	2190	0.0013	0.38	0.30	0.60	0.72
									<u>3.37</u>

These settlements are consistent with those that were observed at a site with these conditions in the 1971 San Fernando earthquake (Tokimatsu and Seed, 1987). The number of significant figures in this example is intended to facilitate understanding of the calculations, not to suggest that the results are accurate to 0.01 in.

9.6.3.2 Settlement of Saturated Sands

The postearthquake densification of saturated sand is influenced by the density of the sand, the maximum shear strain induced in the sand, and the amount of excess pore pressure

generated by the earthquake. Laboratory experiments have shown that the volumetric strain after initial liquefaction varies with relative density and maximum shear strain. Tokimatsu and Seed (1987) used a correlation between $(N_1)_{60}$ and relative density and an estimate of the shear strain potential of liquefied soil from $(N_1)_{60}$ and cyclic stress ratio (Seed et al., 1984) to produce a chart (Figure 9.53) that allows the volumetric strain after liquefaction in a $M = 7.5$ earthquake to be estimated directly from the cyclic stress ratio and SPT resistance. For earthquakes of other magnitudes, an equivalent cyclic stress ratio, CSR_M , can be determined from equation (9.2) and Table 9-2. Note that the volumetric strain after liquefaction can be as high as 2 to 3% for loose to medium dense sands and higher for very loose sands; a 5-m thick (16 ft) layer of very loose sand produced settlements of 50 to 70 cm (20 to 28 in.) in Hachinohe, Japan following the Tokachioki earthquake ($M = 7.9$) in 1968 (Ohsaki, 1970); settlements of 50 to 100 cm (20 to 39 in.) were observed on Port Island and Rokko Island in Kobe, Japan following the 1995 Hyogo-ken Nanbu earthquake. If sand boils are produced, postearthquake settlements are likely to be irregular. The resulting differential movement can be damaging to structures, pavements, or pipelines on or near the ground surface.

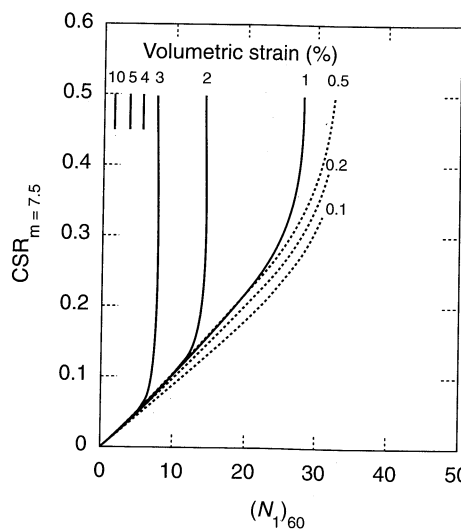


Figure 9.53 Chart for estimation of volumetric strain in saturated sands from cyclic stress ratio and standard penetration resistance. (After Tokimatsu and Seed, 1987. Evaluation of settlements in sand due to earthquake shaking, *Journal of Geotechnical Engineering*, Vol. 113, No. 8. Reprinted by permission of ASCE.)

Example 9.7

Significant settlement was observed in the Marina District of San Francisco following the 1989 Loma Prieta earthquake. Much of this settlement was determined to have resulted from densification of hydraulic fills that were placed to reclaim the area from San Francisco Bay in the 1890s. Subsurface conditions at one location in the Marina District are shown in Figure E9.7 (O'Rourke et al., 1991). Estimate the settlement that would have been expected at this location in the Loma Prieta earthquake. A peak acceleration of 0.20g was measured in the vicinity of the Marina District.

Solution The subsurface profile shows measured (uncorrected) SPT resistances. Assuming that the SPT resistances were measured using standard procedures ($E_m = 0.60E_{ff}$), corrected SPT resistances can be computed using equation (6.30) (column 4 below). The simplified procedure of Seed and Idriss (1971) can be used to estimate the cyclic stress ratio (column 5 below).

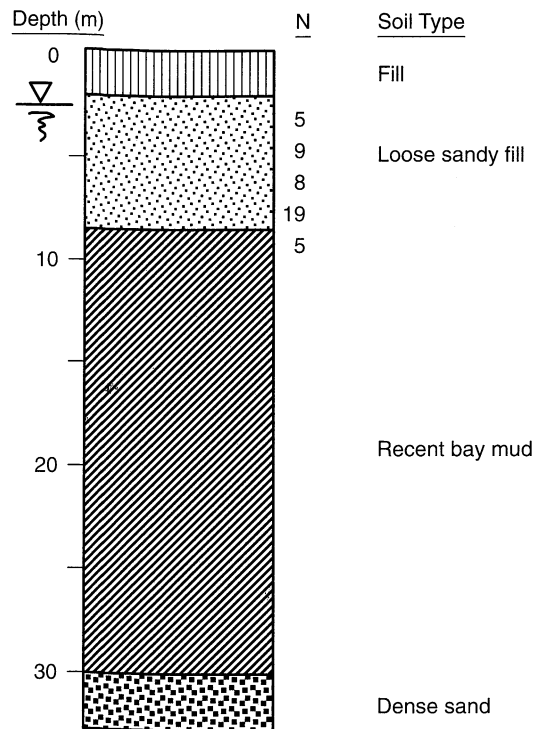


Figure E9.7

(1) Layer	(2) Depth Range (m)	(3) N	(4) $(N_1)_{60}$	(5) CSR	(6) ϵ_v (%)	(7) ΔH (m)
1	2.5–3.5	5	7.5	0.141	3.0	0.030
2	3.5–5.3	9	11.4	0.165	2.4	0.043
3	5.3–6.8	8	8.6	0.180	2.8	0.042
4	6.8–8.5	19	18.7	0.186	0.2	0.003
						0.118

The volumetric strain can then be estimated using Figure 9.53. The settlement of each layer is then computed as the product of the volumetric strain and the layer thickness.

The actual settlements in the vicinity of this site were on the order of 12 to 15 cm. Some of the actual settlements resulted from densification of the dry soil above the water table; that settlement is not accounted for in this example.

In an alternative approach, either the factor of safety against liquefaction [equation (9.14)] or the maximum cyclic shear strain, and the relative density, SPT resistance, or CPT tip resistance, can be used to estimate postliquefaction volumetric strain (Figure 9.54). Integration of these volumetric strains over the thickness of the liquefied layer produces the ground surface settlement.

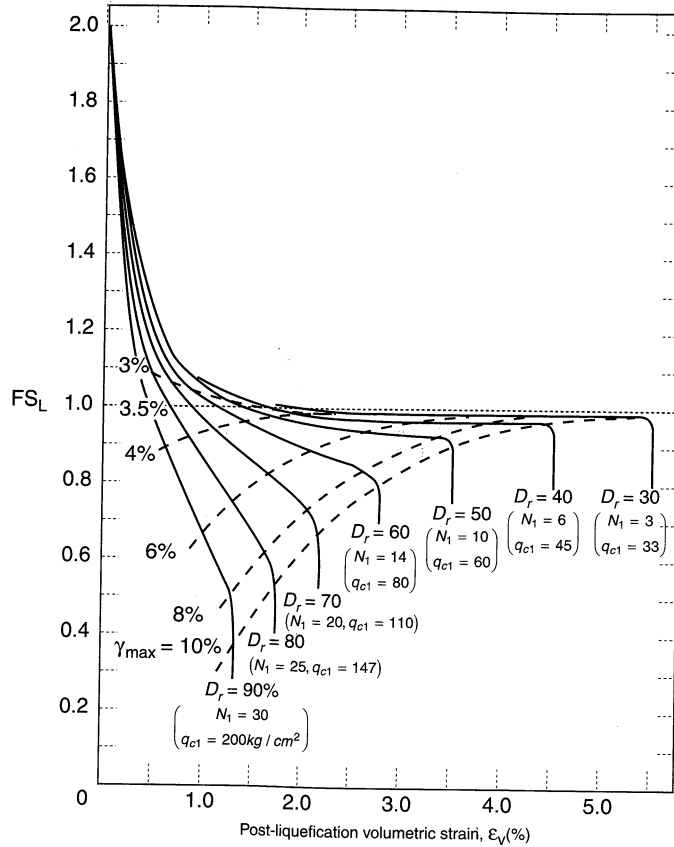


Figure 9.54 Chart for estimating postliquefaction volumetric strain of clean sand as function of factor of safety against liquefaction or maximum shear strain. (After Ishihara and Yoshimine, 1992; used by permission of JSSMFE.)

Example 9.8

Repeat Example 9.7 using the Ishihara–Yoshimine approach.

Solution The Ishihara–Yoshimine approach requires evaluation of the factor of safety against liquefaction. Using the $(N_1)_{60}$ values from Example 9.7 and Figure 9.31, the (magnitude corrected) critical stress ratio required to initiate liquefaction can be determined (column 4 below). Using the CSR values from Example 9.7 and equation (9.11), the factor of safety against liquefaction can be computed for each layer. Then the $(N_1)_{60}$ values must be converted to N_1 values [recall that Japanese SPT procedures typically transmit 20% more energy to the SPT sampler; hence $N_1 \approx 0.833(N_1)_{60}$]. Using the resulting values of FS_L , Figure 9.54 can be used to estimate the volumetric strain in each layer (column 8 below). Again, the settlement of each layer (column 9 below) is given by the product of the volumetric strain and layer thickness.

The total settlement is calculated as 17.7 cm by the Ishihara–Yoshimine procedure. Hence the Tokimatsu–Seed and Ishihara–Yoshimine procedures both provided good estimates

(1) Layer	(2) Depth Range (m)	(3) $(N_1)_{60}$	(4) CSR_L	(5) CSR	(6) FS_L	(7) N_1	(8) ϵ_v (%)	(9) ΔH (m)
1	2.5–3.5	7.5	0.088	0.141	0.62	6.3	4.4	0.044
2	3.5–5.3	11.4	0.134	0.165	0.81	9.5	3.5	0.063
3	5.3–6.8	8.6	0.102	0.180	0.57	7.2	4.2	0.063
4	6.8–8.5	18.7	0.220	0.186	1.18	15.6	0.4	<u>0.007</u> 0.177

of the observed postearthquake settlement at this site. Ishihara (1993) illustrated the use of the Ishihara–Yoshimine procedure for a nearby site (with a smaller thickness of hydraulic fill) using CPT data; a settlement of 7.3 cm was predicted.

In many cases, strong ground motion produces excess pore pressures that are not sufficient to produce initial liquefaction. These pore pressures will dissipate, however, and may produce some volume change. Tokimatsu and Seed (1987) combined a relationship between normalized stress ratio, CSR/CSR_L , and pore pressure ratio (Tokimatsu and Yoshimi, 1983) and a relationship between pore pressure ratio and volumetric strain (Lee and Albaisa, 1974) to develop the relationship shown in Figure 9.55. Figure 9.55 can be used to estimate the volumetric strain for cases in which the maximum pore pressure ratio is less than 100%. Note that postearthquake volume changes are quite small unless the CSR is greater than 70 to 80% of that required to cause initial liquefaction ($r_u = 100\%$).

The rate at which settlement develops depends on the *reconsolidation* characteristics of the liquefied soil. Reconsolidation generally begins at the bottom of the liquefied soil (Florin and Ivanov, 1961; Heidari and James, 1982) and proceeds upward. Because effective stresses can vary over several orders of magnitude during reconsolidation, nonlinear consolidation models are required to predict settlement rates (Whitman et al., 1982; Scott, 1986).

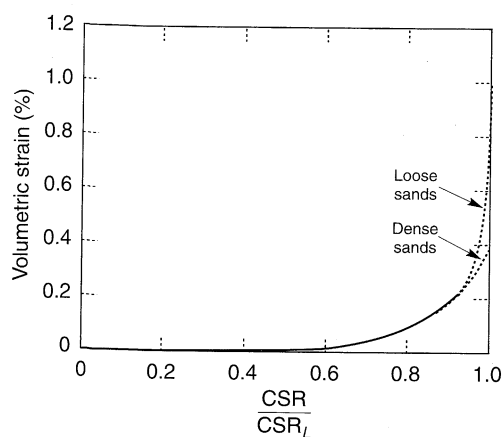


Figure 9.55 Postearthquake volumetric strains for pore pressure ratios less than 100%. (After Tokimatsu and Seed, 1987. Evaluation of settlements in sand due to earthquake shaking, *Journal of Geotechnical Engineering*, Vol. 113, No. 8. Reprinted by permission of ASCE.)

9.6.4 Instability

Liquefaction-induced instabilities are among the most damaging of all earthquake hazards. Their effects have been observed in the form of flow slides, lateral spreads, retaining wall

failures, and foundation failures in countless earthquakes throughout the world. Instability failures can be produced by different liquefaction phenomena, and it is not always clear exactly which is responsible for a given failure. All are strongly influenced, however, by the shear strength of the liquefied soil.

9.6.4.1 Shear Strength of Liquefied Soil

Instability occurs when the shear stresses required to maintain equilibrium of a soil deposit exceed the shear strength of that deposit. The soil then deforms until it reaches a configuration in which the shear stresses do not exceed the shear strength. The amount of deformation required to reach a stable configuration is strongly influenced by the difference between the shear stresses required for equilibrium and the shear strength of the liquefied soil. If the shear strength of the liquefied soil is only slightly lower than the shear stress required for equilibrium, permanent deformations are likely to be small. If the difference between the shear strength and shear stress is large, very large deformations may develop. Accurate evaluation of the effects of liquefaction-induced instability requires accurate estimation of the shear strength of the liquefied soil.

Three different approaches have been developed to estimate the shear strength of liquefied soils. One is based on a program of careful undisturbed sampling and laboratory testing. Another is based on in situ test parameters and interpretation of known liquefaction case histories. The third treats the shear strength of liquefied soil as a normalized strength.

Laboratory Testing Approach: Steady-State Strength. The steady-state strength (defined in Section 9.4.4.2) governs the behavior of liquefied soil. In concept, it is a function solely of the density of the soil, although some experimental studies suggest that it may be influenced by stress path and other factors. For many soils, the steady-state strength is extremely sensitive to density (i.e., small changes in density can result in large changes in steady-state strength).

If cohesionless soils could be sampled “perfectly” (i.e., without any disturbance whatsoever), the steady-state strength, S_{su} , of a given specimen could be measured in a single triaxial test by consolidating the specimen to the in situ stress conditions and then shearing it under undrained conditions following the most appropriate stress path. Unfortunately, the acts of sampling, transportation, handling, and consolidation cause changes in the density of a laboratory specimen by the time it is tested. Given the sensitivity of S_{su} to density, the steady-state strength of a laboratory specimen must be corrected to correspond to the in situ void ratio. Poulos et al. (1985) proposed the following four-step procedure for measurement of in situ steady-state strength. The procedure is illustrated graphically in Figure 9.56.

1. Determine the insitu void ratio from one or more “undisturbed” specimens. This is the most critical, and most difficult, step in the entire procedure. Poulos et al. (1985) suggested three satisfactory sampling procedures: (1) fixed-piston sampling, (2) freezing of the ground and coring, and (3) sampling in test pits. The importance of careful sampling to the success of this procedure cannot be overemphasized.
2. Locate the steady-state line using reconstituted specimens. Since the slope of the SSL is chiefly influenced by grain shape, the SSL from a series of reconstituted specimens should have the same slope as that of the in situ soil. Tests on five or six specimens consolidated to initial states well above the SSL (to ensure contractive behavior) are suggested.

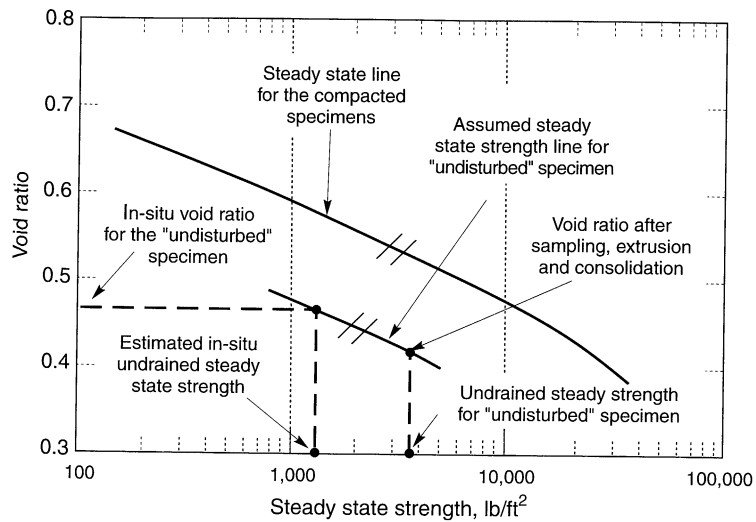


Figure 9.56 Procedure for estimating steady-state shear strength. (After Poulos et al., 1985. Liquefaction evaluation procedure, *Journal of Geotechnical Engineering*, Vol. III, No. 6. Reprinted by permission of ASCE.)

3. Determine the steady-state strength of an undisturbed specimen. A consolidated-undrained triaxial test is performed on a specimen obtained from step 1. To ensure that the steady state is reached at reasonable strain levels, consolidation to elevated effective confining pressures (again, to produce contractive behavior) is suggested.
4. Correct the measured steady state strength to the in situ void ratio. By assuming that the SSL of the undisturbed specimen has the same slope as that of the reconstituted specimens, the in situ steady-state strength can be found by projecting a line through the point describing the undisturbed specimen (from step 3) parallel to the SSL (from step 2) and back to the in situ void ratio (from step 1). The resulting strength is taken as the in situ steady-state strength.

The corrected in situ steady-state strength can then be used to evaluate potential liquefaction hazards. Although this procedure is rational, the user must remain aware of the sensitivity of the results to uncertainties in the input parameters, particularly the in situ void ratio. Kramer (1989) presented a procedure for estimating the uncertainty in S_{su} .

In Situ Testing Approach: Residual Strength. As an alternative to laboratory-based procedures, Seed (1986) developed a correlation between SPT resistance and the apparent shear strength back-calculated from observed flow slides. Since there is no guarantee that all the conditions of the steady state of deformation were satisfied in the case histories—indeed, Stark and Mesri (1992) suggested that partial drainage occurred before some of the flow slides came to rest—the back-calculated strength is termed the *residual strength*. Seed and Harder (1990) reanalyzed many of the flow slides and added new data to

develop a relationship between residual strength and an equivalent clean-sand SPT resistance (Figure 9.57). For sands with more than 10% fines, the equivalent clean-sand SPT resistance is obtained from

$$(N_1)_{60-cs} = (N_1)_{60} + N_{corr} \tag{9.22}$$

where N_{corr} is obtained from Table 9-5.

Table 9-5 Recommended Fines Correction for Estimation of Residual Undrained Strength by Seed-Harder and Stark-Mesri Procedures

Percent Fines	N_{corr} (blows/ft)	
	Seed-Harder	Stark-Mesri
0	0	0
10	1	2.5
15	—	4
20	—	5
25	2	6
30	—	6.5
35	—	7
50	4	7
75	5	7

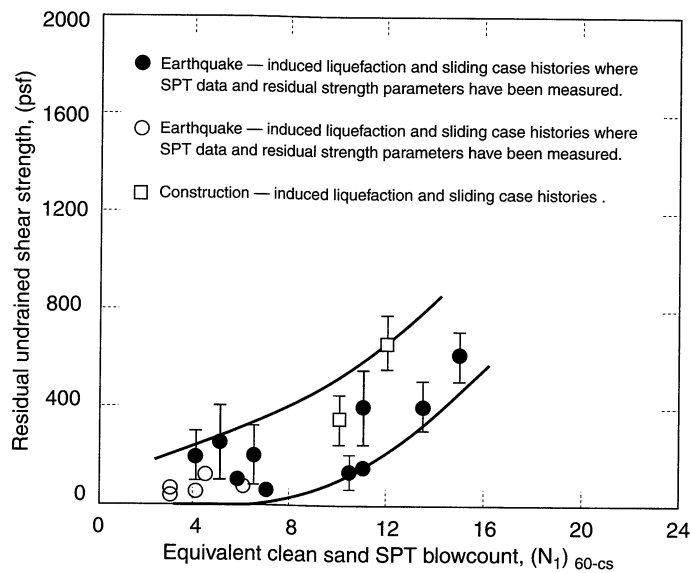


Figure 9.57 Relationship between residual strength and corrected SPT resistance. (After Seed and Harder, 1990. H. Bolton Seed Memorial Symposium Proceedings, Vol. 2, p. 371. Used by permission of BiTech Publishers, Ltd.)

The back-calculation procedures used to obtain the residual strength are not simple—many assumptions and approximations are involved. Combined with the variability of the SPT and the difficulty in selecting a single SPT value to represent each case history, these residual strengths must be considered approximate, as suggested by the wide band in Figure 9.57. As more data become available and as back-calculation procedures improve, this uncertainty is likely to decrease.

Example 9.9

In the 1971 San Fernando earthquake, soil within the upstream slope of Lower San Fernando Dam liquefied and produced a flow slide that nearly breached the dam (Figure 1.7). Subsurface investigations indicated that the hydraulically placed silty sand in the upstream slope contained about 25% fines and had an average measured $(N_1)_{60}$ of about 11.5. Estimate the residual strength of the silty sand.

Solution For a sand with 25% fines, $N_{\text{corr}} = 2$, so

$$(N_1)_{60-cs} = 11.5 + 2 = 13.5$$

Referring to Figure 9.57, the estimated residual strength should be between about 300 lb/ft² and 750 lb/ft² (the values given by the upper and lower curves). Considering that the data from actual case histories of earthquake-induced liquefaction fall in the lower portion of this range, the residual strength appears most likely to be on the order of 300 to 500 lb/ft².

Normalized Strength Approach: Residual Strength Ratio. The concept of *normalized strength* is widely accepted in geotechnical engineering practice for cohesive soils (Ladd and Foott, 1974). The general concept can also be applied to the residual strength of liquefied soils. The significant advantage of this approach is that it allows estimation of residual strength from initial effective stresses, which are much easier to determine accurately than initial void ratios.

If the consolidation curve and steady-state line of a liquefiable soil are parallel, the steady state strength should be proportional to the consolidation stress (i.e., $S_{su}/\sigma'_{1c} = \text{constant}$). Application of this concept is complicated by the fact that sandy soils do not exhibit unique consolidation curves; hence the ratio S_{su}/σ'_{1c} is not unique for a given soil. However, if laboratory specimens are prepared with the same void ratio and soil fabric that exist in the field at comparable initial effective stresses, measured *residual strength ratios* can be representative of field conditions (Vasquez-Herrera et al., 1990; Baziar et al., 1992; Ishihara, 1993). Vasquez-Herrera et al. (1990) found that $S_r/\sigma'_{v0} \approx 0.12$ for reconstituted specimens of silty sand from Lower San Fernando Dam. Byrne et al. (1993) used specimens obtained by freezing and coring at Duncan Dam to measure $S_r/\sigma'_{v0} \approx 0.21$. The normalized strength approach has also been used with residual strength measured in field vane shear tests. Castro and Troncoso (1989) used vane shear tests to measure S_r/σ'_{v0} values of 0.07, 0.11, and 0.08 in very loose slimes (PI = 20 to 22) at three different tailings dams in Chile. For a clayey silt in the foundation of Sardis Dam (Finn et al., 1991), vane shear tests indicated that $S_r/\sigma'_{v0} \approx 0.075$. The limited available data indicate that the normalized strength approach has promise as a practical tool for estimation of the residual strength of liquefied soils. The data also clearly indicate that residual strength ratios can vary over a considerable range and that their evaluation requires careful, site-specific investigation and testing.

The basic normalized strength approach requires site-specific measurement of the residual strength ratio. It is logical to expect that different soils would have different residual

strength ratios; for example, the residual strength ratio of a well-graded angular sand should be greater than that of a uniform rounded sand. Assuming that the factors that influence the residual strength ratio also influence in situ test results, it should be possible to relate the residual strength ratio to in situ test parameters. Stark and Mesri (1992) used back-calculated and laboratory-measured residual strengths from field case histories to correlate values of residual strength ratio to SPT resistance, that is,

$$\frac{S_r}{\sigma'_{v0}} = 0.0055(N_1)_{60-cs} \quad (9.23)$$

where $(N_1)_{60-cs}$ is computed using the values of N_{corr} given in Table 9-5. Although this procedure has the important advantage of allowing the residual strength ratio to be estimated from SPT resistance, equation (9.23) must be recognized as a reasonably conservative approximation to a set of scattered empirical data.

Example 9.10

According to Stark and Mesri (1992), the effective overburden pressure at the center of the liquefied portion of the upstream slope of Lower San Fernando Dam (see Example 9.9) was 3930 lb/ft². Estimate the residual strength of these soils using the Stark–Mesri approach.

Solution According to the Stark–Mesri approach, a silty sand with 25% fines would indicate (from Table 9-6) $N_{corr} = 6$, so

$$(N_1)_{60-cs} = 11.5 + 6 = 17.5$$

Then, using equation (9.23), the residual strength can be estimated as

$$S_r = 0.0055(N_1)_{60-cs} \sigma'_{v0} = (0.0055)(17.5)(3930 \text{ lb/ft}^2) = 378 \text{ lb/ft}^2$$

This value is consistent with the range of values obtained in Example 9.9.

Discussion. Evaluation of the residual strength of a liquefied sand is one of the most difficult problems in contemporary geotechnical earthquake engineering practice. Steady-state concepts are very useful for understanding the behavior of liquefiable soil, but steady-state strengths can be stress path dependent. In the field, failure generally involves different stress paths, and consequently different steady-state strengths, on different parts of the failure surface. Furthermore, some drainage may occur during failure. Given these factors, it is not surprising that residual strengths are difficult to determine.

The laboratory testing approach is rational and based on tests in which the shear stresses are accurately known, but the sensitivity of its results to uncertain input parameters introduces considerable uncertainty into steady-state strength estimates. The in situ testing approach is also rational, but the variability of soil and stress conditions in the case histories on which it is based introduces considerable uncertainty into residual strength estimates. Upon reviewing the application of these approaches to the Lower San Fernando Dam case history, Marcuson et al. (1990) preferred the in situ approach but suggested that both be used where hazards are high. The normalized strength approach offers some advantages over the other approaches, but available data suggest that residual strength ratios vary considerably for different soils.

9.6.4.2 Flow Failures

Liquefaction-induced flow failures occur when the shear stresses required to maintain static equilibrium are greater than the shear strength of a liquefied soil. This situation can arise

in several different ways; the National Research Council (1985) identified four different mechanisms of flow failure. Estimation of the deformations produced by liquefaction-induced flow failures is extremely difficult; available procedures are described in Section 10.6.2.1.

Flow Liquefaction Failures (NRC Mechanism A). Flow liquefaction represents an important flow failure mechanism. Flow liquefaction occurs under totally undrained conditions—no redistribution of pore water (or change in void ratio) is involved. As described in Section 9.5.2.1, flow liquefaction is initiated when sufficient pore pressure is generated to move the effective stress path of an element of soil from its initial position to the flow liquefaction surface. When that occurs, the element becomes unstable and flow liquefaction failure begins in that element of soil. In other words, a flow liquefaction failure occurs at the locations where liquefaction is initiated by earthquake shaking. These characteristics can be used to distinguish between flow liquefaction failures and other types of flow failures. Flow liquefaction failures often occur very quickly and produce large soil movements (Figure 9.58).

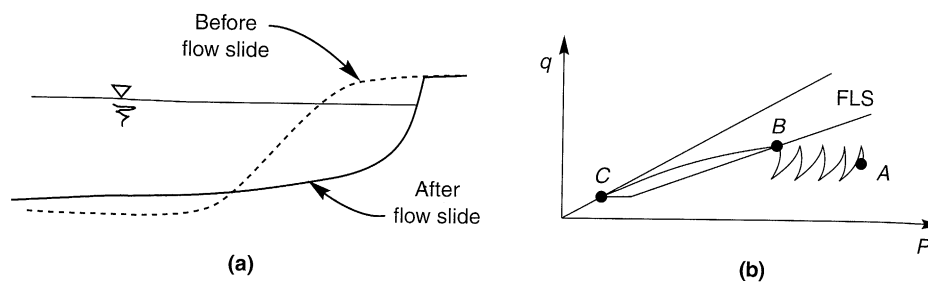


Figure 9.58 (a) Typical cross section through a flow slide showing how liquefied materials can travel large distances and come to rest on very flat surfaces; (b) stress conditions at typical element of soil within failed mass. Prior to earthquake, element is in equilibrium at point A under static shear stress greater than steady state (or residual) strength. Cyclic loading brings stress path to FLS (point B) after which strain softening reduces shearing resistance to steady-state (or residual) strength (point C).

Flow liquefaction failures can develop progressively (i.e., the initiation of flow liquefaction in a small volume of soil may spread to produce a large flow failure). When flow liquefaction is initiated at a particular location, the shearing resistance drops to the steady-state strength. The static shear stresses that were resisted at that location must then be transferred to the surrounding soil, where they may initiate further flow liquefaction. As the redistribution of stresses proceeds, the zone of liquefaction grows. Eventually, a massive flow slide may develop.

Local Loosening Flow Failure (NRC Mechanism B). Since the steady-state strength is very sensitive to the density of many soils, a small amount of loosening can reduce the steady-state strength substantially. In some cases, loosening may reduce the steady-state strength to a value smaller than the shear stress required for equilibrium, thereby producing a flow failure.

If a sand layer is overlain by a less permeable material that does not permit drainage during the earthquake itself, the total volume of the sand will remain constant. If a condition

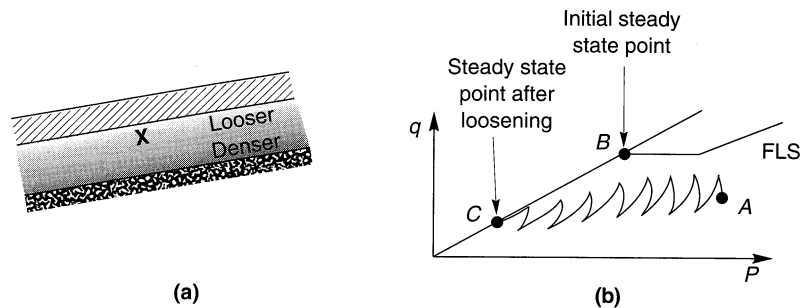


Figure 9.59 Flow failure due to loosening: (a) redistribution of grains in sand layer causes local volume change even though total volume remains constant; (b) stress conditions at point marked with \times . Prior to earthquake, soil is in equilibrium at point A with steady-state strength (point B) that is greater than static shear stress. As effective stresses are reduced during earthquake, loosening of soil reduces steady-state strength to lower value (point C), thereby allowing flow failure to occur.

of initial liquefaction (zero effective stress) is reached, however, the sand particles may rearrange under the action of gravity so that the lower part of the layer becomes denser and the upper part looser. If the upper part loosens sufficiently to reduce the steady-state strength to a value smaller than the static shear stress, a *local loosening flow failure* can occur, as illustrated in Figure 9.59. In extreme cases a water interlayer may form beneath the less permeable material. Since the water interlayer would have zero shear strength, a flow failure could easily be produced.

Global Loosening Flow Failure (NRC Mechanism C). High excess pore pressures generated at depth will cause porewater to flow toward drainage boundaries during and after an earthquake. As illustrated in Figure 9.60a, most of the flow is usually directed toward the ground surface. Shallow soils may be loosened by this flow to the extent that their steady-state strength drops below the shear stress required to maintain equilibrium. In contrast with the local loosening case, this loosening is not compensated for by densification at a different location. The process is illustrated schematically in Figure 9.60b. Since the steady-state strength is not reduced until water flows into the shallower soil, failure may not occur until well after the earthquake. Cracking of the surficial soils may also contribute to the failure.

Interface Flow Failure (NRC Mechanism D). Flow-type failures can also occur when the shear strength of the interface between a liquefiable soil and a structure becomes smaller than the shear stress required for equilibrium. Plunging failure of friction piles (DeAlba, 1983) is an example of an interface flow failure. If the interface is smooth, as with steel or precast concrete piles, interface flow failure does not require volume change of the soil and therefore can occur in contractive or dilative sands.

9.6.4.3 Deformation Failures

Not all liquefaction-related failures involve flow and large displacements. Cyclic mobility can produce small, incremental, permanent deformations that, by the end of an earthquake, may be sufficient to produce extensive damage. Lateral spreading is an example of deformation failure. As illustrated in Figure 9.61, lateral spreading causes surficial

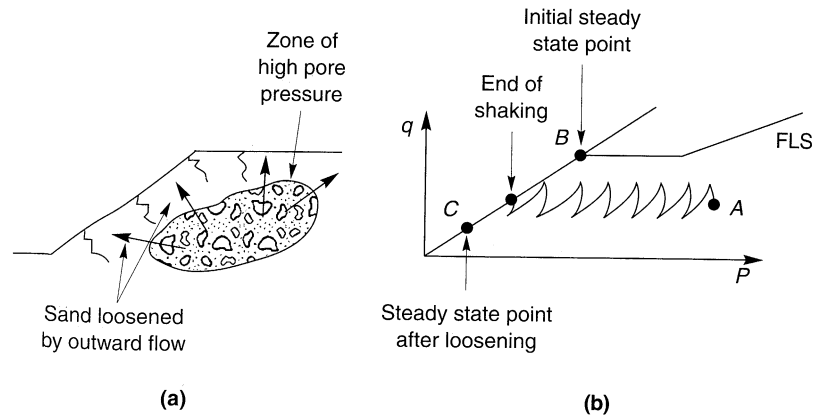


Figure 9.60 (a) Example of global loosening flow failure (after National Research Council, 1985) where earthquake-induced pore pressure at depth causes flow that loosens surficial soils; (b) possible effective stress path for element of surficial soil. Prior to earthquake, static shear stress (point A) is less than steady-state strength (point B). Loosening due to outward flow of porewater reduces steady-state strength (from point B to point C), allowing flow failure to occur.

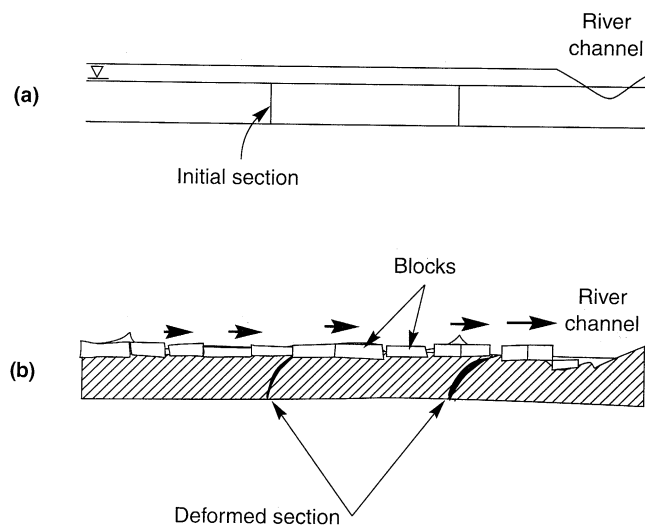


Figure 9.61 Lateral spreading adjacent to a river channel (a) before and (b) after earthquake. Lateral movement of liquefied soil (shaded zone) breaks surface layer into blocks separated by fissures. Blocks may tilt and settle differentially, and sand boils may erupt at fissures. (After Youd, 1984b.)

layers to break into blocks that progressively move downslope or toward a free face (Figure 9.2) during earthquake shaking. The ground surface may exhibit fissures and scarps at the head of the lateral spread, shear zones along its lateral margins, and compressed or buckled

soil at the toe. The surficial blocks usually move irregularly in both horizontal and vertical directions; buildings and pipelines extending across or through the head of a lateral spread may be pulled apart, pipelines crossing the lateral margins may be sheared, and bridges or pipelines near the toe may be buckled (Figure 1.8). Lateral displacements usually range from a few centimeters to a meter or two, but may be larger if shaking is particularly strong or of long duration. Procedures for estimating lateral spreading deformations are described in Section 10.6.2.2.

9.7 SUMMARY

1. The term *liquefaction* has been used to describe a number of related but different phenomena observed in loose, saturated soils. For engineering purposes, these phenomena can be divided into three main groups: flow liquefaction, cyclic mobility, and level-ground liquefaction.
2. Flow liquefaction can occur when the static shear stress in a liquefiable soil deposit is greater than the steady-state strength of the soil. It can produce devastating flow slide failures during or after earthquake shaking. Flow liquefaction can occur only in loose soils.
3. Cyclic mobility can occur when the static shear stress is less than the steady-state strength and the cyclic shear stress is large enough that the steady-state strength is exceeded momentarily. Deformations produced by cyclic mobility develop incrementally but can become substantial by the end of a strong and/or long-duration earthquake. Cyclic mobility can occur in both loose and dense soils but deformation decreases markedly with increased density.
4. Level-ground liquefaction can occur when cyclic loading is sufficient to produce high excess pore pressures, even when static driving stresses are absent. Its occurrence is generally manifested by ground oscillation, postearthquake settlement, and/or the development of sand boils. Permanent lateral displacements due to level-ground liquefaction are usually small. Level-ground liquefaction can occur in loose and dense soils.
5. Liquefaction hazard evaluation requires that questions of liquefaction susceptibility, initiation, and effects be addressed. For a site to be considered free from liquefaction hazards, the soils must be nonsusceptible to liquefaction, the anticipated loading must be insufficient to initiate liquefaction, *or* the effects of liquefaction must be tolerable.
6. Liquefaction susceptibility can be judged on the basis of historical, geologic, compositional, and state considerations. Geologic, compositional, and state criteria must be met for a soil to be susceptible to liquefaction; if any of these criteria are not met, the soil is nonsusceptible to liquefaction.
7. Liquefaction susceptibility is different for different liquefaction phenomena. A soil that is susceptible to cyclic mobility or level-ground liquefaction may not be susceptible to flow liquefaction. Susceptibility to various liquefaction phenomena depends primarily on the state (stress and density conditions) of the soil at the time of the earthquake.

8. Under given loading conditions, any sand will reach a unique combination of effective confining pressure, shear strength, and density at large strains. The combination can be described graphically by a steady-state line. The position of the steady-state line is most strongly influenced by grain size and grain shape characteristics. The behavior of a sand is strongly related to its position relative to the steady-state line.
9. Flow liquefaction is initiated when the principal effective stress ratio reaches a critical value under undrained, stress-controlled conditions. The stress state at the initiation of flow liquefaction can be described graphically in stress path space by the flow liquefaction surface. Once the effective stress path of an element of soil reaches the flow liquefaction surface, additional straining will induce additional excess pore pressure and the available shearing resistance will drop to the steady-state strength.
10. Because the state of a loose sand in equilibrium under high initial shear stress is closer to the flow liquefaction surface than that of a similar soil subjected to lower initial shear stress, less excess pore pressure is required to initiate flow liquefaction. Flow liquefaction can be triggered by small undrained disturbances in soils subjected to high initial shear stresses. Such soils may represent a high liquefaction hazard.
11. Cyclic mobility can produce high excess pore pressures and low effective stresses, but unidirectional movement will cause the soil to dilate. The increased shearing resistance produced by dilation will arrest soil movement so that flow slides cannot develop.
12. The existence of sand boils is often taken as evidence of level-ground liquefaction. Sand boil formation, however, depends on factors such as the depth, thickness, and void volume of the liquefied layer and on the characteristics of overlying soils. Since level-ground liquefaction of a thin and/or silty layer at depth may not be expressed at the ground surface, the absence of sand boils does not necessarily indicate that level-ground liquefaction has not occurred.
13. The cyclic stress approach to evaluation of liquefaction potential characterizes both earthquake loading and soil liquefaction resistance in terms of cyclic stresses. A transient earthquake motion is converted to an equivalent series of uniform cycles of shear stress. The number of equivalent cycles, a function of the duration of the motion, is correlated with the magnitude of the earthquake. Liquefaction resistance is obtained from laboratory or in situ tests. Cyclic triaxial and cyclic simple shear tests are usually used in the laboratory; liquefaction resistance is expressed in terms of the number of cycles required to produce failure of a soil of given density subjected to a particular level of cyclic shear stress. The cyclic stress-based liquefaction resistance, however, is influenced by factors such as soil fabric, stress and strain history, and age that may be destroyed by sampling and are difficult to replicate in the laboratory. In situ test-based procedures characterize liquefaction resistance in terms of in situ test parameters associated with soils that have liquefied in past earthquakes; the SPT resistance is most commonly used, but other insitu parameters, including CPT resistance and shear wave velocity, are gaining acceptance. The cyclic stress approach allows estimation of a factor of safety against liquefaction.
14. In the cyclic strain approach, earthquake loading and liquefaction resistance are characterized by cyclic strains. Since the factors that influence the cyclic shear stresses

required to initiate liquefaction have a similar effect on the shear modulus, the cyclic strain (the ratio of cyclic shear stress to shear modulus) is less sensitive to them. The shear modulus is an important liquefaction resistance parameter in the cyclic strain approach. Liquefaction is expected at locations where the cyclic strain amplitude induced for a particular number of cycles by an earthquake is greater than the cyclic strain amplitude required to initiate liquefaction in the same number of cycles. The cyclic strain approach does not produce a factor of safety against liquefaction.

15. Other approaches to the evaluation of liquefaction potential have been developed. Dissipated energy has been used as a measure of liquefaction resistance; its comparison with the energy content of a ground motion allows liquefaction potential to be evaluated. Effective stress ground response analyses, with cyclic stress–strain and pore pressure models or advanced constitutive models, can be used to predict the generation of excess pore pressure and its redistribution both during and after earthquake shaking. Probabilistic approaches, based both on laboratory tests results and on field performance observations, allow estimation of the likelihood of liquefaction.
16. The effects of liquefaction are different for different liquefaction phenomena. Although flow liquefaction is capable of producing the most spectacular effects, cyclic mobility and level-ground liquefaction can also produce extensive damage.
17. Liquefaction can dramatically alter the amplitude and frequency content of ground surface motions. As the buildup of excess pore pressure causes a layer of liquefiable soil to soften, ground surface displacements may increase even when ground surface accelerations decrease. Ground oscillation may produce chaotic permanent movement of fractured blocks of surficial soil.
18. Ground surface settlement can develop during and/or after earthquakes due to densification of dry or saturated sands. Settlement of dry sand occurs almost immediately, but settlement of saturated sands may not develop until well after earthquake shaking has ended. The magnitude of postearthquake settlement depends on the density of the sand, and on the amplitude and duration of shaking.
19. When earthquake-induced shear stresses exceed the shear strength of a liquefied soil, instability failures can occur. The shear strength of liquefied soil may be evaluated by careful undisturbed sampling and laboratory testing or by comparison with in situ test parameters and back-calculated strengths from liquefaction case histories. All available approaches produce strength estimates with considerable uncertainty.
20. Liquefaction flow failures occur when static shear stresses exceed the shear strength of a liquefied soil. This situation can arise during and/or after an earthquake. The effects of soil loosening due to porewater flow on shear strength must be recognized and accounted for in an evaluation of possible flow failure.
21. Deformation failures, such as lateral spreading, develop incrementally during the period of earthquake shaking. For strong levels and/or long durations of shaking, deformation failures can produce large displacements and cause significant damage. Procedures have been developed to estimate displacements caused by deformation failures.

HOMWORK PROBLEMS

- 9.1 A rounded sand subjected to a series of monotonic triaxial compression tests exhibits the steady-state line (SSL) shown below. Assuming that the sand can mobilize a friction angle of 33° in the steady state, estimate the steady-state strength that would be mobilized by the following test specimens:

Specimen	Initial Void Ratio	Initial σ'_{3c}	Test Condition
A	0.75	100 kPa	Drained
B	0.75	100 kPa	Undrained
C	0.60	50 kPa	Drained
D	0.60	50 kPa	Undrained

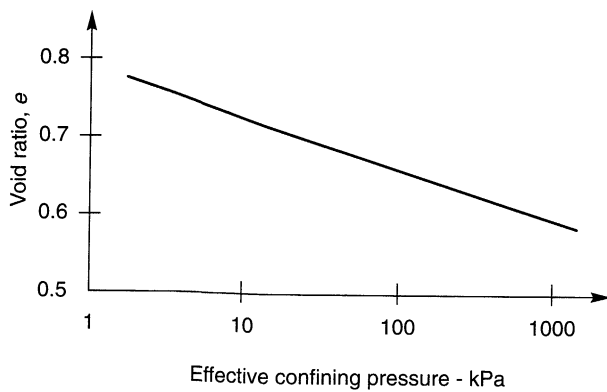


Figure P9.1

- 9.2 Consider an anisotropically consolidated direct simple shear test specimen with the initial conditions shown below. Show graphically how the pore pressure ratio at the initiation of liquefaction, $r_{u,t}$, varies with the amplitude of the cyclic shear stress.

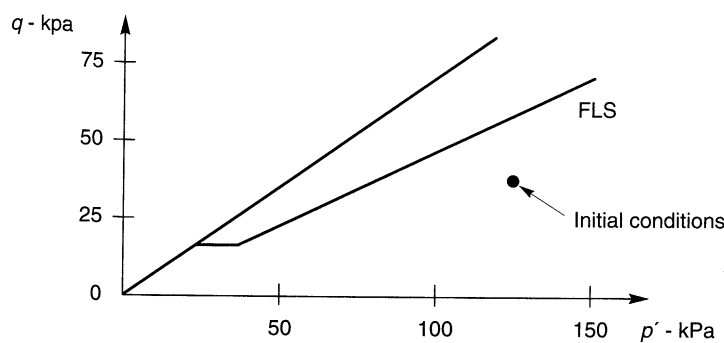


Figure P9.2

- 9.3 A 10 m thick deposit of loose sand is saturated below a depth of 3 m. The soil below the water table is highly susceptible to liquefaction. Estimate the ground surface acceleration that would be required to produce sand boils in a $M = 7.7$ earthquake.
- 9.4 Estimate the variation of uniform cyclic shear stress amplitude with depth for the upper 50 ft of soil (assume $\gamma = 120$ pcf) at the Gilroy No. 2 (soil) station in the Loma Prieta earthquake (see Figure 3.1). Estimate the number of equivalent uniform stress cycles.
- 9.5 A level deposit of saturated clean sand has an average $(N_1)_{60}$ -value of 18 and an average dry unit weight of 105 pcf. Plot the variation of cyclic shear stress required to produce liquefaction in $M = 5.5, 6.5, 7.5,$ and 8.5 earthquakes.
- 9.6 Repeat Problem 9.5 assuming that the sand has 15% fines.
- 9.7 The surface of a thick deposit of silty sand (30% fines) slopes at an angle of 10° . Standard penetration tests indicate an average $(N_1)_{60}$ -value of 12; density tests indicate an average density of 1.80 Mg/m^3 . Compute and plot the cyclic shear stress required to produce liquefaction in the upper 30 ft of the silty sand in a $M = 7.5$ earthquake.
- 9.8 A level deposit of clean sand with an average void ratio of 0.70 has an uncorrected CPT tip resistance of 80 tsf at a depth of 20 ft. The mean grain size of the sand is 0.40 mm and the groundwater table is at a depth of 4 ft. Compute the cyclic shear stress required to produce liquefaction at a depth of 20 ft in a $M = 6.5$ earthquake.
- 9.9 Prior to the 1989 Loma Prieta earthquake, a site investigation at the Hunters Point Navy Base in San Francisco showed 13 to 15 m of clean, hydraulically filled sand with $D_{50} = 0.29$ mm. The water table was at a depth of about 2.5 m. CPT tests produced the following average tip resistances:

Depth Interval (m)	Average q_c (MPa)
3–4	6.5
4–5	5.7
5–6	5.2
6–7	4.9
7–8	5.1
8–9	6.3
9–10	6.9
10–11	7.6

The Loma Prieta earthquake produced peak ground accelerations on the order of $0.15g$ to $0.20g$ at similar sites in the Bay Area. Assuming that the sand has an average dry density of 1.60 Mg/m^3 , compute and plot the factor of safety against liquefaction that would have been expected in the Loma Prieta earthquake.

- 9.10 Plot the estimated porewater pressure distribution at the end of the Loma Prieta earthquake at the Hunters Point site described in Problem 9.9.
- 9.11 Repeat Problem 9.9 for a $M = 7.6$ earthquake that produces a peak ground acceleration of $0.30g$.
- 9.12 Using the energy-based criterion of Law et al. (1990) [(equation (9.16))], plot the limiting hypocentral distance beyond which liquefaction would not be expected in $N_1 = 10$ soils as a function of earthquake magnitude. Compare the result with Figure 9.4 and comment on the differences.

- 9.13** Estimate the vertical settlement that would have been expected at Hunters Point (see Problem 9.9) following the 1989 Loma Prieta earthquake.
- 9.14** Estimate and plot the variation of the post-liquefaction residual strength of the sand at the site described in Example 9.4 using (a) the Seed-Harder approach, and (b) the Stark-Mesri approach.

10

Seismic Slope Stability

10.1 INTRODUCTION

Landslides occur on a regular basis throughout the world as part of the ongoing evolution of landscapes. Many landslides occur in natural slopes, but slides also occur in man-made slopes from time to time. At any point in time, then, slopes exist in states ranging from very stable to marginally stable. When an earthquake occurs, the effects of earthquake-induced ground shaking is often sufficient to cause failure of slopes that were marginally to moderately stable before the earthquake. The resulting damage can range from insignificant to catastrophic depending on the geometric and material characteristics of the slope.

Earthquake-induced landslides, which have been documented from as early as 1789 B.C. (Li, 1990), have caused tremendous amounts of damage throughout history. In many earthquakes, landslides have been responsible for as much or more damage than all other seismic hazards combined. In the 1964 Alaska earthquake, for example, an estimated 56% of the total cost of damage was caused by earthquake-induced landslides (Youd, 1978; Wilson and Keefer, 1985). Kobayashi (1981) found that more than half of all deaths in large ($M > 6.9$) earthquakes in Japan between 1964 and 1980 were caused by landslides. The 1920 Haiyuan earthquake ($M = 8.5$) in the Ningxia Province of China produced hundreds of large landslides that caused more than 100,000 deaths (Close and McCormick, 1922). Evaluation of seismic slope stability is one of the most important activities of the geotechnical earthquake engineer.

This chapter we describes different types of earthquake-induced landslides and the conditions under which they occur. It also reviews the basic principles of slope stability evaluation, including static stability analysis, and then presents several methods for seismic slope stability analysis.

10.2 TYPES OF EARTHQUAKE-INDUCED LANDSLIDES

Many factors, including geologic and hydrologic conditions, topography, climate, weathering, and land use, influence the stability of slopes and the characteristics of landslides. A number of procedures for classification of landslides have been proposed; that of Varnes (1978) is perhaps most widely used in the United States. Similar principles and terminology can be used to classify earthquake-induced landslides (Table 10-1) on the basis of material type (soil

Table 10-1 Types and Characteristics of Earthquake-Induced Landslides

Name	Type of Movement	Internal Disruption ^a	Water content ^b				Velocity ^c	Depth ^d
			D	U	PS	S		
<i>Disrupted Slides and Falls</i>								
Rock falls	Bounding, rolling, free fall	High or very high	×	×	×	×	Extremely rapid	Shallow
Rock slides	Translational sliding on basal shear surface	High	×	×	×	×	Rapid to extremely rapid	Shallow
Rock avalanches	Complex, involving sliding and/or flow, as stream of rock fragments	Very high	×	×	×	×	Extremely rapid	Deep
Soil falls	Bounding, rolling, free fall	High or very high	×	×	×	×	Extremely rapid	Shallow
Disrupted soil	Translational sliding on basal shear surface or zone of weakened, sensitive clay	High	×	×	×	×	Moderate to rapid	Shallow
Soil avalanches	Translational sliding with subsidiary flow	Very high	×	×	×	×	Very rapid to extremely rapid	Shallow
<i>Coherent Slides</i>								
Rock slumps	Sliding on basal shear surface with component of headward rotation	Slight or moderate	?	×	×	×	Slow to rapid	Deep

Table 10-1 Types and Characteristics of Earthquake-Induced Landslides (*continued*)

Name	Type of Movement	Internal Disruption ^a	Water content ^b				Velocity ^c	Depth ^d
			D	U	PS	S		
Rock block slides	Translational sliding on basal shear surface	Slight or moderate	?	×	×	×	Slow to rapid	Deep
Soil slumps	Sliding on basal shear surface with component of headward rotation	Slight or moderate	?	×	×	×	Slow to rapid	Deep
Soil block slides	Translational sliding on basal shear surface	Slight or moderate	?	?	×	×	Slow to rapid	Deep
Slow earth flows	Translational sliding on basal shear surface with minor internal flow	Slight			×	×	Very slow to moderate with very rapid surges	Generally shallow, occasionally deep
<i>Lateral Spreads and Flows</i>								
Soil lateral spreads	Translation on basal zone of liquefied sand, or silt or weakened, sensitive clay	Generally moderate, occasionally slight, occasionally high			×	×	Very rapid	Variable
Rapid soil flows	Flow	Very high	?	?	?	×	Very rapid to extremely rapid	Shallow
Subaqueous landslides	Complex, generally involving lateral spreading, and/or flow; occasionally involving slumping and/or block sliding	Generally high or very high, occasionally moderate or slight			×	×	Generally rapid to extremely rapid, occasionally slow to moderate	Variable

Source: Keefer (1984).

^aInternal disruption: "slight" signifies landslide consists of one or a few coherent blocks; "moderate" signifies several coherent blocks; "high" signifies numerous small blocks and individual soil grains and rock fragments; "very high" signifies nearly complete disaggregation into individual soil grains or small rock fragments.

^bWater content: D, dry; U, moist, but unsaturated; PS, partly saturated; S, saturated.

^cVelocity:

0.6 m/yr	1.5 m/yr	1.5 m/month	1.5 m/day	0.3 m/min	3 m/sec
extremely slow	very slow	slow	moderate	rapid	very rapid
					extremely rapid

^dDepth: "shallow" signifies thickness generally < 3 m; "deep" generally > 3 m.

or rock), character of movement (disrupted or coherent), and other attributes, such as velocity, depth, and water content. Earthquake-induced landslides can be divided into three main categories: disrupted slides and falls, coherent slides, and lateral spreads and flows.

Disrupted slides and falls include rock falls, rock slides, rock avalanches, soil falls, disrupted soil slides, and soil avalanches. The earth materials involved in such failures are sheared, broken, and disturbed into a nearly random order. These types of failures, usually found in steep terrain, can produce extremely rapid movements and devastating damage; rock avalanches and rock falls have historically been among the leading causes of death from earthquake-induced landslides.

Coherent slides, such as rock and soil slumps, rock and soil block slides, and slow earth flows, generally consist of a few coherent blocks that translate or rotate on somewhat deeper failure surfaces in moderate to steeply sloping terrain. Most coherent slides occur at lower velocities than disrupted slides and falls.

Lateral spreads and flows generally involve liquefiable soils, although sensitive clays can produce landslides with very similar characteristics. Due to the low residual strength of these materials, sliding can occur on remarkably flat slopes and produce very high velocities. Liquefaction-induced spreads and flow slides were discussed in detail in Chapter 9.

The different types of earthquake-induced landslides occur with different frequencies. Rock falls, disrupted soil slides, and rock slides appear to be the most common types of landslides observed in historical earthquakes (Table 10-2). Subaqueous landslides, slow earth flows, rock block slides, and rock avalanches are least common, although the difficulty of observing subaqueous slides may contribute to their apparent rarity.

Table 10-2 Relative Abundance of Earthquake-Induced Landslides from Study of 40 Historical Earthquakes Ranging from $M_s = 5.2$ to $M_w = 9.5$

Abundance	Description
Very abundant (> 100,000 in the 40 earthquakes)	Rock falls, disrupted soil slides, rock slides
Abundant (10,000 to 100,000 in the 40 earthquakes)	Soil lateral spreads, soil slumps, soil block slides, soil avalanches
Moderately common (1000 to 10,000 in the 40 earthquakes)	Soil falls, rapid soil flows, rock slumps
Uncommon	Subaqueous landslides, slow earth flows, rock block slides, rock avalanches

Source: Keefer (1984).

10.3 EARTHQUAKE-INDUCED LANDSLIDE ACTIVITY

For preliminary stability evaluations, knowledge of the conditions under which earthquake-induced landslides have occurred in past earthquakes is useful. It is logical to expect that the extent of earthquake-induced landslide activity should increase with increasing earthquake magnitude and that there could be a minimum magnitude below which earthquake-induced

landsliding would rarely occur. It is equally logical to expect that the extent of earthquake-induced landslide activity should decrease with increasing source-to-site distance and that there could be a distance beyond which landslides would not be expected in earthquakes of a given size.

A study of 300 U.S. earthquakes between 1958 and 1977 showed that the smallest earthquakes noted to have produced landslides had local magnitudes of about 4.0 (Keefer, 1984). Minimum magnitudes for different types of landslides were estimated as shown in Table 10-3. Where magnitudes were not available, minimum Modified Mercalli Intensity (MMI) values of IV and V have been observed for disrupted slides or falls and other types of slides, respectively. Although these empirically based limits are useful, their approximate nature must be recognized; failure of slopes that are near the brink of failure under static conditions could be produced by quite weak earthquake shaking.

Table 10-3 Estimates of the Smallest Earthquakes Likely to Cause Landslides

M_L	Description
4.0	Rock falls, rock slides, soil falls, disrupted soil slides
4.5	Soil slumps, soil block slides
5.0	Rock slumps, rock block slides, slow earth flows, soil lateral spreads, rapid soil flows, and subaqueous landslides
6.0	Rock avalanches
6.5	Soil avalanches

Source: After Keefer (1984).

The maximum source-to-site distance at which landslides have been produced in historical earthquakes are different for different types of landslides (Figure 10.1). Disrupted slides or falls, for example, have rarely been found beyond epicentral distances of about 15 km for $M = 5$ events but have been observed as far as about 200 km (124 mi.) in $M = 7$ earthquakes. Note that the curve for lateral spreads and flows correlates reasonably well with the magnitude–distance curve for liquefaction shown in Figure 9.5. Similarly, the area over which earthquake-induced landsliding can be expected also increases with increasing earthquake magnitude (Figure 10.2). Regional differences in attenuation behavior have little apparent influence on the area of earthquake-induced landsliding.

Example 10.1

Estimate the maximum distances at which rock avalanches, soil slumps, and soil lateral spreads would be expected in a $M = 6.5$ earthquake.

Solution Rock avalanches, soil slumps, and soil lateral spreads fall under the headings of disrupted falls and slides, coherent slides, and lateral spreads and flows, respectively. From Figure 10.1, the maximum distances of these types of slides from the fault rupture zone would be

Rock avalanche	61 km
Soil slumps	22 km
Soil lateral spreads	20 km

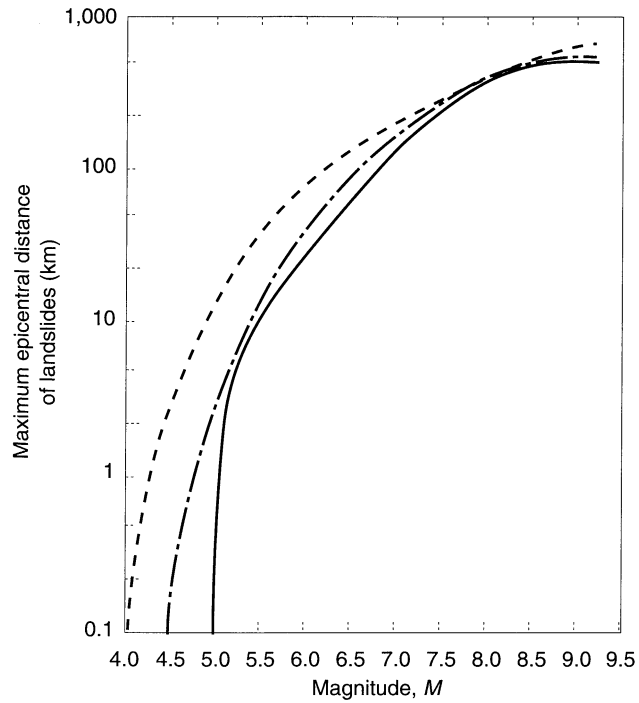


Figure 10.1 Maximum epicentral distance for different types of landslides. Dashed line is for disrupted falls and slides, dash-dot line is for coherent slides, and solid line is for lateral spreads and flows. (After Keefer, 1984. Used by permission of the Geological Society of America.)

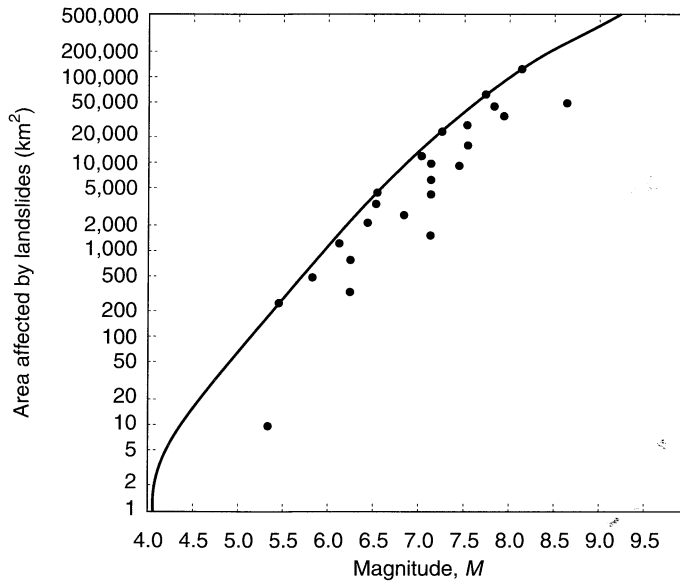


Figure 10.2 Area affected by landslides for earthquakes of different magnitude. (After Keefer, 1984. Used by permission of the Geological Society of America.)

10.4 EVALUATION OF SLOPE STABILITY

The stability of slopes is influenced by many factors, and a complete slope stability evaluation must consider the effects of each. Geological, hydrological, topographical, geometrical, and material characteristics all influence the stability of a particular slope. Information on these characteristics is needed to reliably perform and interpret the results of both static and seismic slope stability analyses. Review of available documents, field reconnaissance, field monitoring, subsurface investigation, and material testing can all be used to obtain this information.

For many sites, considerable useful information can be obtained from previously published documents such as geologic maps, soil survey and/or agricultural maps, topographic maps, natural hazard maps, and geologic and geotechnical engineering reports. Additional information may be obtained from aerial photographs (particularly stereo-paired aerial photographs) and other forms of remote sensing.

Field reconnaissance involves careful observation and detailed mapping of a variety of site characteristics associated with existing or potential slope instability. Features such as scarps; tension cracks; bulges; hummocky terrain; displaced ditches, channels, and fences; cracked foundations, walls, or pavements; and leaning trees or poles can be identified and mapped as evidence of instability. The locations of streams, springs, seeps, ponds, and moist areas, and differences in vegetative cover, can provide evidence of altered or disrupted water flow caused by slope instability.

If time permits, slope movement can be monitored. Surface monuments can be installed at points on and near the slope and surveyed periodically to identify the magnitude and direction of surface movement. Photogrammetric methods can be used to determine relative movements from sets of stereo-paired aerial photographs taken at different times. Inclometers are very useful for monitoring lateral deformation patterns below the ground surface. In many cases, crack gauges, tiltmeters, and extensometers can also be used to observe the effects of slope movement. When, as is commonly the case, pore pressures are important, piezometers and/or observation wells can provide important information on pore pressures and their variation with time.

Subsurface investigation can include excavation and mapping of test pits and trenches, boring and sampling, in situ testing, and geophysical testing. Such investigations can reveal the depth, thickness, density, strength, and deformation characteristics of subsurface units, and the depth and variation of the groundwater table. In situ and geophysical tests are particularly useful for determining the location of an existing failure surface.

Laboratory tests are often used to quantify the physical characteristics of the various subsurface materials for input into a numerical slope stability analysis. Soil density, strength, and stress-strain behavior are of prime importance; other characteristics, such as grain size distribution, plasticity, permeability, and compressibility, are also useful.

Only after this information is obtained can a stability analysis be performed. Although in the remainder of this chapter we focus on methods of slope stability analysis, it is important to remember that the analysis itself is but a single part of a complete slope stability evaluation and that its accuracy will be reduced if careful attention is not given to the other aspects of the evaluation.

10.5 STATIC SLOPE STABILITY ANALYSIS

Slopes become unstable when the shear stresses required to maintain equilibrium reach or exceed the available shearing resistance on some potential failure surface. For slopes in which the shear stresses required to maintain equilibrium under static gravitational loading are high, the additional dynamic stresses needed to produce instability may be low. Hence the seismic stability of a slope is strongly influenced by its static stability. Because of this and the fact that the most commonly used methods of seismic stability analysis rely on static stability analyses, a brief summary of static slope stability analysis is presented.

The procedures for analysis of slope stability under static conditions are well established. An excellent, concise review of the state of the art for static analysis was presented by Duncan (1992). Detailed descriptions of specific methods of analysis can be found in standard references such as National Research Council (1976), Chowdhury (1978), and Huang (1983). Currently, the most commonly used methods of static slope stability analysis are *limit equilibrium analyses* and *stress-deformation analyses*.

10.5.1 Limit Equilibrium Analysis

Limit equilibrium analyses consider force and/or moment equilibrium of a mass of soil above a potential failure surface. The soil above the potential failure surface is assumed to be rigid (i.e., shearing can occur only on the potential failure surface). The available shear strength is assumed to be mobilized at the same rate at all points on the potential failure surface. As a result, the factor of safety is constant over the entire failure surface. Because the soil on the potential failure surface is assumed to be rigid-perfectly plastic (Figure 10.3), limit equilibrium analyses provide no information on slope deformations.

Slope stability is usually expressed in terms of an index, most commonly the *factor of safety*, which is usually defined as

$$FS = \frac{\text{available shear strength}}{\text{shear stress required to maintain equilibrium}} \quad (10.1)$$

Thus the factor of safety is a ratio of capacity (the shear strength of the soil) to demand (the shear stress induced on the potential failure surface). The factor of safety can also be viewed as the factor by which the strength of the soil would have to be divided to bring the slope to the brink of instability. In contrast to the assumptions of limit equilibrium analysis, the strength of the soil in actual slopes is not reached at the same time at all points on the failure surface (i.e., the local factor of safety is not constant).

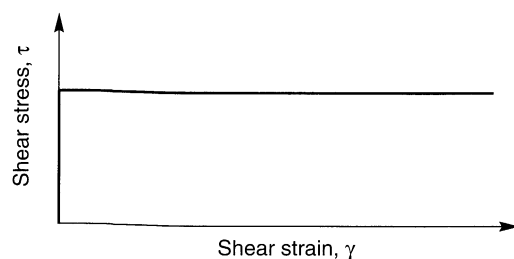


Figure 10.3 Stress-strain curve for a rigid-perfectly plastic material. No shear strain occurs until the strength of the material is reached, after which the material strains at constant shear stress.

A variety of limit equilibrium procedures have been developed to analyze the static stability of slopes. Slopes that fail by translation on a planar failure surface (Figure 10.4a) such as a bedding plane, rock joint, or seam of weak material can be analyzed quite easily by the Culmann method (Taylor, 1948). Slopes in which failure is likely to occur on two or three planes (Figure 10.4b) can be analyzed by wedge methods (e.g., Perloff and Baron, 1976; Lambe and Whitman, 1969). In homogeneous slopes, the critical failure surface usually has a circular (Figure 10.4c) or log-spiral shape. Since the minimum factors of safety for circular and log-spiral failure surfaces are very close, homogeneous slopes are usually analyzed by methods such as the ordinary method of slices (Fellenius, 1927) or Bishop's modified method (Bishop, 1955), which assume circular failure surfaces. When subsurface conditions are not homogeneous (e.g., when layers with significantly different strength, highly anisotropic strength, or discontinuities exist), failure surfaces are likely to be non-circular (Figure 10.4d). In such cases, methods like those of Morgenstern and Price (1965), Spencer (1967), and Janbu (1968) may be used. Nearly all limit equilibrium methods are susceptible to numerical problems under certain conditions. These conditions vary for different methods but are most commonly encountered where soils with high cohesive strength are present at the top of a slope and/or when failure surfaces emerge steeply at the base of the slopes in soils with high frictional strength (Duncan, 1992).

In concept, any slope with a factor of safety above 1.0 should be stable. In practice, however, the level of stability is seldom considered acceptable unless the factor of safety is significantly greater than 1.0. Criteria for acceptable factors of safety recognize (1) uncertainty in the accuracy with which the slope stability analysis represents the actual mechanism of failure, (2) uncertainty in the accuracy with which the input parameters (shear strength, groundwater conditions, slope geometry, etc.) are known, (3) the likelihood and duration of exposure to various types of external loading, and (4) the potential consequences of slope failure. Typical minimum factors of safety used in slope design are about 1.5 for normal long-term loading conditions and about 1.3 for temporary slopes or end-of-construction conditions in permanent slopes (when dissipation of pore pressure increases stability with time).

When the minimum factor of safety of a slope reaches a value of 1.0, the available shear strength of the soil is fully mobilized on some potential failure surface and the slope

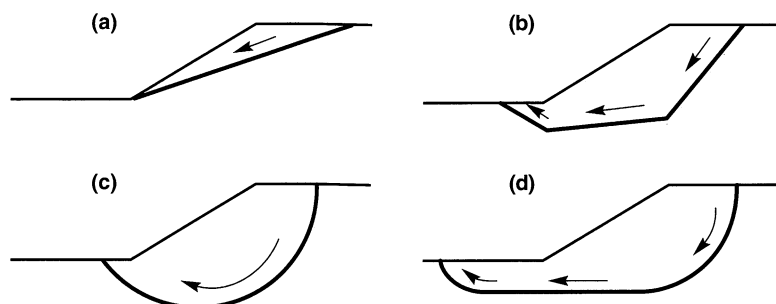


Figure 10.4 Common failure surface geometries: (a) planar; (b) multiplanar; (c) circular; (d) noncircular.

is at the point of incipient failure. Any additional loading will cause the slope to fail (i.e., to deform until it reaches a configuration in which the shear stresses required for equilibrium are less than or equal to the available shear strength of the soil). The limit equilibrium assumption of rigid–perfectly plastic behavior suggests that the required deformation will occur in a ductile manner. Many soils, however, exhibit brittle, strain-softening stress–strain behavior. In such cases the peak shear strength may not be mobilized simultaneously at all points on the failure surface. When the peak strength of a strain-softening soil is reached, such as point A in Figure 10.5a, the available shearing resistance will drop from the peak to the residual strength. As it does so, shear stresses related to the difference between the peak and residual strength of the soil at point A are transferred to the surrounding soil. These redistributed shear stresses may cause the peak strengths in the surrounding soil to be reached (Figure 10.5b) and exceeded, thereby reducing their available shearing resistances to residual values. As the stress redistribution process continues, the zone of failure may grow until the entire slope becomes unstable. Many instances of such progressive failure have been observed in strain-softening soils, even when the limit equilibrium factor of safety (based on peak strength) is well above 1.0. Within the constraints of limit equilibrium analysis, the stability of slopes with strain-softening materials can be analyzed reliably only by using residual shear strengths.

Limit equilibrium analyses must be formulated with great care. Since the available shearing resistance of the soil depends on porewater drainage conditions, those conditions must be considered carefully in the selection of shear strengths and pore pressure conditions for the analysis. Duncan (1992) provided guidelines for the selection of input parameters for limit equilibrium slope stability analyses.

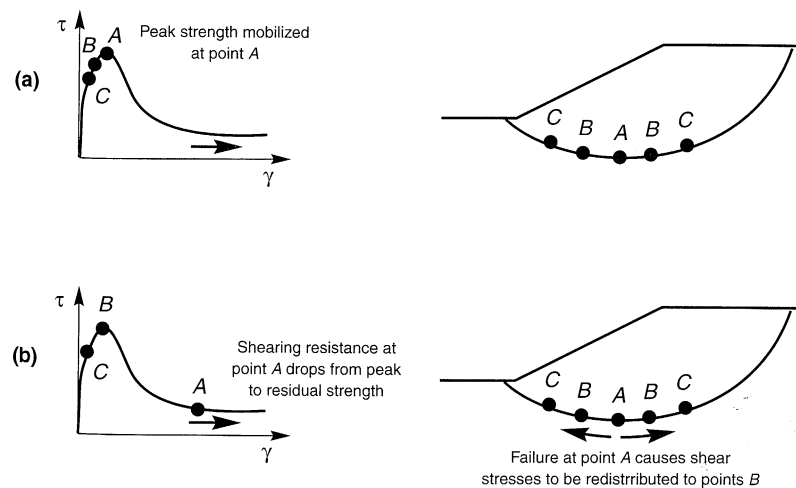


Figure 10.5 Development of progressive failure in slope comprised of strain-softening materials: (a) exceedance of peak strength at any point (A) reduces strength at that point to residual value; (b) redistribution of shear stresses from failure zone to surrounding area produces failure in surrounding zone (points B). Continued redistribution of stresses can eventually lead to failure of the entire slope (points C and beyond).

10.5.2 Stress–Deformation Analyses

Stress–deformation analyses allow consideration of the stress–strain behavior of soil and rock and are most commonly performed using the finite-element method. When applied to slopes, stress–deformation analyses can predict the magnitudes and patterns of stresses, movements, and pore pressures in slopes during and after construction/deposition. Non-linear stress–strain behavior, complex boundary conditions, irregular geometries, and a variety of construction operations can all be considered in modern finite-element analyses.

For static slope stability analysis, stress–deformation analyses offer the advantages of being able to identify the most likely mode of failure by predicting slope deformations up to (and in some cases beyond) the point of failure, of locating the most critically stressed zones within a slope, and of predicting the effects of slope failures. These advantages come at the cost of increased engineering time for problem formulation, characterization of material properties and interpretation of results, and increased computational effort.

The accuracy of stress–deformation analyses is strongly influenced by the accuracy with which the stress–strain model represents actual material behavior. Many different stress–strain models have been used for stress–deformation analysis of slopes; each has advantages and limitations. The accuracy of simple models is usually limited to certain ranges of strain and/or certain stress paths. Models that can be applied to more general stress and strain conditions are often quite complex and may require a large number of input parameters whose values can be difficult to determine. For many problems, the hyperbolic model (Kondner, 1963; Kondner and Zelasko, 1963; Duncan and Chang, 1970; Duncan et al., 1980) offers an appropriate compromise between simplicity and accuracy.

10.6 SEISMIC SLOPE STABILITY ANALYSIS

The previously described procedures for static slope stability analysis have been used for many years and calibrated against many actual slope failures. The database against which seismic slope stability analyses can be calibrated is much smaller. Analysis of the seismic stability of slopes is further complicated by the need to consider the effects of (1) dynamic stresses induced by earthquake shaking, and (2) the effects of those stresses on the strength and stress–strain behavior of the slope materials.

Seismic slope instabilities may be grouped into two categories on the basis of which of these effects is predominant in a given slope. In inertial instabilities, the shear strength of the soil remains relatively constant, but slope deformations are produced by temporary exceedances of the strength by dynamic earthquake stresses. Weakening instabilities are those in which the earthquake serves to weaken the soil sufficiently that it cannot remain stable under earthquake-induced stresses. Flow liquefaction and cyclic mobility (Chapter 9) are the most common causes of weakening instability. A number of analytical techniques, based on both limit equilibrium and stress–deformation analyses, are available for both categories of seismic instability.

10.6.1 Analysis of Inertial Instability

Earthquake motions can induce significant horizontal and vertical dynamic stresses in slopes. These stresses produce dynamic normal and shear stresses along potential failure surfaces within a slope. When superimposed upon the previously existing static shear

stresses, the dynamic shear stresses may exceed the available shear strength of the soil and produce inertial instability of the slope. A number of techniques for the analysis of inertial instability have been proposed. These techniques differ primarily in the accuracy with which the earthquake motion and the dynamic response of the slope are represented. The following sections describe several common approaches to the analysis of inertial instability. The first, pseudostatic analysis, produces a factor of safety against seismic slope failure in much the same way that static limit equilibrium analyses produce factors of safety against static slope failure. All the other approaches attempt to evaluate permanent slope displacements produced by earthquake shaking.

10.6.1.1 Pseudostatic Analysis

Beginning in the 1920s, the seismic stability of earth structures has been analyzed by a *pseudostatic* approach in which the effects of an earthquake are represented by constant horizontal and/or vertical accelerations. The first explicit application of the pseudostatic approach to the analysis of seismic slope stability has been attributed to Terzaghi (1950).

In their most common form, pseudostatic analyses represent the effects of earthquake shaking by pseudostatic accelerations that produce inertial forces, F_h and F_v , which act through the centroid of the failure mass (Figure 10.6). The magnitudes of the pseudostatic forces are

$$F_h = \frac{a_h W}{g} = k_h W \quad (10.2a)$$

$$F_v = \frac{a_v W}{g} = k_v W \quad (10.2b)$$

where a_h and a_v are horizontal and vertical pseudostatic accelerations, k_h and k_v are dimensionless horizontal and vertical pseudostatic coefficients, and W is the weight of the failure mass. The magnitudes of the pseudostatic accelerations should be related to the severity of the anticipated ground motion; selection of pseudostatic accelerations for design is, as discussed in the next section, not a simple matter. Resolving the forces on the potential failure mass in a direction parallel to the failure surface,

$$\text{FS} = \frac{\text{resisting force}}{\text{driving force}} = \frac{c l_{ab} + [(W - F_v) \cos \beta - F_h \sin \beta] \tan \phi}{(W - F_v) \sin \beta + F_h \cos \beta} \quad (10.3)$$

where c and ϕ are the Mohr–Coulomb strength parameters that describe the shear strength on the failure plane and l_{ab} is the length of the failure plane. The horizontal pseudostatic

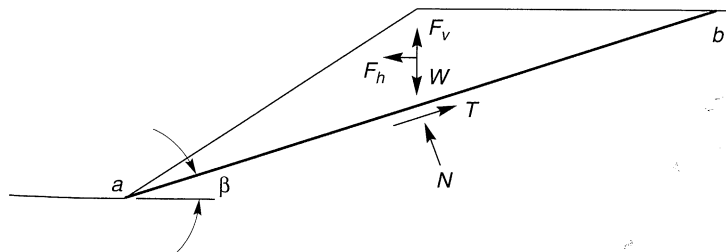


Figure 10.6 Forces acting on triangular wedge of soil above planar failure surface in pseudostatic slope stability analysis.

force clearly decreases the factor of safety—it reduces the resisting force (for $\phi > 0$) and increases the driving force. The vertical pseudostatic force typically has less influence on the factor of safety since it reduces (or increases, depending on its direction) both the driving force and the resisting force—as a result, the effects of vertical accelerations are frequently neglected in pseudostatic analyses. The pseudostatic approach can be used to evaluate pseudostatic factors of safety for planar, circular, and noncircular failure surfaces. Many commercially available computer programs for limit equilibrium slope stability analysis have the option of performing pseudostatic analyses.

Example 10.2

Assuming $k_h = 0.1$ and $k_v = 0.0$, compute the static and pseudostatic factors of safety for the 30-ft-high 2:1 (H:V) slope shown in Figure E10.2.

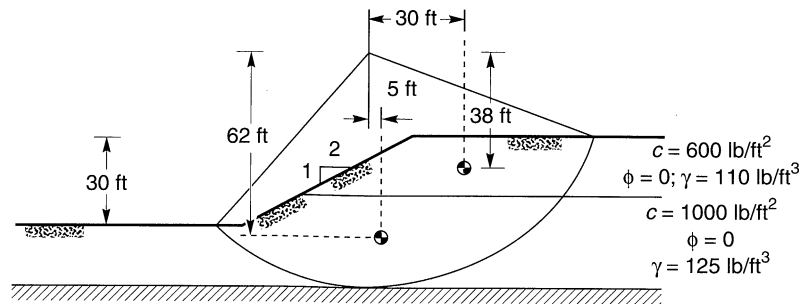


Figure E10.2

Solution Using a simple moment equilibrium analysis, the factor of safety can be defined as the ratio of the moment that resists rotation of a potential failure mass about the center of a circular potential failure surface to the moment that is driving the rotation. The critical failure surface, defined as that which has the lowest factor of safety, is identified by analyzing a number of potential failure surfaces. Shown below are the factor-of-safety calculations for one potential failure surface which may or may not be the critical failure surface.

Computation of the factor of safety requires evaluation of the overturning and resisting moments for both static and pseudostatic conditions. The overturning moment for static conditions results from the weight of the soil above the potential failure surface. The overturning moment for pseudostatic conditions is equal to the sum of the overturning moment for static conditions and the overturning moment produced by the pseudostatic forces. The horizontal pseudostatic forces are assumed to act in directions that produce positive (clockwise, in this case) driving moments. In the calculations shown in tabular form below, the soil above the potential failure mass is divided into two sections.

Overturning moments:

Section	Area (ft ²)	γ (lb/ft ³)	W (kips/ft)	Moment Arm (ft)	Static Moment (kip-ft/ft)	$k_h W$ (kips/ft)	Moment Arm (ft)	Pseudostatic Moment (kip-ft/ft)	Total Moment (kip-ft/ft)
A	1360	110	149.6	30	4488.1	15.0	38	570.0	5058.0
B	2300	125	287.5	5	1437.5	28.8	62	1785.6	3223.1
					5925.5				8281.1

Resisting moment:

Section	Length (ft)	c (lb/ft ²)	Force (kips)	Moment Arm (ft)	Moment (kip-ft/ft)
A	11.5	600	6.9	78	538.2
B	129.3	1000	129.3	78	<u>10,085.4</u>
					10,623.6

Factor of safety:

$$\text{Static FS} = \frac{\text{resisting moment}}{\text{static overturning moment}} = \frac{10,623.6}{5925.5} = 1.79$$

$$\begin{aligned} \text{Pseudostatic FS} &= \frac{\text{resisting moment}}{\text{static + pseudostatic overturning moments}} \\ &= \frac{10,623.6}{8281.1} = 1.28 \end{aligned}$$

Selection of Pseudostatic Coefficient. The results of pseudostatic analyses are critically dependent on the value of the seismic coefficient, k_h . Selection of an appropriate pseudostatic coefficient is the most important, and most difficult, aspect of a pseudostatic stability analysis. The seismic coefficient controls the pseudostatic force on the failure mass, so its value should be related to some measure of the amplitude of the inertial force induced in the potentially unstable material. If the slope material was rigid, the inertial force induced on a potential slide would be equal to the product of the actual horizontal acceleration and the mass of the unstable material. This inertial force would reach its maximum value when the horizontal acceleration reached its maximum value. In recognition of the fact that actual slopes are not rigid and that the peak acceleration exists for only a very short time, the pseudostatic coefficients used in practice generally correspond to acceleration values well below a_{\max} . Terzaghi (1950) originally suggested the use of $k_h = 0.1$ for “severe” earthquakes (Rossi-Forel IX), $k_h = 0.2$ for “violent, destructive” earthquakes (Rossi-Forel X), and $k_h = 0.5$ for “catastrophic” earthquakes. Seed (1979) listed pseudostatic design criteria for 14 dams in 10 seismically active countries; 12 required minimum factors of safety of 1.0 to 1.5 with pseudostatic coefficients of 0.10 to 0.12. Marcuson (1981) suggested that appropriate pseudostatic coefficients for dams should correspond to one-third to one-half of the maximum acceleration, including amplification or deamplification effects, to which the dam is subjected. Using shear beam models, Seed and Martin (1966) and Dakoulas and Gazetas (1986) showed that the inertial force on a potentially unstable slope in an earth dam depends on the response of the dam and that the average seismic coefficient for a deep failure surface is substantially smaller than that of a failure surface that does not extend far below the crest. Seed (1979) also indicated that deformations of earth dams constructed of ductile soils (defined as those that do not generate high pore pressures or show more than 15% strength loss upon cyclic loading) with crest accelerations less than $0.75g$ would be acceptably small for pseudostatic factors of safety of at least 1.15 with $k_h = 0.10$ ($M = 6.5$) to $k_h = 0.15$ ($M = 8.25$). This criteria would allow the use of pseudostatic accelerations as small as 13 to 20% of the peak crest acceleration. Hynes-Griffin and Franklin (1984) applied the Newmark sliding block analysis described in the following section to over 350 accelerograms and concluded that earth dams with pseudostatic factors of safety greater than 1.0 using $k_h = 0.5a_{\max}/g$ would not develop “dangerously large” deformations.

As the preceding discussion indicates, there are no hard and fast rules for selection of a pseudostatic coefficient for design. It seems clear, however, that the pseudostatic coefficient should be based on the actual anticipated level of acceleration in the failure mass (including any amplification or deamplification effects) and that it should correspond to some fraction of the anticipated peak acceleration. Although engineering judgment is required for all cases, the criteria of Hynes-Griffin and Franklin (1984) should be appropriate for most slopes.

Limitations of the Pseudostatic Approach. Representation of the complex, transient, dynamic effects of earthquake shaking by a single constant unidirectional pseudostatic acceleration is obviously quite crude. Even in its infancy, the limitations of the pseudostatic approach were clearly recognized. Terzaghi (1950) stated that “the concept it conveys of earthquake effects on slopes is very inaccurate, to say the least,” and that a slope could be unstable even if the computed pseudostatic factor of safety was greater than 1. Detailed analyses of historical and recent earthquake-induced landslides (e.g., Seed et al., 1969, 1975; Marcuson et al., 1979) have illustrated significant shortcomings of the pseudostatic approach. Experience has clearly shown, for example, that pseudostatic analyses can be unreliable for soils that build up large pore pressures or show more than about 15% degradation of strength due to earthquake shaking. As illustrated in Table 10-4, pseudostatic analyses produced factors of safety well above 1 for a number of dams that later failed during earthquakes. These cases illustrate the inability of the pseudostatic method to reliably evaluate the stability of slopes susceptible to weakening instability. Nevertheless, the pseudostatic approach can provide at least a crude index of relative, if not absolute, stability.

Discussion. The pseudostatic approach has a number of attractive features. The analysis is relatively simple and straightforward; indeed, its similarity to the static limit equilibrium analyses routinely conducted by geotechnical engineers makes its computations easy to understand and perform. It produces a scalar index of stability (the factor of safety) that is analogous to that produced by static stability analyses. It must always be recognized, however, that the accuracy of the pseudostatic approach is governed by the accuracy with which the simple pseudostatic inertial forces represent the complex dynamic inertial forces that actually exist in an earthquake. Difficulty in the assignment of appropriate pseudostatic coefficients and in interpretation of pseudostatic factors of safety, coupled with the development of more realistic methods of analysis, have reduced the use of the pseudostatic approach for seismic slope stability analyses. Methods based on evaluation of permanent slope deformation, such as those described in the following sections, are being used increasingly for seismic slope stability analysis.

Table 10-4 Results of Pseudostatic Analyses of Earth Dams That Failed during Earthquakes

Dam	k_h	FS	Effect of Earthquake
Sheffield Dam	0.10	1.2	Complete failure
Lower San Fernando Dam	0.15	1.3	Upstream slope failure
Upper San Fernando Dam	0.15	~2–2.5	Downstream shell, including crest slipped about 6 ft downstream
Tailings dam (Japan)	0.20	~1.3	Failure of dam with release of tailings

Source: After Seed (1979).

10.6.1.2 Newmark Sliding Block Analysis

The pseudostatic method of analysis, like all limit equilibrium methods, provides an index of stability (the factor of safety) but no information on deformations associated with slope failure. Since the serviceability of a slope after an earthquake is controlled by deformations, analyses that predict slope displacements provide a more useful indication of seismic slope stability. Since earthquake-induced accelerations vary with time, the pseudostatic factor of safety will vary throughout an earthquake. If the inertial forces acting on a potential failure mass become large enough that the total (static plus dynamic) driving forces exceed the available resisting forces, the factor of safety will drop below 1.0. Newmark (1965) considered the behavior of a slope under such conditions. When the factor of safety is less than 1.0, the potential failure mass is no longer in equilibrium; consequently, it will be accelerated by the unbalanced force. The situation is analogous to that of a block resting on an inclined plane (Figure 10.7). Newmark used this analogy to develop a method for prediction of the permanent displacement of a slope subjected to any ground motion.

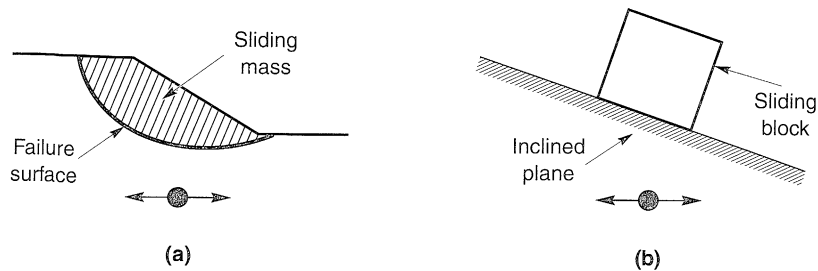


Figure 10.7 Analogy between (a) potential landslide and (b) block resting on inclined plane.

Consider the block in stable, static equilibrium on the inclined plane of Figure 10.7b. Under static conditions, equilibrium of the block (in the direction parallel to the plane) requires that the available static resisting force, R_s , exceed the static driving force, D_s (Figure 10.8a). Assuming that the block's resistance to sliding is purely frictional ($c = 0$)

$$FS = \frac{\text{available resisting force}}{\text{static driving force}} = \frac{R_s}{D_s} = \frac{W \cos \beta \tan \phi}{W \sin \beta} = \frac{\tan \phi}{\tan \beta} \quad (10.4)$$

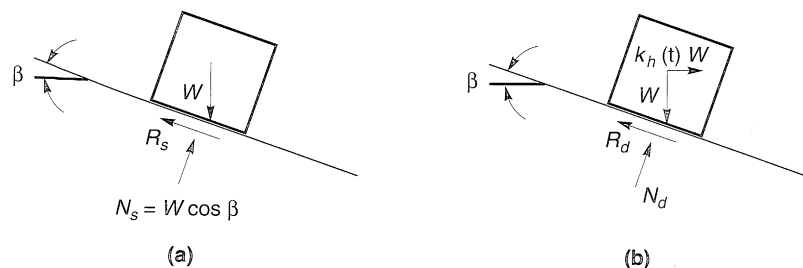


Figure 10.8 Forces acting on a block resting on an inclined plane: (a) static conditions; (b) dynamic conditions.

where ϕ is the angle of friction between the block and the plane. Now consider the effect of inertial forces transmitted to the block by horizontal vibration of the inclined plane with acceleration, $a_h(t) = k_h(t)g$ (the effects of vertical accelerations will be neglected for simplicity). At a particular instant of time, horizontal acceleration of the block will induce a horizontal inertial force, $k_h W$ (Figure 10.8b). When the inertial force acts in the downslope direction, resolving forces perpendicular to the inclined plane gives

$$FS_d(t) = \frac{\text{available resisting force}}{\text{pseudostatic driving force}} = \frac{R_d(t)}{D_d(t)} = \frac{[\cos \beta - k_h(t) \sin \beta] \tan \phi}{\sin \beta + k_h(t) \cos \beta} \quad (10.5)$$

Obviously, the dynamic factor of safety decreases as k_h increases and there will be (for a statically stable block) some positive value of k_h that will produce a factor of safety of 1.0 (Figure 10.9). This coefficient, termed the *yield coefficient*, k_y , corresponds to the *yield acceleration*, $a_y = k_y g$. The yield acceleration is the minimum pseudostatic acceleration required to produce instability of the block. For the block of Figure 10.8,

$$k_y = \tan(\phi - \beta) \quad (10.6)$$

for sliding in the downslope direction. For sliding in the uphill direction (which can occur when β and ϕ are small),

$$k_y = \frac{\tan \phi + \tan \beta}{1 + \tan \phi \tan \beta} \quad (10.7)$$

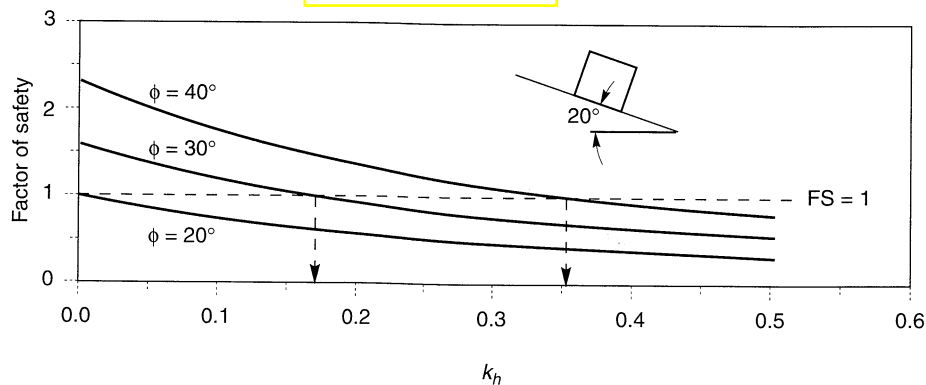


Figure 10.9 Variation of pseudostatic factor of safety with horizontal pseudostatic coefficient for block on plane inclined at 20°. For $\phi = 20^\circ$, block is at the point of failure ($FS = 1$) under static conditions, so the yield coefficient is zero. For $\phi = 30^\circ$ and $\phi = 40^\circ$, yield coefficients are 0.17 and 0.36, respectively.

Example 10.3

Compute the yield acceleration for the slope described in Example 10.2.

Solution The yield acceleration can be computed by trial and error, or computed directly for relatively simple slopes. Reviewing Example 10.2, it is apparent that the total moment is equal to

$$\begin{aligned} M_t &= 4488 \text{ k-ft/ft} + k_h(5685 \text{ k-ft/ft}) + 1438 \text{ k-ft/ft} + k_h(17825 \text{ k-ft/ft}) \\ &= 5926 \text{ k-ft/ft} + k_h(23510 \text{ k-ft/ft}) \end{aligned}$$

The yield coefficient is the value of k_h that produces a pseudostatic factor of safety of 1. Because the resisting moment is equal to the overturning moment when $FS = 1$,

$$5926 \text{ k-ft/ft} + k_h(23510 \text{ k-ft/ft}) = 10624 \text{ k-ft/ft}$$

or

$$k_h = \frac{10624 \text{ k-ft/ft} - 5926 \text{ k-ft/ft}}{23510 \text{ k-ft/ft}} = 0.20$$

Therefore, the yield acceleration is $0.20g$.

When a block on an inclined plane is subjected to a pulse of acceleration that exceeds the yield acceleration, the block will move relative to the plane. To illustrate the procedure by which the resulting permanent displacements can be calculated, consider the case in which an inclined plane is subjected to a single rectangular acceleration pulse of amplitude A and duration Δt . If the yield acceleration, a_y , is less than A (Figure 10.10a), the acceleration of the block relative to the plane during the period from t_0 to $t_0 + \Delta t$ is

$$a_{\text{rel}}(t) = a_b(t) - a_y = A - a_y \quad t_0 \leq t \leq t_0 + \Delta t \quad (10.8a)$$

where $a_b(t)$ is the acceleration of the inclined plane. The relative movement of the block during this period can be obtained by integrating the relative acceleration twice, that is,

$$v_{\text{rel}}(t) = \int_{t_0}^t a_{\text{rel}}(t) dt = [A - a_y](t - t_0) \quad t_0 \leq t \leq t_0 + \Delta t \quad (10.8b)$$

$$d_{\text{rel}}(t) = \int_{t_0}^t v_{\text{rel}}(t) dt = \frac{1}{2}[A - a_y](t - t_0)^2 \quad t_0 \leq t \leq t_0 + \Delta t \quad (10.8c)$$

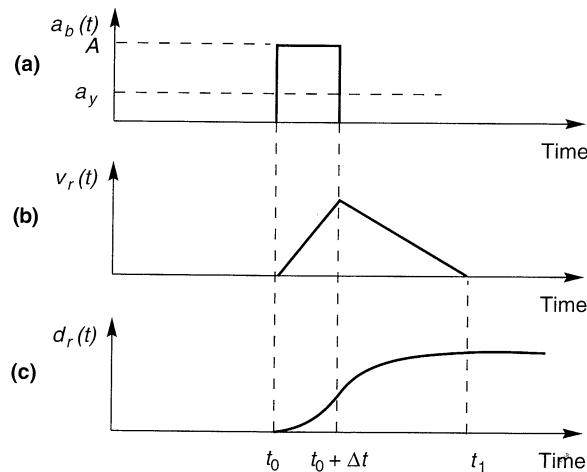


Figure 10.10 Variation of relative velocity and relative displacement between sliding block and plane due to rectangular pulse that exceeds yield acceleration between $t = t_0$ and $t = t_0 + \Delta t$.

At $t = t_0 + \Delta t$, the relative velocity reaches its maximum value. At that time

$$v_{\text{rel}}(t_0 + \Delta t) = [A - a_y]\Delta t \quad (10.9a)$$

$$d_{\text{rel}}(t_0 + \Delta t) = \frac{1}{2}[A - a_y]\Delta t^2 \quad (10.9b)$$

After the base acceleration drops to zero (at $t = t_0 + \Delta t$), the sliding block is decelerated by the friction force acting on its base. The block will continue to slide on the plane, but at a decreasing velocity which eventually reaches zero. The acceleration during this time is given by

$$a_{\text{rel}}(t) = a_b(t) - a_y = 0 - a_y = -a_y \quad t_0 + \Delta t \leq t \leq t_1 \quad (10.10a)$$

where t_1 is the time at which the relative velocity becomes zero (note that the block undergoes negative acceleration, or deceleration, during this period). Between $t_0 + \Delta t$ and t_1 , the relative velocity will decrease with time according to

$$v_{\text{rel}}(t) = v_{\text{rel}}(t_0 + \Delta t) + \int_{t_0 + \Delta t}^t a_{\text{rel}} dt = A \Delta t - a_y(t - t_0) \quad t_0 + \Delta t \leq t \leq t_1 \quad (10.10b)$$

Setting the relative velocity equal to zero at $t = t_1$ gives

$$t_1 = t_0 + \frac{A}{a_y}\Delta t$$

Then

$$d_{\text{rel}}(t) = \int_{t_0 + \Delta t}^t v_{\text{rel}}(t) dt = A \Delta t (t - t_0 - \Delta t) - \frac{1}{2} [t^2 - (t_0 + \Delta t)^2] \quad t_0 + \Delta t \leq t \leq t_1 \quad (10.10c)$$

After time t_1 , the block and inclined plane move together. During the total period of time between $t = t_0$ and $t = t_1$, the relative movement of the block is as shown in Figure 10.10. Between t_0 and $t_0 + \Delta t$, the relative velocity increases linearly and the relative displacement quadratically. At $t_0 + \Delta t$, the relative velocity has reached its maximum value, after which it decreases linearly. The relative displacement continues to increase (but at a decreasing rate) until $t = t_1$. Note that the total relative displacement

$$d_{\text{rel}}(t_1) = \frac{1}{2} (A - a_y) \Delta t^2 \frac{A}{a_y} \quad (10.11)$$

depends strongly on both the amount by which and the length of time during which the yield acceleration is exceeded. This suggests that the relative displacement caused by a single pulse of strong ground motion should be related to both the amplitude and frequency content of that pulse. An earthquake motion, however, can exceed the yield acceleration a number of times and produce a number of increments of displacement (Figure 10.11). Thus the total displacement will be influenced by strong-motion duration as well as amplitude and frequency content. Indeed, application of this approach to a variety of simple waveforms (e.g., Sarma, 1975; Yegian et al., 1991) have shown that the permanent displacement of a sliding block subjected to rectangular, sinusoidal, and triangular periodic base motions is proportional to the *square* of the period of the base motion.

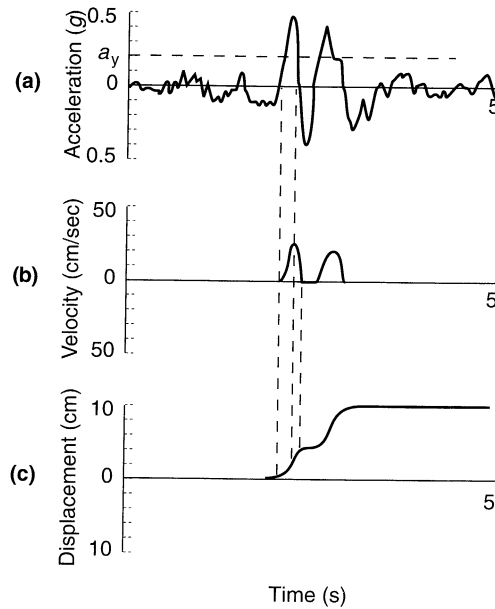


Figure 10.11 Development of permanent slope displacements for actual earthquake ground motion. (After Wilson and Keefer, 1985.)

Influence of Yield Acceleration on Slope Displacements. Obviously, the sliding block model will predict zero permanent slope displacement if earthquake-induced accelerations never exceed the yield acceleration ($a_y/a_{\max} \geq 1.0$) as illustrated in Figure 10.12a. Since the permanent displacement is obtained by double integration of the excess acceleration, the computed displacements for a slope with a relatively low yield acceleration (small a_y/a_{\max}) will be greater than that of a slope with a higher yield acceleration (Figure 10.12b, c). The relationship between slope displacement and a_y/a_{\max} has been investigated by a number of researchers.

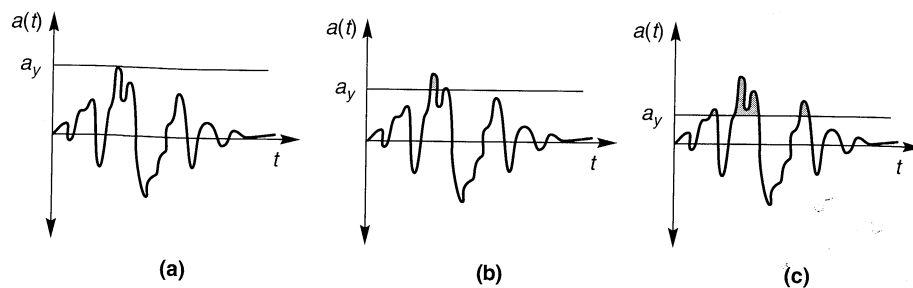


Figure 10.12 Permanent slope displacements depend on the relationship between the yield acceleration and the maximum acceleration. (a) If the yield acceleration of a slope is greater than the maximum acceleration of a particular ground motion, no displacement will occur. As yield accelerations decrease, as in (b) and (c), slope displacements increase quickly.

Using the rectangular pulse solution developed in Section 10.6.1.1, Newmark (1965) related single-pulse slope displacement to peak base velocity, v_{\max} , by

$$d_{\text{rel}} = \frac{v_{\max}^2}{2a_y} \left(\frac{1 - a_y}{A} \right) \tag{10.12}$$

[note that equation (10.12) is equivalent to equation (10.11) with $v_{\max} = A \Delta t$]. Analysis of several earthquake motions normalized to peak accelerations of 0.5g and peak velocities of 30 in./sec (76 cm/sec) suggested that the effective number of pulses in an earthquake motion could be approximated by A/a_y . Newmark found that a reasonable upper bound to the permanent displacements produced by these earthquake motions was given by

$$d_{\text{max}}^j = \frac{v_{\max}^2}{2a_y} \frac{a_{\text{max}}}{a_y} \tag{10.13}$$

where $a_y/a_{\text{max}} \geq 0.17$. Sarma (1975) and Yegian et al. (1988) derived closed-form solutions for the permanent displacements produced by simple periodic (triangular, sinusoidal, and rectangular) input motions (Figure 10.13). Studies of permanent displacements predicted by the sliding block method for actual earthquake motions (e.g., Sarma, 1975; Franklin and Chang, 1977; Makdisi and Seed, 1978; Ambraseys and Menu, 1988) show shapes that are similar to those of the sinusoidal and triangular waves at a_y/a_{max} values greater than about 0.5. Ambraseys and Menu (1988) found that the shape at smaller a_y/a_{max} values was influenced by whether or not upslope movements were considered; for the case in which they were not, permanent displacements (in centimeters) caused by actual ground motions were given by

$$\log u = 0.90 + \log \left[\left(1 - \frac{a_y}{a_{\text{max}}} \right)^{2.53} \left(\frac{a_y}{a_{\text{max}}} \right)^{-1.09} \right] \quad \sigma_{\log u} = 0.30 \tag{10.14}$$

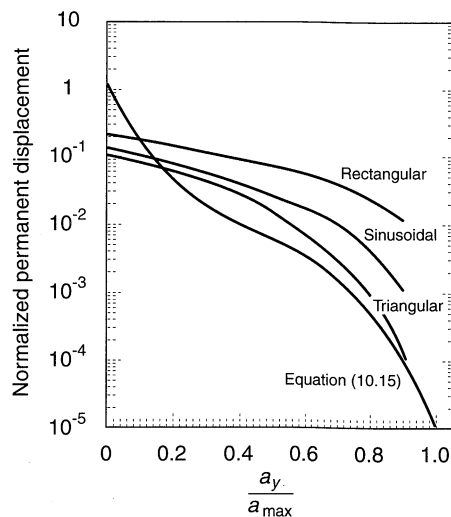


Figure 10.13 Variation of normalized permanent displacement with ratio of yield acceleration to maximum acceleration for simple waveforms. The normalized permanent displacement is defined in equation (10.15). (After Yegian et al., 1991.)

for $0.1 \leq a_y/a_{\max} \leq 0.9$, $6.6 \leq M_s \leq 7.3$, and a_y computed using residual soil strength. To allow measures of frequency content and duration to be considered explicitly, Yegian et al. (1991) used the database of Franklin and Chang (1977) to develop the following expression for the median permanent normalized displacement:

$$\log u^* = \log\left(\frac{u}{a_{\max} N_{\text{eq}} T^2}\right) = 0.22 - 10.12 \frac{a_y}{a_{\max}} + 16.38 \left(\frac{a_y}{a_{\max}}\right)^2 - 11.48 \left(\frac{a_y}{a_{\max}}\right)^3 \quad (10.15)$$

$$\sigma_{\log u^*} = 0.45$$

where N_{eq} is an equivalent number of cycles and T is the predominant period of the input motion. Considering only this source of uncertainty (i.e., neglecting uncertainty in a_{\max} , a_y , N_{eq} , and T), probabilities of exceeding various displacements can be determined (Figure 10.14). Alternative approaches to the probabilistic analysis of slope displacements have been presented by Constantinou and Gazetas (1984) and Lin and Whitman (1986).

Recognition of the limitations of peak acceleration as a sole descriptor of strong ground motion has led to the use of other ground motion parameters in slope-displacement prediction. Sliding block displacements have been correlated with Arias intensity:

$$\log u = 1.460 \log I_a - 6.642 a_y + 1.546 \quad \sigma_{\log u} = 0.409 \quad (10.16)$$

where u is in cm, I_a is in m/sec, and a_y is in g 's (Jibson, 1994) and used to predict areal limits of earthquake-induced landsliding (Wilson and Keefer, 1985).

Two aspects of seismic slope stability are clearly illustrated by the studies described in the preceding paragraphs. First, earthquake-induced slope displacements are very sensitive to the value of the yield acceleration. Consequently, small differences in yield acceleration can produce large variations in predicted slope displacement. Second, the great variability in distributions of acceleration pulse amplitudes between different ground motions produces great variability in predicted slope displacements. Even ground motions with similar amplitudes, frequency contents, and durations can produce significantly different predicted slope

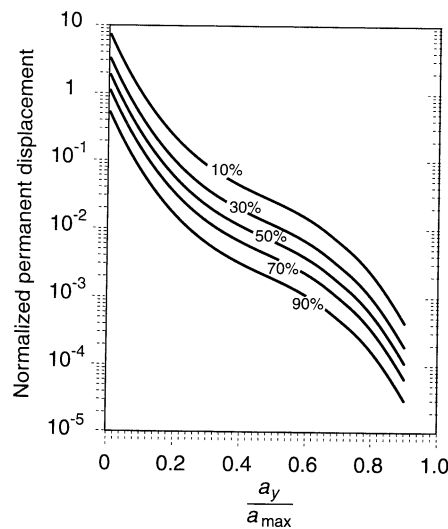


Figure 10.14 Contours of equal probability of exceedance of normalized permanent displacement. (After Yegian et al., 1991.)

displacements. This uncertainty must be recognized in the prediction of earthquake-induced slope deformations.

Example 10.4

Estimate the expected permanent displacement of the slope described in Example 10.3 if subjected to a ground motion equivalent to the Gilroy No. 1 (rock) earthquake motion. Use the procedures of Newmark (Equation 10.13) and Jibson (Equation 10.16).

Solution From Example 3.1, the peak acceleration and velocity of the Gilroy No. 1 (rock) motion are

$$\begin{aligned} a_{\max} &= 0.442 \\ v_{\max} &= 33.7 \text{ cm/sec} \end{aligned}$$

The yield acceleration was computed as 0.20g in Example 10.3. Then, using the Newmark procedure (Equation 10.13), an upper bound estimate of the permanent displacement would be

$$d_{\max} = \frac{(33.7 \text{ cm/sec})^2}{2(0.20g)(981 \text{ cm/sec}^2/g)} \frac{0.442g}{0.200g} = 6.4 \text{ cm}$$

The Arias Intensity of the Gilroy No. 1 (rock) motion was computed as $I_a = 167.7 \text{ cm/sec}$ in Example 3.6. Using the Jibson procedure (Equation 10.16), the average permanent displacement would be given by

$$\log u = 1.460 \log(1.677) - 6.642(0.20) + 1.546 = 0.545$$

so

$$u = 10^{0.545} = 3.5 \text{ cm}$$

Input Motions. The accuracy of a sliding block analysis depends on the accuracy of the input motion applied to the inclined plane. As originally proposed, the sliding block method assumes the potential failure mass to be rigid, in which case the appropriate input motion would be the ground motion at the level of the failure surface. Actual slopes, however, are compliant—they deform during earthquake shaking. Their dynamic response depends on their geometry and stiffness and on the amplitude and frequency content of the motion of the underlying ground. For slopes composed of very stiff soils and/or slopes subjected to low-frequency motion (a combination that produces long wavelengths), lateral displacements throughout the potential failure mass will be nearly in phase (Figure 10.15a) and the rigid block assumption will be at least approximately satisfied. Lateral displacements in

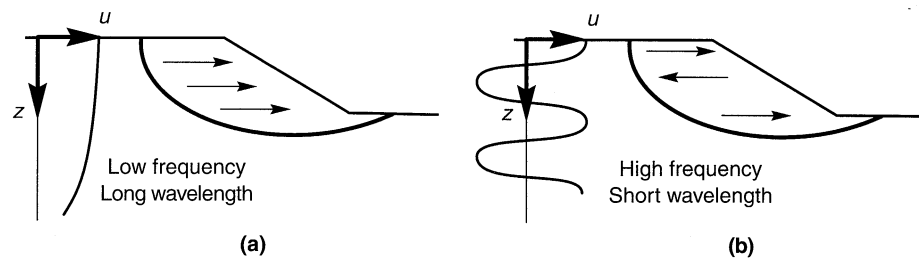


Figure 10.15 Influence of frequency on motions induced in slopes. Long wavelength associated with low-frequency motion (a) causes soil above failure surface to move essentially in phase. For higher-frequency motion (b), portions of soil above failure surface may be moving in opposite directions.

potential failure masses of slopes in softer soils (and/or slopes subjected to higher-frequency motion), however, may be out of phase (Figure 10.15b). When this occurs, the inertial forces at different points within the potential failure mass may be acting in opposite directions and the resultant inertial force may be significantly smaller than that implied by the rigid-block assumption.

The effects of slope response on the inertial force acting on a potential failure mass can be computed using dynamic stress–deformation analyses (Chopra, 1966). Using a dynamic finite-element analysis (Figure 10.16a), the horizontal components of the dynamic stresses acting on a potential failure surface (Figure 10.16b) are integrated over the failure surface to produce the time-varying resultant force that acts on the potential failure surface. This resultant force can then be divided by the mass of the soil above the potential failure surface to produce the average acceleration of the potential failure mass. Although the procedure was developed originally for dams, the basic concept can be applied to any type of slope. The average acceleration time history, which may be of greater or smaller amplitude than the base acceleration time history (depending on the input motions and the amplification characteristics of the slope), provides the most realistic input motion for a sliding block analysis of the potential failure mass.

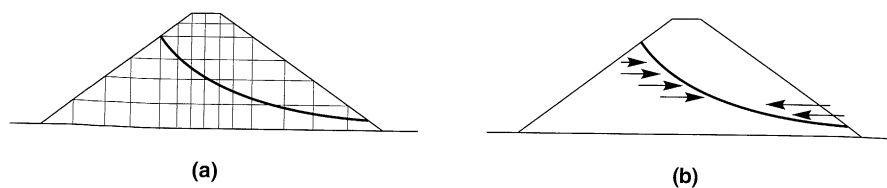


Figure 10.16 Evaluation of average acceleration for slope in embankment. Finite-element analysis predicts variation of shear and normal stresses on potential failure plane with time. Integration of horizontal components of stresses over potential failure surface gives resultant horizontal force acting on potentially unstable soil. Time history of average acceleration is obtained by dividing resultant force by mass of potentially unstable soil.

Other Factors Influencing Slope Displacement. The standard sliding block analysis is based on the assumption of rigid–perfectly plastic stress–strain behavior on a planar failure surface. Conditions for actual slopes may vary from these assumptions in a number of ways.

The shear strength of some soils is rate dependent. Since earthquake-induced shear stresses are applied at different rates, the shear strength (and hence the yield acceleration) can vary with time throughout an earthquake (e.g., Hungr and Morgenstern, 1984; Lemos et al., 1985). Consideration of rate-dependent strength in a sliding block analysis is complicated by differences between strain rates in the field and in the laboratory tests used to measure the strength. Lemos and Coelho (1991) and Tika-Vassilikos et al. (1993) suggested procedures for incorporating rate-dependent field strengths into numerical sliding block analyses.

In the field, soils rarely behave as perfectly plastic materials. Instead, they usually exhibit strain-hardening or strain-softening stress–strain behavior (Figure 10.17) after yielding. The yield accelerations of slopes comprised of strain-hardening or strain-softening soils will vary with slope displacement. Consequently, the permanent displacement of

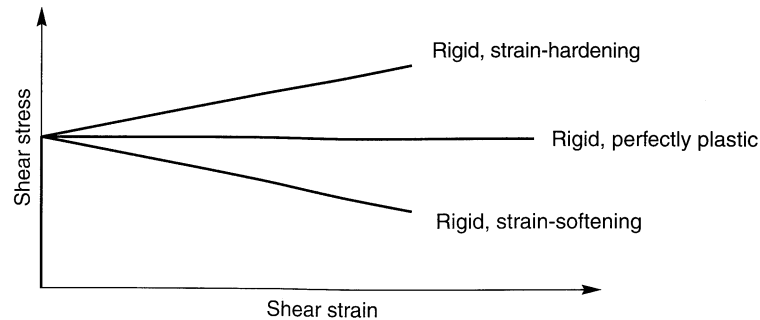


Figure 10.17 Stress–strain behavior of rigid–perfectly plastic, rigid–strain hardening, and rigid–strain softening materials.

a slope in strain-hardening materials will be smaller than predicted by a conventional sliding block analysis; the reverse will be true for strain-softening soils. Modification of sliding block analyses for consideration of displacement-dependent strength is fairly straightforward.

Many slopes fail by mechanisms that differ from the planar failure mechanism assumed in sliding block analyses (see Figure 10.4). Neglecting the effects of rate- and displacement-dependent strength, the stability of a block on a plane will be the same both before and after a pulse of displacement—because the geometry of the block relative to the plane is unchanged. Movement of a slope on a nonplanar failure surface, however, tends to flatten the slope, thereby reducing the driving forces. As a result, the yield acceleration should increase due to changes in the geometry of the unstable soil. For most slopes, however, this effect does not become significant until large displacements have occurred.

10.6.1.3 Makdisi–Seed Analysis

Makdisi and Seed (1978) used average accelerations computed by the procedure of Chopra (1966) and sliding block analyses to compute earthquake-induced permanent deformations of earth dams and embankments. By making simplifying assumptions about the results of dynamic finite element and shear beam analyses of such structures, a simplified procedure for prediction of permanent displacements was developed.

In the simplified procedure, the yield acceleration for a particular potential failure surface is computed using the dynamic yield strength [80% of the undrained strength (Section 6.5.2)] of the soil. The dynamic response of the dam/embankment is accounted for by an acceleration ratio that varies with the depth of the potential failure surface relative to the height of the dam/embankment (Figure 10.18).

By subjecting several real and hypothetical dams to several actual and synthetic ground motions scaled to represent different earthquake magnitudes, Makdisi and Seed computed the variation of permanent displacement with a_y/a_{max} and magnitude. Scatter in the predicted displacements was reduced by normalizing the displacement with respect to the peak base acceleration and the fundamental period of the dam/embankment (note that the normalized displacement has units of seconds). Prediction of permanent displacements by the Makdisi–Seed procedure is accomplished with the charts shown in Figure 10.19.

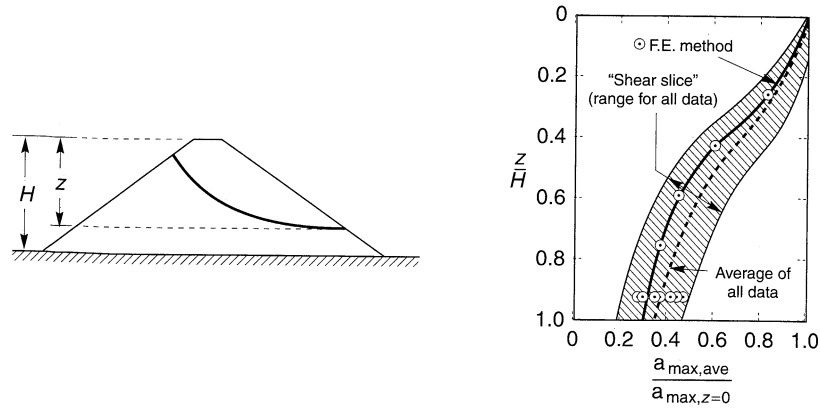


Figure 10.18 Variation of average maximum acceleration with depth of potential failure surface for dams and embankments. (After Makdisi and Seed (1978). Simplified procedure for estimating dam and embankment earthquake-induced deformations, Journal of the Geotechnical Engineering Division, Vol. 104, No. GT7. Reprinted by permission of ASCE.)

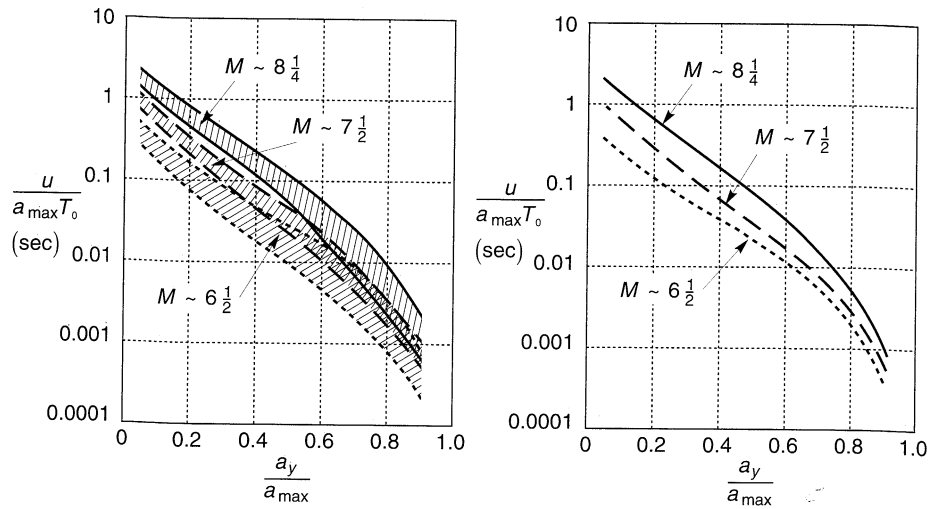


Figure 10.19 Variation of normalized permanent displacement with yield acceleration for earthquakes of different magnitudes: (a) summary for several earthquakes and dams/embankments; (b) average values. (After Makdisi and Seed (1978). Simplified procedure for estimating dam and embankment earthquake-induced deformations, Journal of the Geotechnical Engineering Division, Vol. 104, No. GT7. Reprinted by permission of ASCE.)

Example 10.5

Assume that a failure surface that extends over the upper two-thirds of the earth dam shown in Example 7.6 has a yield acceleration of $0.24g$. Estimate the permanent displacement that would occur if the base of the dam was subjected to the Gilroy No. 1 (rock) motion.

Solution The Gilroy No. 1 motion was recorded in the 1989 Loma Prieta earthquake which had a magnitude of 7.1. The peak acceleration was $0.442g$. From Example 7.6, the fundamental period of the dam is

$$T_o = \frac{2\pi}{19.2 \text{ rad/sec}} = 0.33 \text{ sec}$$

Using Figure 10.19b with $a_y/a_{\max} = 0.24g/0.442g = 0.54$ and $M = 7.1$, the average normalized displacement is about 0.04. Therefore,

$$u = 0.04 a_{\max} T_o = 0.04(0.442g)(32.2 \text{ ft/sec}^2/g)(0.33 \text{ sec}) = 0.19 \text{ ft} = 2.3 \text{ in}$$

The Makdisi–Seed simplified procedure is widely used for estimation of permanent displacements in dams and embankments. Because the procedure is based on the dynamic response characteristics of dams and embankments, its results must be interpreted with caution when applied to other types of slopes.

10.6.1.4 Stress–Deformation Analysis

Just as stress–deformation analyses of static slope stability are usually performed using static finite-element analyses, stress–deformation analyses of seismic slope stability are usually performed using dynamic finite-element analyses (Section 7.3.1). In such analyses the seismically induced permanent strains in each element of the finite-element mesh are integrated to obtain the permanent deformation of the slope. Permanent strains within individual elements can be estimated in different ways. The strain potential and stiffness reduction approaches estimate permanent strains using laboratory test results to determine the “stiffness” of soils subjected to earthquake loading. Nonlinear analysis approaches use the nonlinear inelastic stress–strain behavior of the soil to compute the development of permanent strains throughout an earthquake.

Strain Potential Approach. In their landmark investigation of the slides that occurred in the Upper and Lower San Fernando dams during the 1971 San Fernando earthquake, Seed et al. (1973) developed a procedure for estimating earthquake-induced slope deformation from the results of linear or equivalent linear analyses. In this procedure the cyclic shear stresses are computed in each element of a dynamic finite-element analysis. Using the results of cyclic laboratory tests, the computed cyclic shear stresses are used to predict the *strain potential*, expressed as a shear strain, for each element. Deformations are then estimated as the product of the average strain potential along a vertical section through the slope and the height of that section. The method implicitly assumes that the strains that develop in the field will be the same as those that develop in a similarly loaded laboratory test specimen and that the maximum shear stress acts in the horizontal direction in all elements. Consequently, the strain potential approach estimates only horizontal displacements. Analyses based on the strain potential approach are clearly very approximate, and their results should always be interpreted with that fact in mind.

Stiffness Reduction Approach. Another method for estimation of permanent slope displacement was developed by Lee (1974) and Serff et al. (1976). In this approach, computed strain potentials are used to reduce the stiffness of the soil as illustrated in Figure 10.20. Earthquake-induced slope displacements are then taken as the difference between the nodal point displacements from two static finite-element analyses: one using the initial shear moduli and the other using the reduced shear moduli. The technique can be used with linear or nonlinear models. Unlike the strain potential approach, the stiffness reduction approach can estimate vertical as well as horizontal movements. It is a very approximate procedure, however, and is subject to many of the limitations of the strain potential approach. Work-energy principles can be used to provide a more fundamental procedure for stiffness reduction (Byrne, 1991; Byrne et al., 1992).

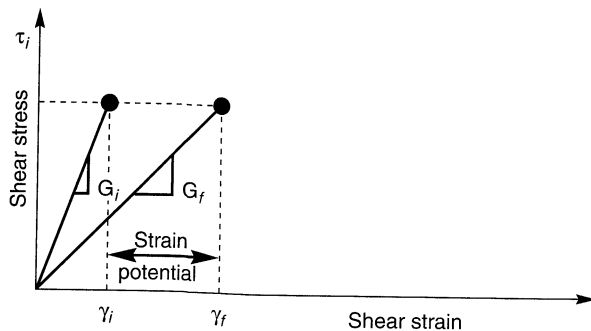


Figure 10.20 Procedure used to reduce stiffness from initial value, G_i , to final value, G_f , in stiffness reduction approach to estimation of permanent slope deformation. (After Serff et al., 1976.)

Nonlinear Analysis Approach. Permanent slope deformations can also be computed by finite-element analyses that employ nonlinear inelastic soil models. The basic procedures of nonlinear finite-element analysis of earth structures were introduced in Section 7.2.3. The seismic performance of slopes has been analyzed with two- and three-dimensional finite-element analyses using both cyclic stress-strain models (e.g., Finn et al., 1986) and advanced constitutive models (e.g., Prevost, 1981; Mizuno and Chen, 1982; Kawai, 1985; Daddazio et al., 1987). The most common application of these techniques, to date, has been the analysis of earth dams. Examples of such analyses can be found in Prevost et al. (1985), Griffiths and Prevost (1988), Finn (1990), Elgamal et al. (1990), and Suncariet et al. (1991). As discussed in Chapter 7, the accuracy of nonlinear finite-element analyses depends primarily on the accuracy of the stress-strain or constitutive models on which they are based.

10.6.2 Analysis of Weakening Instability

Through a process of pore pressure generation and/or structural disturbance, earthquake-induced stresses and strains can reduce the shear strength of a soil. Weakening instabilities can occur when the reduced strength drops below the static and dynamic shear stresses induced in the slope. Weakening instabilities are usually associated with liquefaction

phenomena and can be divided into two main categories, *flow failures* (Section 9.6.3.2) and *deformation failures* (Section 9.6.3.3). Flow failures occur when the available shear strength becomes smaller than the static shear stress required to maintain equilibrium of a slope. Flow failures, therefore, are actually driven by static stresses. They can produce very large deformations that occur quickly and without warning. Deformation failures occur when the shear strength of a soil is reduced to the point where it is temporarily exceeded by earthquake-induced shear stresses. Much like inertial failures, deformation failures occur as a series of “pulses” of permanent displacement that cease at the end of earthquake shaking. Different procedures are available for the analysis of flow failures and deformation failures.

10.6.2.1 Flow Failure Analysis

Because they usually involve significant reduction in soil strength, flow failures usually produce large deformations and severe damage. The first step in their analysis is generally to determine whether or not one will occur. To estimate the extent of the damage produced by flow failures, procedures for estimation of flow failure deformations have also been developed.

Analysis of Stability. Potential flow slide instability is most commonly evaluated by conventional static slope stability analyses using soil strengths based on end-of-earthquake conditions (Marcuson et al., 1990). In a typical analysis, the factors of safety against liquefaction at all points on a potential failure surface is first computed. Residual strengths are then assigned to those portions of the failure surface on which the factor of safety against liquefaction is less than 1. At locations where the factor of safety against liquefaction is greater than 1, strength values are based on the effective stresses at the end of the earthquake (i.e., considering pore pressures generated during the earthquake). With these strengths, conventional limit equilibrium slope stability analyses are used to calculate an overall factor of safety against flow sliding. If the overall factor of safety is less than 1, flow sliding is expected. The possibility of progressive failure (Section 10.5.1) must be considered in stability evaluations of this type—the redistribution of stresses involved in progressive failure are not accounted for directly in limit equilibrium analyses.

Analysis of Deformations. If stability analyses indicate that flow failure is likely, the extent of the zone influenced by the failure can be determined from an analysis of flow failure deformations. By neglecting the small deformations that precede the triggering of flow sliding, rough estimates of flow sliding deformations can be obtained from procedures based on limit equilibrium, fluid mechanics, and stress–deformation analyses.

Simple plane strain, limit equilibrium procedures can be used to estimate the distance a liquefied soil would flow over a gentle (< 3 to 4°) slope (Lucia et al., 1981). By assuming that the liquefied soil would eventually come to rest with a linear surface, a postfailure geometry that satisfies equilibrium and volumetric constraints can be identified. With reference to the notation of Figure 10.21, the procedure can be implemented in the following steps:

1. Using Figure 10.22a, compute values of the height of the slope at the end of flow (when the static factor of safety reaches 1.0) based on strength considerations using

$$H_{T,S} = N_o \frac{S_r}{\gamma} \quad (10.17)$$

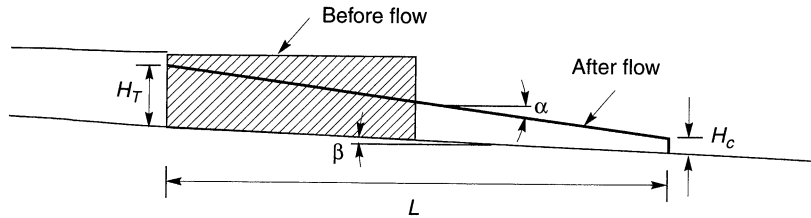


Figure 10.21 Geometric notation for estimation of flow failure distance by procedure of Lucia et al. (1981).

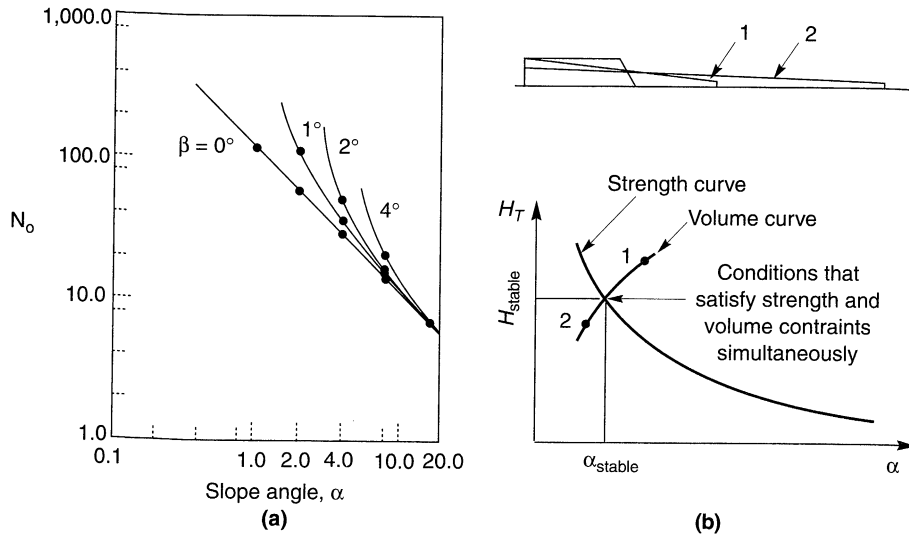


Figure 10.22 Charts for estimation of flow failure distance: (a) stability number charts for computing strength curve; (b) determination of H_T and α values that simultaneously satisfy strength and volume constraints. After Lucia et al. (1981).

for various assumed values of the slope angle, α . Plot the data in the form of a “strength curve” as in Figure 10.22b.

- For various assumed values of α , calculate the height of the slope after flow based on constant-volume conditions using

$$H_{T, V} = \sqrt{A_1^2 H_c^2 + A_2 V_f} - A_3 H_c \tag{10.18}$$

where

$$A_1 = \frac{\tan \alpha}{\tan \alpha - \tan \beta} \quad A_2 = \frac{2 \tan^2 \alpha}{\tan \alpha - \tan \beta}$$

$$A_3 = \frac{\tan \beta}{\tan \alpha - \tan \beta} \quad H_c = \frac{4S_r}{\gamma}$$

and V_f is the estimated volume of soil involved in the flow slide. Plot the resulting data in the form of a “volume curve” as in Figure 10.22b.

3. The strength and volume curves intersect where $H_{T,S} = H_{T,V}$. The resulting H_{stable} and α_{stable} values satisfy both strength and volume requirements with a factor of safety equal to 1. The horizontal distance covered by the flow slide can then be computed as

$$L = \frac{H_{\text{stable}} - H_c}{\tan \alpha_{\text{stable}}} \quad (10.19)$$

Although the procedure involves several simplifying assumptions and requires an estimate of the strength of the liquefied soil (Section 9.6.4.1), it can provide at least a crude estimate of the deformations involved in certain flow slides.

The fluidlike behavior of liquefied soils has motivated fluid mechanics approaches to the modeling of flow slide behavior. Most of this work has been directed toward debris flows (e.g., Johnson, 1970; Iverson and Denlinger, 1987) and tailings dam failures (e.g., Jeyapalan et al., 1981). Rheological modeling of liquefied soils is quite difficult. The Bingham model (strength = $\tau_y + \eta_p \dot{\gamma}$, where τ_y and η_p are the Bingham yield strength and plastic viscosity, respectively, and $\dot{\gamma}$ is the shear strain rate) is most commonly used (Johnson, 1970; Jeyapalan, 1980; O'Brien and Julien, 1988; Phillips and Davies, 1991), although its ability to represent the frictional nature of liquefied soil is limited (Iverson and LaHusen, 1993).

The development of advanced nonlinear dynamic analyses have made an alternative approach possible. The finite-element program TARA-3FL (Finn and Yogendrakumar, 1989), for example, can reduce the strength of any element in the slope to the residual strength at the time liquefaction of the element is initiated. The program periodically updates the finite-element mesh at each time step to allow computation of large deformations (Figure 10.23). Finn (1990) described its application to Sardis Dam in Mississippi, where liquefaction of the core and a thin seam of clayey silt was expected (Figure 10.23). Analyses of this type not only indicate whether flow sliding will occur but also provide an estimate of the distribution and magnitude of any resulting deformations.

10.6.2.2 Deformation Failure Analysis

Although deformation failures generally involve smaller deformations than flow failures, they are capable of causing considerable damage. Lateral spreading is the most common type of deformation failure. In recent years a number of investigators have developed methods to estimate permanent displacements produced by deformation failures. Because the mechanisms that produce deformation failures are so complicated, procedures for prediction of the resulting displacements are largely empirical in nature.

Hamada et al. Approach. Hamada et al. (1986) considered the effects of geotechnical and topographic conditions on permanent ground displacements observed in uniform sands of medium grain size in the 1964 Niigata ($M = 7.5$), 1971 San Fernando ($M = 7.1$), and 1983 Nihonkai-Chubu ($M = 7.7$) earthquakes. Permanent displacements were found to be most strongly influenced by the thickness of the liquefied layer and the slopes of the ground surface and lower boundary of the liquefied zone. Permanent horizontal ground displacement, D , was found to vary according to the empirical relationship

$$D(m) = 0.75H^{1/2}\theta^{1/3} \quad (10.20)$$

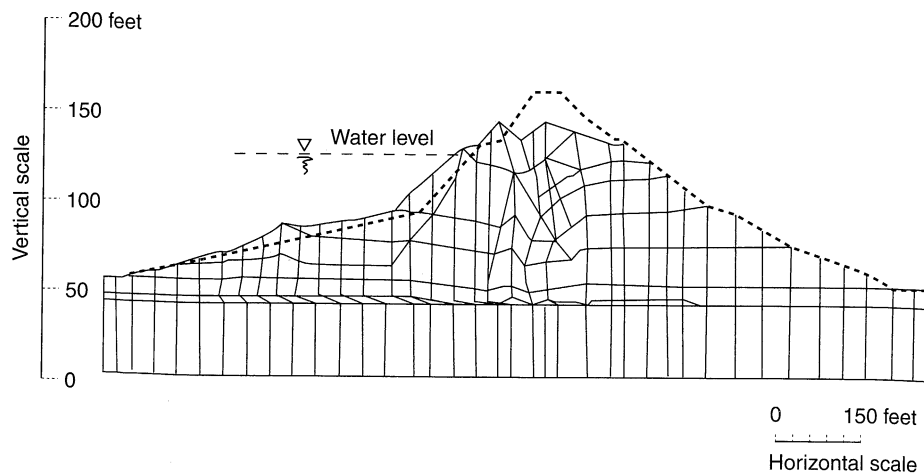


Figure 10.23 Initial (dashed) and postliquefaction (solid) configurations of Sardis Dam in Mississippi from TARA-3FL analyses. Note the large strains due to liquefaction in core and thin seam below the upstream shell. (After Finn, 1990.) Liquefaction hazards were reduced by driving compaction piles into the upstream embankment (see Figure 12.8).

where H is the thickness of the liquefied layer in meters and θ is the larger of the ground surface slope or the slope of the lower boundary of the liquefied zone in percent. For case histories from the three listed earthquakes, 80% of the observed displacements were within a factor of 2 of those predicted by equation (10.20). Note that equation (10.20) does not account for the strength of the liquefied soil; like all such empirical approaches, it must be applied cautiously when conditions vary from those on which it is based.

Youd and Perkins (Liquefaction Severity Index) Approach. Based on observed lateral displacements from a number of case histories in the western United States, Youd and Perkins (1987) defined the *liquefaction severity index* (LSI) as “the general maximum d -value (in inches) for lateral spreads generated on wide active flood plains, deltas, or other areas of gently-sloping Late Holocene fluvial deposits.” As defined, the LSI represents a conservative estimate of ground displacement in a given area; failures with smaller displacements would also be expected in the area. An analysis of the case history database indicated that LSI could be predicted by

$$\log(\text{LSI}) = -3.49 - 1.85 \log R + 0.98 M_w \leq 100 \quad (10.21)$$

where R is the horizontal distance from the seismic energy source in kilometers. The variation of LSI with M and R is shown in Figure 10.24. Qualitative descriptions of the nature of deformation failures for different LSI values are presented in Table 10-5. The dependence of LSI on magnitude and distance lends itself to incorporation into a probabilistic seismic hazard analysis. Youd and Perkins (1987) used this approach to produce probabilistic LSI maps for southern California.

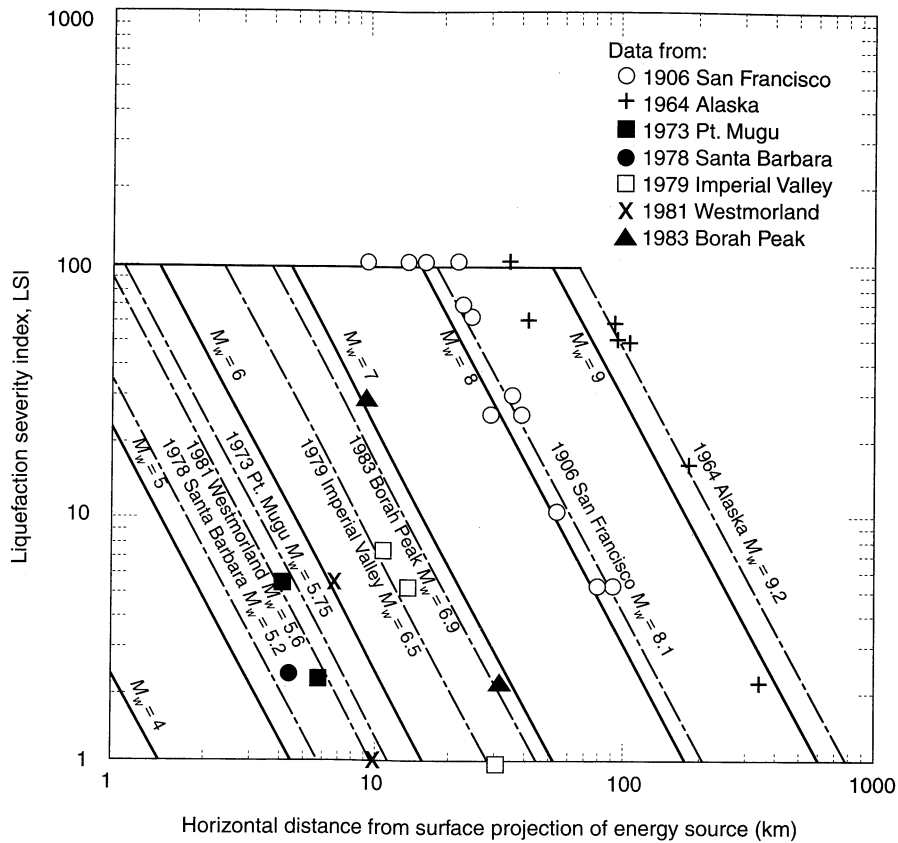


Figure 10.24 Variation of LSI with distance and earthquake magnitude. (After Youd and Perkins, 1986. Mapping of liquefaction severity index, Journal of Geotechnical Engineering, Vol. 103, No. 11. Reprinted by permission of ASCE.)

Byrne Approach. Modeling a slope as a crust of intact soil resting on a layer of liquefied soil (Figure 10.25), Byrne (1991) used work-energy principles with an elastic-perfectly plastic model of liquefied soil to develop expressions for estimation of permanent slope displacement. In this approach, the permanent displacement, D , is obtained from

$$\frac{D^3 S_r}{3(\gamma_{lim} T_L)^2} - D\tau_{st} - \frac{1}{2}mv_0^2 = 0 \quad D < \gamma_{lim} T_L \quad (10.22a)$$

$$D = \frac{3mv_0^2 + 4S_r\gamma_{lim} T_L}{6(S_r - \tau_{st})} \quad D \geq \gamma_{lim} T_L \quad (10.22b)$$

where S_r is the residual strength of the liquefied soil (Figure 9.56), γ_{lim} the limiting shear strain, T_L the thickness of the liquefied layer, τ_{st} the average shear stress required for static equilibrium (on a failure surface passing through the middepth of the liquefied layer), m the mass of the soil above the failure surface, and v_0 the velocity of the mass at the instant of liquefaction. Typical

Table 10-5 Abundance and General Character of Liquefaction Effects for Different LSI Values in Areas with Widespread Liquefiable Deposits

LSI	Description
5	Very sparsely distributed minor ground effects include sand boils with sand aprons up to 0.5 m (1.5 ft) in diameter, minor ground fissures with openings up to 0.1 m (0.3 ft) wide, ground settlements of up to 25 mm (1 in.). Effects lie primarily in areas of recent deposition and shallow groundwater table such as exposed streambeds, active floodplains, mudflats, shorelines, etc.
10	Sparsely distributed ground effects include sand boils with aprons up to 1 m (3 ft) in diameter, ground fissures with openings up to 0.3 m (1 ft) wide, ground settlements of a few inches over loose deposits such as trenches or channels filled with loose sand. Slumps with up to a few tenths of a meter displacement along steep banks. Effects lie primarily in areas of recent deposition with a groundwater table less than 3 m (10 ft) deep.
30	Generally sparse but locally abundant ground effects include sand boils with aprons up to 2 m (6 ft) diameter, ground fissures up to several tenths of a meter wide, some fences and roadways noticeably offset, sporadic ground settlements of as much as 0.3 m (1 ft), slumps with 0.3 m (1 ft) of displacements common along steep stream banks. Larger effects lie primarily in areas of recent deposition with a groundwater table less than 3 m (10 ft) deep.
50	Abundant effects include sand boils with aprons up to 3 m (10 ft) in diameter that commonly coalesce into bands along fissures, fissures with widths up to 1.5 m (4.5 ft), fissures generally parallel or curve toward streams or depressions and commonly break in multiple strands, fences and roadways are offset or pulled apart as much as 1.5 m (4.5 ft) in some places, ground settlements of more than 1 ft (0.3 m) occur locally, slumps with a meter of displacement are common in steep stream banks.
70	Abundant effects include many large sand boils [some with aprons exceeding 6 m (20 ft) in diameter that commonly coalesce along fissures], long fissures parallel to rivers or shorelines, usually in multiple strands with many openings as wide as 2 m (6 ft), many large slumps along streams and other steep banks, some intact masses of ground between fissures displaced 1 to 2 m (3 to 6 ft) down gentle slopes, frequent ground settlements of more than 0.3 m (1 ft).
90	Very abundant ground effects include numerous sand boils with large aprons, 30% or more of some areas covered with freshly deposited sand, many long fissures with multiple parallel streams and shorelines with openings as wide as 2 m or more, some intact masses of ground between fissures are horizontally displaced a couple of meters down gentle slopes, large slumps are common in stream and other steep banks, ground settlements of more than 0.3 m (1 ft) are common.

Source: After Youd and Perkins (1987).

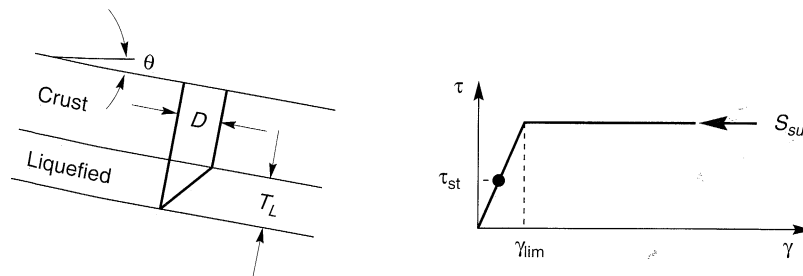


Figure 10.25 Stress, strain, and geometric notation for deformation estimation model of Byrne (1991). Elastic perfectly plastic approximation to stress–strain behavior assumes that residual strength is mobilized at limiting shear strain.

values of γ_{lim} are presented in Table 10-6. Displacements predicted by equations (10.22) agree well with those of equation (10.20) for slopes flatter than about 3% and $(N_1)_{60} = 4$. For higher $(N_1)_{60}$ values, equations (10.22) predict considerably smaller displacements.

Table 10-6 Average Values of Limiting Shear Strain for Clean Sand

$(N_1)_{60}$	γ_{lim}
4	1.00
6	0.80
8	0.63
10	0.50
12	0.40
16	0.25
20	0.16
30	0.05
40	0.015
50	0

Source: Seed et al. (1985).

Byrne et al. (1992) extended this approach to determine factors by which the initial stiffness of a soil should be reduced for finite-element analysis of deformation failures. Deformations predicted by this approach were in good agreement with those observed in the 1971 failure of Upper San Fernando Dam (Figure 10.26).

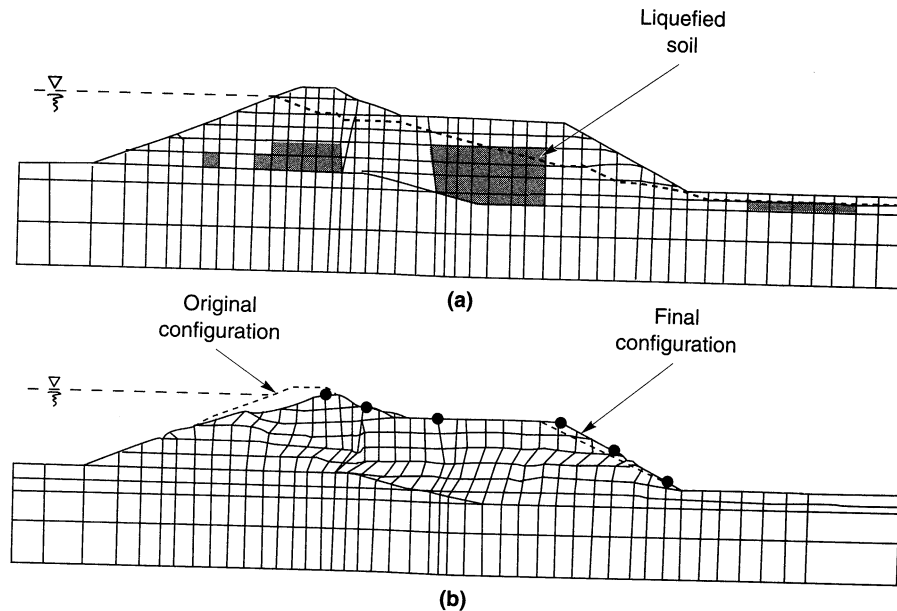
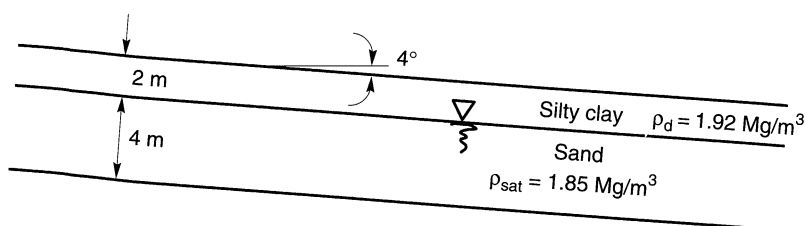


Figure 10.26 (a) Finite-element mesh for analysis of Upper San Fernando Dam with elements determined to have liquefied by Serff et al. (1976) shaded; (b) positions of original and final meshes (displacements exaggerated by factor of 2) by procedure of Byrne et al. (1992). Note large shear strains in liquefied zones.

Example 10.6

The gently sloping site shown below consists of a 2 m thick layer of silty clay overlying a 4 m thick layer of loose, saturated sand. The sand has an average fines content of about 3% and an average $D_{50} = 0.22$ mm. Subsurface investigations indicate that the corrected SPT resistance of the sand is quite consistent with an average value of 11. Estimate the permanent displacement of the slope when subjected to earthquake shaking sufficient to cause liquefaction of the sand.

**Figure E10.6**

Solution The static shear stress at the center of the liquefiable layer is

$$\begin{aligned}\tau_{st} &= \sigma_v \sin \alpha = \left[(2 \text{ m}) \left(1.92 \frac{\text{Mg}}{\text{m}^3} \right) \left(9.81 \frac{\text{m}}{\text{sec}^2} \right) + (2 \text{ m}) \left(1.85 \frac{\text{Mg}}{\text{m}^3} \right) \left(9.81 \frac{\text{m}}{\text{sec}^2} \right) \right] \\ &= 5.2 \text{ kPa}\end{aligned}$$

From Table 10.6, $\gamma_{\text{lim}} = 0.45$ and from Figure 9.57, $S_{su} \approx 300$ psf = 14.4 kPa. Assuming that the slope has no initial velocity ($v_0 = 0$), the direct solution of Equation 10.22b gives

$$D = \frac{0 + 4(14.4 \text{ kPa})(0.45)(4 \text{ m})}{6(14.4 \text{ kPa} - 5.2 \text{ kPa})} = 1.88 \text{ m}$$

Because this displacement is less than $\gamma_{\text{lim}} T_L$, the permanent displacement must be determined using the cubic equation of Equation 10.22a

$$\frac{D^3(14.4 \text{ kPa})}{3[(0.45)(4 \text{ m})]} - D(5.2 \text{ kPa}) - 0 = 0$$

from which

$$D = 1.87 \text{ m}$$

Thus, the estimated permanent displacement would be about 1.9 m. Note that this estimate is based on an average value of the residual strength of the liquefied soil; considering the range of uncertainty of that strength (Figure 9.58), the actual permanent displacement could be considerably smaller or larger.

Baziar et al. Approach. Using a sliding block analysis to describe fundamental aspects of seismic slope stability, Baziar et al. (1992) developed a general expression for permanent lateral displacement

$$d = N \frac{v_{\text{max}}^2}{a_{\text{max}}} f\left(\frac{a_y}{a_{\text{max}}}\right) \quad (10.23)$$

where N is the equivalent number of cycles of harmonic loading, v_{max} is the peak horizontal velocity, a_{max} is the peak horizontal acceleration, and a_y is the yield acceleration. The function $f(a_y/a_{\text{max}})$ was obtained by assuming harmonic accelerations (Figure 10.27). Calibration

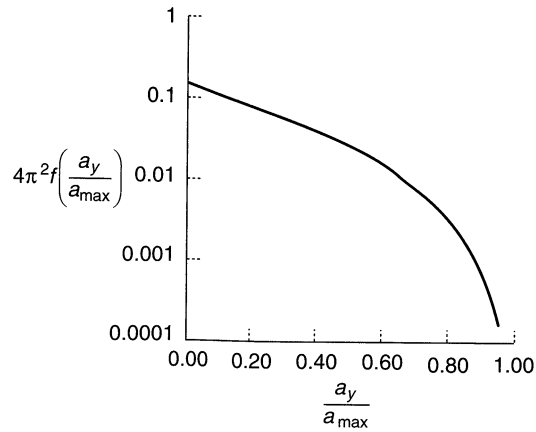


Figure 10.27 Variation of $f(a_y/a_{max})$ with a_y/a_{max} . (After Baziar et al., 1992.)

against case histories from the western United States suggested the use of $N = 2$ for $5.0 \leq M_w \leq 7.7$. By assuming a yield acceleration representative of those associated with the case history database of Youd and Perkins (1987), Baziar et al. (1992) were able to compare displacements predicted by equation (10.23) with the corresponding LSI values. As shown in Figure 10.28, the two approaches are quite consistent at longer site distances, but less so at shorter distances. Until additional near-source data becomes available, the physical basis of equation (10.23) appears to provide a stronger basis than LSI for estimation of displacements.

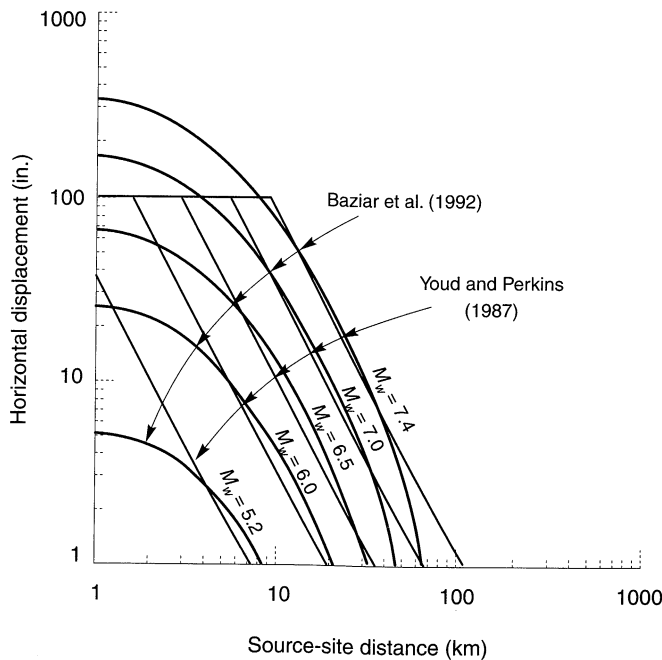


Figure 10.28 Comparison of permanent displacements with LSI. (After Baziar et al., 1992.)

Bartlett and Youd Approach. Bartlett and Youd (1992) used a large database of lateral spreading case histories to develop empirical expressions relating lateral ground displacement to a number of source and site parameters. The database included sites from the western United States and Japan at source–site distances up to 90 km subjected to earthquakes ranging from $M_w = 6.4$ to $M_w = 9.2$. Regression analyses were used to identify the factors that most strongly influenced lateral ground displacements, so that the empirical model could be based on those factors.

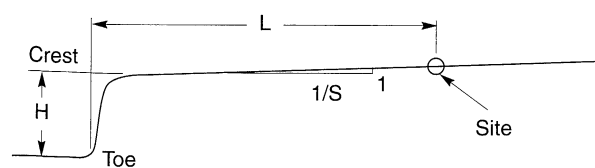
Two empirical models were developed: a *free-face model* for sites near steep banks and a *ground-slope model* for gently sloping sites. For free-face sites, displacements can be obtained from

$$\log D_H = -16.3658 + 1.1782M_w - 0.9275\log R - 0.0133R + 0.6572\log W + 0.3483\log T_{15} + 4.5720\log(100 - F_{15}) - 0.9224(D_{50})_{15} \quad (10.24)$$

where D_H is the estimated lateral ground displacement in meters, M_w the moment magnitude, R the horizontal distance from the seismic energy source in kilometers, W the ratio of the height of the free face to the horizontal distance between the base of the free face and the point of interest (Figure 10.29), T_{15} the cumulative thickness of saturated granular layers with $(N_1)_{60} < 15$ in meters, F_{15} the average fines content for the granular layers comprising T_{15} in percent, and $(D_{50})_{15}$ the average mean grain size for the granular layers comprising T_{15} in millimeters. For gently sloping sites, the *ground-slope model* predicts

$$\log D_H = -16.3658 + 1.1782M_w - 0.9275\log R - 0.0133R + 0.4293\log S + 0.3483\log T_{15} + 4.5720\log(100 - F_{15}) - 0.9224(D_{50})_{15} \quad (10.25)$$

where S is the ground slope in percent (Figure 10.29). Application of these equations to the case history database showed that 90% of the observed displacements were within a factor



- L = Distance from toe of free face to site
- H = Height of free face (crest elev. - toe elev.)
- W = Free-face ratio = $(H/L)(100)$, in percent
- S = Slope of natural ground toward channel in percent

Figure 10.29 Parameters describing slope geometry for free-face and ground-slope deformation models. L , distance from toe of free face to site under consideration; H , height of free face (crest elev. - toe elev.); W , free-face ratio = $(H/L)(100)$, n percent; S , slope of natural ground toward channel = $1/X \cdot 100$, in percent. (After Bartlett and Youd, 1992.)

of 2 of the values predicted. The ranges of input parameters for which predicted results are verified by case history observations are shown in Table 10-7.

Table 10-7 Range of Parameter Values for Which Equations (10.24) and (10.25) Can Be Applied

Input Parameter	Range of Values
Magnitude	$6.0 < M_w < 8.0$
Free-face ratio	$1.0\% < W < 20\%$
Thickness of loose layer	$0.3 \text{ m} < T_{15} < 12 \text{ m}$
Fines content	$0\% < F_{15} < 50\%$
Mean grain size	$0.1 \text{ mm} < (D_{50})_{15} < 1.0 \text{ mm}$
Ground slope	$0.1\% < S < 6\%$
Depth to bottom of section	Depth to bottom of liquefied zone $< 15 \text{ m}$

Source: After Bartlett and Youd (1992).

Example 10.7

Estimate the permanent displacement of the slope described in Example 10.6 due to $M_w = 6.5$ and $M_w = 7.5$ earthquakes occurring at a (horizontal source-site) distance of 30 km.

Solution From the description in Example 10.6, the ground-slope model of Bartlett and Youd is most appropriate. The relevant parameters are

$$S = 4$$

$$T_{15} = 4$$

$$F_{15} = 3$$

$$(D_{50})_{15} = 0.22$$

Then, the permanent displacement due to the $M_w = 6.5$ earthquake can be estimated from equation 10.25 as

$$\begin{aligned} \log D &= -16.3658 + (1.1782)(6.5) - 0.9275 \log(30) - 0.0133(30) + 0.4293 \log(4) \\ &\quad + 0.3483 \log(4) + 4.5270 \log(100 - 3) - 0.9224(0.22) = -1.217 \end{aligned}$$

so

$$D = 10^{-1.217} = 0.061 \text{ m} = 6.1 \text{ cm}$$

For the $M_w = 7.5$ earthquake,

$$\begin{aligned} \log D &= -16.3658 + (1.1782)(7.5) - 0.9275 \log(30) - 0.0133(30) + 0.4293 \log(4) \\ &\quad + 0.3483 \log(4) + 4.5270 \log(100 - 3) - 0.9224(0.22) = -0.039 \end{aligned}$$

so

$$D = 10^{-0.039} = 0.91 \text{ m} = 91 \text{ cm}$$

Discussion. The preceding sections presented a variety of methods for estimation of the permanent displacements produced by deformation failures. Most of these methods are highly empirical, and all produce only approximate estimates of permanent

displacements. The applicability of each method to a particular site depends on the similarity between the conditions at that site and those corresponding to the databases from which the method was developed.

10.7 SUMMARY

1. Historically, earthquake-induced landslides have been among the most damaging of all seismic hazards. Their characteristics are influenced by geologic, hydrologic, topographic, climatic, weathering, and land-use conditions. Slides can be classified on the basis of material type, type of movement, degree of internal disruption, water content, velocity, and depth. Earthquake-induced landslides are usually divided into three main categories: disrupted slides and falls, coherent slides, and lateral spreads and flows.
2. Analysis of historical data allows estimation of the minimum earthquake magnitude required to produce different types of landslides and of the maximum distance to which landslides can be expected in earthquakes of different magnitudes.
3. A slope stability analysis is only one part of a comprehensive evaluation of slope stability. Prior to the analysis, detailed information on geologic, hydrologic, topographic, geometric, and material characteristics must be obtained. The accuracy of the analysis will be only as good as the accuracy of this information.
4. The dynamic shear stresses produced by earthquake shaking represent a source of loading and may also influence the strength and stress-strain behavior of the slope materials. Seismic slope instabilities may be grouped into two categories on the basis of which of these effects is predominant in a given slope. Inertial instabilities are those in which the shear strength of the soil remains essentially constant and slope deformations are caused by its temporary exceedance by dynamic earthquake stresses. Weakening instabilities occur when the earthquake serves to weaken the soil sufficiently that it cannot remain stable under earthquake-induced stresses.
5. Inertial instabilities are most commonly analyzed by pseudostatic, sliding block, or stress-deformation analyses. The Makdisi-Seed approach, based on the results of sliding block analyses, is also used frequently.
6. Pseudostatic analyses represent the effects of an earthquake by applying static horizontal and/or vertical accelerations to a potentially unstable mass of soil. The inertial forces induced by these pseudostatic accelerations increase the driving forces and may decrease the resisting forces acting on the soil. Pseudostatic analyses are not appropriate for soils that build up large pore pressures or show more than about 15% degradation of strength due to earthquake shaking. Stability is expressed in terms of a pseudostatic factor of safety calculated by limit equilibrium procedures. Selection of an appropriate pseudostatic acceleration requires great care; values considerably smaller than the peak acceleration of the sliding mass are usually used.
7. The pseudostatic acceleration required to bring a slope to the point of incipient failure is known as the yield acceleration. If earthquake-induced accelerations in a slope

momentarily exceed the yield acceleration, the unstable soil will momentarily accelerate relative to the material beneath it. Sliding block analyses can be used to calculate the amount of displacement that occurs. The total displacement depends on the amount by which the yield acceleration is exceeded (a function of the ground motion amplitude), the time over which the yield acceleration is exceeded (a function of the frequency content of the ground motion), and the number of times the yield acceleration is exceeded (a function of ground motion duration). Given the highly variable nature of ground motion characteristics, computed displacements can be quite variable.

8. The Makdisi–Seed procedure is based on sliding block analyses of earth dams and embankments. Knowing the fundamental period of vibration of the dam/embankment and the yield acceleration of the slope, simple charts can be used to estimate earthquake-induced permanent displacements.
9. Stress–deformation analyses have been used to estimate permanent deformations caused by inertial instabilities. Strain potential and stiffness reduction approaches allow estimation of permanent deformations from relatively simple analyses; their estimates are highly approximate. Although the computational effort is dramatically increased, permanent deformations can be analyzed more rigorously using nonlinear finite-element techniques. As the accuracy of constitutive models for soils improve, the use of nonlinear finite-element analyses is likely to increase.
10. Weakening instabilities occur when earthquake-induced stresses and strains reduce the shear strength of the soil within a slope. Depending on whether the reduced strength is greater than or less than the stresses required to maintain static equilibrium, weakening instabilities may be classified as flow failures or deformation failures.
11. Flow failure instability is usually evaluated by limit equilibrium analysis. Residual strengths are applied to those portions of the failure surface that pass through liquefied soil. A factor of safety less than 1 suggests that flow failure is likely. Simple limit equilibrium analyses combined with constant-volume constraints can be used to estimate the distance over which materials travel in flow failures. Fluid mechanics models have also been used to estimate flow failure deformations. Nonlinear dynamic analyses that allow weakening of liquefied elements and large strains have also been developed.
12. The effects of deformation failures are usually expressed in terms of slope deformations. A number of approaches, ranging from purely empirical to sliding block model based, have been developed to estimate the displacements produced by deformation failures.

HOMWORK PROBLEMS

- 10.1 The slope shown below is intersected by two 6-inch-thick seams of clayey material. The intact slope materials can be characterized by the parameters, $c = 2500$ psf, $\phi = 0$, $\gamma = 130$ pcf. The clayey seams exhibit $c = 750$ psf, $\phi = 0$, and $\gamma = 120$ pcf. Compute the minimum static factor of safety for the slope.

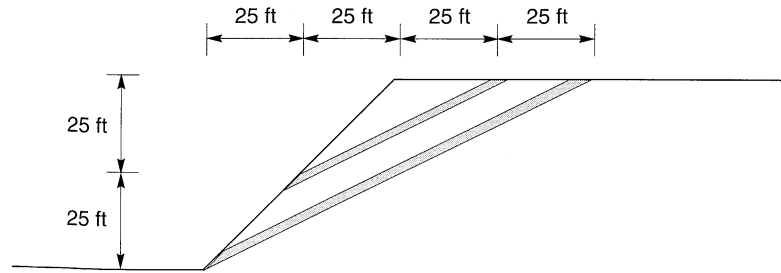


Figure P10.1

- 10.2 Compute the minimum pseudostatic factor of safety for the slope of Problem 10.1 assuming a pseudostatic coefficient of $0.1g$.
- 10.3 Compute the yield acceleration for the slope of Problem 10.1.
- 10.4 Using hand calculations, slope stability charts, or a slope stability analysis computer program, locate the critical circular failure surface for the slope shown below. Considering only this failure surface, compute the yield acceleration for the slope.

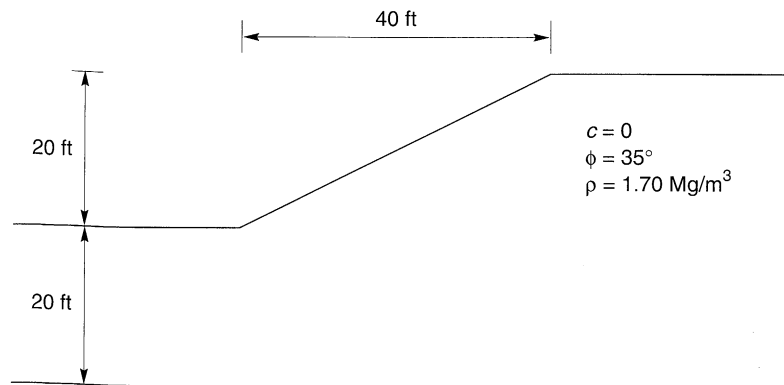


Figure P10.4

- 10.5 The slope shown in Problem 10.4 is subjected to the time history of crest acceleration shown below. Compute the permanent displacement of the slope.

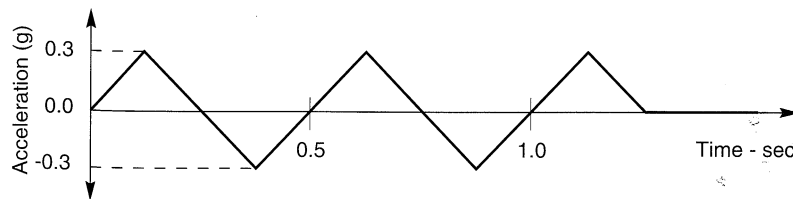


Figure P10.5

- 10.6 An existing embankment is determined to have a yield acceleration of $0.2g$. Using the relationships of Ambraseys and Menu (equation 10.14), estimate the probability that an earthquake

that produces a peak acceleration of $0.3g$ would cause a permanent slope displacement greater than 2.5 cm.

- 10.7** A slope in cohesive soil is determined to have a yield acceleration of $0.17g$. Assuming $N_{eq} = 10$ and using the relationship of Yegian et al. (equation 10.15), compute the expected value of permanent slope displacement if the slope was subjected to (a) the Gilroy No. 1 (rock) motion, and (b) the Gilroy No. 2 (soil) motion. (Note: Peak accelerations and predominant periods of these motions were computed in the example problems in Chapter 3.)
- 10.8** Using the relationship of Jibson (equation 10.16), repeat Problem 10.7. Then compute the permanent slope displacement that would have a 5 percent probability of being exceeded for each ground motion.
- 10.9** The fundamental frequency of the earth dam in Example 7.6 was computed as 3.1 Hz. Pseudo-static slope stability analyses indicate a yield acceleration of $0.21g$. Use the Makdisi-Seed procedure to estimate the permanent displacement of the dam in a $M = 7$ earthquake that produces a peak acceleration of $0.28g$.
- 10.10** The slope shown below consists of 5 m of loose, clean sand overlying very dense clayey gravel with a groundwater table 2 m below the ground surface. Using the Byrne approach, estimate the permanent displacements that would occur if the slope was subjected to earthquake shaking strong enough to initiate liquefaction of the loose sand.

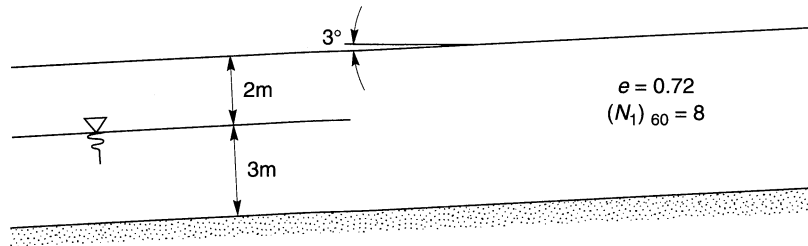


Figure P10.10

- 10.11** Using the approach of Baziar et al., estimate the permanent displacements that would have occurred in identical slopes with yield accelerations of $0.26g$ if subjected to (a) the Gilroy No. 1 (rock) motion, and (b) the Gilroy No. 2 (soil) motion. Comment on the usefulness of peak acceleration as a sole indicator of potential slope deformations.
- 10.12** The slope shown below consists of a loose silty sand overlying stiff clay. Estimate the lateral spreading displacement that would develop if a $M_w = 7.3$ earthquake occurred at a distance (to seismic source) of 40 km.

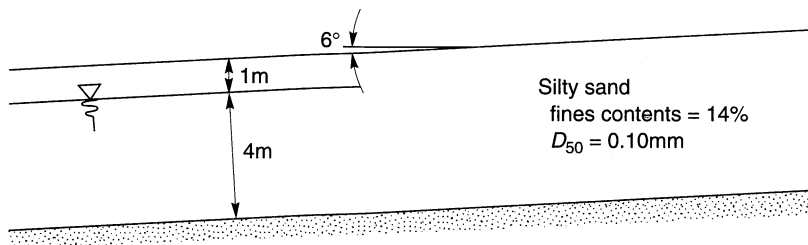


Figure P10.12

11

Seismic Design of Retaining Walls

11.1 INTRODUCTION

Earth retaining structures, such as retaining walls, bridge abutments, quay walls, anchored bulkheads, braced excavations, and mechanically stabilized walls, are used throughout seismically active areas. They frequently represent key elements of ports and harbors, transportation systems, lifelines, and other constructed facilities. Earthquakes have caused permanent deformation of retaining structures in many historical earthquakes. In some cases, these deformations were negligibly small; in others they caused significant damage. In some cases, retaining structures have collapsed during earthquakes, with disastrous physical and economic consequences. This chapter discusses the behavior of retaining walls during earthquakes and presents several of the most common approaches to the seismic design of different types of retaining walls.

11.2 TYPES OF RETAINING WALLS

The problem of retaining soil is one of the oldest in geotechnical engineering; some of the earliest and most fundamental principles of soil mechanics were developed to allow rational design of retaining walls. Many different approaches to soil retention have been developed and used successfully. In recent years, the development of metallic, polymer, and geotextile reinforcement has led to the development of many innovative types of mechanically stabilized earth retention systems.

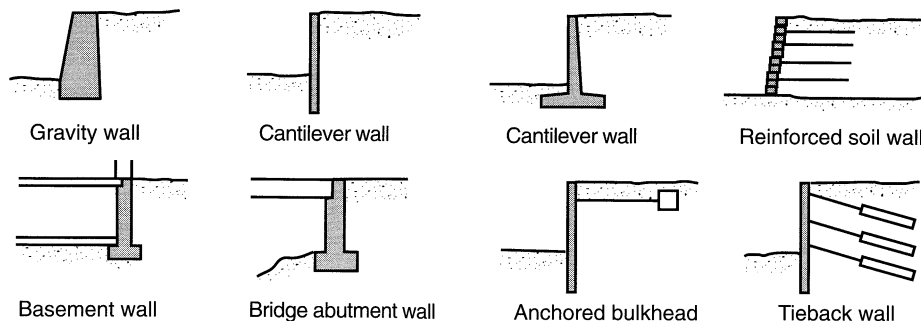


Figure 11.1 Common types of earth retaining structures.

Retaining walls are often classified in terms of their relative mass, flexibility, and anchorage conditions. *Gravity walls* (Figure 11.1) are the oldest and simplest type of retaining wall. Gravity walls are thick and stiff enough that they do not bend; their movement occurs essentially by rigid-body translation and/or rotation. Certain types of composite wall systems, such as crib walls and mechanically stabilized walls, are thick enough that they bend very little and consequently are often designed as gravity walls (with appropriate consideration of internal stability). *Cantilever walls*, which bend as well as translate and rotate, rely on their flexural strength to resist lateral earth pressures. The actual distribution of lateral earth pressure on a cantilever wall is influenced by the relative stiffness and deformation of both the wall and the soil. *Braced walls* are constrained against certain types of movement by the presence of external bracing elements. In the cases of basement walls and bridge abutment walls, lateral movements of the tops of the walls may be restrained by the structures they support. Tieback walls and anchored bulkheads are restrained against lateral movement by anchors embedded in the soil behind the walls. The provision of lateral support at different locations along a braced wall may keep bending moments so low that relatively flexible structural sections can be used.

11.3 TYPES OF RETAINING WALL FAILURES

To design retaining walls, it is necessary to define “failure” and to know how walls can fail. Under static conditions, retaining walls are acted upon by body forces related to the mass of the wall, by soil pressures, and by external forces such as those transmitted by braces. A properly designed retaining wall will achieve equilibrium of these forces without inducing shear stresses that approach the shear strength of the soil. During an earthquake, however, inertial forces and changes in soil strength may violate equilibrium and cause permanent deformation of the wall. Failure, whether by sliding, tilting, bending, or some other mechanism, occurs when these permanent deformations become excessive. The question of what level of deformation is excessive depends on many factors and is best addressed on a site-specific basis.

Gravity walls usually fail by rigid-body mechanisms such as sliding and/or overturning or by gross instability (Figure 11.2). Sliding occurs when horizontal force equilibrium is not maintained (i.e., when the lateral pressures on the back of the wall produce a thrust

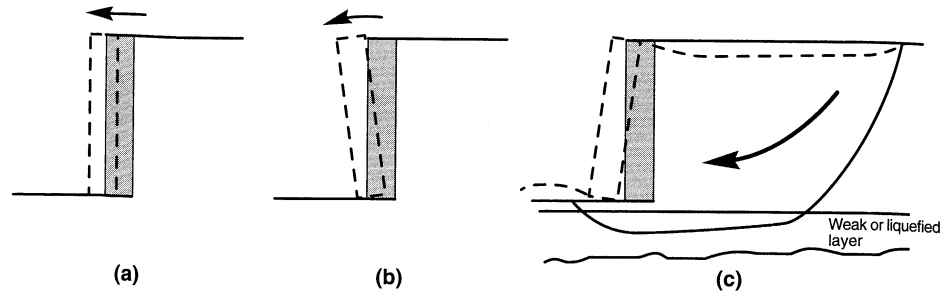


Figure 11.2 Typical failure mechanisms for a gravity retaining wall: (a) sliding (translational) failure; (b) overturning (rotational) failure; (c) gross instability failure.

that exceeds the available sliding resistance on the base of the wall). Overturning failures occur when moment equilibrium is not satisfied; bearing failures at the base of the wall are often involved. Gravity walls may also be damaged by gross instability of the soils behind and beneath them. Such failures may be treated as slope stability failures that encompass the wall. Composite wall systems, such as crib walls, bin walls, and mechanically stabilized walls, can fail in the same ways or by a number of internal mechanisms that may involve shearing, pullout, or tensile failure of various wall elements.

Cantilever walls are subject to the same failure mechanisms as gravity walls, and also to flexural failure mechanisms. Soil pressures and bending moments in cantilever walls depend on the geometry, stiffness, and strength of the wall-soil system (Figure 11.3a,b; pressure and moment diagrams for typical wall). If the bending moments required for equilibrium exceed the flexural strength of the wall, flexural failure may occur (Figure 11.3c). The structural ductility of the wall itself may influence the level of deformation produced by flexural failure.

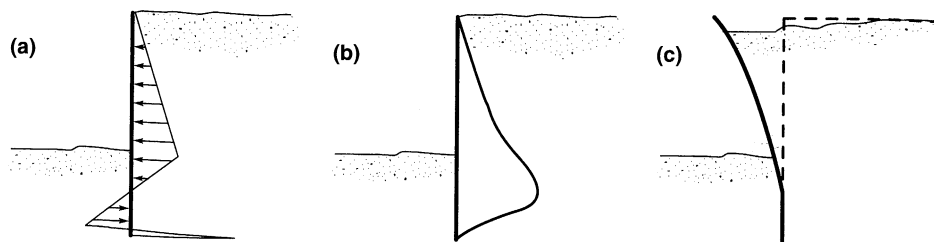


Figure 11.3 (a) Soil pressures, (b) bending moments, and (c) flexural failure mechanism for cantilever retaining wall.

Braced walls usually fail by gross instability, tilting, flexural failure, and/or failure of bracing elements. Tilting of braced walls typically involves rotation about the point at which the brace acts on the wall, often the top of the wall as in the cases of basement and bridge abutment walls (Figure 11.4a). Anchored walls with inadequate penetration may tilt by “kicking out” at their toes (Figure 11.4b). As in the case of cantilever walls, anchored walls may fail in flexure, although the point of failure (maximum bending moment) is likely to be different. Failure of bracing elements can include anchor pullout, tierod failure, or

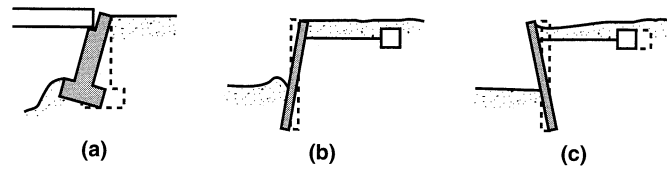


Figure 11.4 Potential modes of failure for braced walls: (a) rotation of bridge abutment about top; (b) rotation of anchored bulkhead due to lack of passive resistance (“kick-out”) at the toe; (c) lack of adequate anchor capacity.

bridge buckling. Backfill settlements can also impose additional axial and transverse loading on bracing elements such as tierods and tiebacks.

11.4 STATIC PRESSURES ON RETAINING WALLS

The seismic behavior of retaining walls depends on the total lateral earth pressures that develop during earthquake shaking. These total pressures include both the static gravitational pressures that exist before an earthquake occurs, and the transient dynamic pressures induced by the earthquake. Since the response of a wall is influenced by both, a brief review of static earth pressures is presented.

Static earth pressures on retaining structures are strongly influenced by wall and soil movements. *Active earth pressures* develop as a retaining wall moves away from the soil behind it, inducing extensional lateral strain in the soil. When the wall movement is sufficient to fully mobilize the strength of the soil behind the wall, *minimum active earth pressures* act on the wall. Because very little wall movement is required to develop minimum active earth pressures (for the usual case of cohesionless backfill materials), free-standing retaining walls are usually designed on the basis of minimum active earth pressures. Where lateral wall movements are restrained, such as in the cases of tieback walls, anchored bulkheads, basement walls, and bridge abutments, static earth pressures may be greater than minimum active. *Passive earth pressures* develop as a retaining wall moves toward the soil, thereby producing compressive lateral strain in the soil. When the strength of the soil is fully mobilized, *maximum passive earth pressures* act on the wall. The stability of many free-standing retaining walls depends on the balance between active pressures acting predominantly on one side of the wall and passive pressures acting on the other.

Even under static conditions, prediction of actual retaining walls forces and deformations is a complicated soil–structure interaction problem. Deformations are rarely considered explicitly in design—the typical approach is to estimate the forces acting on a wall and then to design the wall to resist those forces with a factor of safety high enough to produce acceptably small deformations. A number of simplified approaches are available to evaluate static loads on retaining walls. The most commonly used are described in the following sections.

11.4.1 Rankine Theory

Rankine (1857) developed the simplest procedure for computing minimum active and maximum passive earth pressures. By making assumptions about the stress conditions and

strength envelope of the soil behind a retaining wall (the *backfill soil*), Rankine was able to render the lateral earth pressure problem determinate and directly compute the static pressures acting on retaining walls.

For minimum active conditions, Rankine expressed the pressure at a point on the back of a retaining wall as

$$p_A = K_A \sigma'_v - 2c \sqrt{K_A} \quad (11.1)$$

where K_A is the *coefficient of minimum active earth pressure*, σ'_v is the vertical effective stress at the point of interest, and c is the cohesive strength of the soil. When the principal stress planes are vertical and horizontal (as in the case of a smooth vertical wall retaining a horizontal backfill), the coefficient of minimum active earth pressure is given by

$$K_A = \frac{1 - \sin \phi}{1 + \sin \phi} = \tan^2 \left(45 - \frac{\phi}{2} \right) \quad (11.2)$$

For the case of a cohesionless backfill inclined at an angle β with the horizontal, infinite slope solutions can be used (Terzaghi, 1943; Taylor, 1948) to compute K_A as

$$K_A = \cos \beta \frac{\cos \beta - \sqrt{\cos^2 \beta - \cos^2 \phi}}{\cos \beta + \sqrt{\cos^2 \beta - \cos^2 \phi}} \quad (11.3)$$

for $\beta \leq \phi$ [equation (11.3) is equivalent to equation (11.2) when $\beta = 0$]. The pressure distribution on the back of the wall, as indicated by equations (11.1), depends on the relative magnitudes of the frictional and cohesive components of the backfill soil strength (Figure 11.5). Although the presence of cohesion indicates that tensile stresses will develop between the upper portion of the wall and the backfill, tensile stresses do not actually develop in the field. The creep, stress relaxation, and low-permeability characteristics of cohesive soils render them undesirable as backfill material for retaining structures, and their use in that capacity is generally avoided whenever possible. For dry homogeneous cohesionless backfill, Rankine theory predicts a triangular active pressure distribution oriented parallel to the backfill surface. The active earth pressure resultant, P_A , acts at a point located $H/3$ above the base of a wall of height, H (Figure 11.5a) with magnitude

$$P_A = \frac{1}{2} K_A \gamma H^2 \quad (11.4)$$

Under maximum passive conditions, Rankine theory predicts wall pressures given by

$$p_P = K_P \sigma'_v + 2c \sqrt{K_P} \quad (11.5)$$

where K_P is the *coefficient of maximum passive earth pressure*. For smooth, vertical walls retaining horizontal backfills,

$$K_P = \frac{1 + \sin \phi}{1 - \sin \phi} = \tan^2 \left(45 + \frac{\phi}{2} \right) \quad (11.6)$$

and

$$K_P = \cos \beta \frac{\cos \beta + \sqrt{\cos^2 \beta - \cos^2 \phi}}{\cos \beta - \sqrt{\cos^2 \beta - \cos^2 \phi}} \quad (11.7)$$

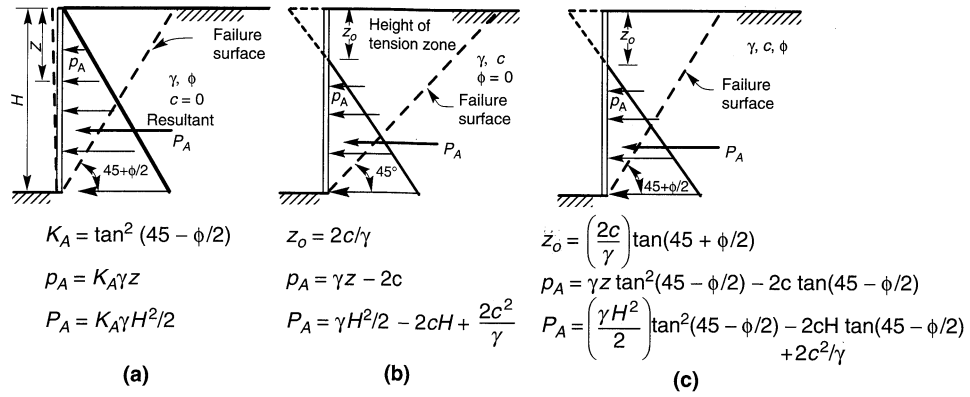


Figure 11.5 Minimum Rankine active earth pressure distributions for backfills with various combinations of frictional and cohesive strength: (a) frictional resistance, no cohesion; (b) cohesive soil, no frictional resistance; (c) combined cohesion and friction. (After NAVFAC, 1982.)

for backfills inclined at β to the horizontal. Passive pressure distributions for various backfill strength characteristics are shown in Figure 11.6. For a dry homogeneous backfill, Rankine theory predicts a triangular passive pressure distribution oriented parallel to the backfill surface. The passive earth pressure resultant, or *passive thrust*, P_p , acts at a point located $H/3$ above the base of a wall of height H (Figure 11.6a) with magnitude

$$P_p = \frac{1}{2} K_p \gamma H^2 \tag{11.8}$$

The presence of water in the backfill behind a retaining wall influences the effective stresses and hence the lateral earth pressure that acts on the wall. For wall design the hydrostatic

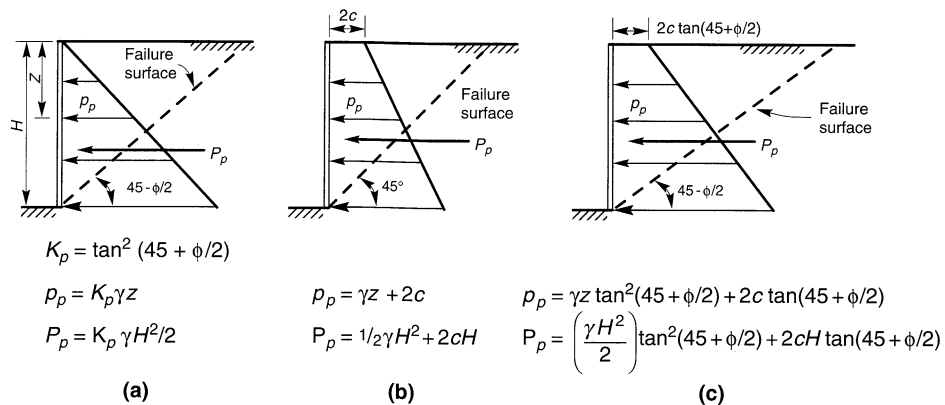


Figure 11.6 Maximum Rankine passive earth pressure distributions for backfills with various combinations of frictional and cohesive strength: (a) frictional resistance, no cohesion; (b) cohesive soil, no frictional resistance; (c) combined cohesion and friction. (After NAVFAC, 1982.)

pressure due to the water must be added to the lateral earth pressure. Because the total lateral thrust on a wall retaining a saturated backfill is considerably greater than that on a wall retaining dry backfill, the provision of backfill drainage is an important part of retaining wall design.

11.4.2 Coulomb Theory

Coulomb (1776) was the first to study the problem of lateral earth pressures on retaining structures. By assuming that the force acting on the back of a retaining wall resulted from the weight of a wedge of soil above a planar failure surface, Coulomb used force equilibrium to determine the magnitude of the soil thrust acting on the wall for both minimum active and maximum passive conditions. Since the problem is indeterminate, a number of potential failure surfaces must be analyzed to identify the critical failure surface (i.e., the surface that produces the greatest active thrust or the smallest passive thrust).

Under minimum active earth pressure conditions, the active thrust on a wall with the geometry shown in Figure 11.7a is obtained from force equilibrium (Figure 11.7b). For the critical failure surface, the active thrust on a wall retaining a cohesionless soil can be expressed as

$$P_A = \frac{1}{2} K_A \gamma H^2 \quad (11.9)$$

where

$$K_A = \frac{\cos^2(\phi - \theta)}{\cos^2\theta \cos(\delta + \theta) \left[1 + \frac{\sin(\delta + \phi)\sin(\phi - \beta)}{\cos(\delta + \theta)\cos(\beta - \theta)} \right]^2} \quad (11.10)$$

δ is the angle of interface friction between the wall and the soil (Table 11-1), and β and θ are as shown in Figure 11.7a. The critical failure surface is inclined at an angle

$$\alpha_A = \phi + \tan^{-1} \left[\frac{\tan(\phi - \beta) + C_1}{C_2} \right] \quad (11.11)$$

to the horizontal where

$$C_1 = \sqrt{\tan(\phi - \beta) [\tan(\phi - \beta) + \cot(\phi - \theta)] [1 + \tan(\delta + \theta)\cot(\phi - \theta)]}$$

$$C_2 = 1 + \{ \tan(\delta + \theta) [\tan(\phi - \beta) + \cot(\phi - \theta)] \}$$

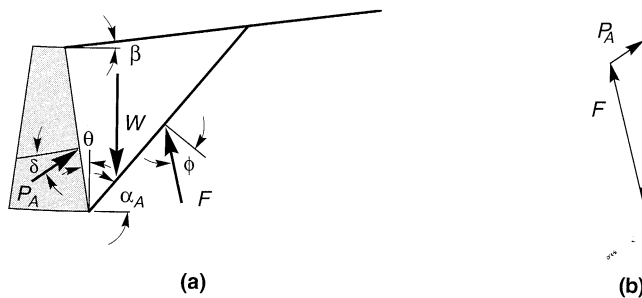


Figure 11.7 (a) Triangular active wedge bounded by planar backfill surface, failure surface, and wall; (b) force polygon for active Coulomb wedge. The critical failure surface is that which gives the largest value of P_A .

Table 11-1 Typical Interface Friction Angles

Interface Materials		Interface Friction Angle δ
Mass concrete against:	clean sound rock	25
	clean gravel, gravel-sand mixtures, coarse sand	29-31
	clean fine to medium sand, silty medium to coarse sand, silty or clayey gravel	24-29
	clean fine sand, silty or clayey fine to medium sand	19-24
	fine sandy silt, nonplastic silt	17-19
Formed concrete against:	medium-stiff and stiff clay and silty clay	17-19
	clean gravel, gravel-sand mixture, well-graded rock fill with spalls	22-26
	clean sand, silty sand-gravel mixture, single-size hard rock fill	17-22
Steel sheet piles against:	silty sand, gravel, or sand mixed with silt or clay	17
	fine sandy silt, nonplastic silt	17
	clean gravel, gravel-sand mixture, well-graded rock fill with spalls	14
	clean sand, silty sand-gravel mixture, single-size hard rock fill	22
	clean sand, silty sand-gravel mixture, single-size hard rock fill	17
	silty sand, gravel, or sand mixed with silt or clay	14
	fine sandy silt, nonplastic silt	11

Source: After NAVFAC (1982).

Coulomb theory does not explicitly predict the distribution of active pressure, but it can be shown to be triangular for linear backfill surfaces with no surface loads. In such cases, P_A acts at a point located $H/3$ above the height of a wall of height H .

For maximum passive conditions in cohesionless backfills (Figure 11.8), Coulomb theory predicts a passive thrust

$$P_P = \frac{1}{2} K_P \gamma H^2 \tag{11.12}$$

where

$$K_P = \frac{\cos^2(\phi + \theta)}{\cos^2\theta \cos(\delta - \theta) \left[1 + \sqrt{\frac{\sin(\delta + \phi)\sin(\phi + \beta)}{\cos(\delta - \theta)\cos(\beta - \theta)}} \right]^2} \tag{11.13}$$

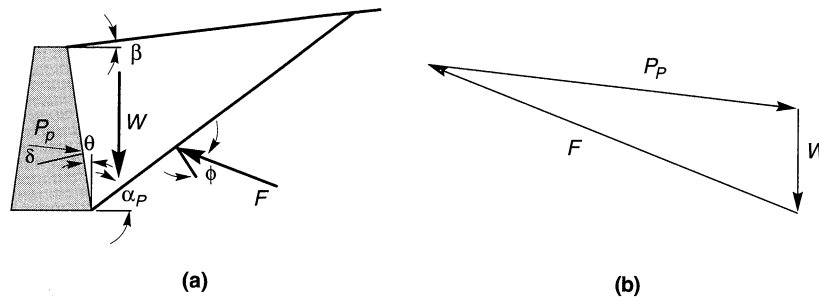


Figure 11.8 (a) Triangular passive wedge bounded by planar backfill surface, failure surface, and wall; (b) force polygon for passive Coulomb wedge. The critical failure surface is that which gives the largest value of P_P .

The critical failure surface for maximum passive earth pressure conditions is inclined to the horizontal at

$$\alpha_p = -\phi + \tan^{-1} \left[\frac{\tan(\phi + \beta) + C_3}{C_4} \right] \quad (11.14)$$

where

$$C_3 = \sqrt{\tan(\phi + \beta) [\tan(\phi + \beta) + \cot(\phi + \theta)] [1 + \tan(\delta - \theta) \cot(\phi + \theta)]}$$

$$C_4 = 1 + \{ \tan(\delta - \theta) [\tan(\phi + \beta) + \cot(\phi + \theta)] \}$$

In contrast to Rankine theory, Coulomb theory can be used to predict soil thrusts on walls with irregular backfill slopes, concentrated loads on the backfill surface, and seepage forces. By considering the soil above a potential failure plane as a free body and including forces due to concentrated loads, boundary water pressures, and so on, the magnitude of the resultant thrust (P_A or P_P) can easily be computed.

11.4.3 Logarithmic Spiral Method

Although the major principal stress axis may be nearly perpendicular to the backfill surface at some distance behind a rough ($\delta > 0$) wall, the presence of shear stresses on the wall-soil interface can shift its position near the back of the wall. If the inclination of the principal stress axes varies within the backfill, the inclination of the failure surface must also vary. In other words, the failure surface must be curved. A logarithmic spiral function has been used to describe such curved failure surfaces for active and passive earth pressure conditions.

For active earth pressure conditions, the critical failure surface consists of a curved portion near the back of the wall and a linear portion that extends up to the ground surface (Figure 11.9a). The active earth pressure distribution is triangular (Figure 11.9b) for walls retaining planar, cohesionless backfills. Thus the active soil thrust can be expressed in the same form as equation (11.4), where the log spiral coefficients of minimum active earth pressure for various wall and backfill inclinations are given in Table 11-2. The active earth pressure coefficients given by the log spiral approach are generally considered to be slightly more accurate than those given by Rankine or Coulomb theory, but the difference is so small that the more convenient Coulomb approach is usually used.

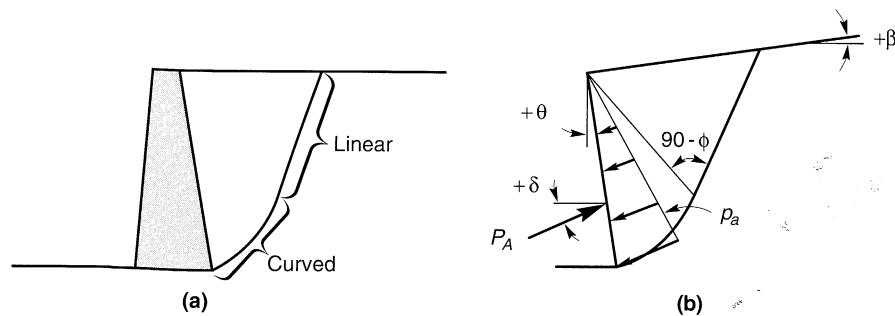


Figure 11.9 (a) Logarithmic spiral representation of the critical failure surface for minimum active earth pressure conditions; (b) orientation of critical failure surface for nonvertical wall with inclined backfill surface.

Table 11-2 Values for K_A for Log-Spiral Failure Surface

δ	β	θ	ϕ					
			20°	25°	30°	35°	40°	45°
0°	-15°	-10°	0.37	0.30	0.24	0.19	0.14	0.11
		0°	0.42	0.35	0.29	0.24	0.19	0.16
		10°	0.45	0.39	0.34	0.29	0.24	0.21
0°	0°	-10°	0.42	0.34	0.27	0.21	0.16	0.12
		0°	0.49	0.41	0.33	0.27	0.22	0.17
		10°	0.55	0.47	0.40	0.34	0.28	0.24
0°	15°	-10°	0.55	0.41	0.32	0.23	0.17	0.13
		0°	0.65	0.51	0.41	0.32	0.25	0.20
		10°	0.75	0.60	0.49	0.41	0.34	0.28
ϕ	-15°	-10°	0.31	0.26	0.21	0.17	0.14	0.11
		0°	0.37	0.31	0.26	0.23	0.19	0.17
		10°	0.41	0.36	0.31	0.27	0.25	0.23
ϕ	0°	-10°	0.37	0.30	0.24	0.19	0.15	0.12
		0°	0.44	0.37	0.30	0.26	0.22	0.19
		10°	0.50	0.43	0.38	0.33	0.30	0.26
ϕ	15°	-10°	0.50	0.37	0.29	0.22	0.17	0.14
		0°	0.61	0.48	0.37	0.32	0.25	0.21
		10°	0.72	0.58	0.46	0.42	0.35	0.31

Source: After Caquot and Kerisel (1948).

The effect of wall friction on the shape of the critical failure surface is more noticeable for passive earth pressure conditions. The passive failure surface also has curved and linear portions (Figure 11.10a), but the curved portion is much more pronounced than for active conditions. For planar cohesionless backfills, the passive earth pressure distribution is triangular (Figure 11.10b), so the passive thrust can be expressed in the form of equation (11.8), where the log spiral coefficients of maximum passive earth pressure are as given in Table 11-3. The passive earth pressure coefficients given by the log spiral method are

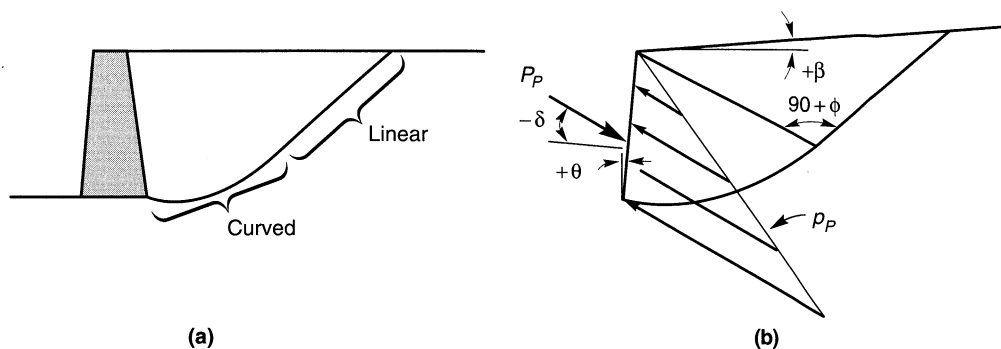


Figure 11.10 (a) Logarithmic spiral representation of the critical failure surface for maximum passive earth pressure conditions; (b) orientation of critical failure surface for nonvertical wall with inclined backfill surface.

Table 11-3 Values for K_p for Log-Spiral Failure Surface

δ	β	θ	ϕ					
			20°	25°	30°	35°	40°	45°
0°	-15°	-10°	1.32	1.66	2.05	2.52	3.09	3.95
		0°	1.09	1.33	1.56	1.82	2.09	2.48
		10°	0.87	1.03	1.17	1.30	1.33	1.54
0°	0°	-10°	2.33	2.96	3.82	5.00	6.68	9.20
		0°	2.04	2.46	3.00	3.69	4.59	5.83
		10°	1.74	1.89	2.33	2.70	3.14	3.69
0°	15°	-10°	3.36	4.56	6.30	8.98	12.2	20.0
		0°	2.99	3.86	5.04	6.72	10.4	12.8
		10°	2.63	3.23	3.97	4.98	6.37	8.20
ϕ	-15°	-10°	1.95	2.90	4.39	6.97	11.8	22.7
		0°	1.62	2.31	3.35	5.04	7.99	14.3
		10°	1.29	1.79	2.50	3.58	5.09	8.86
ϕ	0°	-10°	3.45	5.17	8.17	13.8	25.5	52.9
		0°	3.01	4.29	6.42	10.2	17.5	33.5
		10°	2.57	3.50	4.98	7.47	12.0	21.2
ϕ	15°	-10°	4.95	7.95	13.5	24.8	50.4	115
		0°	4.42	6.72	10.8	18.6	39.6	73.6
		10°	3.88	5.62	8.51	13.8	24.3	46.9

Source: After Caquot and Kerisel (1948).

considerably more accurate than those given by Rankine or Coulomb theory; the Rankine and Coulomb coefficient tend to underpredict and overpredict the maximum passive earth pressure, respectively. Rankine theory greatly underpredicts actual passive earth pressures and is rarely used for that purpose. Coulomb theory overpredicts passive pressures (an unconservative error) by about 11% for $\delta = \phi/2$ and by 100% or more for $\delta = \phi$. For that reason, Coulomb theory is rarely used to evaluate passive earth pressures when $\delta > \phi/2$.

11.4.4 Stress-Deformation Analysis

Since the actual pressures that act on retaining walls depend on interaction between the wall and the surrounding soil, it seems logical to expect that they could be estimated by stress-deformation techniques such as the finite-element method. Finite-element analyses are, in fact, very useful for estimating retaining wall pressures and movements (Clough and Duncan, 1971; Duncan et al., 1990). In addition, they can help explain unexpected or anomalous field measurements of actual wall behavior (Clough and Duncan, 1971; Duncan and Clough, 1971).

The accuracy of stress-deformation analyses, however, depends on how well they are able to model the actual field conditions. A useful method of analysis should be able to describe the stress-strain behavior of the soil (which is nonlinear) and wall (usually assumed to remain linear), the stress-displacement behavior of the soil-wall interface, and the sequence of wall construction and backfill placement. Without careful attention to each of these factors, the results of a finite-element analysis may have limited applicability.

11.5 DYNAMIC RESPONSE OF RETAINING WALLS

The dynamic response of even the simplest type of retaining wall is quite complex. Wall movements and pressures depend on the response of the soil underlying the wall, the response of the backfill, the inertial and flexural response of the wall itself, and the nature of the input motions. Since few well-documented case histories involving field measurements of wall response are available, most of the current understanding of the dynamic response of retaining walls has come from model tests and numerical analyses. These tests and analyses, the majority of which have involved gravity walls, indicate that:

1. Walls can move by translation and/or rotation. The relative amounts of translation and rotation depend on the design of the wall; one or the other may predominate for some walls (Nadim and Whitman, 1984), and both may occur for others (Siddharthan et al., 1992).
2. The magnitude and distribution of dynamic wall pressures are influenced by the mode of wall movement (e.g., translation, rotation about the base, or rotation about the top) (Sherif et al., 1982; Sherif and Fang, 1984a,b).
3. The maximum soil thrust acting on a wall generally occurs when the wall has translated or rotated *toward* the backfill (i.e., when the inertial force on the wall is directed toward the backfill). The minimum soil thrust occurs when the wall has translated or rotated *away* from the backfill.
4. The shape of the earth pressure distribution on the back of the wall changes as the wall moves. The point of application of the soil thrust therefore moves up and down along the back of the wall. The position of the soil thrust is highest when the wall has moved toward the soil and lowest when the wall moves outward.
5. Dynamic wall pressures are influenced by the dynamic response of the wall and backfill and can increase significantly near the natural frequency of the wall-backfill system (Steedman and Zeng, 1990). Permanent wall displacements also increase at frequencies near the natural frequency of the wall-backfill system (Nadim, 1982). Dynamic response effects can also cause deflections of different parts of the wall to be out of phase. This effect can be particularly significant for walls that penetrate into the foundation soils when the backfill soils move out of phase with the foundation soils.
6. Increased residual pressures may remain on the wall after an episode of strong shaking has ended (Whitman, 1990).

Given these complex, interacting phenomena and the inherent variability and uncertainty of soil properties, it is not currently possible to analyze all aspects of the seismic response of retaining walls accurately. As a result, simplified models that make various assumptions about the soil, structure, and input motion are most commonly used for seismic design of retaining walls.

11.6 SEISMIC PRESSURES ON RETAINING WALLS

One common approach to the seismic design of retaining walls involves estimating the loads imposed on the wall during earthquake shaking and then ensuring that the wall can

resist those loads. Because the actual loading on retaining walls during earthquakes is extremely complicated, seismic pressures on retaining walls are usually estimated using simplified methods.

11.6.1 Yielding Walls

Retaining walls that can move sufficiently to develop minimum active and/or maximum passive earth pressures are referred to as *yielding walls*. The dynamic pressures acting on yielding walls are usually estimated by pseudostatic procedures that share many features of those described for seismic slope stability analysis in Section 10.6.1.1. More recently, a pseudodynamic procedure that accounts, in an approximate manner, for the dynamic response of the backfill has been developed.

11.6.1.1 Mononobe–Okabe Method

Okabe (1926) and Mononobe and Matsuo (1929) developed the basis of a pseudo-static analysis of seismic earth pressures on retaining structures that has become popularly known as the Mononobe–Okabe (M-O) method. The M-O method is a direct extension of the static Coulomb theory to pseudostatic conditions. In a M-O analysis, pseudostatic accelerations are applied to a Coulomb active (or passive) wedge. The pseudostatic soil thrust is then obtained from force equilibrium of the wedge.

Active Earth Pressure Conditions. The forces acting on an active wedge in a dry, cohesionless backfill are shown in Figure 11.1a. In addition to the forces that exist under static conditions (Figure 11.7), the wedge is also acted upon by horizontal and vertical pseudostatic forces whose magnitudes are related to the mass of the wedge by the pseudo-static accelerations $a_h = k_h g$ and $a_v = k_v g$. The total active thrust can be expressed in a form similar to that developed for static conditions, that is,

$$P_{AE} = \frac{1}{2} K_{AE} \gamma H^2 (1 - k_v) \tag{11.15}$$

where the dynamic active earth pressure coefficient, K_{AE} , is given by

$$K_{AE} = \frac{\cos^2(\phi - \theta - \psi)}{\cos \psi \cos^2 \theta \cos(\delta + \theta + \psi) \left[1 + \frac{\sin(\delta + \phi) \sin(\phi - \beta - \psi)}{\cos(\delta + \theta + \psi) \cos(\beta - \theta)} \right]^2} \tag{11.16}$$

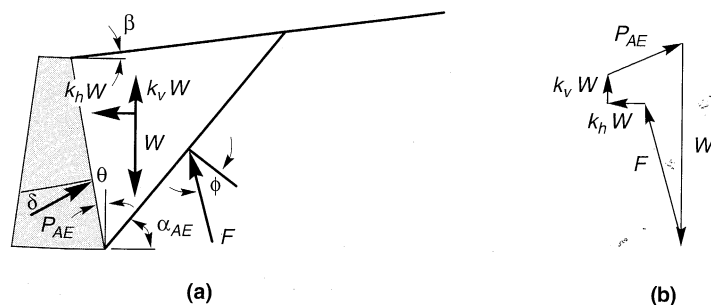


Figure 11.11 (a) Forces acting on active wedge in Mononobe–Okabe analysis, (b) force polygon illustrating equilibrium of forces acting on active wedge.

where $\phi - \beta \geq \psi$, $\gamma = \gamma_d$, and $\psi = \tan^{-1}[k_h/(1 - k_v)]$. The critical failure surface, which is flatter than the critical failure surface for static conditions, is inclined (Zarrabi-Kashani, 1979) at an angle

$$\alpha_{AE} = \phi - \psi + \tan^{-1} \left[\frac{-\tan(\phi - \psi - \beta) + C_{1E}}{C_{2E}} \right] \quad (11.17)$$

where

$$C_{1E} = \frac{\sqrt{\tan(\phi - \psi - \beta) [\tan(\phi - \psi - \beta) + \cot(\phi - \psi - \theta)] [1 + \tan(\delta + \psi + \theta) \cot(\phi - \psi - \theta)]}}{\tan(\delta + \psi + \theta) [\tan(\phi - \psi - \beta) + \cot(\phi - \psi - \theta)]}$$

Although the M-O analysis implies that the total active thrust should act at a point $H/3$ above the base of a wall of height, H , experimental results suggest that it actually acts at a higher point under dynamic loading conditions. The total active thrust, P_{AE} [equation (11.15)], can be divided into a static component, P_A [equation (11.9)], and a dynamic component, ΔP_{AE} :

$$P_{AE} = P_A + \Delta P_{AE} \quad (11.18)$$

The static component is known to act at $H/3$ above the base of the wall. Seed and Whitman (1970) recommended that the dynamic component be taken to act at approximately $0.6H$. On this basis, the total active thrust will act at a height

$$h = \frac{P_A H/3 + \Delta P_{AE} (0.6H)}{P_{AE}} \quad (11.19)$$

above the base of the wall. The value of h depends on the relative magnitudes of P_A and P_{AE} —it often ends up near the midheight of the wall. M-O analyses show that k_v , when taken as one-half to two-thirds the value of k_h , affects P_{AE} by less than 10%. Seed and Whitman (1970) concluded that vertical accelerations can be ignored when the M-O method is used to estimate P_{AE} for typical wall designs.

Example 11.1

Compute the overturning moment about the base of the wall shown below for $k_h = 0.15$ and $k_v = 0.075$.

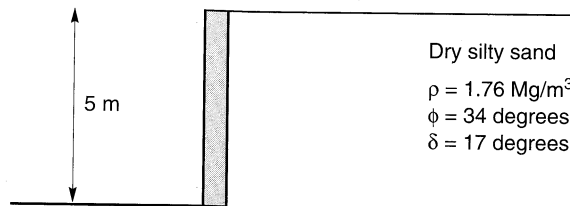


Figure E11.1

Solution First, estimate the static active thrust on the wall. Because the wall is not smooth ($\delta > 0$), Coulomb theory should be used. From equations (11.9) and (11.10),

$$K_A = \frac{\cos^2(34^\circ - 0^\circ)}{\cos^2(0^\circ) \cos(17^\circ + 0^\circ) \left[1 + \frac{\sin(17^\circ + 34^\circ) \sin(34^\circ - 0^\circ)}{\cos(17^\circ + 0^\circ) \cos(0^\circ - 0^\circ)} \right]^2} = 0.256$$

and

$$P_A = \frac{1}{2}K_A\gamma H^2 = \frac{1}{2}(0.256)(1.76 \text{ Mg/m}^3)(9.81 \text{ m/sec}^2)(5 \text{ m})^2 = 55.3 \text{ kN/m}$$

Now, the total active thrust can be computed from equations (11.15) and (11.16). The angle, ψ , is given by

$$\psi = \tan^{-1}\left(\frac{k_h}{1-k_v}\right) = \tan^{-1}\left(\frac{0.15}{1-0.075}\right) = 9.2^\circ$$

and

$$K_{AE} = \frac{\cos^2(34^\circ - 0^\circ - 9.2^\circ)}{\cos(9.2^\circ)\cos^2(0^\circ)\cos(17^\circ + 0^\circ + 9.2^\circ)\left[1 + \sqrt{\frac{\sin(17^\circ + 34^\circ)\sin(34^\circ + 0^\circ - 9.2^\circ)}{\cos(17^\circ + 0^\circ + 9.2^\circ)\cos(0^\circ - 0^\circ)}}\right]^2}$$

$$= 0.362$$

and

$$P_{AE} = \frac{1}{2}K_{AE}\gamma H^2(1-k_v) = \frac{1}{2}(0.362)(1.76 \text{ Mg/m}^3)(9.81 \text{ m/sec}^2)(5 \text{ m})^2(1-0.075)$$

$$= 72.3 \text{ kN/m}$$

The dynamic component of the total thrust is

$$\Delta P_{AE} = P_{AE} - P_A = 72.3 \text{ kN/m} - 55.3 \text{ kN/m} = 17 \text{ kN/m}$$

From equation (11.19), the total thrust acts at a point

$$h = \frac{P_A \frac{H}{3} + \Delta P_{AE}(0.6H)}{P_{AE}} = \frac{55.3 \text{ kN/m} \frac{5 \text{ m}}{3} + 17 \text{ kN/m}(0.6)(5 \text{ m})}{72.3 \text{ kN/m}} = 1.98 \text{ m}$$

above the base of the wall. Because only the horizontal component of the total active thrust contributes to the overturning moment about the base, the overturning moment is given by

$$M_o = (P_{AE})_h h = (72.3 \text{ kN/m})\cos(17^\circ)(1.98 \text{ m}) = 137 \frac{\text{kN}\cdot\text{m}}{\text{m}}$$

Passive Earth Pressure Conditions. The total passive thrust on a wall retaining a dry, cohesionless backfill (Figure 11.12) is given by

$$P_{PE} = \frac{1}{2}K_{PE}\gamma H^2(1-k_v) \quad (11.20)$$

where the dynamic passive earth pressure coefficient, K_{PE} , is given by

$$K_{PE} = \frac{\cos^2(\phi + \theta - \psi)}{\cos\psi \cos^2\theta \cos(\delta - \theta + \psi)\left[1 - \sqrt{\frac{\sin(\delta + \phi)\sin(\phi + \beta - \psi)}{\cos(\delta - \theta + \psi)\cos(\beta - \theta)}}\right]^2} \quad (11.21)$$

The critical failure surface for M-O passive conditions is inclined from horizontal by an angle

$$\alpha_{PE} = \psi - \phi + \tan^{-1}\left[\frac{\tan(\phi + \psi + \beta) + C_{3E}}{C_{4E}}\right] \quad (11.22)$$

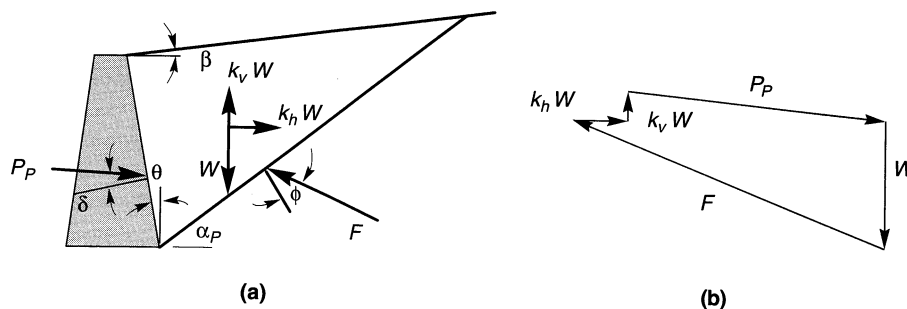


Figure 11.12 (a) Forces acting on passive wedge in Mononobe-Okabe analysis; (b) force polygon illustrating equilibrium of forces acting on passive wedge.

where

$$C_{3E} =$$

$$\sqrt{\tan(\phi + \beta - \psi) [\tan(\phi + \beta - \psi) + \cot(\phi + \theta - \psi)] [1 + \tan(\delta + \psi - \theta) \cot(\phi + \theta - \psi)]}$$

$$C_{4E} = 1 + \{ \tan(\delta + \psi - \theta) [\tan(\phi + \beta - \psi) + \cot(\phi + \theta - \psi)] \}$$

The total passive thrust can also be divided (Towhata and Islam, 1987) into static and dynamic components:

$$P_{PE} = P_P + \Delta P_{PE} \quad (11.23)$$

where P_{PE} and P_P are computed from equations (11.20) and (11.12), respectively. Note that the dynamic component acts in the opposite direction of the static component, thus reducing the available passive resistance.

Discussion. Although conceptually quite simple, the M-O analysis provides a useful means of estimating earthquake-induced loads on retaining walls. A positive horizontal acceleration coefficient causes the total active thrust to exceed the static active thrust and the total passive thrust to be less than the static passive thrust. Since the stability of a particular wall is generally reduced by an increase in active thrust and/or a decrease in passive thrust, the M-O method produces seismic loads that are more critical than the static loads that act prior to an earthquake. The effects of distributed and discrete surface loads and irregular backfill surfaces are easily considered by modifying the free-body diagram of the active or passive wedge. In such cases, equations (11.16) and (11.21) no longer apply—the total thrusts must be obtained from the analysis of a number of potential failure planes.

As a pseudostatic extension of the Coulomb analysis, however, the M-O analysis is subject to all of the limitations of pseudostatic analyses as well as the limitations of Coulomb theory. As in the case of pseudostatic slope stability analyses (Section 10.6.1.1), determination of the appropriate pseudostatic coefficient is difficult and the analysis is not appropriate for soils that experience significant loss of strength during earthquakes (e.g., liquefiable soils). Just as Coulomb theory does under static conditions, the M-O analysis will overpredict the actual total passive thrust, particularly for $\delta > \phi/2$. For these reasons the M-O method should be used and interpreted carefully.

11.6.1.2 Steedman-Zeng Method

As a pseudostatic analysis, the M-O method accounts for the dynamic nature of earthquake loading in a very approximate way. It is possible, however, to account for certain dynamic response characteristics in a relatively simple manner. To account for phase difference and amplification effects within the backfill behind a retaining wall can be considered using a simple pseudodynamic analysis of seismic earth pressures (Steedman and Zeng, 1990).

Consider the fixed-base cantilever wall shown in Figure 11.13. If the base is subjected to harmonic horizontal acceleration of amplitude a_h , the acceleration at a depth z , below the top of the wall can be expressed as

$$a(z, t) = a_h \sin \left[\omega \left(t - \frac{H-z}{v_s} \right) \right] \quad (11.24)$$

If the seismic wall pressures are assumed to result from the soil within a triangular wedge inclined at α to the horizontal, the mass of a thin element of the wedge at depth z is

$$m(z) = \frac{\gamma H - z}{g \tan \alpha} dz \quad (11.25)$$

where γ is the unit weight of the backfill. The total inertial force acting on the wall can therefore be expressed as

$$Q_h(t) = \int_0^H m(z) a(z, t) dz = \frac{\lambda \gamma a_h}{4\pi^2 g \tan \alpha} [2\pi H \cos \omega \zeta + \lambda (\sin \omega \zeta - \sin \omega t)] \quad (11.26)$$

where $\lambda = 2\pi v_s / \omega$ is the wavelength of the vertically propagating shear wave and $\zeta = t - H/v_s$. The special case of a rigid wedge is given, in the limit, as

$$\lim_{v_s \rightarrow \infty} (Q_h)_{\max} = \frac{\gamma H^2 a_h}{2g \tan \alpha} = \frac{a_h}{g} W = k_h W \quad (11.27)$$

which is equivalent to the pseudostatic force assumed by the M-O method. The total (static plus dynamic) soil thrust can be obtained by resolving forces on the wedge, that is,

$$P_{AE}(t) = \frac{Q_h(t) \cos(\alpha - \phi) + W \sin(\alpha - \phi)}{\cos(\delta + \phi - \alpha)} \quad (11.28)$$

and the total earth pressure distribution by differentiating the total soil thrust

$$p_{AE}(t) = \frac{\partial P_{AE}(t)}{\partial z} = \frac{\gamma z}{\tan \alpha} \frac{\sin(\alpha - \phi)}{\cos(\delta + \phi - \alpha)} + \frac{k_h \gamma z}{\tan \alpha} \frac{\cos(\alpha - \phi)}{\cos(\delta + \phi - \alpha)} \sin \left[\omega \left(t - \frac{z}{v_s} \right) \right] \quad (11.29)$$

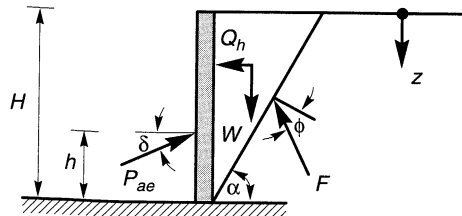


Figure 11.13 Wall geometry and notation for Steedman-Zeng method.

The first term in equation (11.29), which increases linearly with depth and does not vary with time, represents the static earth pressure acting on the wall. The resultant static thrust acts in accordance with static earth pressure theories at a point $h_s = H/3$ above the base of the wall. The second term represents the dynamic earth pressure. It increases as a nonlinear function of depth with a shape that depends on the ratio H/λ . A typical example of the nonlinear dynamic pressure is shown in Figure 11.14. Since the dynamic pressure increases nonlinearly with depth, the position of the dynamic thrust varies with time according to

$$h_d = H - \frac{2\pi^2 H^2 \cos \omega \zeta + 2\pi \lambda H \sin \omega \zeta - \lambda^2 (\cos \omega \zeta - \cos \omega t)}{2\pi H \cos \omega \zeta + \pi \lambda (\sin \omega \zeta - \sin \omega t)} \quad (11.30)$$

The point of application of the dynamic thrust for very low frequency motions (small H/λ , so the backfill moves essentially in phase) is at $h_d = H/3$. For higher-frequency motions, the point of application moves higher on the wall, as indicated in Figure 11.15.

Steedman and Zeng (1989) found that the soil thrusts for backfills of different stiffnesses were close to those obtained when the mean shear wave velocities of the backfill were used in the pseudodynamic analyses. Backfill amplification effects can also be considered by expressing a_h as a function of depth [rather than as a constant in equation (11.24)] and repeating the integration of equation (11.26). Note that backfill amplification will increase both the loads acting on the wall and the height of the resultant soil thrust. Assuming that $a_h(z, t)$ varied linearly from the input acceleration at the base of the wall to a value twice as large at the top, Steedman and Zeng (1990) showed good agreement with the results of centrifuge tests.

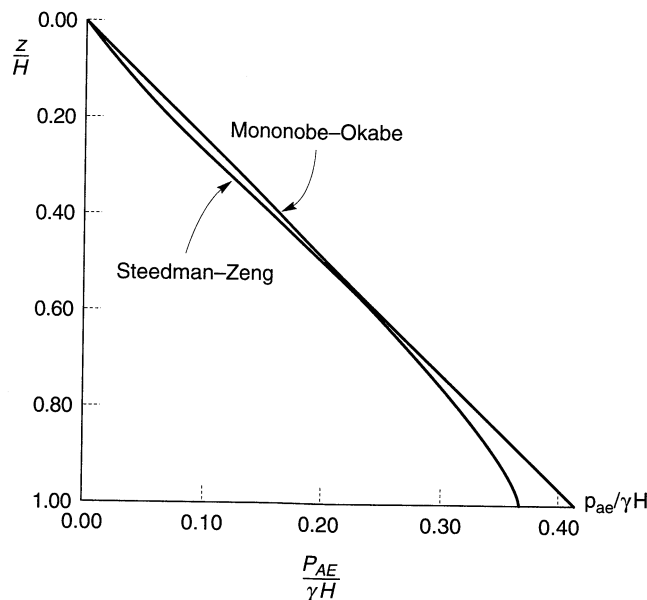


Figure 11.14 Comparison of normalized pressure distributions for M-O and Steedman-Zeng methods assuming that $k_h = 0.2$ and $H/\lambda = 0.3$. (After Steedman and Zeng, 1990.)

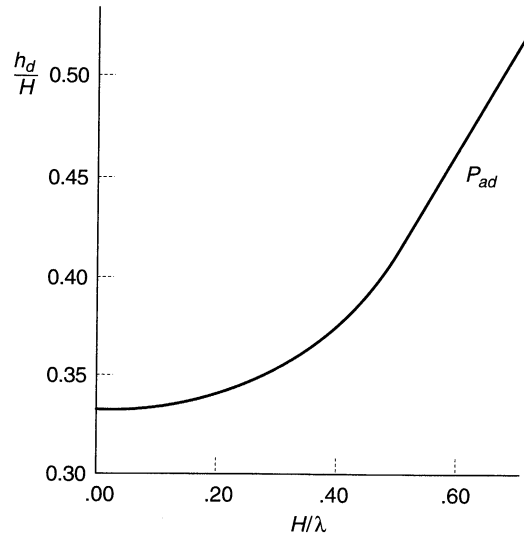


Figure 11.15 Location of dynamic thrust at instant of maximum overturning moment for $k_h = 0.2$. (After Steedman and Zeng, 1990.)

11.6.2 Nonyielding Walls

Some retaining structures, such as massive gravity walls founded on rock or basement walls braced at both top and bottom, do not move sufficiently to mobilize the shear strength of the backfill soil. As a result, the limiting conditions of minimum active or maximum passive earth pressures cannot be developed.

Wood (1973) analyzed the response of a homogeneous linear elastic soil trapped between two rigid walls connected to a rigid base (Figure 11.16). If the two walls are assumed to be spaced far apart, the pressures on one wall will not be strongly influenced by the presence of the other. Wood showed that dynamic amplification was negligible for low-frequency input motions [i.e., motions at less than half the fundamental frequency of the unrestrained backfill ($f_o = v_s/4H$)]. For this range of frequencies, in which many practical problems lie, wall pressures can be obtained from the elastic solution for the case of a uniform, constant, horizontal acceleration applied throughout the soil. For smooth rigid walls, Wood (1973) expressed the dynamic thrust and dynamic overturning moment (about the base of the wall) in the form

$$\Delta P_{eq} = \gamma H^2 \frac{a_h}{g} F_p \quad (11.31)$$

$$\Delta M_{eq} = \gamma H^3 \frac{a_h}{g} F_m \quad (11.32)$$

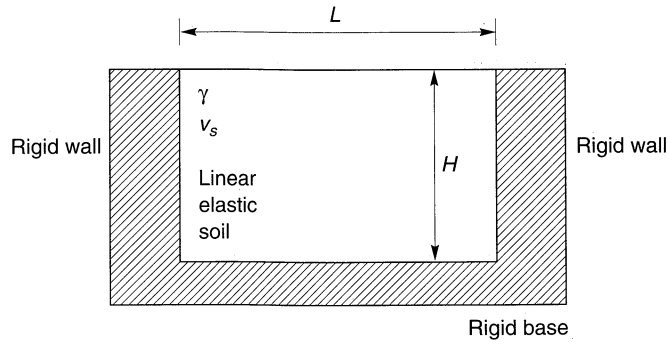


Figure 11.16 Wall geometry and notation for Wood (1973) analysis of pressures on nonyielding walls.

where a_n is the amplitude of the harmonic base acceleration and F_p and F_m are the dimensionless dynamic thrust and moment factors shown in Figures 11.17 and 11.18, respectively. The point of application of the dynamic thrust is at a height

$$h_{eq} = \frac{\Delta M_{eq}}{\Delta P_{eq}} \tag{11.33}$$

above the base of the wall; typically, $h_{eq} \approx 0.63H$.

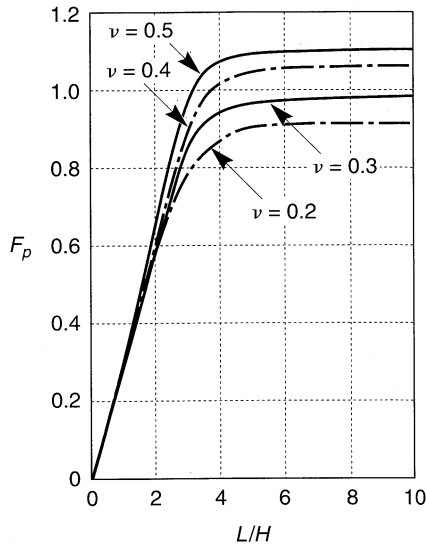


Figure 11.17 Dimensionless thrust factor for various geometries and soil Poisson's ratio values. After Wood (1973).

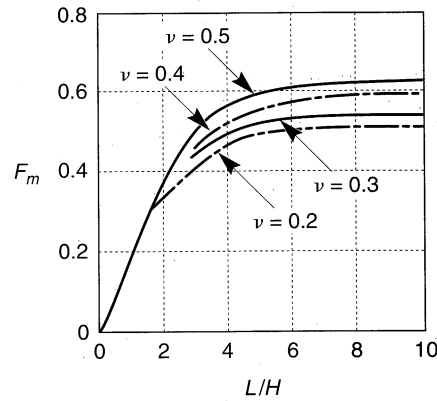


Figure 11.18 Dimensionless moment factor for various geometries and soil Poisson's ratio values. After Wood (1973).

Example 11.2

A reinforced concrete box culvert is used to provide an undercrossing through a railroad embankment as shown below. Estimate the dynamic thrust on a wall of the culvert when subjected to a ground motion with $k_h = 0.2$.

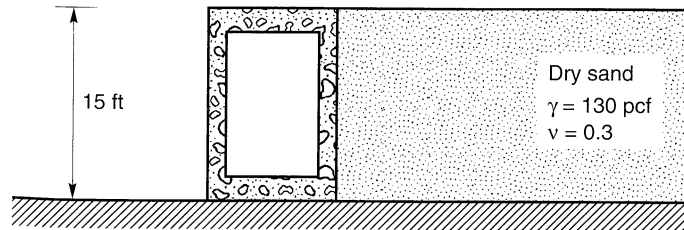


Figure E11.2

Solution Assuming they are properly reinforced and that the culvert cannot slide on its base, the culvert walls will not yield. Consequently, the dynamic thrust can be estimated using equation (11.31) and Figure 11.17

$$\Delta P_{eq} = \gamma H^2 \frac{a_h}{g} F_p = (130 \text{ pcf})(15 \text{ ft})^2 \frac{0.2}{g} (1.0) = 5850 \text{ lb/ft}$$

11.6.3 Effects of Water on Wall Pressures

The procedures for estimation of seismic loads on retaining walls described in the preceding sections have been limited to cases of dry backfills. Most retaining walls are designed with drains to prevent water from building up within the backfill. This is not possible, however, for retaining walls in waterfront areas, where most earthquake-induced wall failures have been observed.

The presence of water plays a strong role in determining the loads on waterfront retaining walls both during and after earthquakes. Water outboard of a retaining wall can exert dynamic pressures on the face of the wall. Water within a backfill can also affect the dynamic pressures that act on the back of the wall. Proper consideration of the effects of water is essential for the seismic design of retaining structures, particularly in waterfront areas. Since few waterfront retaining structures are completely impermeable, the water level in the backfill is usually at approximately the same level as the free water outboard of the wall. Backfill water levels generally lag behind changes in outboard water level—the difference in water level depends on the permeability of the wall and backfill and on the rate at which the outboard water level changes. The total water pressures that act on retaining walls in the absence of seepage within the backfill can be divided into two components: *hydrostatic pressure*, which increases linearly with depth and acts on the wall before, during, and after earthquake shaking, and *hydrodynamic pressure*, which results from the dynamic response of the water itself.

11.6.3.1 Water Outboard of Wall

Hydrodynamic water pressure results from the dynamic response of a body of water. For retaining walls, hydrodynamic pressures are usually estimated from Westergaard's

solution (Westergaard, 1931) for the case of a vertical, rigid dam retaining a semi-infinite reservoir of water that is excited by harmonic, horizontal motion of its rigid base. Westergaard showed that the hydrodynamic pressure amplitude increased with the square root of water depth when the motion is at a frequency lower than the fundamental frequency of the reservoir, $f_o = v_p/4H$, where v_p is the p-wave velocity of water (about 4700 ft/sec (1400 m/sec)) and H is the depth of water in the reservoir (the natural frequency of a 20-ft-deep (6.1 m) reservoir, for example, would be over 58 Hz, well above the frequencies of interest for earthquakes). Westergaard computed the amplitude of the hydrodynamic pressure as

$$P_w = \frac{7}{8} \frac{a_h}{g} \gamma_w \sqrt{z_w H} \quad (11.34)$$

The resultant hydrodynamic thrust is given by

$$P_w = \frac{7}{12} \frac{a_h}{g} \gamma_w H^2 \quad (11.35)$$

The total water pressure on the face of the wall is the sum of the hydrostatic and hydrodynamic water pressures. Similarly, the total lateral thrust due to the water is equal to the sum of the hydrostatic and hydrodynamic thrusts.

Another important consideration in the design of a waterfront retaining wall is the potential for rapid drawdown of the water outboard of the wall. Earthquakes occurring near large bodies of water often induce long-period motion of the water, such as tsunamis or seiches (Section 1.4.7), that cause the water surface to move up and down. While the upward movement of water outboard of a retaining wall will generally tend to stabilize the wall (assuming that it does not rise above the level of the top of the wall), downward movement can create a destabilizing rapid drawdown condition. When liquefiable soils exist under relatively high levels of initial shear stress, failures can be triggered by very small changes in water level. Such failures can originate in the soils adjacent to or beneath the retaining structure rather than in the backfill.

11.6.3.2 Water in Backfill

The presence of water in the backfill behind a retaining wall can influence the seismic loads that act on the wall in three ways: (1) by altering the inertial forces within the backfill, (2) by developing hydrodynamic pressures within the backfill, and (3) by allowing excess porewater pressure generation due to cyclic straining of the backfill soils.

The inertial forces in saturated soils depend on the relative movement between the backfill soil particles and the porewater that surrounds them. If, as is usually the case, the permeability of the soil is small enough (typically $k \leq 10^{-3}$ cm/sec (33×10^{-5} ft/sec) or so) that the porewater moves with the soil during earthquake shaking (no relative movement of soil and water, or *restrained porewater conditions*), the inertial forces will be proportional to the *total* unit weight of the soil. If the permeability of the backfill soil is very high, however, the porewater may remain essentially stationary while the soil skeleton moves back and forth (the soil particles move through the porewater in *free porewater conditions*). In such cases, inertial forces will be proportional to the *buoyant* (or submerged) unit weight of the soil. Hydrodynamic water pressures (Section 11.5.3.1) can also develop under free

pore-water conditions and must be added to the computed soil and hydrostatic pressures to obtain the total loading on the wall.

For restrained porewater conditions, the M-O method can be modified to account for the presence of porewater within the backfill (Matsuzawa et al., 1985). Representing the excess porewater pressure in the backfill by the pore pressure ratio, r_u (Section 9.5.1.1), the active soil thrust acting on a yielding wall can be computed from equation (11.15) using

$$\gamma = \gamma_b(1 - r_u) \quad (11.36)$$

$$\psi = \tan^{-1} \left[\frac{\gamma_{\text{sat}} k_h}{\gamma_b(1 - r_u)(1 - k_v)} \right] \quad (11.37)$$

An equivalent hydrostatic thrust based on a fluid of unit weight $\gamma_{\text{eq}} = \gamma_w + r_u \gamma_b$ must be added to the soil thrust. Note that as r_u approaches 1 (as it could in a liquefiable backfill), the wall thrust approaches that imposed by a fluid of equivalent unit weight, $\gamma_{\text{eq}} = \gamma_{\text{sat}}$. As discussed in Chapter 9, subsequent unidirectional movement of a soil that develops high excess porewater pressures may, depending on its residual (or steady state) strength, cause dilation with accompanying porewater pressure reduction and strength gain.

Soil thrusts from partially submerged backfills may be computed using an average unit weight based on the relative volumes of soil within the active wedge that are above and below the phreatic surface (Figure 11.19):

$$\bar{\gamma} = \lambda^2 \gamma_{\text{sat}} + (1 - \lambda^2) \gamma_d \quad (11.38)$$

Again, the hydrostatic thrust (and hydrodynamic thrust, if present) must be added to the soil thrust.

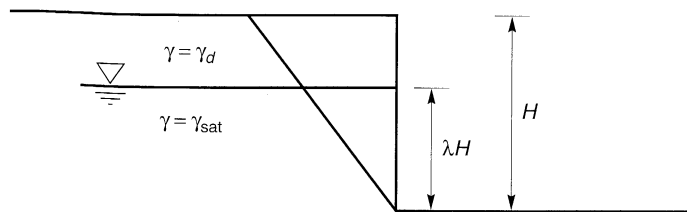


Figure 11.19 Geometry and notation for partially submerged backfill.

Example 11.3

Compute the total thrust that would be expected on the wall shown in Example 11.1 if the wall backfill was completely saturated. Assume that the pore pressure ratio, r_u , reaches a value of 0.5.

Solution The total active thrust can be computed from equation (11.15) using

$$\begin{aligned} \gamma &= \gamma_b(1 - r_u) = \rho_b g(1 - r_u) = \frac{G_s - 1}{G_s} \rho_d g(1 - r_u) \\ &= \frac{2.65 - 1}{2.65} (1.76 \text{ Mg/m}^3) (9.81 \text{ m/sec}^2) (1 - 0.5) = 5.44 \text{ kN/m}^3 \\ \psi &= \tan^{-1} \left[\frac{\gamma_{\text{sat}} k_h}{\gamma_b(1 - r_u)(1 - k_v)} \right] = \tan^{-1} \left[\frac{(10.9 \text{ kN/m}^3 + 9.8 \text{ kN/m}^3)(0.15)}{(10.9 \text{ kN/m}^3)(1 - 0.5)(1 - 0.075)} \right] = 31.6^\circ \end{aligned}$$

Then

$$K_{AE} = \frac{\cos^2(34^\circ - 0^\circ - 31.6^\circ)}{\cos(31.6^\circ)\cos(0^\circ)\cos(17^\circ + 0^\circ + 31.6^\circ) \left[1 + \sqrt{\frac{\sin(17^\circ + 31.6^\circ)\sin(34^\circ - 0^\circ - 31.6^\circ)}{\cos(17^\circ + 0^\circ + 31.6^\circ)\cos(0^\circ - 0^\circ)}} \right]^2}$$

$$= 1.195$$

and

$$P_{AE} = \frac{1}{2}K_{AE}\gamma H^2(1 - k_v) = \frac{1}{2}(1.195)(5.44 \text{ kN/m}^3)(5 \text{ m})^2(1 - 0.075) = 75.2 \text{ kN/m}$$

The hydrostatic thrust is given by

$$P_w = \frac{1}{2}\gamma_{eq}H^2 = \frac{1}{2}(\gamma_w + r_u\gamma_b)H^2 = \frac{1}{2}[9.81 \text{ kN/m}^3 + (0.5)(10.9 \text{ kN/m}^3)](5 \text{ m})^2$$

$$= 190.6 \text{ kN/m}$$

Therefore, the total thrust is

$$P_{tot} = P_{AE} + P_w = 75.2 \text{ kN/m} + 190.6 \text{ kN/m} = 265.8 \text{ kN/m}$$

11.6.4 Finite-Element Analysis

Earthquake-induced pressures on retaining walls can also be evaluated using dynamic response–analyses. A number of computer programs are available for such analyses (Section 7.3). Linear or equivalent linear analyses can be used to estimate wall pressures, although their inability to represent actual modes of failure can make their results difficult to interpret. Nonlinear analyses are capable of predicting permanent deformations (Section 11.6.3) as well as wall pressures.

11.7 SEISMIC DISPLACEMENTS OF RETAINING WALLS

Although the methods of analysis described in the preceding section provide useful information on the seismic loads that act on retaining walls, the postearthquake serviceability of such walls is more closely related to the permanent deformations that occur during earthquakes. While large permanent deformations may be acceptable for some walls, others may be considered to have failed at much smaller deformations. Analyses that predict permanent wall deformations may provide a more useful indication of retaining wall performance. Several methods have been proposed for predicting permanent deformations of yielding walls.

11.7.1 Richards–Elms Method

Richards and Elms (1979) proposed a method for the seismic design of gravity walls based on allowable permanent wall displacements. The method estimates permanent displacements in a manner analogous to the Newmark sliding block procedure (Section 10.6.1.2) developed originally for evaluation of seismic slope stability.

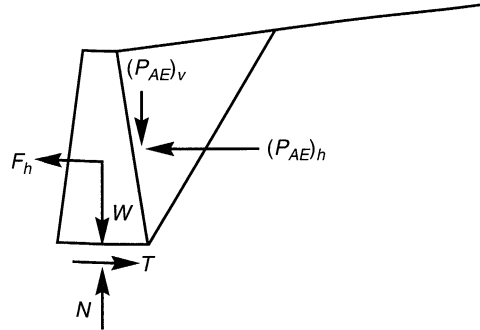


Figure 11.20 Gravity wall acted upon by gravity and pseudostatic accelerations.

Application of the Richards–Elms method requires evaluation of the yield acceleration for the wall–backfill system. Consider the gravity wall shown in Figure 11.20. When the active wedge is subjected to acceleration acting toward the backfill, the resulting inertial forces will act away from the backfill. The level of acceleration that is just large enough to cause the wall to slide on its base is the *yield acceleration*. When the acceleration is equal to the yield acceleration, horizontal and vertical equilibrium require that

$$\begin{aligned} T &= F_h + (P_{AE})_h \\ N &= W + (P_{AE})_v \end{aligned} \quad (11.39)$$

Substituting $T = N \tan \phi_b$, $F_h = a_y W/g$, $(P_{AE})_h = P_{AE} \cos(\delta + \theta)$, and $(P_{AE})_v = P_{AE} \sin(\delta + \theta)$, the yield acceleration can be computed as

$$a_y = \left[\tan \phi_b - \frac{P_{AE} \cos(\delta + \theta) - P_{AE} \sin(\delta + \theta)}{W} \right] g \quad (11.40)$$

Richards and Elms recommended that P_{AE} be calculated using the M–O method (since the M–O method requires that a_y be known, the solution of equation (11.40) must be obtained iteratively). Using the results of sliding block analyses in the same manner as Newmark (1965) and Franklin and Chang (1977), Richards and Elms proposed the following expression for permanent block displacement:

$$d_{\text{perm}} = 0.087 \frac{v_{\text{max}}^2 a_{\text{max}}^3}{a_y^4} \quad \frac{a_y}{a_{\text{max}}} \geq 0.3 \quad (11.41)$$

where v_{max} is the peak ground velocity, a_{max} the peak ground acceleration, and a_y the yield acceleration for the wall–backfill system. Equation (11.41) provides displacement estimates that are close to the estimated maximum displacements [equation (10.13)] of Newmark (1965).

Example 11.4

Estimate the permanent displacement of the concrete gravity wall shown below that would be produced by the Gilroy No. 2 (soil) motion. Assume $k_v = 0$.

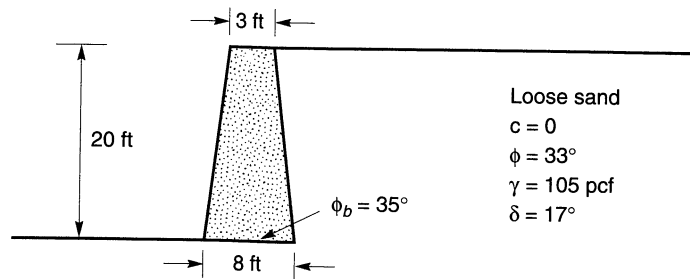


Figure E11.4

Solution The weight of the wall section is

$$W = (20 \text{ ft}) \left(\frac{8 \text{ ft} + 3 \text{ ft}}{2} \right) (150 \text{ lb/ft}^3) = 16500 \text{ lb/ft}$$

The total active thrust can be estimated by the Mononobe–Okabe approach. From equations (11.15) and (11.16). Assuming a trial pseudostatic acceleration of $0.10g$, $\psi = 5.7^\circ$ and

$$K_{AE} = \frac{\cos^2(33^\circ - 7.1^\circ - 5.7^\circ)}{\cos(5.7^\circ) \cos^2(7.1^\circ) \cos(17^\circ + 7.1^\circ + 5.7^\circ) \left[1 + \sqrt{\frac{\sin(17^\circ + 33^\circ) \sin(33^\circ - 0^\circ - 5.7^\circ)}{\cos(17^\circ + 7.1^\circ + 5.7^\circ) \cos(0^\circ - 7.1^\circ)}} \right]^2}$$

$$= 0.385$$

and

$$P_{AE} = \frac{1}{2} (0.385) (105 \text{ pcf}) (20 \text{ ft})^2 = 8085 \text{ lb/ft}$$

Then, from equation (11.40),

$$a_y = \left[\tan(35^\circ) - \frac{(8085 \text{ lb/ft}) \cos(17^\circ + 7.1^\circ) - (8085 \text{ lb/ft}) \sin(17^\circ + 7.1^\circ)}{16500 \text{ lb/ft}} \right] g = 0.45g$$

Because the computed yield acceleration ($0.43g$) is inconsistent with the assumed pseudostatic acceleration ($0.10g$), another iteration is required. For the next iteration, assume that the pseudostatic acceleration is $0.30g$. Then ψ is 16.7° and

$$K_{AE} = \frac{\cos^2(33^\circ - 7.1^\circ - 16.7^\circ)}{\cos(16.7^\circ) \cos^2(7.1^\circ) \cos(17^\circ + 7.1^\circ + 16.7^\circ) \left[1 + \sqrt{\frac{\sin(17^\circ + 33^\circ) \sin(33^\circ - 0^\circ - 16.7^\circ)}{\cos(17^\circ + 7.1^\circ + 16.7^\circ) \cos(0^\circ - 7.1^\circ)}} \right]^2}$$

$$= 0.574$$

and

$$P_{AE} = \frac{1}{2} (0.574) (105 \text{ pcf}) (20 \text{ ft})^2 = 12054 \text{ lb/ft}$$

Then, from equation (11.40),

$$a_y = \left[\tan(35^\circ) - \frac{(12054 \text{ lb/ft})\cos(17 + 7.1) - (12054 \text{ lb/ft})\sin(17 + 7.1)}{16500 \text{ lb/ft}} \right] g = 0.33g$$

Now, the computed yield acceleration is fairly close to the assumed pseudostatic acceleration. Using equation (11.41) with the results of Example 3.1

$$d_{\text{perm}} = 0.087 \frac{(39.2 \text{ cm/sec})^2 [(0.322g)(981 \text{ cm/sec}^2/g)]^3}{[(0.30g)(981 \text{ cm/sec}^2/g)]^4} = 6.5 \text{ cm}$$

11.7.2 Whitman–Liao Method

The Richards–Elms method offers a rational deterministic approach to the estimation of gravity wall displacements. Its simplicity comes, in part, from assumptions that neglect certain aspects of the dynamic earth pressure problem. Whitman and Liao (1985) identified several modeling errors that result from the simplifying assumptions of the Richards–Elms procedure. The most important of these are neglect of the dynamic response of the backfill, neglect of kinematic factors, neglect of tilting mechanisms, and neglect of vertical accelerations. Finite-element analyses of the effects of the dynamic response of the backfill on wall displacements (Nadim, 1982), for example, show that amplification occurs when input motions coincide with the natural period of the backfill and produce considerably greater permanent displacement than the rigid-block model used by Richards and Elms. Analyses in which the backfill wedge and wall were treated as separate blocks (Zarrabi-Kashani, 1979) show that the kinematic requirements of horizontal *and* vertical displacement of the backfill wedge cause systematically smaller displacements than the single-block model of Richards and Elms. Studies of combined tilting and sliding (Nadim, 1980; Siddharthan et al., 1992), indicate that tilting mechanisms generally increase wall displacements over those produced by sliding-only models such as that of Richards and Elms. Consideration of vertical accelerations produces slightly larger displacements than when they are neglected, at least for motions with high peak horizontal acceleration (a_{max} greater than about $0.5g$) and $a_y/a_{\text{max}} \geq 0.4$ (Whitman and Liao, 1985). Whitman and Liao quantified and combined the effects of each of these sources of modeling error to describe the total modeling error by a lognormally distributed random variable with mean value, \bar{M} , and standard deviation, $\sigma_{\ln M}$.

Using the results of sliding block analyses of 14 ground motions by Wong (1982), Whitman and Liao found that the permanent displacements were lognormally distributed with mean value

$$\bar{d}_{\text{perm}} = \frac{37v_{\text{max}}^2}{a_{\text{max}}} \exp\left(\frac{-9.4 a_y}{a_{\text{max}}}\right) \quad (11.42)$$

Uncertainty due to statistical variability of ground motions was characterized by a lognormally distributed random variable, Q , with a mean value of \bar{Q} and standard deviation, $\sigma_{\ln Q}$.

The effects of uncertainty in soil properties, specifically the friction angles, on permanent displacement were also investigated. Using standard deviations of $\sigma_\phi = 2$ to 3° for soil friction angles and $\sigma_\delta = 5^\circ$ for wall–soil interface friction angles, the computed yield acceleration [the only term on the right side of equation (11.40) that is a function of ϕ and

$\delta]$ was defined as a random variable with mean value \bar{a}_y and standard deviation σ_{a_y} . The mean value \bar{a}_y is the yield acceleration computed using the mean values of ϕ and δ .

Combining all of these sources of uncertainty, the permanent displacement can be characterized as a lognormally distributed random variable with mean value

$$\bar{d} = \frac{37v_{\max}^2}{a_{\max}} \exp\left(\frac{-9.4\bar{a}_y}{a_{\max}}\right) \bar{Q}\bar{M} \tag{11.43}$$

and variance

$$\sigma_{\ln d}^2 = \left(\frac{9.4g}{a_{\max}}\right)^2 \sigma_{a_y}^2 + \sigma_{\ln M}^2 + \sigma_{\ln Q}^2 \tag{11.44}$$

Suggested values of the means and standard deviations of the ground motion, soil resistance, and model error factors are shown in Table 11-4.

Table 11-4 Mean and Standard Deviation Values for Gravity Wall Displacement Analysis

Factor	Mean	Standard Deviation
Model error	$\bar{M} = 3.5$	$\sigma_{\ln M} = 0.84$
Soil resistance	$\bar{a}_y = a_y(\bar{\phi}, \bar{\delta})$	$\sigma_{a_y} = 0.04$ to 0.065
Ground motion	$\bar{Q} = 1$	$\sigma_{\ln Q} = 0.58$ to 1.05

Source: After Whitman and Liao (1985).

Using equations (11.43) and (11.44), along with the CDF for the standard normal variable (Table C-1), the probability of exceeding any particular value of d_{all} can easily be computed.

Example 11.5

Estimate the expected permanent displacement of the gravity wall shown in Example 11.4 using the Whitman–Liao approach.

Solution From equation (11.42), the mean or expected value of permanent displacement is given by

$$d_{\text{perm}} = 37 \frac{(39.2 \text{ cm/sec})^2}{[(0.322g)(981 \text{ cm/sec}^2/g)]} \exp [(-9.4)(0.30g)/0.322g] = 0.03 \text{ cm}$$

Note that the mean permanent displacement is considerably smaller than the displacement predicted by the Richards–Elms method in Example 11.4.

11.7.3 Finite-Element Analysis

Earthquake-induced deformations of retaining walls can be predicted by dynamic stress–deformation analyses. Obviously, prediction of permanent deformations requires the use of a nonlinear analysis (Section 7.2.3). A rigorous analysis should be capable of accounting for nonlinear, inelastic behavior of the soil and of the interfaces between the soil and wall elements. Among the relatively few examples of rigorous two-dimensional finite-element analyses that predict permanent deformations are those reported by Alampalli and Elgamel (1990), Finn et al. (1992), and Iai and Kameoka (1993).

11.8 SEISMIC DESIGN CONSIDERATIONS

The design of retaining walls for seismic conditions is similar, in many respects, to designing for static conditions. In both cases, potential modes of failure are identified and the wall designed to avoid initiating them. Although the response of retaining walls under seismic loading conditions is much more complex than under static conditions, conventional design procedures make use of simplifying assumptions that render the problem tractable. Several design approaches for different types of retaining walls are described in the following sections.

11.8.1 Gravity Walls

Gravity walls are the simplest type of retaining wall, and more attention has been paid to their design than to the design of other types of walls. Gravity wall design procedures, however, are commonly adapted as part of the design of cantilever walls and composite wall systems. Gravity walls are customarily designed by one of two approaches: a seismic pressure-based approach or a permanent displacement-based approach. Although the gravity wall design procedures are oriented toward prevention of sliding failure, the possibility of overturning due to bearing failure of the soil beneath the base of a wall must also be considered in design.

11.8.1.1 Design Based on Seismic Pressures

Gravity walls have traditionally been designed on the basis of seismic earth pressures. The M-O method is most commonly used along with an inertial force, using the same pseudostatic acceleration applied to the active wedge, applied to the wall itself. Pseudostatic accelerations are generally considerably smaller than anticipated peak accelerations. Values between 0.05g and 0.15g, corresponding to one-third to one-half of the peak ground surface acceleration, are commonly used with factors of safety of 1.0 to 1.2 (Whitman, 1990).

Despite the considerable simplification of their complex actual behavior, gravity walls designed by the traditional approach have generally performed quite well in earthquakes. The reason, however, may have more to do with the conservatism commonly used in static wall design than with the accuracy of the M-O method. Design pressures that account for backfill amplification, such as those that can be obtained by the Steedman-Zeng method, should be considered for design of unusually tall or unusually displacement-sensitive walls.

11.8.1.2 Design Based on Allowable Displacements

Gravity walls are being designed on the basis of allowable displacements more and more frequently. This approach allows the designer to consider the consequences of permanent displacement for an individual wall when selecting an allowable displacement for design. Design procedures based on the Richards-Elms and Whitman-Liao procedures for estimation of permanent displacement are available.

The Richards-Elms design procedure involves calculation of the wall weight that would be required to ensure that permanent displacements are less than or equal to some allowable value. The procedure can be summarized as follows:

1. Select an allowable permanent displacement, d_{all} .
2. Calculate the yield acceleration required to produce the allowable permanent displacement from equation (11.41), rearranged in the form

$$a_y = \left(\frac{0.087 v_{\text{max}}^2 a_{\text{max}}^3}{d_{\text{all}}} \right)^{1/4} \quad (11.45)$$

3. Calculate P_{AE} using the M-O method with the yield acceleration from step 2 as the pseudostatic acceleration. This represents the soil thrust that would be expected to cause a maximum permanent displacement equal to d_{all} .
4. Calculate the wall weight required to limit the permanent displacement to the allowable permanent displacement using equation (11.40) rearranged in the form

$$W = \frac{P_{AE} \cos(\delta + \theta) - P_{AE} \sin(\delta + \theta) \tan \phi_b}{\tan \phi_b - a_y/g} \quad (11.46)$$

5. Apply a factor of safety to the weight of the wall. Richards and Elms originally suggested a factor of safety of 1.5, but subsequent research has shown that a wall weight factor of safety of 1.1 to 1.2 should be sufficient to reduce the probability of exceeding the allowable permanent displacement to 5% or less (Whitman and Liao, 1985).

Using the Whitman–Liao approach, gravity walls can be designed on the basis of allowable displacements that have defined probabilities of exceedance. The selection of an acceptable probability of exceedance is a complicated matter that may depend on the importance of the wall, the effects of failure, the cost of repair, and other technical and/or non-technical factors. The actual wall design is accomplished by using equation (11.43) to compute the yield acceleration as

$$a_y = \frac{a_{\text{max}}}{9.4} \ln \frac{37 \bar{M} v_{\text{max}}^2}{a_{\text{max}} d_{\text{all}}} \quad (11.47)$$

and then using the M-O method to size the wall to meet or exceed the computed yield acceleration. Whitman and Liao suggest a conservative design (corresponding to a probability of exceedance of about 5%) can be obtained by assuming $d_{\text{all}} = 4 \bar{d}_{\text{perm}}$, where \bar{d}_{perm} is calculated from equation (11.42). A less conservative design (corresponding to about 10% probability of exceedance) is obtained by taking $d_{\text{all}} = 2.5 \bar{d}_{\text{perm}}$.

11.8.2 Cantilever Walls

Cantilever walls are designed in much the same way as gravity walls, except that bending failure must also be considered. Maximum bending moments are usually calculated using the M-O method to compute the maximum soil thrust, which is taken to act at the height given by equation (11.19). The maximum overturning moment is used for structural design of wall elements (to prevent flexural failure of the wall itself) and to determine the size of the wall footing required to prevent bearing failure of the supporting soils.

11.8.3 Braced Walls

Because their lateral displacements are constrained by bracing elements, braced walls do not develop minimum active (or maximum passive) earth pressures in the vicinity of the

bracing elements. The earth pressures that do develop depend on the stiffness of the brace and the relative stiffness of the wall and soil. Analysis of actual soil–wall–brace interaction is quite complicated, and simplified methods are generally adopted for design purposes.

11.8.3.1 Non-Yielding Braced Walls

Walls that are braced sufficiently that they do not move at all, such as braced walls founded on rock, are usually designed to resist the earth pressures predicted by Wood's (1973) analysis. To avoid cracking or yielding of such walls, design pressures are usually based on the peak acceleration (Whitman, 1991). This approach, however, can lead to very high design pressures and some data [e.g., Chang et al. (1990)], indicates that the pressures on braced walls that can move slightly are lower. Dynamic finite-element analyses of stiff, embedded basement walls suggest that the M-O method with the peak ground surface acceleration outside the structure produces reasonable design earth pressures (Whitman, 1990).

Specifications for design of bridge abutments (e.g., AASHTO, 1991) recommend that nonyielding abutments be designed to resist lateral thrust obtained from the M-O method with a pseudostatic horizontal acceleration 50% greater than the effective peak acceleration.

11.8.3.2 Flexible Braced Walls

The seismic response of flexible braced walls such as anchored bulkheads and tieback walls is particularly complicated. Again, these complexities require that simplified methods be used for design. Because these types of walls are very commonly used in waterfront areas, and because the great majority of earthquake-induced retaining wall failures occur in waterfront areas, special attention to their design is required. In the case of anchored bulkheads, the simplified design procedures can be supplemented by a useful empirical model of damage potential based on observations of actual wall performance.

Anchored Bulkheads. The design of anchored bulkheads in waterfront areas is strongly influenced by liquefaction hazards. If widespread liquefaction occurs, experience indicates that bulkhead failures are very likely. Consequently, steps should be taken prior to construction to ensure that such liquefaction will not occur. Permanent seaward movements of anchored bulkheads in the absence of widespread liquefaction, however, has also been observed. Conventional design procedures seek to minimize this type of damage using pseudostatically determined design pressures.

A recent design procedure uses the free earth support method and Rowe's moment reduction method, with earthquake effects represented by pseudostatic inertial forces. A brief summary of the procedure is presented below; a detailed description with a worked example may be found in Ebeling and Morrison (1993).

1. Design the anchored bulkhead for static loading conditions.
2. Select pseudostatic accelerations a_h and a_v .
3. Compute the active soil thrust on the back of the wall using the M-O method. The active wedge is assumed to originate at the bottom of the wall.
4. Compute the passive soil thrust acting on the front of the wall using the M-O method. The passive wedge is also assumed to originate at the bottom of the wall.
5. Compute the minimum required depth of wall penetration by summing moments about the wall–tierod connection. All water pressures (hydrostatic, hydrodynamic, and excess porewater, if present) must be included.

6. Compute the required anchor resistance by summing the horizontal forces acting on the wall. All water pressures (hydrostatic, hydrodynamic, and excess porewater, if present) must be included. The computed anchor resistance is termed the *free earth support anchor resistance*.
7. Compute the distribution of bending moments over the height of the wall. All water pressures (hydrostatic, hydrodynamic, and excess porewater, if present) must be included. The maximum bending moment is termed the *free earth support moment*.
8. Compute the design bending moment as the product of the free earth support moment and Rowe's moment reduction factor (Rowe, 1952).
9. Set the design tierrod force at a level 30% greater than the free earth support anchor resistance.
10. Determine the required size of the anchor block to satisfy horizontal force equilibrium considering the active and passive pressures, as well as all water pressures, on both sides of the block. The effects of any water pressures on the bottom and top surfaces of the anchor block should also be considered.
11. Locate the anchor block at a sufficient distance behind the wall that the active wedge behind the wall does not intersect the passive wedge in front of the anchor block. Since the active and passive failure surfaces are flatter for seismic loading than for static loading, seismic design may require a considerably longer tierrod than static design.
12. Check the effects of redistribution of any earthquake-induced excess porewater pressure after earthquake shaking has ended.

Case histories of anchored bulkhead performance (neglecting cases in which widespread liquefaction was observed) suggest that anchored bulkhead damage levels can be predicted approximately with the aid of two dimensionless indices: the *effective anchor index* and the *embedment participation index* (Gazetas et al., 1990). Referring to Figure 11.21a, the effective anchor index describes the relative magnitude of the available anchor capacity as

$$EAI = \frac{d}{H} \quad (11.48)$$

where d is the horizontal distance between the active wedge and the tierrod–anchor connection and H is the height of the wall. The critical active failure plane is taken to originate at the effective *point of rotation* of the wall, which can be located using soil–structure interaction analyses or estimated as

$$f \approx \left(\frac{1 + k'_e}{2} - \frac{\phi - 20^\circ}{50^\circ} \right) H \leq D \quad (11.49)$$

where

$$k'_e = \begin{cases} \frac{k_h}{1 - k_v} & \text{above the water table} \\ \frac{(a_h/g)_{\max}}{1 - 2(a_v/g)_{\max}/3} & \text{below the water table} \end{cases}$$

The inclination of the critical active failure plane can be approximated (Dennehy, 1985) as

$$\alpha_{AE} \approx 45^\circ + \frac{\phi}{2} - 135^\circ (k'_e)^{1.75} \quad (11.50)$$

for $0.10 \leq k'_e \leq 0.50$ and $25^\circ \leq \phi \leq 35^\circ$. Beyond these ranges, equation (11.17) can be used to estimate the inclination of the active wedge. The embedment participation index is defined as

$$EPI = \frac{F_{PE}}{F_{AE}} \left(1 + \frac{f}{f+H} \right) \quad (11.51)$$

where F_{AE} and F_{PE} are the potential active and passive thrusts, respectively. For uniform backfill and foundation soils,

$$EPI \approx \frac{K_{PE}}{K_{AE}} r^2 (1+r) \quad (11.52)$$

where $r = f/(f+H)$. Values of EAI and EPI have been computed for 75 anchored bulkheads for which degrees of damage in earthquake had been categorized as indicated in Table 11-5 (Gazetas et al., 1990). Comparison of degrees of damage with EAI and EPI showed significant trends in the characteristics of anchored bulkheads that performed well and those that performed poorly. As illustrated in Figure 11.21b, anchored bulkheads with high EAI and EPI values (zone I) generally suffered little or no damage. Anchored bulkheads with low EAI and EPI values (zone III) usually suffered severe damage. Moderate damage was generally associated with intermediate combinations of EAI and EPI (zone II). The chart of Figure 11.21b is a very useful tool for checking the design of anchored bulkheads in waterfront areas.

Table 11-5 Qualitative and Quantitative Descriptions of Reported Degrees of Damage to Anchored Bulkheads during Earthquakes

Degree of Damage	Description of Damage	Permanent Horizontal Displacement at Top of Sheetpile (cm)
0	No damage	< 2
1	Negligible damage to the wall itself; noticeable damage to related structures	2–10
2	Noticeable damage to the wall	10–30
3	General shape of anchored sheetpile preserved, but significantly damaged	30–60
4	Complete destruction	> 60

Source: After Kitajima and Uwabe (1979).

Tieback Walls. Because their use was originally restricted to temporary support of excavations, the seismic performance of tieback walls has received relatively little attention. As permanent tieback walls have become more common, however, recognition of the need to consider seismic loading in their design has increased. With respect to seismic performance, tieback walls are similar to anchored bulkheads—the primary differences are that tieback walls have multiple anchors and that the anchors are generally inclined. Although

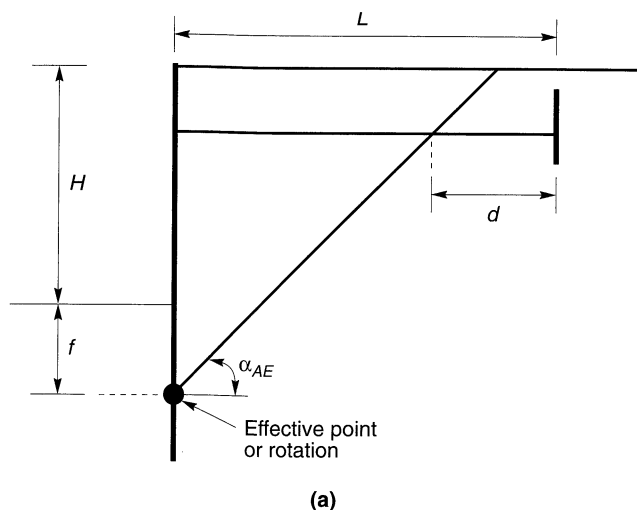
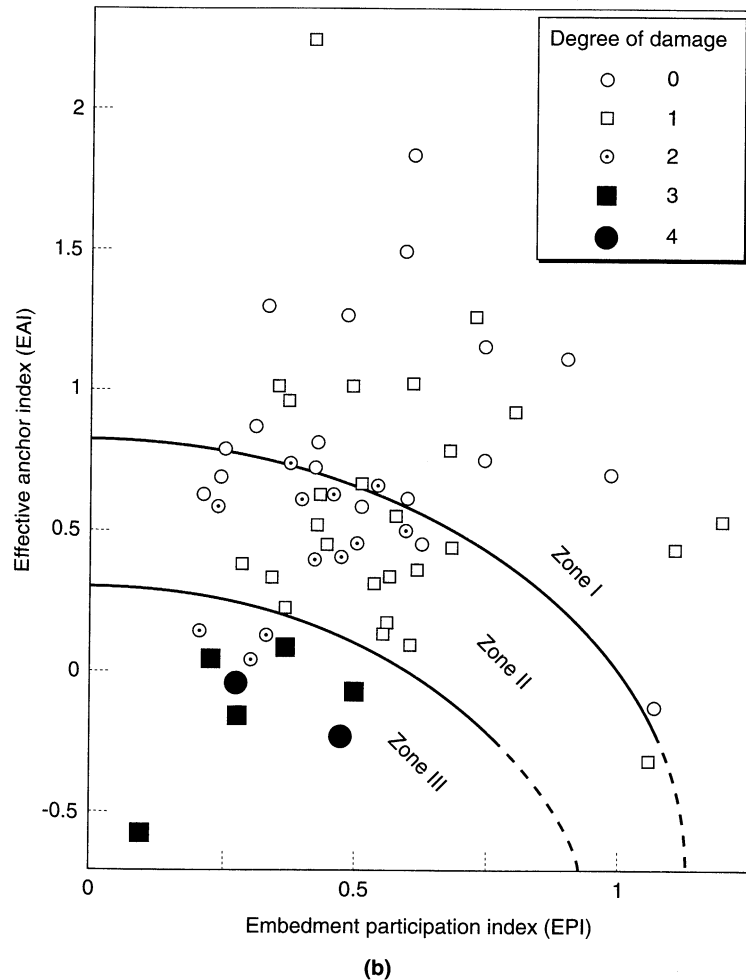


Figure 11.21 (a) Geometry and notation for evaluation of anchored bulkhead design; (b) correlation between damage levels and dimensionless anchored bulkhead indices. After Gazetas et al. (1990). Empirical design method for waterfront anchored sheetpile walls, *Design and Performance of Earth Retaining Structures*. Reprinted by permission of ASCE.

formalized design procedures are not currently available, the results of a limited number of experimental and numerical investigations provide insight into special considerations for seismic design of tieback walls. Few observations of the seismic performance of tieback walls have been made, but those that are available generally indicate good performance (Ho et al., 1990).

Numerical analyses indicate that the stiffness and spacing of the anchors strongly influences the permanent displacements of a tieback wall (Siller and Frawley, 1992). In general, tieback walls with stiff anchors will develop smaller permanent displacements than walls with softer anchors. Tieback walls with smaller vertical spacing between anchors will experience smaller and more uniform permanent displacements than walls with greater anchor spacing. Earthquake-induced permanent displacements also appear sensitive to static design pressures—walls designed for higher static pressures suffer smaller permanent displacements during earthquakes than walls designed for lower static pressures. Tieback walls also tend to develop smaller permanent when higher rather than lower initial anchor preloads are used (Siller and Dolly, 1992).

Tieback walls can also be influenced by phase differences between the response of the soil behind the wall and the foundation soil (Fragaszy et al., 1987). Wall elements that extend into the foundation soils may be subjected to very high bending moments at the base of the wall. Further, inclined anchors that extend below the bottom of the excavation may experience very high tensile forces when the soil end moves one way and the wall end the other.



(b)
Figure 11.21 (continued)

11.8.4 Reinforced Soil Walls

Reinforced soil walls have become very popular in recent years. Although many different materials are used, reinforced soil walls consist of a zone of reinforced soil that retains unreinforced soil behind it. During an earthquake, a reinforced soil wall is subjected to a dynamic soil thrust at the back of the reinforced zone and to inertial forces within the reinforced zone in addition to static forces. The wall must be designed to avoid *external instability* (sliding or overturning failure of the reinforced zone) and *internal instability* (tensile or pullout failure of the reinforcement). Current design procedures, such as those described below (Christopher et al., 1990), use a pseudostatic approach, but displacement-based design procedures are likely to be developed in the future.

Reinforced soil walls use different materials and provide support by different mechanisms than do conventional retaining walls. Their design requires careful consideration of loading, time, and environmental factors that may not be significant for conventional retaining walls. The following sections are restricted to seismic aspects of reinforced soil wall design. Other aspects of design are discussed in detail by Mitchell and Villet (1987), Christopher et al. (1990), and Koerner (1994).

11.8.4.1 External Stability

For evaluation of external stability, a reinforced wall is treated much like a gravity wall. As illustrated in Figure 11.22, the reinforced zone is assumed to be acted on by its own weight, W , and the static soil thrust, P_A . Earthquake loading is represented pseudostatically by the dynamic soil thrust, ΔP_{AE} , and the inertial force on the reinforced zone, P_{IR} . The external stability of a particular wall design can be evaluated by the following procedure:

1. Determine the peak horizontal ground surface acceleration, a_{max} .
2. Calculate the peak acceleration at the centroid of the reinforced zone from the equation

$$a_c = \left(1.45 - \frac{a_{max}}{g} \right) a_{max} \tag{11.53}$$

3. Calculate the dynamic soil thrust from

$$\Delta P_{AE} = 0.375 \frac{a_c \gamma^{(b)} H^2}{g} \tag{11.54}$$

where $\gamma^{(b)}$ is the unit weight of the backfill soil.

4. Calculate the inertial force acting on the reinforced zone from

$$P_{IR} = \frac{a_c \gamma^{(r)} HL}{g} \tag{11.55}$$

where $\gamma^{(r)}$ is the unit weight of the reinforced zone.

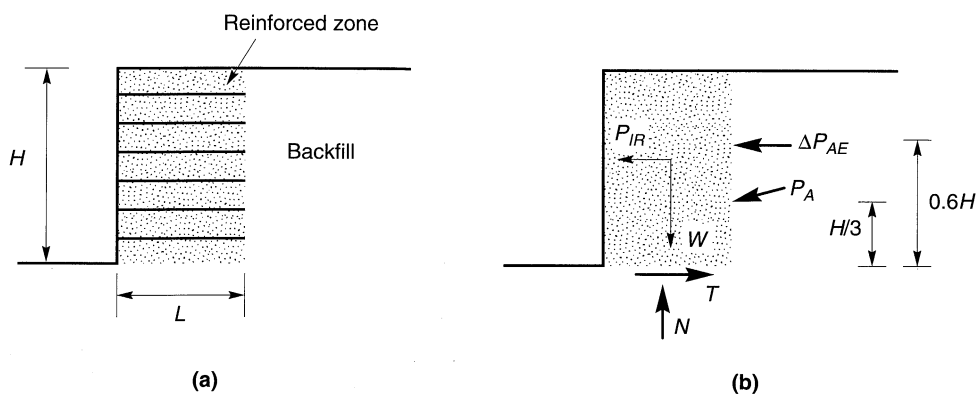


Figure 11.22 (a) Geometry and notation for reinforced soil walls; (b) static and pseudostatic forces acting on reinforced zone.

5. Add P_{AE} and 50% of P_{IR} to the static forces acting on the reinforced zone and check sliding and overturning stability (the reduced value of P_{IR} is allowed to account for the fact that the maximum values of ΔP_{AE} and P_{IR} are unlikely to occur at the same time). For seismic design, factors of safety against sliding and overturning should be greater than or equal to 75% of the minimum acceptable factors of safety for static loading.

11.8.4.2 Internal Stability

Internal stability evaluation depends on the nature of the reinforcement since the critical internal failure surface is different for inextensible and extensible reinforcement (Figure 11.23). Internal stability for seismic conditions can be evaluated in the following steps:

1. Determine the pseudostatic inertial force acting on the potentially unstable internal failure zone,

$$P_{IA} = \frac{a_c W_A}{g} \quad (11.56)$$

where W_A is the weight of the failure mass (the trapezoidal or triangular zones in Figure 11.23a and b for inextensible or extensible reinforcement, respectively).

2. Distribute P_{IA} to each reinforcement layer in proportion to its resistant area (the area of reinforcement that extends beyond the potential internal failure surface). This process produces a dynamic component of tensile force for each layer of reinforcement.
3. Add the dynamic components of tensile force to the static components of tensile force to obtain the total tensile force for each layer of reinforcement.
4. Check to see that the allowable tensile strength of the reinforcement is at least 75% of the total tensile force in each layer of reinforcement.
5. Check to see that each layer of reinforcement extends far enough beyond the potential internal failure surface to avoid pullout failure with a factor of safety not less than 75% of the minimum static factor of safety when the total tensile force is applied.

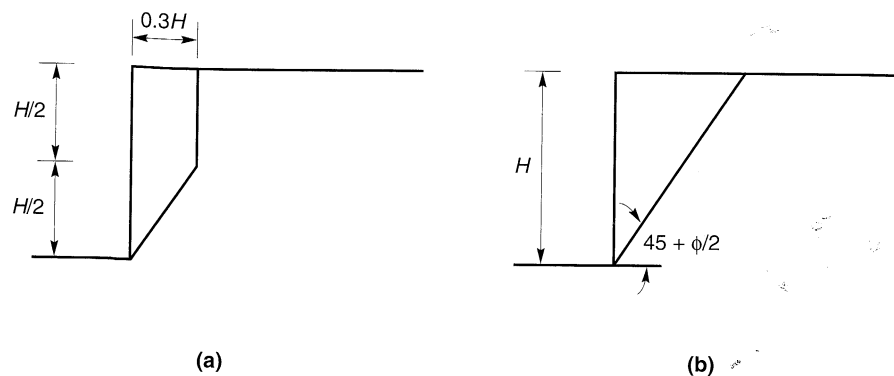


Figure 11.23 Critical potential failure surfaces for evaluation of internal seismic stability of reinforced soil walls: (a) inextensible reinforcement; (b) extensible reinforcement.

11.9 SUMMARY

1. A variety of different systems are used to retain soil; many innovative systems have been developed and used in the last 20 years. For seismic design purposes, most retaining systems fall into three general categories: gravity walls, cantilever walls, and braced walls. Each of these types of walls resists the lateral pressures of the retained soil differently.
2. Retaining walls can fail in many different ways. Gravity walls fail by sliding, overturning, or gross instability. Cantilever walls can fail in the same ways as gravity walls, but can also fail in bending. Braced walls can fail in the same ways as cantilever walls, but also by bracing element failure or rotation about the brace connection.
3. The seismic performance of a retaining wall depends on the total pressures (i.e., static plus dynamic pressures) that act on it during an earthquake. Consequently, the level of dynamic pressures required to damage the wall depends on the level of static pressures that exist before the earthquake. Analysis of the seismic behavior of a retaining wall, therefore, requires an initial analysis of the behavior under static conditions.
4. The seismic response of retaining walls is a complex example of soil–structure interaction. Because of this complexity, design procedures are usually based on a number of simplifying assumptions. Although the simplified procedures do not represent all aspects of wall–soil behavior accurately, they have been shown to provide a reasonable basis for design.
5. The soil pressure on a retaining wall depends on whether the wall is able to move relative to the soil. The dynamic pressures acting on a yielding wall are usually estimated by the pseudostatic Mononobe–Okabe analysis. The dynamic pressures on nonyielding walls are usually estimated by an elastic analysis.
6. The presence of water on either side of a retaining wall strongly influences the seismic behavior of the wall. Water on the outboard side of the wall can exert dynamic, in addition to hydrostatic, pressures on the face of the wall. Water within the backfill can influence the inertial forces acting on the wall and can develop hydrodynamic or excess porewater pressures.
7. Earthquake-induced displacements of retaining walls can be estimated by procedures analogous to the Newmark sliding block analysis for displacements of slopes. Refinements to this approach allow consideration of factors such as backfill amplification, wall tilting, kinematic constraints, and vertical acceleration. Procedures for estimation of probabilities of various displacement levels are also available.
8. Seismic design of retaining walls is generally based on seismic pressures or allowable displacements. In the former approach, pseudostatic or pseudodynamic analyses are used to estimate seismically induced wall pressures, and the wall is designed to resist those pressures without failing or causing failure of the surrounding soil. The latter approach involves designing the wall such that its seismically induced permanent displacement does not exceed a predetermined allowable displacement.
9. The majority of observed failures of retaining walls during earthquakes have occurred in waterfront areas; many have involved liquefaction of the backfill. Excessive permanent displacements of anchored bulkheads in waterfront areas have often been associated with inadequate wall embedment depths and/or insufficient anchor capacity.

HOMWORK PROBLEMS

- 11.1 Compute the static thrust and overturning moment at the base of the concrete retaining wall shown below.

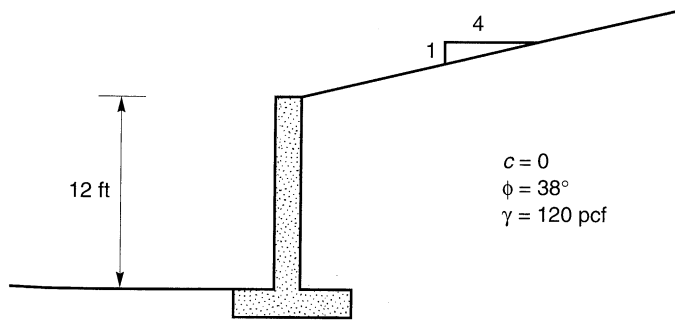


Figure P11.1

- 11.2 The wall shown in Problem 11.1 is subjected to earthquake shaking with a peak horizontal acceleration of $0.28g$. Assuming a pseudostatic coefficient, $k_h = 0.3 a_{\max}/g$, estimate (a) the total active thrust acting on the wall, (b) the height of the resultant of the total active thrust, and (c) the total overturning moment about the base of the wall.
- 11.3 Using the Steedman-Zeng approach, plot the distributions of maximum and minimum lateral pressure if the wall shown below is subjected to a $0.15g$ harmonic base motion at (a) a frequency of 0.5 Hz , and (b) a frequency of 5.0 Hz .

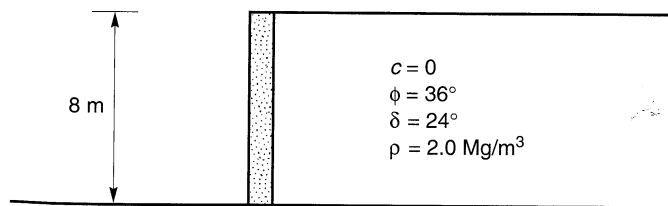


Figure P11.3

- 11.4 A 12 ft deep rigid basement wall is backfilled with dense gravelly sand: $c = 0$, $\phi = 45^\circ$, $\gamma = 140 \text{ pcf}$. Estimate the maximum dynamic thrust acting on the wall when subjected to a ground motion with $a_{\max} = 0.33g$.
- 11.5 Compute the yield acceleration for the concrete gravity wall shown below.

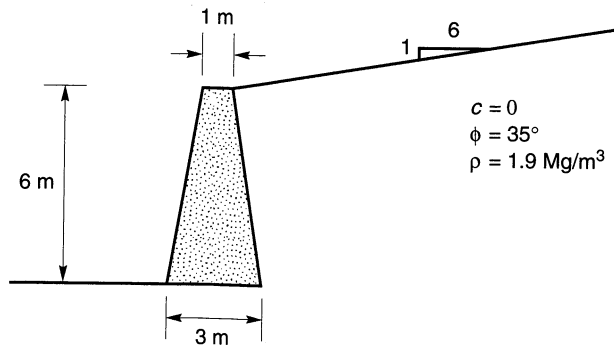


Figure P11.5

- 11.6 Using the Richards–Elms procedure, estimate the permanent displacement of the wall of Problem 11.5 when subjected to (a) the Gilroy No. 1 (rock) ground motion, and (b) the Gilroy No. 2 (soil) ground motion.
- 11.7 Using the Whitman–Liao procedure, estimate the permanent displacement of the wall of Problem 11.5 when subjected to (a) the Gilroy No. 1 (rock) ground motion, and (b) the Gilroy No. 2 (soil) ground motion.
- 11.8 Estimate the permanent displacement of the wall in Problem 11.5 that would have a 10% probability of exceedance if subjected to the Gilroy No. 2 (soil) motion.
- 11.9 A 15 ft tall gravity wall is to retain a level sand backfill ($c = 0$, $\phi = 35^\circ$, $\gamma = 115$ pcf). The wall will be placed on a layer of dense sandy gravel ($c = 0$, $\phi = 44^\circ$, $\gamma = 140$ pcf). Determine the wall weight that would be required to limit the permanent displacement of the wall to 1/4-inch if subjected to the Gilroy No. 2 (soil) ground motion.
- 11.10 The anchored bulkhead shown below is located in a seismically active area. Neglecting the effect of vertical motions, estimate the minimum peak acceleration levels that would be likely to produce (a) moderate damage, and (b) severe damage.

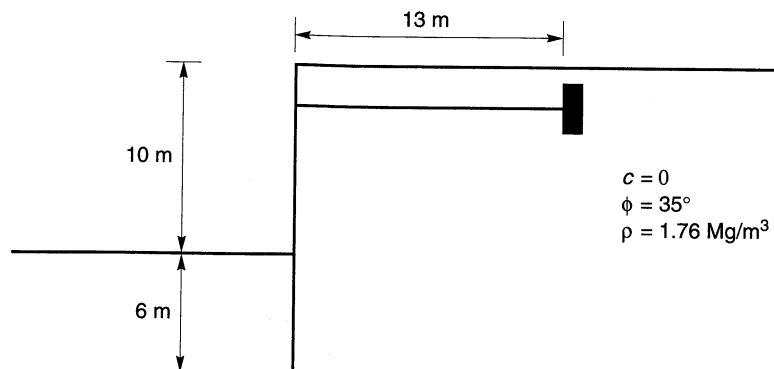


Figure P11.10

12

Soil Improvement for Mitigation of Seismic Hazards

12.1 INTRODUCTION

Soils have been modified to improve their engineering properties for hundreds of years. In the past 75 years, however, improved knowledge of soil behavior and geotechnical hazards has led to the development and verification of many innovative soil improvement techniques. Increased recognition of seismic hazards and improved understanding of the factors that control them have led these techniques to be applied to the mitigation of seismic hazards in the past 30 years.

In both seismically active and inactive areas, soil improvement techniques are commonly used at sites where the existing soil conditions are expected to lead to unsatisfactory performance. Unsatisfactory performance can take many forms, but usually involves unacceptably large soil movements. The movements may include horizontal or vertical (or both) components and may take place during and/or after earthquake shaking. In the absence of earthquake shaking, unacceptable movements usually result from insufficient soil strength and/or stiffness. Consequently, most soil improvement techniques were developed to increase the strength and stiffness of soil deposits. These techniques are described in detail in a number of useful references (e.g., Welsh, 1987; Van Impe, 1989; Hausmann, 1990;

Broms, 1991; Bell, 1993; Mosely, 1993); those which are not commonly used for mitigation of *seismic* hazards are not discussed in this chapter.

During earthquakes, other factors can contribute to unacceptable performance. In particular, the buildup of excess porewater pressure can lead to very large deformations. Consequently, commonly used techniques for mitigation of seismic hazards often involve reducing the tendency of the soil to generate positive excess porewater pressure during earthquake shaking as well as increasing the strength and stiffness of the soil.

The topic of soil improvement is somewhat different from topics presented in earlier chapters. Advances in soil improvement technology have generally resulted from the initiative and imagination of contractors. Research and explanatory “theories” have followed, rather than led, implementation; for some widely used techniques, proven theories have yet to be developed. In such cases, indirect or empirical evidence must be relied upon and the study of case histories is particularly important. This chapter does not attempt to describe all available soil improvement techniques in detail; instead, it presents an introduction to the soil improvement techniques that are most commonly used for mitigation of seismic hazards. References to more complete descriptions of the techniques are presented. Because soil improvement technology changes rapidly as new techniques are developed and existing techniques are tested by actual earthquakes, the relevant geotechnical engineering literature should be reviewed on a regular basis. Methods for verification of the effectiveness of soil improvement techniques are also described.

At present, a wide variety of soil improvement techniques are available for mitigation of seismic hazards. The costs of these methods vary widely, and the conditions under which they can be used are influenced by the nature and proximity of structures and constructed facilities. On the basis of the mechanisms by which they improve the engineering properties of the soil, the most common of these can be divided into four major categories: densification techniques, reinforcement techniques, grouting/mixing techniques, and drainage techniques. However, not all soil improvement techniques fall neatly into a single category.

12.2 DENSIFICATION TECHNIQUES

The particles that comprise a particular soil can be arranged in many different ways. However, the strength and stiffness of the soil is higher when the particles are packed in a dense configuration than when they are packed loosely. Also, the tendency to generate positive excess porewater pressure due to cyclic loading is lower when the soil is dense than when it is loose. As a result, *densification* is one of the most effective and commonly used means of improving soil characteristics for mitigation of seismic hazards. At the same time, it should be recognized that the increased stiffness of a densified soil deposit will cause it to respond differently to earthquake motion; displacement amplitudes are likely to decrease, but accelerations may be somewhat greater than they would have been had the soil not been improved.

Densification produces permanent volume changes that often result in settlement of the ground surface. Different densification techniques produce different amounts of

settlement; with some techniques additional soil is placed at or beneath the ground surface during the process of densification in order to minimize the settlement. Despite such efforts, some densification techniques are limited to sites without existing structures or facilities that could be damaged by ground settlement.

The most common approaches to densification include vibro techniques, dynamic compaction, blasting, and compaction grouting. Of these techniques, the first three make use of the tendency of granular soils to densify when subjected to vibrations. As such, their effectiveness is greatest for cohesionless soils such as clean sands and gravels. Just as fines tend to inhibit liquefaction during earthquakes, they tend to inhibit densification by vibration.

12.2.1 Vibro Techniques

Vibro techniques use probes that are vibrated through a soil deposit in a grid pattern to densify the soil over the entire thickness of the deposit. Vibro techniques can be divided into those based on horizontal vibration (*vibroflotation*) and those based on vertical vibration (*vibro rod systems*). Vibro techniques are among the most commonly used techniques for mitigation of seismic hazards.

12.2.1.1 Vibroflotation

In vibroflotation, a torpedolike probe (the *vibroflot*) suspended by a crane is used to densify a soil deposit. Vibroflots, usually 12 to 18 in. (30 to 46 cm) in diameter and about 10 to 16 ft (3.0 to 4.9 m) long, contain weights mounted eccentrically on a central shaft driven by electric or hydraulic power (Figure 12.1).

The vibroflot is initially lowered to the bottom of the deposit by a combination of vibration and water or air jetting through ports in its pointed nose cone. The vibroflot is then incrementally withdrawn in 2 to 3 ft (60 to 90 cm) intervals at an overall rate of about 1 ft/min (30 cm/min) while still vibrating. Water may be jetted through ports in the upper part of the vibroflot to loosen the soil above the vibroflot temporarily and aid in its withdrawal. The vibrations produce a localized zone of temporary liquefaction that causes the soil surrounding the vibroflot to densify. A conical depression usually forms at the ground surface above the probe. This depression can be filled with granular material (such as clean sand or gravel) as the vibroflot is withdrawn. Alternatively, vibroflots with bottom-feed systems can introduce granular material through the tip of the vibroflot. As the vibroflot is removed, it leaves behind a densified column of soil. When gravel or crushed stone is introduced into the soil, the resulting *stone column* provides benefits of reinforcement and drainage in addition to densification. The use of bottom-feed systems has increased rapidly in recent years. Air delivery systems have become quite common and tend to be preferred over water delivery systems at congested sites and in environmentally sensitive areas.

Vibroflotation is most effective in clean granular soils with fines contents less than 20% and clay contents below 3%. In such soils it typically produces high densities (relative densities of about 100%) within 12 to 18 in. (30 to 46 cm) of the vibroflot and lower densities at greater radial distances. To densify an entire site, vibroflotation is performed in a grid pattern with a spacing that depends on the soil conditions and the power of the vibroflot; spacings of 6 to 10 ft (2 to 3 m) are common. Vibroflotation has been used successfully

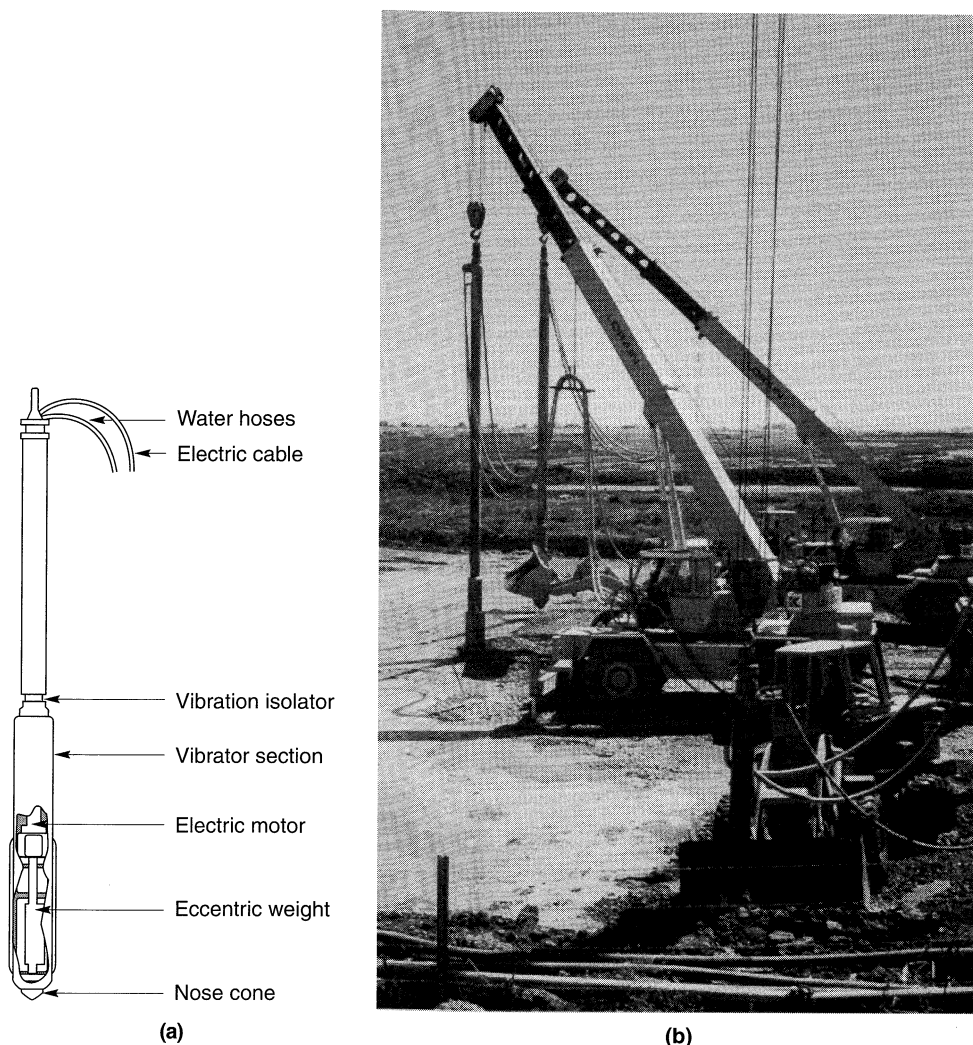


Figure 12.1 (a) Schematic illustration of a typical vibroflot (after Bell, 1993), and (b) vibroflots densifying liquefiable soils at a wastewater treatment facility in California (photo courtesy of Hayward Baker).

to densify soils to depths of up to 115 ft (35 m). Case histories of vibroflotation have been reported by Harder et al. (1984) and Dobson (1987).

12.2.1.2 Vibro Rod

Vibro rod systems use a vibratory pile driving hammer to vibrate a long probe into the soil. The probe is then withdrawn while still being vibrated to densify the soil. To minimize densification-induced settlement, additional soil may be introduced at the ground surface or

at depth. Several types of probes have been used in vibrocompaction. In the *Terraprobe* system, a 30-in. (76-cm) open-ended steel pipe is vibrated into the ground; the vibrations densify the soil both inside and outside the pipe. The *Vibro-Wing* consists of a central rod with diametrically opposed 31-in. (80-cm) "wings" spaced 19 in. (50 cm) apart along the length of the rod (Figure 12.2). The *Franki Y-probe* consists of three 19-in. (50-cm)-wide steel plates welded to a central rod at 120° angles from each other. Horizontal cross-ribs may be welded to the faces of the steel plates to facilitate densification. By adjusting the frequency of vibration, these probes can be "tuned" to the resonant frequency of the soil-probe system to increase vibration amplitudes and densify the soil more efficiently (Massarch, 1991).

Vibro rod systems are most effective in soils similar to those for which vibroflotation is most effective. Because vibro rods use vertical vibrations, their radius of influence is usually smaller than that observed for vibroflotation. As a result, the grid spacing for soil improvement by vibro rods is generally smaller than for vibroflotation. The effectiveness of vibro rods also appears to vary with depth (Janes, 1973). Case histories of vibro rod systems have been reported by Massarch (1991), Neely and Leroy (1991), and Senneset and Nestvold (1992).

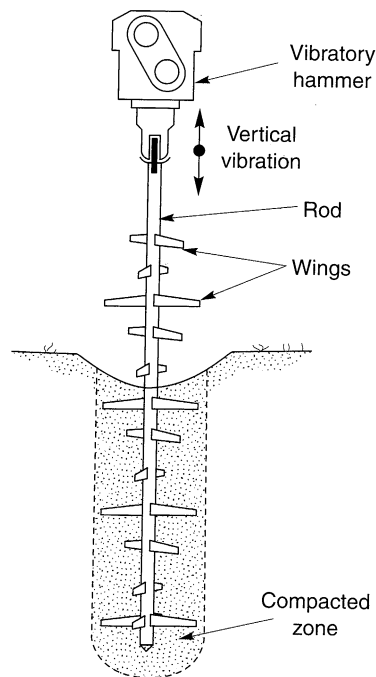


Figure 12.2 Vibro-wing system. Each pair of wings is oriented at a 120° angle to those located immediately above and below. After Broms (1991).

12.2.2 Dynamic Compaction

Dynamic compaction is performed by repeatedly dropping a heavy weight in a grid pattern on the ground surface (Figure 12.3). The weights, usually constructed of steel plates and/or reinforced concrete, generally range from 6 to 30 tons (53 to 267 kN), although weights of up to 170 tons (1500 kN) have been used. Drop heights usually range from about 35 to 100



Figure 12.3 Aerial view of site undergoing soil improvement by dynamic compaction. The grid pattern on which the dynamic compaction weight is dropped, and the need for subsequent regrading and surface compaction, are evident from this photograph. (Photo courtesy of Hayward Baker).

ft (10 to 30 m), although weights have been dropped from up to 130 ft (40 m). The weights are usually dropped three to eight times before moving to the next point on the grid. A detailed description of dynamic compaction was prepared by Lukas (1986).

At a particular site, dynamic compaction is generally performed in several stages, or passes. Empirical evidence suggests that the effective depth of influence (the depth to which significant improvement can be detected) increases with impact energy and that the greatest degree of improvement is usually observed at about half the effective depth of influence (Mayne et al., 1984). To avoid developing a shallow zone of dense soil that could inhibit the transmission of energy to greater depths, the deepest soil is densified first with a series of high-energy (heavy weight and/or high drop height) drops on a widely spaced grid. After the craters produced by the first pass have been filled (preferably with well-graded granular soil), soils at intermediate depth are then compacted using a greater number of drops from a smaller height at closer spacing (often half the spacing of the original grid). Finally, the

near-surface soils are compacted by dropping relatively light weights on a virtually continuous pattern to smooth or “iron” the ground surface. Additional smoothing by conventional surface grading and compaction equipment is usually required.

The kinetic energy of the weight at impact produces stress waves that travel through the soil. The total energy delivered to the soil is a function of the weight, drop height, grid spacing, and number of drops per grid point. When the groundwater table is near the surface, placement of a gravel or sand blanket may be required prior to compaction. Although dynamic compaction has been used successfully for cohesive soils, its most common use for mitigation of seismic hazards is for potentially liquefiable soils. At each grid point, a series of drops causes the porewater pressure to increase so that the soil particles can more easily move into a denser configuration. Dissipation of the excess porewater pressure results in further densification within a short period (1 to 2 days for sand and gravels; 1 to 2 weeks for sandy silts) after treatment.

Dynamic compaction is generally effective to depths of 30 to 40 ft (9 to 12 m), although extremely high impact energies may produce densification at greater depths. Because the process is rather intrusive—it can produce considerable noise, dust, flying debris, and vibration—it is rarely used near occupied or vibration-sensitive structures. Case histories of dynamic compaction of potentially liquefiable soil have been described by Hussein and Ali (1987), Keller et al. (1987), Koutsoftas and Kiefer (1990), Mitchell and Wentz (1991), and others.

12.2.3 Blasting

Loose granular soils have also been compacted by *blasting*. Blasting densification involves the detonation of multiple explosive charges vertically spaced 10 to 20 ft (3 to 6 m) apart in drilled or jetted boreholes. The boreholes are usually spaced between 15 to 50 ft (5 to 15 m) apart and backfilled prior to detonation. To increase the efficiency of the densification process, the charges at different elevations may be detonated at small time delays. Immediately after detonation, the ground surface rises and gas and water are expelled from fractures (Figure 12.4). The ground surface then settles as the excess gas and water pressure dissipates. Although the efficiency of densification decreases with each round of blasting, two or three rounds (with later rounds detonated at locations between those of the earlier rounds) are often used to achieve the desired degree of densification.

Blasting is most effective in loose sands that contain less than 20% silt and less than 5% clay. Even small amounts of clay, or small clay seams, can substantially reduce the effectiveness of blasting. Blasting can be effective in dry soils, but the effects of capillary tension and gas bubbles in partially saturated soils virtually negates its effectiveness. As a result, blasting is most commonly used to densify completely saturated soils. In such soils the shock wave produced by the charges produces localized, temporary liquefaction which allows the soil grains to move into a more dense configuration.

Although blasting is quite economical, its use is limited by several practical considerations. It produces strong vibrations that may damage nearby structures or produce significant ground movements. It requires the use of potentially hazardous explosives for which strict regulations on handling and storage usually apply. Finally, its effectiveness is difficult to predict in advance. Case histories of the use of blasting to mitigate seismic

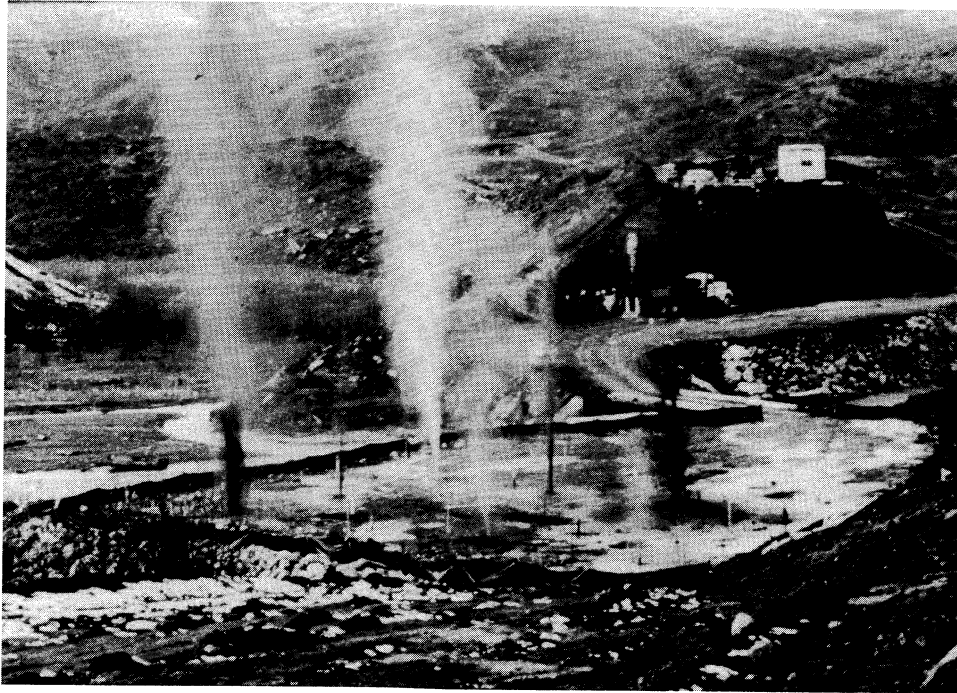


Figure 12.4 Ground surface shortly after detonation of explosives during blast densification of loose soil beneath an abutment prior to construction of Coldwater Creek bridge near Mt. St. Helens in Washington state. (Photo by A. P. Kilian; used with permission).

hazards have been described by Klohn et al. (1981), Solymar and Reed (1986), LaFosse and von Rosenvinge (1992), and Hachey et al. (1994).

12.2.4 Compaction Grouting

Soft or weak soils can be densified by injecting a very low slump [generally less than 1 in. (2.5 cm)] grout into the soil under high pressure, a process known as *compaction grouting*. Because the grout is highly viscous, it forms an intact bulb or column that densifies the surrounding soil by displacement (Figure 12.5). Compaction grouting may be performed at a series of points in a grid or along a line. Grout point spacings ranging from 3 to 15 ft (1 to 4.6 m) have been used. Because higher overburden pressures allow the use of higher grout pressures, larger spacings are generally used when treating deeper soils. At shallow depths, compaction grouting may be used to lift settled slabs or structures; indeed, remediation of foundation settlement is probably the most common application of compaction grouting.

Compaction grouting may be performed from the top down (*downstage grouting*) or from the bottom up (*upstage grouting*). Upstage grouting is less expensive and more commonly used than downstage grouting. However, the downstage procedure is preferred (Stilley, 1982; Bell, 1993) for underpinning of structures or for sites where loose soils

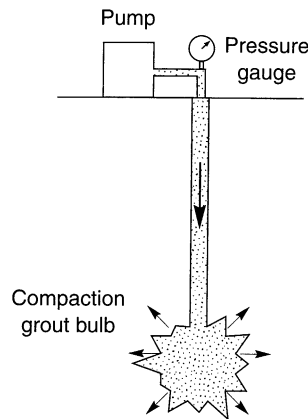


Figure 12.5 Compaction grouting. Low-slump grout is pumped under high pressure to form a bulb that displaces and densifies the surrounding soils. By raising the grout tube while pumping, a column of grout can be created in the soil. (After Hausmann, 1990.)

extend to the ground surface. By working from the top down, placement of an upper grout bulb reduces the possibility of subsequent grout escaping at the surface and grout heave, and also provides additional strength and confinement that allows the use of higher grouting pressures at greater depths.

Because it does not rely on vibration, compaction grouting can be used in all soil types. It is most commonly used in sands and nonplastic silts. Compaction grouting can be used to virtually any depth and can easily be used within a given range of depths. The size and shape of the grout bulb or column is influenced by the stiffness and strength of the soil and also by the rate and pressure at which the grout is injected. An important feature of compaction grouting is that its greatest effects occur where the soil is softest and weakest. Compaction grout masses with diameters greater than 3 ft (1 m) are not uncommon (Warner, 1982). Compaction grouting has been used to depths of 100 ft (30 m). Case histories of compaction grouting have been described by Salley et al. (1987), Warner (1982), Graf (1992), and Baez and Henry (1993).

12.2.5 Areal Extent of Densification

An important consideration in the densification of soils for construction of individual structures and foundations is the areal extent of soil improvement required for satisfactory performance during earthquakes. The areal extent should be evaluated on a case-by-case basis since site-specific soil conditions, performance requirements, and failure consequences must be addressed.

The required areal extent of improvement depends on the mechanism of failure that the improvement is intended to eliminate. For potential stability failures, the areal extent of improvement will depend on the degree of improvement that can be achieved and on the extent of the potential failure surface(s). By estimating the residual strength of the soil after improvement, stability analyses can be used to estimate the extent of improvement that will produce an acceptable level of stability. To minimize postearthquake settlement of a structure or foundation on loose, saturated sand, densification is usually performed within a zone defined by a 30 to 45° line from the edge of the structure, as illustrated in Figure 12.6. Available research and field experience indicates that this approach is likely to produce a satisfactory extent of improvement (Iai et al., 1988).

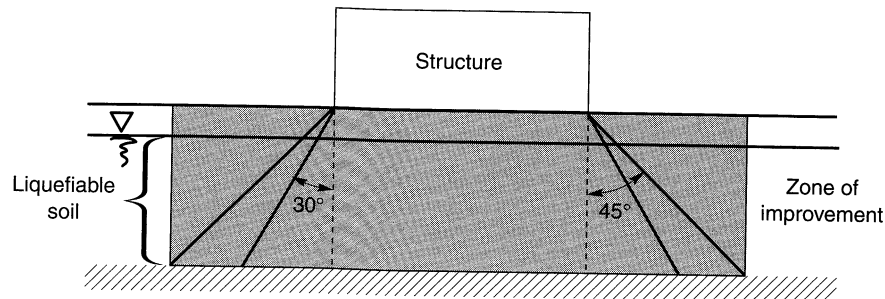


Figure 12.6 Typical areal extent of improvement for densification of potentially liquefiable soil beneath a structure.

12.3 REINFORCEMENT TECHNIQUES

In some cases it is possible to improve the strength and stiffness of an existing soil deposit by installing discrete inclusions that reinforce the soil. These inclusions may consist of structural materials, such as steel, concrete, or timber, and geomaterials such as densified gravel. Reinforcement of new engineered fills using geosynthetic or metallic reinforcement is beyond the scope of this chapter.

12.3.1 Stone Columns

Soil deposits can be improved by the installation of dense columns of gravel known as *stone columns*. Stone columns may be used in both fine- and coarse-grained soils. In fine-grained soils, stone columns are usually used to increase shear strength beneath structures and embankments by accelerating consolidation (by allowing radial drainage) and introducing columns of stronger material. For mitigation of seismic hazards, they are commonly used for improvement of liquefiable soil deposits.

Stone columns can be installed in a variety of ways. As discussed previously, stone columns may be constructed by introducing gravel during the process of vibroflotation (Brown, 1977). Several other methods of installation are also available. In the *Franki method*, a steel casing initially closed at the bottom by a gravel plug is driven to the desired depth by an internal hammer (Figure 12.7). At that depth, part of the plug is driven beyond the bottom of the casing to form a bulb of gravel. Additional gravel is then added and compacted as the casing is withdrawn. The diameter of the resulting stone column depends on the stiffness and compressibility of the surrounding soil; in loose sand, a 0.5- to 0.7-m (19 to 28 in.) casing will typically produce a 0.8-m (31 in.) diameter column. Casings with trap doors at the bottom have also been used to install stone columns (Solyman and Reed, 1986). The trap door allows the casing to be driven as a closed-end pile but also allows gravel to be placed during withdrawal of the casing. The gravel can be densified by pausing to redrive the casing at various intervals during the withdrawal process.

Stone columns combine at least four different mechanisms for improvement of liquefiable soil deposits. First, they improve the deposit by virtue of their own high density, strength, and stiffness—in this sense they reinforce the soil deposit. Second, they provide closely spaced drainage boundaries that inhibit the development of high excess porewater

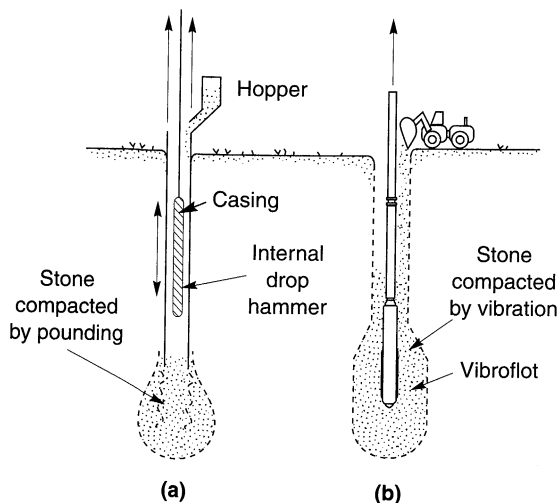


Figure 12.7 Methods of stone column installation: (a) Franki method; (b) by vibroflotation. (After Broms, 1991.)

pressures (Section 12.6). Third, the processes by which they are installed densify the surrounding soil by the combined effects of vibration and displacement. Finally, the installation process increases the lateral stresses in the soil surrounding the stone columns. These multiple benefits have made the use of stone columns very popular. Case histories of seismic hazard mitigation by stone columns have been presented by Priebe (1991), Hayden and Welch (1991), and Mitchell and Wentz, (1991).

12.3.2 Compaction Piles

Granular soils can be improved by the installation of *compaction piles*. Compaction piles are displacement piles, usually prestressed concrete or timber, that are driven into a loose sand or gravel deposit in a grid pattern (Figure 12.8) and left there. Compaction piles improve the seismic performance of a soil deposit by three different mechanisms. First, the flexural strength of the piles themselves provides resistance to soil movement (reinforcement). Second, the vibrations and displacements produced by their installation cause densification. Finally, the installation process increases the lateral stresses in the soil surrounding the piles.

Compaction piles generally densify the soil within a distance of 7 to 12 pile diameters (Robinsky and Morrison, 1964; Kishida, 1967), and consequently, are usually installed in a grid pattern. Between compaction piles, relative densities of up to 75 to 80% are usually achieved (Solymar and Reed, 1986). Improvement can be obtained with reasonable economy to depths of about 60 ft. Case histories describing the use of compaction piles have been presented by Lindqvist and Petaja (1981), Marcuson et al. (1991), Mitchell and Wentz (1991), and Kramer and Holtz (1991).

12.3.3 Drilled Inclusions

Structural reinforcing elements can also be installed in the ground by drilling or augering. Drilled shafts, sometimes with very large diameters, have been used to stabilize many slopes. Such shafts may be installed closely enough to form tangent or secant pile walls. Soil

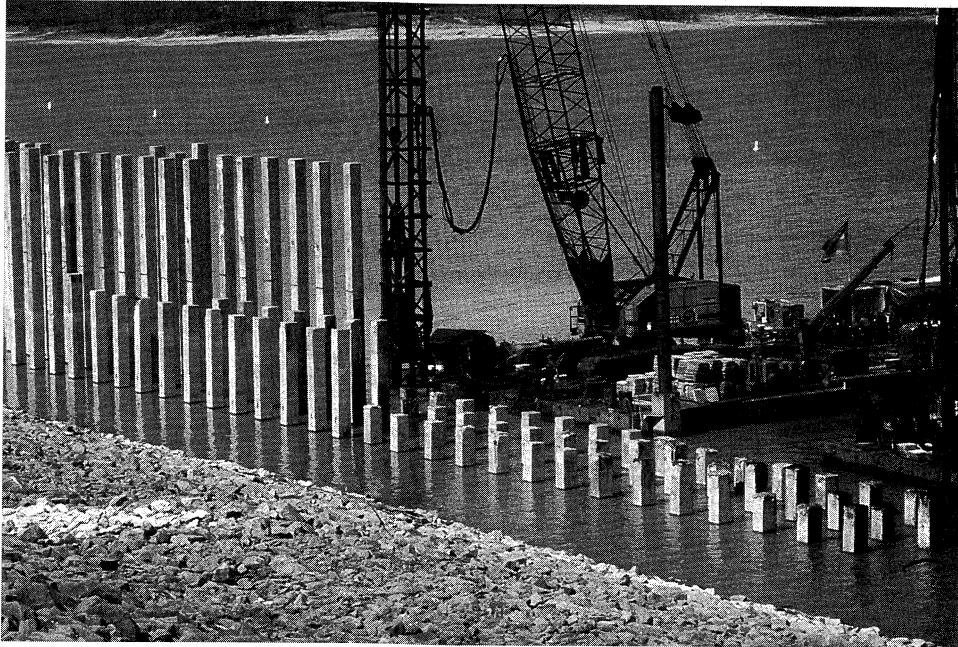


Figure 12.8 Compaction piles driven into the upstream embankment of Sardis Dam to reduce liquefaction hazards. The contractor drove the piles to this level with a barge-mounted conventional hammer; the piles were later driven below the water surface with a different hammer. (Photo by T. D. Stark; used with permission.)

nails, tiebacks, micropiles, and root piles have also been used. The installation of such drilled inclusions can be quite difficult, however, in the loose granular soils that contribute to many seismic hazards. Although soil nailed walls performed well in the 1989 Loma Prieta earthquake (Felio et al., 1990), there is currently no consensus on their design for seismic loading.

12.4 GROUTING AND MIXING TECHNIQUES

The engineering characteristics of many soil deposits can be improved by injecting or mixing cementitious materials into the soil. These materials both strengthen the contacts between soil grains and fill the void space between the grains. *Grouting* techniques involve the injection of such materials into the voids of the soil or into fractures in the soil so that the particle structure of the majority of the soil remains intact. *Mixing* techniques introduce cementitious materials by physically mixing them with the soil, completely disturbing the particle structure of the soil. The mixing can be accomplished mechanically or hydraulically. Grouting and mixing techniques tend to be expensive but can often be accomplished with minimal settlement or vibration. As a result, grouting and mixing techniques can often be used in situations where other soil improvement techniques cannot.

12.4.1 Grouting

The term *grouting* is used to describe a variety of processes by which cementitious material is introduced into the ground. Grouting techniques are often classified according to the method by which the grout is placed in the ground (Hausmann, 1990). In this chapter, however, soil improvement techniques are classified according to the primary mechanisms by which they produce improvement. As a result, compaction grouting is described with other densification techniques in Section 12.3, and jet grouting is considered as a mixing technique in the following section. With this convention, there are two primary types of grouting techniques.

12.4.1.1 Permeation Grouting

Permeation grouting involves the injection of low-viscosity liquid grout into the voids of the soil without disturbing the soil structure (Figure 12.9). *Particulate grouts* (i.e., aqueous suspensions of cement, fly ash, bentonite, microfine cement, or some combination thereof) or *chemical grouts* (e.g., silica and lignin gels, or phenolic and acrylic resins) may be used.

The suitability of different types of grouts for different soil conditions is most strongly influenced by the grain size of the soil. Virtually any type of grout, even relatively viscous cement grouts, can be used in soil with large voids such as gravels and coarse sands. Chemical grouts generally exhibit lower viscosity than particulate grouts (although the viscosity of microfine cements grouts may be as low as some chemical grouts) and can therefore be used in fine sands. The presence of fines can significantly reduce the effectiveness of permeation grouting.

Grout pipes are typically installed in a grid pattern at spacings of 4 to 8 ft (1.2 to 2.4 m) (Hayden, 1994). The grout may be injected in different ways. In *stage grouting*, a boring is advanced a short distance before grout is injected through the end of the drill rod. After the grout sets up, the boring is advanced another short distance and grouted again. This process continues until grout has been placed to the desired depth. In the *tube-à-manchette* approach, a grout tube with injection ports every 12 to 24 in. (30 to 61 cm) along its length is installed in a borehole. Rubber sleeves (manchettes) that serve as one-way valves cover the injection ports on the outer surface of the grout tube and internal packer systems are used to control the depths at which grout is injected.

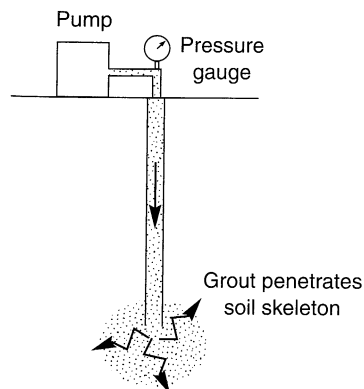


Figure 12.9 Permeation grouting. (After Hausmann, 1990).

Permeation grouting produces soil improvement by two primary mechanisms. First the grout tends to strengthen the contacts between individual soil grains, thereby producing a soil skeleton that is stronger and stiffer than that of the ungrouted soil. Second, the grout takes up space in the voids between soil particles, reducing the tendency for densification (or excess pore pressure generation) upon cyclic loading. Soils improved by permeation grouting can have shear strengths of 50 to 300 psi (345 to 2070 kPa). Case histories in which permeation grouting was used to mitigate seismic hazards were described by Zacher and Graf (1979), Graf (1992), and Bruce (1992).

12.4.1.2 Intrusion Grouting

In the process of *intrusion grouting*, fluid grout is injected under pressure to cause controlled fracturing of the soil (Figure 12.10). Because the grout is not intended to flow through the small voids between soil particles, relatively viscous (and strong) cement grouts can be used. In theory, the first fractures should be parallel to the minor principal stress planes, but observations show that they usually follow weak bedding planes. After allowing the initially placed grout to cure, repeated intrusion grouting fractures the soil along different planes. Eventually, a three-dimensional network of intersecting grout lenses can be formed. Some densification of the soil may occur, but the primary mechanism of improvement results from the increased stiffness and strength of the soil mass due to the hardened lenses of grout.

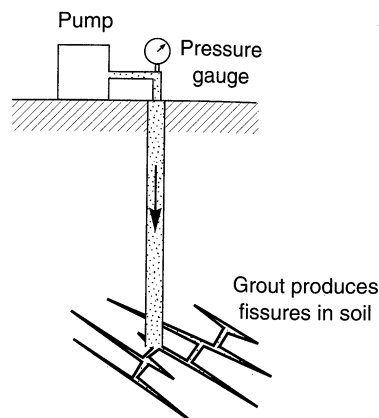


Figure 12.10 Intrusion grouting process. (After Hausmann, 1990).

12.4.2 Mixing

Localized improvement of soil columns can be achieved by in situ mixing of the soil with cementitious material. Because the cementitious material is physically mixed with the soil, it need not have an extremely low viscosity—strong, cement slurries are commonly used. For mitigation of seismic hazards, this approach is most commonly accomplished by *soil mixing* and *jet grouting*.

12.4.2.1 Soil Mixing

The term *soil mixing* describes a specific technique in which cementitious material is mechanically mixed into the soil using a hollow stem auger and paddle arrangement (Figure 12.11). Soil mixing rigs may have single augers (0.5 to 4 m (1.6 to 13 ft) in diameter) or

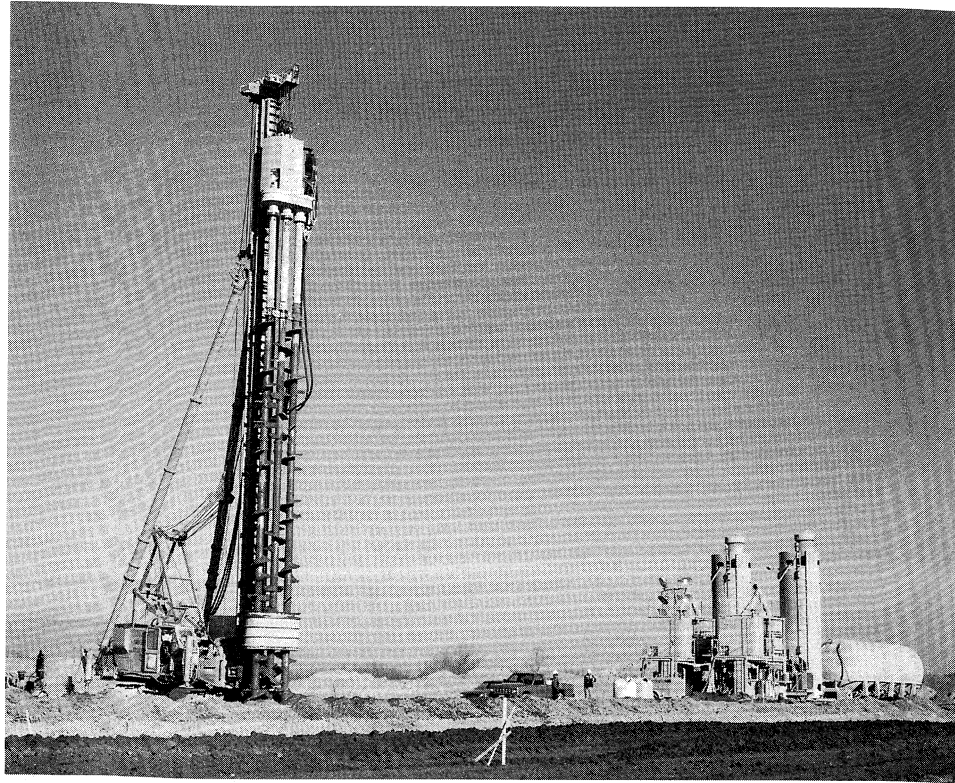


Figure 12.11 Triple auger soil mixing rig improving liquefiable soils at Jackson Lake Dam in Wyoming. Grout batch plant is at right (photo courtesy of SMW Seiko, Inc.)

gangs of two to eight augers (usually about 1 m (3.1 ft) in diameter). As the mixing augers are advanced into the soil, grout is pumped through their stems and injected into the soil at their tips. The grout is thoroughly mixed with the soil by the auger flights and mixing paddles. After the design depth has been reached, the augers are withdrawn while the mixing process continues. The soil mixing process leaves behind a uniform (constant width) column of soil-cement. By overlapping the columns before the grout cures, walls and cellular structures can be constructed below the ground surface.

Soil mixing can be used in virtually any type of inorganic soil. It has been used to depths of over 20 m (66 ft) in the United States and up to 60 m (200 ft) in Japan. The strength of the soil-cement mixture depends on the type of grout, type of soil, and degree of mixing; strengths of 200 psi (1380 kPa) or more are commonly achieved. Case histories involving the use of soil mixing for mitigation of seismic hazards have been presented by Ryan and Jasperse (1989), Babasaki et al. (1991), and Taki and Yang (1991).

12.4.2.2 Jet Grouting

In *jet grouting*, the soil is mixed with cement grout injected horizontally under high pressure in a previously drilled borehole (Figure 12.12). The injection nozzle is rotated to

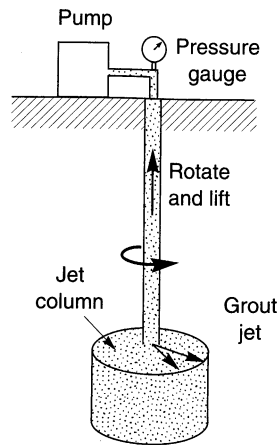


Figure 12.12 Jet grouting process. (After Hausmann, 1990).

allow the grout to be placed in all directions. Air or air and water may also be injected to aid in the mixing process. Jet grouting begins at the bottom of the borehole and proceeds to the top, leaving behind a relatively uniform column of mixed soil–cement. By overlapping the columns before the grout cures, walls and cellular structures can be constructed below the ground surface.

The diameter of a jet grouted column depends on the soil condition and the manner in which the jet grouting is performed. Column diameters are generally greater in coarse-grained soils than in fine-grained soils. By varying the air, water, and grout pressures and the rates of rotation and lifting of the grout tubes, a jet grouting operator can control the effective dimensions of the column. Diameters ranging from 0.4 to 0.5 m (16 to 20 in.) in clayey silt to 0.9 to 1.0 m (36 to 39 in.) in sandy gravel can be expected using a single-jet (grout only) system (Bell, 1993). Diameters of 0.8 to 1.0 m (31 to 39 in.) in clayey silt and 2.0 to 2.4 m (6.5 to 7.9 ft) in sandy gravel can be expected with a triple-jet (air, water, and grout) system. Jet grouting can be performed in any type of inorganic soil to depths limited only by the range of the drilling equipment. Case histories of the use of jet grouting for mitigation of seismic hazards have been presented by Hayden (1994).

12.5 DRAINAGE TECHNIQUES

Unacceptable movements of slopes, embankments, retaining structures, and foundations can frequently be eliminated by lowering the groundwater table prior to earthquake shaking. A number of dewatering techniques have been developed and proven useful in engineering practice. Procedures for the design of dewatering systems are well established and widely used (e.g., Cedergren, 1989; Powers, 1992). These standard techniques may be used to increase the stiffness and strength of a soil deposit for mitigation of seismic as well as nonseismic hazards.

The buildup of excess porewater pressure during earthquake shaking can be suppressed using drainage techniques, although drainage alone is rarely relied upon for the mitigation of liquefaction hazards. The installation of stone columns, for example, introduces

columns of freely draining gravel into a liquefiable soil deposit (though mixing of the gravel and the native soil during installation may reduce the permeability of the stone column). Earthquake-induced excess pore pressures may be rapidly dissipated by horizontal flow of porewater into the stone columns. The rate of pore pressure dissipation depends on the diameter and spacing of the stone columns and on the permeability and compressibility of the surrounding soil. Seed and Booker (1976, 1977) developed procedures for selecting the sizes and spacings of gravel drains (or stone columns) for mitigation of liquefaction hazards. The use of gravel drains for suppression of excess porewater pressure requires careful attention to drain permeability and filtration behavior of the drain–soil boundary. Even though drainage techniques can mitigate liquefaction hazards by suppressing excess porewater pressure buildup, postearthquake settlement may still occur. Case histories of the use of drainage techniques for mitigation of seismic hazards have been described by Ishihara et al. (1980), Aboshi et al. (1991), and Iai et al. (1994).

12.6 VERIFICATION OF SOIL IMPROVEMENT

All attempts at soil improvement should be checked to confirm that the desired improvement has taken place. The most direct way of verifying the effectiveness of a particular soil improvement technique is to measure the soil characteristic that was considered deficient both before and after improvement. For example, if the improvement was undertaken to increase the strength of the soil, measurement of the strength before and after improvement would provide the most direct verification of the effectiveness of the improvement process. However, it is not always feasible to measure the deficient characteristic directly. In such cases, verification is usually accomplished using related characteristics that are more easily measured.

Verification may be based on the results of laboratory or field tests. While laboratory tests have historically been commonly used for verification of soil improvement, recent advances in field testing techniques have provided additional means for verification. Field testing techniques may be divided into in situ testing techniques and geophysical testing techniques. Common verification techniques were summarized by Ledbetter (1985).

12.6.1 Laboratory Testing Techniques

Laboratory testing techniques have a number of advantages over other methods for verification of soil improvement, but they also suffer from drawbacks that can significantly limit their usefulness for certain types of soil improvement. The requirement of obtaining a sample of the improved soil leads directly to many of the advantages of using laboratory testing techniques and also to many of the disadvantages. Obtaining a sample of improved soil allows visual inspection of the effects of improvement. For many improvement techniques (e.g., permeation grouting, soil mixing, etc.), the ability to inspect the treated soil provides direct and valuable evidence of the effectiveness of the treatment. Laboratory tests allow greater control and more accurate measurement of stress, strain, and environmental conditions than are possible in field tests. In some cases this flexibility may allow more accurate characterization of the properties of the improved soil.

On the other hand, laboratory tests only provide verification at discrete points. When soil improvement is used to improve or eliminate localized zones or seams of weakness, verification by methods that require discrete sampling may be ineffective. Laboratory tests may also be influenced by the inevitable effects of sample disturbance, a problem that is particularly significant in the improvement of liquefiable soils. The density changes produced by even thin-walled samplers (Marcuson et al., 1977; Seko and Tobe, 1977; Singh et al., 1979) can lead to considerable uncertainty in the evaluation of improvement effectiveness.

12.6.2 In Situ Testing Techniques

Many of the limitations of laboratory testing based approaches to the verification of soil improvement effectiveness may be overcome by the use of in situ tests. Indeed, the use of in situ tests for verification of soil improvement effectiveness has increased dramatically in the past 15 to 20 years. Because many geotechnical seismic hazards are evaluated using in situ test parameters, those parameters can provide direct evidence of hazard mitigation. Indeed, soil improvement specifications may be written to require that a certain parameter value (e.g., a minimum SPT resistance) be achieved after improvement. Mitchell (1986) and Welsh (1986) described the use of in situ tests for verification of soil improvement effectiveness.

The SPT, CPT, PMT, and DMT (Section 6.3.1.2) can all be used for verification of soil improvement effectiveness. The SPT and CPT tests are performed relatively quickly and inexpensively compared to sampling and laboratory testing. The CPT is particularly useful because it provides a continuous record with depth. The PMT is more expensive, but it also allows measurement of lateral stresses and direct measurement of strength. For gravelly soils, the Becker hammer penetration test (Section 6.3.1.2) may be used for verification purposes.

Interpretation of soil improvement effectiveness from in situ test results must be performed carefully. The penetration resistance of granular soils, for example, is influenced not only by density and overburden stress, but also by lateral stress. Soil improvement techniques that result in increased lateral stress may produce unconservative estimates of the density of the improved soil if the postimprovement stress state is not carefully considered in the interpretation of penetration test results. Because time-dependent changes in strength, stiffness, and penetration resistance are often observed after densification (Mitchell and Solymar, 1984; Mitchell, 1986), in situ tests performed immediately after densification may not reflect the actual degree of improvement of the soil. Verification testing is usually performed at least 72 hours after densification has taken place. Many soil improvement techniques are applied at a grid of treatment points, and the degree of improvement usually decreases with distance from the treatment point. The relationship between the locations of in situ tests and the locations of treatment points should be considered in the interpretation of soil improvement effectiveness from in situ test results. In situ tests have limited effectiveness for verification of grouting effectiveness (Welsh, 1986).

12.6.3 Geophysical Testing Techniques

Many soil improvement techniques increase the stiffness of the treated soil. The effectiveness of these techniques can be verified using seismic geophysical techniques (Section 6.3.1.1). In most cases it is desirable to perform seismic tests both before and after improvement.

Cross-hole and downhole (including seismic cone) tests are most commonly used for verification of soil improvement. These techniques can measure p- or s-wave velocities over considerable distances, thereby providing spatially averaged stiffness measurements. However, each requires at least one borehole. For sites where soil improvement has been performed over a large area, seismic reflection and seismic refraction tests may be useful for verification purposes. SASW tests provide similar information without the need for boreholes. At sites where stiffness changes irregularly in two or three dimensions or sites that contain inclusions, the results of SASW tests may be very difficult to interpret. Such tests must also be performed when background noise (including that produced by on-going soil improvement work) will not adversely affect their results. Tests that measure average wave propagation velocities may not accurately reflect the degree of improvement of thin, loose zones unless the distance over which velocities are averaged is quite small.

12.7 OTHER CONSIDERATIONS

The application of soil improvement techniques to the mitigation of seismic hazards is relatively new. The theoretical underpinnings of many soil improvement techniques are poorly developed, and empirical observations of the performance of improved soil in actual earthquakes are rare. Because of these factors, it is particularly important to review the relevant geotechnical engineering literature before attempting to mitigate seismic hazards by soil improvement.

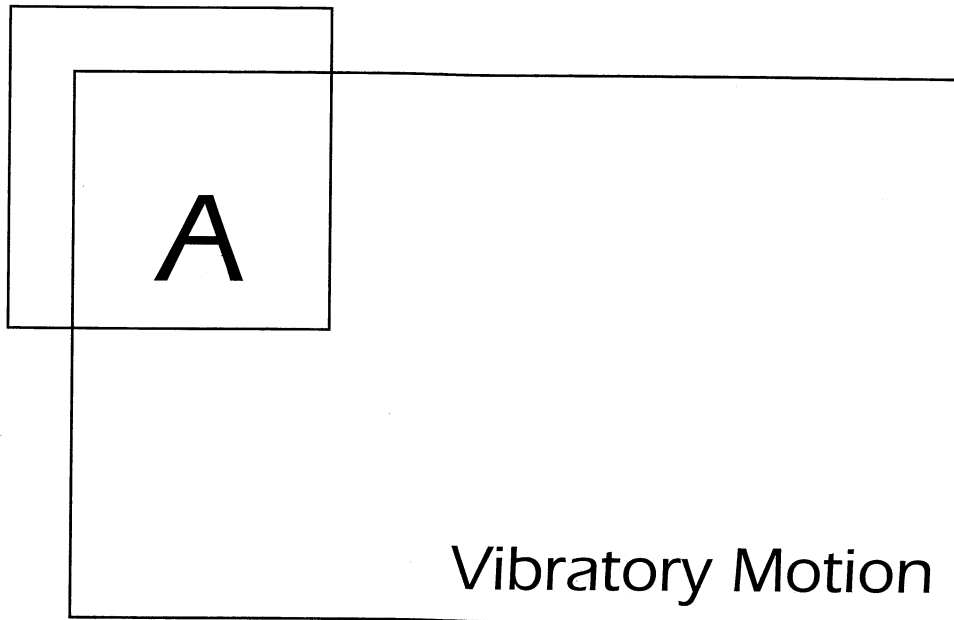
The effectiveness of many soil improvement techniques can be difficult to predict in advance for a particular site. Furthermore, the equipment, procedures, experience, and skill of the soil improvement contractor can strongly influence soil improvement effectiveness. For these reasons, it is frequently beneficial to construct *test sections* before beginning production work or even before final selection of a soil improvement technique. Test sections allow site- and procedure-specific evaluation of soil improvement effectiveness at a moderate cost; their use is advisable whenever possible.

12.8 SUMMARY

1. Unfavorable soil conditions can frequently be improved using soil improvement techniques. A variety of soil improvement techniques have been developed—some apply to long-term, static loading conditions and others also apply to seismic loading conditions.
2. The cost of different soil improvement techniques vary widely. Costs are influenced by the volume and extent of the soil to be treated, access to the site, site sensitivity to vibration and permanent ground movement, and other factors.
3. The presence of existing structures, pipelines, and other constructed facilities can eliminate many soil improvement techniques from consideration at a given site. The techniques that can be used at such sites tend to be among the more expensive.
4. Most soil improvement techniques are intended to increase the strength and stiffness of a soil deposit. Increased strength and stiffness is generally desirable for both static and seismic loading conditions.

5. Current soil improvement techniques can be divided into four broad categories: densification techniques, reinforcement techniques, grouting/mixing techniques, and drainage techniques. Not all techniques fall entirely within a single category; for example, stone columns can improve a soil deposit by densification, reinforcement, and drainage functions.
6. Several soil improvement techniques that are commonly used to mitigate seismic hazards are intended to reduce the tendency of loose, saturated granular soils to generate excess porewater pressure during earthquake shaking. These techniques typically involve densification of the soil.
7. Densification is probably the most commonly used soil improvement technique for mitigation of seismic hazards. Most densification techniques rely on the tendency of granular soils to densify when subjected to vibration. Densification can produce substantial settlement, although some procedures allow the introduction of new material to balance the volume change caused by densification.
8. Many densification techniques rely on vibrations that can be potentially damaging to structures, pipelines, and other constructed facilities. Such vibrations may also be too objectionable to people who live or work near sites that require improvement to allow their use.
9. Most vibratory techniques produce a temporary, localized zone of liquefaction in loose, saturated sand. Densification occurs as the sand particles are rearranged during reconsolidation. The presence of fines, particularly plastic fines, inhibits the development of high pore pressures and the rearrangement of soil particles. As a result, vibratory techniques may have limited effectiveness in soils with significant fines contents.
10. Reinforcement techniques introduce discrete inclusions that stiffen and strengthen a soil deposit. The high stiffness and strength of the inclusions also tend to reduce the stresses imposed on the weaker material between the inclusions.
11. Cementitious materials may be injected or mixed into a soil deposit. The materials improve the soil by strengthening the contacts between individual grains and filling the space between the grains.
12. Grouting techniques involve the injection of such materials into the voids of the soil or into fractures in the soil so that the particle structure of the majority of the soil remains intact. In permeation grouting, very low viscosity grouts are injected into the voids of the soil without disturbing the soil structure. In intrusion grouting, thicker and more viscous grouts are injected under pressure to cause controlled fracturing of the soil.
13. Mixing techniques introduce cementitious materials by physically mixing them with the soil, completely disturbing the particle structure of the soil. The mixing can be accomplished mechanically (soil mixing) or hydraulically (jet grouting). Both soil mixing and jet grouting leave behind relatively uniform columns of mixed soil-cement. By overlapping the columns, walls or cellular structures can be constructed below the ground surface.
14. Drainage techniques minimize the buildup of porewater pressure during earthquakes by shortening the drainage paths in a soil deposit. The installation of drains generally involves some degree of densification and the drains themselves may also provide some reinforcement.

15. Verification of the effectiveness of soil improvement is an important part of seismic hazard mitigation. Direct or indirect measurement of stiffness, strength, or density characteristics both before and after improvement can allow reliable evaluation of soil improvement effectiveness. These characteristics may be measured by laboratory, in situ, or geophysical tests. The relative advantages and limitations of these types of tests, discussed in detail in Chapter 6, apply to their use in verification applications.



A.1 INTRODUCTION

Many different types of dynamic loading can induce vibratory motion in soils and structures. To solve problems involving the dynamic response of soils and structures, it is necessary to be able to describe dynamic events. They can be described in different ways, and the geotechnical earthquake engineer must be familiar with each. This appendix provides a brief description of vibratory motion and introduces the nomenclature and mathematical forms by which it is usually described.

A.2 TYPES OF VIBRATORY MOTION

Vibratory motion can be divided into two broad categories: *periodic motion* and *nonperiodic motion*. Periodic motions are those which repeat themselves at regular intervals of time. Mathematically, a motion, $u(t)$, is periodic if there exists some period, T_f , for which $u(t + T_f) = u(t)$ for all t . The simplest form of periodic motion is *simple harmonic motion* in which displacement varies sinusoidally with time. *Nonperiodic motions*, which do not repeat themselves at constant intervals, can result from impulsive loads (e.g., explosions or falling weights), or from longer-duration transient loadings (e.g., earthquakes or traffic). Examples of periodic and nonperiodic motions are shown in Figure A.1.

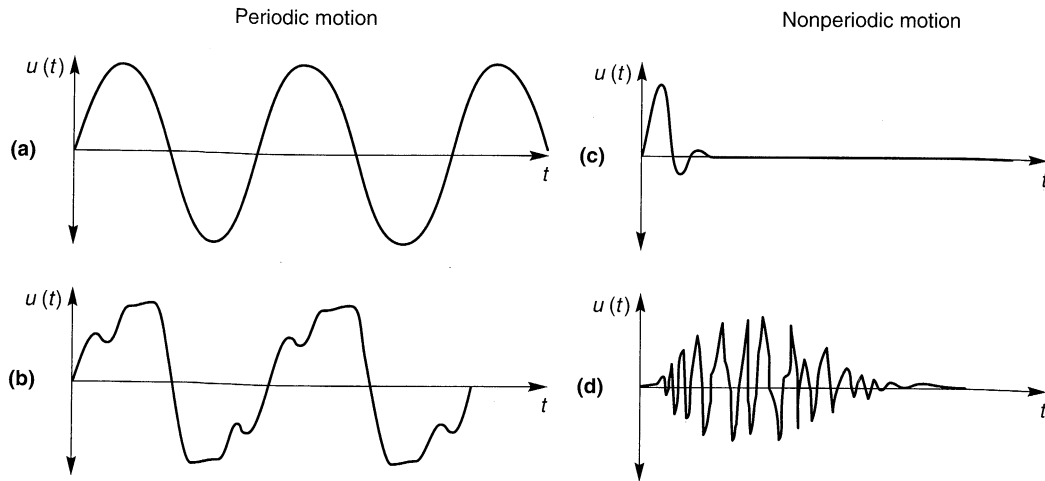


Figure A.1 Periodic and nonperiodic motion: (a) simple harmonic motion; (b) general periodic motion; (c) transient motion (response to impact loading); (d) transient motion (earthquake ground motion).

Some forms of periodic motion (e.g., Figure A.1b) may appear to be much more complex than simple harmonic motion, but with the use of mathematical techniques described later in this appendix, they can be expressed as the sum of a series of simple harmonic motions. Even transient, nonperiodic motions such as those of Figure A.1c and d can be represented as periodic motions by assuming that they repeat themselves after some “quiet” zone during which no motion occurs (Figure A.2). Using this technique, even a transient motion can also be expressed as a periodic motion. This becomes a very powerful tool for the dynamic analysis of linear systems, where the principle of superposition allows the response to transient loading to be expressed as the sum of the responses to a series of simple harmonic loads.

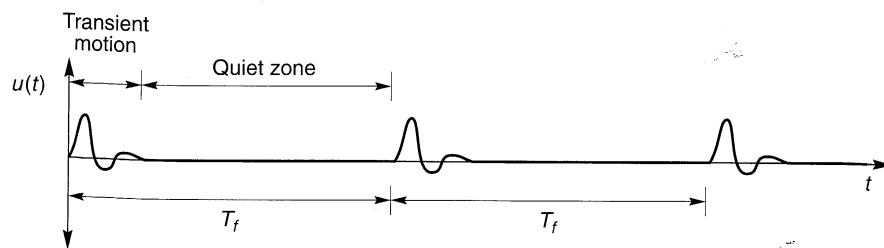


Figure A.2 Representation of a transient motion as a periodic motion using an artificial quiet zone. The motion repeats itself indefinitely at period T_f .

A.2.1 Simple Harmonic Motion

Simple harmonic motion can be characterized by sinusoidal motion at constant frequency. Its most important features can be defined by three quantities: *amplitude*, *frequency*, and

phase. Simple harmonic motion can be described in different ways, two of which will be presented in the following sections: using *trigonometric notation* or using *complex notation*. Both notations are equivalent and both are commonly used in geotechnical earthquake engineering.

A.2.2 Trigonometric Notation for Simple Harmonic Motion

In its simplest form, simple harmonic motion can be expressed in terms of a displacement, $u(t)$, using trigonometric notation: for example,

$$u(t) = A \sin(\omega t + \phi) \tag{A.1}$$

where A represents the displacement *amplitude*, ω the *circular frequency*, and ϕ the *phase angle*. The time history of this simple harmonic displacement is shown in Figure A.3. The amplitude, A , is occasionally referred to as the *single amplitude* to distinguish it from the *double amplitude* (which represents the peak-to-peak displacement) referred to in some of the older geotechnical earthquake engineering literature. The circular frequency describes the rate of oscillation in terms of radians per unit time, where 2π radians corresponds to one cycle of motion. The phase angle describes the amount of time by which the peaks (and zero points) are shifted from those of a pure sine function, as illustrated in Figure A.4. The displacement will be zero when $\omega t + \phi = 0$ or, consequently, when $t = -\phi/\omega$. A positive phase angle indicates that the motion *leads* the sine function; it *lags* the sine function if the phase angle is negative. The concept of circular frequency is more easily understood by considering the motion of the

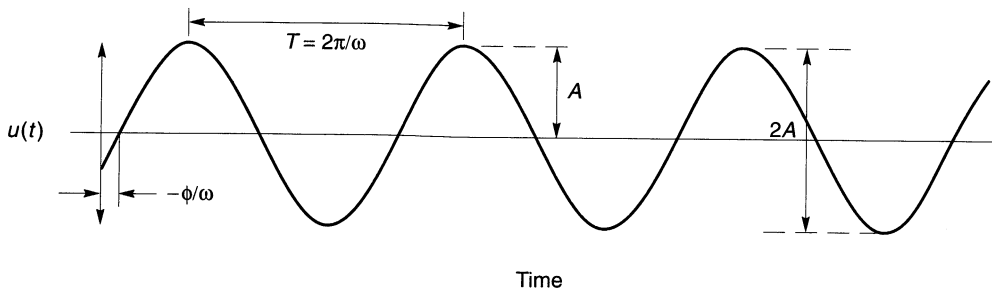


Figure A.3 Time history of simple harmonic displacement.

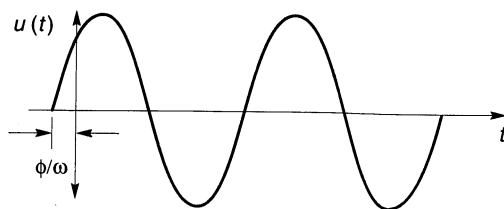


Figure A.4 Influence of phase angle on position of sinusoid.

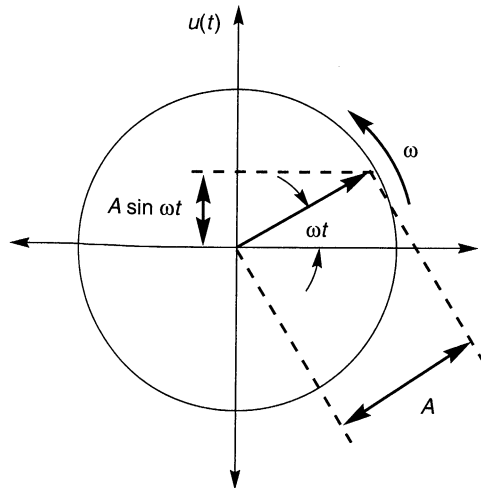


Figure A.5 Rotating vector representation of simple harmonic motion with zero phase angle.

rotating vector of length A shown in Figure A.5. If the vector rotates counterclockwise about its origin at an angular speed, ω , from its initial horizontal position, the displacement, $u(t)$, is given by the vertical component of the vector

$$u(t) = A \sin \omega t$$

The vertical component increases to a maximum value at $\omega t = \pi/2$, then decreases through zero (at $\omega t = \pi$) and reaches its maximum negative value at $\omega t = 3\pi/2$. It continues back to its original position and then repeats the entire process.

The time required for the rotating vector to make one full revolution is the time required for one *cycle* of the motion. This time is referred to as the *period of vibration*, T , and is related to the circular frequency by

$$T = \frac{\text{angular distance for one revolution}}{\text{angular speed}} = \frac{2\pi}{\omega} \quad (\text{A.2})$$

Another common measure of the frequency of oscillation is expressed in terms of the number of cycles that occur in a particular period of time. Since the period of vibration represents the time per cycle, the number of cycles per unit time must be its reciprocal, that is,

$$f = \frac{1}{T} = \frac{\omega}{2\pi} \quad (\text{A.3})$$

which is usually expressed in cycles per second or hertz (abbreviated Hz).

Simple harmonic motion can also be described as the sum of a sine function and a cosine function, that is,

$$u(t) = a \cos \omega t + b \sin \omega t \quad (\text{A.4})$$

As shown in Figure A.6, the sum of the sine and cosine functions is also a sinusoid that oscillates at circular frequency, ω . However, its amplitude is not the simple sum of the amplitudes of the sine and cosine functions, and its peaks do not occur at the same times as those of the sine or cosine functions. The rotating vector representation of this function is illustrated in

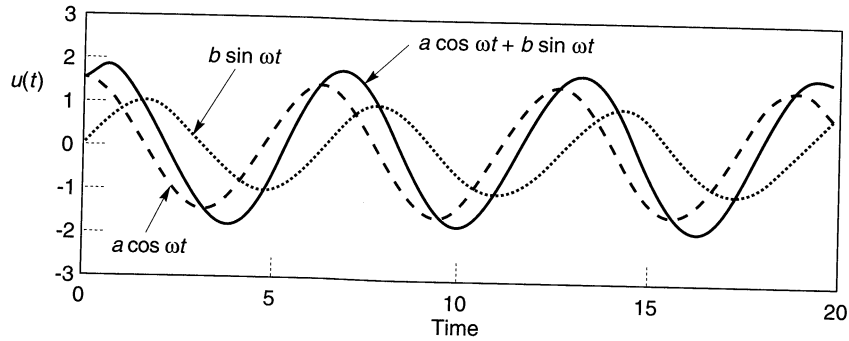


Figure A.6 Summation of sine and cosine functions of the same frequency produces a sinusoid of the same frequency. Amplitude and phase of the sinusoid depends on the amplitudes of the sine and cosine functions.

Figure A.7. Since $\cos \theta = \sin(\theta + 90^\circ)$, the rotating vector of length a must be 90° ahead of the vector of length b . The vertical components of vectors a and b are $a \cos \omega t$ and $b \sin \omega t$, respectively. As illustrated in Figure A.7a, the total value of $u(t)$ is given by $u(t) = a \cos \omega t + b \sin \omega t$. The motion can be expressed in a different form by considering the resultant of vectors a and b , as in Figure A.7b. The length of the resultant will be $\sqrt{a^2 + b^2}$ and it will lead b by an angle $\phi = \tan^{-1}(a/b)$. Accordingly, the vertical component of the resultant is

$$u(t) = A \sin(\omega t + \phi) \tag{A.5}$$

where $A = \sqrt{a^2 + b^2}$ is the amplitude and $\phi = \tan^{-1}(a/b)$ is the phase angle of the motion.

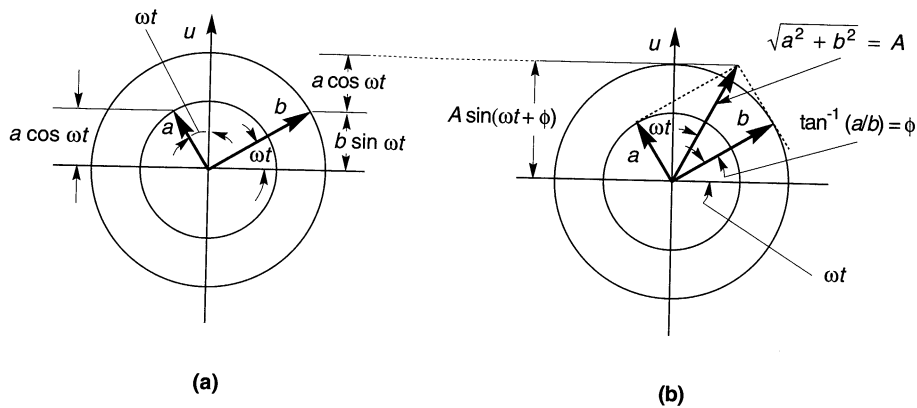


Figure A.7 Rotating vector representation of simple harmonic motion. Sum of vertical components of sine and cosine components in (a) is equal to vertical component of resultant of sine and cosine components in (b).

A.2.2.1 Complex Notation for Simple Harmonic Motion

Trigonometric descriptions of simple harmonic motion use familiar functions that are easy to visualize. For many dynamic analyses, however, the use of trigonometric notation

leads to very long and awkward equations. These analyses become much simpler when motions are described using complex notation (the word *complex* indicates that complex variables are used, not that the notation is particularly complicated). Complex notation can be derived directly from trigonometric notation using *Euler's law*:

$$e^{i\alpha} = \cos \alpha + i \sin \alpha \quad (\text{A.6})$$

where i is the imaginary number $i = \sqrt{-1}$. The quantity $e^{i\alpha}$ is a complex number; it has two parts, a *real part* and an *imaginary part*, which can be written as

$$\text{Re}(e^{i\alpha}) = \cos \alpha$$

$$\text{Im}(e^{i\alpha}) = \sin \alpha$$

Euler's law can be used to show that

$$\cos \alpha = \frac{e^{i\alpha} + e^{-i\alpha}}{2} \quad \sin \alpha = -i \frac{e^{i\alpha} - e^{-i\alpha}}{2} \quad (\text{A.7})$$

Substituting these expressions into the general expression for harmonic motion equation (A.4) gives

$$\begin{aligned} u(t) &= a \frac{e^{i\omega t} + e^{-i\omega t}}{2} - bi \frac{e^{i\omega t} - e^{-i\omega t}}{2} \\ &= \frac{a - ib}{2} e^{i\omega t} + \frac{a + ib}{2} e^{-i\omega t} \end{aligned} \quad (\text{A.8})$$

This form of the displacement may be visualized as a pair of rotating vectors in an *Argand diagram*. An Argand diagram represents a complex number graphically as a vector with orthogonal real and imaginary components. Although usually drawn with the real axis oriented horizontally, the rotated Argand diagram of Figure A.8a will help illustrate how this complex notation describes simple harmonic motion. In the Argand diagram, the term $e^{i\omega t}$

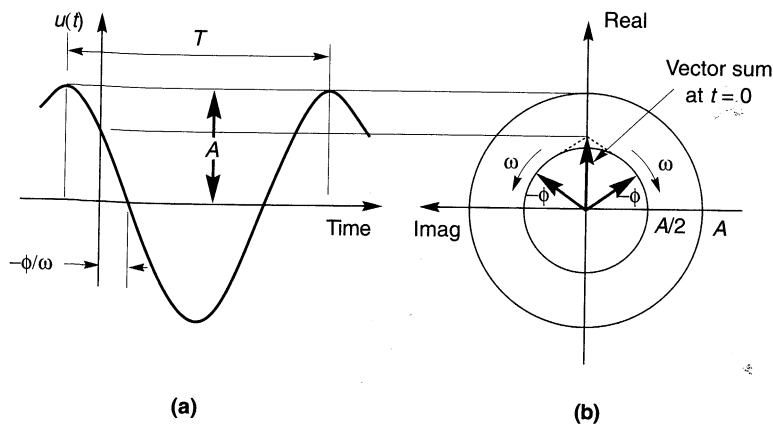


Figure A.8 How counterrotating vectors of length $A/2$ produce simple harmonic motion. Note that the phase angles are measured from the horizontal axis in the direction of vector rotation.

is represented by a vector of unit length rotating clockwise at an angular speed, ω . The term $e^{-i\omega t} = e^{i(-\omega)t}$ therefore can be represented by a unit vector rotating clockwise at angular speed, $-\omega$, which is equivalent to rotating counterclockwise at angular speed, ω . Accordingly, the first term in equation (A.8) can be represented by a vector of real part, $a/2$, and imaginary part, $-b/2$, rotating clockwise at ω , and the second term by another vector with the same real part, but an imaginary part, $b/2$, rotating counterclockwise at ω . The length of each vector is $\sqrt{(a/2)^2 + (b/2)^2} = \frac{1}{2}\sqrt{a^2 + b^2}$. As shown in Figure A.8a, the sum of the vectors is real (the imaginary parts always cancel each other). Figure A.8b shows how the vector sum describes a simple harmonic motion of amplitude $A = \sqrt{a^2 + b^2}$ and circular frequency ω .

A.2.3 Other Measures of Motion

Displacement is not the only parameter that can be used to describe vibratory motion. In fact, other parameters are often of greater interest. If the variation of displacement with time is known, however, the other parameters of interest can be determined. Differentiating the expression for simple harmonic displacement produces expressions for *velocity* and *acceleration*:

$$u(t) = A \sin(\omega t + \phi) \quad \text{displacement} \quad (\text{A.9a})$$

$$\dot{u}(t) = \frac{du}{dt} = \omega A \cos(\omega t + \phi) \quad \text{velocity} \quad (\text{A.9b})$$

$$\ddot{u}(t) = \frac{d^2u}{dt^2} = -\omega^2 A \sin(\omega t + \phi) = -\omega^2 u \quad \text{acceleration} \quad (\text{A.9c})$$

Note that when the *displacement amplitude* is A , the *velocity amplitude* is ωA , and the *acceleration amplitude* is $\omega^2 A$. Thus frequency and the displacement, velocity, and acceleration amplitudes of a harmonic motion are related in such a way that knowledge of the frequency and any one amplitude, or knowledge of any two amplitudes, allows calculation of all other quantities. This important and useful property of harmonic motions allows the use of *tripartite plots*, in which a harmonic motion can be completely described in terms of frequency and displacement, velocity, and acceleration amplitudes by a single point. Tripartite plots, an example of which is shown in Figure A.9, are commonly used to describe earthquake ground motions. It is important to note that these relationships apply only to harmonic motions and that the relationships between displacement, velocity, and acceleration for other types of motion must be obtained by differentiation and/or integration.

Examination of equations (A.8) reveals that in addition to having different amplitudes, the displacement, velocity, and acceleration are out of phase with each other (Figure A.10). The velocity can be seen to lead the displacement by $\pi/2$ radians, or 90° , and the acceleration to lead the velocity by the same amount. The relationships between displacement, velocity, and acceleration for harmonic motions, in both trigonometric and complex notation, are

$$u(t) = A \sin \omega t \quad u(t) = A e^{i\omega t} \quad (\text{A.10a})$$

$$\dot{u}(t) = \omega A \cos \omega t = \omega A \sin(\omega t + \pi/2) \quad \dot{u}(t) = i\omega A e^{i\omega t} \quad (\text{A.10b})$$

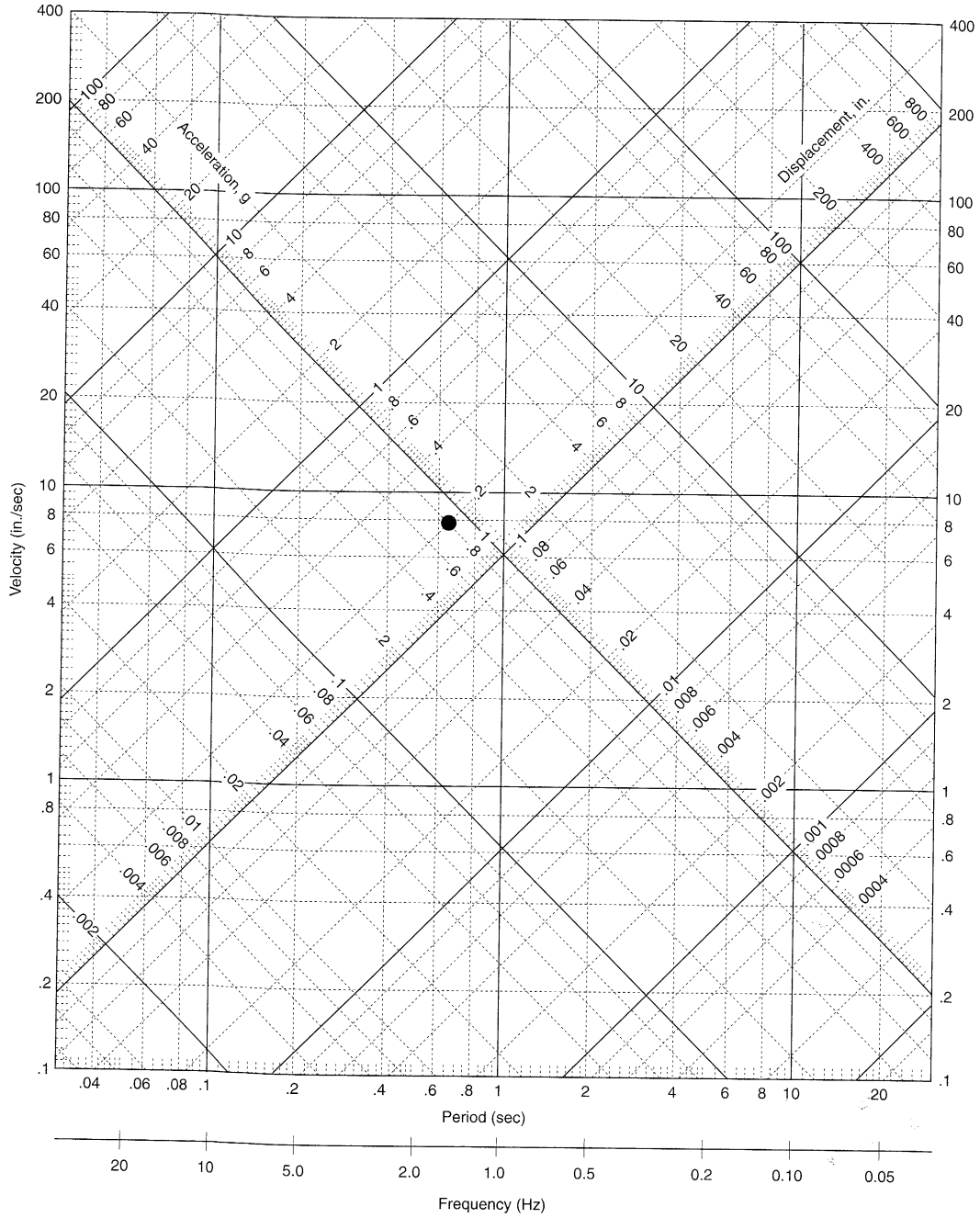


Figure A.9 Tripartite plot for harmonic motion. Point at center describes harmonic motion at a period of 0.65 sec with displacement amplitude of 0.8 in., velocity amplitude of 8.0 in./sec, and acceleration amplitude of 0.20g. (After Richart, et al., 1970.)

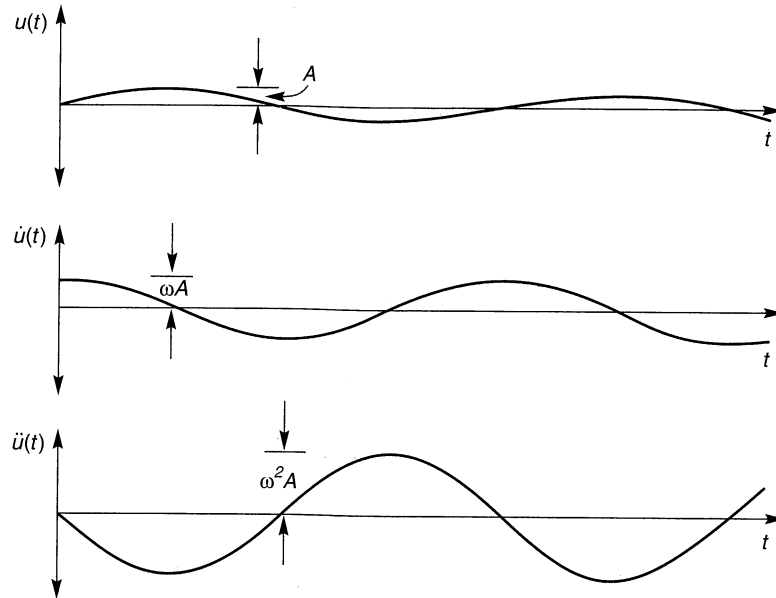


Figure A.10 Time histories of displacement, velocity, and acceleration. Note that acceleration leads velocity by one-quarter cycle and displacement by one-half cycle.

$$\ddot{u}(t) = -\omega^2 A \sin \omega t = \omega^2 A \sin(\omega t + \pi) \quad \ddot{u}(t) = i^2 \omega^2 A e^{i\omega t} = -\omega^2 A e^{i\omega t} \quad (\text{A.10c})$$

The relationship between harmonic displacements, velocities, and accelerations can be visualized in terms of three vectors rotating counterclockwise at an angular speed ω (Figure A.11). The acceleration vector is 90° (or $\pi/2$ radians) ahead of the velocity vector and 180° (or π radians) ahead of the displacement vector.

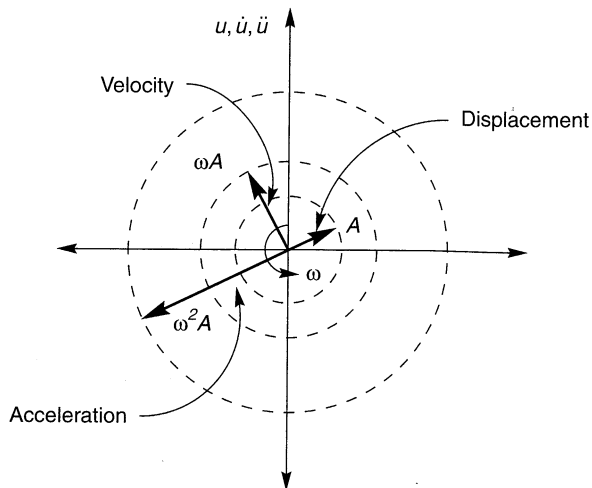


Figure A.11 Rotating vector representation of displacement, velocity, and acceleration. Note how acceleration leads velocity by 90° and displacement by 180° .

A.3 FOURIER SERIES

While studying heat flow problems in the early nineteenth century, the French mathematician J. B. J. Fourier showed that any periodic function that meets certain conditions can be expressed as the sum of a series of sinusoids of different amplitude, frequency, and phase. Since the conditions for existence of a Fourier series are nearly always met for functions that accurately describe physical processes (Ramirez, 1985), it is an extraordinarily useful tool in many branches of science and engineering.

Geotechnical earthquake engineering is no exception. By breaking down a complicated loading function such as that imposed by an earthquake ground motion into the sum of a series of simple harmonic loading functions, the principle of superposition allows available solutions for harmonic loading to be used to compute the total response (provided that the system is linear), as illustrated schematically in Figure A.12.

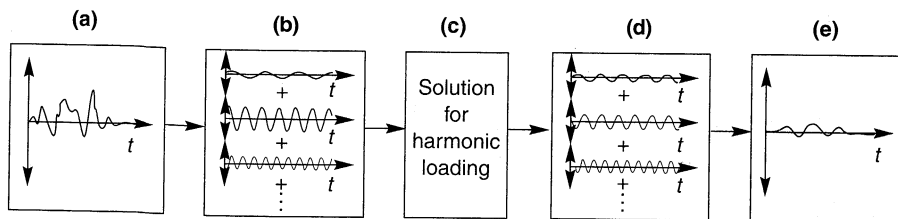


Figure A.12 Process by which Fourier series representation of complicated loading can allow relatively simple solutions for harmonic loading to be used to produce the total response: (a) time history of loading; (b) representation of time history of loading as sum of series of harmonic loads; (c) calculation of response for each harmonic load; (d) representation of response as sum of series of harmonic responses; (e) summation of harmonic responses to produce time history of response.

A.3.1 Trigonometric Form

Since a Fourier series is simply a summation of simple harmonic functions, it can be expressed using either trigonometric notation or complex notation. The general trigonometric form of the Fourier series for a function of period, T_f , is

$$x(t) = a_0 + \sum_{n=1}^{\infty} (a_n \cos \omega_n t + b_n \sin \omega_n t) \quad (\text{A.11})$$

where the *Fourier coefficients* are

$$a_0 = \frac{1}{T_f} \int_0^{T_f} x(t) dt$$

$$a_n = \frac{2}{T_f} \int_0^{T_f} x(t) \cos \omega_n t dt$$

$$b_n = \frac{2}{T_f} \int_0^{T_f} x(t) \sin \omega_n t dt$$

and $\omega_n = 2\pi n/T_f$. The term a_0 represents the average value of $x(t)$ over the range $t = 0$ to $t = T_f$; its value is zero in many geotechnical earthquake engineering applications. Note that the frequencies, ω_n , are not arbitrary; rather, they are evenly spaced at a constant frequency increment, $\Delta\omega = 2\pi/T_f$.

Example A.1

The Fourier coefficients are not difficult to calculate for simple functions. Consider the square-wave function shown in Figure EA.1. Over its period, T_f , the square wave is described by

$$x(t) = \begin{cases} +A & 0 < t \leq \frac{T_f}{4} \\ -A & \frac{T_f}{4} < t \leq \frac{3T_f}{4} \\ +A & \frac{3T_f}{4} < t \leq T_f \end{cases}$$

Since the average value of $x(t)$ is easily seen to be zero, the coefficient $a_0 = 0$. The value of a_1 can be computed as

$$\begin{aligned} a_1 &= \frac{2}{T_f} \int_0^{T_f} x(t) \cos \omega_1 t \, dt \\ &= \frac{2}{T_f} \left[A \int_0^{T_f/4} \cos \omega_1 t \, dt - A \int_{T_f/4}^{3T_f/4} \cos \omega_1 t \, dt + A \int_{3T_f/4}^{T_f} \cos \omega_1 t \, dt \right] \\ &= \frac{2A}{\omega_1 T_f} \left[\sin \frac{\omega_1 T_f}{4} - \left(\sin \frac{3\omega_1 T_f}{4} - \sin \frac{\omega_1 T_f}{4} \right) + \left(\sin \omega_1 T_f - \sin \frac{3\omega_1 T_f}{4} \right) \right] \end{aligned}$$

Substituting $\omega_1 T_f = 2\pi$ yields

$$a_1 = \frac{A}{\pi} (1 + 2 + 1) = \frac{4A}{\pi}$$

Repeating for all n yields

$$a_n = \begin{cases} \frac{+4A}{n\pi} & n = 1, 5, 9, \dots \\ \frac{-4A}{n\pi} & n = 3, 7, 11, \dots \\ 0 & n = \text{even integers} \end{cases}$$

$$b_n = 0 \quad \text{all } n$$

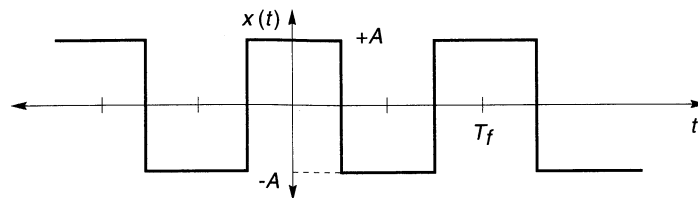


Figure EA.1 Square-wave function.

so the Fourier series is

$$x(t) = \frac{4A}{\pi} \left(\cos \omega_1 t - \frac{1}{3} \cos 3\omega_1 t + \frac{1}{5} \cos 5\omega_1 t - \frac{1}{7} \cos 7\omega_1 t + \dots \right)$$

where $\omega_1 = 2\pi/T_f$. The sine terms are all zero because the square wave, like the cosine function, is an *even function* [i.e., one for which $f(t) = f(-t)$]. For an *odd function* [$f(t) = -f(-t)$], the cosine terms are zero. For a function that is neither even nor odd, the Fourier series will contain both sine and cosine terms.

The Fourier series represents a function exactly only for $n = \infty$. If the series is truncated at some finite value of n , the Fourier series only approximates the function. For many functions, however, the approximation can be quite good even when n is relatively small. This characteristic is often used to great advantage in dynamic analyses of soils and structures.

From equations (A.5) and (A.11), it is apparent that the Fourier series can also be expressed as

$$x(t) = c_0 + \sum_{n=1}^{\infty} c_n \sin(\omega_n t + \phi_n) \quad (\text{A.12})$$

where $c_0 = a_0$, $c_n = \sqrt{a_n^2 + b_n^2}$, and $\phi_n = \tan^{-1}(a_n/b_n)$. In this form, c_n and ϕ_n are the amplitude and phase, respectively, of the n th harmonic. A plot of c_n versus ω_n is known as a Fourier amplitude spectrum; a plot of ϕ_n versus ω_n gives a Fourier phase spectrum. Fourier amplitude spectra are very useful in geotechnical earthquake engineering—as discussed in Chapter 3, they effectively describe the frequency content of an earthquake motion.

Example A.2

The Fourier amplitude and phase spectra for the square wave of Example A.1 are easily determined. The values of c_n and ϕ_n for the first eight terms of the series are

$$\begin{aligned} c_0 &= 0 \\ c_1 &= \frac{4A}{\pi} & \phi_1 &= \frac{\pi}{2} \\ c_2 &= 0 \\ c_3 &= \frac{4A}{3\pi} & \phi_3 &= \frac{-\pi}{2} \\ c_4 &= 0 \\ c_5 &= \frac{4A}{5\pi} & \phi_5 &= \frac{\pi}{2} \\ c_6 &= 0 \\ c_7 &= \frac{4A}{7\pi} & \phi_7 &= \frac{-\pi}{2} \end{aligned}$$

The spectra are plotted in Figure EA.2.

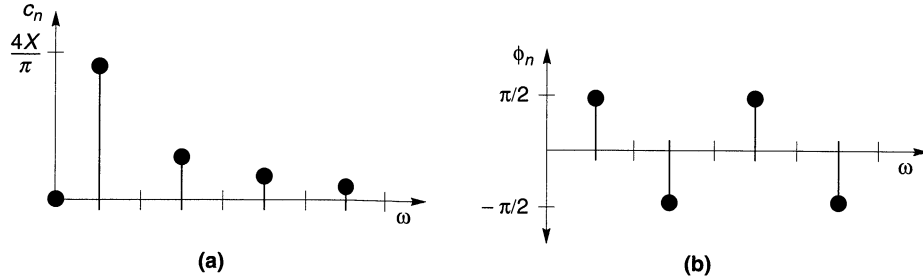


Figure EA.2 Fourier spectra for square wave of Example A.1: (a) Fourier amplitude spectrum; (b) Fourier phase spectrum.

A.3.2 Exponential Form

The Fourier series can also be expressed in exponential form. Substituting Equations A.7 into A.10 for all n gives

$$x(t) = a_0 + \sum_{n=1}^{\infty} \left(\frac{a_n - ib_n}{2} e^{i\omega_n t} + \frac{a_n + ib_n}{2} e^{-i\omega_n t} \right) \quad (\text{A.13})$$

Defining new Fourier coefficients,

$$\begin{aligned} c_0^* &= a_0 \\ c_n^* &= \frac{a_n - ib_n}{2} \\ c_{-n}^* &= \frac{a_n + ib_n}{2} \end{aligned}$$

where the $*$ indicates the complex nature of the coefficient, the Fourier series can be rewritten as

$$x(t) = c_0^* + \sum_{n=1}^{\infty} (c_n^* e^{i\omega_n t} + c_{-n}^* e^{-i\omega_n t}) \quad (\text{A.14})$$

Since $\omega_{-n} = -\omega_n$, the limits of summation can be changed to write the Fourier series in the more compact form

$$x(t) = \sum_{n=-\infty}^{\infty} c_n^* e^{i\omega_n t} \quad (\text{A.15})$$

The complex Fourier coefficients, c_n^* , can be determined directly from $x(t)$ as

$$c_n^* = \frac{1}{T_f} \int_0^{T_f} x(t) e^{-i\omega_n t} dt \quad (\text{A.16})$$

Example A.3

Compute the complex Fourier coefficients for the square wave of Example A.1.

Solution Since the average value of the square wave is zero, $c_0^* = 0$. For $n = +1$, equation (A.16) gives

$$\begin{aligned} c_1^* &= \frac{1}{T_f} \left[X \int_0^{T_f/4} e^{i\omega_1 t} dt - X \int_{T_f/4}^{3T_f/4} e^{i\omega_1 t} dt + X \int_{3T_f/4}^{T_f} e^{i\omega_1 t} dt \right] \\ &= \frac{X}{i\omega_1 T_f} [e^{i\omega_1 T_f/4} - (e^{i3\omega_1 T_f/4} - e^{i\omega_1 T_f/4}) + (e^{i\omega_1 T_f} - e^{i3\omega_1 T_f/4})] \\ &= \frac{X}{i2\pi} (2e^{i\pi/2} - 2e^{i3\pi/2} + e^{i2\pi}) \\ &= \frac{X}{i2\pi} (2i + 2i + 0) = \frac{2X}{\pi} \end{aligned}$$

Note that although $c_0^* = c_0 = a_0$, the definitions of c_n^* and c_{-n}^* indicate that

$$\begin{aligned} |c_n^*| &= \sqrt{[\operatorname{Re}(c_n^*)]^2 + [\operatorname{Im}(c_n^*)]^2} = \sqrt{\left(\frac{a_n}{2}\right)^2 + \left(\frac{b_n}{2}\right)^2} = \frac{\sqrt{a_n^2 + b_n^2}}{2} = \frac{c_n}{2} \\ |c_{-n}^*| &= \sqrt{[\operatorname{Re}(c_{-n}^*)]^2 + [\operatorname{Im}(c_{-n}^*)]^2} = \sqrt{\left(\frac{a_n}{2}\right)^2 + \left(\frac{b_n}{2}\right)^2} = \frac{\sqrt{a_n^2 + b_n^2}}{2} = \frac{c_n}{2} \end{aligned} \quad (\text{A.17})$$

(i.e., in exponential form, half of the amplitude is associated with positive frequencies and half with negative frequencies). The phase angles at positive and negative frequencies are equal but of opposite sign; consequently, the imaginary parts cancel each other [as they must if $x(t)$ is a real function]. The complex Fourier coefficients are sometimes (although rarely in geotechnical earthquake engineering applications) used to plot *two-sided spectra* which are related to the more conventional *one-sided spectra* as shown in Figure EA.3.

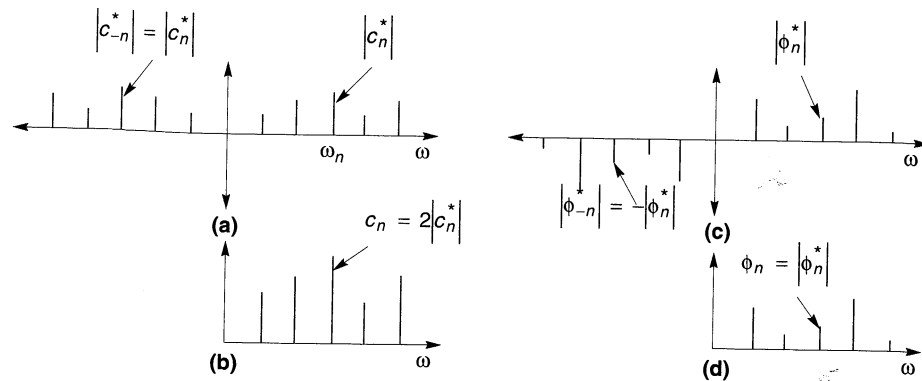


Figure EA.3 Comparison of one- and two-sided Fourier spectra. The two-sided Fourier amplitude spectrum (a) is symmetrical with amplitudes on each side of the $\omega = 0$ axis equal to half the amplitude of the one-sided spectrum (b). (The amplitude at $\omega = 0$ is the same for both.) The two-sided phase spectrum (c) is antisymmetric, but phase at positive frequencies is equal to phase of one-sided spectrum (d).

A.3.3 Discrete Fourier Transform

In many geotechnical earthquake engineering applications, loading or motion parameters are described by a finite number of data points rather than by an analytical function. In such cases the Fourier coefficients are obtained by summation rather than integration. For a variable $x(t_k)$, $k = 1, N$, where $t_k = k \Delta t$, the *discrete Fourier transform* (DFT) is given by

$$X(\omega_n) = \Delta t \sum_{k=1}^N x(t_k) e^{-i\omega_n t_k} \quad (\text{A.18a})$$

where $\omega_n = n \Delta \omega = 2\pi n / N \Delta t$. Using Euler's law, the DFT can also be written as

$$X(\omega_n) = \Delta t \sum_{k=1}^N [x(t_k) \cos \omega_n t_k - ix(t_k) \sin \omega_n t_k] \quad (\text{A.18b})$$

Note that the Fourier coefficients of the DFT have units of the original variable multiplied by time.

The DFT can also be inverted; that is, a set of data spaced at equal frequency intervals, $\Delta \omega$, can be expressed as a function of time, using the *inverse discrete Fourier transform* (IDFT):

$$x(t_k) = \Delta \omega \sum_{n=1}^N X(\omega_n) e^{i\omega_n t_k} \quad (\text{A.19a})$$

or

$$x(t_k) = \Delta \omega \sum_{n=1}^N [X(\omega_n) \cos \omega_n t_k + iX(\omega_n) \sin \omega_n t_k] \quad (\text{A.19b})$$

Either of these expressions can easily be programmed on a personal computer; since n takes on N different values, the summation operation will be performed N times. The time required for computation of a DFT (or IDFT), therefore, is proportional to N^2 .

A.3.4 Fast Fourier Transform

The DFT was developed long before computers were available, and its use, for even modest values of N , was extremely labor intensive. As early as 1805, the beginning of a more efficient approach to the DFT was described (Brigham, 1974). As digital computers were developed in the 1960s, Cooley and Tukey (1965) developed a computational algorithm for the case where N is a power of 2 that has become known as the *fast Fourier transform* (FFT). By performing repeated operations on groups that start with a single number and increase in size by a factor of 2 at each of j stages (where $N = 2^j$), the time required to complete the transform is proportional to $N \log_2 N$. Consequently, the FFT is much more efficient than the DFT. For example, at $N = 2048$, the FFT is more than 180 times faster than the DFT. The *inverse fast Fourier transform* (IFFT) operates with equal speed.

A.3.5 Power Spectrum

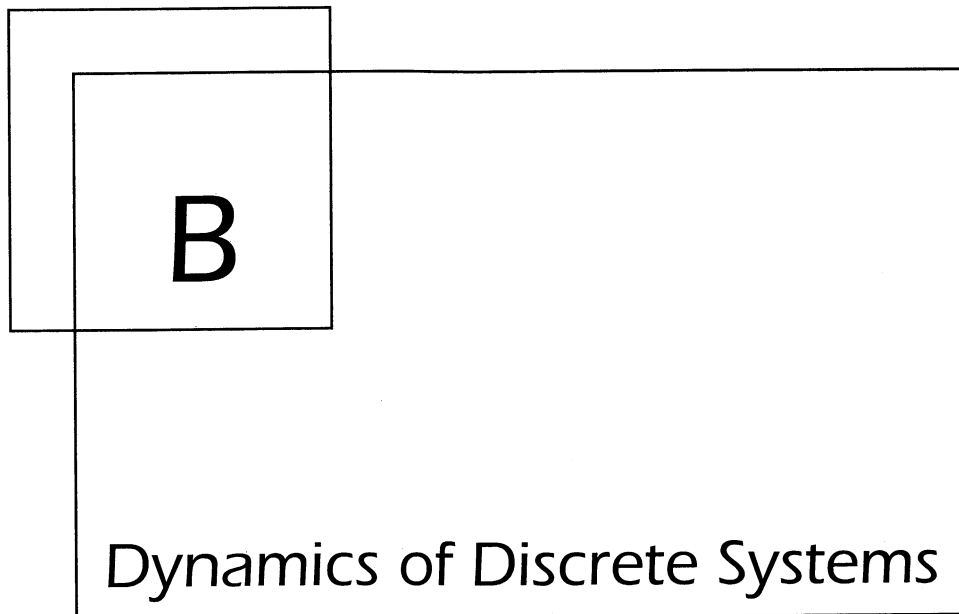
The Fourier amplitude spectrum illustrates how the strength of a quantity varies with frequency. This information can also be expressed in terms of *power*. The power of a signal, $x(t)$, that can be expressed in the form of equation (A.11) or (A.12), is defined as

$$P(\omega_n) = \frac{1}{2}(a_n^2 + b_n^2) = \frac{1}{2}c_n^2$$

Note that this definition of power can be applied to any signal (it is not related to mechanical—force times velocity—power). Power can be plotted as a function of frequency to obtain a power spectrum. The total power of the signal is the same whether it is computed in the time domain or the frequency domain:

$$\text{total power} = \sum_{n=1}^{\infty} P(\omega_n) = \int_0^{T_f} [x(t)]^2 dt = \frac{1}{2} \int_0^{\omega_n} c_n^2 d\omega$$

Power spectra are often used to describe earthquake-induced ground motions.



B.1 INTRODUCTION

Many vibrating systems consist of discrete elements such as masses and springs, or can at least be idealized as such. For most practical problems of structural dynamics, the structure is idealized as a system of rigid masses connected by massless springs. Even continuous systems such as soil deposits have been idealized as assemblages of many discrete elements, though that approach is seldom taken any more. Since the geotechnical earthquake engineer often provides input to the structural engineer, a firm understanding of the dynamic response of discrete systems is required. Also, many of the concepts and terminologies used in geotechnical earthquake engineering analyses are analogous to those of discrete system dynamics and are more easily introduced in that framework.

This appendix introduces the dynamics of discrete systems. It begins with very simple systems, and adds complicating factors such as damping, base motion, and nonlinearity. Analytical and numerical solutions in the time domain and frequency domain are presented. Finally, the response of multiple-degree-of-freedom systems is introduced. While many of the basic concepts of structural dynamics are presented, much more complete treatments may be found in a number of structural dynamics texts (e.g., Clough and Penzien, 1975; Paz, 1980; Berg, 1989; Chopra, 1995).

B.2 VIBRATING SYSTEMS

Vibrating systems can be divided into two broad categories: *rigid systems* and *compliant systems*. A rigid system is one in which no strains occur. All points within a rigid system move in phase with each other, and the description of rigid-body motion is a relatively simple matter of kinematics. In compliant systems, however, different points within the system may move differently (and out of phase) from each other. A given physical system may behave very nearly as a rigid system under certain conditions and as a compliant system under other conditions. Since neither soils nor structures are rigid, the dynamic response of compliant systems is central to the study of soil and structural dynamics and to earthquake engineering.

Compliant systems can be characterized by the distribution of their mass. *Discrete systems* are those whose mass can be considered to be concentrated at a finite number of locations, where the mass of a *continuous system* is distributed throughout the system. The number of independent variables required to describe the position of all the significant masses of a system is the number of *dynamic degrees of freedom* of the system. Systems of interest in earthquake engineering may have anywhere from 1 to an infinite number of degrees of freedom. Figure B.1 illustrates several commonly encountered systems with varying numbers of degrees of freedom (DOF). Discrete systems have a finite number of degrees of freedom; the number of degrees of freedom of a continuous system is infinite. Certain types of analyses idealize continuous systems as discrete systems with large numbers of degrees of freedom, and other types represent discrete systems with many degrees of freedom as continuous systems.

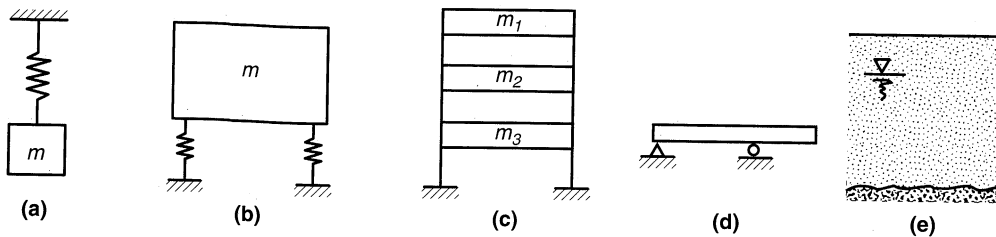


Figure B.1 Vibrating systems with various numbers of degrees of freedom: (a) one DOF, vertical translation; (b) two DOF, vertical translation and rocking; (c) three DOF, horizontal translation; (d) infinite DOF; (e) infinite DOF.

B.3 SINGLE-DEGREE-OF-FREEDOM SYSTEMS

A discrete system whose position can be described completely by a single variable is known as a *single-degree-of-freedom* (SDOF) system. That single degree of freedom may represent translational displacement, as in the SDOF systems of Figure B.2a–c, or rotational displacement, as in the case of the pendulum of Figure B.2d.

A typical SDOF system is one in which a rigid *mass*, m , is connected in parallel to a *spring* of stiffness, k , and a *dashpot* of viscous damping coefficient, c , and subjected to some external load, $Q(t)$, as shown in Figure B.3. The spring and dashpot are assumed to be massless and the displacement origin to coincide with the static equilibrium position.

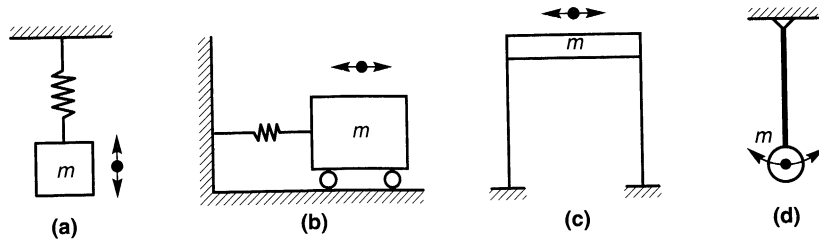


Figure B.2 Various SDOF systems. The degrees of freedom are (a) vertical translation, (b) and (c) horizontal translation, and (d) rotation.

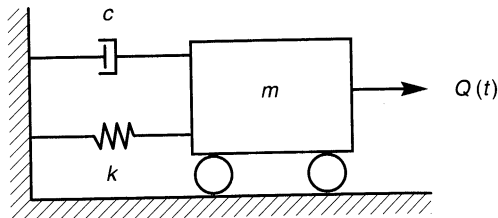


Figure B.3 Damped SDOF system subjected to external dynamic load, $Q(t)$.

B.4 EQUATION OF MOTION FOR SDOF SYSTEM

Many SDOF systems are acted upon by externally applied loads. In earthquake engineering, dynamic loading often results from another source—movement of the supports of the system. The dynamic response of a SDOF system such as that shown in Figure B.3 is governed by an *equation of motion*. The equation of motion can be derived in a number of ways; a simple, force equilibrium approach will be used here.

B.4.1 Equation of Motion: External Loading

When a dynamic load is applied to the mass of a SDOF system (Figure B.3), the tendency for motion is resisted by the inertia of the mass and by forces that develop in the dashpot and spring. Thus the external load, $Q(t)$, acting in the positive x -direction is opposed by three forces (Figure B.4) that act in the negative x -direction: the *inertial force*, f_i , the *viscous damping force*, f_D , and the *elastic spring force*, f_S . The equation of motion can be expressed in terms of the dynamic equilibrium of these forces:

$$f_i(t) + f_D(t) + f_S(t) = Q(t) \tag{B.1}$$

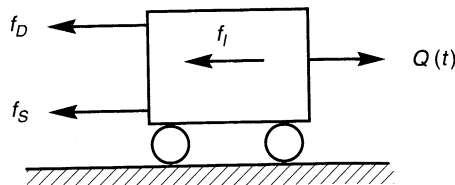


Figure B.4 Dynamic forces acting on mass from Figure B.3.

These forces can also be expressed in terms of the motion of the mass. Newton's second law states that the inertial force acting on a mass is equal to its rate of change of momentum, which for a system of constant mass produces

$$f_I(t) = \frac{d}{dt} \left(m \frac{du(t)}{dt} \right) = m \frac{d^2 u(t)}{dt^2} = m\ddot{u}(t) \quad (\text{B.2a})$$

For a viscous dashpot, the damping force is proportional to the velocity of the mass:

$$f_D(t) = c \frac{du(t)}{dt} = c\dot{u}(t) \quad (\text{B.2b})$$

and the force provided by the spring is simply the product of its stiffness and the amount by which it is displaced

$$f_S(t) = ku(t) \quad (\text{B.2c})$$

The behavior of these forces is illustrated graphically in Figure B.5. The inertial force is proportional to the acceleration and the constant of proportionality is the mass. Similarly, the viscous damping force and the elastic spring force are proportional to the velocity and displacement with the damping and spring coefficients serving as the respective constants of proportionality.

Substituting equations (B.2) into equation (B.1), the equation of motion for the SDOF system can be written as

$$m\ddot{u}(t) + c\dot{u}(t) + ku(t) = Q(t) \quad (\text{B.3})$$

This second-order differential equation is commonly used to describe the behavior of oscillating systems ranging from the mechanical systems considered in earthquake engineering problems to electrical circuits. The differential equation of motion is linear (i.e., all of its terms have constant coefficients). This linearity allows a closed-form analytical solution to be readily obtained and, importantly, it allows the principle of superposition to be used. When any of the coefficients are not constant, the behavior is not linear and the solution becomes considerably more difficult. In most cases, the response of nonlinear systems must be evaluated numerically (Section B.7).

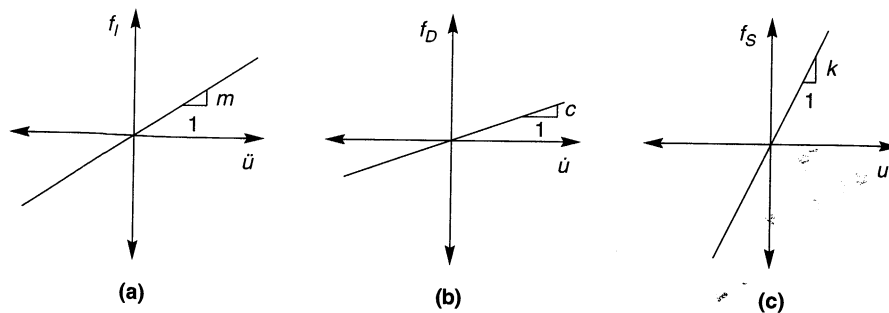


Figure B.5 Variation of (a) inertial, (b) viscous, and (c) elastic forces with acceleration, velocity, and displacement, respectively.

B.4.2 Equation of Motion: Vibration of Supports (Base Shaking)

For earthquake engineering problems, dynamic loading often results from vibration of the supports of a system rather than from dynamic external loads. To evaluate the response of such systems, it is necessary to develop an equation of motion for loading caused by base shaking. Consider the damped SDOF system shown in Figure B.6a. When subjected to dynamic base shaking, $u_b(t)$, it will deform into a configuration that might look like that shown in Figure B.6b at a particular time, t . The total displacement of the mass, $u_t(t)$, can be broken down as the sum of the base displacement, $u_b(t)$, and the displacement of the mass relative to the base, $u(t)$. The inertial force will depend on the total acceleration of the mass, while the viscous damping and elastic spring forces will depend on the relative velocity and displacement, respectively. Using the notation shown in Figure B.6b, the equation of motion can be written as

$$m\ddot{u}_t + c\dot{u} + ku = 0$$

or substituting $\ddot{u}_t(t) = \ddot{u}_b(t) + \ddot{u}(t)$ and rearranging,

$$m\ddot{u} = c\dot{u} + ku = -m\ddot{u}_b \tag{B.4}$$

In other words, the response of the system to base shaking is equivalent to the response that the system would have if its base was fixed and the mass was subjected to an external load $Q(t) = -m\ddot{u}_b(t)$. Thus any solutions for the response of an SDOF system subjected to external load can be used to evaluate the response of the system to base shaking.

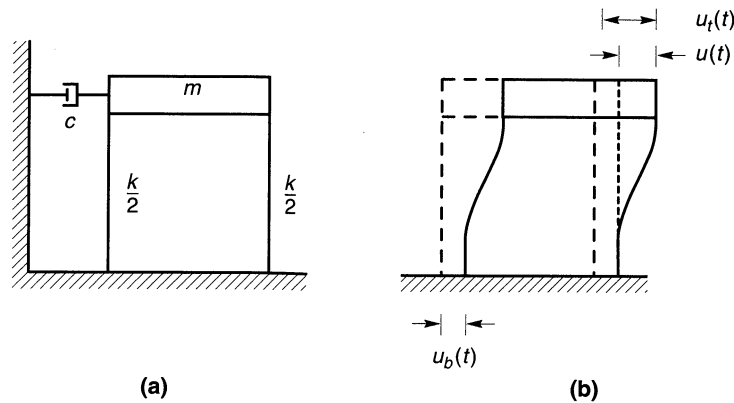


Figure B.6 Damped SDOF system subjected to base shaking.

B.5 RESPONSE OF LINEAR SDOF SYSTEMS

In order to evaluate the dynamic response of a linear SDOF system, the differential equation of motion must be solved. There are several types of conditions under which the dynamic response of SDOF systems are commonly calculated. *Forced vibration* occurs when the mass

is subjected to some external loading, $Q(t)$. The loading may be periodic or nonperiodic and it may correspond to an actual physical force applied to the mass or to some known level of base shaking. *Free vibration* occurs in the absence of external loading or base shaking. It may result from the release of the mass from some initial displacement or may occur after some transient forced vibration has ended. The following sections will develop solutions to the equation of motion for cases in which damping is and is not present, and for cases in which external loading is and is not present. The resulting four permutations of these conditions are

1. Undamped free vibrations: $c = 0, Q(t) = 0$
2. Damped free vibrations: $c > 0, Q(t) = 0$
3. Undamped forced vibrations: $c = 0, Q(t) \neq 0$
4. Damped forced vibrations: $c > 0, Q(t) \neq 0$

The solution of the equation of motion for each of these conditions will be presented in turn.

B.5.1 Undamped Free Vibrations

A SDOF system undergoes free vibration when it oscillates without being acted upon by any external loads. When damping is not present ($c = 0$) the equation of motion (for undamped free vibration) reduces to

$$m\ddot{u} + ku = 0 \quad (\text{B.5})$$

or after dividing both sides by the mass,

$$\ddot{u} + \frac{k}{m}u = 0 \quad (\text{B.6})$$

The solution to this simple differential equation can be found in any elementary text on differential equations as

$$u = C_1 \sin \sqrt{\frac{k}{m}}t + C_2 \cos \sqrt{\frac{k}{m}}t \quad (\text{B.7})$$

where the values of the constants C_1 and C_2 depend on the initial conditions of the system. The quantity $\sqrt{k/m}$ is very important—it represents the *undamped natural circular frequency* of the system

$$\omega_0 = \sqrt{\frac{k}{m}} \quad (\text{B.8})$$

Then the *natural frequency*, f_0 , and *natural period of vibration*, T_0 , can be written as

$$f_0 = \frac{\omega_0}{2\pi} = \frac{1}{2\pi} \sqrt{\frac{k}{m}} \quad (\text{B.9})$$

$$T_0 = \frac{2\pi}{\omega_0} = 2\pi \sqrt{\frac{m}{k}} \quad (\text{B.10})$$

Substituting equation (B.8) into the solution for the equation of motion [equation (B.7)] yields

$$u = C_1 \sin \omega_0 t + C_2 \cos \omega_0 t \quad (\text{B.11})$$

which indicates that an undamped system in free vibration will oscillate harmonically at its undamped natural frequency. C_1 and C_2 , can be evaluated by assuming the initial ($t = 0$) conditions to be represented by an initial displacement, u_0 , and initial velocity, \dot{u}_0 . Then

$$\begin{aligned} u_0 &= C_1 \sin(0) + C_2 \cos(0) = C_2 \\ \dot{u}_0 &= \omega_0 C_1 \cos(0) - \omega_0 C_2 \sin(0) = \omega_0 C_1 \end{aligned}$$

Therefore, $C_1 = \dot{u}_0/\omega_0$ and $C_2 = u_0$, so the complete solution to the undamped free vibration response of an SDOF system is given by

$$u = \frac{\dot{u}_0}{\omega_0} \sin \omega_0 t + u_0 \cos \omega_0 t \quad (\text{B.12})$$

The response of such a system is shown in Figure B.7.

Referring back to equation (A.5), the free vibration response can also be expressed as

$$u = A \sin(\omega_0 t + \phi) \quad (\text{B.13})$$

where the amplitude, A , and phase angle, ϕ , are given by

$$\begin{aligned} A &= \sqrt{u_0^2 + \left(\frac{\dot{u}_0}{\omega_0}\right)^2} \\ \phi &= \tan^{-1} \frac{u_0 \omega_0}{\dot{u}_0} \end{aligned}$$

The solution to the equation of motion of an undamped system indicates that the response of the system depends on its initial displacement and velocity. Note that the amplitude remains constant with time. Because no energy is lost in an undamped system, it will continue to oscillate forever. Obviously, truly undamped systems do not exist in the real world; however, some systems can have such low damping that their response over short periods of time may approximate that of an undamped system.

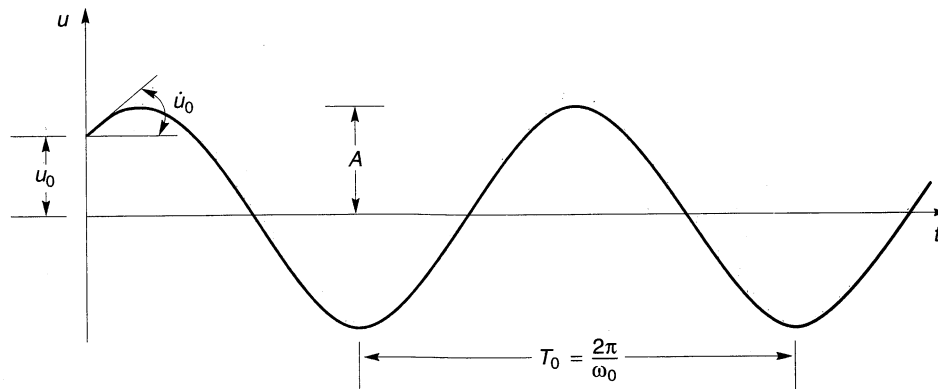


Figure B.7 Time history of displacement for undamped free vibration with initial displacement u_0 and initial velocity \dot{u}_0 .

Example B.1

The SDOF structure shown in Figure EB.1a consists of a 10-kip weight supported by a massless column. Application of a 5-kip static horizontal force to the weight produces a horizontal deflection of 0.04 in. Compute (a) the natural circular frequency, (b) the natural period of vibration, and (c) the time history of response if the horizontal force was suddenly removed.

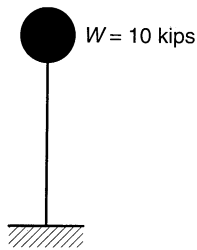


Figure EB.1a

Solution (a) The problem statement indicates that the stiffness of the column is

$$k = \frac{5 \text{ kips}}{0.04 \text{ in.}} = 125 \text{ kips/in.}$$

The natural circular frequency is given by

$$\omega_0 = \sqrt{\frac{k}{m}} = \sqrt{\frac{kg}{W}} = \sqrt{\frac{(125 \text{ kips/in.})(12 \text{ in./ft})(32.2 \text{ ft/sec}^2)}{10 \text{ kips}}} = 69.5 \text{ rad/sec}$$

(b) The natural period would be

$$T_0 = \frac{2\pi}{\omega_0} = \frac{2\pi \text{ rad}}{69.5 \text{ rad/sec}} = 0.09 \text{ sec}$$

(c) The horizontal force produced a static deflection of 0.04 in. Consequently, the initial conditions for free vibration would be

$$u_0 = 0.04 \text{ in.} \quad \dot{u}_0 = 0$$

Then

$$u(t) = \frac{\dot{u}_0}{\omega_0} \sin \omega_0 t + u_0 \cos \omega_0 t = (0.04 \text{ in.}) \cos (69.5t)$$

The response is plotted in Figure EB.1b.

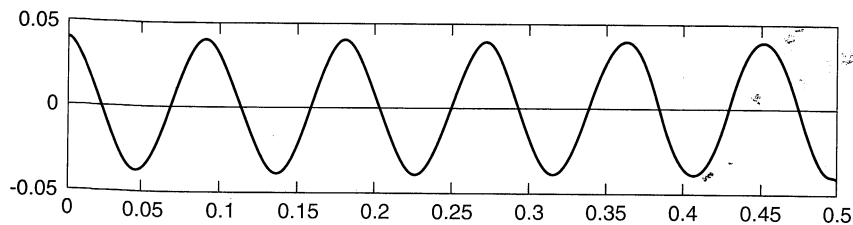


Figure EB.1b

B.5.2 Damped Free Vibrations

In real systems, energy may be lost as a result of friction, heat generation, air resistance, or other physical mechanisms. Hence the free vibration response of a damped SDOF system will diminish with time. For damped free vibrations, the equation of motion is written as

$$m\ddot{u} + c\dot{u} + ku = 0 \quad (\text{B.14})$$

or, dividing by m and substituting [from equation (B.17)] $k = m\omega_0^2$, we have

$$\ddot{u} + 2\frac{c}{2\sqrt{km}}\omega_0 u + \omega_0^2 u = 0 \quad (\text{B.15})$$

The quantity $2\sqrt{km}$, called the *critical damping coefficient*, c_c , allows the *damping ratio*, ξ , to be defined as the ratio of the damping coefficient to the critical damping coefficient, that is,

$$\xi = \frac{c}{c_c} = \frac{c}{2\sqrt{km}} = \frac{c}{2m\omega_0} = \frac{c\omega_0}{2k} \quad (\text{B.16})$$

With this notation, the equation of motion can be expressed as

$$\ddot{u} + 2\xi\omega_0\dot{u} + \omega_0^2 u = 0 \quad (\text{B.17})$$

The solution of this differential equation of motion depends on the value of the damping ratio. When $\xi < 100\%$ ($c < c_c$), the system is said to be *underdamped*. When $\xi = 100\%$ ($c = c_c$) the system is *critically damped*, and when $\xi > 100\%$ ($c > c_c$) the system is *overdamped*. Separate solutions must be obtained for each of the three cases, but structures of interest in earthquake engineering are virtually always underdamped.

For the case in which damping is less than critical, the solution to the equation of motion is of the form

$$u = e^{-\xi\omega_0 t} \left[C_1 \sin(\omega_0 \sqrt{1 - \xi^2} t) + C_2 \cos(\omega_0 \sqrt{1 - \xi^2} t) \right] \quad (\text{B.18})$$

Note the exponential term by which the term in brackets is multiplied. This exponential term gets smaller with time and eventually approaches zero, indicating that the response of an underdamped system in free vibration decays exponentially with time. The rate of decay depends on the damping ratio—for small ξ the response decays slowly and for larger ξ the response decays *more* quickly. Defining the *damped natural circular frequency* of the system as $\omega_d = \omega_0 \sqrt{1 - \xi^2}$ the solution can be expressed as

$$u = e^{-\xi\omega_0 t} (C_1 \sin \omega_d t + C_2 \cos \omega_d t) \quad (\text{B.19})$$

The natural frequency of a damped system is always lower than that of an undamped system, and it decreases with increasing damping ratio.

The coefficients C_1 and C_2 can be determined from the initial conditions in the same manner as for the undamped case. The initial displacement and velocity are

$$u_0 = e^{-\xi\omega_0(0)} [C_1 \sin(0) + C_2 \cos(0)] = C_2$$

$$\begin{aligned} \dot{u}_0 &= e^{-\xi\omega_0(0)} [\omega_d C_1 \cos \omega_d(0) - \omega_d C_2 \sin \omega_d(0)] - \xi \omega_0 e^{-\xi\omega_0(0)} [C_1 \sin \omega_d(0) + C_2 \cos \omega_d(0)] \\ &= \omega_d C_1 - \xi \omega_0 C_2 \end{aligned}$$

Therefore, $C_1 = (\dot{u}_0 + \xi \omega_0 u_0) / \omega_d$ and $C_2 = u_0$, so the solution for damped free vibrations can be expressed as

$$u = e^{-\xi \omega_0 t} \left(\frac{\dot{u}_0 + \xi \omega_0 u_0}{\omega_d} \sin \omega_d t + u_0 \cos \omega_d t \right) \quad (\text{B.20})$$

The free vibration response of an underdamped system is shown in Figure B.8. Note the exponential decay of displacement amplitude with time. The ratio of the amplitudes of any two successive peaks will be

$$\frac{u_n}{u_{n+1}} = \exp\left(2\pi\xi \frac{\omega_0}{\omega_d}\right) \quad (\text{B.21})$$

Defining the *logarithmic decrement* as $\delta = \ln(u_n/u_{n+1})$; then

$$\delta = 2\pi\xi \frac{\omega_0}{\omega_d} = \frac{2\pi\xi}{\sqrt{1-\xi^2}} \quad (\text{B.22})$$

Rearranging allows the damping ratio to be determined from the logarithmic decrement

$$\xi = \frac{\delta}{\sqrt{4\pi^2 + \delta^2}} \quad (\text{B.23})$$

For small values of δ , $\xi \approx \delta/2\pi$. Therefore, a simple way to estimate the damping ratio of an SDOF system is to perform a *free vibration test*, in which the logarithmic decrement is measured when a system is displaced by some initial displacement, u_0 , and released with initial velocity $\dot{u}_0 = 0$.

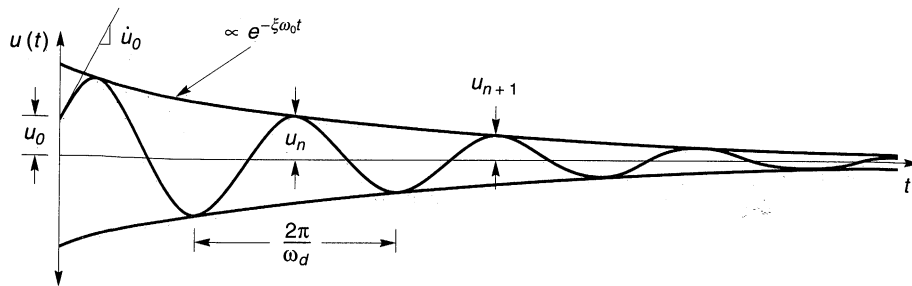


Figure B.8 Time history of damped free vibration with initial displacement u_0 and initial velocity \dot{u} .

Example B.2

The structure shown in Figure EB.2a is released from an initial displacement of 1 cm with an initial velocity of -5 cm/sec. Compute (a) the damped natural frequency and (b) the time history of response of the mass.

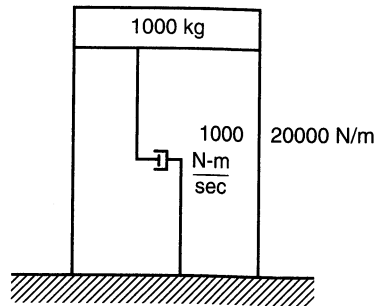


Figure EB2.a

Solution (a) The undamped natural frequency is

$$f_0 = \frac{\omega_0}{2\pi} = \frac{1}{2\pi} \sqrt{\frac{k}{m}} = \frac{1}{2\pi} \sqrt{\frac{20000 \text{ N/m}}{1000 \text{ kg}}} = 0.71 \text{ Hz}$$

and the damping ratio is

$$\xi = \frac{c}{2\sqrt{km}} = \frac{1000 \text{ N-m/sec}}{2\sqrt{(20000 \text{ N/m})(1000 \text{ kg})}} = 0.118$$

Then

$$f_d = f_0 \sqrt{1 - \xi^2} = (0.71 \text{ Hz}) \sqrt{1 - (0.118)^2} = 0.70 \text{ Hz}$$

(b) The undamped and damped natural circular frequencies will be $\omega_0 = 2\pi f_0 = 4.47$ rad/sec and $\omega_d = f_d 2\pi = 4.44$ rad/sec, respectively. From equation (B.20), the displacement response is

$$\begin{aligned} u &= e^{-\xi\omega_0 t} \left(\frac{\dot{u}_0 + \xi\omega_0 u_0}{\omega_d} \sin \omega_d t + u_0 \cos \omega_d t \right) \\ &= \exp[-(0.118)(4.47)t] \left[\frac{-0.05 + (0.118)(4.47)(0.01)}{4.44} \sin(4.44t) + (1) \cos(4.44t) \right] \\ &= e^{-0.527t} [\cos(4.44t) - 0.010 \sin(4.44t)] \end{aligned}$$

which is plotted in Figure EB.2b.

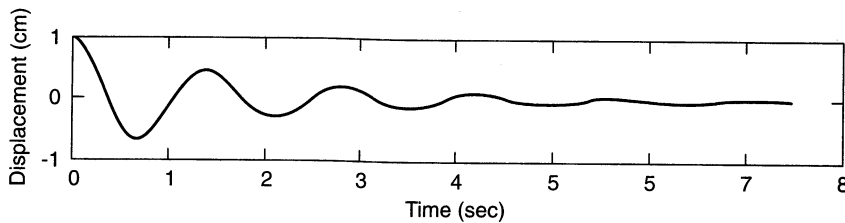


Figure EB.2b

B.5.3 Response of SDOF Systems to Harmonic Loading

A SDOF system is said to undergo forced vibration when acted upon by some external dynamic force, $Q(t)$. Dynamic loading may come from many different sources and may be

periodic or nonperiodic. For problems of soil and structural dynamics, the response to harmonic loading is very important. One form of simple harmonic loading $Q(t)$ can be expressed as $Q(t) = Q_0 \sin \bar{\omega}t$, where Q_0 is the amplitude of the harmonic load and $\bar{\omega}$ is the circular frequency at which the load is applied.

B.5.3.1 Undamped Forced Vibrations

The equation of motion for an undamped system subjected to such simple harmonic loading is

$$m\ddot{u} + ku = Q_0 \sin \bar{\omega}t \quad (\text{B.24})$$

The general solution to this equation of motion is given by the sum of the *complementary solution* (for the homogeneous case in which the right side of the equation is zero) and the *particular solution* [which must satisfy the right side of equation (B.24)].

The homogeneous equation is

$$m\ddot{u} + ku = 0$$

so the complementary solution is simply the solution to the undamped free vibration problem

$$u_c(t) = C_1 \sin \omega_0 t + C_2 \cos \omega_0 t \quad (\text{B.25})$$

The portion of the response described by the complementary solution is that which results from the initial conditions of the system. It consists of a simple harmonic oscillation at the undamped natural frequency of the system.

The particular solution describes the portion of the response caused by the external loading. This portion of the response can be assumed to be of the same form and to be in phase with the harmonic loading; thus

$$u_p(t) = U_0 \sin \bar{\omega}t \quad (\text{B.26})$$

where U_0 is the amplitude of the harmonic response. Substituting equation (B.26) into equation (B.24) yields

$$-m\bar{\omega}^2 U_0 \sin \bar{\omega}t + kU_0 \sin \bar{\omega}t = Q_0 \sin \bar{\omega}t \quad (\text{B.27})$$

Substituting $k/m = \omega_0^2$ and rearranging gives

$$U_0 = \frac{Q_0/k}{1 - \bar{\omega}^2/\omega_0^2} = \frac{Q_0/k}{1 - \beta^2} \quad (\text{B.28})$$

where $\beta = \bar{\omega}/\omega_0$ is referred to as the *tuning ratio*. Now the general solution of the equation of motion can be obtained by combining the complementary and particular solutions:

$$u(t) = u_c(t) + u_p(t) = C_1 \sin \omega_0 t + C_2 \cos \omega_0 t + \frac{Q_0/k}{1 - \beta^2} \sin \bar{\omega}t \quad (\text{B.29})$$

The general solution must satisfy the initial conditions. From equation (B.29), the velocity can be written as

$$\dot{u}(t) = \frac{du}{dt} = \omega_0 C_1 \cos \omega_0 t - \omega_0 C_2 \sin \omega_0 t + \bar{\omega} \frac{Q_0/k}{1 - \beta^2} \cos \bar{\omega}t \quad (\text{B.30})$$

For a given initial displacement, u_0 , and initial velocity, \dot{u}_0 ,

$$u_0 = C_1 \sin \omega_0(0) + C_2 \cos \omega_0(0) + \frac{Q_0/k}{1-\beta^2} \sin \bar{\omega}(0) = C_2 \quad (\text{B.31})$$

and

$$\begin{aligned} \dot{u}_0 = \omega_0 C_1 \cos \omega_0(0) - \omega_0 C_2 \sin \omega_0(0) + \bar{\omega} \frac{Q_0/k}{1-\beta^2} \cos \bar{\omega}(0) = \omega_0 C_1 \\ + \bar{\omega} \frac{Q_0/k}{1-\beta^2} \end{aligned} \quad (\text{B.32})$$

from which

$$C_1 = \frac{\dot{u}_0 - \bar{\omega} [(Q_0/k)/(1-\beta^2)]}{\omega_0} = \frac{\dot{u}_0}{\omega_0} - \frac{Q_0\beta}{k(1-\beta^2)} \quad (\text{B.33})$$

Now the general response can finally be written as

$$u = \left[\frac{\dot{u}_0}{\omega_0} - \frac{Q_0\beta}{k(1-\beta^2)} \right] \sin \omega_0 t + u_0 \cos \omega_0 t + \frac{Q_0/k}{1-\beta^2} \sin \bar{\omega} t \quad (\text{B.34})$$

It is interesting to consider the case in which the system is initially at rest in its equilibrium position, (i.e., $u_0 = \dot{u}_0 = 0$). For this case the response is given by

$$u = \frac{Q_0}{k} \frac{1}{1-\beta^2} (\sin \bar{\omega} t - \beta \sin \omega_0 t) \quad (\text{B.35})$$

which indicates that the response has two components. One component occurs in response to the applied loading and occurs at the frequency of the applied loading. The other is a free vibration effect induced by the initial conditions; it occurs at the natural frequency of the system. It is useful to realize that the term Q_0/k in equation (B.35) represents the displacement of the mass that would occur if the load Q_0 was applied statically. The term $1/(1-\beta^2)$ can then be thought of as a magnification factor that describes the amount by which the static displacement amplitude is magnified by the harmonic load. The magnification factor varies with the tuning ratio, β , as shown in Figure B.9. Note that the displacement amplitude is greater than the static displacement for loading frequencies lower than $\sqrt{2} \omega_0$. At higher loading frequencies, the displacement amplitude is less than the static displacement and can become very small at high frequencies. However, the response of an undamped SDOF system becomes very large as $\bar{\omega}$ approaches ω_0 . When harmonic loading is applied at the natural frequency of an undamped SDOF system, the response goes to infinity indicating *resonance* of the system. However, since truly undamped systems do not exist, true resonance is never really achieved. The concept of the tuning ratio that relates the frequency of loading to the natural frequency of the system is an important one, as evidenced by its strong influence on the response.

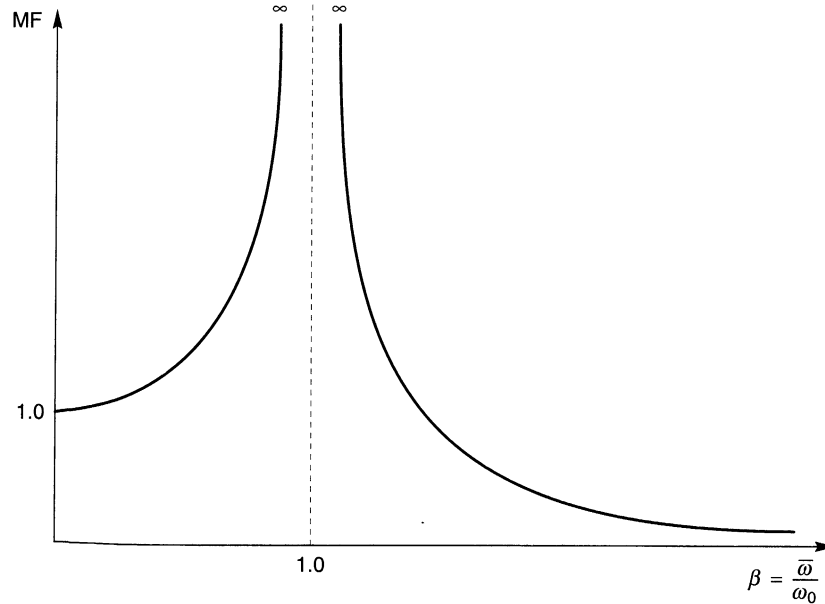


Figure B.9 Variation of magnification factor with tuning ratio for undamped SDOF system.

Example B.3

From an initial stationary state, the undamped SDOF system of Example B.1 is subjected to a harmonic base acceleration of $0.20g$ at a frequency of 2 Hz. Compute the response of the system.

Solution Expressing the base motion as

$$\ddot{u}_b(t) = (0.2)(32.2 \text{ ft/sec}^2) \sin 4\pi t = 6.44 \sin 4\pi t$$

the equivalent external force would be

$$Q(t) = -\frac{W}{g}\ddot{u}_b(t) = -\frac{10,000 \text{ lb}}{32.2 \text{ ft/sec}^2}(6.44 \text{ ft/sec}^2) \sin 4\pi t = -(2000 \text{ lb}) \sin 4\pi t$$

The tuning ratio would be

$$\beta = \frac{\bar{\omega}}{\omega_0} = \frac{2\pi\bar{f}}{\omega_0} = \frac{2\pi(2)}{69.5} = 0.181$$

Then, from equation (B.35),

$$\begin{aligned} u(t) &= \frac{Q_0}{k} \frac{1}{1-\beta^2} (\sin \bar{\omega}t - \beta \sin \omega_0 t) \\ &= \frac{-2 \text{ kips}}{1500 \text{ kips/ft}} \frac{1}{1-(0.181)^2} [\sin 4\pi t - 0.181 \sin (69.5t)] \\ &= 0.00138 \sin 4\pi t - 0.00025 \sin 69.5t \end{aligned}$$

which is plotted in Figure EB.3.

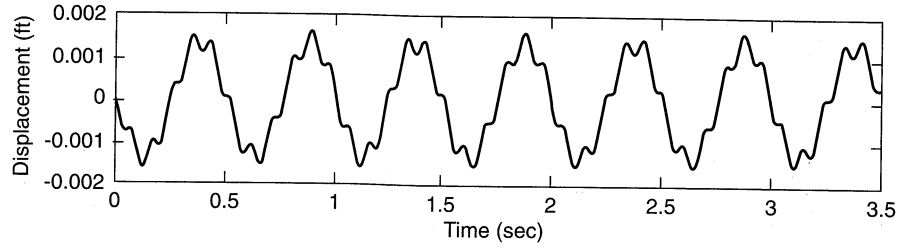


Figure EB.3

B.5.3.2 Damped Forced Vibrations

The most general case is that of a damped system subjected to forced harmonic loading. Each of the three prior cases can be considered as a subset of this one since their equations of motion can be obtained by setting various terms of the equation of motion for damped forced vibrations shown below to zero. The equation of motion for a damped SDOF system subjected to simple harmonic loading of the form $Q(t) = Q_0 \sin \bar{\omega}t$ is

$$m\ddot{u} + c\dot{u} + ku = Q_0 \sin \bar{\omega}t \quad (\text{B.36})$$

After dividing by m and using the relationships $\xi = c/2m\omega_0$ and $\omega_0^2 = k/m$, equation (B.36) can be rewritten as

$$\ddot{u} + 2\xi\omega_0\dot{u} + \omega_0^2u = \frac{Q_0}{m} \sin \bar{\omega}t \quad (\text{B.37})$$

The complementary solution represents the damped free vibration response, which was expressed for an underdamped system by equation (B.19).

$$u_c(t) = e^{-\xi\omega_0 t} (C_1 \sin \omega_d t + C_2 \cos \omega_d t)$$

Since the response of a damped SDOF system is generally out of phase with the external loading, a harmonic particular solution of the form

$$u_p(t) = C_3 \sin \bar{\omega}t + C_4 \cos \bar{\omega}t \quad (\text{B.38a})$$

can be assumed. The corresponding velocity and acceleration are

$$\dot{u}_p(t) = C_3 \bar{\omega} \cos \bar{\omega}t - C_4 \bar{\omega} \sin \bar{\omega}t \quad (\text{B.38b})$$

$$\ddot{u}_p(t) = -\bar{\omega}^2 C_3 \sin \bar{\omega}t - \bar{\omega}^2 C_4 \cos \bar{\omega}t \quad (\text{B.38c})$$

Substituting equations (B.38) into the equation of motion [equation (B.37)] and grouping the $\sin \bar{\omega}t$ and $\cos \bar{\omega}t$ terms gives

$$\begin{aligned} & (C_3\omega_0^2 - C_3\bar{\omega}^2 - 2\xi\omega_0 C_4\bar{\omega}) \sin \bar{\omega}t \\ & + (C_4\omega_0^2 - C_4\bar{\omega}^2 + C_3\bar{\omega}2\xi\omega_0) \cos \bar{\omega}t = \frac{Q_0}{m} \sin \bar{\omega}t \end{aligned} \quad (\text{B.39})$$

Now, at the instances where $\bar{\omega}t = 0 + n\pi$ (where n is any positive integer), $\sin \bar{\omega}t = 0$ and $\cos \bar{\omega}t = 1$. Thus the relationship

$$C_4 \omega_0^2 - C_4 \bar{\omega}^2 + C_3 \bar{\omega} 2\xi \omega_0 = 0 \quad (\text{B.40a})$$

must be satisfied. Further, at $\bar{\omega}t = \pi/2 + n\pi$, $\cos \bar{\omega}t = 0$ and $\sin \bar{\omega}t = 1$, which means that

$$C_3 \omega_0^2 - C_3 \bar{\omega}^2 - 2\xi \omega_0 C_4 \bar{\omega} = \frac{Q_0}{m} \quad (\text{B.40b})$$

must also be satisfied. Equations (B.40) represent two simultaneous equations with the two unknowns C_3 and C_4 . Solving for the unknowns yields

$$C_3 = \frac{Q_0}{k} \frac{1 - \beta^2}{(1 - \beta^2)^2 + (2\xi\beta)^2} \quad (\text{B.41a})$$

$$C_4 = \frac{Q_0}{k} \frac{-2\xi\beta}{(1 - \beta^2)^2 + (2\xi\beta)^2} \quad (\text{B.41b})$$

The general solution to the equation of motion for damped forced vibration can now be obtained by combining the complementary and particular solutions

$$u(t) = e^{-\xi\omega_0 t} (C_1 \sin \omega_d t + C_2 \cos \omega_d t) + \frac{Q_0}{k} \frac{1}{(1 - \beta^2)^2 + (2\xi\beta)^2} [(1 - \beta^2) \sin \bar{\omega}t - 2\xi\beta \cos \bar{\omega}t] \quad (\text{B.42})$$

where the constants C_1 and C_2 depend on the initial conditions. There are several important characteristics of this solution. Note that the complementary solution (which represents the effects of the initial conditions) decays with time. The complementary solution therefore describes a *transient response* caused by the requirement of satisfying the initial conditions. After the transient response dies out, only the *steady-state response* described by the particular solution remains. The steady-state response occurs at the frequency of the applied harmonic loading but is out of phase with the loading.

Example B.4

The SDOF system shown in Figure EB.4a is at rest when the sinusoidal load is applied. Determine the transient, steady state, and total motion of the system.

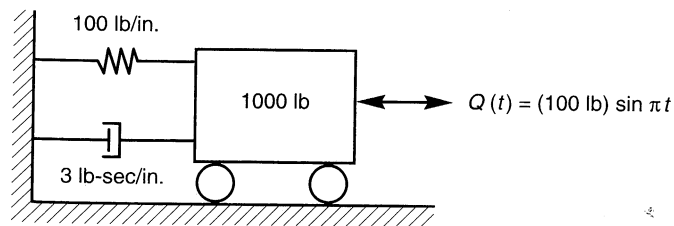


Figure EB.4a

Solution From equation (B.42), the total response is given by

$$u(t) = e^{-\xi\omega_0 t} (C_1 \sin \omega_d t + C_2 \cos \omega_d t) + \frac{Q_0}{k} \frac{1}{(1-\beta^2)^2 + (2\xi\beta)^2} [(1-\beta^2) \sin \bar{\omega} t - 2\xi\beta \cos \bar{\omega} t]$$

For zero initial displacement,

$$\begin{aligned} u(t=0) &= 0 \\ &= e^{-\xi\omega_0(0)} [C_1 \sin \omega_d(0) + C_2 \cos \omega_d(0)] \\ &\quad + \frac{Q_0}{k} \frac{1}{(1-\beta^2)^2 + (2\xi\beta)^2} [(1-\beta^2) \sin \bar{\omega}(0) - 2\xi\beta \cos \bar{\omega}(0)] \\ &= C_2 + \frac{Q_0}{k} \frac{-2\xi\beta}{(1-\beta^2)^2 + (2\xi\beta)^2} \end{aligned}$$

or

$$C_2 = \frac{Q_0}{k} \frac{2\xi\beta}{(1-\beta^2)^2 + (2\xi\beta)^2}$$

For zero initial velocity,

$$\begin{aligned} \dot{u} &= 0 \\ &= \omega_d e^{-\xi\omega_0(0)} [C_1 \cos \omega_d(0) - C_2 \sin \omega_d(0)] - \xi\omega_0 e^{-\xi\omega_0 t} [C_1 \sin \omega_d(0) - C_2 \cos \omega_d(0)] \\ &\quad + \frac{Q_0}{k} \frac{\bar{\omega}}{(1-\beta^2)^2 + (2\xi\beta)^2} [(1-\beta^2) \cos \bar{\omega}(0) + 2\xi\beta \sin \bar{\omega}(0)] \\ &= \omega_d C_1 - \xi\omega_0 C_2 + \frac{Q_0}{k} \frac{\bar{\omega}(1-\beta^2)}{(1-\beta^2)^2 + (2\xi\beta)^2} \end{aligned}$$

or

$$C_1 = \frac{Q_0 \bar{\omega}}{k \omega_d} \frac{\beta^2 - 1}{(1-\beta^2)^2 + (2\xi\beta)^2}$$

Then the transient motion is given by

$$u_c(t) = \frac{Q_0}{k} \frac{1}{(1-\beta^2)^2 + (2\xi\beta)^2} e^{-\xi\omega_0 t} \left[\frac{\bar{\omega}}{\omega_d} (\beta^2 + 2\xi^2 - 1) \sin \omega_d t + 2\xi\beta \cos \omega_d t \right]$$

and the steady-state motion by

$$u_p(t) = \frac{Q_0}{k} \frac{1}{(1-\beta^2)^2 + (2\xi\beta)^2} [(1-\beta^2) \sin \bar{\omega} t - 2\xi\beta \cos \bar{\omega} t]$$

The total motion is the sum of the transient and steady-state motions. For the system shown in Figure EB.1a,

$$\omega_0 = \sqrt{\frac{k}{m}} = \sqrt{\frac{kg}{W}} = \sqrt{\frac{(100 \text{ lb/in.})(12 \text{ in./ft})(32.2 \text{ ft/sec/sec})}{1000 \text{ lb}}} = 6.22 \text{ rad/sec}$$

$$\xi = \frac{c}{2m\omega_0} = \frac{cg}{2W\omega_0} = \frac{(3 \text{ lb-sec/in.})(12 \text{ in./ft})(32.2 \text{ ft/sec/sec})}{2(1000 \text{ lb})(6.22 \text{ rad/sec})} = 0.093$$

$$\omega_d = \omega_0 \sqrt{1 - \xi^2} = \sqrt{1 - (0.092)^2} = 6.19 \text{ rad/sec}$$

$$\beta = \frac{\bar{\omega}}{\omega_0} = \frac{\pi \text{ rad/sec}}{6.22 \text{ rad/sec}} = 0.505$$

Substituting these values into the solutions gives the response shown in Figure EB.4b

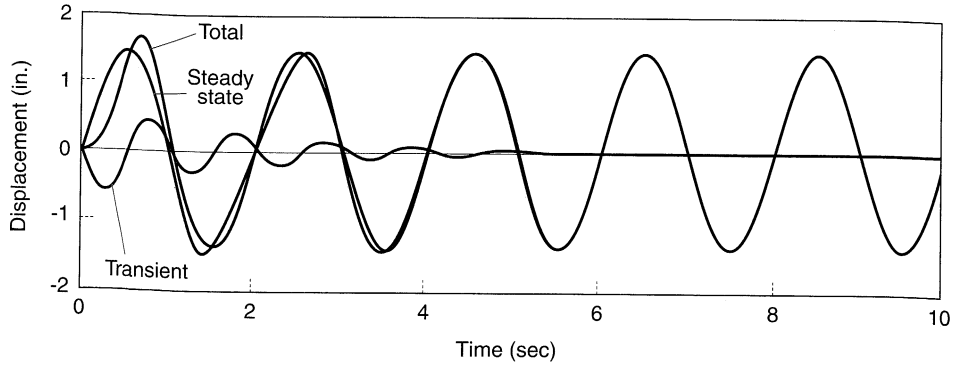


Figure EB.4b

The steady-state response could also be described by

$$u = A \sin (\bar{\omega} t + \phi) \tag{B.43}$$

where

$$A = \frac{Q_0}{k} \frac{1}{\sqrt{(1 - \beta^2)^2 + (2\xi\beta)^2}}$$

$$\phi = \tan^{-1} \left(-\frac{2\xi\beta}{1 - \beta^2} \right)$$

The steady-state response can be visualized with the aid of rotating vectors, both for the response and for the forces induced in the system, as shown in Figure B.10. Note that the spring, dashpot, and inertial forces act opposite to the displacement, velocity and acceleration vectors, and that the displacement lags the applied loading vector by the negative phase

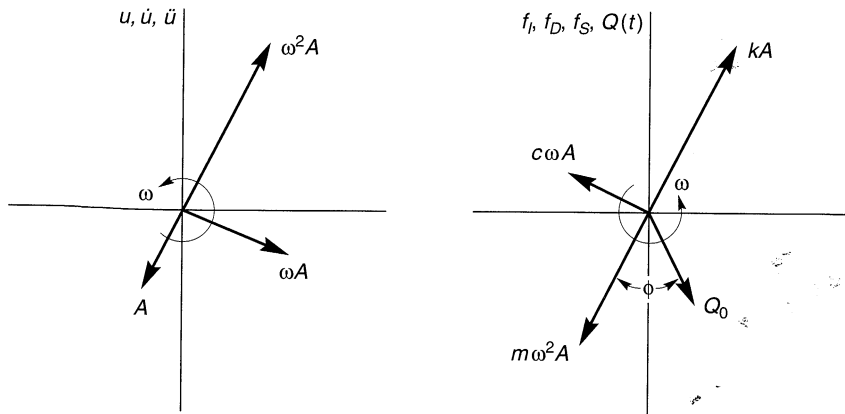


Figure B.10 Rotating vector representation of response and forces in vibrating SDOF system.

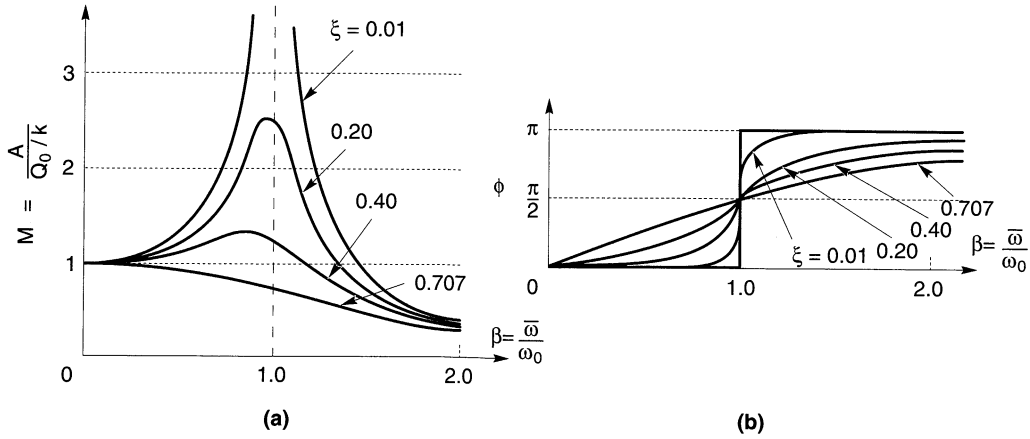


Figure B.11 Variation of (a) magnification factor, and (b) phase angle with damping ratio and tuning ratio.

angle, ϕ . For harmonic loading the phase angle varies with both damping ratio and tuning ratio, as shown in Figure B.11a.

The influence of the tuning ratio can be illustrated by the use of the magnification factor, again defined as the ratio of the amplitude to the static displacement:

$$M = \frac{A}{Q_0/k} = \frac{1}{\sqrt{(1 - \beta^2)^2 + (2\xi\beta)^2}} \tag{B.44}$$

The variation of the magnification factor with tuning ratio and damping ratio is shown in Figure B.11b. The damping ratio influences the peak magnification factor and also the variation of magnification factor with frequency. The magnification factor curves broaden with increasing damping ratio. Note that the magnification is unbounded (resonance) only for $\xi = 0$ and $\beta = 1$. For nonzero damping, there is some maximum magnification, M_{\max} ,

$$M_{\max} = \frac{1}{2\xi\sqrt{1 - \xi^2}} \tag{B.45}$$

which occurs when the tuning ratio $\beta = \sqrt{1 - 2\xi^2}$. The shape of the magnification curve is obviously controlled by the damping ratio. Although a system with low damping may produce large magnification at a tuning ratio near 1, it will exhibit significant magnification over a smaller range of frequencies than a system with higher damping.

B.5.4 Response of SDOF Systems to Periodic Loading

The solutions for the response of a SDOF system to harmonic loading developed in the preceding section can be used to develop solutions for the more general case of periodic loading. As shown in Appendix A, periodic loading can be approximated by a Fourier series (i.e., as the sum of a series of harmonic loads). The response of a SDOF system to the periodic loading, using the principle of superposition, is simply the sum of the responses to each term in the loading series. The required calculations can be performed using trigonometric or exponential notation.

B.5.4.1 Trigonometric Notation

From equation (A.11) a periodic load, $Q(t)$, can be expressed by the Fourier series

$$Q(t) = a_0 + \sum_{n=1}^{\infty} a_n \cos \omega_n t + b_n \sin \omega_n t$$

where the *Fourier coefficients* are

$$a_0 = \frac{1}{T_f} \int_0^{T_f} Q(t) dt$$

$$a_n = \frac{2}{T_f} \int_0^{T_f} Q(t) \cos \omega_n t dt$$

$$b_n = \frac{2}{T_f} \int_0^{T_f} Q(t) \sin \omega_n t dt$$

and $\omega_n = 2\pi n/T_f$. Using the steady-state portion of equation (B.42), the response to each sine term in the Fourier series is

$$u_{n, \sin}(t) = \frac{b_n}{k} \frac{1}{(1 - \beta_n^2)^2 + (2\xi\beta_n)^2} [(1 - \beta_n^2) \sin \bar{\omega}t - 2\xi\beta_n \cos \bar{\omega}t]$$

where $\beta_n = \omega_n T_f / 2\pi$. In the same way, the steady-state response to each cosine term can be shown to be

$$u_{n, \cos}(t) = \frac{a_n}{k} \frac{1}{(1 - \beta_n^2)^2 + (2\xi\beta_n)^2} [(1 - \beta_n^2) \cos \bar{\omega}t + 2\xi\beta_n \sin \bar{\omega}t]$$

Since the steady-state response to the constant load term is the static displacement, $u_0 = a_0/k$, the total steady-state response is given by

$$\begin{aligned} u(t) &= u_0 + \sum_{n=1}^{\infty} u_{n, \sin}(t) + u_{n, \cos}(t) \\ &= \frac{1}{k} \left(a_0 + \sum_{n=1}^{\infty} \frac{1}{(1 - \beta_n^2)^2 + (2\xi\beta_n)^2} \{ [a_n 2\xi\beta_n + b_n (1 - \beta_n^2)] \sin \omega_n t \right. \\ &\quad \left. + [a_n (1 - \beta_n^2) - b_n 2\xi\beta_n] \cos \omega_n t \} \right) \end{aligned} \quad (\text{B.46})$$

2.5.4.2 Exponential Notation

Periodic loading can also be described by the Fourier series in exponential form. Using equation (A.15), a periodic load can be expressed as

$$Q(t) = \sum_{n=-\infty}^{\infty} q_n^* e^{i\omega_n t}$$

The complex Fourier coefficients, q_n^* , can be determined directly from $Q(t)$ as

$$q_n^* = \frac{1}{T_f} \int_0^{T_f} Q(t) e^{-i\omega_n t} dt$$

The response of a SDOF system loaded by the n th harmonic would be governed by the equation of motion

$$m\ddot{u}_n(t) + (c\dot{u}_n(t) + ku_n(t)) = q_n^* e^{i\omega_n t} \quad (\text{B.47})$$

The response of the system can be related to the loading by

$$u_n(t) = H(\omega_n) q_n^* e^{i\omega_n t} \quad (\text{B.48})$$

where $H(\omega_n)$ is a *transfer function* [i.e., a function that relates one parameter (in this case, the displacement of the oscillator) to another (the external load)]. Substituting equation (B.48) into the equation of motion gives

$$-m\omega_n^2 H(\omega_n) q_n^* e^{i\omega_n t} + ic\omega_n H(\omega_n) q_n^* e^{i\omega_n t} + kH(\omega_n) q_n^* e^{i\omega_n t} = q_n^* e^{i\omega_n t}$$

or

$$H(\omega_n) = \frac{1}{-m\omega_n^2 + ic\omega_n + k} = \frac{1}{k(-\beta_n^2 + 2i\beta_n\xi + 1)} \quad (\text{B.49})$$

Since $A^* = a + ib = Ae^{i\theta}$, where the *modulus*, $A = \sqrt{a^2 + b^2}$, and the *argument*, $\theta = \tan^{-1}(b/a)$, the transfer function can also be written as

$$H(\omega_n) = \frac{1/k}{\sqrt{(1 - \beta_n^2)^2 + (2\xi\beta_n)^2}} \exp\left(i \tan^{-1} \frac{2\xi\beta_n}{\beta_n^2 - 1}\right)$$

Note the close relationship between the modulus of the transfer function and the magnification factor of equation (B.44). Because the transfer function can be used for any frequency in the series, the principle of superposition gives the total response as

$$u(t) = \sum_{n=-\infty}^{\infty} H(\omega_n) q_n^* e^{i\omega_n t} \quad (\text{B.50})$$

Many different transfer functions can be developed. For example, a transfer function relating the acceleration of the SDOF system to the external load could have been developed just as easily. The advantages of the transfer function approach lie in its simplicity and in the ease with which it allows computation of the response to complicated loading patterns.

The transfer function may be viewed as a *filter* that acts upon some input signal to produce an output signal. In the case just considered, the input signal was the time history of loading, $Q(t)$, and the output was the displacement, $u(t)$. If the input signal has Fourier amplitude and phase spectra, $F_i(\omega_n)$ and $\phi_i(\omega_n)$, the Fourier amplitude spectra of the output signal will be given by

$$F_o(\omega_n) = H(\omega_n) F_i(\omega_n) \quad (\text{B.51a})$$

$$\phi_o(\omega_n) = H(\omega_n) \phi_i(\omega_n) \quad (\text{B.51b})$$

Thus the procedure for Fourier analysis of SDOF system response can be summarized in the following steps:

1. Obtain the Fourier series for the applied loading (or base motion). In doing so, the loading (or base motion) is expressed as a function of frequency rather than a function of time.
2. Multiply the Fourier series coefficients by the appropriate value of the transfer function at each frequency, ω_n . This will produce the Fourier series of the output motion.
3. Express the output motion in the time domain by obtaining the inverse Fourier transform of the output motion.

It is precisely this approach that forms the backbone of several of the most commonly used methods for analysis of ground response and soil–structure interaction. These methods are presented in Chapter 7.

B.5.5 Response of SDOF Systems to General Loading

Not all loading is harmonic or even periodic. To determine the response of SDOF systems to general loading conditions, a more general solution of the equation of motion is required.

B.5.5.1 Response to Step Loading

Consider a damped SDOF system subjected to a step load of intensity, Q_0 , which is applied instantaneously at $t = 0$ and removed instantaneously at $t = t_1$ as shown in Figure B.12. For $t \leq t_1$, the complementary solution to the equation of motion for this system [equation (B.19)],

$$u_c(t) = e^{-\xi\omega_0 t} [C_1 \sin \omega_d t + C_2 \cos \omega_d t]$$

describes the transient response of the system. The equation of motion for the steady-state condition is given by

$$m\ddot{u}_p + c\dot{u}_p + ku_p = Q_0$$

Since the applied load does not vary with time, the steady-state response will be a constant displacement,

$$u_p(t) = \frac{Q_0}{k}$$

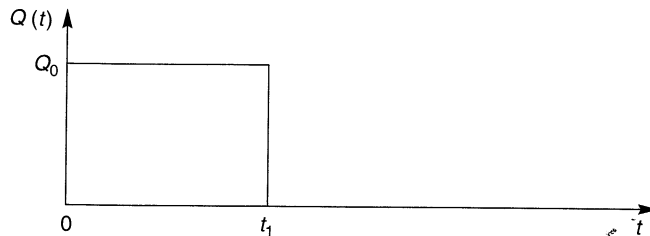


Figure B.12 Time history of step loading.

The general solution to the step loading problem for $t \leq t_1$ can then be written as

$$u(t) = \frac{Q_0}{k} + e^{-\xi\omega_0 t} (C_1 \sin \omega_d t + C_2 \cos \omega_d t) \quad (\text{B.52})$$

with free vibration occurring at $t > t_1$ (when no external load is applied). The constants are determined by the initial conditions, u_0 and \dot{u}_0 . At $t = 0$,

$$\begin{aligned} u_0 &= \frac{Q_0}{k} + e^{-\xi\omega_0(0)} [C_1 \sin \omega_d(0) + C_2 \cos \omega_d(0)] = \frac{Q_0}{k} + C_2 \\ \dot{u}_0 &= e^{-\xi\omega_0(0)} [\omega_d C_1 \cos \omega_d(0) - \omega_d C_2 \sin \omega_d(0)] \\ &\quad - \xi\omega_0 e^{-\xi\omega_0(0)} [C_1 \sin \omega_d(0) + C_2 \cos \omega_d(0)] = \omega_d C_1 - \xi\omega_0 C_2 \end{aligned}$$

from which

$$\begin{aligned} C_1 &= \frac{\dot{u}_0 + \xi\omega_0(u_0 - Q_0/k)}{\omega_d} \\ C_2 &= u_0 - \frac{Q_0}{k} \end{aligned}$$

so that

$$u(t) = \frac{Q_0}{k} + e^{-\xi\omega_0 t} \left[\frac{\dot{u}_0 + \xi\omega_0(u_0 - Q_0/k)}{\omega_d} \sin \omega_d t + \left(u_0 - \frac{Q_0}{k} \right) \cos \omega_d t \right] \quad (\text{B.53})$$

describes the response of the system up to the beginning of free vibration at $t = t_1$.

B.5.5.2 Dirac Pulse

A particular type of step loading can be described using a Dirac delta function. A Dirac delta function is one whose value is zero at all values of x except one at which it goes to infinity in such a way that the area under the function is unity. Mathematically, the Dirac delta function satisfies the conditions

$$\delta(x) = \begin{cases} 0 & \text{for } x \neq a \\ \infty & \text{for } x = a \end{cases} \quad (\text{B.54a})$$

$$\int_{-\infty}^{\infty} \delta(x) dx = 1 \quad (\text{B.54b})$$

Define a Dirac pulse as a constant force Q_0 applied over a duration t_1 that approaches zero as shown in Figure B.13. From impulse-momentum principles, $Q_0 t_1 = m \dot{u}_0(t_1)$. As t_1 approaches zero, the effect of the Dirac pulse is to cause an initial velocity $\dot{u}_0 = Q_0 t_1 / m$, with no initial displacement. Thus the steady-state response occurs only over an infinitesimal period of time, and the system is immediately set into free vibration. From equation (B.20), the response to a Dirac pulse disturbance at $t = 0$ is given by

$$u(t) = e^{-\xi\omega_0 t} \left(\frac{Q_0 t_1}{m \omega_d} \sin \omega_d t \right) \quad (\text{B.55})$$



Figure B.13 Dirac pulse loading.

B.5.5.3 Duhamel Integral

A general loading function such as that shown in Figure B.14 can be thought of as a train of load pulses, each of infinitesimal duration. Looking at one of these pulses, the pulse of duration $d\tau$ occurring at $t = \tau$ (Figure B.14), the response it causes at a later time, $t = \tilde{t}$, follows from equation (B.55):

$$du(\tilde{t}) = e^{-\xi\omega_0(\tilde{t}-\tau)} \frac{Q_0(\tau)d\tau}{m\omega_d} \sin \omega_d(\tilde{t}-\tau) \quad (\text{B.56})$$

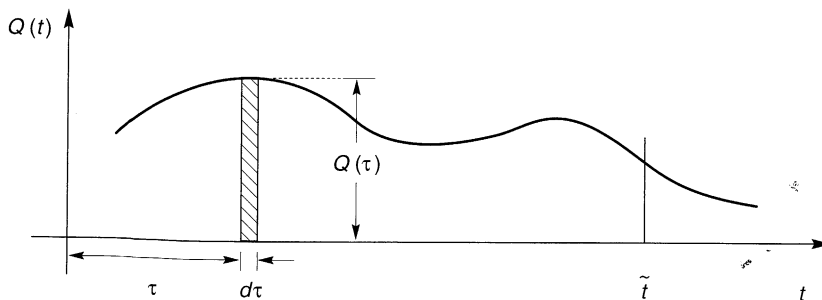
The response induced by the entire train of load pulses can be obtained by summing the responses of all of the individual pulses up to the time $t = \tilde{t}$, that is,

$$u(\tilde{t}) = \frac{1}{m\omega_d} \sum_{i=1}^n Q(\tau_i) \sin \omega_d(\tilde{t}-\tau_i) d\tau \quad (\text{B.57})$$

where n is the total number of pulses up to $t = \tilde{t}$. As $d\tau$ approaches zero, the summation becomes an integral with which the total response can be calculated as

$$u(\tilde{t}) = \frac{1}{m\omega_d} \int_0^{\tilde{t}} Q(\tau) e^{-\xi\omega_0(\tilde{t}-\tau)} \sin \omega_d(\tilde{t}-\tau) d\tau \quad (\text{B.58})$$

This equation describing the response of a linear system is known as *Duhamel's integral*. It is usually very difficult to solve analytically, but can be integrated numerically by a variety of procedures. Its use, however, is constrained to linear systems.

Figure B.14 Pulse of duration $d\tau$ occurring at $t = \tau$.

B.6 DAMPING

Energy is dissipated in soils and structures by several mechanisms, including friction, heat generation, and plastic yielding. For specific soils and structures, however, the operative mechanisms are not understood sufficiently to allow them to be explicitly modeled. As a result, the effects of the various energy loss mechanisms are usually lumped together and represented by some convenient damping mechanism.

B.6.1 Viscous Damping

The most commonly used mechanism for representing energy dissipation is viscous damping. When a viscous damped SDOF system such as that shown in Figure B.3 is subjected to a harmonic displacement

$$u(t) = u_0 \sin \bar{\omega}t$$

the net force exerted on the mass by the spring and dashpot is

$$F(t) = ku(t) + c\dot{u}(t) = ku_0 \sin \bar{\omega}t + c\bar{\omega}u_0 \cos \bar{\omega}t$$

Evaluating these functions from time t_0 to time $t_0 + 2\pi/\bar{\omega}$ yields the force–displacement values for one cycle of a *hysteresis loop*. When the viscous damping coefficient, c , is zero, the force and displacement are in phase and proportional to each other, implying a linear elastic stress–strain relationship. For nonzero damping, however, the hysteresis loop is elliptical, as shown in Figure B.15. Note that when the displacement is zero, the spring force is zero and the net force comes entirely from the dashpot. Similarly, when the velocity is zero (at $\bar{\omega}t = \pi/2 + n\pi$), the dashpot force vanishes and the net force consists entirely of the spring force. The aspect ratio of the hysteresis loop decreases with increasing damping; the loop becomes a circle when $c = k/\bar{\omega}$.

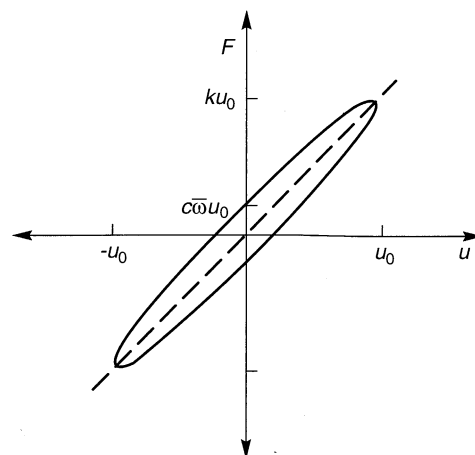


Figure B.15 Stress–strain behavior implied by viscous damping. Hysteresis loop is elliptical.

Obviously, the shape of the hysteresis loop depends on the viscous damping coefficient and therefore on the damping ratio. Hence we should be able to determine the damping ratio from a known hysteresis loop. The energy dissipated in one cycle of oscillation is given by the area inside the hysteresis loop and can be obtained from

$$W_D = \int_{t_0}^{t_0 + 2\pi/\bar{\omega}} F \frac{du}{dt} dt = \pi c \bar{\omega} u_0^2 \quad (\text{B.59})$$

At maximum displacement, the velocity is zero and the strain energy stored in the system is given by

$$W_S = \frac{1}{2} k u_0^2 \quad (\text{B.60})$$

Equations (B.59) and (B.60) show that $c = W_D / (\pi \omega u_0^2)$ and $k = 2W_S / u_0^2$. Substituting these into equation (B.16) with $\bar{\omega} = \omega_0$ gives an expression

$$\xi = \frac{W_D}{4\pi W_S}$$

that is commonly used for graphical determination of the damping ratio from a measured hysteresis loop. Referring to Figure B.16, the damping ratio is taken as the ratio of the area of the hysteresis loop to the area of the shaded triangle, all divided by 4π . This graphical evaluation of the damping ratio is commonly used in the interpretation of many of the laboratory tests discussed in Chapter 6.

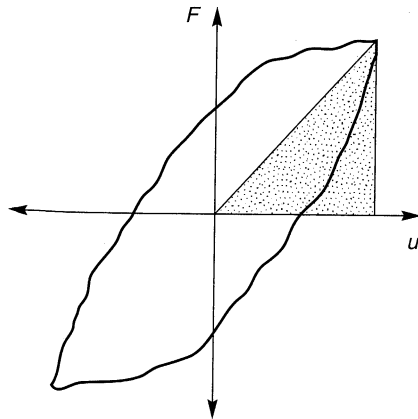


Figure B.16 Graphical evaluation of damping ratio from measured hysteresis loop. The damping ratio is proportional to the ratio of the shaded area to the area of the hysteresis loop.

The damping characteristics of a linear system can also be evaluated from its frequency response characteristics. Setting the magnification factor expression [equation (B.44)] equal to $M_{\max} / \sqrt{2}$, the *half-power tuning ratios*, shown in Figure B.17, can be approximated as

$$\beta_1 \approx 1 - \xi - \xi^2$$

$$\beta_2 \approx 1 + \xi - \xi^2$$

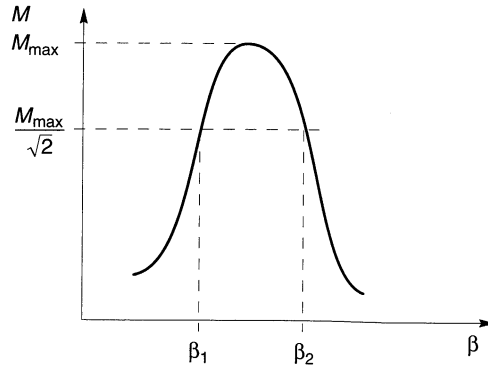


Figure B.17 Half-power tuning ratios for evaluation of damping ratio from magnification curve.

Therefore, the damping ratio is given by half the difference between the half-power tuning ratios

$$\xi \approx \frac{\beta_2 - \beta_1}{2} \tag{B.61}$$

or, when the response is expressed in terms of frequency, where $\omega_1 = \beta_1 \omega_0$ and $\omega_2 = \beta_2 \omega_0$,

$$\xi \approx \frac{\omega_2 - \omega_1}{\omega_2 + \omega_1} \tag{B.62}$$

Thus the damping ratio of a system can be measured by exciting the system at different frequencies and determining the amplitude of the magnification factor at each frequency.

B.6.2 Other Measures of Energy Dissipation

In addition to the damping ratio, ξ , a number of other parameters have been used to describe energy dissipation characteristics. Seismologists, for example, often work with the *quality factor*

$$Q = \frac{1}{2\xi} \tag{B.63}$$

In vibration analysis, the *loss factor*

$$\eta = 2\xi \tag{B.64}$$

and *specific damping capacity*

$$\psi = 2\pi\xi \tag{B.65}$$

are often used (Goodman, 1988).

It is important to remember that the damping ratio, and any of these other parameters, are simply parameters used to describe the effects of phenomena that are often poorly understood. They allow the effects of energy dissipation to be represented in a mathematically convenient manner. For most soils and structures, however, energy is dissipated hysteretically (i.e., by yielding or plastic straining of the material). In such cases the behavior is more accurately characterized by evaluating the nonlinear response of the system.

B.6.3 Complex Stiffness

A viscously damped system can be represented conveniently in a different but equivalent way for a class of techniques known as *complex response analysis*. Consider a damped SDOF system subjected to simple harmonic loading of amplitude Q_0 and loading frequency $\bar{\omega}$. The loading can be represented by

$$Q(t) = Q_0 e^{i\bar{\omega}t} \quad (\text{B.66})$$

Assuming that $u(t) = U_0 e^{i\bar{\omega}t}$, the steady-state solution to the equation of motion

$$m\ddot{u} + c\dot{u} + ku = Q_0 e^{i\bar{\omega}t} \quad (\text{B.67})$$

is

$$u(t) = \frac{Q_0}{k - m\bar{\omega}^2 + ic\bar{\omega}} e^{i\bar{\omega}t} \quad (\text{B.68})$$

Now consider the SDOF system of Figure B.18, which has no dashpot but which has a spring of *complex stiffness* $k^* = k_1 + ik_2$. The equation of motion for this system is

$$m\ddot{u} + k^* u = Q_0 e^{i\bar{\omega}t} \quad (\text{B.69})$$

Again assuming that $u(t) = U_0 e^{i\bar{\omega}t}$, the steady-state solution can be expressed as

$$u(t) = \frac{Q_0}{k^* - \bar{\omega}^2 m} e^{i\bar{\omega}t} \quad (\text{B.70})$$

Comparing equations (B.68) and (B.70), it is apparent that

$$k^* = k + ic\bar{\omega} \quad (\text{B.71})$$

By the appropriate choice of k^* , the displacement amplitude of equation (B.70) can be made equal to that of equation (B.68), (although a small phase difference between the two solutions will remain). To accomplish this, the complex stiffness is represented as

$$k^* = k(1 - 2\xi^2 + 2i\xi\sqrt{1 - \xi^2}) \quad (\text{B.72})$$

where $\xi \leq 1$. For the usual small damping ratios considered in earthquake engineering problems, the ξ^2 terms can be neglected so that $k^* \approx k(1 + 2i\xi)$. Using this expression for k^* , the error in phase angle between the responses given by equations (B.68) and (B.70) is $\Delta\theta \approx 2\xi/(1 + \beta)$. As a result, a viscously damped system can be represented as an undamped system with complex stiffness. The use of this approach, however, is restricted to cases of harmonic motion. For problems in which loading is characterized as periodic (and therefore as the sum as a series of harmonic loads), the use of complex stiffness greatly simplifies calculation of the response of damped systems.

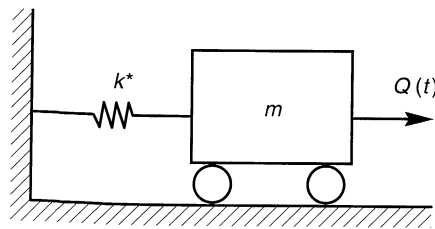


Figure B.18 SDOF system with spring of complex stiffness.

For small damping ratios, the complex stiffness then consists of real and imaginary parts

$$\text{Re}(k^*) = k \tag{B.73a}$$

$$\text{Im}(k^*) = 2k\xi \tag{B.73b}$$

Consequently, the damping ratio can be expressed as

$$\xi = \frac{\text{Im}(k^*)}{2\text{Re}(k^*)} \tag{B.74}$$

which is useful to remember in the interpretation of quantities such as complex impedance functions, which are usually expressed in terms of their real and imaginary parts.

B.7 RESPONSE SPECTRA

For earthquake-resistant design, the entire time history of response may not be required. Instead, earthquake-resistant design may be based on the maximum (absolute) value of the response of a structure to a particular base motion. Obviously, the response will depend on the mass, stiffness, and damping characteristics of the structure and on the characteristics of the base motion.

The *response spectrum* describes the maximum response of a single-degree-of-freedom (SDOF) system to a particular input motion as a function of the natural frequency (or natural period) and damping ratio of the SDOF system (Figure B.19). The response may be expressed in terms of acceleration, velocity, or displacement. The maximum values of each of these parameters depend only on the natural frequency and damping ratio of the SDOF

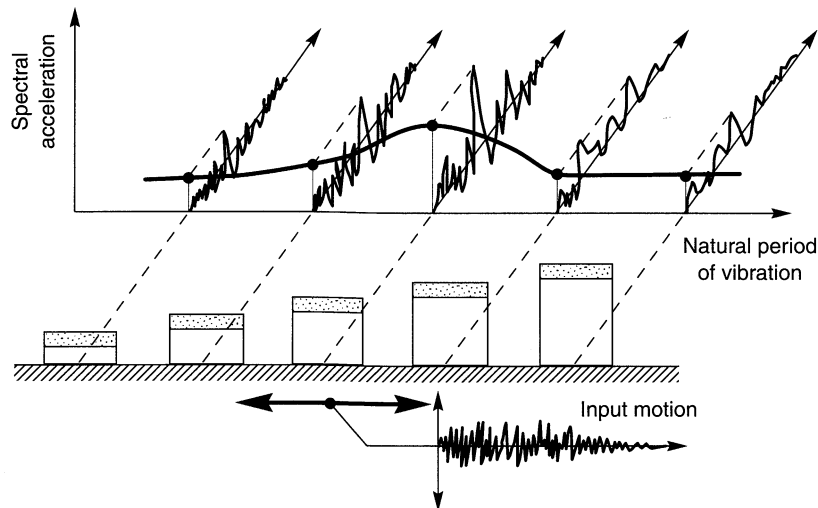


Figure B.19 Response spectrum. Spectral accelerations are the maximum acceleration amplitudes of SDOF systems in response to the same input motion. The response system is obtained by plotting the spectral accelerations against the periods of vibrations of the SDOF systems.

system (for a particular input motion). The maximum values of acceleration, velocity, and displacement are referred to as the spectral acceleration (S_a), spectral velocity (S_v), and spectral displacement (S_d), respectively. Note that a SDOF system of zero natural period (infinite natural frequency) would be rigid, and its spectral acceleration would be equal to the peak ground acceleration.

Application of the Duhamel integral to a linear elastic SDOF system produces expressions for the acceleration, velocity, and displacement time histories that are proportional (by a factor of ω), except for a phase shift. Because the phase shift does not significantly influence the maximum response values, the spectral acceleration, velocity, and displacement can be approximately related to each other by the following simple expressions:

$$S_d = |u|_{\max} \quad (\text{B.75a})$$

$$S_v = |\dot{u}|_{\max} \approx \omega_0 S_d = \text{PSV} \quad (\text{B.75b})$$

$$S_a = |\ddot{u}|_{\max} \approx \omega_0^2 S_d = \omega_0 \cdot \text{PSV} = \text{PSA} \quad (\text{B.75c})$$

where u and ω_0 are the displacement and natural frequency of the SDOF system, PSV is the *pseudospectral velocity*, and PSA is the *pseudospectral acceleration*. Although the PSV and PSA are not the true maximum values of velocity and acceleration, they are usually very close to the maxima for recorded strong ground motions. In practice, the pseudospectral values are generally assumed to be equal to the spectral values.

B.8 RESPONSE OF NONLINEAR SDOF SYSTEMS TO GENERAL LOADING

Numerical integration of the Duhamel integral is very useful for calculation of the response of linear systems to general loading. Many systems for which the seismic response is to be calculated, however, exhibit nonlinear behavior. In such systems the mass is usually constant, but the damping coefficient and/or the stiffness may vary with time, deflection, or velocity. It will be useful to develop methods for analysis of the response of nonlinear systems, recognizing that they will be appropriate for linear systems as well when damping and stiffness values are held constant.

The most common approach to nonlinear analysis is the direct integration of *incremental equations of motion* that govern the response of the system over small time increments. The response is calculated for each time increment after adjusting the stiffness and damping at the beginning of the increment. By using the conditions at the end of one time increment as the initial conditions for the next time increment, the nonlinear system is approximated as an incrementally changing linear system.

B.8.1 Incremental Equation of Motion

Consider the SDOF system shown in Figure B.20, which has a nonlinear spring and dashpot (i.e., the spring force is not proportional to displacement and the dashpot force is not proportional to velocity). Dynamic equilibrium at time τ requires that

$$f_I(\tau) + f_D(\tau) + f_S(\tau) = Q(\tau) \quad (\text{B.76})$$

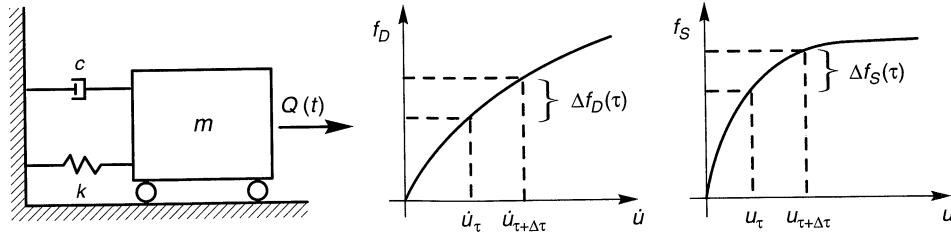


Figure B.20 SDOF system with nonlinear damping and spring forces.

and that

$$f_I(\tau + \Delta\tau) + f_D(\tau + \Delta\tau) + f_S(\tau + \Delta\tau) = Q(\tau + \Delta\tau) \tag{B.77}$$

at time $\tau + \Delta\tau$. Defining

$$\begin{aligned} \Delta f_I(\tau) &= f_I(\tau + \Delta\tau) - f_I(\tau) \\ \Delta f_D(\tau) &= f_D(\tau + \Delta\tau) - f_D(\tau) \\ \Delta f_S(\tau) &= f_S(\tau + \Delta\tau) - f_S(\tau) \\ \Delta Q(\tau) &= Q(\tau + \Delta\tau) - Q(\tau) \end{aligned}$$

and subtracting equation (B.76) from equation (B.77), the incremental equation of motion for the time interval from t to $\tau + \Delta\tau$ is

$$\Delta f_I(\tau) + \Delta f_D(\tau) + \Delta f_S(\tau) = \Delta Q(\tau) \tag{B.78}$$

or expressing the incremental forces in terms of incremental displacements, velocities, and accelerations, as

$$m \Delta \ddot{u}(\tau) + c(\tau) \Delta \dot{u}(\tau) + k(\tau) \Delta u(\tau) = \Delta Q(\tau) \tag{B.79}$$

By integrating this incremental equation of motion in a series of small time steps, the response of the nonlinear system can be obtained. It should be noted that this approach can be used to calculate the response of linear elastic, nonlinear elastic, or nonlinear inelastic materials with stress–strain behaviors shown in Figure B.21. The third of these is particularly important because it allows representation of the hysteretic damping displayed by cyclically loaded soils.

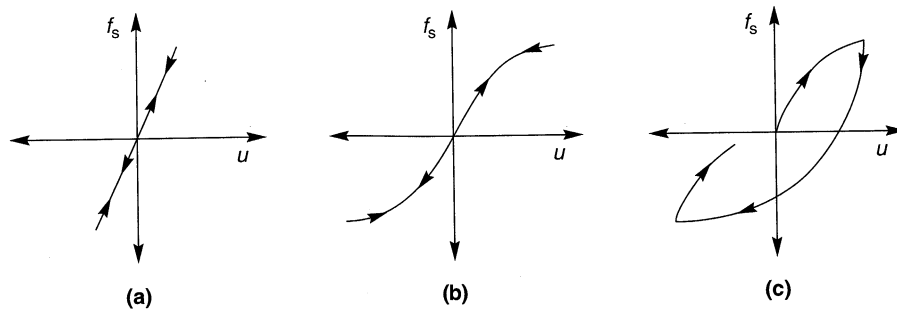


Figure B.21 Stress–strain behavior of (a) linear elastic, (b) nonlinear elastic, and (c) nonlinear inelastic materials under cyclic loading conditions.

B.8.2 Numerical Integration

There are many ways to numerically integrate the incremental equation of motion. One of the simplest and most easily coded of these is the *linear acceleration method*. It is based on the assumption that the acceleration varies linearly within each time increment. If the acceleration in the time increment varies linearly, the velocity and displacement will vary quadratically and cubically, respectively, as shown in Figure B.22. Therefore, expressions for the incremental velocity and displacement can be written in terms of the incremental acceleration, that is,

$$\Delta \dot{u}(\tau) = \ddot{u}(\tau)\Delta t + \Delta \ddot{u}(\tau)\frac{\Delta t}{2} \quad (\text{B.80})$$

$$\Delta u(\tau) = \dot{u}(\tau)\Delta t + \Delta \dot{u}(\tau)\frac{\Delta t^2}{2} + \Delta \ddot{u}(\tau)\frac{\Delta t^2}{6} \quad (\text{B.81})$$

Rearranging, the incremental acceleration and velocity can be expressed in terms of the incremental displacement

$$\Delta \ddot{u}(\tau) = \frac{6}{\Delta t^2}\Delta u(\tau) - \frac{6}{\Delta t}\dot{u}(\tau) - 3\ddot{u}(\tau) \quad (\text{B.82a})$$

$$\Delta \dot{u}(\tau) = \frac{3}{\Delta t}\Delta u(\tau) - 3\dot{u}(\tau) - \frac{\Delta t}{2}\ddot{u}(\tau) \quad (\text{B.82b})$$

Substituting equations (B.82) into the incremental equation of motion gives

$$m \left[\frac{6}{\Delta t^2}\Delta u(\tau) - \frac{6}{\Delta t}\dot{u}(\tau) - 3\ddot{u}(\tau) \right] + c(\tau) \left[\frac{3}{\Delta t}\Delta u(\tau) - 3\dot{u}(\tau) - \frac{\Delta t}{2}\ddot{u}(\tau) \right] + k(\tau)\Delta u(\tau) = \Delta Q(\tau) \quad (\text{B.83})$$

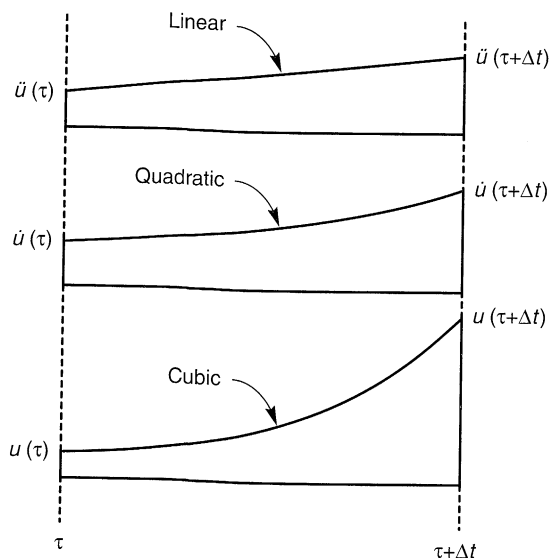


Figure B.22 Variation of acceleration, velocity, and displacement over time increment.

which can be solved for the unknown incremental displacement

$$\Delta u(\tau) = \frac{\Delta Q(\tau) + m [(6/\Delta t)\dot{u}(\tau) + 3\ddot{u}(\tau)] + c(\tau) [3\dot{u}(\tau) + (\Delta t/2)\ddot{u}(\tau)]}{k(\tau) + (6/\Delta t^2)m + (3/\Delta t)c(\tau)} \quad (\text{B.84})$$

Equation (B.84) shows that if the displacement, velocity, and acceleration at time τ are known, the incremental displacement during the succeeding time increment $\Delta\tau$ based on the loading and the stiffness and damping during that time increment can be calculated. From this incremental displacement, the incremental velocity and acceleration, and from these the displacement, velocity, and acceleration at the end of the time increment, can be determined. The conditions at the end of the time increment are then taken as the initial conditions for the next time increment and are used to calculate the appropriate stiffness and damping values for the next time increment. To prevent the accumulation of errors resulting from the assumptions of the linear acceleration method, the acceleration at the beginning of each time step should be calculated by subtracting the damping and spring forces from the total external load and dividing the result by the mass. This will ensure that total equilibrium is satisfied at each step of the analysis.

For numerical stability, it is necessary that the time steps be relatively small, typically less than about 55% of the undamped natural period of the system. These small time steps can lead to considerable computational effort, particularly when such direct integration methods are applied to multiple-degree-of-freedom systems. A number of other numerical integration techniques are available; Berg (1989) describes the application of several to structural dynamics problems.

B.9 MULTIPLE-DEGREE-OF-FREEDOM SYSTEMS

In most physical systems, the motion of the significant masses cannot be described by a single variable; such systems must be treated as *multiple-degree-of-freedom* (MDOF) systems. With the exception of only the simplest cases, the types of buildings, bridges, and other structures that are of interest in earthquake engineering have multiple degrees of freedom. Some structures can be idealized with only a few degrees of freedom; others may require hundreds or even thousands.

In many respects, the response of MDOF systems is similar to the response of SDOF systems, and procedures for analysis are analogous to those described previously for SDOF systems. Although the additional degrees of freedom complicate the algebra, the procedures are conceptually quite similar. In fact, a very useful approach to the response of linear MDOF systems allows their response to be computed as the sum of the responses of a series of SDOF systems.

B.9.1 Equations of Motion

In evaluating the response of an MDOF system, dynamic equilibrium of all masses must be ensured simultaneously. Consider the idealized two-story structure shown in Figure B.23. The structure has two degrees of freedom: horizontal translation of the upper mass and horizontal translation of the lower mass. For each mass the externally applied load must be balanced by the inertial, damping, and elastic forces that resist motion:

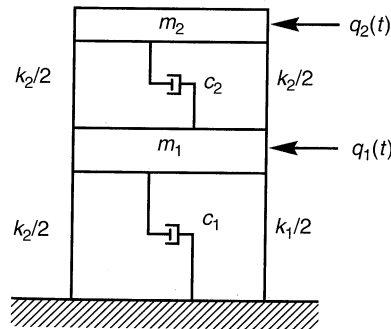


Figure B.23 Two-degree-of-freedom system. Displacements of masses 1 and 2 from equilibrium positions are u_1 and u_2 , respectively.

$$f_{I1} + f_{D1} + f_{S1} = q_1(t) \quad (\text{B.85a})$$

$$f_{I2} + f_{D2} + f_{S2} = q_2(t) \quad (\text{B.85b})$$

or, in matrix form,

$$\mathbf{f}_I + \mathbf{f}_D + \mathbf{f}_S = \mathbf{q}(t) \quad (\text{B.86})$$

If the structure exhibits linear behavior, the principle of superposition is valid. Then the forces that resist motion at each level can be expressed in terms of coefficients by which the motion parameter at all levels are multiplied. For example, the elastic force resisting motion at level 1 can be expressed as

$$f_{S1} = k_{11}u_1 + k_{12}u_2$$

where the stiffness coefficients k_{ij} represent the force induced at level i due to a unit displacement at level j (with the displacements at all levels except j held equal to zero). In matrix form

$$\begin{Bmatrix} f_{S1} \\ f_{S2} \end{Bmatrix} = \begin{bmatrix} k_{11} & k_{12} \\ k_{21} & k_{22} \end{bmatrix} \begin{Bmatrix} u_1 \\ u_2 \end{Bmatrix}$$

or

$$\mathbf{f}_S = \mathbf{k}\mathbf{u}$$

in which \mathbf{k} is the *stiffness matrix* of the structure.

Similarly, a *damping matrix* and a *mass matrix* can be developed in which the elements c_{ij} (or m_{ij}) represent the damping (or inertial) forces resisting motion at level i due to a unit velocity (or acceleration) of level j . Dynamic equilibrium of the MDOF system can then be described by a set of simultaneous equations of motion, which can be expressed in matrix form as

$$\mathbf{m}\ddot{\mathbf{u}} + \mathbf{c}\dot{\mathbf{u}} + \mathbf{k}\mathbf{u} = \mathbf{q}(t) \quad (\text{B.87})$$

MDOF systems also respond to base motions. The equation of motion for the case of base shaking is easily developed following the same procedure applied to the SDOF case in Section B.4.2. The resulting equation of motion is

$$\mathbf{m}\ddot{\mathbf{u}} + \mathbf{c}\dot{\mathbf{u}} + \mathbf{k}\mathbf{u} = -\mathbf{m}\mathbf{1}\ddot{u}_b(t) \quad (\text{B.88})$$

Equation (B.95) indicates that the response of an N -story structure to base motion is equal to the response to equivalent external loads, where $q_i = -m_i \ddot{u}_b(t)$ ($i = 1, N$) is the load applied to the i th floor.

B.9.2 Undamped Free Vibrations

For undamped free vibrations, all terms of the damping matrix are zero, so the equations of motion reduce to

$$\mathbf{m}\ddot{\mathbf{u}} + \mathbf{k}\mathbf{u} = \mathbf{0} \tag{B.89}$$

Assuming that the response of each mass (degree of freedom) is harmonic, we have

$$\mathbf{u}(t) = \mathbf{U} \sin(\omega t + \boldsymbol{\theta}) \tag{B.90}$$

where \mathbf{U} is a vector containing the displacement amplitudes and $\boldsymbol{\theta}$ is a vector containing the phase angles at each level of the structure (or for each degree of freedom). Differentiating equation (B.90) twice gives

$$\ddot{\mathbf{u}}(t) = -\omega^2 \mathbf{U} \sin(\omega t + \boldsymbol{\theta}) = -\omega^2 \mathbf{u}(t) \tag{B.91}$$

Substituting the expressions for displacement [equation (B.90)] and acceleration [equation (B.91)] into the equation of motion [equation (B.89)] yields

$$-\mathbf{m}\omega^2 \mathbf{U} \sin(\omega t + \boldsymbol{\theta}) + \mathbf{k}\mathbf{U} \sin(\omega t + \boldsymbol{\theta}) = \mathbf{0}$$

or

$$[\mathbf{k} - \omega^2 \mathbf{m}]\mathbf{U} = \mathbf{0} \tag{B.92}$$

which is a set of linear algebraic equations with unknown \mathbf{U} . A nontrivial solution (one that gives values other than $\mathbf{U} = \mathbf{0}$) can be obtained only if

$$\det(\mathbf{k} - \omega^2 \mathbf{m}) = |\mathbf{k} - \omega^2 \mathbf{m}| = 0 \tag{B.93}$$

Equation (B.93) is the *frequency equation* (or *characteristic equation*) of the system, which for a system of N degrees of freedom, will give a polynomial of N th degree in ω^2 . The N roots of the frequency equations $\{\omega_1^2, \omega_2^2, \omega_3^2, \dots, \omega_N^2\}$ represent the frequencies at which the undamped system can oscillate in the absence of external forces. These frequencies are called the *natural circular frequencies* of the system.

Example B.5

Compute the natural frequencies of the three-story structure shown in Figure EB.5.

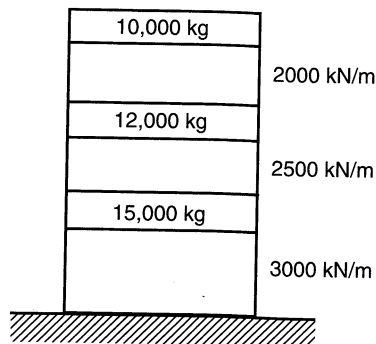


Figure EB.5

Solution The mass matrix for this simple structure is

$$\mathbf{m} = 1000 \begin{bmatrix} 10 & 0 & 0 \\ 0 & 12 & 0 \\ 0 & 0 & 15 \end{bmatrix} \quad \text{kg}$$

The stiffness matrix can be determined by applying a unit displacement to each floor (with zero displacement at the other floors) and evaluating the resulting forces. By this procedure the stiffness matrix is

$$\mathbf{k} = 1,000,000 \begin{bmatrix} 5.5 & -2.5 & 0 \\ -2.5 & 4.5 & -2.0 \\ 0 & -2.0 & 2.0 \end{bmatrix} \quad \text{N/m}$$

Then

$$\mathbf{k} - \omega^2 \mathbf{m} = 1,000,000 \begin{bmatrix} 5.5 - 10\alpha & -2.5 & 0 \\ -2.5 & 4.5 - 12\alpha & -2.0 \\ 0 & -2.0 & 2.0 - 15\alpha \end{bmatrix} \quad \text{where } \alpha = \frac{\omega^2}{1000}$$

Setting the determinant $|\mathbf{k} - \omega^2 \mathbf{m}| = 0$ gives the frequency equation

$$1800\alpha^3 - 1905\alpha^2 + 459.5\alpha - 15 = 0$$

The roots of the frequency equation are $\alpha_1 = 0.0386$, $\alpha_2 = 0.3000$, and $\alpha_3 = 0.7197$. Consequently,

$$\begin{Bmatrix} \omega_1^2 \\ \omega_2^2 \\ \omega_3^2 \end{Bmatrix} = \begin{Bmatrix} 38.6 \\ 300.0 \\ 719.7 \end{Bmatrix} \Rightarrow \begin{Bmatrix} \omega_1 \\ \omega_2 \\ \omega_3 \end{Bmatrix} = \begin{Bmatrix} 6.21 \\ 17.62 \\ 26.83 \end{Bmatrix} \frac{\text{rad}}{\text{sec}} \Rightarrow \begin{Bmatrix} f_1 \\ f_2 \\ f_3 \end{Bmatrix} = \begin{Bmatrix} 0.99 \\ 2.76 \\ 4.27 \end{Bmatrix} \text{ Hz}$$

Each natural frequency is associated with a *mode of vibration* of the system. At the natural frequencies, the amplitude of the displacement vector, \mathbf{U} , is indeterminate [scaling the displacements up or down by a constant factor will still satisfy equation (B.92)]. The vector \mathbf{U} does describe the shape of the vibrating system, which is different at each natural frequency. This shape is often made dimensionless by dividing the elements of \mathbf{U} by one (often the first, sometimes the largest) element. The resulting vector describes the mode shape; the *mode shape* for the n^{th} mode of vibration would be

$$\boldsymbol{\phi}_n^T = [\phi_{1n} \ \phi_{2n} \ \cdots \ \phi_{Nn}] = \frac{1}{U_{Nn}} [U_{1n} \ U_{2n} \ \cdots \ 1] \quad (\text{B.94})$$

All mode shapes satisfy the relationship, $|\mathbf{k} - \omega_n^2 \mathbf{m}| \boldsymbol{\phi}_n = \mathbf{0}$ for $n = [1, N]$. The values of the vector $\boldsymbol{\phi}_n$ at each natural frequency describe the mode shape of the corresponding mode of vibration. Thus a system of N degrees of freedom will have N natural frequencies corresponding to N modes of vibration. Each mode of vibration occurs at a particular natural frequency and causes the structure to deform with a particular mode shape. The mode corresponding to the lowest natural frequency is called the first mode or *fundamental mode*, the second lowest natural frequency is called the second mode, and so on. The mode shapes can be shown to be *orthogonal*, that is, for $m \neq n$

$$\boldsymbol{\phi}_m^T \mathbf{m} \boldsymbol{\phi}_n = 0$$

$$\boldsymbol{\phi}_m^T \mathbf{k} \boldsymbol{\phi}_n = 0$$

Example B.6

Compute the mode shapes for the structure shown in Example B.5.

Solution Substituting the fundamental frequency into equation (B.99) yields

$$1,000,000 \begin{bmatrix} 5.114 & -2.5 & 0 \\ -2.5 & 4.037 & -2.0 \\ 0 & -2.0 & 1.421 \end{bmatrix} \begin{Bmatrix} U_{11} \\ U_{21} \\ U_{31} \end{Bmatrix} = \begin{Bmatrix} 0 \\ 0 \\ 0 \end{Bmatrix}$$

Normalizing by the top floor displacement, U_{31} , the mode shape

$$\phi_1 = \frac{1}{U_{31}} \begin{Bmatrix} U_{11} \\ U_{21} \\ U_{31} \end{Bmatrix} = \begin{Bmatrix} \phi_{11} \\ \phi_{21} \\ 1 \end{Bmatrix}$$

must satisfy $[\mathbf{k} - \omega_1^2 \mathbf{m}] \phi_1 = \mathbf{0}$. Then, using the known value of $\phi_{31} = 1$, ϕ_{11} and ϕ_{21} can be determined. The process can be repeated to yield the mode shapes of all three modes of vibration:

$$\phi_1 = \begin{Bmatrix} 0.347 \\ 0.711 \\ 1.000 \end{Bmatrix} \quad \phi_2 = \begin{Bmatrix} -1.250 \\ -1.250 \\ 1.000 \end{Bmatrix} \quad \phi_3 = \begin{Bmatrix} 6.479 \\ -4.398 \\ 1.000 \end{Bmatrix}$$

The mode shapes are shown graphically in Figure EB.6.

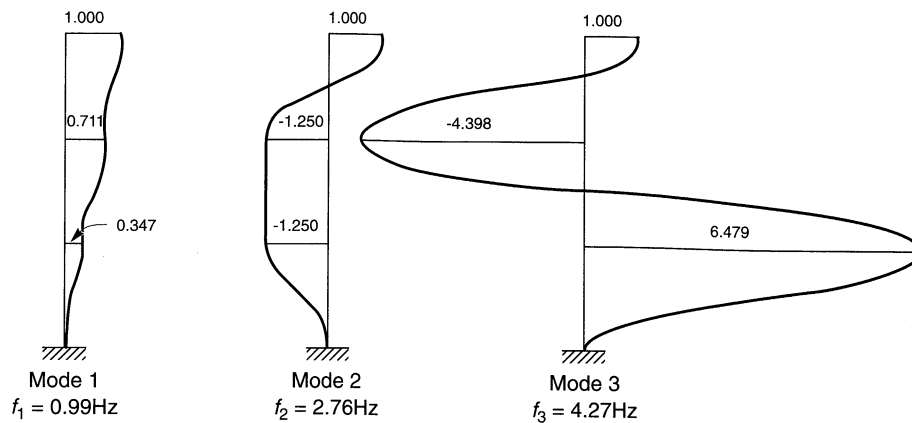


Figure EB.6

B.9.3 Mode Superposition Method

For linear structures with certain types of damping, the response in each mode of vibration can be determined independently of the response in the other modes. The independent modal responses can then be combined to determine the total response. This is the basis of the *mode superposition method*.

Recalling that the mode shape vector, ϕ_n , describes only the shape of the n th mode, the displacements can be expressed as the product of the mode shape and the modal amplitude, y_n :

$$\mathbf{U}_n(t) = \boldsymbol{\phi}_n y_n(t) \quad (\text{B.95})$$

Then, by substituting equation (B.95) into equation (B.87) and premultiplying each term by $\boldsymbol{\phi}_n^T$, the equation of motion can be written for the n th mode of vibration as

$$M_n \ddot{y}_n + C_n \dot{y}_n + K_n y_n = Q_n(t) \quad (\text{B.96})$$

where $M_n = \boldsymbol{\phi}_n^T \mathbf{m} \boldsymbol{\phi}_n$, $C_n = \boldsymbol{\phi}_n^T \mathbf{c} \boldsymbol{\phi}_n$, $K_n = \boldsymbol{\phi}_n^T \mathbf{k} \boldsymbol{\phi}_n$, and $Q_n(t) = \boldsymbol{\phi}_n^T \mathbf{q}(t)$. This equation of motion is based on the assumption that the damping matrix is orthogonal (i.e., that $\boldsymbol{\phi}_m^T \mathbf{c} \boldsymbol{\phi}_n = 0$ for $m \neq n$). *Rayleigh damping*, in which the damping matrix can be broken into a component proportional to the mass matrix and a component proportional to the stiffness matrix, satisfies the orthogonality requirement. Other procedures are described in standard structural dynamics texts. Alternatively, the equation of motion can be written as

$$\ddot{y}_n + 2\xi_n \omega_n \dot{y}_n + \omega_n^2 y_n = \frac{Q_n(t)}{M_n} \quad (\text{B.97})$$

For the case of base shaking, the equation of motion can be expressed as

$$\ddot{y}_n + 2\xi_n \omega_n \dot{y}_n + \omega_n^2 y_n = -\frac{L_n}{M_n} \ddot{u}_b(t) \quad (\text{B.98})$$

where $L_n = \sum_{j=1}^N m_j \phi_{jn}$.

By this process, the system of N simultaneous equations (the original equations of motion) is transformed to a system of N independent equations. Each of these independent equations can be solved for $y_n(t)$ using the SDOF procedures described earlier in this appendix. Then the total displacement is obtained by superposition of the modal contributions:

$$\mathbf{u}(t) = \boldsymbol{\phi}_1 y_1(t) + \boldsymbol{\phi}_2 y_2(t) + \cdots + \boldsymbol{\phi}_N y_N(t) \quad (\text{B.99})$$

Once the displacements are known, they can be used to compute forces, stresses, and other parameters of interest. The displacements can also be used to compute a set of *equivalent lateral forces*, $\mathbf{f}(t)$, which would produce the displacements $\mathbf{u}(t)$ if they were applied as static loads:

$$\mathbf{f}(t) = \mathbf{k} \boldsymbol{\phi}_1 y_1(t) + \mathbf{k} \boldsymbol{\phi}_2 y_2(t) + \cdots + \mathbf{k} \boldsymbol{\phi}_N y_N(t) \quad (\text{B.100})$$

Internal forces can be computed by static analysis of the structure subjected to the equivalent lateral forces. These internal forces can be used for design of the various elements of the structure.

Example B.7

Compute the response of the structure shown in Example B.4 to the Gilroy No. 2 E-W earthquake motion using the mode superposition method. Assume 5% damping for all modes.

Solution The Gilroy No. 2 earthquake motion, illustrated in Figure 3.1, was recorded on the surface of a thick deposit of stiff soil in the 1989 Loma Prieta earthquake. Use of the mode superposition method requires evaluation of the modal equations of motion. For the first mode,

$$M_1 = \boldsymbol{\phi}_1^T \mathbf{m} \boldsymbol{\phi}_1 = (1000 \text{ kg}) \{0.347 \quad 0.711 \quad 1.000\} \begin{bmatrix} 10 & 0 & 0 \\ 0 & 12 & 0 \\ 0 & 0 & 15 \end{bmatrix} \begin{Bmatrix} 0.347 \\ 0.711 \\ 1.000 \end{Bmatrix} = 22,270 \text{ kg}$$

$$\begin{aligned} L_1 &= m_1 \phi_{11} + m_2 \phi_{21} + m_3 \phi_{31} \\ &= (10,000)(0.347) + (12,000)(0.711) + (15,000)(1.000) \\ &= 27,002 \text{ kg} \end{aligned}$$

so the equation of motion [equation (B.98)] is

$$\ddot{y}_1 + 0.621\dot{y}_1 + 38.56y_1 = -1.212\ddot{u}_b(t)$$

Repeating this process for the second and third modes gives

$$\ddot{y}_2 + 1.732\dot{y}_2 + 300.0y_2 = 0.253\ddot{u}_b(t)$$

$$\ddot{y}_3 + 2.683\dot{y}_3 + 719.8y_3 = -0.041\ddot{u}_b(t)$$

B.9.4 Response Spectrum Analysis

The mode superposition method produces the entire time history of the response of the structure. For design purposes, however, the entire time history may not be needed; the maximum response values may be sufficient. Because each mode of vibration can be treated as an independent SDOF system, maximum values of modal response can be obtained from the response spectrum. The modal maxima can then be combined to estimate the maximum total response.

B.9.4.1 Calculation of Modal Response Maxima

Let S_{dn} , S_{vn} , and S_{an} denote the spectral displacement, velocity, and acceleration associated with the n th mode of vibration, respectively (these values would be obtained from the response spectrum at a period, $T_n = 2\pi/\omega_n$). Then the maximum modal displacement is given by

$$(y_n)_{\max} = \frac{L_n}{M_n} S_{dn} = \frac{L_n T_n^2}{4\pi^2 M_n} S_{an} \quad (\text{B.101})$$

Using equation (B.95), the maximum displacement of the j th floor would be

$$(U_{jn})_{\max} = \frac{L_n}{M_n} S_{dn} \phi_{jn} = \frac{L_n T_n^2}{4\pi^2 M_n} S_{an} \phi_{jn} \quad (\text{B.102})$$

The maximum value of the equivalent lateral force at the j th floor is

$$(f_{jn})_{\max} = \frac{L_n}{M_n} m_j \phi_{jn} S_{an} \quad (\text{B.103})$$

Maximum values of the internal forces can be computed by static analysis of the structure subjected to the maximum equivalent lateral forces.

B.9.4.2 Combination of Modal Response Maxima

Section B.9.4.1 showed how the response spectrum can be used to predict maximum values of various modal response parameters. The mode superposition method showed that

time histories of modal response can be combined by simple superposition to obtain the total time history of response. However, combination of modal response maxima to obtain the maximum total response is not as straightforward.

The exact value of the maximum total response cannot be obtained directly from the modal maxima because the modal maxima occur at different times. Direct superposition of the modal maxima, which implies that the maxima do occur simultaneously, produces an upper bound to the maximum total response; for any response parameter $r(t)$,

$$r_{\max} \leq \sum_{n=1}^N (r_n)_{\max} \quad (\text{B.104})$$

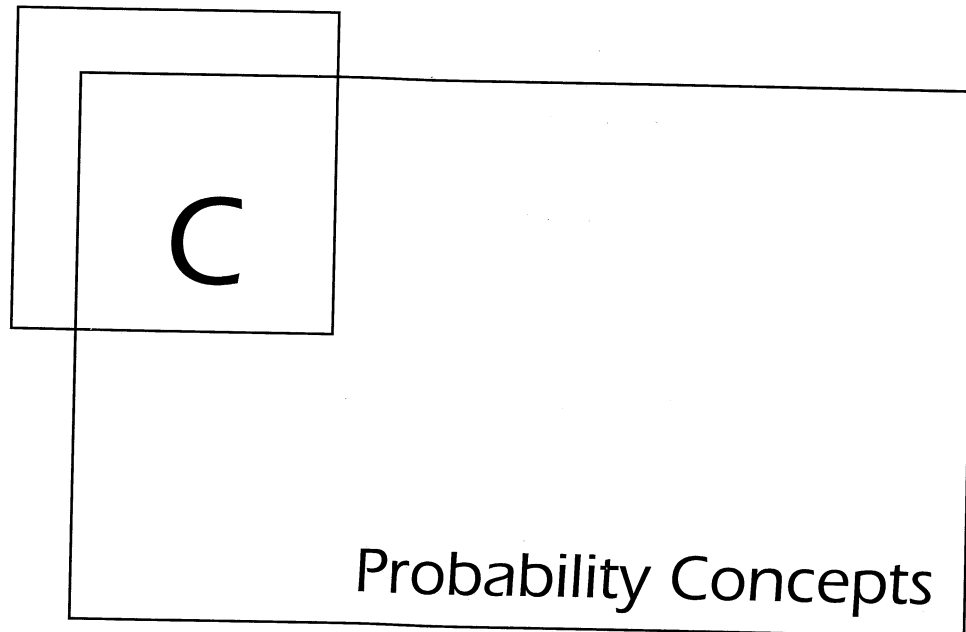
This upper bound value is usually too conservative and is rarely used for design. Instead, modal combination procedures based on random vibration theory are used. The simplest of these is the root-sum-square value

$$r_{\max} = \sqrt{\sum_{n=1}^N (r_n)_{\max}^2} \quad (\text{B.105})$$

The root-sum-square procedure provides a good estimate of maximum total response when the natural periods are well separated (by a factor of about 1.5 or more for 5% damping). Procedures that account for correlation between modes are available (Newmark and Rosenblueth, 1971; Chopra, 1995) for cases of closely spaced modes.

B.9.5 Discussion

The mode superposition method and response spectrum analysis procedures both rely on representation of a MDOF system by a set of SDOF systems. The characteristics of the set of SDOF systems are such that those corresponding to the lower natural frequencies contribute more to the total response than those corresponding to the higher natural frequencies. For practical purposes, the response of a MDOF system can be computed with reasonable accuracy by considering only the lower modes that contribute significantly to the total response of the structure. For some structures, only a small number of modes may need to be considered. All of the analyses described in this section apply to linear structures. Procedures for analysis of nonlinear MDOF structures are available but are well beyond the scope of this appendix.



C.1 INTRODUCTION

Geotechnical earthquake engineering problems are fraught with uncertainty. At a particular site, earthquake-induced loading depends on the size and location of the earthquake—none of which can be predicted with certainty. Because of the inherent variability of soils and the inevitable limits on exploration of subsurface conditions, the resistance of the soil to that loading is not known with certainty. When both loading and resistance are uncertain, the resulting effects are uncertain as well. A number of geotechnical earthquake engineering analyses attempt to quantify the uncertainty in the various input parameters for a particular problem, and compute the resulting uncertainty in the output.

In this appendix we provide a brief introduction to some basic concepts of probability and describe several probability distributions that are used in the body of the book. More detailed information on these topics can be found in texts such as Benjamin and Cornell (1970), Ang and Tang (1975a,b, 1984), and Harr (1987).

C.2 SAMPLE SPACES AND EVENTS

Probability theory deals with the results, or outcomes, of processes that are usually described in a general sense as *experiments*. The set of all possible outcomes of an experiment is called the *sample space*, and each outcome of an experiment is called a *sample*

point. The sample space therefore consists of all possible sample points. The sample space may be *continuous*, in which case the number of sample points is infinite, or it may be *discrete*, as when the number of sample points are finite and countable.

An *event* is a subset of a sample space, and therefore represents a set of sample points. A *single event* consists of a single sample point, and a *compound event* consists of more than one sample point. If Ω represents a sample space and A represents an event, the *complementary event*, \bar{A} , is the set of all sample points in Ω that are not in A . The interrelationships among sets can be conveniently illustrated by means of a *Venn diagram* (Figure C.1). In Figure C.1 the sample space is represented by the rectangle Ω and the event A by the circle. Thus A is a subset of Ω . The complementary event \bar{A} corresponds to the part of the rectangle that lies outside the circle. Because no sample points are in both A and \bar{A} , the *intersection* of A and \bar{A} is the *null set*, ϕ (i.e., $A \cap \bar{A} = \phi$). Similarly, all sample points are in either A or \bar{A} , so the *union* of A and \bar{A} is Ω (i.e., $A \cup \bar{A} = \Omega$). Two events, A and B , are said to be mutually exclusive if they share no common sample points (i.e., $A \cap B = \phi$).

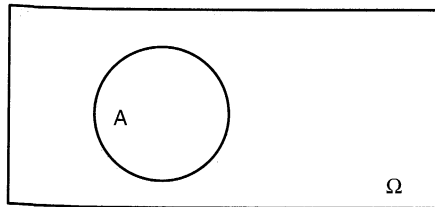


Figure C.1 Venn diagram illustrating event A in sample space Ω .

Example C.1

Consider the Venn diagram for the three events, A , B , and C , shown in Figure EC.1.

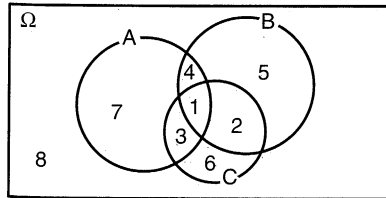


Figure EC.1

$$A \cap B = \text{regions 1 and 4}$$

$$B \cup C = \text{regions 1, 2, 3, 4, 5, and 6}$$

$$A \cap B \cap C = \text{region 1}$$

$$A \cap \bar{B} = \text{regions 3 and 7}$$

$$(A \cup B) \cap C = \text{regions 1, 2, and 3}$$

$$\bar{A} \cap \bar{B} \cap \bar{C} = \text{region 8}$$

C.3 AXIOMS OF PROBABILITY

A probability measure, P , can be assigned to each sample point or set of sample points in a sample space. The probability of an event A is denoted by the symbol $P[A]$. The entire theory of probability is based on the following three fundamental axioms.

Axiom 1. The probability of an event is represented by a number greater than or equal to zero but less than or equal to 1:

$$0 \leq P[A] \leq 1 \quad (\text{C.1a})$$

Axiom 2. The probability of an event equal to the entire sample space Ω is 1:

$$P[\Omega] = 1 \quad (\text{C.1b})$$

Axiom 3. The probability of an event representing the union of two mutually exclusive events is equal to the sum of the probabilities of the events:

$$P[A \cup B] = P[A] + P[B] \quad (\text{C.1c})$$

These axioms can be used to develop the rules and theorems that comprise the mathematical theory of probability.

C.4 PROBABILITIES OF EVENTS

Probabilities are often thought of in terms of relative frequencies of occurrence. If the existence of a water content greater than the optimum water content in a compacted fill is considered to be an event, the probability of that event can be estimated by determining the relative frequency of water content measurements that exceed the water content. If the total number of water content measurements is small, the relative frequency may only approximate the actual probability, but as the number of measurements becomes large, the relative frequency will approach the actual probability. This frequentist point of view is not very helpful, however, for situations in which an experiment cannot be repeated. In such cases, probabilities can be viewed as relative likelihoods (or degrees of belief), as in the probability that a newly discovered fault is capable of producing maximum earthquake magnitudes of 7.0 or 7.5. The latter interpretation lends itself to the subjective evaluation of probability.

Regardless of how probabilities are interpreted, the axioms of probability allow statements to be made about the probabilities of occurrence of single or multiple events. These can be visualized with the help of *Venn diagrams* drawn such that the area of the rectangle representing the sample space Ω is 1 and the areas of all events within the sample space are equal to their probabilities. Consider the nonexclusive events A and B in Figure C.2. The event $A \cap B$ (which means that *both A and B occur*) is represented by the shaded region in Figure C.2a; $P[A \cap B]$ is given by the area of the shaded region. The event $A \cup B$ (which means that *either A or B occurs*) is represented by the shaded region in Figure C.2b; $P[A \cup B]$ is given by the area of that shaded region, or

$$P[A \cup B] = P[A] + P[B] - P[A \cap B] \quad (\text{C.2})$$

In many instances, the probability of one event depends on the occurrence of another event. The *conditional probability* of event A given the occurrence of event B is denoted $P[A|B]$ and is defined (for $P[B] > 0$) by

$$P[A|B] = \frac{P[A \cap B]}{P[B]} \quad (\text{C.3})$$

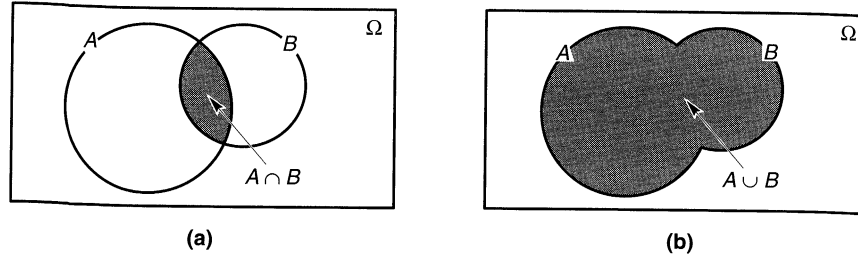


Figure C.2 Venn diagrams for events A and B in sample space Ω . (a) The set $A \cap B$ is given by the shaded area; if the area of Ω is 1, $P[A \cap B]$ is equal to the area that is shaded. (b) The set $A \cup B$ is given by the shaded area; $P[A \cup B]$ is equal to the shaded area.

The conditional probability is easily visualized with the Venn diagram (Figure C.2a) as the ratio of the area of $A \cap B$ to the area of B . Event A is *statistically independent* of event B if the occurrence of B does not affect the probability of occurrence of A ; that is,

$$P[A|B] = P[A] \quad (\text{C.4})$$

Rearranging equation (C.2), the probability that both A and B occur, is given by

$$P[A \cap B] = P[A|B] P[B] \quad (\text{C.5})$$

which if A and B are statistically independent becomes

$$P[A \cap B] = P[A] P[B] \quad (\text{C.6})$$

This is known as the *multiplication rule* and can be extended to the multiple, mutually independent events A, B, C, \dots, N by

$$P[A \cap B \cap C \cap \dots \cap N] = P[A] P[B] P[C] \dots P[N] \quad (\text{C.7})$$

The multiplication rule states that the probability of joint occurrence of statistically independent events is equal to the product of their individual probabilities.

Example C.2

Consider the rolling of a single fair die as an experiment. Then the resulting sample space, $\Omega = \{1, 2, 3, 4, 5, 6\}$, is the set of all possible outcomes of the experiment. Let the following three events be defined as

$$\begin{aligned} A &= \{1\} && \text{(a single roll produces a 1)} \\ B &= \{1, 3, 5\} && \text{(a single roll produces an odd number)} \\ C &= \{4, 5, 6\} && \text{(a single roll produces a number greater than 3)} \end{aligned}$$

Define the sets $A \cap B$, $A \cup B$, and $B \cup C$, and compute their probabilities.

Solution The set $A \cap B$ includes all outcomes that are in both A and B (i.e., $A \cap B = \{1\}$). The set $A \cup B$ includes all outcomes that are in either A or B (i.e., $A \cup B = \{1, 3, 5\}$). The set $B \cup C$ includes all outcomes that are in either B or C (i.e., $B \cup C = \{1, 3, 4, 5, 6\}$). The probabilities of each set can be computed as

$$\begin{aligned} P[A \cap B] &= P[A|B] P[B] = \left(\frac{1}{3}\right)\left(\frac{1}{2}\right) = \frac{1}{6} \\ P[A \cup B] &= P[A] + P[B] - P[A \cap B] = \frac{1}{6} + \frac{1}{2} - \frac{1}{6} = \frac{1}{2} \\ P[B \cup C] &= P[B] + P[C] - P[B \cap C] = \frac{1}{2} + \frac{1}{2} - \frac{1}{6} = \frac{5}{6} \end{aligned}$$

Example C.3

One hundred field compaction tests were performed in the early stages of construction of an earth dam. The results of the tests are presented in terms of the numbers that satisfied specifications for minimum relative compaction and for compaction water content in the table below.

Water Content	Relative Compaction	
	Acceptable	Not Acceptable
Acceptable	80	10
Not acceptable	6	4

Assume that the contractor's performance in the future will be the same as in the first 100 tests and that the fill material does not change. Estimate the probability that the relative compaction specification will be satisfied in the next test if the water content specification is satisfied. Estimate that probability for the case in which the water content specification is not satisfied.

Solution Define two events, R and W , such that

R = relative compaction specification satisfied

W = water content specification satisfied

From the table the probability that both the relative compaction and water content specifications are satisfied can be estimated as $P[W \cap R] = 80/100$. Then the probability that the relative compaction specification will be satisfied in the next test if the water content specification is satisfied is the conditional probability $P[R|W]$, which can be computed as

$$P[R|W] = \frac{P[W \cap R]}{P[W]} = \frac{80/100}{80/100 + 10/100} = \frac{80}{90} = 0.889$$

The probability that the relative compaction specification is satisfied given that the water content specification is not satisfied can be estimated as $P[R|\bar{W}]$, or

$$P[R|\bar{W}] = \frac{P[\bar{W} \cap R]}{P[\bar{W}]} = \frac{6/100}{6/100 + 4/100} = \frac{6}{10} = 0.600$$

For a set of events, B_1, B_2, \dots, B_N , which are mutually exclusive ($B_i \cap B_j = \emptyset$) for all $i \neq j$ but collectively exhaustive ($B_1 \cup B_2 \cup \dots \cup B_N = \Omega$), like that shown in the Venn diagram of Figure C.3, the probability of another event A can be expressed as

$$P[A] = P[A \cap B_1] + P[A \cap B_2] + \dots + P[A \cap B_N] \tag{C.8}$$

Using equation (C.5) for each term on the right side of equation (C.8) yields

$$\begin{aligned} P[A] &= P[A|B_1]P[B_1] + P[A|B_2]P[B_2] + \dots + P[A|B_N]P[B_N] \\ &= \sum_{i=1}^N P[A|B_i]P[B_i] \end{aligned} \tag{C.9}$$

which is known as the *total probability theorem*. The total probability theorem forms the backbone of the probability calculations required for probabilistic seismic hazard analyses (Chapter 4).

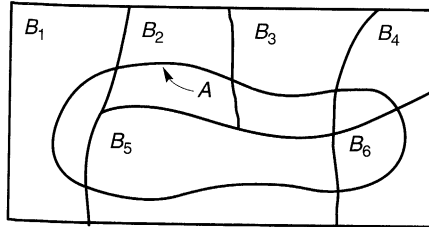


Figure C.3 Intersection of event A with mutually exclusive but collectively exhaustive events B_i .

Example C.4

A structural engineer has determined that a structure will collapse in an earthquake that produces a peak acceleration of $0.3g$. The probability that a given earthquake on fault A, B, or C would be strong enough to cause the structure to collapse are 0.5, 0.2, and 0.1, respectively. The probabilities that that such earthquakes will occur on faults A, B, and C during the life of the building are 0.01, 0.05, and 0.08, respectively. What is the probability that the structure will collapse in an earthquake?

Solution Define the following events as

A = the structure collapses in an earthquake

D_1 = an earthquake capable of collapsing the structure occurs on fault A

D_2 = an earthquake capable of collapsing the structure occurs on fault B

D_3 = an earthquake capable of collapsing the structure occurs on fault C

Then the probability that the structure collapses in an earthquake is given by

$$\begin{aligned} P[A] &= P[A|D_1]P[D_1] + P[A|D_2]P[D_2] + P[A|D_3]P[D_3] \\ &= (0.5)(0.01) + (0.2)(0.05) + (0.1)(0.10) \\ &= 0.025 \end{aligned}$$

C.5 RANDOM VARIABLES

All fields of science and engineering attempt to describe various quantities or phenomena with numerical values. In most cases, the precise numerical value cannot be predicted in advance of some process, or experiment, of interest. In such cases, a particular quantity or phenomenon is described by a *random variable*. The random variable is used to describe an event in a sample space in quantitative terms.

A *continuous random variable* can take on any value within one or more intervals. Because a continuous random variable can take on any of an infinite number of values, the probability of it taking on any specific value is $1/\infty = 0$. The probability distribution of a continuous random variable can also be described by its *probability density function* or PDF, $f_X(x)$, which must satisfy the conditions

$$f_X(x) \geq 0 \quad \text{for all } x$$

$$\int_{-\infty}^{\infty} f_X(x) dx = 1$$

$$P[a \leq X \leq b] = \int_a^b f_X(x) dx$$

According to these conditions, the area under the PDF between two values a and b represents the probability that the random variable will have a value in the interval bounded by a and b . The probability distribution of a random variable can also be described by its *cumulative distribution function* (CDF), which is given by

$$F_X(x) = P[X \leq x] = \int_{-\infty}^x f_X(x) dx \tag{C.10}$$

Therefore, the probability that a random variable, X , falls between two values a and b is

$$P[a \leq X \leq b] = F_X(b) - F_X(a) \tag{C.11}$$

Obviously, the PDF and CDF are closely related—one can be obtained from the other by integration or differentiation. The PDF and CDF of a typical probability distribution are shown in Figure C.4.

From the total probability theorem and the definition of the PDF, the probability of the random variable Y having some value y given that the random variable X is between two values, a and b , can be expressed as

$$\begin{aligned} P[Y = y] &= P[Y = y | a \leq X \leq x_2] P[x_1 \leq X \leq x_2] \\ &= \int_a^b P[Y = y | a \leq X \leq x_2] f_X(X) dx \end{aligned} \tag{C.12}$$

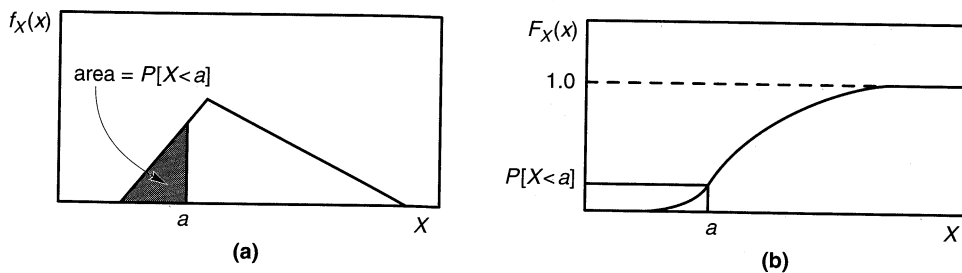


Figure C.4 (a) PDF for a random variable, X . The probability that $X < a$ is given by the area under the PDF to the left of a . (b) CDF for the same random variable. The probability that $X < a$ is given by the value of the CDF at $X = a$.

C.6 EXPECTED VALUES AND STANDARD DEVIATIONS

The uncertainty of a random variable can often be characterized with reasonable accuracy by a few statistical parameters. The *mean*, or *expected value*, of a continuous random variable, X , is given by

$$\bar{x} = \int_{-\infty}^{\infty} x f_X(x) dx \tag{C.13}$$

The mean is a very useful measure of the central tendency of the random variable. By itself, however, it does not adequately describe the shape of the PDF. The dispersion of the random

variable about the mean is also very important. This dispersion is usually characterized by the *variance*

$$\sigma_x^2 = \int_{-\infty}^{\infty} (x - \bar{x})^2 f_X(x) dx \quad (\text{C.14})$$

or the *standard deviation*

$$\sigma_x = \sqrt{\sigma_x^2} \quad (\text{C.15})$$

Both of these parameters reflect how widely the random variable is dispersed about the mean. Because its units are the same as those of the random variable, the standard deviation is more commonly used than the variance. This characteristic also allows the dispersion to be expressed in dimensionless form by the coefficient of variation

$$\text{COV}_x = \frac{\sigma_x}{\bar{x}} \quad (\text{C.16})$$

The mean and standard deviation (or mean and coefficient of variation) go far toward describing the uncertainty in a random variable. Many simple probability distributions, including those most commonly used in geotechnical earthquake engineering, are completely described by these two parameters. Other distributions may require additional parameters to characterize their symmetry, limits, and/or other characteristics.

C.7 COMMON PROBABILITY DISTRIBUTIONS

The results of statistical experiments often exhibit the same general type of behavior. As a result, the random variables associated with those experiments can be described by essentially the same PDF. Many probability density functions exist, but only a few are required for the geotechnical earthquake engineering analyses described in this book.

C.7.1 Uniform Distribution

The simplest probability distribution is one in which all possible values of the random variable are equally likely. Such a random variable is described by a *uniform distribution*. The PDF for a continuous random variable, X , that is uniformly distributed between two values a and b is

$$f_X(x) = \begin{cases} 0 & \text{for } x \leq a \\ \frac{1}{b-a} & \text{for } a < x \leq b \\ 0 & \text{for } x > b \end{cases} \quad (\text{C.17})$$

The PDF and CDF for a uniform distribution are illustrated in Figure C.5.

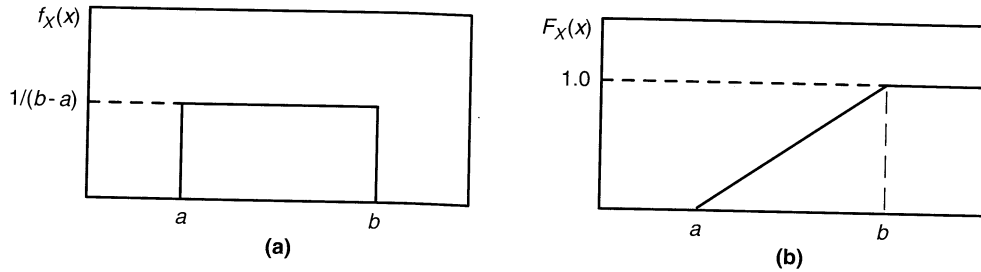


Figure C.5 Uniform distribution: (a) probability density function; (b) cumulative distribution function.

C.7.2 Normal Distribution

The most commonly used probability distribution in statistics is the *normal distribution* (or *Gaussian distribution*). Its PDF, which plots as the familiar bell-shaped curve of Figure C.6a, describes sets of data produced by a wide variety of physical processes. The normal distribution is completely defined by two parameters: the mean and standard deviation. Mathematically, the PDF of a normally distributed random variable X with mean \bar{x} and standard deviation σ_x is given by

$$f_X(x) = \frac{1}{\sqrt{2\pi}\sigma_x} \exp\left[-\frac{1}{2}\left(\frac{x-\bar{x}}{\sigma_x}\right)^2\right] \quad (C.18)$$

The PDF and CDF for a normal distribution are illustrated in Figure C.6. Examples of normal pdf's for random variables with different means and standard deviations are shown in Figure C.7.

Integration of the PDF of the normal distribution does not produce a simple expression for the CDF, so values of the normal CDF are usually expressed in tabular form. The

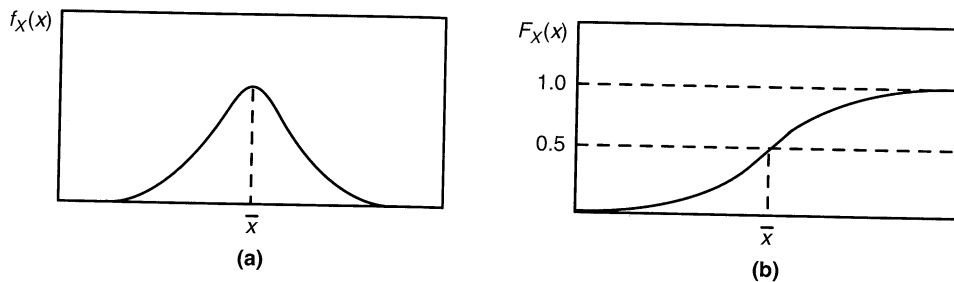


Figure C.6 Normal distribution: (a) probability density function; (b) cumulative distribution function.

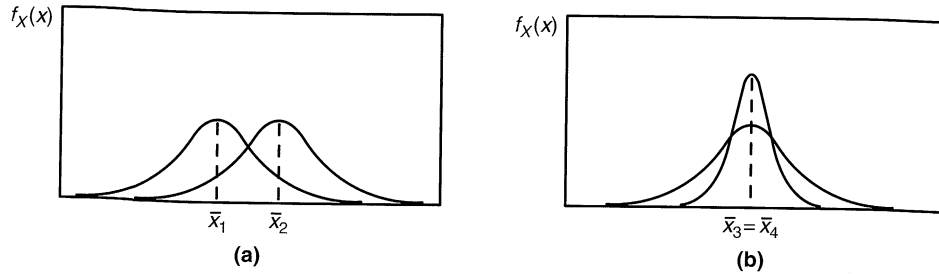


Figure C.7 Normal distributions for (a) two random variables, X_1 and X_2 , with different means but the same standard deviation, and (b) two random variables, X_3 and X_4 , with the same mean but different standard deviations.

normal CDF is most efficiently expressed in terms of the *standard normal variable*, Z , which can be computed for any random variable, X , using the transformation

$$Z = \frac{X - \bar{x}}{\sigma_x} \quad (\text{C.19})$$

Whenever X has a value, x , the corresponding value of Z is $z = (x - \bar{x})/\sigma_x$. Thus, the mean value of Z is $\bar{z} = 0$ and the standard deviation is $\sigma_z = 1$. Tabulated values of the standard normal CDF are presented in Table C-1.

Example C.5

Given a normally distributed random variable, X , with $\bar{x} = 270$ and $\sigma_x = 40$, compute the probability that (a) $X < 300$, (b) $X > 350$, and (c) $200 < X < 240$.

Solution (a) For $X = 300$,

$$Z = \frac{X - \bar{x}}{\sigma_x} = \frac{300 - 270}{40} = 0.75$$

Then

$$P[X < 300] = P[Z < 0.75] = F_z(0.75) = 1 - F_z(-0.75) = 1 - 0.2266 = 0.7734$$

(b) For $X = 350$,

$$Z = \frac{X - \bar{x}}{\sigma_x} = \frac{350 - 270}{40} = 2.0$$

Then

$$P[X > 350] = P[Z > 2.0] = 1 - F_z(2.0) = F_z(-2.0) = 0.0228$$

(c) For $X = 200$,

$$Z = \frac{X - \bar{x}}{\sigma_x} = \frac{200 - 270}{40} = -1.75$$

For $X = 240$,

$$Z = \frac{X - \bar{x}}{\sigma_x} = \frac{240 - 270}{40} = -0.75$$

Then

$$\begin{aligned}
 P[200 < X < 240] &= P[-1.75 < Z < -0.75] = F_z(-0.75) - F_z(-1.75) \\
 &= 0.2266 - 0.0401 = 0.1865
 \end{aligned}$$

TABLE C-1 Values of the CDF of the standard normal distribution, $F_Z(z) = 1 - F_Z(-z)$

<i>z</i>	0.00	0.01	0.02	0.03	0.04	0.05	0.06	0.07	0.08	0.09
-3.4	0.0003	0.0003	0.0003	0.0003	0.0003	0.0003	0.0003	0.0003	0.0003	0.0002
-3.3	0.0005	0.0005	0.0005	0.0004	0.0004	0.0004	0.0004	0.0004	0.0004	0.0003
-3.2	0.0007	0.0007	0.0006	0.0006	0.0006	0.0006	0.0005	0.0005	0.0005	0.0005
-3.1	0.0010	0.0009	0.0009	0.0009	0.0008	0.0008	0.0008	0.0008	0.0007	0.0007
-3.0	0.0013	0.0013	0.0013	0.0012	0.0012	0.0011	0.0011	0.0011	0.0010	0.0010
-2.9	0.0019	0.0018	0.0017	0.0017	0.0016	0.0016	0.0015	0.0015	0.0014	0.0014
-2.8	0.0026	0.0025	0.0024	0.0023	0.0023	0.0022	0.0021	0.0021	0.0020	0.0019
-2.7	0.0035	0.0034	0.0033	0.0032	0.0031	0.0030	0.0029	0.0028	0.0027	0.0026
-2.6	0.0047	0.0045	0.0044	0.0043	0.0041	0.0040	0.0039	0.0038	0.0037	0.0036
-2.5	0.0062	0.0060	0.0059	0.0057	0.0055	0.0054	0.0052	0.0051	0.0049	0.0048
-2.4	0.0082	0.0080	0.0078	0.0075	0.0073	0.0071	0.0069	0.0068	0.0066	0.0064
-2.3	0.0107	0.0104	0.0102	0.0099	0.0096	0.0094	0.0091	0.0089	0.0087	0.0084
-2.2	0.0139	0.0136	0.0132	0.0129	0.0125	0.0122	0.0119	0.0116	0.0113	0.0110
-2.1	0.0179	0.0174	0.0170	0.0166	0.0162	0.0158	0.0154	0.0150	0.0146	0.0143
-2.0	0.0228	0.0222	0.0217	0.0212	0.0207	0.0202	0.0197	0.0192	0.0188	0.0183
-1.9	0.0287	0.0281	0.0274	0.0268	0.0262	0.0256	0.0250	0.0244	0.0239	0.0233
-1.8	0.0359	0.0352	0.0344	0.0336	0.0329	0.0322	0.0314	0.0304	0.0301	0.0294
-1.7	0.0446	0.0436	0.0427	0.0418	0.0409	0.0401	0.0392	0.0384	0.0375	0.0367
-1.6	0.0548	0.0537	0.0526	0.0516	0.0505	0.0495	0.0485	0.0475	0.0465	0.0455
-1.5	0.0668	0.0655	0.0643	0.0630	0.0618	0.0606	0.0594	0.0582	0.0571	0.0559
-1.4	0.0808	0.0793	0.0778	0.0764	0.0749	0.0735	0.0722	0.0708	0.0694	0.0681
-1.3	0.0968	0.0951	0.0934	0.0918	0.0901	0.0885	0.0859	0.0853	0.0838	0.0823
-1.2	0.1151	0.1131	0.1112	0.1093	0.1075	0.1056	0.1038	0.1020	0.1003	0.0985
-1.1	0.1357	0.1335	0.1314	0.1292	0.1271	0.1251	0.1230	0.1210	0.1190	0.1170
-1.0	0.1587	0.1562	0.1539	0.1515	0.1492	0.1469	0.1446	0.1423	0.1401	0.1379
-0.9	0.1841	0.1814	0.1788	0.1762	0.1736	0.1711	0.1685	0.1660	0.1635	0.1611
-0.8	0.2119	0.2090	0.2061	0.2033	0.2005	0.1977	0.1949	0.1922	0.1894	0.1867
-0.7	0.2420	0.2389	0.2358	0.2327	0.2296	0.2266	0.2236	0.2206	0.2177	0.2148
-0.6	0.2743	0.2709	0.2676	0.2643	0.2611	0.2578	0.2546	0.2514	0.2483	0.2451
-0.5	0.3085	0.3050	0.3015	0.2981	0.2946	0.2912	0.2877	0.2843	0.2810	0.2776
-0.4	0.3446	0.3409	0.3372	0.3336	0.3300	0.3264	0.3228	0.3192	0.3156	0.3121
-0.3	0.3821	0.3783	0.3745	0.3707	0.3669	0.3632	0.3594	0.3557	0.3520	0.3483
-0.2	0.4207	0.4168	0.4129	0.4090	0.4052	0.4013	0.3974	0.3936	0.3897	0.3859
-0.1	0.4602	0.4562	0.4522	0.4483	0.4443	0.4404	0.4365	0.4325	0.4286	0.4247
-0.0	0.5000	0.4960	0.4920	0.4880	0.4840	0.4801	0.4761	0.4721	0.4681	0.4641

C.7.3 Lognormal Distribution

Some problems, particularly those involving ground motion parameters (Chapter 3), are formulated in terms of the logarithm of a parameter rather than the parameter itself. If X is a random variable, then $Y = \ln X$ is also a random variable. If Y is normally distributed, then X is *lognormally distributed*. In other words, a random variable is lognormally distributed if its logarithm is normally distributed. The PDF of a lognormally distributed random variable X is given by

$$f_X(x) = \frac{1}{x\sqrt{2\pi}\sigma_{\ln x}} \exp\left[-\frac{1}{2}\left(\frac{\ln x - \overline{\ln x}}{\sigma_{\ln x}}\right)^2\right] \quad (\text{C.20})$$

The shape of the lognormal distribution is shown in Figure C.8. Note that the PDF is not symmetric, and that it assigns zero probability to negative values of the random variable. These characteristics can be very useful for some random variables [the normal distribution, for example, assigns nonzero probabilities for values ranging from $-\infty$ to $+\infty$; when applied to a random variable such as soil density, it can assign some (hopefully small) probability that the soil will have a negative density].

Values of the CDF of the lognormal distribution are usually obtained from Table C-1, using the modified transformation

$$Z = \frac{\ln X - \overline{\ln x}}{\sigma_{\ln x}} \quad (\text{C.21})$$

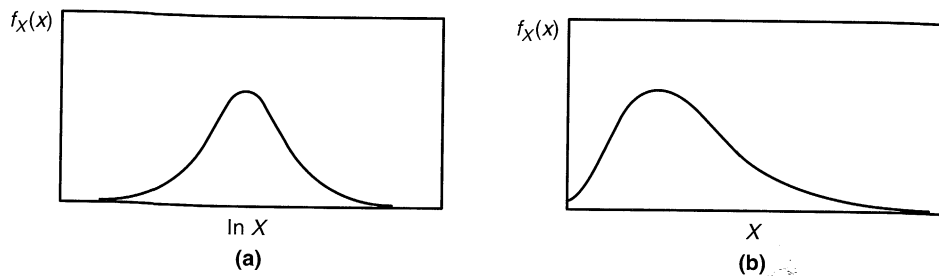


Figure C.8 Two views of the lognormal distribution. (a) Because the logarithm of a lognormally distributed random variable, X , is normally distributed, the probability density function of $\ln X$ is a bell-shaped curve. (b) The probability density function of X itself has no negative values and is not symmetric.

Example C.6

A random variable, X , is lognormally distributed with $\overline{\ln x} = 5$ and $\sigma_{\ln x} = 1.2$. Compute (a) the probability that $X < 100$, and (b) the value of X that has a 10% probability of being exceeded.

Solution (a) For $X = 100$,

$$Z = \frac{\ln X - \overline{\ln x}}{\sigma_{\ln x}} = \frac{\ln 100 - 5}{1.2} = -0.33$$

From Table C-1,

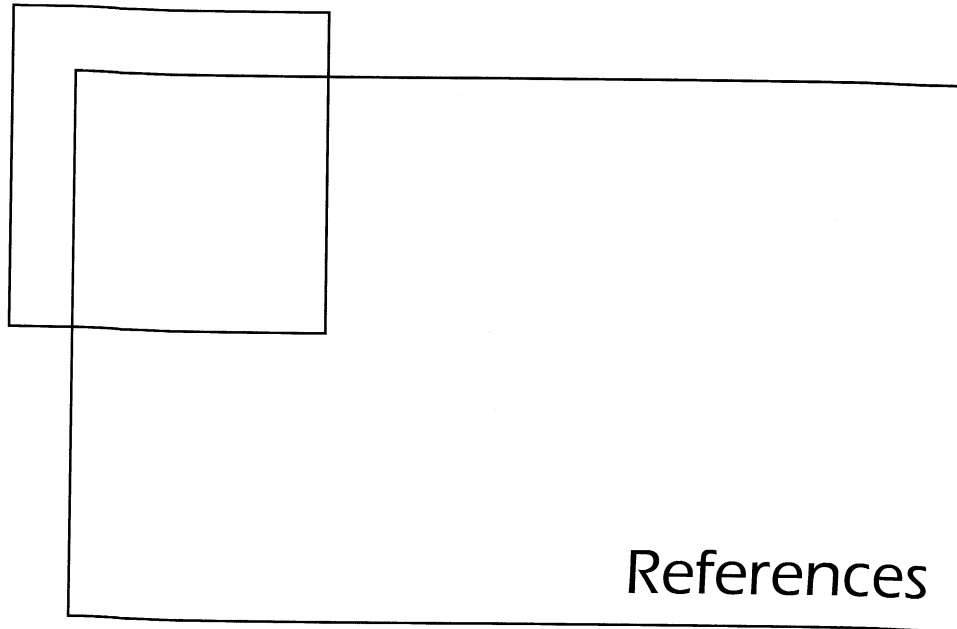
$$P[X < 100] = P[Z < -0.33] = F_z(-0.33) = 0.3707$$

(b) From Table C-1, the value of Z that would have a 10% probability of exceedance is 1.282 [i.e., $F_z(1.282) = 0.90$]. Then, rearranging equation (C.21) yields

$$\ln X = Z\sigma_{\ln x} + \overline{\ln x} = (1.282)(1.2) + 5 = 6.54$$

so

$$X = e^{6.54} = 691$$



- AASHTO (1991). *Interim Specification: Bridges - 1991*, American Association of State Highway and Transportation Officials, Washington, D.C., 470 pp.
- ABDEL-GHAFFAR, A.M. AND SCOTT, R.F. (1979). "Shear moduli and damping factors of earth dam," *Journal of the Geotechnical Engineering Division*, ASCE, Vol. 105, No. GT12, pp. 1405-1426.
- ABOSHI, H., MIZUNO, Y., AND KUWABARA, M. (1991). Present state of sand compaction pile in Japan, *Deep Foundation Improvements: Design, Construction, and Testing*, ASTM STP 1089, M.I. Esrig and R.C. Bachus, eds., ASTM, Philadelphia, pp. 32-46.
- ABRAHAMSON, N.A. (1991). "Spatial coherency of ground motion from the SMART 1 array," *Geotechnical News*, Vol. 9, No. 1, pp. 31-34.
- ABRAHAMSON, N.A. AND LITEHISER, J.J. (1989). "Attenuation of vertical peak acceleration," *Bulletin of the Seismological Society of America*, Vol. 79, pp. 549-580.
- ABRAHAMSON, N.A. AND SINGH, J.P. (1986). "Importance of phasing of strong ground motion in the estimation of structural response," *Proceedings, 3rd Engineering Mechanics Specialty Conference on Dynamic Response of Structures*, ASCE, Los Angeles.
- ABRAHAMSON, N.A., SCHNEIDER, J.F., AND STEPP, J.C. (1991). "Empirical spatial coherency functions for application to soil-structure interaction analyses," *Earthquake Spectra*, Vol. 7, No. 1, pp. 1-28.
- ACHARAYA, H.K. (1979). "Regional variations in the rupture-length magnitude relationships and their dynamical significance," *Bulletin of the Seismological Society of America*, Vol. 69, No. 6, pp. 2063-2084.

- ADAIR, M.J. (1979). "Geologic evaluation of a site for a nuclear power plant," in A.W. Hatheway and C.R. McClure, eds., *Geology in the Siting of Nuclear Power Plants*, Geological Society of America Reviews in Engineering Geology, Boulder, Colorado, Vol. 4, pp. 27-39.
- AIREY, D.W. AND WOOD, D.M. (1987). "An evaluation of direct simple shear tests on clay," *Geotechnique*, Vol. 37, No. 1, pp. 25-35.
- AKI, K. (1969). Analysis of the seismic coda of local earthquakes as scattered waves, *Journal of Geophysical Research*, Vol. 74, pp. 615-631.
- AKI, K. (1979). "Characterization of barriers on an earthquake fault," *Journal of Geophysical Research*, Vol. 86, pp. 6140-6148.
- AKI, K. (1984). "Asperities, barriers, characteristic earthquakes, and strong motion prediction," *Journal of Geophysical Research*, Vol. 89, pp. 5867-5872.
- AKI, K. (1988). Local site effects on strong ground motion, *Proceedings, Earthquake Engineering and Soil Dynamics II - Recent Advances in Ground Motion Evaluation*, ASCE, Geotechnical Special Publication No. 20, pp. 103-155.
- AKI, K. (1993). "Local site effects on weak and strong ground motion," *Tectonophysics*, Vol. 218, No. 1-3, pp. 93-112.
- AKI, K. AND RICHARDS, P.G. (1980). *Quantitative Seismology: Theory and Methods*, Volumes 1 and 2, W.H. Freeman, San Francisco, California.
- AL-SANAD, H. AND AGGOUR, M.S. (1984). "Dynamic soil properties from sinusoidal and random vibrations," *Proceedings, 8th World Conference on Earthquake Engineering*, San Francisco, Vol. 3, pp. 15-22.
- ALAMPALLI, S. AND ELGAMEL, A.-W. (1990). "Dynamic response of retaining walls including supported soil backfill: A computational model," *Proceedings, 4th U.S. National Conference on Earthquake Engineering*, Earthquake Engineering Research Institute, Palm Springs, California, Vol. 3, pp. 623-632.
- Alarcon-Guzman, A., Leonards, G.A., and Chameau, J.L. (1988). "Undrained monotonic and cyclic strength of sands," *Journal of Geotechnical Engineering*, ASCE, Vol. 114, No. 10, pp. 1089-1108.
- ALGERMISSEN, S.T., PERKINS, D.M., THENHAUS, P.C., HANSON, S.L., AND BENDER, B.L. (1982). "Probabilistic estimates of maximum acceleration and velocity in rock in the contiguous United States," *Open-File Report 82-1033*, U.S. Geological Survey, Washington, D.C., pp. 99.
- ALGERMISSEN, S.T., PERKINS, D.M., THENHAUS, P.C., HANSON, S.L., AND BENDER, B.L. (1990). Probabilistic earthquake acceleration and velocity maps for the United States and Puerto Rico, Miscellaneous Field Studies Map MF-2120, U.S. Geological Survey, Washington, D.C.
- ALLEN, C.R. (1975). "Geologic criteria for evaluating seismicity," *Bulletin of the Geological Society of America*, Vol. 86, No. 8, pp. 1041-1057.
- AMBRASEYS, N.N. (1960). "On the shear response of a two-dimensional truncated wedge subjected to an arbitrary disturbance," *Bulletin of the Seismological Society of America*, Vol. 50, No. 1, pp. 45-56.
- AMBRASEYS, N.N. (1971). "Value of historical records of earthquakes," *Nature*, Vol. 232, pp. 375-379.
- AMBRASEYS, N.N. (1978). "Middle East - A reappraisal of the seismicity," *Quarterly Journal of Engineering Geology*, Vol. 11, pp. 19-32.
- AMBRASEYS, N.N. (1988). "Engineering seismology," *Earthquake Engineering and Structural Dynamics*, Vol. 17, pp. 1-105.
- AMBRASEYS, N.N. AND MENU, J.M. (1988). "Earthquake-induced ground displacements," *Earthquake Engineering and Structural Dynamics*, Vol. 16, pp. 985-1006.
- ANAGNOS, T., AND KRREMIDJIAN, A.S. (1982). Stochastic time-predictable model for earthquake occurrences, *Bulletin of the Seismological Society of America*, Vol. 74, No. 6, pp. 2593-2611.

- ANDERSEN, K.H., KLEVEN, A., AND HEIEN, D. (1988). "Cyclic soil data for design of gravity structures," *Journal of Geotechnical Engineering*, ASCE, Vol. 114, No. 5, pp. 517-539.
- ANDERSON, D.G. AND STOKOE, K.H. (1978). "Shear modulus: A time-dependent soil property," *Dynamic Geotechnical Testing*, ASTM STP 654, ASTM, Philadelphia, pp. 66-90.
- ANDERSON, D.G. AND WOODS, R.D. (1975). "Comparison of field and laboratory shear modulus," *Proceedings, ASCE Conference on In Situ Measurement of Soil Properties*, Vol. 1, pp. 69-92.
- ANDERSON, D.G. AND WOODS, R.D. (1976). "Time-dependent increase in shear modulus of clay," *Journal of the Geotechnical Engineering Division*, ASCE, Vol. 102, No. GT5, pp. 525-537.
- ANDERSON, J.G. (1991). "Guerrero accelerograph array: Seismological and geotechnical lessons," *Geotechnical News*, Vol. 9, No. 1, pp. 34-37.
- ANDERSEN, A. AND BJERRUM, L. (1968). "Slides in subaqueous slopes in loose sand and silt," *Publication 81*, Norwegian Geotechnical Institute, Publication 8, Oslo, pp. 1-9.
- ANG, A.H.S. (1990). Reliability bases for seismic safety assessment and design, *Proceedings, Fourth U.S. National Conference on Earthquake Engineering*, Earthquake Engineering Research Institute, Palm Springs, Vol. 1, pp. 29-45.
- ANG, A.H.S. AND TANG, W.H. (1975a). *Probability Concepts in Engineering Planning and Design*, Vol. I: *Basic Principles*, Wiley, New York.
- ANG, A.H.S. AND TANG, W.H. (1975b). *Probability Concepts in Engineering Planning and Design*, Vol. II: *Decision, Risk, and Reliability*, Wiley, New York.
- APPLEGATE, J.K. (1974). "A torsional seismic source," Thesis, Colorado School of Mines, Boulder, Colorado.
- ATC (1978). "Tentative provisions for the development of seismic regulations for buildings, ATC 3-06," Applied Technology Council, Palo Alto, California.
- ARIAS, A. (1970) "A measure of earthquake intensity," in R.J. Hansen, ed. *Seismic Design for Nuclear Power Plants*, MIT Press, Cambridge, Massachusetts, pp. 438-483.
- ARULMOLI, K., ARULANANDAN, K., AND SEED, H.B. (1985). "New method for evaluating liquefaction potential," *Journal of Geotechnical Engineering*, ASCE, Vol. 111, No. 1, pp. 95-114.
- ATWATER, T. AND SVERINGHAUS, J. (1989). "Tectonic map of the north Pacific," in E.L. Winterer, D.M. Hussong, and R.W. Decker, eds., *DNAG: The Eastern Pacific Ocean and Hawaii*, Geologic Society of America Publication, Boulder, Colorado, Vol. N, pp. 15-20.
- ATWATER, B.F. (1987). Evidence for great Holocene earthquakes along the outer coast of Washington state" *Science*, Vol. 236, pp. 942-944.
- ATWATER, B.F., HULL, A.G., AND BEVIS, K.A. (1987). "Aperiodic Holocene recurrence of widespread, probably coseismic subsidence in southwestern Washington," *Eos*, Vol. 68, 1468 pp.
- AULD, B. (1977). "Cross-hole and down-hole v_s by mechanical impulse," *Journal of the Geotechnical Engineering Division*, ASCE, Vol. 103, No. GT12, pp. 1381-1398.
- BABASAKI, R., SUZUKI, K., SAITOH, S., SUZUKI, Y., AND TOKITOH, K. (1991). "Construction and testing of deep foundation improvement using the deep cement mixing method," *Deep Foundation Improvements: Design Construction and Testing*, ASTM STP 1089, ASTM, Philadelphia, pp. 224-233.
- BAEZ, J.I. AND HENRY, J.F. (1993). "Reduction of liquefaction potential by compaction grouting at Pinopolis Dam, South Carolina," *Geotechnical Practice in Dam Rehabilitation*, Geotechnical Special Publication 35, ASCE, New York, pp. 430-466.
- BALDI, G., BELLOTTI, R., GHIONNA, V., JAMIOLKOWSKY, M., MARCHETTI, S., AND PASQUELINI, E. (1986). "Flat dilatometer tests in calibration chambers," *Proceedings, In Situ '86*, Geotechnical Special Publication 6, ASCE, New York, pp. 431-446.

- BALDI, G., BRUZZI, D., SUPERBO, S., BATTAGLIO, M. AND JAMIOLKOWSKY, M. (1988). "Seismic cone in Po River sand," *Penetration Testing 1988*, ISOPT-1 Symposium, Orlando, Florida, Vol. 2, pp. 643-650.
- BALDI, G., BELLOTTI, R., GHIONNA, V., JAMIOLKOWSKY, M., AND LO PRESTI, D.C.F. (1989). "Modulus of sands from CPT's and DMT's," *Proceedings, 12th International Conference on Soil Mechanics and Foundation Engineering*, Rio de Janeiro, Brazil, Vol. 1, pp. 165-170.
- BARD, P.Y. AND GARIEL, J.C. (1986). "The seismic response of two-dimensional sedimentary deposits with large vertical velocity gradients," *Bulletin of the Seismological Society of America*, Vol. 76, pp. 343-356.
- BARTLETT, S.F. AND YOUND, T.L. (1992). "Empirical analysis of horizontal ground displacement generated by liquefaction-induced lateral spread," *Technical Report NCEER-92-0021*, National Center for Earthquake Engineering Research, Buffalo, New York.
- BATH, M. (1979). *Introduction to seismology*, Birkhauser, Boston, 428 pp.
- BATHE, K.J. (1982). *Finite Element Procedures in Engineering Analysis*, Prentice Hall, Englewood Cliffs, New Jersey, 735 pp.
- BAYLOR, J.L. (1974). "TRANL: a 3-D finite element code for transient nonlinear analysis," *DNA 3501F*, Weidlinger Associates, New York.
- BAZIAR, M.H., DOBRY, R., AND ELGAMEL, A.W.M. (1992). "Engineering evaluation of permanent ground deformations due to seismically-induced liquefaction," *Technical Report NCEER-92-0007*, National Center for Earthquake Engineering Research, State University of New York, Buffalo.
- BEEN, K. AND JEFFRIES, M.G. (1985). "A state parameter for sands," *Geotechnique*, Vol. 35, No. 2, pp. 99-112.
- BEEN, K., CROOKS, J.H.A., BECKER, D.E., AND JEFFRIES, M.G. (1986). "The cone penetration test in sands; Part I: State parameter interpretation," *Geotechnique*, Vol. 36, No. 2, pp. 239-249.
- BEEN, K., JEFFRIES, M.G., CROOKS, J.H.A., AND ROTHENBURG, L. (1987). "The cone penetration test in sands, Part II: General inference of state," *Geotechnique*, Vol 37, No. 3, pp. 285-300.
- BELL, F.G. (1993). *Engineering treatment of soils*, E & FN Spon, London, 302 pp.
- BELLOTTI, R., GHIONNA, V., JAMIOLKOWSKY, M., LANCELLOTTA, R., AND MANFREDINI, G. (1986). "Deformation characteristics of cohesionless soils in insitu tests," *Proceedings, In Situ '86*, Geotechnical Special Publication 6, ASCE, New York, pp. 47-73.
- BEN-MENACHEM, A. (1961). "Radiation patterns of seismic surface waves from finite moving sources," *Bulletin of the Seismological Society of America*, Vol. 51, pp. 401-435.
- BENDER, B. (1984). "Incorporating acceleration variability into seismic hazard analysis," *Bulletin of the Seismological Society of America*, Vol. 74, No. 4, pp. 1451-1462.
- BENIOFF, H. (1955). "Mechanism and strain characteristics of the White Wolf fault as indicated by the aftershock sequence," *Earthquakes in Kern County, California During 1955*, California Division of Mines, Bulletin 171, G.B. Oakeshott, ed., pp. 199-202.
- BENJAMIN, J.R. AND ASSOCIATES (1988). "A criterion for determining exceedance of the Operating Basis Earthquake," *EPRI Report NP-5930*, Electric Power Research Institute, Palo Alto, California.
- BENJAMIN, J.R., AND CORNELL, C.A. (1970). *Probability, Statistics, and Decision for Civil Engineers*, McGraw-Hill, New York.
- BERG, G.V. (1983). *Seismic design codes and procedures*, Earthquake Engineering Research Institute, Berkeley, California, 119 pp.
- BERG, G.V. (1989). *Elements of Structural Dynamics*, Prentice Hall, Englewood Cliffs, New Jersey, 268 pp.

- BERGER, J. BAKER, L.M., BRUNE, J.N., FLETCHER, J.B., HANKS, T.C. AND VERNON, F.L. (1984). "The Anza array: A high-dynamic-range, broadband, digitally radiotelemetered seismic array," *Bulletin of the Seismological Society of America*, Vol. 74, No. 4, pp 1469-1481.
- BERLIN, G.L. (1980). *Earthquakes and the Urban Environment*, CRC Press, Boca Raton, Florida, Vol. 1, 211 pp.
- BISHOP, A.W. (1955). "The use of the slip circle in the stability analysis of slopes," *Geotechnique*, Vol. 5, No. 1, pp. 7-17.
- BJERRUM, L., (1971). "Subaqueous slope failures in Norwegian fjords," *Publication 88*. Norwegian Geotechnical Institute, Oslo.
- BOLT, B. A. (1969) "Duration of strong motion," *Proceedings of the 4th World Conference on Earthquake Engineering*, Santiago, Chile, pp. 1304-1315.
- BOLT, B.A. (1975). *Nuclear Explosions and Earthquakes*, W.H. Freeman, San Francisco.
- BOLT, B.A. (1988). *Earthquakes*, W.H. Freeman and Company, New York, 282 pp.
- BOLT, B.A. (1989). The nature of earthquake ground motion, in F. Naeim, ed., *The Seismic Design Handbook*, Van Nostrand Reinhold, New York.
- BOLT, B.A. (1993). *Earthquakes*, W.H. Freeman, New York, 331 pp.
- BONILLA, M.G. AND BUCHANAN, J.M. (1970). "Interim report on world-wide historic surface faulting," *Open-File Report*, U.S. Geological Survey, Reston, Virginia, 32 pp.
- BONILLA, M.G., MARK, R.K. AND LIENKAEMPER, J.J. (1984). "Statistical relations among earthquake magnitude, surface rupture length, and surface fault displacement," *Bulletin of the Seismological Society of America*, Vol. 74, pp. 2379-2411.
- BOORE, D.M. (1977). The motion of the ground during earthquakes, *Scientific American*, Vol. 237, No. 6, pp. 68-78.
- BOORE, D.M. (1983). "Stochastic simulation of high-frequency ground motions based on seismological models of the radiated spectra," *Bulletin of the Seismological Society of America*, Vol. 73, pp. 1865-1884.
- BOORE, D.M., JOYNER, W.B., AND FUMAL, T.E. (1993). Estimation of response spectra and peak accelerations from western North America earthquakes: An interim report, *Open-File-Report 93-509*, U.S. Geological Survey, Reston, Virginia, 72 pp.
- BORCHERDT, R. D., FLETCHER, J. B., JENSEN, E. G., MAXWELL, G. L., VAN SCHAACK, J. R., WARRICK, R. E., CRANSWICK, E., JOHNSON, M.J.S., AND MCCLEARN, R. (1985) "A general earthquake observation system," *Bulletin of the Seismological Society of America*, 75, 1783-1825.
- BOULANGER, R.W., CHAN, C.K., SEED, H.B., SEED, R.B., AND SOUSA, J. (1993). "A low-compliance bidirectional cyclic simple shear apparatus," *Geotechnical Testing Journal*, ASTM, Vol. 16, No. 1, pp. 36-45.
- BRIGHAM, E.O. (1974). *The Fast Fourier Transform*, Prentice Hall, Englewood Cliffs, New Jersey, 252 pp.
- BROMS, B. (1991). "Deep compaction of granular soil," in H.-Y. Fang, ed., *Foundation Engineering Handbook*, 2nd ed., Van Nostrand Reinhold, New York, pp. 814-832.
- BROMS, B. AND BENNERMARK, H. (1967). Free discussion, *Proceedings, Geotechnical Conference*, Vol. 2, Oslo, Norway, pp. 118-120.
- BROWN, R.E. (1977). "Vibroflotation compaction of cohesionless soils," *Journal of the Geotechnical Engineering Division*, ASCE, Vol. 103, No. GT12, pp. 1437-1451.
- BRUCE, D.A. (1992). "Progress and development in dam rehabilitation by grouting," *Grouting, Soil Improvement, and Geosynthetics*, Geotechnical Special Publication 30, ASCE, New York, Vol. 1, pp. 601-613.

- BRUNE, J.N. (1970). "Tectonic stress and the spectra of seismic shear waves from earthquakes," *Journal of Geophysical Research*, Vol. 75, pp. 4997-5009.
- BRUNE, J.N. (1971). "Correction," *Journal of Geophysical Research*, Vol. 76, p. 5002.
- BSSC (1994A). *NEHRP Recommended Provisions for the Development of Seismic Regulations for New Buildings, Part I: Provisions*, Building Seismic Safety Council, Federal Emergency Management Agency, Washington, D.C.
- BSSC (1994B). *NEHRP Recommended Provisions for the Development of Seismic Regulations for New Buildings, Part II: Commentary*, Building Seismic Safety Council, Federal Emergency Management Agency, Washington, D.C.
- BULLARD, E.C., EVERETT, J.E., AND SMITH, A.G. (1965). "Fit of Continents around Atlantic, in P.M.S. Blackett, *On Continental Drift. Philosophical Transactions of the Royal Society of London, Series A*, Vol. 258, pp. 41-75.
- BULLEN, K.E. (1953). *An introduction to the theory of seismology*, Cambridge University Press, London, 296 pp.
- BULLEN, K.E. (1975). *The Earth's Density*, Chapman & Hall, London.
- BULLEN, K.E. AND BOLT, B.A. (1985). *An Introduction to the Theory of Seismology*, Cambridge University Press, Cambridge.
- BURLAND, J.B. AND SYMES, M.J. (1982) "A simple axial displacement gauge for use in the triaxial apparatus," *Geotechnique*, Vol. 32, No. 1, pp. 62-65.
- BUTLER, K.K., SLOGLUND, G.R., AND LANDERS, G.B. (1978). "Crosshole: An interpretive computer code for crosshole seismic test results, Documentation and examples," *Miscellaneous Paper S-78-6*, U.S. Army Corps of Engineers Waterways Experiment Station, Vicksburg, Mississippi.
- BYCROFT, G. N. (1978) "The effect of soil-structure interaction on seismometer readings," *Bulletin of the Seismological Society of America*, Vol. 68, pp. 823-843.
- BYRNE, P.M. (1991). "A model for predicting liquefaction induced displacement," *Proceedings, 2nd International Conference on Recent Advances in Geotechnical Earthquake Engineering and Soil Dynamics*, St. Louis, Missouri, Vol. 2, pp. 1027-1035.
- BYRNE, P.M., IMRIE, A.S., AND MORGENSTERN, N.R. (1993). "Results and implications of seismic response studies - Duncan Dam," *Proceedings, 46th Annual Canadian Geotechnical Conference*, Saskatoon, Saskatchewan, pp. 271-281.
- BYRNE, P.M., JITNO, H., AND SALGADO, R. (1992). "Earthquake-induced displacements of soil-structures systems," *Proceedings, 10th World Conference on Earthquake Engineering*, Madrid, Vol. 3, pp. 1407-1412.
- BYRNE, P.M., MORRIS, D.V., AND CALDWELL, J.A. (1984). "Seismic stability of a tailings impoundment on soft clayey silt deposits," *Proceedings, 8th World Conference on Earthquake Engineering*, San Francisco, Vol. 3.
- BYRNE, P.M., SALGADO, F., AND HOWIE, J.A. (1991). " G_{max} from pressuremeter tests: theory, chamber tests, and field measurements," *Proceedings, 2nd International Conference on Recent Advances in Geotechnical Earthquake Engineering and Soil Dynamics*, St. Louis, Missouri, Vol. 1, pp. 57-63.
- CAMPBELL, K. W. (1981) "Near source attenuation of peak horizontal acceleration," *Bulletin of the Seismological Society of America*, 71, 2039-2070.
- CAMPBELL, K.W. (1985). Strong ground motions attenuation relations: A ten-year perspective, *Earthquake Spectra*, Vol. 1, No. 4, pp. 759-804.
- CAMPBELL, K.W. AND BOZORGNI, Y. (1994). Near-source attenuation of peak horizontal acceleration from worldwide accelerograms recorded from 1957 to 1993, *Proceedings, Fifth U.S. National*

- Conference on Earthquake Engineering*, Earthquake Engineering Research Institute, Berkeley, California, Vol. 1, pp. 283-292.
- CAMPBELL, K.W. AND DUKE, C.M. (1974). Bedrock intensity, attenuation, and site factors from San Fernando earthquake records, *Bulletin of the Seismological Society of America*, Vol. 64, No. 1, pp. 173-185.
- CAQUOT, A, AND KERISEL, F. (1948). *Tables for the calculation of passive pressure, active pressure and bearing capacity of foundations*, Gauthier-Villars, Paris.
- CARTER, D.P. AND SEED, H.B. (1988). "Liquefaction potential of sand deposits under low levels of excitation," *Report UCB/EERC-88/11*, Earthquake Engineering Research Center, University of California, Berkeley, 309 pp.
- CASAGRANDE, A. (1936). "Characteristics of cohesionless soils affecting the stability of slopes and earth fills," *Journal of the Boston Society of Civil Engineers*, reprinted in *Contributions to Soil Mechanics*, Boston Society of Civil Engineers, 1940, pp.257-276.
- CASAGRANDE, A. (1976). "Liquefaction and cyclic mobility of sands: a critical review," *Harvard Soil Mechanics Series 88*, Harvard University, Cambridge, Massachusetts.
- CASTRO, G. (1969). "Liquefaction of sands," *Harvard Soil Mechanics Series 87*, Harvard University, Cambridge, Massachusetts.
- CASTRO, G. (1975). "Liquefaction and cyclic mobility of sands," *Journal of the Geotechnical Engineering Division*, ASCE, Vol. 101, No. GT6, pp. 551-569.
- CASTRO, G. (1991). "On the behavior of soils during earthquakes - liquefaction," *Proceedings, NSF/EPRI Workshop on Dynamic Soil Properties and Site Characterization*, EPRI NP-7337, Vol. 2, Electric Power Research Institute, Palo Alto, California, pp. 1-36.
- CASTRO, G. AND CHRISTIAN, J.T. (1976). "Shear strength of soils and cyclic loading," *Journal of the Geotechnical Engineering Division*, ASCE, Vol. 102, No. GT9, pp. 887-894.
- CASTRO, G. AND POULOS, S.J. (1977). "Factors affecting liquefaction and cyclic mobility," *Journal of the Geotechnical Engineering Division*, ASCE, Vol. 106, No. GT6, pp. 501-506.
- CASTRO, G. AND TRONCOSO, J. (1989). "Effects of 1989 Chilean earthquake on three tailings dams," *Proceedings, 5th Chilean Conference on Seismology and Earthquake Engineering*, Santiago, Chile.
- CASTRO, R.R., ANDERSON, J.G., AND SINGH, S.K. (1990). "Site response, attenuation and source spectra of s-waves along the Guerrero, Mexico, subduction zone," *Bulletin of the Seismological Society of America*, Vol. 80, No. 6, pp. 1489-1523.
- CEDERGREN, H. (1989). *Seepage, Drainage, and Flow Nets*, 3rd ed., Wiley, New York, 465 pp.
- CHAMEAU, J.L. AND CLOUGH, G.W. (1983). "Probabilistic pore pressure analysis for seismic loading," *Journal of Geotechnical Engineering*, ASCE, Vol. 109, No. 4, pp. 507-524.
- CHANG, C.-Y., MOK, C.M., POWER, M.S., TANG, Y.K., TANG, H.T., AND STEPP, J.C. (1991). "Development of shear modulus reduction curves based on Lotung downhole ground motion data," *Proceedings, 2nd International Conference on Recent Advances in Geotechnical Earthquake Engineering and Soil Dynamics*, St. Louis, Missouri, Vol. 1, pp. 111-118.
- CHANG, C.-Y., POWER, M.S., IDRIS, I.M., SOMERVILLE, P.G., SILVA, W., AND CHEN, P.C. (1986). "Engineering characterization of ground motion, Task II: Observational data on spatial variations of earthquake ground motions," *Report NUREG/CR-3805*, Vol. 3, U.S. Nuclear Regulatory Commission, Washington, D.C.
- CHANG, C.Y., POWER, M.S., MOK, C.M., TANG, Y.K., AND TANG, H.T. (1990). "Analysis of dynamic lateral earth pressures recorded on Lotung reactor containment model structure," *Proceedings, 4th U.S. National Conference on Earthquake Engineering*, Earthquake Engineering Research Institute, Palm Springs, California, Vol. 3, pp. 643-652.

- CHANG, F. K. AND KRINITZSKY, E. L. (1977) "Duration, spectral content, and predominant period of strong motion earthquake records from western United States," *Miscellaneous Paper 5-73-1*, U.S. Army Corps of Engineers Waterways Experiment Station, Vicksburg, Mississippi.
- CHANG, K.T. (1978). "An Analysis of Damage of Slope Sliding by Earthquake on the Paiho Main Dam and its Earthquake Strengthening," Tseng-hua Design Section, Dept. of Earthquake-Resistant Design and Flood Control Command of Miyna Reservoir, Peoples Republic of China.
- CHANG, M., KWIATOWSKI, H., NAU, R., OLIVER, R. AND PISTER, K. (1982). "ARMA models for earthquake ground motions," *Earthquake Engineering and Structural Dynamics*, Vol. 10, pp. 651-662.
- CHANG, N.Y., JUANG, M.J., LIEN, B.H., AND CHANG, F.K. (1986). "EQGEN: a user-friendly artificial earthquake simulation program," *Proceedings, 3rd U.S. National Conference on Earthquake Engineering*, Charleston, South Carolina, Vol. 1, pp. 439-450.
- CHEN, D. (1984). "Some empirical formulae for hazard analysis in China," *Proceedings, 8th World Conference on Earthquake Engineering*, San Francisco, Vol. 1, pp. 173-180.
- CHOPRA, A.K. (1966). "Earthquake effects on dams," Ph.D. dissertation, University of California, Berkeley.
- CHOPRA, A.K. (1995). *Dynamics of Structures*. Prentice Hall, Englewood Cliffs, New Jersey, 729 pp.
- CHOWDHURY, R.N. (1978). *Slope analysis*, Elsevier, New York, 423 pp.
- CHRISTIAN, J.T. (1988). "Developing design ground motions in practice," in *Geotechnical Special Publication 20, Earthquake Engineering and Soil Dynamics II: Recent Advances in Ground Motion Evaluation*, Geotechnical Special Publication 20, ASCE, New York, pp. 405-429.
- CHRISTIAN, J.T. AND SWIGER, W.F. (1973). "Statistic of liquefaction and SPT results," *Journal of the Geotechnical Engineering Division*, ASCE, Vol. 101, No. GT11, pp. 1135-1150.
- CHRISTIAN, J.T., ROESSET, J.M., AND DESAI, C.S. (1977). "Two- and three-dimensional dynamic analyses," Chapter 20 in *Numerical Methods in Geotechnical Engineering*, C.S. Desai and J.T. Christian, eds., McGraw Hill Book Company, New York, New York, pp. 683-718.
- CHRISTIAN, J.T., BORJESON, R.W., AND TRINGALE, P.T. (1978). "Probabilistic evaluation of OBE for nuclear plant," *Journal of the Geotechnical Engineering Division*, ASCE, Vol. 104, No. GT7, pp. 907-919.
- CHRISTOPHER, B.R., GILL, S.A., GIROUD, J.-P., JURAN, I. MITCHELL, J.K., SCHLOSSER, F., AND DUNNICLIFF, J. (1990). "Reinforced soil structures - design and construction guidelines," *Report FHWA-RD-89-043*, Vol. 1, Federal Highway Administration, Washington, D.C., 285 pp.
- CLOSE, U. AND MCCORMICK, E. (1922). "Where the mountains walked," *National Geographic*, Vol. 41, No. 5, pp. 445-464.
- CLOUGH, G.W. AND DUNCAN, J.M. (1971). Finite element analyses of retaining wall behavior, *Journal of the Soil Mechanics and Foundations Division*, ASCE, Vol. 97, No. SM12, pp. 1657-1674.
- CLOUGH, R.W. AND PENZIEN, J. (1975). *Dynamics of Structures*, McGraw-Hill, New York, 634 pp.
- CLUFF, L.S. AND CLUFF, J.L. (1984). "Importance of assessing degrees of fault activity for engineering decisions," *Proceedings, 8th World Conference on Earthquake Engineering*, San Francisco, Vol. 2, pp. 629-636.
- CLUFF, L.S., HANSON, W.R., TAYLOR, C.L., WEAVER, K.D., BROGAN, G.E., IDRIS, I.M., MCCLURE, F.E., AND BLAYNEY, J.A. (1972). "Site evaluation in seismically active regions: an interdisciplinary approach," *Proceedings, First International Conference on Microzonation*, Seattle, Washington, Vol. 2, pp. 957-987.
- CLUFF, L.S., PATARDHAN, A.S., AND COPPERSMITH, K.J. (1980). "Estimating the probability of occurrences of surface faulting earthquakes on the Wasatch fault zone," *Bulletin of the Seismological Society of America*, Vol. 70, No. 5, pp. 1463-1478.

- Code of Federal Regulations* (1978). "Title 10, Energy; Part 100 [10 CFR 100] *Reactor Site Criteria*; Appendix A, Seismic and geologic siting criteria for nuclear power plants," Nuclear Regulatory Commission, Washington, D.C.
- COMMITTEE ON EARTHQUAKE ENGINEERING RESEARCH (1982). *Earthquake engineering research - 1982*, National Research Council, National Academy Press, Washington, D.C., 266 pp.
- COMMITTEE ON NUCLEAR STRUCTURES AND MATERIALS (1979). *Analyses for Soil-Structure Interaction Effects for Nuclear Power Plants*, ASCE, New York, 155 pp.
- COMMITTEE ON SEISMIC RISK (1984). "Glossary of terms for probabilistic seismic-risk and hazard analysis," *Earthquake Spectra*, Vol. 1, No. 1, pp. 33-40.
- CONLON, R. (1966). "Landslide at Toulmoustouc River, Quebec," *Canadian Geotechnical Journal*, Vol. 3, No. 3, pp. 113-144.
- CONSTANTINO, M. AND GAZETAS, G. (1984). "Probabilistic seismic sliding deformations of earth dams and slopes," *Proceedings, 4th ASCE Specialty Conference on Probabilistic Mechanics and Structural Reliability*, pp. 318-321.
- CONVERSE, A.M. (1992). "BAP: Basic strong-motion accelerogram processing software, Version 1.0" *Open-File Report 92-296A*, U. S. Geological Survey, U.S. Department of the Interior, Denver, Colorado.
- COOLEY, P.M., AND TUKEY, J.W. (1965). An algorithm for the machine computation of complex Fourier series, *Mathematics of Computation*, Vol. 19, No. 4, pp. 297-301.
- COPPERSMITH, K.J. (1981). "Probabilities of earthquake occurrences on the San Andreas fault based on geologic risk," *EOS*, Vol. 62, No. 17, p. 322.
- COPPERSMITH, K.J. AND YOUNGS, R.R. (1986). "Capturing uncertainty in probabilistic seismic hazard assessments with intraplate tectonic environments," *Proceedings, 3rd U.S. National Conference on Earthquake Engineering*, Charleston, South Carolina, Vol. 1, pp. 301-312.
- CORNELL, C.A. (1968). Engineering seismic risk analysis, *Bulletin of the Seismological Society of America*, Vol. 58, pp. 1583-1606.
- CORNELL, C.A. AND WINTERSTEIN, S.R. (1986). "Applicability of the Poisson earthquake-occurrence model," in *Seismic Hazard Methodology for the Central and Eastern United States*, EPRI Research Report NP-4726, Electric Power Research Institute, Palo Alto, California.
- CORNELL, C.A. AND WINTERSTEIN, S.R. (1988). "Temporal and magnitude dependence in earthquake recurrence models," *Bulletin of the Seismological Society of America*, Vol. 78, pp. 1522-1537.
- CORNELL, C.A., BANON, H., AND SHAKAL, A.F. (1979). Seismic motion and response prediction alternatives, *Earthquake Engineering and Structural Dynamics*, Vol. 7, No. 4, pp. 295-315.
- CORNFORTH, D.H., WORTH, E.G. AND WRIGHT, W.L., (1975). "Observations and analysis of a flow slide in sand fill," in British Geotechnical Society, *Field Instrumentation in Geotechnical Engineering*, Wiley, New York, 136-151.
- CORPS OF ENGINEERS (1979). "Geophysical exploration," *Engineer Manual 1110-1-1802*, U. S. Department of the Army, Corps of Engineers.
- COULOMB, C.A. (1776). "Essai sur une application des regles des maximis et minimis a quelques problemes de statique relatifs a l'architecture," *Memoires de l'Academie Royale pres Divers Savants*, Vol. 7.
- COULTER, M. AND MIGLIACCIO, L. (1966). "Effects of the earthquake of March 27, 1964 at Valdez, Alaska." *Professional Paper 542-C*, U.S. Geological Survey, U.S. Department of the Interior, Washington, D.C.
- CROUSE, C. B. AND HUSHMAND, B. (1989). "Soil-structure interaction at CDMG and USGS accelerograph stations," *Bulletin of the Seismological Society of America*, Vol. 79, No. 1, pp. 1-14.

- CROUSE, C. B., LIANG, G. C., AND MARTIN, G. R. (1984). "Experimental study of soil-structure interaction at an accelerograph station," *Bulletin of the Seismological Society of America*, Vol. 74, pp. 1995-2013.
- CROUSE, C.B. (1991). "Ground motion attenuation equations for earthquakes on the Cascadia subduction zone," *Earthquake Spectra*, Vol. 7, No. 2, pp. 201-236.
- CROUSE, C.B. AND HUSHMAND, B. (1989). Soil-structure interaction at CDMG and USGS accelerograph stations, *Bulletin of the Seismological Society of America*, Vol. 79, No. 1, pp. 1-14.
- CUNDALL, P.A. AND STRACK, O.D.L. (1979). "A discrete numerical model for granular assemblies," *Geotechnique*, Vol. 29, No. 1, pp. 47-65.
- DADDAZIO, R.P., ETTOUNEY, M.M., AND SANDLER, I.S. (1987). "Nonlinear dynamic slope stability analysis," *Journal of Geotechnical Engineering*, ASCE, Vol. 113, No. 4, pp. 285-298.
- DAFALIAS, Y.F. AND HERRMANN, L.R. (1982). "Bounding surface formulation of soil plasticity," Chapter 10 in G.N. Pande and O.C. Zienkiewicz, eds., *Soil Mechanics: Transient and Cyclic Loads*, Wiley, New York, pp. 253-282.
- DAFALIAS, Y.F. AND POPOV, E.P. (1979). "A model for nonlinearly hardening materials for complex loading," *Acta Mechanica*, Vol. 21, No. 3, pp. 173-192.
- DAKOULAS, P. (1985). "Contributions to seismic analysis of earth dams," Ph.D. dissertation, Rensselaer Polytechnic Institute, Troy, New York.
- DAKOULAS, P. AND GAZETAS, G. (1985). "A class of inhomogeneous shear models for seismic response of dams and embankments," *Soil Dynamics and Earthquake Engineering*, Vol. 4, No. 4, pp. 166-182.
- DAKOULAS, P. AND GAZETAS, G. (1986). "Seismic lateral vibration of embankment dams in semi-cylindrical valleys," *Earthquake Engineering and Structural Dynamics*, Vol. 13, No. 1, pp. 19-40.
- DAKOULAS, P. AND GAZETAS, G. (1986). "Seismic shear strains and seismic coefficients in dams and embankments," *Soil Dynamics and Earthquake Engineering*, Vol. 5, No. 2, pp. 75-83.
- DAVIS, J.L. (1986). *Finite Difference Methods in Dynamics of Continuous Media*, Macmillan, New York, 238 pp.
- DAVIS, R.O. AND BERRILL, J.B. (1982). "Energy dissipation and seismic liquefaction in sands," *Earthquake Engineering and Structural Dynamics*, Vol. 10, No. 1, pp. 59-68.
- DBAIBO, N.T. (1989). "Investigation of collapse surface behavior of sands," *M.S.E. Thesis*, Department of Civil Engineering, University of Washington, Seattle, Washington, 268 pp.
- DE ALBA, P. AND PYKE, R.M. (1987). "Behavior of embankments on soft soils under earthquake loading," *Proceedings*, International Symposium on Geotechnical Engineering of Soft Soils, Mexico City, Vol. 2, pp. 125-141.
- DE ALBA, P., BALDWIN, K., JANOO, V., ROE, G. AND CELIKKEL, B. (1984). "Elastic-wave velocities and liquefaction potential," *Geotechnical Testing Journal*, ASTM, Vol. 7, No. 2, pp. 77-88.
- DEALBA, P. (1983). "Pile settlement in a liquefying soil deposit," *Journal of Geotechnical Engineering*, ASCE, Vol. 109, No. 9, pp. 1165-1180.
- DEALBA, P., CHAN, C.K., AND SEED, H.B. (1975). "Determination of soil liquefaction characteristics by large-scale laboratory tests," *Report EERC 75-14*, Earthquake Engineering Research Center, University of California, Berkeley.
- DENG, N., ASHFORD, S.A., AND LYSMER, J. (1995). GROUND2D: A two-dimensional seismic site response analysis program, *Report*, Earthquake Engineering Research Center, University of California, Berkeley.
- DENNEHY, K.T. (1985). Seismic vulnerability, analysis, and design of anchored bulkheads, *Ph.D. Dissertation*, Rensselaer Polytechnic Institute, Troy, New York.

- DER-KIUREGHIAN, A. AND ANG, A.H.S. (1977). "A fault-rupture model for seismic risk analysis," *Bulletin of the Seismological Society of America*, Vol. 67, No. 4, pp. 1173-1194.
- DESAI, C.S. AND ABEL, J.F. (1972). *Introduction to the Finite Element Method*, Van Nostrand Reinhold, New York.
- DESAI, C.S. AND SIRIWARDANE, H.J. (1984). *Constitutive Laws for Engineering Materials, with Emphasis on Geologic Materials*, Prentice Hall, Englewood Cliffs, New Jersey, 468 pp.
- DEWEY, J.W. (1979). "A consumer's guide to instrumental methods for determination of hypocenters," A.W. Hatheway and C.R. McClure, Jr., eds., *Geology in the Siting of Nuclear Power Plants, Geologic Society of America Reviews in Engineering Geology*, Vol. 4, pp. 109-117.
- DIKMEN, S.U. AND GHABOUSSI, J. (1984). "Effective stress analysis of seismic response and liquefaction, theory," *Journal of Geotechnical Engineering*, ASCE, Vol. 110, No.5, pp. 628-644.
- DOBRY, R. AND LADD, R.S. (1980). Discussion to "Soil liquefaction and cyclic mobility evaluation for level ground during earthquakes," by H.B. Seed and "Liquefaction potential: science versus practice," by R.B. Peck, *Journal of the Geotechnical Engineering Division*, ASCE, Vol. 106, No. GT6, pp. 720-724.
- DOBRY, R. AND VUCETIC, M. (1987). "Dynamic properties and seismic response of soft clay deposits," *Proceedings, International Symposium on Geotechnical Engineering of Soft Soils*, Mexico City, Vol. 2, pp. 51-87.
- DOBRY, R., IDRISS, I.M., AND NG, E. (1978). "Duration characteristics of horizontal components of strong motion earthquake records," *Bulletin of the Seismological Society of America*, Vol. 68, No. 5, pp. 1487-1520.
- DOBRY, R., LADD, R.S., YOKEL, F.Y., CHUNG, R.M., AND POWELL, D. (1982). "Prediction of pore water pressure buildup and liquefaction of sands during earthquakes by the cyclic strain method," *NBS Building Science Series 138*, National Bureau of Standards, Gaithersburg, Maryland, 150 pp.
- DOBRY, R., MOHAMAD, R., DAKOULAS, P., AND GAZETAS, G. (1984). "Liquefaction evaluation of earth dams - a new approach," *Proceedings, 8th World Conference on Earthquake Engineering*, Vol. 3, pp.333-340.
- DOBRY, R., VASQUEZ-HERRERA, A., MOHAMMAD, R. AND VUCETIC, M. (1985). "Liquefaction flow failure of silty sand by torsional cyclic tests," *Advances in the Art of Testing Soils Under Cyclic Loading Conditions*, ASCE, New York, pp. 29-50.
- DOBSON, T. (1987). "Case histories of the vibro systems to minimize the risk of liquefaction," in *Soil Improvement: A Ten Year Update*, Geotechnical Special Publication 12, ASCE, New York, pp. 167-183.
- DOUGLAS, B.J., OLSEN, R.S., AND MARTIN, G.R. (1981). Evaluation of the cone penetrometer test for SPT liquefaction assessment, *Proceedings, In Situ Testing to Evaluate Liquefaction Susceptibility*, ASCE, New York.
- DRNEVICH, V.P. (1967). "Effect of strain history on the dynamic properties of sand," Ph.D. Dissertation, University of Michigan, 151 pp.
- DRNEVICH, V.P. (1972). "Undrained cyclic shear of saturated sand," *Journal of the Soil Mechanics and Foundations Division*, ASCE, Vol. 98, No. SM8, pp. 807-825.
- DRNEVICH, V.P. AND RICHART, F.E. JR. (1970). "Dynamic prestraining of dry sand," *Journal of the Soil Mechanics and Foundations Division*, ASCE, Vol. 96, No. SM2, pp. 453-469.
- DUNCAN, J.M. (1992). "State-of-the-art: static stability and deformation analysis," in R.B. Seed and R.W. Boulanger, eds., *Proceedings, Specialty Conference on Stability and Performance of Slopes and Embankments*, II, ASCE, New York, Vol. 1, pp. 222-266.

- DUNCAN, J.M. AND CHANG, C.Y. (1970). "Nonlinear analysis of stress and strain in soils," *Journal of the Soil Mechanics and Foundations Division*, ASCE, Vol. 96, No. SM5, pp. 1629-1653.
- DUNCAN, J.M., BYRNE, P.M., WONG, K.S., AND MABRY, P. (1980). "Strength, stress-strain, and bulk modulus parameters for finite element analysis of stresses and movements in soil masses," *Report UCB/GT/80-01*, University of California, Berkeley.
- DUNCAN, J.M., CLOUGH, G.W., AND EBELING, R.M. (1990). "Behavior and design of gravity earth retaining structures," *Proceedings, ASCE Specialty Conference on Design and Performance of Earth Retaining Structures*, Special Technical Publication 25, Cornell University, Ithaca, New York, pp. 251-277.
- DUSSOM, K.B., HADJ-HAMOU, T., AND BAKEER, R. (1991). "QUAKE: An expert system for the selection of design earthquake accelerogram," *Computers and Structures*, Vol. 40, No. 1, pp. 161-167.
- DYVIK, R. AND MADSHUS, C. (1985). "Laboratory measurements of G_{max} using bender elements," *Advances in the Art of Testing Soils Under Cyclic Conditions*, ASCE, New York, pp. 186-196.
- EBELING, R.M. AND MORRISON, E.E. (1993). "The seismic design of waterfront retaining structures," *NCEL Report R-939*, Naval Civil Engineering Laboratory, Port Hueneme, California, 256 pp.
- ECKERSLEY, J.D. (1985). "Flowslides in stockpiled coal," *Engineering Geology*, Vol 22, No. 1, pp. 13-22.
- EIBY, G.A. (1980). *Earthquakes*, Van Nostrand Reinhold, New York.
- EILER, E.E. AND WHITTIER, R.M. (1988). "Piezoelectric and piezoresistive transducers," Chapter 12 in *Shock and Vibration Handbook*, 3rd edition, C.M. Harris, editor, McGraw Hill Book Company, New York.
- ELGAMAL, A.M., SCOTT, R.F., SUCCARIEH, M.F., AND YAN, L.P. (1990). "La Villita Dam response during five earthquake including permanent deformation," *Journal of Geotechnical Engineering*, ASCE, Vol. 116, No. 10, pp. 1443-1462.
- ELGAMAL, A.W., ABDEL-GHAFFAR, M., AND PREVOST, J.H. (1985). "Elasto-plastic earthquake shear response of one-dimensional earth dam models," *Earthquake Engineering and Structural Dynamics*, Vol. 13, pp. 617-633.
- ELGHADAMSI, F. E., MOHRAZ, B., LEE, C. T. AND MOAYYAD, P. (1988) "Time dependent power spectral density of earthquake motion," *International Journal of Soil Dynamics and Earthquake Engineering*, 7 No. (1), pp. 15-21.
- EPRI (1986). "Seismic hazard methodology for the central and eastern United States," *Report NP-4726*, Electric Power Research Institute, Palo Alto, California.
- EPRI (1993). *Guidelines for determining design basis ground motions*, Electric Power Research Institute, Palo Alto, California, Vol. 1, pp. 8-1 through 8-69.
- ESTEVA, L. (1970). "Seismic risk and seismic design decisions," in R.J. Hansen, ed., *Seismic Design of Nuclear Power Plants*, MIT Press, Cambridge, Massachusetts.
- EVANS, M.D. AND SEED, H.B. (1987). "Undrained cyclic triaxial testing of gravels: the effect of membrane compliance," *Report UCB/EERC-87/08*, Earthquake Engineering Research Center, University of California, Berkeley, California.
- EWING, M., JARDESKY, W. AND PRESS, F. (1957). *Elastic Waves in Layered Media*, McGraw-Hill, New York, 380 pp.
- FACCIOLI, E. (1991). "Seismic amplification in the presence of geological and topographic irregularities," *Proceedings, 2nd International Conference on Recent Advances in Geotechnical Earthquake Engineering and Soil Dynamics*, St. Louis, Missouri, Vol. 2, pp. 1779-1797.
- FARDIS, M.N. AND VENEZIANO, D. (1982). "Probabilistic analysis of deposit liquefaction," *Journal of the Geotechnical Engineering Division*, ASCE, Vol. 108, No. GT3, pp. 395-417.

- FELIO, G., VUCETIC, M., HUDSON, M., BARAR, P. AND CHAPMAN, R. (1990). "Performance of soil nailed walls during the October 17, 1989 Loma Prieta earthquake," *Proceedings, 43rd Canadian Geotechnical Conference*, Quebec City, Vol. 1, pp. 165-173.
- FELLENIUS, B. (1953). "The landslide at Guntorp," *Geotechnique*, Vol. 5, No. 1, pp. 120-125.
- FELLENIUS, W. (1927). *Erdstatische Berechnungen mit Reibung und Kohäsion*, Ernst, Berlin.
- FERRITTO, J.M. (1992). "Optimized earthquake time history and response spectra, User's guide," *Report UG-0025*, Naval Civil Engineering Laboratory, Port Hueneme, California, 14 pp.
- FIEGEL, G.L. AND KUTTER, B.L. (1992). "The mechanism of liquefaction in layered soils," *Report CR92.009*, Naval Civil Engineering Laboratory, Port Hueneme, California, 34 pp.
- FIGUEROA, J.L. AND DAHISARIA, N. (1991). "An energy approach in defining soil liquefaction," *Proceedings, 2nd International Conference on Recent Advances in Geotechnical Earthquake Engineering and Soil Dynamics*, St. Louis, Missouri, Vol. 1, pp. 407-410.
- FINN, W.D.L. (1988). "Dynamic analysis in geotechnical engineering," *Earthquake Engineering and Soil Dynamics II: Recent Advances in Ground-Motion Evaluation*, Geotechnical Special Publication 20, ASCE, New York, pp. 523-591.
- FINN, W.D.L. (1990). "Analysis of post-liquefaction deformations in soil structures," *Proceedings, H. Bolton Seed Memorial Symposium*, University of California, Berkeley, Vol. 2, pp. 291-312.
- FINN, W.D.L. (1991). "Assessment of liquefaction potential and post-liquefaction behavior of earth structures: Developments 1981-1991 (State-of-the-art paper)," *Proceedings, 2nd International Conference on Recent Advances in Geotechnical Earthquake Engineering and Soil Dynamics*, St. Louis, Missouri, Vol. 3, pp. 1833-1850.
- FINN, W.D.L. (1991). "Geotechnical engineering aspects of microzonation," *Proceedings, 4th International Conference on Microzonation*, Earthquake Engineering Research Institute, Stanford University, Palo Alto, California, Vol. 1, pp. 199-259.
- FINN, W.D.L. AND BHATIA, S.K. (1981). "Prediction of seismic pore-water pressures," *Proceedings, 10th International Conference on Soil Mechanics and Foundation Engineering*, Rotterdam, The Netherlands, Vol. 3, pp. 201-206.
- FINN, W.D.L. AND YOGENDRAKUMAR, M. (1989). *TARA-3FL - Program for analysis of liquefaction induced flow deformations*, Department of Civil Engineering, University of British Columbia, Vancouver, British Columbia.
- FINN, W.D.L., BRANSBY, P.L., AND PICKERING, D.J. (1970). "Effect of strain history on liquefaction of sands," *Journal of the Soil Mechanics and Foundations Division*, ASCE, Vol. 96, No. SM6, pp. 1917-1934.
- FINN, W.D.L., PICKERING, D.J., AND BRANSBY, P.L. (1971). "Sand liquefaction in triaxial and simple shear tests," *Journal of the Soil Mechanics and Foundations Division*, ASCE, Vol. 97, No. SM4, pp. 639-659.
- FINN, W.D.L., LEE, K.W., AND MARTIN, G.R. (1977). "An effective stress model for liquefaction," *Journal of the Geotechnical Engineering Division*, ASCE, Vol. 103, No. GT6, pp. 517-533.
- FINN, W.D.L., YOGENDRAKUMAR, M., YOSHIDA, M., AND YOSHIDA, N. (1986). *TARA-3: A Program to Compute the Response of 2-D Embankments and Soil-Structure Interaction Systems to Seismic Loadings*, Department of Civil Engineering, University of British Columbia, Vancouver.
- FINN, W.D.L., LEDBETTER, R.H., FLEMING, R.L., JR., TEMPLETON, A.E., FORREST, T.W., AND STACY, S.T. (1991). "Dam on liquefiable foundation: Safety assessment and remediation," *Proceedings, 17th International Conference on Large Dams*, Vienna, pp. 531-553.

- FINN, W.D.L., WU, G., AND YOSHIDA, N. (1992). "Seismic response of sheet pile walls," *Proceedings, 10th World Conference on Earthquake Engineering*, Madrid, Vol. 3, pp. 1689-1694.
- FINN, W.D.L., LEDBETTER, R.H., AND WU, G. (1994). "Liquefaction in silty soils: Design and analysis," *Ground Failures under Seismic Conditions*, Geotechnical Special Publication 44, ASCE, New York, pp. 51-76.
- FLORIN, V.A. AND IVANOV, P.L. (1961). "Liquefaction of saturated sand soil," *Proceedings, 5th International Conference on Soil Mechanics and Foundation Engineering*, Paris.
- FOSTER, R. J. (1971). *Physical Geology*, Charles E. Merrill, Columbus, Ohio.
- FOWLER, C.M.R. (1990). *The solid earth. An introduction to global geophysics*, Cambridge University Press, Cambridge, England, 472 pp.
- FRAGASZY, R.J., ALI, A., DENBY, G., AND KILIAN, A.P. (1987). "Seismic response of tieback walls," *Transportation Research Record*, Transportation Research Board, Washington, D.C.
- FRANKLIN, A.G. AND CHANG, F.K. (1977). Permanent displacements of earth embankments by Newmark sliding block analysis, *Report 5, Miscellaneous Paper S-71-17*, U.S. Army Corps of Engineers Waterways Experiment Station, Vicksburg, Mississippi.
- FRENCH ASSOCIATION FOR EARTHQUAKE ENGINEERING (1990). *Recommendations AFPS90 for the reduction of rules relative to the structures and installations built in regions prone to earthquakes*, Saint-Remy-les-Chevreuse, France.
- GAO, Z., HO, B., AND CHANG, D. (1983). "Some geological considerations for the damage during the Tangshan earthquake," *North China Earthquake Sciences*, Vol. 1, pp. 64-72 (in Chinese).
- GARFUNKEL, Z. (1975). "Growth, shrinking, and long-term evolution of plates and their implications for flow patterns in the mantle," *Journal of Geophysical Research*, Vol. 80, p. 4425.
- GAZETAS, G. (1982). "Shear vibrations of vertically inhomogeneous earth dams," *International Journal for Numerical and Analytical Methods in Geomechanics*, Vol. 6, No. 1, pp. 219-241.
- GAZETAS, G. (1987). "Seismic response of earth dams; some recent developments," *Soil Dynamics and Earthquake Engineering*, Vol. 6, No. 1, pp. 3-47.
- GAZETAS, G. (1991). Foundation vibrations, Chapter 15 in *Foundation Engineering Handbook*, 2nd edition, H.-Y. Fang, ed., Van Nostrand Reinhold, New York, pp. 553-593.
- GAZETAS, G., DAKOULAS, P., AND DENNEHY, K. (1990). Empirical seismic design method for water-front anchored sheetpile walls, *Proceedings, ASCE Specialty Conference on Design and Performance of Earth Retaining Structures*, Geotechnical Specialty Publication 25, pp. 232-250.
- GELI, L., BARD, P.Y., AND JULLIEN, B. (1988). "The effect of topography on earthquake ground motion: A review and new results," *Bulletin of the Seismological Society of America*, Vol. 78, No. 1, pp. 42-63.
- GILBERT, F. AND DZIEWONSKI, A.M. (1975). "An application of normal mode theory to the retrieval of structural parameters and source mechanisms from seismic spectra," *Phil. Trans. R. Soc. Lond.*, 278, 187-269.
- GLASER, S. (1995). System identification and its application to estimating soil properties, *Journal of Geotechnical Engineering*, Vol. 121, No. 7, pp. 553-560.
- GLEN, W. (1975). *Continental Drift and Plate Tectonics*, Charles E. Merrill, Columbus, Ohio.
- GOODMAN, L.E. (1988). Material damping and slip damping, Chapter 36 in C.M. Harris, ed., *Shock and Vibration Handbook*, 3rd ed., McGraw-Hill, New York.
- GOTO, S., TATSUOKA, F., SHIBUYA, S., KIM, Y.-S., AND SATO, S. (1991). "A simple gauge for local small strain measurements in the laboratory," *Soils and Foundations*, Vol. 31, No. 1, pp. 169-180.

- GOULOIS, A.M., WHITMAN, R.V., AND HOEG, K. (1985). "Effect of sustained shear stress on the cyclic degradation of clay," *Proceedings, Symposium on Strength Testing of Marine Sediments*, R.C. Chaney and K.R. Demars, eds., ASTM STP 883, ASTM, Philadelphia, pp. 336-351.
- GRAF, E.D. (1992). "Earthquake support grouting in sands," in *Grouting, Soil Improvement, and Geosynthetics*, Geotechnical Special Publication 30, ASCE, New York, Vol. 2, pp. 879-888.
- GRIFFITHS, D.H. AND KING, R.F. (1965). *Applied geophysics for engineers and geologists*, Pergamon Press, New York, 223 pp.
- GRIFFITHS, D.V. AND PREVOST, J.H. (1988). "Two- and three-dimensional finite element analyses of the Long Valley Dam," *Technical Report NCEER-88-0015*, National Center for Earthquake Engineering Research, Buffalo, New York.
- GUAGENTI-GRANDORI, E. AND MOLINA, D. (1984). "Semi-Markov processes in seismic risk analysis," *Proceedings, International Symposium of Semi-Markov Processes and Their Applications*, Brussels.
- GUBBINS, D. (1990). *Seismology and Plate Tectonics*, University Press, Cambridge, 339 pp.
- GUCUNSKI, N. AND WOODS, R.D. (1991). "Use of Rayleigh modes in interpretation of SASW test," *Proceedings, 2nd International Conference on Recent Advances in Geotechnical Earthquake Engineering and Soil Dynamics*, St. Louis, Missouri, Vol. 2, pp. 1399-1408.
- GUTENBERG, B. (1927). *Grundlagen der Erdlebenkunde*, Berlin.
- GUTENBERG, B. (1945). "Magnitude determination for deep-focus earthquakes," *Bulletin of the Seismological Society of America*, Vol. 35, pp. 117-130.
- GUTENBERG, B., AND RICHTER, C.F. (1936). "On Seismic Waves (third paper)," *Gerlands Beitrage zur Geophysik*, Vol. 47, pp. 73-131.
- GUTENBERG, B. AND RICHTER, C.F. (1942). "Earthquake magnitude, intensity, energy, and acceleration," *Bulletin of the Seismological Society of America*, Vol. 32, pp. 163-191.
- GUTENBERG, B. AND RICHTER, C. F. (1944). "Frequency of Earthquakes in California," *Bulletin of the Seismological Society of America*, Vol. 34, No. 4, pp. 1985-1988.
- GUTENBERG, B. AND RICHTER, C.F. (1954). *Seismicity of the Earth and Related Phenomena*, Princeton University Press, Princeton, New Jersey, 310 pp.
- GUTENBERG, B. AND RICHTER, C.F. (1956). "earthquake magnitude: intensity, energy, and acceleration," *Bulletin of the Seismological Society of America*, Vol. 46, pp. 104-145.
- HACHEY, J.E., PLUM, R.L., BYRNE, R.J., KILIAN, A.P., AND JENKINS, D.V. (1994). Blast densification of a thick, loose debris flow at Mt. St. Helen's, Washington, *Proceedings, Vertical and Horizontal Deformations of Foundations and Embankments*, Geotechnical Special Publication No. 40, ASCE, College Station, Texas, pp. 502-512.
- HAGER, B.H. (1978). "Oceanic plate driven by lithospheric thickening and subducted slabs," *Nature*, Vol. 276, pp. 156-159.
- HAGIWARA, Y. (1974). "Probability of earthquake occurrence as obtained from a Weibull distribution analysis of crustal strain," *Tectonophysics*, Vol. 23, No. 3, pp. 313-318.
- HALDAR, A. AND TANG, W.H. (1979). "Probabilistic evaluation of liquefaction potential," *Journal of the Geotechnical Engineering Division*, ASCE, Vol. 105, No. GT2, pp. 145-163.
- HALDAR, A. AND TANG, W.H. (1981). "Statistical study of uniform cycles in earthquakes," *Journal of the Geotechnical Engineering Division*, ASCE, Vo. 107, No. GT5, pp. 577-589.
- HALL, W.J. (1988). "Part I: Vibration of structures induced by ground motion," Chapter 24 in *Shock and Vibration Handbook*, 3rd edition, C.M. Harris, editor, McGraw Hill Book Company, New York.
- HAMADA, M., YASUDA, S., ISOYAMA, R., AND EMOTO, K. (1986). "Study on liquefaction induced permanent ground displacements," *Report for the Association for the Development of Earthquake Prediction*.

- HAMADA, M. AND O'ROURKE, T.D. (1992). Case histories of liquefaction and lifeline performance during past earthquakes, *Technical Report NCEER-92-0001*, National Center for Earthquake Engineering Research, Buffalo, New York, 2 Vol.
- HANKS, T.C. (1982). " f_{max} ," *Bulletin of the Seismological Society of America*, Vol. 72, pp. 1867-1879.
- HANKS, T.C. AND KANAMORI, H. (1979). "A moment magnitude scale," *Journal of Geophysical Research*, Vol. 84, pp. 2348-2350.
- HANKS, T. C. AND MCGUIRE, R. K. (1981) "The character of high-frequency strong ground motion," *Bulletin of the Seismological Society of America*, Vol. 71, pp. 2071-2095.
- HANZAWA, H., ITOH, Y., AND SUZUKI, K. (1979). "Shear characteristics of a quick sand in the Arabian Gulf," *Soils and Foundations*, Vol., 19, No. 4, pp.1-15.
- HAO, H., OLIVEIRA, C.S., AND PENZIEN, J. (1989). "Multiple station ground motion processing and simulation based on SMART-1 array data," *Nuclear Engineering and Design*, Vol. 111, pp. 293-310.
- HARDER, L. F. AND SEED, H.B. (1986). "Determination of penetration resistance for coarse-grained soils using the Becker hammer drill," *Report UCB/EERC-86/06*, Earthquake Engineering Research Center, University of California, Berkeley, 126 pp.
- HARDER, L.F., JR., HAMMOND, W.D., AND ROSS, P.S. (1984). "Vibroflotation compaction at Thermalito Afterbay," *Journal of Geotechnical Engineering*, ASCE, Vol. 110, No. 1, pp. 57-72.
- HARDIN, B.O. (1978). "The nature of stress-strain behavior of soils," *Proceedings, Earthquake Engineering and Soil Dynamics*, ASCE Pasadena, California, Vol. 1, pp. 3-89.
- HARDIN, B.O. AND BLACK, W.L. (1968). "Vibration modulus of normally consolidated clay," *Journal of the Soil Mechanics and Foundations Division*, ASCE, Vol. 94, No. SM2, pp. 353-369.
- HARDIN, B.O. AND DRNEVICH, V.P. (1972a). "Shear modulus and damping in soils: Measurement and parameter effects," *Journal of the Soil Mechanics and Foundations Division*, ASCE, Vol. 98, No. SM6, pp. 603-624.
- HARDIN, B.O. AND DRNEVICH, V.P. (1972b). "Shear modulus and damping in soils: design equations and curves," *Journal of the Soil Mechanics and Foundations Division*, ASCE, Vol. 98, No. SM7, pp. 667-692.
- HARICHARAN, R.S. AND VANMARCKE, E.H. (1986). "Stochastic variation of earthquake ground motion in space and time," *Journal of Engineering Mechanics*, Vol. 112, No. 2, pp. 154-174.
- HART, M.E. (1987). *Reliability-based Design in Civil Engineering*, McGraw-Hill, New York.
- HARTZELL, S. (1978). "Earthquake aftershocks as Green's functions," *Geophysical Research Letters*, Vol. 5, No. 1, pp. 1-4.
- HASKELL, N.H. (1953). "The dispersion of surface waves in multilayered media," *Bulletin of the Seismological Society of America*, Vol. 43, pp. 17-34.
- HATANAKA, M. (1952). "3-dimensional consideration on the vibration of earth dams," *Journal of the Japanese Society of Civil Engineers*, Vol. 37, No. 10.
- HATHEWAY, A.W. AND LEIGHTON, F.B. (1979). "Trenching as an exploratory method," in A.W. Hatheway and C.R. McClure eds. *Geology in the Siting of Nuclear Power Plants*, Reviews in Engineering Geology, Geological Society of America, Vol. 4, pp. 169-198.
- HAUSMANN, M.R. (1990). *Engineering Principles of Ground Modification*, McGraw-Hill, New York, 632 pp.
- HAYDEN, R.F. (1994). "Utilization of liquefaction countermeasures in North America," *Proceedings, 5th U.S. National Conference on Earthquake Engineering*, Chicago, Vol. 4, pp. 149-158.

- HAYDEN, R.F. AND WELCH, J.P. (1991). "Design and installation of stone columns at naval air station," in M.I. Esrig and R.C. Bachus, eds., *Deep Foundation Improvement: Design, Construction, and Testing*, ASTM STP 1089, ASTM, Philadelphia, pp. 172-184.
- HEATON, T.H. AND KANAMORI, H. (1984). "Seismic potential associated with subduction in the northwestern United States," *Bulletin of the Seismological Society of America*, Vol. 73, No. 3, pp. 933-941.
- HEIDARI, M. AND JAMES, R.G. (1982). "Centrifuge modelling of earthquake induced liquefaction in a column of sand," *Proceedings, Conference on Soil Dynamics and Earthquake Engineering*, A.A. Balkema, Rotterdam, The Netherlands, Vol. 1, pp. 271-281.
- HEISEY, J.S., STOKOE, K.H., AND MEYER, A.H. (1982). "Moduli of pavement systems from spectral analysis of surface waves," *Transportation Research Record 853*, Transportation Research Board Washington, D.C.
- HENKE, W. AND HENKE, R. (1991). "In situ torsional cylindrical shear test - laboratory results," *Proceedings, 2nd International Conference on Recent Advances in Geotechnical Earthquake Engineering and Soil Dynamics*, St. Louis, Missouri, Vol. 1, pp. 131-136.
- HERSHBERGER, J. (1956). "A comparison of earthquake accelerations with intensity ratings," *Bulletin of the Seismological Society of America*, Vol. 46, pp. 317-320.
- Hertz, H. (1881). "Über die Berührung fester elastischer Körper," *Journal Für die Reine und Angewandte Mathematik*, Vol. 92, pp. 156-171.
- HETTLER, A. AND GUDEHUS, G. (1985). "A pressure-dependent correction for displacement results from 1 g model tests with sand," *Geotechnique*, Vol. 35, No. 4, pp. 497-510.
- HEUKELOM, W. AND FOSTER, C.R. (1960). "Dynamic testing of pavements," *Journal of the Soil Mechanics and Foundations Division*, ASCE, Vol. 86, No. SM1, pp. 1-28.
- HILTUNEN, D.R. AND WOODS, R.D. (1988). "SASW and crosshole test results compared," *Proceedings, Earthquake Engineering and Soil Dynamics II: Recent Advances in Ground Motion Evaluation*, Geotechnical Special Publication 20, ASCE, New York, pp. 279-289.
- HO, C.L., DENBY, G.M., AND FRAGASZY, R.J. (1990). Seismic performance of tied-back walls, *Proceedings*, ASCE Specialty Conference on Design and Performance of Earth Retaining Structures, Geotechnical Specialty Publication No. 25, pp. 843-853.
- HOAR, R.J. AND STOKOE, K.H. (1984). "Field and laboratory measurements of material damping of soil in shear" *Proceedings, 8th World Conference on Earthquake Engineering*, San Francisco, Vol. 3, pp. 47-54.
- HOLTZ, R.D. AND KOVACS, W.D. (1981). *An Introduction to Geotechnical Engineering*, Prentice Hall, Englewood Cliffs, New Jersey, 733 pp.
- HORN, H.M. (1978). "North American experience in soil sampling and its influence on dynamic laboratory testing," Preprint Session No. 79, ASCE Annual Convention, Chicago.
- HOU, S. (1968). "Earthquake simulation models and their applications," *Report R68-17*, Department of Civil Engineering, Massachusetts Institute of Technology, Cambridge, Massachusetts.
- HOUSNER, G.W. (1947). "Characteristics of strong-motion earthquakes," *Bulletin of the Seismological Society of America*, Vol. 37, No. 1, pp. 19-31.
- HOUSNER, G. W. (1959) "Behavior of structures during earthquakes," *Journal of the Engineering Mechanics Division*, ASCE, Vol. 85, No. EM14, 109-129.
- HOUSNER, G.W. ET AL. (1990). *Competing Against Time*, Report to the Governor, Governor's Board of Inquiry, State of California.
- HOUSTON, W.N. AND HERRMANN, H.G. (1980). Undrained cyclic strength of marine soil, *Journal of the Geotechnical Engineering Division*, ASCE, Vol. 106, No. GT6, pp. 691-712.

- HRYCIW, R.D. (1989). "Ray-path curvature in shallow seismic investigations," *Journal of Geotechnical Engineering*, ASCE, Vol. 115, No. 9, pp. 1268-1284.
- HRYCIW, R.D. (1990). Small-strain-shear modulus of soil by dilatometer, *Journal of Geotechnical Engineering*, ASCE, Vol. 116, No. 11, pp. 1700-1716.
- HRYCIW, R.D., VITTON, S., AND THOMANN, T.G. (1990). "Liquefaction and flow failure during seismic exploration," *Journal of Geotechnical Engineering*, ASCE, Vol. 116, No. 12, pp. 1881-1889.
- HUANG, Y.H. (1983). *Stability Analysis of Earth Slopes*, Van Nostrand Reinhold, New York, 305 pp.
- HUDSON, D.E. (1958). "The Wilmot survey type strong-motion earthquake recorder," *Earthquake Engineering Laboratory Research Report*, California Institute of Technology, Pasadena, California.
- HUDSON, D.E. (1979). *Reading and Interpreting Strong Motion Accelerograms*, Earthquake Engineering Research Institute, Berkeley, California, 112 pp.
- HUDSON, D.E. (1984). "Strong motion accelerograph systems - problems and prospects," *Proceedings, 8th World Conference on Earthquake Engineering*, Vol. 2, pp. 39-45.
- HUNGR, O. AND MORGENSTERN, N.R. (1984). "High velocity ring shear tests on sand," *Geotechnique*, Vol. 34, No. 3, pp. 415-421.
- HUSSIN, J.D. AND ALI, S. (1987). "Soil improvement of the Trident submarine facility," in *Soil Improvement: A Ten Year Update*, Geotechnical Special Publication 12, ASCE, New York, pp. 215-231.
- HVORSLEV, M.J. (1949). *Subsurface Exploration and Sampling of Soils for Civil Engineering Purposes*, Report of Committee on Sampling and Testing, Soil Mechanics and Foundations Division, ASCE, New York, 521 pp.
- HYNES-GRIFFIN, M.E. AND FRANKLIN, A.G. (1984). "Rationalizing the seismic coefficient method," *Miscellaneous Paper GL-84-13*, U.S. Army Corps of Engineers Waterways Experiment Station, Vicksburg, Mississippi, 21 pp.
- IAI, S. (1989). "Similitude for shaking table tests on soil-structure-fluid model in 1g gravitational field," *Soils and Foundations*, Vol. 29, No. 1, pp. 105-118.
- IAI, S. AND KAMEOKA, T. (1993). "Finite element analysis of earthquake induced damage to anchored steel sheet pile quay walls," *Soils and Foundations*, Vol. 33, No. 1, pp. 71-91.
- IAI, S., NODA, S., AND TSUCHIDA, H. (1988). "Basic consideration for designing the area of the ground compaction as a remedial measure against liquefaction," *Proceedings, U.S.-Japan Joint Workshop on Remedial Measures for Liquefiable Soils*.
- IAI, S., MATSUNAGA, Y., MORITA, T., MIYODA, M., SAKURAI, H., OISHI, H., OGURA, H., ANDO, Y., TANAKA, Y., AND KATO, M. (1994). "Effects of remedial measures against liquefaction at 1993 Kushiro-Oki earthquake," *Proceedings, 5th Japan-U.S. Workshop on Earthquake Resistant Design of Lifeline Facilities and Countermeasures for Soil Liquefaction*, Snowbird, Utah.
- ICBO, (1994). *Uniform Building Code, 1991*, International Conference of Building Officials, Whittier, California.
- Idriss, I.M. (1985). "Evaluating seismic risk in engineering practice," *Proceedings of the 11th International Conference on Soil Mechanics and Foundation Engineering*, San Francisco, Vol. 1, 255-320.
- IDRISS, I.M. (1990). "Response of soft soil sites during earthquakes," in J.M. Duncan, ed., *Proceedings, H. Bolton Seed Memorial Symposium*, BiTech Publishers, Vancouver, British Columbia, Vol. 2, pp. 273-289.
- IDRISS, I.M. (1991). "Earthquake ground motions at soft soil sites," *Proceedings, 2nd International Conference on Recent Advances in Geotechnical Earthquake Engineering and Soil Dynamics*, Vol. III, pp. 2265-2271.

- IDRISS, I.M. AND SEED, H.B. (1968). "An analysis of ground motions during the 1957 San Francisco earthquake," *Bulletin of the Seismological Society of America*, Vol. 58, No. 6, pp. 2013-2032.
- IDRISS, I.M. and Sun, J.I. (1992). "SHAKE91: a computer program for conducting equivalent linear seismic response analyses of horizontally layered soil deposits," *User's Guide*, University of California, Davis, 13 pp.
- IDRISS, I.M., DOBRY, R., AND SINGH, R.D. (1978). "Nonlinear behavior of soft clays during cyclic loading," *Journal of the Geotechnical Engineering Division*, ASCE, Vol. 104, No. GT12, pp. 1427-1447.
- IDRISS, I.M., MORIWAKI, Y., WRIGHT, S.G., DOYLE, E.H., AND LADD, R.S. (1980). "Behavior of normally consolidated clay under simulated earthquake and ocean wave loading conditions, *Proceedings, International Symposium on Soils under Cyclic and Transient Loading*, Swansea, United Kingdom, Vol. 1, pp. 437-445.
- IIDA, K., COX, D.C., AND PARARAS-CARAYANNIS, G. (1967). "Preliminary catalog of tsunamis occurring in the Pacific Ocean," *Report No. HIG-67-10*, Hawaii Institute of Geophysics, University of Hawaii, Honolulu, Hawaii.
- IMAI, T. AND TONOUCI, K. (1982). "Correlation of N-value with s-wave velocity and shear modulus," *Proceedings, 2nd European Symposium on Penetration Testing*, Amsterdam, pp. 57-72.
- ISENHOWER, W.M. AND STOKOE, K.H. (1981). Strain rate dependent shear modulus of San Francisco Bay Mud, *Proceedings, Internatinoal Conference on Recent Advances in Geotechnical Earthquake Engineering and Soil Dynamics*, St. Louis, Missouri, Vol. 2, pp. 597-602.
- ISHIBASHI, I. (1992). Discussion to "Effect of soil plasticity on cyclic response," by M. Vucetic and R. Dobry, *Journal of Geotechnical Engineering*, ASCE, Vol. 118, No. 5, pp. 830-832.
- ISHIBASHI, I. AND ZHANG, X. (1993). "Unified dynamic shear moduli and damping ratios of sand and clay," *Soils and Foundations*, Vol. 33, No. 1, pp. 182-191.
- ISHIHARA, K. (1984). "Post-earthquake failure of a tailings dam due to liquefaction of the pond deposit," *Proceedings, International Conference on Case Histories in Geotechnical Engineering*, University of Missouri, St. Louis, Vol. 3, pp. 1129-1143.
- ISHIHARA, K. (1985). "Stability of natural deposits during earthquakes," *Proceedings, 11th International Conference on Soil Mechanics and Foundation Engineering*, Vol. 1, pp. 321-376.
- ISHIHARA, K. (1993). Liquefaction and flow failure during earthquakes, *Geotechnique*, Vol. 43, No. 3, pp. 351-415.
- ISHIHARA, K. AND KOSEKI, J. (1989). Discussion of "Cyclic shear strength of fines-containing sands," *Earthquake Geotechnical Engineering, 12th International Conference on Soil Mechanics and Foundation Engineering*, Rio de Janeiro, pp. 101-106.
- ISHIHARA, K. AND LI, S. (1972). "Liquefaction of saturated sand in triaxial torsion shear test," *Soils and Foundations*, Vol. 12, No. 2, pp. 19-39.
- ISHIHARA, K. AND TOWHATA, I. (1980). "One-dimensional soil response analysis during earthquakes based on effective stress model," *Journal of the Faculty of Engineering*, University of Tokyo, Vol. 35, No. 4.
- ISHIHARA, K. AND YOSHIMINE, M. (1992). "Evaluation of settlements in sand deposits following liquefaction during earthquakes," *Soils and Foundations*, Vol. 32, No. 1, pp. 173-188.
- ISHIHARA, K., TATSUOKA, F., AND YASUDA, S. (1975). "Undrained deformation and liquefaction of sand under cyclic stresses," *Soils and Foundations*, Vol. 15, No. 1, pp. 29-44.
- ISHIHARA, K., KAWASE, Y., AND NAKAJIMA, M. (1980). Liquefaction characteristics of sand deposits at an oil tank site during the 1978 Miyagiken-Oki earthquake, *Soils and Foundation*, Vol. 20, No. 2, pp. 97-111.
- ISHIMOTO, M. (1932). "Echelle d'intensité sismique et accélération maxima," *Bulletin of the Earthquake Research Institute*, Tokyo University, Vol. 10, pp. 614-626.

- IVERSON, R.M. AND DENLINGER, R.P. (1987). "The physics of debris flows: a conceptual assessment," in R.L. Beschta, T. Blinn, G.E. Grant, G.G. Ice, and F.J. Swanson, eds. *Proceedings, Erosion and Sedimentation in the Pacific Rim*, International Association of Hydrological Science, Corvallis, Oregon, pp. 155-165.
- IVERSON, R.M. AND LAHUSEN, R.G. (1993). "Friction in debris flows: Inferences from large-scale flume experiments," *Proceedings, Hydraulics Engineering '93*, ASCE, San Francisco, pp. 1604-1609.
- IWAN, W.D. (1967). "On a class of models for the yielding behavior of continuous and composite systems," *Journal of Applied Mechanics*, Vol. 34, No. E3, pp. 612-617.
- IWASAKI, T., TATSUOKA, F., AND TAKAGI, Y. (1978). "Shear modulus of sands under torsional shear loading," *Soils and Foundations*, Vol. 18, No. 1, pp. 39-56.
- JACOB, K.H. (1991). "Seismic zonation and site response: Are building-code soil-factors adequate to account for variability of site conditions across the US?" *Proceedings, 4th International Conference on Microzonation*, Earthquake Engineering Research Institute, Stanford University, Palo Alto, California, Vol. 1, pp. 695-702.
- JAKOBSEN, B. (1952). "The landslide at Surte on the Gota River, September 29, 1952," *Proceedings 5*, Royal Swedish Geotechnical Institute, Stockholm.
- JAMIOLKOWSKY, M. AND LOPRESTI, D.C.F. (1992). Discussion of "Correlation between liquefaction resistance and shear wave velocity," by K. Tokimatsu and A. Uchida, *Soils and Foundations*, Vol. 32, No. 2, pp. 145-148.
- JAMIOLKOWSKI, M., LEROUÉIL, S., AND LOPRESTI, D.C.F. (1991). "Theme lecture: Design parameters from theory to practice," *Proceedings, Geo-Coast '91*, Yokohama, Japan, pp. 1-41.
- JANBU, N. (1968). "Slope stability computations," *Soil Mechanics and Foundation Engineering Report*, Technical University of Norway, Trondheim.
- JANES, H.W. (1973). "Densification of sand for drydock by Terra-probe," *Journal of the Soil Mechanics and Foundations Division*, ASCE, Vol. 99, No. SM6, pp. 451-470.
- JAPAN SOCIETY OF CIVIL ENGINEERS (1980). "Earthquake resistant design of quaywalls and piers in Japan," *Earthquake Resistant Design for Civil Engineering Structures*, Earth Structures and Foundations, pp. 31-85.
- JENNINGS, J.E. (1979). "The failure of a slimes dam at Bafokeng," *Civil Engineering in South Africa*, Vol. 6, pp. 135-140.
- JENNINGS, P.C. (1985). "Ground motion parameters that influence structural damage," in R.E. Scholl and J.L. King, eds. *Strong Ground Motion Simulation and Engineering Applications*, EERI Publication 85-02, Earthquake Engineering Research Institute, Berkeley, California.
- JEYAPALAN, J.K. (1980). "Analyses of flow failures of mine tailings impoundments," Ph.D. Dissertation, University of California, Berkeley, 298 pp.
- JEYAPALAN, J.K., DUNCAN, J.M., AND SEED, H.B. (1981). "Summary of research on flow failures of mine tailings impoundments," *Information Circular 8857*, Technology Transfer Workshop on Mine Waste Disposal Techniques, U.S. Bureau of Mines, Denver, Colorado, pp. 54-63.
- JIBSON, R. (1987). "Summary of research on the effects of topographic amplification of earthquake shaking on slope stability," *Open-File Report 87-268*, U.S. Geological Survey, Menlo Park, California.
- JIBSON, R. (1994). "Predicting earthquake-induced landslide displacements using Newmark's sliding block analysis," *Transportation Research Record 1411*, Transportation Research Board, Washington, D.C., pp. 9-17.
- JOHNSON, A.M. (1970). *Physical Processes in Geology*, Freeman, Cooper, San Francisco, 577 pp.

- JOHNSON, H.V. (1982). "The effects of end platens, methods of loading and specimen size in monotonic triaxial R tests," *Miscellaneous Paper GL-82-10*, U.S. Army Engineering Waterways Experiment Station, Vicksburg, MS.
- JOHNSON, L.R. AND SILVA, W. (1981). "The effects of unconsolidated sediments upon the ground motion during local earthquakes," *Bulletin of the Seismological Society of America*, Vol. 71, No. 1, pp. 127-142.
- JOHNSON, S.A., GREENLEAF, J.F., RITMAN, E.L., HARRIS, L.D., AND RAJAGOPOLAN, B. (1978). "Three-dimensional analysis and display of rock and soil masses for site characterization: potential contributions from medical imaging techniques," *Proceedings, Specialty Workshop on Site Characterization and Exploration*, Northwestern University, Evanston, Illinois, pp. 322-334.
- JOHNSTON, A.C. (1990). "An earthquake strength scale for the media and the public," *Earthquakes and Volcanoes*, Vol. 22, No. 5, pp. 214-216.
- JOYNER, W.B. (1977). "NONLI3: A Fortran program for calculating nonlinear ground response," *Open File Report 77-761*, U.S. Geological Survey, Menlo Park, California.
- JOYNER, W. B. AND BOORE, D. M. (1981) "Peak horizontal acceleration and velocity from strong-motion records including records from the 1979 Imperial Valley, California earthquake," *Bulletin of the Seismological Society of America*, 71, 2011-2038.
- JOYNER, W.B. AND BOORE, D.M. (1982). "Prediction of earthquake response spectra," *Proceedings, 51st Annual Convention of the Structural Engineers of California*, also *USGS Open-File Report 82-977*, 16 pp.
- JOYNER, W.J. AND BOORE, D.M. (1991). Strong earthquake ground motion and engineering design, *Geotechnical News*, Vol. 9, No. 1, pp. 21-26.
- JOYNER, W. B. AND BOORE, D.M. (1988) "Measurement, characterization, and prediction of strong ground motion," in *Earthquake Engineering and Soil Dynamics II - Recent Advances in Ground-Motion Evaluation*, Geotechnical Special Publication 20, ASCE, New York, pp. 43-102.
- JOYNER, W.B. AND CHEN, A.T.F. (1975) "Calculation of nonlinear ground response in earthquakes," *Bulletin of the Seismological Society of America*, Vol. 65, pp. 1315-1336.
- JOYNER, W.B., WARRICK, R.E., AND OLIVER, A.A., III (1976). "Analysis of seismograms from a downhole array in sediments near San Francisco Bay," *Bulletin of the Seismological Society of America*, Vol. 66, No. 5, pp. 937-958.
- KAGAWA, T. (1977). "Shaking table tests and analysis of soil-structure systems," Ph.D. Dissertation, University of California, Berkeley.
- KAGAWA, T., MEJIA, L., SEED, H.B., AND LYSMER, J. (1981). "TLUSH: a computer program for three-dimensional dynamic analysis of earth dams," *Report UCB/EERC-81/14*, University of California, Berkeley.
- KANAI, K. (1957) "Semi-empirical formula for the seismic characteristics of the ground," *Bulletin of the Earthquake Research Institute*, Tokyo University, Vol. 35, pp. 308-325.
- KANAMORI, H. (1977). "The Energy Release in Great Earthquakes," *Journal of Geophysical Research*, Vol. 82, pp. 2981-2987.
- KANAMORI, H. (1983). Magnitude scale and quantification of earthquakes, *Tectonophysics*, Vol. 93, pp. 185-199.
- KANAMORI, H. (1988). "Importance of historical seismograms for geophysical research," in W.H.K. Lee, H. Meyers, and K. Shimazaki, eds. *Historical Seismograms and Earthquakes of the World*, Academic Press, San Diego, California, pp. 16-31.

- KANAMORI, H. AND STEWART, G.S. (1978). "Seismological aspects of the Guatemala earthquake of February 4, 1976," *Journal of Geophysical Research*, Vol. 83, pp. 3427-3434.
- KATAYAMA, I. (1991). "Wave scattering effect in soil-structure interaction," *Proceedings, 11th International Conference on Structural Mechanics in Reactor Technology*, Tokyo, Vol. K, pp. 153-158.
- KATAYAMA, T. AND SATO, N. (1982). "Ground strain measurement by a very densely located seismometer array," *Proceedings, 6th Japan Earthquake Engineering Symposium*, pp. 241-248.
- KAVAZANJIAN, E., ECHEZURIA, H., AND MCCANN, M.W. (1985). "RMS acceleration hazard for San Francisco," *Soil Dynamics and Earthquake Engineering*, Vol. 4, No. 3, pp.
- KAVAZANJIAN, E., JR., SNOW, M.S., MATASOVIC, N., PORAN, C., AND SATOH, T. (1994). "Non-intrusive Rayleigh wave investigations at solid waste landfills," *Proceedings, First International Conference on Environmental Geotechnics*, Edmonton, Alberta, Canada.
- KAWAI, T. (1985). DIANA - Dynamic interaction approach and non-linear analysis, *Summary Report*, Science University of Tokyo.
- KAWASUMI, H. (1951). "Measures of earthquake danger and expectancy of maximum intensity throughout Japan as inferred from the seismic activity in historical times," *Bulletin of the Earthquake Research Institute*, Tokyo University, Vol. 29, pp. 469-482.
- KAYEN, R.E., MITCHELL, J.K., SEED, R.B., LODGE, A., NISHIO, S., AND COTINHO, R. (1992). Evaluation of SPT-, CPT-, and shear wave-based methods for liquefaction potential assessment using Loma Prieta data, *Proceedings, 4th U.S. - Japan Workshop on Earthquake Resistant Design of Lifeline Facilities and Countermeasures for Soil Liquefaction*, Vol. 1, pp. 177-204.
- KEAREY, P. AND VINE, F.J. (1990). *Global Tectonics*, Blackwell, Oxford, 302 pp.
- KEEFER, D.K. (1984). "Landslides caused by earthquakes," *Geologic Society of America Bulletin*, Vol. 95, No. 2, pp. 406-421.
- KELLER, T.O., CASTRO, G., AND ROGERS, J.H. (1987). "Steel Creek Dam foundation densification," in *Soil Improvement: A Ten Year Update*, Geotechnical Special Publication 12, ASCE, New York, pp. 136-166.
- KENNEDY, R.P. (1980). "Ground motion parameters useful in structural design," presented at the Conference on Evaluation of Regional Seismic Hazards and Risk, Santa Fe, New Mexico.
- KHOURI, N.Q. (1984). "Dynamic properties of soils," *Masters Thesis*, Department of Civil Engineering, Syracuse University, Syracuse, New York.
- KING, J.L. AND TUCKER, B.E. (1984). "Dependence of sediment-filled valley response on the input amplitude and the valley properties," *Bulletin of the Seismological Society of America*, Vol. 74, No. 1, pp. 153-165.
- KIREMIDJIAN, A. AND ANAGNOS, T. (1984). "Stochastic slip-predictable model for earthquake occurrences," *Bulletin of the Seismological Society of America*, Vol. 74, pp. 739-755.
- KISHIDA, H. (1967). "Ultimate bearing capacity of piles driven into loose sand," *Soils and Foundations*, Vol. 7, No. 3, pp. 20-29.
- KITAJIMA, S. AND UWABE, T. (1979). "Analysis of seismic damage in anchored sheet-piling bulkheads," *Report of the Japanese Port and Harbor Research Institute*, Vol. 18, No. 1, pp. 67-130 (in Japanese).
- KLEINER, D.E. (1976). "Design and construction of an embankment dam to impound gypsum wastes," *Proceedings, 12th International Congress on Large Dams, International Commission on Large Dams*, Mexico City, pp. 235-249.
- KLEYN, A.H. (1983). *Seismic Reflection Interpretation*, Applied Science Publishers, London, 269 pp.

- KLOHN, E.J., GARGA, V.K., AND SHUKIN, W. (1981). "Densification of sand tailings by blasting," *Proceedings, 10th International Conference on Soil Mechanics and Foundation Engineering*, Stockholm, Vol. 3, pp. 725-730.
- KOBAYASHI, Y. (1981). "Causes of fatalities in recent earthquakes in Japan," *Journal of Disaster Science*, Vol. 3, pp. 15-22.
- KOERNER, R.M. (1994). *Designing with geosynthetics*, Prentice Hall, Englewood Cliffs, New Jersey, 783 pp.
- KOESTER, J.P. (1994). The influence of fines type and content on cyclic strength, *Ground Failures Under Seismic Conditions*, Geotechnical Special Report No. 44, ASCE, New York, pp. 17-33.
- KOKUSHO, T. (1980). "Cyclic triaxial test of dynamic soil properties for wide strain range," *Soils and Foundations*, Vol. 20, No. 2, pp. 45-60.
- KOKUSHO, T., YOSHIDA, Y., AND ESASHI, Y. (1982). "Dynamic properties of soft clay for wide strain range," *Soils and Foundations*, Vol. 22, No. 4, pp. 1-18.
- KOLSKY, H. (1963). *Stress waves in solids*, Dover Publications, New York, 213 pp.
- KONDNER, R.L. (1963). "Hyperbolic stress-strain response: cohesive soils," *Journal of the Soil Mechanics and Foundations Division*, ASCE, Vol 89, No. SM1, pp. 115-.
- KONDNER, R.L. AND ZELASKO, J.S. (1963). "A hyperbolic stress-strain formulation of sands," *Proceedings, 2nd Pan American Conference on Soil Mechanics and Foundation Engineering*, Brazil, Vol. 1, p. 281.
- KONNO, T., SUZUKI, Y., TATOISHI, A., ISHIHARA, K., AKINO, K., AND SATSUO, I. (1993). "Gravelly soil properties by field and laboratory tests," *Proceedings, 3rd International Conference on Case Histories in Geotechnical Engineering*, St. Louis, Missouri, Vol. 1, pp. 575-594.
- KONRAD, J.-M. (1988). "Interpretation of flat plate dilatometer tests in sands in terms of the state parameter," *Geotechnique*, Vol. 38, No. 2, pp. 263-278.
- KOPPEJAN, A.W., WAMELAN, B.M. AND WEINBERG, L.J. (1948), "Coastal flowslides in the Dutch Province of Zeeland," *Proceedings, 2nd International Conference on Soil Mechanics and Foundation Engineering*, Vol. 5, pp. 89-96.
- KOUTSOFTAS, D.C. (1978). "Effect of cyclic loads on undrained strength of two marine clays," *Journal of the Geotechnical Engineering Division*, ASCE, Vol. 104, No. GT5.
- KOUTSOFTAS, D.C. AND KIEFER, M.L. (1990). "Improvement of mine spoils in southern Illinois," in *Geotechnics of Waste Fills*, Special Technical Publication 1070, ASTM, Philadelphia, pp. 153-167.
- KOVACS, W.D. AND LEO, E. (1981). "Cyclic simple shear of large-scale sand samples: Effects of diameter to height ratio," *Proceedings, International Conference on Recent Advances in Geotechnical Earthquake Engineering and Soil Dynamics*, St. Louis, Vol. 3, pp. 897-907.
- KOVACS, W.D. AND SALOMONE, L.A. (1982). "SPT hammer energy measurement," *Journal of the Geotechnical Engineering Division*, ASCE, Vol. 108, No. GT4, pp. 599-620.
- KOVACS, W.D., EVANS, J.C., AND GRIFFITH, A.H. (1977). "Toward a more standardized SPT," *Proceedings, 9th International Conference on Soil Mechanics and Foundation Engineering*, Tokyo, Vol. 2, pp. 269-276.
- KOZIN, F. (1988). "Autoregressive moving average models of earthquake records," *Journal of Probabilistic Engineering Mechanics*, Vol. 3, No. 2.
- KRAMER, S.L. (1985). "Liquefaction of sands due to non-seismic loading," *Ph.D. Dissertation*, University of California, Berkeley, California.
- KRAMER, S.L. (1988). "Triggering of liquefaction flow slides in coastal soil deposits," *Engineering Geology*, Vol. 26, No. 1, pp. 17-31.

- KRAMER, S.L. (1989). "Uncertainty in Steady State Liquefaction Evaluation Procedures," *Journal of Geotechnical Engineering*, ASCE, Vol. 115, No. 10, pp. 1402-1419.
- KRAMER, S.L. AND HOLTZ, R.D. (1991). *Soil improvement and foundation remediation with emphasis on seismic hazards*, University of Washington, Seattle, Washington, 106 pp.
- KRAMER, S.L. AND SEED, H.B. (1988). "Initiation of soil liquefaction under static loading condition," *Journal of Geotechnical Engineering*, ASCE, Vol. 114, No. 4, pp. 412-430.
- KRAMER, S.L. AND SIVANESWARAN, N. (1989a). "A non-destructive, specimen-specific method for measurement of membrane penetration in the triaxial test," *Geotechnical Testing Journal*, ASTM, Vol. 12, No. 1, pp. 50-59.
- KRAMER, S.L. AND SIVANESWARAN, N. (1989b). "Stress-path-dependent correction for membrane penetration," *Journal of Geotechnical Engineering*, ASCE, Vol. 115, No. 12, pp. 1787-1804.
- KRINITZSKY, E.L. AND CHANG, F.K. (1979). "State-of-the-art for assessing earthquake hazards in the United States: specifying peak motions for design earthquakes," *Miscellaneous Paper S-73-1, Report 7*, U.S. Army Corps of Engineers Waterways Experiment Station, Vicksburg, Mississippi.
- KRINITZSKY, E.L. AND CHANG, F.K. (1987). "Parameters for specifying intensity-related earthquake ground motions," *Miscellaneous Paper S-73-1, Report 25*, U.S. Army Corps of Engineers Waterways Experiment Station, Vicksburg, Mississippi, 43 pp.
- KRINITZSKY, E.L., GOULD, J.P., AND EDINGER, P.H. (1993). *Fundamentals of Earthquake-Resistant Construction*, John Wiley and Sons, New York, 299 pp.
- KUHLEMAYER, R.L. AND LYSMER, J. (1973). Finite element method accuracy for wave propagation problems, *Journal of the Soil Mechanics and Foundations Division*, ASCE, Vol. 99, No. SM5, pp. 421-427.
- KULKARNI, R. B., SUDIGH, K., AND IDRIS, I. M. (1979) "Probabilistic evaluation of seismic exposure," *Proceedings, 8th World Conference on Earthquake Engineering*, San Francisco, pp. 90-98.
- KULKARNI, R.B., YOUNGS, R.R., AND COPPERSMITH, K.J. (1984). "Assessment of confidence intervals for results of seismic hazard analysis," *Proceedings, 8th World Conference on Earthquake Engineering*, San Francisco, Vol. 1, pp. 263-270.
- KUTTER, B.L. AND JAMES, R.G. (1989). "Dynamic centrifuge model tests on clay embankments," *Geotechnique*, Vol. 39, No. 1, pp. 91-106.
- LADD, C.C. AND FOOT, R. (1974). "New design procedure for stability of soft clays," *Journal of the Geotechnical Engineering Division*, ASCE, Vol. 100, No. GT7, pp. 763-786.
- LADD, R.J. AND DUTKO, P. (1985). "Small-strain measurements using triaxial apparatus," in V. Koshla, ed., *Advances in the Art of Testing Soils Under Cyclic Conditions*, ASCE, New York, pp. 148-166.
- LADD, R.S. (1974). "Specimen preparation and liquefaction of sands," *Journal of the Geotechnical Engineering Division*, ASCE, Vol. 100, No. GT10, pp. 1180-1184.
- LADE, P.V. (1988). "Effects of voids and volume changes on the behaviour of frictional materials," *International Journal for Numerical and Analytical Methods in Geomechanics*, Vol. 12, pp. 351-370.
- LADE, P.V. (1992). "Static instability and liquefaction of loose fine sandy slopes," *Journal of Geotechnical Engineering*, ASCE, Vol. 118, No. 1, pp. 51-71.
- LADE, P.V. AND HERNANDEZ, S.B. (1977). "Membrane penetration effects in undrained tests," *Journal of the Geotechnical Engineering Division*, ASCE, Vol. 103, No. GT2, pp. 109-125.
- LAFOSSÉ, U. AND VON ROSENVIINGE, T. (1992). "Densification of loose sands by blasting," *Grouting, Soil Improvement, and Geosynthetics*, Geotechnical Special Publication 30, ASCE, New York, Vol. 2, pp. 954-968.

- LAI, C.D. (1977). "A two-dimensional 'immigration-branching' model with application to earthquake occurrence times and energies," *Journal of Applied Probability*, Vol. 14, pp. 464-474.
- LAI, S.P. (1982). "Statistical characterization of strong motions using power spectral density function," *Bulletin of the Seismological Society of America*, Vol. 72, No. 1, pp 259-274.
- LAMBE, T.W. AND WHITMAN, R.V. (1969). *Soil Mechanics*, Wiley, New York.
- LAW, K.T., CAO, Y.L., AND HE, G.N. (1990). "An energy approach for assessing seismic liquefaction potential," *Canadian Geotechnical Journal*, Vol. 27, No. 3, pp. 320-329.
- LAWRENCE, F.V. JR. (1963). "Propagation velocity of ultrasonic waves through sand," *MIT Research Report R63-8*, Massachusetts Institute of Technology, Cambridge, Massachusetts.
- LAY, T. AND WALLACE, T.C. (1995). *Modern Global Seismology*, Academic Press, San Diego, 521 pp.
- LEDBETTER, R.H. (1985). "Improvement of liquefiable foundation conditions beneath existing structures," *Technical Report REMR-GT-2*, U.S. Army Corps of Engineers, Waterways Experiment Station, Vicksburg, Mississippi, 51 pp.
- LEE, K.L. (1974). Seismic permanent deformations in earth dams, *Report No. UCLA-ENG-7497*, School of Engineering and Applied Science, University of California at Los Angeles.
- LEE, K.L. AND ALBAISA, A. (1974). "Earthquake induced settlements in saturated sands," *Journal of the Soil Mechanics and Foundations Division*, ASCE, Vol. 100, No. GT4.
- LEE, K.L. AND FOCHT, J.A. (1976). "Strength of clay subjected to cyclic loading," *Marine Geotechnology*, Vol. 1, No. 3.
- LEE, M.K.W AND FINN, W.D.L. (1978). "DESRA-2, Dynamic effective stress response analysis of soil deposits with energy transmitting boundary including assessment of liquefaction potential," *Soil Mechanics Series No. 38*, University of British Columbia, Vancouver.
- LEMOS, L.J.L. AND COELHO, P.A.L.F. (1991). Displacements of slopes under earthquake loading, *Proceedings, 2nd International Conference on Recent Advances in Geotechnical Earthquake Engineering and Soil Dynamics*, St. Louis, Missouri, Vol. 2, pp. 1051-1056.
- LEMOS, L.J.L., SKEMPTON, A.W., AND VAUGHAN, P.R. (1985). "Earthquake loading of shear surfaces in slopes," *Proceedings, 11th International Conference on Soil Mechanics and Foundation Engineering*, San Francisco, Vol. 4, pp. 1955-1958.
- LI, T. (1990). "Landslide management in mountain areas of China," *Occasional Paper 15*, International Centre for Integrated Mountain Development, Kathmandu, Nepal, 50 pp.
- LIAO, S.S.C. AND WHITMAN, R.V. (1986). "Overburden correction factors for SPT in sand," *Journal of Geotechnical Engineering*, ASCE, Vol. 112, No. 3, pp. 373-377.
- LIAO, S.S.C., VENEZIANO, D., AND WHITMAN, R.V. (1988). "Regression models for evaluating liquefaction probability," *Journal of Geotechnical Engineering*, ASCE, Vol. 114, No. 4, pp. 389-411.
- LIN, J.S. AND WHITMAN, R.V. (1986). "Earthquake induced displacements of sliding blocks," *Journal of Geotechnical Engineering*, ASCE, Vol. 112, No. 1, pp. 44-59.
- LINDQVIST, L. AND PETAJA, J. (1981). "Experience in the evaluation of the bearing capacity of tapered friction piles in postglacial sand and silt strata," *Proceedings, 10th International Conference on Soil Mechanics and Foundation Engineering*, Stockholm, Vol. 2, pp. 759-766.
- LIU, H. AND QIAO, T. (1984). "Liquefaction potential of saturated sand deposits underlying foundation of structure," *Proceedings, 8th World Conference on Earthquake Engineering*, San Francisco, Vol. 3, pp. 199-206.
- LIU, S.C. (1970). "Evolutionary power spectral density of strong-motion earthquakes," *Bulletin of the Seismological Society of America*, Vol. 60, No. 3, pp. 891-900.

- LODDE, P.F. (1982). "Dynamic response of San Francisco Bay mud," *M.S. Thesis*, University of Texas, Austin, Texas.
- LOMNITZ-ADLER, J. AND LOMNITZ, C. (1979). "A modified form of the Gutenberg-Richter magnitude-frequency law," *Bulletin of the Seismological Society of America*, Vol. 63, pp. 1999-2003.
- LOVE, A.E.H. (1927). *The Mathematical Theory of Elasticity*, 4th Ed., University Press, Cambridge.
- LUCIA, P.C., DUNCAN, J.M., AND SEED, H.B. (1981). "Summary of research on case histories of flow failures of mine tailings impoundments," *Information Circular 8857*, Technology Transfer Workshop on Mine Waste Disposal Techniques, U.S. Bureau of Mines, Denver, Colorado, pp. 46-53.
- LUCO, J.E. AND WONG, H.L. (1982). "Response of structures to nonvertically incident seismic waves," *Bulletin of the Seismological Society of America*, Vol. 72, No 1, pp. 265-302.
- LUCO, J.E. AND WONG, H.L. (1986). "Response of a rigid foundation to a spatially random ground motion," *Earthquake Engineering and Structural Dynamics*, Vol. 14, pp. 891-908.
- LUKAS, R.G. (1986). "Dynamic compaction for highway construction, Vol. I: Design and construction guidelines," *Report FHWA/RD-86/133*, Federal Highway Administration, Washington, D.C.
- LYSMER, J., UDAKA, T., SEED, H.B., AND HWANG, R. (1974). "LUSH: a computer program for complex response analysis of soil-structure systems," *Report EERC 74-4*, Earthquake Engineering Research Center, University of California, Berkeley.
- LYSMER, J., UDAKA, T., TSAI, C.F., AND SEED, H.B. (1975). "FLUSH: a computer program for approximate 3-D analysis of soil-structure interaction problems," *Report EERC 75-30*, Earthquake Engineering Research Center, University of California, Berkeley, 83 pp.
- LYSMER, J., TABATABAIE, M., TAJIRIAN, F., VAHDANI, S., AND OSTADAN, F. (1981). "SASSI: a system for analysis of soil-structure interaction," *Report UCB/GT81-02*, University of California, Berkeley.
- LYTLE, R.J. (1978). "Geophysical characterization using advanced data processing," *Proceedings, Specialty Workshop on Site Characterization and Exploration*, Northwestern University, Evanston, Illinois, pp. 291-300.
- MACMURDO, J. (1824). "Papers relating to the earthquake which occurred in India in 1819," *Philosophical Magazine*, Vol. 63, pp. 105-177.
- MAIR, R.J. AND WOOD, D.M. (1987). *Pressuremeter Testing: Methods and Interpretation*, Butterworth, London, 160 pp.
- MAKDISI, F.I. AND SEED, H.B. (1978). "Simplified procedure for estimating dam and embankment earthquake-induced deformations," *Journal of the Geotechnical Engineering Division*, ASCE, Vol. 104, No. GT7, pp. 849-867.
- MALLET, R. (1862). *Great Neapolitan Earthquake of 1857*, London, 2 vols.
- MARCHETTI, S. (1980). "In situ tests by flat dilatometer," *Journal of the Geotechnical Engineering Division*, ASCE, Vol. 106, No. GT3, pp. 299-321.
- MARCHETTI, S. (1982). "Detection of liquefiable sand layers by means of quasi-static penetration tests," *Proceedings, 2nd European Symposium on Penetration Testing*, Amsterdam, Vol. 2, pp. 458-482.
- MARCUSON, W.F., III (1981). "Moderator's report for session on 'Earth dams and stability of slopes under dynamic loads'," *Proceedings, International Conference on Recent Advances in Geotechnical Earthquake Engineering and Soil Dynamics*, St. Louis, Missouri, Vol. 3, p. 1175.
- MARCUSON, W.F. III, COOPER, S.S., AND BIEGANOUSKY, W.A. (1977). "Laboratory sampling study conducted on fine sands," *Proceedings of Specialty Session 2, 9th International Conference on Soil Mechanics and Foundation Engineering*, Tokyo, pp. 15-22.
- MARCUSON, W.F. AND HYNES, M.E. (1990). Stability of slopes and embankments during earthquakes, *Proceedings, ASCE/Pennsylvania Department of Transportation Geotechnical Seminar*, Hershey, Pennsylvania.

- MARCUSON, W.F., III, BALLARD, R.F., JR., AND LEDBETTER, R.H. (1979). "Liquefaction failure of tailings dams resulting from the Near Izu Oshima earthquake, 14 and 15 January, 1978," *Proceedings, 6th Pan American Conference on Soil Mechanics and Foundation Engineering*, Lima, Peru.
- MARCUSON, W.F. III, HYNES, M.E., AND FRANKLIN, A.G. (1990). Evaluation and use of residual strength in seismic safety analysis of embankments, *Earthquake Spectra*, Vol. 6, No. 3, pp. 529-572.
- MARCUSON, W.F. III, HADALA, P.F., AND LEDBETTER, R.H. (1991). "Seismic rehabilitation of earth dams," *Geotechnical Practice in Dam Rehabilitation*, Geotechnical Special Publication 35, ASCE, New York, pp. 430-466.
- MARK, R.K. AND BONILLA, M.G. (1977). "Regression analysis of earthquake magnitude and surface fault length using the 1970 data of Bonilla and Buchanan," Open File Report, U.S. Geological Survey, 10 pp.
- MARTIN, G.R. (1992). Evaluation of soil properties for seismic stability analysis of slopes, *Proceedings, Stability and Performance of Slopes and Embankments*, Geotechnical Special Publication No. 31, ASCE, Vol. 1, pp. 116-142.
- MARTIN, G.R., FINN, W.D.L., AND SEED, H.B. (1978). "Effects of system compliance on liquefaction tests," *Journal of Geotechnical Engineering*, ASCE, Vol. 104, No. GT4, pp. 463-479.
- MARTIN, G.R., FINN, W.D.L., AND SEED, H.B. (1975). "Fundamentals of liquefaction under cyclic loading," *Journal of the Geotechnical Engineering Division*, ASCE, Vol. 101, No. GT5, pp. 423-438.
- MARTIN, G.R., LAM, I.P., MCCASKIE, S.L., AND TSAI, C.-F. (1981). "A parametric study of an effective stress liquefaction model," *Proceedings, International Conference on Geotechnical Earthquake Engineering and Soil Dynamics*, St. Louis, Missouri, Vol. 2, pp. 699-705.
- MARTIN, P.P. AND SEED, H.B. (1978). "MASH - A computer program for the nonlinear analysis of vertically propagating shear waves in horizontally layered soil deposits," *Report No. UCB/EERC-78/23*, Earthquake Engineering Research Center, University of California, Berkeley, California.
- MASING, G. (1926). "Eigenspannungen und Verfertigung beim Messing," *Proceedings, 2nd International Congress on Applied Mechanics*, Zurich.
- MASSARCH, K.R. (1991). "Deep soil compaction using vibratory probes," in M.I. Esrig and R.C. Bachus, eds., *Deep Foundation Improvement: Design, Construction, and Testing*, ASTM STP 1089, ASTM, Philadelphia, pp. 297-319.
- MATSUZAWA, H., ISHIBASHI, I., AND KAWAMURA, M. (1985). Dynamic soil and water pressures of submerged soils, *Journal of Geotechnical Engineering*, ASCE, Vol. 111, No. 10, pp. 1161-1176.
- MATTHIENSEN, J., ET AL. (1982). "Recommendations concerning seismic design of zonation," *Critical Aspects of Earthquake Ground Motion and Building Damage Potential*, ATC-10-1, Applied Technology Council, Redwood City, California, pp. 213-246.
- MAYNE, P.W. AND RIX, G.J. (1993). " G_{max} - q_c relationship for clays," *Geotechnical Testing Journal*, ASTM, Vol. 16, No. 1, pp. 54-60.
- MAYNE, P.W., JONES, J.S., AND DUMAS, J.C. (1984). Ground response to dynamic compaction, *Journal of Geotechnical Engineering*, Vol. 110, No. 6, pp. 757-774.
- MCCAMY, K., MEYER, R.P., AND SMITH, T.J. (1962). "Generally applicable solutions of Zoeppritz' amplitude equations," *Bulletin of the Seismological Society of America*, Vol. 52, No. 4, pp. 923-955.
- MCCANN, M.W. AND SHAH, H. C. (1979) "Determining strong motion duration of earthquakes," *Bulletin of the Seismological Society of America*, Vol. 69, No.4, pp. 1253-1265.
- MCGUIRE, R. K. (1977) "Seismic design spectra and mapping predures using hazard analysis based directly on oscillator response," *Journal of Earthquake Engineering and Structural Dynamics*, 5, 211-234.
- MCGUIRE, R. K. (1978) "Seismic ground motion parameter relations," *Journal of the Geotechnical Engineering Division*, ASCE, Vol. 104, No. GT4, pp. 481-490.

- MCGUIRE, R.K. AND ARABASZ, W.J. (1990). "An introduction to probabilistic seismic hazard analysis," in S.H. Ward, ed. *Geotechnical and Environmental Geophysics*, Society of Exploration Geophysicists, Vol. 1, pp. 333-353.
- MCGUIRE, R.M. AND HANKS, T.C. (1980). "RMS accelerations and spectral amplitudes of strong ground motion during the San Fernando, California earthquake," *Bulletin of the Seismological Society of America*, Vol. 70, pp. 1907-1919.
- MCGUIRE, R.K., BECKER, A.M., AND DONOVAN, N.C. (1984). "Spectral estimates of seismic shear waves," *Bulletin of the Seismological Society of America*, Vol. 74, No. 4, pp. 1427-1440.
- MCKENZIE, D.P. (1970). "Plate tectonics of the Mediterranean region," *Nature, London*, pp. 226-239.
- MEDVEDEV, S.V. AND SPONHEUR, V. (1969). "Scale of seismic intensity," *Proceedings, 4th World Conference on Earthquake Engineering*, Santiago, Chile, pp. 143-153.
- MEIMON, Y. AND HICHER, P.Y. (1980). "Mechanical behavior of clays under cyclic loading," in G.N. Pande and O.C. Zienkiewicz, eds., *Proceedings, International Symposium on Soils Under Cyclic and Transient Loading*, Balkema, Vol. 1, Rotterdam, The Netherlands.
- MEJIA, L.H. AND SEED, H.B. (1981). "Three-dimensional dynamic response analysis of earth dams," *Report No. UCB/EERC-81/15*, Earthquake Engineering Research Center, University of California, Berkeley, 238 pp.
- MERZ, H. A. AND CORNELL, C. A. (1973a). "Seismic risk based on a quadratic magnitude-frequency law," *Bulletin of the Seismological Society of America*, Vol. 73, No. 6, pp. 1949-2006.
- MERZ, H. A. AND CORNELL, C. A. (1973b). "Aftershocks in engineering seismic risk analysis," *Report R73-25*, Department of Civil Engineering, Massachusetts Institute of Technology, Cambridge, Massachusetts.
- MIDDLEBROOKS, T.A. (1942) "Fort Peck Slide," *Transactions, ASCE*, Vol. 107, pp. 723-764.
- MILLER, G.F. AND PURSEY, H. (1955). "On the partition of energy between elastic waves in a semi-infinite solid," *Proceedings of the Royal Society, London, Series A*, Vol. 233, pp. 55-69.
- MINDLIN, R.D. AND DERESIEWICZ, H. (1953). "Elastic spheres in contact under varying oblique forces," *Journal of Applied Mechanics*, ASME, Vol. 20, pp. 327-344.
- MITCHELL, D.E. (1984). "Liquefaction slides in hydraulically placed sands," *Proceedings, 4th International Symposium on Landslides*, Toronto.
- MITCHELL, J.K. (1986). "Ground improvement evaluation by insitu tests," *Proceedings, In Situ '86*, Geotechnical Special Publication 6, ASCE, New York, pp. 221-236.
- MITCHELL, J.K. AND SOLYMAR, Z.V. (1984). "Time-dependent strength gain in freshly deposited or densified sand," *Journal of Geotechnical Engineering*, ASCE, Vol. 110, No. 11, pp. 1559-1576.
- MITCHELL, J.K. AND TSENG, D.-J. (1990). "Assessment of liquefaction potential by cone penetration resistance," in J.M. Duncan ed., *Proceedings, H. Bolton Seed Memorial Symposium*, Berkeley, California, Vol. 2, pp. 335-350.
- MITCHELL, J.K. AND VILLET, W.C.B. (1987). Reinforcement of earth slopes and embankments, *National Cooperative Highway Research Program Report 290*, Transportation Research Board, Washington, D.C., 323 pp.
- MITCHELL, J.K. AND WENTZ, F.L. (1991). "Performance of improved ground during the Loma Prieta earthquake," *Report UCB/EERC-91/12*, Earthquake Engineering Research Center, University of California, Berkeley.
- MIZUNO, E. AND CHEN, W.F. (1982). "Plasticity models for seismic analysis of slopes," *Report CE-STR-82-2*, School of Civil Engineering, Purdue University, West Lafayette, Indiana.
- MOGAMI, T., AND KUBU, K. (1953). The behavior of soil during vibration, *Proceedings, 3rd International Conference on Soil Mechanics and Foundation Engineering*, Zurich, Vol. 1, pp. 152-155.

- MOHAMAD, R. AND DOBRY, R. (1986). "Undrained monotonic and cyclic triaxial strength of sand," *Journal of Geotechnical Engineering*, ASCE, Vol. 112, No. 10, pp. 941-958.
- MOHRAZ, B. AND ELGHADAMSI, F. E. (1989) "Earthquake ground motion and response spectra," in *The Seismic Design Handbook*, F. Naeim, ed., Van Nostrand Reinhold, New York, 32-80.
- MOK, Y.-J., SANCHEZ-SALINERO, I., STOKOW, K.H., AND ROESSET, J.M. (1988). "In situ damping measurements by crosshole seismic method," *Proceedings, Earthquake Engineering and Soil Dynamics II: Recent Advances in Ground Motion Evaluation*, Geotechnical Special Publication 20, ASCE, New York, pp. 305-320.
- MONONOBE, H.A. ET AL. (1936). "Seismic stability of the earth dam," *Proceedings, 2nd Congress on Large Dams*, Washington, D.C., Vol. 4.
- MONONOBE, N. AND MATSUO, H. (1929). "On the determination of earth pressures during earthquakes," *Proceedings, World Engineering Congress*, 9 p.
- MORGENSTERN, N.R. AND PRICE, V.E. (1965). "The analysis of the stability of general slip surfaces," *Geotechnique*, Vol. 15, No. 1, pp. 79-93.
- MOSELY, M.P., ED. (1993). *Ground Improvement*, Blackie, London, 218 pp.
- MROZ, Z. (1967). "On the description of anisotropic work hardening," *Journal of Mechanics and Physics of Solids*, Vol. 15, pp. 163-175.
- MULILIS, J.P., CHAN, C.K. AND SEED, H.B. (1975). "The effects of method of sample preparation on the cyclic stress-strain behavior of sands," *Report EERC 75-18*, Earthquake Engineering Research Center, University of California, Berkeley.
- MURPHY, J.R. AND O'BRIEN, L.J. (1977). The correlation of peak ground acceleration amplitude with seismic intensity and other physical parameters, *Bulletin of the Seismological Society of America*, Vol. 67, pp. 877-915.
- NACCI, V.A. AND TAYLOR, K.J. (1967). "Influence of clay structure on elastic wave velocities," *Proceedings, International Symposium on Wave Propagation and Dynamic Properties of Earth Materials*, Albuquerque, New Mexico, pp. 491-502.
- NADIM, F. (1980). "Tilting and sliding of gravity retaining walls," *S.M. Thesis*, Department of Civil Engineering, Massachusetts Institute of Technology, Cambridge, Massachusetts.
- NADIM, F. (1982). "A numerical model for evaluation of seismic behavior of gravity retaining walls," Sc.D. thesis, *Research Report R82-33*, Department of Civil Engineering, Massachusetts Institute of Technology, Cambridge, Massachusetts.
- NADIM, F. AND WHITMAN, R.V. (1984). "Coupled sliding and tilting of gravity retaining walls during earthquakes," *Proceedings, 8th World Conference on Earthquake Engineering*, San Francisco, Vol. 3, pp. 477-484.
- NAEIM, F. AND LEW, M. (1995). On the use of design-spectrum compatible time histories, *Earthquake Spectra*, Vol. 11, No. 1, pp. 111-127.
- NATIONAL RESEARCH COUNCIL (1976). Landslides, analysis and control, *Special Report 176*, R.L. Schuster and R.J. Krizek, eds., Transportation Research Board, Washington, D.C., 234 pp.
- NATIONAL RESEARCH COUNCIL (1985). *Liquefaction of Soils during Earthquakes*, National Academy Press, Washington, D.C., 240 pp.
- NATIONAL RESEARCH COUNCIL (1988). *Probabilistic Seismic Hazard Analysis*, National Academy Press, Washington, D.C., 97 pp.
- NAVFAC (1982). "Foundations and earth structures," *Design Manual 7.2*, Naval Facilities Engineering Command, Department of the Navy, Alexandria, Virginia, 244 pp.
- NAZARIAN, S. (1984). "In situ determination of elastic moduli of soil deposits and pavement systems by spectral-analysis-of-surface-waves method," Ph.D. dissertation, University of Texas, Austin, 458 pp.

- NAZARIAN, S. AND STOKOE, K.H. (1983). "Use of spectral analysis of surface waves for determination of moduli and thicknesses of pavement systems, *Transportation Research Record 954*, Transportation Research Board, Washington, D.C.
- NEELY, W.J. AND LEROY, D.A. (1991). "Densification of sand using a variable frequency vibratory probe," in M.I. Esrig and R.C. Bachus, eds., *Deep Foundation Improvement: Design, Construction, and Testing*, ASTM STP 1089, ASTM, Philadelphia, pp. 320-332.
- NEHRP (1993) *Building for the future*, Fiscal Years 1991-1992 Report to Congress, National Earthquake Hazard Reduction Program, Washington, D.C., 123 pp.
- NEMAT-NASSER, S. AND SHOKOOH, A. (1979). "A unified approach to densification and liquefaction of cohesionless sand in cyclic shearing," *Canadian Geotechnical Journal*, Vol. 16, No. 4, pp. 649-678.
- NEWMARK, N. (1965). "Effects of earthquakes on dams and embankments," *Geotechnique*, Vol. 15, No. 2, pp. 139-160.
- NEWMARK, N.M. (1973) "A Study of Vertical and Horizontal Earthquake spectra," N.M. Newmark Consulting Engineering Services, Directorate of Licensing, U.S. Atomic Energy Commission, Washington, D.C.
- NEWMARK, N.M. AND HALL, W.J. (1973). "Procedures and criteria for earthquake-resistant design," *Building Practices for Disaster Mitigation*, Washington, D.C., Building Science Series 46, U.S. Department of Commerce, pp. 209-236.
- NEWMARK, N.M. AND HALL, W.J. (1978). "Development of criteria for earthquake resistant design," *Report NUREG/CR-0098*, Nuclear Regulatory Commission, Washington, D.C., 49 pp.
- NEWMARK, N.M. AND HALL, W.J. (1982). *Earthquake Spectra and Design*, EERI Monograph, Earthquake Engineering Research Institute, Berkeley, California, 103 pp.
- NEWMARK, N.M. AND ROSENBLUETH, E. (1971). *Fundamentals of Earthquake Engineering*, Prentice Hall, Englewood Cliffs, New Jersey, 640 pp.
- NG, T.-T. AND DOBRY, R. (1994). "Numerical simulations of monotonic and cyclic loading of granular soil," *Journal of Geotechnical Engineering*, ASCE, Vol. 20, No. 2, pp. 388-403.
- NIGBOR, R.L. AND IMAI, T. (1994). The suspension p-s velocity logging method, *Geophysical Characterization of Sites*, R.D. Woods, ed., A.A. Balkema, Rotterdam, pp. 57-61.
- NISHIOKA, T. AND SHAH, H.C. (1980). "Application of the Markov chain on probability of earthquake occurrences," *Proceedings of the Japanese Society of Civil Engineering*, Vol. 1, pp. 137-145.
- NOSON, L.L., QAMAR, A., AND THORSEN, G.W. (1988). Washington state earthquake hazards, *Information Circular 85*, Washington Division of Geology and Earth Resources, Olympia, Washington.
- NOVAK, M., SHETA, M., EL-HIFNAWY, L., EL-MARSAFAWI, H., AND RAMADAN, O. (1993). "DYNA4: a computer program for calculation of foundation response to dynamic loads" *Report GEOP 93-01*, Geotechnical Research Centre, The University of Western Ontario, London, Ontario.
- NUTTLI, O.W. (1973). Seismic wave attenuation and magnitude relations for eastern North America, *Journal of Geophysical Research*, Vol. 78, pp. 876-885.
- NUTTLI, O.W. (1979). "The relation of sustained maximum ground acceleration and velocity to earthquake intensity and magnitude," *Miscellaneous Paper S-73-1*, Report 16, U.S. Army Corps of Engineers Waterways Experiment Station, Vicksburg, Mississippi, 74 pp.
- NUTTLI, O.W. AND HERRMANN, R.B. (1984). "Ground motion of Mississippi Valley earthquakes," *Journal of Technical Topics in Civil Engineering*, ASCE, Vol. 110, pp. 54-69.
- O'BRIEN, J.S. AND JULIEN, P.Y. (1988). "Laboratory analysis of mudflow properties," *Journal of Hydraulic Engineering*, ASCE, Vol. 114, pp. 877-887.
- O'REILLY, M.P. (1991). "Cyclic load testing of soils," in M.P. O'Reilly and S.F. Brown, eds., *Cyclic Loading of Soils*, Blackie, London, pp. 70-121.

- O'ROURKE, T.D., GOWDY, T.E., STEWART, H.E., AND PEASE, J.W. (1991). "Lifeline and geotechnical aspects of the 1989 Loma Prieta earthquake," *Proceedings, 2nd International Conference on Recent Advances in Geotechnical Earthquake Engineering and Soil Dynamics*, St. Louis, Missouri, Vol. 2, pp. 1601-1612.
- OHSAKI, Y. (1969). "The effects of local soil conditions upon earthquake damage," *Proceedings of Specialty Session 2, 7th International Conference on Soil Mechanics and Foundation Engineering*, Mexico City.
- OHSAKI, Y. (1970). "Effects of sand compaction on liquefaction during Tokachioki earthquake," *Soils and Foundations*, Vol. 10, No. 2, pp. 112-128.
- OHSAKI, Y. (1979). "On the significance of phase content in earthquake ground motion," *Earthquake Engineering and Structural Dynamics*, Vol. 7, pp. 427-439.
- OHTA, Y. AND GOTO, N. (1976). Estimation of s-wave velocity in terms of characteristic indices of soil, *Butsuri-Tanku*, Vol. 29, No. 4, pp. 34-41.
- OKABE, S. (1926). "General theory of earth pressures," *Journal of the Japan Society of Civil Engineering*, Vol. 12, No. 1.
- OKAMOTO, S. (1973). *Introduction to Earthquake Engineering*, John Wiley, New York, New York.
- ORPHAL, D. L. AND LAHOUD, J. A. (1974) "Prediction of peak ground motion from earthquakes," *Bulletin of the Seismological Society of America*, 64, 1563-1574.
- PAGE, R.A., BOORE, D.M., HOUNER, W.B., AND CAULTER, H.W. (1972). "Ground motion values for use in the seismic design of the Trans-Alaska pipeline system," *USGS Circular 672*, U.S. Geological Survey, Reston, Virginia.
- PAPAGEORGIOU, A.S. AND AKI, K. (1983). "A specific barrier for the quantitative description of inhomogeneous faulting and the prediction of strong ground motion. II. Applications of the model," *Bulletin of the Seismological Society of America*, Vol. 73, pp. 953-978.
- PARK, T. AND SILVER, M.L. (1975). "Dynamic soil properties required to predict the dynamic behavior of elevated transportation structures," *Report DOT-TST-75-44*, U.S. Department of Transportation, Washington, D. C.
- PATWARDHAN, A.S., KULKARNI, R.B., AND TOCHER, D. (1980). "A semi-Markov model for characterizing recurrence of great earthquakes," *Bulletin of the Seismological Society of America*, Vol. 70, No. 1, pp. 323-347.
- PAZ, M. (1950). *Structural Dynamics: Theory and Computation*, van Nostrand Reinhold, New York.
- PEREZ, V. (1974). "Time dependent spectral analysis of thirty-one strong motion earthquake records," *Open File Report 74-48*, U.S. Geological Survey, Reston, Virginia.
- PERLOFF, W.H. AND BARON, W. (1976). *Soil Mechanics*, Ronald Press, New York.
- PHILLIPS, C.J. AND DAVIES, T.R. (1991). "Determining rheological parameters of debris flow material," *Geomorphology*, Vol. 4, pp. 101-110.
- PILLAI, V.S. (1991). "Liquefaction analysis of sands: Some interpretation of Seed's $K\alpha$ (sloping ground) and $K\sigma$ (depth) correction factors using steady state concept," *Proceedings, 2nd International Conference on Recent Advances in Geotechnical Earthquake Engineering and Soil Dynamics*, St. Louis, Missouri, Vol. 1, pp. 579-587.
- POULOS, S.J. (1981). "The steady state of deformation," *Journal of the Geotechnical Engineering Division*, ASCE, Vol. 107, No. GT5, pp. 553-562.
- POULOS, S.J., CASTRO G., AND FRANCE, J.W. (1985). "Liquefaction evaluation procedure," *Journal of Geotechnical Engineering*, ASCE, Vol. 111, No. 6, pp. 772-792.

- POWER, M.S., COPPERSMITH, K.J., YOUNGS, R.R., SCHWARTZ, D.P., AND SWAN, R.H. (1981). *Seismic Exposure Analysis for the WNP-2 and WNP-1/4 Site: Appendix 2.5K to Amendment No. 18 Final Safety Analysis Report for WNP-2*, Woodward-Clyde Consultants, San Francisco, 63 pp.
- POWERS, J.P. (1992). *Construction Dewatering: New Methods and Applications*, Wiley, Inc., New York, 492 pp.
- PRANGE, B. (1981). "Stochastic excitation of rock masses," *Proceedings, 10th International Conference on Soil Mechanics and Foundation Engineering*, Stockholm, Vol. 4, pp. 89-880.
- PREVOST, J.H. (1977). "Mathematical modelling of monotonic and cyclic undrained clay behavior," *International Journal of Numerical and Analytical Methods in Geomechanics*, Vol. 1, No. 2, pp. 195-216.
- PREVOST, J.H. (1981). *DYNAFLOW: A Nonlinear Transient Finite Element Analysis Program*, Department of Civil Engineering, Princeton University, Princeton, New Jersey.
- PREVOST, J.H. (1989). *DYNA1D: a computer program for nonlinear seismic site response analysis - Technical documentation, Report NCEER-89-0025*, National Center for Earthquake Engineering Research, Buffalo, New York.
- PREVOST, J.H., ABDEL-GHAFFAR, A.M., AND LACY, S.J. (1985). "Nonlinear dynamic analysis of earth dams: a comparative study," *Journal of Geotechnical Engineering*, ASCE, Vol. 111, No. 2, pp. 882-897.
- PRIEBE, H.J. (1990). The prevention of liquefaction by vibro replacement, *Proceedings, International Conference on Earthquake Resistant Construction*, Berlin.
- PRIESTLEY, M.B. (1965). "Evolutionary spectra and non-stationary processes," *Journal of the Royal Statistical Society, Series B*, Vol. 27, pp. 204-237.
- PRIESTLEY, M.B. (1967). "Power spectral analysis of non-stationary random processes," *Journal of Sound and Vibration*, Vol. 6, No. 1, pp. 86-97.
- PYKE, R.M. (1973). "Settlement and liquefaction of sands under multi-directional loading," Ph.D. dissertation, University of California, Berkeley.
- PYKE, R.M. (1979). "Nonlinear soil models for irregular cyclic loadings," *Journal of the Geotechnical Engineering Division*, ASCE, Vol. 105, No. GT6, pp. 715-726.
- PYKE, R.M. (1985). *TESSI: A Computer Program for Nonlinear Ground Response Analysis. User's Manual*, TAGA Engineering Software Services, Lafayette, California.
- PYKE, R., SEED, H.B., AND CHAN, C.K. (1975). "Settlement of sands under multi-directional loading," *Journal of the Geotechnical Engineering Division*, ASCE, Vol. 101, No. GT4, pp. 379-398.
- RAJU, V.S. AND VENKATARAMANA, K. (1980). "Undrained triaxial tests to assess liquefaction potential of sands: Effect of membrane penetration," *Proceedings, International Symposium on Soils under Cyclic and Transient Loading*, Swansea, United Kingdom, pp. 483-494.
- RAMBERG, W. AND OSGOOD, W.R. (1943). "Description of stress-strain curves by three parameters," *Technical Note 902*, National Advisory Committee for Aeronautics, Washington, D.C.
- RAMIREZ, R.W. (1985). *The FFT: Fundamentals and Concepts*, Prentice Hall, Englewood Cliffs, New Jersey, 178 pp.
- RANKINE, W. (1857). "On the stability of loose earth," *Philosophical Transactions of the Royal Society of London*, Vol. 147.
- RAYLEIGH, LORD (1885). "On waves propagated along the plane surface of an elastic solid," *Proceedings of the London Mathematical Society*, Vol. 17, pp. 4-11.
- REAL, C.R. AND TENG, T. (1973). "Local Richter magnitude and total signal duration in southern California," *Bulletin of the Seismological Society of America*, Vol. 63, No. 5.

- REDPATH, B.B. (1973). "Seismic refraction exploration for engineering site investigations," *Technical Report E-73-4*, U.S. Army Corps of Engineers Waterways Experiment Station, Explosive Excavation Research Laboratory, Livermore, California, 55 pp.
- REDPATH, B.B. AND LEE, R.C. (1986). "In situ measurements of shear wave attenuation at a strong-motion recording site," *Report*, U.S. Geological Survey Contract 14-08-001-21823, URS/John A. Blume and Associates, San Francisco.
- REDPATH, B.B., EDWARDS, R.B., HALE, R.J., AND KINTZER, F.Z. (1982). "Development of field techniques to measure damping values for near-surface rocks and soils," *Report* URS/John A. Blume and Associates, San Francisco, 120 pp.
- REID, H.F. (1910). *The California Earthquake of April 18, 1906*, Publication 87, Vol. 21, Carnegie Institute of Washington, Washington, D.C.
- REID, H.F. (1911). "The elastic rebound theory of earthquakes," *Bulletin of the Department of Geology*, University of Berkeley, Vol. 6, pp. 413-444.
- REITER, L. (1990). *Earthquake Hazard Analysis - Issues and Insights*, Columbia University Press, New York, 254 pp.
- REYNA, F. AND CHAMEAU, J.-L. (1991). "Dilatometer based liquefaction potential of sites in the Imperial Valley," *Proceedings, 2nd International Conference on Recent Advances in Geotechnical Earthquake Engineering and Soil Dynamics*, St. Louis, Missouri, Vol. 1, pp. 385-392.
- RIAL, J.A., SALTZMAN, N.G., AND LING, H. (1992). "Earthquake-induced resonance in sedimentary basins," *American Scientist*, Vol. 80, No. 6, pp. 566-578.
- RICHARDS, R. AND ELMS, D. (1979). Seismic behavior of gravity retaining walls, *Journal of the Geotechnical Engineering Division*, ASCE, Vol. 105, No. GT4, pp. 449-464.
- RICHART, F.E., HALL, J.R., AND WOODS, R.D. (1970). *Vibrations of Soils and Foundations*, Prentice Hall, Englewood Cliffs, New Jersey, 401 pp.
- RICHTER, C.F. (1935). "An instrumental earthquake scale," *Bulletin of the Seismological Society of America*, Vol. 25, pp. 1-32.
- RICHTER, C.F. (1958). *Elementary Seismology*, W.H. Freeman, San Francisco.
- RIEMER, M.F. AND SEED, R.B. (1992). "Observed effects of testing conditions on the residual strength of loose, saturated sands at large strains," *Proceedings, 4th Japan-U.S. Workshop on Earthquake Resistant Design of Lifeline Facilities and Countermeasures for Soil Liquefaction*, in M. Hamada and T.D. O'Rourke, eds., Technical Report NCEER-92-0019, National Center for Earthquake Engineering Research, Buffalo, New York, Vol. 1, pp. 223-238.
- RIX, G.J. AND STOKOE, K.H. (1991). "Correlation of initial tangent modulus and cone penetration resistance," *Calibration Chamber Testing*, International Symposium on Calibration Chamber Testing, A.B. Huang, ed., Elsevier Publishing, New York, pp. 351-362.
- ROBERTSON, P.K. (1982). "Insitu testing of soil with emphasis on its application to liquefaction assessment," Ph.D. Thesis, University of British Columbia, Vancouver, British Columbia.
- ROBERTSON, P.K. AND CAMPANELLA, R.G. (1985). "Liquefaction potential of sands using the CPT," *Journal of Geotechnical Engineering*, ASCE, Vol. 111, No. 3, pp. 384-403.
- ROBERTSON, P.K. AND CAMPANELLA, R.G. (1986). "Estimating liquefaction potential of sands using the flat dilatometer," *Geotechnical Testing Journal*, ASTM, Vol. 9, No. 1, pp. 38-40.
- ROBERTSON, P.K., CAMPANELLA, R.G., GILLESPIE, D., AND RICE, A. (1985). "Seismic CPT to measure in-situ shear wave velocity," in *Measurement and Use of Shear Wave Velocity for Evaluating Dynamic Soil Properties*, ASCE, New York, pp. 18-34.
- ROBINSKY, E.I. AND MORRISON, D.E. (1964). "Sand displacement and compaction around model friction piles," *Canadian Geotechnical Journal*, Vol. 1, No. 2, pp. 81-

- ROESLER, S.K. (1977). "Correlation methods in soil dynamics," *Proceedings, DMSR 77*, Karlsruhe, Germany, Vol. 1, pp. 309-334.
- ROESLER, S.K. (1979). "Anisotropic stress modulus due to stress anisotropy," *Journal of the Geotechnical Engineering Division*, ASCE, Vol. 105, No. GT7, pp. 871-880.
- ROESSET, J.M. (1977). "Soil amplification of earthquakes," Chapter 19 in C.S. Desai and J.T. Christian, eds., *Numerical Methods in Geotechnical Engineering*, McGraw-Hill, New York, pp. 639-682.
- ROMO, M.P. AND SEED, H.B. (1986). "Analytical modelling of dynamic soil response in the Mexico earthquake of September 19, 1985," *Proceedings, ASCE International Conference on the Mexico Earthquakes - 1985*, Mexico City, pp. 148-162.
- ROSCOE, K.H. AND BURLAND, J.B. (1968). "On the generalized stress-strain behavior of 'wet' clay," in J. Heyman and F.A. Leckie, eds., *Engineering Plasticity*, University Press, Cambridge, pp. 535-609.
- ROSCOE, K.H. AND POOROSHASB, H.B. (1963). "A fundamental principle of similarity in model tests for earth pressure problems," *Proceedings, 2nd Asian Regional Conference on Soil Mechanics*, Tokyo, Vol. 1, pp. 134-140.
- ROSCOE, K.H. AND SCHOFIELD, A.N. (1963). "Mechanical behavior of an idealised 'wet' clay," *Proceedings, 2nd European Conference on Soil Mechanics*, Wiesbaden, Germany, Vol. 1, pp. 47-54.
- ROWE, P.W. (1952). "Anchored sheet pile walls," *Proceedings of the Institution of Civil Engineers*, Vol. 1, No. 1, pp. 27-70.
- RUFF, L. AND KANAMORI, H. (1980). "Seismicity and subduction processes," *Physics of the Earth and Planetary Interiors*, Vol. 23, pp. 240-252.
- RYAN, C.R. AND JASPERSE, B.H. (1989). "Deep soil mixing at the Jackson Lake Dam," in *Foundation Engineering: Current Principles and Practices*, Geotechnical Special Publication 22, ASCE, New York, Vol. 1, pp. 354-367.
- SALLEY, J.R., FOREMAN, B., BAKER, W.H., AND HENRY, J.F. (1987). "Compaction grouting test program Pinopolis West Dam," in *Soil Improvement: A Ten Year Update*, Geotechnical Special Publication 12, ASCE, New York, pp. 245-269.
- SANCHEZ-SESMA, F. (1990). "Elementary solutions for response of a wedge-shaped medium to incident SH- and SV-waves," *Bulletin of the Seismological Society of America*, Vol. 80, pp. 737-742.
- SANCHEZ-SESMA, F. AND CAMPILLO, M. (1993). "Topographic effects for incident P, SV, and Rayleigh waves," *Tectonophysics*, Vol. 218, No. 1-3, pp. 113-125.
- SANGREY, D.A., HENKEL, D.J., AND ESRIG, M.I. (1969). "The effective stress response of a saturated clay soil to repeated loading," *Canadian Geotechnical Journal*, Vol. 6, No.3.
- SARAGONI, G.R. AND HART, G.C. (1974). Simulation of artificial earthquakes, *Earthquake Engineering and Structural Dynamics*, Vol. 2, No. 2, pp. 249-267.
- SARMA, S.K. (1975). "Seismic stability of earth dams and embankments," *Geotechnique*, Vol. 25, pp. 743-761.
- SAVARENSKY, Y.F. AND KIRNOS, D.P. (1955). *Elements of Seismology and Seismometry*, State Press of Technical-Theoretical Literature, Moscow, 543 pp.
- SAVY, H.B., SHAH, H.C., AND BOORE, D.M. (1980). "Nonstationary risk model with geophysical input," *Journal of the Structural Division*, ASCE, Vol. 106, No. ST1, pp. 145-164.
- SAYAO, A.S.F. AND VAID, Y.P. (1989). "Deformations due to principal stress rotation," *Proceedings, 12th International Conference on Soil Mechanics and Foundation Engineering*, Rio de Janeiro, Brazil, Vol. 1, pp. 107-110.
- SCHMERTMANN, J.H., SMITH, T.V., AND HO, R. (1978). "Example of an energy calibration report on a standard penetration test (ASTM Standard D1586-67) drill rig," *Geotechnical Testing Journal*, ASTM, Vol. 1, No. 1, pp. 57-61.

- SCHNABEL, P.B., LYSMER, J., AND SEED, H.B. (1972). "SHAKE: a computer program for earthquake response analysis of horizontally layered sites," *Report EERC 72-12*, Earthquake Engineering Research Center, University of California, Berkeley.
- SCHOFIELD, A.N. (1980). "Cambridge geotechnical centrifuge operations," *Geotechnique*, Vol. 30, No. 3, pp. 227-268.
- SCHOFIELD, A.N. AND WROTH, C.P. (1968). *Critical state soil mechanics*, McGraw-Hill, London.
- SCHWARTZ, D.P. (1988). "Geology and seismic hazards: Moving into the 1990s," *Proceedings, Earthquake Engineering and Soil Dynamics II: Recent Advances in Ground Motion Evaluation*, Geotechnical Special Publication 20, ASCE, New York, pp. 1-42.
- SCHWARTZ, D.P. AND COPPERSMITH, K.J. (1984). "Fault behavior and characteristic earthquakes: examples from the Wasatch and San Andreas fault zones," *Journal of Geophysical Research*, Vol. 89 No. B7, pp. 5681-5698.
- SCHWARTZ, D.P. AND COPPERSMITH, K.J. (1986). "Seismic hazards: New trends in analysis using geologic data," in R.E. Wallace, ed., *Active Tectonics*, Academic Press, Orlando, Florida, pp. 215-230.
- SCHWARZ, S.D. AND MUSSER, J.M., JR. (1972). "Various techniques for making in situ shear wave velocity measurements - a description and evaluation," *Proceedings, International Conference on Microzonation*, Seattle, Washington, Vol. 2, pp. 594-608.
- SCOTT, R.F. (1972). "The calculation of horizontal accelerations from seismoscope records," presented at Seismological Society of America Conference, Hawaii.
- SCOTT, R.F. (1986). "Solidification and consolidation of a liquefied sand column," *Soils and Foundations*, Vol. 26, No. 4, pp. 23-31.
- SEAOC (1990). *Recommended Lateral Force Requirements and Tentative Commentary*, Structural Engineers Association of California, San Francisco, 64 pp.
- SEED, H.B. (1976). "Some aspects of sand liquefaction under cyclic loading," *Proceedings, Conference on Behavior of Offshore Structures*, Norwegian Institute of Technology, Oslo.
- SEED, H.B. (1979). Considerations in the earthquake-resistant design of earth and rockfill dams, *Geotechnique*, Vol. 29, No. 3, pp. 215-263.
- SEED, H.B. (1979). Soil liquefaction and cyclic mobility evaluation for level ground during earthquakes, *Journal of the Geotechnical Engineering Division*, ASCE, Vol. 105, No. GT2, pp. 201-255.
- SEED, H.B. (1980). Closure to "Soil liquefaction and cyclic mobility evaluation for level ground during earthquakes," *Journal of the Geotechnical Engineering Division*, ASCE Vol. 106, No. GT6, p. 724.
- SEED, H.B. (1983). "Earthquake-resistant design of earth dams," in T.R. Howard, ed., *Proceedings, Symposium on Seismic Design of Earth Dams*, ASCE, New York, pp. 41-64.
- SEED, H.B. (1986). "Design problems in soil liquefaction," *Journal of Geotechnical Engineering*, ASCE, Vol. 113, No. 8, pp. 827-845.
- SEED, H.B. AND BOOKER, J.R. (1976). "Stabilization of potentially liquefiable sand deposits using gravel drain systems," *Report EERC-76-10*, Earthquake Engineering Research Center, University of California, Berkeley.
- SEED, H.B. AND BOOKER, J.R. (1977). "Stabilization of potentially liquefiable sand deposits using gravel drains," *Journal of the Geotechnical Engineering Division*, ASCE, Vol. 103, No. GT7, pp. 757-768.
- SEED, H.B. AND CHAN, C.K. (1966). "Clay strength under earthquake loading conditions," *Journal of the Soil Mechanics and Foundations Division*, ASCE, Vol. 92, No. SM2, pp. 53-78.
- SEED, H.B. AND DE ALBA, P. (1986). "Use of SPT and CPT tests for evaluating the liquefaction resistance of soils," *Proceedings, In situ '86*, ASCE.
- SEED, H.B. AND IDRIS, I.M. (1969). "Rock motion accelerograms for high-magnitude earthquakes," *EERC Report 69-7*, Earthquake Engineering Research Center, University of California, Berkeley.

- SEED, H.B. AND IDRIS, I.M. (1970). "Soil moduli and damping factors for dynamic response analyses," *Report EERC 70-10*, Earthquake Engineering Research Center, University of California, Berkeley.
- SEED, H.B. AND IDRIS, I.M. (1971). "Simplified procedure for evaluating soil liquefaction potential," *Journal of the Soil Mechanics and Foundations Division*, ASCE, Vol. 107, No. SM9, pp. 1249-1274.
- SEED, H.B. AND IDRIS, I.M. (1982). *Ground Motions and Soil Liquefaction During Earthquakes*, Earthquake Engineering Research Institute, Berkeley, California, 134 pp.
- SEED, H.B. AND LEE, K.L. (1965). "Studies of liquefaction of sands under cyclic loading conditions," *Report TE-65-65*, Department of Civil Engineering, University of California, Berkeley.
- SEED, H.B. AND LEE, K.L. (1966). "Liquefaction of saturated sands during cyclic loading," *Journal of the Soil Mechanics and Foundations Division*, ASCE, Vol. 92, No. SM6, pp. 105-134.
- SEED, H.B. AND MARTIN, G.R. (1966). "The seismic coefficient in earth dam design," *Journal of the Soil Mechanics and Foundations Division*, ASCE, Vol. 92, No. SM3, pp. 25-58.
- SEED, H.B. AND PEACOCK, W.H. (1971). "Test procedures for measuring soil liquefaction characteristics," *Journal of the Soil Mechanics and Foundations Division*, ASCE, Vol. 97, No. SM8, pp. 1099-1119.
- SEED, H.B. AND SILVER, M.L. (1972). "Settlement of dry sands during earthquakes," *Journal of the Soil Mechanics and Foundations Division*, Vol. 98, No. SM4, pp. 381-397.
- SEED, H.B. AND WHITMAN, R.V. (1970). "Design of earth retaining structures for dynamic loads," *Proceedings, ASCE Specialty Conference on Lateral Stresses in the Ground and Design of Earth Retaining Structures*, pp. 103-147.
- SEED, H.B., IDRIS, I.M., AND KIEFER, F.W. (1969). "Characteristics of rock motions during earthquakes," *Journal of the Soil Mechanics and Foundations Division*, ASCE, Vol. 95, No. SM5, pp. 1199-1218.
- SEED, H.B., LEE, K.L., AND IDRIS, I.M. (1969). "Analysis of Sheffield Dam failure," *Journal of the Soil Mechanics and Foundations Division*, ASCE, Vol. 95, No. SM6, pp. 1453-1490.
- SEED, H.B., LEE, K.L., IDRIS, I.M., AND MAKDISI, R. (1973). "Analysis of the slides in the San Fernando dams during the earthquake of Feb. 9, 1971," *Report No. EERC 73-2*, Earthquake Engineering Research Center, University of California, Berkeley, 150 pp.
- SEED, H.B., MORI, K., AND CHAN, C.K. (1975). "Influence of seismic history on the liquefaction characteristics of sands," *Report EERC 75-25*, Earthquake Engineering Research Center, University of California, Berkeley, 21 pp.
- SEED, H.B., LEE, K.L., IDRIS, I.M., AND MAKDISI, F.I. (1975). "The slides in the San Fernando Dams during the earthquake of February 9, 1971," *Journal of the Geotechnical Engineering Division*, ASCE, Vol. 101, No. GT7, pp. 651-688.
- SEED, H. B., IDRIS, I. M., MAKDISI, F., AND BANERJEE, N. (1975) "Representation of irregular stress time histories by equivalent uniform stress series in liquefaction analyses," *EERC 75-29*, Earthquake Engineering Research Center, University of California, Berkeley.
- SEED, H.B., MURARKA, R., LYSMER, J., AND IDRIS, I.M. (1976). "Relationships of maximum acceleration, maximum velocity, distance from source and local site conditions for moderately strong earthquakes," *Bulletin of the Seismological Society of America*, Vol. 66, No. 4, pp. 1323-1342.
- SEED, H.B., UGAS, C., AND LYSMER, J. (1976). "Site-dependent spectra for earthquake-resistant design," *Bulletin of the Seismological Society of America*, Vol. 66, pp. 221-243.
- SEED, H.B., IDRIS, I.M., AND ARANGO, I. (1983). "Evaluation of liquefaction potential using field performance data," *Journal of Geotechnical Engineering*, ASCE, Vo. 109, No. 3, pp. 458-482.

- SEED, H.B., TOKIMATSU, K., AND HARDER, L. (1984). "The influence of SPT procedures in evaluating soil liquefaction resistance," *Report UCB/EERC-84-15*, Earthquake Engineering Research Center, University of California, Berkeley.
- SEED, H.B., WONG, R.T., IDRIS, I.M., AND TOKIMATSU, K. (1984). Moduli and damping factors for dynamic analyses of cohesionless soils," *Journal of Geotechnical Engineering*, ASCE, Vol. 112, No. 11, pp. 1016-1032.
- SEED, H.B., TOKIMATSU, K., HARDER, L.F., AND CHUNG, R.M. (1985). "Influence of SPT procedures in soil liquefaction resistance evaluations," *Journal of Geotechnical Engineering*, Vol. 111, No. 12, pp.1425-1445.
- SEED, H.B., WONG, R.T., IDRIS, I.M., AND TOKIMATSU, K. (1986). Moduli and damping factors for dynamic analyses of cohesionless soils, *Journal of Geotechnical Engineering*, ASCE, Vol. 112, No. GT11, pp. 1016- 1032.
- SEED, R.B. AND ANWAR, H. (1986). "Development of a laboratory technique for correcting results of undrained triaxial shear tests on soils containing coarse particles for effects of membrane penetration," *Research Report SR/GT/86-02*, Department of Civil Engineering, Stanford University, Stanford, California.
- SEED, R.B. AND HARDER, L.F. (1990). "SPT-based analysis of cyclic pore pressure generation and undrained residual strength," in J.M. Duncan ed., *Proceedings, H. Bolton Seed Memorial Symposium*, University of California, Berkeley, Vol. 2, pp. 351-376.
- SEED, R.B., DICKENSON, S.E., REIMER, M.F., BRAY, J.D., SITAR, N., MITCHELL, J.K., IDRIS, I.M., KAYEN, R.E., KROPP, A., HARDER, L.F., AND POWER, M.S. (1990). "Preliminary report on the principal geotechnical aspects of the October 17, 1989 Loma Prieta earthquake," *Report UCB/EERC-90/05*, Earthquake Engineering Research Center, University of California, Berkeley, 137 pp.
- SEEKINS, L.C., BRADY, A.G., CARPENTER, C., AND BROWN, N. (1992). Digitized strong-motion accelerograms of North and Central American earthquakes 1933-1986, *Digital Data Series DDS-7* (CD-ROM), U.S. Geological Survey, Golden, Colorado.
- SEKO, T. AND TOBE, K. (1977). "An experimental investigation of sand sampling," *Proceedings of Specialty Session 2, 9th International Conference on Soil Mechanics and Foundation Engineering*, Tokyo, pp. 37-42.
- SENNESET, K. AND NESTVOLD, J. (1992). "Deep compaction by vibro wing technique and dynamic compaction," in *Grouting, Soil Improvement, and Geosynthetics*, Geotechnical Special Publication 30, ASCE, New York, Vol. 2, pp. 889-901.
- SERFF, N., SEED, H.B., MAKDISI, F.I., AND CHANG, C.-Y. (1976). "Earthquake-induced deformations of earth dams," *Report EERC 76-4*, Earthquake Engineering Research Center, University of California, Berkeley, 140 pp.
- SHAH, H. C., MORTGAT, C. P., KIREMIDJIAN, A. S., AND ZSUTTY, T. C. (1975). "A Study of Seismic Risk for Nicaragua, Part I," *Report 11*, The John A. Blume Earthquake Engineering Center, Stanford University, Stanford, California.
- SHAKAL, A.F. AND BERNREUTER, D.L. (1981). "Empirical analysis of near-source ground motion," Nuclear Regulatory Commission *Report NUREG/CR-2095*, Washington, D. C.
- SHAKAL, A.F., HUANG, M.-J., AND VENTURA, C.E. (1988). "The California Strong Motion Instrumentation Program: Objectives, status and recent data," *Proceedings, 9th World Conference on Earthquake Engineering*, Tokyo, Vol. 8, pp. 105-116.
- SHARMA, M.P. AND SHAH, H.C. (1986). "Time varying parameter domain modeling of strong ground motion," *Proceedings, 3rd Engineering Mechanics Specialty Conference on Dynamics of Structures*, ASCE, University of California, Los Angeles.

- SHERIF, M.A. AND FANG, Y.S. (1984a). "Dynamic earth pressures on wall rotating about the top," *Soils and Foundations*, Vol. 24, No. 4, pp. 109-117.
- SHERIF, M.A. AND FANG, Y.S. (1984b). "Dynamic earth pressures on wall rotating about the base," *Proceedings, 8th World Conference on Earthquake Engineering*, San Francisco, Vol. 6, pp. 993-1000.
- SHERIF, M.A., ISHIBASHI, I., AND LEE, C.D. (1982). "Earth pressure against rigid retaining walls," *Journal of the Geotechnical Engineering Division*, ASCE, Vol. 108, No. GT5, pp. 679-695.
- SHINOZUKA, M. (1973). "Digital simulation of strong ground accelerations," *Proceedings, 5th World Conference on Earthquake Engineering*, Vol. 2, pp. 2829-2838.
- SHINOZUKA, M. AND DEODATIS, G. (1988). "Stochastic process models for earthquake ground motion," *Journal of Probabilistic Engineering Mechanics*, Vol. 3, No. 3, pp. 187-221.
- SHIRLEY, D.J. AND ANDERSON, A.L. (1975). "Acoustic and engineering properties of sediments," *Report ARL-TR-75-58*, Applied Research Laboratory, University of Texas, Austin.
- SHLIEN, S. AND TOKOSZ, M.N. (1970). "A clustering model for earthquake occurrences," *Bulletin of the Seismological Society of America*, Vol. 60, pp. 1765-1787.
- SIDDHARTHAN, R., ARA, S., AND NORRIS, G.M. (1992). "Simple rigid plastic model for seismic tilting of rigid walls," *Journal of Structural Engineering*, ASCE, Vol. 118, No. 2, pp. 469-487.
- SILLER, T.J. AND DOLLY, M.O. (1992). "Design of tied-back walls for seismic loading," *Journal of Geotechnical Engineering*, ASCE, Vol. 118, No. 11, pp. 1804-1821.
- SILLER, T.J. AND FRAWLEY, D.D. (1992). "Seismic response of multianchored retaining walls," *Journal of Geotechnical Engineering*, ASCE, Vol. 118, No. 11, pp. 1787-1803.
- SILVA, W.J. (1987). "WES RASCAL code for synthesizing earthquake ground motions," *Miscellaneous Paper S-73-1, Report 24*, U.S. Army Corps of Engineers, Waterways Experiment Station, Vicksburg, Mississippi, 73 pp.
- SILVA, W.J. (1988). "Soil response to earthquake ground motion," *EPRI Report NP-5747*, Electric Power Research Institute, Palo Alto, California.
- SILVA, W.J. (1988). "Soil response to earthquake ground motion," *EPRI Report NP-5747*, Electric Power Research Institute, Palo Alto, California.
- SILVER, N.L. AND SEED, H.B. (1971). "Volume changes in sands during cyclic loading," *Journal of the Soil Mechanics and Foundations Division*, ASCE, Vol 97, No. SM9, pp. 1171-
- SIMCOCK, K.J., DAVIS, R.O., BERRILL, J.B., AND MULLENGER, G. (1983). "Cyclic triaxial tests with continuous measurement of dissipated energy," *Geotechnical Testing Journal*, ASTM, Vol. 6, No. 1, pp. 35-39.
- SINGH, J.P. (1985). Earthquake ground motions: Implications for designing structures and reconciling structural damage, *Earthquake Spectra*, Vol. 1, No. 2, pp. 239-270.
- SINGH, S., SEED, H.B., AND CHAN, C.K. (1979). "Undisturbed sampling and cyclic load testing of sands," *Report UCB/EERC-79/33*, Earthquake Engineering Research Center, University of California, Berkeley, 131 pp.
- SLADEN, J.A. (1985). "Problems with interpretation of sand state from cone penetration test," *Geotechnique*, Vol. 39, No. 2, pp. 323-332.
- SLADEN, J.A., D'HOLLANDER, R.D., AND KRAHN, J. (1985). "The liquefaction of sands, a collapse surface approach," *Canadian Geotechnical Journal*. Vol. 22., No. 4, pp. 564-578.
- SLEMMONS, D.B. (1977). "Faults and earthquake magnitude," *Miscellaneous Paper S-73-1, Report 6*, U.S. Army Corps of Engineers Waterways Experiment Station, Vicksburg, Mississippi, 129 pp.
- SLEMMONS, D.B. (1982). "Determination of design earthquake magnitudes for microzonation," *Proceedings, 3rd International Earthquake Microzonation Conference*, Seattle, Washington, Vol. 1, pp. 119-130.

- SLEMMONS, D.B. AND MCKINNEY, R. (1977). "Definition of 'active fault'," *Miscellaneous Paper S-77-8*, U.S. Army Corps of Engineers Waterways Experiment Station, Vicksburg, Mississippi.
- SMITH, S.W. (1976). "Determination of maximum earthquake magnitude," *Geophysical Research Letters*, Vol. 3, No. 6, pp. 351-354.
- SOLYMAR, Z.V. AND REED, D.J. (1986). "A comparison of foundation compaction techniques," *Canadian Geotechnical Journal*, Vol. 23, No. 3, pp. 271-280.
- SOSKE, J.L. (1959). "The blind zone problem in engineering geophysics," *Geophysics*, Vol. 24, pp. 359-365.
- SPAETH, M.G. AND BERKMAN, S.C. (1967). "The tsunami of March 28, 1964 as recorded at tide stations," *ESSA Technical Report C and GS 33*, U.S. Coast and Geodetic Survey, Rockville, Maryland.
- SPENCER, E. (1967). "A method of analysis of the stability of embankments assuming parallel interslice forces," *Geotechnique*, Vol 17, No. 1, pp. 11-26.
- STARA-GAZETAS, E. (1986). "A method for inelastic response analysis of earth dams," Ph.D. dissertation, Rensselaer Polytechnic Institute, Troy, New York.
- STARA-GAZETAS, E. AND DOBRY, R. (1991). "Inelastic seismic response of San Fernando and Santa Felicia dams," *Proceedings, 2nd International Conference on Recent Advances in Geotechnical Earthquake Engineering and Soil Dynamics*, St. Louis, Missouri, Vol. 2, pp. 1129-1135.
- STARK, T.D. AND MESRI, G. (1992). "Undrained shear strength of sands for stability analysis," *Journal of Geotechnical Engineering*, ASCE, Vol. 118, No. 11, pp. 1727-1747.
- STEEDMAN, R.S. (1991). "Centrifuge modelling for dynamic geotechnical studies," *Proceedings, 2nd International Conference on Recent Advances in Geotechnical Earthquake Engineering and Soil Dynamics*, St. Louis, Missouri, Vol. 3, pp. 2401-2417.
- STEEDMAN, R.S. AND ZENG, X. (1990). "The seismic response of waterfront retaining walls," *Proceedings, ASCE Specialty Conference on Design and Performance of Earth Retaining Structures, Special Technical Publication 25*, Cornell University, Ithaca, New York, pp. 872-886.
- STEINBRUGGE, K.V. AND CLOUD, W. (1962). "Epicentral intensities and damage in the Hebgen Lake, Montana earthquake of August 17, 1959," *Bulletin of the Seismological Society of America*, Vol. 52, No. 2, pp. 181-234.
- STEPP, J.C. (1972). "Analysis of completeness in the earthquake sample in the Puget Sound area and its effect on statistical estimates of earthquake hazard," *Proceedings, International Conference on Microzonation*, Seattle, Washington, Vol. 2, pp. 897-910.
- STEWART, W.P. AND CAMPANELLA, R.G. (1991). "In-situ measurement of damping in sands and silts," *Proceedings, 2nd International Conference on Recent Advances in Geotechnical Earthquake Engineering and Soil Dynamics*, St. Louis, Missouri, Vol. X, pp.
- STILLEY, A.N. (1982). "Compaction grouting for foundation stabilization," *Proceedings, ASCE Specialty Conference on Grouting in Geotechnical Engineering*, New Orleans, Louisiana, pp. 923-937.
- STOKOE, K.H. AND ABDUL-RAZZAK, K.G. (1975). "Shear moduli of two compacted fills," *Proceedings, In-Situ Measurement of Soil Properties Specialty Conference*, Raleigh, North Carolina, Vol. 1, pp. 422-449.
- STOKOE, K.H. AND HOAR, R.J. (1978). "Generation and measurement of shear waves in situ," *Dynamic Geotechnical Testing*, ASTM STP 654, ASTM, Philadelphia, pp. 3-29.
- STOKOE, K.H. AND LODDE, P.F. (1978). "Dynamic response of San Francisco Bay mud," *Proceedings, ASCE Specialty Conference on Earthquake Engineering and Soil Dynamics*, Pasadena, Vol. 2, pp. 940-959.

- STOKOE, K.H., LEE, S.H.H., AND KNOX, D.P. (1985). "Shear moduli measurements under true triaxial stresses," *Proceedings, Advances in the Art of Testing Soils under Cyclic Conditions*, ASCE, New York, pp. 166-185.
- STOKOE, K.H., NAZARIAN, S., RIX, G.J., SANCHEZ-SALINERO, R., SHEU, J.-C., AND MOK, Y.-J. (1988). "In situ seismic testing of hard-to-sample soils by surface wave method," *Proceedings, Earthquake Engineering and Soil Dynamics II: Recent Advances in Ground Motion Evaluation*, Geotechnical Special Publication 20, ASCE, New York, pp. 264-278.
- STOKOE, K.H., ROESSET, J.M., BIRSCHWALE, J.G., AND AOUAD, M. (1988). "Liquefaction potential of sands from shear wave velocity," *Proceedings, 9th World Conference on Earthquake Engineering*, Tokyo, Vol. 3, pp. 213-218.
- STOKOE, K.H., WRIGHT, S.G., BAY, J.A. AND ROESSET, J.M. (1994). Characterization of geotechnical sites by SASW method, *Geophysical Characterization of Sites*, R.D. Woods, ed., A.A. Balkema, Rotterdam, pp. 15-25.
- STONE, W.C., YOKEL, F.Y., CELEBI, M., HANKS, T., AND LEYENDECKER, E.V. (1987). "Engineering aspects of the September 19, 1985 Mexico earthquake," *NBS Building Science Series 165*, National Bureau of Standards, Washington, D.C., 207 pp.
- STREETER, V.L., WYLIE, E.B. AND RICHART, F.E. (1973). "Soil motion computations by characteristics methods," *Proceedings, ASCE National Structural Engineering Conference*, San Francisco.
- SUCCARIEH, M.F., YAN, L., AND ELGAMAL, A.M. (1991). "Modelling of observed deformation at La Villita dam," *Proceedings, 2nd International Conference on Recent Advances in Geotechnical Earthquake Engineering and Soil Dynamics*, St. Louis, Missouri, Vol. 2, pp. 1079-1086.
- SUMNER, J.S. (1969). *Geophysics, Geologic Structures, and Tectonics*, Wm. C. Brown, Dubuque, Iowa.
- SUN, J.I., GOLESORKHI, R., AND SEED, H.B. (1988). "Dynamic moduli and damping ratios for cohesive soils," Report No. EERC-88/15, Earthquake Engineering Research Center, University of California, Berkeley.
- SWAN, F.H. III, SCHWARTZ, D.P., AND CLUFF, L.S. (1980). Recurrence of moderate-to-large magnitude earthquakes produced by surface faulting on the Wasatch fault, *Bulletin of the Seismological Society of America*, Vol. 70, No. 5, pp. 1431-1462.
- SY, A. AND CAMPANELLA, R.G. (1994). Becker and standard penetration tests (BPT-SPT) correlations with consideration of casing friction, *Canadian Geotechnical Journal*, Vol. 31, No. 3, pp. 343-356.
- SYMES, M.J., GENS, A., AND HIGHT, D.W. (1988). "Drained principal stress rotation in saturated sand," *Geotechnique*, Vol. 38, No. 1, pp. 59-81.
- TAJIMI, H. (1960) "A statistical method of determining the maximum response of a building structure during an earthquake," *Proceedings of the 2nd World Conference on Earthquake Engineering*, Tokyo, Vol. 2, pp. 781-797.
- TAJIRIAN, R. (1981). "Impedance matrices and interpolation techniques for 3-D interaction analysis by the flexible volume method," Ph.D. dissertation, University of California, Berkeley.
- TAKI, D. AND YANG, D.S. (1991). "Soil-cement mixed wall technique," *Geotechnical Engineering Congress*, Geotechnical Special Publication 27, ASCE, New York, Vol. 1, pp. 298-309.
- TAN, K. AND VUCETIC, M. (1989). "Behavior of medium and low plasticity clays under cyclic simple shear conditions," *Proceedings, 4th International Conference on Soil Dynamics and Earthquake Engineering*, A.S. Cakmak and I. Herrera, eds., Mexico City, pp. 131-142.
- TANG, H.T. (1987). "Large scale soil-structure interaction," *Report EPRI NP-5513-SR*, Electric Power Research Institute, Palo Alto, California.

- TATSUOKA, F., SASAKI, T., AND YAMADA, S. (1984). "Settlement in saturated sand induced by cyclic undrained simple shear," *Proceedings, 8th World Conference on Earthquake Engineering*, San Francisco, Vol. 3, pp. 255-262.
- TATSUOKA, F., OCHI, K., FUJII, S., AND OKAMOTO, M. (1986). "Cyclic undrained triaxial and torsional shear strength of sands for different sample preparation methods," *Soils and Foundations*, Vol. 26, No. 3, pp. 23-41.
- TAWFIQ, K.S., AGGOUR, M.S., AND AL-SANAD, H.A. (1988). "Dynamic properties of cohesive soils from impulse testing," *Proceedings, 9th World Conference on Earthquake Engineering*, Tokyo, Vol. 3, pp. 11-16.
- TAYLOR, D.W. (1948). *Fundamentals of Soil Mechanics*, Wiley, New York, 700 pp.
- TAYLOR, F.B. (1910). "Bearing of the Tertiary mountain belt on the origin of the Earth's plan," *Bulletin of the Geological Society of America*, Vol. 21, pp. 179-226.
- TERZAGHI, K. (1943). *Theoretical Soil Mechanics*, Wiley, Inc., New York.
- TERZAGHI, K. (1950). Mechanisms of landslides, *Engineering Geology (Berkey) Volume*, Geological Society of America.
- THIERS, G.R. AND SEED, H.B. (1978). "Strength and stress-strain characteristics of clays subjected to seismic loading conditions," in *Vibration Effects of Earthquakes on Soils and Foundations*, Special Technical Publication 450, ASTM, Philadelphia, pp. 3-56.
- THOMANN, T.G. AND HRYCIW, R.D. (1991). "Seismic downhole, CPT, and DMT correlations in sand," *Proceedings, 2nd International Conference on Recent Advances in Geotechnical Earthquake Engineering and Soil Dynamics*, St. Louis, Vol. 1, pp. 97-101.
- THOMSON, W.T. (1950). "Transmission of elastic waves through a stratified solid," *Journal of Applied Physics*, Vol. 21, pp. 89-93.
- TIKA-VASSILIKOS, T.E., SARMA, S.K., AND AMBRASEYS, N. (1993). "Seismic displacements on shear surfaces in cohesive soils," *Earthquake Engineering and Structural Dynamics*, Vol. 22, pp. 709-721.
- TIMOSHENKO, S.P. AND GOODIER, J.N. (1951). *Theory of elasticity*, McGraw-Hill, New York, 506 pp.
- TING, J.M., CORKUM, B.T., KAUFFMAN, C.R. AND GRECO, C. (1989). "Discrete numerical model for soil mechanics," *Journal of Geotechnical Engineering*, ASCE, Vol. 115, No. 3, pp. 379-398.
- TOCHER, D. (1958). "Earthquake energy and ground breakage," *Bulletin of the Seismological Society of America*, Vol. 48, No. 2, pp. 147-153.
- TOKI, S., TATSUOKA, F., MIURA, S., YOSHIMI, Y., YASUDA, S., AND MAKIHARA, Y. (1986). "Cyclic undrained triaxial strength of sand by a cooperative test program," *Soils and Foundations*, Vol. 26, No. 3, pp. 117-128.
- TOKIMATSU, K. AND MIDORIKAWA, S. (1981). "Nonlinear soil properties estimated from strong motion accelerograms," *Proceedings, International Conference on Recent Advances in Geotechnical Earthquake Engineering and Soil Dynamics*, St. Louis, Missouri, Vol. 1, pp. 117-122.
- TOKIMATSU, K. AND NAKAMURA, K. (1986). "A liquefaction test without membrane penetration effects," *Soils and Foundations*, Vol. 26, No. 4, pp. 127-138.
- TOKIMATSU, K. AND SEED, H.B. (1987). "Evaluation of settlements in sand due to earthquake shaking," *Journal of Geotechnical Engineering*, ASCE, Vol. 113, No. 8, pp. 861-878.
- TOKIMATSU, K. AND YOSHIMI, Y. (1983). "Empirical correlation of soil liquefaction based on SPT N-value and fines content," *Soils and Foundations*, Vol. 23, No. 4, pp. 56-74.
- TOKIMATSU, K., KUWAYAMA, S., AND TAMURA, S. (1991). "Liquefaction potential evaluation based on Rayleigh wave investigation and its comparison with field behavior," *Proceedings, 2nd Interna-*

- tional Conference on Recent Advances in Geotechnical Earthquake Engineering and Soil Dynamics*, St. Louis, Missouri, Vol. 1, pp. 357-364.
- TOKIMATSU, K., TAMURA, S., AND KOJIMA, H. (1992). "Effects of multiple modes on Rayleigh wave dispersion characteristics," *Journal of Geotechnical Engineering*, Vol. 118, No. 10, pp. 1529-1543.
- TORO, G.R., ABRAHAMSON, N.A., AND SCHNEIDER, J.F. (1995). "Engineering model of strong ground motions from earthquakes in the central and eastern United States," *Earthquake Spectra*, in press.
- TOWHATA, I. AND ISLAM, S. (1987). "Prediction of lateral movement of anchored bulkheads induced by seismic liquefaction," *Soils and Foundations*, Vol. 27, No. 4, pp. 137-147.
- TRIFUNAC, M.D. (1976). "Preliminary empirical model for scaling Fourier amplitude spectra of strong ground acceleration in terms of earthquake magnitude, source-to-station distance, and recording site conditions," *Bulletin of the Seismological Society of America*, Vol. 66, No. 4, pp. 1343-1373.
- TRIFUNAC, M.D. AND BRADY, A.G. (1975a). "On the correlation of seismic intensity with peaks of recorded strong ground motion," *Bulletin of the Seismological Society of America*, Vol. 65, pp. 139-162.
- TRIFUNAC, M. D. AND BRADY, A. G. (1975b) "A study of the duration of strong earthquake ground motion," *Bulletin of the Seismological Society of America*, Vol., 65, pp. 581-626.
- TRIFUNAC, M.D. AND HUDSON, D.E. (1971). "Analysis of the Pacoima Dam accelerograms - San Fernando earthquake of 1971," *Bulletin of the Seismological Society of America*, Vol. 61, No. 5, pp. 1393-1411.
- TRIFUNAC, M.D. AND LEE, V.W. (1987). "Frequency dependent attenuation of strong earthquake ground motion," in *Selection of Earthquake-Resistant Design Criteria for Nuclear Power Plants: Methodology and Technical Cases*, Report NUREG/CR-4903, Vol. 1, Nuclear Regulatory Commission, Washington, D. C.
- TRIFUNAC, M.D. AND WESTERMO, B. (1977). "A note on the correlation of frequency-dependent duration of strong earthquake ground motion with the MMI and geologic condition at the recording stations," *Bulletin of the Seismological Society of America*, Vol. 67, No. 3, pp. 917-927.
- TRIFUNAC, M.D., LEE, V.W., AND ANDERSON, J.G. (1987). "Methods for introduction of geologic data into characterization of active faults and seismicity and upgrading of the URS technique," *Report NUREG/CR*, Vol. 2, Nuclear Regulatory Commission, Washington, D. C.
- TSUCHIDA, H. (1970). "Prediction and countermeasure against the liquefaction in sand deposits," *Abstract of the Seminar in the Port and Harbor Research Institute*, pp. 3.1-3.33 (in Japanese).
- U. S. GEOLOGICAL SURVEY (1975). "A study of earthquake losses in the Puget Sound, Washington area," USGS Open File Report 75-375, 298 pp.
- U.S. GEOLOGICAL SURVEY (1975). *The Interior of the Earth*, U.S. Government Printing Office, Washington, D.C.
- U.S. DEPARTMENT OF THE NAVY (1982). Foundations and earth structures, *NAVFAC DM-7.2*, Naval Facilities Engineering Command, U.S. Government Printing Office, Washington, D.C., 244 pp.
- USCOLD (1985). Guidelines for selecting seismic parameters for dam projects, *Report of Committee on Earthquakes*, U.S. Committee on Large Dams.
- VAGLIENTE, V.H. (1973). "Forecasting risk inherent in earthquake-resistant design," *Technical Report 174*, Department of Civil Engineering, Stanford University, Stanford, California.
- VAID, Y.P. AND CHERN, J.C. (1983). "Effect of static shear on resistance of liquefaction," *Soils and Foundations*, Vol. 23, No. 1, pp. 47-60.
- VAID, Y.P. AND CHERN, J.C. (1985). "Cyclic and monotonic undrained response of saturated sands," in V. Khosla ed., *Advances in the Art of Testing Soils under Cyclic Conditions*, ASCE, New York, pp. 120-147.

- VAID, Y.P. AND NEGUSSEY, D. (1984). "A critical assessment of membrane penetration in the triaxial test," *Geotechnical Testing Journal*, Vol. 7, No. 2, pp. 70-76.
- VAID, Y.P., CHUNG, E.K.F., AND KUERBIS, R.H. (1990). "Stress path and steady state," *Canadian Geotechnical Journal*, Vol. 27, No. 1, pp. 1-7.
- VAID, Y.P. AND THOMAS, J. (1995). Liquefaction and post-liquefaction behavior of sand, *Journal of Geotechnical Engineering*, ASCE, Vol. 121, No. 2, pp. 163-173.
- VAN IMPE, W.F. (1989). *Soil improvement techniques and their evolution*, A.A. Balkema, Rotterdam, The Netherlands, 125 pp.
- VANMARCKE, E.H. (1972). "Properties of spectral moments with application to random vibration," *Journal of the Engineering Mechanics Division*, ASCE, Vol. 98, No. 3, pp. 425-442.
- VANMARCKE, E.H. (1976). "Structural response to earthquakes," Chapter 8 in C. Lomnitz and E. Rosenblueth, eds., *Seismic Risk and Engineering Decisions*, Elsevier, Amsterdam, pp. 287-338.
- VANMARCKE, E.H. (1979). "State-of-the-art for assessing earthquake hazards in the United States: Representation of earthquake ground motion: scaled accelerograms and equivalent response spectra," *Miscellaneous Paper S-73-1, Report 14*, U.S. Army Corps of Engineers Waterways Experiment Station, Vicksburg, Mississippi.
- VANMARCKE, E.H. AND LAI, S.P. (1977). "Strong motion duration of earthquakes," *Report R77-16*, Massachusetts Institute of Technology, Cambridge, Massachusetts.
- VANMARCKE, E.H. AND LAI, S.P. (1980). Strong motion duration and rms amplitude of earthquake records, *Bulletin of the Seismological Society of America*, Vol. 70, pp. 1293-1307.
- VARNES, D.J. (1978). "Slope movement types and processes," in *Landslides: Analysis and Control*, Transportation Research Board Special Report 176, National Academy of Sciences, Washington, D.C., pp. 12-33.
- VASQUEZ-HERRERA, A. AND DOBRY, R. (1988). "The behavior of undrained contractive sand and its effect on seismic liquefaction flow failures of earth structures," *Report to U.S. Army Corps of Engineers*, Rensselaer Polytechnic Institute, Troy, New York, 510 pp.
- VASQUEZ-HERRERA, A., DOBRY, R., AND BAZIAR, M.H. (1990). "Re-evaluation of liquefaction triggering and flow sliding in the Lower San Fernando Dam during the 1971 earthquake," *Proceedings, 4th U.S. National Conference on Earthquake Engineering*, Palm Springs, California, pp. 783-792.
- VAUGHAN, D.K. (1983). *FLEX User's Guide*, Document UG8298, Weidlinger Associates, New York.
- VENEZIANO, D. AND CORNELL, C.A. (1974). Earthquake models with spatial and temporal memory for engineering seismic risk analysis, *Research Report R74-78*, Department of Civil Engineering, Massachusetts Institute of Technology, Cambridge, Massachusetts.
- VENEZIANO, D. AND LIAO, S. (1984). "Statistical analysis of liquefaction data," *Proceedings, 4th ASCE Specialty Conference on Probabilistic Mechanics and Structural Reliability*, pp. 206-209.
- VERDUGO, R. (1992). Discussion of "Correlation between liquefaction resistance and shear wave velocity," by K. Tokimatsu and A. Uchida, *Soils and Foundations*, Vol. 32, No. 2, pp. 144-145.
- VERE-JONES, D. AND OZAKI, T. (1982). "Some examples of statistical estimation applied to earthquake data. I. Cyclic Poisson and self-exciting models," *Annals of the Institute of Statistics and Mathematics*, Vol. 34, Part B, pp. 189-207.
- VERE-JONES, D.A. (1966). "A Markov model for aftershock occurrence," *Pure and Applied Geophysics*, Vol. 64, pp. 31-42.
- VERE-JONES, D.A. AND DAVIES, R.B. (1966). "Statistical survey of earthquakes in the main seismic region of New Zealand, Part 2: Time series analysis," *New Zealand Journal of Geology and Geophysics*, Vol. 9, pp. 251-284.

- VERHOODAN, J. (1960). "Temperatures inside the earth," *American Scientist*, Vol. 48, No. 2, pp. 134-159.
- VERNEY, P. (1979). *The Earthquake Handbook*, Paddington Press, New York.
- VIDALE, J.E. AND HELMBERGER, D.V. (1988). "Elastic finite difference of the 1971 San Fernando earthquake," *Bulletin of the Seismological Society of America*, Vol. 78, No. 1, pp. 122-141.
- VON THUN, J. L., ROCHIM, L. H., SCOTT, G. A., AND WILSON, J. A. (1988) "Earthquake ground motions for design and analysis of dams," in *Earthquake Engineering and Soil Dynamics II - Recent Advance in Ground-Motion Evaluation*, Geotechnical Special Publication 20, ASCE, New York, pp. 463-481.
- VUCETIC, M. (1990). "Normalized behavior of clay under irregular cyclic loading," *Canadian Geotechnical Journal*, Vol. 27, No. 1, pp. 29-46.
- VUCETIC, M. (1994). "Cyclic threshold shear strains in soils," *Journal of Geotechnical Engineering*, ASCE, Vol. 120, No. 12, pp. 2208-2228.
- VUCETIC, M. AND DOBRY, R. (1989). "Degradation of marine clays under cyclic loading," *Journal of Geotechnical Engineering*, ASCE, Vol. 114, No. 2, pp. 133-149.
- VUCETIC, M. AND DOBRY, R. (1991). "Effect of soil plasticity on cyclic response," *Journal of Geotechnical Engineering*, ASCE, Vol. 117, No. 1, pp. 89-107.
- WALLACE, R.E. (1981). "Active faults, paleoseismology, and earthquake hazards in the western United States," in D.W. Simpson and T.G. Richards, eds. *Earthquake Prediction: An International Review*, Maurice Ewing Series 4, American Geophysical Union, Washington, D. C., pp. 209-216.
- WANG, W. (1979). "Some findings in soil liquefaction," Water Conservancy and Hydroelectric Power Scientific Research Institute, Beijing, China.
- WARD, W.A. (1986). "Interpretation of CPT data for design of earth dams near Tehachapi, California," *Proceedings, In Situ '86*, Blacksburg, Virginia, Geotechnical Special Publication 6, ASCE, New York, pp. 1119-1133.
- WARNER, J. (1982). "Compaction grouting - the first thirty years," *Proceedings, ASCE Specialty Conference on Grouting in Geotechnical Engineering*, New Orleans, Louisiana, pp. 694-707.
- WEGENER, A. (1915). *Die Entstehung der Kontinente und Ozeane*, Vieweg, Braunschweig, Germany.
- WEICHERT, D. (1980). "Estimation of the earthquake recurrence parameters for unequal observation periods for different magnitudes," *Bulletin of the Seismological Society of America*, Vol. 70, No. 4, pp. 1337-1347.
- WEILER, W.A. (1988). "Small strain shear modulus of clay," *Proceedings, ASCE Conference on Earthquake Engineering and Soil Dynamics II: Recent Advances in Ground Motion Evaluation*, Geotechnical Special Publication 20, ASCE, New York, pp. 331-335.
- WELLS, D.L. AND COPPERSMITH, K.J. (1994). "New empirical relationships among magnitude, rupture length, rupture width, rupture area, and surface displacement," *Bulletin of the Seismological Society of America*, Vol. 84, No. 4, pp. 974-1002.
- WELSH, J.P. (1986). "In situ testing for ground modification techniques," *Proceedings, In Situ '86*, Geotechnical Special Publication 6, ASCE, New York, pp. 322-335.
- WELSH, J.P., ED. (1987). *Soil Improvement: A Ten Year Update*, Geotechnical Special Publication No. 12, ASCE, New York, 331 pp.
- WESNOUSKY, S.G. (1994). "The Gutenberg-Richter or characteristic earthquake distribution, which is it?" *Bulletin of the Seismological Society of America*, Vol. 84, No. 6, pp. 1940-1959.
- WESNOUSKY, S.G., SCHOLZ, C.H., SHIMAZAKI, K., AND MATSUDE, T. (1984). "Integration of geological and seismological data for the analysis of seismic hazard: A case study of Japan," *Bulletin of the Seismological Society of America*, Vol. 74, pp. 687-708.

- WESSON, R.L., HELLEY, E.J., LAJOIE, K.R., AND WENTWORTH, C.M. (1975). "Faults and future earthquakes," in R.D. Borcherdt, ed. *Studies for Seismic Zonation of the San Francisco Bay Region*, Professional Paper 941-A, U. S. Geological Survey, Reston, Virginia, pp. A5-A30.
- WESTERGAARD, H. (1931). "Water pressure on dams during earthquakes," *Transactions of ASCE*, Paper No. 1835, pp. 418-433.
- WHITMAN, R.V. (1971). "Resistance of soil to liquefaction and settlement," *Soils and Foundations*, Vol. 11, No. 4, pp. 59-68.
- WHITMAN, R.V. (1989). "Workshop on ground motion parameters for seismic hazard mapping," *Technical Report NCEER-89-0038*, National Center for Earthquake Engineering Research, State University of New York, Buffalo, 41 pp.
- WHITMAN, R.V. (1990). "Seismic design behavior of gravity retaining walls," *Proceedings, ASCE Specialty Conference on Design and Performance of Earth Retaining Structures*, Geotechnical Specialty Publication 25, ASCE, New York, pp. 817-842.
- WHITMAN, R.V. (1992). "Proceedings for the site effects workshop," *Technical Report NCEER-92-0006*, National Center for Earthquake Engineering Research, State University of New York, Buffalo, 35 pp.
- WHITMAN, R.V. AND LIAO, S. (1985). Seismic design of retaining walls, *Miscellaneous Paper GL-85-1*, U.S. Army Engineer Waterways Experiment Station, Vicksburg, Mississippi.
- WHITMAN, R.V., LAMBE, P.C., AND AKIYAMA, H. (1982). "Consolidation during dynamic tests on a centrifuge," *Preprint 82-063*, ASCE National Convention, Las Vegas, Nevada.
- WILSON, J.T. (1965). "A new class of faults and their bearing on continental drift," *Nature*, Vol. 207, pp. 343-347.
- WILSON, R.C. (1993). "Relation of Arias Intensity to magnitude and distance in California," *Open-File Report 93-556*, U.S. Geological Survey, Reston, Virginia, 42 pp.
- WILSON, R. C. AND KEEFER, D. K. (1985) "Predicting areal limits of earthquake-induced landsliding," in *Evaluating Earthquake Hazards in the Los Angeles Region*, Ziony, J. I., ed., U. S. Geological Survey, Reston, Virginia, Professional Paper 1360, 317-345.
- WOLF, J.P. (1985). *Dynamic Soil-Structure Interaction*, Prentice Hall, Englewood Cliffs, New Jersey, 466 pp.
- WOLF, J.P. (1991). "Consistent lumped-parameter models for unbounded soil: physical representation," *Earthquake Engineering and Structural Dynamics*, Vol. 20, No. 1, pp. 11-32.
- WONG, C.P. (1982). "Seismic analysis and an improved design procedure for gravity retaining walls," *S.M. Thesis*, Department of Civil Engineering, Massachusetts Institute of Technology; Cambridge, Massachusetts.
- WONG, R.K.S. AND ARTHUR, J.R.F. (1986). "Sand shear by stresses with cyclic variations in direction," *Geotechnique*, Vol. 36, No. 2, pp. 215-226.
- WONG, R.T., SEED, H.B., AND CHAN, C.K. (1975). "Liquefaction of gravelly soil under cyclic loading conditions," *Journal of the Geotechnical Engineering Division*, ASCE, Vol. 101 No. GT6, pp. 574-583.
- WONG, W. (1984). "Earthquake damages to earth dams and levees in relation to soil liquefaction and weakness in soft clays," *Proceedings, International Conference on Case Histories in Geotechnical Engineering*, Vol. 1, pp. 511-521.
- WOOD, D.M. (1991). Approaches to modelling the cyclic stress-strain response of soils, Chapter 2 in M.P. O'Reilly and S.F. Brown, eds, *Cyclic Loading of Soils*, Blackie, London, pp. 19-69.
- WOOD, H.O. (1908). "Distribution of apparent intensity in San Francisco, in the California earthquake of April 18, 1906," *Report of the State Earthquake Investigation Commission*, Carnegie Institute of Washington, Washington, D.C., Vol. 1, pp. 220-245.

- WOOD, J. (1973). "Earthquake-induced soil pressures on structures," *Report EERL 73-05*, California Institute of Technology, Pasadena, California, 311 pp.
- WOODS, R.D. (1978). "Measurement of dynamic soil properties," *Proceedings, Earthquake Engineering and Soil Dynamics Specialty Conference*, ASCE, Pasadena, California, Vol. 1, pp. 91-178.
- WOODS, R.D. (1991). "Field and laboratory determination of soil properties at low and high strains," *Proceedings, 2nd International Conference on Recent Advances in Geotechnical Earthquake Engineering and Soil Dynamics*, St. Louis, Missouri, Vol. 3, pp. 1727-1741.
- WOODWARD-CLYDE CONSULTANTS (1979). "Report of the evaluation of maximum earthquake and site ground motion parameters associated with the Offshore Zone of deformation, San Onofre Nuclear Generating Station," *Report to Southern California Edison Company*, Woodward-Clyde Consultants, San Francisco.
- WROTH, C.P. AND HOULSBY, G.T. (1985). "Soil mechanics - Property characterization and analysis procedures," *Proceedings, 11th International Conference on Soil Mechanics and Foundation Engineering*, San Francisco, Vol. 1, pp. 1-55.
- WU, S.-C., CORNELL, C.A., AND WINTERSTEIN, S.R. (1995). "A hybrid recurrence model and its implication on seismic hazard results," *Bulletin of the Seismological Society of America*, Vol. 85, No. 1, pp. 1-16.
- WYSS, M. (1979). "Estimating maximum expected magnitude of earthquakes from fault dimensions," *Geology*, Vol. 7, No. 7, pp. 336-340.
- YAN, L., AND BYRNE, P.M. (1990). "Simulation of downhole and crosshole seismic tests on sand using the hydraulic gradient similitude method," *Canadian Geotechnical Journal*, Vol. 27, No. 4.
- YAN, L. AND BYRNE, P.M. (1991). "Stress state and stress ratio effects in downhole and crosshole shear wave velocity tests on sands," *Proceedings, 2nd International Conference on Recent Advances in Geotechnical Earthquake Engineering and Soil Dynamics*, St. Louis, Missouri, Vol. 1, pp. 299-306.
- YANG, C.Y. (1986). *Random Vibration of Structures*, John Wiley and Sons, New York, 295 pp.
- YASUDA, N. AND MATSUMOTO, N. (1993). "Dynamic deformation characteristics of sands and rock-fill materials," *Canadian Geotechnical Journal*, Vol. 30, No. 5, pp. 747-757.
- YEGIAN, M.K. AND WHITMAN, R.V. (1978). "Risk analysis for ground failure by liquefaction," *Journal of the Geotechnical Engineering Division*, ASCE, Vol 104, NO. GT7, pp. 921-938.
- YEGIAN, M.K., GHARAMAN, V.G., AND HARUTIUNYAN, R.N. (1994). "Liquefaction and embankment failure case histories, 1988 Armenai earthquake," *Journal of Geotechnical Engineering*, ASCE, Vol. 120, No. 3, pp. 581-596.
- YEGIAN, M.K., MARCIANO, E.A., AND GHARAMAN, V.G. (1988). "Integrated seismic risk analysis for earth dams," *Report 88-15*, Northeastern University, Boston.
- YEGIAN, M.K., MARCIANO, E., AND GHARAMAN, V.G. (1991). "Earthquake-induced permanent deformations: probabilistic approach," *Journal of Geotechnical Engineering*, ASCE, Vol. 117, No. 1, pp. 35-50.
- YOSHIMI, Y., TOKIMATSU, K., AND HASAKA, Y. (1989). "Evaluation of liquefaction resistance of clean sands based on high-quality undisturbed samples," *Soils and Foundations*, Vol. 29, No. 1, pp. 93-104.
- YOUND, T.L. (1972). "Compaction of sands by repeated shear straining," *Journal of the Soil Mechanics and Foundations Division*, ASCE, Vol. 98, No. SM7, pp. 709-725.
- YOUND, T.L. (1978). "Major cause of earthquake damage is ground failure," *Civil Engineering*, ASCE, Vol. 48, No. 4, pp. 47-51.

- YOUNG, T.L. (1984a). "Recurrence of liquefaction at the same site," *Proceedings, 8th World Conference on Earthquake Engineering*, Vol. 3, pp. 231-238.
- YOUNG, T.L. (1984b). "Geologic effects - Liquefaction and associated ground failure," *Proceedings, Geologic and Hydrologic Hazards Training Program*, Open File Report 84-760, U.S. Geological Survey, Menlo Park, California, pp. 210-232.
- YOUNG, T.L. (1991). "Mapping of earthquake-induced liquefaction for seismic zonation," *Proceedings, 4th International Conference on Seismic Zonation*, Earthquake Engineering Research Institute, Stanford University, Vol. 1, pp. 111-147.
- YOUNG, T.L. (1993). "Liquefaction-induced lateral spread displacement," *Report TN-1862*, Naval Civil Engineering Laboratory, Port Hueneme, California, 44 pp.
- YOUNG, T.L. AND GARRIS, C.T. (1995). Liquefaction-induced ground surface disruption, *Journal of Geotechnical Engineering*, ASCE, Vol. 121, No. 11, in press.
- YOUNG, T.L. AND HOOSE, S.N. (1977). "Liquefaction susceptibility and geologic setting," *Proceedings, 6th World Conference on Earthquake Engineering*, New Delhi, Vol. 3, pp. 2189-2194.
- YOUNG, T.L. AND PERKINS, D.M. (1987). "Mapping of Liquefaction Severity Index," *Journal of Geotechnical Engineering*, ASCE, Vol. 113, No. 11, pp. 1374-1392.
- YOUNG, T.L., ET AL. (1985). "The Borah Peak, Idaho earthquake of October 28, 1983--liquefaction," *Earthquake Spectra*, Vol. 2, No. 1, pp. 71-89.
- YOUNGS, R. R. AND COPPERSMITH, K. J. (1985). "Implications of fault slip rates and earthquake recurrence models to probabilistic seismic hazard assessments," *Bulletin of the Seismological Society of America*, Vol. 75, No. 4, pp. 939-964.
- YOUNGS, R.R., DAY, S.M., AND STEVENS, J.L. (1988). "Near field ground motions on rock for large subduction earthquakes," *Proceedings, Earthquake Engineering and Soil Dynamics II: Recent Advances in Ground Motion Evaluation*, Geotechnical Special Publication 20, ASCE, New York, pp. 445-462.
- YU, H.S. (1994). "State parameter from self-boring pressuremeter tests in sand," *Journal of Geotechnical Engineering*, Vol. 120, No. 12, pp. 2118-2135.
- ZACHER, E.G. AND GRAF, E.D. (1979). "Chemical grouting of sand for earthquake resistance," *Civil Engineering*, ASCE, New York, Vol. 49, No. 1, pp. 67-69.
- ZARRABI-KASHANI, K. (1979). "Sliding of gravity retaining wall during earthquakes considering vertical accelerations and changing inclination of failure surface," S.M. thesis, Department of Civil Engineering, Massachusetts Institute of Technology, Cambridge, Massachusetts.
- ZELIKSON, A. (1969). "Geotechnical models using the hydraulic gradient similarity methods," *Geotechnique*, Vol. 19, pp. 495-508.
- ZEMELL, S. W. (1984) "Imposed upper limit for probabilistic seismic risk," *Proceedings, 8th World Conference on Earthquake Engineering*, San Francisco, pp. 239-245.
- ZEN, K., UMEHARA, Y., AND HAMADA, K. (1978). "Laboratory tests and in-situ seismic survey on vibratory shear modulus of clayey soils with different plasticities," *Proceedings, Fifth Japan Earthquake Engineering Symposium*, Tokyo, pp. 721-728.
- ZIENKIEWICZ, O.C. AND TAYLOR, R.L. (1989). *The Finite Element Method*, McGraw-Hill, London.
- ZOEPPRITZ, K. (1919). "Nach d. Konigl. Gessel d. Wissen, z. Gottingen," *Math-Phys.*, Berlin, pp. 66-94.



Index

A

Acceleration spectrum intensity, 83, 100
Accelerogram, 56
Accelerograph, 56
Accelerometer, 58
 force balance, 58
 piezoelectric, 59
Accretionary wedge, 31
Active earth pressure (see Retaining walls)
Active fault, 109-111
Aftershock (see Earthquake)
Amplification function, 310-312
Amplitude, 55, 529, 531, 533
Anchored bulkheads, 496-498
Apparent dip angle, 198-199
Argand diagram, 53
Arias intensity, 82, 99-100
Aseismic deformation, 25

Asperities, 38
Autocovariance, 101
Axioms of probability, 584-585

B

Backbone curve, 231-232, 240-243
Bandwidth, 76
Barriers, 38
Baseline error, 59, 62
Basin effects, 321-323
Becker hammer penetration test, 211-212
Bedrock motion (see Ground motion)
Bedrock outcropping motion (see Ground motion)
Benioff zone, 31
Blasting densification (see Soil improvement)
Blind zone, 197

- Body wave, 19-20, 144-156
- Body wave magnitude (see Magnitude)
- Borehole torsional shear test, 215
- Bracketed duration, 79-80, 95, 99
- Brune spectrum, 92-93

- C**
- Central frequency, 76-77
- Centrifuge test, 226-227
- Characteristic earthquake (see Recurrence law)
- Characteristic (frequency) equation, 577
- Characteristic intensity, 82
- Characteristic site period, 261
- Chiba array, 63
- Circular frequency, 529
- Coda, 48
- Coda magnitude (see Magnitude)
- Coefficient of variation (see Random variable)
- Coherency, 101-102
- Collapse surface, 363
- Compaction grouting (see Soil improvement)
- Compaction piles (see Soil improvement)
- Complex shear modulus, 177
- Complex stiffness, 570-571
- Complex wave number, 177, 260
- Conditional probability, 585-588
- Cone penetration (CPT) test, 212-213
 - correlation to G_{max} , 235
 - correlation to liquefaction resistance, 383-385
- Constitutive models, 243-244
- Continental collision, 31
- Continental drift, 23-28
- Controlling earthquake, 114
- Convection, 28
- Core (see Earth), 22
- Corner frequency, 72
- Critical angle of incidence, 172, 196
- Critical damping coefficient, 551
- Critical distance, 196
- Critical level of repeated loading (CLRL), 245
- Critical void ratio, 355-357
- Cross-hole test, 205-207

- Crust (see Earth), 20
- Cumulative absolute velocity, 83
- Cumulative distribution function (see Probability)
- Cutoff frequency, 72
- Cyclic direct simple shear test, 223-224
- Cyclic mobility (see Liquefaction)
- Cyclic nonlinear models, 240-243
- Cyclic strength curves, 374-375
- Cyclic strength ratio, 245
- Cyclic stress ratio, 374-376
- Cyclic torsional shear test, 224-225
- Cyclic triaxial test, 220-223

- D**
- Damped natural frequency, 551
- Damping
 - complex stiffness, 570-571
 - effect on ground response, 260, 263
 - from half-power bandwidth method, 568-569
 - from hysteresis loop, 567-568
 - from logarithmic decrement, 552
 - material, 175-178
 - quality factor, 92, 569
 - radiation, 264
 - viscous, 567-571
- Damping ratio
 - definition, 551
 - measurement of, 208, 217, 222
 - of soils, 238-240
- Deaggregation (see Seismic hazard analysis)
- Deconvolution (see Ground response analysis)
- Degradation of shear modulus, 238-239
- Degrees of freedom, 544
- Dependent events, 122
- Design earthquakes
 - and deterministic seismic hazard analysis, 114-117
 - maximum credible earthquake, 324
 - maximum probable earthquake, 324
 - operating basis earthquake, 324
 - safe shutdown earthquake, 324

- Design ground motion
 - code-based development, 328-339
 - from design earthquakes, 324
 - design response spectrum, 325-327, 334
 - site-specific development, 327-328
 - time history development, 340-345
 - uniform risk spectrum, 327
 - Deterministic seismic hazard analysis, 114-117
 - Dilatometer test, 213-214
 - correlation to G_{max} , 235
 - correlation to liquefaction resistance, 385-386
 - Dip-slip movement (see Fault)
 - Dirac function, 565
 - Direct wave (see Seismic refraction test)
 - Directivity effect, 39
 - Dispersion, 164-165, 203-205
 - Down-hole test, 207-208
 - Drilled inclusions (see Soil improvement)
 - Ductility
 - effect on design base shear, 330, 338
 - factor, 75
 - Duhamel integral, 566
 - Duration
 - and liquefaction, 369-370
 - definitions, 79-82
 - prediction of, 95
 - Duration magnitude (see Magnitude)
 - Dynamic compaction (see Soil improvement)
- E**
- Earth, 18-22
 - Benioff zone, 31
 - core, 22
 - crust, 20
 - mantle, 21
 - Mohorovicic discontinuity, 21
 - temperature, 21
 - wave velocities, 22
 - Earth pressure (see Retaining walls)
 - Earthquake
 - aftershock, 38, 122
 - energy, 50-51
 - epicenter, 43
 - focus, 43
 - foreshock, 38, 122
 - historical, 1, 14-17
 - hypocenter, 43
 - intensity, 45-46
 - intraplate, 32
 - location, 44
 - magnitude, 46-50
 - multiple-event, 39
 - reservoir-induced, 42
 - Earthquake-resistant design, 106
 - Effective acceleration, 69
 - Effective design acceleration, 70
 - Effective peak acceleration, 83-84
 - Effective peak velocity, 83-84
 - Effective shear strain, 271-273
 - Elastic rebound, 36-42
 - Epicenter, 43
 - Epicentral distance, 43
 - Epicentral intensity (see Intensity), 45
 - Equation of motion, 144, 152-154, 546, 575
 - Equivalent lateral force, 580
 - Equivalent linear model
 - advantages and limitations of, 279-280
 - and ground response analysis, 270-275, 284-286, 292
 - soil properties, 230-240
 - Equivalent stress cycles, 369-371
 - Evolutionary power spectrum, 73
 - Expected value (see Random variable)
 - Extended source effect, 101
- F**
- Fault
 - activity, 109-111
 - geometry, 33-34
 - movement, 34
 - types
 - dip-slip, 34-35
 - normal, 34-35
 - reverse, 34
 - strike-slip, 34, 36

- Fault (*cont.*)
 - thrust, 34
- Finite difference method, 275-279
- Finite element method, 281-286
 - boundary conditions, 283-284
 - discretization considerations, 283
 - elemental equations of motion, 281-283
 - global equations of motion, 283
- Fling, 39-40
- Flow failure (see Liquefaction)
- Flow liquefaction surface (see Liquefaction)
- Focal depth, 43
- Focus, 43
- Forced vibration, 548, 553-566
- Foreshock (see Earthquake)
- Fourier amplitude spectrum, 71-72, 92-93, 538
- Fourier phase spectrum, 71-72, 538
- Fourier series, 536-542; 562-563
 - discrete Fourier transform, 541
 - Fast Fourier transform, 541
- Free-field motion, 61, 255, 294, 300-302
- Free surface motion, 255-256
- Free vibration, 548-553
- Frequency
 - content, 55, 70
 - definition, 530
 - fundamental, 261, 577-578
 - equation, 577
- Fundamental mode of vibration, 578

- G**
- Gaussian distribution (see Normal distribution)
- Geophone, 59, 195
- Geotomography, 215
- Global Digital Seismographic Network, 62
- G_{\max} , 232-235
- Gravity walls, 489-492, 494-495
- Green's function
 - (see Time history development)
- Ground motion
 - bedrock motion, 255
 - bedrock outcropping motion, 255
 - coherency, 101-102
 - free surface motion, 255
 - measurement
 - accelerogram, 56
 - accelerograph, 56
 - accelerometer, 58
 - baseline error, 59, 62
 - instrument arrays, 62-64
 - seismogram, 56
 - seismograph, 56
 - seismometer, 58
 - seismoscope, 59
 - parameters
 - acceleration spectrum intensity, 83, 100
 - Arias intensity, 82, 99-100
 - bandwidth, 76
 - bracketed duration, 79-80, 95, 99
 - central frequency, 76-77
 - characteristic intensity, 82
 - cumulative absolute velocity, 83
 - effective acceleration, 69
 - effective design acceleration, 70
 - effective peak acceleration, 83-84
 - effective peak velocity, 83-84
 - Kanai-Tajimi parameters, 78
 - peak acceleration, 67-68, 88-91
 - peak displacement, 68
 - peak velocity, 68, 90
 - predominant period, 76, 91-92
 - response spectrum intensity, 83
 - rms acceleration, 82, 98-99
 - shape factor, 77-78
 - sustained maximum acceleration, 69-70
 - sustained maximum velocity, 69-70
 - velocity spectrum intensity, 83, 100
 - v_{\max}/a_{\max} , 78-79, 94
 - rock outcropping motion, 255
- Ground oscillation (see Liquefaction)
- Ground response analysis, 254-305
 - comparison of equivalent linear and nonlinear, 279-280, 291
 - deconvolution, 274-275
 - equivalent linear, 270-275, 284-286, 292
 - nonlinear, 275-279, 286, 292-293
 - one-dimensional, 255-280

- Ground response analysis (*cont.*)
 three-dimensional, 291-294
 transfer functions, 256-275
 two-dimensional, 280-291
- Group velocity, 165
- Grouting (see Soil improvement)
- Gutenberg discontinuity, 22
- Gutenberg-Richter recurrence law
 (see Recurrence law)
- H**
- Half-power bandwidth method, 568-569
- Haskell-Thomson solution, 204
- Head wave (see Seismic refraction test)
- Historical seismicity, 113-114
- Hydrodynamic pressure, 486
- Hypocenter, 43
- Hypocentral depth, 43
- Hypocentral distance, 43
- Hysteresis loop, 567-568
- I**
- Impedance ratio
 complex, 265
- Impedance ratio, 167-169
- Instrument arrays, 62-64
 Chiba, 63
 El Centro, 63, 64
 GSDN, 62
 Lotung, 63
 WWSSN, 62
- Instrumental seismicity, 114
- Intensity
 and peak horizontal acceleration, 67
 epicentral, 45
 isoseismal map, 45, 47
 Japanese Meteorological Agency, 45
 Medvedev-Spoonheuer-Kornik, 45
 modified Mercalli, 45-46
 Rossi-Forel, 45
- Interface friction angle, 472-473
- Intraplate earthquakes, 32
- Intrusion grouting (see Soil improvement)
- Isoseismal map (see Intensity)
- J**
- Jet grouting (see Soil improvement)
- JMA intensity (see Intensity)
- JMA magnitude (see Magnitude)
- K**
- Kanai-Tajimi power spectrum
 (see Power spectrum)
- L**
- Landslide (see Slope stability)
- Lateral spreading, 5-8, 349-351, 367-368,
 453-462
- Lifelines, 11
- Linear acceleration method, 574-575
- Liquefaction, 348-422
 cyclic mobility, 349-350, 367-368
 effects, 5-8, 397-418
 alteration of ground motion, 398-401
 development of sand boils, 8, 400-402
 ground oscillation, 399-400
 instability, 5-8, 408-417, 451-462
 residual shear strength, 410-413
 settlement, 402-408
 steady state shear strength, 409-410
 flow liquefaction, 5-7, 349, 361-366, 413-
 415
 initiation, 361-398
 cyclic strain approach, 390-394
 cyclic stress approach, 369-390
 effective stress-based response analysis,
 395-396
 energy dissipation approach, 394-395
 factor of safety against liquefaction,
 386-390
 flow liquefaction surface, 361-369
 initial liquefaction, 368-369
 probabilistic approach, 396-397

- Liquefaction (*cont.*)
- resistance
 - effect of fines, 378-380
 - laboratory characterization of, 373-377
 - insitu test characterization of, 377-387
 - specimen preparation effects on, 377
 - settlement dry sand, 402-404
 - saturated sand, 404-408
 - susceptibility, 351-360
 - compositional criteria, 354-355
 - geologic criteria, 353-354
 - historical criteria, 352-353
 - state criteria, 355-360
 - Liquefaction Severity Index, 454-456
 - Local magnitude (see Magnitude)
 - Local site effects, 309-323
 - Logarithmic decrement, 552
 - Logic tree, 137-138
 - Lognormal distribution, 594-595
 - Loma Prieta earthquake, 316-317
 - Lotung array, 63
 - Love wave, 20, 162-164
- M**
- Magnification factor, 561
 - Magnitude
 - and fault rupture area, 111-113
 - and maximum fault displacement, 111-113
 - and surface rupture length, 111-113
 - body wave, 48
 - coda, 48
 - duration, 48-49
 - Japanese Meteorological Agency, 49
 - moment, 49
 - Richter local, 48
 - saturation, 49
 - surface wave, 48
 - Makdisi-Seed analysis (see Slope stability)
 - Mantle (see Earth), 21
 - Markov model, 129
 - Masing behavior, 241-242
 - Material damping, 175-178
 - Maximum credible earthquake, 115
 - Maximum probable earthquake, 115
 - Mean (see Random variable)
 - Membrane penetration, 220
 - Mexico City, 313-315
 - Micromechanical modeling, 230
 - Microplates, 23
 - Microseismic activity, 54
 - Mode of vibration
 - of earth dam, 289-290
 - of MDOF structure, 578
 - of soil deposit, 261-262
 - Mode shape, 261, 578
 - Mode superposition method, 579-581
 - Model tests, 225-228
 - Modified Mercalli intensity (see Intensity)
 - Modulus reduction curve (see Shear modulus)
 - Mohorovicic discontinuity, 21
 - Mohr circle of stress, 186
 - Moment magnitude (see Magnitude)
 - Mononobe-Okabe method
 - (see Retaining walls)
 - Multiple degree of freedom systems, 575-582
 - equations of motion, 575-577
 - response of linear MDOF systems, 577-582
 - mode superposition method, 579-581
 - response spectrum analysis, 581-582
 - undamped free vibrations, 577-579
 - Multiplication rule, 586
- N**
- Natural frequency, 548
 - Natural hazards, 2
 - Natural period of vibration, 548
 - NEHRP Provisions
 - effective peak acceleration coefficient
 - 335-336, 338
 - effective peak velocity-related acceleration coefficient, 335, 337-338
 - equivalent lateral force procedure, 338-340
 - Newmark sliding block analysis
 - (see Slope stability)
 - Newmark-Hall design response spectrum, 325-326

- Nonlinear analysis
 of SDOF systems, 572-575
 of soil deposits, 275-280, 286, 290, 292-293
- Nonperiodic motion, 527-528
- Normal distribution, 591-593
 cumulative distribution function values, 593
 standard normal variable, 592
- Normal fault (see Fault)
- Normal stress, 150
- Nyquist frequency, 73
- O**
- Operating basis earthquake, 115
- P**
- p-wave, 19, 154-156
- Paleoseismology, 107
- Pangaea, 23
- Passive earth pressure (see Retaining walls)
- Peak acceleration, 67-68, 88-91
- Peak displacement, 68
- Peak velocity, 68, 90
- Period of vibration, 530
- Periodic motion, 527-528
- Permeation grouting (see Soil improvement)
- Phase angle, 529, 531
- Phase transformation, 357-358
- Phase velocity, 165
- Piezoelectric bender element test, 219-220
- Plane wave, 156
- Plates
 boundary types
 spreading ridge, 29
 subduction zone, 30-31
 transform fault, 32
 major, 23, 26
 microplates, 23
 plate tectonics, 24-28
 platelets, 23
- Poisson model, 128-129, 134-135
- Pore pressure ratio, 362, 376, 388
- Power spectrum, 72, 542
- Predictive relationships, 86-100, 126-127
 acceleration spectrum intensity, 100
 and probabilistic seismic hazard analysis,
 126-127
 Arias intensity, 99-100
 bracketed duration, 95, 99
 Fourier spectrum ordinates, 92-93
 peak acceleration, 88-91
 peak velocity, 90
 predominant period, 91-92
 response spectrum ordinates, 94-98
 rms acceleration, 98-99
 velocity spectrum intensity, 100
 v_{\max}/a_{\max} , 94
- Predominant period, 76, 91-92
- Pressuremeter test, 214-215, 235
- Principal stresses, 187-188
 rotation of, 189-190
- Probabilistic seismic hazard analysis, 117-139
- Probability, 585-595
 axioms of, 584-585
 cumulative distribution function, 589
 multiplication rule, 586
 of events, 585-588
 probability density function, 588
 total probability theorem, 587-588
- Progressive failure, 432
- Pseudo-spectral acceleration, 572
- Pseudo-spectral velocity, 572
- Pseudostatic analysis, 434-437, 478-481
- Q**
- Quality factor, 92, 569
- Quiet zone, 528
- R**
- Radiation damping, 179-180, 266, 283-284,
 298-299
- Random variable, 588-589
 coefficient of variation, 590
 expected value, 589
 mean, 589

- Random variable (*cont.*)
 - standard deviation, 590
 - variance, 590
 - Rate effects, 234
 - Ray path, 101, 170-171
 - Rayleigh damping, 580
 - Rayleigh wave, 20, 156-161
 - displacement, 160-161
 - use in subsurface exploration, 203-205
 - velocity, 159-160
 - Recurrence laws, 117, 120-126
 - Gutenberg-Richter, 121-124
 - characteristic earthquake, 124-125
 - Reflection, 165, 170, 193-195
 - Refraction, 171, 195-202
 - Reinforced soil walls
 - external stability, 501-502
 - internal stability, 502
 - Remnant magnetism, 29-30
 - Reservoir-induced seismicity, 42
 - Residual shear strength (see Liquefaction)
 - Resonance
 - of soil deposit, 257-260
 - of structure, 555
 - spurious, 279
 - Resonance, 555
 - Resonant column test, 216-219
 - Response spectrum, 73-75, 94-98, 571-572
 - Response spectrum analysis, 581-582
 - Response spectrum intensity, 83
 - Retaining walls, 11-12, 466-502
 - active earth pressure, 470-476
 - dynamic response, 477
 - failures, 11-12, 467-469
 - interface friction angles, 472-473
 - passive earth pressure, 470-476
 - seismic design considerations, 494-502
 - anchored bulkheads, 496-498
 - braced walls, 495-500
 - gravity walls, 494-495
 - reinforced soil walls, 500-502
 - tieback walls, 498-499
 - seismic displacements, 489-493
 - Richards-Elms method, 489-492
 - Whitman-Liao method, 492-493
 - seismic pressures, 477-489
 - effects of water, 486-489
 - Mononobe-Okabe method, 478-481
 - nonyielding walls, 484-486
 - Steedman-Zeng method, 482-484
 - static pressures, 469-477
 - types, 467
 - Reverse fault (see Fault)
 - Richards-Elms method (see Retaining walls)
 - Richter magnitude (see Magnitude)
 - Ridge push, 28
 - RMS acceleration, 82, 98-99
 - Rock outcropping motion, 255
 - Rossi-Forel intensity (see Intensity)
- S**
- s-wave, 19, 154-156
 - Safe shutdown earthquake, 115
 - Sample space, 583
 - Sampling, 215-216
 - Sand boil, 8, 401-403
 - Saturation (see Magnitude)
 - Scaling (see Time history development)
 - Scattering, 174
 - Seiche, 13
 - Seismic cone test, 208
 - Seismic gap, 40-41
 - Seismic hazard analysis, 106-139
 - deterministic, 114-117
 - probabilistic, 117-139
 - deaggregation, 135, 137
 - seismic hazard curve, 129-134
 - Seismic moment, 42
 - Seismic reflection test, 193-195
 - Seismic refraction test, 195-202
 - direct wave, 196
 - head wave, 196
 - Seismic safety evaluation earthquake, 115
 - Seismicity
 - characteristic earthquake, 125-125
 - Gutenberg-Richter recurrence law, 121-124
 - historical, 113-114

- Seismicity (*cont.*)
 - instrumental, 114
- Seismogram, 56
- Seismograph, 56
- Seismology, 18
- Seismometer, 58
- Seismoscope, 59
- Settlement (see Liquefaction)
- SH-wave, 20, 170-174
- Shaking table test, 225-226
- Shape factor, 77-78
- Shear beam analysis
 - linear inelastic shear beam, 290-291
 - three-dimensional, 293
 - two-dimensional, 286-291
- Shear modulus
 - and s-wave velocity, 147, 155
 - degradation of, 238-239
 - maximum, 232-234
 - modulus reduction curve, 232, 234-238
 - variation with shear strain, 234-238
- Shear strain, 150
- Shear stress, 150
- Similitude, 227
- Simple harmonic motion, 527-533
- Single degree of freedom systems, 544-575
 - equation of motion, 545-547
 - response of linear SDOF systems, 547-575
 - damped forced vibrations, 557-561
 - damped free vibrations, 551-553
 - undamped forced vibrations, 554-557
 - undamped free vibrations, 548-550
 - response of nonlinear SDOF systems, 572-575
- Slab pull, 28
- Slip-predictable model, 129
- Slope stability
 - inertial instability, 433-450
 - Makdisi-Seed analysis, 447-449
 - Newmark sliding block analysis, 438-442
 - pseudostatic analysis, 434-437
 - stress-deformation analyses, 449-450
 - landslides, 9-11, 424-428
 - static, 430-433
 - weakening instability, 450-462
 - flow failure analysis, 451-453
 - deformation failure analysis, 453-462
- Soil improvement, 506-522
 - densification techniques
 - blasting, 512-513
 - compaction grouting, 513-514
 - dynamic compaction, 510-512
 - required extent of treatment, 514-515
 - vibro rod, 509-510
 - vibroflotation, 508-509
 - drainage techniques, 521-522
 - grouting and mixing techniques
 - intrusion grouting, 519
 - jet grouting, 520-521
 - permeation grouting, 518-519
 - soil mixing, 519-520
 - reinforcement techniques
 - compaction piles, 516
 - drilled inclusions, 516-517
 - stone columns, 515-516
 - verification of effectiveness, 522-524
- Soil mixing (see Soil improvement)
- Soil-structure interaction, 294-303
 - inertial interaction, 302-303
 - kinematic interaction, 300-303
- Source spectrum (see Brune spectrum)
- Source zone, 114, 118-120
- Source-site distance, 86, 118-120
- Spatial variability (see Coherency)
- Specific impedance, 167
- Spectral analysis of surface waves (SASW)
 - test, 203-205
- Spreading ridge (see Plates), 29
- Spurious resonance, 279
- Standard deviation (see Random variable)
- Standard normal variable, 592
- Standard penetration (SPT) test
 - correlation to G_{max} , 235
 - correlation to liquefaction resistance, 378-382
 - energy correction, 209
 - overburden correction, 209-210
- State parameter, 360

- Static liquefaction, 361-366
 - Steady state of deformation, 357-360
 - definition, 357-358
 - state parameter, 360
 - steady state line, 358-360
 - steady state shear strength, 410-411
 - Steady state vibration response, 558-559
 - Steady state vibration test, 203
 - Steedman-Zeng method (see Retaining walls)
 - Stone columns (see Soil improvement)
 - Strain energy, 36, 41-42
 - Strain-displacement relationships, 145, 150
 - Stress drop, 93
 - Stress path, 188-190
 - Stress reversal, 221-222
 - Stress-strain relationships, 145, 151-152
 - Strike-slip movement (see Fault)
 - Strong ground motion (see Ground motions)
 - Subduction zone (see Plates)
 - Surface wave magnitude (see Magnitude)
 - Surface wave, 19-20, 156-164
 - Suspension logging test, 202
 - Sustained maximum acceleration, 69-70
 - Sustained maximum velocity, 69-70
 - SV-wave, 19, 170-174
 - System compliance, 220
- T**
- Thrust fault, 34
 - Tieback walls, 498-499
 - Time-predictable model, 129
 - Threshold strain
 - volumetric, 230
 - linear, 230, 236
 - Time history development
 - frequency domain generation, 343
 - Green's function techniques, 343-345
 - scaling of actual ground motions, 340-341
 - time domain generation, 341-342
 - Topographic effects, 319-321, 323
 - Total probability theorem, 587-588
 - Transfer function, 256-275, 285, 562-564
 - argument, 563
 - modulus, 257, 563
 - Transform fault (see Plates)
 - Transient response, 558-559
 - Trigger model, 129
 - Tripartite plot, 533-534
 - Tsunami, 13
 - Tuning ratio, 57, 554
- U**
- Ultrasonic pulse test, 219
 - Uniform Building Code
 - design base shear, 330-332
 - design response spectrum, 334
 - importance factor, 330, 332
 - seismic zone factor, 330-331
 - soil coefficient, 330, 334
 - Uniform distribution, 590-591
 - Uniform risk spectrum, 327
 - Up-hole test, 207-208
- V**
- Variance (see Random variable)
 - Velocity
 - group, 165
 - Love wave, 163-164
 - p-wave, 145, 155
 - particle, 145
 - phase, 165
 - Rayleigh wave, 159-160
 - reversal, 197
 - s-wave, 147, 155
 - Velocity spectrum intensity, 83, 100
 - Venn diagram, 585
 - Vibro rod (see Soil improvement)
 - Vibroflotation (see Soil improvement)
 - Viscous damping, 175-178, 567-570
 - v_{\max}/a_{\max} , 78-79, 94
- W**
- Wave number, 148
 - Wave passage effect, 101

Wave propagation, 143-183
 body waves, 19, 154-156
 one-dimensional, 144-149, 165-170
 three-dimensional, 149-165, 170-174
 surface waves, 20, 156-164
 Rayleigh waves, 156-161
 Love waves, 162-164
Wavefront, 170-171

Wavelength, 148
Whitman-Liao method (see Retaining walls)
Wood-Anderson seismograph, 48, 57
Worldwide Standard Seismographic Network, 62

Y

Yield acceleration, 439, 442-445

GEOTECHNICAL EARTHQUAKE ENGINEERING

STEVEN L. KRAMER

In countless earthquakes, damage to buildings, bridges, and other structures has been strongly influenced by soil and rock conditions. For the first time, the basic principles, theories, and methods of geotechnical earthquake engineering have been compiled in a comprehensive textbook.

Written for graduate students and practicing geotechnical engineers, this book was designed to help readers understand the fundamental principles and practical methods of geotechnical earthquake engineering. The author begins with basic concepts of seismology, earthquakes, and strong ground motion and introduces procedures of deterministic and probabilistic seismic hazard analysis. Basic principles of wave propagation are used to develop procedures for ground response analysis and to provide insight into such important problems as local site effects, liquefaction, seismic slope stability, and seismic design of retaining structures. Concepts are fully developed and illustrated with examples. Each chapter includes a point-by-point summary of its most important concepts and principles.

Topics include:

- Seismology and Earthquakes
- Strong Ground Motion
- Seismic Hazard Analysis
- Wave Propagation
- Dynamic Soil Properties
- Ground Response Analysis
- Local Site Effects and Design Ground Motions
- Liquefaction
- Seismic Slope Stability
- Seismic Design of Retaining Structures
- Mitigation of Seismic Hazards

PRENTICE HALL
Upper Saddle River, NJ 07458

<http://www.prenhall.com>

ISBN 0-13-374943-6



9 780133 749434